Measurements of isolated-photon production inclusively and in association with jets at $\sqrt{s} = 13$ TeV with the ATLAS detector

Memoria de Tesis Doctoral realizada por

Ana Rosario Cueto Gómez

presentada ante el Departamento de Física Teórica
de la Universidad Autónoma de Madrid
para optar al Título de Doctor en Física Teórica

Tesis Doctoral dirigida por **Juan Terrón Cuadrado** y **Claudia Glasman Kuguel,**

Profesores titulares de la Universidad Autónoma de Madrid

Departamento de Física Teórica
Universidad Autónoma de Madrid



Madrid, Junio de 2018

Abstract

This document summarises most of my work during the years of my Ph.D. It covers ATLAS Standard Model measurements with a single photon in the final state, as well as the jet energy scale in situ measurements using γ+jet events and data quality inspection of the liquid argon calorimeter.

The production of prompt photons in proton–proton collisions, $pp \to \gamma + \mathrm{X}$, provides a testing ground for the theory of quantum chromodynamics (QCD) with a hard colourless probe not affected by hadronisation. A quantitative understanding of the features of photon production is not only relevant for precision Standard Model measurements but also important for Higgs production and searches for resonances predicted by models beyond the Standard Model.

Measurements of prompt-photon production at the Large Hadron Collider (LHC) provide a handle on the gluon density in the proton by means of the Compton scattering and can be used to constrain the gluon density function inside the proton. The constraining power of the measurements can be enhanced if they are combined with measurements at different centre-of-mass energies. The requirement of jets in the final state allows to probe the dynamics of the hard-scattering process by measuring the correlations between the photon and the jets. Measurements of the photon plus one jet cross section as a function of the scattering angle in the centre-of-mass frame are sensitive to the spin of the particle exchanged in the t-channel and thus provide insight on the dominant production mechanism. When two jets are required, the production mechanisms can be studied in detail by selecting different regions of the phase space in which their contributions are enhanced according to whether the photon is the object with highest or lowest transverse momentum among the three objects considered in the final state.

All the measurements presented here refer to isolated photons. Isolation was achieved by limiting the transverse energy allowed inside a cone of size $\Delta R = 0.4$ around the photon. Jets were reconstructed using the anti-k_t algorithm with jet radius $R = 0.4$.

The results of four different analyses at $\sqrt{s} = 13$ TeV are presented, namely the measurement of inclusive isolated-photon cross sections, the ratio of inclusive isolated-photon cross sections at $\sqrt{s} = 13$ and 8 TeV, the measurement of the cross section for isolated-photon plus jet production and the cross-section measurements for isolated-photon plus two jets production.

Leading order (LO) Monte Carlo predictions of Pythia and Sherpa, which include different treatments of the production mechanisms already at the matrix-element level, were compared to the measurements. In addition, comparisons with the next-to-leading order (NLO) fixed-order calculations of JetPhox corrected for non-perturbative effects and Sherpa NLO predictions, which include matrix elements of γ+1 and 2 jets computed at NLO and γ+3 and 4 jets computed at LO supplemented with parton shower, are provided. In general, agreement was found between the measurements and QCD predictions with different features in the predicted cross-section normalisation and shape that depend on the analysis.

Resumen

Este documento resume la mayor parte de mi trabajo como doctorando, el cual cubre medidas hechas del Modelo Estándar con el detector ATLAS con un fotón en el estado final así como medidas in situ de la escala de energía de los jets usando eventos con un fotón y un jet y la inspección de la calidad de los datos del calorímetro de argón líquido.

La producción de fotones provenientes de la interacción dura en colisiones protón–protón, $pp \to \gamma + \mathrm{X}$, proporciona un marco de pruebas para examinar la teoría de cromodinámica cuántica (QCD) con una partícula sin color que no está afectada por los efectos de la hadronización. Un entendimiento cuantitativo de las características de la producción de fotones no es solo relevante para medidas de precisión del Modelo Estándar, sino que también son de gran importancia en estudios de las desintegraciones del bosón de Higgs y búsquedas de resonancias predichas por modelos más allá del Modelo Estándar.

Las medidas de producción de fotones son sensibles a la densidad de gluones dentro del protón a través de la dispersión de Compton y pueden ser usadas para restringir la función de densidad de gluones dentro del protón. El poder de restricción de estas medidas se puede reforzar cuando son combinadas con medidas del mismo proceso a diferentes energías del centro de masas. La presencia de jets en el estado final permite sondear la dinámica de la dispersión dura por medio de las medidas de las correlaciones angulares entre el fotón y los jets. Si solo se requiere un jet en el estado final, las medidas de la sección eficaz en función del ángulo de dispersión en el centro de masa son sensibles al spin de la partícula intercambiada en el canal t proporcionando mayor conocimiento sobre el mecanismo de producción dominante. Cuando se requieren dos jets, los distintos mecanismos de producción se pueden estudiar en detalle seleccionando distintas regiones del espacio de fases en las cuales la contribución de uno de los mecanismos de producción se realza respecto al otro.

Todas las medidas que aquí se presentan se refieren a fotones aislados. El aislamiento se consiguió limitando la cantidad de energía transversa permitida en un cono de radio $\Delta R = 0.4$ alrededor del fotón. Los jets fueron reconstruidos usando el algoritmo anti-k_t con un radio del jet de $R = 0.4$.

Los resultados de cuatro análisis a una energía en el centro de masas ($\sqrt{s}$) de 13 TeV son descritos: las medidas de la sección eficaz inclusiva de producción de fotones aislados, el cociente de las secciones eficaces de producción de fotones aislados a $\sqrt{s} = 13$ y 8 TeV, las medidas de la sección eficaz de producción de un fotón aislado acompañado de un jet y las medidas de la sección eficaz de producción de un fotón aislado acompañado de dos jets.

Las medidas han sido comparadas con las predicciones de los generadores Monte Carlo de primer orden (LO) Pythia y Sherpa que incluyen un tratamiento diferente para los distintos mecanismos de producción en los elementos de matriz. Además, se proporciona la comparación con los datos de las predicciones de QCD al siguiente orden (NLO) de JetPhox a nivel partónico corregidas por efectos no perturbativos y de las predicciones de Sherpa NLO que incluyen elementos de matriz calculados a NLO para procesos de γ+1 y 2 jets y a LO para procesos de γ+3 y 4 jets complementados con cascada de partones. En general, se ha observado un acuerdo adecuado entre las medidas y las predicciones de QCD con diferentes características en la normalización y forma de la sección eficaz que dependen de cada medida individual.

Contents

1 Introduction **1**

2 Experimental setup **7**
2.1 The LHC accelerator . . . 7
2.2 The ATLAS detector . . . 9
2.3 Data quality assessment of the LAr calorimeter . . . 17

3 The theoretical framework **23**
3.1 The Standard Model . . . 23
3.2 Concepts of Quantum Chromodynamics . . . 24
3.3 Jets . . . 33
3.4 Theory of prompt-photon production . . . 34
3.5 Monte Carlo event generators . . . 39
3.6 Fixed-order pQCD predictions with JetPhox . . . 47

4 Photon reconstruction, identification and calibration **48**
4.1 Photon reconstruction . . . 48
4.2 Photon calibration . . . 50
4.3 Photon identification . . . 56
4.4 Photon isolation . . . 60

5 Jet reconstruction and calibration **62**
5.1 In situ calibration with γ+jet events . . . 67

6 Measurement of inclusive isolated-photon cross sections **77**
6.1 Data selection . . . 77
6.2 Trigger efficiency . . . 80
6.3 Background estimation and subtraction . . . 88
6.4 Control plots . . . 97
6.5 Unfolding . . . 99
6.6 Systematic uncertainties . . . 112
6.7 Next-to-leading-order QCD calculations . . . 138
6.8 Results . . . 148
6.9 Further research using the published cross-section measurements . . . 153

7 Ratio of inclusive isolated-photon cross sections at $\sqrt{s} = 13$ and 8 TeV **158**
7.1 Analysis strategy . . . 158
7.2 Experimental systematic uncertainties . . . 159
7.3 Next-to-leading-order QCD predictions . . . 180
7.4 Theoretical predictions for $D_{13/8}^{\gamma/Z}$ . . . 193

7.5 Results . . . 204

8 Measurement of the cross section for isolated-photon plus jet production 212
8.1 Data selection . . . 212
8.2 Background estimation and subtraction . . . 224
8.3 Control Plots . . . 237
8.4 Unfolding . . . 239
8.5 Systematic uncertainties . . . 263
8.6 Next-to-leading-order QCD calculations . . . 291
8.7 Results . . . 307

9 Cross-section measurements for isolated-photon production plus two jets 312
9.1 Data selection . . . 312
9.2 Background estimation and subtraction . . . 320
9.3 Control plots . . . 335
9.4 Unfolding . . . 339
9.5 Systematic uncertainties . . . 359
9.6 Results . . . 411

10 Summary and conclusions 425

A Cross check for converted photon fraction 431

B Event displays 436

C Sources of photon energy scale systematic uncertainties 439

D Additional cleaning requirement on jets 441

E Correlation between the jet and photon energy scale 444

F Tables of results 449
F.1 Tables for the inclusive photon analysis . . . 449
F.2 Tables for the photon plus jet analysis . . . 454
F.3 Tables for the ratio of cross sections for inclusive-photon production . . . 460

G NLO calculations for $pp \to \gamma$ + jet + jet + X 461

Bibliography 476

1 Introduction

The Large Hadron Collider (LHC) was foreseen as an ideal machine for exploring physics in the TeV scale. One of the main goals of the LHC program was the discovery of the Higgs boson. In 2012, the ATLAS and CMS collaborations announced the observation of a new particle with properties compatible with the Higgs boson as predicted by the Standard Model (SM) [1, 2]. After this major breakthrough, the LHC potential has been exploited in different areas such as the characterisation of the new particle, the search for physics beyond the SM or precision measurements of the SM parameters. All of them are connected to the interactions of quarks and gluons at large momentum transfers of the colliding particles. An optimal exploitation of the LHC is thus unimaginable without a solid understanding of the underlying theory, quantum chromodynamics (QCD), and its implementation in accurate Monte Carlo programs.

The production of prompt photons in proton–proton collisions, $pp \to \gamma + \mathrm{X}$, provides a testing ground for perturbative QCD (pQCD) with a hard colourless probe, insensitive to the effects of hadronisation. By definition, prompt photons are those not secondaries to hadron decays. At the LHC, two processes contribute to prompt-photon production: the direct process, in which the photon originates directly from the hard interaction, and the fragmentation process, in which the photon is emitted in the fragmentation of a high transverse momentum (p_{T}) parton [3–6] (also referred to as the bremsstrahlung contribution).

Since the dominant production mechanism in pp collisions at the LHC proceeds via the $qg \to q\gamma$ process, measurements of prompt-photon production are sensitive at leading order (LO) to the gluon density in the proton [7–10]. The gluon parton density function (PDF) is constrained in the current global PDF fits indirectly by scaling violations in deep-inelastic scattering (DIS) and momentum sum rules and constrained directly mostly by inclusive jet-production (measurements of the Z boson p_{T} and $t\bar{t}$ production are also considered by some groups). Prompt-photon production can provide new observables with independent information to constrain the gluon PDF and help to improve the accuracy of its determination and associated uncertainties. The improvement in the determination of the gluon PDF is of special interest for the prediction of Higgs cross sections via the gluon–gluon production channel. Although prompt-photon data were initially included in the determination of the proton PDFs, their use was abandoned some years ago. Since then, theoretical developments [9, 10] have shown ways to improve the description of the data in terms of pQCD, and recent studies quantified the impact of prompt-photon data from hadron colliders on the gluon density in the proton [11] at next-to-next-to-leading order (NNLO), demonstrating a good agreement of prompt-photon data with global PDF fits and a moderate reduction of the gluon PDF uncertainties. New measurements of prompt-

photon production at higher centre-of-mass energies are expected to constrain further the gluon density in the proton when combined with previous data. These measurements can also be used to tune the Monte Carlo (MC) models to improve the understanding of prompt-photon production. In addition, precise measurements of these processes aid those searches for which they are an important background, such as the search for new phenomena in final states with a photon and missing transverse momentum.

Measurements of inclusive prompt-photon production were used recently to investigate novel approaches to the description of parton radiation [12] and the importance of resummation of threshold logarithms in QCD and of the electroweak corrections [13]. The recent NNLO pQCD calculations [14] allow a more stringent test of pQCD. To make such a test with small experimental and theoretical uncertainties, it is optimal to perform measurements of prompt-photon production at high photon transverse energies and at the highest possible centre-of-mass energies of the colliding particles.

Comparisons of measurements of prompt-photon production with pQCD are usually limited by the theoretical uncertainties associated to the missing higher-order terms in the perturbative expansion. This was the case in the inclusive isolated-photon cross sections performed by ATLAS at 8 TeV [15]. The uncertainties on the next-to-leading order (NLO) pQCD predictions are larger than those of experimental nature, preventing a more precise test of the theory. A stringent test of the theory can be achieved either by the inclusion of the NNLO QCD corrections in the calculations [14] or by making measurements of the ratio of cross sections for inclusive isolated-photon production at different centre-of-mass energies and confront them with the predictions as suggested in Reference [16]. A significant reduction of the experimental systematic and theoretical uncertainties is expected in this ratio due to the presence of correlations between measurements, allowing a more accurate comparison between data and theory. It is then of paramount importance to account properly for the correlations in the uncertainties affecting the measurements and the predictions.

The production of prompt photons in association with jets can be used to probe the dynamics of the hard-scattering process through the measurements of angular correlations between the photon and the jets. The production of isolated photons in association with jets in pp collisions at $\sqrt{s} = 7$ and 8 TeV was studied by ATLAS [17–19] and CMS [20–22]. The increase in the centre-of-mass energy of pp collisions at the LHC to 13 TeV allows the exploration of the dynamics of photon+jet production in a new energy regime with the goal of extending the test of pQCD predictions to higher energy transfers. In addition, the description of parton-shower generators, such as Sherpa and Pythia, can be validated by means of these measurements; this is useful for searches for physics beyond the Standard Model involving photons, such as the search for new phenomena in final states with a photon and a jet [23, 24], in which the same generators are used for the estimation of the SM background.

The photon plus one jet measurements are useful to test t–channel quark exchange [18]. The dynamics of the underlying processes in $2 \to 2$ hard-collinear scattering can be investigated using the variable $\theta^\star$, where $\cos\theta^\star \equiv \tanh(\Delta y/2)$ and Δy is the difference in rapidity between the two final-state particles. The variable $\theta^\star$ coincides with the scattering polar angle in the centre-of-mass frame for collinear scattering of massless particles, and its distribution is sensitive to the spin, s, of the exchanged particle. The differential cross sections behave as $(1 - |\cos\theta^\star|)^{-2s}$ when $|\cos\theta^\star| \to 1$. The direct-photon contribution is dominated by the t-channel quark exchange and expected to exhibit a $(1 - |\cos\theta^\star|)^{-1}$

dependence in the limit $|\cos\theta^\star| \to 1$, whereas that of fragmentation processes is predicted to be the same as in di-jet production, $(1 - |\cos\theta^\star|)^{-2}$. For both processes, there are also s-channel contributions which are, however, non-singular when $|\cos\theta^\star| \to 1$. As a result, a measurement of the cross section for prompt-photon plus jet production as a function of $|\cos\theta^\star|$ provides a handle on the relative contributions of the direct and fragmentation components as well as the possibility to test the dominance of the t-channel quark exchange.

The photon plus two-jets final state provides direct access to the fragmentation production process. The rate of photon radiation is small compared to the gluon radiation, however, the dijet-production cross section is sufficiently large that bremsstrahlung production is expected to be of the order of the direct production. The interplay between the direct and bremsstrahlung underlying mechanisms can be studied in different phase-space regions, distinguished according to whether the photon is the object with the highest or the lowest p_{T} in the event [25].

This document is organised as follows. Chapter 2 presents an overview of the LHC and the ATLAS detector. During the time of my Ph.D., I had the opportunity to contribute to the offline data quality assessment of the Liquid Argon (LAr) calorimeter [26], where the data are validated before being used for physics analyses. The main purpose of the task is to quickly identify issues that would affect the ATLAS detector performance. The assessment procedure is described in Section 2.3. Chapter 3 covers the most relevant aspects of the theory underlying the measurements presented in this dissertation. In Chapter 4, the procedure followed in ATLAS to reconstruct, identify and calibrate photons is presented, as well as the procedure to estimate the photon isolation transverse energy. Chapter 5 summarises the jet reconstruction and calibration techniques. I contributed to the jet in situ calibration using photon plus jet events. The good resolution of photons in the electromagnetic calorimeter is used to measure the jet energy scale in events in which a single jet recoils against a photon. This is described in Section 5.1. The following chapters are dedicated to cross section measurements performed during my Ph.D. Prompt-photon production was measured inclusively or in association with jets in the four measurements presented in this dissertation. Chapter 6 presents the measurement of isolated inclusive-photon production performed with the ATLAS detector at $\sqrt{s} =$ 13 TeV. This measurement has been published in the journal Physics Letter B [27] and overviewed in the proceedings published in Il Nuovo Cimento C journal [28]. Details of the measurement of the cross-section ratios at $\sqrt{s} = 8$ and 13 TeV can be found in Chapter 7. This analysis is under ATLAS review process and the details of the analysis can be found as an ATLAS Internal Note [29]. Chapter 8 presents the measurement of isolated-photon production in association with one jet, which has been published in the journal Physics Letter B [30]. All these $\sqrt{s} = 13$ TeV measurements were performed with the data recorded by the ATLAS detector in 2015. The last measurement described here, which can be found in Chapter 9, was performed with a larger dataset collected in 2015 and 2016 and consists of the cross-section measurement of photon plus two jets production. This analysis is also under ATLAS internal review [31].

Introducción en español

El gran colisionador de hadrones (LHC) fue previsto como una máquina ideal para explorar la física a la escala de los TeV. Uno de los principales propósitos del programa del LHC era el descubrimiento del bosón de Higgs. En 2012 las colaboraciones ATLAS y CMS anunciaron la observación de una nueva partícula con propiedades compatibles con las del bosón de Higgs que predice el Modelo Estándar (SM) [1, 2]. Tras este gran logro, el potencial del LHC ha sido explotado en diferentes áreas tales como la caracterización de la nueva partícula, la búsqueda de física más allá del SM o medidas de precisión de los parámetros del SM. Todas ellas están conectadas a la interacción de quarks y gluones en las que se transfiere una gran cantidad de momento entre lass partículas que colisionan. Una explotación óptima de las capacidades del LHC sería, por tanto, inimaginable sin un entendimiento sólido de la teoría que subyace a estas interacciones, la cromodinámica cuántica (QCD), y su implementación en programas de Monte Carlo precisos.

La producción de fotones provenientes de la interacción dura entre partones en las colisiones protón–protón, $pp \to \gamma + \mathrm{X}$, proporciona un banco de pruebas de pQCD con una partícula insensible a los efectos de hadronización. En el LHC, dos tipos de procesos contribuyen a la producción de fotones: la producción directa, en la que el fotón se origina directamente en la interacción dura, y la producción por fragmentación, en la que el fotón es emitido en la fragmentación de un partón de momento transverso (p_{T}) alto [3–6] a la que también nos referiremos como radiación de frenado.

Dado que el mecanismo de producción dominante en las colisiones pp en el LHC proviene del proceso $qg \to q\gamma$, las medidas de la producción de fotones son sensibles a la densidad de gluones en el protón a primer orden (LO) [7–10]. La función de densidad de partones (PDF) del gluón se constriñe indirectamente en los ajustes globales a través de las violaciones de escala en dispersión inelástica profunda (DIS) y la regla de la suma de momentos y directamente principalmente por la producción de jets, aunque algunos grupos también consideran medidas del p_T del bosón Z y de producción de parejas del quark top. La producción de fotones puede proveer nuevos observables con información independiente sobre la PDF del gluón y ayudar a mejorar la precisión de su determinación y sus incertidumbres asociadas. La mejora en la determinación de la PDF tiene especial interés en la predicción de la sección eficaz de producción del bosón de Higgs en el canal de fusión de gluones. Las medidas de fotones fueron inicialmente incluidas en la determinación de las PDFs, sin embargo, su uso se abandonó hace unos años. Desde entonces, el desarrollo teórico [9, 10] ha demostrado maneras de mejorar la descripción de los datos en términos de pQCD, y un estudio reciente ha cuantificado el impacto de estos datos en colisionadores de hadrones para la densidad de gluones en el protón [11] a tercer orden (NNLO), demostrando un buen acuerdo de los datos de fotones en los ajustes de las PDFs y una reducción moderada de las incertidumbres de la PDF del gluón. Se espera que nuevas medidas de producción de fotones a una energía en el centro de masas aún más elevada ayuden a constreñir más la PDF del gluón al ser combinadas con datos previos. Estas medidas también pueden ser útiles para ajustar los modelos de MC y mejorar el entendimiento de la producción de fotones. Además, medidas precisas de estos procesos ayudan a aquellas búsquedas en las que éstas representan un ruido de fondo importante, tales como la búsqueda de nuevos fenómenos en estados finales con un fotón y energía transversa faltante.

Medidas de la producción inclusiva de fotones han sido usadas recientemente para investigar nuevas estrategias en la descripción de la radiación de partones [12] y la impor-

tancia de la resumación de logaritmos umbrales en QCD y de las correcciones electrodébiles [13]. Los nuevos cálculos a NNLO [14] permiten un test mas preciso de pQCD. Para realizar estos tests con incertidumbres experimentales y teóricas pequeñas, es óptimo realizar las medidas de producción inclusiva de fotones a energías transversas altas del fotón a la energía de centro de masas de las partículas colisionantes lo más alta posible.

La comparación de las predicciones de QCD con las medidas de la producción de fotones suele estar limitada por las incertidumbres teóricas asociadas a los órdenes ausentes en la expansión perturbativa. Este ha sido el caso en las medidas de secciones eficaces hechas en ATLAS a 8 TeV [15]. Las incertidumbres en las predicciones de pQCD a NLO son más grandes que aquellas de naturaleza experimental, impidiendo un test más preciso de la teoría. Un test más estricto se puede realizar o bien con la inclusión de las correcciones a NNLO de QCD en los cálculos [14] o realizando medidas del cociente de secciones eficaces a diferentes energías en el centro de masas y comparándolas con las teoría [16]. En dicho cociente, se espera una reducción significativa de las incertidumbres teóricas y experimentales debido a la presencia de correlaciones entre las medidas, permitiendo una comparación más detallada y precisa entre los datos y la teoría. Por tanto, es de vital importancia tratar adecuadamente las correlaciones que afectan a la medida y a las predicciones.

La producción de fotones acompañados de jets se puede usar para testear la dinámica del proceso de interacción dura a través de las medida de las correlaciones angulares entre el fotón y los jets. La producción de fotones aislados acompañados de jets en colisiones pp a $\sqrt{s} = 7$ y 8 TeV ha sido estudiada por las colaboraciones ATLAS [17–19] y CMS [20–22]. El incremento de la energía en el centro de masas en las colisiones pp en el LHC a 13 TeV permiten explorar la dinámica de la producción de fotón+jet en un nuevo régimen de energía con el objetivo de extender el test de las predicciones de pQCD a transferencias de energías transversas más altas. Por otro lado, la descripción de los generadores con cascada de partones como Sherpa y Pythia, puede ser validada usando estas medidas. Estas predicciones son útiles para búsquedas de física más allá del SM con fotones, como la búsqueda de nuevos fenómenos en estados finales con un fotón y un jet [23, 24], en las que los mismos generadores se usan para estimar la radiación de fondo del SM.

Las medidas de un fotón acompañado de un jet son útiles para examinar el canal t en el que se intercambia un quark [18]. La dinámica del proceso subyacente en la dispersión $2 \to 2$ colineal dura se puede investigar con la variable $\theta^\star$, donde $\cos\theta^\star \equiv \tanh(\Delta y/2)$ y Δy es la diferencia en rapidez entre las dos partículas del estado final. La variables $\theta^\star$ coincide con el ángulo polar de la dispersión en el sistema de referencia del centro de masas para dispersiones colineales de partículas no masivas, y su distribución es sensible al spin s de la partícula intercambiada. La sección eficaz diferencial se comporta como $(1 - |\cos\theta^\star|)^{-2s}$ cuando $|\cos\theta^\star| \to 1$. La contribución de fotones directos está dominada por el intercambio de quarks en el canal t y se espera que exhiba una dependencia de $(1 - |\cos\theta^\star|)^{-1}$ en el límite $|\cos\theta^\star| \to 1$, mientras que para fotones de fragmentación se espera que la dependencia sea la misma que en la producción de di-jets, $(1 - |\cos\theta^\star|)^{-2}$. Para ambos procesos, también hay contribuciones del canal s que no son singulares cuando $|\cos\theta^\star| \to 1$. Como resultado, la medida de la sección eficaz de producción de fotón más jet en función de $|\cos\theta^\star|$ da información sobre las contribuciones relativas de fotones directos y de fragmentación y proporciona la posibilidad de testear la dominancia del intercambio de quarks en el canal t.

El estado final de fotón más dos jets proporciona acceso directo al proceso de

producción por radiación de frenado. La proporción de radiación de fotones es pequeña comparada con la de radiación de gluones, sin embargo, la sección eficaz de producción de di-jets es lo suficientemente alta como para que la producción de fotones por fragmentación sea del orden de la producción de fotones directos. La relación entre los mecanismos subyacentes de producción de fotones directos y de fragmentación se puede estudiar en diferentes espacios de fase, que pueden distinguirse de acuerdo a si el fotón es el objeto con mayor o menor p_{T} del evento [25].

Este documento se organiza de la siguiente manera. El Capítulo 2 presenta un resumen del LHC y del detector ATLAS. Durante mi doctorado, tuve la oportunidad de contribuir a la inspección de la calidad de los datos recogidos por el calorímetro de argón líquido [26], donde los datos se validan antes de que sean usados por los análisis de física. El propósito de esta tarea es identificar rápidamente cualquier problema que pueda afectar al rendimiento del detector. El procedimiento de examen de los datos se describe en la Sección 2.3. El Capítulo 3 cubre los aspectos más importantes de la teoría subyacente a las medidas presentadas en esta tesis. En el Capítulo 4 se presenta el procemiento seguido en ATLAS para reconstruir, identificar y calibrar fotones, así como el procedimiento para estimar la energía transversa de aislamiento del fotón. El Capítulo 5 resume las técnicas usadas para la reconstrucción y calibración de jets. También pude contribuir a la calibración in situ de la escala de energía de los jets usando eventos de fotón más jet. La buena resolución de los fotones en el calorímetro electromagnético se usa para medir la escala de energía de los jets en eventos en los que un jet recula frente a un fotón. Ésto está descrito en la Sección 5.1. Los siguientes capítulos están dedicados a medidas de secciones eficaces realizadas durante mi doctorado. La producción de fotones ha sido medida de manera inclusiva o acompañados de jets en los cuatro análisis presentados en esta tesis. En el Capítulo 6 se presentan las medidas de la producción inclusiva de fotones hechas con el detector ATLAS a $\sqrt{s} = 13$ TeV. Esta medida ha sido publicada en la revista Physics Letter B [27] y resumida en actas publicadas en la revista Il Nuovo Cimento C [28]. Los detalles de la medida del cociente de las secciones eficaces a $\sqrt{s} = 8$ y 13 TeV se encuentran en el Capítulo 7. Este análisis está bajo el proceso interno de revisión de ATLAS y los detalles se pueden encontrar en la Nota Interna de ATLAS [29]. En el Capítulo 8 se describe la medida de producción de fotones aislados acompañados de un jet que ha sido publicado en la revista Physics Letter B [30]. Todas estas medidas a $\sqrt{s} = 13$ TeV se hicieron usando los datos recogidos por el detector ATLAS durante 2015. La última medida descrita en esta tesis, que se puede encontrar en el Capítulo 9, fue hecha con un conjunto de datos mayor correspondiente a los datos recogidos en 2015 y 2016 y consiste en la medida de fotones aislados acompañados de dos jets. Este análisis también está bajo revisión interna de ATLAS [31].

2
Experimental setup

In this section, the most relevant aspects of the LHC [32] and the ATLAS (A Toroidal LHC ApparatuS) [33] detector are described. An overview of the trigger system is also given at the end of the section.

2.1 The LHC accelerator

The LHC, located at the European Organization for Nuclear Research (CERN) site, is a super-conducting accelerator and collider installed in a 26.7 km long circular tunnel buried 100 m underground. The tunnel was constructed between 1984 and 1989 for the CERN LEP (Large Electron-Positron collider) machine [34]. The LHC was always foreseen as the natural long-range extension of the CERN facilities beyond LEP and considered an ideal machine for exploring physics at the TeV scale.

Inside the LHC, two beams of protons travel in opposite directions in separated beam pipes around the accelerator ring guided by a strong magnetic field maintained by super-conducting magnets. Unlike electron-positron accelerators, hadrons can be accelerated to higher energies than electrons since they are heavier and so less synchrotron radiation is produced. Protons collide at a nominal center-of-mass energy of 13 TeV since 2015 at four different locations along the accelerator ring. These locations correspond to the position of the four detectors: ALICE (A Large Ion Collider Experiment) [35], ATLAS, CMS (Compact Muon Solenoid) [36] and LHCb (Large Hadron Collider beauty) [37]. Three other smaller experiments, with very specific purposes, are situated near the larger detectors: TOTEM (TOTal Elastic and diffractive cross-section Measurements) [38], LHCf (LHC forward experiment) [39] and MoEDAL (Monopole and Exotic Detector At the LHC) [40].

The LHC ring is the final step of an accelerating chain. The starting step is a simple bottle of hydrogen. After stripping the hydrogen atoms of their electrons with an electric field, the remaining protons circulate successively through a series of accelerators to increase their speed. The linear accelerator Linac 2 is the first accelerator of the chain. It accelerates protons to 50 MeV, then the beam is injected into the Proton Synchrotron Booster (PSB), which increases the energy of the protons up to 1.4 GeV. It is followed by the Proton Synchrotron (PS), which pushes the beam to an energy of 25 GeV. Before getting into the LHC, the protons are accelerated to an energy of 450 GeV in the Super Proton Synchrotron (SPS). Figure 2.1 shows the layout of this accelerator chain.

The first particle beams circulated in the LHC on September 10th, 2008. Nine days later, an electrical fault induced a mechanical damage that was sorted out one year later.

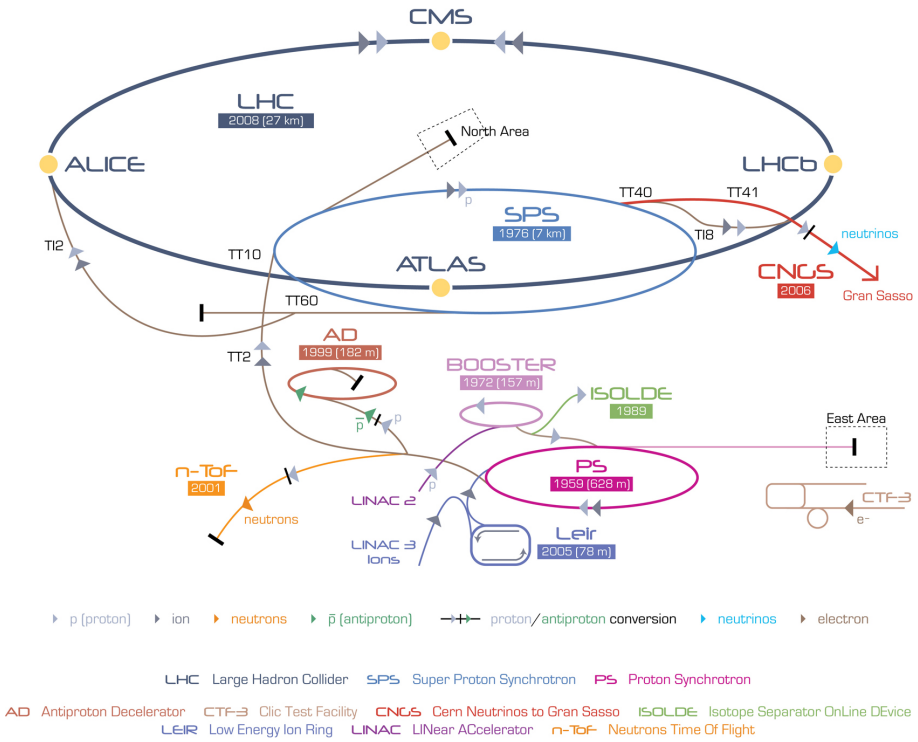


Figure 2.1: Layout of the CERN accelerator complex. From [41]

On December 2009, the LHC ended its first full period of operation with collisions at 2.36 TeV, setting a new world record. After a short technical stop, the first collisions at 7 TeV arrived on March 2010 and in April 2012 the centre-of-mass energy was increased up to 8 TeV. This successful Run-1 period, in which the Higgs boson was discovered [1], ended in 2013 and the first shutdown begun. The accelerator and detectors were improved to increase the centre-of-mass energy and the luminosity. A new era of the LHC (Run-2) started on June 2015, with recorded collisions at 13 TeV; all the results presented in this thesis make use of data recorded during the 2015 or 2015+2016 data taking periods of Run-2.

The main achievements of the LHC do not only lie on beating world records on centre-of-mass energy at the collision points, but also on the luminosity provided to the experiments. The luminosity is a measurement of the number of collisions per area and time. It relates the total number of events and the cross section of the process studied, σ, as:

$$N = \mathcal{L} \cdot \sigma, \tag{2.1}$$

where the instantaneous luminosity $\mathcal{L}$ can be expressed, for a Gaussian beam distribution, as:

$$\mathcal{L} = \frac{N_b^2 n_b f_{rev} \gamma_r F}{4\pi \epsilon_n \beta^*}, \tag{2.2}$$

where N_b is the number of particles per bunch, n_b is the number of bunches per beam, f_{rev} is the revolution frequency, γ_r is the relativistic gamma factor, ϵ_n is the normalized transverse beam emittance, β^* is the beta function at the interaction point (IP) and F, the geometric luminosity reduction factor due to the crossing angle at the IP. Typical values of these parameters are: $N_b \sim 1 \times 1^{11}$, $f_{rev} \sim 11$ kHz, $\beta^* \sim 0.55$ m and $F \sim 0.85$. These

operating parameters have been optimised to be able to provide a high luminosity. The size of the beams is reduced when they meet at the centre of the experiments, leading to a lower emittance and higher luminosity. The peak instantaneous luminosity has surpassed the initial expectations defined by the original designs for the LHC, 1×10^{34} cm^{-2}s^{-1}. The integrated luminosity

$$L = \int \mathcal{L} \mathrm{d}t \tag{2.3}$$

is a measurement of the collected data size. Figure 2.2 shows a comparison of the integrated luminosity of the LHC for proton-proton collisions during the last years. In 2016, it has surpassed the expectations and doubled that achieved in 2012.

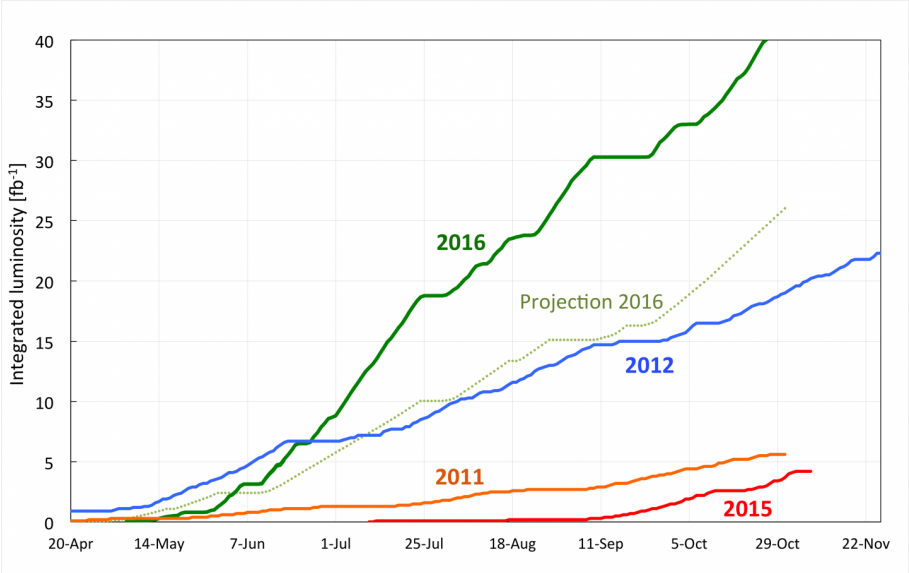


Figure 2.2: Expected and provided integrated luminosity for LHC in 2016. The integrated luminosity of previous years is also presented for comparison. © 1998-2018 CERN

2.2 The ATLAS detector

The ATLAS experiment is a general-purpose detector for the LHC, whose design was guided by the need to accommodate a wide spectrum of possible physics signatures. The major goal of the ATLAS experiment is the exploration of the TeV mass scale where ground-breaking discoveries are expected, and the search for the Higgs boson, discovered in 2012, as well as the search for physics beyond the Standard Model.

High luminosity, with an inelastic proton-proton cross section of 80 mb at $\sqrt{s} =$ 13 TeV [42], presents a serious experimental difficulty as it implies that every candidate event for new physics will on average be accompanied by ∼20 inelastic events per bunch-crossing (separated only by 25 ns) for the designed instantaneous luminosity. Identifying final states of rare processes imposes further demands on the luminosity needed, and on the identification capabilities of the detector.

To achieve these physics goals, a set of general requirements for an LHC detector should be fulfilled:

- due to the experimental conditions at the LHC, the detector requires fast, radiation-hard electronics and sensor elements. Also, high detector granularity is needed to handle the particle fluxes and to reduce the influence of overlapping events;
- large pseudorapidity (η) acceptance with almost full azimuthal angle (ϕ) coverage;
- good charged-particle momentum resolution and reconstruction efficiency in the inner-tracker. Secondary vertex observation is also required for offline τ-leptons and b-jets tagging;
- very good electromagnetic (EM) calorimetry for electron and photon identification and measurements, complemented by full-coverage hadronic calorimetry for accurate jet and missing transverse energy ($E_{\mathrm{T}}^{\mathrm{miss}}$) measurements;
- good muon identification and momentum resolution over a wide range of momenta and ability to determine unambiguously the charge of high p_T muons;
- triggering on low transverse momentum objects is important to maintain high kinematic efficiency with sufficient background rejection to realise an acceptable trigger rate for most physics processes of interest.

The overall ATLAS detector layout is shown in Figure 2.3 and its main performance goals are listed in Table 2.1. The ATLAS detector has a forward-backward symmetry with respect to the IP. A thin superconducting solenoid surrounds the inner-detector (ID) cavity, and three large superconducting toroids (one in the barrel and two in the end-caps) are arranged with an eight-fold azimuthal symmetry around the electronic and hadronic calorimeters.

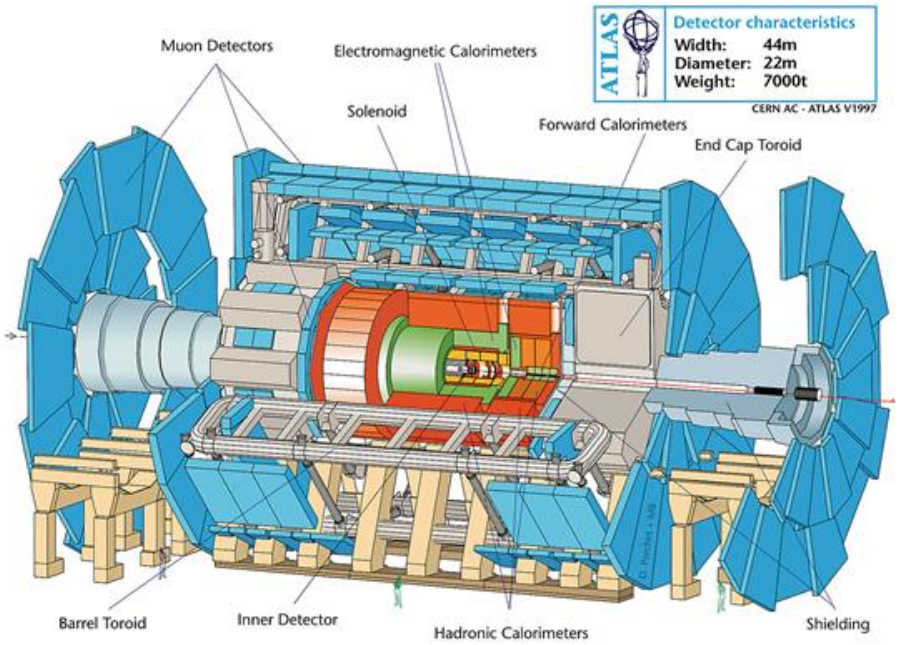


Figure 2.3: Computer generated image of the ATLAS detector. © 1998-2018 CERN

A common coordinate system is used throughout ATLAS. The origin of the coordinate system is defined by the interaction point and the z-axis runs along the beam line. The

Detector component	**Required resolution**	**η coverage**
Tracking	$\sigma_{p_T}/p_T = 0.05\% \oplus 1\%$	± 2.5
EM calorimetry	$\sigma_E/E = 10\%/\sqrt{E} \oplus 0.7\%$	± 3.2
Hadronic calorimeters (jets)		
barrel and end-cap	$\sigma_E/E = 50\%/\sqrt{E} \oplus 3\%$	± 3.2
forward	$\sigma_E/E = 100\%/\sqrt{E} \oplus 10\%$	$3.1 < \lvert\eta\rvert < 4.9$
Muon spectrometer	$\sigma_{p_T}/p_T = 10\%$ at $p_T = 1$ TeV	± 2.7

Table 2.1: General performance goals of the ATLAS detector. The units for E and p_T are in GeV.

x–y plane is perpendicular to the beam line and referred to as the transverse plane. The positive x-axis points from the IP to the centre of the LHC ring; the positive y-axis points upward to the surface of the earth. The positive (negative) z-values are referred to as the "A-side" ("C-side"). Cylindrical coordinates, r and ϕ, are also used. The azimuthal angle ϕ is measured from the x-axis around the beam while the radial dimension, r, measures the distance from the beam line. The polar angle θ is defined as the angle from the positive z-axis; it is often reported in terms of the pseudorapidity, defined as $\eta = -\ln\tan(\theta/2)$. The angular distance is measured in units of $\Delta R \equiv \sqrt{(\Delta\eta)^2 + (\Delta\phi)^2}$. The rapidity is defined as $y = 0.5 \ln\left[(E + p_z)/(E - p_z)\right]$, where E is the energy and p_z is the z-component of the momentum. The transverse energy is defined as $E_{\mathrm{T}} = E \sin\theta$.

2.2.1 Tracking

The ID, immersed in a 2 T solenoidal field, was designed to provide hermetic and robust pattern recognition, excellent momentum resolution and both primary- and secondary-vertex measurements for charged tracks above a given p_T threshold. High-resolution semiconductor pixel and silicon microstrip (SCT) detectors in the inner part used in conjunction with straw tubes from a Transition Radiation Tracker (TRT) offer these features.

The precision tracking detectors (pixels and SCT) cover the region $|\eta| < 2.5$. In the barrel region, they are arranged on concentric cylinders around the beam axis while in the end-cap regions they are located on disks perpendicular to the beam axis. The highest granularity is achieved around the vertex region using silicon pixel detectors. The pixel layers are segmented in $R \times \phi$ and z with a pixel size of 50×400 μm^2 and typically three pixel layers are crossed by each track. For the SCT, eight strip layers are crossed by each track. In the barrel region, this detector uses small-angle (40 mrad) stereo strips to measure both coordinates with one set of strips in each layer parallel to the beam direction, measuring $R - \phi$. In the end-cap region, the detectors have a set of strips running radially and a set of stereo strips at an angle of 40 mrad.

During the first long shutdown phase in 2013 and 2014, a fourth pixel layer (insertable b-layer or IBL [43]) was added to the pixel detector between the new and smaller beam pipe and the previous innermost pixel layer at 3.2 cm from the IP. The benefits of the introduction of this new layer include: increased tracking robustness against failure of pixel modules, higher tagging efficiency of secondary vertices of hadrons with a bottom quark (b-tagging) and better vertexing performance and tracking precision due to the closer location to the interaction point.

The TRT is located at large radii. A large number of hits (typically 36 per track) is provided by the 4 mm diameter straw tubes of the TRT, which enables track-following up to $|\eta|$=2.0, with much less material per point than silicon. The TRT only provides $R \times \phi$ information with an intrinsic accuracy of 130 μm. In the barrel region, the straws are parallel to the beam axis and are 144 cm long, divided into two lengths. In the end-cap region, the 37 cm long straws are arranged radially on wheels.

The combination of precision trackers at small radii with TRTs at larger radii gives very robust pattern recognition and high precision in both ϕ and z coordinates. The straw hits at the outer radius contribute significantly to the momentum measurement since the lower precision per point compared to the silicon is compensated by the large number of measurements and longer measured track length.

2.2.2 Calorimetry

The ATLAS calorimeters are sampling calorimeters that measure the energy that a particle losses as it passes through the detector. They interleave layers of a passive medium of high-density material, that produces a shower of particles that evolves quickly in a limited space, with layers of active medium, a scintillator material in which it is possible to sample the shape of the resulting shower.

Calorimeters cover the range $|\eta| < 4.9$, using different techniques suited to the widely varying requirements of the desired physics processes and radiation environment over this large η-range. Over the η region matched to the ID, the fine granularity of the EM calorimeter is ideally suited for precision measurements of electrons and photons. The coarser granularity of the rest of the calorimeter is sufficient to satisfy the two main physics requirements: the reconstruction of jets (i.e. clusters of particles) which appear as energy clusters in the calorimeter emerging from the collision point, and measurement of $E_{\mathrm{T}}^{\mathrm{miss}}$, which is a strong signal that one or more undetectable neutral particles were produced in the collision. Within the region $|\eta| < 3.2$, electromagnetic calorimetry is provided by the barrel and end-cap high-granularity LAr electromagnetic calorimeters, within an additional thin LAr presampler covering $|\eta| < 1.8$; for $|\eta| < 2.5$ the LAr calorimeters are divided into three layers in depth. Hadronic calorimetry is provided by a steel/scintillator-tile calorimeter, segmented into three barrel structures within $|\eta| < 1.7$, and two copper/LAr hadronic end-cap calorimeters, which cover the region $1.5 < |\eta| < 3.2$.

LAr electromagnetic calorimeter

The EM calorimeter is divided into a barrel part ($|\eta| < 1.475$) and two end-caps ($1.375 < |\eta| < 3.2$). Eight out of the 16 modules of the end-cap EM calorimeter were assembled at UAM [1]. One module consists of 96 (32) layers for the outer (inner) wheel stacked on top of each other. The position of the central solenoid in front of the EM calorimeter demands optimisation of the material to achieve the desired calorimeter performance. The barrel calorimeter consists of two identical half barrels, separated by a small gap (4 mm) at $z = 0$. Each end-cap calorimeter is mechanically divided into two coaxial wheels: an outer wheel covering the region $1.375 < |\eta| < 2.5$, and an inner wheel covering the region $2.5 < |\eta| < 3.2$. The EM calorimeter is a lead-LAr detector with accordion-shaped kapton electrodes and lead absorber plates over its full coverage. The accordion geometry provides

[1] Universidad Autónoma de Madrid.

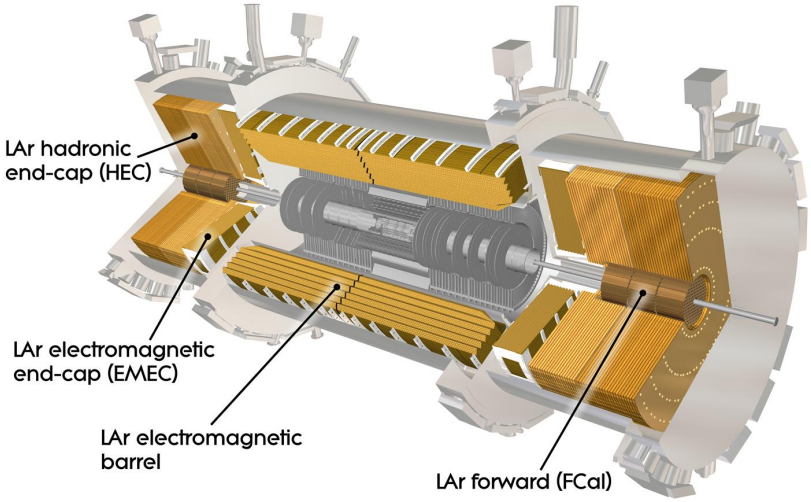


Figure 2.4: Cut-away view of the ATLAS liquid argon calorimeter system [33].

complete ϕ symmetry without azimuthal cracks. The lead thickness in the absorber plates has been optimised as a function of η in terms of EM calorimeter performance in energy resolution.

The EM calorimeter is composed of three sampling layers for $|\eta| < 2.5$. The first layer has a thickness of about 4.4 radiation lengths (X_0). In the ranges $|\eta| < 1.4$ and $1.5 < |\eta| < 2.4$, the first layer is segmented into high-granularity strips in the η direction, with a cell size of 0.0003×0.0982 in the $\eta - \phi$ plane. For $1.4 < |\eta| < 1.5$ and $2.4 < |\eta| < 2.5$, the η-segmentation of the first layer is coarser. The fine granularity in η of the strips is sufficient to provide discrimination between single photon showers and two overlapping showers coming from the decays of neutral hadrons. The second layer has a thickness of about 17 X_0 and a granularity of 0.025×0.0245 in the $\eta - \phi$ plane. It collects most of the energy deposited in the calorimeter by photon and electron showers. The third layer has a granularity of 0.05×0.0245 in $\eta - \phi$ and a depth of about 2 X_0. It is used to correct for leakage beyond the EM calorimeter of high-energy showers. A thin presampler in front of the accordion calorimeter covers the interval $|\eta| < 1.8$ and is used to correct for energy loss upstream of the calorimeter. The presampler consists of an active LAr layer with a thickness of 1.1 cm (0.5 cm) in the barrel (end-cap) and has a granularity of 0.025×0.0982 in the $\eta - \phi$ plane. The LAr calorimeter system is displayed in Figure 2.4 and its main parameters are summarised in Table 2.2.

The tile calorimeter

The tile calorimeter is placed directly outside the EM calorimeter envelope. This sampling calorimeter makes use of steel-plates as the absorber and scintillating tiles as the active material. The region $|\eta| < 1$ is covered by the barrel section and two additional extended barrels cover the range $0.8 < |\eta| < 1.7$. The barrel and extended barrels are divided

azimuthally into 64 modules. It is segmented in depth in three layers of approximately 1.5, 4.1 and 1.8 interaction lengths [2] (λ) for the barrel and 1.5, 2.6 and 3.3 λ in the extended barrels.

The hadronic LAr end-cap calorimeter

The hadronic end-cap calorimeter (HEC) consists of two independent wheels per end-cap located just behind the electromagnetic end-cap calorimeter. Liquid Argon is used as the active material and, instead of lead, copper is used as the absorbent material. The HEC extends out to $|\eta| < 3.2$ to avoid material density drop at the transition between the end-cap and the forward calorimeter, overlapping with the forward calorimeter (around $|\eta| < 3.1$). Similarly, the HEC η also overlaps with the tile calorimeter by extending up to $\eta = 1.5$.

The forward calorimeter

The forward calorimeters (FCal) are located in the same cryostat as the end-cap calorimeters and cover the region $3.1 < |\eta| < 4.9$. The close vicinity and coupling between these systems minimise energy losses in cracks between the calorimeter systems and also limits the background which reaches the muon system. The FCal is approximately 10 λ deep, and consists of three modules in each end-cap: the first, made of copper, is optimised for electromagnetic measurements, while the other two, made of tungsten, measure predominantly the energy of hadronic interactions. Each module consists of a metal matrix, with regularly spaced longitudinal channels filled with the electrode structure consisting of concentric rods and tubes parallel to the beam axis.

2.2.3 The Muon spectrometer

The muon spectrometer is located at the outer part of the ATLAS detector. Its main goals are to detect charged particles that exit the barrel and end-cap calorimeters and to measure their momentum in the pseudorapidity range $|\eta| < 2.7$. It has an excellent resolution at large transverse momentum.

It includes three large superconducting air-core toroids, precision tracking chambers for accurate momentum resolution, and an effective trigger system based on chambers with fast response. The conceptual layout of the muon spectrometer is shown in Figure 2.5.

In the range $|\eta| < 1.4$, magnetic bending is provided by the large toroid. For $1.6 < |\eta| < 2.7$, muon tracks are bent by two smaller end-cap magnets inserted into both ends of the barrel toroid. In the range $1.4 < |\eta| < 1.6$, the transition region, magnetic deflection is provided by a combination of barrel and end-cap fields.

In the barrel region, tracks are measured in chambers arranged in three cylindrical layers around the beam axis. In the transition and end-cap regions, the chambers are

[2] In a hadronic shower, the interaction length is defined as the distance that the shower has to cross inside a specific material to reduce the number of particles by a factor $1/e$,

$$N(x) = N_0 \exp(-x/\lambda),$$

where $N(x)$ is the number of particles after distance x, and N_0 is the initial number of particles.

EM calorimeter	Barrel (EMB)	End-cap (EMEC)	
Coverage	$\|\eta\| < 1.475$	$1.375 < \|\eta\| < 3.2$	
Longitudinal segmentation	3 samplings	3 samplings	$1.5 < \|\eta\| < 2.5$
		2 samplings	$1.375 < \|\eta\| < 1.5$
		2 samplings	$2.5 < \|\eta\| < 3.2$
Granularity ($\Delta\eta \times \Delta\phi$)			
Sampling 1	0.003×0.1 ($\|\eta\| < 1.4$)	0.05×0.1	$1.375 < \|\eta\| < 1.425$
	0.025×0.025 ($1.4 < \|\eta\| < 1.475$)	0.025×0.1	$1.425 < \|\eta\| < 1.5$
		0.003×0.1	$1.5 < \|\eta\| < 1.8$
		0.004×0.1	$1.8 < \|\eta\| < 2.0$
		0.006×0.1	$2.0 < \|\eta\| < 2.4$
		0.025×0.1	$2.4 < \|\eta\| < 2.5$
		0.1×0.1	$2.5 < \|\eta\| < 3.2$
Sampling 2	0.025×0.025 ($\|\eta\| < 1.4$)	0.05×0.025	$1.375 < \|\eta\| < 1.425$
	0.075×0.025 ($1.4 < \|\eta\| < 1.475$)	0.025×0.025	$1.425 < \|\eta\| < 2.5$
		0.1×0.1	$2.5 < \|\eta\| < 3.2$
Sampling 3	0.05×0.025	0.05×0.025	$1.5 < \|\eta\| < 2.5$
Presampler	Barrel	End-cap	
Coverage	$\|\eta\| < 1.52$	$1.5 < \|\eta\| < 1.8$	
Longitudinal segmentation	1 sampling	1 sampling	
Granularity ($\Delta\eta \times \Delta\phi$)	0.025×0.1	0.025×0.1	
Hadronic Tile	Barrel	End-cap	
Coverage	$\|\eta\| < 1.0$	$0.8 < \|\eta\| < 1.7$	
Longitudinal segmentation	3 samplings	3 samplings	
Granularity ($\Delta\eta \times \Delta\phi$)			
Samplings 1 and 2	0.1×0.1	0.1×0.1	
Sampling 3	0.2×0.1	0.2×0.1	
Hadronic LAr		End-cap	
Coverage		$1.5 < \|\eta\| < 3.2$	
Longitudinal segmentation		4 samplings	
Granularity ($\Delta\eta \times \Delta\phi$)		0.1×0.1	$1.5 < \|\eta\| < 2.5$
		0.2×0.2	$2.5 < \|\eta\| < 3.2$
Forward calorimeter		Forward	
Coverage		$3.1 < \|\eta\| < 4.9$	
Longitudinal segmentation		3 samplings	
Granularity ($\Delta\eta \times \Delta\phi$ (cm))		FCal1: 3.0×2.6	$3.15 < \|\eta\| < 4.30$
		FCal1: $\sim$ four times finer	$3.10 < \|\eta\| < 3.15$
			$4.30 < \|\eta\| < 4.83$
		FCal2: 3.3×4.2	$3.24 < \|\eta\| < 4.50$
		FCal2: $\sim$ four times finer	$3.20 < \|\eta\| < 3.24$
			$4.50 < \|\eta\| < 4.81$
		FCal3: 5.4×4.7	$3.32 < \|\eta\| < 4.60$
		FCal3: $\sim$ four times finer	$3.29 < \|\eta\| < 3.32$
			$4.60 < \|\eta\| < 4.75$

Table 2.2: Main parameters of the calorimetry system. The numbers for the granularity have been rounded.

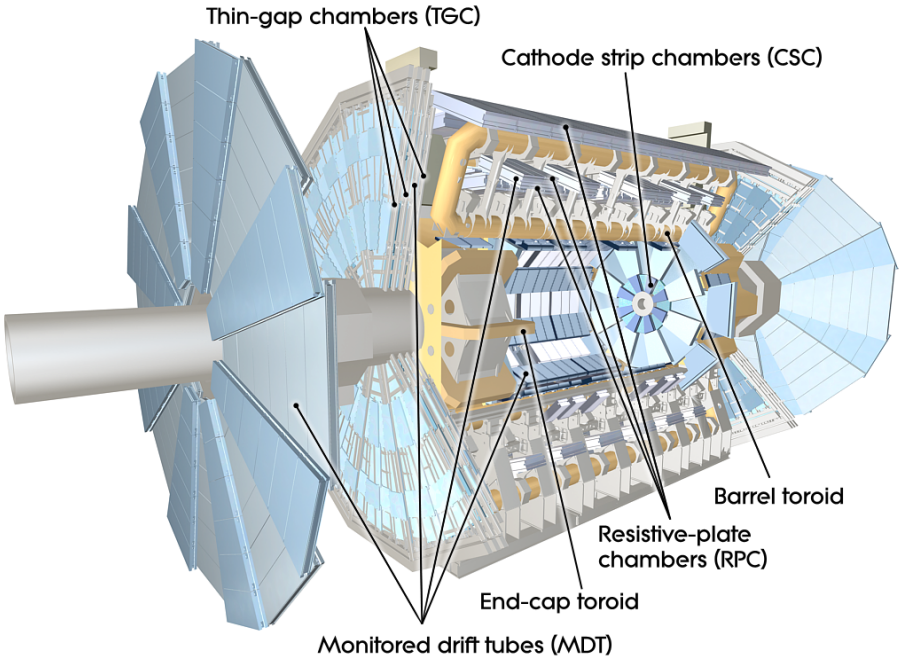


Figure 2.5: Cut-away view of the ATLAS muon spectrometer instrumentation [33].

installed in planes perpendicular to the beam, also in three layers. The main parameters of the muon chambers are listed in Table 2.3.

2.2.4 Forward detectors

The forward region of the ATLAS detector is covered by three smaller detector systems [44]. The first system (ordered according to their distance to the interaction point) is a Cherenkov detector called LUCID (LUminosity measurement using Cherenkov Integrating Detector) [45]. It is placed at ± 17 m from the interaction point and detects inelastic pp scattering in the forward direction determining the on-line relative-luminosity delivered to

Monitored drift tubes	**MDT**
- Coverage	$\lvert\eta\rvert < 2.7$ (innermost layer: $\lvert\eta\rvert < 2.0$)
- Function	Precision tracking
Cathode strip chambers	**CSC**
- Coverage	$2.0 < \lvert\eta\rvert < 2.7$
- Function	Precision tracking
Resistive plate chambers	**RPC**
- Coverage	$\lvert\eta\rvert < 1.05$
- Function	Triggering, second coordinate
Thin gap chambers	**TGC**
- Coverage	$1.05 < \lvert\eta\rvert < 2.7$ (2.4 for triggering)
- Function	Triggering, second coordinate

Table 2.3: Main parameters of the muon spectrometer.

ATLAS.

The beam-pipe is divided into two separate pipes at ±140 m, where the second detector, the Zero-Degree Calorimeter (ZDC) [46] is situated and is used to determine the centrality of heavy-ion collisions.

At ± 240 m lies the third detector, ALFA (Absolute Luminosity For ATLAS) [47]; it consists of scintillating fibre trackers located inside Roman pots which are designed to approach as close as 1 mm to the beam.

2.2.5 Trigger and data-acquisition system

The main challenges of the trigger system at the LHC are to select the rare and interesting events with high efficiency while rejecting the overwhelming background processes. Decisions must be taken for every bunch crossing, happening with a frequency of 40 MHz (every 25 ns). Each of them contains around 20 pp interactions. At the end of the trigger decision chain, the event storage rate is limited to approximately 1kHz.

The trigger system, upgraded for Run-2 [48], consists of a hardware-based first level trigger (level-1) and a software-based high-level trigger (HLT). The level-1 trigger searches for high transverse-momentum muons, electrons, photons, jets, τ-leptons decaying into hadrons, and missing and total transverse energy. It makes use of custom electronics to determine Regions-of-Interest (RoIs), i.e the coordinates in η and ϕ, of those regions within the detector where its selection process has identified interesting features. It requires about 2.5 μs to reach its decision, including the propagation delays on cables between the detector and the underground counting room where the trigger logic is housed. At the end of the level-1 trigger, the event rate is reduced to approximately 100 kHz.

The level-1 trigger decision uses calorimeter information to build a RoI consisting of 4×4 trigger towers with granularity 0.1×0.1 in the $\eta - \phi$ plane. A η-dependent p_{T} requirement is applied to account for energy losses and the geometry of the detector. A sliding-window algorithm identifies local energy maxima using four overlapping towers within a 2×2 central region for EM energy reconstruction. The EM and hadronic isolation rings are formed from the 12 towers surrounding the central cluster in the EM and hadronic layers, respectively. These rings are used to discriminate against hadronic activity. The hadronic core energy behind the EM cluster provides additional hadronic rejection.

The HLT is seeded by the RoIs information formed at level-1. Sophisticated selection algorithms are run using full granularity detector information in either the RoI or the whole event. The output rate is reduced by the HLT to 1kHz on average within a processing time of about 200 ms.

At the HLT, the full detector granularity is used within the RoI for the final trigger decision. The calorimeter reconstruction of photons and electrons is typically less expensive in terms of computing than that of based on tracks. Therefore, the calorimeter reconstruction precedes the track reconstruction to reject events early. Additional details about photon triggers are found in Section 6.1.1.

2.3 Data quality assessment of the LAr calorimeter

The main purpose of the LAr calorimeter is the measurement of electron and photon kinematic properties. It also provides important input for measuring jets and missing

transverse energy. A data monitoring procedure [49] was designed to quickly identify issues that could affect the detector performance and ensure that no bad-quality data are used in physics analyses. The monitoring infrastructure is common to online (during data-taking periods) and offline (after data-taking periods for data reprocessing) environments with an increasing refinement in the analysis of the data from online to offline. In the online analysis, only problems that are unrepairable are treated.

After trigger decision, the ATLAS data are organised in *streams* which can be divided into two categories: calibration and physics streams. The calibration streams are designed to provide detailed information about the run conditions (pile-up, luminosity, electronic noise, etc.) and are also used to monitor all detector components while physics streams are devoted to physics analysis. Four main calibration streams are considered in the LAr calorimeter data quality assessment as follows.

- the *Express stream* contains a small fraction of the data representative of the most common trigger chains used during collision runs;
- the *CosmicCalo stream* contains events triggered in empty bunch groups, where no collisions are expected;
- the *LArCells stream* contains partially-built collision events, where only a fraction of the LAr data is stored. The reduced event size allows looser trigger conditions and more events recorded in the data sample;
- the *LArCellsEmpty stream* also makes use of "partial event building", but the trigger is restricted to empty bunches.

The calibration streams containing collision events (Express and LArCells) are used to identify data corruption issues, timing misalignments and large coherent noise while those filled during empty bunches (CosmicCalo and LArCellsEmpty) are used to identify isolated noisy cells.

The information contained in the calibration streams are needed to reconstruct physics data and thus are promptly processed shortly after the beginning of the run. The first quality assessment is completed within the 48 hours following the end of the run, before the start of the physics stream reconstruction. The 48-hour period for the primary quality check is called *calibration loop*. The conditions database is updated, if needed, during the calibration loop.

After the end of the calibration loop, the processing of all the physics streams (the *bulk*) is launched. Once the complete dataset is available the final data-quality assessment is performed to check if the problems first observed during the calibration loop were properly fixed by the conditions updates. Any imperfection found in the bulk is collected in the database, but is not taken into account until the next data processing.

2.3.1 Data quality logging

Data losses are documented by assigning a *defect* [50] to a luminosity block. These defects can affect the whole calorimeter or be limited to one partition of the calorimeter. A defect can be either *intolerable*, implying a systematic rejection of the affected luminosity block, or *tolerable* and mainly set for bookkeeping while the data are still suitable for physics analyses.

The smallest time granularity available to reject a sequence of data is a luminosity block, which lasts approximately one minute. However, problems affecting the calorimeter may last less than one minute. Therefore, a complementary method that allows event-by-event data rejection is used to reduce data losses. To avoid bias in the luminosity computation, small time periods are rejected rather than isolated events in this *time-window veto* procedure.

The main sources of defects are briefly discussed in the next sections.

2.3.2 High-voltage conditions

The high voltage (HV) is distributed among 3250 sectors and is applied for charge collection in the active liquid argon gaps of the calorimeter. The HV conditions impact the amount of signal collected by the electrodes and, therefore, are crucial input for the energy computation.

The most common issue encountered is a trip of one HV line (a sudden voltage drop due to a current spike). The HV line can be ramped up automatically although this process may fail. During the calibration loop reconstruction, a correction factor is automatically applied based on the HV reading. A variation of HV conditions also requires an update of the expected noise per cell. During a trip, the HV, and therefore the energy scale, vary too quickly to be accurately assessed. In addition, the luminosity block in which the trip happened is usually affected by a large burst of coherent noise (see Section 2.3.6). The luminosity blocks in which a HV drop occurred are marked with a tolerable defect after a careful study of the noise behaviour.

2.3.3 Calorimeter coverage

The LAr calorimeter provides full hermeticity in azimuth and longitudinal coverage up to $|\eta| < 4.9$. However, when hardware failures occur (they are very rare), this coverage may be degraded. The inefficiencies can be caused, for example, by a faulty HV sector. The degraded coverage might significantly affect the physics performance and the corresponding data are systematically rejected by marking them with an intolerable defect.

2.3.4 Data integrity

The more than 180000 calorimeter channels are read out by 1524 front-end-boards (FEBS) that shape the signal and send the digitised samples via optical links. The FEB outputs are the basic detector information building block. Checks are performed to look for any error word sent by the different chips of each FEB or inconsistency of data (bunch crossing identification (BCID), event identifier, etc.). The information provided by each channel is expected to be uniform, but is not propagated individually to the data-acquisition system. A software algorithm performs additional checks which require: presence of all data blocks, unchanged data block length from the FEBs to the central data acquisition system and uniform data type and number of digitised samples. A FEB integrity error indicates a fatal and irrecoverable data corruption. To ensure a readout coverage as uniform as possible, any event containing a corrupted block is discarded. This event rejection is performed online by applying a time-window veto.

Due to hardware or software failures, the database information about the instantaneous luminosity may be missing. Under these conditions, the reconstruction of the LAr calorimeter energy is not optimal and data are rejected by assigning an intolerable defect associated with the luminosity detectors.

2.3.5 Global timing

The global timing is extracted by averaging (energy weighted) the mean signal peak time of each individual cell to optimise the phase of the clock delivered to each FEB. Only minor incidents have been related to FEBs desynchronisation with negligible impact on data quality.

2.3.6 Large-scale coherent noise

With increased luminosity, large burst of coherent noise (mainly located in the end-caps) affect the LAr with a larger occurrence rate.

The coherent noise is estimated by considering the variable $Y_{3\sigma}$ in each calorimeter partition, which is defined as the fraction of channels with a signal greater than three times the Gaussian electronic noise[3]. Assuming a perfect and uncorrelated Gaussian noise behaviour, the variable $Y_{3\sigma}$ peaks around 0.13%. Tails above 1% are characteristic of large coherent noise.

In collision streams, the $Y_{3\sigma}$ variable is positively biased by the presence of energy deposits due to collisions and cannot be used to identify coherent noise. The discrimination of noise bursts is based on the quality factor [51] of the channels, which quantifies whether the pulses matched the expectations or they may be mismeasured. A veto is imposed if more than five FEBs containing more than 30 channels with quality factor greater than 4000 is found (*Standard flag*).

Most of the noise bursts consist of a peak of *hard* events surrounded by peripheral *soft* events: the hard events are characterised by a large $Y_{3\sigma}$ and are properly identified by the Standard flag, whereas the soft ones are characterised by $Y_{3\sigma}$ around 2–3% and are not identified by the Standard flag. A time-window veto is applied around the well-identified hard events. The $Y_{3\sigma}$ variable is improved after the application of this time-window veto.

2.3.7 Per-channel noise

Individual channel behaviour is constantly monitored during collision runs. It relies on data streams with empty bunches (CosmicCalo and LArCellsEmpty streams), where no energy deposit is expected. The Gaussian noise is checked by looking at distributions of the mean energy and noise per cell as well as the fraction of cells with energy above 3σ (where σ is the measured electronic noise). If pathologies are found, the team responsible for the calibration is informed and they request a new calibration procedure. The Gaussian noise is usually very stable.

Non-Gaussian noise behaviours are also identified. Some of the characteristics observed are:

- the noise is not constant over time;

[3]The electronic noise is measured in calibration runs, using a simple clock-generated trigger.

- the measured signal can reach up to 100 GeV in a single cell;
- the noise does not always affect the same cells from one run to another;
- lowering the HV settings in the affected sector reduces the noise amplitude;
- no coherent behaviour is observed between the affected channels.

This phenomenon has a typical time scale much longer than the noise burst mentioned above, making the treatment with a time-window veto impractical. Instead, the affected channels are masked and the cell energy is estimated from the eight neighbouring cells in the same layer. The list of affected channels is extracted in each run and updated in the corresponding database during the calibration loop. When too many contiguous cells are noisy, this method may produce an ineffective detection area in the calorimeter and there is no other solution than rejecting the whole dataset affected. The masking efficiency is double-checked on the same data streams after bulk processing. If the masking procedure fails, the noisy luminosity blocks are excluded from the express processing. Still, the database is updated to include additional noisy channels so that the masking can be applied during any future data reprocessing to recover the lost luminosity.

The data rejection due to intolerable defects (time-window veto or luminosity block rejection) as a function of the data taking period[4] is shown in Figure 2.6 (Figure 2.7) for the whole 2017 data-taking period in which the luminosity recorded under LAr "ready" conditions was 43.6 fb^{-1}.

[4] A period corresponds to a data set acquired under similar operating conditions.

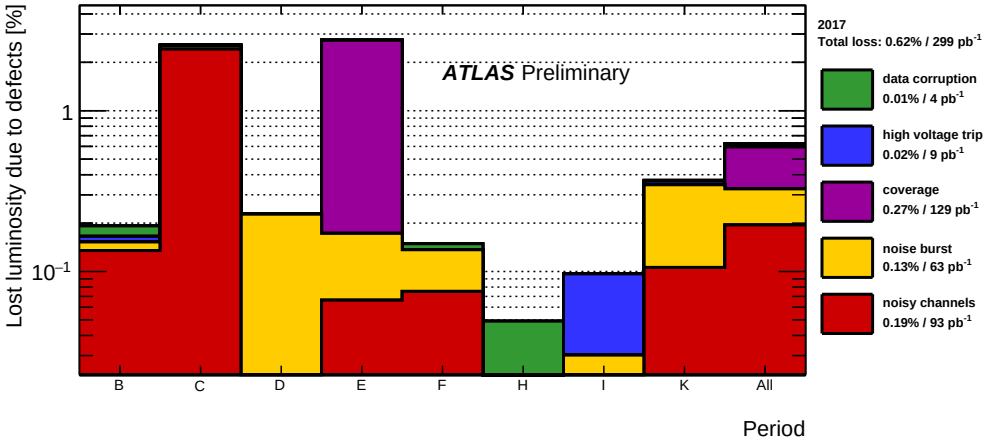


Figure 2.6: Data rejection due to defects set in the LAr data quality assessment during the 2017 data-taking periods.

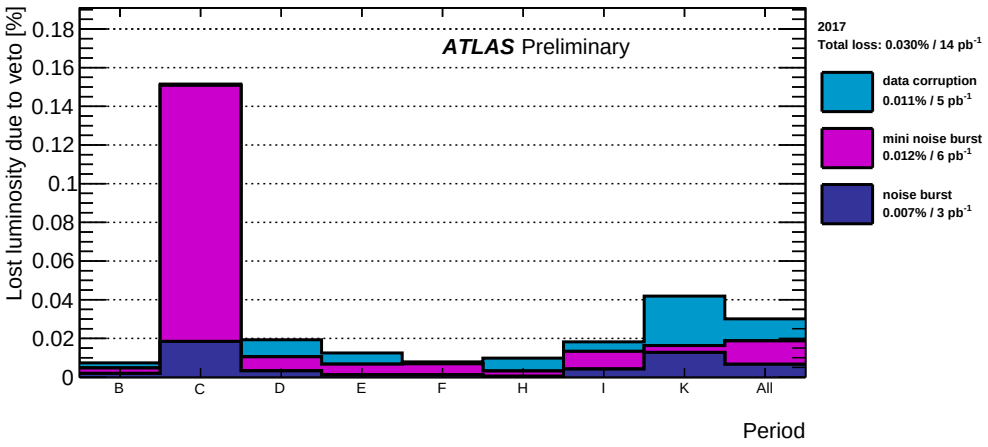


Figure 2.7: Data rejection due to time vetoes set in the LAr data quality assessment during the 2017 data-taking periods. "Mini noise burst" refers to noise bursts affecting only a region of the calorimeter.

3

The theoretical framework

The most relevant theoretical aspects underlying the work presented in this dissertation are reviewed in this chapter.

3.1 The Standard Model

The Standard Model (SM) [52–54] of particle physics is the theory that describes the interactions between the elementary particles that constitute matter and radiation. It was developed in the early 1970s and, so far, has successfully explained almost all experimental results and its predictions have been tested with high precision in a wide variety of phenomena.

The SM unifies three forces of nature: the weak, electromagnetic and strong forces. These fundamental forces are the result of the exchange of force-carrier particles (bosons). The strong force is carried by gluons, the electromagnetic force is carried by photons and the massive W and Z bosons are responsible for the weak force. The fundamental forces have different ranges and strengths. The electromagnetic force has infinite range while the weak and strong forces act only at a subatomic level.

All matter particles participate in the weak interaction, but only quarks feel the strong force. Both quark and charged leptons interact via the electromagnetic force. Neutrinos are matter particles that only interact via the weak force. A schema of the particle content of the Standard Model is shown in Figure 3.1.

In a mathematical framework, interactions are governed by local gauge symmetries. The symmetry group of the Standard Model is

$$SU(3)_c \times SU(2)_L \times U(1)_Y. \tag{3.1}$$

It has 12 generators (8+3+1) with a nontrivial commutator algebra. There are 8 gluons associated with the $\mathrm{SU}(3)_c$ color generators that describe the strong interaction and four gauge bosons W^+, W^-, Z^0 and γ associated with the electroweak $SU(2)_Y \times U(1)$ sector (unifying the electromagnetic and weak forces). The SM lagrangian can be then separated into two terms; the first one describing the electroweak interactions and the second one describing the strong interaction or better known as quantum chromodynamics:

$$\mathcal{L}_{SM} = \mathcal{L}_{EW} + \mathcal{L}_{QCD}. \tag{3.2}$$

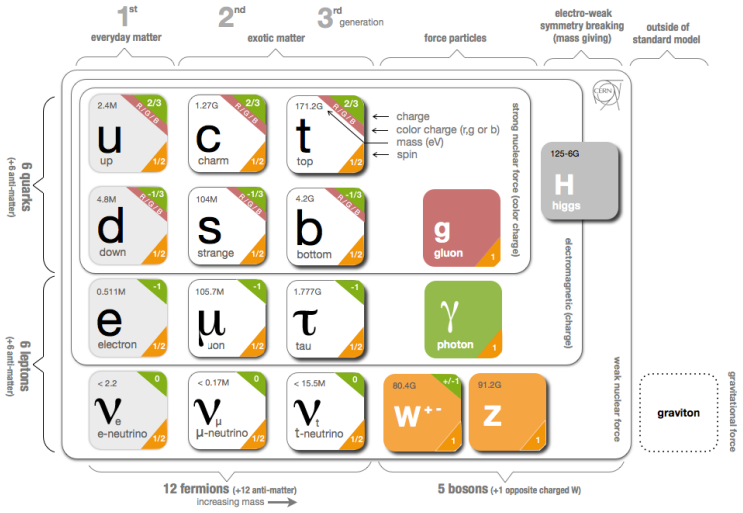


Figure 3.1: Particle content of the SM

3.2 Concepts of Quantum Chromodynamics

QCD [55, 56] is the theory that describes the strong interactions. It is a local non-abelian gauge theory formulated in terms of elementary fields: quarks, antiquarks and gluons. $SU(3)_c$ is the gauge group with gluons as gauge bosons and c stands for the color quantum number, which makes reference to the three different states of quarks. The QCD Lagrangian contains quark-gluon interactions as well as gluon self-interactions, a novel feature compared to quantum electrodynamics (QED) due to the non-abelian character of QCD.

Local gauge symmetry is achieved by the introduction of the covariant derivative D_μ defined as:

$$D_\mu \equiv \partial_\mu - ig_s T_a G^a_\mu, \tag{3.3}$$

where g_s is the strong coupling constant, more typically referred as $\alpha_s \equiv g_s^2/4\pi$, T_a are the $SU(3)_c$ generators and G^a_μ are the gluon fields. After introducing the covariant derivative the QCD Lagrangian[1] can be written as:

$$\mathcal{L}_{QCD} = \bar{q}(i\gamma^\mu D_\mu - m)q - \frac{1}{4} G^a_{\mu\nu} G^{a\mu\nu}, \tag{3.4}$$

where γ^μ are the Dirac matrices, q is the quark field of three components corresponding to the different colours of a given quark type and m the mass of the quark. The interactions between quarks and gluons are enclosed in the definition of the covariant derivative of equation 3.4. The gluon field strength tensor $G^a_{\mu\nu}$ is given by:

$$G^a_{\mu\nu} = \partial_\mu G^a_\nu - \partial_\nu G^a_\mu - g_s f_{abc} G^b_\mu G^c_\nu, \tag{3.5}$$

where f_{abc} are the structure constants of the SU(3) group.

[1] The given description of QCD ommits ghost fields and possible gauge-fixing terms, which are introduced during the quantisation of the theory.

One of the basic principles of QCD is that hadronic matter is made of quarks. The idea of quarks arose from the need to have a physical manifestation of the $SU(3)$ group observed in the spectrum of the lowest-mass mesons and baryons. Quarks, as any other particle in the Standard Model, are characterised by their quantum numbers. The third component of the weak isospin (T_3) describes how they transform under $SU(2)$, while the hypercharge (Y_W) describes how it transforms under $U(1)$. Under the unitary irreducible representation of $SU(2)\times SU(1)$ they transform according to the electric charge (Q) related to T_3 and Y_W as

$$Q = T_3 + \frac{1}{2}Y_W. \tag{3.6}$$

The properties of the six known quarks are summarised in Table 3.1.

Quark	Mass	Charge (Q)	Weak Isospin (T_3)	Weak hypercharge (Y_W)
u	≈ 2.3MeV	$+\frac{2}{3}$	$\frac{1}{2}$	$\frac{1}{3}$
d	≈ 4.8MeV	$-\frac{1}{3}$	$-\frac{1}{2}$	$\frac{1}{3}$
c	≈ 1.275GeV	$+\frac{2}{3}$	$\frac{1}{2}$	$\frac{1}{3}$
s	≈ 95MeV	$-\frac{1}{3}$	$-\frac{1}{2}$	$\frac{1}{3}$
t	≈ 173.21GeV	$+\frac{2}{3}$	$\frac{1}{2}$	$\frac{1}{3}$
b	≈ 4.18GeV	$-\frac{1}{3}$	$-\frac{1}{2}$	$\frac{1}{3}$

Table 3.1: Properties of the quarks.

Baryons are made of three quarks (or antiquarks) while mesons are made of quark-antiquark pairs. These are the so-called valence quarks, which determine the charge and flavour of the hadron. However, the internal structure of hadrons cannot be explained just in these simple terms. Due to the dynamics and interactions between quarks, gluons can be radiated by the valence quarks with a latter split into quark-antiquark pairs. Therefore, there is a non-zero probability of finding gluons and quarks with different flavours from those of the valence quarks. These kind of quarks are known as sea quarks. As a result, hadrons are made of quarks, antiquarks and gluons.

3.2.1 Renormalisation Group Equations

In QCD gluons are massless, therefore, the theory contains divergences that result in infinities in the cross sections calculations. A renormalisation procedure is then necessary so that the theory yields physical meaningful results that can be compared to the experimental measurements.

This renormalisation procedure is done by some specified (but arbitrary) prescription, which introduces a new dimensional scale μ. Renormalised quantities, such as the basic vertex coupling g_s, depend explicitly on μ. Different renormalisation prescriptions with different μ must all lead to the same observable amplitudes. The transformations of renormalised operators, as the renormalisation scale, μ, is changed, form a Lie group named the *Renormalisation Group* [57]. The equations that express the invariance of the physics under changes of the parameter μ are known as the *Renormalisation Group Equations* (RGE).

A dimensionless physical observable R, which depends on a single large energy scale Q, can be calculated as a perturbation series in the coupling α_s, introducing a renormalisation scale μ (the point at which the subtractions which remove the ultraviolet

divergences are performed). Since R is dimensionless, it can only depend on the ratios Q^2/μ^2 and m/Q (where m is the mass of the quark) and the coupling α_s. Mathematically, the μ independence of R, assuming massless quarks, may be expressed by:

$$\mu^2 \frac{d}{d\mu^2} R(Q^2/\mu^2, \alpha_s) \equiv \left[\mu^2 \frac{\partial}{\partial \mu^2} + \mu^2 \frac{\partial \alpha_s}{\partial \mu^2} \frac{\partial}{\partial \alpha_s} \right] R = 0. \tag{3.7}$$

This equation corresponds to the RGE for the massless case. Taking $t = \ln\left(\frac{Q^2}{\mu^2}\right)$ and $\beta(\alpha_s) = \mu^2 \frac{\partial \alpha_s}{\partial \mu^2}$, equation (3.7) can be rewritten as:

$$\left[-\frac{\partial}{\partial t} + \beta(\alpha_s) \frac{\partial}{\partial \alpha_s} \right] R(e^t, \alpha_s) = 0. \tag{3.8}$$

This first order partial differential equation is solved by implicitly defining a new function, the *running coupling* $\alpha_S(Q^2)$, as follows:

$$t = \int_{\alpha_s}^{\alpha_s(Q^2)} \frac{dx}{\beta(x)}, \qquad \alpha_s(\mu^2) \equiv \alpha_s \tag{3.9}$$

A solution of equation (3.7) is $R(1, \alpha_s(Q^2))$. This shows that all the scale dependence in R enters through the running of the coupling $\alpha_s(Q^2)$.

3.2.2 The β function

The function $\beta(\alpha_s)$ defined above determines the behaviour of the running coupling at different scales. In QCD, the perturbative expansion of this function is:

$$\beta(\alpha_s) = -b_0 \alpha_s^2 + \mathcal{O}(\alpha_s^3), \tag{3.10}$$

with

$$b_0 = \frac{33 - 2n_f}{12\pi}, \tag{3.11}$$

where b_0 is the 1-loop beta function coefficient and n_f the number of active light flavours. The equation

$$Q^2 \frac{\partial \alpha_s(Q^2)}{\partial Q^2} = -b\alpha_s^2(Q^2) + \mathcal{O}(\alpha_s^3(Q^2)), \tag{3.12}$$

leads to the LO solution

$$\alpha_s(Q^2) = \frac{\alpha_s(\mu^2)}{1 + \alpha_s(\mu^2) bt}, \tag{3.13}$$

that determines the relation between $\alpha_s(Q^2)$ and $\alpha_s(\mu^2)$ provided that both are in the perturbative region. The renormalisation scale introduced will be referred as μ_R in other sections and chapters.

3.2.3 Confinement and asymptotic freedom

Confinement and asymptotic freedoms are two limiting cases of the theory at small and large energy scales, respectively. Contrary to QED, where the coupling increases with the scale of the process, gluon self-interactions lead the β function to be negative (as in

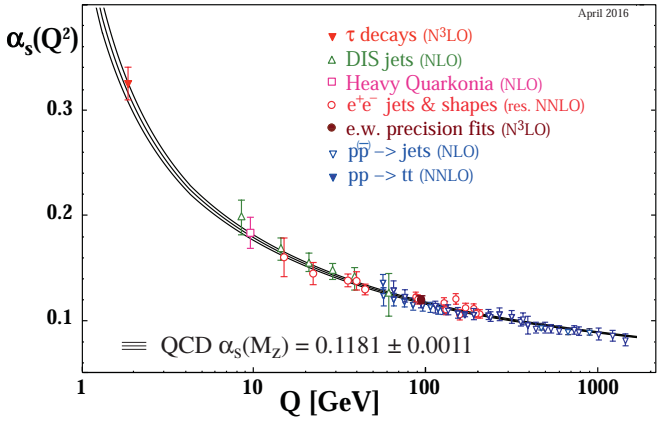


Figure 3.2: Summary of measurements of α_s as a function of the energy scale Q [60].

Equation 3.10) changing the overall behaviour of the theory. In Figure 3.2 the value of α_s as a function of the energy scale Q is plotted. As t increases in equation (3.13) the running coupling approaches zero, therefore QCD becomes weakly interacting at high energy scales and that explains why the methods of perturbation theory are useful in this regime. This is known as asymptotic freedom. On the other hand, when t decreases the coupling increases making α_s to be sizeable at low Q^2 and the theory to be strongly interacting, leading to confined partons. Therefore, confinement explains why the quark and gluon degrees of freedom are not observed as states which propagate over macroscopic distances.

Asymptotic freedom and confinement have relevant experimental consequences in hadron-hadron collisions. Quarks and gluons cannot be observed directly. Interactions with high energy probes are required to eject these particles from the nucleon; collimated shower of hadrons are detected instead.

3.2.4 Parton model and parton distribution functions

Asymptotic freedom allows a description of QCD using point-like constituents at sufficiently large energy scales. The parton model [58] succeeded in explaining the first evidence of this behaviour given by the SLAC-MIT experiments. To accommodate the momentum scale introduced by renormalisation, the *improved parton model* was developed. Starting from these ideas, the perturbative evolution of the quarks and gluons behaviour can be predicted separately from the soft, non-perturbative physics, allowing for theoretical calculation of QCD processes.

The differential cross section for lepton-hadron (lh) inelastic scattering can be written as

$$\frac{d^2\sigma(lh)}{dxdQ^2} = \frac{1}{Q^4}(f(y)xF_1(x,Q^2) + g(y)F_2(x,Q^2)). \tag{3.14}$$

$F_{1,2}$ are *structure functions* that encapsulate the lack of knowledge on the nucleon behaviour and x is a variable that, at LO, represents the fraction of hadron momentum taken by the scattered quark. F_1 and F_2 are related by the Callan-Gross equation, given that quarks have spin 1/2, that reads

$$2xF_1(x) = F_2(x). \tag{3.15}$$

The structure function F_2 can be identified, when compared to the cross section for incoherent scattering (where quarks that compose the hadrons are independent from each other), with

$$F_2 = \sum_i^{N_q} e_i^2 x q_i(x), \tag{3.16}$$

where e_i is the electric charge of the quark i and $q_i(x)$ are functions that can be interpreted at LO as the probability density of finding a quark with flavour i carrying a fraction x of the hadron momentum. The momentum distribution for a given quark or gluon is also called a parton distribution function or PDF. The independence of the structure function from the momentum transfer Q^2 at fixed values of x is known as Bjorken scaling. However, this scaling does not hold exactly, scaling-breaking terms appear invariably order-by-order in perturbative calculations. A mild violation is possible in QCD due to its asymptotic freedom.

Quarks and gluons are dynamical objects which interact with each other varying their hadron momentum fraction leading to scaling violations. The DGLAP formalism (see next section) models these interactions through *splitting functions* using them to evolve perturbatively the renormalised parton densities that contain the Q^2 dependence. This formalism only provides information about the evolution of the PDFs, but not on the shape, which is derived using a combination of experimental data on the structure functions. Probability conservation requires that the area of the total momentum distributions in a hadron is equal to unity (*momentum sum rule*). The PDFs obtained at NNLO in the NNPDF analysis [59] at two different scales, $\mu^2 = 10$ and 10^4 GeV^2, are shown in Figure 3.3.

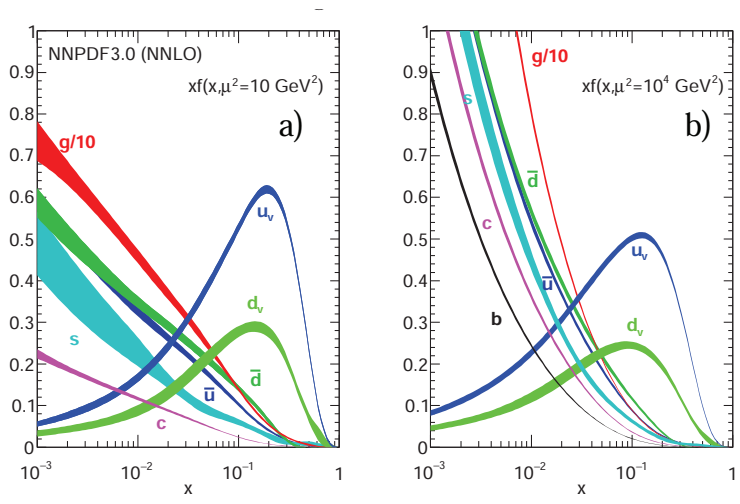


Figure 3.3: The bands are x times the unpolarised parton distributions $f(x)$ (with $f = u_v, d_v, \bar{u}, \bar{d}, s \approx \bar{s}, c = \bar{c}, b = \bar{b}$ and g) obtained in the NNLO NNPDF3.0 global analysis [59] at scales $\mu^2 = 10$ and 10^4 GeV^2, with $\alpha_S(M_Z^2) = 0.118$.

3.2.5 Factorisation

One of the main reasons of the success of QCD as a predictive theory is that the short-distance component of the scattering process described by perturbative QCD can be separated from the non-perturbative long-distance component when computing the cross sections. This is known as the factorisation theorem and implies that perturbation theory can be used to calculate the hard-scattering cross section, while universal functions such as the PDFs can be determined separately to obtain the full theoretical prediction. For a hard hadronic process

$$d\sigma(p_A, p_B, Q^2) = \sum_{ab} \int dx_a dx_b f_{a/A}(x_a, \mu_F^2) f_{b/B}(x_b, \mu_F^2) \times d\hat{\sigma}_{ab\to cd}(\alpha_s(\mu_R^2), Q^2/\mu_R^2), \tag{3.17}$$

where $d\hat{\sigma}$ is the differential cross section for the parton underlying process, x_a (x_b) is the momentum fraction of parton a (b) with respect to the colliding hadron A (B) and $f_{a/A}$ ($f_{b/B}$) is the parton momentum density for the interacting parton a (b) with respect to hadron A (B). Since the factorisation procedure absorbs singularities in the same fashion as renormalisation, a new scale μ_F^2 is introduced. As the choice of the factorisation scale is arbitrary, the cross section at all orders cannot depend on μ_F, that is, $d\sigma/d\mu_F = 0$; however, order-by-order it depends on μ_F. It is rather common to set $\mu_F = Q$.

Initial-state infrared and collinear divergences

Two kinds of divergences appear when a gluon is radiated by the initial-state quarks:

- infrared divergences: the energy of the emitted gluon tends to zero;
- collinear divergences: the emitted gluon is collinear to the quark.

Infrared (IR) divergences cancel by virtue of the Kinoshita-Lee-Nauenberg theorem: the infrared divergences coming from loop integrals are cancelled by infrared divergences coming from phase-space integrals. The collinear singularities are not cancelled but absorbed into the bare distribution of the PDFs at a certain factorisation scale. The invariance of the PDF with the factorisation scale is expressed as

$$\frac{d}{d\ln\mu_F} f_{a/H}(x, \mu_F) = \sum_b \int_x^1 \frac{d\xi}{\xi} P_{ab}(x/\xi, \alpha_s(\mu_F)) f_{b/H}(\xi, \mu_F). \tag{3.18}$$

These are the Dokshitzer-Gribov-Lipatov-Altarelli-Parisi (DGLAP) equations in which $f_{a/H}$ ($f_{b/H}$) is the PDF of parton a (b) in hadron H and P_{ab} are the splitting functions, which are related to the probability of emission of a parton a by a parton b. It is the analogue of the beta function equation and one of the most important equations in pQCD.

A practical consequence of the cancellation of the IR divergences is that observables that are inclusive enough to be insensitive to processes that distinguish between different numbers of partons are IR safe. In experimental measurements, detectors have a finite

spatial resolution and cannot resolve the products of individual partons. If the objects that represent the partons in the final state have a well-defined behaviour both in theory and experiment, the parton kinematics are reflected in the final-state object. Here is where the definition of *jets* becomes essential for QCD measurements. Naively speaking, a jet can be seen as a group of collimated particles generated by the hadronisation of a parton coming from the hard-scattering process. A detailed definition of jets and the algorithm used for jet finding are given in Section 3.3.

The DGLAP splitting functions

The splitting functions P_{ab}, where a, b represents different partons, have a perturbative expansion in terms of the running coupling:

$$P_{ab}(z, \alpha_s) = P_{ab}^{(1)}(z)\left(\frac{\alpha_s}{2\pi}\right) + P_{ab}^{(2)}(z)\left(\frac{\alpha_s}{2\pi}\right)^2 + \mathcal{O}(\alpha_s^3). \tag{3.19}$$

Strictly speaking, only the leading-order DGLAP splitting functions $P_{ab}^{(1)}(z)$ have a physical interpretation of the probability that a parton b emits a parton a with a fraction z of the longitudinal momentum of the parent parton and a transverse momentum squared much less that μ^2. At LO, the splitting function $P_{q_i q_j}$ is only different from zero if $i = j$. The interpretation as probabilities implies that the splitting functions are positive definite for $x < 1$, and satisfy the sum rules

$$\begin{aligned} \int_0^1 dz P_{qq}^{(1)}(z) &= 0 \\ \int_0^1 dz z \left[P_{qq}^{(1)}(z) + P_{gq}^{(1)}(z)\right] &= 0 \\ \int_0^1 dz z \left[2n_f P_{qg}^{(1)}(z) + P_{gg}^{(1)}(z)\right] &= 0, \end{aligned} \tag{3.20}$$

which corresponds to quark-number and momentum conservation in the splittings of quarks and gluons, respectively. The expressions of the splitting functions at LO are:

$$\begin{aligned} P_{qq}^{(1)}(x) &= C_F\left[\frac{1+x^2}{(1-x)_+} + \frac{3}{2}\delta(1-x)\right], \\ P_{qg}^{(1)}(x) &= T_R\left[x^2 + (1-x)^2\right], \\ P_{gq}^{(1)}(x) &= C_F\left[\frac{1+(1-x)^2}{x}\right], \\ P_{gg}^{(1)}(x) &= 2C_A\left[\frac{x}{(1-x)_+} + \frac{1-x}{x} + x(1-x)\right] + \delta(1-x)\frac{11C_A - 4n_f T_R}{6}, \end{aligned}$$

where $T_R = 1/2$, $C_A = 3$ and $C_F = 4/3$ are the SU(3) group factors and the '+' distribution is defined as

$$\int_0^1 \frac{f(x)}{(1-x)_+} dx = \int_0^1 \frac{f(x) - f(1)}{1-x} dx. \tag{3.21}$$

Scaling violations

An independent fragmentation model would predict scale-independence in the parton momenta distribution. The interaction of quarks and gluons inside hadrons is modelled through the splitting functions. Due to this fact, the DGLAP equations that describe the change in quark, antiquark and gluon densities with Q^2 are coupled. This leads to scaling violations in the PDFs. As the scale increases, the x distribution is shifted toward lower values. Physically, this can be understood as an increase in the phase space for gluon emission by the quarks as μ^2 increases, with a corresponding reduction in the quark momentum. Figure 3.4 shows how the structure function F_2 varies with the scale.

The emergence of computable scale-dependence of dimensionless physical quantities at high energies in an asymptotically free quantum field theory with dimensionless coupling, like QCD, is a remarkable feature of relativistic quantum mechanics. The mechanism through which the scale-dependence arises is sometimes referred to as *dimensional transmutation.*

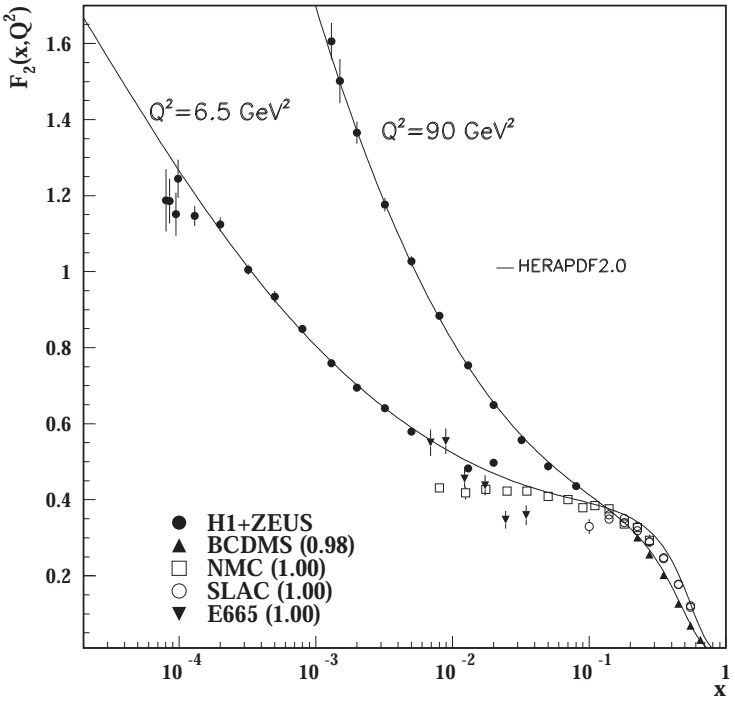
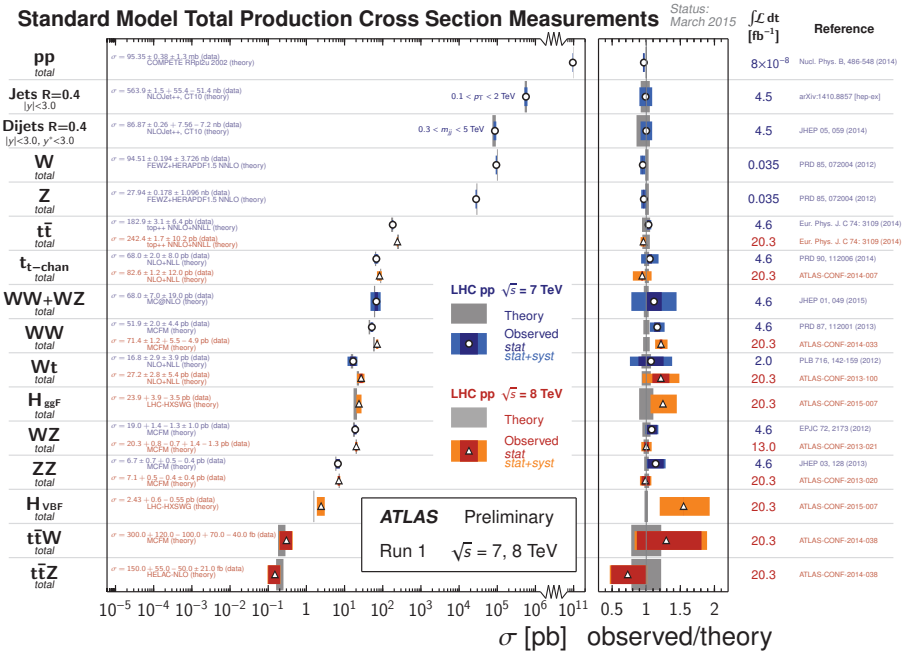


Figure 3.4: The proton structure function F_2^p measured in electromagnetic scattering of electrons and positrons on protons (collider experiments H1 and ZEUS for $Q^2 \geq 2\text{GeV}^2$), in the kinematic domain of the HERA data, and for electrons (SLAC) and muons (BCDMS, E665, NMC) on a fixed target experiment [60, 61].

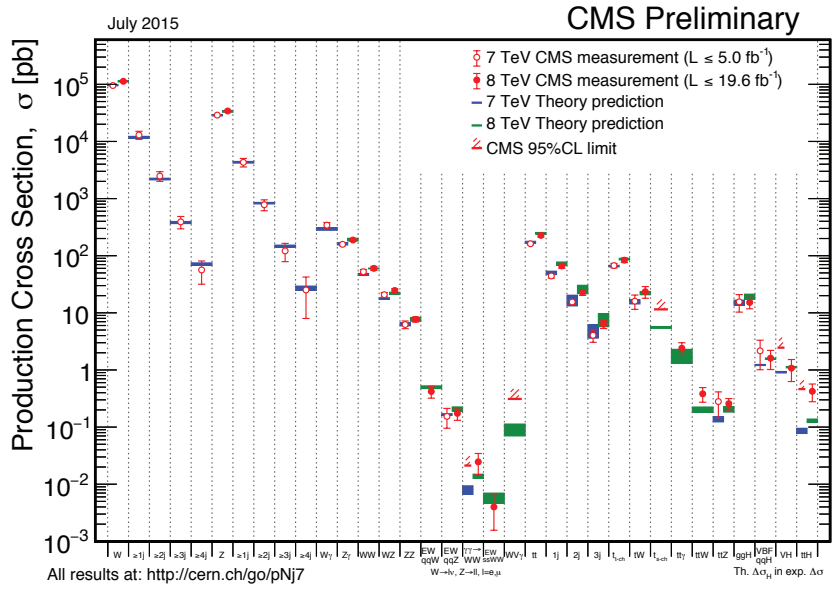
3.2.6 QCD tests at the LHC

At hadron colliders, the variety of observables and the number of measurements performed is enormous. They probe many regions of phase space measuring processes with very different cross sections as shown in Figure 3.5 for the ATLAS and CMS experiments.

Besides representing a general test of the SM, they serve several purposes like probing pQCD and its various approximations and implementations in MC models or extracting and constraining parameters such as the strong coupling constant or PDFs.



(a)



(b)

Figure 3.5: Overview of cross section measurements for a wide class of processes and observables, as obtained by the ATLAS [62] and CMS [63] experiments at the LHC, for centre-of-mass energies of 7, 8 and 13 TeV. Also shown are the theoretical predictions and their uncertainties.

3.3 Jets

Final-state partons and hadrons appear predominantly in collimated bunches, which are generically called *jets*. To a first approximation, a jet can be thought as a hard parton that has undergone soft and collinear showering and hadronisation. These objects are the closest to single quarks or gluons in colliders. The cross section for the production of these objects has to be finite at all orders of perturbation theory and as insensitive as possible to the parton to hadron transition through the non-perturbative hadronisation process.

Defining a jet requires a procedure to associate either particles or energy deposits to a single jet (*jet algorithm*) and a *recombination scheme* that specifies how to combine the four-momenta of the jet constituents. There is no universal jet algorithm for all topologies of interest.

3.3.1 Theoretical requirements for a jet algorithm

A jet algorithm must satisfy the following requirements to have a well defined behaviour from the theoretical side:

- **infrared safety**: the presence or absence of additional infinitely soft particles radiated by the primary partons should not modify the result of the jet finding (e.g. the number of jets);
- **collinear safety**: jets should not be sensitive to particles radiated at very small angles with respect to the original parton. The configurations in which a certain amount of transverse momentum is carried by one particle or if the particle splits into two collinear particles should lead to e.g. the same number of jets;
- **independence on input-object**: the same jet topology should be reconstructed regardless of the input type (partons, particles, ...) to be as much independent as possible of the non-perturbative effects.

Another desirable requirement for a jet algorithm to be successfully used in a high-energy physics experiment is to be computationally fast.

3.3.2 Types of jet algorithms

Jet algorithms can be divided into two main subgroups: cluster and cone-type algorithms.

Cone algorithms define jets based on the dominant direction of energy flow, that is, they try to maximise the energy density within a cone of fixed size. It starts from inputs with energy above a certain threshold (seeds) and sums the four-momenta of all particles in a surrounding cone of radius R. The jet candidate is accepted if its p_{T} is larger than some critical value. In the last step, a split-merge technique is used to disentangle the overlapping constituents of stable cones. This simple algorithm cannot be used to describe the full wealth of features predicted in QCD without introducing further complications. A problem arises when trying to find more than one jet in multijet configurations in which jets may overlap.

Cluster algorithms, such as k_t or anti-k_t, are based on the sequential recombination of objects that iteratively merge pairs according to a distance that usually involves the

angular separation between the objects and their transverse momenta. The usage of the transverse energy flow in the rapidity-azimuth plane with respect to the colliding axis ensures Lorentz invariance under longitudinal boosts.

A general definition of distance between a pair of objects (i, j) for this last type of jet algorithms is

$$d_{ij} = \min\left(E_{T,i}^{2p}, E_{T,j}^{2p}\right) \frac{\Delta_{ij}^2}{R^2} \tag{3.22}$$

$$d_{iB} = E_{T,i}^{2p}, \tag{3.23}$$

where $d_{i,B}$ is the distance between the object i and the beam B, R is the usual radius parameter, $\Delta_{ij} = (y_i - y_j)^2 + (\phi_i - \phi_j)^2$ and $E_{T,i}$, y_i and ϕ_i are the transverse momentum, rapidity and azimuth of object i, respectively. The algorithm proceeds by identifying the smallest distance between the two given definitions d_{ij} and d_{iB} . If d_{ij} is the smallest, the entities i and j are recombined into a single object. Otherwise, the object i is called a jet and removed from the list. The process is iterated until no objects remain.

Depending on the value of the parameter p different jet algorithms are defined. For $p = 1$, the inclusive k_t algorithm is obtained and softer objects are recombined first. The value $p = 0$ corresponds to the Cambridge/Aachen algorithm in which the recombination is purely based on angular distances. The case of $p = -1$ corresponds to the anti-k_t jet clustering algorithm and harder objects are recombined first. Values of $p > 0$ and $p < -1$ have the same behaviour with respect to soft radiation as the k_t and anti-k_t jet algorithms, respectively. Since in the case of negative values of p are the hard particles those who modified the shape of the jet, the jet boundary in the anti-k_t algorithm is resilient to soft radiation, but flexible with respect to hard radiation. Furthermore, it behaves as an idealised cone algorithm in which active and passive areas are equal. The knowledge on the shape of the jets facilitates experimental calibration of jets and soft radiation resilience can simplify certain theoretical calculations, as well as eliminate some contributions to the momentum-resolution loss caused by underlying event and pile-up.

Another important feature of jet algorithms is the recombination scheme. The so-called E-scheme was used for the results presented in this thesis: the four-momentum of the combined particle is the sum of the four-momenta of the two clustered objects.

3.4 Theory of prompt-photon production

At hadron colliders, high transverse momentum prompt-photon[2] production, $pp \to \gamma$+(jets) + X, is separated into two categories depending on the production mechanism:

- direct photons (DP) that come directly from the hard interaction and are likely to be well separated from the hadronic activity;
- fragmentation photons (F), which are the products of the collinear fragmentation of a final-state parton [3–6]. This collinear singularity does not cancel (as opposed to gluon radiation, in which the collinear singularity is cancelled when real and virtual gluon contributions are summed) and it has to be absorbed into a *photon*

[2] All photons produced in pp collisions that are not secondaries from hadron decays are considered as "prompt".

fragmentation function $D_q^\gamma(z,\mu_f^2)$ ($D_g^\gamma(z,\mu_f^2)$) representing the probability of finding a photon carrying longitudinal momentum fraction z in a quark (gluon) jet at scale μ_f. When this fragmentation scale, μ_f, is large with respect to $\sim$ 1 GeV, the photon fragmentation function behaves as $\sim \alpha_{\rm EM}/\alpha_s(M_F^2)$, becoming of the same order in α_s as the Born-level term of the direct mechanism, $\alpha_{EM}\alpha_s$. Besides, due to the high value of the gluon parton densities at small x, the fragmentation photons can dominate the inclusive production rate in the lower range of the $p_{\rm T}$ spectrum. Fragmentation is a non-perturbative process but obeys a DGLAP evolution equation. At LO, the contribution to the cross section is of the form

$$\hat{\sigma}^{\rm LO}(qg \to qg) \otimes D_q^\gamma(z,\mu_f), \tag{3.24}$$

while at higher orders, final-state multiple collinear singularities appear in any subprocess where a high-$p_{\rm T}$ parton undergoes a cascade of successive collinear splittings ending up with a quark-photon splitting.

Some examples of Feynman diagrams for prompt-photon production are presented in Figure 3.6.

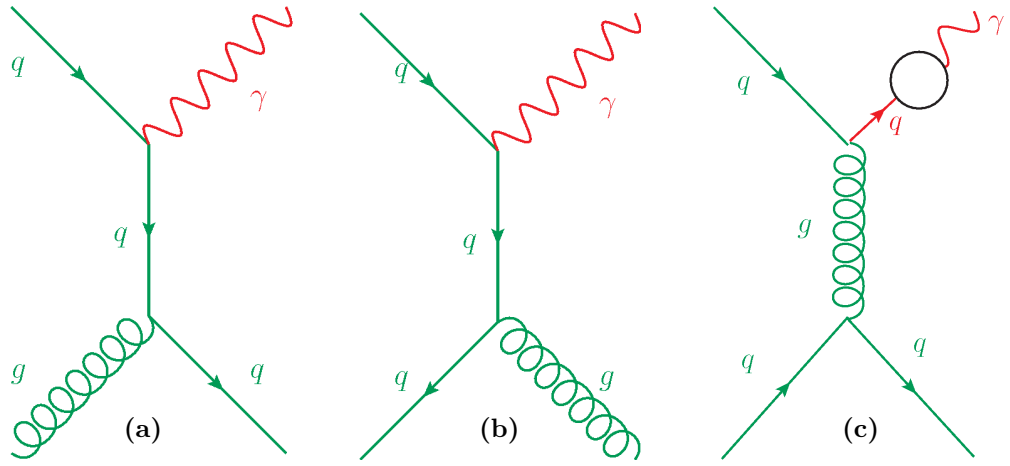


Figure 3.6: Leading-order diagrams for prompt-photon production. Gluon Compton scattering, (*a*), and annihilation, (*b*), are both direct production processes. (*c*) is an example of the production of a prompt-photon coming from a fragmentation process.

The LO differential cross section as a function of the transverse momentum of the photon ($E_{\rm T}^\gamma$) is given by the sum of the direct and fragmentation contributions,

$$\frac{d\sigma^{LO}}{dE_{\rm T}^\gamma} = \frac{d\hat{\sigma}^{LO,\gamma}}{dE_{\rm T}^\gamma}(E_{\rm T}^\gamma,\mu_F) + \sum_a \int_0^1 \frac{dz}{z}\frac{d\hat{\sigma}^{LO,a}}{dE_{\rm T}^\gamma}(E_{\rm T}^\gamma/z,\mu_F,\mu_f) D_a^{LO,\gamma}(z,\mu_f), \tag{3.25}$$

where $\frac{d\sigma^{LO}}{dE_{\rm T}^\gamma}$ and $\frac{d\hat{\sigma}^{LO,\gamma}}{dE_{\rm T}^\gamma}$ are the corresponding partonic cross sections convoluted with the PDFs, $a = q, g$ and z represent the fractional momentum carried by the photon. The expression is analogous to that of Equation (3.17). From Equation (3.25), it is concluded that at high-p_T values, the dynamics can be computed perturbatively in terms of partonic cross sections, while the dominant non-perturbative phenomena can be factorised into the PDFs and the fragmentation function of the final-state photon. Beyond LO, the

classification into F and DP has no longer any physical meaning and the distinction between both processes is an arbitrary choice which follows from the need of factorising the cross section. The scale introduced in this process, μ_f, is an unphysical parameter. Only the sum of the fragmentation and direct processes cancels the dependence on μ_f and is a physical observable. The full expression for the cross section for inclusive isolated prompt-photon production at NLO is presented in Reference [64].

3.4.1 Isolated prompt photons

One of the main challenges in a prompt-photon analysis is the suppression of the overwhelming background coming mainly from the decay of light mesons (π^0, η, ω) into photons. Photons are produced copiously inside jets; however, these secondary photons are not isolated. Therefore, isolation from hadronic activity becomes an essential requirement for the study of prompt photons. A widely used technique to implement photon isolation is the *cone criterion*: the hadronic transverse energy in a cone of radius R defined in the rapidity and azimuthal plane around the direction of the photon as

$$(\eta - \eta^\gamma)^2 + (\phi - \phi^\gamma)^2 \leq R^2, \tag{3.26}$$

is required to be less than a given limiting amount

$$E_{\mathrm{T,had}} \leq E_{\mathrm{T,max}}. \tag{3.27}$$

The application of the isolation criteria reduces part of the fragmentation contribution as well as the background. If z is the transverse momentum fraction of the final-state parton taken by the photon, the transverse momentum of the parton produced after fragmentation is

$$p_T^p = (1-z)P_T^{p,bf} = \frac{1-z}{z}E_{\mathrm{T}}^\gamma, \tag{3.28}$$

where bf stands for "before fragmentation". The quantity p_T^p should be smaller than the maximal hadronic activity allowed in the cone. Taking this into account, fragmentation photons survive the isolation requirement provided that

$$z \geq \left(1 + \frac{E_{\mathrm{T,max}}}{E_{\mathrm{T}}^\gamma}\right)^{-1}. \tag{3.29}$$

The cross section for the production of isolated photons depends on the isolation parameters R and $E_{\mathrm{T,max}}$. Since the isolation criteria impose phase-space restrictions, the cross section is not fully inclusive and factorisation cannot always be applied. However, it has been proven [3] that if the isolation criteria fulfils certain requirements, the cross section satisfies the factorisation property and is finite to all orders in perturbation theory for non-zero R and $E_{\mathrm{T,max}}$. The requirements for any isolation criteria specified in terms of a function

$$F_{\mathrm{isol.}}^{(n+1)}(p_A, p_B; p_\gamma; p_1, ..., p_{n+1}), \tag{3.30}$$

where $p_{A,B}$ are the momenta of initial partons and p_i the final-state partons momenta, are:

(i) Infrared safety:

$$F_{\mathrm{isol.}}^{(n+1)}(p_A, p_B; p_\gamma; p_1, ..., p_i, ..., p_{n+1}) \xrightarrow{p_i \to 0} F_{\mathrm{isol.}}^{(n)}(p_A, p_B; p_\gamma; p_1, ..., p_{n+1}). \tag{3.31}$$

The cross section is insensitive to soft particle momenta.

(ii) Collinear safety:

$$F_{\text{isol.}}^{(n+1)}(p_A, p_B; p_\gamma; p_1, ..., p_i, p_j, ..., p_{n+1}) \xrightarrow{p_i||p_j} F_{\text{isol.}}^{(n)}(p_A, p_B; p_\gamma; p_1, ..., p_i + p_j, ..., p_{n+1}). \tag{3.32}$$

It implies that in the case that some final-state particles are produced collinear to each other, the cross section depends on the sum of their momenta and not on the momentum of each of them.

(iii) Final-state factorisability:

$$F_{\text{isol.}}^{(n+1)}(p_A, p_B; p_\gamma; p_1, ..., p_i, ..., p_{n+1}) \xrightarrow{p_i||p_\gamma} F_{\text{isol.}}^{(n)}(p_A, p_B; p_\gamma + p_i; p_1, ..., p_{n+1}). \tag{3.33}$$

It means that long-distance phenomena related to the low momentum fragmentation of the photon can be absorbed and factorised in the universal fragmentation function $D_a^\gamma(z; \mu_f)$. By universal it is meant that it does not depend on the process and, in particular, it does not depend on the isolation parameters.

(iv) Initial-state factorisability:

$$F_{\text{isol.}}^{(n+1)}(p_A, p_B; p_\gamma; p_1, ..., p_i, ..., p_{n+1}) \xrightarrow{p_i||p_A} F_{\text{isol.}}^{(n)}(p_A - p_i, p_B; p_\gamma; p_1, ..., p_{n+1}). \tag{3.34}$$

In hadron-hadron collisions, the cross section is affected by additional long-distance phenomena related to the non-perturbative binding of the colliding partons within the incoming hadrons. At parton level, these phenomena lead to initial-state singularities that have to be absorbed and factorised into the non-perturbative parton distribution of the colliding hadrons. This property guarantees that the photon isolation criterion does not spoil the factorisation of the initial-state singularities.

The QCD factorisation is valid at any order in perturbation theory and the fragmentation function is the same that appears for non-isolation, provided that the isolation criterion satisfies the requirements mentioned above.

Cone-isolation is not the only isolation criterion used. The democratic approach [65] treats the photon as a parton in a jet-finding algorithm. At the end of the clustering procedure, the configuration corresponds to an isolated photon event only if the ratio of the hadronic energy found inside the jet containing the photon over the total energy of the jet is smaller than a fixed amount. The smooth-cone isolation criterion [66] modifies the cone approach so that the photon cross section only depends on the direct process. This is achieved by eliminating the dependence on the fragmentation functions while radiation is allowed in all regions of the phase space. According to this approach, events are rejected unless they fulfil the following condition:

$$\sum_i E_i \Theta(\delta - R_{i\gamma}) \leq \chi(\delta) \quad \text{for all} \quad \delta \leq \delta_0, \tag{3.35}$$

where E_i is the energy of hadron i, $R_{i\gamma}$ is the angular distance between hadron i and the photon and δ_0 is the radius of the cone in which the condition is applied. The function $\chi(\delta)$ is defined as

$$\chi(\delta) = E_{\text{T}}^\gamma \epsilon_\gamma \left(\frac{1 - \cos\delta}{1 - \cos\delta_0} \right)^n, \tag{3.36}$$

where E_{T}^{γ} is the transverse energy of the photon and ϵ_{γ} and n are adjustable parameters of the method. The main feature of $\chi(\delta)$ is that

$$\lim_{\delta \to 0} \chi(\delta) = 0, \tag{3.37}$$

avoiding collinear divergences around the photon.

3.4.2 State-of-the-art of Standard Model photon physics

The quark and gluon fragmentation functions into photons were constrained using LEP data at the end of last century [4]. These fragmentation functions have been used in generators able to perform a full NLO computation of inclusive-photon production cross sections, such as JetPhox [64] or MCFM [67] and which have represented the best knowledge of inclusive photon-production during the last fifteen years. The fragmentation contribution has always been a difficulty for advances in higher-order calculations and the fragmentation functions are considered to be a source of large uncertainties.

In 2016, calculations of the cross section for inclusive prompt-photon production were released including threshold resummation of next-to-next-to-next-to-leading logarithm ($\mathrm{N^3LL}$) [13] and at NNLO [14]. In both cases, a smooth-cone isolation criterion was adopted and an N-jettiness slicing technique was used in Reference [14]. The leading-logarithmic (LL) electroweak virtual corrections were studied and proved to be important at high E_{T}^{γ}.

The smooth-cone isolation criterion is not possible to implement at experimental level due to the finite size of the calorimeter cells. Some concerns may arise if experimental data (with the standard cone isolation) are compared to predictions in which only the direct-photon production is taken into account. Predictions obtained with the smooth-cone criterion are expected to give a lower bound for the production cross section. In the context of photon-pair production at NLO, it was shown that for very strict isolation parameters, the results for standard- and smooth-cone isolation are similar with regards to the scale dependence of the cross section [68, 69]. At NNLO, such a comparison is not yet possible but studies have been performed to quantify the impact of different smooth-cone isolation parameters on the cross sections [70].

The current knowledge of the inclusive photon and photon+jet cross sections at NNLO is now comparable to that of Z+jet production. The ratio of the cross sections for the two processes has been exploited to provide a better understanding of the $Z \to \nu\bar{\nu}$+jet process, which gives rise to a significant background in searches for dark matter and supersymmetry [71, 72].

Direct-photon production probes the gluon density inside the proton already at LO through the Compton scattering process, $qg \to \gamma q$. Exploiting these measurements to constrain the gluon PDF is complicated due to the fragmentation contribution. In spite of this fact, direct-photon production data from fixed-target experiments were used in early PDF fits [73–75]; however, the use of prompt-photon data was abandoned. The constraining potential of LHC data at NLO was demonstrated in [8]; it has not been until the release of NNLO calculations that photon data have been considered in a NNLO PDF global analysis. Very recent studies have shown that LHC photon-production data lead to both a moderate reduction of the gluon uncertainties at medium x and a preference for a somewhat softer central value at large x [11].

3.5 Monte Carlo event generators

In general, Monte Carlo (MC) methods are used to evaluate difficult integrals that may be intractable using numerical methods. They rely on a "random number generator" which generates uniform statistically-independent values.

A Monte Carlo event generator simulates events aleatory weighted with statistical distributions derived from the cross section of the simulated process. In high-energy physics, they are used to provide fully exclusive modelling of high-energy collisions. The structure of a proton-proton collision at the LHC as built up by event generators is factorised into different well defined phases, corresponding to different kinematic regimes:

- hard process;
- parton shower;
- hadronisation;
- underlying event;
- unstable particle decays into stable particles.

The final output should be in the form of *events*, with final particles (i.e. hadrons, leptons and photons) together with their momenta, with the same average behaviour and the same fluctuations as the data. Whereas in the data the fluctuations arise from the quantum mechanical character of the underlying theory, in generators these fluctuations are the result of the (quasi-)randomness of the Monte Carlo approach. The generated events are passed through a detector simulation that reconstructs the signals produced in the different parts of the detector by the final-state particles based on the energy, position and type of particle. The full MC programs used in this dissertation are Pythia 8.186 [76], Sherpa 2.1.1 [77] and Sherpa 2.2.2 [77]. The GEANT4-based [78] detector simulation is used.

3.5.1 Hard process

The event simulation for the LHC begins with a relatively simple subprocess resulting from a collision of the constituents of the proton beams. This *hard scatter* is the highest momentum transfer process in the event. The momenta of the colliding constituents are selected by sampling the PDFs of the proton at the energy scale of the subprocess. These distributions have been measured at lower energies and in other processes and are evolved to higher scales using the QCD evolution equations for parton densities derived by renormalisation group techniques (DGLAP equations; see Section 3.2.5). Convolution with the differential cross section of the subprocess and integration over phase space gives the relevant production cross section.

Any of the incoming or outgoing objects of the hard subprocess that carry colour is eligible for parton showering in the next stage of the simulation. The main difference in this step between the generators used is that while Pythia can only calculate $2 \to 2$ matrix elements, Sherpa 2.1.1 (Sherpa LO from now on) uses LO matrix elements for photon plus jets final states with up to four additional partons. This fact makes a difference when a large number of hard jets are required in the final state.

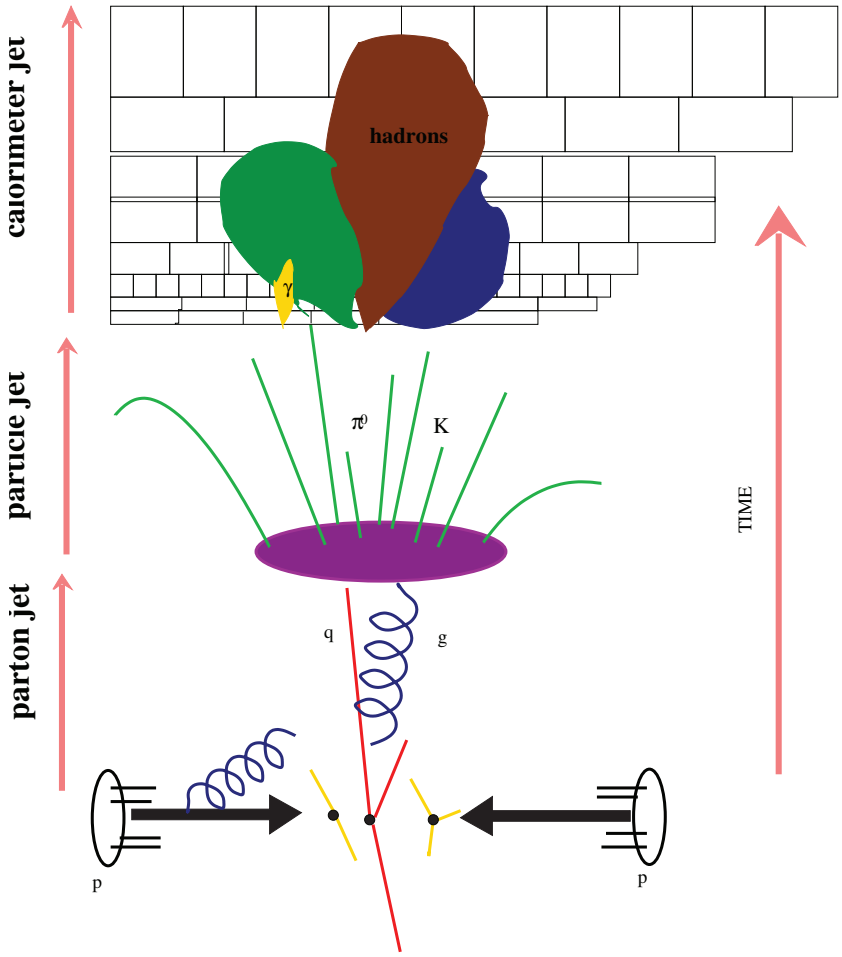


Figure 3.7: Diagram of a proton-proton interaction. Different colours correspond to different stages of the event generation: red for the hard process, blue for the parton shower, green for hadronisation and yellow for the underlying event.

3.5.2 Parton shower

Scattered colour charges radiate gluons. Contrary to QED, gluons themselves are coloured and therefore, a gluon can also radiate. This fact leads to an extended shower that fills up the phase space with mostly soft gluons. Parton-shower evolution starts from the hard process and works downwards to lower momentum scales until the point where perturbation theory breaks down. The structure of the showers is given in terms of the branchings $a \to bc$. These processes are characterised by a splitting functions $P_{a\to bc}(z)$[3]; the branching rate is proportional to $\int P_{a\to bc}(z)dz$ where z, is the fraction of the energy of the mother taken by the daughter b. A matching between the hard-scattering generator and the parton shower has to be performed such that double counting of parton emission in the same phase-space region is avoided.

In Pythia, the initial-state radiation is space-like. That is, in the sequence of

[3] $P(z, \alpha_s)$ are the DGLAP splitting functions (see Section 3.2.5) and depend on flavour and spin of the involved particles.

branchings $a \to bc$, particles a and b have $m^2 = E^2 - p^2 < 0$. The "side branch" particle c, which does not participate in the hard scattering, may be on-shell or have a time-like virtuality. To a first approximation, the evolution of the space-like main branch is characterised by a p_T-ordered shower algorithm, where the evolution variable $Q^2 = -p_{\mathrm{T}}^2 = -(1-z)m^2$ is required to be strictly increasing along the shower. In contrast, final-state radiation is time-like; i.e. partons have $m^2 = E^2 - p^2 > 0$. Starting from some maximum scale Q^2_{max}, an original parton evolves downwards in Q^2 until a branching occurs. The selected Q^2 value defines the p_{T} of the branching. SHERPA makes use of a virtuality-ordered shower. For the simulation of events with a photon in the final state, the PYTHIA MC also includes a QED shower.

3.5.3 Hadronisation

To take into account the QCD strong interacting regime at long distances, it is necessary to resort to hadronisation models. The hadronisation process cannot be described from first principles. Therefore, a number of different phenomenological models have been developed to treat this regime. The string fragmentation (SF) and cluster fragmentation (CF) are two of the most frequently used models.

String fragmentation model

The string fragmentation model or *Lund string model* is the default for PYTHIA simulations. It is based on the assumption that the colour potential between two partons ($V(r) \approx -\frac{4}{3}\frac{\alpha_s}{r} + \kappa r$) increases with their separation for distances larger than about 1 fm, leading to colour-field strings between them. As the distance increases, it reaches a certain threshold above which it is energetically beneficial to create a $q\bar{q}$ pair from the string energy, which breaks the string into two separate colour-singlet parts. This process is assumed to proceed until only on-mass-shell hadrons remain, each hadron corresponding to a small piece of string with a quark in one end and an antiquark in the other end. A schema of the model is shown in Figure 3.8(a).

Cluster fragmentation model

The colour preconfinement property of the angular-ordered parton shower is used as the basis of the hadronisation cluster models. Due to this property, the colour structure of the shower at any evolution scale is such that colour singlet combinations of partons (clusters) can be formed with an asymptotically universal[4] invariant mass distribution. All gluons are first split into $q\bar{q}$ pairs, before quarks that are close to each other in phase space are grouped into colourless clusters. After splitting heavy clusters to lighter ones, the remaining light clusters finally decay isotropically in their rest frames into pairs of hadrons. A schema of the model is shown in Figure 3.8(b).

SHERPA uses a modified cluster fragmentation model with new features: soft colour reconnection is accounted for in the formation and decay of clusters. The flavour-dependent separation of the cluster regime from the region of hadron resonances yields the selection of specific cluster-transition modes. The two regimes are distinguished by comparing the

[4]Here universal means that it only depends on Q_0 and the QCD scale Λ and not on the scale Q or the nature of the hard process initiating the shower.

mass of the cluster with the masses of the accessible hadrons matching the clusters flavour structure.

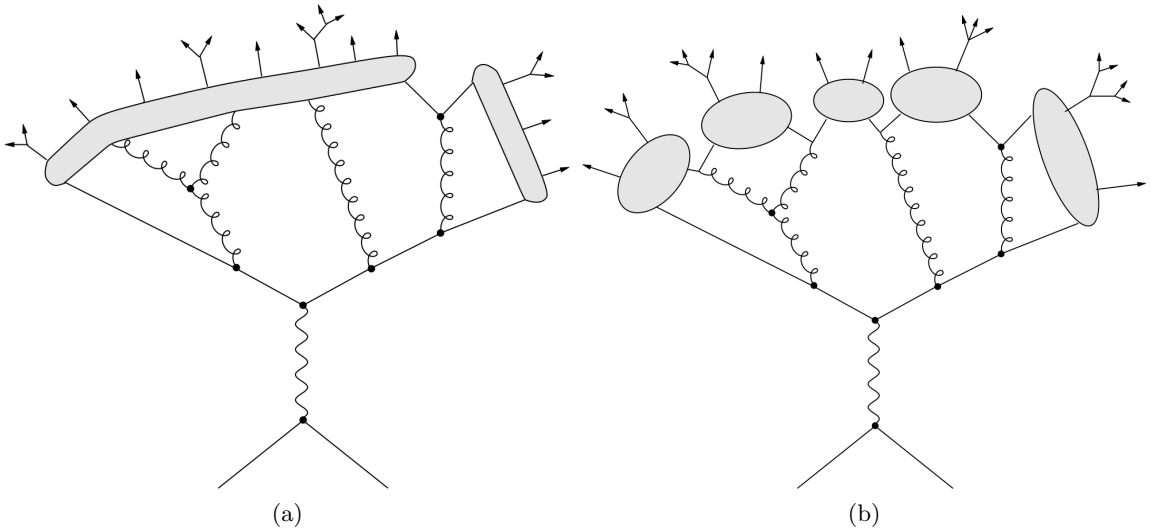


Figure 3.8: Examples of the string fragmentation (a) and cluster fragmentation (b) models of hadronisation.

3.5.4 Underlying event

Partons that initiate the hard interaction are accompanied by the other constituents of the colliding hadrons, which form the so-called beam remnants. These are coloured and therefore, hadronise as well, providing additional particles in the final state. Furthermore, the beam remnants might also interact with each other, leading to multiple parton interactions (MPI). All these effects that do not derive from the primary hard interaction are collectively referred to as the *underlying event* (UE).

High p_{T} jets are generally accompanied by a level of UE higher than the average level. This experimental observation is called the jet pedestal effect. In peripheral collisions, with larger impact parameter, only a small fraction of events contain any high-p_{T} activity; whereas central collisions, with smaller impact parameter, are more likely to contain at least one hard scattering. The description of the jet pedestal by the MC models depends on the ability to describe the number of interactions as a function of the impact parameter, which is one of the main tuning parameters.

The UE is closely linked to what is often called *minimum bias* event. It consists of a small number of hadrons at low transverse momentum distributed across a wide range of rapidities in the final state of a proton-proton collision. It has been widely assumed that the effect of the UE can be removed by the subtraction of the minimum bias events. However, fluctuations in the amount of underlying event and correlations between the UE and the measured jets makes this procedure to possibly underestimate the size of the UE corrections.

3.5.5 Decays of unstable particles

Following the hadronisation phase of the event generation, a number of unstable hadrons are produced, which must decay into particles that are stable on collider timescales. This is an important part of the event simulation, because the observed final-state hadrons result from a convolution of hadronisation and decay, so that a particular set of tuned hadronisation parameters is applicable only in combination with a particular decay package.

The first choice that must be made is which hadrons to include in the simulation. This choice is generator specific and closely connected with the tuning of hadronisation parameters. In the cluster model, in particular, it is important that all the light members of a multiplet are included, as the absence of members can lead to isospin or $SU(3)$ flavour violation at an unphysical rate. All the general-purpose event generators include the lightest pseudoscalar (see Figure 3.9), vector, scalar, even and odd charge conjugation pseudovector, and tensor multiplets of light mesons. In addition, some excited vector multiplets of light mesons are often included.

Historically, the standard generators included few matrix elements for hadron decays and at best used a naive Breit-Wigner smearing of the masses of the particles. More sophisticated simulation of hadronic decays was then performed using specialised external packages such as EvtGen [79] for hadron decays. This still holds true for Pythia8, while Sherpa now includes much better simulation of hadronic, and particularly tau lepton decays.

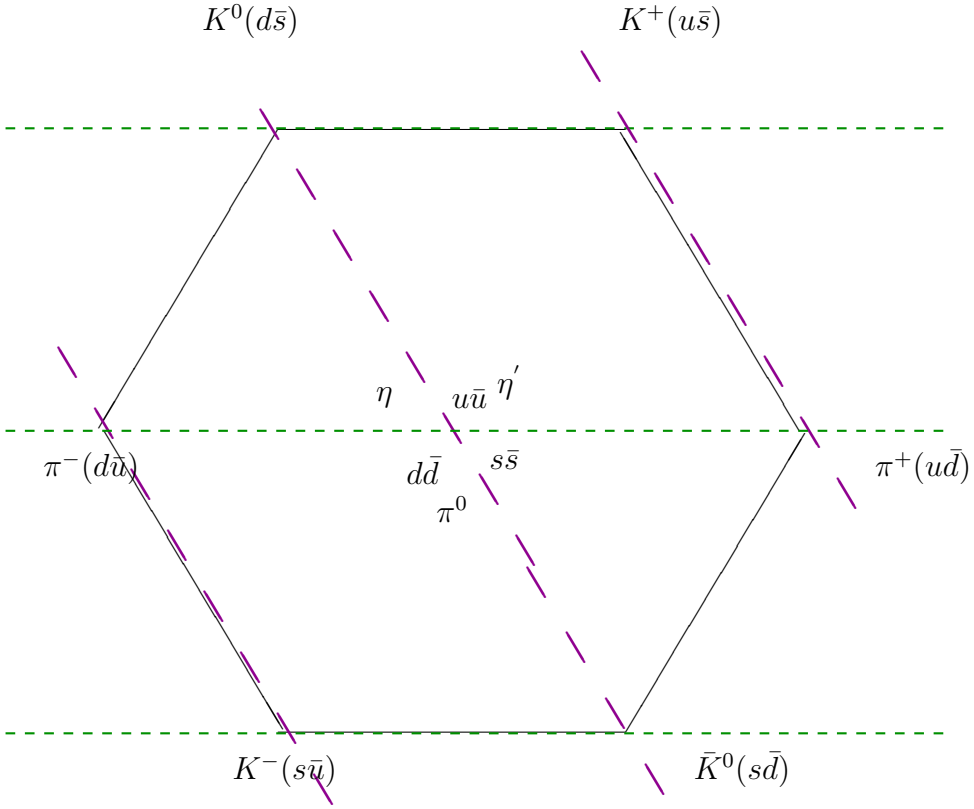


Figure 3.9: SU(3) octet of lightest mesons. The dashed green line join particles with same strangeness quantum number while magenta dashed lines pass through particles with the same electric charge.

3.5.6 Detector simulation

The simulation of the ATLAS detector was carried out using the GEANT4 package. Once the final-state particles have been generated, the signals that these particles produced in the different parts of the detectors based on their energy, position and kind of particle must be simulated. The GEANT4 particle simulation toolkit uses a highly-detailed detector description and provides detailed models for physics processes and the infrastructure for particle transportation through a given detector geometry.

To be able to reconstruct these signals, all the samples of generated events were passed through the GEANT4-based [78] detector simulation.

3.5.7 Monte Carlo programs used in the analyses

To study the characteristics of the signal and perform the unfolding of the measurements to particle level, MC samples were used in the analyses presented in this thesis. In addition, these samples are used to estimate the hadronisation corrections to parton-level NLO QCD calculations. As mentioned at the beginning of this chapter, samples of Pythia 8.186 [76] and Sherpa LO are used for these purposes while Sherpa 2.2.2 (Sherpa NLO), with NLO matrix elements, are used to compare with the measurements.

The PDF sets used to parameterise the proton structure are NNPDF2.3 [80] in Pythia and NLO CT10 [81] for Sherpa. The event generator parameters were set according to the "A14" tune for Pythia [82] and the "CT10" tune for Sherpa (the default tune for Sherpa, not fitted to ATLAS data).

The fragmentation contribution (or bremsstrahlung contribution) is simulated differently in Pythia and Sherpa LO. In Pythia, photons can be radiated in the parton shower without a restriction on the opening angle with respect to the parent parton and, as a result, the photons can be emitted very close to the parton direction. In Sherpa, photons are not emitted in the parton shower and the bremsstrahlung component is simulated through matrix elements of $2 \to n$ processes with $n \geq 3$. Collinear singularities are avoided by restricting the emission through the implementation of a smooth-cone isolation requirement with parameters ($\delta_0 = 0.3$, $n = 2$ and $\epsilon = 0.025$); as a result, photons are not emitted close to the parent parton in Sherpa.

Although there is no straightforward mapping between the smooth-cone isolation criterion and the standard-cone criterion, a twofold concern may arise in the use of Sherpa samples due to isolation imposed at the matrix-element level:

- the modelling of non-isolated photons, which is needed for background subtraction (see Section 6.3), could be biased. This is tackled by assessing a systematic uncertainty in the measurements in which a comparison is made with Pythia. The resulting systematic uncertainty is subdominant in all the analyses performed;

- the predictions of the differential cross sections could also be underestimated in some regions of the phase space in which the smooth-cone isolation is tighter than the one applied at particle level with the standard-cone isolation. This was studied using Sherpa NLO samples, generated with a looser isolation requirement (see below). The tighter isolation of the LO samples at parton level was mimicked in the Sherpa NLO samples and the differential cross-section predictions for isolated photons were

confronted with the default results obtained with NLO SHERPA. The differences in the predictions were found to be typically lower than 0.5% and, thus, neglected.

The MC samples were subjected to different filters during the generation of the events in the following way:

- PYTHIA:
  - The samples were generated with a cut on $\hat{p}_{\mathrm{T}}$. For each slice, the cut on $\hat{p}_{\mathrm{T}}$ is 0.5 times the lowest threshold in E_{T}^{γ} requirement, e.g. for the slice 70–140 GeV the cut on $\hat{p}_{\mathrm{T}}$ was 35 GeV. This was made to ensure that there is no bias in the spectrum in the region close to the lowest threshold.
  - The samples were filtered in E_{T}^{γ}. A particle-level photon (after the parton-shower) was required to fulfil the (double-sided) conditions of the slice, i.e. for the slice 70–140 GeV a photon in that range was required. In the same filter, a cut on the photon pseudorapidity (η^{γ}) was applied ($|\eta^{\gamma}| < 2.5$). This is the reason why the cutoff for each slice is so sharp in Figure 3.10(a).
- SHERPA:
  - The samples were generated with a cut on E_{T}^{γ} at the matrix-element level (e.g. 70–140 GeV for the corresponding slice). There was no restriction on η^{γ} and no filter was applied. For this reason, each slice extends both below and above the E_{T}^{γ} requirements (no sharp cutoff as in PYTHIA). However, this was done in such way that the different slices can be simply added (without double counting). There is a bias in the region close to the lowest threshold for the first slice (70–140 GeV), which does not affect this analysis since the phase-space region starts at 125 GeV.

For the PYTHIA samples, it was found that in events in which more than one photon is generated, the leading photon may fall out of the E_{T}^{γ} range of the given slice[5]. In such cases, it was observed that peaks appear at values of E_{T}^{γ} higher than the one corresponding to the given range; e.g. the peaks at ~ 700 GeV and ~ 1 TeV from the 70–140 GeV slice seen in Figure 3.10(a) (black histogram). The contribution of the events from the 70–140 GeV slice to the region ~ 700 GeV would then be of the same size as that from events in the "relevant" slice (500–800 GeV slice), but it is affected by a huge statistical uncertainty. Therefore, events in which the leading photon is not within the given range in each slice are removed[6]. Figure 3.10(b) shows the E_{T}^{γ} spectrum after this removal. This problem is not present in the SHERPA samples (see Figure 3.10(c)). Dedicated MC samples without underlying event were generated at particle and parton levels to correct the NLO calculations for hadronisation and underlying-event effects.

To compare the measurements with QCD NLO predictions, signal samples of SHERPA NLO were also generated. The SHERPA NLO program consistently combines parton-level

[5]The photon filter used in the generation of the PYTHIA MC samples selects an event if there is at least one true photon fulfilling the conditions; this photon might not be the leading true photon, which is the one considered in this analysis.

[6]The fraction of events removed in each slice is: $3.1 \cdot 10^{-4}$ for the $70-140$ GeV slice, $2.0 \cdot 10^{-4}$ for the $140-280$ GeV slice, $1.5 \cdot 10^{-4}$ for the $280-500$ GeV slice, $1.6 \cdot 10^{-4}$ for the $500-800$ GeV slice, $2.5 \cdot 10^{-4}$ for the $800-1000$ GeV slice, $1.0 \cdot 10^{-4}$ for the $1000-1500$ GeV slice, $7.1 \cdot 10^{-5}$ for the $1500-2000$ GeV slice, $4.2 \cdot 10^{-5}$ for the $2000-2500$ GeV slice and $3.1 \cdot 10^{-5}$ for the $2500-3000$ GeV slice.

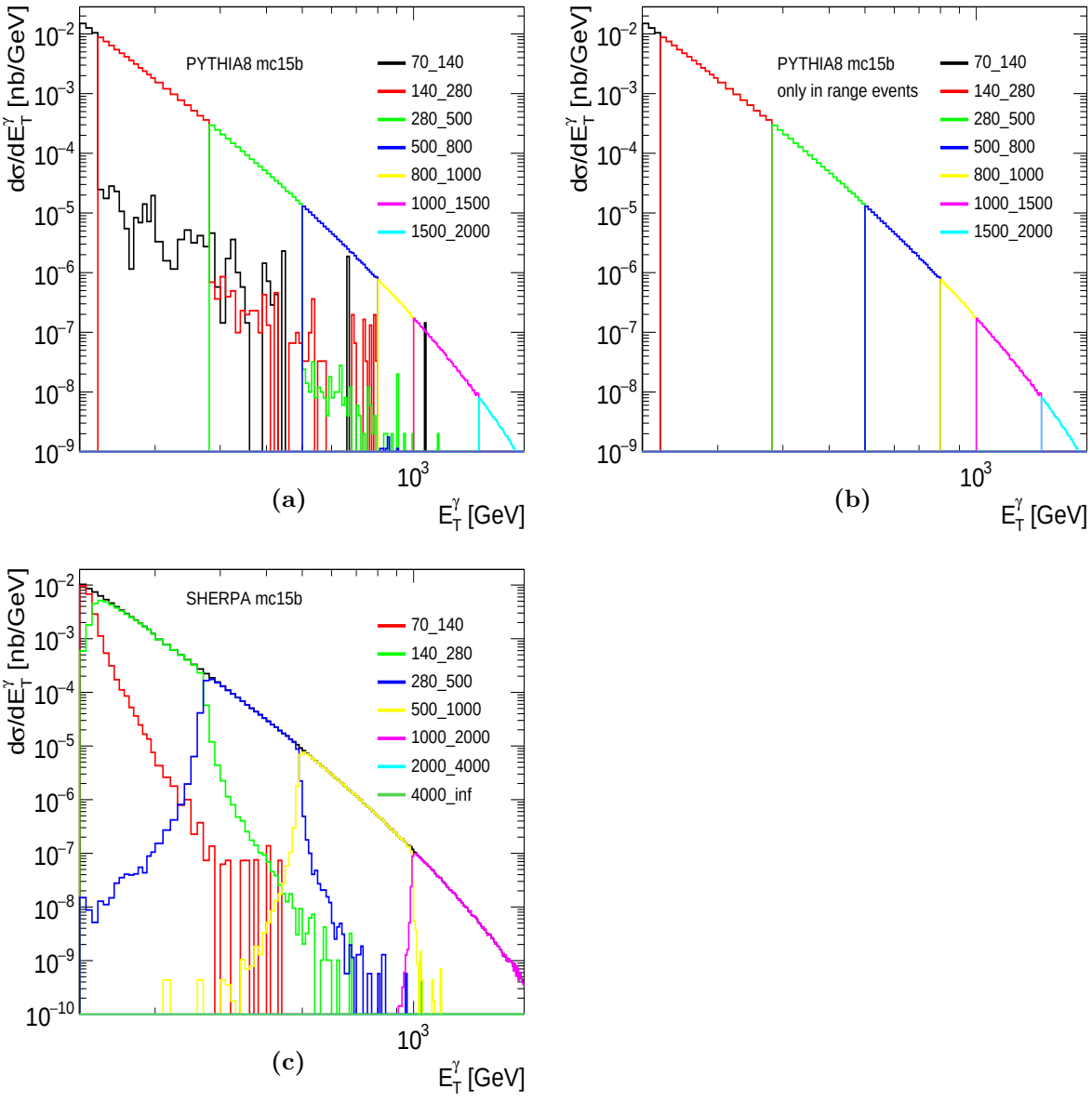


Figure 3.10: Generated E_{T}^{γ} distributions for the different slices of (a) Pythia, (b) Pythia after restriction of the E_{T}^{γ} ranges in each slice and (c) Sherpa LO.

calculations of $\gamma + 1,\ 2$ jets at NLO and $\gamma + 3,\ 4$ jets at LO [83] supplemented with a parton shower [84] while avoiding double-counting effects [85]. A requirement on the photon isolation at the matrix-element level was imposed using a smooth-cone criterion with $\delta_0 = 0.1$, $n = 2$ and $\epsilon = 0.1$. The factorisation and renormalisation scales of the core process was set to E_{T}^{γ}, while α_{EM} was evaluated in the Thomson limit. The merging scale was set up dynamically in the scheme of [86] using as fixed cut $\bar{Q}_{cut} = 20$ GeV. The strong coupling constant was set to $\alpha_s(m_Z) = 0.118$. Fragmentation into hadrons and simulation of the UE were performed using the same models as for the LO SHERPA samples. The NNPDF3.0NNLO PDFs [59] are used in conjunction with the corresponding SHERPA tuning. The samples were generated with additional weights for the NNPDF3.0NNLO replicas, α_s variations of ± 0.002 around the nominal value of 0.118, as well as 7-point scale variations of the factorisation and renormalisation scales. These samples were used in the photon plus jet and photon plus two jets analyses.

3.6 Fixed-order pQCD predictions with JETPHOX

In the inclusive photon and photon plus jet analyses the fixed-order NLO QCD predictions were computed using the JETPHOX program based on the MMHT2014 [87] parameterisation of the PDFs inside the proton. This program includes a full NLO QCD calculation of both the DP and F contributions to the cross section. It also adds the dual gluon-initiated box diagram. The calculations are based on a combination of the phase-space slicing and subtraction methods to treat the soft and collinear singular parts of the perturbative matrix elements [64]. For the calculations presented here, the number of active flavours was set to five. The renormalisation (μ_R), factorisation (μ_F) and fragmentation (μ_f) scales were chosen to be $\mu_R = \mu_F = \mu_f = E_{\mathrm{T}}^{\gamma}$. The set of photon fragmentation functions used in the calculation was the BFG set II [4]. The strong coupling constant was calculated at two loops with $\alpha_s(m_Z) = 0.120$. Photon isolation was ensured by applying the same cone-isolation criterion as in the particle level of each analysis. The anti-k_t algorithm was applied to partons in the events generated by this program to compute the cross-section predictions.

After applying the analyses requirements, the parton level cross sections extracted from the program were corrected for hadronisation and UE effects to compare with the measured cross sections. The correction factor, C_{NLO} was defined as the ratio of the cross section at particle level with UE and that at parton level without UE and computed using MC samples of events. This correction factor corrects only for the residual effects of hadronisation and UE after subtraction using the jet-area method [88]. The correction factor can be factorised into two parts:

$$C_{NLO} = C_{\mathrm{had}} \cdot C_{UE},$$

where C_{had} is the ratio of the cross sections at particle level and at parton level without UE effects and C_{UE} corrects the NLO QCD calculations to include the residual effects of the UE. The latter is computed as the ratio of the cross section at particle level with UE and that without such an effect. Specific details are discussed in the chapters dedicated to each analysis.

4

Photon reconstruction, identification and calibration

In this chapter, the features of prompt photons (those not secondaries to hadron decays) as seen in the ATLAS detector are presented and the procedure to identify them, by exploiting these characteristics, is explained.

4.1 Photon reconstruction

The electromagnetic shower originated when an energetic photon interacts with the material of the EM calorimeter deposits a significant amount of energy in a small number of neighbouring calorimeter cells. Due to their similar signatures in the EM calorimeter, the reconstruction of photons and electrons proceeds in parallel.

The reconstruction of photon candidates in the region $|\eta| < 2.5$ begins with a preliminary set of seed clusters of EM calorimeter cells. Seed clusters of size $\Delta\eta \times \Delta\phi = 0.075 \times 0.175$ (corresponding to 3×7 EM calorimeter towers) with $p_{\mathrm{T}} > 2.5$ GeV are formed by a sliding-window algorithm [89] with an estimated initial cluster reconstruction close to 100% for photons with $E_{\mathrm{T}} > 20$ GeV. Clusters of 5×5 cells of the middle layer are used in the end-caps.

After cluster reconstruction, tracks that are *loosely matched* to the cluster are searched for in the inner detector. These are useful for the reconstruction of electrons and e^+e^- pairs in the case of photon conversions. A track is loosely matched if the angular distance between the cluster barycentre and the extrapolated intersection point of the track with the second sampling of the calorimeter is smaller than 0.05 (0.2) along the ϕ in the direction of (opposite to) the bending of tracks in the magnetic field of the ATLAS solenoid, and smaller than 0.05 along η for tracks with hits in the pixel and SCT detectors. Tracks are then extrapolated from the point of closest approach to the primary vertex if they have hits in the silicon detectors or otherwise from the last measured point to the position corresponding to the expected maximum energy deposit for EM showers. Tracks can suffer significant bremsstrahlung losses before reaching the calorimeter, lowering the momentum of the track; in those cases, they are also considered after rescaling the track momentum to the cluster energy. Tracks loosely matched to a cluster and with hits in the silicon detectors are refitted with a Gaussian-sum-filter technique to improve the track parameter resolution.

Tracks from photon conversion are parallel at the place of conversion and geometric requirements are used to select these track pairs. Three categories are built to classify

these pairs: both tracks (Si-Si), only one of them (Si-TRT) or none of them (TRT-TRT) with hits in the silicon detectors. The following requirements must be satisfied by the tracks to be retained:

- $\Delta \cot \theta$, where θ is the polar angle taken at the track's points of closest approach to the primary vertex, between the two tracks must be less than 0.3 for Si-Si tracks and 0.5 for the other two categories. This requirement is not applied to TRT-TRT track pairs with both tracks in the central region, $|\eta| < 0.6$;
- the distance of closest approach between the two tracks must be less than 10 mm (50 mm) for Si-Si track pairs (TRT-TRT or Si-TRT pairs);
- the difference between the sum of the radii of the helices that can be constructed from the electron and positron tracks and the distance between the centres of the two helices is between -5 and 5 mm, -50 and 10 mm, -25 and 10 mm for Si-Si, TRT-TRT and Si-TRT respectively;
- the difference in azimuthal angle between the two tracks must be less than 0.05 (0.2) for Si-Si tracks and 0.2 for the other two categories.

Furthermore, requirements related to the conversion vertex are applied:

- the χ^2 of the conversion vertex fit must be less than 50. The fit is performed taking into account helix parameters of both tracks in the pair;
- the distance from the vertex to the beam line in the transverse plane, known as the radius of the conversion vertex, must be greater than 20, 70 and 250 mm for vertices from Si-Si, Si-TRT and TRT-TRT track pairs, respectively;
- the azimuthal difference between the vertex position and the direction of the reconstructed conversion must less than 0.2.

For conversions happening in the outermost layers of the inner detector, the efficiency of photon-conversion reconstruction as double-track vertex candidates decreases significantly. This effect is due to photon conversions in which one of the two electron tracks is not reconstructed either because it is very soft (asymmetric conversion), or because the two tracks are very close to each other and cannot be adequately separated. Therefore, tracks without hits in the $b-$layer with no hits in TRT or with an electron likelihood greater than 95% are considered as *single-track* conversion vertex candidates. In this case, the conversion vertex is defined with respect to the location of the first measurement of the track. Unless they miss the hit in the second pixel layer, a track which passes through a passive region of the b-layer is not considered as a single-track.

The matching of the conversion vertices to the clusters also relies on an extrapolation of the conversion candidates to the second sampling layer of the calorimeter. The details of the extrapolation depend on the type of conversion vertex candidate. For a double-track conversion vertex candidate with track transverse momenta that differ by less than a factor of four from each other, each track is extrapolated to the second sampling layer of the calorimeter and is required to be matched to the cluster. If the ratio between the tracks momenta is larger than four times the photon direction is reconstructed from the electron and positron directions determined by the conversion vertex fit and matched

with a straight line to the second layer of the calorimeter. For single-track conversion candidates, the track is extrapolated from its last measurement.

The final distinction of the reconstructed objects in converted photons, unconverted photons and electrons for the reconstructed objects is performed as follows:

- clusters to which neither a conversion vertex candidate nor any track matched to it are considered as unconverted-photon candidates;
- electromagnetic clusters matched to a conversion vertex candidate are considered as converted photon candidates. The object is removed from the converted photon candidates if the track does not coincide with any of the tracks assigned to the conversion vertex candidates unless the track p_{T} is smaller than the p_{T} of the converted photon candidate or if the coinciding track has a hit in the $b-$layer, while the other track lacks one;
- single-track converted photon candidates are recovered from objects that are only reconstructed as electron candidates with $p_{\mathrm{T}} > 2$ GeV and $E/p < 10$, where E is the cluster energy and p the track momentum, if the track has no hit in the silicon detectors;
- unconverted-photon candidates are recovered from electron candidates if the electron candidate has a corresponding track without hits in the silicon detectors and with $p_T < 2$ GeV, or if the electron candidate is not considered as single-track converted photon and its matched track has a transverse momentum lower than 2 GeV or E/p greater than 10.

From simulations, it was determined that only 4% of prompt photons are incorrectly reconstructed as electrons for $E_{\mathrm{T}} > 25$ GeV. The efficiency to reconstruct photon conversions decreases at high E_{T} (> 150 GeV), where it becomes more difficult to separate the two tracks from the conversions. More details about photon identification can be found in Reference [90] and references therein.

The final photon energy measurement is performed using a cluster size that depends on the classification of the photon candidates. The photon energy calibration accounts for upstream energy loss and both lateral and longitudinal leakage and it is described in the next section.

4.2 Photon calibration

Electrons and photons entering the LAr calorimeter develop EM showers through their interaction with lead absorbers. The EM showers ionise the LAr in the gaps between absorbers. The ionising electrons drift and induce an electrical signal on the electrodes which is proportional to the energy deposited in the active volume of the calorimeter. The signal is brought via cables to read-out Front End Boards, where it is first amplified. To optimise the total noise due to electronics and out-of-time pile-up (inelastic pp collisions coming from previous bunch crossings), the signal is shaped by a bipolar filter and simultaneously amplified with three linear gains: low (LG), medium (MG) and high (HG). The sample corresponding to a maximum amplitude of the physical pulse stored in MG is first digitised by an analog-to-digital converter (ADC). Based on this sample, a hardware

gain selection is used to choose the most suited gain which is then digitised. The total energy deposited in an EM calorimeter cell is reconstructed as:

$$E_{cell} = F_{\mu A \to MeV} \times F_{DAC \to \mu A} \times \frac{1}{\frac{M_{phys}}{M_{cali}}} \times G \times \sum_{j=1}^{N_{samples}} a_j (s_j - p_j), \tag{4.1}$$

where s_j are the samples of the shaped ionisation signal digitised in the selected electronic gain, measured in ADC counts in $N_{samples}$ ($N_{samples} = 4$ in Run-2) time slices spaced by 25 ns; p is the read-out electronic pedestal measured for each gain in dedicated calibration runs; a_j are the weights of the optimal filter coefficients (OFC) derived from the predicted shape of the ionisation pulse and the noise autocorrelation; G is the cell gain computed by injecting a known calibration signal and reconstructing the corresponding cell response; the factor $\frac{M_{phys}}{M_{cali}}$ quantifies the ratio of the maxima of the physical and calibration pulses corresponding to the same input current and corrects for the gain factor G; the factor $F_{DAC \to \mu A}$ converts digital-to-analog converter (DAC) counts set on the calibration board current to μA and the factor $F_{\mu A \to MeV}$ converts the ionisation current to the total deposited energy at the *EM scale*; this factor is determined from test-beam studies. The EM scale measures correctly the energy deposited in the calorimeter by particles produced in the electromagnetic showers.

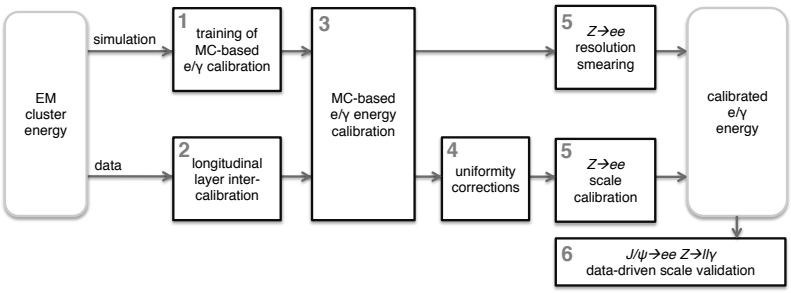


Figure 4.1: Schematic overview of the procedure used to calibrate the energy response of electrons and photons in ATLAS.

The photon energy calibration is done in different steps as follows:

1. The electromagnetic cluster properties, including its longitudinal development, are calibrated to the original photon energy simulated in MC samples using multivariate techniques. This constitutes the core of the MC-based photon response calibration that will be covered later in step 3 (see Figure 4.1). The calibration constants are determined using a multivariate algorithm (MVA) separately for electrons, converted and unconverted photons in different η and p_{T} bins. This correction takes into account the energy lost in the material upstream of the calorimeter, the energy deposited in the cells neighbouring the cluster and the energy lost beyond the LAr calorimeter. The quantities used in the MVA are the total energy measured in the calorimeter, E_{calo}; the ratio of the presampler energy to the calorimeter energy, E_0/E_{calo}; the shower depth ($X = \sum_i X_i E_i / \sum_i E_i$, where E_i and X_i are the cluster energy and the calorimeter thickness in radiation length in layer i); the cluster barycentre pseudorapidity in the ATLAS coordinate system, $\eta_{cluster}$; and the cluster barycentre in η and ϕ within the calorimeter frame. The variable $\eta_{cluster}$ is used to take into account the different quantity of passive-material in front of the calorimeter.

The barycentre location in the calorimeter frame is used to correct for the increase of lateral energy leakage for particles that hit the cell close to the edge and for the sampling fraction variation as a function of the particle impact point with respect to the calorimeter absorbers. For converted photons, the conversion radius is used as an additional variable in the MVA if the momenta of the conversion track, p_{T}^{conv}, is larger than 3 GeV. For Si-TRT and TRT-TRT photon conversions, additional quantities are considered: the ratio $p_{\mathrm{T}}^{conv}/E_{calo}$ and the momentum fraction carried by the highest-p_T track. At the end of the optimisation, the energy response is optimised while the root mean square resolution is minimised. The presence of tails in the energy response results in remaining non-linearities; these non-linearities are removed by adjusting the peak position of the ratio of the output energy and the true energy to unity.

A prerequisite of the MC-based calibration is that the detector geometry and the interaction of particles with matter are accurately described in the simulations. The material distribution is measured in data using the ratio of the first to the second-layer energy in the EM calorimeter ($E_{1/2}$). Measuring this ratio in data with samples of electron and unconverted photons allows a precise determination of the amount of material in front of the EM calorimeter. Higher values of $E_{1/2}$ in data would indicate earlier shower development and local excess of material in comparison with the simulation. Electrons are sensitive to all detector material crossed along their trajectory; unconverted photons are insensitive to the inner-detector material upstream of the conversion radius. Within the presampler acceptance ($|\eta| < 1.82$), a veto on the presampler activity can be required to minimise the probability that a conversion happened in front of the presampler, making the photon candidate sensitive to the passive material between the presampler and the first layer of the EM calorimeter. The sensitivity of these two probes to $E_{1/2}$ is evaluated in different simulated samples with distorted geometry. The simulations are improved after this measurement and the MC-based energy calibration explained above is applied using the new detector description. Systematic uncertainties are considered for the LAr $E_{1/2}$ modelling, the GEANT4 simulation of the material, the first layer gain and data-driven uncertainties in the material determination.

2. The electromagnetic calorimeter is longitudinally segmented and the scales of the different longitudinal layers have to be equalised in data and MC prior to the overall energy scale determination to ensure the correct extrapolation of the response in the full p_{T} range used in the various analyses. The intercalibration of the first and second layers uses muons from $Z \to \mu\mu$ decays as probes, while the presampler energy is determined from energy distributions of electrons in data and simulation. The contribution of the third layer to the energy scale is generally negligible and no intercalibration is performed. Muon energy deposits in the calorimeter are insensitive to the amount of passive material upstream of the EM calorimeter and are a direct probe of the energy response. Muon energy deposits are very localised (most of the energy is deposited in one or two cells) and since the critical energy for muons interacting with the calorimeter is of the order of 100 GeV, most of the muons from Z decays are minimum ionising particles. The calorimeter cells crossed by the muons are determined by extrapolating the muon tracks to each layer of the calorimeter. The observed muon energy distribution in each layer is given by the convolution of a Landau distribution describing the energy deposit, and a Gaussian

distribution corresponding to the electronic noise. Denoting by $\langle E_{1/2} \rangle$ the ratio of the most probable value (MPV) of the energy deposits in the first and second layer, the resulting intercalibration is defined as $\alpha_{1/2} = \langle E_{1/2} \rangle^{data} / \langle E_{1/2} \rangle^{MC}$. Two different methods are used to determine the MPV of the deposited energy: a fit using the convolution model or a truncated mean. The difference between these two methods is taken as a systematic uncertainty. Uncertainties in the intercalibration are also propagated to the uncertainty in the modelling of $E_{1/2}$ for electrons and photons. The bias induced by data–MC differences is removed by applying a $|\eta|$–dependent correction to the layer intercalibration in data. The resulting uncertainty on the relative calibration of the first and second layer rises from 1% to 1.5% with the pseudorapidity in the barrel and is 1.5% in the end-cap.

The presampler energy scale, α_{PS}, is determined from the ratio of presampler energies in data and simulations using electrons from W and Z decays after the effects of passive-material mismodelling is taken into account. This is addressed by exploiting the expected correlation between $E_{1/2}$ and the presampler energy deposit, E_0, for electrons under variations of the passive material upstream of the presampler. The measured α_{PS} constitutes a correction factor that is applied to the data. This measurement is accurate, up to 2-3%, depending on η.

3. The MC-based e/γ response calibration is applied to the cluster energies reconstructed from both data and MC simulated samples.

4. Uniformity corrections to account for response variations not included in the simulation are performed. This is investigated using the E/p ratio for electrons in $W \to e\nu$ events and the electron pair invariant mass in Z decays. These corrections include: high voltage inhomogeneities, time dependence of the presampler response, energy loss between the barrel calorimeter modules, difference of the energy response in HG and MG and the azimuthal non-uniformity and operation stability after previous corrections.

5. Using a large sample of $Z \to ee$ events, the overall electron response in data is calibrated so it agrees with the expectation from simulation. The difference is parameterised as follows:

$$E^{\text{data}} = E^{\text{MC}}(1 + \alpha_i), \tag{4.2}$$

where the parameter α_i represents the departure from optimal calibration in a given pseudorapidity bin i. The relative energy resolution is parameterised as

$$\frac{\sigma(E)}{E} = \frac{a}{\sqrt{E}} \oplus \frac{b}{E} \oplus c, \tag{4.3}$$

where a is the sampling term related to shower fluctuations in the calorimeter, b the electronic noise term measured in calibration runs and c is the constant term.

The invariant mass in $Z \to ee$ events is used for the calibration and an analogous parameterisation is used,

$$m_{ij}^{\text{data}} = m_{ij}^{\text{MC}}(1 + \alpha_{ij}); \quad \alpha_{ij} \sim \frac{\alpha_i + \alpha_j}{2}, \tag{4.4}$$

neglecting second-order terms and assuming that the angle between both electrons is well known. The α_{ij} term is the induced shift in the mass peak. The resolution

curve is assumed to be well modelled by the simulation up to a Gaussian constant term, c'. For each (η_i, η_j) category, the mass resolution satisfies:

$$\left(\frac{\sigma_m}{m}\right)_{ij}^{\text{data}} = \left(\frac{\sigma_m}{m}\right)_{ij}^{\text{MC}} \oplus c'_{ij} \quad \text{with} \quad c'_{ij} = \frac{c'_i \oplus c'_j}{2}. \tag{4.5}$$

For these categories, templates are built with energy scale and resolution perturbations to the detector-level quantities, in a range covering the expected uncertainty in narrow steps, building a two-dimensional grid in the plane (α_{ij}, c'_{ij}). The optimal values, uncertainties and correlations for α_{ij} and c'_{ij} are obtained through a χ^2 minimisation. An alternative method replaces the templates by a parameterisation of the MC distributions and performs a likelihood fit to the energy scales. The parameterisation is based on the convolution of a Breit-Wigner function and a Gaussian distribution. The minimisation of the following likelihood

$$-\ln L_{\text{tot}} = \sum_{k=1}^{N_{\text{events}}} -\ln L_{ij}\left(\frac{m_k}{1+\alpha_{ij}}\right) \tag{4.6}$$

with respect to α_{ij} determines the energy scales.

6. The calibrated electron energy is validated with electron candidates from $J/\psi \to ee$ events in data. The scale factors extracted from $Z \to ee$ events are assumed to be valid also for photons. The assumption is validated using photon candidates from $Z \to ll\gamma$ events in data.

The final photon energy, E, is estimated from the energies E_i measured in the cluster cells of each electromagnetic calorimeter layer:

$$\begin{aligned} E = \Big[& a(E_{\text{tot}}^{\text{EM}}, |\eta|) + b(E_{\text{tot}}^{\text{EM}}, |\eta|) \times E_{\text{ps}} + c(E_{\text{tot}}^{\text{EM}}, |\eta|) \times E_{\text{ps}}^2 \\ & + \frac{s_{cl}^{\text{EM}}(X, |\eta|)}{f_{out}^{\text{EM}}(X, |\eta|)} \times \Big(\sum_{i=1,3} E_i\Big) \times (1 + f_{\text{leak}}(X, |\eta|)) \Big] \times F(|\eta|, \phi), \end{aligned} \tag{4.7}$$

where $a(E_{\text{tot}}^{\text{EM}}, |\eta|)$, $b(E_{\text{tot}}^{\text{EM}}, |\eta|)$ and $c(E_{\text{tot}}^{\text{EM}}, |\eta|)$ are parameters determined as functions of the energy deposited in the three layers of the calorimeter, $E_{\text{tot}}^{\text{EM}}$, and $|\eta|$; E_{ps} is the part of the cluster energy measured in the presampler corrected for the fraction deposited in the passive materials; X is the longitudinal barycentre of the EM shower; $s_{cl}^{\text{EM}}(X, |\eta|)$ is the correction factor that accounts for the EM sampling fraction; $f_{out}(X, |\eta|)$ is the lateral leakage correction; $f_{leak}(X, |\eta|)$ is the longitudinal leakage correction and $F(|\eta|, \phi)$ is an energy correction that refines previous corrections. Photon-specific uncertainties are considered to take into account inefficiencies (such as conversion reconstruction inefficiencies or fake conversions) and possible mismodelling of the correction parameters applied in the final photon calibration.

The preliminary photon calibration for Run-2 (used in the inclusive photon and the photon plus jet analyses) was based on corrections measured in Run-1. The data and MC samples used in Run-1 were reprocessed using the Run-2 reconstruction software. Some systematic uncertainties were re-estimated and others were added to take into account

the differences between the 2012 and 2015 data-taking periods. A total of 71 nuisance parameters were considered. The changes between the uncertainties for Run-2 and Run-1 are listed below:

- The LAr temperature was different in Run-1 and Run-2. From test-beam studies, the signal in the EM calorimeter shows a $-2\%/K$ dependence due to density and drift velocity variations. The difference in the α parameter between 2012 and the checks performed in 2015, $\Delta\alpha = \alpha_{2015} - \alpha_{2012}$, was taken into account in the systematics and it amounts to -0.45% in (end-cap C), -0.46% (barrel C), -0.42% (barrel A) and 0.0% (end-cap A). A systematic uncertainty due the temperature corrections was assigned to the energy of the photon candidates in the barrel (0.15%) and end-cap (0.25%).

- The relative difference in the layer intercalibration ratio, $E_{1/2}$, with the different reconstruction software used in 2012 and 2015 showed a maximum peak-to-peak deviation of $\sim (1.5 - 2)\%$. A conservative uncertainty of 1.5% constant in η was considered.

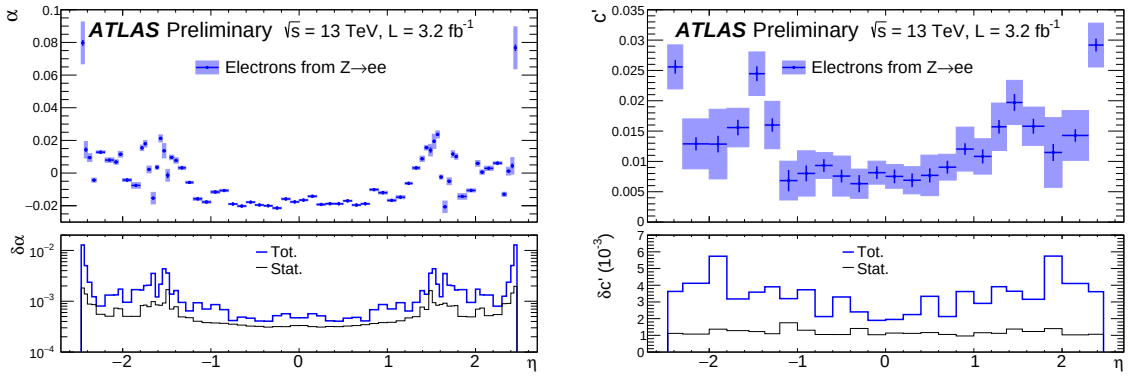
- Regarding the $Z \to ee$ in situ measurements, two additional uncertainties were considered:

  - For 2015, a double number of bins, 34, was taken for η_{calo}. This change revealed additional sub-patterns. A systematic uncertainty was defined as the absolute difference between the value of α for 34 bins and the simple average of two sub-bins. The results exhibit a variation of about 0.9% in the crack region and $|\eta_{\text{calo}}| > 2.4$ while remaining below 0.05% in the barrel and end-cap regions.
  - A systematic uncertainty was assigned to cover for the difference in the centre-of-mass energy. The measurement procedure was applied, using 13 TeV MC as data, and the resulting values of α and C were taken as systematic uncertainties. The resulting uncertainty is around 1% for C while the uncertainty on α is below 0.5%, except in the crack region, where it reaches up to 4%.

The same schema of systematic uncertainties was also considered for the analysis of the inclusive photon cross section ratios. In this case, a new uncertainty was considered to take into account the relative difference in photon energy response between the MG to HG ratio in Run-2 and Run-1. The value of the input uncertainty was based on the change in the cell energy observed for the change in the number of LAr-time samples (changed from five to four) and the optimal filter coefficients for these new timing samples. The resulting uncertainties on E_{T}^{γ} are $\approx 0.4\%$, except in $0.8 < |\eta| < 1.37$ where it increases up to $\approx 0.8\%$.

A more refined estimation of the photon energy scale uncertainties was used in the photon plus two-jets analysis. New energy scale corrections α_i and additional constant terms for the energy resolution (c_i') were estimated using the template procedure based on $Z \to ee$ events with Run-2 data. The results are shown in Figure 4.2. More details about the photon calibration procedure and the extrapolations between Run-1 and Run-2 can be found in References [91–93].

All other corrections were also estimated with Run-2 data. The only remaining extrapolation in the uncertainties between Run-1 and Run-2 is that of the material



(a) (b)

Figure 4.2: Energy scale α (a) and constant term c' (b) corrections derived from $Z \to ee$ events using the template method [91].

upstream of the calorimeter, for which an extra uncertainty was introduced to take into account the mismodelling of the new IBL material and the inner-detector patch panel region (PP0; significant discrepancies were observed between data and MC simulation at $\sqrt{s} = 8$ TeV in this PP0 region between $|\eta| = 2.2$ and $|\eta| = 2.5$ with important amounts of passive material). This more refined model consists of 67 nuisance parameters for the energy scale uncertainty.

Photon energy resolution accuracy

The main way to probe the resolution in data is provided by the study of the Z resonance width, which provides a constraint on the total resolution at a given η at $\langle E_{\mathrm{T}}^{e} \rangle \sim 40$ GeV, the average transverse energy of electrons from Z decays. The resolution corrections c (see equation 4.3) are obtained from the in-situ $Z \to ee$ measurements as an effective constant term to be added in quadrature to the expected resolution. However, c absorbs the potential mismodelling of the resolution sampling term, the electronic noise term, the asymptotic resolution at high energy, and the effect of passive material upstream of the calorimeter. The uncertainties on the photon resolution are parameterised with 9 nuisance parameters.

4.3 Photon identification

Energy deposits of single photons in the EM calorimeter are typically narrower and have smaller leakage in the hadronic calorimeter than those coming from the background of photon pairs originated from neutral meson decays (e.g. $\pi^0 \to \gamma\gamma$). The latter are often characterised by two separate local energy maxima in the finely segmented strips of the first layer of the EM calorimeter. All these differences are exploited by means of a cut-based algorithm applying independent requirements to several discriminating variables (DV) to achieve a good photon identification and background rejection from transverse momenta from 10 GeV to the TeV scale [90]. The presence of pile-up can distort the expected shape of the energy depositions, for both background and single photons, since

the pile-up tends to broaden the distributions of the DV and, thus, reduces the separation between background and single-photon candidates.

The set of discriminating variables used are:

- **Leakage in the hadronic calorimeter.**
  The *normalised hadronic leakage*, R_{had}, is defined as the total transverse energy, $E_{\text{T}}^{\text{had}}$, deposited in the hadronic calorimeter normalised to the total transverse energy, E_{T}, of the photon candidate:
  $$R_{\text{had}} = \frac{E_{\text{T}}^{\text{had}}}{E_{\text{T}}}. \tag{4.8}$$
  In the region $0.8 < |\eta| < 1.37$, the energy deposited in the whole hadronic calorimeter is used, while in other pseudorapidity intervals only the leakage in the first layer of the hadronic calorimeter is used (R_{had1}).

- **Variables using the second layer of the EM calorimeter.**
  The *middle η energy ratio, R_η,* is the ratio between the sum of the energies of the second layer of the EM calorimeter contained in a 3×7 rectangle in $\eta\times\phi$ ($E_{3\times7}^{S2}$), and the sum of the energies in the same layer in a 7×7 rectangle ($E_{7\times7}^{S2}$), both centred around the cluster seed:
  $$R_\eta = \frac{E_{3\times7}^{S2}}{E_{7\times7}^{S2}}. \tag{4.9}$$
  The *middle ϕ energy ratio*,
  $$R_\phi = \frac{E_{3\times3}^{S2}}{E_{3\times7}^{S2}}, \tag{4.10}$$
  uses the energy contained in a 3×3 rectangle and behaves differently for unconverted and converted photons, since the electron-positron pair bend in different directions in ϕ because of the solenoid magnetic field, producing larger showers in the ϕ direction for converted than for unconverted photons.

  The *middle lateral width*,
  $$w_2 = \sqrt{\frac{\sum E_i\eta_i^2}{\sum E_i} - \left(\frac{\sum E_i\eta_i}{\sum E_i}\right)^2}, \tag{4.11}$$
  measures the shower lateral width in the second layer of the EM calorimeter, using all cells in a window $\eta\times\phi = 3\times5$ measured in cell units.

- **Variables using the first layer of the EM calorimeter.**

  The *front side energy ratio*,
  $$F_{side} = \frac{E(\pm3) - E(\pm1)}{E(\pm1)}, \tag{4.12}$$
  measures the lateral containment of the shower, along the η direction, where $E(\pm n)$ is the energy in the $\pm n$ strip cells around the one with the largest energy.

The *front-lateral width (3 strips)*,

$$w_{s,3} = \sqrt{\frac{\sum E_i (i - i_{\max})^2}{\sum E_i}}, \tag{4.13}$$

measures the shower width along η in the first layer of the EM calorimeter, using two strip cells around the maximal energy deposit. In Equation 4.13, $i_{\max}$ identifies the strip with the highest energy and E_i is the energy deposited in each strip. The variables $w_{s,3}$ and F_{side} discriminate single showers from two showers merged into a wider maximum.

The *front-lateral width (total)*, $w_{s,tot}$, has a similar definition to $w_{s,3}$ but it makes use of all the cells in a window $\Delta\eta \times \Delta\phi = 0.0625 \times 0.196$, corresponding approximately to 20×2 strip cells in $\eta \times \phi$. This variable identifies wide showers consistent with jets.

The *front second-maximum energy difference*,

$$\Delta E = \left[E^{S1}_{2^{nd}\max} - E^{S1}_{\min} \right], \tag{4.14}$$

is the difference between the energy of the strip cell with the second-highest energy, $E^{S1}_{2^{nd}\max}$, and the energy in the strip cell with the smallest energy found between the first and second maxima, $E^{S1}_{\min}$ ($\Delta E = 0$ when there is no second maximum).

The *front maxima relative energy ratio*,

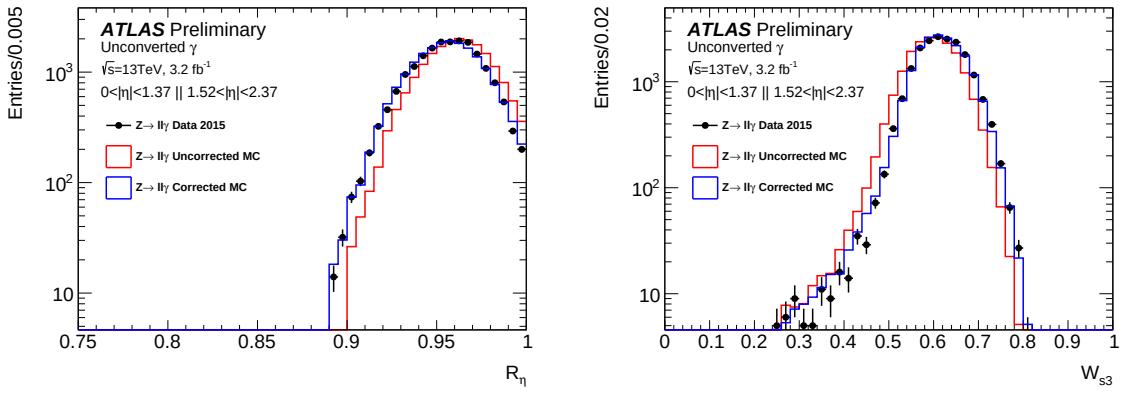
$$E_{\text{ratio}} = \frac{E^{S1}_{1^{st}\max} - E^{S1}_{2^{nd}\max}}{E^{S1}_{1^{st}\max} + E^{S1}_{2^{nd}\max}}, \tag{4.15}$$

measures the relative difference between the energy of the strip cell with the highest energy $E^{S1}_{1^{st}\max}$ and the energy in the strip cell with second-highest energy $E^{S1}_{2^{nd}\max}$ (E_{ratio} is set to unity if there is no second maximum). This variable, together with ΔE, provides rejection against showers with two different energy maxima, typical of light mesons decays into photons.

Two reference identification criteria are defined: *loose* and *tight*. The loose criterion is identical for converted and unconverted-photon candidates, it imposes loose cuts in the hadronic leakage, R_{had} and the variables computed using the second layer of the EM calorimeter. The tight selection is optimised separately for converted and unconverted photons and applies tighter cuts in the variables used in the loose selection plus cuts on the variables computed using the first layer of the calorimeter. Three other identification criteria are used in the analyses presented in this dissertation:

- *loose'*: imposes tight requirements on R_{had}, R_η, ω_2, R_ϕ and $\omega_{s,tot}$;
- *looser loose'*: same as loose', except for the exclusion of $\omega_{s,tot}$ (referred to as "LoosePrime5");
- *tighter loose'*: adds ΔE and E_{ratio} to the loose' ("LoosePrime2"). An alternative definition adding only E_{ratio} to the loose' definition is also investigated ("LoosePrime3").

The selection criteria for shower-shape variables are independent of the photon-candidate transverse energy, but vary as functions of η^{γ}, to take into account significant changes in the total thickness of the upstream material and variations in the calorimeter geometry and granularity. To improve the description of the photon DVs, corrections are applied to simulated events by applying a shift to each of them; the value of the shift is optimised separately for unconverted and converted photons as a function of η. Examples of DV distributions are shown in Figure 4.3 for Run-2 data. Photons with $E_{\mathrm{T}}^{\gamma} < 25$ GeV were selected from $Z \to l^{+}l^{-}\gamma$ decay events, while those with $E_{\mathrm{T}}^{\gamma} \geq 25$ GeV were required to fulfil isolation and tight ID criteria.



(a) (b)

Figure 4.3: Examples of shower-shape variables (R_{η} in (a) and ω_{s3} in (b)) for unconverted photons from [94]. $Z \to l^{+}l^{-}\gamma$ data are represented with black dots, the red histogram represents the MC simulations before applying any correction and the blue histogram shows the prediction of the corrected MC.

A systematic uncertainty was considered in the analyses to take into account the photon-identification efficiency. For the analyses with 2015 data only, the efficiency was set to unity and its uncertainty was estimated by switching the MC corrections to the identification DV on and off. For the photon plus two jets analysis, scale factors to be propagated in the analysis and its corresponding uncertainties were derived using data-driven photon-efficiency measurements [90]. Three different methods with partial overlaps are used within ATLAS:

- radiative Z boson decays: this method relies on the use of a pure photon sample selected from radiative decays of the Z boson, $Z \to l^{+}l^{-}\gamma$, and allows precise measurements in the low E_{T}^{γ} region. The $e^{+}e^{-}\gamma$ and $\mu^{+}\mu^{-}\gamma$ channels were combined after checking that they were giving consistent results;

- electron extrapolation: an electron sample from $Z \to ee$ decays is used to obtain a pure sample of electromagnetic showers from data. The differences between photon and electron showers are taken from the simulation and applied to the observed showers from electrons to describe those produced by photons. This method covers an intermediate E_{T}^{γ} range;

- matrix method: this method exploits photons reconstructed in collision data, which are contaminated by hadronic background. The isolation of reconstructed photons

is used as a discriminating property to extract the purity of the sample before and after photon identification. It is the only method that covers a wide range of E_{T}^{γ}.

4.4 Photon isolation

The isolation transverse energy, $E_{\mathrm{T}}^{\mathrm{iso}}$, is reconstructed by using topoclusters calibrated at the EM scale within a cone of radius $R = 0.4$ in the $\eta - \phi$ plane around the photon-cluster barycentre. Topological clusters [95] are clusters seeded by cells with an energy significantly above the noise threshold for that cell. The clusters are then expanded by adding neighbouring cells in the three spatial directions across all calorimeter layers that have an energy more than two times above the noise level. These topological clusters are not further calibrated, that is, they remain at the EM scale. All positive-energy topological clusters with a barycentre within the isolation cone are summed into the raw isolation variable $E_{\mathrm{T,raw}}^{\mathrm{iso}}$. This is illustrated in Figure 4.4.

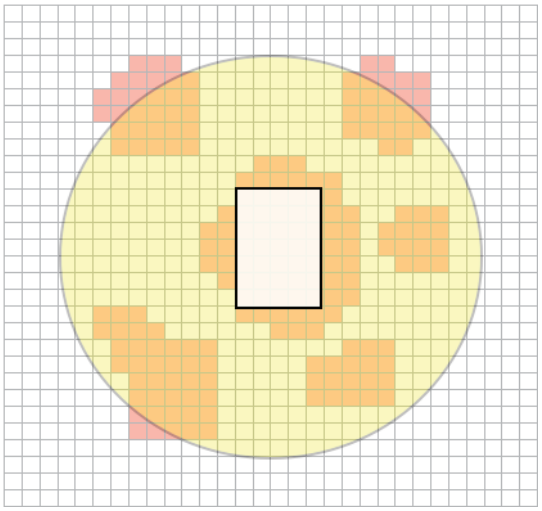


Figure 4.4: Schema of the $E_{\mathrm{T,raw}}^{\mathrm{iso}}$ variable: the grid represents the middle calorimeter cells in the $\eta \times \phi$ plane. The photon is located in the centre of the yellow cone representing the isolation cone. Topological clusters with a barycentre within the isolation cone are represented in red. The 5×7 cells in the white rectangle corresponds to the photon core.

The photon energy included in the $E_{\mathrm{T,raw}}^{\mathrm{iso}}$ computation, which is referred to as the core energy, $E_{\mathrm{T,core}}$, has to be subtracted from the raw isolation variable. For photons, this is done by removing the cells included in the 5×7 rectangle around the photon direction. This provides a stable subtraction for real or fake objects for any transverse momentum and pile-up conditions. After the core removal, there is still some leakage of the photon energy into the cone which is further subtracted. The leakage is evaluated by using single-particle Monte Carlo samples without pile-up. The leakage is estimated for converted and unconverted photons in different η bins as a function of E_{T}^{γ}. The estimator used to quantify the leakage energy is the most probable value of a Crystal-Ball function [96] as

$$E_{\mathrm{T,leakage}}(p_{\mathrm{T}}) = \mu_{CB}(p_{\mathrm{T}}) \times E_{\mathrm{cal}} / \cosh(\eta_{\mathrm{cluster}}), \tag{4.16}$$

where E_{cal} is the calibrated energy of the photon and η_{cluster} is the associated cluster η position. This technique has two important limitations: it is evaluated on average (it does

not account for shower-shape fluctuations at a given E_{T}) and relies on the MC description of the lateral shower shapes.

Further corrections are applied to the isolation to account for the effects from underlying-event modelling and pile-up effects and to match the definition between data and theory. Those corrections are estimated using the so-called *jet area method* [88]. In this method, low-energy jets are used to compute an ambient transverse energy density in an event-by-event basis using the FastJet package [97] as follows:

- positive-energy topological clusters in the calorimeter acceptance up to $|\eta| = 5$ are used to reconstruct jets with the anti-k_t algorithm (see Section 3.3.2) with $R = 0.5$;
- the area, A_i, of each jet in the event is estimated from a Voronoi tessellation algorithm;
- the transverse energy density of each jet is computed as $\rho_i = p_{T,i}/A_i$;
- the median of the distribution of all the transverse energy densities in the event, $\langle\rho\rangle$, is used as an estimator of the transverse energy density of the event.

The pile-up and underlying-event corrections are then evaluated as:

$$E_{\mathrm{T,pile-up+UE}}(\eta) = \langle\rho\rangle(\eta) \times (\pi R^2 - A_{\mathrm{core}}), \tag{4.17}$$

where R is the radius of the isolation cone and A_{core} is the area of the core. The final isolation value is computed as:

$$E_{\mathrm{T}}^{\mathrm{iso}} = E_{\mathrm{T,raw}}^{\mathrm{iso}} - E_{\mathrm{T,core}} - E_{\mathrm{T,leakage}}(p_{\mathrm{T}}) - E_{\mathrm{T,pile-up+UE}}(\eta). \tag{4.18}$$

5 Jet reconstruction and calibration

Jets are reconstructed using the anti-k_t algorithm (see Section 3.3.2) using the FastJet package. The jet radius used in the analyses presented here is $R = 0.4$. Jets are formed using different inputs: stable particles from event generator of simulated events (particle jets or *truth jets*); reconstructed calorimeter topoclusters (calorimeter jets); or, inner detector tracks (track jets). In the first case, candidate particles are required to have a lifetime of $c\tau > 10$ mm and muons, neutrinos and pile-up activity are excluded. The exclusion of muons and neutrinos ensures that the particle jets are built from particles that leave significant energy deposits in the calorimeter. Calorimeter and track jets are reconstructed in data as well as in MC events.

Calorimeter jets are built from topoclusters. A topocluster is assigned an energy equal to the sum of the associated calorimeter-cell energies calibrated at the EM scale. The direction of a topocluster is defined from the centre of the ATLAS detector to the energy-weighted barycentre of the associated calorimeter cells, and the mass is set to zero. This calibration takes into account different effects, such as: calorimeter non-compensation (different scales of energy measured from hadronic and EM showers), inactive areas of the calorimeter, leakage outside the calorimeter, energy deposits below noise thresholds and energy of particles which are not included in the reconstructed jets or pile-up.

Jets are further calibrated offline to restore the jet energy scale to that of jets reconstructed at the particle-level scale. The calibration consists of several sequential steps represented in Figure 5.1 and explained below:

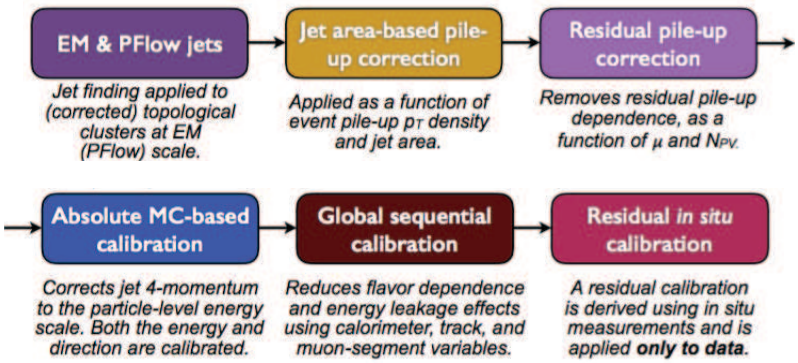


Figure 5.1: Overview of the ATLAS jet calibration.

- **Origin correction**. The four-momentum of the jets is recalculated to point to

the hard-scattering primary vertex rather than to the centre of the detector, while keeping the jet energy constant. This correction improves the η resolution of the jets.

- **Pile-up correction**. The pile-up correction removes the energy contamination due to in-time and out-of-time pile-up. This correction consists of two components; an area-based p_{T} density subtraction [88] applied at the per-event level, and a residual correction derived from the MC simulation. The area-based method subtracts the per-event pile-up contribution to the p_{T} of each jet according to its area. The pile-up contribution is calculated from the median p_{T} density ρ of jets in the $\eta - \phi$ plane. The calculation of ρ uses only positive-energy topoclusters within $|\eta| < 2$ that are clustered using the k_t algorithm with a jet radius of $R = 0.4$. The k_t algorithm is chosen for its sensitivity to soft radiation and is only used in the area-based method. The central $|\eta|$ selection is needed by the higher calorimeter occupancy in the forward region. The p_{T} density of each jet is taken to be p_{T}/A, where the area A of a jet is calculated using ghost association. In this procedure, simulated ghost particles of infinitesimal momentum are added uniformly in solid angle to the event before jet reconstruction. The area of a jet is measured from the relative number of ghost particles associated to a jet after clustering. The ratio between the ρ-subtracted jet p_{T} and the uncorrected jet p_{T} is taken as a correction factor applied to the jet four-momentum and does not affect the jet angular coordinates. The calculation of ρ is derived from the central, lower-occupancy regions of the calorimeter, since it does not describe fully the pile-up sensitivity in the forward calorimeter region or in the higher-occupancy core of high-p_{T} jets. It is observed that after this correction some dependence of the anti-k_t jet p_{T} on the amount of pile-up remains and an additional residual correction is derived. A dependence is seen on the number of primary vertices, N_{PV}, which is sensitive to in-time pile-up, and μ, which is sensitive to out-of-time pile-up. The residual p_{T} dependence on N_{PV} (α) and μ (β) are observed to be fairly linear and independent of each other. Linear fits are used to derive the α and β coefficients separately in bins of p_{T} and η. The pile-up corrected, p_{T}^{corr}, after the area-based and residual corrections, is given by

$$p_T^{corr} = p_T^{reco} - \rho \times A - \alpha \times (N_{PV} - 1) - \beta \times \ \mu, \tag{5.1}$$

where p_T^{reco} refers to the EM-scale p_T of the reconstructed jet before any pile-up correction is applied.

- **Monte Carlo-based jet energy scale and η calibration.** The jet energy scale and η calibration corrects the reconstructed jet four-momentum to the particle-level scale and accounts for biases in the jet η reconstruction. Such biases are primarily caused by the transition between different calorimeter technologies and the sudden change in calorimeter granularity. The calibration is derived from MC simulation using reconstructed jets after the application of the origin and pile-up corrections. The jet energy scale (JES) calibration is derived first as a correction of the reconstructed jet energy to the particle-level jet energy. Reconstructed jets are matched geometrically to particle-level jets within $\Delta R < 0.3$. Only isolated jets are used to avoid any ambiguities in the matching of calorimeter jets to particle-level jets. An isolated calorimeter jet is required to have no other calorimeter jet of $p_{\mathrm{T}} > 5$ GeV within $\Delta R = 1$, and only one particle-level jet of $p_{\mathrm{T}}^{truth} > 7$ GeV within

$\Delta R = 0.6$. The average energy response is defined as the mean of a Gaussian fit to the core of the ratio of the energy of the jet measured in the calorimeter (E^{reco}) and the jet energy at particle level (E^{truth}), E^{reco}/E^{truth}, binned in E^{truth} and the jet η pointing from the geometrical centre of the detector (η_{det}). The response is derived as a function of η_{det}, to remove any ambiguity as to which region of the detector is being measured. Gaps and transitions between calorimeter subdetectors result in a lower energy response due to absorbed or undetected particles, evident when parameterised in η_{det}. For each (E^{truth}, η_{det}) bin, the average jet energy response $\langle E^{reco} \rangle$ is derived from the mean of the E^{reco} distribution. The jet response calibration function is obtained for each η_{det} bin by a fit to the $\langle E^{reco} \rangle$ and $\langle \frac{E^{reco}}{E^{truth}} \rangle$ values obtained in each E^{truth} bin. The jet-calibration factor is taken as the inverse of the jet response calibration function. Good closure of the JES calibration is seen across the entire η range. A bias is seen in the reconstructed jet η as a function of η_{det} which is largest in jets that encompass two calorimeter regions with different energy responses caused by changes in calorimeter geometry or technology. This artificially increases the energy of one side of the jet with respect to the other, altering the reconstructed four momentum. The barrel-end-cap ($|\eta_{det}| \sim 1.4$) and end-cap-forward ($|\eta_{det}| \sim 3.1$) transition regions are the most affected by this effect. A second correction is therefore derived as the difference between the reconstructed η^{reco} and the particle-level η^{truth}, parameterised as a function of E^{truth} and $|\eta_{det}|$. Unlike the other calibration steps, the η calibration alters only the jet p_{T} and η, not the full four-momentum. Jets calibrated with the full energy scale and η calibration are considered to be at the EM+JES scale.

- **Global sequential calibration.** Following the previous calibrations, a residual dependence of the JES on longitudinal and transverse features of the jet is observed. Such differences may arise due to details of the detector interaction and of the particle composition of jets, with the response varying between quark- and gluon-initiated jets. Five observables are identified which improve the resolution of the jet energy through a global sequential calibration (GSC). For each observable, an independent jet four-momentum correction is derived by inverting the jet response in MC. An overall constant is applied to each numerical inversion to ensure the average energy is unchanged at each stage. The effect of each correction is to remove the dependence of the jet response for each observable while maintaining the overall energy scale at the EM+JES level. Corrections for each observable are applied independently and sequentially to the jet four-momentum, neglecting correlations between observables. No improvement was found from including such correlations or altering the sequence of the corrections. The five stages of the GSC account for the dependence of the jet response on (in order):

  - f_{Tile0}, the fraction of jet energy measured in the first layer of the hadronic Tile calorimeter ($|\eta_{det}| < 1.7$);
  - f_{LAr3}, the fraction of jet energy measured in the third layer of the electromagnetic LAr calorimeter ($|\eta_{det}| < 3.5$);
  - $width_{trk}$, the average p_{T}-weighted transverse distance in the $\eta-\phi$ plane between the jet axis and all tracks with $p_{\mathrm{T}} > 1$ GeV ghost-associated to the jet ($|\eta_{det}| < 2.5$);

  - n_{trk}, the number of tracks with $p_{\mathrm{T}} > 1$ GeV ghost-associated to the jet ($|\eta_{det}| < 2.5$);
  - $N_{segments}$, the number of muon segments associated to the jet ($|\eta_{det}| < 2.7$).

  The $N_{segments}$ correction reduces the tails of the response distribution caused by high-p_{T} jets that are not fully contained in the calorimeter, referred to as punch-through jets. The first four corrections are derived as a function of jet p_{T}, while the punch-through correction is derived as a function of jet energy, being better correlated with the energy escaping the calorimeters. The underlying distributions of these five observables are fairly well modelled by MC simulation. Slight differences with data have a negligible impact on the GSC as long as the dependence of the average jet response on the observables is well modelled in MC simulation. This average response dependence was tested using the dijet tag-and-probe method. The average p_{T} asymmetry between back-to-back jets was measured as a function of each observable and found to be compatible between data and MC; the differences are small compared to the size of the corrections.

- **In situ calibration methods.** The last step of the jet calibration accounts for differences in the jet response between data and MC simulation. Such differences arise from limitations in the description of the detector response and detector material, as well as in the simulation of the hard scatter, underlying event, pile-up, jet formation and electromagnetic and hadronic interactions with the detector. Differences between data and MC simulation are quantified by balancing the p_{T} of a jet against other well-measured reference objects. The η-intercalibration corrects the response of forward jets to well-measured central jets using dijet events. Three other in situ calibrations correct for differences in the response of central jets with respect to well-measured reference objects, each focusing on a different p_{T} region using Z-boson, photon and multijet systems. For each in situ calibration, a response $\mathcal{R}_{in\ situ}$ is defined in data and MC as the average p_{T} ratio between a jet and a reference object in a given region of p_{T}^{ref} of the reference object. It is proportional to the jet response in the calorimeter at the EM+JES scale, but it is also sensitive to secondary effects such as gluon radiation and the loss of energy outside of the jet radius. Assuming that these secondary effects are well modelled in the MC simulation, the ratio $c = \mathcal{R}^{data}_{in\ situ}/\mathcal{R}^{MC}_{in\ situ}$ is a useful estimation of the ratio between the JES in data and MC. The correction to the jet four-momentum is derived through a mapping from p_{T}^{ref} to the jet p_{T}. Event selections are designed to reduce the impact of any secondary effects, and their mismodelling in simulation is covered by systematic uncertainties derived from the choice of MC generator. The correction is derived as a function of jet p_{T}, and also as a function of jet η in the η-intercalibration. The η-intercalibration corrects the jet energy scale of forward jets ($0.8 < |\eta_{det}| < 4.5$) to that of central jets ($|\eta_{det}| < 0.8$) in a dijet system. The boson balance analyses use a well-calibrated photon or Z-boson, the latter decaying into an electron or muon pair, to measure the p_{T} response of the recoiling jet in the central region up to a p_{T} of about 950 GeV. The multijet balance analysis calibrates central ($|\eta| <1.2$), high-p_{T} jets ($300 < p_{\mathrm{T}} < 2000$ GeV) recoiling against a collection of well-calibrated, lower-p_{T} jets. While the Z/γ and multijet balance calibrations are derived from central jets, their corrections are applicable for forward jets whose energy scale have been equalised by the η-intercalibration procedure. The calibration constants derived

in each of these analyses are statistically combined into a final in situ calibration covering the region $20 < p_{\mathrm{T}} < 2000$ GeV.

The final calibration includes a set of 76 JES systematic uncertainty terms propagated from the individual calibrations and studies. The majority (65) of uncertainties come from the Z/γ-jet and multijet balance in situ calibrations and account for assumptions made in the event topology, MC simulations, sample statistics, and propagated uncertainties on the electron, muon and photon energy scales. The remaining 11 uncertainties are derived from other sources. Four pile-up uncertainties are included to account for potential mismodelling of N_{PV}, μ, ρ, and the residual p_{T} dependence. Three η-intercalibration uncertainties account for potential physics mismodelling, statistical uncertainties, and the method non-closure in the region $2.0 < |\eta_{det}| < 2.6$. Two additional uncertainties account for differences in the jet response and simulated jet composition of light-quark and gluon-initiated jets. An uncertainty is also considered on the GSC punch-through correction, derived as the maximum difference in the jet response in data and MC as a function of the number of muon segments. A high-p_{T} jet uncertainty is derived from single-particle response studies and is applied to jets above 2 TeV, beyond the reach of the in situ methods. The full combination of all uncertainties is shown in Figure 5.2 as a function of jet transverse momentum ($p_{\mathrm{T}}^{\mathrm{jet}}$) at jet pseudorapidity (η^{jet}) set to zero and as a function of η^{jet} at $p_{\mathrm{T}}^{\mathrm{jet}} = 80$ GeV. Each uncertainty is generally treated independently of one another but fully correlated across $p_{\mathrm{T}}^{\mathrm{jet}}$ and η^{jet}. Exceptions are the correlated electron and photon energy scale measurements and the propagated multijet-balance uncertainties related to pile-up, punch-through, η-intercalibration, and jet flavour. The uncertainty is largest at low $p_{\mathrm{T}}^{\mathrm{jet}}$, starting at 5.7% and decreasing to 1% at 200 GeV. It rises after 200 GeV due to the statistical uncertainties related to the in situ calibrations, and increases sharply after 2 TeV where the multijet-balance measurements end and larger uncertainties are taken from the single-particle response. The uncertainty is fairly constant as a function of η^{jet} and reaches a maximum of 3.7% for the most forward jets. A peak can be seen at $2.0 < |\eta^{\mathrm{jet}}| < 2.6$ due to the non-closure uncertainty of the η-intercalibration.

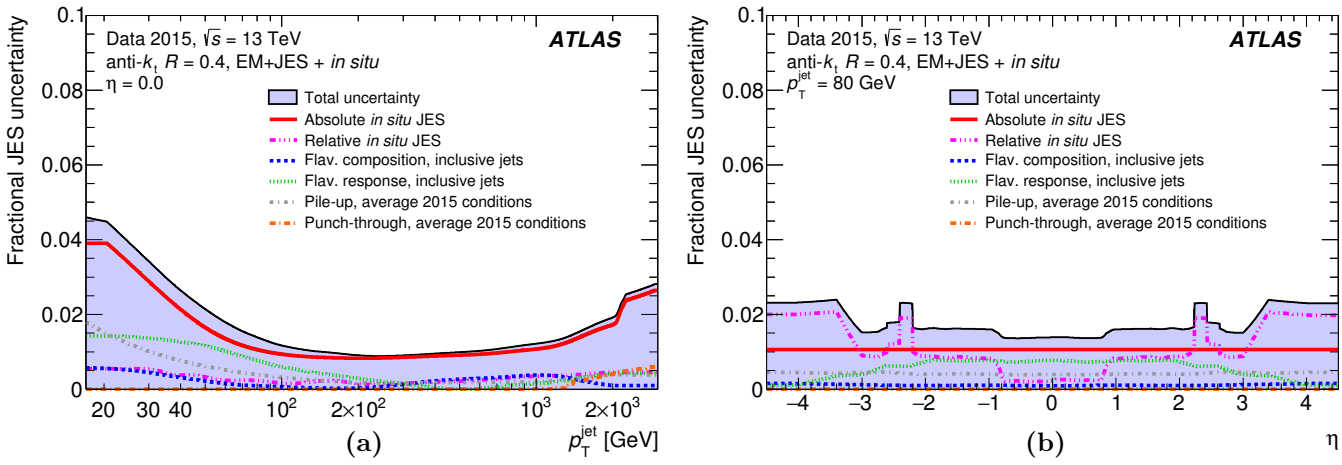


Figure 5.2: JES uncertainty as a function of (a) $p_{\mathrm{T}}^{\mathrm{jet}}$ and (b) η^{jet} [98].

The jet energy scale calibration model used in the photon plus two jet analysis is

based on the same procedure, but the η calibration and the in situ corrections were derived with 2015+2016 data. The decorrelation model of the jet energy scale uncertainty consists of 86 nuisance parameters. The increase in this number with respect to the one used in 2015 comes only from the extended binning used in the in situ measurements, which are treated as separated nuisance parameters.

5.1 In situ calibration with γ+jet events

The jet energy scale corrections derived from the in situ calibrations with the software release used during 2015 or 2016 running periods were used in the physics analyses presented in this dissertation. The results were re-computed using 2015 + 2016 data reprocessed with the software release used during 2017 to provide pre-recommendations for the jet energy scale. For this purpose, two methods were investigated: the direct balance (DB) and the missing projection fraction (MPF) [99]. The studies presented in this chapter are preliminary and detailed studies and improvements are being developed during the first half of 2018.

The DB method uses events with one jet recoiling against a photon and compares their transverse momenta. Assuming a perfect detector measurement and that the jet cone collects all particles recoiling against the photon, the jet and the photon must have the same p_{T} at LO. In practice, this is not usually the case since this measurement is affected by:

- additional parton radiation contributing to the recoil against the photon;
- particles originated in a fragmentation process from the parent parton that are not included in the jet cone, referred to as out-of-cone radiation;
- contributions from the pile-up and underlying event;
- the uncertainty on the photon energy scale;

To reduce, at least partly, the effect of additional parton radiation perpendicular to the jet axis in the transverse plane, the variable $p_{\mathrm{T}}^{\mathrm{ref}}$, defined as

$$p_{\mathrm{T}}^{\mathrm{ref}} = E_{\mathrm{T}}^{\gamma} \cdot |\cos \Delta\phi(\mathrm{jet}, \gamma)|, \tag{5.2}$$

was used, where $\Delta\phi(\mathrm{jet}, \gamma)$ is the azimuthal separation between the photon and the jet. Additionally, requirements on $\Delta\phi(\mathrm{jet}, \gamma)$ and the p_{T} of the sub-leading jet ($p_{\mathrm{T}}^{\mathrm{sub-lead}}$) were applied.

The measurement of the p_{T} balance between the photon and the jet, $R_{\mathrm{bal}} = p_{\mathrm{T}}^{\mathrm{jet}}/p_{\mathrm{T}}^{\mathrm{ref}}$ is sensitive to the jet energy scale. The response

$$\mathcal{R}_{in\ situ} = \langle \frac{p_{\mathrm{T}}^{\mathrm{jet}}}{p_{\mathrm{T}}^{\mathrm{ref}}} \rangle = \langle R_{\mathrm{bal}} \rangle \tag{5.3}$$

is measured in data and compared to the MC predictions.

The precision of the DB method is limited by the out-of-cone effects. The MPF technique represents an alternative less sensitive to the out-of-cone radiation and more robust against pile-up and UE effects.

The MPF formalism considers the balance between the reference object against the whole hadronic recoil. Applying transverse momentum conservation at LO:

$$\vec{p_{\mathrm{T}}}^{\gamma} + \vec{p_{\mathrm{T}}}^{\mathrm{parton}} = 0, \tag{5.4}$$

where $\vec{p_{\mathrm{T}}}^{\gamma}$ ($\vec{p_{\mathrm{T}}}^{\mathrm{parton}}$) is the momentum of the outgoing photon (parton), while at particle level:

$$\vec{p_{\mathrm{T}}}^{\gamma} + \vec{p_{\mathrm{T}}}^{\mathrm{recoil}} = 0, \tag{5.5}$$

where $\vec{p_{\mathrm{T}}}^{\mathrm{recoil}}$ is the momentum of all particles recoiling against the photon. It is assumed that the momentum balance is not affected by the parton fragmentation. The higher-order effects originated by initial- or final-state radiation are mitigated by the selection criteria applied on the event topology. Accounting for the interactions with the calorimeters of particles produced by the hard-scattering, Equation 5.5 can be re-written as:

$$R_{\mathrm{EM}}\ \vec{p_{\mathrm{T}}}^{\gamma} + R_{\mathrm{MPF}} \cdot \vec{p_{\mathrm{T}}}^{\mathrm{recoil}} = -\vec{E_{\mathrm{T}}}^{\mathrm{miss}}, \tag{5.6}$$

where R_{EM} is the response of particles interacting electromagnetically in the calorimeter, R_{MPF} is the calorimeter response to the hadronic recoil and $\vec{E_{\mathrm{T}}}^{\mathrm{miss}}$ is the missing transverse momentum in the event. The $\vec{E_{\mathrm{T}}}^{\mathrm{miss}}$ is assumed to be mostly due to the reduced calorimeter signal for the jet because of non-compensation or the loss of particles in the inactive material in front of the calorimeters. The photon is measured with a good resolution and thus $R_{\mathrm{EM}} \approx 1$ was assumed. Considering this approximation and using again Equation 5.5,

$$\vec{p_{\mathrm{T}}}^{\gamma} + R_{\mathrm{MPF}} \cdot \vec{p_{\mathrm{T}}}^{\mathrm{recoil}} = -\vec{E_{\mathrm{T}}}^{\mathrm{miss}} = \vec{p_{\mathrm{T}}}^{\gamma} - R_{\mathrm{MPF}} \cdot \vec{p_{\mathrm{T}}}^{\gamma}. \tag{5.7}$$

The result is projected into the direction of the photon $\hat{n_{\gamma}}$ yielding

$$E_{\mathrm{T}}^{\gamma} - R_{\mathrm{MPF}} E_{\mathrm{T}}^{\gamma} = -\hat{n_{\gamma}} \cdot \vec{E_{\mathrm{T}}}^{\mathrm{miss}}. \tag{5.8}$$

The previous equation is divided by E_{T}^{γ} to obtain the final MPF equation:

$$R_{\mathrm{MPF}} = 1 + \frac{\hat{n_{\gamma}} \cdot \vec{E_{\mathrm{T}}}^{\mathrm{miss}}}{E_{\mathrm{T}}^{\gamma}}, \tag{5.9}$$

where R_{MPF} is assumed to be a good estimator of the jet response. The $\vec{E_{\mathrm{T}}}^{\mathrm{miss}}$ was chosen to be consistent with the jet energy scale being calibrated, EM+JES in this study. In the following sections, $p_{\mathrm{T}}^{\mathrm{ref}} \equiv E_{\mathrm{T}}^{\gamma}$ was used for the MPF method.

One of the main characteristics of this technique is that it is almost independent of the jet algorithm and the only residual contribution enters via the selection cuts.

The ratios $\frac{\langle R_{\mathrm{bal}}^{\mathrm{data}} \rangle}{\langle R_{\mathrm{bal}}^{\mathrm{MC}} \rangle}$ and $\frac{\langle R_{\mathrm{MPF}}^{\mathrm{data}} \rangle}{\langle R_{\mathrm{MPF}}^{\mathrm{MC}} \rangle}$ of the mean balances (MPF responses) measured in data and MC simulations were used to quantify the level of agreement between data and MC in the DB (MPF) method to validate the MC-based jet calibration. The nominal MC used in this study was Pythia while Sherpa was used to estimate the systematic uncertainty on the modelling of the final state.

5.1.1 Event selection

Events collected by the group of single photon triggers included in Table 5.1 with E_{T}^{γ} thesholds of 20, 25, 35, 40, 45, 50, 60, 70, 80, 100, 120 and 140 GeV and loose photon identification criteria were selected. The use of several triggers allows to accommodate the fast increase in luminosity during the data-taking periods of 2015 and 2016. The trigger selection was designed such that, for a given E_{T} threshold, the efficiency was better than 99% in the E_{T}^{γ} range in which it was applied (see Table 5.1). The lowest E_{T}^{γ} threshold unprescaled triggers were the HLT_g120_loose during 2015 and beginning of 2016 and HLT_g140_loose during most of the 2016 data-taking period. Events selected by prescaled triggers were weighted according to the combination of trigger prescales [100]. The trigger string may change between 2015 and 2016 data-taking periods depending on the seed required at level-1.

Trigger	E_{T}^{γ} range
HLT_g20_loose	25 GeV$< E_{\mathrm{T}}^{\gamma} <$ 100 GeV
HLT_g25_loose	30 GeV$< E_{\mathrm{T}}^{\gamma} <$ 110 GeV
HLT_g35_loose	40 GeV$< E_{\mathrm{T}}^{\gamma} <$ 110 GeV
HLT_g40_loose	45 GeV$< E_{\mathrm{T}}^{\gamma} <$ 120 GeV
HLT_g45_loose	50 GeV$< E_{\mathrm{T}}^{\gamma} <$ 120 GeV
HLT_g50_loose	55 GeV$< E_{\mathrm{T}}^{\gamma} <$ 130 GeV
HLT_g60_loose	65 GeV$< E_{\mathrm{T}}^{\gamma} <$ 130 GeV
HLT_g70_loose	75 GeV$< E_{\mathrm{T}}^{\gamma} <$ 140 GeV
HLT_g80_loose	85 GeV$< E_{\mathrm{T}}^{\gamma} <$ 140 GeV
HLT_g100_loose	105 GeV$< E_{\mathrm{T}}^{\gamma} <$ 150 GeV
HLT_g120_loose	125 GeV$< E_{\mathrm{T}}^{\gamma} <$ 160 GeV
HLT_g140_loose	145 GeV$< E_{\mathrm{T}}^{\gamma}$

Table 5.1: List of single photon triggers used for the event selection.

Only events with a highest-p_{T} (or leading) photon with $E_{\mathrm{T}}^{\gamma} > 25$ GeV within the barrel region of the calorimeter ($|\eta^{\gamma}| < 1.37$) were considered. Tight identification criteria as well as isolation (on the tracks and at calorimeter level) requirements were applied to the photon. The $E_{\mathrm{T}}^{\mathrm{iso}}$ measured in the calorimeter within a radius $R = 0.4$ was limited to a maximum value of $0.022 \cdot E_{\mathrm{T}}^{\gamma} + 2.45$ GeV. Track isolation was also required so that the sum of the p_{T} of the tracks in a cone of radius $R = 0.2$ was lower than $0.05 \cdot E_{\mathrm{T}}^{\gamma}$. To achieve a better jet-background rejection a requirement on transverse momentum of the photon cluster, $E_{\mathrm{T,cluster}}^{\gamma}$, compared to the scalar sum of the transverse momentum of the tracks coming from the vertex at which the photon was originated ($\sum p_{\mathrm{T}}^{\mathrm{tracks}}$) was applied for converted photons as follows:

- if two tracks are matched to the leading photon cluster, events with $0.5 < \frac{E_{\mathrm{T,cluster}}^{\gamma}}{\sum p_{\mathrm{T}}^{\mathrm{tracks}}} < 1.5$ were retained;
- if only one track is consistent with the photon conversion vertex, events with $\frac{E_{\mathrm{T,cluster}}^{\gamma}}{\sum p_{\mathrm{T}}^{\mathrm{tracks}}} < 2$ were retained.

Jets were reconstructed using the anti-k_t algorithm with radius $R = 0.4$ and calibrated to the EM+JES scale. Only jets within the full calorimeter acceptance ($|\eta| < 4.5$) with calibrated $p_{\mathrm{T}} > 8$ GeV were considered. Background jets were rejected by requiring jet quality criteria. To assess whether a given jet comes from the primary hard-scattering or pile-up vertex, requirements on the jet-vertex fraction (JVT) were imposed. The JVT variable is defined as the scalar sum of those tracks matched to a given jet that are associated with the hard-scattering primary vertex divided by the scalar sum of all tracks matched to a jet. Central jets with $|\eta| < 2.4$, $p_{\mathrm{T}} < 60$ GeV and JVT < 0.59 are more probable to be originated from a pile-up vertex and thus were excluded. The overlap between the leading photon and the jets was avoided by rejecting jets with a distance between the jet axis and the photon of $\Delta R < 0.2$. After this pre-selection cuts, only events with a leading jet with $p_{\mathrm{T}}^{\mathrm{jet}} > 10$ GeV and $|\eta| < 0.8$ were considered.

Two additional cuts on the topology of the photon plus jet events were applied to avoid events affected by initial- or final-state radiation:

- a veto on the jet with the second-highest p_{T} was imposed:
  $p_{\mathrm{T}}^{\mathrm{sublead-jet}} < \max(0.3 \times E_{\mathrm{T}}^{\gamma}, 12)$ GeV for the MPF and
  $p_{\mathrm{T}}^{\mathrm{sublead-jet}} < \max(0.1 \times E_{\mathrm{T}}^{\gamma}, 20)$ GeV for the DB method;
- the difference in azimuth between the jet and the photon was required to be $\Delta\phi(\mathrm{jet}, \gamma) > 2.9$ rad for the MPF method and 2.8 rad for the DB method.

5.1.2 Fitting procedure

The DB (MPF) distributions in each bin of $p_{\mathrm{T}}^{\mathrm{ref}}$ were fitted using a maximum likelihood method to a Poisson (Gaussian) distribution. The Poisson distribution in the DB was extended to non-integer values. The mean value of the underlying fitting distribution was taken as the mean balance $\mathcal{R}_{in\ situ}$ ($\langle R_{\mathrm{MPF}} \rangle$). The fit range was limited to a width equal to ± 1.6 times the root mean square (RMS) of the balance distribution around its arithmetic mean to minimise the impact on the final result of mismodelling of the tails of the balance distribution by the MC simulation. A fit was preferred to an arithmetic mean calculation because the cut on $p_{\mathrm{T}}^{\mathrm{jet}}$ biases the mean value of the balance distribution at low-$p_{\mathrm{T}}^{\mathrm{jet}}$ due to the jet energy resolution and the steeply falling photon plus jet cross section.

The results of the fits in data are shown in Figure 5.3 (Figure 5.4) for the DB (MPF) technique. The bias induced by the kinematic cuts in the first bin, 25 GeV$< p_{\mathrm{T}}^{\mathrm{ref}} <$ 45 GeV, affects the quality of the fit of the DB distributions and must be revisited. In any case, this region is covered by the in situ measurements using Z boson decays to electrons or muons.

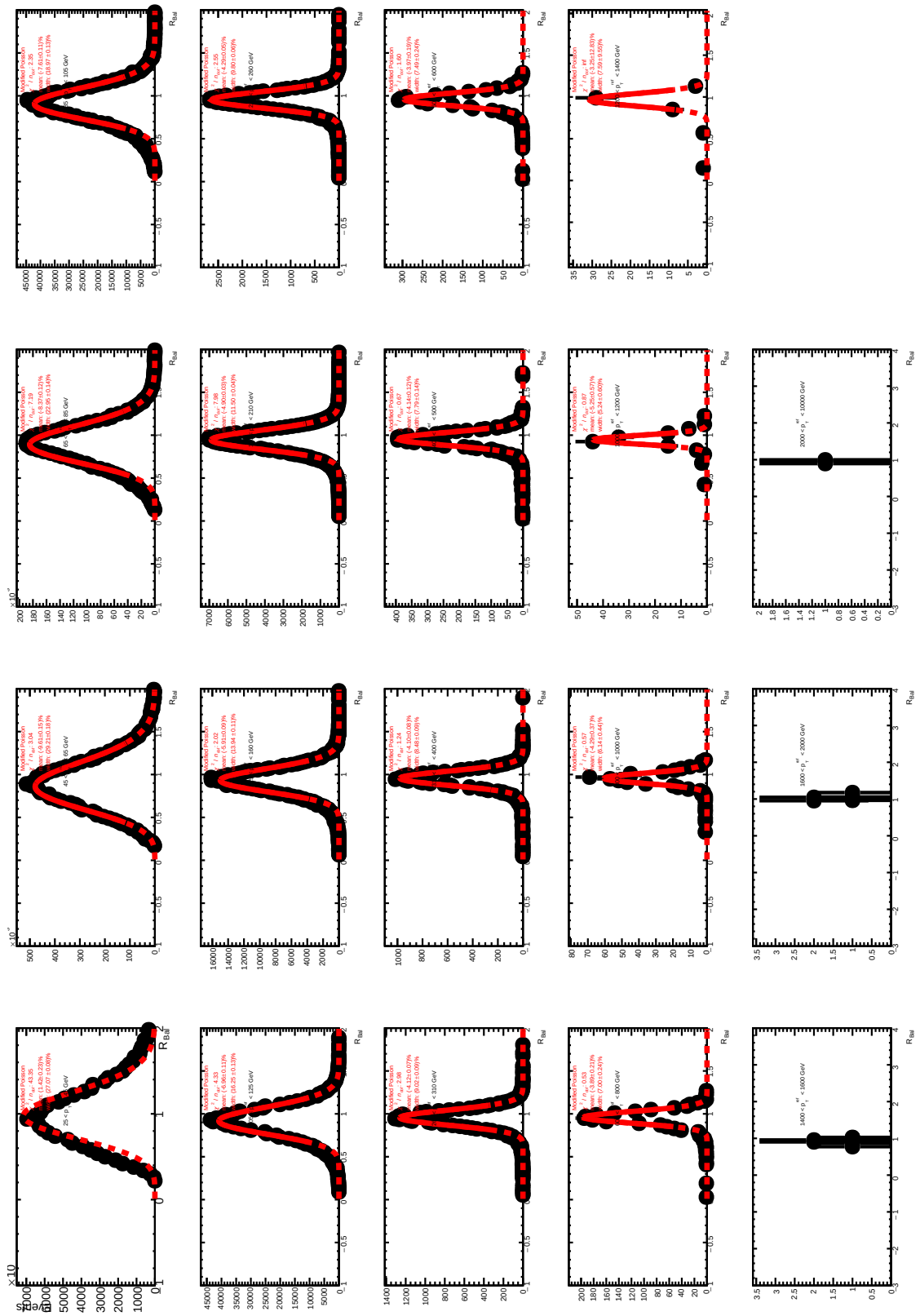


Figure 5.3: Distributions of $p_{\mathrm{T}}^{\mathrm{jet}}/p_{\mathrm{T}}^{\mathrm{ref}}$ (R_{bal}) in data for different bins of $p_{\mathrm{T}}^{\mathrm{ref}}$ fitted with a modified Poisson distribution.

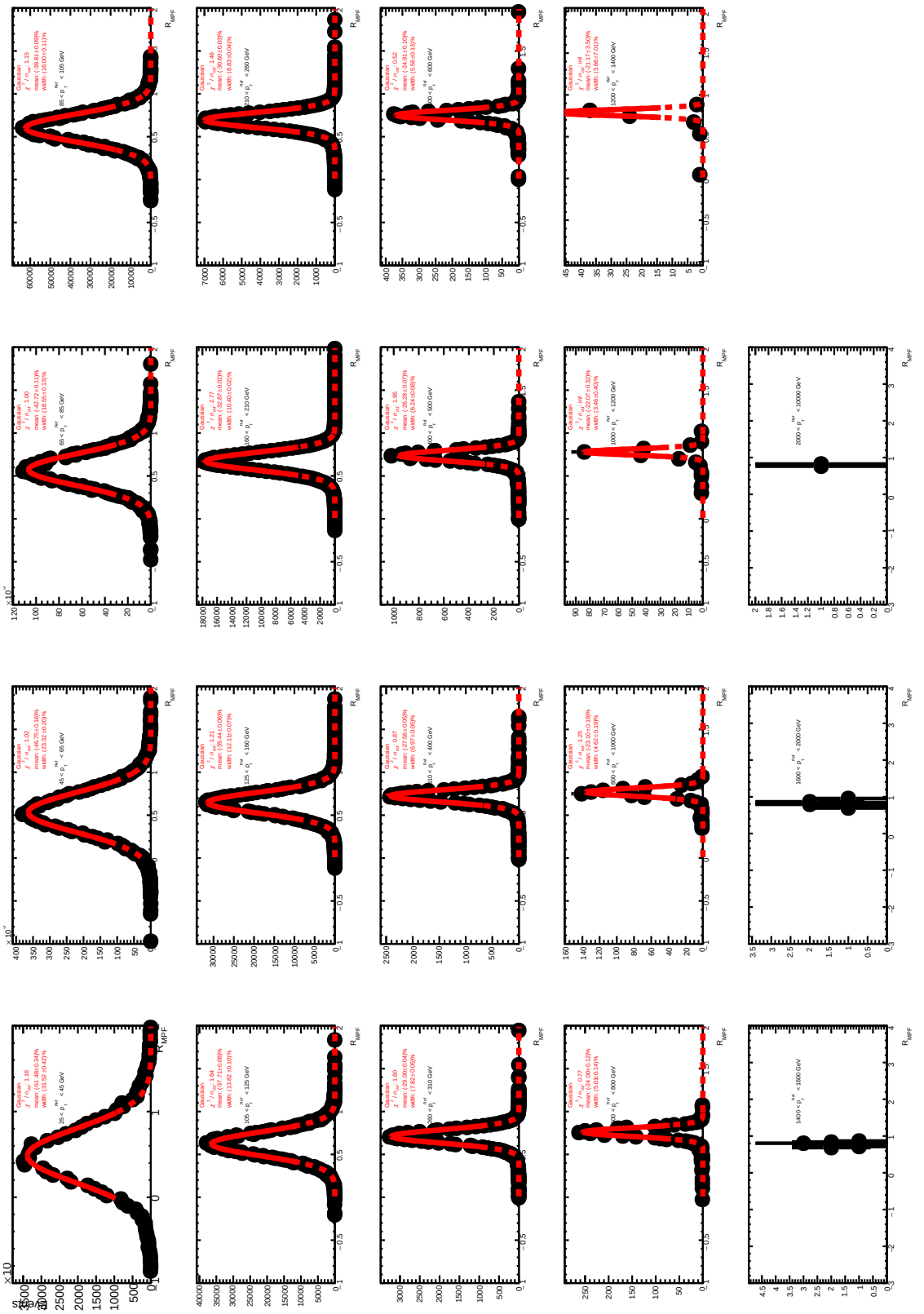


Figure 5.4: Distributions of R_{MPF} in data for different bins of $p_{\mathrm{T}}^{\mathrm{ref}}$ fitted with a Gaussian distribution.

5.1.3 Mapping from $p_{\mathrm{T}}^{\mathrm{ref}}$ to $p_{\mathrm{T}}^{\mathrm{jet}}$

Since the trigger selection imposes cuts on E_{T}^{γ}, the measurements of R_{MPF} and R_{bal} were performed as functions of $p_{\mathrm{T}}^{\mathrm{ref}}$. However, it is desirable to have the final calibration as a function of $p_{\mathrm{T}}^{\mathrm{jet}}$. Therefore, $p_{\mathrm{T}}^{\mathrm{ref}}$ was projected over $p_{\mathrm{T}}^{\mathrm{jet}}$. The correlation between $p_{\mathrm{T}}^{\mathrm{ref}}$ and $p_{\mathrm{T}}^{\mathrm{jet}}$ was measured in data. Starting at an arbitrary fixed value of 28 GeV, the value of $p_{\mathrm{T}}^{\mathrm{jet}}$ at each bin centre of $p_{\mathrm{T}}^{\mathrm{ref}}$ was evaluated to obtain the binning as a function of $p_{\mathrm{T}}^{\mathrm{jet}}$.

5.1.4 Signal purity estimations

To remove the background from jets faking photons, which could be especially sizeable at low E_{T}^{γ}, the 2-D sideband method was used. This technique is explained in detail in Section 6.3 and is extrapolable to what was performed in this study taking into account the different calorimetric isolation criteria and that here the upper limit in isolation of the isolated regions coincides with the lower limit of the non-isolated control regions. Additionally, the signal purity ($\mathcal{P}$) was estimated using[1] $R^{\mathrm{bg}} = 1.45$. The nominal results were obtained assuming a signal purity of 100% and the differences obtained for the purity estimations with $R^{\mathrm{bg}} = 1.45$ were taken into account in the systematic uncertainties. The uncertainty on the balance distribution due to background contamination of the signal was estimated for each bin i as:

$$(1 - \mathcal{P}_i) \times \frac{\mathcal{R}_{in\ situ,i}^{\mathrm{dijet}} - \mathcal{R}_{in\ situ,i}^{\gamma-\mathrm{jet}}}{\mathcal{R}_{in\ situ,i}^{\gamma-\mathrm{jet}}}, \tag{5.10}$$

where $\mathcal{R}_{in\ situ,i}^{\mathrm{dijet}}$ is the balance estimated in the MC for the dijet background in which one jet is misidentified as a photon and $\mathcal{R}_{in\ situ,i}^{\gamma-\mathrm{jet}}$ is the response of the γ–jet events estimated from the signal MC. The second factor of Equation 5.10 estimates how much the balance is changed by the background events. Careful studies were performed in Run-1 [101] in which it was concluded that the relative balance difference between signal and background was covered by a conservative 5% difference across the whole $p_{\mathrm{T}}^{\mathrm{ref}}$ spectrum. For Run-2, the value was validated using as an estimator for the background the balance of photons passing the loose' identification criteria but failing the tight identification. The same procedure was followed for the MPF response.

The estimations of the signal purity are shown in Figure 5.5.

5.1.5 Comparisons between data and MC

Figure 5.6 shows the DB and MPF distributions as functions of $p_{\mathrm{T}}^{\mathrm{jet}}$ calibrated up to the GSC correction (the final η-intercalibration was still not ready when these studies were performed). The MPF technique is less sensitive to the signal modelling by the MC and thus similar results are found with either Pythia or Sherpa except in the first bin of the distribution, not covered by the Sherpa samples.

5.1.6 Systematic uncertainties

The following systematic uncertainties were considered in the γ+jet in situ measurements:

[1] This value was conserved from previous studies and was not estimated for this data set.

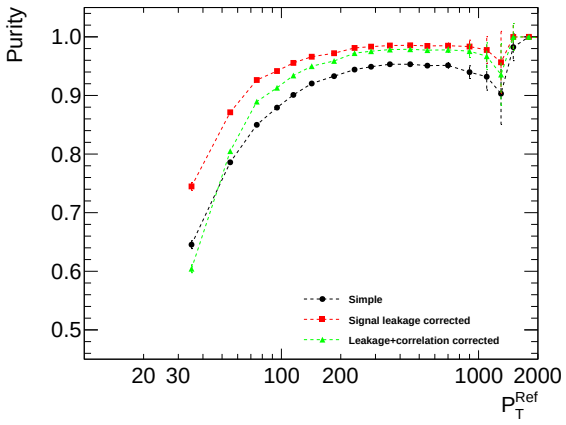


Figure 5.5: Purity estimation as a function of $p_{\mathrm{T}}^{\mathrm{ref}}$ using only data (black dots), the signal leakage corrections extracted from Pythia (red squares) and the signal leakage corrections extracted from Pythia plus a correlation between the isolation and the photon identification of $R^{\mathrm{bg}} = 1.45$ (green triangles).

- the uncertainty on the photon energy scale, "EG_SCALE_ALL", was estimated using a simplified model in which only one nuisance parameter was varied within its uncertainties and propagated to the $\mathcal{R}_{in\ situ}$ or $\langle R_{\mathrm{MPF}} \rangle$ to assess the final uncertainty due to the photon energy scale;

- the uncertainty on the photon energy resolution, "EG_RESOLUTION_ALL", was estimated similarly to the photon energy scale using a single nuisance parameter;

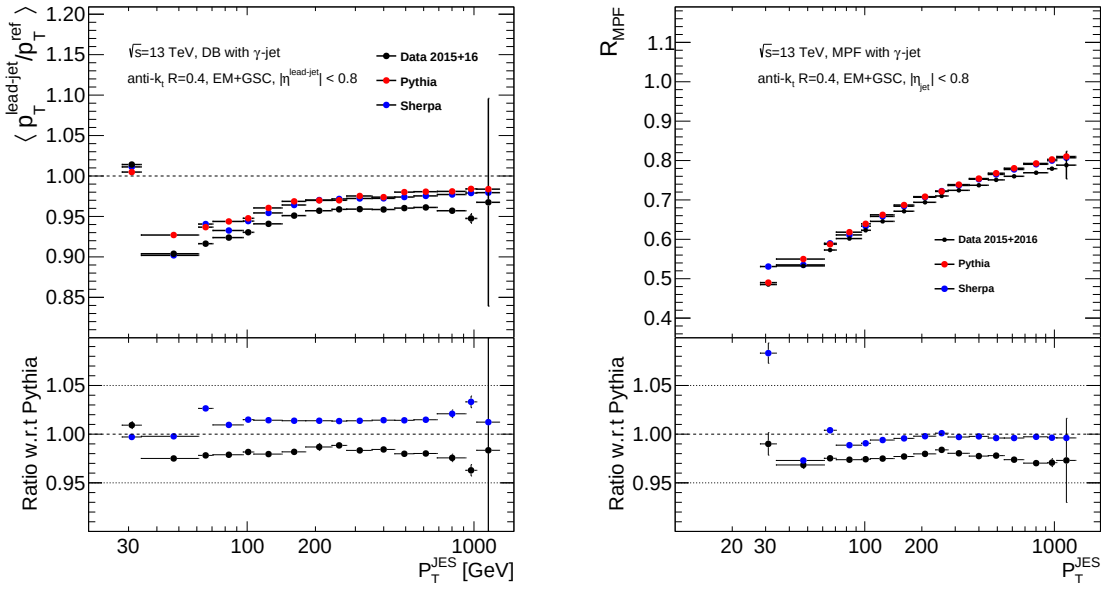
- the uncertainty on JVT, "JVT", was evaluated by comparing the results obtained with JVT<0.11 or JVT<0.91 to reject pile-up jets to the nominal results;

- the uncertainty on the requirements on the sub-leading jet, "Veto", was estimated by varying this requirement to $p_{\mathrm{T}}^{\mathrm{sub-lead}} < \max(0.15 \times p_{\mathrm{T}}^{\mathrm{jet}}, 20)$ GeV or $p_{\mathrm{T}}^{\mathrm{sub-lead}} < \max(0.05 \times p_{\mathrm{T}}^{\mathrm{jet}}, 10)$ GeV ($p_{\mathrm{T}}^{\mathrm{sub-lead}} < \max(0.4 \times p_{\mathrm{T}}^{\mathrm{jet}}, 12)$ GeV or $p_{\mathrm{T}}^{\mathrm{sub-lead}} < \max(0.2 \times p_{\mathrm{T}}^{\mathrm{jet}}, 12)$ GeV) for the DB (MPF) method;

- the uncertainty on the difference in azimuth between the photon and the jet requirement, "dPhi", was estimated by varying this requirement to $\Delta\phi(jet, \gamma) < 2.7$ rad or $\Delta\phi(jet, \gamma) < 2.9$ rad ($\Delta\phi(jet, \gamma) < 2.8$ rad or $\Delta\phi(jet, \gamma) < 3.0$ rad) for the DB (MPF) method;

- the uncertainty due to the MC signal modelling, "MC", was estimated by comparing the results obtained with Sherpa to the nominal results obtained with Pythia. As the Sherpa sample starts at 35 GeV, the "MC" uncertainty in the first bin of the spectrum can not be evaluated and the same value as in the second bin was assigned;

- the uncertainty due to the signal purity, "Purity", was estimated by evaluating the differences from unity obtained with the purity estimates using Pythia and $R^{\mathrm{bg}} = 1.45$ measured as functions of $p_{\mathrm{T}}^{\mathrm{ref}}$ and propagating the result to the measurements of $\mathcal{R}_{in\ situ}$ and $\langle R_{\mathrm{MPF}} \rangle$ (see Section 5.1.4).



(a) (b)

Figure 5.6: The $\mathcal{R}_{in\ situ}$ (a) and $\langle R_{\mathrm{MPF}} \rangle$ (b) distributions as functions of $p_{\mathrm{T}}^{\mathrm{jet}}$ as measured in data (black dots), with Pythia (red dots) or Sherpa (blue dots). The lower part of the figures shows the ratios of data and Sherpa to the results obtained with Pythia.

All the systematic uncertainties as well as the statistical uncertainty, "Stat", were evaluated using the bootstrap technique with 100 replicas. The data and MC replicas were assigned a weight randomly generated with a Poisson distribution with a mean set to unity. The mean of the distribution filled with the measurements or systematic variations obtained for all the replicas was used as an estimator of the central value of the measurement or systematic variation and the RMS as an estimator of its statistical uncertainty. The statistical uncertainty on the systematic variations was used to combine bins if statistical fluctuations were found. Starting from the first bin, a bin was combined with the following one if the relative uncertainty was larger than 50%. The weighted average of the combined bins was taken as the central value of the new bin. The same procedure was performed starting from the last bin. The combination that resulted in a larger number of bins was chosen. This bin-combination procedure was not performed at this stage for the "Stat" and "Purity" uncertainties. The statistical uncertainty was rebinned after the combination with in situ measurements using Z decays to muons or electrons. The total uncertainty was computed by summing in quadrature all the components listed above. Figure 5.7 shows a summary of all the systematic uncertainties together with the statistical uncertainty obtained for the DB and MPF methods. An additional systematic uncertainty must be considered in the DB method to take into account the uncertainty on the out-of-cone radiation which was assigned from the values obtained in previous years. The dominant systematic uncertainty for $p_{\mathrm{T}}^{\mathrm{jet}} > 100$ GeV is that on the photon energy scale uncertainty while the low-$p_{\mathrm{T}}^{\mathrm{jet}}$ region is dominated by the uncertainty on the photon purity (expected to increase in this region in which the jet background becomes important) and the differences in the modelling between Pythia

and SHERPA. The total uncertainty is ≈1% in most of the phase-space, from 60 GeV up to 1 TeV.

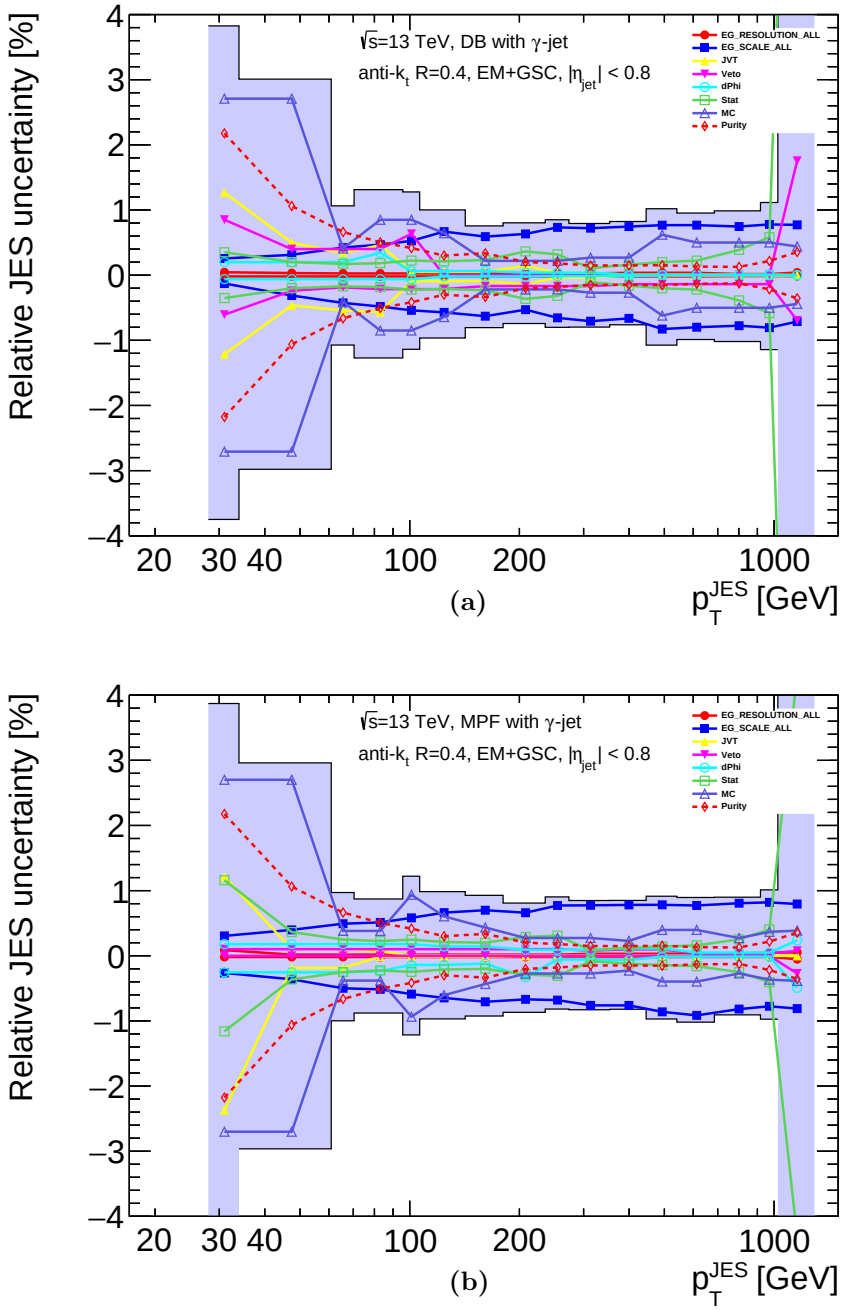


Figure 5.7: Systematic and statistical uncertainties for the in situ γ+jet measurement using the DB (a) or the MPF (b) method. The total uncertainty is shown as a shaded blue area. The "EG_RESOLUTION_ALL" uncertainty is represented as dots, the "EG_SCALE_ALL" uncertainty is represented as squares, the "JVT" uncertainty is represented as upwards triangles, the "Veto" uncertainty is represented as downwards triangles, the "dPhi" uncertainty is represented as open circles, the "Stat" uncertainty is represented as open squares, the "MC" uncertainty is represented as open upwards triangles and the "Purity" uncertainty is represented as open diamonds.

6

Measurement of inclusive isolated-photon cross sections

In this chapter, the measurement of isolated-prompt photon production in pp collisions at $\sqrt{s} = 13$ TeV with the ATLAS detector using an integrated luminosity of 3.2 fb^{-1} is presented [27,28]. Previous measurement of this process have been performed at the LHC by ATLAS [15,102–104] and CMS [105,106]. The phase-space region of the measurement, as well as the analysis strategy, follows closely that of the ATLAS publication at $\sqrt{s} =$ 8 TeV. Differential cross sections as functions of the photon transverse energy E_T^γ have been measured in different regions of the photon pseudorapidity, η^γ, for $E_T^\gamma > 125$ GeV and $|\eta^\gamma| < 2.37$, excluding the region $1.37 < |\eta^\gamma| < 1.56$. The photon was required to be isolated by imposing a standard cone isolation with $R = 0.4$ with a limiting transverse energy inside the cone, E_T^{iso}, of 4.8 GeV + $4.2 \cdot 10^{-3} \cdot E_{\text{T}}^\gamma$ [GeV]. The NLO predictions of pQCD were compared to the measurements.

6.1 Data selection

The data used in this analysis correspond to those collected with the ATLAS detector during the 25 ns proton-proton collision running period of 2015, when the LHC operated at a centre-of-mass energy of $\sqrt{s} = 13$ TeV.

The corresponding integrated luminosity of this data set is 3.16 ± 0.07 fb^{-1}. The events in this data set were recorded after passing data quality requirements and the "HLT_g120_loose" trigger requirements. Events in which the inner detectors or calorimeters were not fully operational or showed data quality problems were excluded. This was achieved by using a Good Runs List (GRL) in which problematic data intervals were marked as "bad" and did not pass the selection. The data rejected were not taken into account in the luminosity calculation.

6.1.1 Trigger requirements

The data sample used consists of events triggered by a single-photon high-level trigger with a nominal transverse energy threshold of 120 GeV (HLT_g120_loose), seeded by a level-1 trigger with nominal threshold equal to 22 GeV. The level-1 EM triggers are based on towers of 0.1×0.1 in the $\eta \times \phi$ plane. The E_{T} of the candidate is estimated using the sum of two electromagnetic towers, adjacent either in η or ϕ with a precision resolution of ~ 0.5 GeV. For towers with energy below 50 GeV, a hadronic veto as well as a loose isolation requirement was applied [107]. Events passing the level-1 trigger selection are

processed by the HLT. Photons are identified by making extensive use of calorimeter shower shapes and energy ratios (see Section 4.3). The selection criteria applied by the trigger on shower-shape variables computed from the energy profiles of the showers in the calorimeters are looser than the photon identification criteria applied in the offline analysis and allow a plateau of constant efficiency close to 100% for true prompt photons of $E_{\mathrm{T}}^{\gamma} = 125$ GeV and $|\eta^{\gamma}| < 2.37$, as explained in Section 4.3. The HLT_g120_loose trigger was the lowest-threshold unprescaled photon trigger during the 2015 25 ns data-taking period. The trigger requirement was not applied on the MC samples since the trigger efficiency was measured in data.

6.1.2 Event selection

The sample of isolated-photon events was selected offline using similar criteria to those reported in the previous ATLAS measurement at 8 TeV [15]. The event selection criteria applied are:

- the events were required to have at least one reconstructed primary vertex, with at least two associated tracks of $p_{\mathrm{T}} > 400$ MeV, consistent with the average beam-spot position;
- events with problems associated to noise burst and data-integrity errors in the LAr calorimeter were rejected. This requirement was applied only to data;
- a part of the detector information was missing in some events; these events were removed from the sample. This requirement was applied only to data;
- events were rejected if the tile calorimeter output was corrupted. This requirement was applied only to data;
- events with SCT problems were rejected. This requirement was applied only to data.

The selection criteria applied to photons are described in the following section.

6.1.3 Photon selection

The selection of photons is based on those isolated electromagnetic clusters reconstructed in the calorimeter without an associated track in the inner detector ("unconverted" photons). To recover photon conversions, clusters matched to pairs of tracks originating from reconstructed conversion vertices in the inner detector are considered as "converted" photon candidates; clusters matched to a single track consistent with originating from a photon conversion were also considered.

There is an intrinsic ambiguity in reconstructing an electromagnetic object as electron or photon. The EM objects reconstructed as photons only are called "un-ambiguous", while those reconstructed both as photons and electrons are called "ambiguous". In particular, EM clusters matched to single tracks without hits in an active region of the pixel layer nearest to the beam pipe are considered both as converted photon candidates and electron candidates. Un-ambiguous and ambiguous photons were considered in the analysis (see Section 4.1 for further details). In events in which multiple photon candidates satisfy the selection criteria, only the leading photon (the one with highest transverse

momentum) was considered for the analysis. The candidates were required to pass a "loose′" identification criteria based on five discriminating variables computed from the lateral and longitudinal profiles of the energy deposited in the calorimeter. The leading photon was required to pass a "tight" identification criteria which makes use of nine discriminating variables. More details about the photon identification are given in Section 4.3.

Events in which the leading photon had transverse energy $E_{\mathrm{T}}^{\gamma} > 125$ GeV and $|\eta^{\gamma}| < 2.37$, excluding the region $1.37 < |\eta^{\gamma}| < 1.56$, were selected. The isolation transverse energy of the leading photon was required to be lower than $4.8\ \mathrm{GeV} + 4.2 \cdot 10^{-3} \cdot E_{\mathrm{T}}^{\gamma}$ [GeV] (see Section 4.4). This cut was found to have a constant efficiency in the 8 TeV analysis [15]. Additional corrections were applied to the simulated events to match the overall event conditions of the data sample and to account for known differences between data and MC. They are explained in Section 6.1.4.

After this selection, the number of events in the signal region of tight and isolated photons was $1,253,508$. Figure 6.1 shows the E_{T}^{γ}, $|\eta^{\gamma}|$ and ϕ^{γ} data and MC distributions.

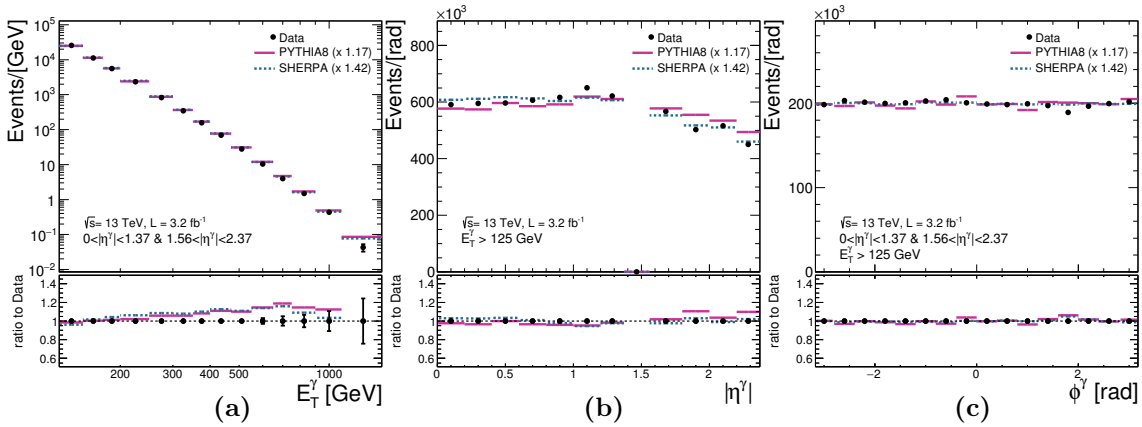


Figure 6.1: The measured (a) E_{T}^{γ}, (b) $|\eta^{\gamma}|$ and (c) ϕ^{γ} distributions for events with $E_{\mathrm{T}}^{\gamma} > 125$ GeV (dots). For comparison, the MC simulations of the signal from Pythia (solid histograms) and Sherpa (dashed histograms) are also included. The MC distributions are normalised to the number of data events using the factors in parentheses. The lower part of each figure shows the ratio of the MC distributions to the data.

6.1.4 Corrections to simulated events

Corrections were applied to the simulated events to match the overall event conditions of the data sample and to account for known differences between data and simulations. These corrections are:

- as explained in Section 4.3, the discriminant variables based on the prompt photon shower-shapes features used for the photon identification were shifted in the MC to

match the shapes observed in data;

- a correction was applied to the photon isolation (see Section 4.4) to remove the effect of the pile-up and underlying event. The average ambient transverse energy density is shown in Figure 6.2 and was typically 4 GeV for the central region in 2015; therefore, the average correction in the isolation cone with $R = 0.4$ was typically 2 GeV;
- the previously corrected isolation value in the MC simulations was further corrected so that the isolation peak observed in data was correctly described. More details are given in Section 6.6.4;
- to match the in-time and out-of-time pile-up conditions in the data, the distribution of $\langle\mu\rangle$ in simulated events was reweighted to that of the data. Figure 6.3 shows the distribution of $\langle\mu\rangle$ for data, after applying a general scale factor of 1/1.16, to achieve a better agreement between data and MC for the distribution on the number of primary vertices, and Pythia and Sherpa MC before and after this reweighting was applied. The reweighting factors for both MC simulations are very similar.

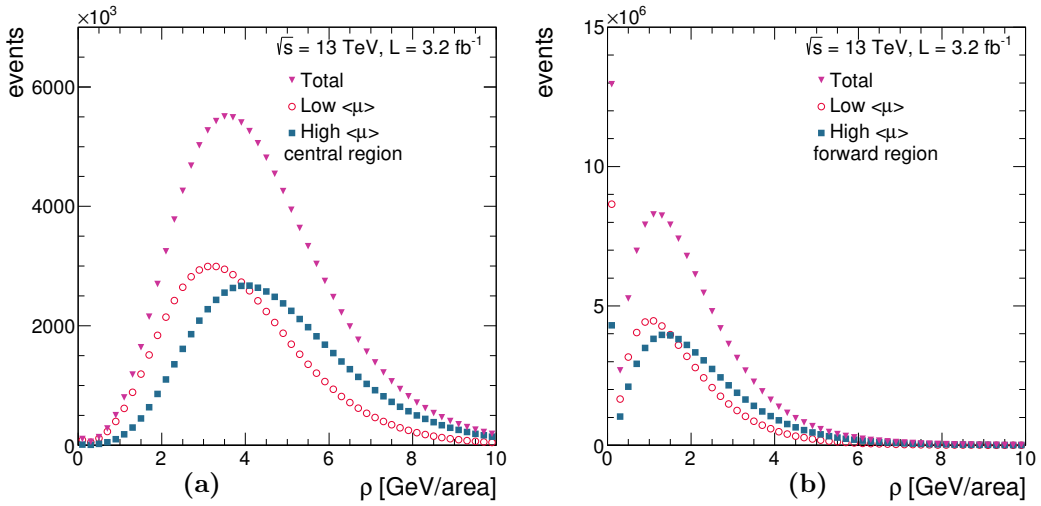


Figure 6.2: Distribution of the ambient transverse-energy density in the (a) central and (b) forward regions for data.

6.2 Trigger efficiency

The efficiency of the trigger used in this analyis (HLT_g120_loose) was evaluated in data using a bootstrap method in which the reference trigger was HLT_g100_loose as

$$\epsilon_{\text{trigger}} = \frac{N_{\text{HLT_g100_loose}\otimes\text{HLT_g120_loose}}}{N_{\text{HLT_g100_loose}}}, \tag{6.1}$$

where $N_{\text{HLT_g100_loose}\otimes\text{HLT_g120_loose}}$ is the number of events that pass all the selection criteria listed in Section 6.1.2 and fulfil the conditions of the triggers HLT_g100_loose

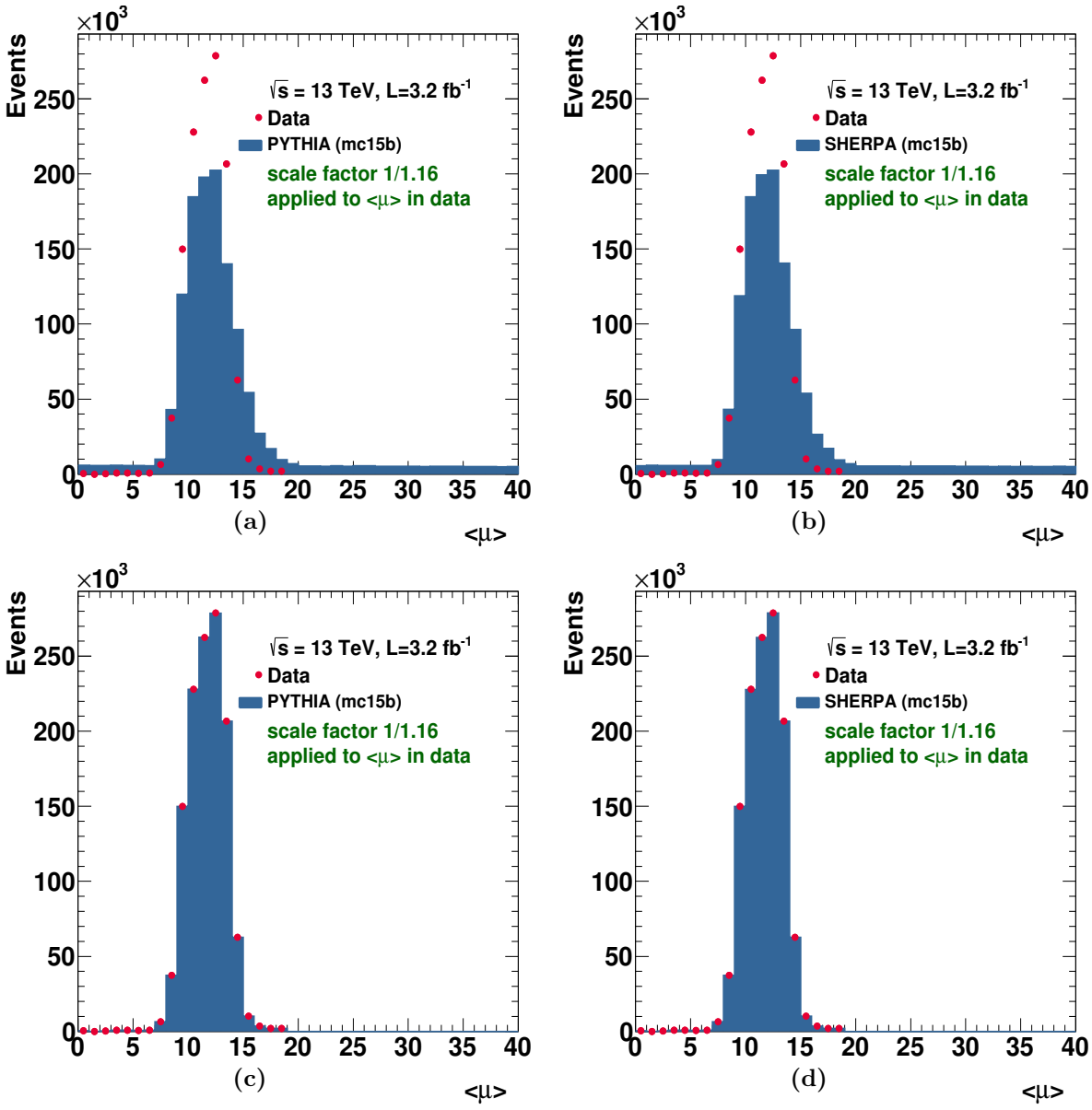


Figure 6.3: Distribution of the average number of interactions per bunch crossing for the sample of tight and isolated photons in data (dots) and Pythia and Sherpa MC (histograms) (a,b) before and (c,d) after reweighting.

and HLT_g120_loose; and $N_{\text{HLT_g100_loose}}$ is the number of events that pass all the selection criteria listed in Section 6.1.2 and fulfil the conditions of the trigger HLT_g100_loose. The reference trigger was checked to be fully efficient at 125 GeV with 2015 data [108]. The resulting efficiencies of the HLT_g120_loose trigger were evaluated for the different photon samples used in the background subtraction (See Section 6.3). The values for $E_{\text{T}}^{\gamma} > 125$ GeV photons are:

- tight and isolated selection: $> 99.3\%$ (signal region);
- tight and non-isolated selection: $> 98.4\%$;
- non-tight and isolated selection: $> 98.3\%$;
- non-tight and non-isolated: $> 97.4\%$.

Figures 6.4 to 6.7 show the trigger efficiency for different η^{γ} regions as a function of E_{T}^{γ} for the four samples listed above. The measurements of the differential cross sections presented on Section 6.8 were corrected for the trigger inefficiency at the turn-on.

An uncertainty was assigned to the trigger efficiency to cover the statistical uncertainty and the differences between data and simulation. The statistical uncertainty was computed using Bayesian confidence intervals. In Bayesian statistics, a likelihood-function (how probable it is to get the observed data assuming a true efficiency) and a prior probability (what is the probability that a certain true efficiency is actually realised) are used to determine a posterior probability using Bayes theorem. In this case, the prior was chosen to be the "least informative" to guarantee objective results. For the trigger efficiency (binomial model), this prior coincides with Jeffrey's prior:

$$Prior(\epsilon) = \frac{1}{B(1/2, 1/2)} \times \epsilon^{-1/2} \times (1-\epsilon)^{-1/2}, \tag{6.2}$$

where $B(1/2, 1/2)$ is the beta function with both free parameters set to 1/2. The mode was chosen as the best estimator of the trigger efficiency [112]. The statistical uncertainty was obtained as the one sigma confidence interval of the probability density function. The systematic uncertainty was calculated as the standard deviation between data and MC; the data are expected to contain the effect of the background in the data sample. This is a conservative approach since these differences also account for inaccuracies of the detector description in the MC, small differences in the kinematics of signal events, etc. The integrated efficiencies in each region of η^{γ} are:

- for $|\eta^{\gamma}| < 0.6$: efficiency $= 99.90 \pm 0.02$ (stat) ± 0.07 (syst) %;
- for $0.6 < |\eta^{\gamma}| < 1.37$: efficiency $= 99.70 \pm 0.03$ (stat) ± 0.21 (syst) %;
- for $1.56 < |\eta^{\gamma}| < 1.81$: efficiency $= 98.58^{+0.10}_{-0.11}$ (stat) ± 0.99 (syst) %;
- for $1.81 < |\eta^{\gamma}| < 2.37$: efficiency $= 99.65 \pm 0.04$ (stat) ± 0.24 (syst) %.

Comparisons between the trigger efficiency in data and MC are shown in Figure 6.8.

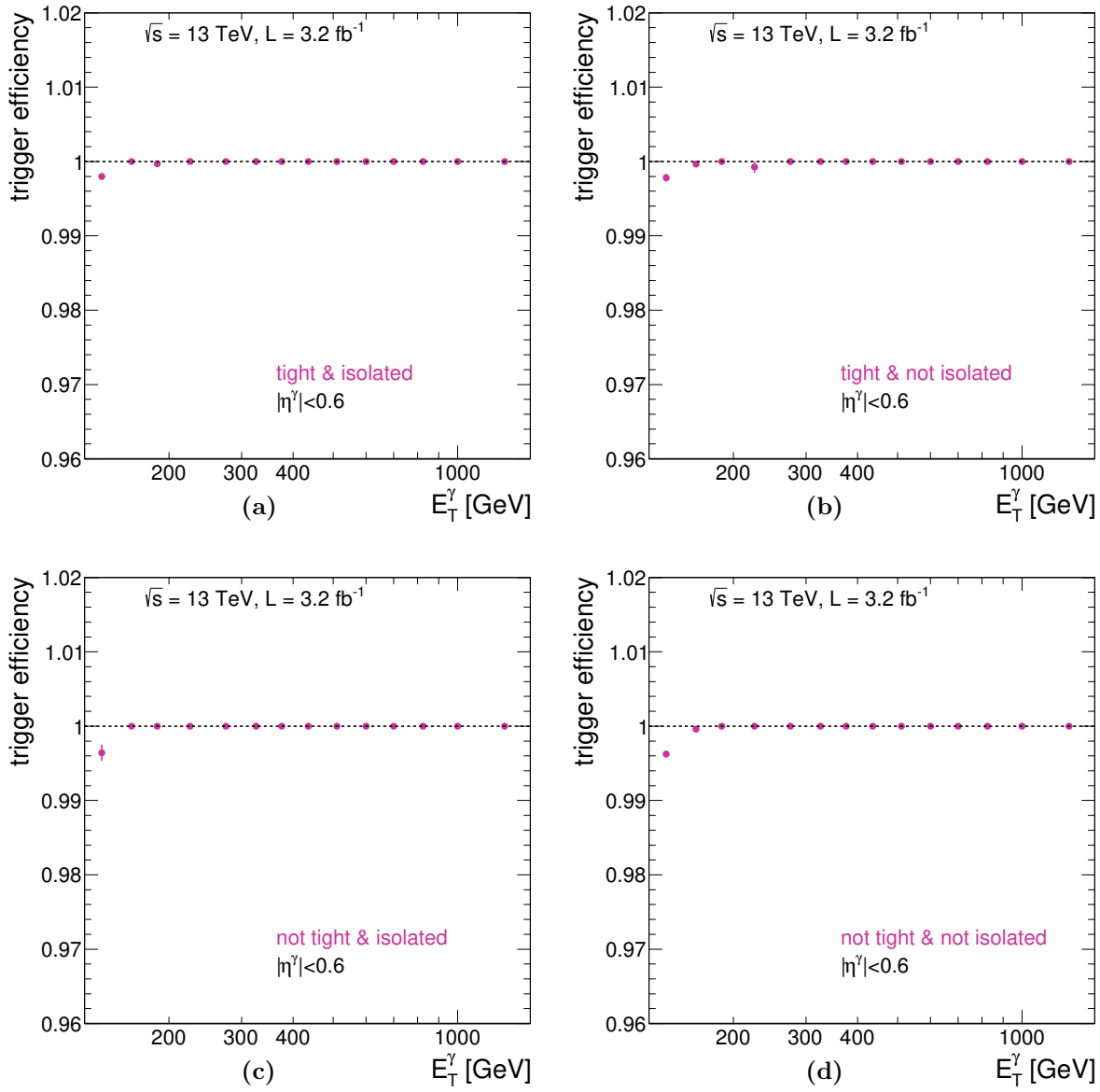


Figure 6.4: Trigger efficiency for $|\eta^{\gamma}| < 0.6$ as a function of E_{T}^{γ} for (a) tight and isolated (signal region), (b) tight and non-isolated (control region B), (c) non-tight and isolated (control region C) and (d) non-tight and non-isolated (control region D) photons. See Section 6.3 for the definition of the regions.

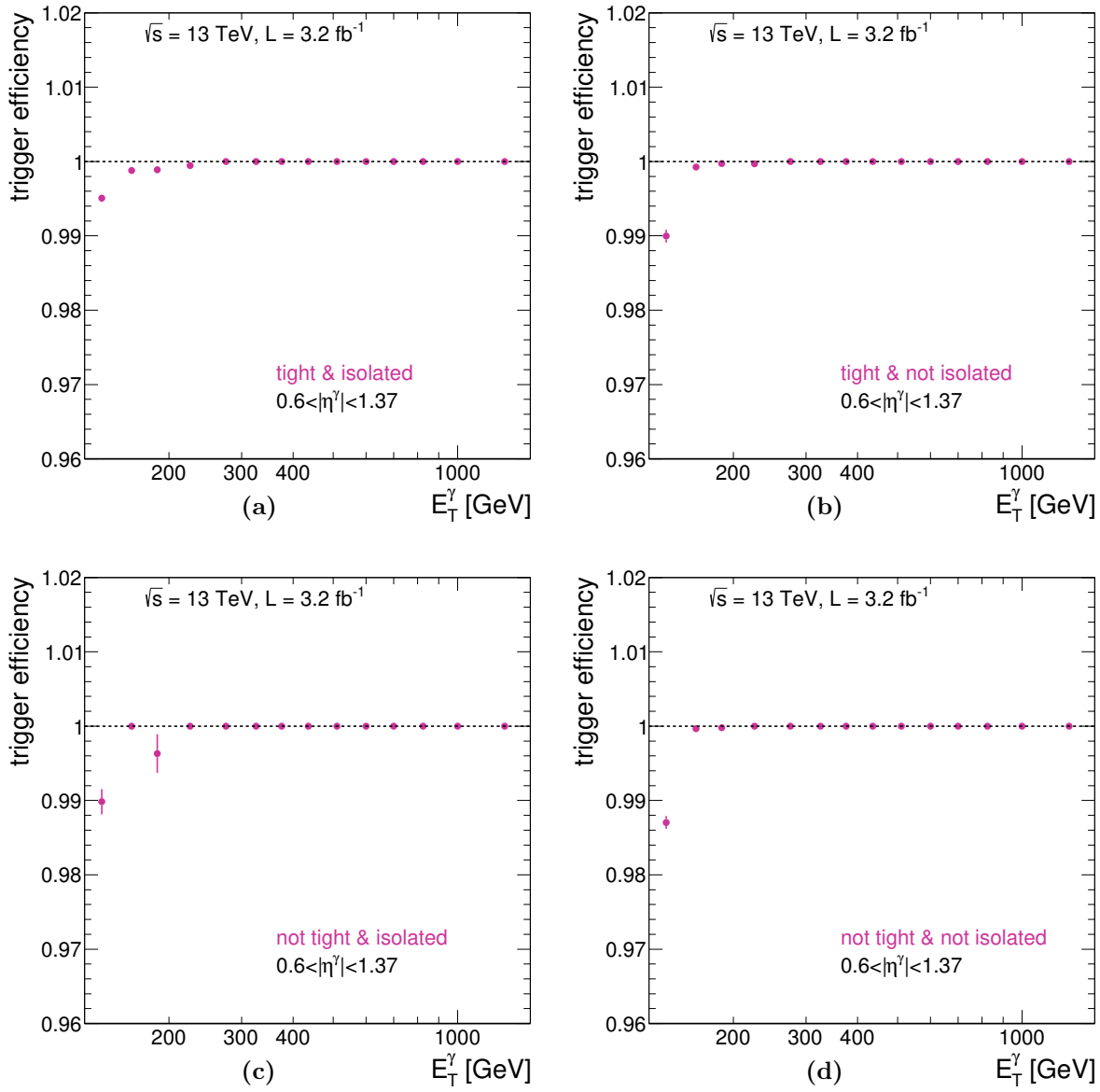


Figure 6.5: Trigger efficiency for $0.6 < |\eta^{\gamma}| < 1.37$ as a function of E_{T}^{γ} for (a) tight and isolated (signal region), (b) tight and non-isolated (control region B), (c) non-tight and isolated (control region C) and (d) non-tight and non-isolated (control region D) photons. See Section 6.3 for the definition of the regions.

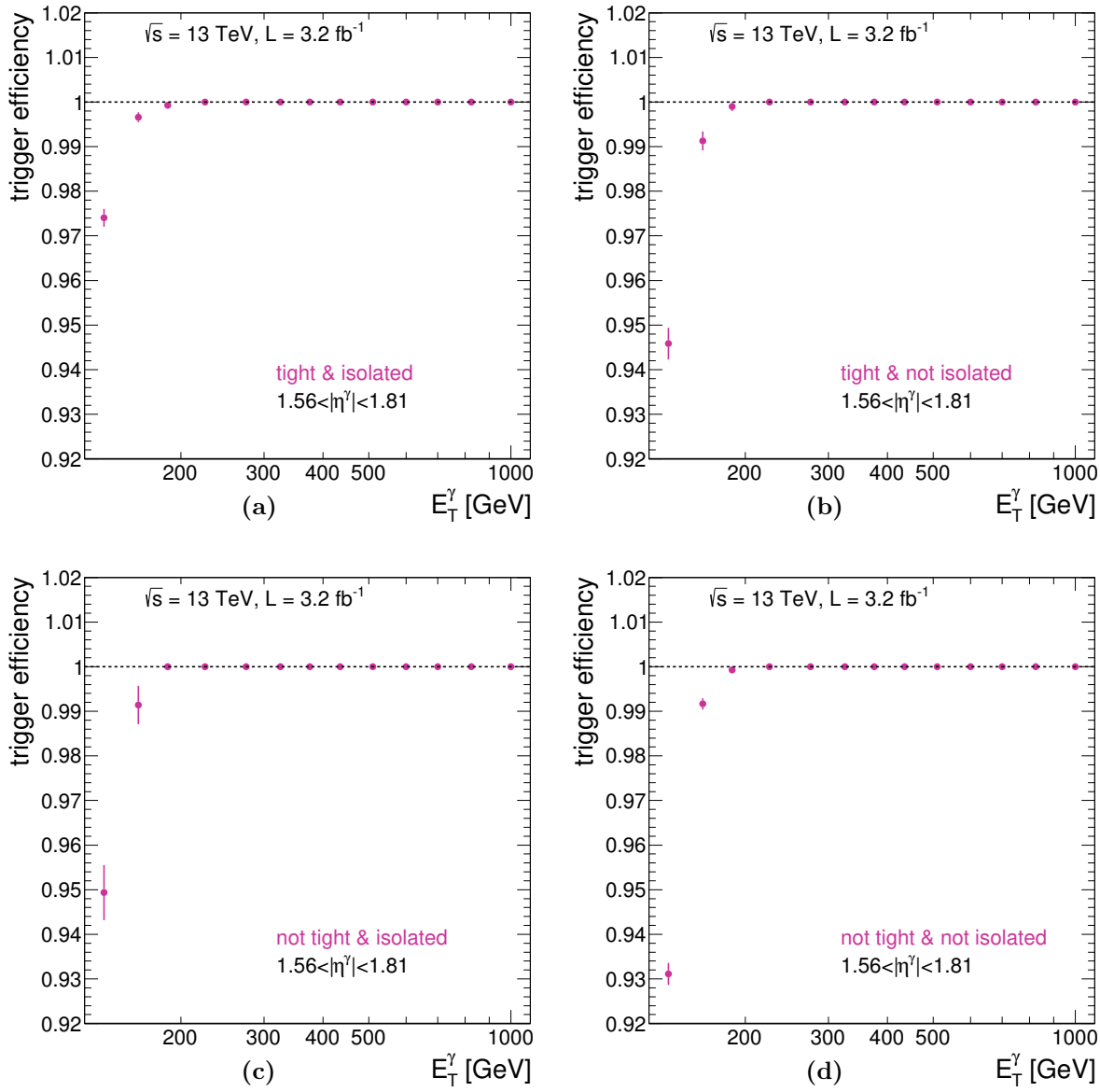


Figure 6.6: Trigger efficiency for $1.56 < |\eta^{\gamma}| < 1.81$ as a function of E_{T}^{γ} for (a) tight and isolated (signal region), (b) tight and non-isolated (control region B), (c) non-tight and isolated (control region C) and (d) non-tight and non-isolated (control region D) photons. See Section 6.3 for the definition of the regions.

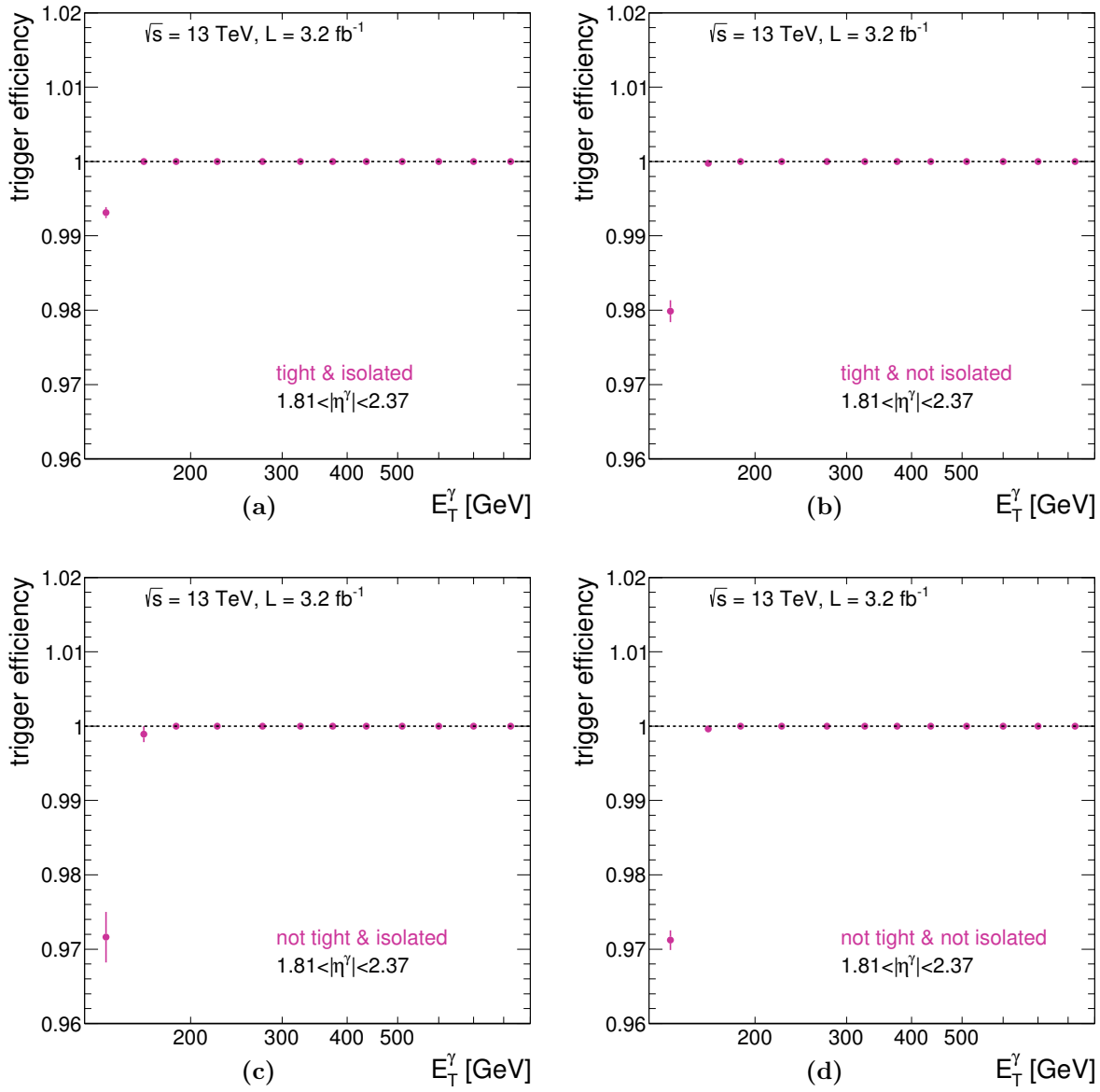


Figure 6.7: Trigger efficiency for $1.81 < |\eta^{\gamma}| < 2.37$ as a function of E_{T}^{γ} for (a) tight and isolated (signal region), (b) tight and non-isolated (control region B), (c) non-tight and isolated (control region C) and (d) non-tight and non-isolated (control region D) photons. See Section 6.3 for the definition of the regions.

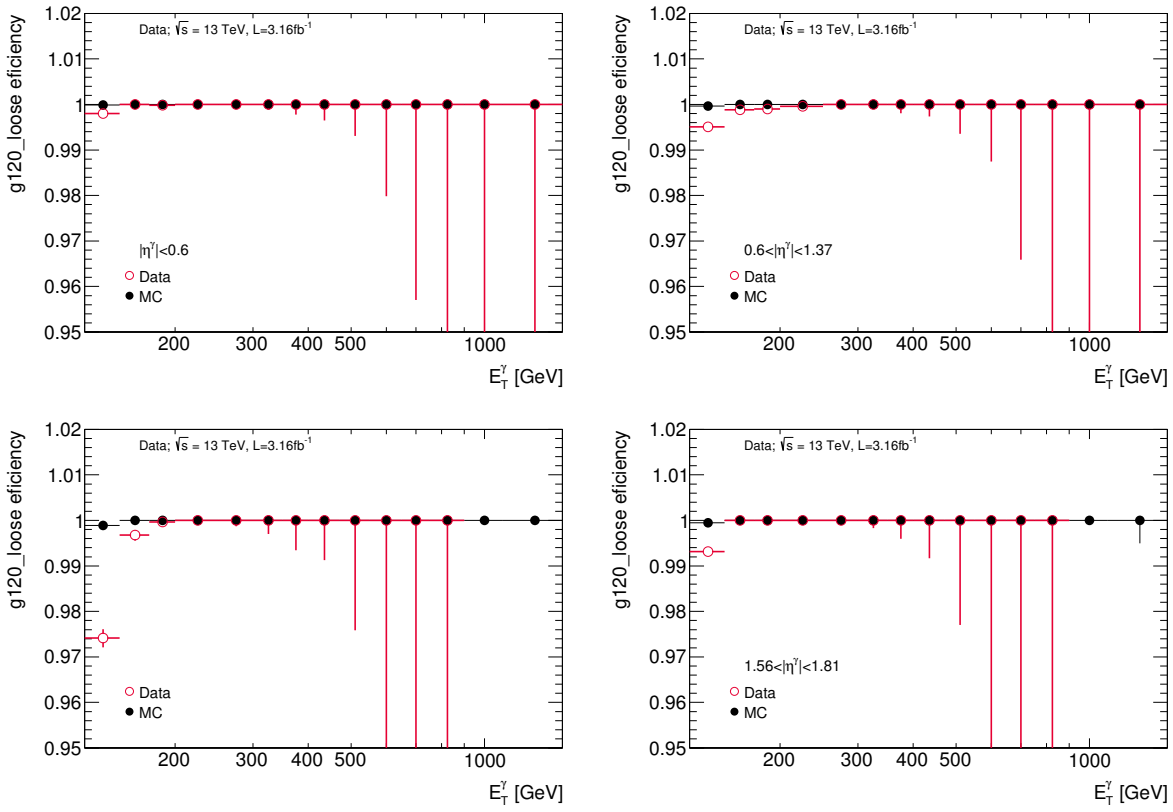


Figure 6.8: Trigger efficiency in data (red open circles) and MC (black dots) for selected photon candidates as a function of E_{T}^{γ} in different regions of $|\eta^{\gamma}|$. The error bars display the Bayesian confidence intervals for the efficiency measured in data.

6.3 Background estimation and subtraction

Even after the application of the tight identification and isolation requirements, a non-negligible contribution of background contaminates the selected signal sample. This background originates mainly from multi-jet processes in which one jet is mis-identified as a photon. This jet usually contains a light neutral meson, predominantly a π^0 that decays into two collimated photons, which carry most of the energy of the jet and allows it to pass the isolation requirement. In this configuration, the two energy deposits in the EM calorimeter left by neutral pions cannot be distinguished and the energy deposit features resemble more that of a single-photon deposit.

The contribution of the background in the signal-enriched sample can be estimated from the $E_{\mathrm{T}}^{\mathrm{iso}}$ distributions of tight photons and that of photons passing the loose' identification criteria, as defined in Section 4.3, but failing the tight requirements (non-tight subsample). The non-tight subsample is expected to be enriched in background candidates. The isolation profile of fake-photon candidates is expected to have the same shape in the tight and non-tight subsamples. The isolation distribution of non-tight candidates was scaled to that of tight candidates in the region of $E_{\mathrm{T}}^{\mathrm{iso}} > 10$ GeV, where the contribution of prompt photons is expected to be negligible. The prompt-photon signal was observed as a clear peak around zero in the isolation distribution, while the background was estimated from the contribution of the non-tight candidates in the signal region of $E_{\mathrm{T}}^{\mathrm{iso}}$<4.8 GeV+4.2$\cdot 10^{-3} \cdot E_{\mathrm{T}}^{\gamma}$ [GeV], which corresponds to an isolation cut of 5.3 (9) GeV for E_{T}^{γ} 125 (1000) GeV. The rescaled background distribution was subtracted from that of tight photon candidates, as shown in Figure 6.9. The isolation profile is compared to that of the prompt-photon MC simulations of Pythia and Sherpa in Figure 6.9.

Similar assumptions as in the previous study were considered in the data-driven method used in this analysis for background subtraction. This method is a counting technique based on the observed number of events in control regions of a two-dimensional plane, known as the 2D-sideband method, widely used within ATLAS and, especially, in previous photon analyses [15,102–104]. Two non-correlated variables, $E_{\mathrm{T}}^{\mathrm{iso}}$ and the photon identification variables, γ_{ID}, were chosen as the axes of the plane. The plane is divided in one signal region and three signal-depleted control regions as shown in Figure 6.10 and defined below:

- "A" is the signal region, which contains tight and isolated ($E_{\mathrm{T}}^{\mathrm{iso}}$< 4.8 GeV + $4.2 \cdot 10^{-3} \cdot E_{\mathrm{T}}^{\gamma}$ [GeV]) photon candidates;
- "B" is the control region with non-isolated background, which contains tight and non-isolated ($E_{\mathrm{T}}^{\mathrm{iso}}$> (4.8 + 2) GeV + $4.2 \cdot 10^{-3} \cdot E_{\mathrm{T}}^{\gamma}$ [GeV]) photon candidates. An upper cut on $E_{\mathrm{T}}^{\mathrm{iso}}$ of 50 GeV is also imposed;
- "C" is the control region with non-tight background, which contains isolated ($E_{\mathrm{T}}^{\mathrm{iso}}$< 4.8 GeV + $4.2 \cdot 10^{-3} \cdot E_{\mathrm{T}}^{\gamma}$ [GeV]) and non-tight photon candidates;
- "D" is the background control region, which contains non-isolated ($E_{\mathrm{T}}^{\mathrm{iso}}$> (4.8 + 2) GeV + $4.2 \cdot 10^{-3} \cdot E_{\mathrm{T}}^{\gamma}$ [GeV]) and non-tight photon candidates. An upper cut on $E_{\mathrm{T}}^{\mathrm{iso}}$ of 50 GeV is also imposed.

The advantage of the method is that no precise knowledge of the signal is needed. It assumes that background control regions have weak signal contamination. The number

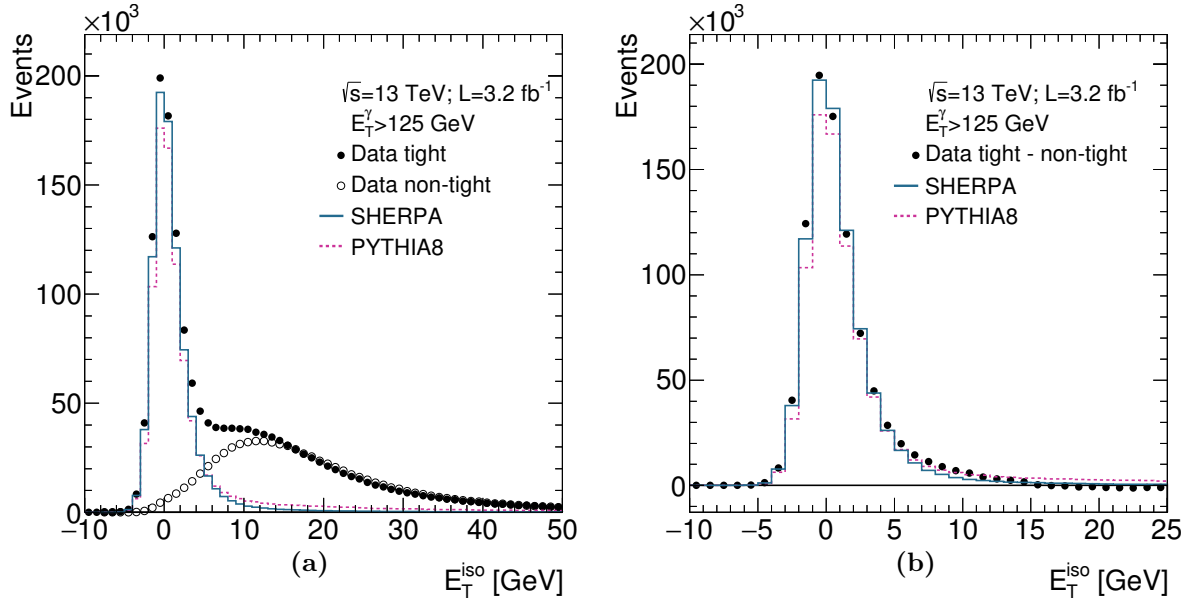


Figure 6.9: (a) The measured $E_{\mathrm{T}}^{\mathrm{iso}}$ distribution before the isolation requirement and after applying the tight identification requirement (black dots) and for those events which fail the tight identification ("non-tight") (open circles). The "non-tight" distribution was normalised so that the integral of the "tight" and "non-tight" distributions for $E_{\mathrm{T}}^{\mathrm{iso}}>$ 10 GeV coincide. For comparison, the MC simulations of the signal from SHERPA (solid histogram) and PYTHIA (dashed histogram) are also included. The MC distributions are normalised to the number of data events in the tight distribution for $E_{\mathrm{T}}^{\mathrm{iso}}<$ 10 GeV. (b) The measured $E_{\mathrm{T}}^{\mathrm{iso}}$ distribution before the isolation requirement and after applying the tight identification requirement and after subtracting the non-tight events (dots).

of signal events in A (N_A^{sig}) is the number of events in the region minus the number of background events (N_A^{bg}),

$$N_A^{\mathrm{sig}} = N_A - N_A^{\mathrm{bg}}. \tag{6.3}$$

Since the method assumes that the axes variables, $E_{\mathrm{T}}^{\mathrm{iso}}$ and γ_{ID}, are not correlated, the following proportion holds:

$$\frac{N_A^{\mathrm{bg}}}{N_B^{\mathrm{bg}}} = \frac{N_C^{\mathrm{bg}}}{N_D^{\mathrm{bg}}} \rightarrow R^{\mathrm{bg}} \equiv \frac{N_A^{\mathrm{bg}} \cdot N_D^{\mathrm{bg}}}{N_B^{\mathrm{bg}} \cdot N_C^{\mathrm{bg}}} = 1. \tag{6.4}$$

The signal leakage into the control regions is taken into account by rewriting

$$N_K^{\mathrm{bg}} = N_K - \epsilon_K N_A^{\mathrm{sig}}, \tag{6.5}$$

where ϵ_K are the signal leakage fractions ($\epsilon_K = N_{K,MC}^{\mathrm{sig}}/N_{A,MC}^{\mathrm{sig}}$) in each background control region (K =B, C, D) and are extracted from the MC simulations of the signal.

The final number of signal events in the region A is

$$N_A^{\mathrm{sig}} = N_A - R^{\mathrm{bg}} \cdot (N_B - \epsilon_B N_A^{\mathrm{sig}}) \cdot \frac{N_C - \epsilon_C N_A^{\mathrm{sig}}}{N_D - \epsilon_D N_A^{\mathrm{sig}}}. \tag{6.6}$$

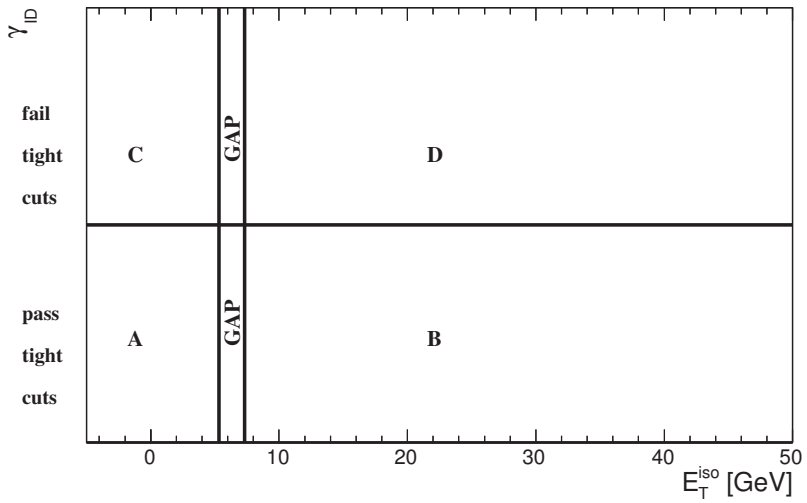


Figure 6.10: Illustration of the two-dimensional plane of the photon identification variables vs. the transverse isolation energy used to estimate the background yield in the signal region, A, from the observed yields in three control regions, B, C and D. The vertical lines correspond to the requirements on $E_{\mathrm{T}}^{\mathrm{iso}}$ for $E_{\mathrm{T}}^{\gamma} = 125$ GeV (line on the left to define regions A and C and line on the right to define regions B and D).

Equation (6.6) leads to a second-order polynomial equation in N_A^{sig} that has only one physical solution. The factor R^{bg} is kept since a systematic uncertainty was considered in which the assumption of $R^{\mathrm{bg}} = 1$ was modified.

The signal leakage fractions are shown in Figures 6.11. The fractions ϵ_C, which represent the signal leaking into the non-tight and isolated control region, are approximately constant in all η^{γ} regions and around $0.02 - 0.03$ and very similar for Pythia and Sherpa. The fractions ϵ_B, signal leakage into the tight and non-isolated control region, are approximately constant for all η^{γ} regions and take values of ≈ 0.1 for Pythia and ≈ 0.05 for Sherpa; this difference between Pythia and Sherpa is due to the different treatment of the bremsstrahlung component in both MC generators (see Section 3.5.7). The fractions ϵ_D, the signal leakage into the non-tight and non-isolated control region, increase as a function of E_{T}^{γ}; they take very different values for Pythia or Sherpa. This is the control region most affected by the different treatment of the bremsstrahlung component in both models.

It was observed (see Figure 6.12) that the upper cut on $E_{\mathrm{T}}^{\mathrm{iso}}$ of 50 GeV is safe to avoid the regions in which the tail of the MC distribution overestimates the data. In this way, the effect on the signal leakage fractions of the contribution at large values of $E_{\mathrm{T}}^{\mathrm{iso}}$ is suppressed and, thereby, it makes the results of the subtraction using the 2D-sideband method more robust than by not using an upper cut on $E_{\mathrm{T}}^{\mathrm{iso}}$ for the background control regions B and D.

The signal purity was computed as $P = N_A^{\mathrm{sig}}/N_A$, where N_A^{sig} is obtained from Equation (6.6). The signal purity is shown in Figure 6.13, with signal leakage fractions estimated with the Pythia or Sherpa MC samples. The lack of events in bins of the background control regions leads to purity values larger than unity. In these cases, the background subtraction method explained does not hold and the signal yield was fixed to the number of events observed in the signal region. Low statistics can cause dips in the

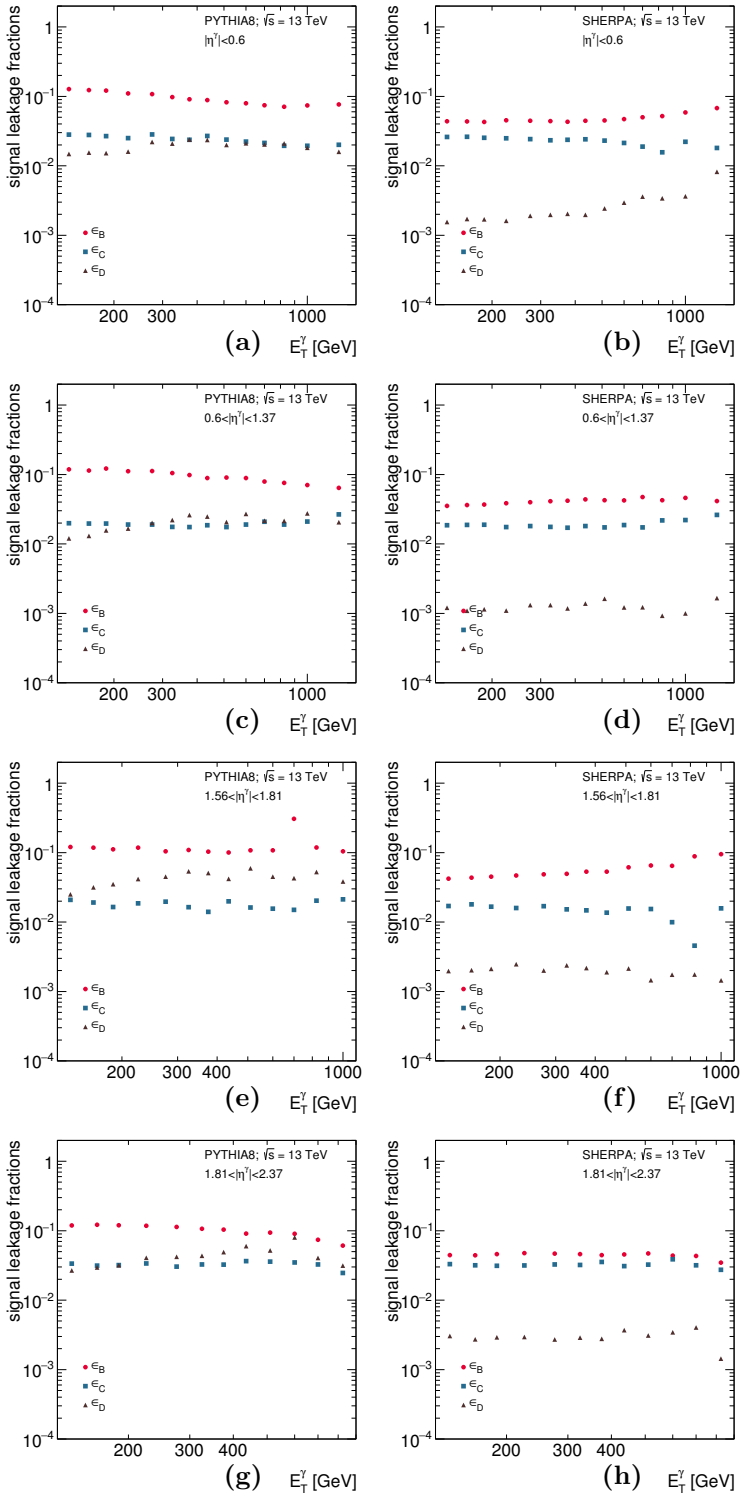


Figure 6.11: Signal leakage fractions from Pythia (a,c,e,g) and Sherpa (b,d,f,h) for the B (dots), C (squares) and D (triangles) control regions as functions of E_{T}^{γ} in different regions of η^{γ}.

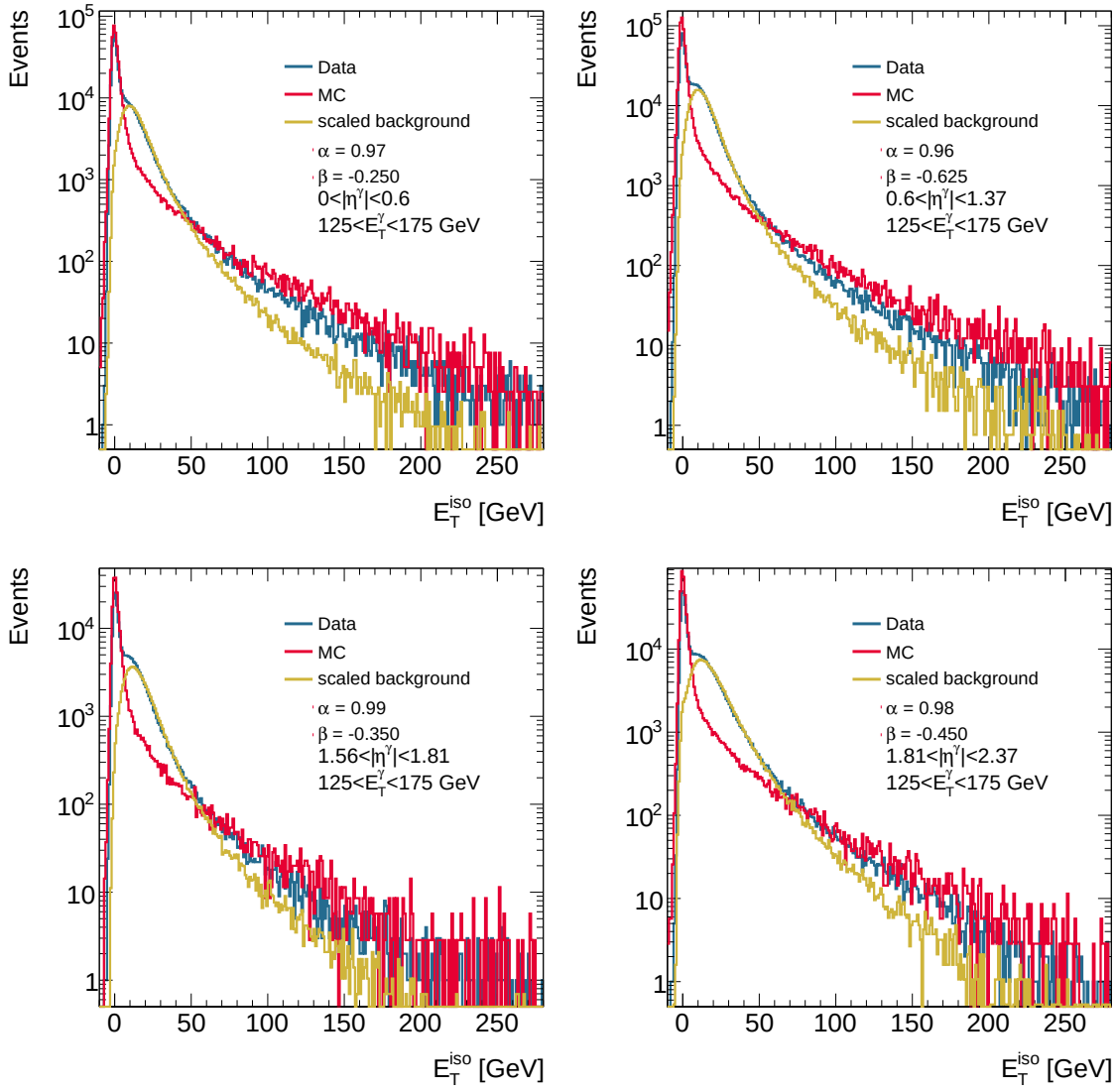


Figure 6.12: Measured $E_{\mathrm{T}}^{\mathrm{iso}}$distribution for tight (blue histograms) and non-tight (golden histograms, normalised according to the results of the fit) photons for $125 < E_{\mathrm{T}}^{\gamma} < 175$ GeV in different regions of $|\eta^{\gamma}|$. For comparison, the MC simulations of the signal from PYTHIA (red histograms, normalised according to the results of the fit) are also included.

purity distribution; the purity was set to unity in these cases if the statistical uncertainty was consistent with such value.

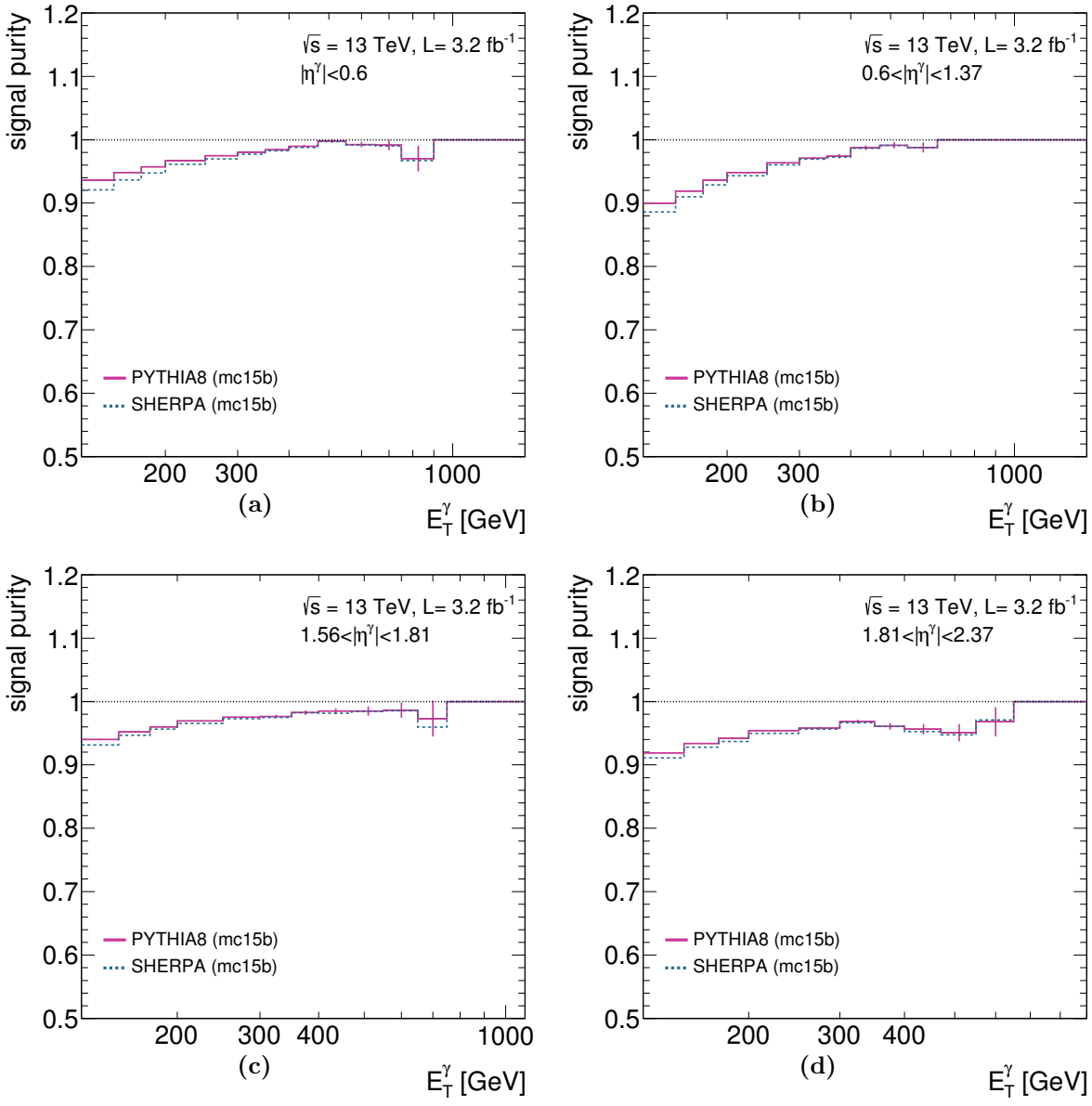


Figure 6.13: Estimated signal purities in data using signal leakage fractions from PYTHIA (solid lines) and SHERPA (dashed lines) as functions of E_{T}^{γ} in different regions of η^{γ}.

6.3.1 Background from electrons faking photons

In addition to the fake photons arising from jets, the background from isolated electrons faking photons was studied. The MC samples of SHERPA 2.2 and ALPGEN for W/Z + jets were used to investigate the contribution of this background. As expected, this background is negligible in this phase-space region. The use of the MC samples for the estimation of this source of background is supported by the data-driven studies performed in [109]; the studies performed in that analysis correspond to the same phase-space region and dataset as used here. The normalisation of the MC predictions was corrected using factors computed with NNLO calculations. After such corrections, the MC predictions agree with the measurements of W/Z production [110,111]. The results are summarised in Tables 6.1 to 6.4.

Sample	Number of events	Fraction of Background
W + jets Sherpa 2.2 no-match	465 ± 285	$0.14\% \pm 0.08\%$
W + jets Sherpa 2.2 matched	429 ± 17	$0.127\% \pm 0.005\%$
Z + jets Sherpa 2.2 no-match	157 ± 267	$0.05\% \pm 0.08\%$
Z + jets Sherpa 2.2 matched	146.0 ± 8.8	$0.043\% \pm 0.003\%$
Total W/Z + jets Sherpa2.2 matched		0.17%
W + jets Alpgen no-match	516 ± 26	$0.153\% \pm 0.008\%$
W + jets Alpgen matched	458 ± 26	$0.135\% \pm 0.008\%$
Z + jets Alpgen no-match	131.5 ± 3.6	$0.039\% \pm 0.001\%$
Z + jets Alpgen matched	119.4 ± 3.5	$0.035\% \pm 0.001\%$
Total W/Z + jets Alpgen matched		0.17%

Table 6.1: Overview of the estimations of the background from electrons faking photons for inclusive photon production in the range $|\eta^{\gamma}| < 0.6$. First column: the MC sample and whether truth matching to $e^{\pm}$ was applied. Second column: estimated number of background events. Third column: fraction of background with respect to the data.

Sample	Number of events	Fraction of Background
W + jets Sherpa2.2 no-match	736 ± 428	$0.17\% \pm 0.10\%$
W + jets Sherpa2.2 matched	685 ± 24	$0.155\% \pm 0.005\%$
Z + jets Sherpa2.2 no-match	206 ± 366	$0.05\% \pm 0.08\%$
Z + jets Sherpa2.2 matched	205 ± 10	$0.046\% \pm 0.002\%$
Total W/Z + jets Sherpa2.2 matched		0.20%
W + jets Alpgen no-match	856 ± 48	$0.194\% \pm 0.011\%$
W + jets Alpgen matched	779 ± 48	$0.176\% \pm 0.011\%$
Z + jets Alpgen no-match	218.2 ± 4.9	$0.049\% \pm 0.001\%$
Z + jets Alpgen matched	200.4 ± 4.7	$0.045\% \pm 0.001\%$
Total W/Z + jets Alpgen matched		0.22%

Table 6.2: Overview of the estimations of the background from electrons faking photons for inclusive photon production in the range $0.6 < |\eta^{\gamma}| < 1.37$. First column: the MC sample and whether truth matching to $e^{\pm}$ was applied. Second column: estimated number of background events. Third column: fraction of background with respect to the data.

Sample	Number of events	Fraction of Background
W + jets Sherpa2.2 no-match	366 ± 442	$0.27\% \pm 0.33\%$
W + jets Sherpa2.2 matched	348 ± 13	$0.26\% \pm 0.01\%$
Z + jets Sherpa2.2 no-match	122 ± 179	$0.09\% \pm 0.13\%$
Z + jets Sherpa2.2 matched	119.1 ± 7.3	$0.088\% \pm 0.005\%$
Total W/Z + jets Sherpa2.2 matched		0.35%
W + jets Alpgen no-match	416 ± 34	$0.306\% \pm 0.025\%$
W + jets Alpgen matched	396 ± 34	$0.292\% \pm 0.025\%$
Z + jets Alpgen no-match	112.4 ± 3.2	$0.083\% \pm 0.002\%$
Z + jets Alpgen matched	109.3 ± 3.2	$0.081\% \pm 0.002\%$
Total W/Z + jets Alpgen matched		0.37%

Table 6.3: Overview of the estimations of the background from electrons faking photons for inclusive photon production in the range $1.56 < |\eta^{\gamma}| < 1.81$. First column: the MC sample and whether truth matching to $e^{\pm}$ was applied. Second column: estimated number of background events. Third column: fraction of background with respect to the data.

Sample	Number of events	Fraction of Background
W + jets Sherpa2.2 no-match	915 ± 354	$0.36\% \pm 0.14\%$
W + jets Sherpa2.2 matched	887 ± 24	$0.345\% \pm 0.009\%$
Z + jets Sherpa2.2 no-match	329 ± 336	$0.13\% \pm 0.13\%$
Z + jets Sherpa2.2 matched	322 ± 14	$0.125\% \pm 0.005\%$
W/Z + jets Sherpa2.2 matched		0.47%
W + jets Alpgen no-match	991 ± 43	$0.385\% \pm 0.017\%$
W + jets Alpgen matched	950 ± 43	$0.370\% \pm 0.017\%$
Z + jets Alpgen no-match	279.6 ± 5.3	$0.109\% \pm 0.002\%$
Z + jets Alpgen matched	272.2 ± 5.2	$0.106\% \pm 0.002\%$
W/Z + jets Alpgen matched		0.48%

Table 6.4: Overview of the estimations of the background from electrons faking photons for inclusive photon production in the range $1.81 < |\eta^{\gamma}| < 2.37$. First column: the MC sample and whether truth matching to $e^{\pm}$ was applied. Second column: estimated number of background events. Third column: fraction of background with respect to the data.

6.4 Control plots

The estimated signal yields divided by the bin width using the signal leakage fractions from Pythia or Sherpa are shown in Figs. 6.14 and 6.15 as functions of E_{T}^{γ} in different regions of η^{γ}. The measured distributions decrease with increasing E_{T}^{γ} by approximately five orders of magnitude within the measured range. This range covers from 125 GeV to 1500 GeV for $|\eta^{\gamma}| < 0.6$ and $0.6 < |\eta^{\gamma}| < 1.37$, up to 1100 GeV for $1.56 < |\eta^{\gamma}| < 1.81$ and up to 900 GeV for $1.81 < |\eta^{\gamma}| < 2.37$. The simulations of Pythia and Sherpa are also shown for comparison; the simulations were normalised to the data in each region of η^{γ} with the factors indicated in parenthesis. Both simulations provide a reasonable description of the data.

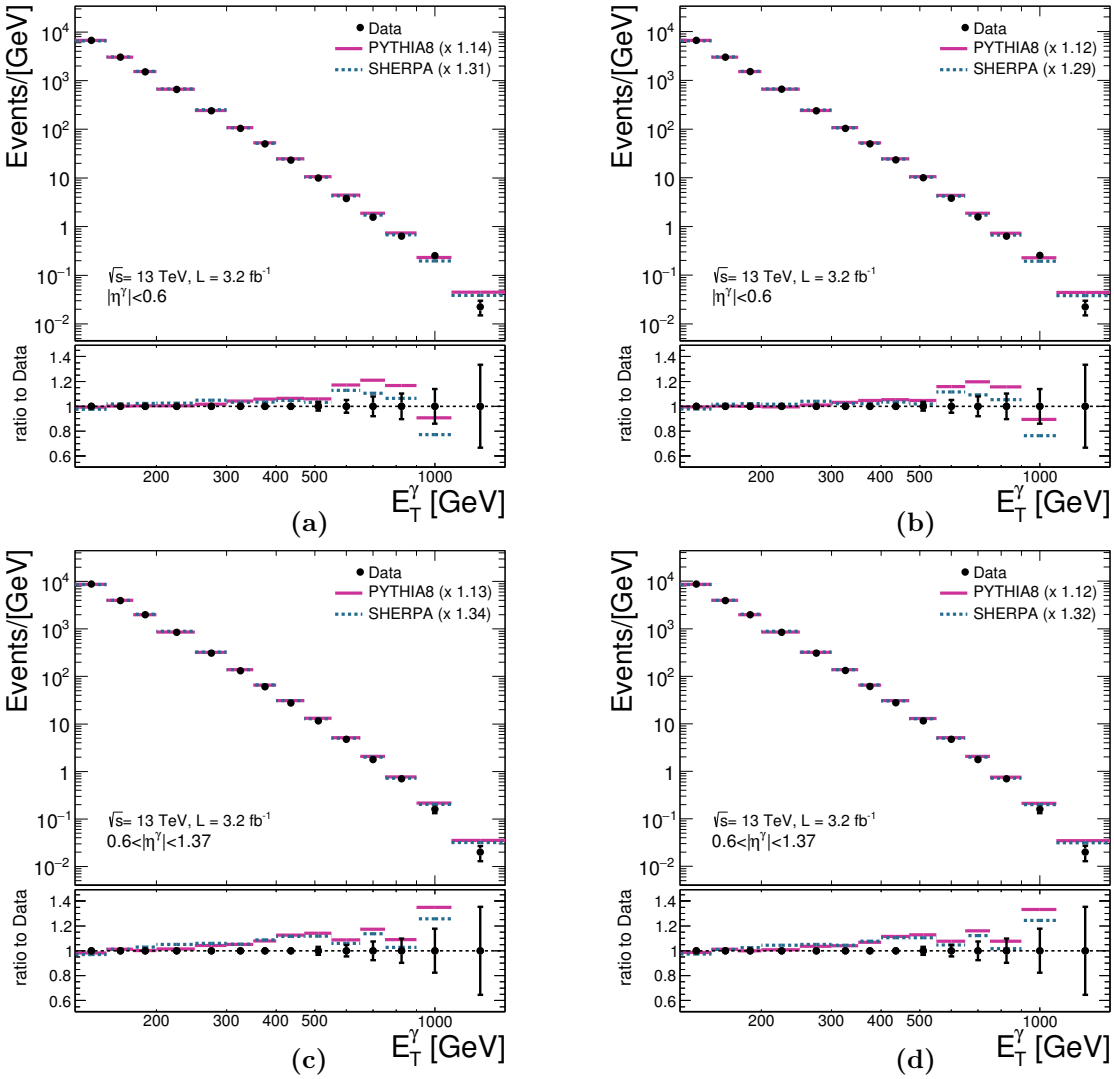


Figure 6.14: The estimated signal yields in data (dots) using signal leakage fractions from Pythia (a,c) or Sherpa (b,d) as functions of E_{T}^{γ} in different regions of η^{γ}. For comparison, the MC simulations of the signal from Pythia (solid histograms) and Sherpa (dashed histograms) are also included. The MC distributions are normalised to the number of data events using the factor indicated in parentheses. The ratio of the MC and data distributions is shown in the lower part of the figures.

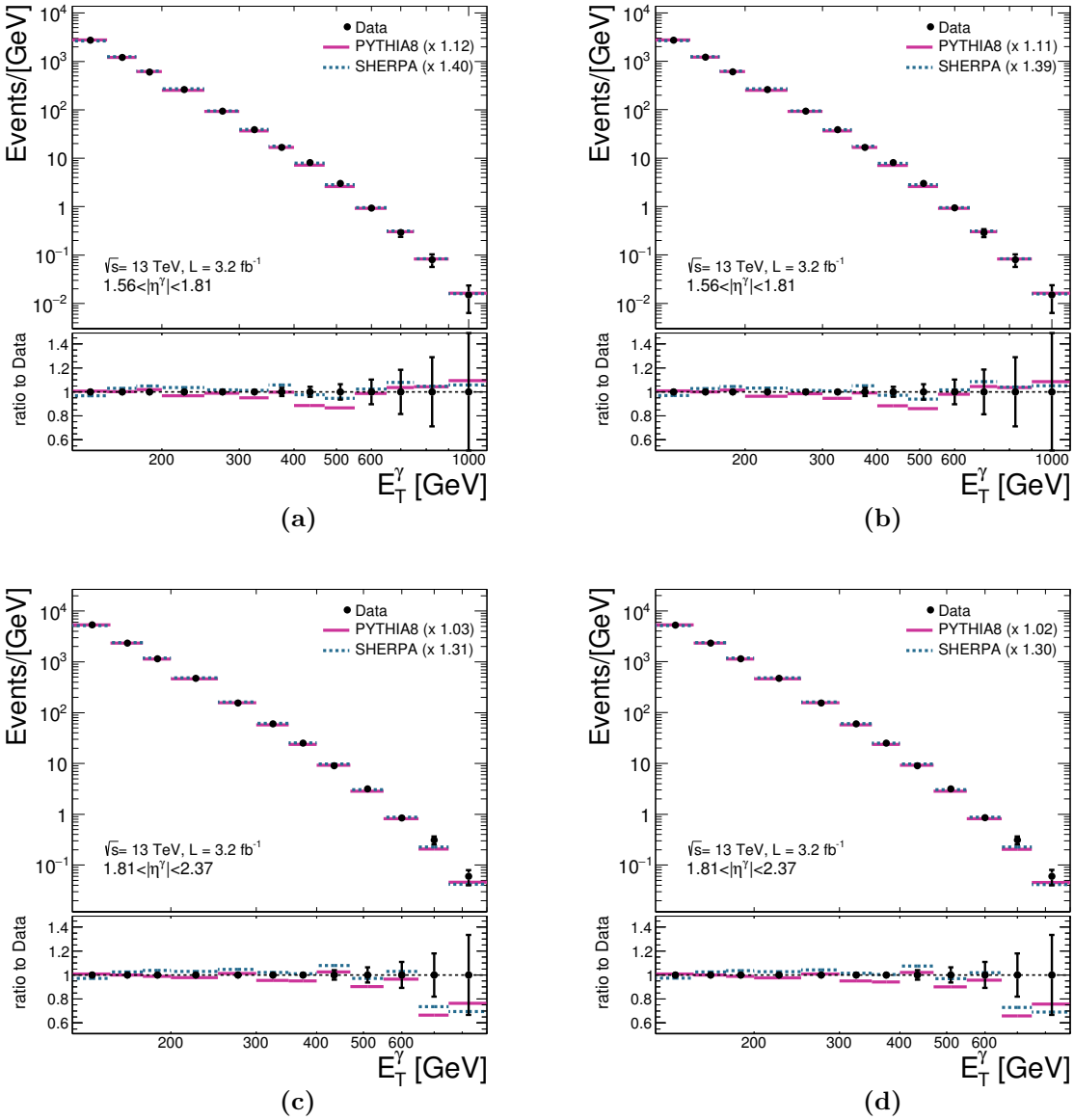


Figure 6.15: The estimated signal yields in data (dots) using signal leakage fractions from Pythia (a,c) or Sherpa (b,d) as functions of E_{T}^{γ} in different regions of η^{γ}. For comparison, the MC simulations of the signal from Pythia (solid histograms) and Sherpa (dashed histograms) are also included. The MC distributions are normalised to the number of data events using the factor indicated in parentheses. The ratio of the MC and data distributions is shown in the lower part of the figures.

6.5 Unfolding

The effects of the detector resolution as well as inefficiencies were corrected for to obtain particle-level kinematic cross-section distributions, easier to compare with the theoretical predictions. The Pythia generator provides a reasonable description of the E_{T}^{γ} distributions in all η^{γ} regions and was the nominal generator used in the unfolding procedure. In this analysis, a bin-by-bin unfolding technique was used in which correction factors were derived using the MC samples. These correction factors were computed for each bin as

$$C_i^{MC} = \frac{N_{\mathrm{part}}^{\mathrm{MC}}(i)}{N_{\mathrm{reco}}^{\mathrm{MC}}(i)}, \tag{6.7}$$

where $N_{\mathrm{part}}^{\mathrm{MC}}(i)$ is the number of events which fulfil the kinematic constraints of the phase-space region at the particle level, i.e. the leading photon at particle level has to satisfy the bin requirements in E_{T}^{γ}, the requirement on η^{γ} and the constraint on the photon isolation at particle level, and $N_{\mathrm{reco}}^{\mathrm{MC}}(i)$ is the number of events which fulfil all the selection criteria at reconstruction level. The correction factors for the Pythia and Sherpa generator are shown in Figure 6.16 and the difference between both generators was taken into account as a systematic uncertainty.

The differential cross section for bin i as a function of a given observable A, $\frac{d\sigma}{dA}(i)$ was obtained with this unfolding method as

$$\frac{d\sigma}{dA}(i) = \frac{N_A^{\mathrm{sig}}(i) C^{\mathrm{MC}}(i)}{\mathcal{L}\Delta A(i)}, \tag{6.8}$$

where $N_A^{\mathrm{sig}}(i)$ is the number of background-subtracted data events in bin i, $C^{\mathrm{MC}}(i)$ is the correction factor in bin i, $\mathcal{L}$ is the integrated measured luminosity and $\Delta A(i)$ is the width of bin i.

The bin-by-bin unfolding technique can be safely applied if the MC sample describes adequately the shape of the measured distribution, the quality of the reconstruction is good, the values of the reconstruction efficiency and purity are sufficiently high and the same binning used at reconstruction level is desired at particle level.

The quality of the reconstruction was studied by means of the correlation at particle and reconstruction levels in the MC samples. The particle- and reconstructed-level photons were required to be geometrically matched using the requirement $\Delta R < 0.2$. The correlations between the reconstruction and particle levels are shown for Pythia in Figure 6.17 and for Sherpa in Figure 6.18. Thanks to the good resolution of the photon energy, a very good reconstruction quality was achieved.

The selection efficiency and purity were evaluated using the MC samples of Pythia and Sherpa. The integrated selection efficiency, ϵ, was computed as

$$\epsilon = \frac{N^{\mathrm{reco,part}}}{N^{\mathrm{part}}}, \tag{6.9}$$

where $N^{\mathrm{reco,part}}$ is the number of MC events that pass all the selection requirement both at reconstruction and particle level and N^{part} is the number of MC events that pass the selection requirements at particle level. The integrated selection efficiency was found to be 86.4% (86.6%) from the Pythia (Sherpa) samples.

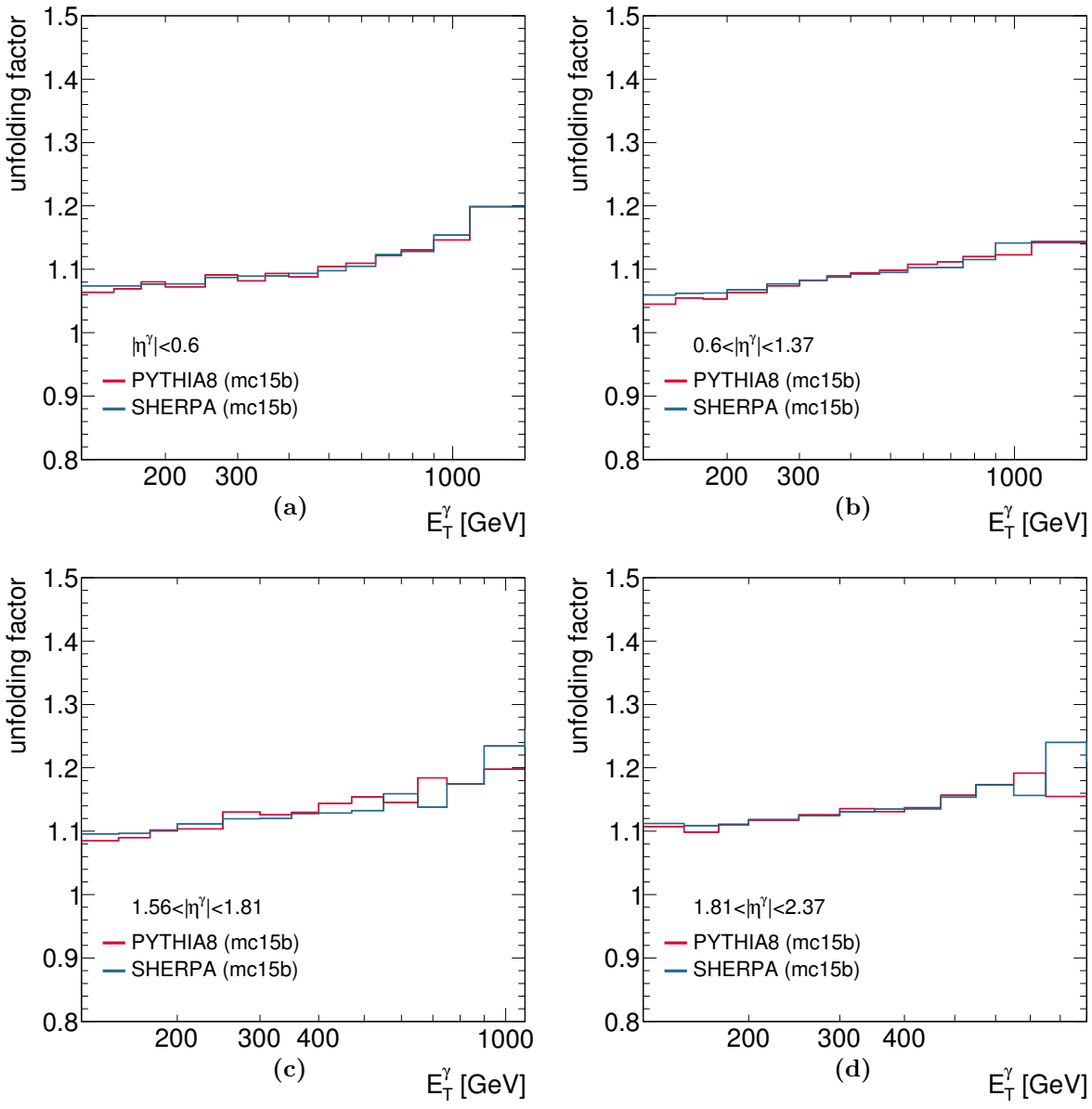


Figure 6.16: Correction factors from PYTHIA (red lines) and SHERPA (blue lines) as functions of E_{T}^{γ} in different regions of η^{γ}.

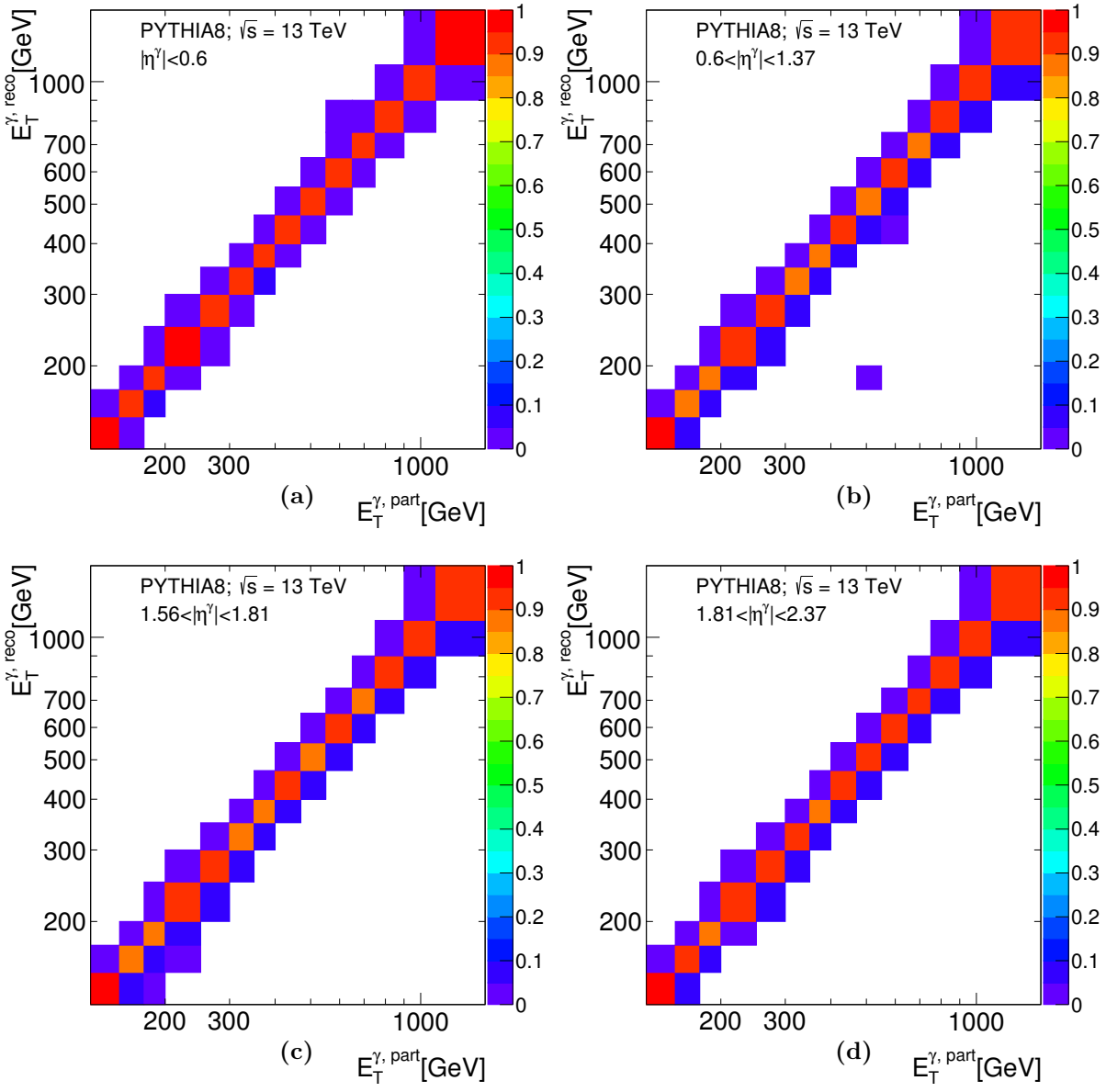


Figure 6.17: The $E_{\mathrm{T}}^{\gamma,\mathrm{reco}}$ vs. $E_{\mathrm{T}}^{\gamma,\mathrm{part}}$ correlation for the PYTHIA MC samples as functions of E_{T}^{γ} in different regions of η^{γ}.

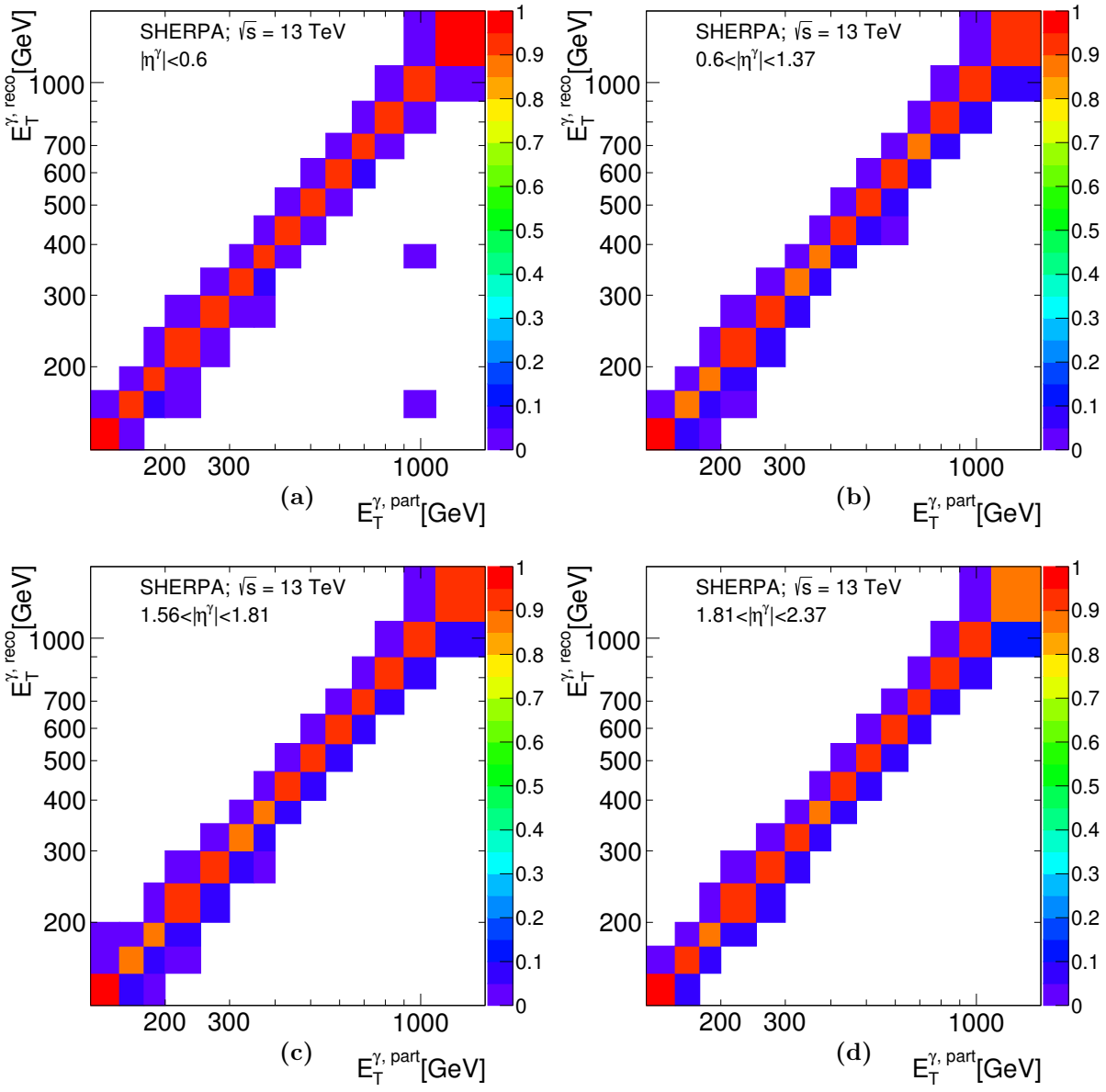


Figure 6.18: The $E_{\mathrm{T}}^{\gamma,\mathrm{reco}}$ vs. $E_{\mathrm{T}}^{\gamma,\mathrm{reco}}$ correlation for the SHERPA MC samples as functions of E_{T}^{γ} in different regions of η^{γ}.

The bin-to-bin selection efficiency was computed for each bin i as

$$\epsilon_i = \frac{N_i^{\text{reco,part}}}{N_i^{\text{part}}}. \tag{6.10}$$

In this case, migrations between different E_{T}^{γ} bins and η^{γ} regions affect the estimation of the efficiency. The bin-to-bin selection efficiency is shown in Figure 6.19. It is typically 75-85% and very similar for both of the generators studied.

The integrated selection purity, $\mathcal{P}$, was computed as

$$\mathcal{P} = \frac{N^{\text{reco,part}}}{N^{\text{reco}}}, \tag{6.11}$$

where N^{reco} is the number of events that pass all the selection requirements at reconstruction level. The integrated selection purity was found to be 92.9% (93.7%) from the PYTHIA (SHERPA) samples. The bin-to-bin selection purity in bin i was computed as $\mathcal{P}_i = \frac{N_i^{\text{reco,part}}}{N_i^{\text{reco}}}$ and measures the fraction of events observed in bin i at reconstruction level which were generated in the same bin at particle level. The bin-to-bin selection purity (Figure 6.20) lies above $\approx 85\%$ and is very similar for both of the generators studied.

The bin-to-bin reconstruction efficiency and purity were taken into account in the correction factors used to unfold the measurements since the correction factor can be written as

$$C_i^{MC} = \frac{\mathcal{P}_i}{\epsilon_i}. \tag{6.12}$$

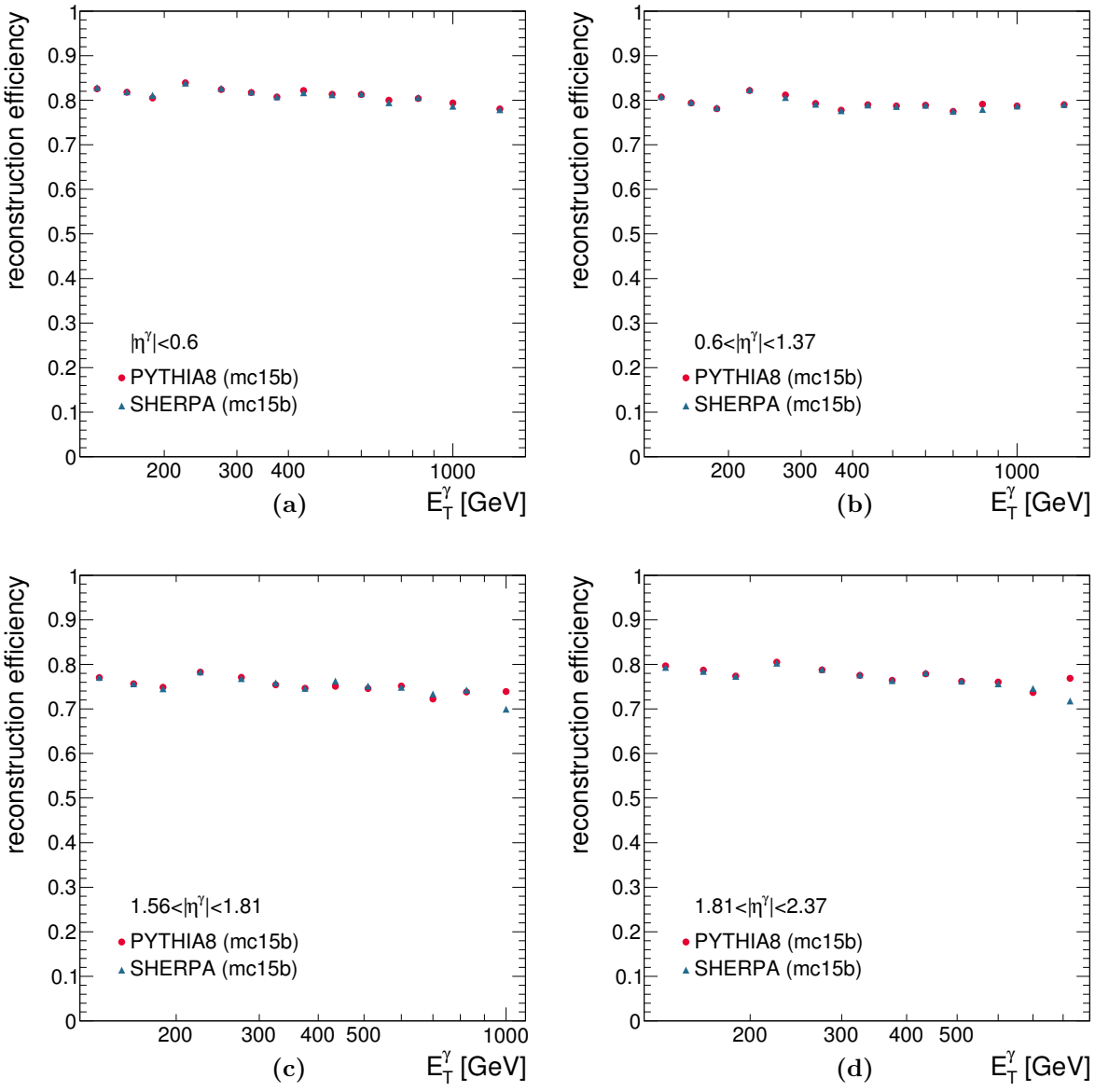


Figure 6.19: Selection efficiency from PYTHIA (dots) and SHERPA (triangles) as functions of E_{T}^{γ} in different regions of η^{γ}.

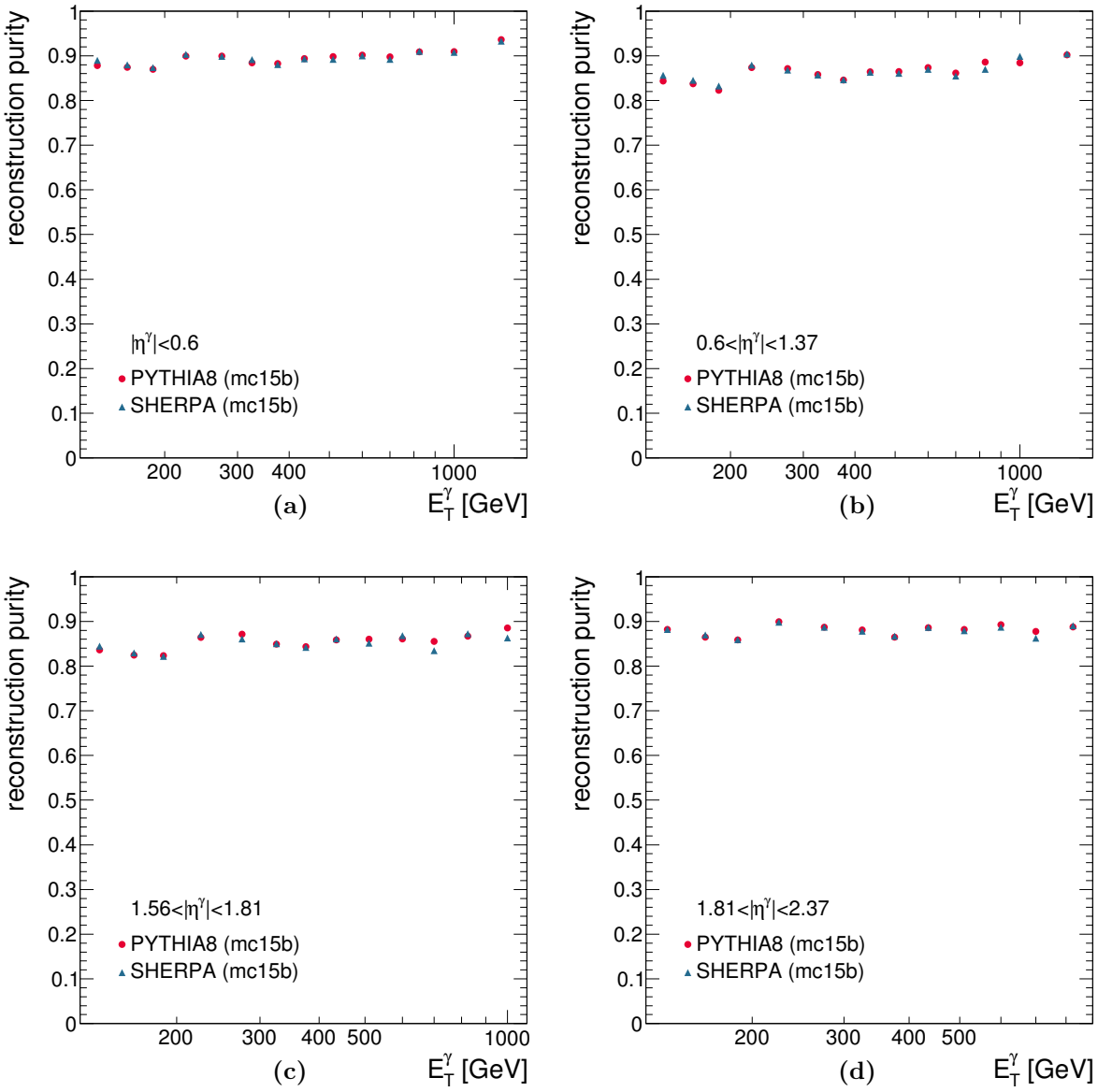


Figure 6.20: Selection purity from PYTHIA (dots) and SHERPA (triangles) as functions of E_{T}^{γ} in different regions of η^{γ}.

6.5.1 Iterative Bayesian unfolding

A more sophisticated unfolding method, based on the iterative application of Bayes' theorem [113], was investigated to validate the results obtained using the bin-by-bin method explained above. The Bayesian technique infers the "true" distribution (the particle-level distribution) taking properly into account the migrations between bins and the reconstruction purity and efficiency when the MC description of the data is not adequate. One weak point of the Bayes approach is the need of knowledge of the initial distribution, this is overcome by an iterative procedure. This unfolding procedure was implemented using the RooUnfold package [114].

In the case of 1-dimensional distributions, as the ones treated in this analysis, the true distribution bins, T_j, can be obtain by applying an unfolding matrix, R_{ij}, to the measured bins, M_i. For the iterative Bayesian unfolding, this matrix is obtained applying Bayes' theorem. The correlation between the reconstructed distribution and the true distribution is needed for this method. This correlation matrix, also known as the transfer matrix, is obtained from the MC and contains the information of bin migrations from the particle to the reconstruction level and reconstruction efficiency. The folding matrix can be obtained from the transfer matrix by normalising the sum of entries in a bin of the true physical quantity to unity. This matrix gives the probability for a value of the true physical quantity to be reconstructed at a given value and it is shown in Figures 6.21 to 6.24. The unmatched events are those events that fulfil the selection criteria only at particle or reconstruction level (but not both), but do not fulfil a matching criterion between both levels. The fractions of unmatched events are shown in Figures 6.21 to 6.24. The particle-level unmatched events were taken into account by scaling the response matrix by the efficiency (ε_i in Equation 6.14) of each truth bin, while the reconstruction-level unmatched events were taken into account through the correction of the output by the fraction of reconstructed events in a given bin i that are matched to particle level (independently on the bin in which the event was generated) over the total number of reconstruction-level events in bin i in the MC. This correction fraction is referred to as κ_j.

The goal of the approach is to estimate the probability that events generated in a true bin i are reconstructed in a bin j. Using Bayes' theorem:

$$P(T_i|M_j) = \frac{P(M_j|T_i)P_0(T_i)}{\sum_{l=1}^{n_T} P(M_j|T_l)P_0(T_l)} \tag{6.13}$$

$$\hat{n}(T_i) = \frac{1}{\varepsilon_i}\sum_{j=1}^{n_M} n(M_j)P(T_i|M_j), \quad \varepsilon_i \neq 0, \tag{6.14}$$

where $\hat{n}(T_i)$ is the expected number of true events in bin i, $n(M_j)$ is the number of data events in the measured bin j after background subtraction, $P_0(T_i)$ is the initial probability, ε_i is the efficiency for true events in bin i measured at reconstruction level, n_T is the number of bins at particle level and n_M is the number of measured bins ($n_T = n_M$ in this analysis). This can be rewritten in terms of the unfolding matrix R as

$$\hat{n}(T_i) = \sum_{j=1}^{n_M} R_{ij} n(M_j), \tag{6.15}$$

$$R_{ij} = \frac{P(M_j|T_i)P_0(T_i)}{\left[\sum_{l=1}^{n_M} P(M_l|T_i)\right]\left[\sum_{l=1}^{n_T} P(M_j|T_l)P_0(T_l)\right]}. \tag{6.16}$$

The initial prior is obtained from the true distribution in which the number of entries in each bin is normalised to the total number of events at particle level. It is updated to $\hat{n}(T_i)$ normalised to $\hat{n}(T) = \sum_{i=1}^{n_T} \hat{n}(T_i)$ for the next iteration. The values of $P(M_j|T_i)$ are taken from the j,i entry of the transfer matrix normalised to the total number of generated events in bin i.

The differential cross section for a bin i as a function of a given observable A, $\frac{d\sigma}{dA}(i)$ was obtained with this unfolding method as

$$\frac{d\sigma}{dA}(i) = \frac{1}{\mathcal{L}\Delta A(i)} \sum_{j=1}^{n_M} R_{ij}\kappa_j N_A^{\text{sig}}(j), \tag{6.17}$$

where $N_A^{\text{sig}}(j)$ is the number of background-subtracted data events in bin j, R is the unfolding matrix, $\mathcal{L}$ is the measured integrated luminosity and $\Delta A(i)$ is the width of bin i.

The number of iterations is a regularisation parameter for this iterative unfolding method. A reasonable performance is obtained with only a few iterations. Since the method converges quickly, the optimal number of iterations was extracted by comparing the unfolding results obtained at consecutive iteration steps and choosing the number of iterations for which the change is small with respect to the following iterations. A lower value of iterations is preferred since the statistical uncertainty increases with the number of iterations. The chosen number of iterations was four and comparisons of the unfolded distributions with a different number of iterations are shown in Figures 6.21 to 6.24.

The comparisons between the cross sections unfolded via the bin-by-bin and the Bayes techniques are shown in Figures 6.21 to 6.24 as functions of E_{T}^{γ} for the different regions of $|\eta^{\gamma}|$. The differences between the cross sections obtained via the two methods are generally much smaller than 1%. In the regions of phase space where the MC statistics is poor some deviations are observed, but they are well within the statistical uncertainty of the data. The relative statistical uncertainty coming from the data in the cross sections is shown in the figures for comparison. The folding matrix as well as the reconstructed photons not matched to a truth photon ("reco unmatched") as well as reconstruction inefficiencies ("truth unmatched") are shown in Figure 6.21 to 6.24.

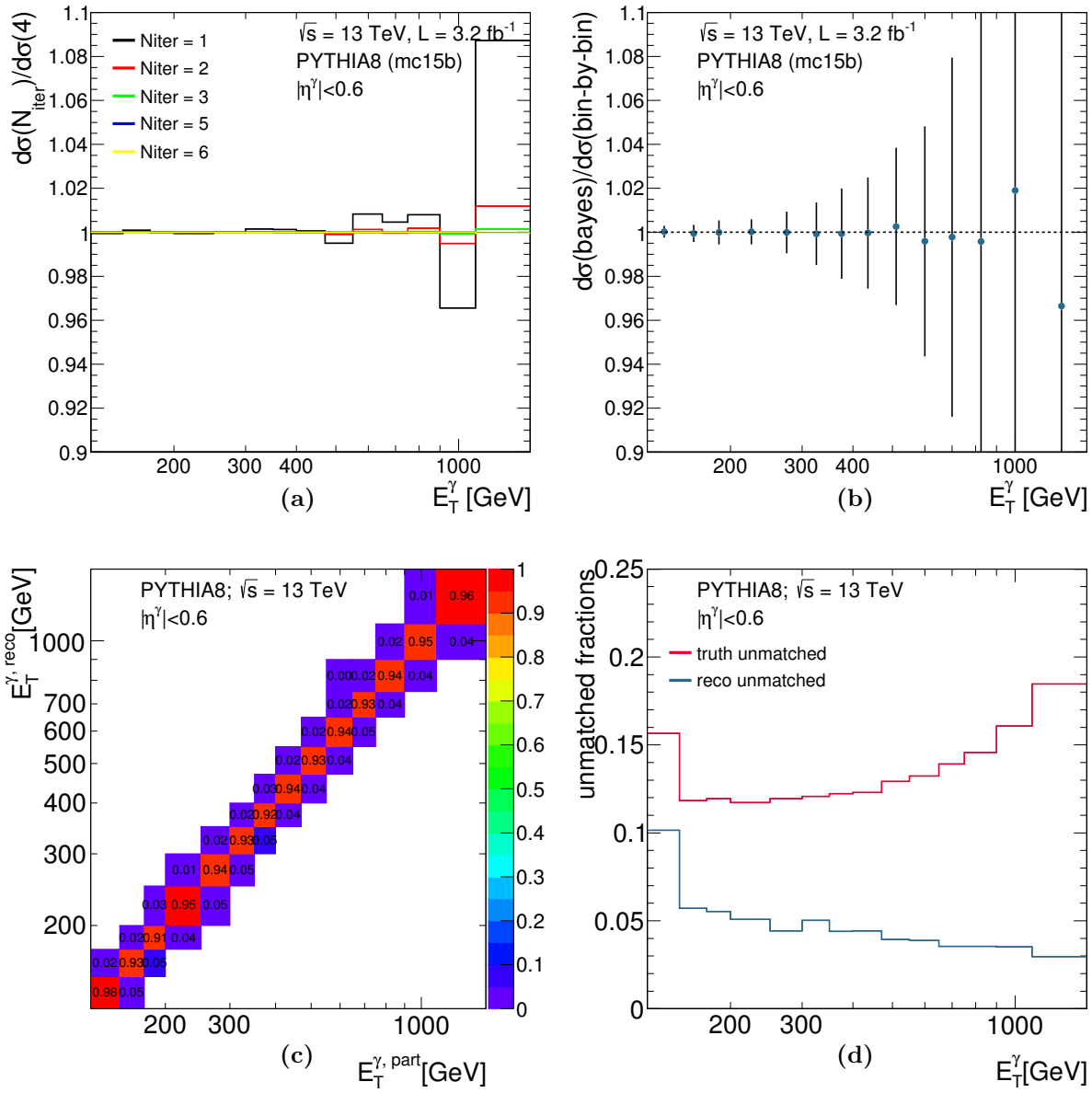


Figure 6.21: (a) Ratio between the cross sections unfolded using the Bayesian method with N iterations and the results unfolded using 4 iterations (PYTHIA MC was used) as a function of E_{T}^{γ} for $|\eta^{\gamma}| < 0.6$. (b) Ratio between the cross sections unfolded using the Bayesian method with four iterations and the nominal cross sections as a function of E_{T}^{γ} for $|\eta^{\gamma}| < 0.6$. The error bars display the statistical uncertainty on the cross section. (c) Folding matrix from PYTHIA for E_{T}^{γ} for $|\eta^{\gamma}| < 0.6$. (d) Fraction of unmatched truth (red lines) and reco (blue lines) events.

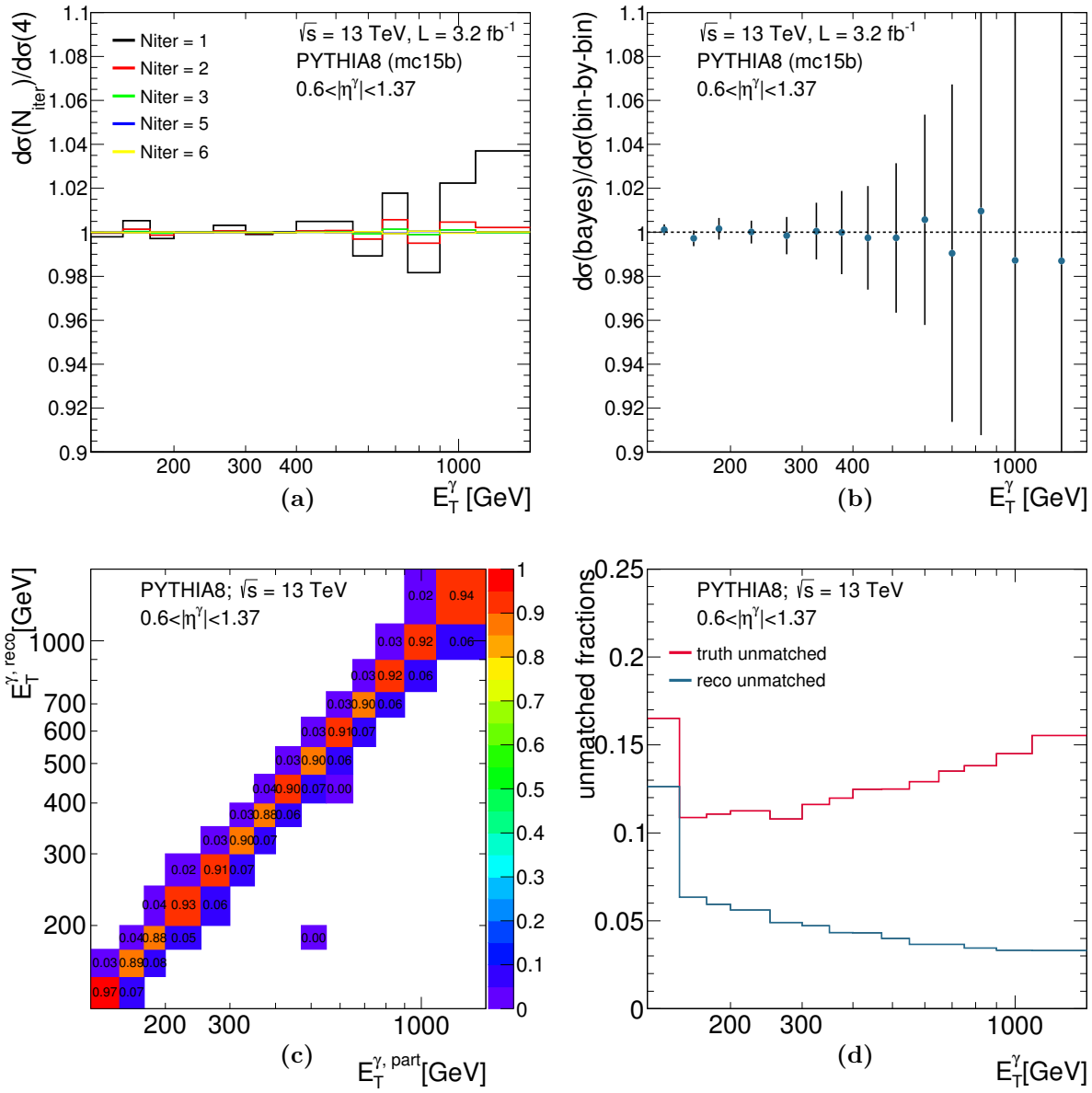


Figure 6.22: (a) Ratio between the cross sections unfolded using the Bayesian method with N iterations and the results unfolded using 4 iterations (PYTHIA MC was used) as a function of E_{T}^{γ} for $0.6 < |\eta^{\gamma}| < 1.37$. (b) Ratio between the cross sections unfolded using the Bayesian method with four iterations and the nominal cross sections as a function of E_{T}^{γ} for $0.6 < |\eta^{\gamma}| < 1.37$. The error bars display the statistical uncertainty on the cross section. (c) Folding matrix from PYTHIA for E_{T}^{γ} for $0.6 < |\eta^{\gamma}| < 1.37$. (d) Fraction of unmatched truth (red lines) and reco (blue lines) events.

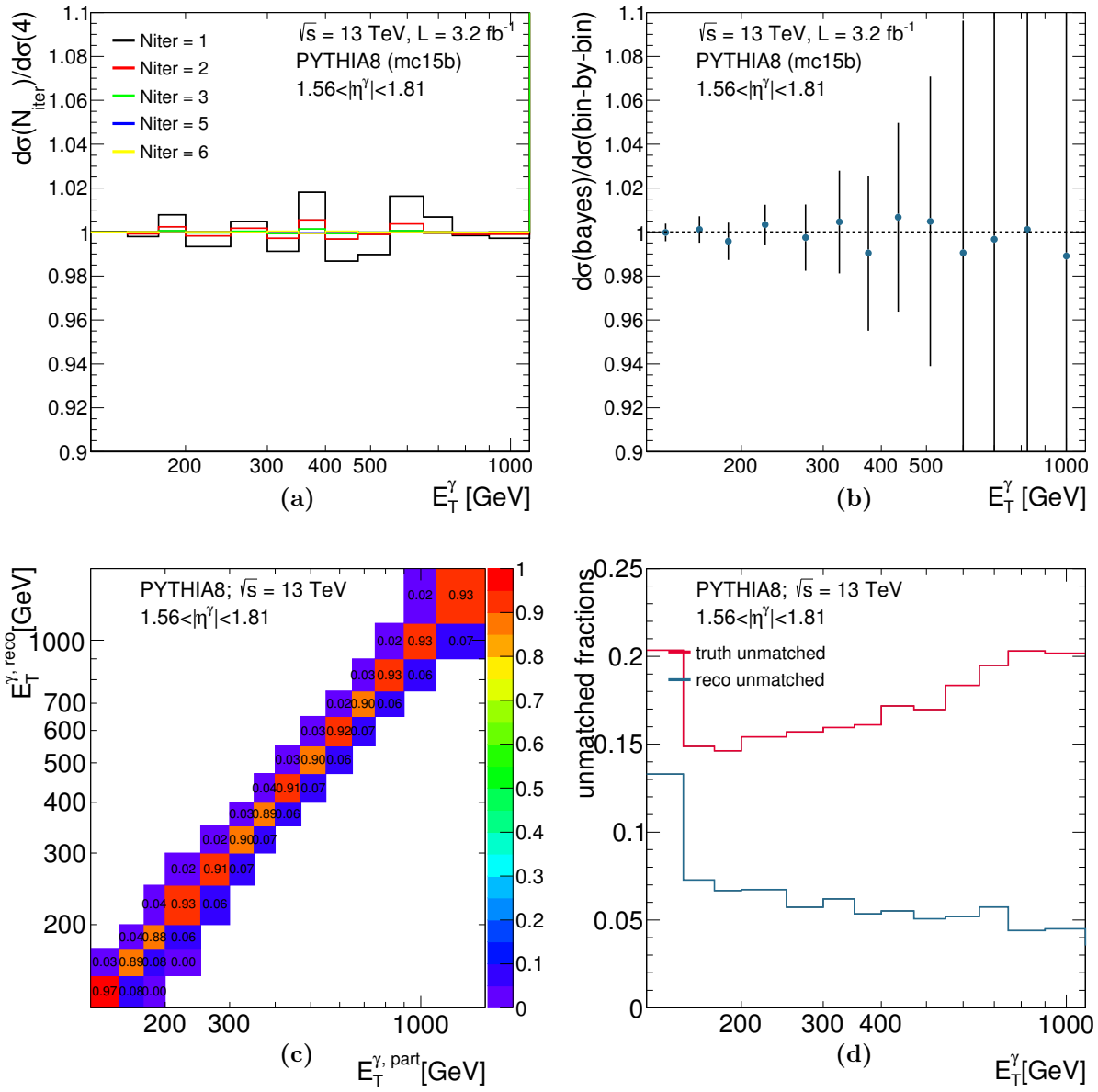


Figure 6.23: (a) Ratio between the cross sections unfolded using the Bayesian method with N iterations and the results unfolded using 4 iterations (PYTHIA MC was used) as a function of E_{T}^{γ} for $1.56 < |\eta^{\gamma}| < 1.81$. (b) Ratio between the cross sections unfolded using the Bayesian method with four iterations and the nominal cross sections as a function of E_{T}^{γ} for $1.56 < |\eta^{\gamma}| < 1.81$. The error bars display the statistical uncertainty on the cross section. (c) Folding matrix from PYTHIA for E_{T}^{γ} for $1.56 < |\eta^{\gamma}| < 1.81$. (d) Fraction of unmatched truth (red lines) and reco (blue lines) events.

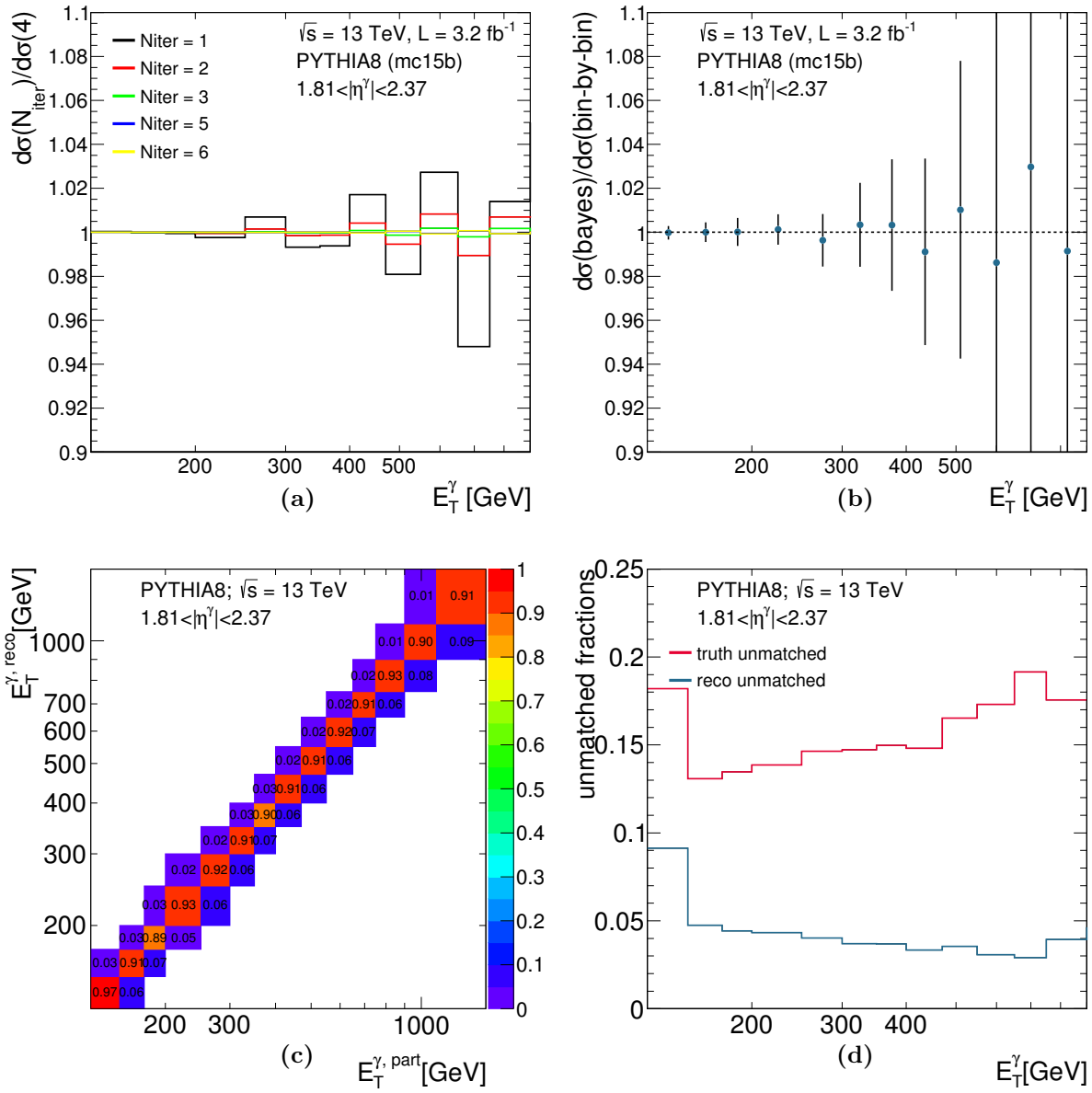


Figure 6.24: (a) Ratio between the cross sections unfolded using the Bayesian method with N iterations and the results unfolded using 4 iterations (PYTHIA MC was used) as a function of E_{T}^{γ} for $1.81 < |\eta^{\gamma}| < 2.37$. (b) Ratio between the cross sections unfolded using the Bayesian method with four iterations and the nominal cross sections as a function of E_{T}^{γ} for $1.81 < |\eta^{\gamma}| < 2.37$. The error bars display the statistical uncertainty on the cross section. (c) Folding matrix from PYTHIA for E_{T}^{γ} for $1.81 < |\eta^{\gamma}| < 2.37$. (d) Fraction of unmatched truth (red lines) and reco (blue lines) events.

6.6 Systematic uncertainties

The main sources of systematic uncertainties that affect the measurements were investigated. These sources include the photon energy scale and resolution, the model dependence, the QCD-cascade and hadronisation model dependence, the photon identification efficiency, the MC isolation correction, the choice of background control regions, the identification and isolation correlation in the background, the signal modelling, pile-up reweighting, MC sample statistics, the trigger efficiency and the luminosity-measurement uncertainties. Each source is detailed below.

6.6.1 Photon energy scale and resolution

Differences between the energy scale and resolution in data and simulations lead to systematic uncertainties in the cross-section measurements. The preliminary photon energy scale uncertainties for Run-2 were used in this analysis. The photon calibration procedure as well as details on the uncertainties were explained in Section 4.2.

The systematic uncertainties on the measured cross section due to the uncertainty in the photon energy scale were estimated by varying each individual source of uncertainty (71 nuisance parameters in total) separately in the MC simulations and, then, added in quadrature. Figure 6.25 shows the resulting uncertainties together with the largest contribution in each region of η^{γ}. In most of the regions, the uncertainty arising from the dependence of the energy response from the gain used in the read-out chain in the second layer of the EM calorimeter is the dominant uncertainty.

The statistical uncertainty of the systematic variations was obtained by a bootstrap technique in which several MC replicas were used. For each replica, events were weighted according to a Poisson distribution with unity mean and the photon energy scale was varied according to each nuisance parameter. The mean value of the relative uncertainty was obtained from the mean of the differences in the cross section with respect to the nominal and the statistical uncertainty from the RMS of the same distribution for each bin. The uncertainty coming from each variation was then fitted, taking into account its statistical uncertainty, to a smooth function and added in quadrature to obtain the value of the total systematic uncertainty due to the photon energy scale without statistical fluctuations. The final uncertainty is shown in Figure 6.26.

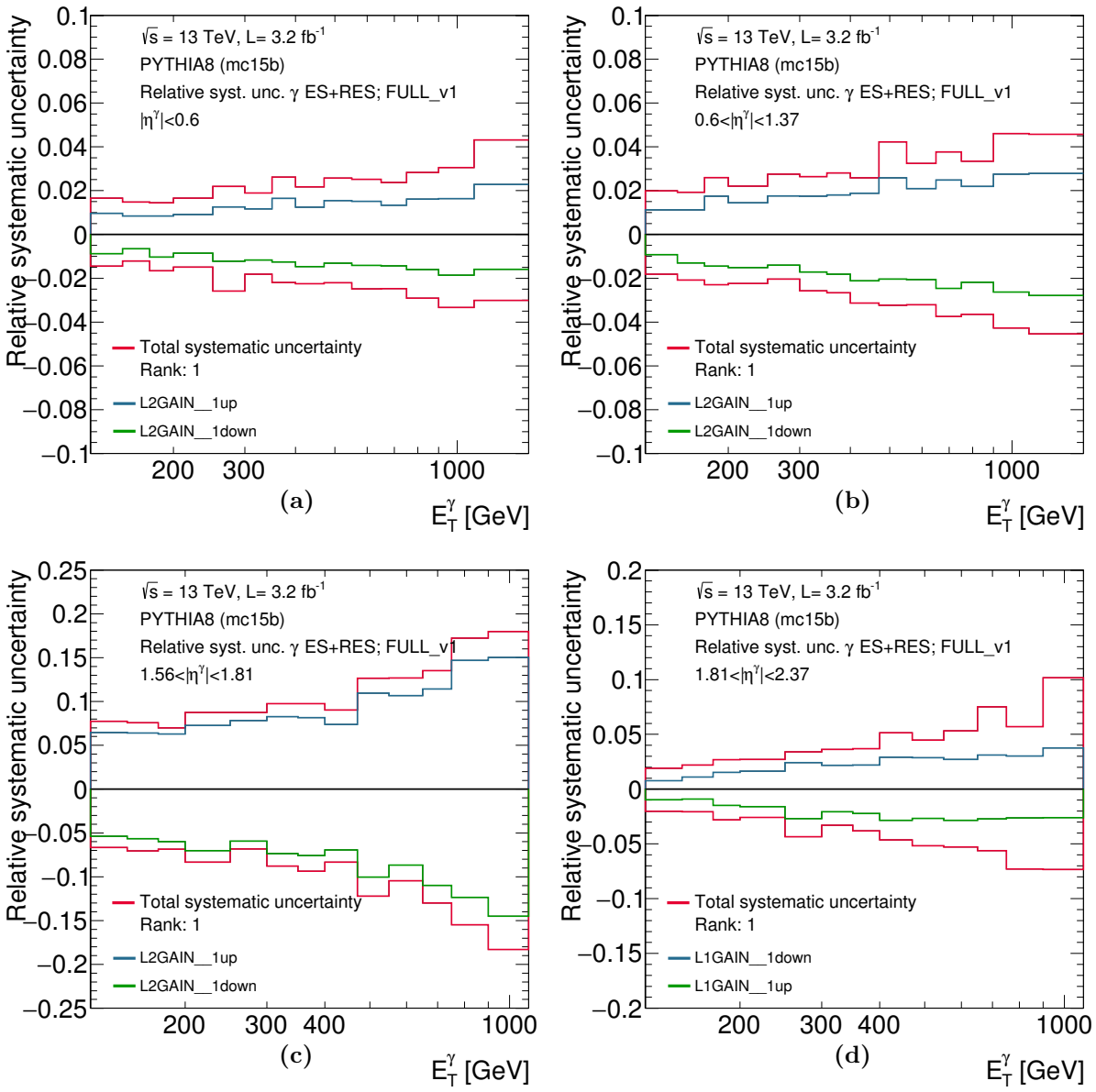


Figure 6.25: Systematic uncertainties on the measured cross section due to the uncertainty in the photon energy scale and resolution as functions of E_{T}^{γ} in different regions of η^{γ} (red lines). The blue (green) lines represent the upwards (downwards) largest contribution to this uncertainty.

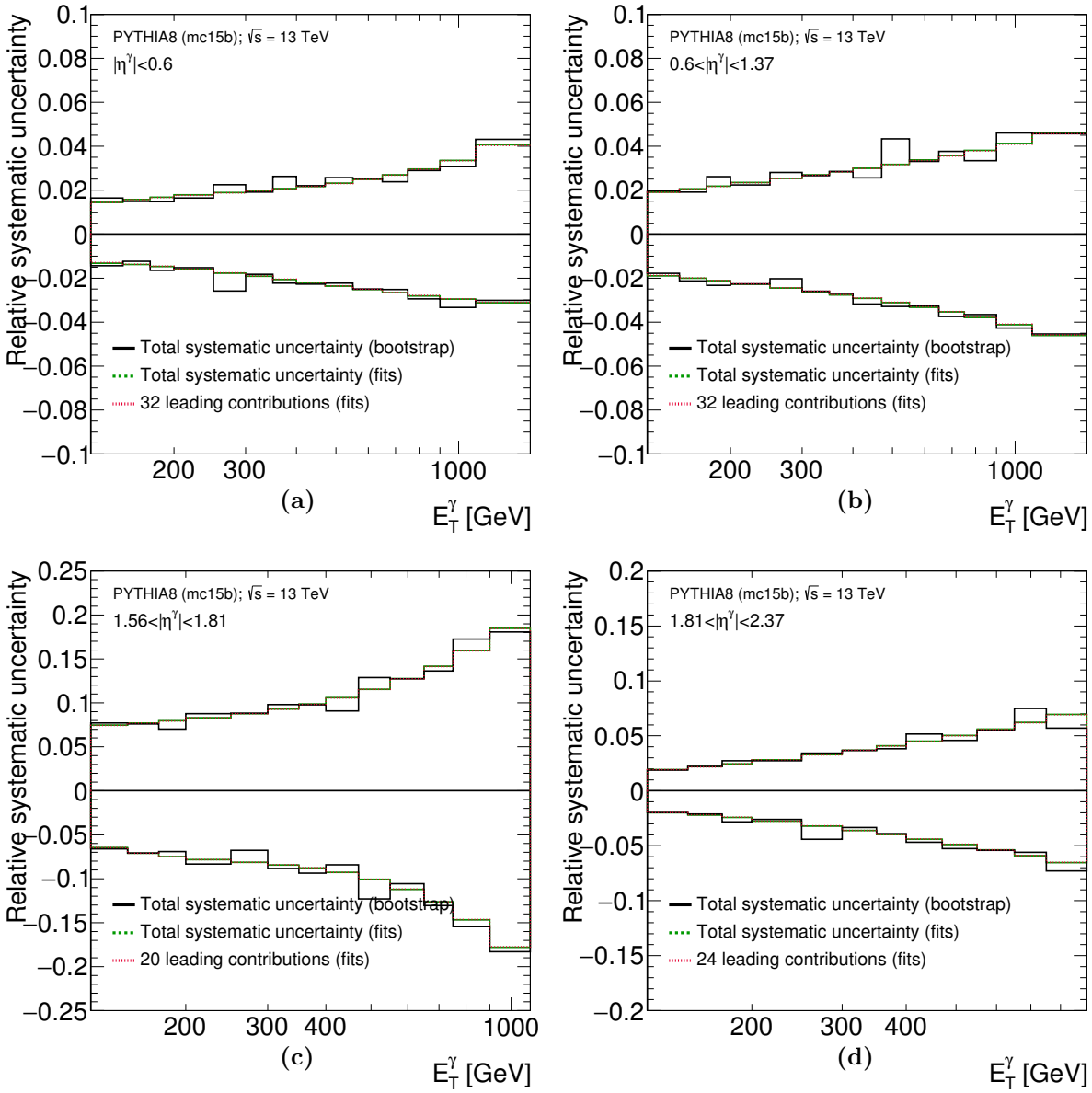


Figure 6.26: Systematic uncertainties on the measured cross section due to the uncertainty in the photon energy scale and resolution as functions of E_{T}^{γ} in different regions of η^{γ} using a bootstrap technique (black lines). The sum in quadrature of the fits to the bootstrap results for each nuisance parameter is represented by the green dashed line. The sum in quadrature of the fits for a certain number of leading contributions is shown by the red dotted line.

6.6.2 QCD-cascade and hadronisation model dependence

The effects due to the different parton-shower ordering and hadronisation models between Pythia and Sherpa in the signal purity and correction factors were estimated. The deviations observed from the nominal results obtained with Pythia by using Sherpa MC determined the size of the uncertainties. Both effects were separated into two uncertainties following a conservative approach to avoid possible partial cancellations of the two effects:

- the signal leakage fractions of Sherpa were used to subtract the background via the 2D-sideband method. The unfolding was performed with Pythia. The differences with respect to the nominal results (with signal leakage fractions from Pythia) are shown in Figure 6.27;
- the unfolding was performed with Sherpa while the signal leakage fractions were estimated with Pythia. The differences with respect to the nominal results (with unfolding factors from Pythia) are shown in Figure 6.28.

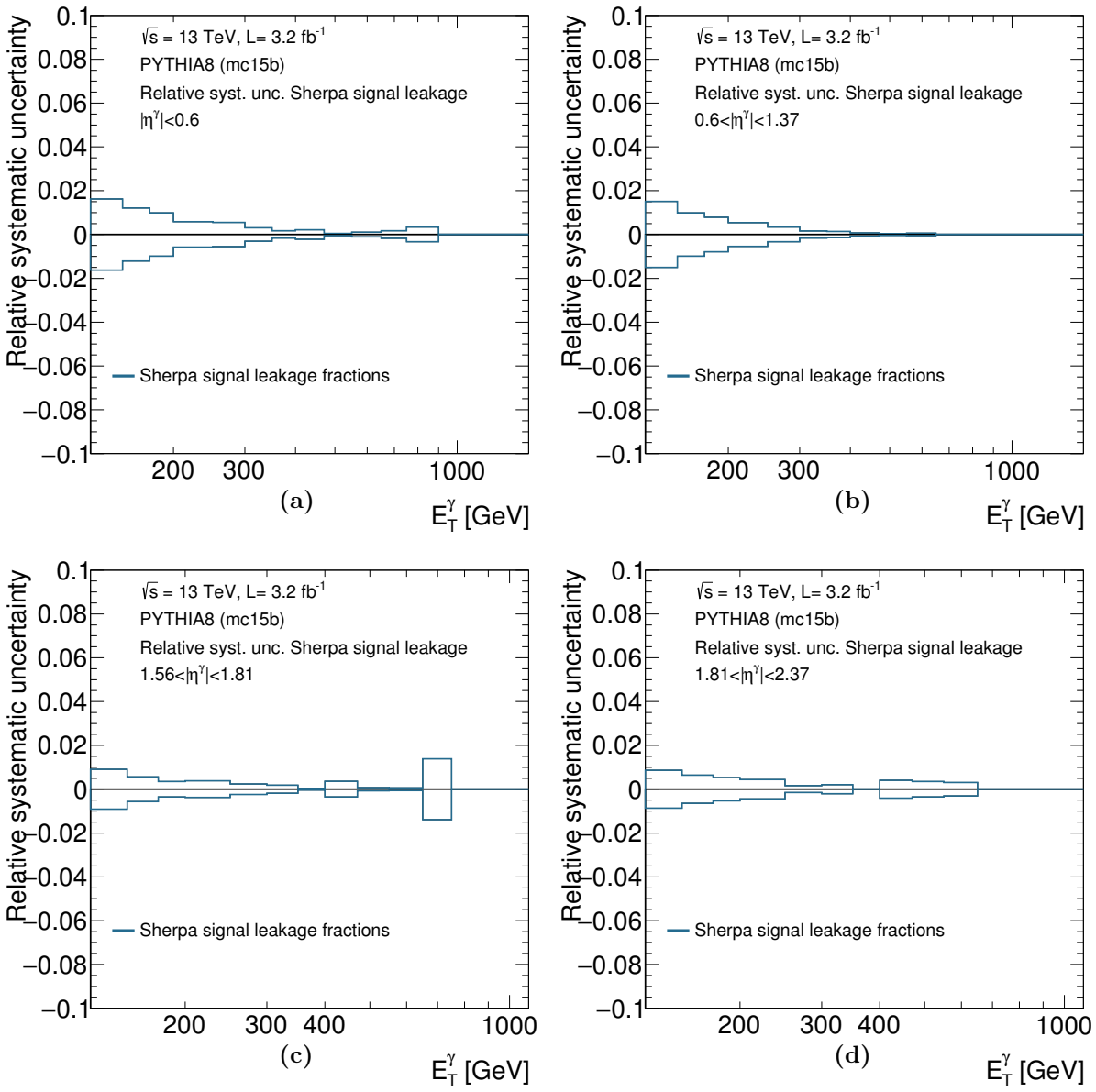


Figure 6.27: Systematic uncertainties on the measured cross section due to the QCD-cascade and hadronisation model as functions of E_{T}^{γ} in different regions of η^{γ} using SHERPA to estimate the signal purity. This uncertainty has been symmetrised.

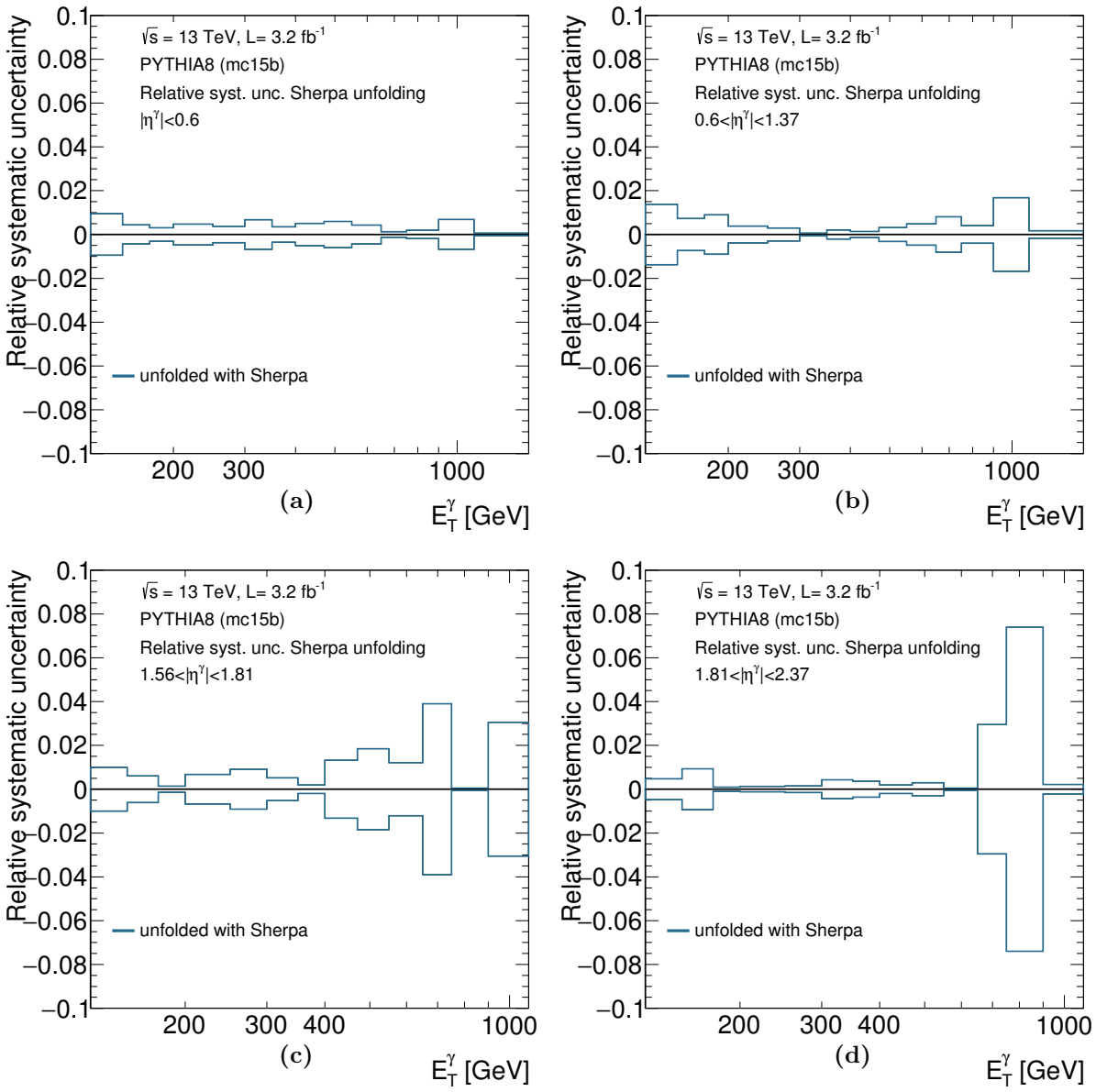


Figure 6.28: Systematic uncertainties on the measured cross section due to the QCD-cascade and hadronisation model as functions of E_{T}^{γ} in different regions of η^{γ} using SHERPA to estimate the correction factors. This uncertainty has been symmetrised.

6.6.3 Photon identification

The uncertainty on the photon identification efficiency was estimated using pre-recommendations for 2015 data. They assumed that the "tight" identification efficiency was well modelled in the MC and the systematic uncertainties were obtained by switching on and off the corrections applied to the shower-shape variables used in the photon identification. The photon identification efficiencies from data-driven methods and MC simulations were compared in Reference [90]. No significant difference is observed between the data-driven measurements and the nominal or corrected (for the small differences in the average values of the shower-shape values between data and simulation) simulation for $E_{\mathrm{T}}^{\gamma} > 60$ GeV. The resulting uncertainties are shown in Figure 6.29.

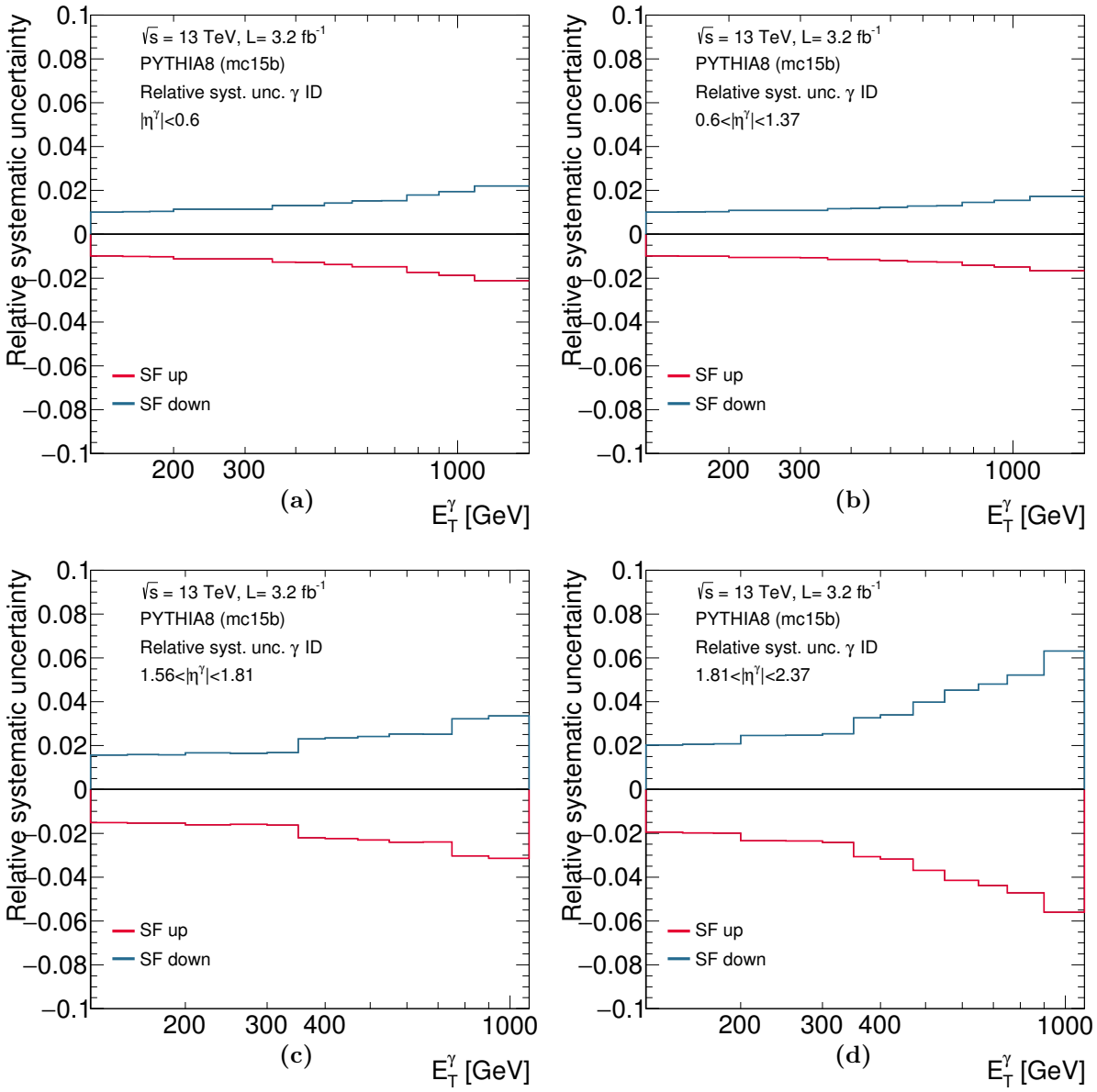


Figure 6.29: Systematic uncertainties on the measured cross sections due to the uncertainty in the photon-ID efficiency as functions of E_{T}^{γ} in different regions of η^{γ}.

6.6.4 Isolation correction

A systematic uncertainty was assigned to the mismodelling of the $E_{\mathrm{T}}^{\mathrm{iso}}$ distribution of signal photons by the MC simulations. The nominal results were obtained by shifting the MC predictions with data-driven corrections. These corrections were extracted in an independent analysis by fitting the isolation distributions with a Crystal Ball function with parameters depending on E_{T}^{γ} in different η^{γ} bins for converted and unconverted photons separately. After this final correction to the isolation values, the $E_{\mathrm{T}}^{\mathrm{iso}}$ distributions in data and MC were compared. For this purpose, the distribution of non-tight photons, which simulates the background, and the MC simulation distribution for prompt photons were added according to a χ^2 fit to the measured $E_{\mathrm{T}}^{\mathrm{iso}}$ distribution of tight photons measured in data. These comparisons were made in the different regions of η^{γ} of the analysis and different E_{T}^{γ} bins. As an example, Figure 6.30 shows the comparison for $125 < E_{\mathrm{T}}^{\gamma} < 175$ GeV in different η^{γ} regions. The resulting uncertainties on the cross section were estimated by comparing the nominal results to those obtained without applying the data-driven corrections to $E_{\mathrm{T}}^{\mathrm{iso}}$ and are shown in Figure 6.31. This uncertainty is not symmetrised for the final results.

6.6.5 Choice of background control regions

The estimation of the background contamination in the signal region may be affected by the choice of the background control regions. Several uncertainties were considered as follows.

- The definition of the non-isolated control regions was changed in two different ways:
  - the lower limit of isolation of these regions was varied from the nominal value, $E_T^{\mathrm{iso}} > (4.8 + 2) + 4.2 \cdot 10^{-3} E_{\mathrm{T}}^{\gamma}$ [GeV] by 1 GeV up and down. The results are shown in Figure 6.32;
  - the upper limit on $E_{\mathrm{T}}^{\mathrm{iso}}$ for regions B and D (set at 50 GeV for the nominal results) was removed. The resulting uncertainty is shown in Figure 6.33.
- The definition of the non-tight control regions was varied. The looser loose' and the tighter loose' criteria were used to select the events with a leading photon passing the modified loose' criteria but failing the tight selection. The uncertainty was smoothed following the same recipe as explained in Section 6.6.1 for the photon energy scale uncertainty. The original results without bootstrapping, the bootstrap results and the χ^2 fits are shown in Figures 6.34 and 6.35. In some cases, the fitting function crosses zero; in those cases, upper and lower bounds were determined to avoid the estimated uncertainty being artificially zero at some value of E_T^{γ}; the upper and lower bands are presented by in Figures 6.34 and 6.35. Figure 6.36 shows the resulting uncertainties on the cross sections.

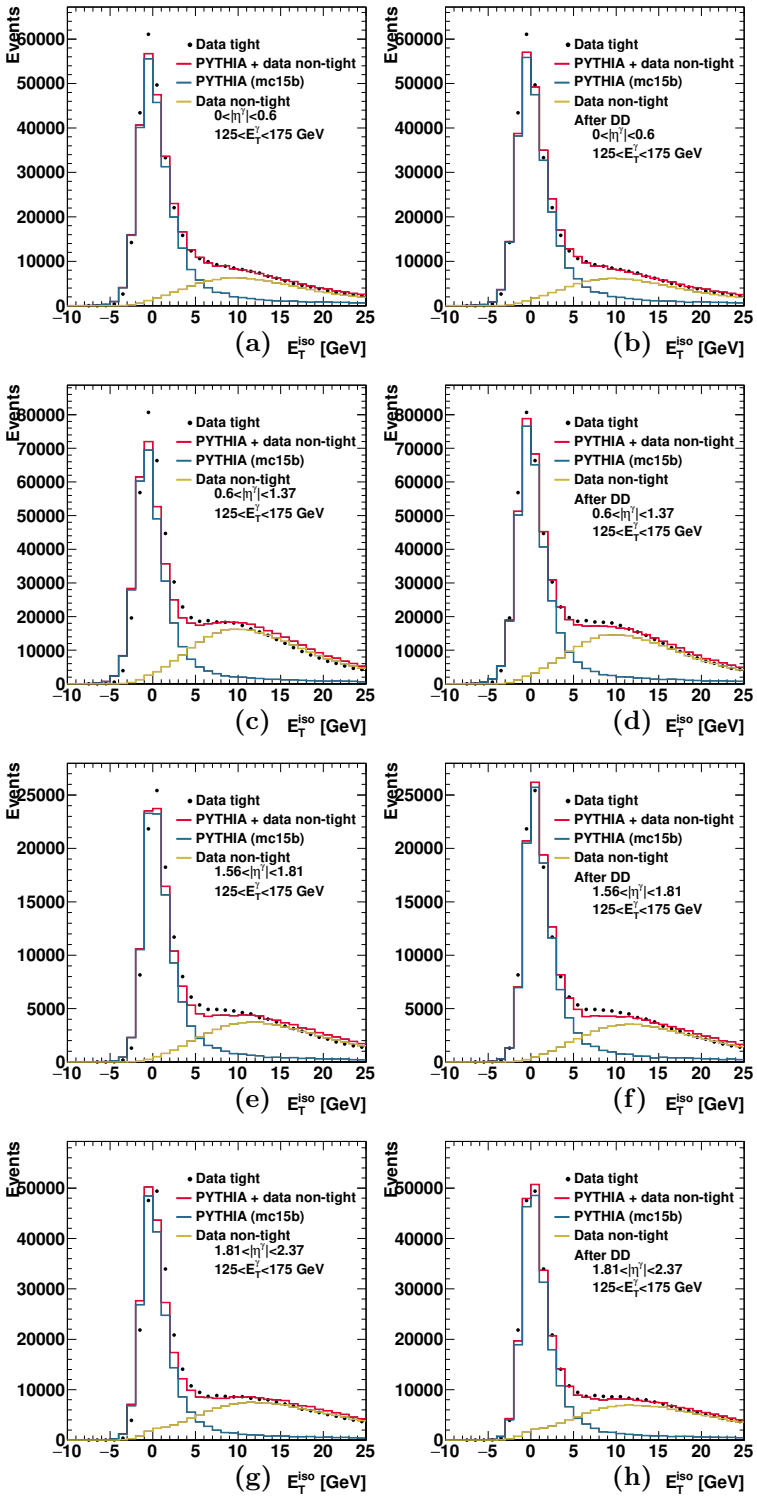


Figure 6.30: Measured $E_{\mathrm{T}}^{\mathrm{iso}}$ distribution for tight (dots) and non-tight (golden histograms, normalised according to the results of the fit explained in the text) photons for $125 < E_{\mathrm{T}}^{\gamma} < 175$ GeV in different regions of η^{γ}. For comparison, the MC simulations of the signal from Pythia (blue histograms, normalised according to the results of the fit explained in the text), after (before) the application of the data-driven correction in a,c,e and g (b,d,f and h), are also included. The red histograms are the sum of the contributions from the MC simulation and the non-tight photons in each region.

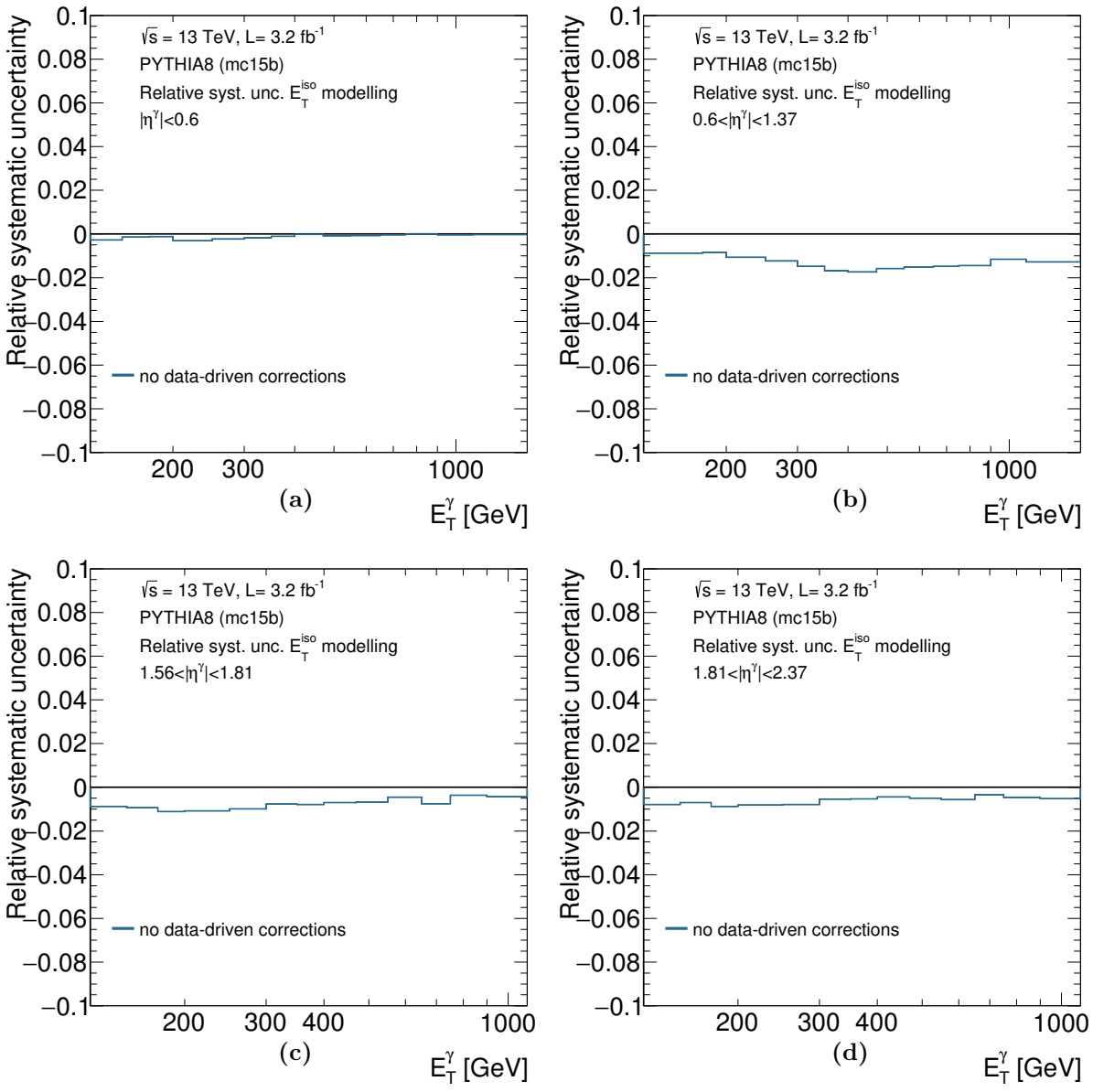


Figure 6.31: Systematic uncertainties on the measured cross sections due to the effect of the isolation corrections as functions of E_{T}^{γ} in different regions of η^{γ}.

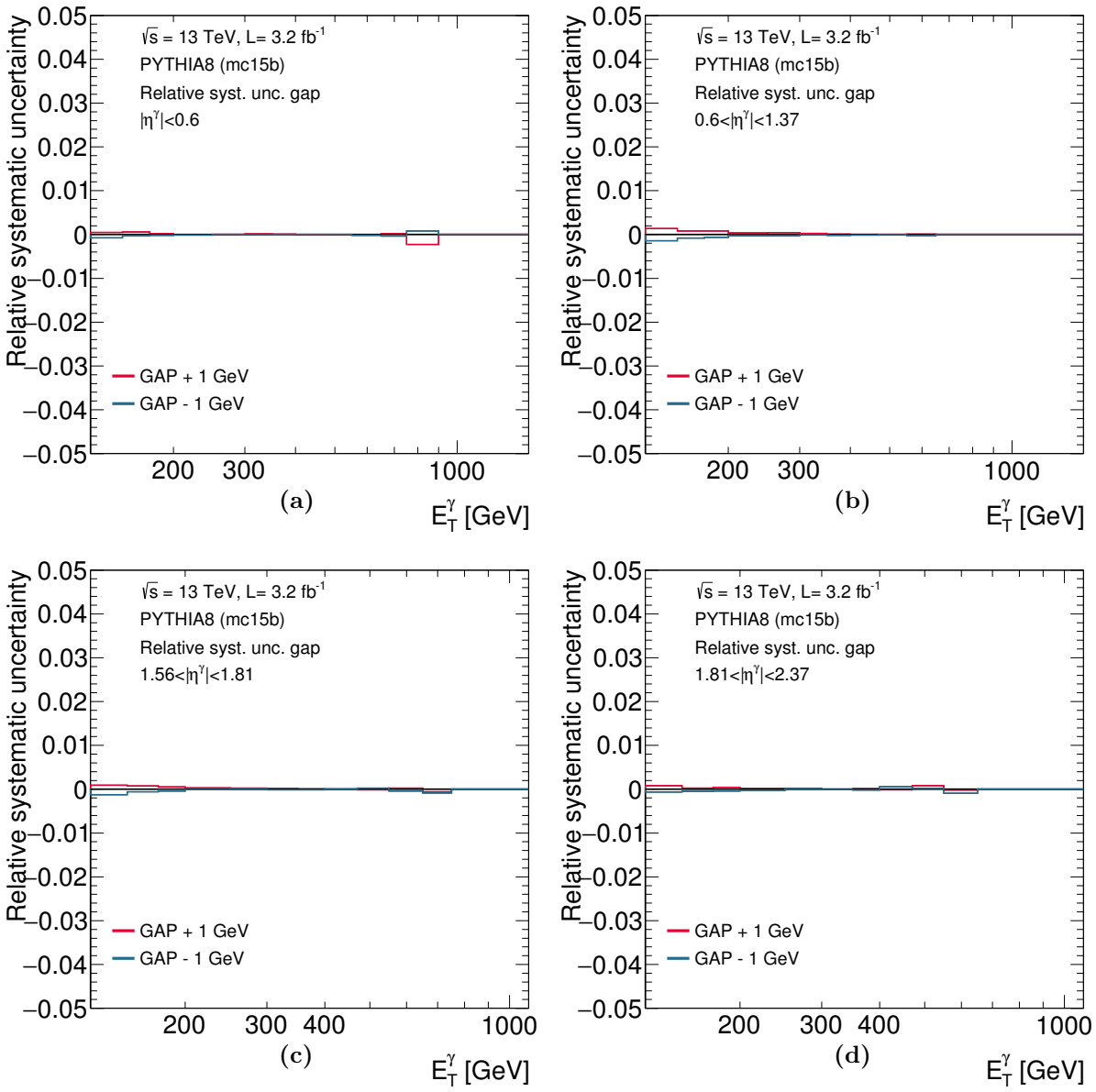


Figure 6.32: Systematic uncertainties on the measured cross sections due to the choice of background control regions (different $E_{\mathrm{T}}^{\mathrm{iso}}$ requirements) as functions of E_{T}^{γ} in different η^{γ} regions.

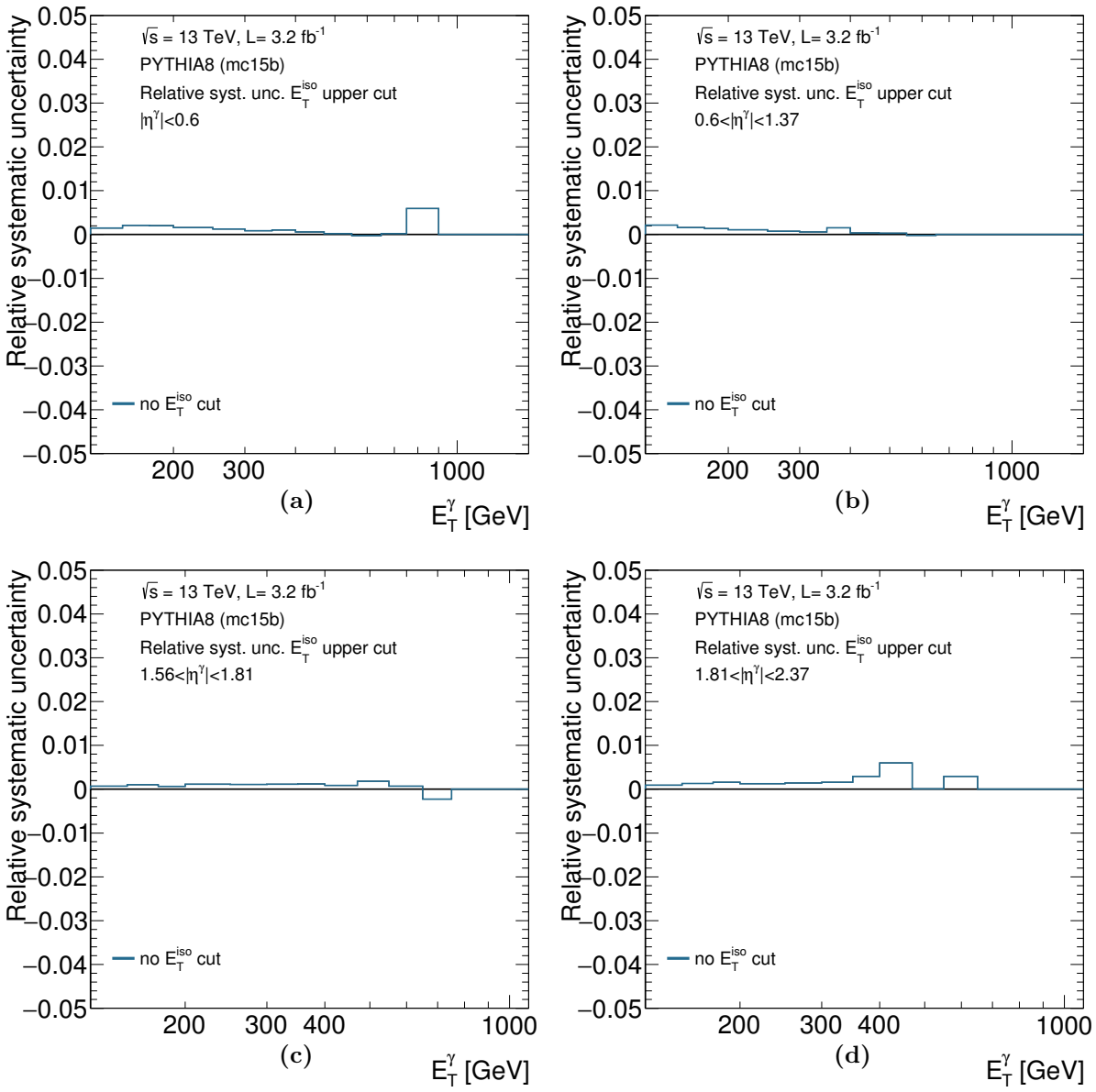


Figure 6.33: Systematic uncertainties on the measured cross sections due to the choice of background control regions (removal of the upper cuts on $E_{\mathrm{T}}^{\mathrm{iso}}$ for regions B and D) as functions of E_{T}^{γ} in different η^{γ} regions.

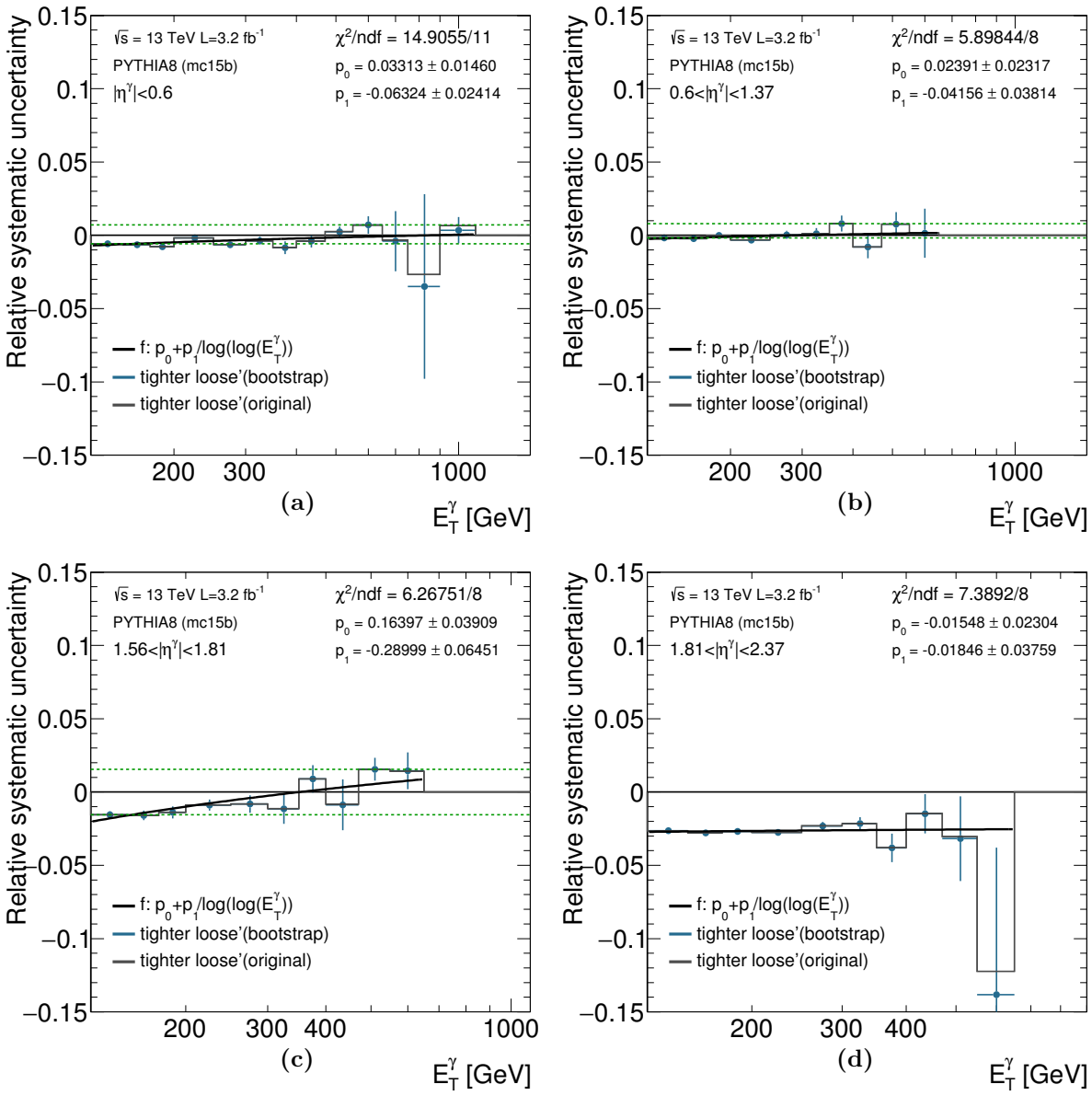


Figure 6.34: Systematic uncertainties on the measured cross sections due to the choice of background control regions (tighter loose′ definition) as functions of E_{T}^{γ} in different η^{γ} regions. The results of the bootstrap method, the fits and the lower and upper bounds are also shown.

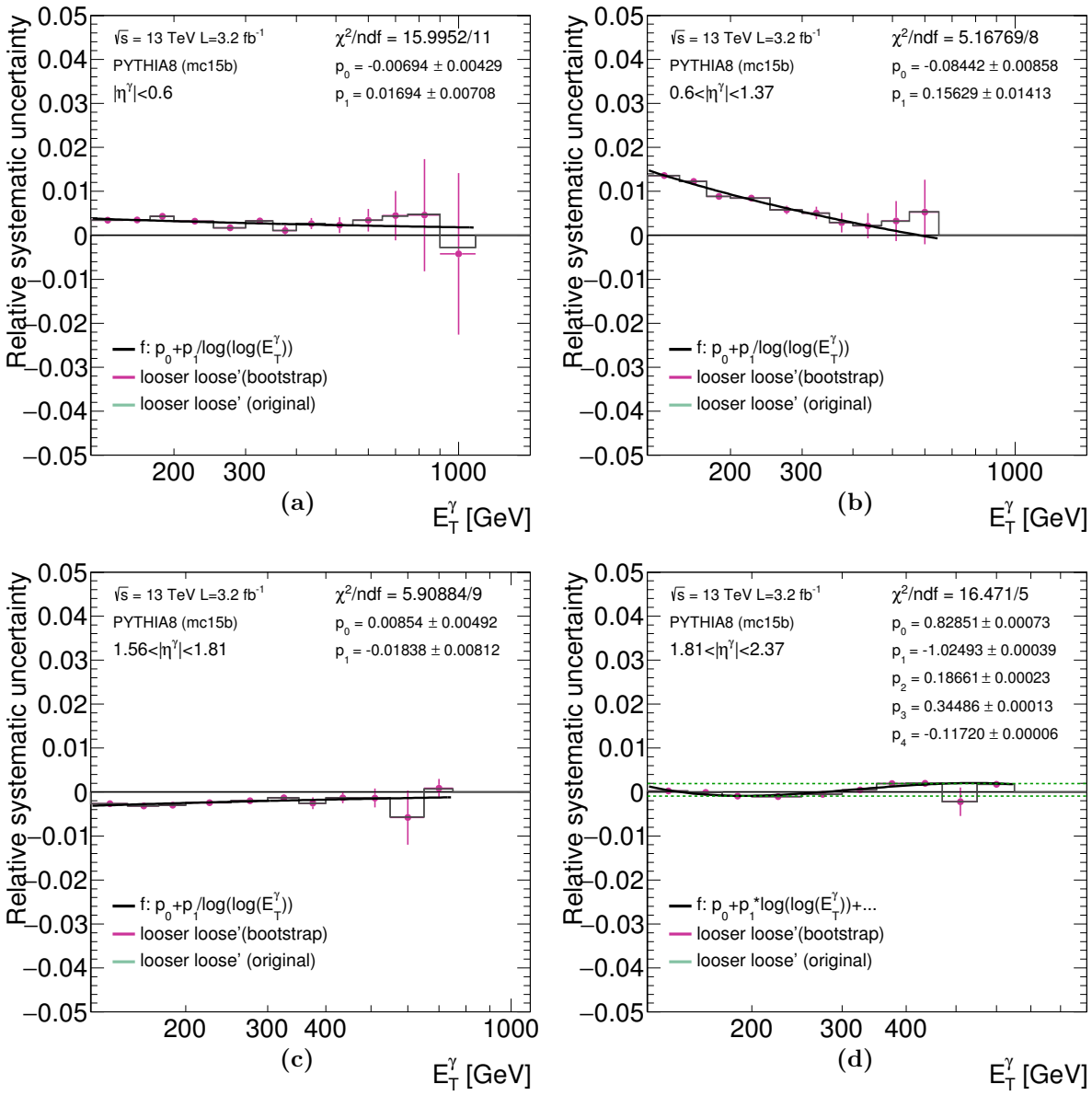


Figure 6.35: Systematic uncertainties on the measured cross sections due to the choice of background control regions (looser loose′ definition) as functions of E_{T}^{γ} in different η^{γ} regions. The results of the bootstrap method, the fits and the lower and upper bounds are also shown.

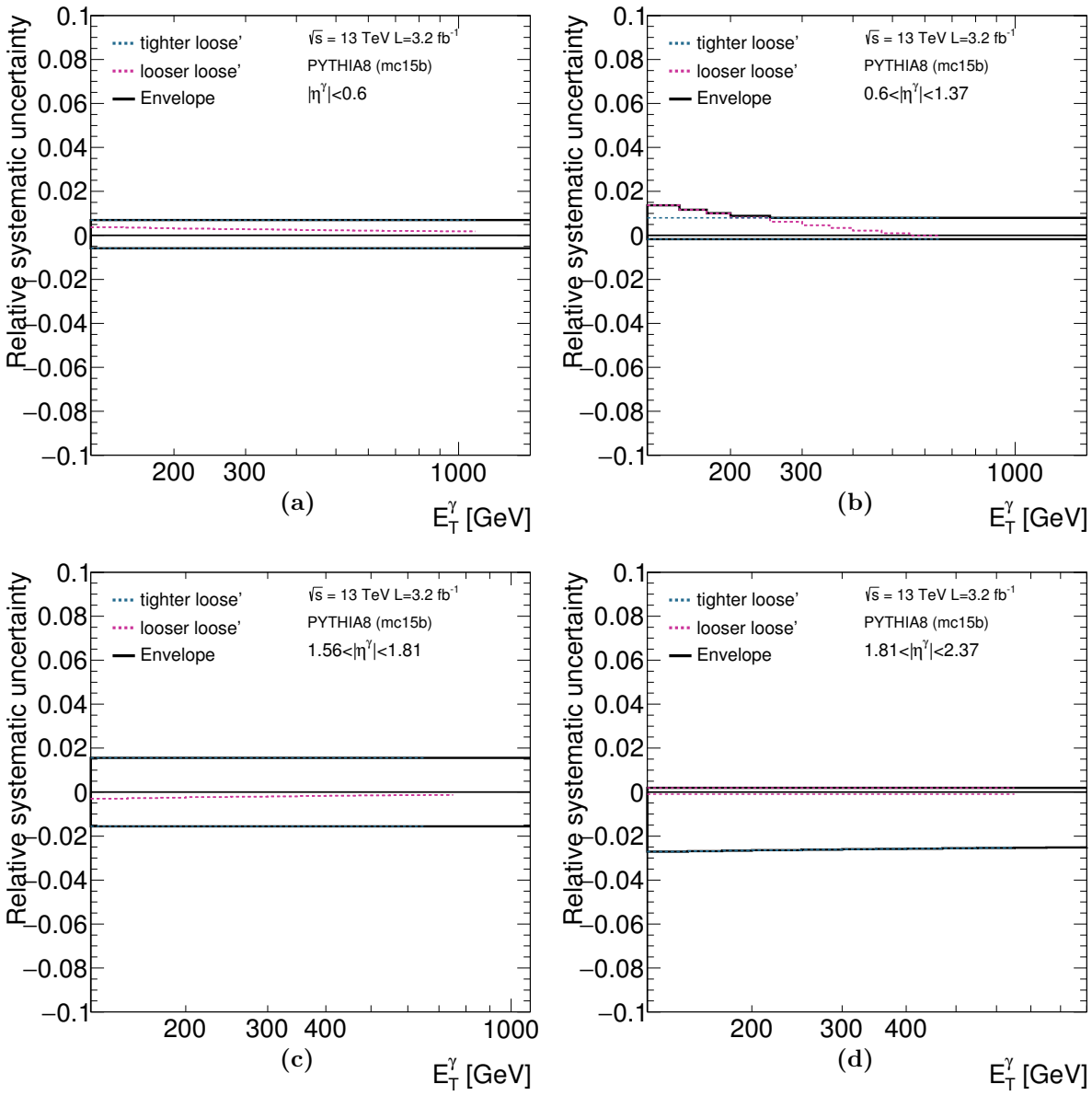


Figure 6.36: Systematic uncertainties on the measured cross sections due to the choice of background control regions (different loose′ definitions) as functions of E_{T}^{γ} in different η^{γ} regions.

6.6.6 Identification and isolation correlation in the background

The background subtraction method explained in Section 6.3 relies on the assumption that the photon identification variables and $E_{\mathrm{T}}^{\mathrm{iso}}$ are uncorrelated for the background photons, that is, $R^{\mathrm{bg}} = 1$ (R^{bg} is also referred as R_{bckg} in the figures). Variations of R^{bg} from unity were investigated. The variations applied were estimated using a data-driven method since the statistics of the background MC samples was found to be very poor for the phase space considered in this analysis. The data-driven method consists in measuring the background ratio between new defined control regions in the high $E_{\mathrm{T}}^{\mathrm{iso}}$ region, which is expected to be clearly dominated by the background. The possible signal leakage coming from photons produced in a bremsstrahlung process was taken into account by using the fractions estimated from the MC in the new control regions. It could be questioned whether the results for R^{bg} obtained in this high $E_{\mathrm{T}}^{\mathrm{iso}}$ region could be extrapolated to the signal region. This fact was investigated by defining several new control regions which are closer in isolation to the signal region and checking that the results were consistent. Details of the method are given below:

- the non-isolated control regions B and D are further divided into two regions: B', B", D' and D";
- the upper limit of regions B' and D' is fixed to 8 GeV higher than the lower limits of these regions. The value coincides with the lower limit of regions B" and D". These subdivisions were set to ensure enough statistics in all the new regions;
- the ratio

$$R^{\mathrm{bg}} = \frac{N_{B'}^{\mathrm{bg}} \cdot N_{D''}^{\mathrm{bg}}}{N_{B''}^{\mathrm{bg}} \cdot N_{D'}^{\mathrm{bg}}} \tag{6.18}$$

  is computed. It uses the number of background events in each region B', B", D' and D" computed in an analogous way as in Equation 6.5 with the number of signal events estimated with $R^{\mathrm{bg}} = 1$;
- the ratio was computed using a new definition of the region in which the lower limits (referred to as "threshold" in the figures) are moved by 1 GeV towards higher $E_{\mathrm{T}}^{\mathrm{iso}}$;
- the final estimation was obtained from the regions defined with lower limit of the regions B' and D' set to $E_{\mathrm{T}}^{\mathrm{iso}} = 4.2 \cdot 10^{-3} E_{\mathrm{T}}^{\gamma} + 4.8 + 7$ [GeV].

As a result of this study, a range in R^{bg} was set to cover the largest deviations from unity observed for the estimations subtracting the signal leakage in the regions studied with either Pythia (see Figure 6.38) or Sherpa (see Figure 6.39). The results obtained without taking into account the signal leakage in the regions considered in the study are shown in Figure 6.37. The ranges are shown in Figures 6.38 and 6.39: for the regions $0.6 < |\eta^{\gamma}| < 1.37$ and $1.81 < |\eta^{\gamma}| < 2.37$ the range is $0.8 < R^{\mathrm{bg}} < 1.2$; for the regions $|\eta^{\gamma}| < 0.6$ and $1.56 < |\eta^{\gamma}| < 1.81$ the range depends on E_{T}^{γ}. Figure 6.40 shows the resulting uncertainties on the measured cross sections.

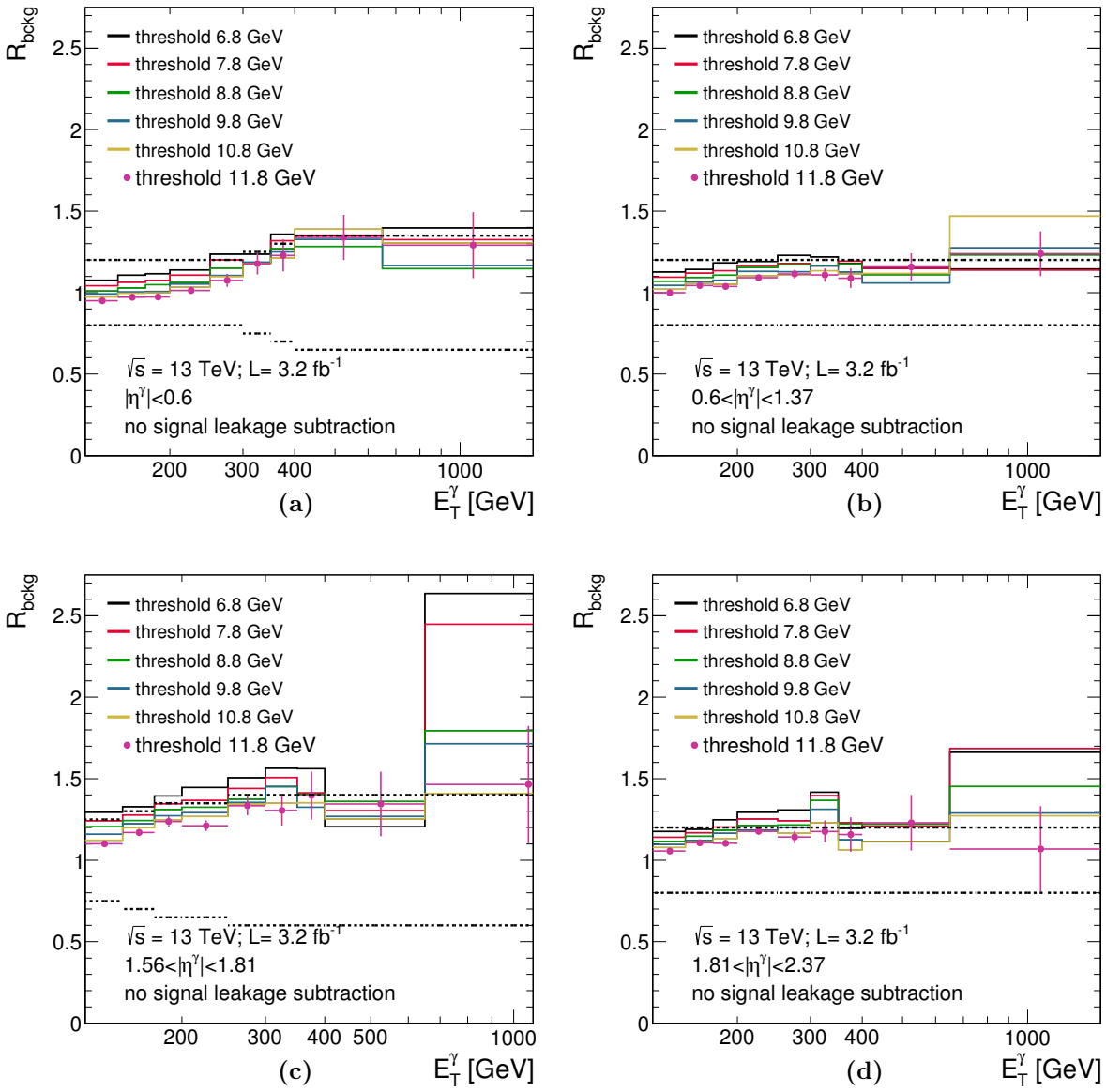


Figure 6.37: R_{bckg} as a function of E_{T}^{γ} in different regions of η^{γ} and for different definitions of the control regions. No signal leakage subtraction was applied. The range in R_{bckg}, which was taken as the uncertainty, is indicated by the dotted lines.

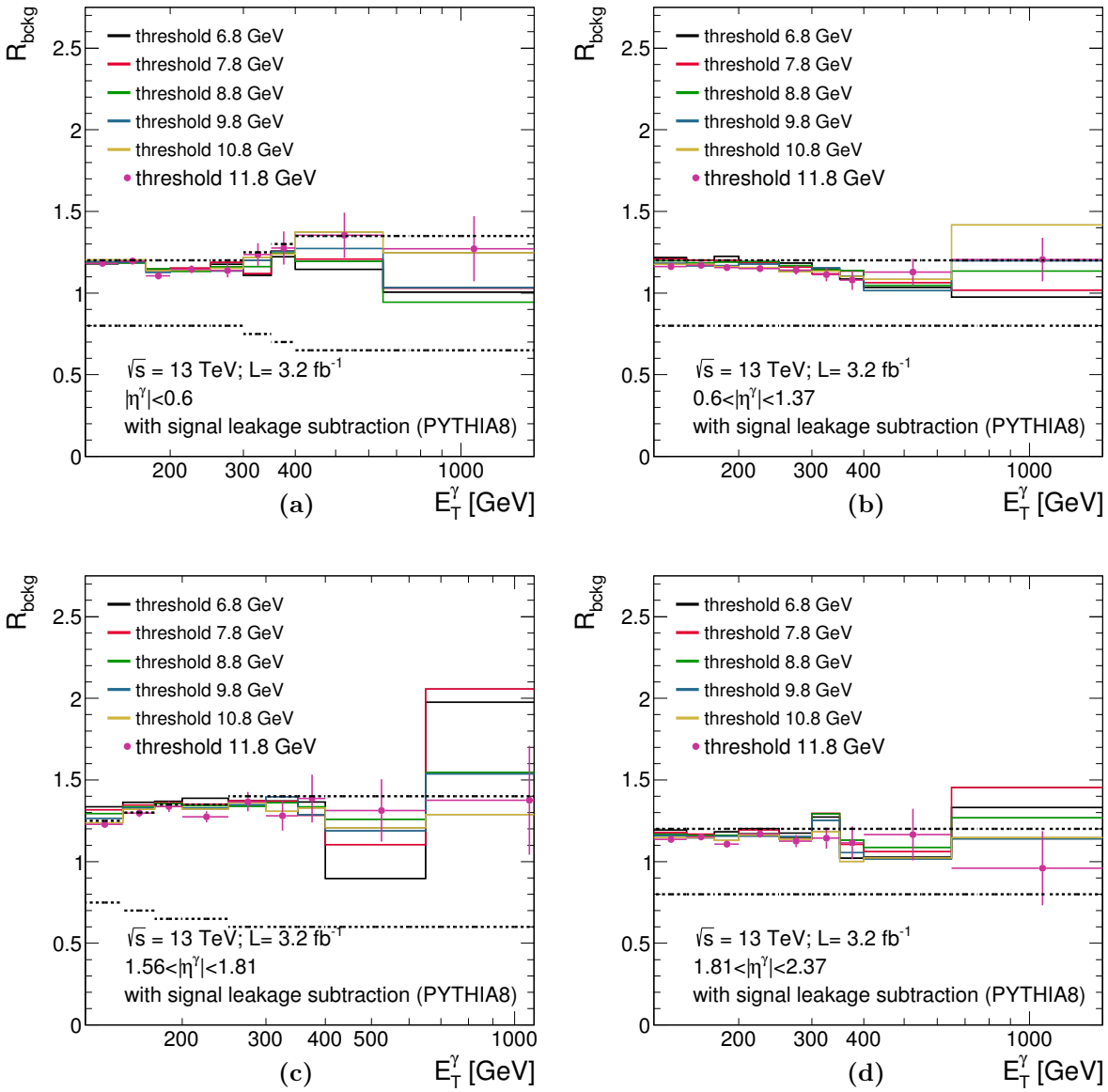


Figure 6.38: R_{bckg} as a function of E_{T}^{γ} in different regions of η^{γ} and for different definitions of the control regions. The signal leakage contributions in the control regions were removed using the PYTHIA samples. The range in R_{bckg}, which was taken as the uncertainty, is indicated by the dotted lines.

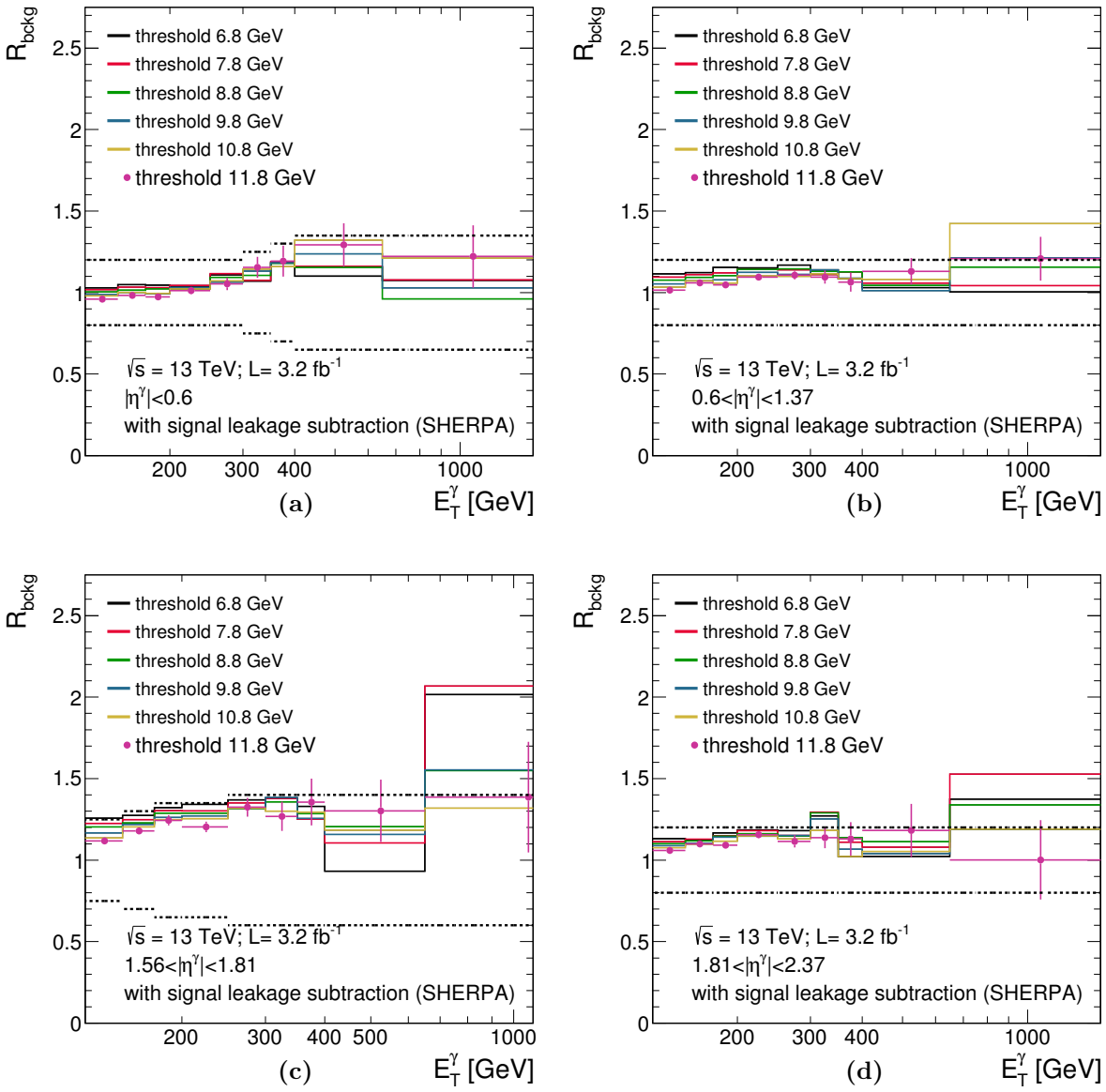


Figure 6.39: R_{bckg} as a function of E_{T}^{γ} in different regions of η^{γ} and for different definitions of the control regions. The signal leakage contributions in the control regions were removed using the SHERPA samples. The range in R_{bckg}, which was taken as the uncertainty, is indicated by the dotted lines.

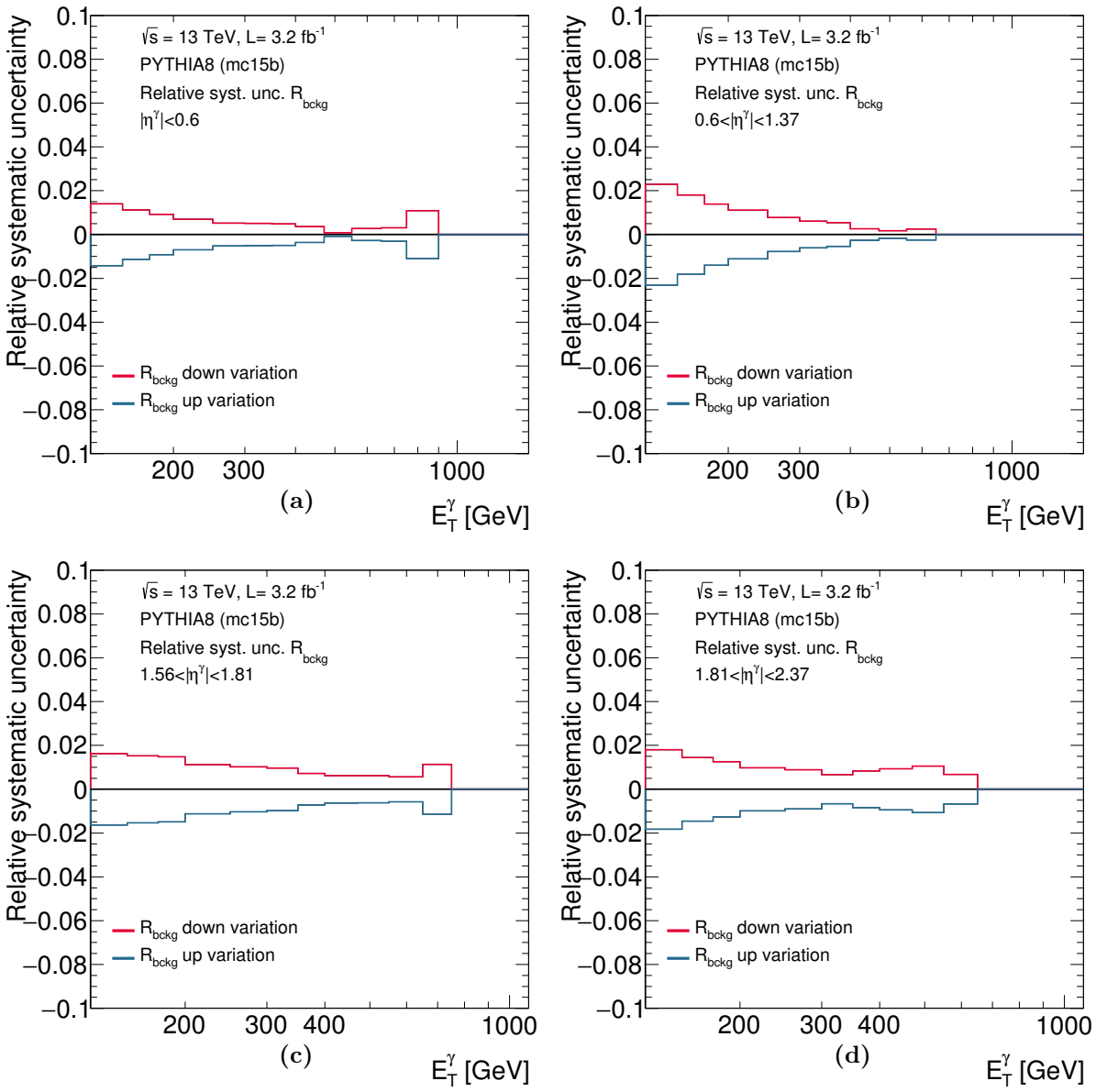


Figure 6.40: Systematic uncertainties on the measured cross sections due to the background identification and isolation correlation (R_{bckg}) as functions of E_{T}^{γ} in different regions of η^{γ}.

6.6.7 Signal modelling

The PYTHIA simulation was used with the default mixture of the hard and bremsstrahlung contributions to yield the background-subtracted data distributions and to compute the correction factors. The uncertainty related to the simulation of the hard and bremsstrahlung components was estimated by performing the background subtraction and the estimation of the correction factors by enhancing the bremsstrahlung contribution by a factor 2 or suppressing it completely. The resulting uncertainty is shown in Figure 6.41.

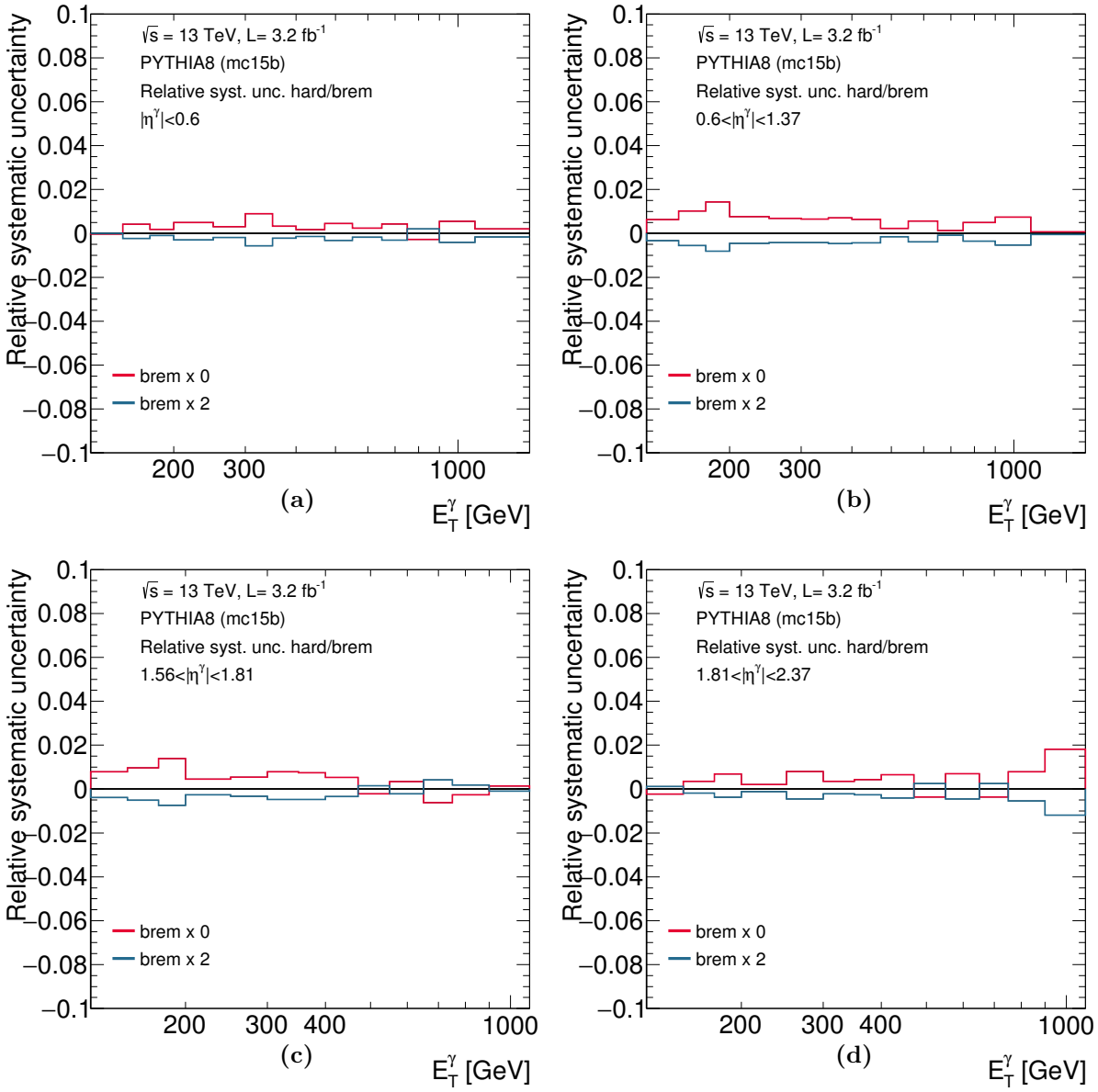


Figure 6.41: Systematic uncertainties on the measured cross sections due to the effect of the signal modelling as functions of E_{T}^{γ} in different regions of η^{γ}.

6.6.8 Pile-up reweighting

To match the in-time and out-of-time pile-up conditions in the data, the distribution of $\langle\mu\rangle$ in simulated events was reweighted to that of the data after applying a factor 1/1.16 (see Section 6.1.4). An uncertainty due to this reweighting was estimated by changing this factor applied to the data to 1/1.09 or 1/1.23 and repeating the reweighting procedure. Figure 6.42 shows the resulting uncertainties on the cross sections.

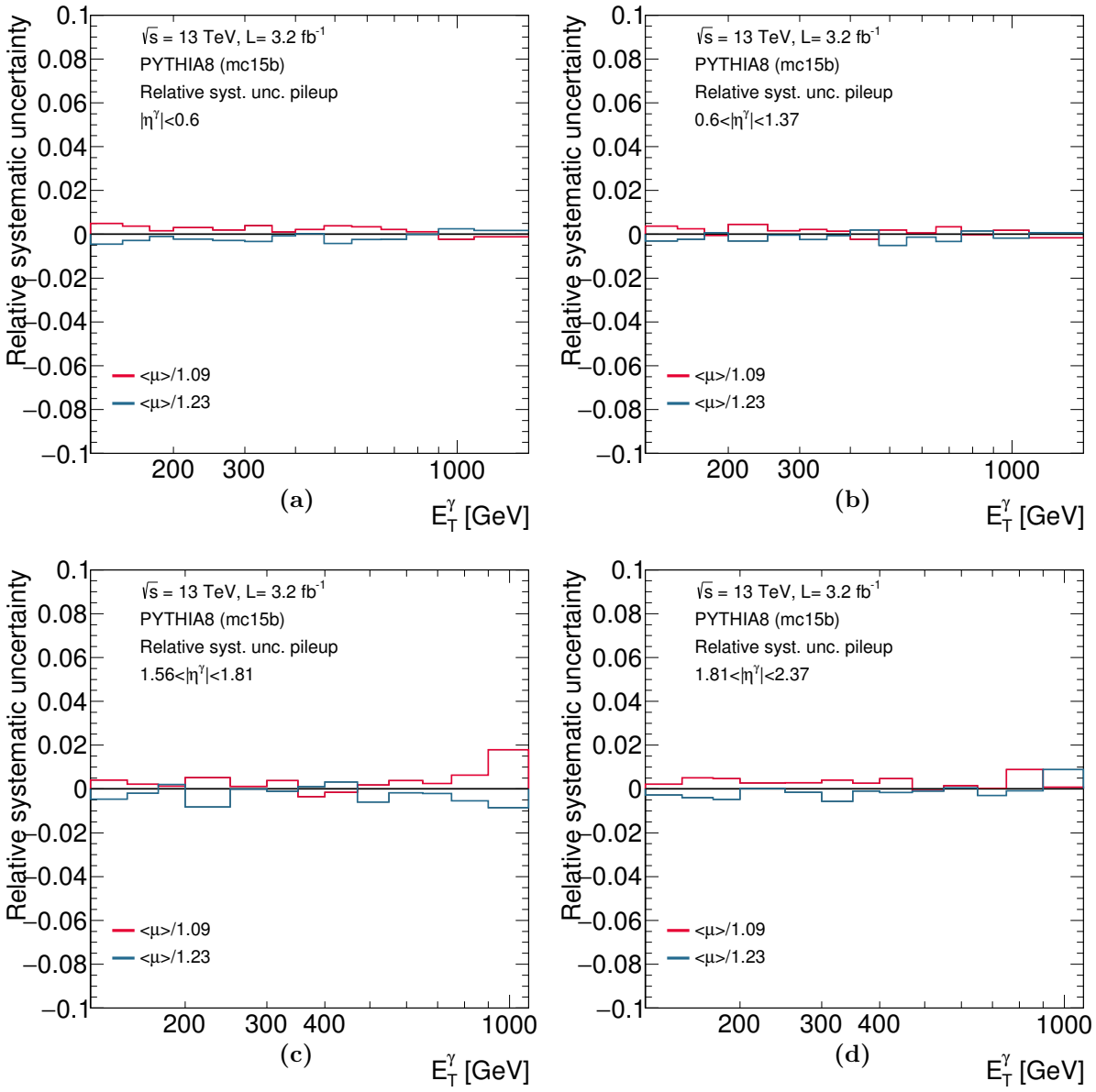


Figure 6.42: Systematic uncertainties on the measured cross sections due to the pile-up reweighting as functions of E_{T}^{γ} in different regions of η^{γ}.

6.6.9 MC sample statistics

The limited MC statistics affects mainly the bin-by-bin correction factors. Figure 6.43 shows the statistical uncertainty of the MC samples.

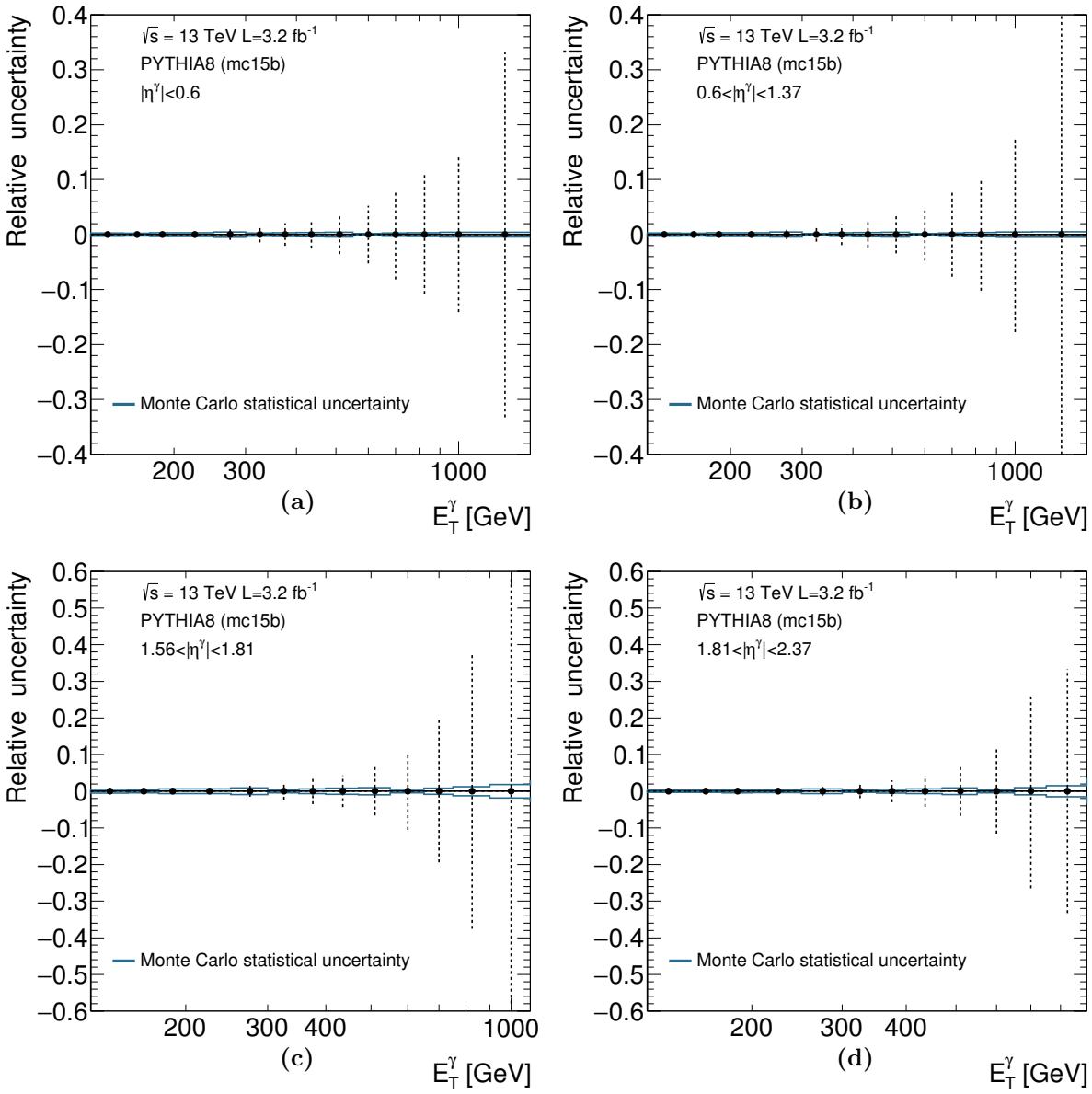


Figure 6.43: Statistical uncertainty of the MC samples as functions of E_{T}^{γ} in different regions of η^{γ}. For comparison, the vertical error bars display the data statistical uncertainty.

6.6.10 Uncertainty on the trigger efficiency

The uncertainty on the trigger efficiency (see Section 6.2) has been propagated into the measured cross sections.

6.6.11 Uncertainty on the measurement of the integrated luminosity

The uncertainty on the integrated luminosity is ±2.1% [115]. This uncertainty is fully correlated in all bins of all the measured cross sections and it was not added in quadrature to the other uncertainties.

6.6.12 Total systematic uncertainty

The total systematic uncertainty was computed by adding in quadrature the sources of uncertainty listed in the previous sections, except that on the integrated luminosity. Figure 6.44 shows the resulting total systematic uncertainty, together with the statistical uncertainty. For $E_{\mathrm{T}}^{\gamma} \lesssim 600$ GeV, the systematic uncertainty dominates while for higher E_{T}^{γ} values, the statistical uncertainty of the data limits the precision of the measurements.

The total relative systematic uncertainty as a function of E_{T}^{γ} in different regions of $|\eta^{\gamma}|$ as well as the contributions from the dominant systematic uncertainties, namely the photon energy scale and resolution, the photon identification and R^{bg}, are shown in Figure 6.45.

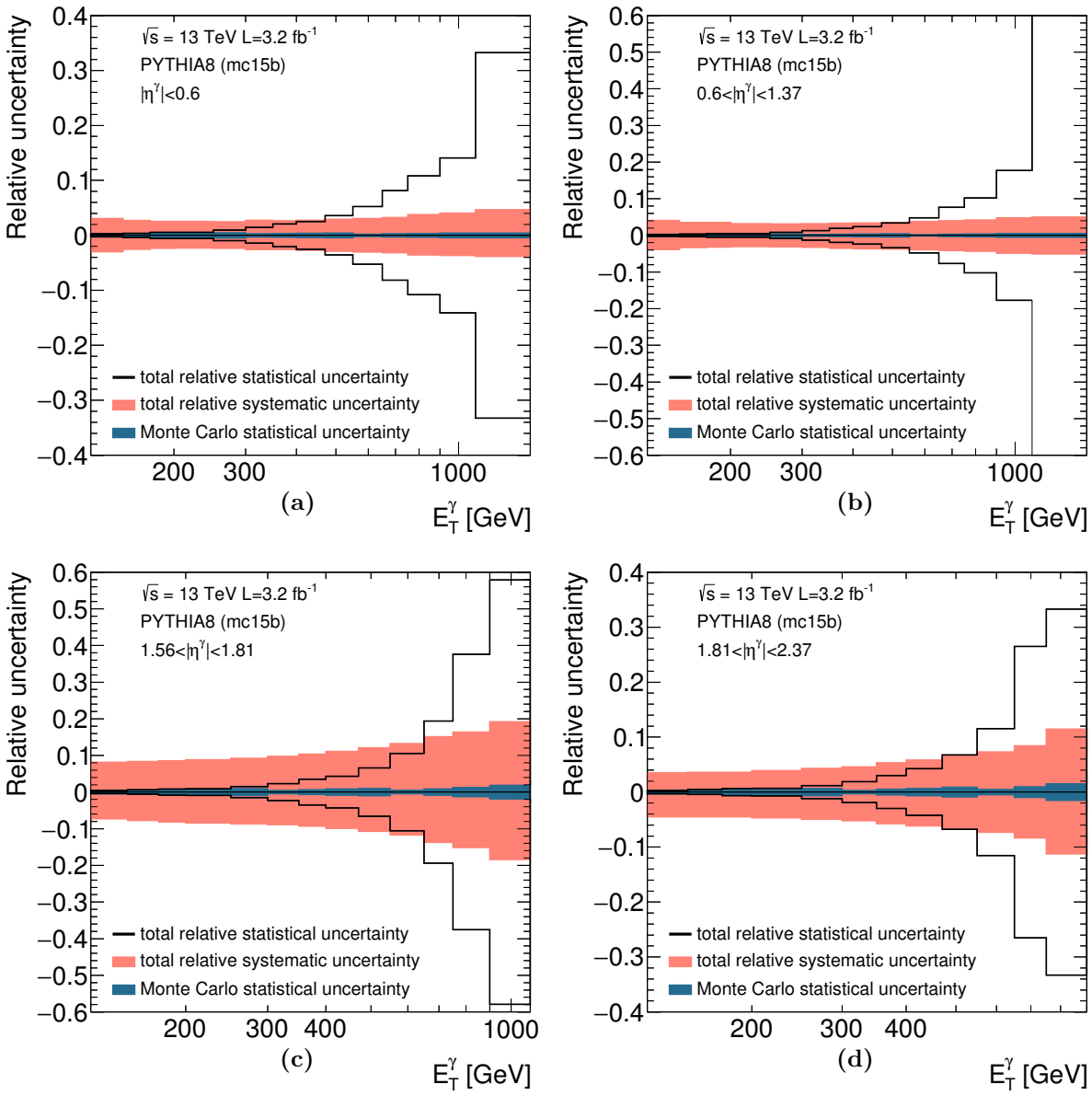


Figure 6.44: Total systematic (pink shaded area) and statistical uncertainties from the data (white histogram) and MC (blue shaded area) as functions of E_{T}^{γ} in different regions of η^{γ}.

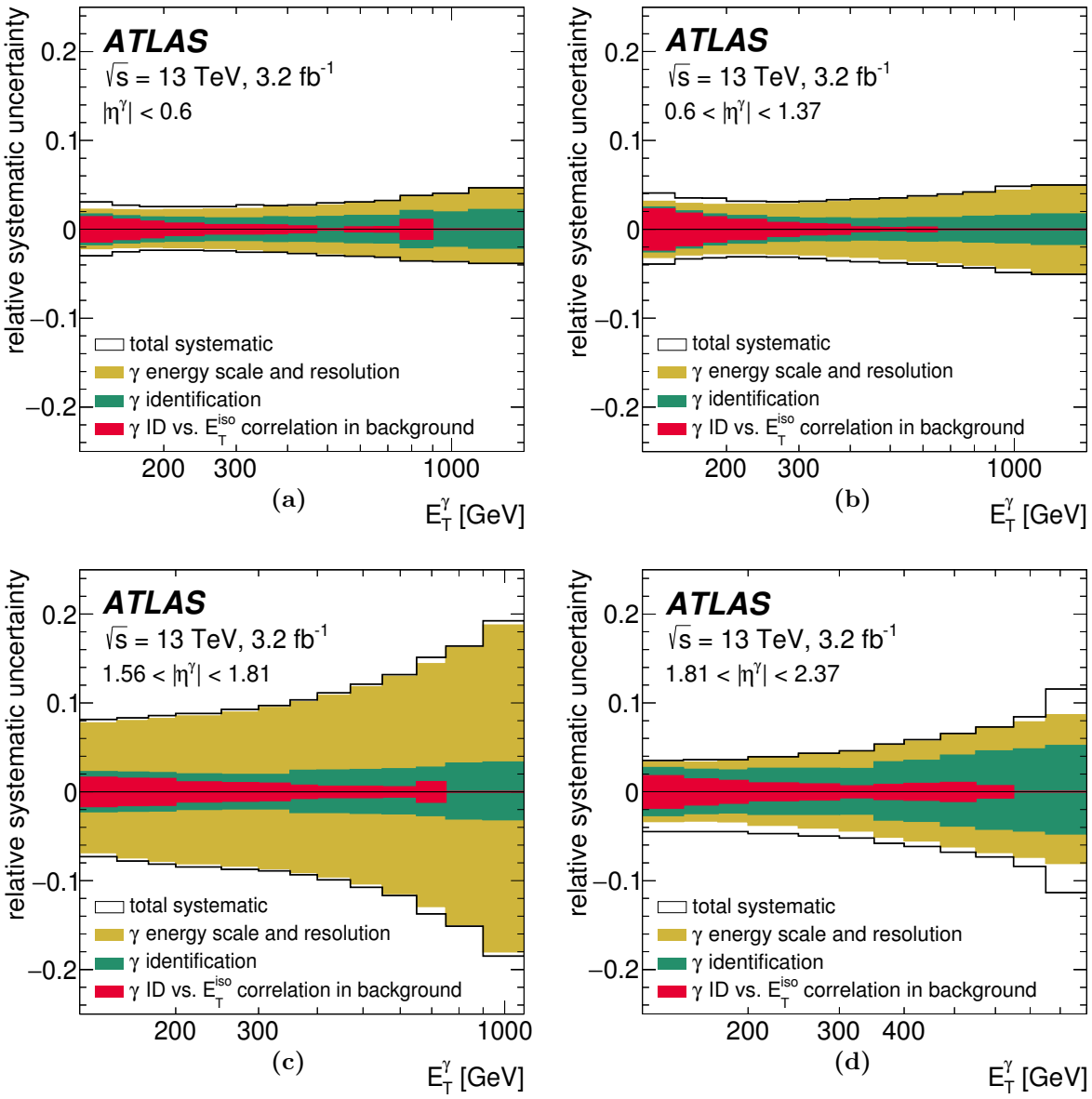


Figure 6.45: Total relative systematic uncertainty, excluding that in the luminosity measurement, as a function of E_{T}^{γ} in different regions of $|\eta^{\gamma}|$ (black histogram) as well as the contributions from the photon energy scale and resolution (yellow histogram), the photon identification (green histogram) and the photon identification vs. $E_{\mathrm{T}}^{\mathrm{iso}}$ correlation in the background (red histogram). The histograms show the stacked contributions.

6.7 Next-to-leading-order QCD calculations

Details about the NLO pQCD calculations were given in Section 3.5.7. In this section, the non-perturbative corrections applied to the parton-level NLO pQCD calculations of JetPhox as well as the theoretical uncertainties are presented.

6.7.1 Non-perturbative corrections

The corrections from the parton- to the particle-level calculations were obtained using the Pythia MC samples. For these corrections to be valid, the MC simulations must be close in shape to the NLO QCD calculations. The parton-level predictions of Pythia are compared to the NLO QCD calculations of JetPhox based on the MMHT2014 parameterisations of the PDFs in Figure 6.47. They provide an adequate description of the shape of the NLO QCD calculations.

The non-perturbative correction factors, C_{NLO}, as defined in Section 3.5.7, are shown in Figure 6.48 and are close to unity. The two contributions to this term, C_{had} and C_{UE}, are shown in Figures 6.49 and 6.50, respectively; the contribution of the correction for the underlying event is larger than that for hadronisation. No significant dependence on η^{γ} was observed and, therefore, the correction factors were evaluated in the inclusive η^{γ} range to be less affected by lack of statistics in the samples (see Figure 6.46). Since the C_{NLO} factors are very close to unity, no corrections were applied to the calculations and an uncertainty of 1% was assigned.

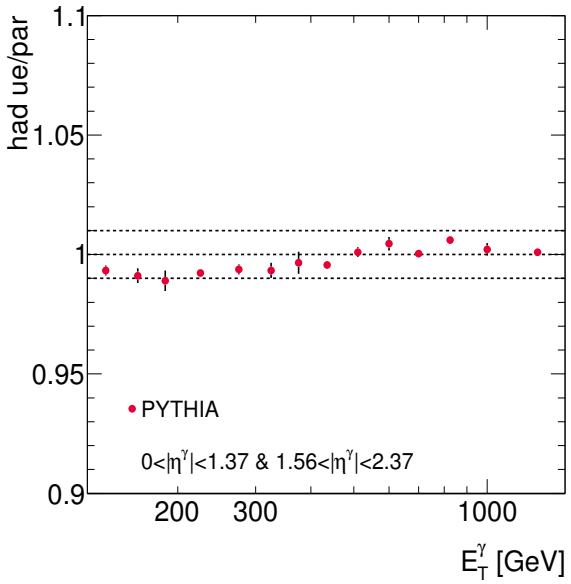


Figure 6.46: C_{NLO} correction factors from Pythia (dots) as functions of E_{T}^{γ}.

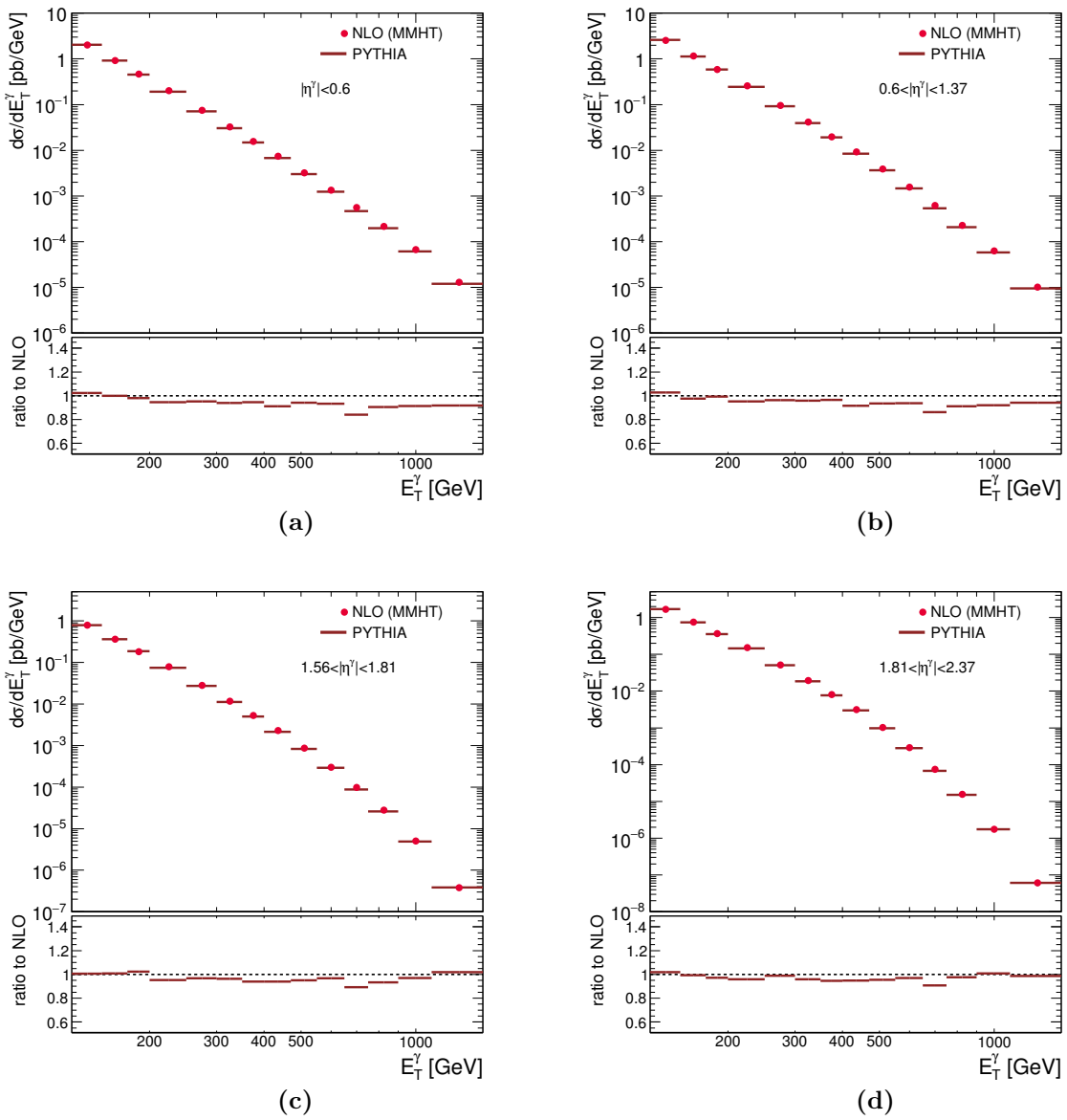


Figure 6.47: Predicted NLO QCD cross sections (dots) as functions of E_{T}^{γ} in different regions of η^{γ}. The predictions at parton level of PYTHIA (lines) are also shown. The lower part of the figures shows the ratio of the parton-level MC and NLO QCD calculations.

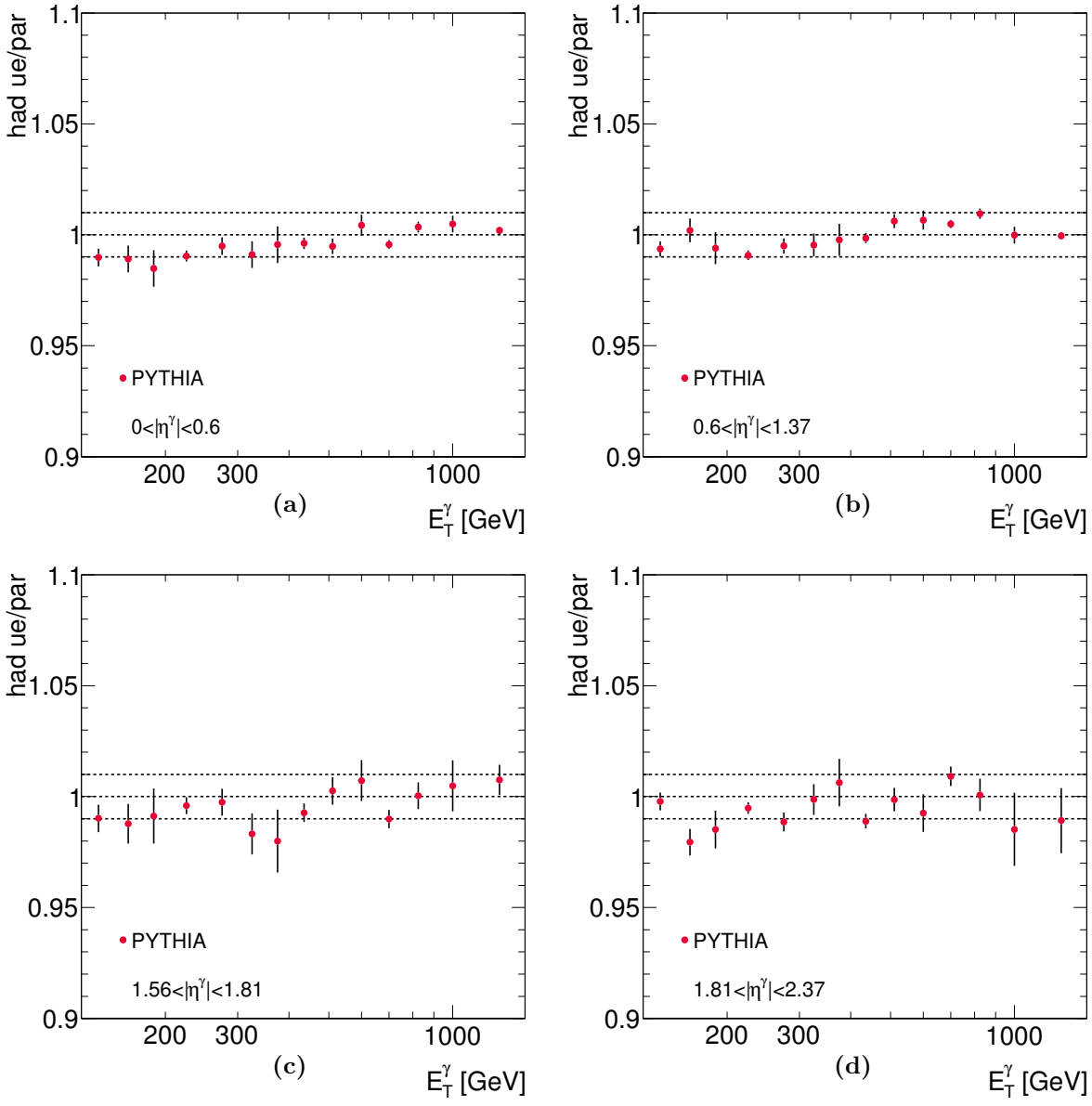


Figure 6.48: C_{NLO} correction factors from PYTHIA (dots) as functions of E_{T}^{γ} in different regions of η^{γ}.

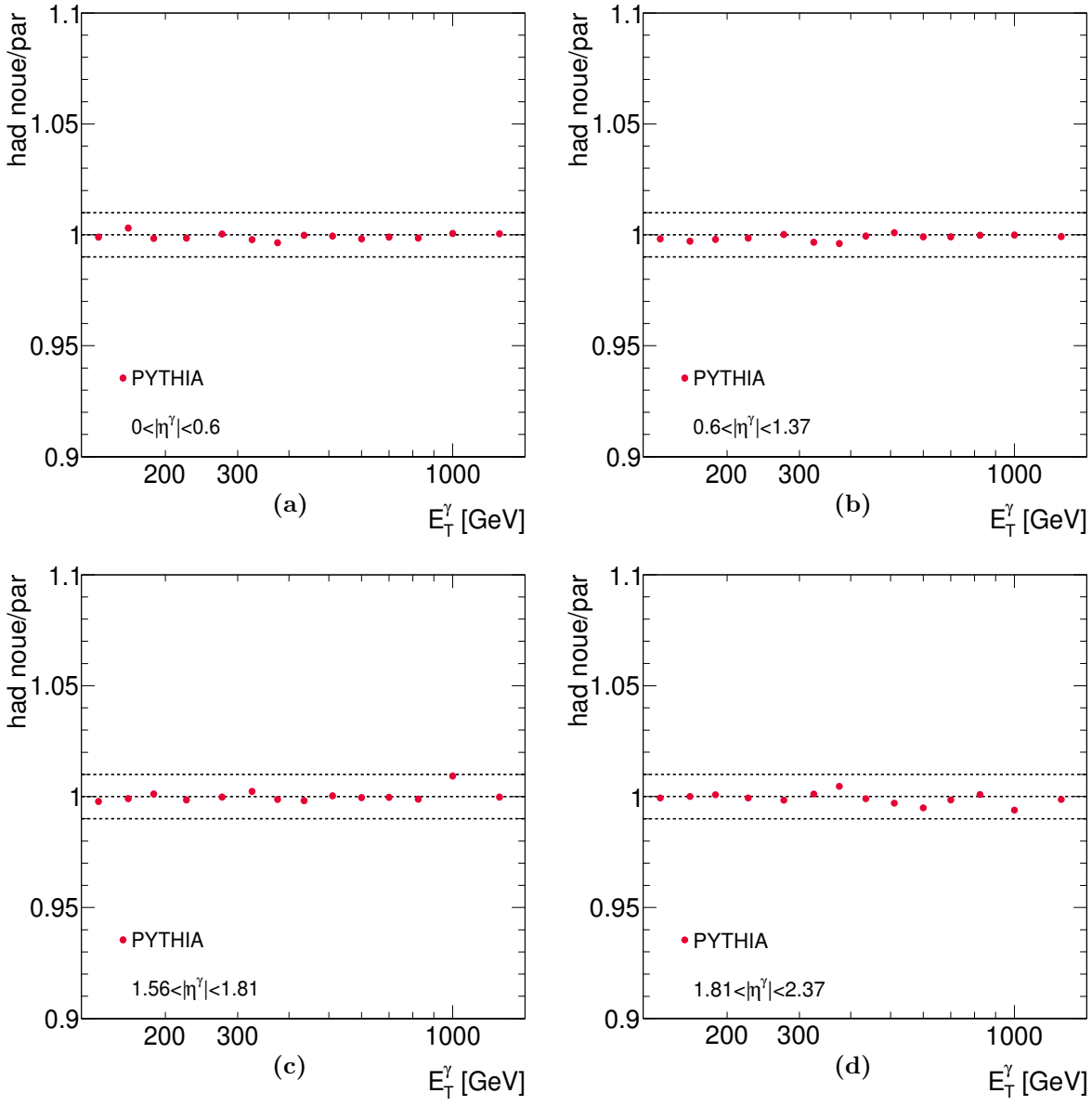


Figure 6.49: C_{had} correction factors from PYTHIA (dots) as functions of E_{T}^{γ} in different regions of η^{γ}.

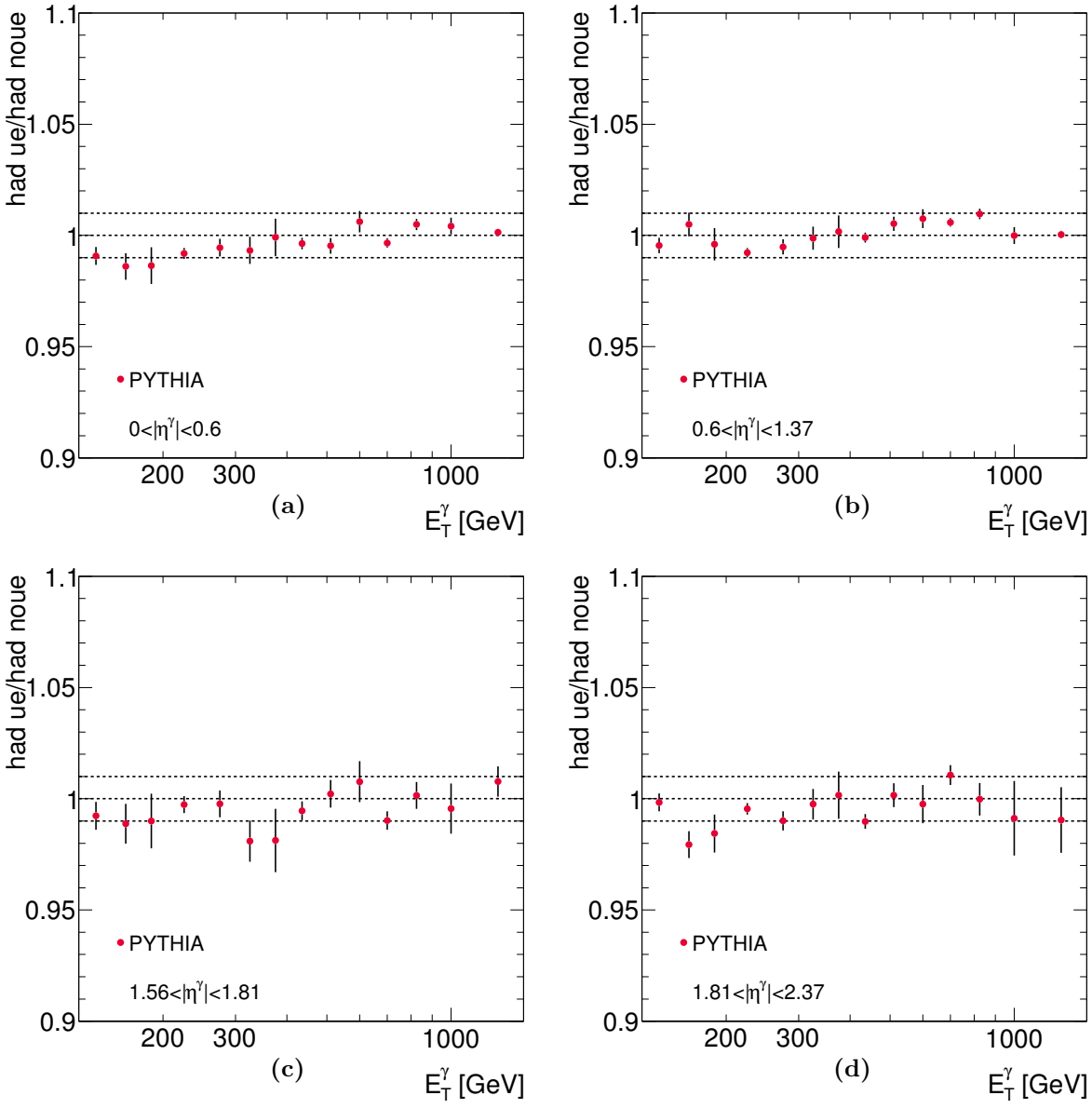


Figure 6.50: C_{UE} correction factors from PYTHIA (dots) as functions of E_{T}^{γ} in different regions of η^{γ}.

6.7.2 Theoretical uncertainties

The baseline theoretical calculations were performed setting some parameters to arbitrary but well motivated values. Theoretical uncertainties were assigned for this choice as explained below:

- the different scales used in the calculations: μ_R, μ_F and μ_f, were varied by factors 0.5 or 2. The three scales were either varied simultaneously, individually or by fixing one and varying the other two. In all cases, the condition $0.5 < \mu_A/\mu_B < 2$ was imposed, where $A, B = R, F, f$, to avoid combinations in which the variations have opposite directions in the theoretical uncertainty. Some representative variations are shown in Figures 6.51 to 6.52. The final uncertainty was taken as the largest deviation from the nominal value among the 14 possible variations and is shown in Figure 6.52. This uncertainty should estimate the missing higher-order terms of the perturbative calculations, which are expected to cancel the dependence of the final cross-section prediction on these scales;

- the uncertainty due to the lack of perfect knowledge of the proton PDF was estimated by repeating the calculations with 50 additional sets from the MMHT2014 error analysis using the eigenvectors from the Hessian method [118]. These results were used to approximate the PDF uncertainty through the use of a "Master Equation" [119] which separates the maximal positive and negative variations of the predicted cross sections. The impact of this uncertainty on the predicted cross section is shown in Figure 6.53;

- the uncertainty in the NLO pQCD predictions due to that in the value of $\alpha_s(m_Z)$ was estimated by repeating the calculations using two additional sets of proton PDFs from the MMHT2014 analysis, for which different values of $\alpha_s(m_Z)$ were assumed in the fits, namely $\alpha_s(m_Z) = 0.118$ and $\alpha_s = 0.122$. In this way, the correlation between α_s and the PDFs is preserved. The differences in the variations were scaled by a factor 0.0015/0.002 to obtain the results with 1σ confidence level [120] and are shown in Figure 6.53;

- An uncertainty of 1% was assigned due to the non-perturbative effects of hadronisation and UE, as explained in the previous section.

The dominant theoretical uncertainty is that arising from the terms beyond NLO and amounts to $10-15\%$ for all the η^γ regions. The uncertainty arising from those in the PDFs increases from 1% at $E_{\mathrm{T}}^{\gamma} = 125$ GeV to $3-4\%$ at high E_{T}^{γ}. The uncertainty arising from the value of $\alpha_s(m_Z)$ is below 2%. The total theoretical uncertainty was obtained by adding in quadrature the individual uncertainties listed above and is shown in Figure 6.54.

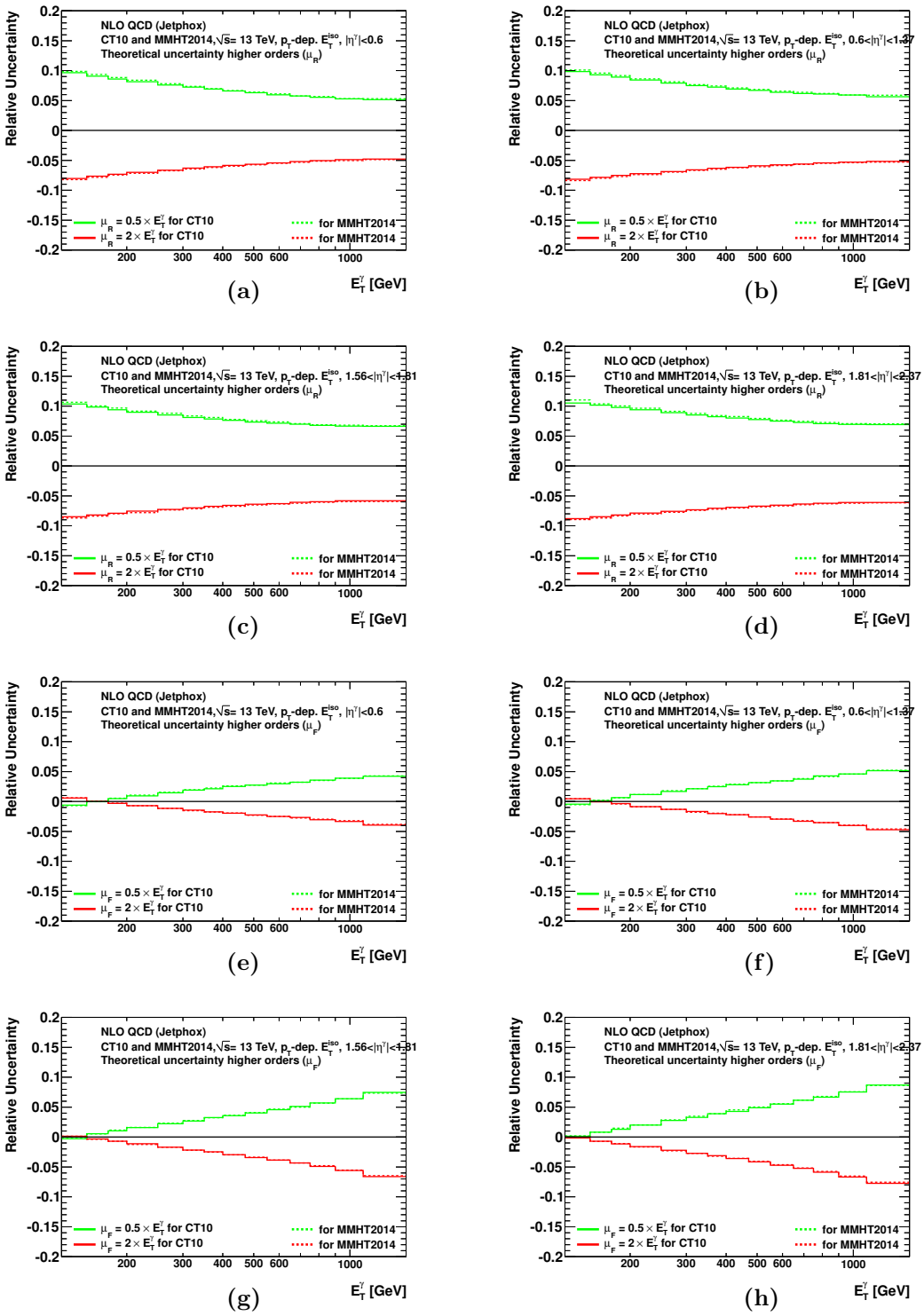


Figure 6.51: Theoretical uncertainty arising from terms beyond NLO (variation of μ_R in (a,b,c,d) and μ_F in (e,f,g,h)) using MMHT2014 (dotted lines) and CT10 (solid lines) as a function of E_{T}^{γ} in different regions of η^{γ}.

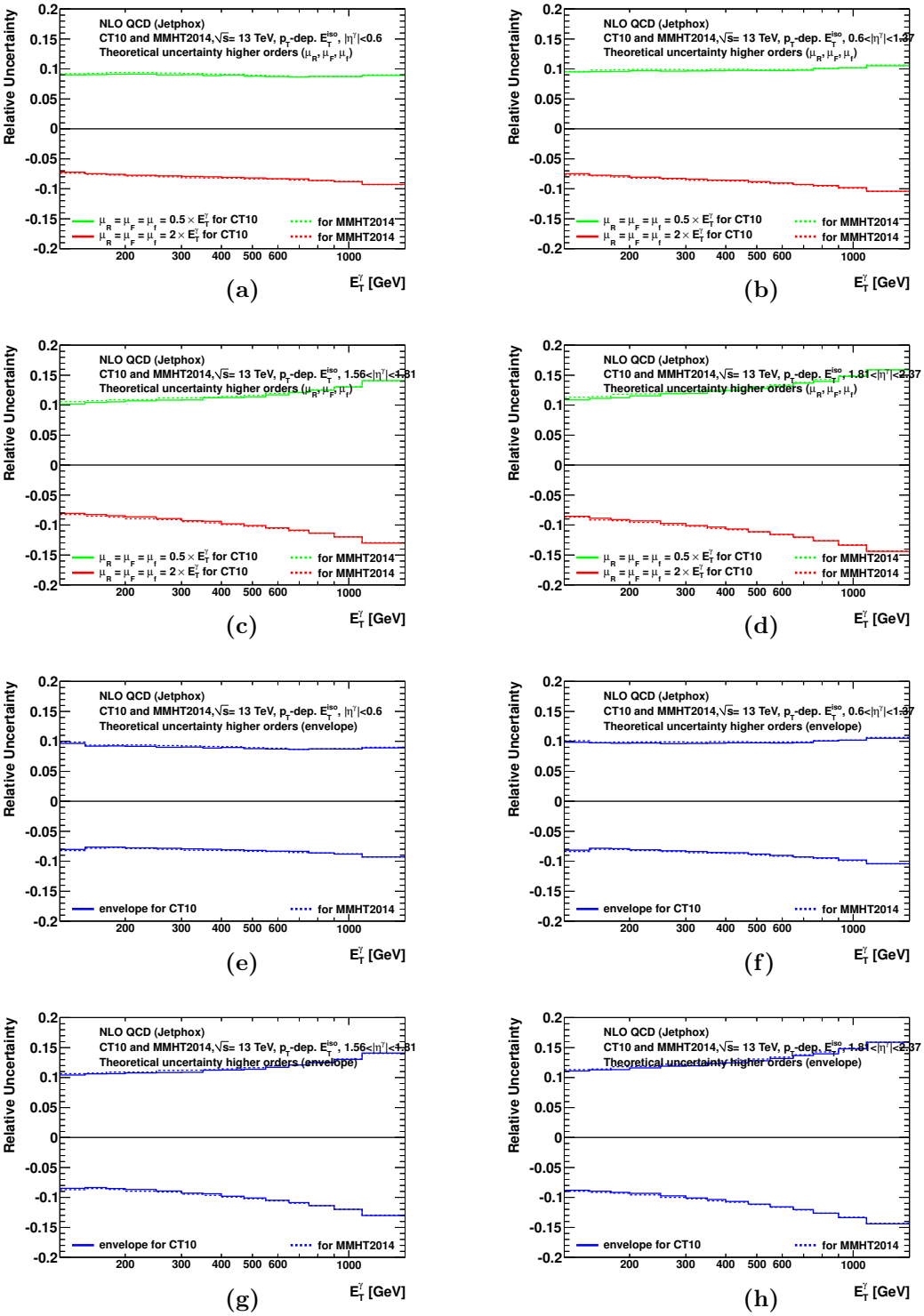


Figure 6.52: Theoretical uncertainty arising from terms beyond NLO (simultaneous variations of μ_R, μ_F and μ_f (a,b,c,d) and envelope of the variations of the scales (e,f,g,h)) using MMHT2014 (dotted lines) and CT10 (solid lines) as a function of E_{T}^{γ} in different regions of η^{γ}.

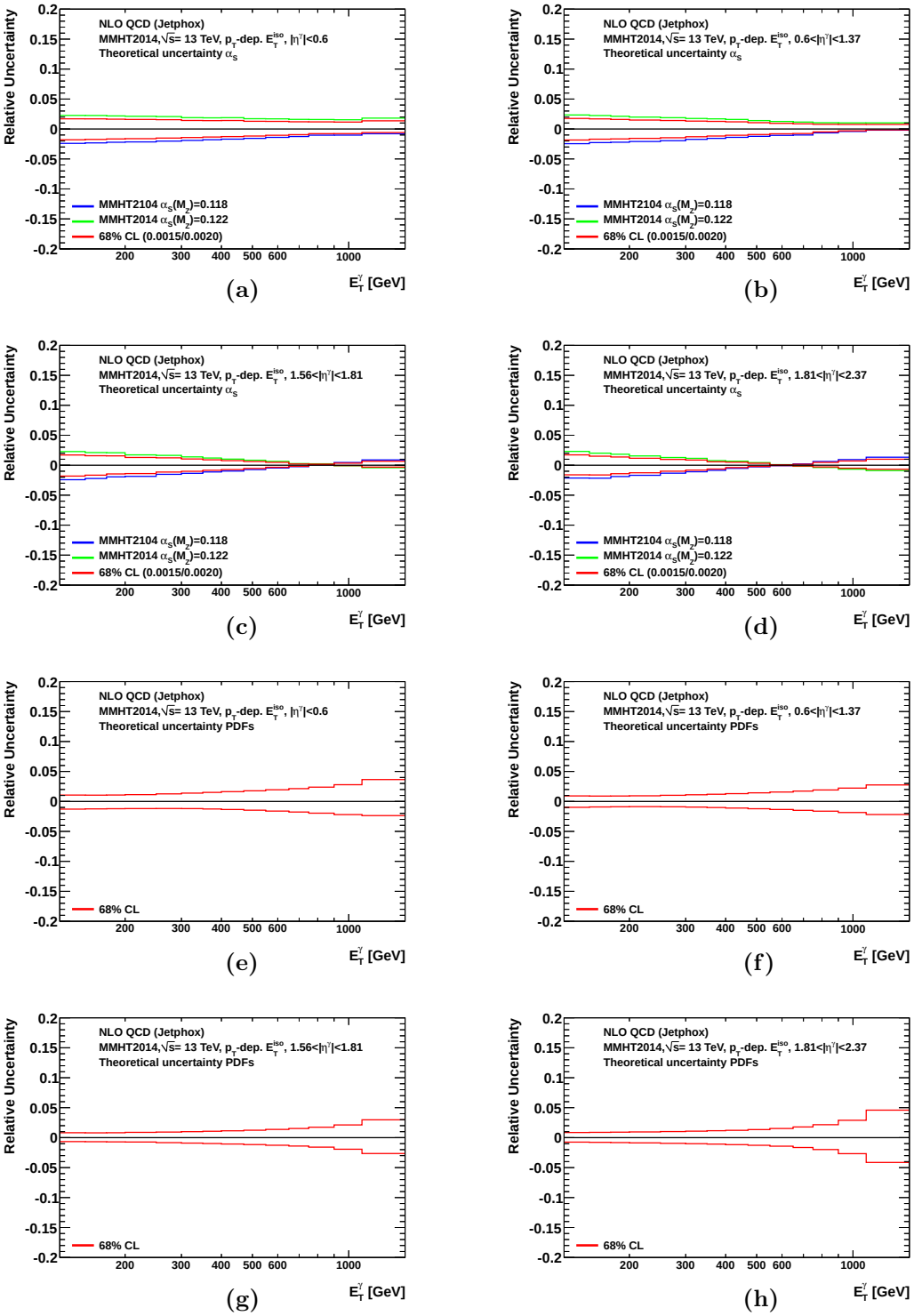


Figure 6.53: Theoretical uncertainty arising from the uncertainty in α_s (a,b,c,d) and the PDFs (e,f,g,h) as a function of E_T^γ in different regions of η^γ using MMHT2014.

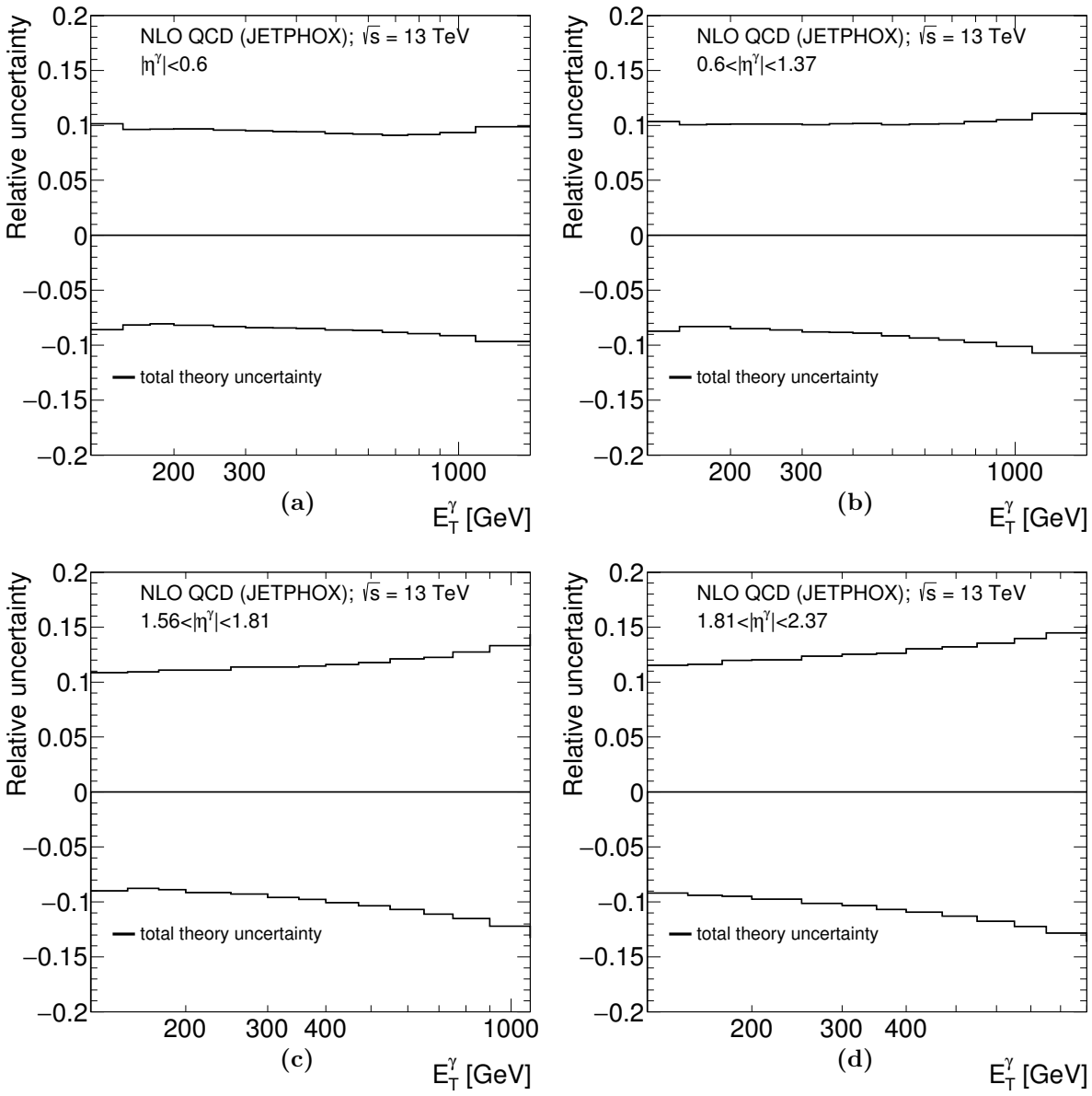


Figure 6.54: Total theoretical uncertainty as a function of E_{T}^{γ} in different regions of η^{γ} using the calculations based on the MMHT2014 PDFs. The total theoretical uncertainty includes the envelope of the variations of the scales, the uncertainties on the PDFs and α_{s} as well as the uncertainty (1%) on the non-perturbative corrections.

6.8 Results

Figure 6.55 shows the isolated-photon cross section as a function of E_{T}^{γ} in four different regions of η^{γ}. The measured cross sections decrease by approximately five orders of magnitude in the measured range. Values of E_{T}^{γ} up to 1.5 TeV were accessed. The cross-section distributions measured in the four different regions of η^{γ} have similar shapes.

The predictions of the Pythia and Sherpa MC models are compared to the measurements in Figure 6.55. These predictions are normalised to the measured integrated cross section in each η^{γ} region. The difference in normalisation between data and Pythia (Sherpa) is $\sim +10\%$ ($+30\%$) and is attributed to the fact that these generators are based on tree-level matrix elements, which are affected by a large normalisation uncertainty due to missing higher-order terms. The predictions of both Pythia and Sherpa give a good description of the shape of the measured cross-section distributions for $E_{\mathrm{T}}^{\gamma} \lesssim 500$ GeV in the range $|\eta^{\gamma}| < 1.37$ and in the whole measured E_{T}^{γ} range for $1.56 < |\eta^{\gamma}| < 2.37$.

Figure 6.56 shows the measured isolated-photon cross sections as functions of E_{T}^{γ} in four different regions of η^{γ} compared with the predictions of the NLO pQCD calculations of JetPhox based on the MMHT2014 proton PDF set. The ratios of the theoretical predictions based on different PDF sets to the measured cross sections are shown in Figure 6.57 and 6.58. The predictions based on MMHT2014, CT14 [116] and NNPDF3.0 [59], HERAPDF2.0 [61] and AMB11 [117] are similar, the differences being much smaller than the total theoretical uncertainties dominated by the scale variations. For most of the points, the theoretical uncertainties are larger than those of experimental origin. Differences are observed between data and the predictions of up to 10–15% depending on E_{T}^{γ} and $|\eta^{\gamma}|$; since the theoretical uncertainties are 10–15% and cover those differences, it is concluded that the NLO pQCD predictions provide an adequate description of the measurements. The measured cross sections are larger than those at $\sqrt{s} = 8$ TeV [15] by approximately a factor of two at low E_{T}^{γ} ($E_{\mathrm{T}}^{\gamma} \sim 125$ GeV) and by approximately an order of magnitude at the high end of the spectrum in each region of $|\eta^{\gamma}|$. Such increases in the measured cross section are expected from the increase in the centre-of-mass energy. For both centre-of-mass energies the NLO theoretical uncertainties are of similar size and comparable to the differences between the predictions and the data; since, in addition, the experimental uncertainties are smaller than those differences, the inclusion of NNLO pQCD corrections might improve the description of the two sets of measurements.

The measured fiducial cross section for inclusive isolated-photon production in the phase-space region given by $E_{\mathrm{T}}^{\gamma} > 125$ GeV and $|\eta^{\gamma}| < 2.37$ (excluding the region of $1.37 < |\eta^{\gamma}| < 1.56$) and isolation $E_{\mathrm{T}}^{\mathrm{iso}}$<4.8 GeV $+ 4.2 \cdot 10^{-3} \cdot E_{\mathrm{T}}^{\gamma}$ [GeV] is

$$\sigma_{\mathrm{meas}} = 399 \pm 13\ (\mathrm{exp.})\ \pm 8\ (\mathrm{lumi.})\ \mathrm{pb},$$

where "exp." denotes the sum in quadrature of the statistical and systematic uncertainties and "lumi." denotes the uncertainty due to that in the integrated luminosity. The fiducial cross section predicted at NLO in pQCD by JetPhox using the MMHT2014 PDFs is

$$\sigma_{\mathrm{NLO}} = 352^{+36}_{-29}\ (\mathrm{scale})\ \pm 3\ (\mathrm{PDF})\ \pm 6\ (\alpha_{\mathrm{s}})\ \pm 4\ (\mathrm{non-perturb.})\ \mathrm{pb},$$

which is 12% lower than the measurement, but consistent within the experimental and theoretical uncertainties.

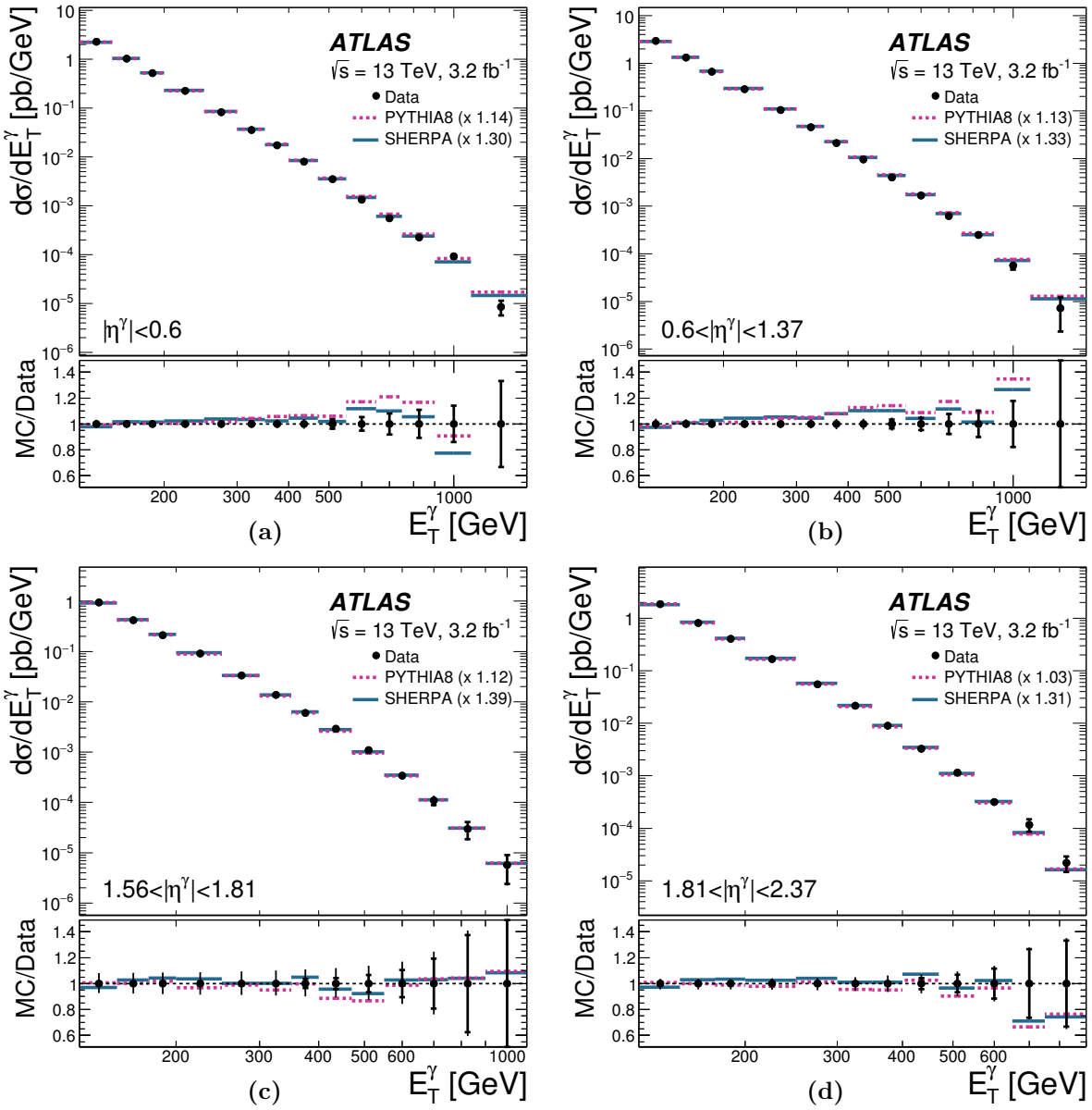


Figure 6.55: Measured cross sections for isolated-photon production (dots) as functions of E_{T}^{γ} in (a) $|\eta^{\gamma}| < 0.6$, (b) $0.6 < |\eta^{\gamma}| < 1.37$, (c) $1.56 < |\eta^{\gamma}| < 1.81$ and (d) $1.81 < |\eta^{\gamma}| < 2.37$. The predictions from Pythia (dashed lines) and Sherpa (solid lines) are also shown; these predictions are normalised to the measured integrated cross section in each region of $|\eta^{\gamma}|$ using the values indicated in parentheses. The bottom part of each figure shows the ratio of the MC predictions to the measured cross section. The inner (outer) error bars represent the statistical uncertainties (the statistical and systematic uncertainties, excluding that on the luminosity, added in quadrature). For most of the points, the inner error bars are smaller than the marker size and, thus, not visible.

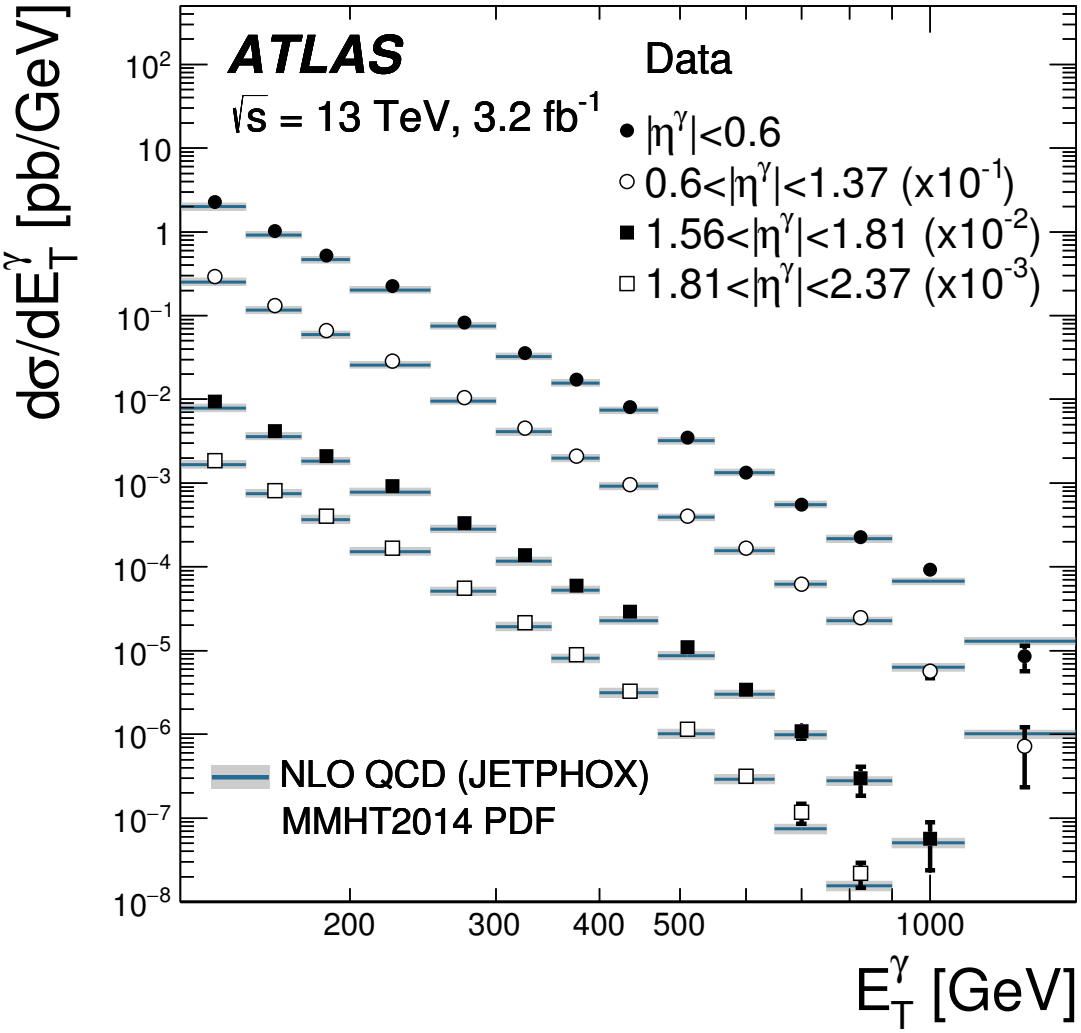


Figure 6.56: Measured cross sections for isolated-photon production as functions of E_{T}^{γ} in $|\eta^{\gamma}| < 0.6$ (black dots), $0.6 < |\eta^{\gamma}| < 1.37$ (open circles), $1.56 < |\eta^{\gamma}| < 1.81$ (black squares) and $1.81 < |\eta^{\gamma}| < 2.37$ (open squares). The NLO pQCD predictions from JetPhox based on the MMHT2014 PDFs (solid lines) are also shown. The measurements and the predictions are normalised by the factors shown in parentheses to aid visibility. The error bars represent the statistical and systematic uncertainties added in quadrature. The shaded bands display the theoretical uncertainty.

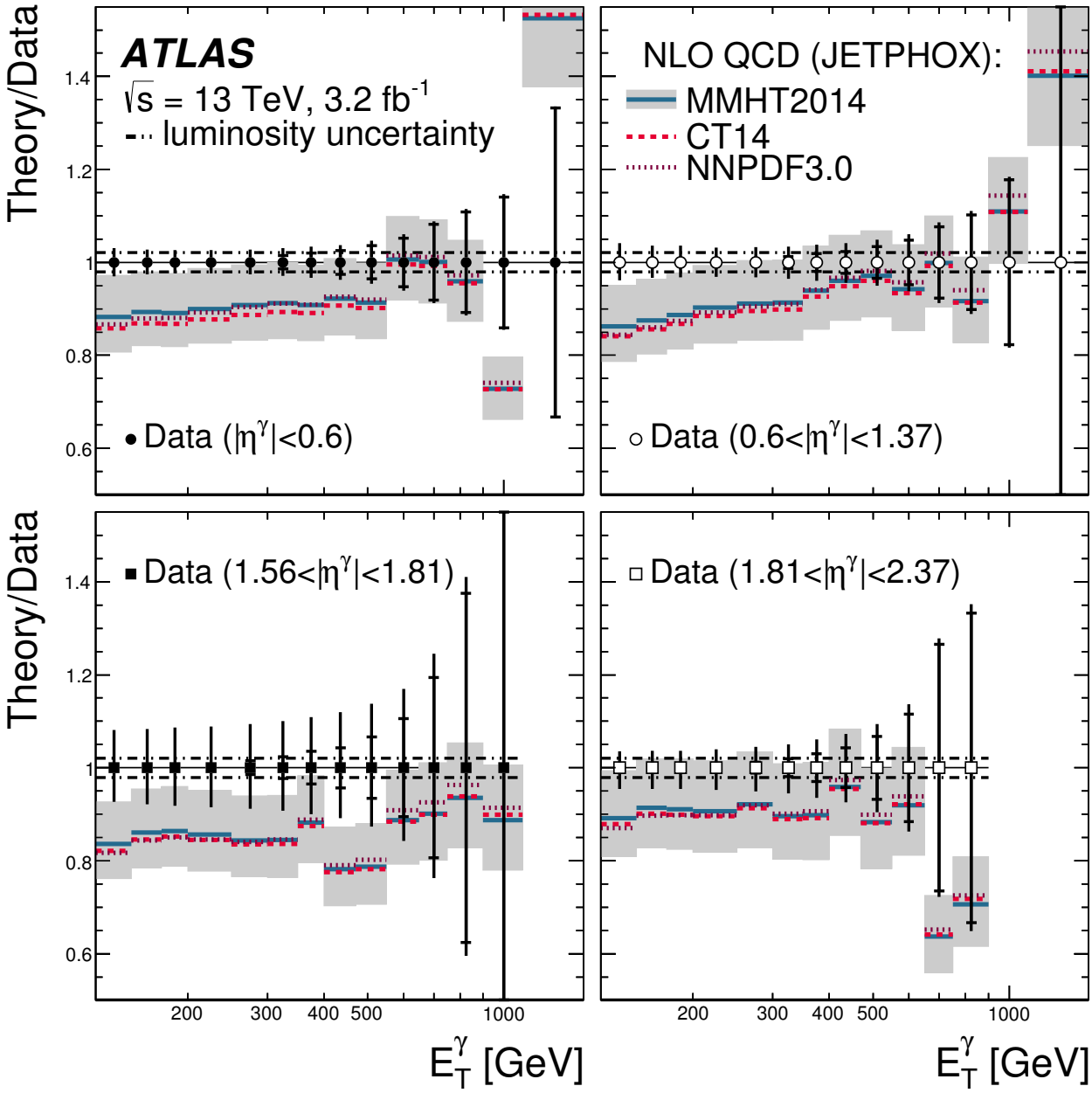


Figure 6.57: Ratio of the NLO pQCD predictions from JetPhox based on the MMHT2014 PDFs to the measured cross sections for isolated-photon production (solid lines) as a function of E_{T}^{γ} in (a) $|\eta^{\gamma}| < 0.6$, (b) $0.6 < |\eta^{\gamma}| < 1.37$, (c) $1.56 < |\eta^{\gamma}| < 1.81$ and (d) $1.81 < |\eta^{\gamma}| < 2.37$. The inner (outer) error bars represent the statistical uncertainties (statistical and systematic uncertainties, excluding that on the luminosity, added in quadrature), the dot-dot-dashed lines represent the uncertainty due to the luminosity measurement and the shaded bands display the theoretical uncertainty of the calculation based on the MMHT2014 PDFs. The ratio of the NLO pQCD predictions based on the CT14 (dashed lines) or NNPDF3.0 (dotted lines) PDF sets to the data are also included.

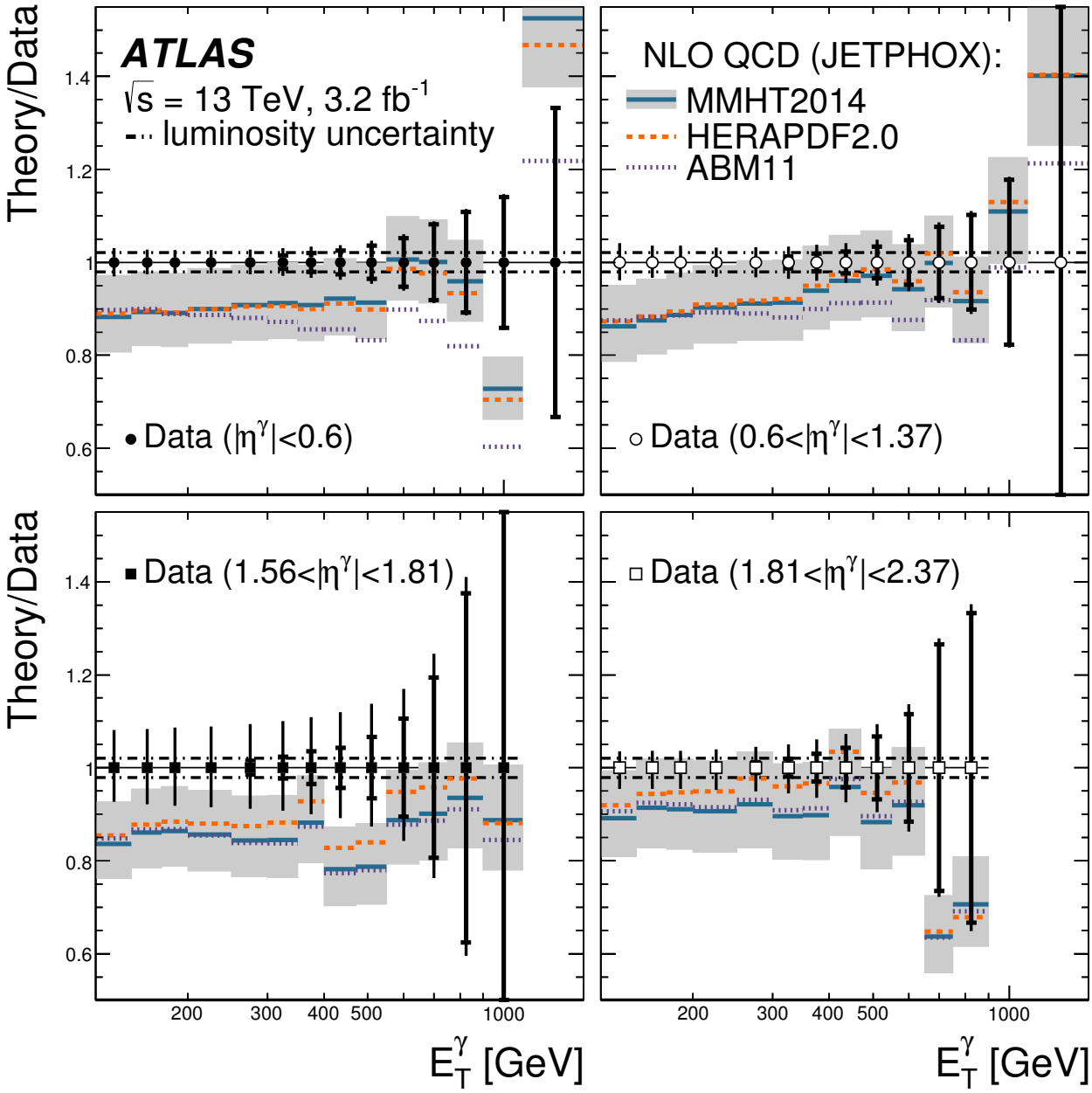


Figure 6.58: Ratio of the NLO pQCD predictions from JetPhox based on the MMHT2014 PDFs to the measured cross sections for isolated-photon production (solid lines) as a function of E_{T}^{γ} in (a) $|\eta^{\gamma}| < 0.6$, (b) $0.6 < |\eta^{\gamma}| < 1.37$, (c) $1.56 < |\eta^{\gamma}| < 1.81$ and (d) $1.81 < |\eta^{\gamma}| < 2.37$. The inner (outer) error bars represent the statistical uncertainties (statistical and systematic uncertainties, excluding that on the luminosity, added in quadrature), the dot-dot-dashed lines represent the uncertainty due to the luminosity measurement and the shaded bands display the theoretical uncertainty of the calculation based on the MMHT2014 PDFs. The ratio of the NLO pQCD predictions based on the HERAPDF2.0 (dashed lines) or ABM11 (dotted lines) PDF sets to the data are also included.

6.9 Further research using the published cross-section measurements

As mentioned in Section 3.4.2, improvements in the knowledge of the direct inclusive-photon production have been achieved by different theoretical groups. The measurements provided to the scientific community by the inclusive-photon analyses have been used to compare with new theoretical computations.

The NNLO QCD plus LL electroweak predictions for direct inclusive-photon production were compared to the measurements presented in this chapter in Reference [11]. The NNLO calculations were based on the NNPDF3.1NNLO PDF set. The smooth cone isolation criterion with parameters $\epsilon = 0.1$, $n = 2$ and $\delta_0 = 0.4$ was adopted in the calculations. The renormalisation and factorisation scales were set to E_{T}^{γ}. To account for the impact of Sudakov effects induced by virtual loops of heavy electroweak gauge bosons, the resummation of electroweak Sudakov logarithms at LL accuracy was included. The QED coupling constant was set to $\alpha_{\mathrm{EM}}(m_Z) = 1/127.9$.

The calculations were performed at $\sqrt{s} = 8$ and 13 TeV and the former were included in the NNPDF3.1NNLO global analysis to assess the impact of these data on the medium-x gluon PDF. In NNPDF3.1, the gluon PDF is constrained by measurements of inclusive-jet production, $Z_{p_{\mathrm{T}}}$ and $t\bar{t}$ production. The (x, Q^2) range covered by the inclusive-photon measurements is only partly covered by other experiments (see Figure 6.59). The new PDF set is referred to as NNPDF3.1+ATLAS$_\gamma$. The comparisons between the calculations based on the NNPDF3.1NNLO PDF set and the NNPDF3.1+ATLAS$_\gamma$ PDF set and 13 TeV ATLAS inclusive-photon data are illustrated in Figure 6.60.

The scale uncertainties were estimated by independently varying the μ_R and μ_F scales by a factor of two. For the majority of the E_{T}^{γ} bins, the scale uncertainty is $\approx 5\%$, reaching a maximum of 10% in the most forward rapidity bin at high E_{T}^{γ}. A significant reduction of the scale uncertainties was achieved with respect to the NLO calculations, where this uncertainty lies typically in the range 10–15%. The NNLO calculations describe the shape and normalisation of the data within the reduced theoretical uncertainties.

As the direct-photon predictions were also made at $\sqrt{s} = 8$ TeV, the ratio of the cross-section predictions at $\sqrt{s} = 13$ and 8 TeV was computed in Reference [11]. Figure 6.61 shows the comparison for $R_{13/8}$, as defined in Chapter 7, between data and predictions. The theoretical uncertainties include only the contribution of the PDF uncertainties and the experimental uncertainties were not estimated following the careful procedure presented in Chapter 7. The ratio of theory and data for $R_{13/8}$ is shown in Figure 6.62.

After the detailed studies performed in Reference [11], it was demonstrated that there is no reason to exclude recent LHC photon data from a global PDF analysis. These measurements lead to a moderate reduction of the gluon PDF uncertainties at medium x.

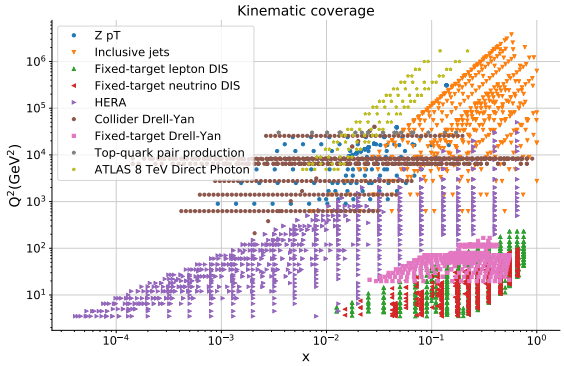


Figure 6.59: Kinematic coverage of the ATLAS inclusive photon data at $\sqrt{s} = 8$ TeV (stars) together with other measurements used in the global PDF fit [11].

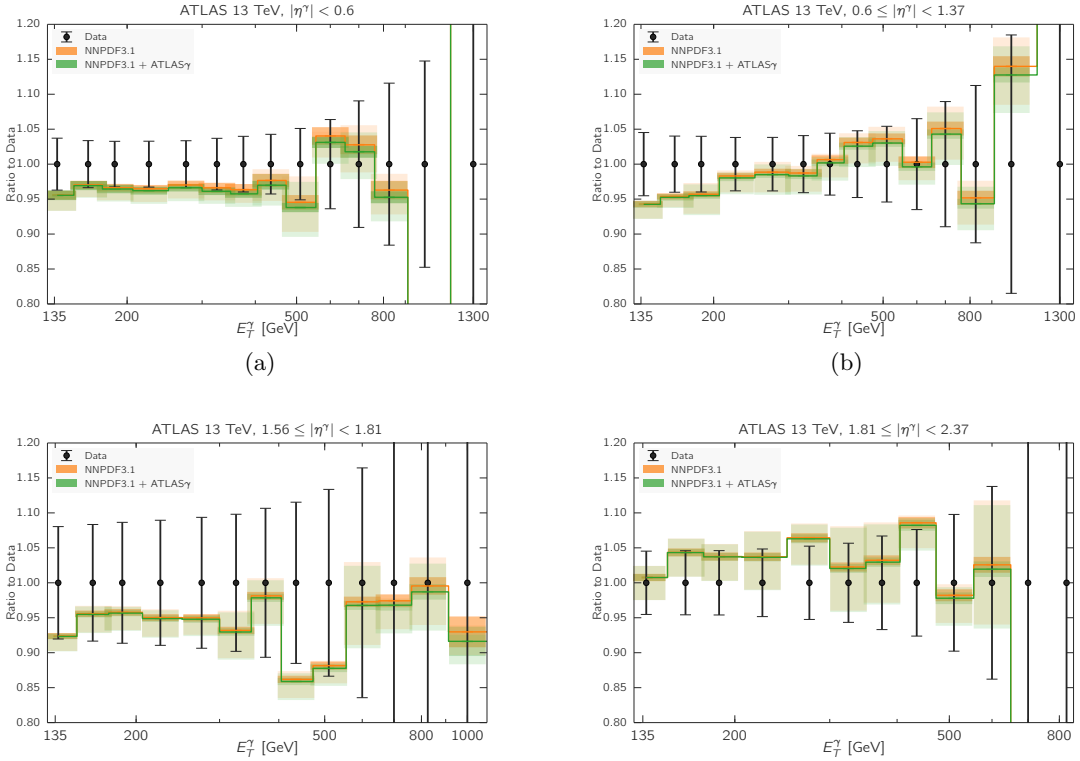


Figure 6.60: Comparisons shown in [11] between the ATLAS 13 TeV inclusive photon data presented in Chapter 6 and NNLO theoretical predictions for direct photon production computed with the NNPDF3.1 PDF set (orange histograms) and a modified set (green histogram), NNPDF3.1+ATLAS$_\gamma$, in which the ATLAS 8 TeV inclusive photon data were used in the PDF fits. The experimental statistical and systematic uncertainties have been added in quadrature and displayed as error bars. The error bands show the scale uncertainties associated with the NNLO calculations (shown as the lighter error bands) in addition to the PDF uncertainties.

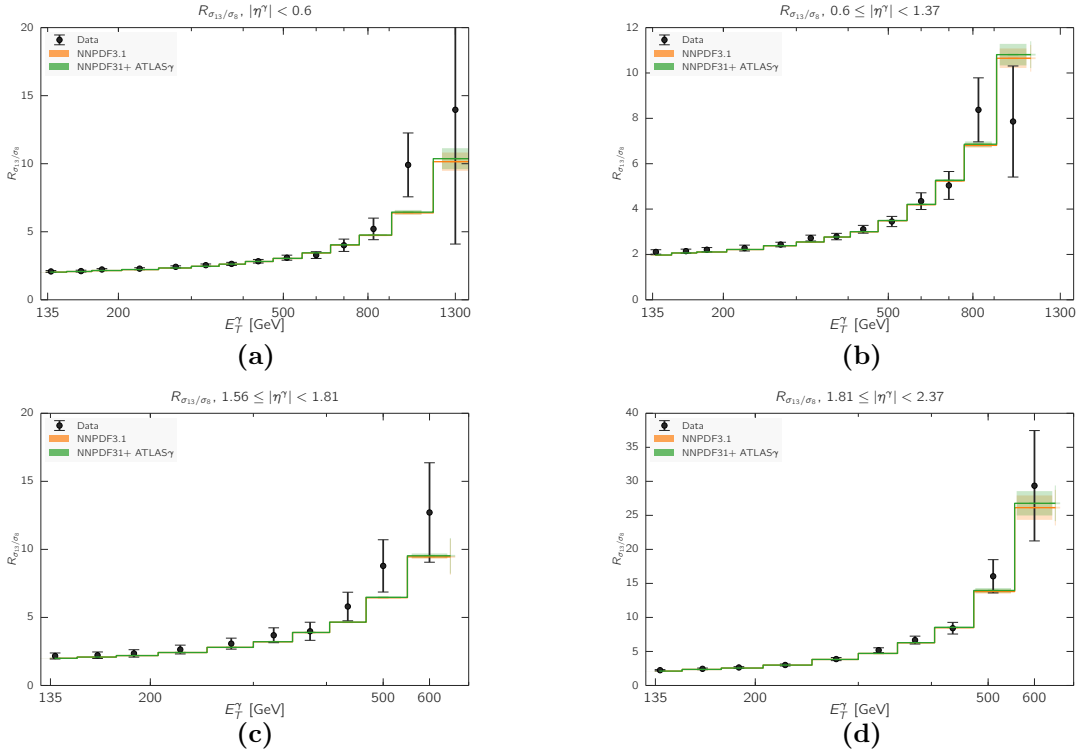


Figure 6.61: Comparisons shown in Reference [11] between the experimental measurements of $R_{13/8}$ ratio and the corresponding theoretical calculations using NNPDF3.1 and NNPDF3.1+ATLAS$_\gamma$. The theory band includes only the contribution of the PDF uncertainties.

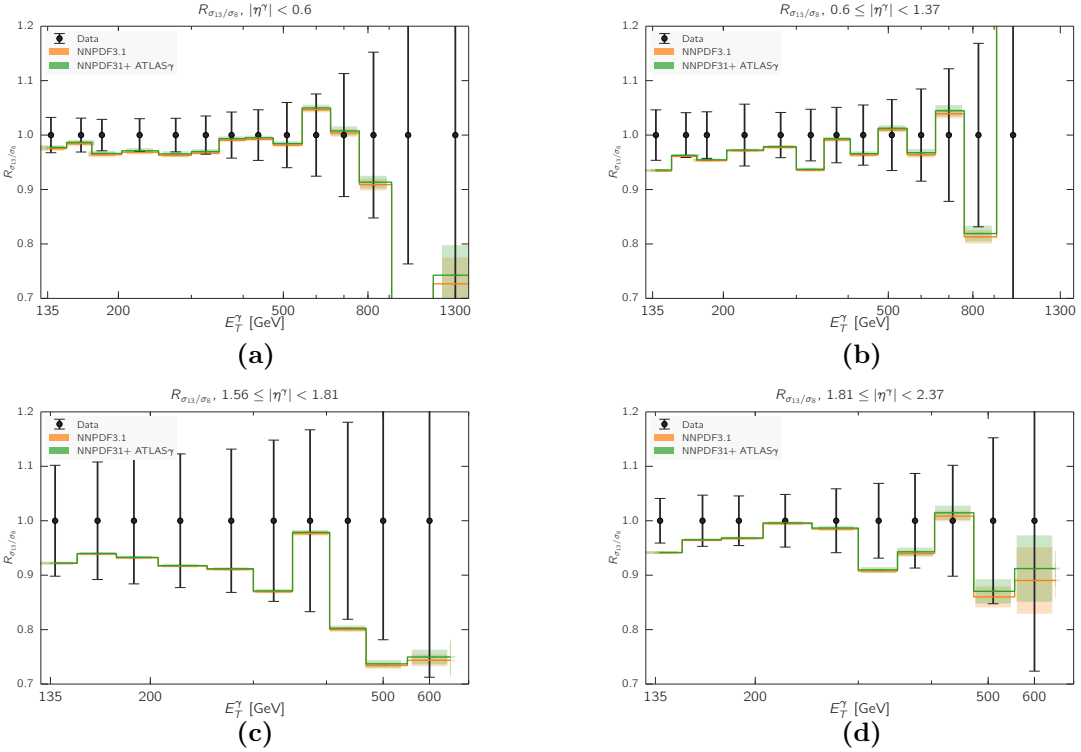


Figure 6.62: Ratio theory over data shown in Reference [11] for $R_{13/8}$ using NNPDF3.1 and NNPDF3.1+ATLAS$_\gamma$. The theory band includes only the contribution of the PDF uncertainties.

To estimate the uncertainties due to the MC parton shower and the hadronisation model used in the unfolding of the measurements, at least two comparable MC generators are desirable. For all the measurements presented in this dissertation, LO MCs (Pythia and Sherpa) were used since there are no alternative MC samples to Sherpa NLO with NLO matrix elements available within the ATLAS framework. However, this alternative already exists with POWHEG [121]. In POWHEG, the LO direct-photon production processes $q\bar{q} \to \gamma g$ and $qg \to \gamma q$ were calculated taking into account colour and spin correlations. The virtual corrections were computed at one-loop level with renormalisation performed in the modified minimal subtraction scheme. For the real corrections, the tree-level processes with additional gluon radiation or gluon splitting into quark-antiquark pairs were computed. The process $gg \to \gamma q\bar{q}$ was also taken into account. The total NLO partonic calculation based on the NNPDF3.1NLO PDF set was checked to agree with that of JetPhox. The latter includes the fragmentation contribution at NLO, whereas in the Powheg approach, this contribution was taken into account at NLO by partonic scatterings supplemented with a QED parton shower. The renormalisation and factorisation scales were set to E_{T}^{γ}. To estimate the theoretical uncertainties, the scales were then varied by relative factors of two. The matching between the NLO calculations with the parton shower was made with the FKS method [133]. The parton-shower algorithm used was that of Pythia 8.226 [76] with its p_{T}-ordered parton shower and string hadronisation model.

Figures 6.63 and 6.64 show the comparison between the measurements presented in Section 6.8 and the following predictions:

- the LO predictions of Pythia using the Monash 2013 tune and based on the NNPDF-2.3QEDLO PDF set with $\alpha_{\mathrm{s}}(m_{\mathrm{Z}}) = 0.130$;
- the NLO predictions of Powheg supplemented with the Pythia parton shower as described in this section based on the NNPDF3.1NLO PDF set with $\alpha_{\mathrm{s}}(m_{\mathrm{Z}}) = 0.118$;
- the fixed-order calculations of JetPhox based on the NNPDF3.1NLO PDF set with $\alpha_{\mathrm{s}}(m_{\mathrm{Z}}) = 0.118$ and the BFG II fragmentation functions.

The uncertainties of the LO calculations are considerably larger than those of the NLO and NLO supplemented with parton shower (NLO+PS) calculations. The NLO JetPhox predictions have a different shape in the second rapidity bin and globally underestimate the data. The central predictions of Powheg NLO+PS predictions still underestimate the data in the central rapidity bin, but generally offer the best agreement with the data and are always within the scale uncertainties. Since the purely partonic process of Powheg agrees with that in JetPhox, the better agreement of Powheg NLO+PS with the data seems to indicate that the parton-shower fragmentation in Pythia describes the data slightly better that the BFG II fragmentation function.

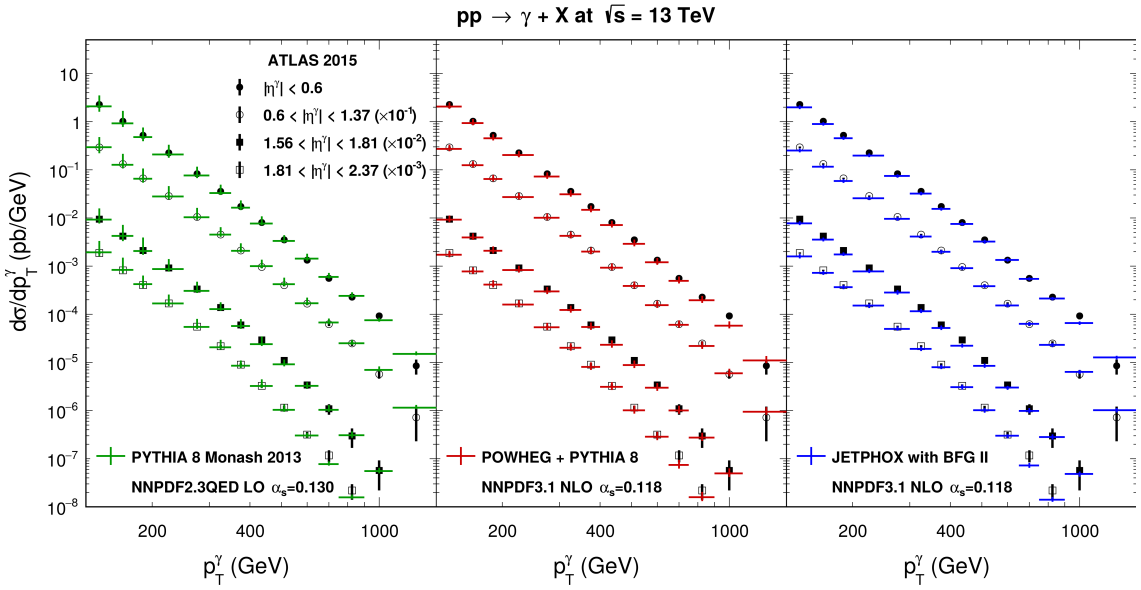


Figure 6.63: Figure from Reference [121]. ATLAS inclusive photon data at $\sqrt{s} = 13$ TeV compared to the predictions of Pythia LO (left), JetPhox NLO (right) and PowHeg at NLO supplemented with Pythia parton shower (centre). More details can be found in Reference [121].

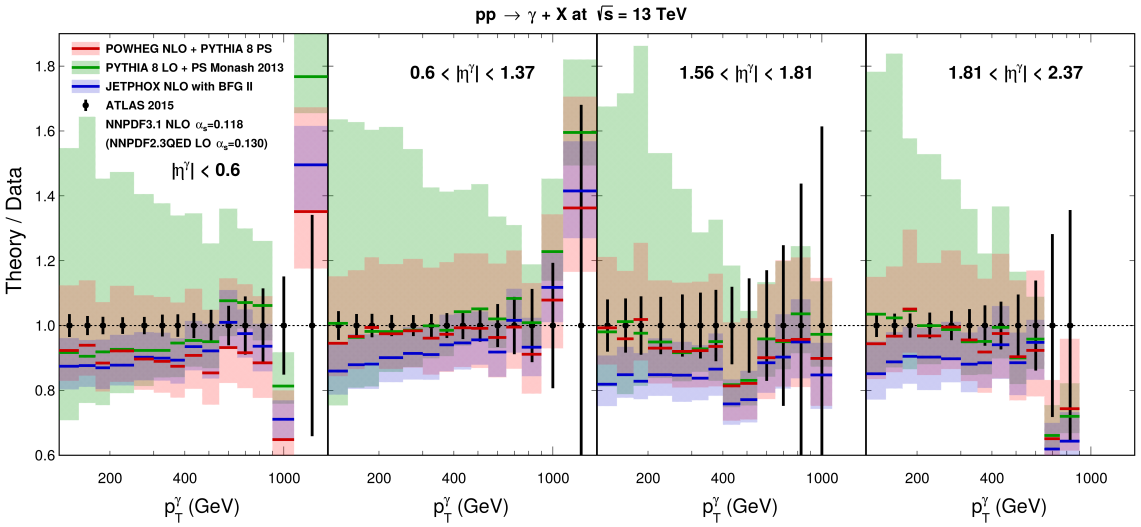


Figure 6.64: Figure from Reference [121]. Ratio of the predictions of Pythia LO, JetPhox NLO and PowHeg at NLO supplemented with Pythia parton shower to ATLAS inclusive photon data at $\sqrt{s} = 13$ TeV in different regions of η^{γ}. More details can be found in Reference [121].

7

Ratio of inclusive isolated-photon cross sections at $\sqrt{s} = 13$ and 8 TeV

A measurement of the ratio of cross sections, $R_{13/8}$, for inclusive isolated-photon production in pp collisions at $\sqrt{s} = 13$ [27] and 8 TeV [15] using the ATLAS detector is presented in this chapter. The ratio $R_{13/8}$ was measured as a function of E_{T}^{γ} in different regions of η^{γ} for photons with $E_{\mathrm{T}}^{\gamma} > 125$ GeV and $|\eta^{\gamma}| < 2.37$, excluding the region $1.37 < |\eta^{\gamma}| < 1.56$. The experimental systematic uncertainties in $R_{13/8}$ take into account the correlations between the experimental uncertainties at the two centre-of-mass energies. As a result, the uncertainties in $R_{13/8}$ were significantly reduced. The predictions from NLO pQCD were compared to the measured $R_{13/8}$. The NLO pQCD predictions based on current parameterisations of the proton PDFs agree with the data within the reduced experimental and theoretical uncertainties. Additionally, the double ratio of $R_{13/8}$ over the ratio of the fiducial cross sections for Z boson production at 13 and 8 TeV [122], $D_{13/8}^{\gamma/Z}$, was also measured. The ratio $D_{13/8}^{\gamma/Z}$ benefits from the complete cancellation of the uncertainty on the measured integrated luminosity.

7.1 Analysis strategy

The measurement of $R_{13/8}$ makes use of the results presented in Chapter 6 and a similar measurement performed previously at 8 TeV [15]. Relevant details on the latter are given throughout this chapter. The measurement at 13 TeV was made in such a way as to make possible the measurement of $R_{13/8}$: the phase-space region to which the data distributions were unfolded to is the same as that at 8 TeV in what concerns the photon isolation and the regions in $|\eta^{\gamma}|$; regarding the range in E_{T}^{γ}, the analysis at 13 TeV covers the range $E_{\mathrm{T}}^{\gamma} > 125$ GeV with the same binning[1] as used at 8 TeV.

Given the dominance of the systematic uncertainty arising from the photon energy scale on the cross sections, it is of vital importance that this source of uncertainty is treated properly. This is discussed in Section 7.2.1. The decomposition of this source of uncertainty in independent components and the treatment of the correlations of these components between the measurements at 13 and 8 TeV results in a significant reduction of the systematic uncertainty in $R_{13/8}$.

The proper evaluation of the theoretical uncertainties reduces the theoretical uncertain-

[1] There are a few bins at the high end of the spectrum in E_{T}^{γ} for which the cross section was measured at 13 TeV and not at 8 TeV. These bins, which are present only in the regions $0.6 < |\eta^{\gamma}| < 1.37$, $1.56 < |\eta^{\gamma}| < 1.81$ and $1.81 < |\eta^{\gamma}| < 2.37$, are not used in the analysis presented in this chapter.

ty on $R_{13/8}$ after taking into account the correlations between both centre-of-mass energies; the theoretical uncertainty is of $\mathcal{O}(10\text{–}15\%)$ for the individual measurements and dominated by the uncertainty on the terms beyond NLO. These uncertainties are much larger than those of experimental nature and limit the precision with which the predictions are tested. The treatment of the theoretical uncertainties in $R_{13/8}$ is described in Section 7.2.

The measurement of $D_{13/8}^{\gamma/Z}$ is based on the measurement of $R_{13/8}$ described above as well as on the measurement of the ratio of the fiducial cross sections for Z boson production at 13 and 8 TeV [122], $\sigma_Z^{\text{fid}}(13\text{TeV})/\sigma_Z^{\text{fid}}(8\text{TeV})$. The ratio $R_{13/8}$ was measured as a function of E_{T}^{γ} in different ranges of η^{γ} while the ratio $\sigma_Z^{\text{fid}}(13\text{TeV})/\sigma_Z^{\text{fid}}(8\text{TeV})$ is a single number.

The uncertainty due to the luminosity cancels out in $D_{13/8}^{\gamma/Z}$, which is the main reason to consider this double ratio. The experimental uncertainty on $\sigma_Z^{\text{fid}}(13\text{TeV})/\sigma_Z^{\text{fid}}$ (8TeV) is dominated by the lepton reconstruction and efficiency while that on the electron energy scale is a subdominant uncertainty (see Section 7.2.4). Therefore, the correlation between the contribution due to the electron energy scale and the photon energy scale in $R_{13/8}$ can be neglected safely.

The predictions for $D_{13/8}^{\gamma/Z}$ were obtained from NLO pQCD calculations for $R_{13/8}$ and NNLO pQCD calculations for $\sigma_Z^{\text{fid}}(13\text{TeV})/\sigma_Z^{\text{fid}}(8\text{TeV})$. The correlations arising from the PDFs and $\alpha_{\text{s}}(m_Z)$ were taken into account by obtaining the predictions of $R_{13/8}$ with the same PDF sets as for $\sigma_Z^{\text{fid}}(13\text{TeV})/\sigma_Z^{\text{fid}}(8\text{TeV})$.

7.2 Experimental systematic uncertainties

In this section, the treatment of the systematic uncertainties in $R_{13/8}$ is presented. The individual measurements are dominated by the photon energy scale in the phase-space region considered for the ratio. The procedure followed to correlate this uncertainty between the measurements at 8 and 13 TeV is explained in Section 7.2.1. The type of correlation considered for all the other uncertainties is presented in Section 7.2.2.

7.2.1 Photon energy scale

The photon energy scale correction parameters and uncertainties for the 13 TeV inclusive photon measurement were based on those estimated at 8 TeV and taking also into account the difference between both data-taking periods, as explained in Section 4.2, allowing an easier determination of the correlation between the different sources of the uncertainty. The 13 TeV measurement was performed using the full decorrelated model in which the sources of the uncertainties were separated into different bins of η^{γ}. However, this model was not available when the 8 TeV measurement was published and a simplified decorrelation model based on 20 nuisance parameters was used. To correlate properly both measurements, the measurement at 13 TeV was repeated using the same model and adding two additional parameters specific to $\sqrt{s} = 13$ TeV. All the components influencing the energy measurement of the photon are summarised in Table 7.1 and described in Appendix C.

The ratio of the measurements at $\sqrt{s} = 13$ TeV and 8 TeV was made taking all the uncertainty components as correlated except for those related to the in situ corrections with

Common to $\sqrt{s} = 13$ and 8 TeV			
ZeeStatUncert	ZeeSystUncert	LArCalibUncert	LArUnconvCalibUncert
LArElecUnconvUncert	LArElecCalibUncert	G4Uncert	PSUncert
S12Uncert	MatIDUncert	MatCryoUncert	MatCaloUncert
L1GainUncert	L2GainUncert	LeakageConvUncert	LeakageUnconvUncert
ConvEfficiencyUncert	ConvFakeRateUncert	PedestalUncert	ConvRadiusUncert
Only for $\sqrt{s} = 13$ TeV			
LARCALIB_EXTRA2015PRE		LARTEMPERATURE_EXTRA2015PRE	

Table 7.1: List of the individual sources of systematic uncertainty in the photon energy scale.

$Z \to e^+e^-$, since it increased in $\sqrt{s} = 13$ TeV due to the extra uncertainties considered and explained in Section 4.2, that is, "ZeeStat" and "ZeeSyst", and the specific components for the 13 TeV measurement: "LARCALIB_EXTRA2015PRE" and "LARTEMPERATURE_-EXTRA2015PRE".

The relative uncertainties in the cross-section measurements as functions of E_{T}^{γ} for the dominant common components for $|\eta^{\gamma}| < 0.6$ are shown in Figure 7.1. All other components are lower than 0.5% in the whole E_{T}^{γ} range and very similar between 8 and 13 TeV. For $0.6 < |\eta^{\gamma}| < 1.37$, the common dominant uncertainties are shown in Figure 7.2; all other components are smaller and very similar between 8 and 13 TeV. The dominant uncertainties in the forward region $1.56 < |\eta^{\gamma}| < 1.81$ ($1.81 < |\eta^{\gamma}| < 2.37$) are displayed in Figure 7.3 (Figure 7.4).

The total systematic uncertainty in $R_{13/8}$ due to the correlated components of the photon energy scale (γ-ES) uncertainty is shown in Figure 7.5. For comparison, the estimated uncertainty when treating these components as uncorrelated is also shown in the figure. The results obtained, after the proper correlation treatment is used, exhibit a large reduction in size when compared to those in which the correlation is ignored.

The extra uncertainties considered for the $\sqrt{s} = 13$ TeV measurement are shown in Figure 7.6. The size of these two uncertainties lies between 1 and 2% depending on E_{T}^{γ} and η^{γ}.

An additional uncertainty in $R_{13/8}$ was considered, which does not affect the individual measurements. This source of uncertainty arises from the relative difference in the photon energy response between the MG to HG ratio in Run-2 and Run-1, as mentioned in Section 4.2. The impact of this uncertainty on $R_{13/8}$ is shown in Figure 7.7. The resulting uncertainty (denoted as MG/HG Run2/Run1) was added in quadrature to the estimation of the γ-ES uncertainty due to the sources described above.

The final uncertainty due to the γ-ES on $R_{13/8}$ was obtained by adding in quadrature the contribution of those uncertainties treated as correlated (shown in Figure 7.5), those treated as uncorrelated, the extra uncertainties considered for the $\sqrt{s} = 13$ TeV measurement (see Figure 7.6) and the MG/HG Run2/Run1 uncertainty.

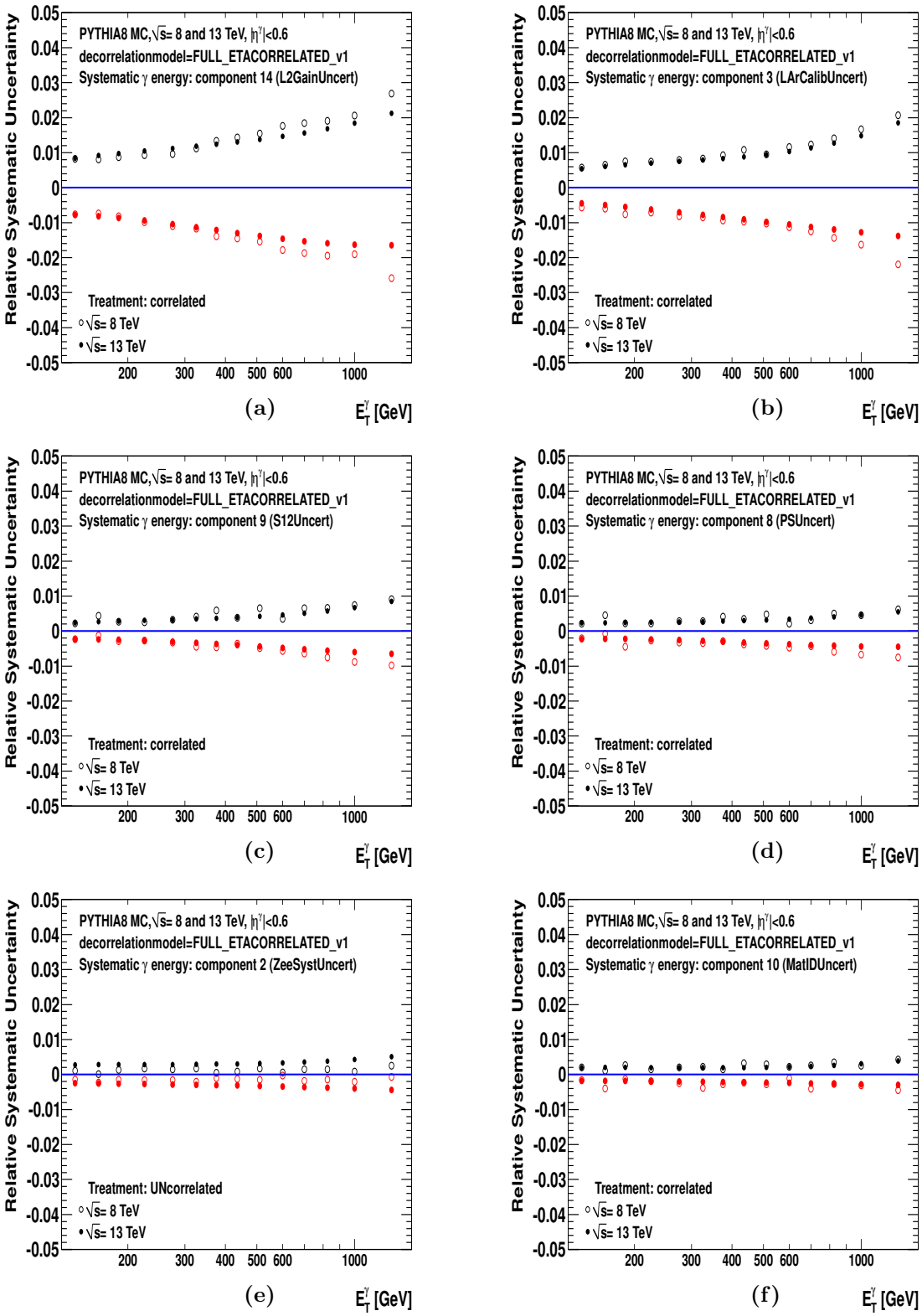


Figure 7.1: Relative systematic uncertainty in the measured cross sections as a function of E_{T}^{γ} for the region $|\eta^{\gamma}| < 0.6$ due to the following γ-ES components: (a) "L2GainUncert", (b) "LArCalibUncert", (c) "S12Uncert", (d) "PSUncert", (e) "ZeeSystUncert", (f) "MatIDUncert". Results are presented for both $\sqrt{s} = 8$ (open circles) and 13 TeV (dots).

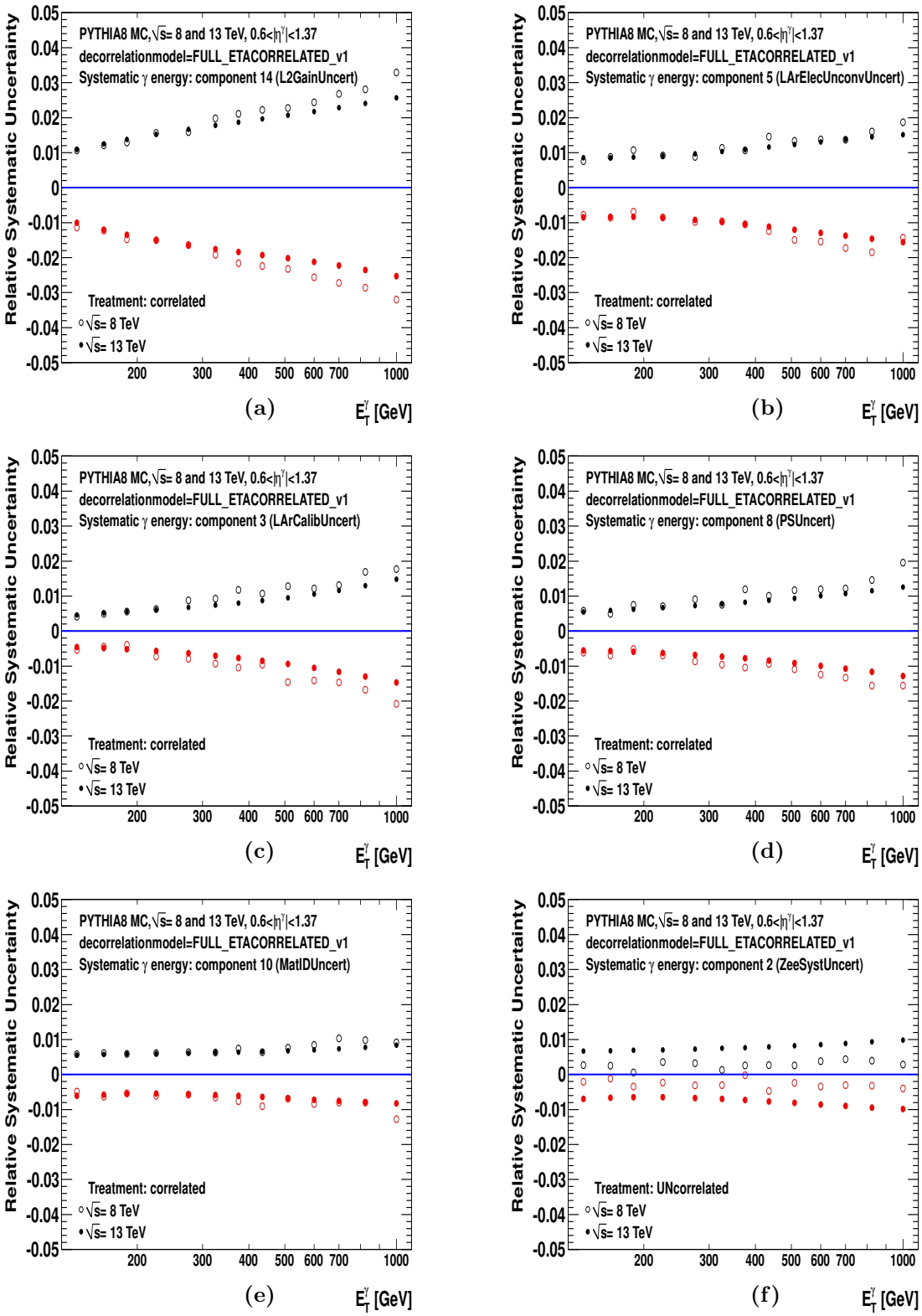


Figure 7.2: Relative systematic uncertainty in the measured cross sections as a function of E_{T}^{γ} for the region $0.6 < |\eta^{\gamma}| < 1.37$ due to the following γ-ES components: (a) "L2GainUncert", (b) "LArElecUnconvUncert", (c) "LArCalibUncert", (d) "PSUncert", (e) "MatIDUncert", (f) "ZeeSystUncert". Results are presented for both $\sqrt{s} = 8$ (open circles) and 13 TeV (dots).

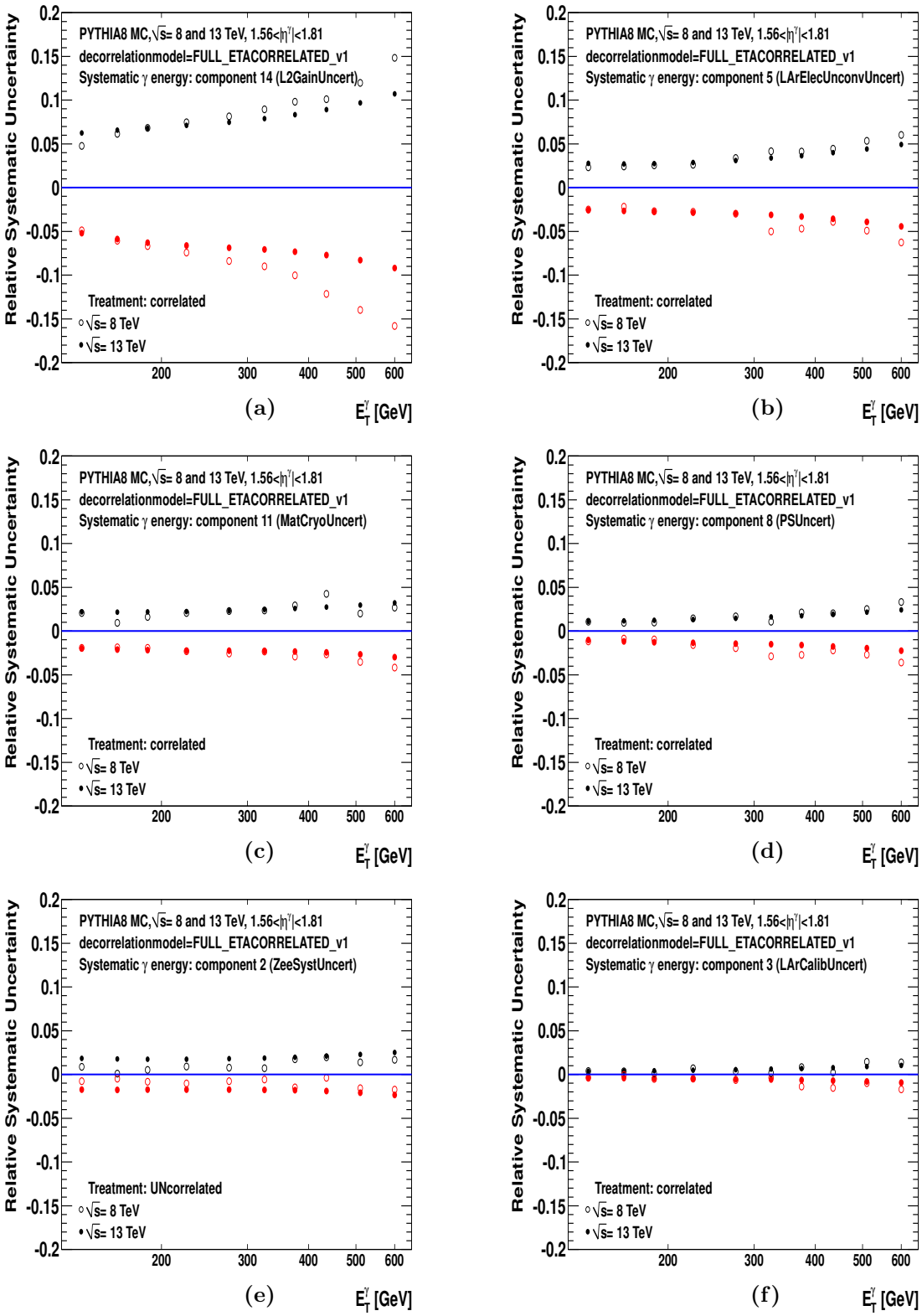


Figure 7.3: Relative systematic uncertainty in the measured cross sections as a function of E_{T}^{γ} for the region $1.56 < |\eta^{\gamma}| < 1.81$ due to the following γ-ES components: (a) "L2GainUncert", (b) "LArElecUnconvUncert", (c) "MatCryoUncert", (d) "PSUncert", (e) "ZeeSystUncert", (f) "LArCalibUncert". Results are presented for both $\sqrt{s} = 8$ (open circles) and 13 TeV (dots).

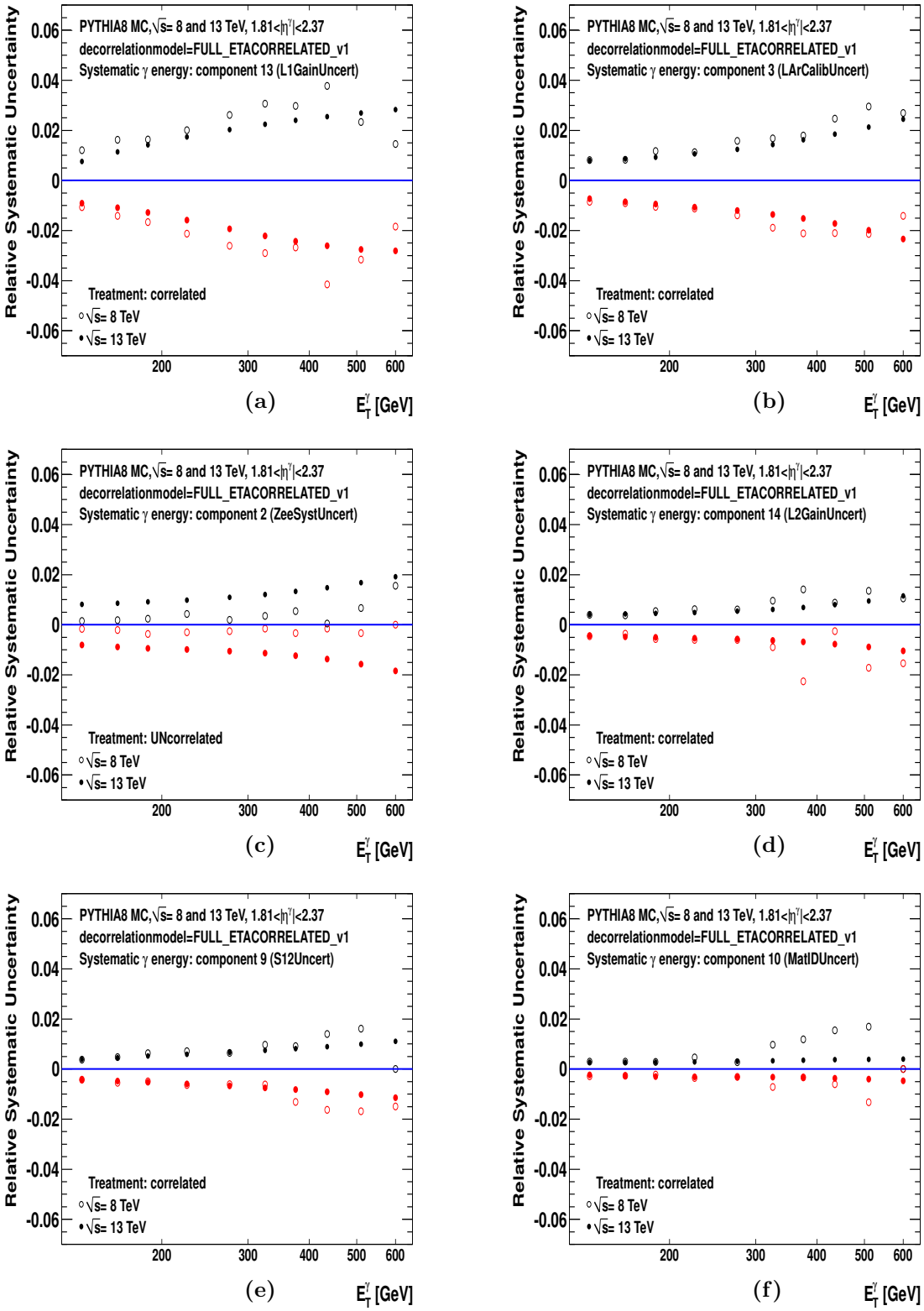


Figure 7.4: Relative systematic uncertainty in the measured cross sections as a function of E_{T}^{γ} for the region $1.81 < |\eta^{\gamma}| < 2.37$ due to the following γ-ES components: (a) "L1GainUncert", (b) "LArCalibUncert", (c) "ZeeSystUncert", (d) "L2GainUncert", (e) "S12Uncert", (f) "MatIDUncert". Results are presented for both $\sqrt{s} = 8$ (open circles) and 13 TeV (dots).

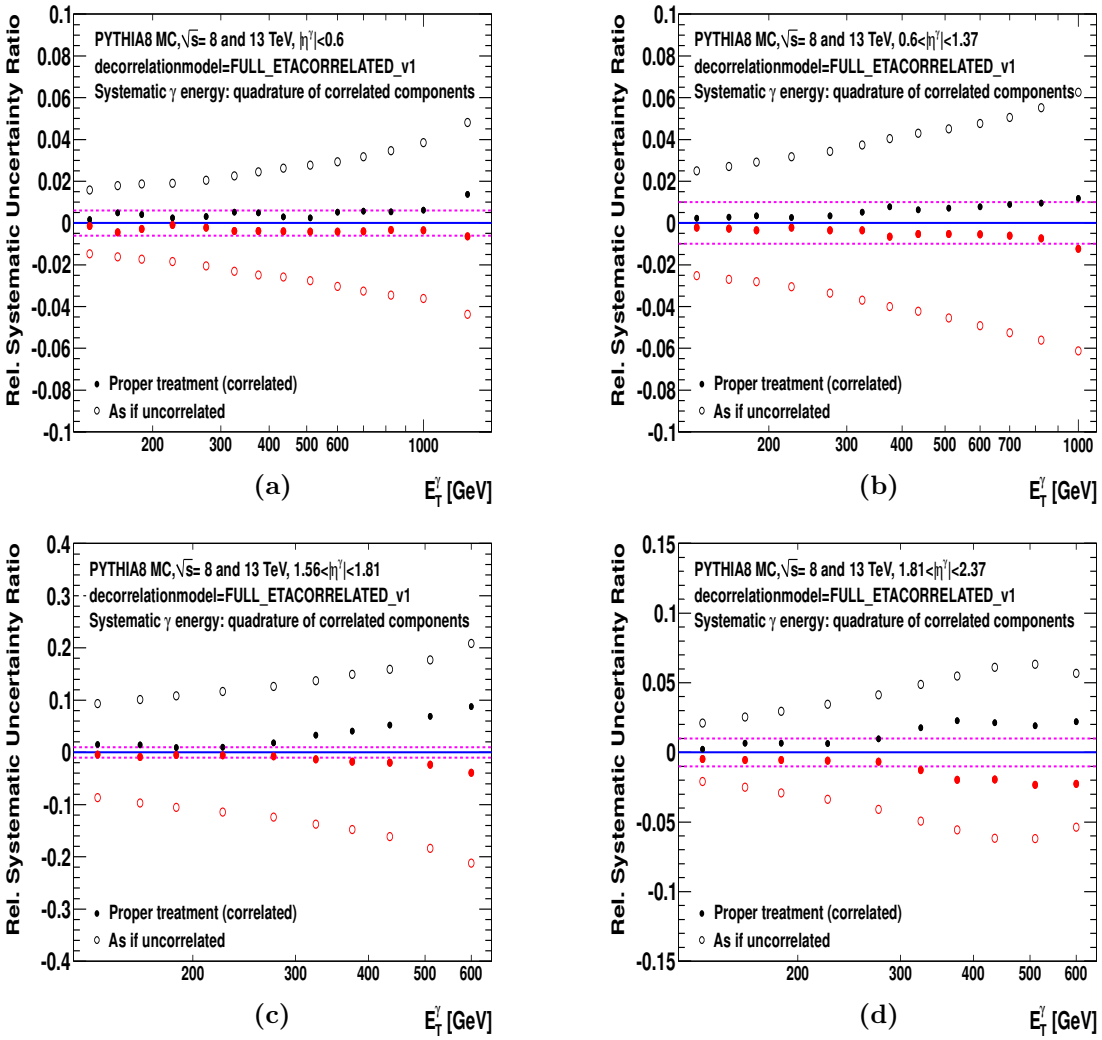


Figure 7.5: Relative systematic uncertainty in $R_{13/8}$ as a function of E_{T}^{γ} due to the γ-ES components that are correlated between both centre-of-mass energies. For comparison, the results of considering the components as uncorrelated are shown as open circles.

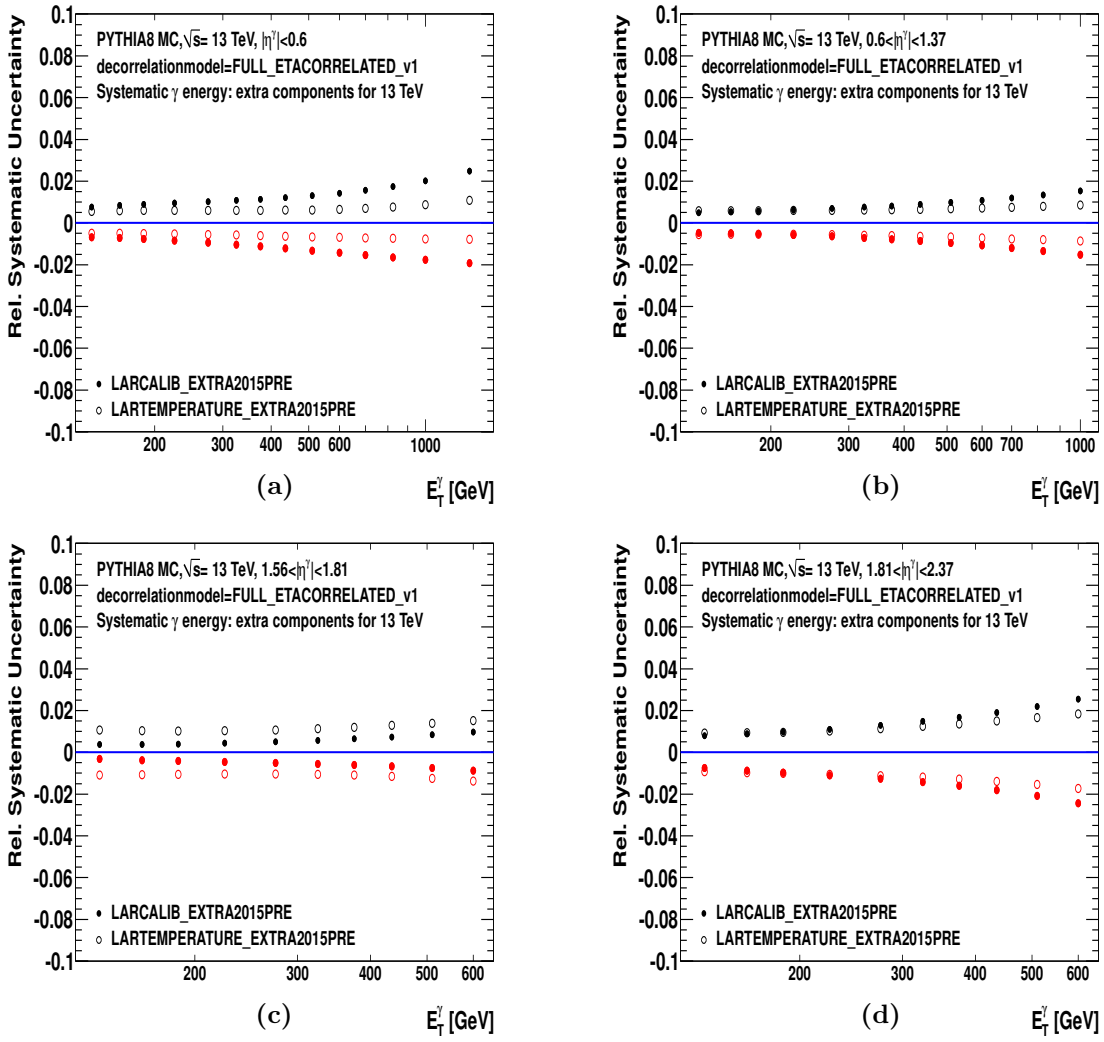


Figure 7.6: Relative systematic uncertainty in the measured cross sections as a function of E_{T}^{γ} for different regions in $|\eta^{\gamma}|$ due to the following γ-ES components: LARCALIB_EXTRA2015PRE (dots) and LARTEMPERATURE_EXTRA2015PRE (open circles). Results are presented only for 13 TeV.

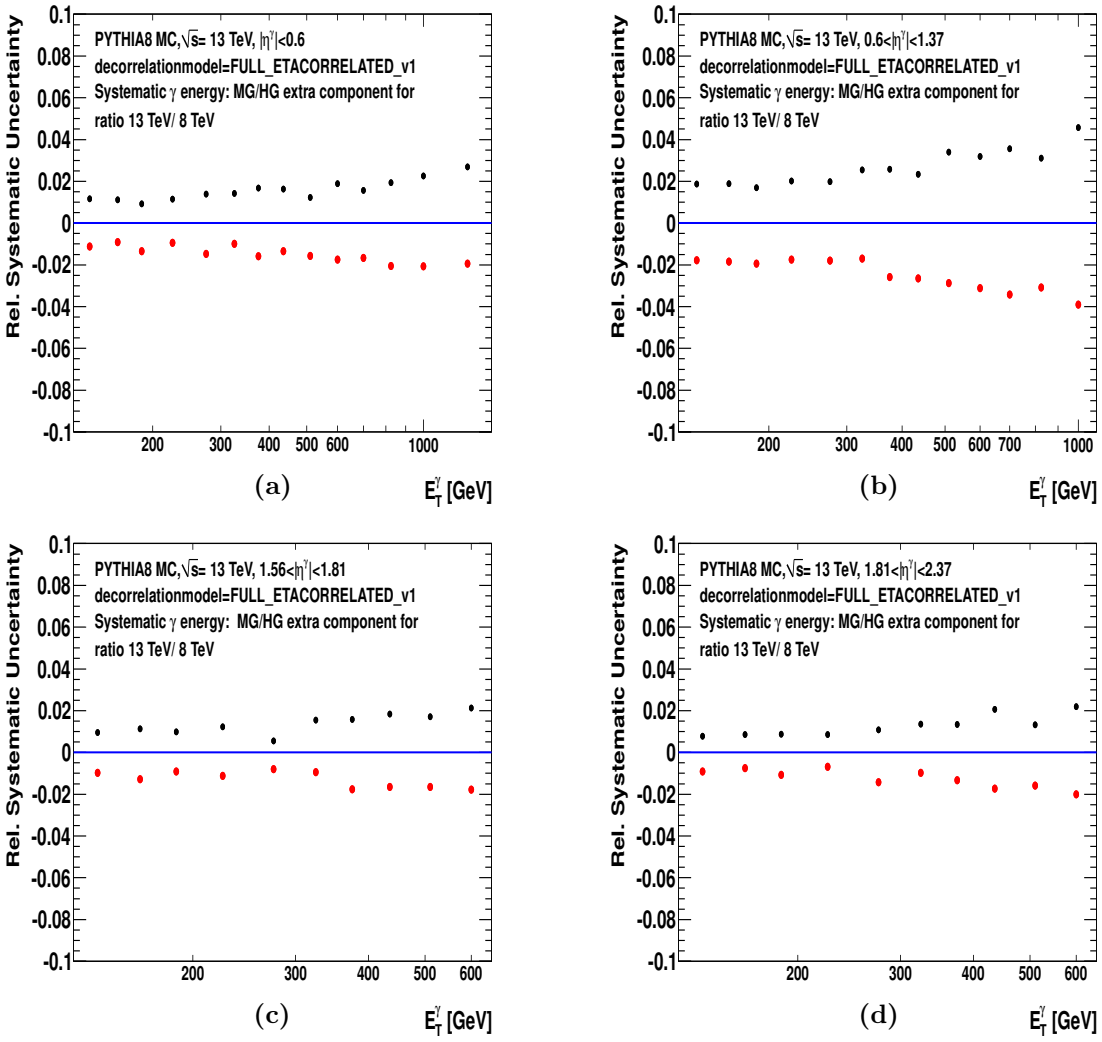


Figure 7.7: Relative systematic uncertainty in $R_{13/8}$ as a function of E_{T}^{γ} for different regions in $|\eta^{\gamma}|$ due to the MG/HG Run2/Run1 uncertainty in the photon energy scale.

7.2.2 Other uncertainties

The other sources of experimental uncertainty affecting the measurement of $R_{13/8}$ were treated as follows:

1. **Statistical uncertainty.** The statistical uncertainty in both data and MC simulations at $\sqrt{s} = 13$ and 8 TeV was treated as uncorrelated.

2. **Luminosity uncertainty.** The luminosity uncertainties were treated as uncorrelated for data at $\sqrt{s} = 13$ and 8 TeV due to different luminometers used, different methods used in the estimation of the dominant uncertainty and intrinsic non-correlation of uncertainties related to the beam conditions. The relative uncertainty in $R_{13/8}$ amounts to $\sqrt{(1.9\%)^2 + (2.1\%)^2} = 2.8\%$.

3. **Trigger uncertainty.** The uncertainties in the trigger efficiency were treated as uncorrelated for data at different centre-of-mass energies.

4. **Photon-identification uncertainty.** These uncertainties were treated as uncorrelated since different methods were used at $\sqrt{s} = 13$ and 8 TeV. At $\sqrt{s} = 13$ TeV, the shower-shape corrections were turned on and off, whereas the uncertainties on the data-driven determination of the tight efficiency were used at $\sqrt{s} = 8$ TeV. Furthermore, the photon identification criteria were re-optimised for data taking at 13 TeV.

5. **Modelling of the photon isolation in MC.** These uncertainties were treated as uncorrelated since different methods were used at $\sqrt{s} = 13$ and 8 TeV. In the former, data-driven corrections were turned off and compared to the nominal results with this correction. At 8 TeV, a dedicated fit in the selected data sample was made to set the shift that had to be applied to the simulations to describe the isolation peak observed in the data. The uncertainty was then computed with twice the fit accuracy on the shift.

6. **Choice of background control regions.** These uncertainties were treated as uncorrelated since, as mentioned above, the photon identification requirements were re-optimised for data-taking at 13 TeV.

7. **Photon identification and isolation correlation in the background.** These uncertainties were treated as uncorrelated since, as mentioned above, the photon identification requirements were re-optimised for data-taking at 13 TeV.

8. **Signal modelling.** These uncertainties were treated as uncorrelated since different methods were used at $\sqrt{s} = 13$ and 8 TeV. The bremsstrahlung contribution in Pythia was enhanced by a factor of two or suppressed completely for the former, while the results of using either Pythia default or Pythia optimised, as described in Section 8.2.1, were used at 8 TeV.

9. **QCD-cascade and hadronisation model dependence.** These uncertainties were treated as uncorrelated since different versions and tunes of the MC generators[2]

[2]The MC samples of events of Pythia were used as nominal to unfold the distributions for the analyses at 13 and 8 TeV, whereas the MC samples of events of Sherpa were used for the evaluation of some systematic uncertainties.

were used at $\sqrt{s} = 13$ and 8 TeV. PYTHIA 8.165 with the CTEQ6L1 PDF parameterisation and tune AU2 was used at $\sqrt{s} = 8$ TeV and PYTHIA 8.186 with the NNPDF2.3 PDFs and the A14 tune was used at $\sqrt{s} = 13$ TeV. Also different versions of SHERPA to estimate the uncertainty were used: SHERPA 1.4.0 at $\sqrt{s} = 8$ TeV and SHERPA 2.1.1 at $\sqrt{s} = 13$ TeV.

10. **Pile-up uncertainties.** These uncertainties were treated as uncorrelated due to the different running conditions in the 2012 and 2015 data-taking periods.

To illustrate the size of the uncertainties in the individual measurements at $\sqrt{s} = 13$ and 8 TeV, the contributions from various components are shown separately for both centre-of-mass energies. The sources of uncertainty in the measurements have been separated in different sets. The sets considered for the $\sqrt{s} = 8$ TeV measurement are listed below:

- **Set1 ("mix,loose′,gap,rbckg,mod,unf"):** admixture of hard and bremsstrahlung in PYTHIA ("mix"); variations of inverted shower-shape variables in the background subtraction ("loose′"); lower limit in $E_{\mathrm{T}}^{\mathrm{iso}}$ for the control regions B and D ("gap"); uncertainty in "rbckg"; use of SHERPA ("mod"); unfolding uncertainty ("unf");
- **Set2 ("pid"):** photon identification ("pid");
- **Set3:** the sum in quadrature of the contributions of "Set1" and "Set2" as well as that of the photon-energy resolution[3];
- **Set4:** the sum in quadrature of the contributions of "Set3" and that of the luminosity uncertainty (1.9%);
- **Set5:** the sum in quadrature of the contributions of "Set4" and that of the statistical uncertainty.

The resulting uncertainties of Set1 to Set4 are shown in Figure 7.8.

The list of uncertainties gathered in each set for the measurements at $\sqrt{s} = 13$ TeV are listed below:

- **Set1 ("mix,loose′,upp,gap,rbckg,leak,mod,isomc,pu,mcstat,trigg"):** admixture of hard and bremsstrahlung in PYTHIA ("mix"); variations of inverted shower-shape variables in the background subtraction ("loose′"); upper limit in $E_{\mathrm{T}}^{\mathrm{iso}}$ for the control regions B and D ("upp"); lower limit in $E_{\mathrm{T}}^{\mathrm{iso}}$ for the control regions B and D ("gap"); uncertainty in "rbckg"; leakage factors of SHERPA ("leak"); unfolding with SHERPA ("mod"); modelling of $E_{\mathrm{T}}^{\mathrm{iso}}$ in MC ("isomc"); pile-up ("pu"); statistics of the MC samples ("mcstat"); trigger uncertainty ("trigg");
- **Set2 ("pid"):** photon identification ("pid").
- **Set3:** the sum in quadrature of the contributions of "Set1" and "Set2" as well as that of the photon-energy resolution;
- **Set4:** the sum in quadrature of the contributions of "Set3" and that of the luminosity uncertainty (2.1%);

[3]Due to the non-availability of the decomposition in components of the photon-energy resolution (γER) for the measurements at 8 TeV, it is treated as uncorrelated with respect to the measurements at 13 TeV.

- **Set5:** the sum in quadrature of the contributions of "Set4" and that of the statistical uncertainty.

The resulting uncertainties of Set1 to Set4 considered at $\sqrt{s} = 13$ TeV are shown in Figure 7.9.

Not all the uncertainties were considered at both centre-of-mass energies. For the measurements at $\sqrt{s} = 8$ TeV, the following uncertainties were found to be negligible and were not considered in the overall uncertainty: trigger ("trigg"); modelling of $E_{\mathrm{T}}^{\mathrm{iso}}$ in MC ("isomc"); the upper limit in $E_{\mathrm{T}}^{\mathrm{iso}}$ for the control regions B and D was not applied and, as a consequence, this was not considered as a source of uncertainty ("upp"); pile-up ("pu"). For the measurements at $\sqrt{s} = 8$ TeV, an uncertainty associated to the unfolding procedure was included ("unf"), which is negligible for $E_{\mathrm{T}}^{\gamma} > 125$ GeV and was not considered for the measurements at $\sqrt{s} = 13$ TeV. The MC statistical uncertainties were added to the data statistical uncertainties for the measurements at $\sqrt{s} = 8$ TeV, whereas they were considered separately for the measurements at $\sqrt{s} = 13$ TeV.

A summary of the size of the uncorrelated uncertainties grouped in Set4 is given below comparing both $\sqrt{s}$:

- region $|\eta^{\gamma}| < 0.6$: At 8 TeV, the "Set4" uncertainty is $\approx 2\%$ from $E_{\mathrm{T}}^{\gamma} = 125$ GeV up to 550 GeV, and increases up to $\approx 3\%$ at $E_{\mathrm{T}}^{\gamma} = 1.3$ TeV. For the 13 TeV measurement, the "Set4" uncertainty is $\approx 3\%$ from $E_{\mathrm{T}}^{\gamma} = 125$ GeV up to 1.5 TeV;
- region $0.6 < |\eta^{\gamma}| < 1.37$: At 8 TeV, the "Set4" uncertainty is $\approx 2\%$ from $E_{\mathrm{T}}^{\gamma} = 125$ GeV up to 550 GeV, and is $\approx 3\%$ beyond. For the 13 TeV measurement, the "Set4" uncertainty is $\approx 3\%$ from $E_{\mathrm{T}}^{\gamma} = 200$ GeV up to 1.1 TeV and increases up to $\approx 4\%$ for $E_{\mathrm{T}}^{\gamma} = 125$ GeV;
- region $1.56 < |\eta^{\gamma}| < 1.81$: At 8 TeV, the "Set4" uncertainty is $\approx 2\%$ from $E_{\mathrm{T}}^{\gamma} = 125$ GeV up to 550 GeV and is $\approx 4\%$ for higher E_{T}^{γ} values. For the 13 TeV measurement, the "Set4" uncertainty is $\approx 4\%$ from $E_{\mathrm{T}}^{\gamma} = 125$ GeV up to 650 GeV;
- region $1.81 < |\eta^{\gamma}| < 2.37$: At 8 TeV, the "Set4" uncertainty is $\approx 2\%$ from $E_{\mathrm{T}}^{\gamma} = 125$ GeV up to 400 GeV and increases up to $\approx 6\%$ for higher E_{T}^{γ} values. For the 13 TeV measurement, the "Set4" uncertainty is $\approx^{+3.5}_{-4.5}$ % from $E_{\mathrm{T}}^{\gamma} = 125$ GeV up to 350 GeV, and increases up to $\approx^{+5}_{-5.5}$ % for $E_{\mathrm{T}}^{\gamma} = 650$ GeV.

The increase in the uncorrelated experimental uncertainties after adding the statistical uncertainty (Set5) is presented in Figure 7.10 (Figure 7.11) for 8 TeV (13 TeV).

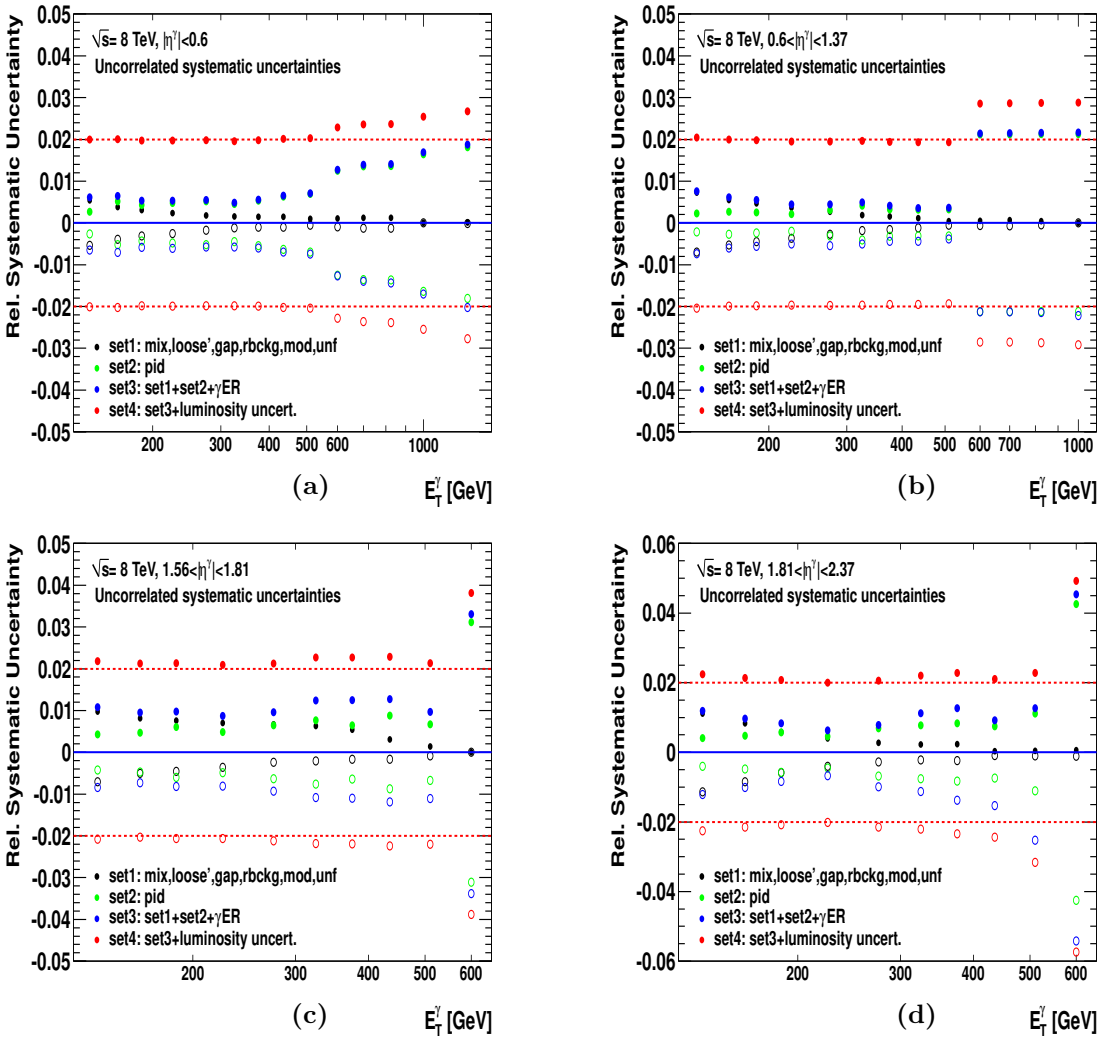


Figure 7.8: Relative systematic uncertainty in the measured cross sections at 8 TeV as a function of E_{T}^{γ} for the different regions in $|\eta^{\gamma}|$ due to different sources: Set1 (black), Set2 (green), Set3 (blue) and Set4 (red); see text for details. The dashed red line shows the typical values of Set4.

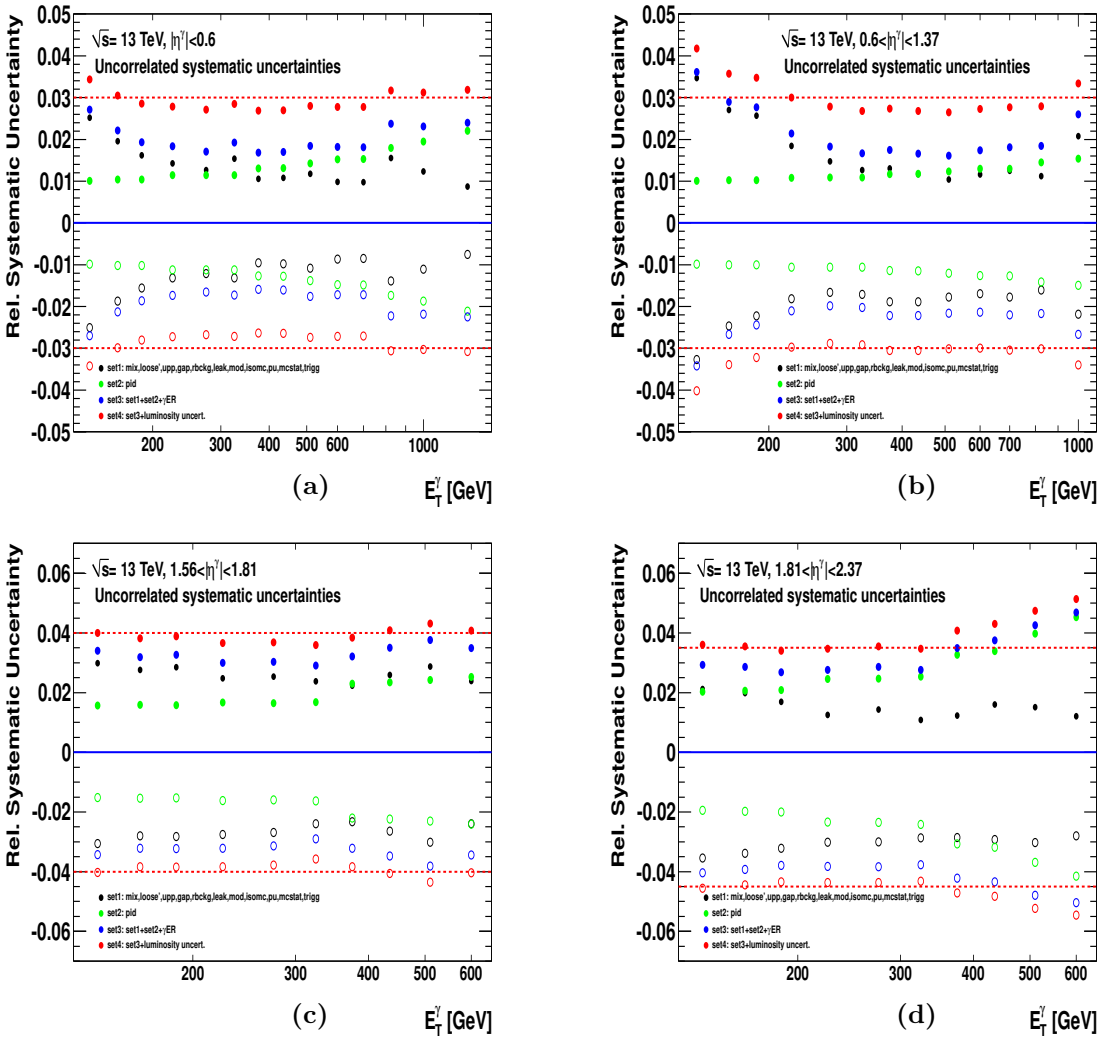


Figure 7.9: Relative systematic uncertainty in the measured cross sections at 13 TeV as a function of E_{T}^{γ} for the different regions in $|\eta^{\gamma}|$ due to different sources: Set1 (black), Set2 (green), Set3 (blue) and Set4 (red); see text for details. The dashed red line shows the typical values of Set4.

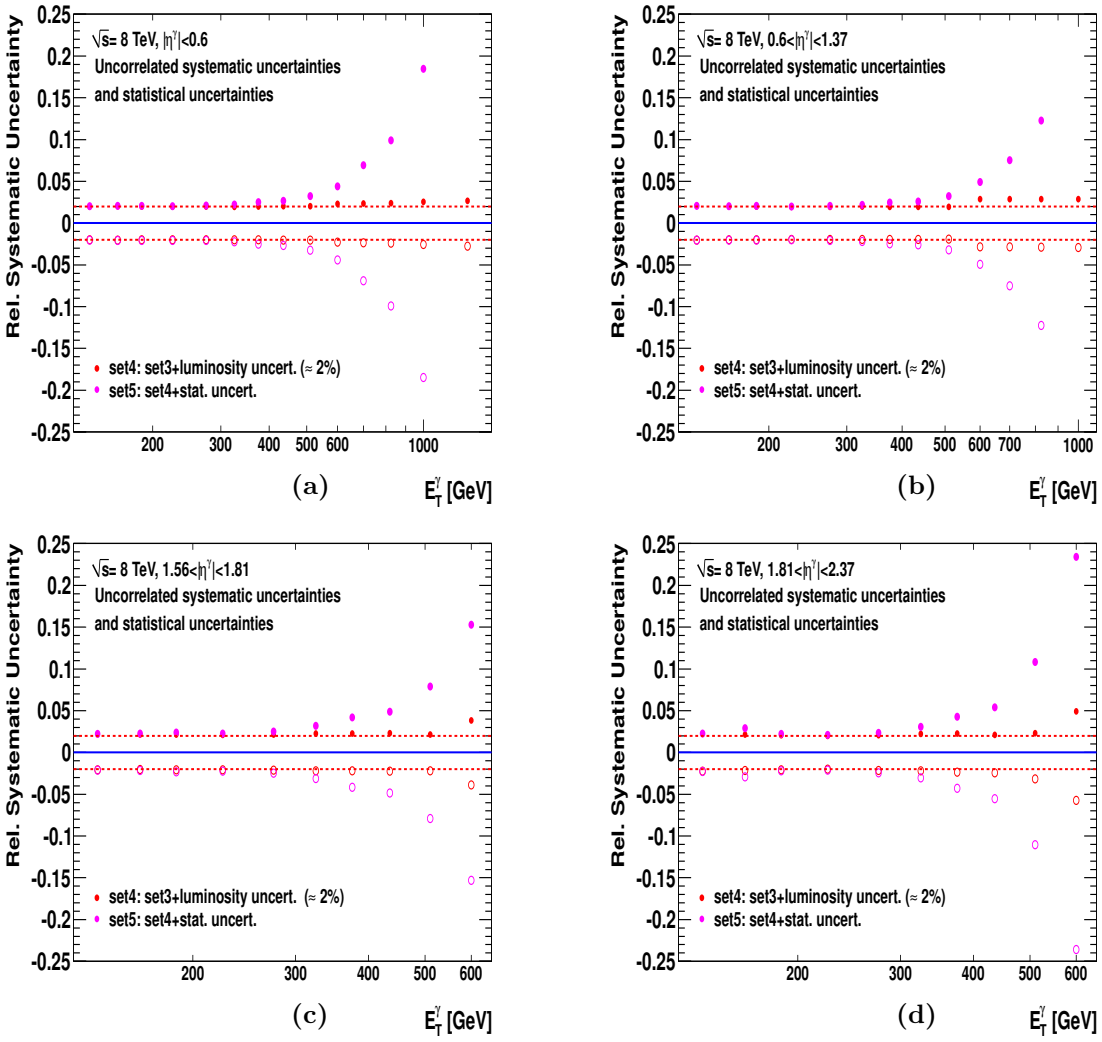


Figure 7.10: Relative systematic uncertainty in the measured cross sections at 8 TeV as a function of E_{T}^{γ} due to different sources: Set4 (red) and Set5 (pink); see text for details.

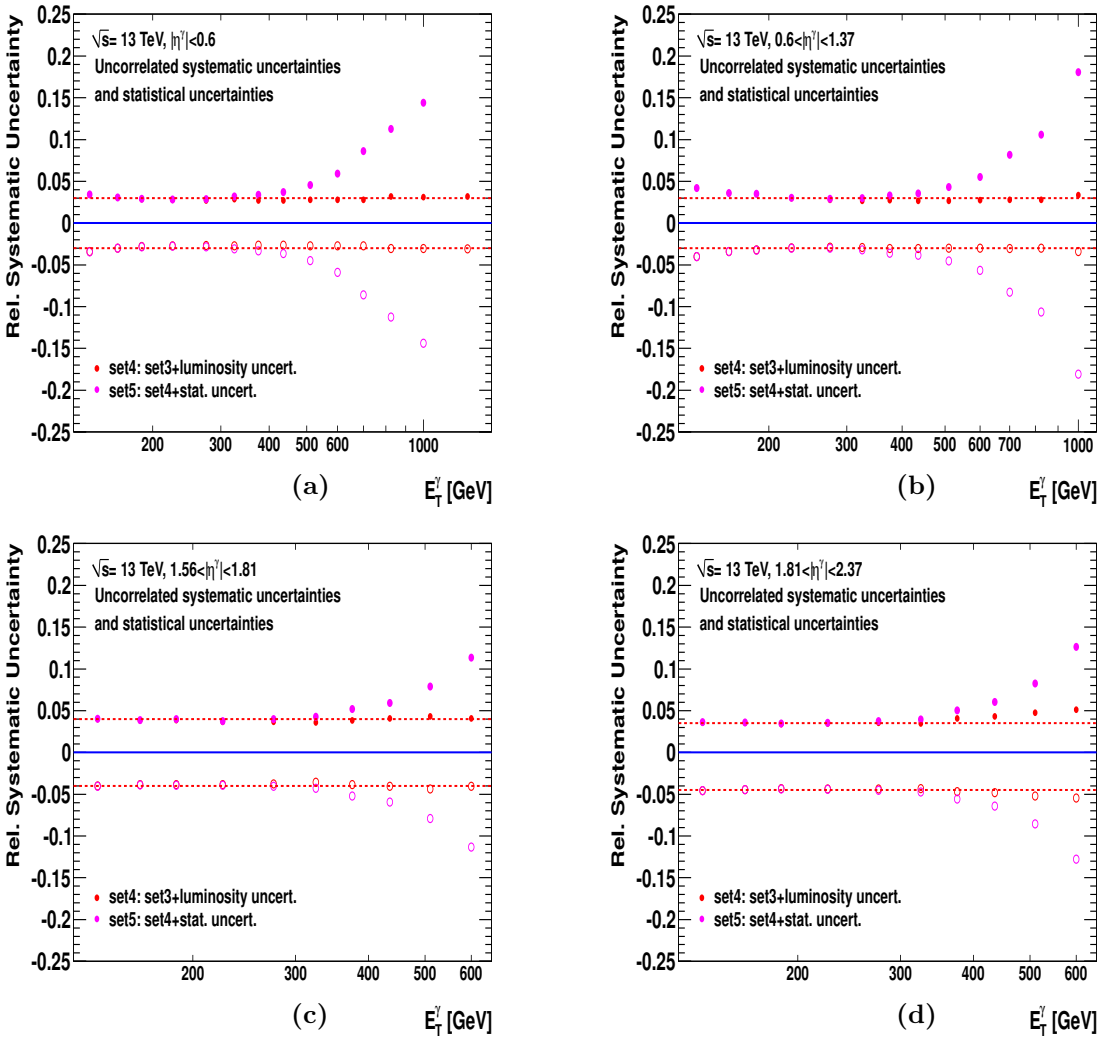


Figure 7.11: Relative systematic uncertainty in the measured cross sections at 13 TeV as a function of E_{T}^{γ} due to different sources: Set4 (red) and Set5 (pink); see text for details.

7.2.3 Total experimental uncertainty in $R_{13/8}$

The relative uncertainties in $R_{13/8}$ due to the photon energy scale, including the correlated and uncorrelated sources as well as the extra contribution associated to 2015 data and the contribution MG/HG Run2/Run1, are shown in Figure 7.12. This uncertainty is compared to the size of the uncertainty in $R_{13/8}$ due to the uncorrelated uncertainties from Set3 and Set4. It is concluded that the relative uncertainty in $R_{13/8}$ due to the photon energy scale is no longer the dominant uncertainty, except for the range $E_{\mathrm{T}}^{\gamma} > 300$ GeV in the regions $0.6 < |\eta^{\gamma}| < 1.37$ and $1.56 < |\eta^{\gamma}| < 1.81$. For comparison, the relative uncertainties in $R_{13/8}$ due to Set3, Set4 and the sum in quadrature of Set4 and the photon energy scale uncertainty (denoted by "Set6") are also shown in Figure 7.13.

The total relative experimental uncertainty in $R_{13/8}$ as a function of E_{T}^{γ} is shown separately for each region of $|\eta^{\gamma}|$ in Figure 7.14. The total experimental uncertainty is referred to as "Set7" in the figures and is the sum in quadrature of the total systematic and statistical uncertainties. For comparison, the total experimental systematic uncertainty (i.e. excluding the statistical uncertainties) is referred to as "Set6" and is also shown in Figure 7.14. The following values are obtained for the total systematic uncertainty in each η^{γ} region:

- region $|\eta^{\gamma}| < 0.6$: the total systematic uncertainty is $\approx 4\%$ in the range $125 \leq E_{\mathrm{T}}^{\gamma} \leq 750$ GeV; it rises up to $\approx 6\%$ at the end of the spectrum. The total experimental uncertainty is $\approx 4\%$ from $E_{\mathrm{T}}^{\gamma} = 125$ GeV up to $E_{\mathrm{T}}^{\gamma} = 400$ GeV; it rises up to 71% for $E_{\mathrm{T}}^{\gamma} \sim 1.3$ TeV;
- region $0.6 < |\eta^{\gamma}| < 1.37$: the total systematic uncertainty is $\approx 4.5\%$ in the range $150 \leq E_{\mathrm{T}}^{\gamma} \leq 470$ GeV; it rises up to $\approx 7\%$ at the end of the spectrum and up to $\approx 5\%$ for $E_{\mathrm{T}}^{\gamma} = 125$ GeV; The total experimental uncertainty is $\approx 4.5\%$ from $E_{\mathrm{T}}^{\gamma} = 150$ GeV up to $E_{\mathrm{T}}^{\gamma} = 350$ GeV; it rises up to 31% (5%) for $E_{\mathrm{T}}^{\gamma} \sim 1$ TeV (125 GeV);
- region $1.56 < |\eta^{\gamma}| < 1.81$: the total systematic uncertainty is $\approx 5\%$ in the range $125 \leq E_{\mathrm{T}}^{\gamma} \leq 300$ GeV; it rises up to $\approx 11\%$ at the end of the spectrum. The total experimental uncertainty is $\approx 5\%$ from $E_{\mathrm{T}}^{\gamma} = 125$ GeV up to $E_{\mathrm{T}}^{\gamma} = 300$ GeV; it rises up to 21% for $E_{\mathrm{T}}^{\gamma} \sim 600$ GeV;
- region $1.81 < |\eta^{\gamma}| < 2.37$: the total systematic uncertainty is $\approx 5\%$ in the range $125 \leq E_{\mathrm{T}}^{\gamma} \leq 300$ GeV; it rises up to $\approx 9\%$ at the end of the spectrum. The total experimental uncertainty is $\approx 5\%$ from $E_{\mathrm{T}}^{\gamma} = 125$ GeV up to $E_{\mathrm{T}}^{\gamma} = 300$ GeV; it rises up to 27% for $E_{\mathrm{T}}^{\gamma} \sim 600$ GeV.

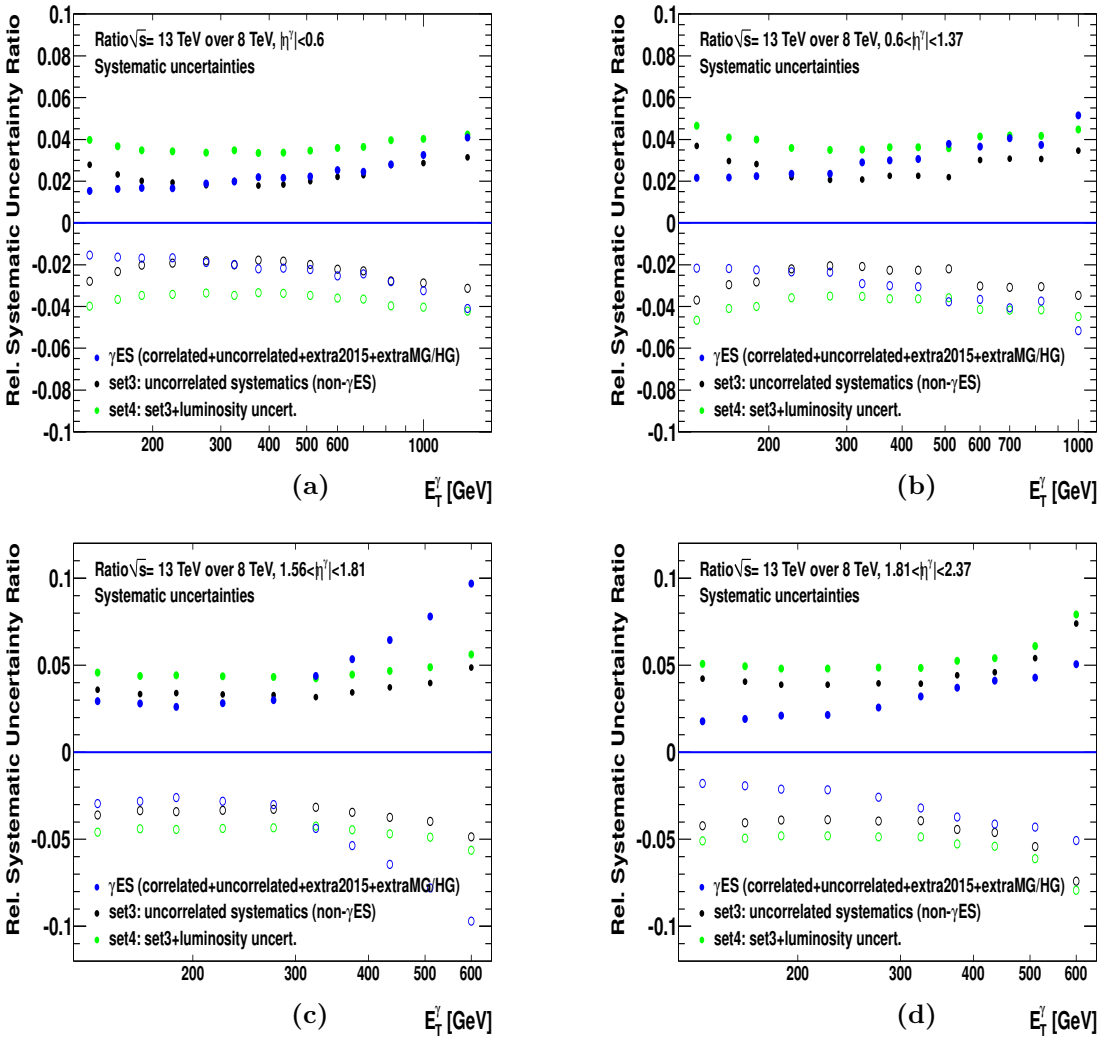


Figure 7.12: Relative systematic uncertainty in $R_{13/8}$ as a function of E_{T}^{γ} for the different $|\eta^{\gamma}|$ regions due to different sources: γES (correlated and uncorrelated terms as well as the additional terms for 2015 data and the MG/HG Run1/Run2 uncertainty; blue), Set3 (black) and Set4 (green); see text for details.

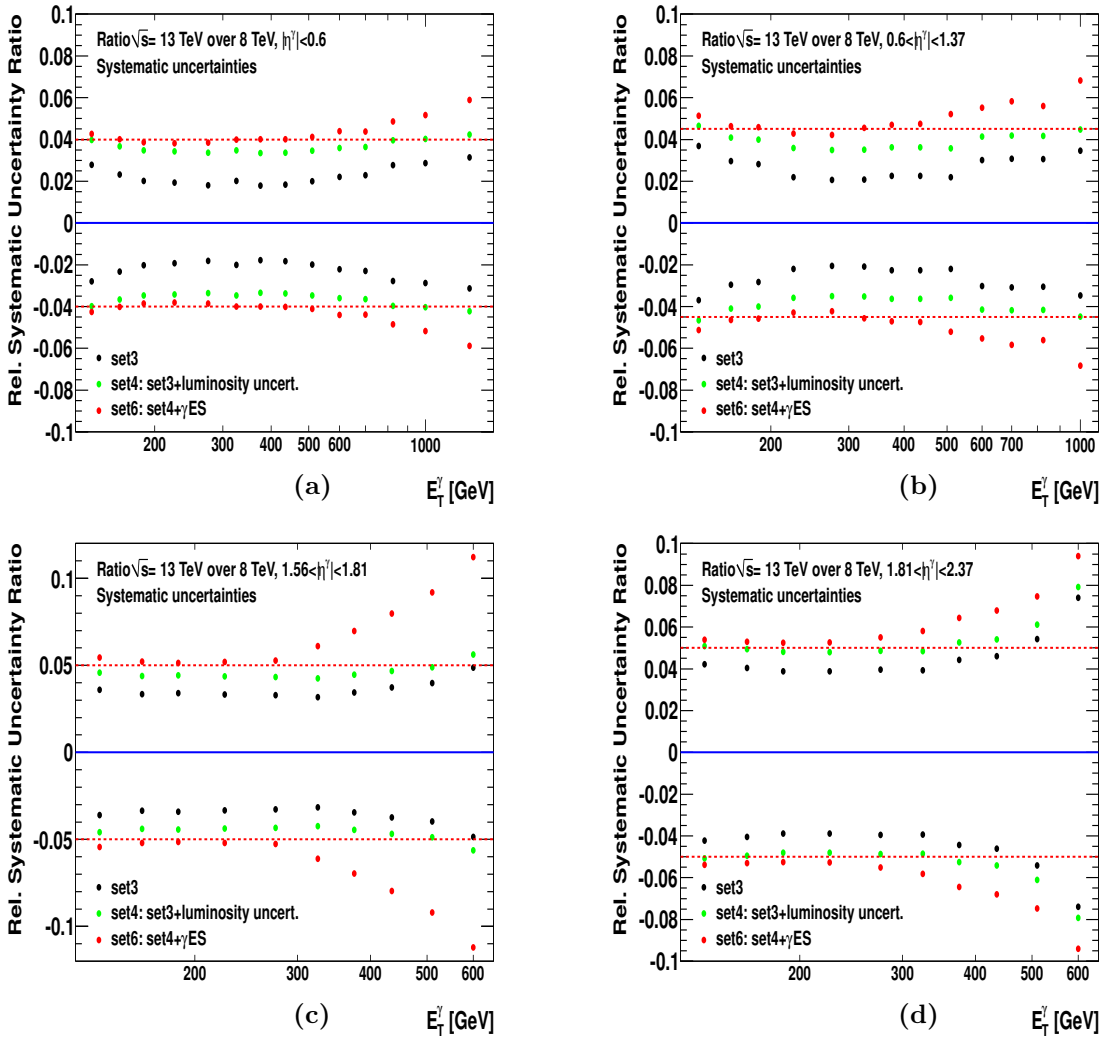


Figure 7.13: Relative systematic uncertainty in $R_{13/8}$ as a function of E_{T}^{γ} for the different regions in $|\eta^{\gamma}|$ due to different sources: Set3 (black), Set4 (green) and Set6 (red); see text for details.

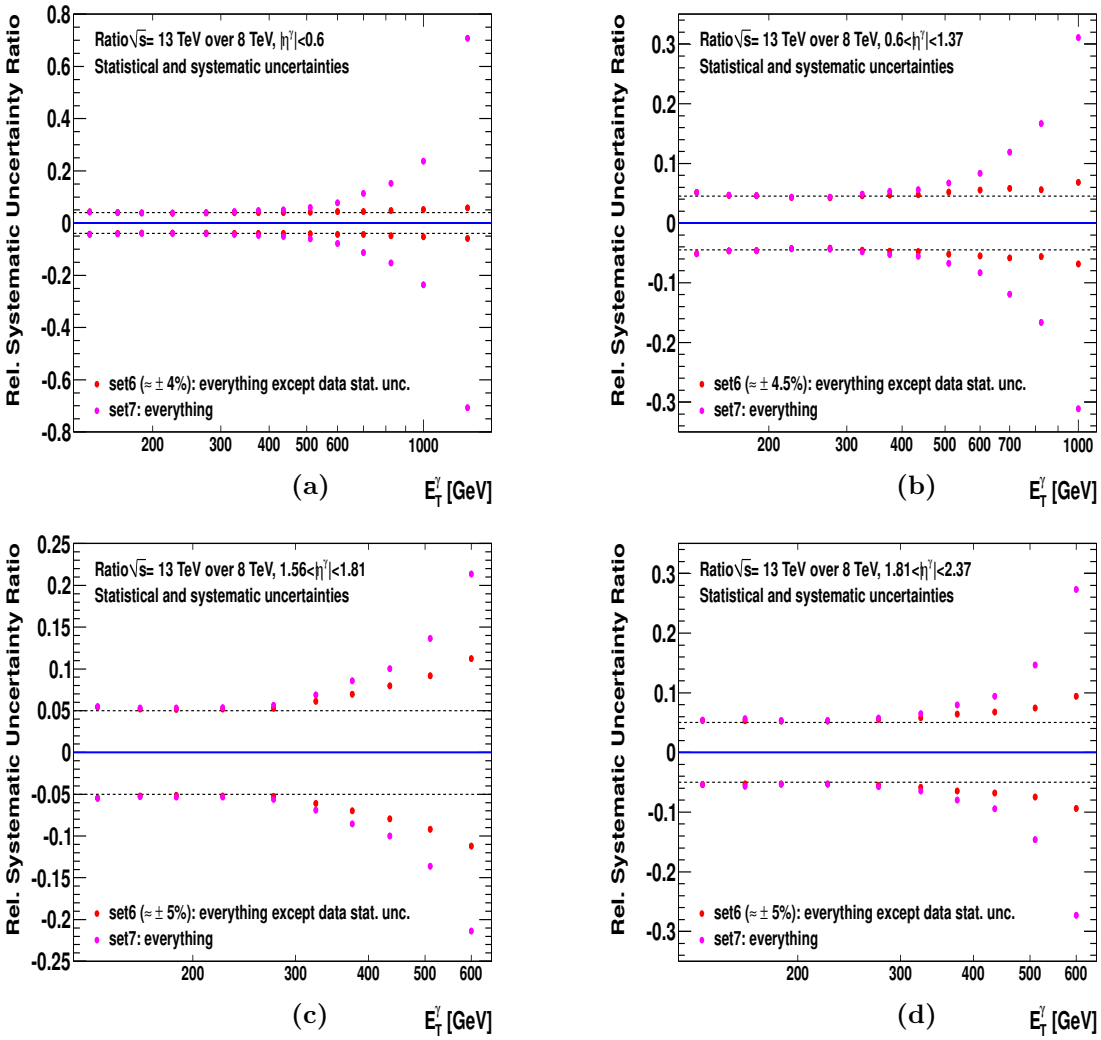


Figure 7.14: Relative systematic uncertainty in $R_{13/8}$ as a function of E_{T}^{γ} for the different regions in $|\eta^{\gamma}|$ due to different sources: Set6 (red) and Set7 (pink); see text for details.

7.2.4 Total experimental uncertainty in $D_{13/8}^{\gamma/Z}$

The measured result of $\sigma_Z^{\text{fid}}(13TeV)/\sigma_Z^{\text{fid}}(8TeV)$ quoted in [122] is:

$$\sigma_Z^{\text{fid}}(13TeV)/\sigma_Z^{\text{fid}}(8TeV) = 1.537 \pm 0.001 \text{ (stat.)} \pm 0.010 \text{ (syst.)} \pm 0.044 \text{ (lumi.)}.$$

The decomposition of the uncertainties for each centre-of-mass energy is collected in Table 7.2. Excluding the luminosity and beam energy uncertainties, the dominant experimental uncertainties are that on the muon and electron reconstruction and identification, which were treated as uncorrelated since different lepton reconstruction and algorithms were employed at 8 and 13 TeV. The impact on $D_{13/8}^{\gamma/Z}$ of the correlation between the photon and the electron energy scales is neglected since the electron energy scale is a subdominant uncertainty for $\sigma_Z^{\text{fid}}(13TeV)/\sigma_Z^{\text{fid}}(8TeV)$.

Source	$\sqrt{s} = 13$ TeV (%)	$\sqrt{s} = 8$ TeV (%)
Luminosity	2.10	1.90
Beam energy	0.69	0.62
Muon trigger	0.12	0.55
Muon reco and id.	0.68	0.45
Muon isolation	0.41	0.04
Muon momentum scale	0.06	0.03
Electron trigger	0.01	0.19
Electron reco and ID	0.41	0.80
Electron isolation	0.14	0.00
Electron energy scale	0.25	0.07
Background	0.08	0.15
Signal modelling	0.12	0.08

Table 7.2: Systematic uncertainties for the measurement of Z boson production cross section at different $\sqrt{s}$ values [123].

The total relative experimental uncertainty in $D_{13/8}^{\gamma/Z}$ was obtained as follows:

- using the uncertainty in $R_{13/8}$ as presented in Section 7.2.3 except for the contribution from the luminosity. The uncertainty in the luminosity was not included since it cancels out in $D_{13/8}^{\gamma/Z}$;
- adding in quadrature to the estimate above the statistical (0.1%) and systematic (0.7%) uncertainties in $\sigma_Z^{\text{fid}}(13 \text{ TeV})/\sigma_Z^{\text{fid}}(8 \text{ TeV})$ [122].

The relative total experimental uncertainty in the measured $D_{13/8}^{\gamma/Z}$ as a function of E_{T}^{γ} is shown separately for each region in $|\eta^{\gamma}|$ in Figure 7.15.

For comparison, the relative total experimental uncertainty, excluding that arising from the luminosity, in $R_{13/8}$ is also shown in Figure 7.15. Since the systematic uncertainty of 0.7% in $\sigma_Z^{\text{fid}}(13 \text{ TeV})/\sigma_Z^{\text{fid}}(8 \text{ TeV})$ is at least a factor of three smaller than the systematic uncertainty in $R_{13/8}$, the effect of adding in quadrature such a contribution has a small impact. On the other hand, the cancellation of the luminosity uncertainty in $D_{13/8}^{\gamma/Z}$ has a significant impact, leading to a more precise measurement to be confronted with the predictions.

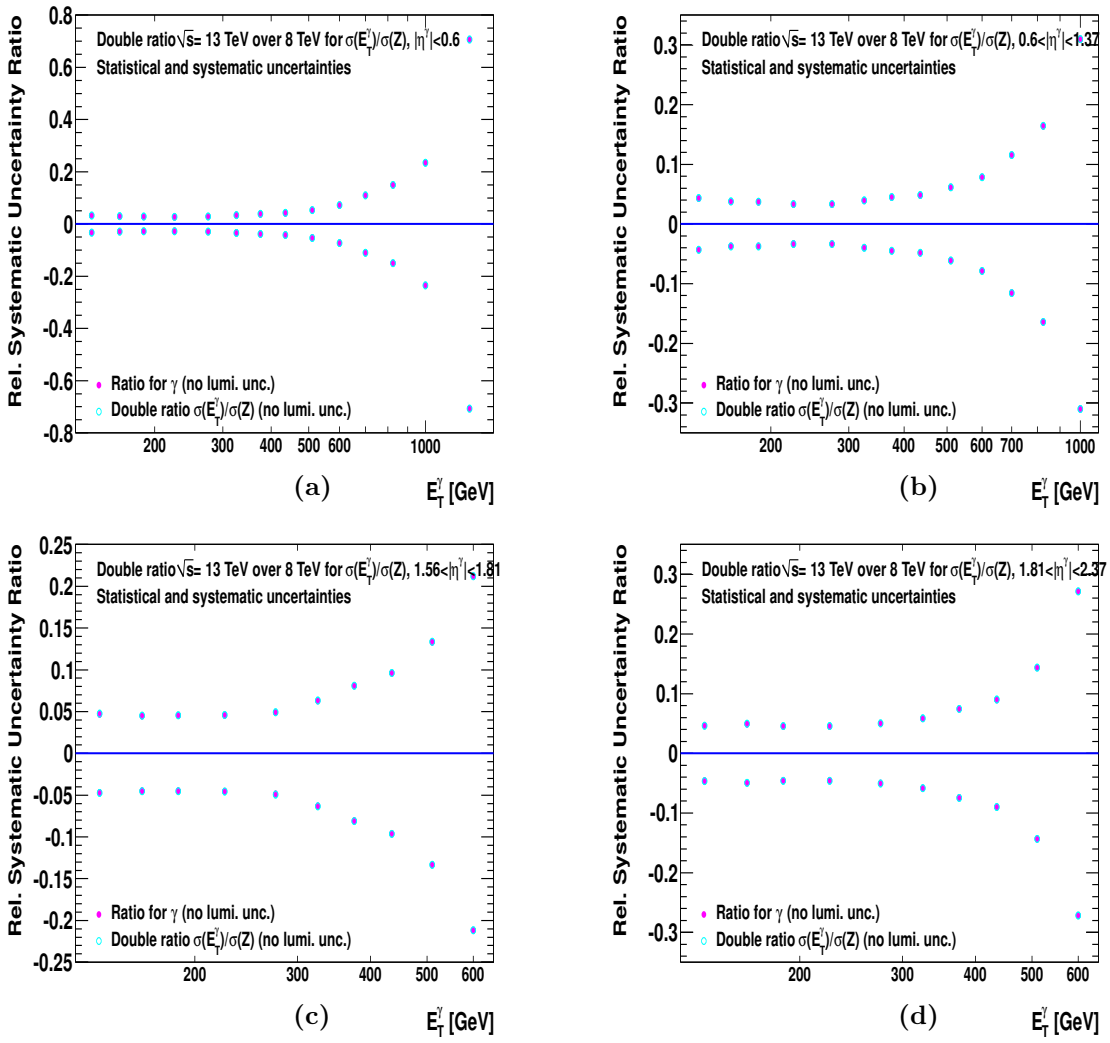


Figure 7.15: Relative experimental uncertainty in $R_{13/8}$ (pink dots) and in $D^{\gamma/Z}_{13/8}$ (light blue open points) as a function of E^{γ}_{T} for the different regions in $|\eta^{\gamma}|$.

7.3 Next-to-leading-order QCD predictions

The NLO QCD predictions for $R_{13/8}$ were computed using the program JetPhox 1.3.1_2. The details on the set-up of the program are found in Section 3.5.7. The baseline calculations were based on the MMHT2014 PDFs. Predictions are also obtained with other PDFs such as CT14, HERAPDF2.0, NNPDF3.0 and ABMP16 [124].

The estimation of the theoretical uncertainties considered follows the same methodology as in the inclusive-photon analysis and described in Section 6.7 for the uncertainty due to terms beyond NLO in pQCD, the PDF- and the α_{s}-induced uncertainties. In addition, an uncertainty in the beam energy was considered. It was computed by repeating the calculations with $\sqrt{s}$ varied by its uncertainty of 0.1%.

For the differential cross-section predictions at both centre-of-mass energies, the dominant theoretical uncertainty is that arising from the terms beyond NLO. The envelopes

of the relative uncertainties in the predictions at $\sqrt{s} = 13$ and 8 TeV due to the variations of the scales are shown in Figure 7.16. The uncertainties in the predictions at $\sqrt{s} = 13$ and 8 TeV due to that in the PDFs ($\alpha_s(m_Z)$) are shown in Figure 7.17 (Figure 7.18). The uncertainty on the beam energy is lower than 1% in the whole measured range.

For $R_{13/8}$, all the sources of uncertainties are considered as correlated between the two centre-of-mass energies. The resulting uncertainties are shown in Figure 7.19. Large cancellations in the uncertainties of the predictions for $R_{13/8}$ due to the scale variations are achieved, they decreased from a $\mathcal{O}(10\%)$ for the individual predictions down to $< 2\%$ for $R_{13/8}$ across most of the range in E_T^γ. The relative uncertainty in $R_{13/8}$ due to the uncertainties in $\alpha_s(m_Z)$ also exhibits a significant cancellation with respect to the individual predictions. The cancellations in the PDF uncertainty are more modest than the ones in the scale and α_s since different momentum fractions are probed at the same E_T^γ for different centre-of-mass energies. The uncertainty on the beam energy is negligible. The total uncertainty is also displayed in Figure 7.19 and the following values for the total relative uncertainties are obtained:

- region $|\eta^\gamma| < 0.6$: the total relative uncertainty is below 2% in the range $125 \leq E_T^\gamma \leq 750$ GeV; it rises up to $\approx 3.5\%$ at the end of the spectrum. It is dominated by the variation of the scales except for the downward variation for $E_T^\gamma \gtrsim 500$ GeV, where it is dominated by the uncertainties in the PDFs;
- region $0.6 < |\eta^\gamma| < 1.37$: the total relative uncertainty is below 2% in the range $125 \leq E_T^\gamma \leq 650$ GeV; it rises up to $\approx 3\%$ at the end of the spectrum. It is dominated by the variation of the scales except for the downward variation for $E_T^\gamma \gtrsim 900$ GeV, where the contribution from the uncertainties in the PDFs is equally important;
- region $1.56 < |\eta^\gamma| < 1.81$: the total relative uncertainty is below 2% in the range $125 \leq E_T^\gamma \leq 350$ GeV; it rises up to $\approx 3\%$ at the end of the spectrum. It is dominated by the variation of the scales;
- region $1.81 < |\eta^\gamma| < 2.37$: the total relative uncertainty is below 3% in the range $125 \leq E_T^\gamma \leq 470$ GeV; it rises up to $\approx 3.5\%$ at the end of the spectrum. It is dominated by the variation of the scales.

There is some ambiguity in the correlation of the scale uncertainties, since at very different centre-of-mass energies the contribution of the different production processes may change significantly. Large differences in the final theoretical uncertainties are found whether full or null correlation is assumed and can be inferred from the differences between Figure 7.19 (full correlation) and Figure 7.20 (null correlation). For example, in the most central region, the uncertainty on $R_{13/8}$ due to the scale variations is 1–3% for full correlation and 14% for null correlation between both $\sqrt{s}$. A different approach, free from the ambiguity on the correlations, is to consider the difference between NLO and LO predictions for $R_{13/8}$, which is expected to be larger than the difference between the missing higher-orders in the calculation and the NLO for inclusive photon production at high-E_T^γ. The LO and NLO relative difference for $R_{13/8}$ is shown in Figure 7.21 and the differences are much closer to the assumption of full correlation.

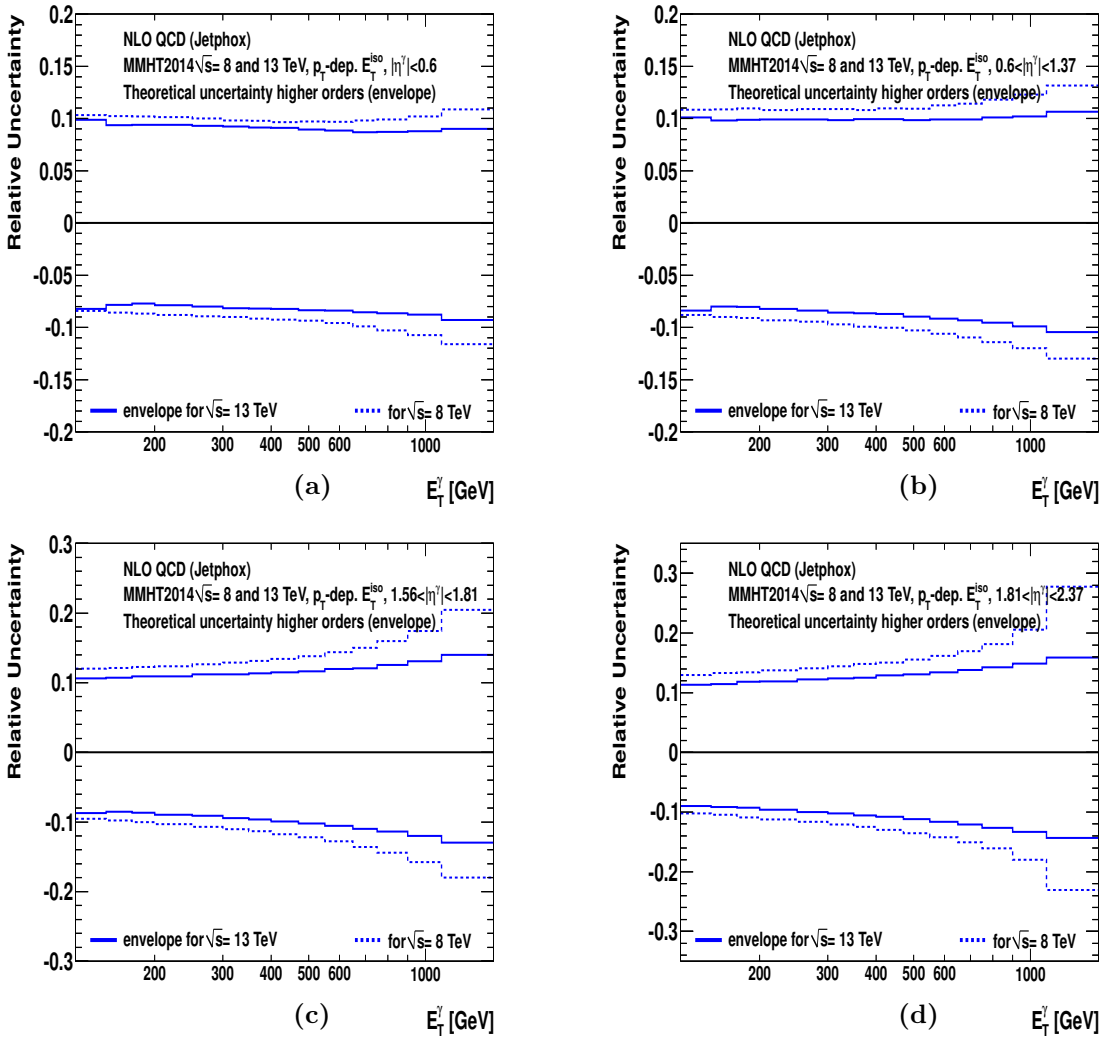


Figure 7.16: Theoretical uncertainty in the differential cross sections arising from terms beyond NLO (envelope of all variations) as a function of E_{T}^{γ} in different regions of $|\eta^{\gamma}|$. Results are presented for both $\sqrt{s} = 8$ (dashed lines) and 13 TeV (solid lines).

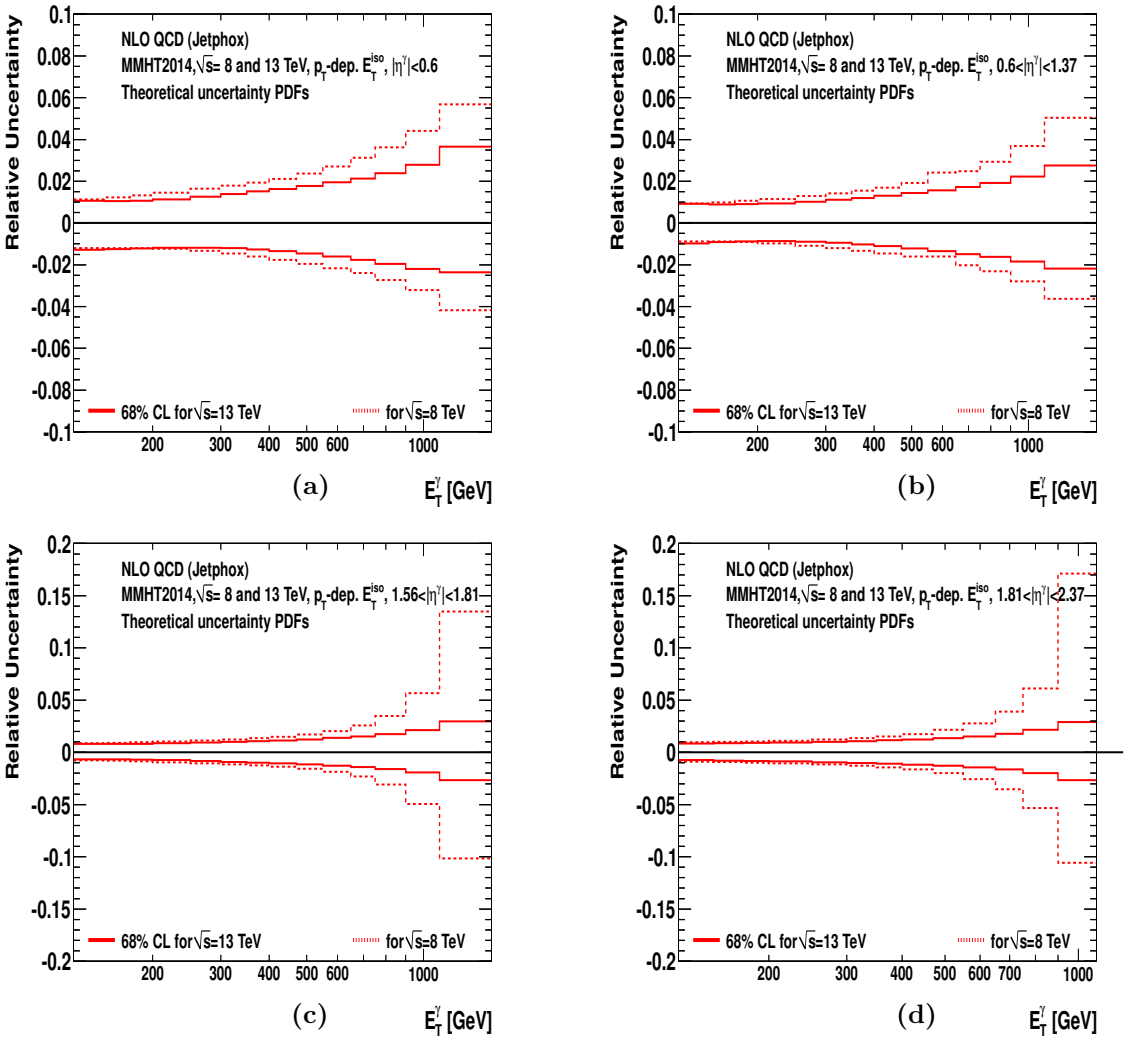


Figure 7.17: Theoretical uncertainty in the differential cross sections arising from the uncertainty in the PDFs as a function of E_{T}^{γ} in different regions of $|\eta^{\gamma}|$. Results are presented for both $\sqrt{s} = 8$ (dashed lines) and 13 TeV (solid lines).

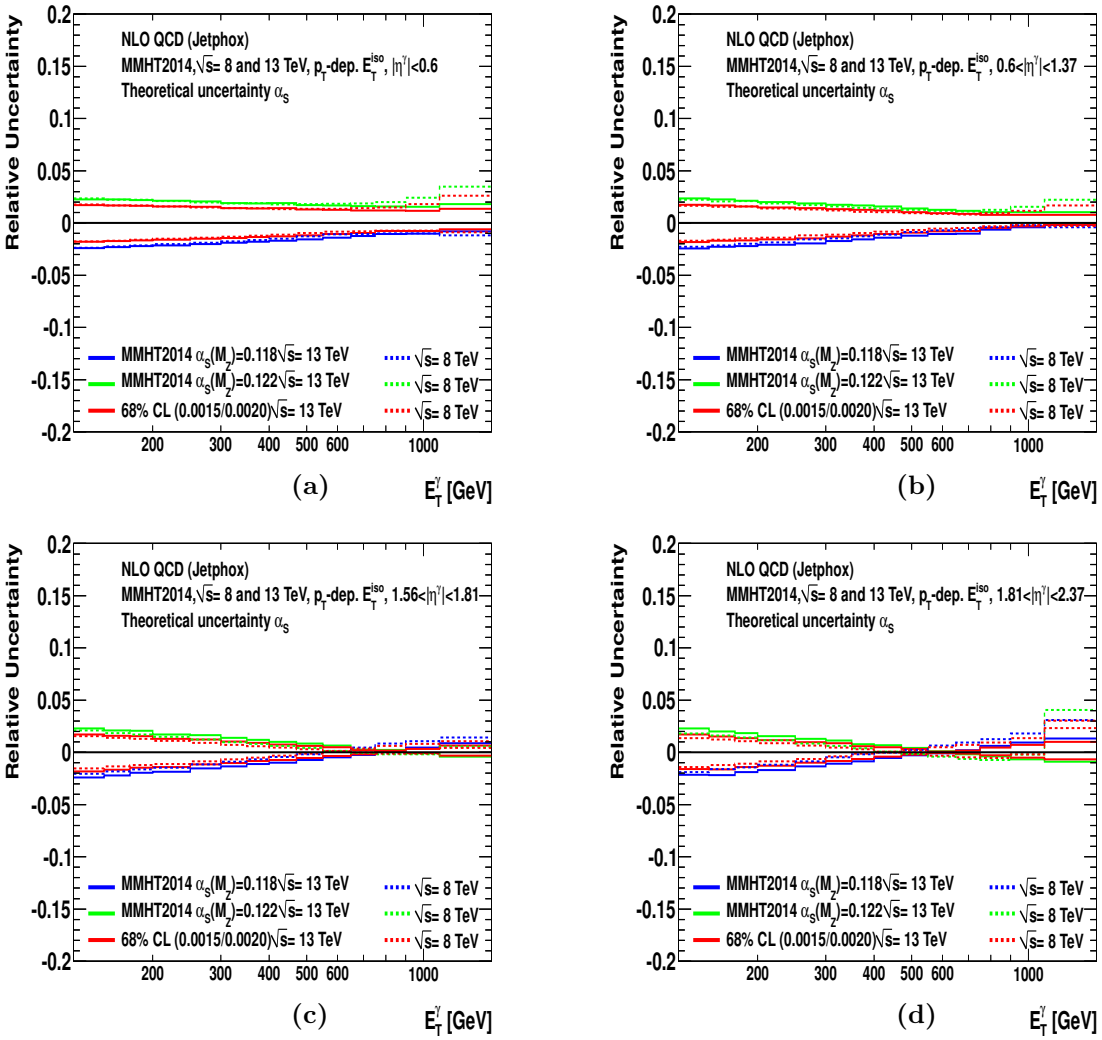


Figure 7.18: Theoretical uncertainty in the differential cross sections arising from the uncertainty in $\alpha_S(m_Z)$ as a function of E_T^γ in different regions of $|\eta^\gamma|$. Results are presented for both $\sqrt{s} = 8$ (dashed lines) and 13 TeV (solid lines).

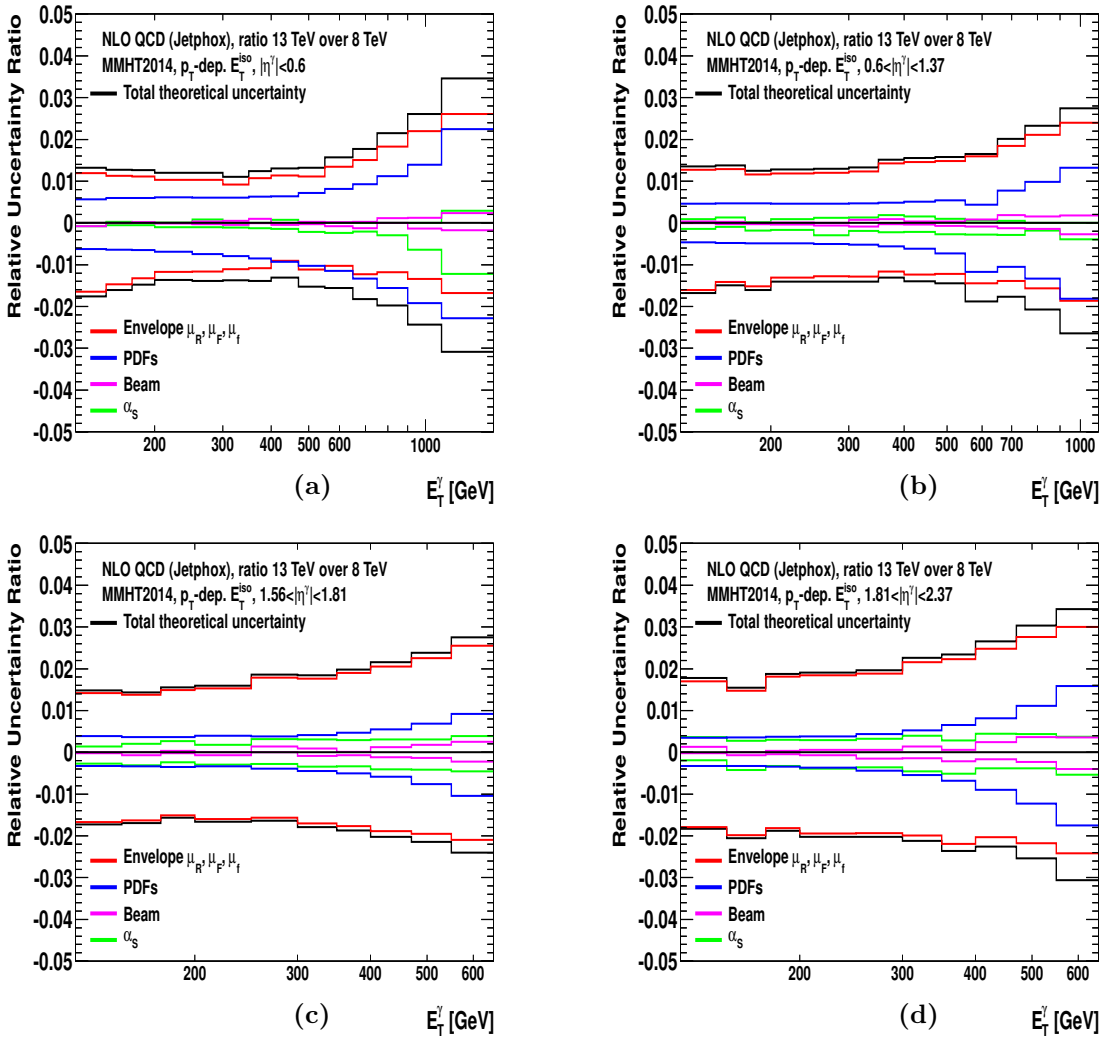


Figure 7.19: Total theoretical uncertainty (black histogram) in $R_{13/8}$ as a function of E_{T}^{γ} in the different regions of $|\eta^{\gamma}|$. The contributions from the envelope of the variation of the scales (red histogram; treated as correlated), the PDFs (blue histogram), the beam energy (violet histogram) and $\alpha_{\mathrm{S}}(m_Z)$ (green histogram) are also shown.

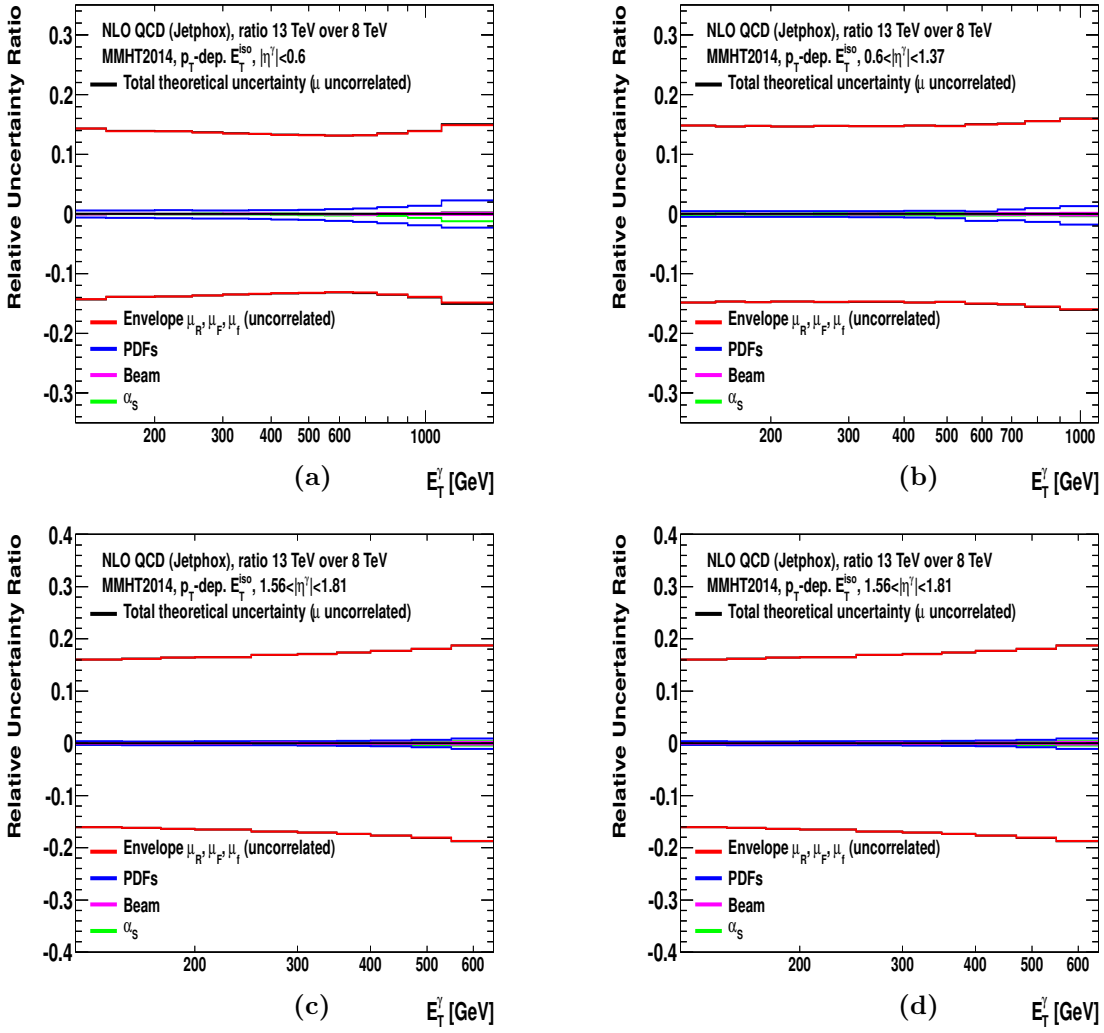


Figure 7.20: Total theoretical uncertainty (black histogram) in $R_{13/8}$ as a function of E_{T}^{γ} in the different regions of $|\eta^{\gamma}|$. The contributions from the envelope of the variation of the scales (red histogram; treated as uncorrelated), the PDFs (blue histogram), the beam energy (violet histogram) and $\alpha_{\mathrm{S}}(m_Z)$ (green histogram) are also shown.

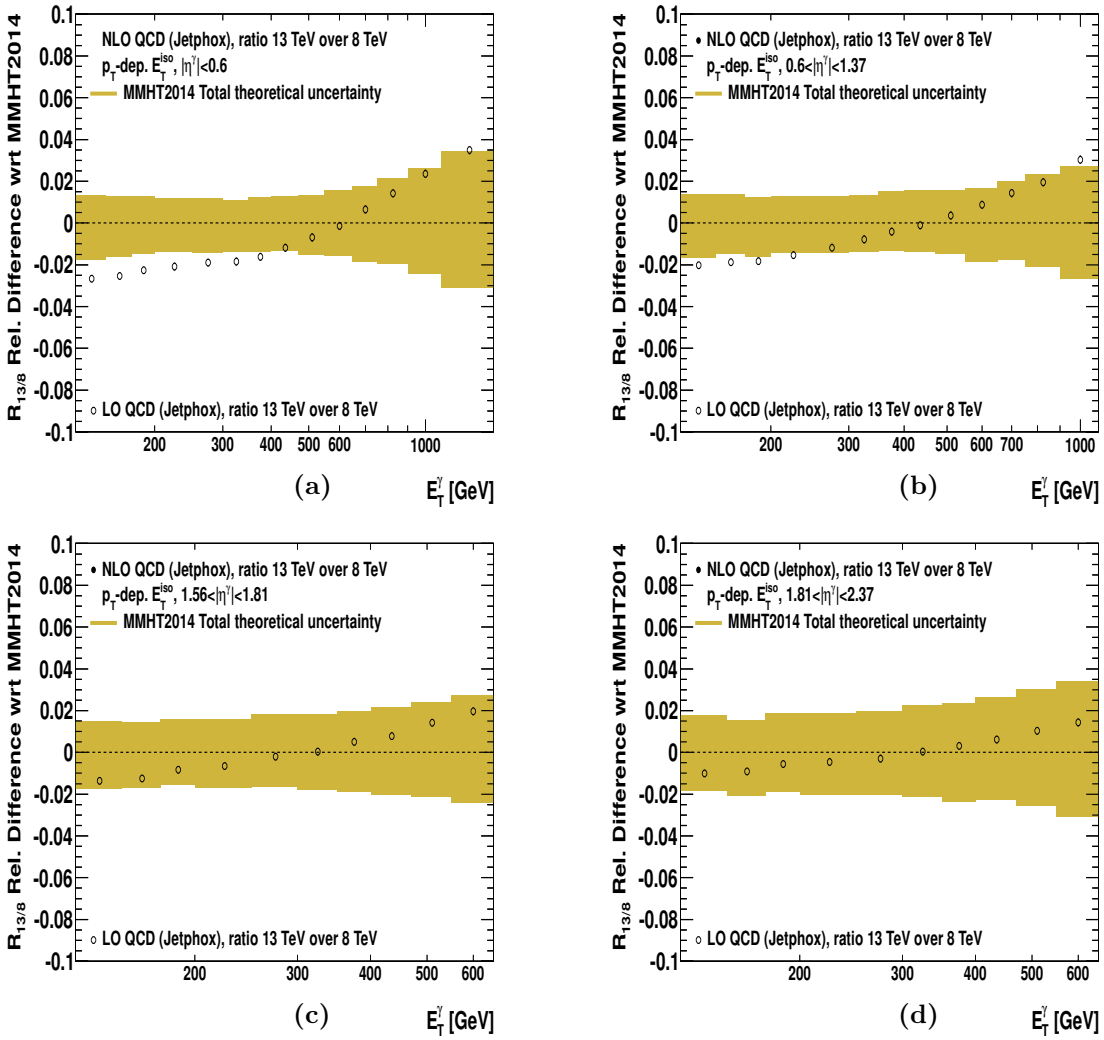


Figure 7.21: Relative difference between the predictions for $R_{13/8}$ at NLO and LO (open circles). The shaded bands represent the NLO relative theoretical uncertainty based on the MMHT2014 PDF parameterisations.

7.3.1 Comparisons of predictions for $R_{13/8}$ based on different PDFs

The NLO pQCD predictions of JetPhox based on the MMHT2014 parameterisations of the proton PDFs are shown in Figure 7.22: the predictions for $R_{13/8}$ as well as the theoretical uncertainties are shown as functions of E_{T}^{γ} for each region in $|\eta^{\gamma}|$. The predicted $R_{13/8}$ is approximately a factor of two at $E_{\mathrm{T}}^{\gamma} = 125$ GeV and increases as E_{T}^{γ} increases reaching a factor of 10 at the end of the spectrum; the increase is larger for the forward η^{γ} regions than for the central η^{γ} regions. The predictions based on other parameterisations of the proton PDFs are compared to those based on MMHT2014 in Figures 7.23 and 7.24.

To illustrate the differences between the predictions based on different sets of PDFs, the double ratio with respect to the predictions based on MMHT2014 is shown as a function of E_{T}^{γ} separately for each region in $|\eta^{\gamma}|$ in Figure 7.25:

- region $|\eta^{\gamma}| < 0.6$: the predictions based on MMHT2014, NNPDF3.0, CT14 and HERAPDF2.0 are similar, while those based on ABMP16 deviate significantly for E_{T}^{γ} above 650 GeV. The predicted $R_{13/8}$ using ABMP16 increases more rapidly than the others, showing differences up to +8% at $E_{\mathrm{T}}^{\gamma} \sim 1.3$ TeV;
- region $0.6 < |\eta^{\gamma}| < 1.37$: the predictions based on MMHT2014, NNPDF3.0, CT14, HERAPDF2.0 and ABMP16 are similar up to $E_{\mathrm{T}}^{\gamma} \sim 750$ GeV; for E_{T}^{γ} above 750 GeV the predictions based on HERAPDF2.0 and ABMP16 increase more rapidly than the others, showing differences up to +8% at $E_{\mathrm{T}}^{\gamma} \sim 1$ TeV;
- region $1.56 < |\eta^{\gamma}| < 1.81$: the predictions based on MMHT2014, NNPDF3.0, CT14, HERAPDF2.0 and ABMP16 are similar up to $E_{\mathrm{T}}^{\gamma} \sim 470$ GeV; for E_{T}^{γ} above 470 GeV those based on HERAPDF2.0 have larger values for $R_{13/8}$, which increases as E_{T}^{γ} increases up to +8% at $E_{\mathrm{T}}^{\gamma} \sim 600$ GeV;
- region $1.81 < |\eta^{\gamma}| < 2.37$: the predictions based on MMHT2014, NNPDF3.0, CT14, HERAPDF2.0 and ABMP16 are similar up to $E_{\mathrm{T}}^{\gamma} \sim 350$ GeV; for E_{T}^{γ} above 350 GeV, those based on HERAPDF2.0 have larger values for $R_{13/8}$, which increases as E_{T}^{γ} increases up to a maximum of +22% at $E_{\mathrm{T}}^{\gamma} \sim 600$ GeV;

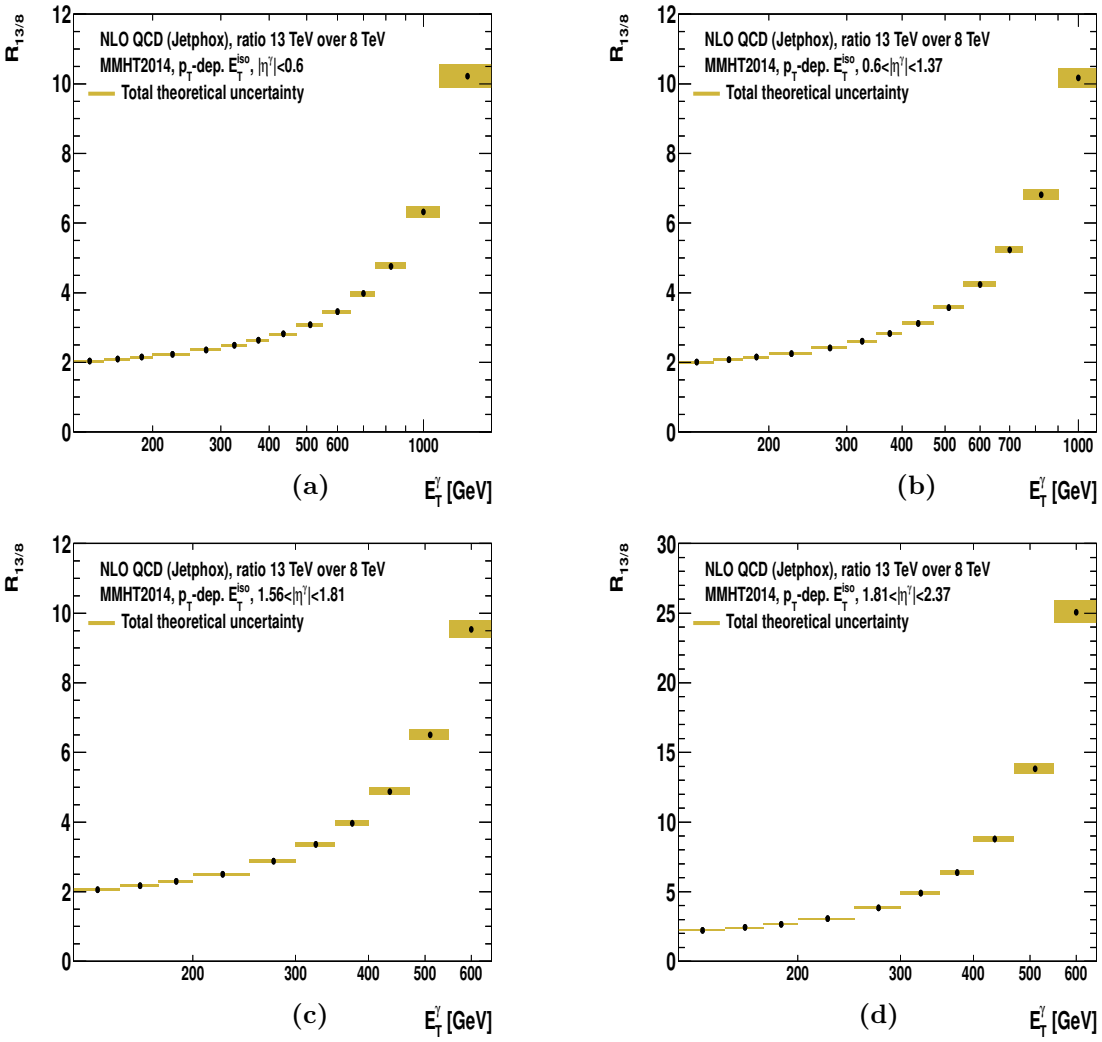


Figure 7.22: Theoretical prediction (black dots) for $R_{13/8}$ as a function of E_{T}^{γ} in different regions of $|\eta^{\gamma}|$. The shaded band shows the total theoretical uncertainty.

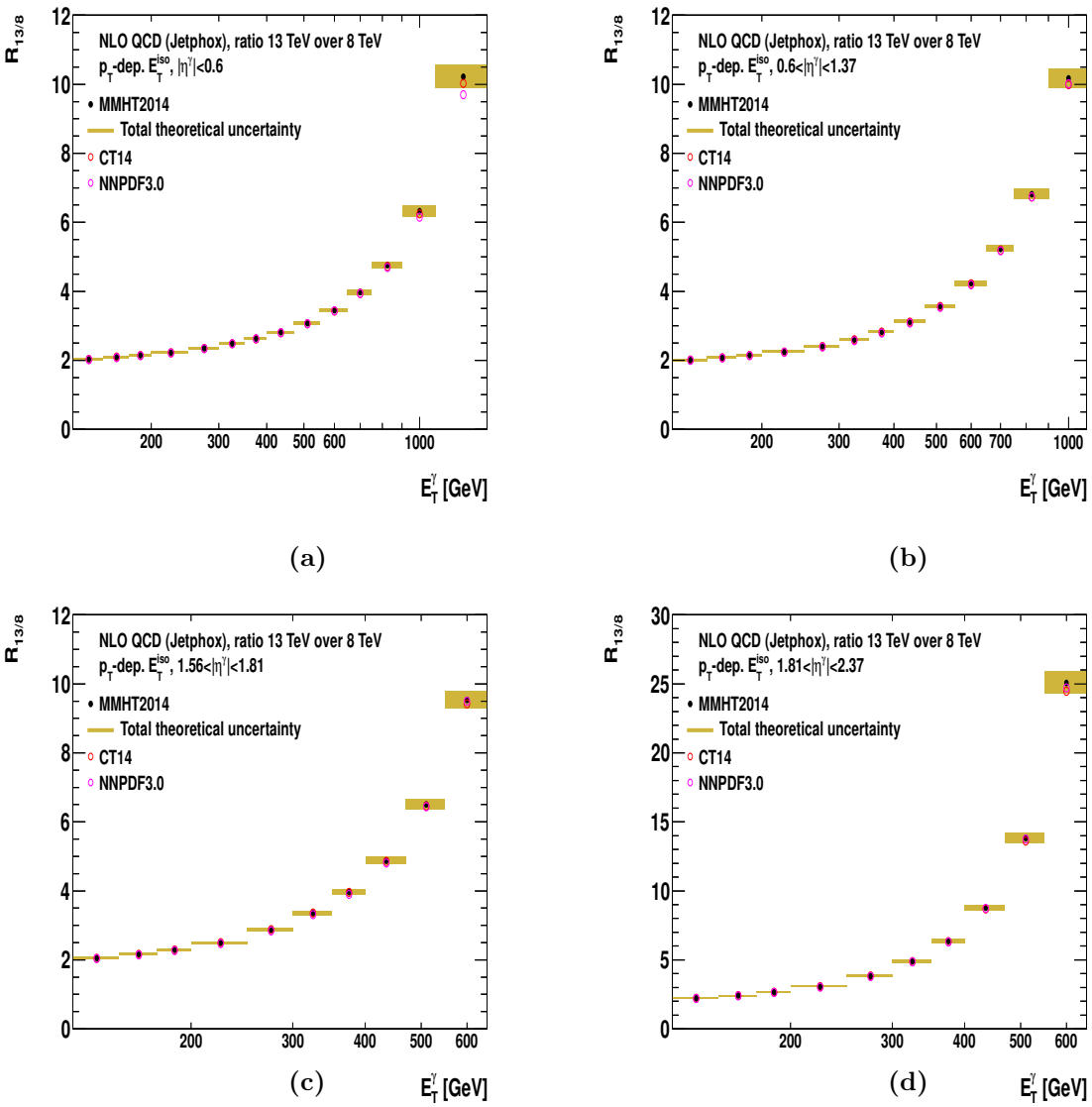


Figure 7.23: Theoretical prediction (black dots) for $R_{13/8}$ as a function of E_{T}^{γ} in different regions of $|\eta^{\gamma}|$. The shaded band shows the total theoretical uncertainty using MMHT2014. The predictions based on the CT14 (open red circles) and NNPDF3.0 (open pink circles) PDFs are also shown.

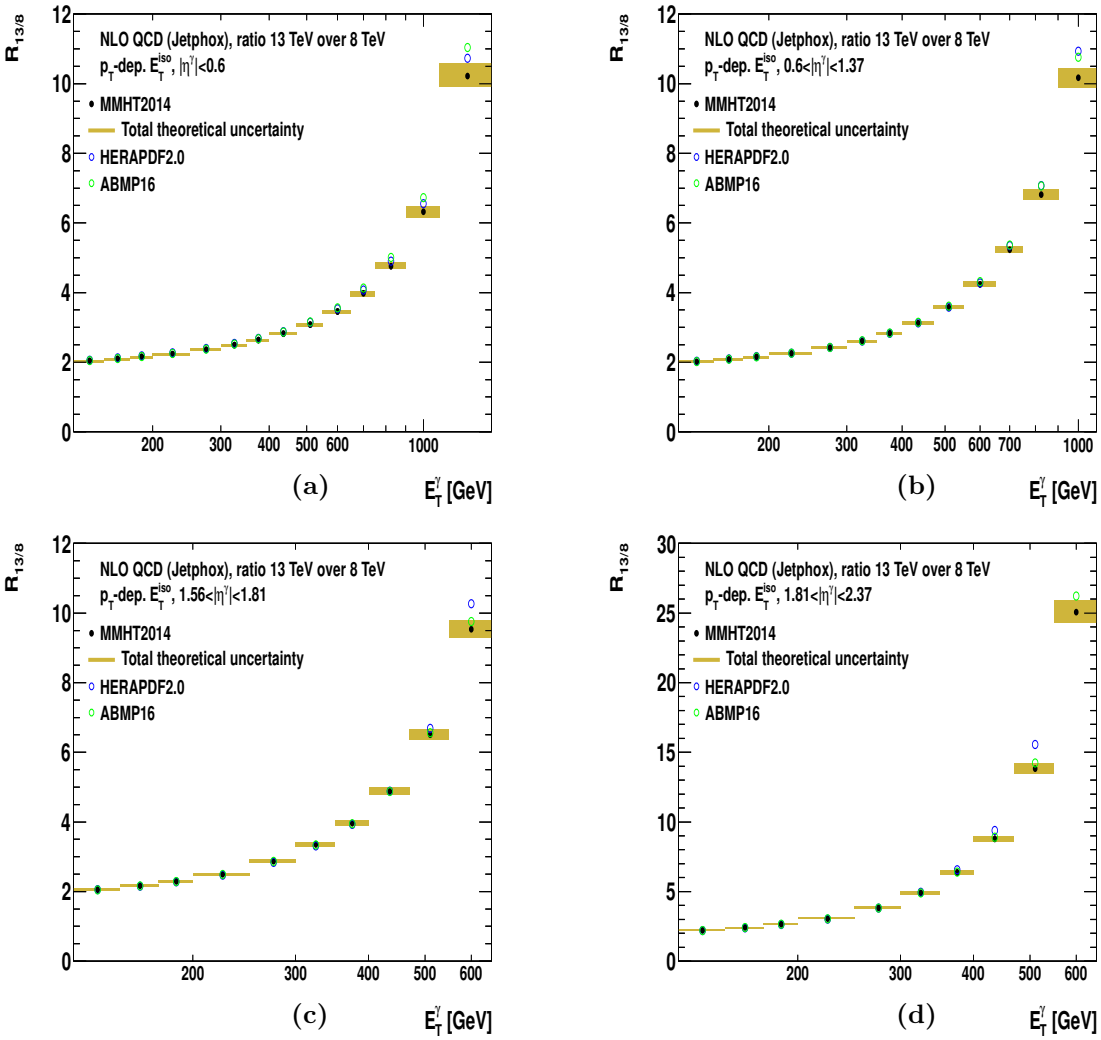


Figure 7.24: Theoretical prediction (black dots) for $R_{13/8}$ as a function of E_{T}^{γ} in different regions of $|\eta^{\gamma}|$. The shaded band shows the total theoretical uncertainty using MMHT2014. The predictions based on the HERAPDF2.0 (open blue circles) and ABMP16 (open green circles) PDFs are also shown.

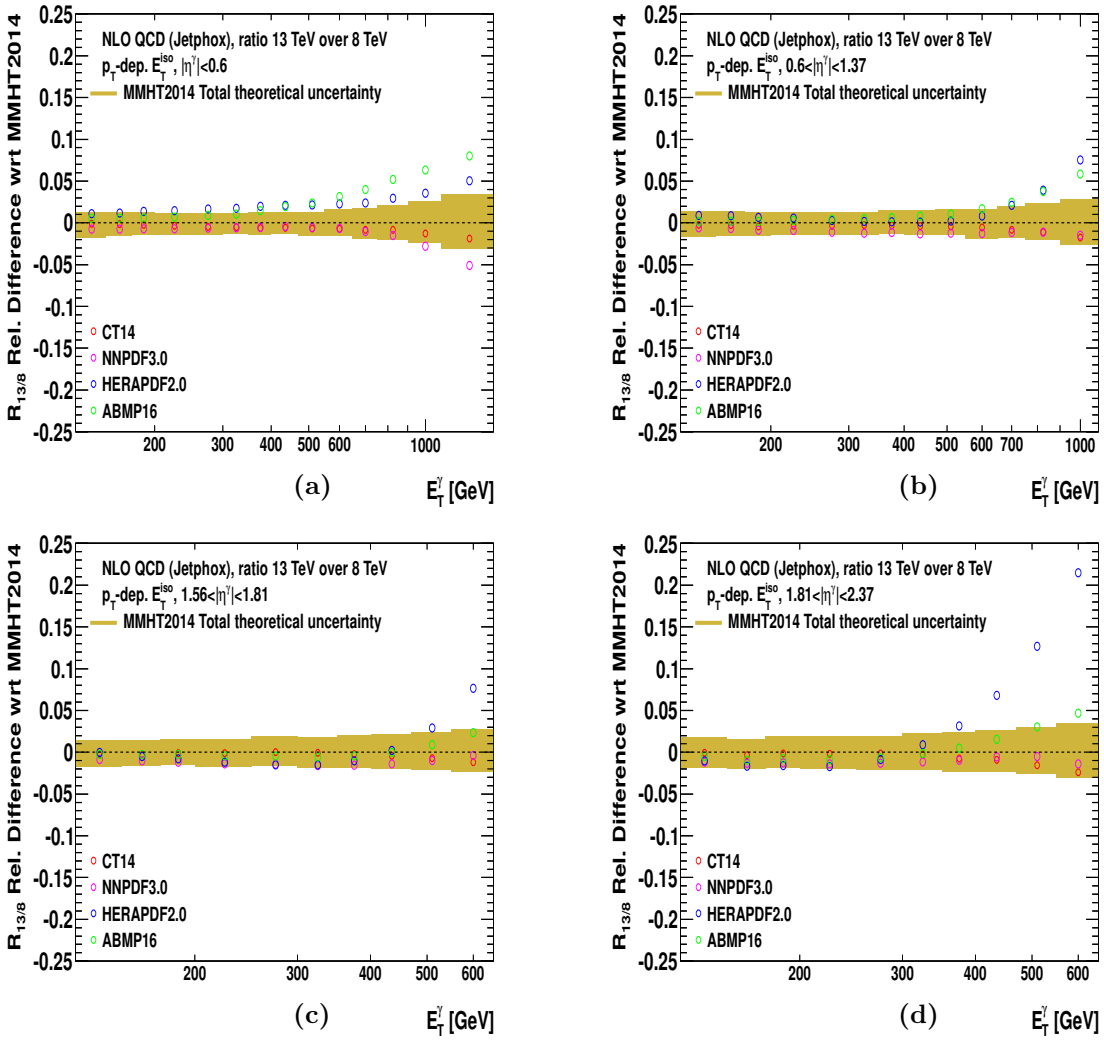


Figure 7.25: Relative difference of the theoretical predictions for $R_{13/8}$ with respect to that based on MMHT2014 as a function of E_{T}^{γ} in the different regions in $|\eta^{\gamma}|$: CT14 (open red circles), NNPDF3.0 (open pink circles), HERAPDF2.0 (open blue circles) and ABMP16 (open green circles). The shaded band shows the relative total theoretical uncertainty using MMHT2014.

7.4 Theoretical predictions for $D_{13/8}^{\gamma/Z}$

The predictions for $D_{13/8}^{\gamma/Z}$ were computed using the NNLO QCD calculations from DYTURBO[4] for $\sigma_Z^{\text{fid}}(13\text{ TeV})/\sigma_Z^{\text{fid}}(8\text{ TeV})$ and the NLO QCD calculations using JetPhox for the ratio $R_{13/8}$. The NNLO QCD calculations of DYTURBO are available for the ATLAS Collaboration in [123]. They were made based on sets of PDFs extracted with NNLO QCD fits, namely MMHT2014nnlo, CT14nnlo, HERAPDF2.0nnlo and NNPDF3.0nnlo. For consistency, and to take into account properly the correlations in the PDF uncertainties, the calculations of JetPhox for $R_{13/8}$ were repeated using the same PDF sets determined at NNLO QCD. The same settings as for the results presented in Section 7.3 were used for the number of active flavours, scales and fragmentation functions. The strong coupling constant $\alpha_s(m_Z)$ was set to the value assumed in the fit to determine the PDFs. In the case of the MMHT2014nnlo PDF set, the assumed value is $\alpha_s(m_Z) = 0.118$.

7.4.1 Theoretical uncertainties

The following sources of uncertainty in the theoretical predictions based on MMHT2014nnlo are considered for $R_{13/8}$:

- the uncertainty on the NLO QCD calculations due to terms beyond NLO was estimated by repeating the calculations using values of μ_R, μ_F and μ_f scaled by the factors 0.5 and 2. The three scales were either varied simultaneously, individually or by fixing one and varying the other two. In all cases, the condition $0.5 \leq \mu_A/\mu_B \leq 2$ is imposed, where $A, B = R, F, f$ and $A \neq B$. The final uncertainty is taken as the largest deviation from the nominal value among the 14 possible variations and is shown in Figure 7.26;
- the uncertainty on the NLO QCD calculations due to those on the proton PDFs was estimated by repeating the calculations using the 50 additional sets from the MMHT2014 error analysis. The results were added according to the asymmetric Master Formula [119] to get the final uncertainty, which is shown in Figure 7.27;
- the uncertainty on the NLO QCD calculations due to that on the value of $\alpha_s(m_Z)$ is estimated by repeating the calculations using two additional sets of proton PDFs, for which different values of $\alpha_s(m_Z)$ were assumed in the fits, namely $\alpha_s(m_Z) = 0.116$ and 0.120. The results were scaled by a factor 1.5/2.0 to quote the final uncertainty at 68% of confidence level, which is shown in Figure 7.28.

The uncertainty due to that on the beam energy was neglected. The correlation between different centre-of-mass energies for the uncertainties was the same as in the results presented in Section 7.3, that is, all uncertainties were treated as correlated for $R_{13/8}$.

For the prediction of $D_{13/8}^{\gamma/Z}$, the uncertainties were estimated based on the results available in Reference [123] as follows:

- the scale variations were considered uncorrelated between Z production and isolated-photon production. The uncertainty in the prediction of $\sigma_Z^{\text{fid}}(13\text{ TeV})/\sigma_Z^{\text{fid}}$ (8 TeV) due to the scale variations is $^{+0.02}_{-0.3}$% [123];

[4] DYTURBO is an optimised [123] version of the DYNNLO program [125, 126].

- the PDF uncertainties were considered correlated between Z production and isolated-photon production. The uncertainty in the prediction of $\sigma_Z^{\text{fid}}(13\text{ TeV})/\sigma_Z^{\text{fid}}$ (8 TeV) due to the PDFs is $^{+0.9}_{-0.8}\%$ [123]. The cross-section predictions for $\sigma_Z^{\text{fid}}(13\text{ TeV})$ and $\sigma_Z^{\text{fid}}(8\text{ TeV})$ for each eigenvector PDF of MMHT2014nnlo are available in Reference [123]. Therefore, it has been possible to make the correlation without any approximation;

- the $\alpha_s(m_Z)$ uncertainties were considered correlated between Z production and isolated-photon production. The uncertainty in the prediction of $\sigma_Z^{\text{fid}}(13\text{ TeV})/\sigma_Z^{\text{fid}}$ (8 TeV) due to $\alpha_s(m_Z)$ is -0.03% ($\alpha_s(m_Z)$ up) and -0.3% ($\alpha_s(m_Z)$ down) [123].

The total relative uncertainty affecting the $D_{13/8}^{\gamma/Z}$ predictions as well as the contributions from the variations of the scales, the uncertainty in $\alpha_s(m_Z)$ and the uncertainties in the PDFs are shown as functions of E_T^γ separately for each region in $|\eta^\gamma|$ in Figure 7.29. The following values for the total relative uncertainty were obtained:

- region $|\eta^\gamma| < 0.6$: the total relative uncertainty is below 2% from $E_T^\gamma = 125$ GeV up to $E_T^\gamma = 650$ GeV; it rises up to $\approx 4.5\%$ at the end of the spectrum. It is dominated by the variation of the scales for $E_T^\gamma \lesssim 300$ GeV; for $E_T^\gamma \gtrsim 300$ GeV, it is dominated by the uncertainties in the PDFs;

- region $0.6 < |\eta^\gamma| < 1.37$: the total relative uncertainty is below 2% from $E_T^\gamma = 125$ GeV up to $E_T^\gamma = 650$ GeV; it rises up to $\approx 3.3\%$ at the end of the spectrum. It is dominated by the variation of the scales except for $E_T^\gamma \gtrsim 750$ GeV, where the contribution from the uncertainties in the PDFs is equally important;

- region $1.56 < |\eta^\gamma| < 1.81$: the total relative uncertainty is below 2% from $E_T^\gamma = 125$ GeV up to $E_T^\gamma = 350$ GeV; it rises up to $\approx 3\%$ at the end of the spectrum. It is dominated by the variation of the scales;

- region $1.81 < |\eta^\gamma| < 2.37$: the total relative uncertainty is below 3% from $E_T^\gamma = 125$ GeV up to $E_T^\gamma = 470$ GeV; it rises up to $\approx 3.6\%$ at the end of the spectrum. It is dominated by the variation of the scales except for the downward variation for $E_T^\gamma \gtrsim 550$ GeV, where the contribution from the uncertainty in the PDFs is equally important;

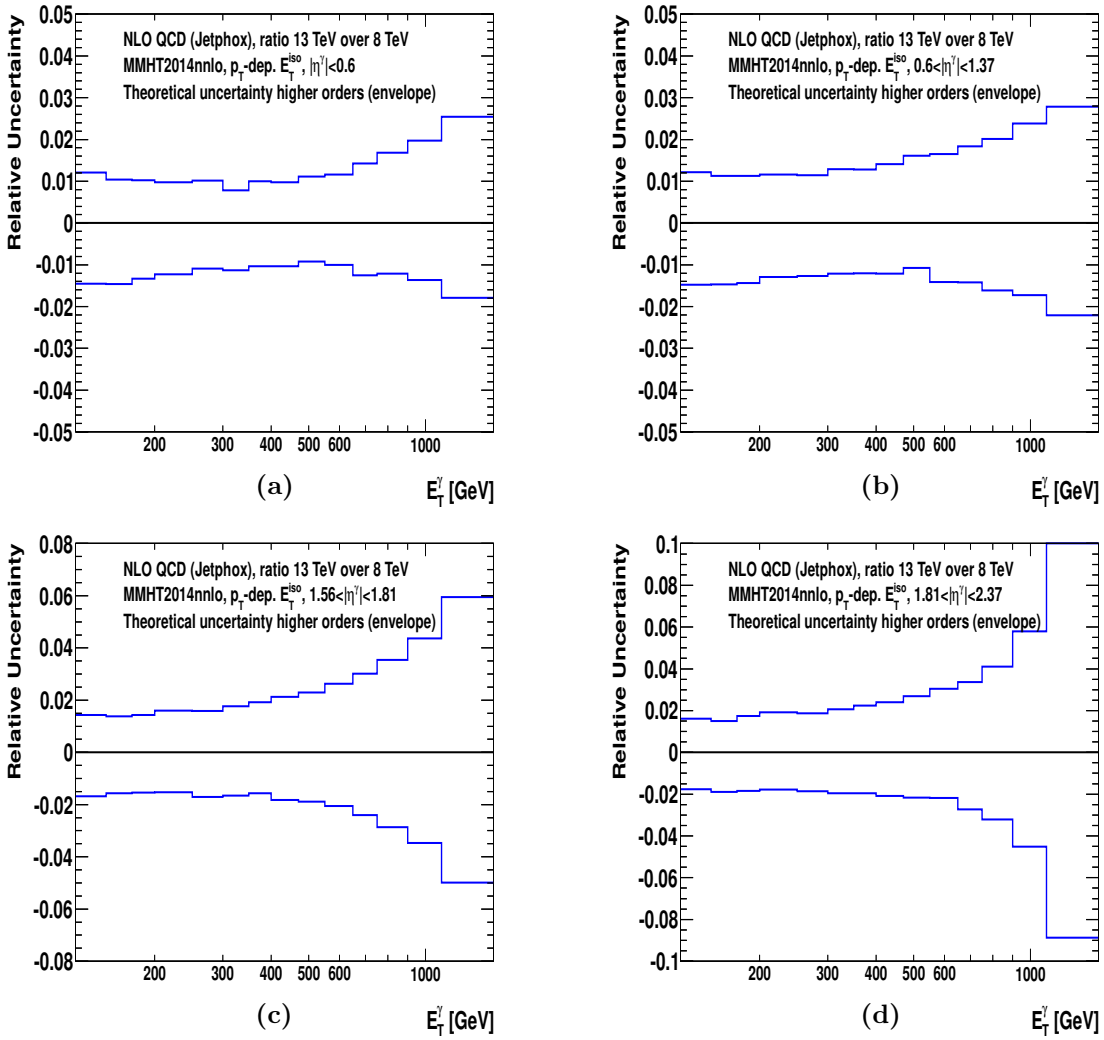


Figure 7.26: Theoretical uncertainty in $R_{13/8}$ from terms beyond NLO (envelope of all variations) as a function of E_{T}^{γ} in different regions of $|\eta^{\gamma}|$. The MMHT2014nnlo PDFs are used. The uncertainty was treated as correlated between different $\sqrt{s}$.

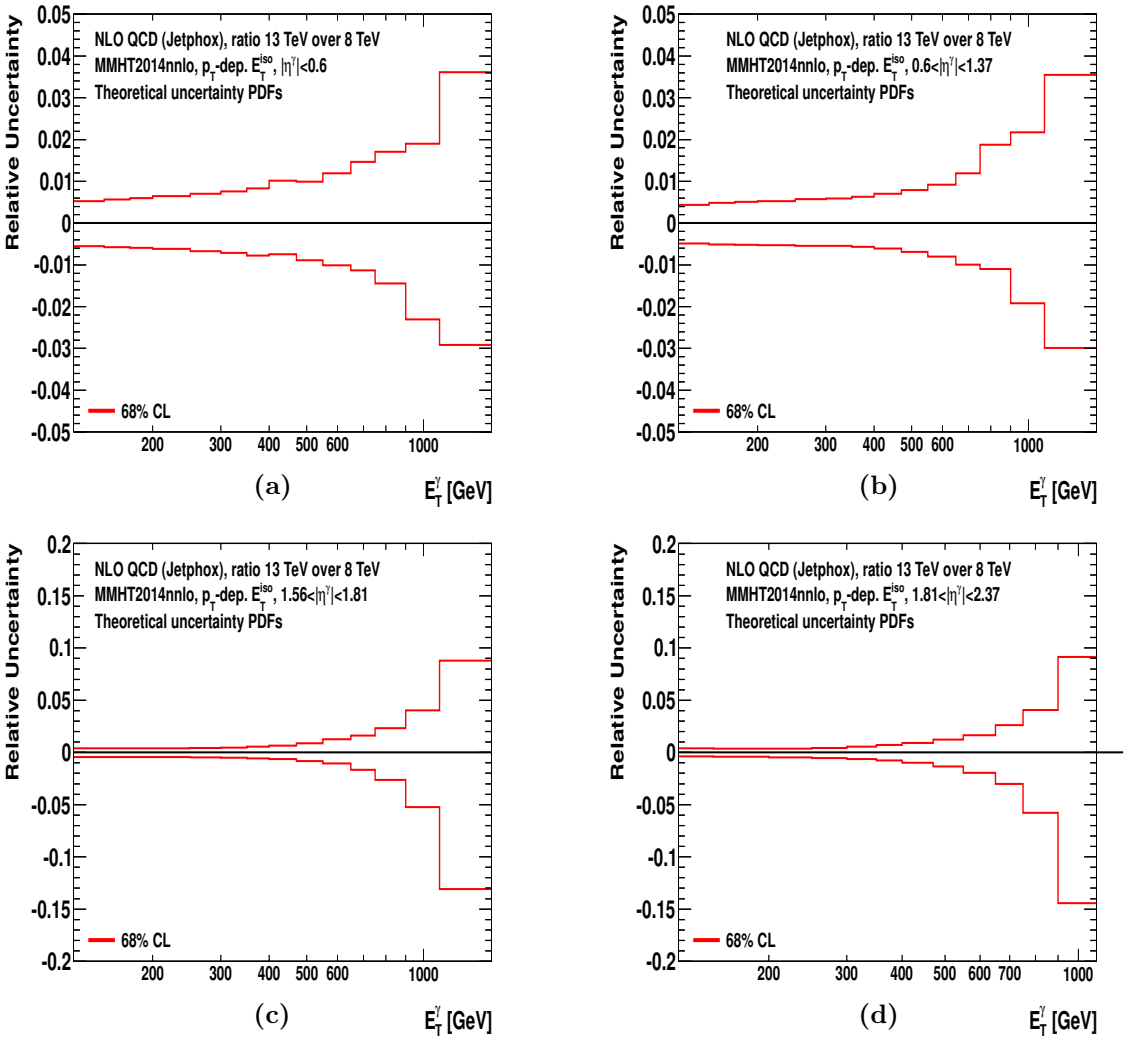


Figure 7.27: Theoretical uncertainty in $R_{13/8}$ arising from the uncertainty in the PDFs as a function of E_{T}^{γ} in different regions of $|\eta^{\gamma}|$. The MMHT2014nnlo PDFs are used.

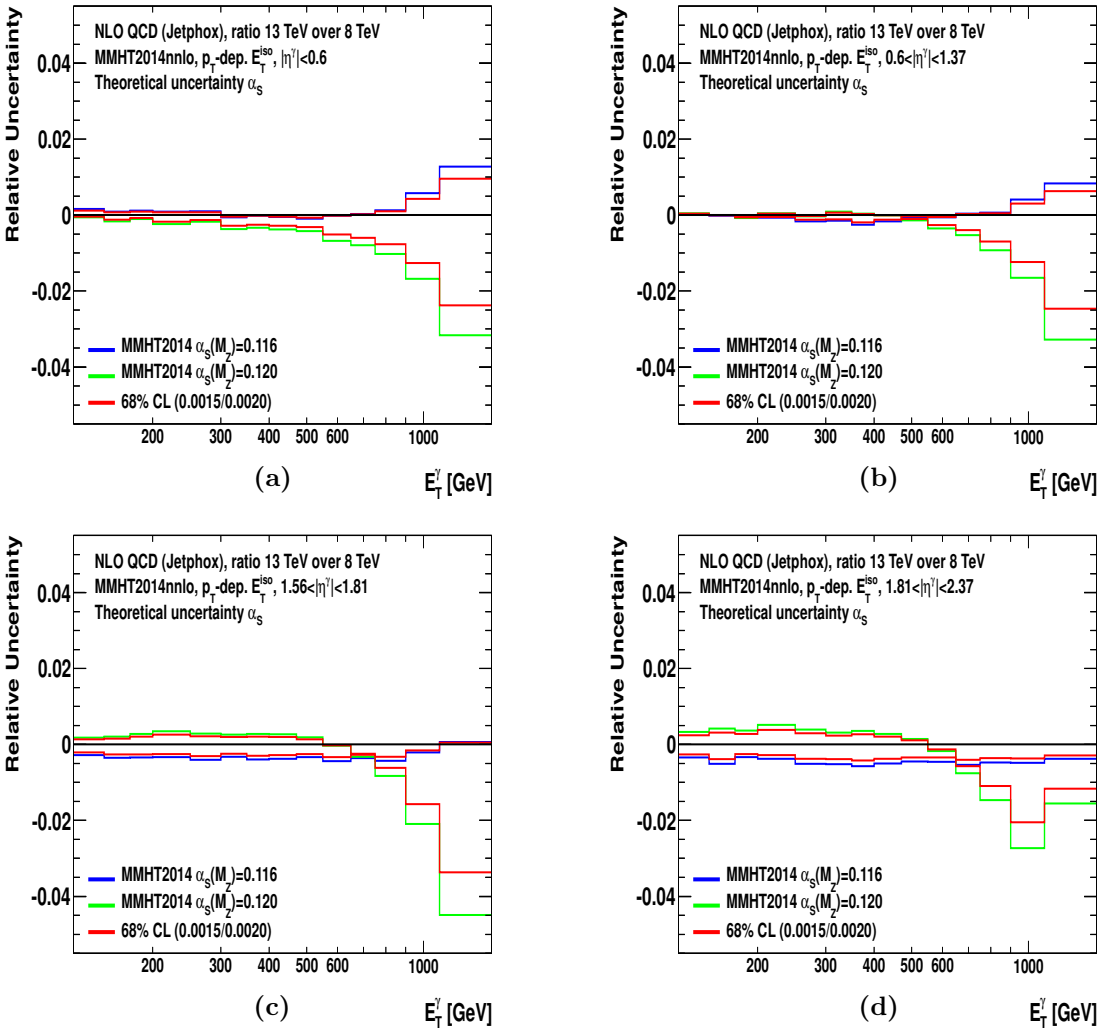


Figure 7.28: Theoretical uncertainty in $R_{13/8}$ arising from the uncertainty in $\alpha_{\mathrm{S}}(m_Z)$ as a function of E_{T}^{γ} in different regions of $|\eta^{\gamma}|$. The MMHT2014nnlo PDFs are used.

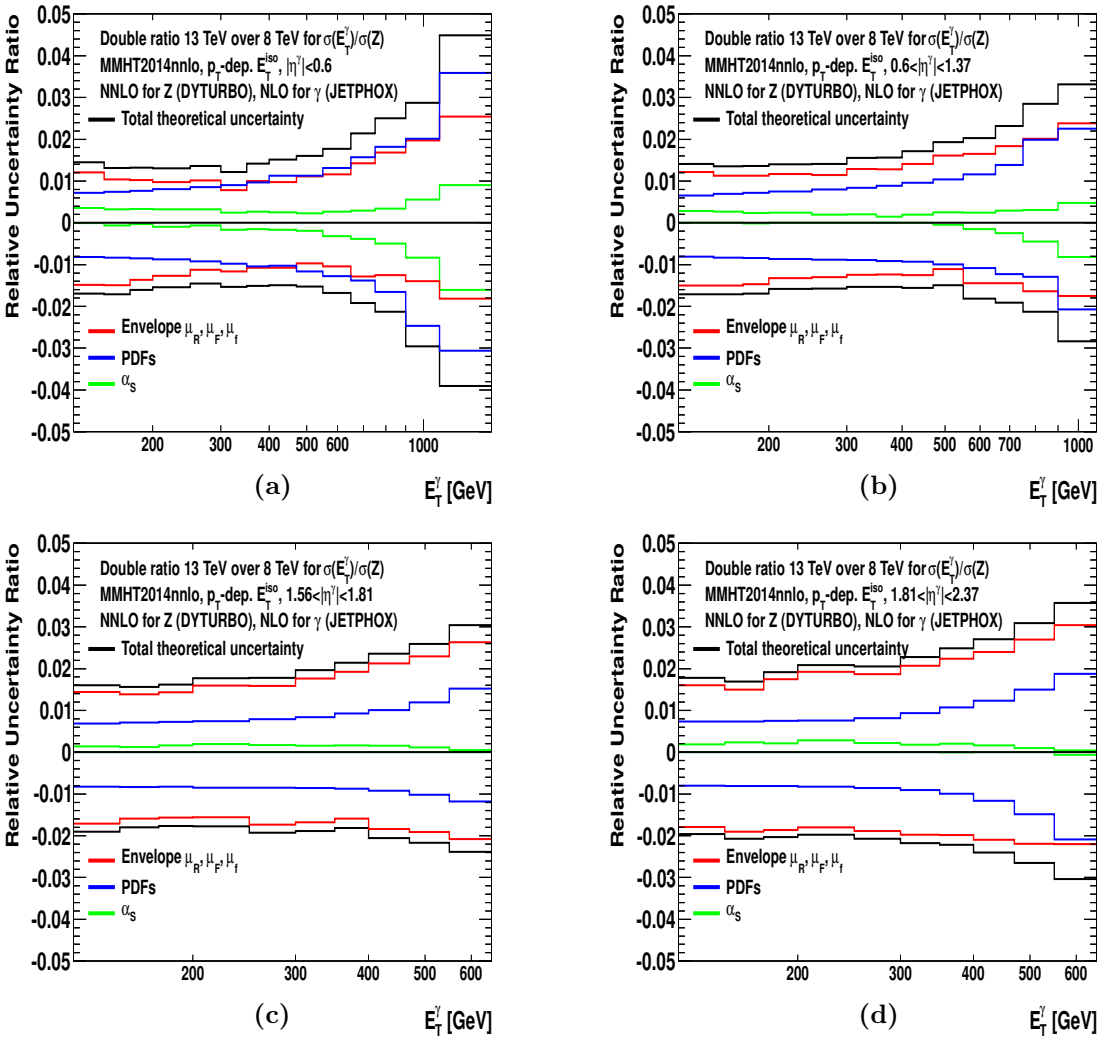


Figure 7.29: Total theoretical uncertainty (black histogram) in $D_{13/8}^{\gamma/Z}$ as a function of E_{T}^{γ} in the different regions of $|\eta^{\gamma}|$. The contributions from the envelope of the variation of the scales (red histogram), the PDFs (blue histogram) and $\alpha_{\mathrm{S}}(m_Z)$ (green histogram) are also shown.

7.4.2 Comparisons of $D_{13/8}^{\gamma/Z}$ predictions based on different PDFs

The theoretical predictions for $D_{13/8}^{\gamma/Z}$ based on the MMHT2014nnlo parameterisations of the proton PDFs are shown in Figure 7.30: the predictions for $D_{13/8}^{\gamma/Z}$ as well as the theoretical uncertainties are shown as functions of E_{T}^{γ} for each region in $|\eta^{\gamma}|$. The trends observed in the double ratio are the same as in $R_{13/8}$. The predicted $D_{13/8}^{\gamma/Z}$ is approximately a factor of 1.4 at $E_{\mathrm{T}}^{\gamma} = 125$ GeV and increases as E_{T}^{γ} increases reaching a factor of 6–17 at the end of the spectrum; the increase is larger for the forward η^{γ} regions than for the central η^{γ} regions. The predictions based on other parameterisations of the proton PDFs are compared to those based on MMHT2014nnlo in Figures 7.31 and 7.32.

To illustrate the differences between the predictions based on different sets of PDFs, the ratio with respect to the predictions based on MMHT2014nnlo is shown as a function of E_{T}^{γ} separately for each region in $|\eta^{\gamma}|$ in Figure 7.33:

- region $|\eta^{\gamma}| < 0.6$: the predictions based on MMHT2014nnlo, NNPDF3.0nnlo, CT14-nnlo and HERAPDF2.0nnlo are similar up to $E_{\mathrm{T}}^{\gamma} \sim 650$ GeV; for E_{T}^{γ} above 650 GeV, the prediction based on HERAPDF2.0nnlo increases more rapidly than the others, showing differences up to +13% at $E_{\mathrm{T}}^{\gamma} \sim 1.3$ TeV;
- region $0.6 < |\eta^{\gamma}| < 1.37$: the predictions based on MMHT2014nnlo, NNPDF3.0nnlo, CT14nnlo and HERAPDF2.0nnlo are similar up to $E_{\mathrm{T}}^{\gamma} \sim 750$ GeV; for E_{T}^{γ} above 750 GeV the prediction based on HERAPDF2.0nnlo increases more rapidly than the others, showing differences up to +8% at $E_{\mathrm{T}}^{\gamma} \sim 1$ TeV;
- region $1.56 < |\eta^{\gamma}| < 1.81$: the predictions based on MMHT2014nnlo, NNPDF3.0nnlo, CT14nnlo and HERAPDF2.0nnlo are similar up to $E_{\mathrm{T}}^{\gamma} \sim 550$ GeV; for E_{T}^{γ} above 550 GeV the prediction based on HERAPDF2.0nnlo exhibits a larger ratio (+5%);
- region $1.81 < |\eta^{\gamma}| < 2.37$: the predictions based on MMHT2014nnlo, NNPDF3.0nnlo, CT14nnlo and HERAPDF2.0nnlo are similar up to $E_{\mathrm{T}}^{\gamma} \sim 400$ GeV; for E_{T}^{γ} above 400 GeV, the prediction based on HERAPDF2.0nnlo exhibits a larger ratio, which increases as E_{T}^{γ} increases up to a maximum of +17% at $E_{\mathrm{T}}^{\gamma} \sim 600$ GeV.

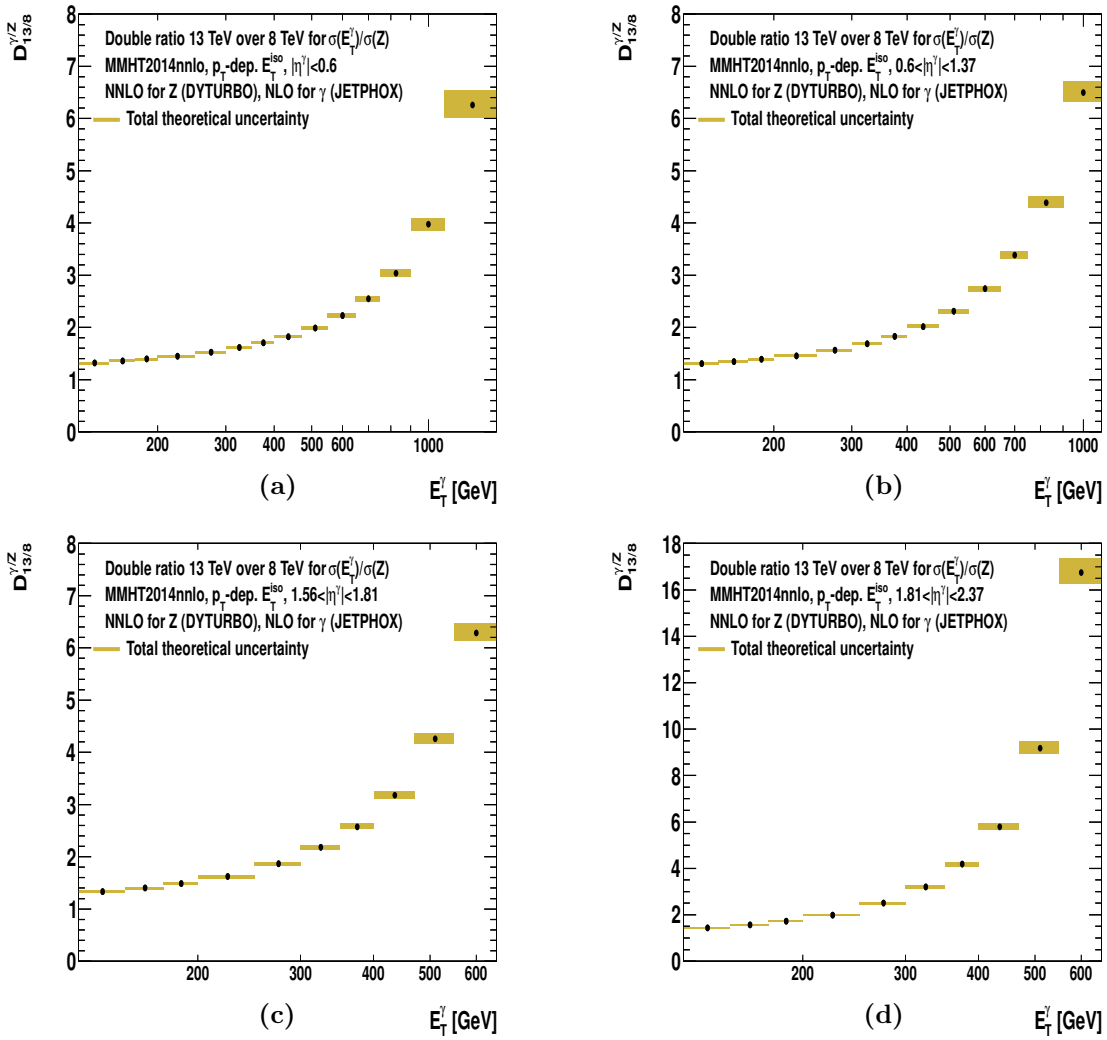


Figure 7.30: Theoretical prediction (black dots) for $D_{13/8}^{\gamma/Z}$ as a function of E_{T}^{γ} in different regions of $|\eta^{\gamma}|$. The shaded band shows the total theoretical uncertainty.

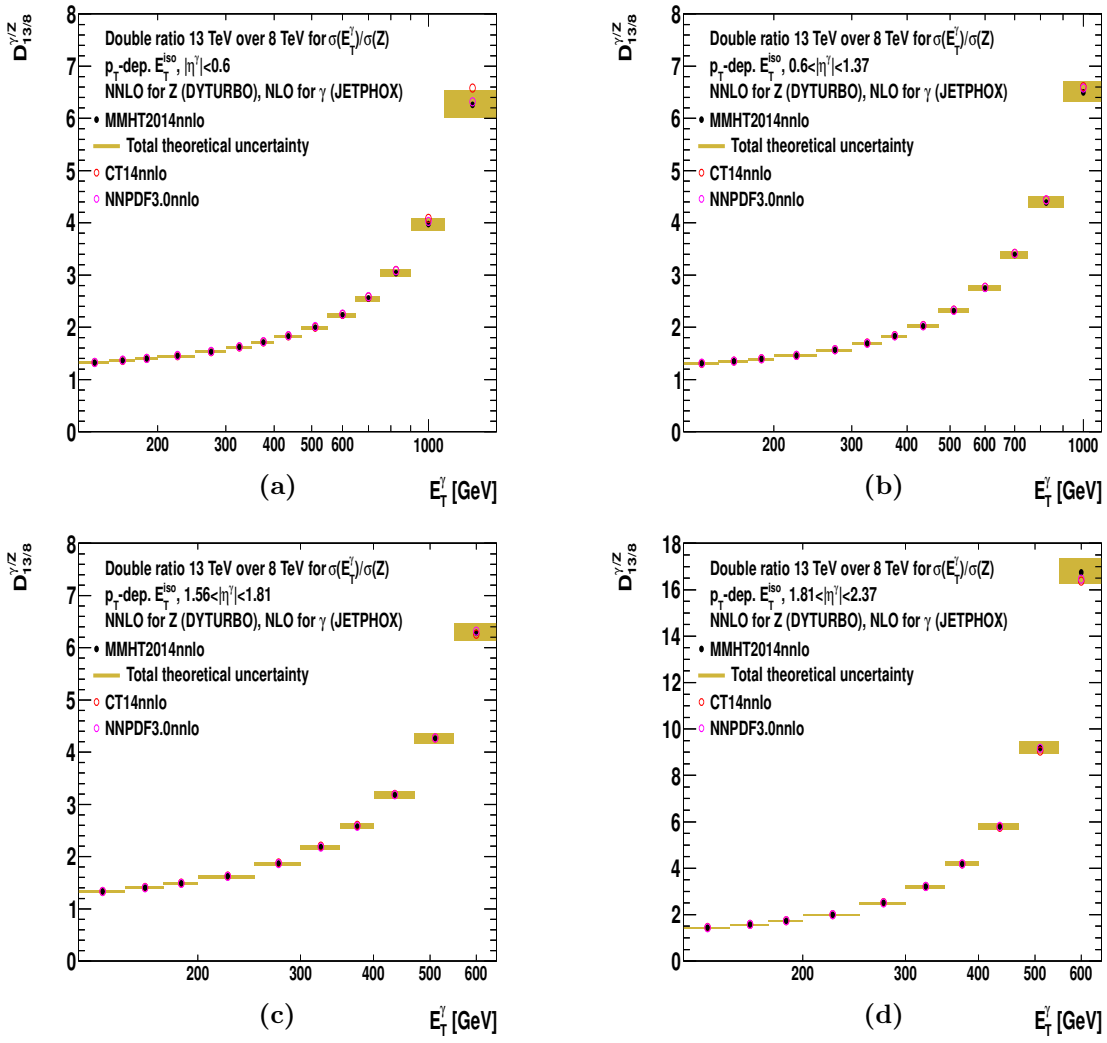


Figure 7.31: Theoretical prediction (black dots) for $D_{13/8}^{\gamma/Z}$ as a function of E_{T}^{γ} in different regions of $|\eta^{\gamma}|$. The shaded band shows the total theoretical uncertainty using MMHT2014nnlo. The predictions based on the CT14nnlo (open red circles) and NNPDF3.0nnlo (open pink circles) PDFs are also shown.

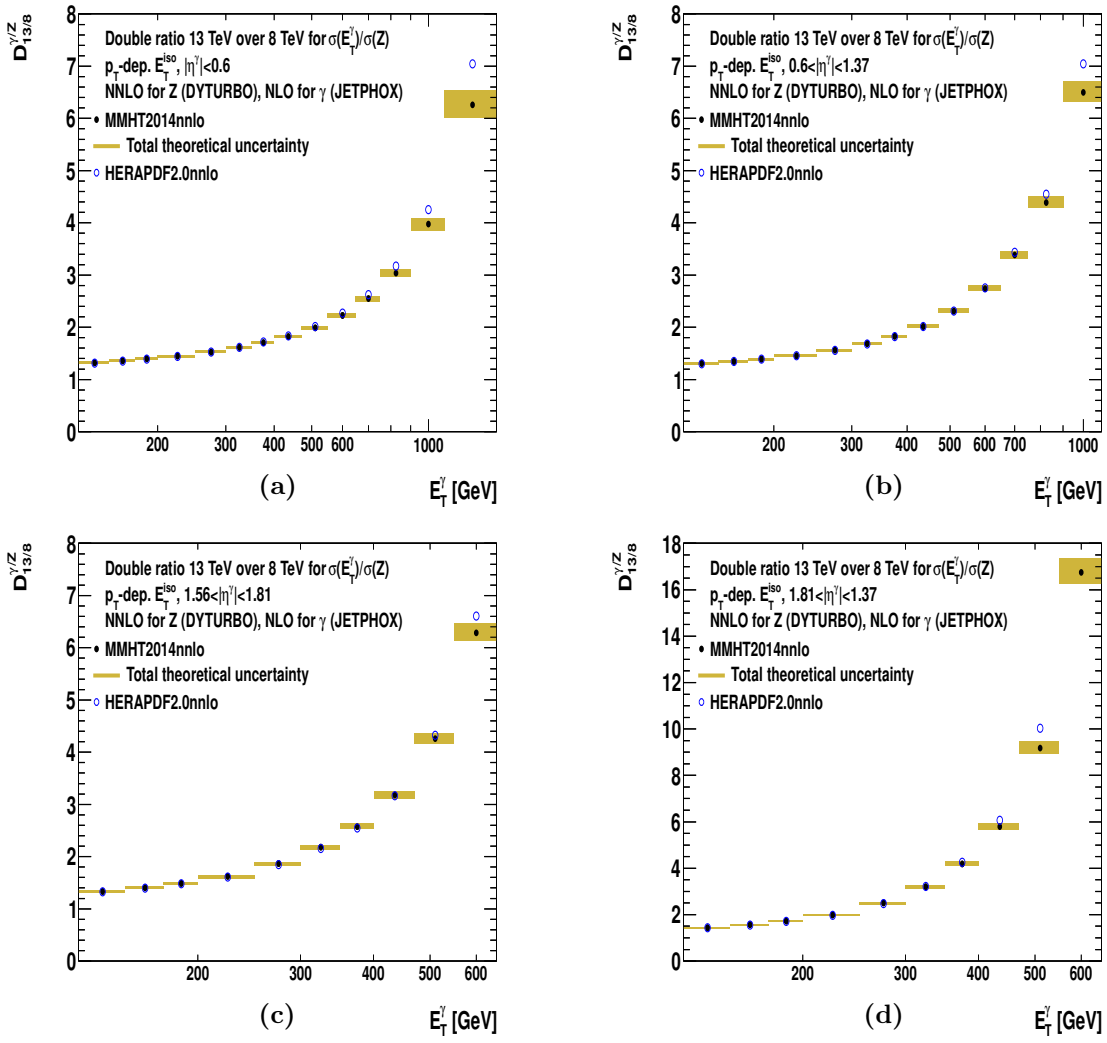


Figure 7.32: Theoretical prediction (black dots) for $D_{13/8}^{\gamma/Z}$ as a function of E_{T}^{γ} in different regions of $|\eta^{\gamma}|$. The shaded band shows the total theoretical uncertainty using MMHT2014nnlo. The predictions based on the HERAPDF2.0nnlo (open blue circles) PDFs are also shown.

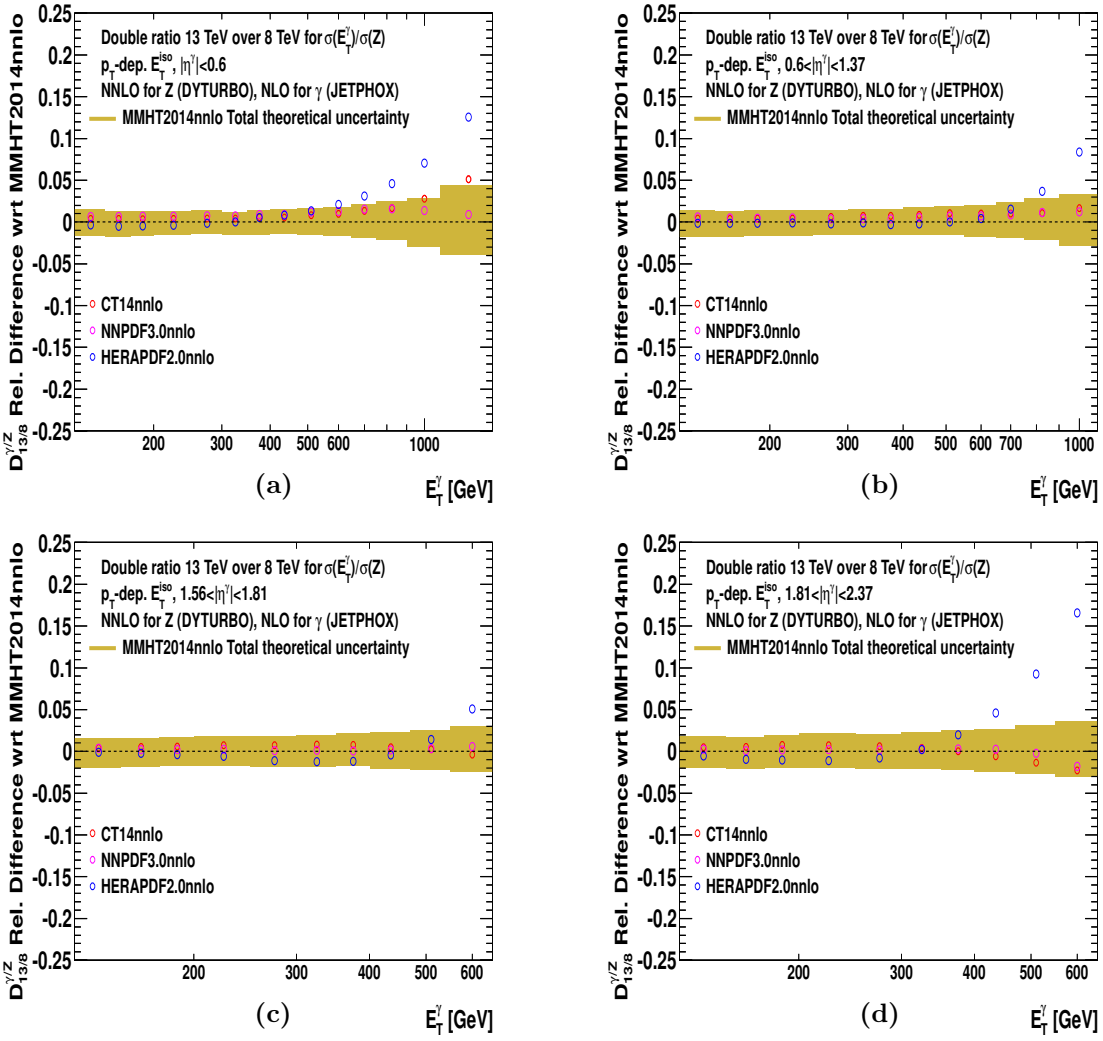


Figure 7.33: Relative difference of the theoretical predictions for $D_{13/8}^{\gamma/Z}$ with respect to that based on MMHT2014nnlo as a function of E_{T}^{γ} in the different regions of $|\eta^{\gamma}|$: CT14nnlo (open red circles), NNPDF3.0nnlo (open pink circles) and HERAPDF2.0nnlo (open blue circles). The shaded band shows the relative total theoretical uncertainty using MMHT2014nnlo.

7.5 Results

The results of $R_{13/8}$ are shown as functions of E_{T}^{γ} in different regions of $|\eta^{\gamma}|$ in Figure 7.34. The measured ratio increases as E_{T}^{γ} increases, from approximately 2 at $E_{\mathrm{T}}^{\gamma} = 125$ GeV up to approximately an order of magnitude higher at the high-end of the spectrum.

The measured ratio at the highest value of E_{T}^{γ} in each $|\eta^{\gamma}|$ region is $R_{13/8} = 13.9 \pm 9.8$ at $E_{\mathrm{T}}^{\gamma} = 1.3$ TeV for $|\eta^{\gamma}| < 0.6$, $R_{13/8} = 7.9 \pm 2.4$ at $E_{\mathrm{T}}^{\gamma} = 1$ TeV for $0.6 < |\eta^{\gamma}| < 1.37$, $R_{13/8} = 12.5 \pm 2.7$ at $E_{\mathrm{T}}^{\gamma} = 0.6$ TeV for $1.56 < |\eta^{\gamma}| < 1.81$ and $R_{13/8} = 29.3 \pm 8.0$ at $E_{\mathrm{T}}^{\gamma} = 0.6$ TeV for $1.81 < |\eta^{\gamma}| < 2.37$. At a fixed value of E_{T}^{γ}, the measured $R_{13/8}$ increases as $|\eta^{\gamma}|$ increases. For example, the measured $R_{13/8}$ at $E_{\mathrm{T}}^{\gamma} = 600$ GeV is $R_{13/8} = 3.3 \pm 0.3$ for $|\eta^{\gamma}| < 0.6$, $R_{13/8} = 4.4 \pm 0.4$ for $0.6 < |\eta^{\gamma}| < 1.37$, $R_{13/8} = 12.5 \pm 2.7$ for $1.56 < |\eta^{\gamma}| < 1.81$ and $R_{13/8} = 29.3 \pm 8.0$ for $1.81 < |\eta^{\gamma}| < 2.37$.

The predictions for $R_{13/8}$ from NLO pQCD using the MMHT2014 PDFs are compared to the measurements in Figures 7.34. The NLO pQCD predictions reproduce the measured $R_{13/8}$ and, in particular, the increase as E_{T}^{γ} increases as well as the dependence with $|\eta^{\gamma}|$. To study the description of the measured $R_{13/8}$ by the NLO pQCD predictions, the ratio $R_{13/8}(\mathrm{NLO})/\mathrm{R}_{13/8}(\mathrm{Data})$ is shown as a function of E_{T}^{γ} in different regions of $|\eta^{\gamma}|$ in Figure 7.35 (a zoom is provided in Figure 7.36). The ratio is shown for NLO pQCD predictions based on different parameterisations of the proton PDFs: MMHT2014, CT14, NNPDF3.0, HERAPDF2.0 and ABMP16. The predictions agree with the measured $R_{13/8}$ within the experimental and theoretical uncertainties for all PDFs considered.

The comparison of $d\sigma/dE_{\mathrm{T}}^{\gamma}$ between data and NLO pQCD in the previous ATLAS analyses at 8 and 13 TeV is limited by the theoretical uncertainties, which are larger than those of experimental nature and dominated by the uncertainties due to the terms beyond NLO. The theoretical uncertainties in $d\sigma/dE_{\mathrm{T}}^{\gamma}$ are 10–15%. In contrast, the theoretical uncertainties in $R_{13/8}$ are below 2% for most of the phase space considered and smaller than the experimental uncertainties. The experimental uncertainties in $R_{13/8}$ also benefit from a significant reduction due to the partial cancellation of the systematic uncertainties due to the photon energy scale; the total systematic uncertainty is below 5% for most of the phase space considered. Thus, the significant reduction of the experimental and theoretical uncertainties in $R_{13/8}$ allows a stringent test of NLO pQCD. The agreement between data and the NLO pQCD predictions based on current parameterisations of the proton PDFs within these reduced uncertainties validates the description of the evolution of isolated-photon production in pp collisions with the centre-of-mass energy.

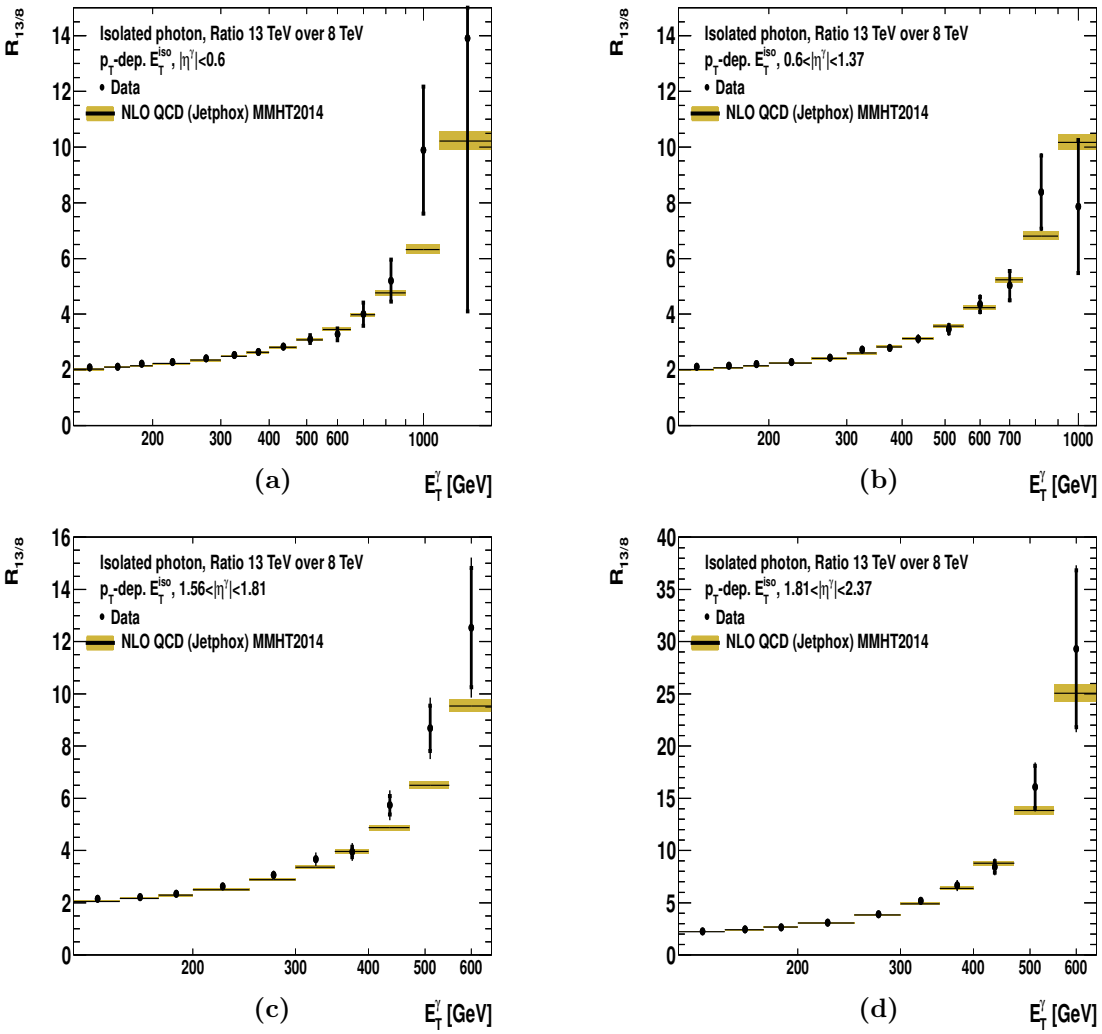


Figure 7.34: Measured $R_{13/8}$ (dots) as a function of E_{T}^{γ} in (a) $|\eta^{\gamma}| < 0.6$, (b) $0.6 < |\eta^{\gamma}| < 1.37$, (c) $1.56 < |\eta^{\gamma}| < 1.81$ and (d) $1.81 < |\eta^{\gamma}| < 2.37$. The predictions from NLO pQCD (black lines) using the MMHT2014 PDFs are also shown. The inner (outer) error bars represent the statistical uncertainties (the statistical and systematic uncertainties added in quadrature). The shaded band represents the theoretical uncertainty on the predictions. For most of the points, the error bars are smaller than the marker size and, thus, not visible.

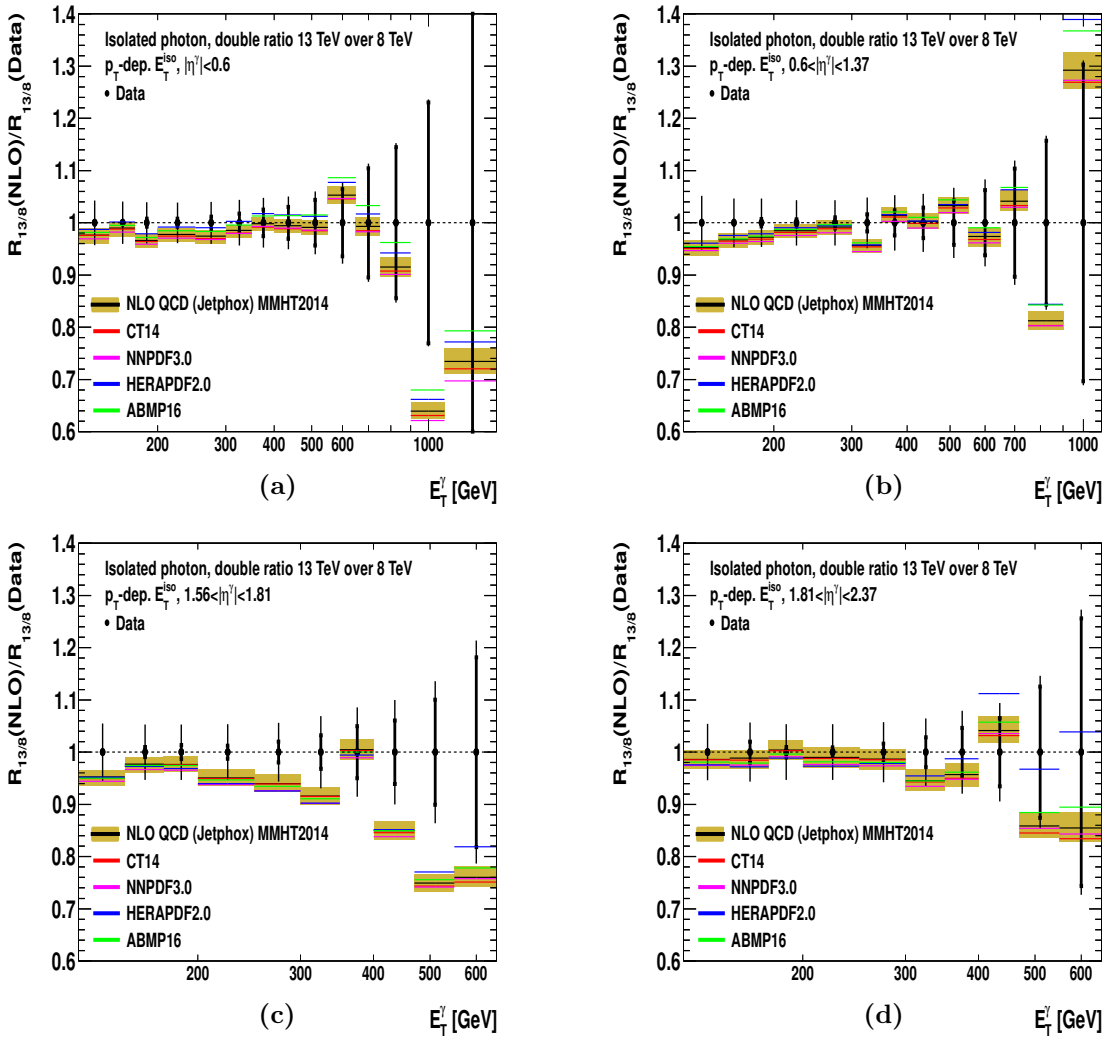


Figure 7.35: Ratio $R_{13/8}$(NLO)/$R_{13/8}$(Data) as a function of E_T^γ in (a) $|\eta^\gamma| < 0.6$, (b) $0.6 < |\eta^\gamma| < 1.37$, (c) $1.56 < |\eta^\gamma| < 1.81$ and (d) $1.81 < |\eta^\gamma| < 2.37$. The predictions from NLO pQCD using the MMHT2014, CT14, NNPDF3.0, HERAPDF2.0 and ABMP16 PDFs are shown. The inner (outer) error bars represent the statistical uncertainties (the statistical and systematic uncertainties added in quadrature). The shaded band represents the theoretical uncertainty on the predictions.

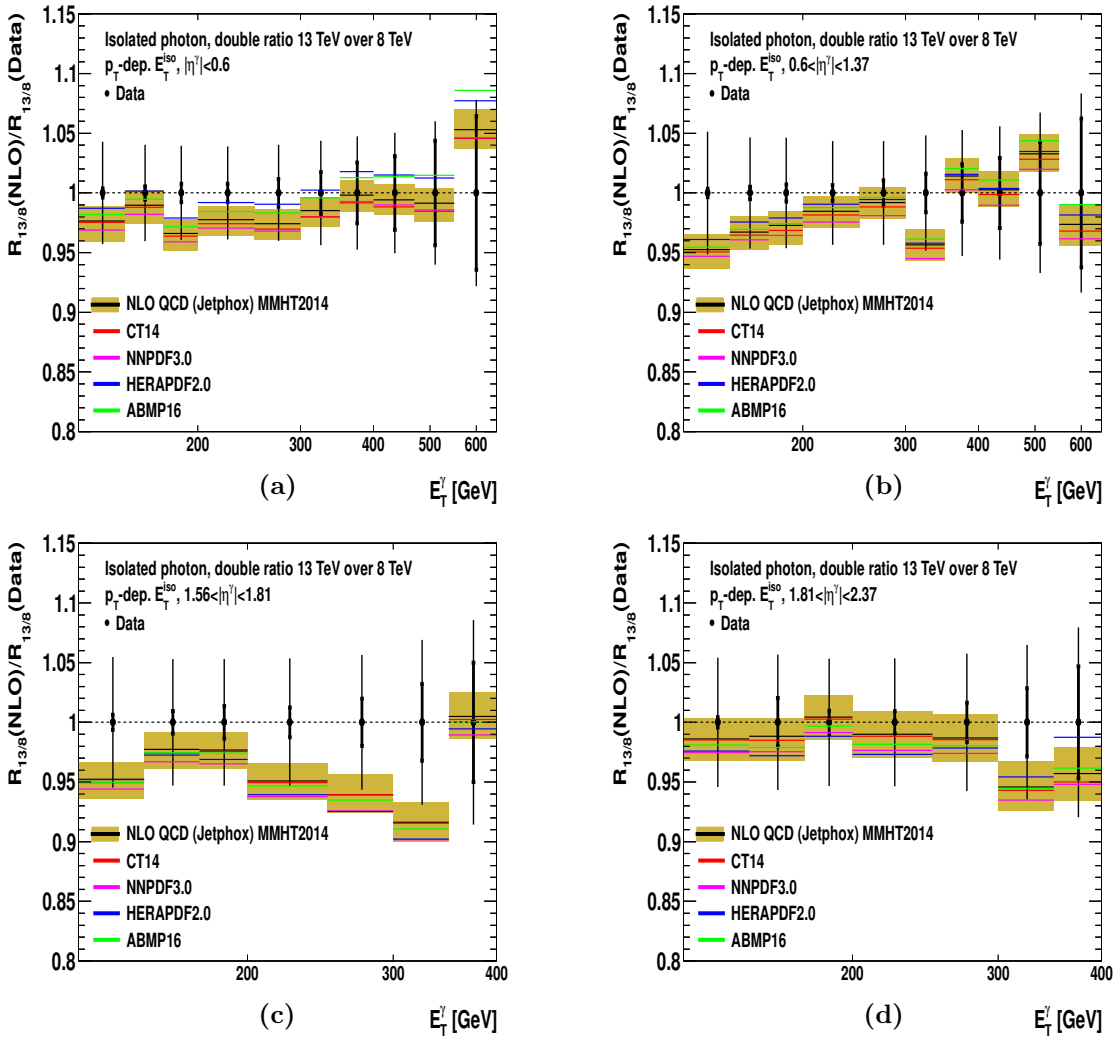


Figure 7.36: Ratio $R_{13/8}$(NLO)/$R_{13/8}$(Data) as a function of E_T^γ in (a) $|\eta^\gamma| < 0.6$, (b) $0.6 < |\eta^\gamma| < 1.37$, (c) $1.56 < |\eta^\gamma| < 1.81$ and (d) $1.81 < |\eta^\gamma| < 2.37$. The predictions from NLO pQCD using the MMHT2014, CT14, NNPDF3.0, HERAPDF2.0 and ABMP16 PDFs are shown. The inner (outer) error bars represent the statistical uncertainties (the statistical and systematic uncertainties added in quadrature). The shaded band represents the theoretical uncertainty on the predictions.

7.5.1 Results for $D_{13/8}^{\gamma/Z}$

The results of $D_{13/8}^{\gamma/Z}$ are shown as functions of E_{T}^{γ} in different regions of $|\eta^{\gamma}|$ in Figure 7.37. The measured ratio of the fiducial cross section for Z boson production at 13 TeV over that at 8 TeV is [122]

$$\sigma_Z^{\mathrm{fid}}(13\ \mathrm{TeV})/\sigma_Z^{\mathrm{fid}}(8\ \mathrm{TeV}) = 1.537 \pm 0.001\ (\mathrm{stat}) \pm 0.010\ (\mathrm{syst}) \pm 0.044\ (\mathrm{lumi}).$$

As mentioned in Section 7.2.3, the uncertainty in the luminosity measurement cancels out in $D_{13/8}^{\gamma/Z}$. The systematic uncertainty in $\sigma_Z^{\mathrm{fid}}(13\ \mathrm{TeV})/\sigma_Z^{\mathrm{fid}}(8\ \mathrm{TeV})$ amounts to 0.7%, which is at least a factor three smaller than the systematic uncertainty in $R_{13/8}$. As a result, the measured $D_{13/8}^{\gamma/Z}$ benefits from a significant reduction of the experimental uncertainty with respect to $R_{13/8}$. The measured $D_{13/8}^{\gamma/Z}$ increases as E_{T}^{γ} increases, from approximately 1.4 at $E_{\mathrm{T}}^{\gamma} = 125$ GeV up to approximately 5–19 at the high-end of the spectrum. The measured $D_{13/8}^{\gamma/Z}$ at the highest value of E_{T}^{γ} in each $|\eta^{\gamma}|$ region is $D_{13/8}^{\gamma/Z} = 9.1 \pm 6.4$ at $E_{\mathrm{T}}^{\gamma} = 1.3$ TeV for $|\eta^{\gamma}| < 0.6$, $D_{13/8}^{\gamma/Z} = 5.1 \pm 1.6$ at $E_{\mathrm{T}}^{\gamma} = 1$ TeV for $0.6 < |\eta^{\gamma}| < 1.37$, $D_{13/8}^{\gamma/Z} = 8.2 \pm 1.7$ at $E_{\mathrm{T}}^{\gamma} = 0.6$ TeV for $1.56 < |\eta^{\gamma}| < 1.81$ and $D_{13/8}^{\gamma/Z} = 19.1 \pm 5.2$ at $E_{\mathrm{T}}^{\gamma} = 0.6$ TeV for $1.81 < |\eta^{\gamma}| < 2.37$. At a fixed value of E_{T}^{γ} the measured $D_{13/8}^{\gamma/Z}$ increases as $|\eta^{\gamma}|$ increases. For example, the measured $D_{13/8}^{\gamma/Z}$ at $E_{\mathrm{T}}^{\gamma} = 600$ GeV is $D_{13/8}^{\gamma/Z} = 2.1 \pm 0.2$ for $|\eta^{\gamma}| < 0.6$, $D_{13/8}^{\gamma/Z} = 2.8 \pm 0.2$ for $0.6 < |\eta^{\gamma}| < 1.37$, $D_{13/8}^{\gamma/Z} = 8.2 \pm 1.7$ for $1.56 < |\eta^{\gamma}| < 1.81$ and $D_{13/8}^{\gamma/Z} = 19.1 \pm 5.2$ for $1.81 < |\eta^{\gamma}| < 2.37$. The predictions for $D_{13/8}^{\gamma/Z}$ using the MMHT2014nnlo PDFs are compared to the measured $D_{13/8}^{\gamma/Z}$ in Figures 7.37. The predictions reproduce the measured $D_{13/8}^{\gamma/Z}$ and, in particular, the increase as E_{T}^{γ} increases as well as the dependence with $|\eta^{\gamma}|$. To study the description of the measured $D_{13/8}^{\gamma/Z}$ by the predictions, the ratio $D_{13/8}^{\gamma/Z}$(Theory)/$\mathrm{D}_{13/8}^{\gamma/Z}$(Data) is shown as a function of E_{T}^{γ} in different regions of $|\eta^{\gamma}|$ in Figure 7.38 (a zoom is provided in Figure 7.39). The ratio is shown for predictions based on different parameterisations of the proton PDFs: MMHT2014nnlo, CT14nnlo, NNPDF3.0nnlo and HERAPDF2.0nnlo. The predictions agree with the measured $D_{13/8}^{\gamma/Z}$ within the experimental and theoretical uncertainties for all PDFs considered.

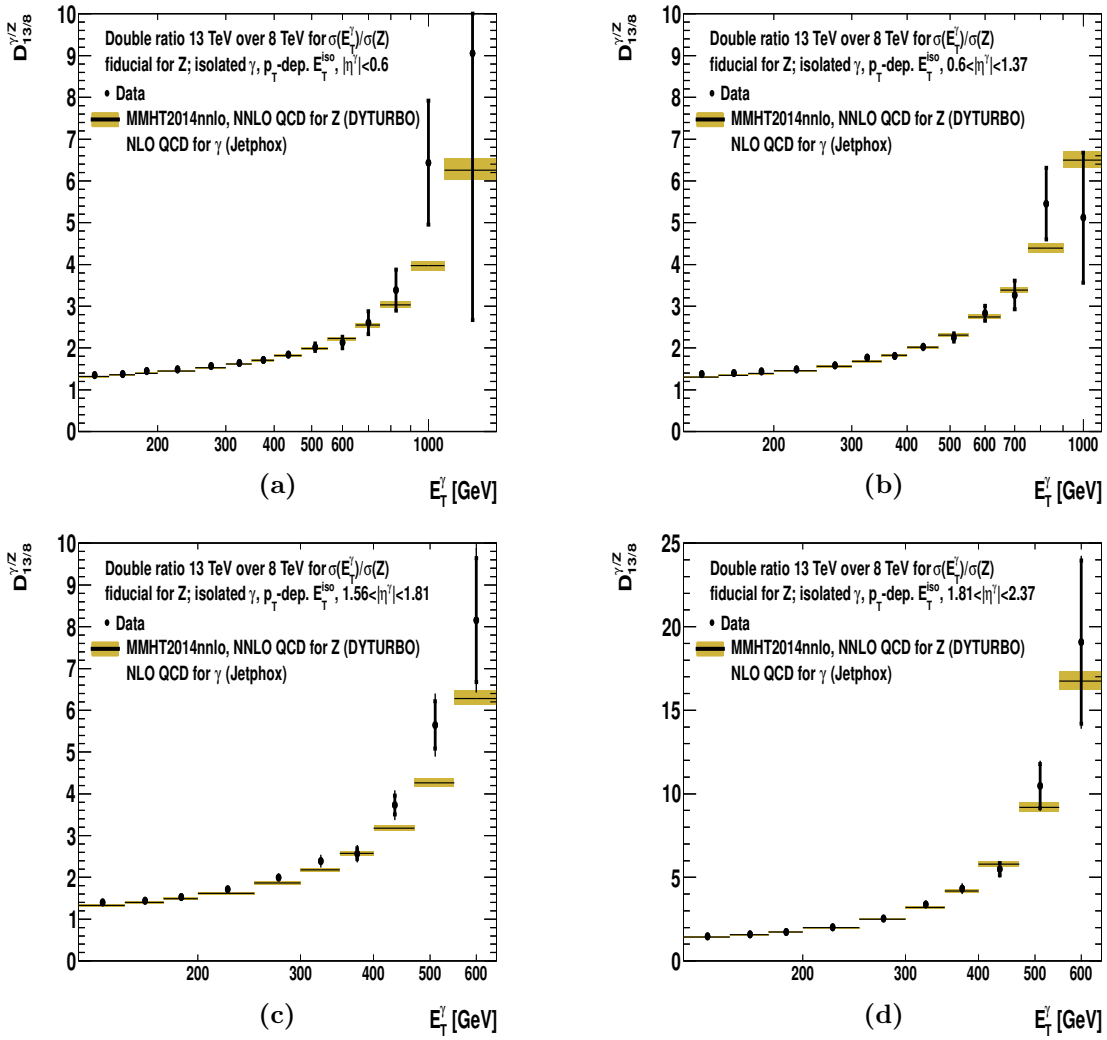


Figure 7.37: Measured $D_{13/8}^{\gamma/Z}$ as a function of E_{T}^{γ} in (a) $|\eta^{\gamma}| < 0.6$, (b) $0.6 < |\eta^{\gamma}| < 1.37$, (c) $1.56 < |\eta^{\gamma}| < 1.81$ and (d) $1.81 < |\eta^{\gamma}| < 2.37$. The predictions (black lines) using the MMHT2014nnlo PDFs are also shown. The inner (outer) error bars represent the statistical uncertainties (the statistical and systematic uncertainties added in quadrature). The shaded band represents the theoretical uncertainty on the predictions. For most of the points, the error bars are smaller than the marker size and, thus, not visible.

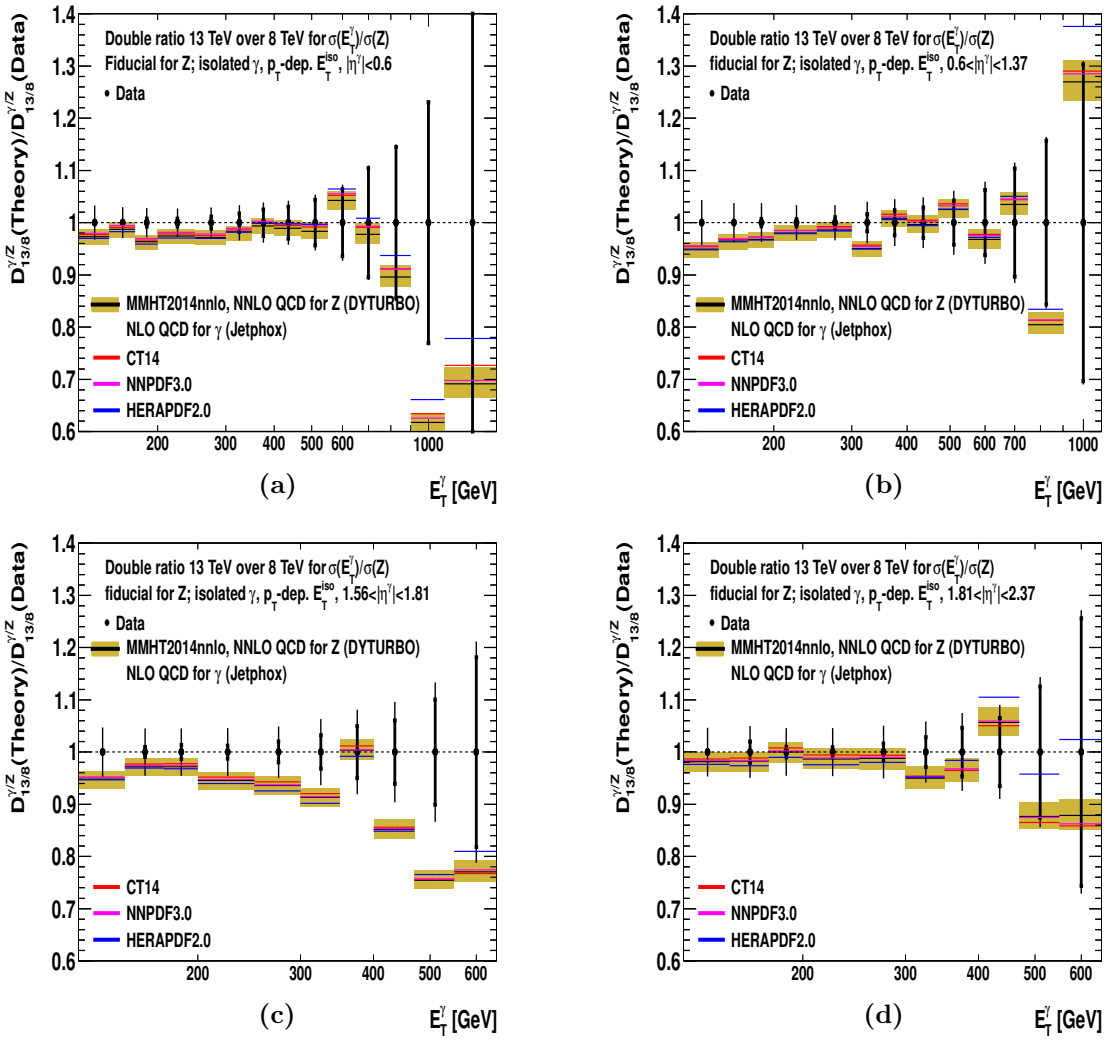


Figure 7.38: The ratio $D^{\gamma/Z}_{13/8}$(Theory)/$D^{\gamma/Z}_{13/8}$(Data) as a function of E^{γ}_{T} in (a) $|\eta^{\gamma}| < 0.6$, (b) $0.6 < |\eta^{\gamma}| < 1.37$, (c) $1.56 < |\eta^{\gamma}| < 1.81$ and (d) $1.81 < |\eta^{\gamma}| < 2.37$. The predictions using the MMHT2014nnlo, CT14nnlo, NNPDF3.0nnlo and HERAPDF2.0nnlo PDFs are shown. The inner (outer) error bars represent the statistical uncertainties (the statistical and systematic uncertainties added in quadrature). The shaded band represents the theoretical uncertainty on the predictions.

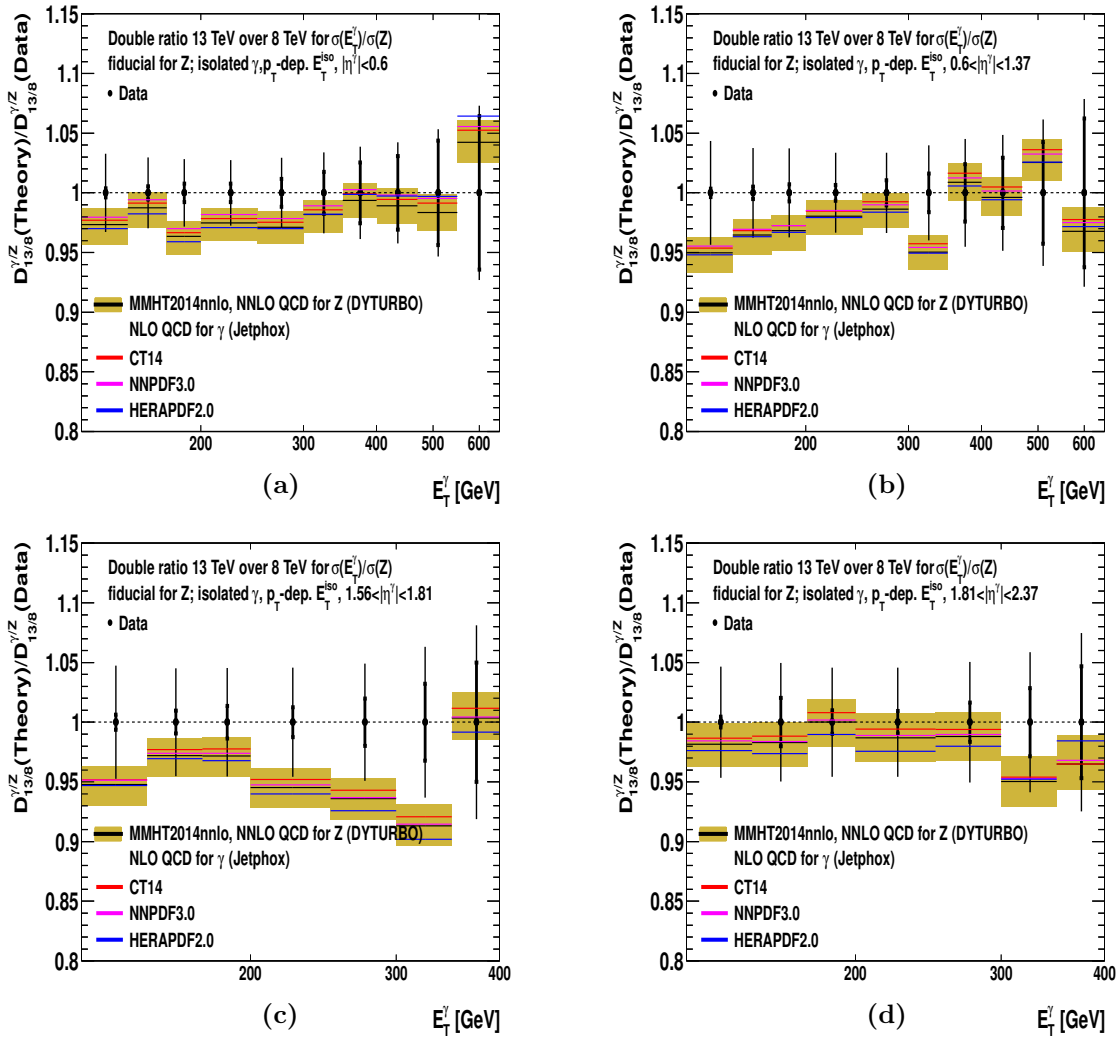


Figure 7.39: The ratio $D^{\gamma/Z}_{13/8}$(Theory)/$D^{\gamma/Z}_{13/8}$(Data) as a function of E^{γ}_{T} in (a) $|\eta^{\gamma}| < 0.6$, (b) $0.6 < |\eta^{\gamma}| < 1.37$, (c) $1.56 < |\eta^{\gamma}| < 1.81$ and (d) $1.81 < |\eta^{\gamma}| < 2.37$. The predictions using the MMHT2014nnlo, CT14nnlo, NNPDF3.0nnlo and HERAPDF2.0nnlo PDFs are shown. The inner (outer) error bars represent the statistical uncertainties (the statistical and systematic uncertainties added in quadrature). The shaded band represents the theoretical uncertainty on the predictions.

8

Measurement of the cross section for isolated-photon plus jet production

In this chapter, a study of the dynamics of isolated-photon production in association with a jet in pp collisions at a centre-of-mass energy of 13 TeV performed with the ATLAS detector with an integrated luminosity of 3.2 fb^{-1} is presented [30]. Photons were required to have transverse energies above 125 GeV. Jets were identified using the anti-k_t algorithm with radius parameter $R = 0.4$ and required to have transverse momenta above 100 GeV. The cross-section measurements were presented as functions of the leading photon transverse energy, the leading jet transverse momentum, the angular separation in azimuth between the photon and the jet, the photon-jet invariant mass and the scattering angle in the photon-jet centre-of-mass system. The tree-level plus parton-shower predictions from Sherpa and Pythia as well as NLO QCD predictions from JetPhox and Sherpa were compared to the measurements.

8.1 Data selection

The data selection, trigger requirements, event selection and photon selection for this analysis follow the same strategy as explained in Section 6.1. Also the corrections to the MC simulations are the ones mentioned in Section 6.1.4. The jet selection is explained below.

8.1.1 Jet selection

Jets were reconstructed using the anti-k_t algorithm [128] with radius parameter $R = 0.4$ using as input positive-energy topological clusters of calorimeter cell energies. The jet four-momentum calibration following a EM+GSC scheme and jet reconstruction are explained in Chapter 5. The jet selection criteria were:

- the event was rejected if there was at least one jet above $p_{\mathrm{T}}^{\mathrm{jet}} > 60$ GeV not fulfilling jet quality criteria. These criteria were applied to suppress background jets coming from beam-gas events, beam-halo events, cosmic-ray muons overlapping in-time with collision events or calorimeter noise. The discrimination between collisions and background jet candidates is based on several pieces of experimental information, including the quality of the energy reconstruction at the cell level, jet energy deposits in the direction of the shower development, and reconstructed tracks matched to the jets;

- events with at least one jet candidate with $|y^{\text{jet}}| < 2.37$ were selected;
- if the jet axis lay within a cone of radius $R = 0.8$ around the photon candidate, the jet was discarded. This requirement avoids contributions from the jet to the isolation transverse energy of the photon and the selection of jets with singular shapes (different from a cone) for which the calibration scheme is not valid;
- the event was retained if the jet with the highest transverse energy (leading jet) had $p_{\text{T}}^{\text{jet}} > 100$ GeV. A lower threshold for jets than for the photon was chosen to avoid infrared sensitivity in the calculations if the same cuts for the photon and the jet are applied [127].

8.1.2 Data sample

Figures 8.1 and 8.2 show the measured distributions as functions of the leading-photon transverse energy (E_{T}^{γ}), the leading-photon pseudorapidity (η^{γ}), the absolute value of the leading-photon pseudorapidity ($|\eta^{\gamma}|$) and the leading-photon azimuthal angle (ϕ^{γ}) as well as of the leading-jet transverse momentum ($p_{\text{T}}^{\text{jet}-\text{lead}}$), the leading-jet rapidity ($y^{\text{jet}-\text{lead}}$), the absolute value of the leading-jet rapidity ($|y^{\text{jet}-\text{lead}}|$) and the leading-jet azimuthal angle ($\phi^{\text{jet}-\text{lead}}$) for the selected photon+jet sample. Figure 8.3 shows the measured distributions as functions of the absolute value of the difference in rapidity between the leading photon and the leading jet ($|\Delta\eta^{\gamma-\text{jet lead}}| \equiv |\eta^{\gamma} - y^{\text{jet}-\text{lead}}|$) and the azimuthal angle between the leading photon and the leading jet ($\Delta\phi^{\gamma-\text{jet lead}} \equiv |\phi^{\gamma} - \phi^{\text{jet}-\text{lead}}|$) for the selected photon+jet sample. The distribution on the number of jets (N_{jets}) is shown in Figure 8.4. The simulations of Sherpa and Pythia are compared to the data in these figures and are normalised to the data.

For the measurements of the cross sections as functions of the invariant mass of the leading-photon and leading-jet system ($m^{\gamma-\text{jet}}$) and $|\cos\theta^{\star}|$, additional requirements were imposed to remove the bias due to the rapidity and transverse-momentum cuts on the photon and the jet. To perform unbiased measurements for $m^{\gamma-\text{jet}}$ and $|\cos\theta^{\star}|$, the additional requirements $|\eta^{\gamma} + y^{\text{jet}-\text{lead}}| < 2.37$, $|\eta^{\gamma} - y^{\text{jet}-\text{lead}}| < 2.37$ (or equivalently $|\cos\theta^{\star}| < 0.83$) and $m^{\gamma-\text{jet}} > 450$ GeV were imposed. The first two requirements avoid the bias induced by cuts on η^{γ} and $y^{\text{jet}-\text{lead}}$, yielding slices of $\cos\theta^{\star}$ with the same length along the $\eta^{\gamma} + y^{\text{jet}-\text{lead}}$ axis (see Figure 8.5(a)). The diagonal slices show the different possible values of $|\cos\theta^{\star}|$. The dashed line shows the limitation of the new phase-space in which all slices have the same length. The third requirement avoids the bias due to the $E_{\text{T}}^{\gamma} > 125$ GeV cut, which can be seen in the $|\cos\theta^{\star}| - m^{\gamma-\text{jet}}$ plane (see Figure 8.5(b)). In the limit of back-to-back massless particles, the lower bound of the invariant mass of the photon-jet system can be written as $m^{\gamma-\text{jet}} = 2 \cdot E_{\text{T}}^{\gamma} / \sin\theta^{\star}$. The minimum allowed value is obtained from the minimum value of $E_{\text{T}}^{\gamma} = 125$ GeV and the maximum value of $\cos\theta^{\star} = 0.83$, which gives a rounded value of 450 GeV. The unbiased kinematic region is shown as a shaded blue area in Figure 8.5. The $\cos\theta^{\star}$ and $m^{\gamma-\text{jet}}$ measured distributions in the unbiased kinematic region are shown in Figure 8.6.

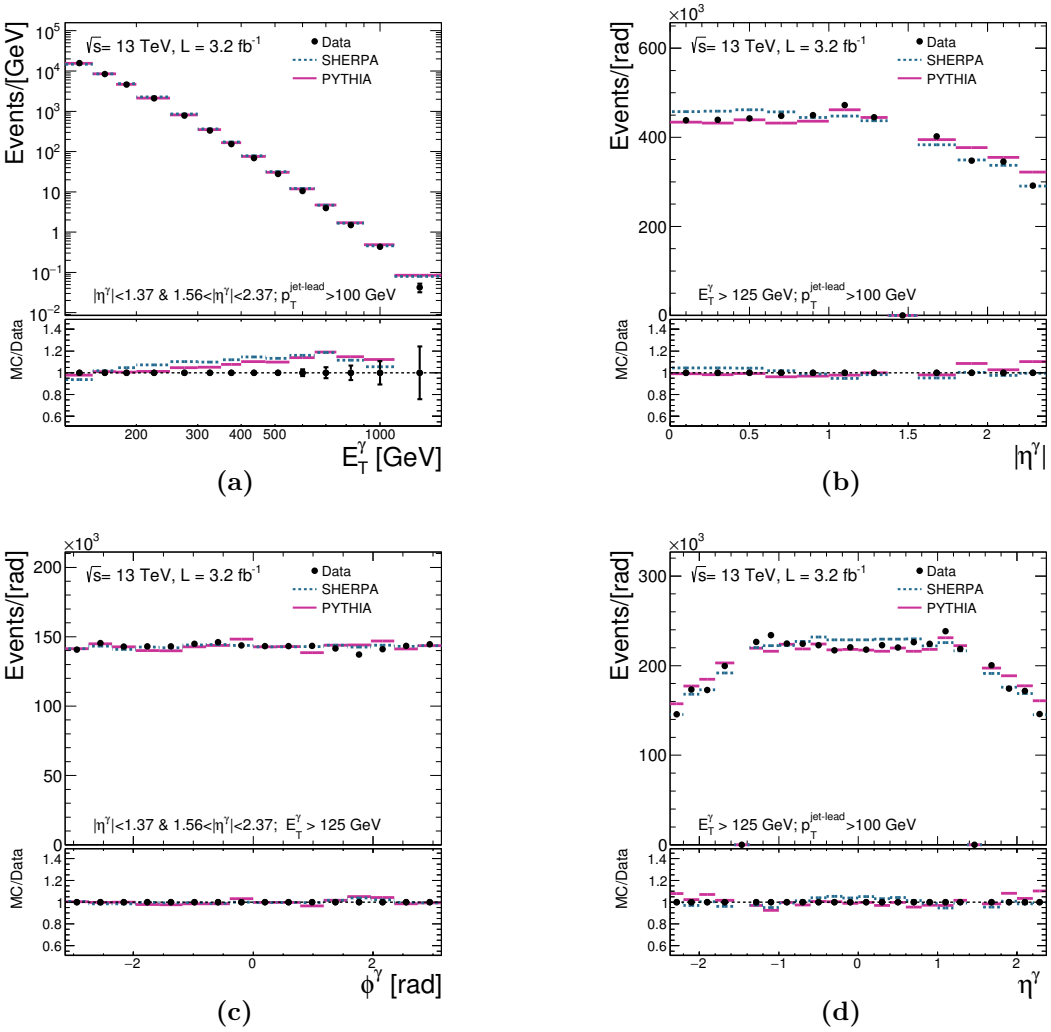


Figure 8.1: The measured (a) E_{T}^{γ}, (b) $|\eta^{\gamma}|$, (c) ϕ^{γ} and (d) η^{γ} distributions for the leading photon in the photon+jet selected sample divided by the bin width (dots). The measured distributions include background, which has not been subtracted. For comparison, the MC simulations of the signal from Pythia (solid histograms) and Sherpa (dashed histograms) are also included. The MC distributions are normalised to the data. The lower part of the figure shows the ratio of the MC and data distributions.

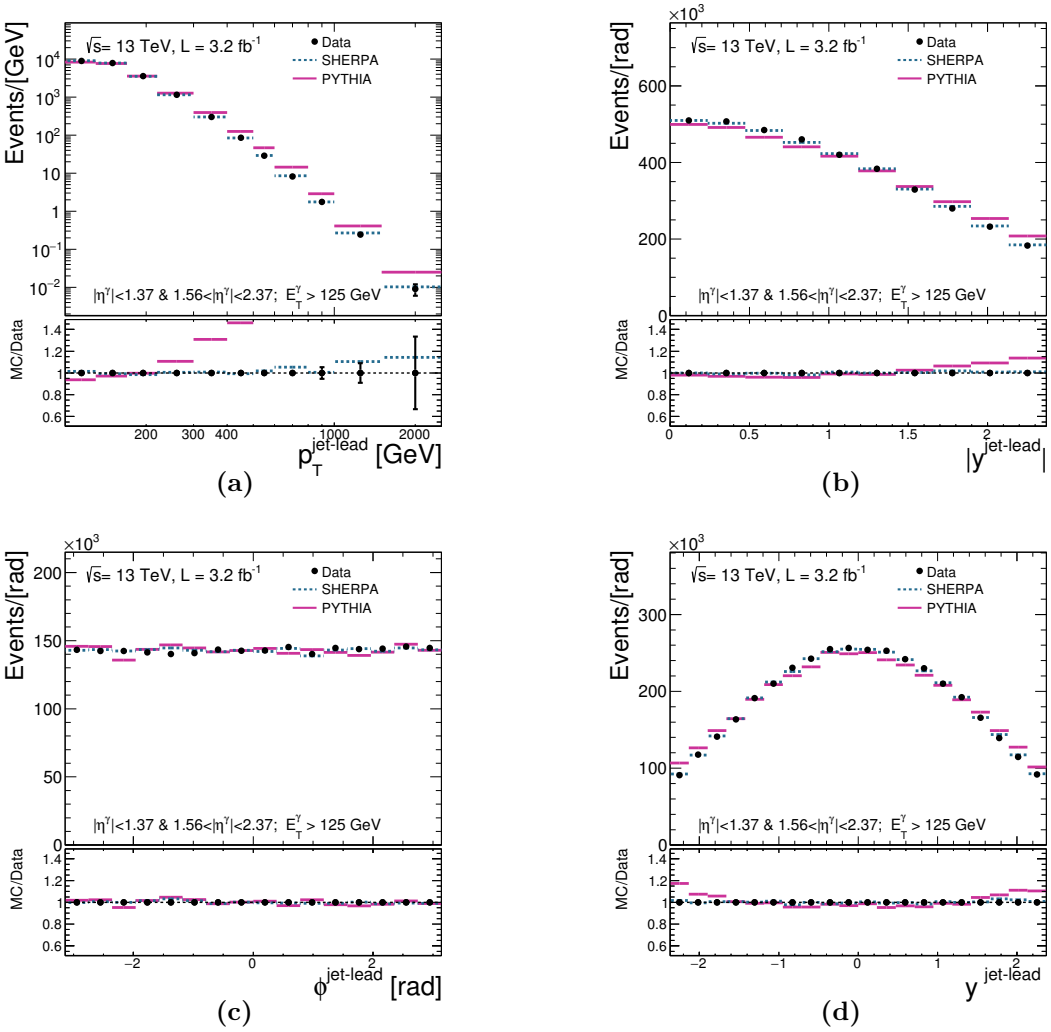


Figure 8.2: The measured (a) $p_{\mathrm{T}}^{\mathrm{jet-lead}}$, (b) $|y^{\mathrm{jet-lead}}|$, (c) $\phi^{\mathrm{jet-lead}}$ and (d) $y^{\mathrm{jet-lead}}$ distributions for the leading jet in the photon+jet selected sample divided by the bin width (dots). The measured distributions include background, which has not been subtracted. For comparison, the MC simulations of the signal from Pythia (solid histograms) and Sherpa (dashed histograms) are also included. The MC distributions are normalised to the data. The lower part of the figure shows the ratio of the MC and data distributions.

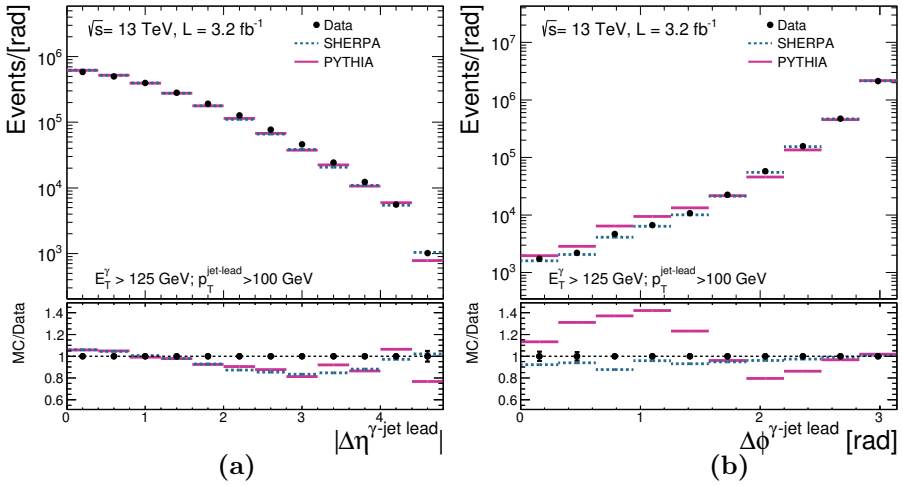


Figure 8.3: The measured (a) $|\Delta\eta^{\gamma-\text{jet lead}}|$ and (b) $\Delta\phi^{\gamma-\text{jet lead}}$ distributions in the photon+jet selected sample divided by the bin width (dots). The measured distributions include background, which has not been subtracted. For comparison, the MC simulations of the signal from Pythia (solid histograms) and Sherpa (dashed histograms) are also included. The MC distributions are normalised to the data. The lower part of the figure shows the ratio of the MC and data distributions.

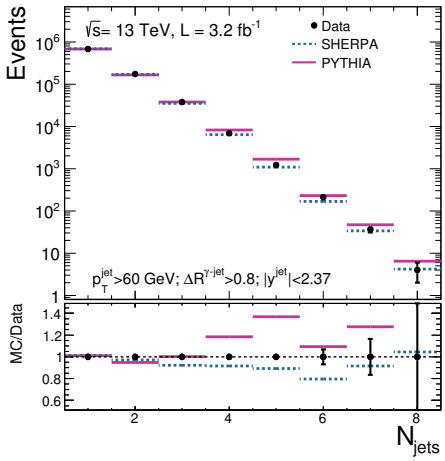
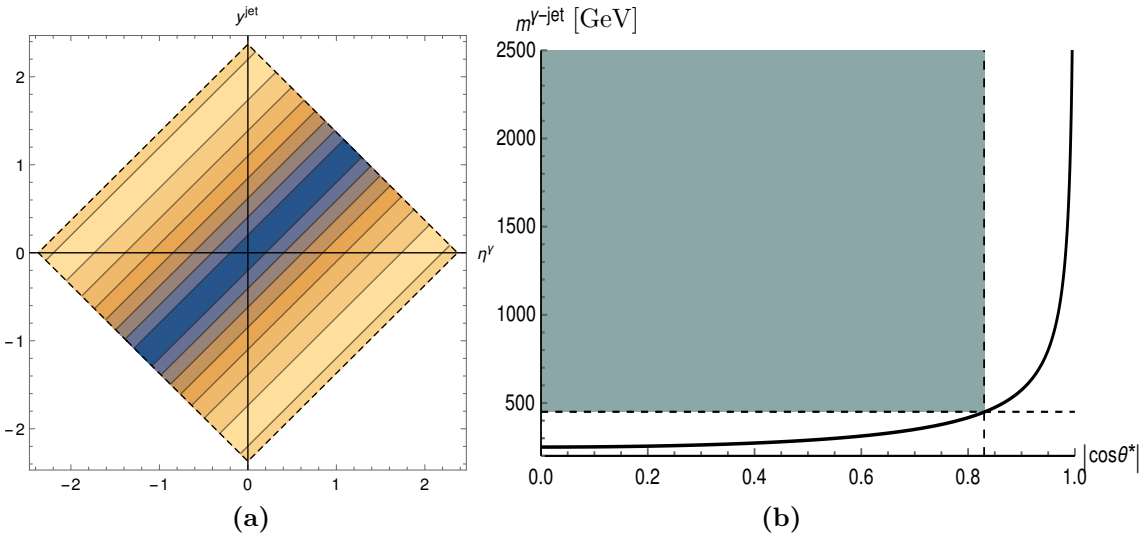
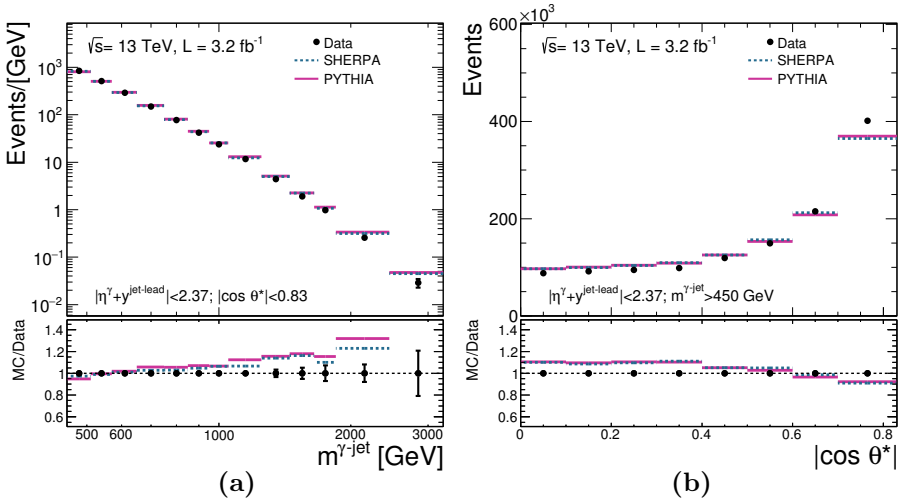


Figure 8.4: Distribution of the number of jets (N_{jets}) in the photon+jet selected sample (dots). The measured distributions include background, which has not been subtracted. For comparison, the MC simulations of the signal from Pythia (solid histograms) and Sherpa (dashed histograms) are also included. The MC distributions are normalised to the data. The lower part of the figure shows the ratio of the MC and data distributions.



(a) (b)

Figure 8.5: The selected regions in the (a) η^{γ}-y^{jet} and (b) $m^{\gamma-\text{jet}}$-$|\cos\theta^{\star}|$ planes. In (a), the dashed lines correspond to: $\eta^{\gamma} + y^{\text{jet}} = 2.37$ (first quadrant), $\eta^{\gamma} - y^{\text{jet}} = 2.37$ (second quadrant), $\eta^{\gamma} + y^{\text{jet}} = -2.37$ (third quadrant) and $\eta^{\gamma} - y^{\text{jet}} = -2.37$ (fourth quadrant). In (b), the horizontal (vertical) dashed lines delimiting the blue shaded rectangle correspond to $m^{\gamma-\text{jet}} = 450$ GeV ($|\cos\theta^{\star}| = 0.83$) and the solid line corresponds to the lower bound of the invariant mass of the photon-jet system for $E_{\text{T}}^{\gamma} = 125$ GeV.



(a) (b)

Figure 8.6: The measured (a) $m^{\gamma-\text{jet}}$ and (b) $|\cos\theta^{\star}|$ distributions divided by the bin width (dots). The measured distributions include background, which has not been subtracted. For comparison, the MC simulations of the signal from Pythia (solid histograms) and Sherpa (dashed histograms) are also included. The MC distributions are normalised to the data. The lower part of the figure shows the ratio of the MC and data distributions.

8.1.3 Trigger efficiency

The trigger requirements and efficiency were computed in the same way as in the inclusive photon analysis (see Section 6.2). The resulting efficiencies of the HLT_g120_loose trigger for the selected photon+jet sample are:

- tight and isolated selection: $> 99.4\%$ (signal region);
- tight and non-isolated selection: $> 98.4\%$;
- non-tight and isolated selection: $> 98.3\%$;
- non-tight and non-isolated: $> 97.5\%$.

The above four selected samples correspond to the regions A, B, C and D, respectively, of the data-driven background-subtraction method; the details can be found in Section 6.3. The number of events in the signal region as well as in each of the control regions for background subtraction were corrected by the trigger efficiency observed in each bin of the distribution. Figures 8.7 to 8.10 show the trigger efficiency as a function of E_{T}^{γ}, $p_{\mathrm{T}}^{\mathrm{jet-lead}}$, $m^{\gamma-\mathrm{jet}}$, $|\cos\theta^{\star}|$ and $\Delta\phi^{\gamma-\mathrm{jet}}$. An uncertainty on the trigger efficiency was evaluated taking into account the differences between data and simulations and the statistical uncertainty in data (see Figure 8.11):

- photon+jet: efficiency $= 99.70 \pm 0.02$ (stat) ± 0.21 (syst) %;
- photon+jet with additional requirements for $m^{\gamma-\mathrm{jet}}$ and $|\cos\theta^{\star}|$ distributions: efficiency $= 99.92 \pm 0.03$ (stat) ± 0.05 (syst) %.

As for the trigger-efficiency corrections, the reference trigger was the HLT_g100_loose (fully efficient at 125 GeV [108]). However, this estimation does not account for the efficiency of the "loose" requirement of the trigger. The effect of this requirement on the efficiency of HLT_g120_loose was estimated using a level-1 trigger with an E_{T} threshold of 7 GeV in the electromagnetic cluster. This study was only performed in the first two bins of the measurement as a function of E_{T}^{γ} due to the lack of statistics in the reference trigger (see Figure 8.12). The efficiency obtained in the first bin is $\approx 99\%$. This inefficiency of 1% is larger than the trigger uncertainty estimated before and so this value was taken as a systematic uncertainty on the trigger efficiency for all bins.

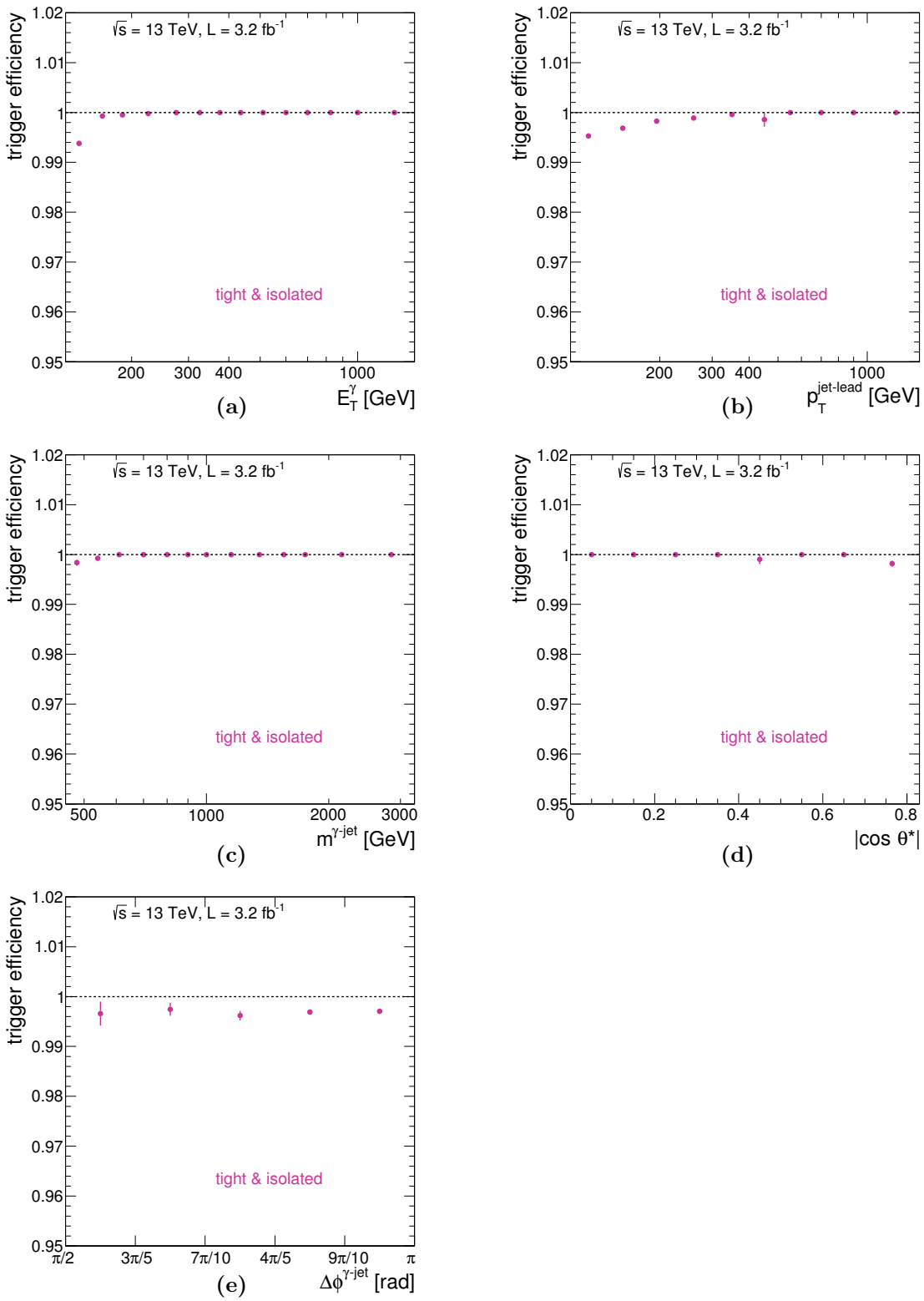


Figure 8.7: Trigger efficiency as a function of (a) E_{T}^{γ}, (b) $p_{\mathrm{T}}^{\mathrm{jet-lead}}$, (c) $m^{\gamma-\mathrm{jet}}$, (d) $|\cos\theta^{\star}|$ and (e) $\Delta\phi^{\gamma-\mathrm{jet}}$ for the tight and isolated (signal) region.

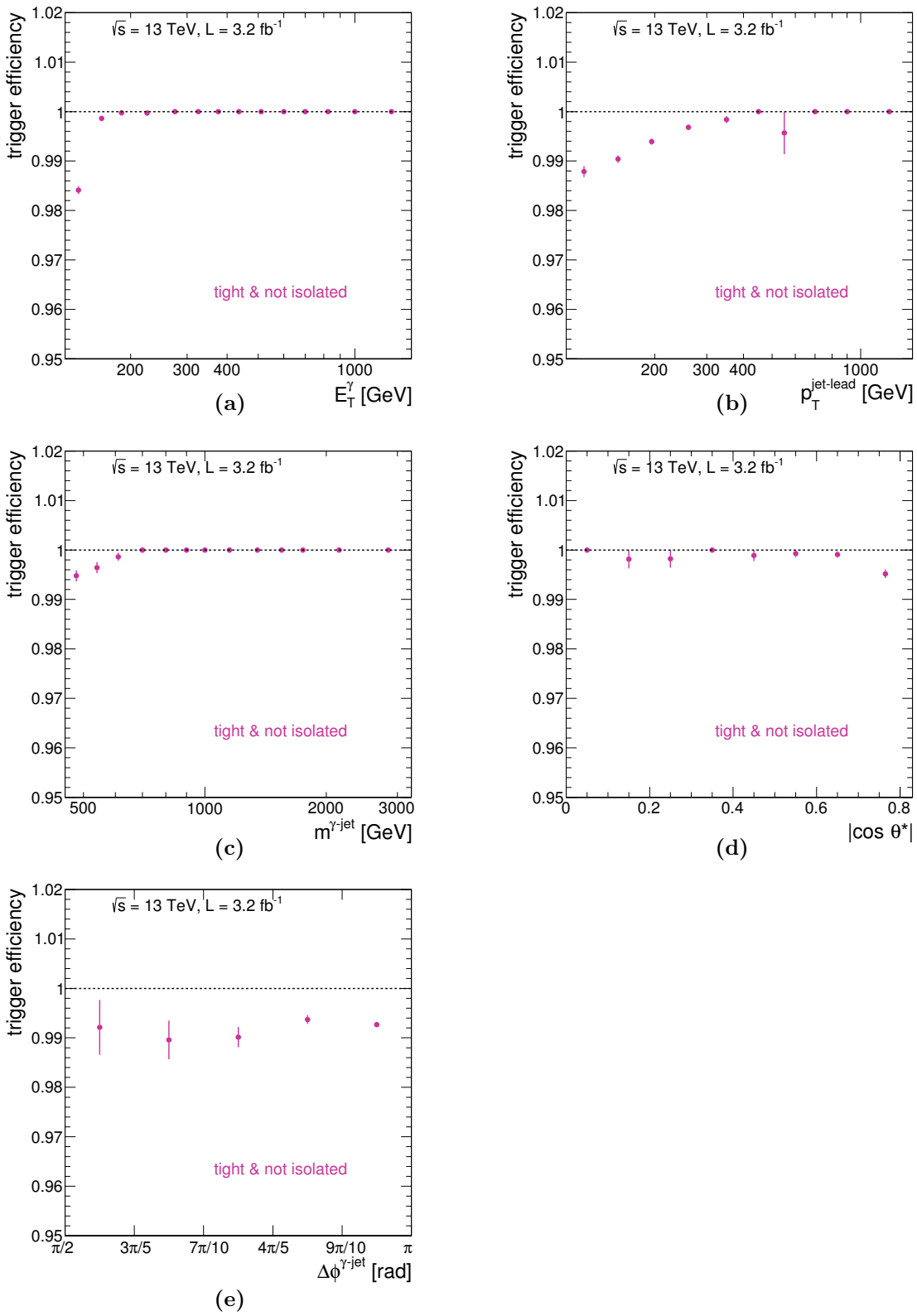


Figure 8.8: Trigger efficiency as a function of (a) E_{T}^{γ}, (b) $p_{\mathrm{T}}^{\mathrm{jet-lead}}$, (c) $m^{\gamma-\mathrm{jet}}$, (d) $|\cos\theta^{\star}|$ and (e) $\Delta\phi^{\gamma-\mathrm{jet}}$ for the tight and non-isolated region.

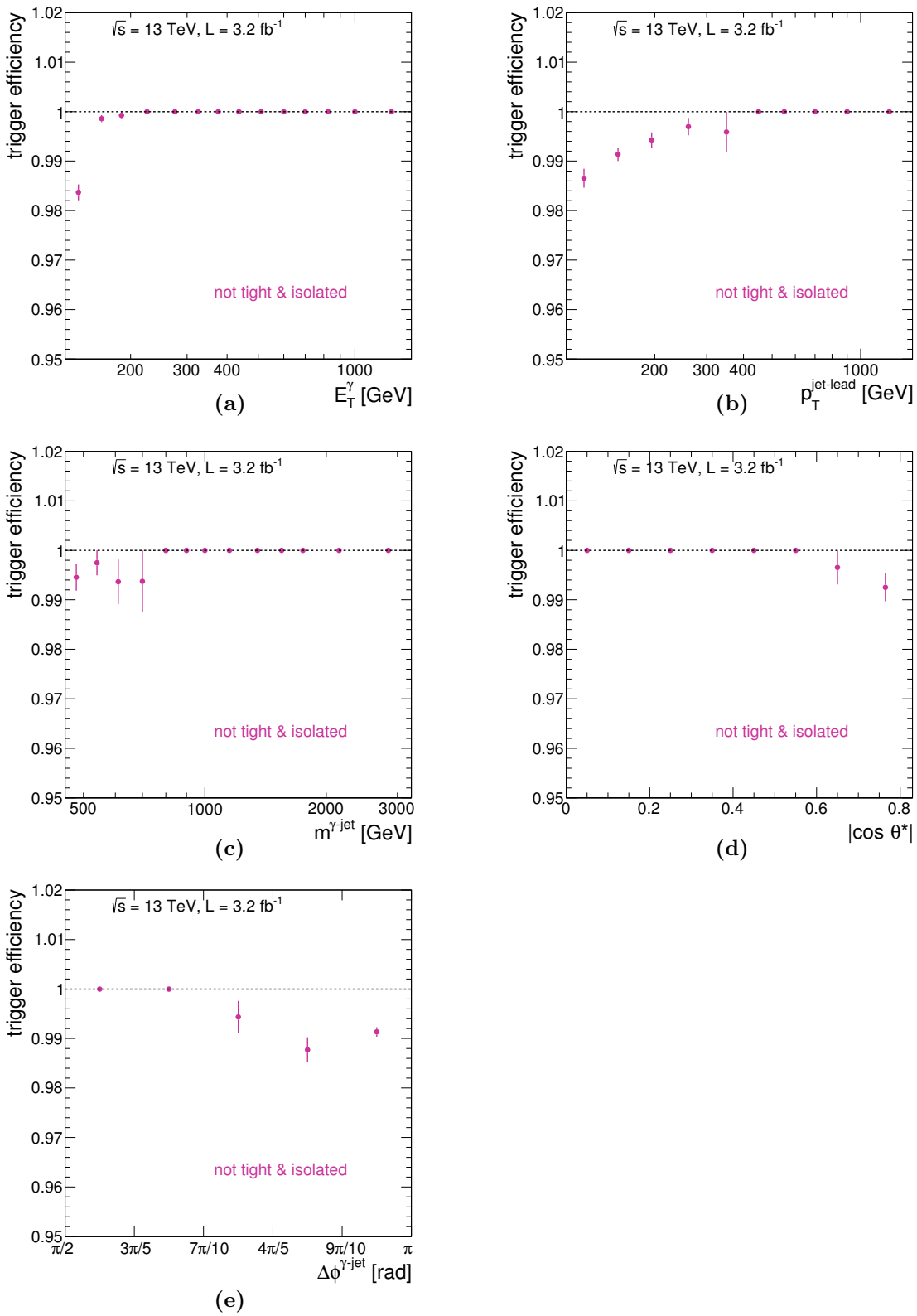


Figure 8.9: Trigger efficiency as a function of (a) E_{T}^{γ}, (b) $p_{\mathrm{T}}^{\mathrm{jet-lead}}$, (c) $m^{\gamma-\mathrm{jet}}$, (d) $|\cos\theta^{\star}|$ and (e) $\Delta\phi^{\gamma-\mathrm{jet}}$ for the non-tight and isolated region.

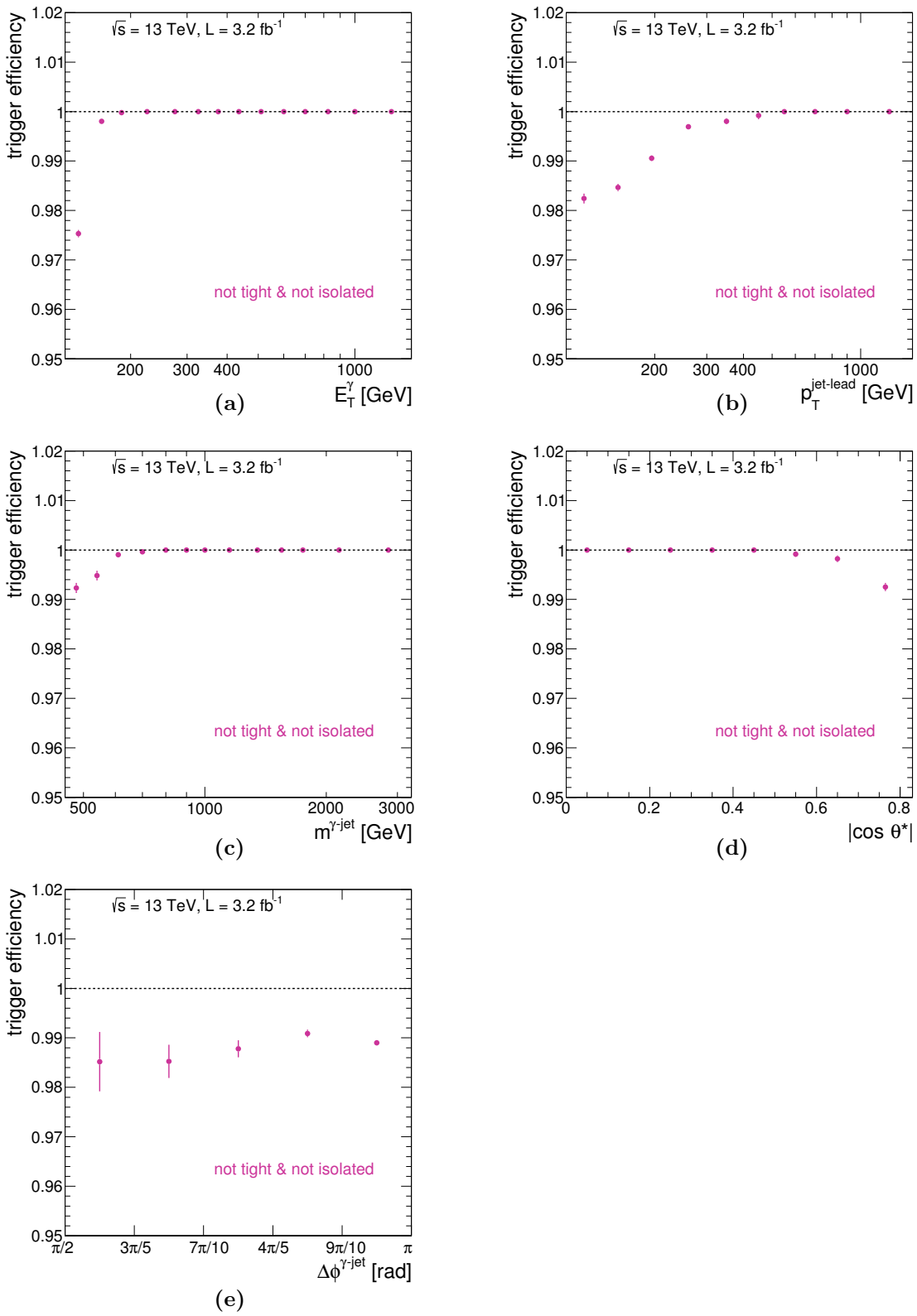


Figure 8.10: Trigger efficiency as a function of (a) E_{T}^{γ}, (b) $p_{\mathrm{T}}^{\mathrm{jet-lead}}$, (c) $m^{\gamma-\mathrm{jet}}$, (d) $|\cos\theta^{\star}|$ and (e) $\Delta\phi^{\gamma-\mathrm{jet}}$ for the non-tight and non-isolated region.

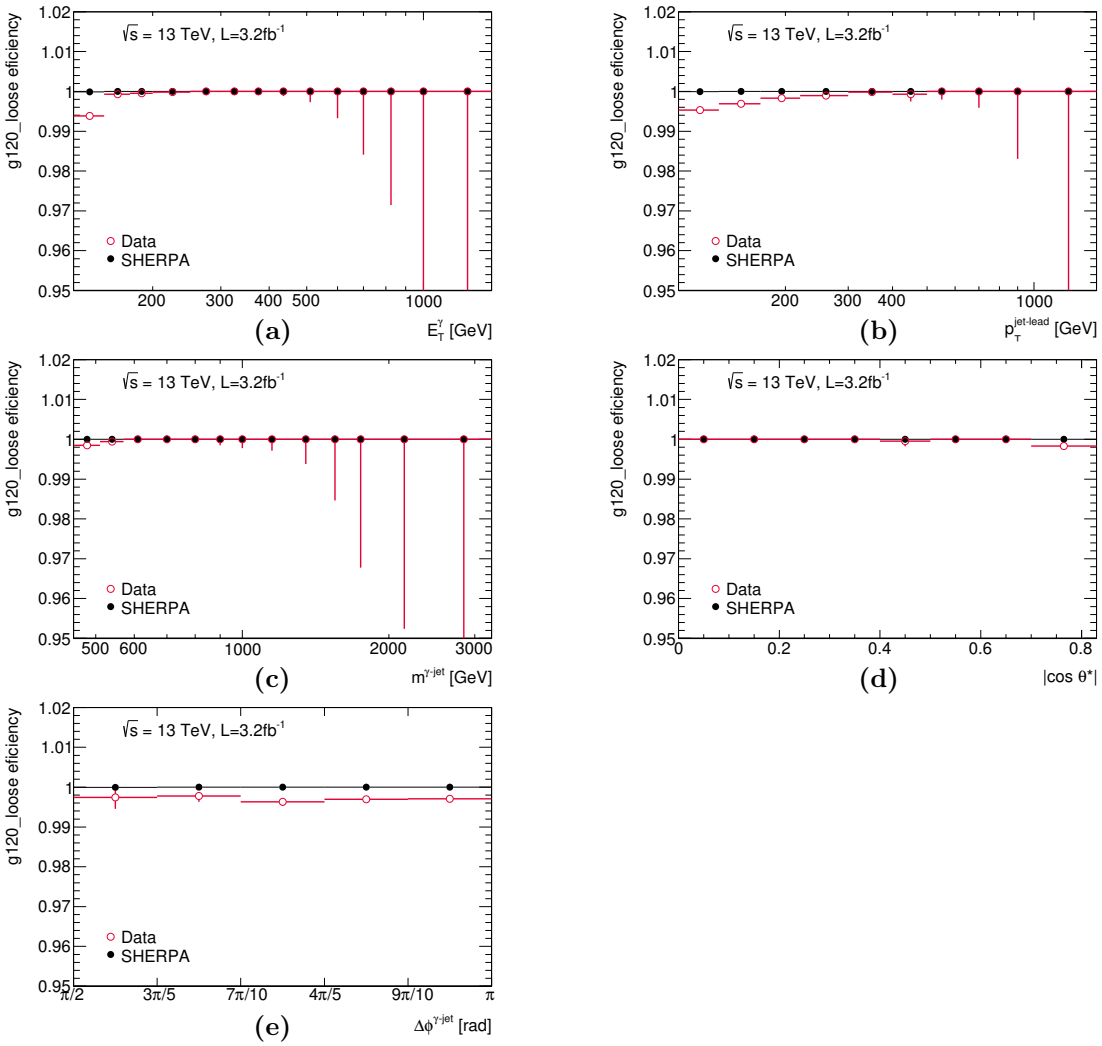


Figure 8.11: Trigger efficiency in data (red open circles) and SHERPA MC (black dots) for the selected photon candidates as a function of (a) E_{T}^{γ}, (b) $p_{\mathrm{T}}^{\mathrm{jet-lead}}$, (c) $m^{\gamma-\mathrm{jet}}$, (d) $|\cos\theta^{\star}|$ and (e) $\Delta\phi^{\gamma-\mathrm{jet}}$. The error bars display the Bayesian confidence intervals for the efficiency measured in data.

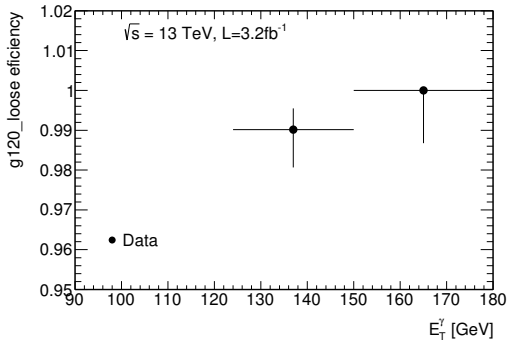


Figure 8.12: HLT_g120_loose trigger efficiency measured as a function of E_{T}^{γ} using a level-1 trigger as reference.

8.2 Background estimation and subtraction

The background-subtraction technique applied here is the same followed in the inclusive photon analysis (see Section 6.3). A comparison of the distributions in $E_{\mathrm{T}}^{\mathrm{iso}}$ for tight and non-tight photon candidates in data after the leading photon and jet selection in this analysis is needed to support the adequacy of the background control regions in the 2D-sideband method. This is shown in Figure 8.13. It was checked that, as expected, the distribution in $E_{\mathrm{T}}^{\mathrm{iso}}$ from the non-tight photon candidates in data reproduces the tail of the distribution of tight-photon candidates and that the MC simulations of signal photons exhibits a peak around $E_{\mathrm{T}}^{\mathrm{iso}} \approx 0$ GeV that reproduces the one observed in data, thanks to the data-driven corrections applied to $E_{\mathrm{T}}^{\mathrm{iso}}$ in the MC. To avoid the effect of fake photons in the simulations, a geometrical matching criteria was imposed between particle and reconstruction level with $\Delta R = 0.2$, where $\Delta R = \sqrt{(\Delta\eta)^2 + (\Delta\phi)^2}$.

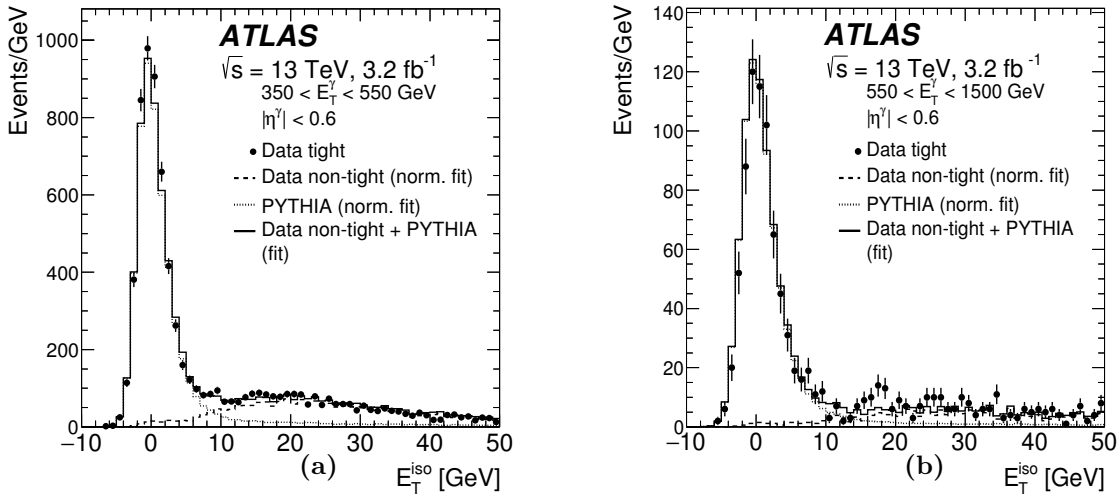


Figure 8.13: The measured $E_{\mathrm{T}}^{\mathrm{iso}}$ distribution before the isolation requirement for photon candidates passing the tight identification requirements (dots) and for those which fail the tight identification criteria (*non-tight*) (dashed histogram) in data with $|\eta^{\gamma}| < 0.6$ for $350 < E_{\mathrm{T}}^{\gamma} < 550$ GeV (a) and $350 < E_{\mathrm{T}}^{\gamma} < 1500$ GeV (b). The MC simulations of the signal using Pythia is also shown (dotted histogram). The solid histogram is the sum of the contributions of the MC simulation of the signal using Pythia and that of the non-tight photon candidates normalised according to a χ^2 fit that provides the best description of the $E_{\mathrm{T}}^{\mathrm{iso}}$ distribution of tight photon candidates.

The expected fraction of signal events in the three background control regions, extracted from the MC, are shown in Figures 8.14 and 8.15. The fraction ϵ_C, which represents the signal leaking into the non-tight and isolated control region, is approximately constant for all observables and around $0.02 - 0.03$ and very similar for Pythia and Sherpa. The fraction ϵ_B, the signal leakage into the tight and non-isolated control region, is smaller for Sherpa than Pythia and can be explained in terms of how the bremsstrahlung component is simulated in Pythia and Sherpa. The fraction ϵ_D, the signal leakage into the non-tight non-isolated control region, is very different for Pythia and Sherpa, also affected by the different treatment of the bremsstrahlung component in both models. The fractions ϵ_B and ϵ_D grow as functions of some of the observables, most

noticeably for $p_{\mathrm{T}}^{\mathrm{jet-lead}}$, due to the increasing fraction of the bremsstrahlung component as $p_{\mathrm{T}}^{\mathrm{jet-lead}}$ increases.

The signal purity, computed as $P = N_A^{\mathrm{sig}}/N_A$, is shown in Figure 8.16 for the PYTHIA and SHERPA MC samples. For some of the points at high E_{T}^{γ}, $p_{\mathrm{T}}^{\mathrm{jet-lead}}$ or $m^{\gamma-\mathrm{jet}}$ in which the purity is above unity (due to lack of statistics in the background control regions) or consistent with unity but with a large statistical uncertainty, the purity was set to unity. The purity is $\gtrsim 90\%$ and very similar for the estimation using either PYTHIA or SHERPA to compute the signal leakage fractions.

As shown in Figures 8.1 to 8.3, the default description of tight and isolated photon candidates before background subtraction by PYTHIA fails to describe some of the observables; especially $p_{\mathrm{T}}^{\mathrm{jet-lead}}$, $\Delta\phi^{\gamma-\mathrm{jet}}$ and $m^{\gamma-\mathrm{jet}}$. Since the signal purity is high, the description of PYTHIA is not expected to improve significantly after background subtraction. Therefore, it would not be adequate to perform the final background estimation with the default description of the signal by PYTHIA. Hence, the description of the signal by PYTHIA was optimised by changing the simulated fractions of hard and bremsstrahlung photons (see next Section). The fraction of bremsstrahlung photons are shown in Figure 8.17.

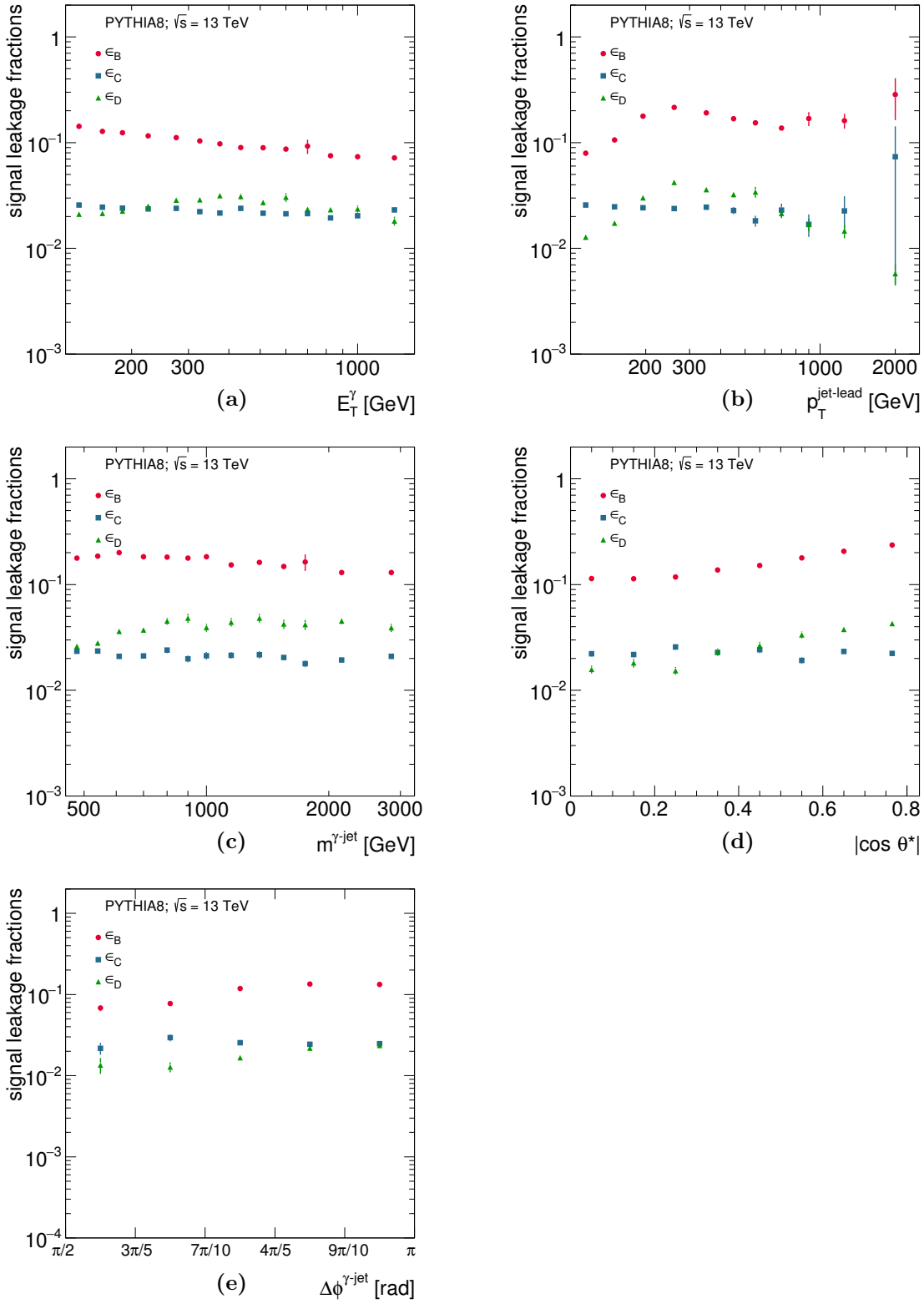


Figure 8.14: Signal leakage fractions from PYTHIA default for the B (dots), C (squares) and D (triangles) control regions as functions of the observables studied.

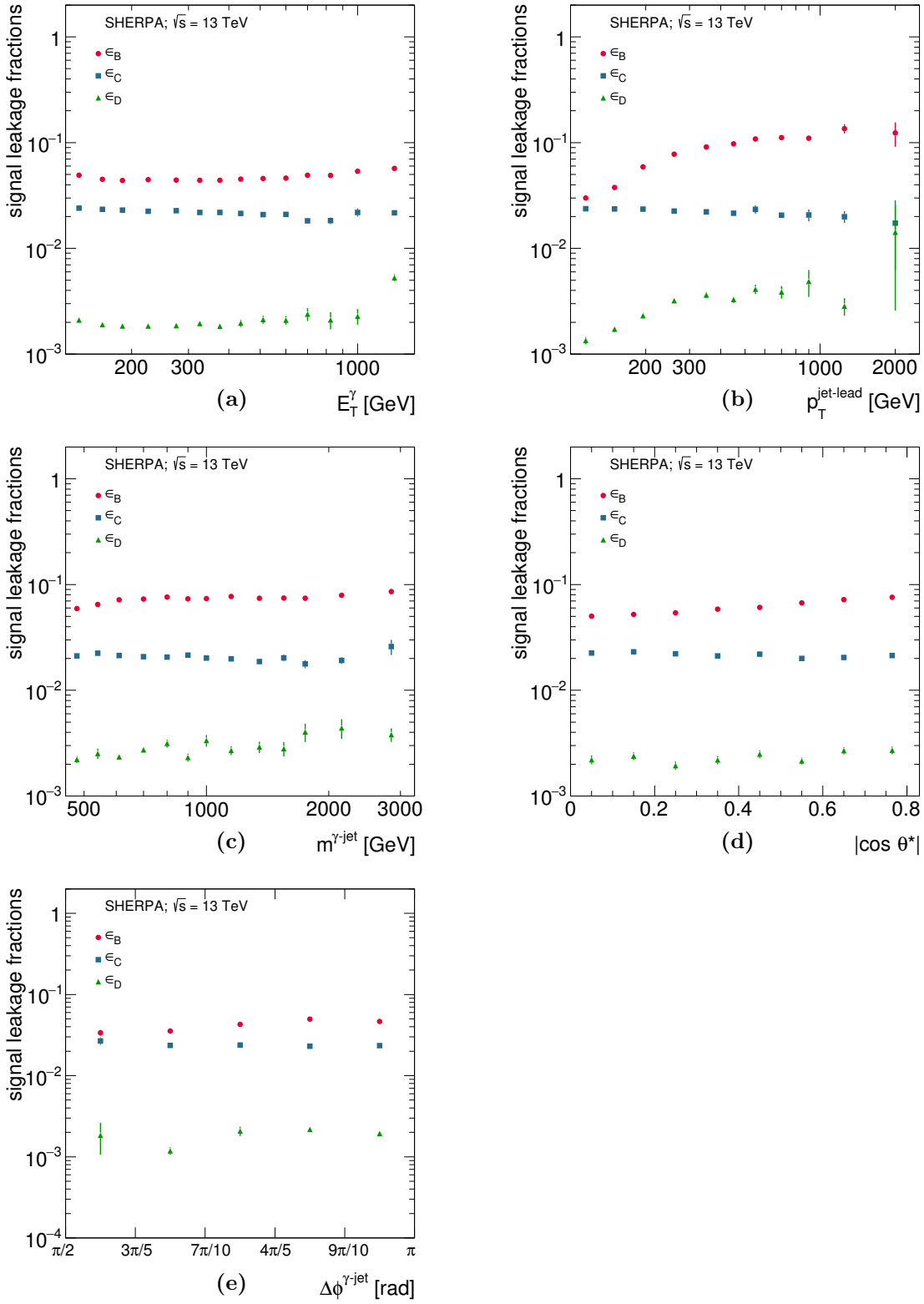


Figure 8.15: Signal leakage fractions from SHERPA default for the B (dots), C (squares) and D (triangles) control regions as functions of the observables studied.

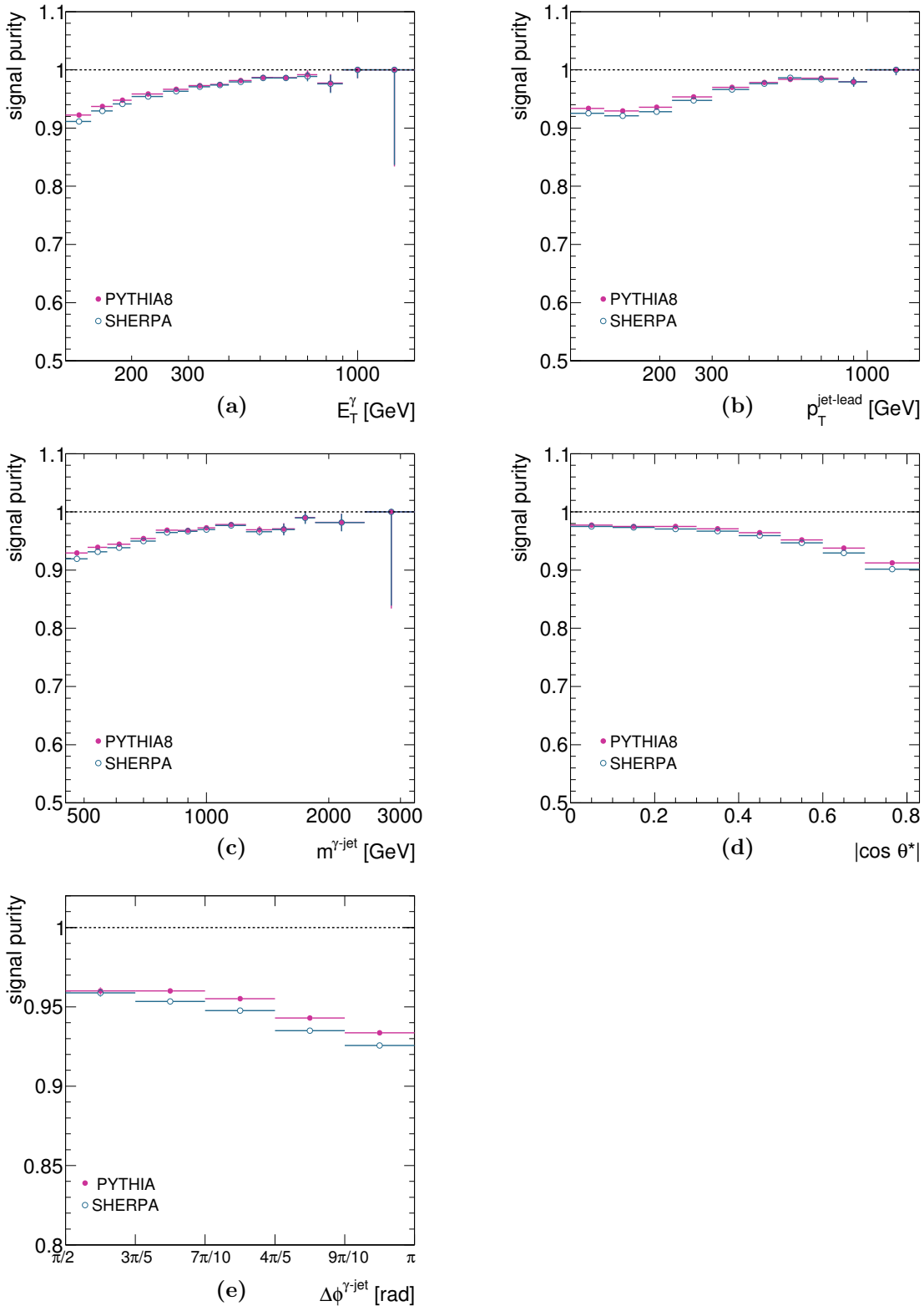


Figure 8.16: Estimated signal purities in data using signal leakage fractions from PYTHIA (dots) and SHERPA (open circles) as functions of (a) E_{T}^{γ}, (b) $p_{\mathrm{T}}^{\mathrm{jet-lead}}$, (c) $m^{\gamma-\mathrm{jet}}$, (d) $|\cos\theta^{\star}|$ and (e) $\Delta\phi^{\gamma-\mathrm{jet}}$.

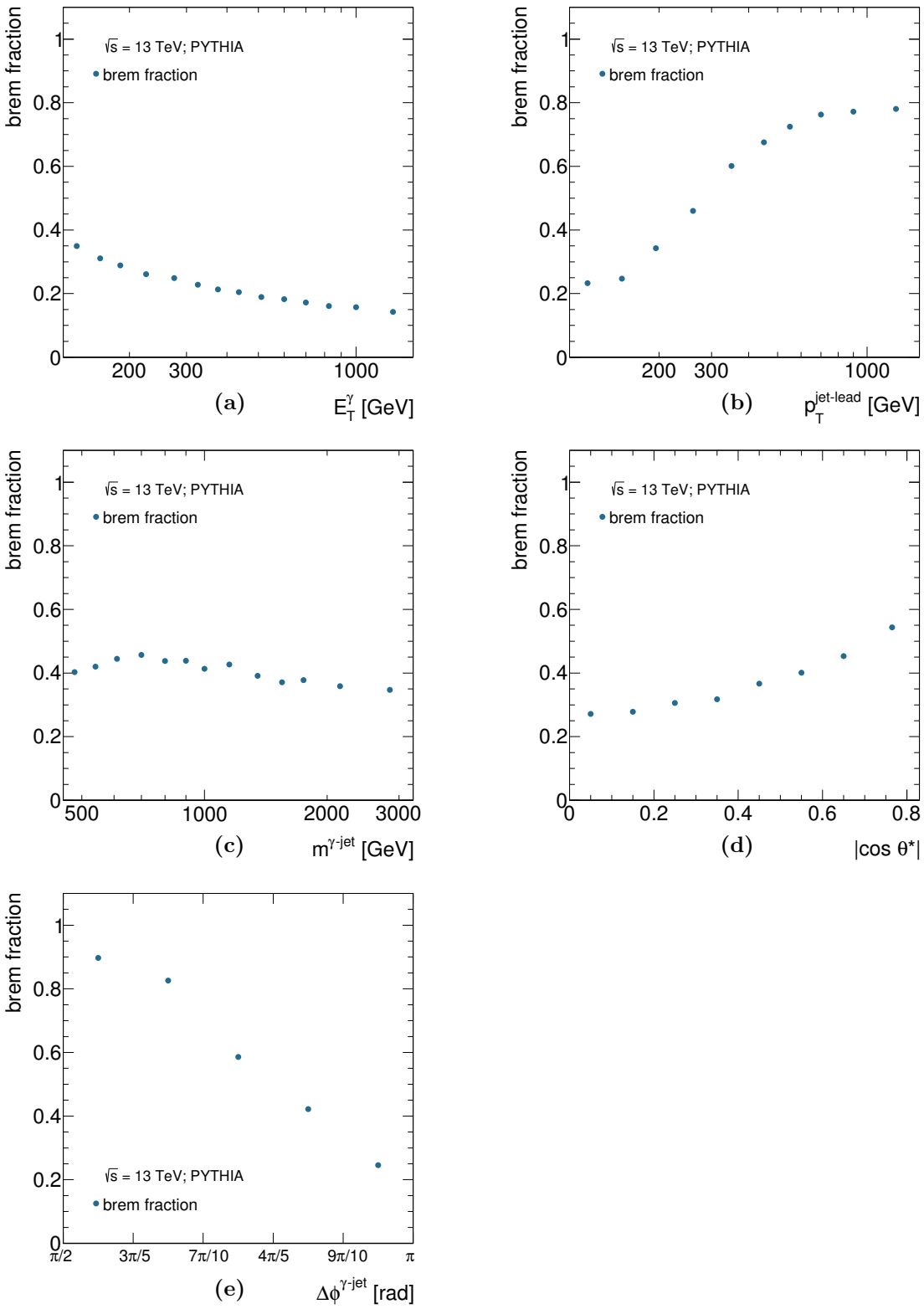


Figure 8.17: The fraction of the bremsstrahlung component in PYTHIA default (dots) as a function of (a) E_{T}^{γ}, (b) $p_{\mathrm{T}}^{\mathrm{jet-lead}}$, (c) $m^{\gamma-\mathrm{jet}}$, (d) $|\cos\theta^{\star}|$ and (e) $\Delta\phi^{\gamma-\mathrm{jet}}$.

8.2.1 Optimisation of the MC description

To study in more detail the success or failure of the PYTHIA MC simulations to describe the data distributions, Figure 8.18 shows, in addition to the full MC distributions, the individual hard and bremsstrahlung PYTHIA contributions. It is observed that the shape of these two components is quite different for the observables studied. Therefore, the shape of the MC distributions depends on the relative fraction of these two contributions. An improvement of the description of the data by the PYTHIA MC was achieved by performing a χ^2 fit to each data distribution of the relative fraction of the hard (α) and the bremsstrahlung ($1-\alpha$) contributions as the free parameter; $\alpha = 0.5$ reproduces the original prediction of PYTHIA. The χ^2 function used is

$$\chi^2(\alpha) = \sum_i \left(\frac{N_A^{\rm sig}(i) - N_A^{\rm MC}(i,\alpha)}{\Delta N_A^{\rm sig}(i)} \right)^2 ,$$

where the sum runs over the bins of a given distribution (i being the bin index), $\Delta N_A^{\rm sig}(i)$ is the statistical uncertainty in the data signal yield in bin i,

$$N_A^{\rm MC}(i,\alpha) = \frac{N_A^{\rm sig,TOT}}{\alpha\ N_A^{\rm MC,H,TOT} + (1-\alpha)\ N_A^{\rm MC,B,TOT}} \left(\alpha\ N_A^{\rm MC,H}(i) + \ (1-\alpha)\ N_A^{\rm MC,B}(i) \right)$$

and α is the free parameter in the fit[1]. The other symbols used are defined as follows: $N_A^{\rm MC,H}(i)$ ($N_A^{\rm MC,B}(i)$) is the number of simulated events from the hard (bremsstrahlung) component in bin i; $N_A^{\rm MC,H,TOT}$ ($N_A^{\rm MC,B,TOT}$) is the total number of simulated events from the hard (bremsstrahlung) component; $N_A^{\rm sig,TOT}$ is the total signal yield in data. The optimisation was done in two steps. In the first step, the distributions of the signal yield in data using the leakage fractions from PYTHIA default were fitted. In the second step, the signal yields in data were re-evaluated using the leakage fractions from PYTHIA in which the hard and bremsstrahlung contributions were mixed according to the fitted value of α obtained in the first step; the resulting distributions of the signal yield in data were again fitted. The fitted values of α of the two steps were very similar and so no further iterations were performed. This version of PYTHIA in which the fraction of bremsstrahlung and hard components were changed to describe better the data is referred to as PYTHIA *optimised*.

The signal leakage fractions and signal purity estimated with PYTHIA optimised are shown in Figures 8.19 and 8.20, respectively. The fitted values of α, shown in Table 8.1, are different for each observable. This variation is expected since the two components are simulated at LO; the NLO QCD radiative corrections are expected to affect them differently and, furthermore, to entangle them, making any distinction physically impossible. In fact, variations between different observables were also observed in the application of the same procedure at parton level: the optimal value of α resulting from a fit of the parton-level predictions of the two components in PYTHIA to the NLO QCD calculations depends also on the observable. Thus, it is understood that the variation of the optimal value of α with the observable arises from higher-order effects; they can be mimicked by mixing the LO descriptions of the two components in an observable-dependent way.

[1]The fit to the data was performed using MINUIT and the error treatment was done using MIGRAD.

	Pythia	
	α	$\Delta\alpha$
E_{T}^{γ}	0.4691	0.0070
$p_{\mathrm{T}}^{\mathrm{jet-lead}}$	0.6968	0.0030
$m^{\gamma-\mathrm{jet}}$	0.770	0.043
$\lvert\cos\theta^{\star}\rvert$	0.3896	0.0067
$\Delta\phi^{\gamma-\mathrm{jet}}$	0.4023	0.0021

Table 8.1: Values of the free parameter α and its statistical uncertainty in the admixture of the hard and bremsstrahlung components in Pythia resulting from the fit to the data distributions (in the second step, see text).

8.2.2 Background from electron faking photons

Following the details given in Section 6.3.1, the background from isolated electrons faking photons was studied using Sherpa 2.2 and Alpgen samples of W/Z+jets. The fraction of W+jets and Z+jets background to the photon+jet production as a function of the different observables are shown in Figure 8.21 and 8.22, respectively. This background was found to be negligible and, therefore, was neglected in the measurement.

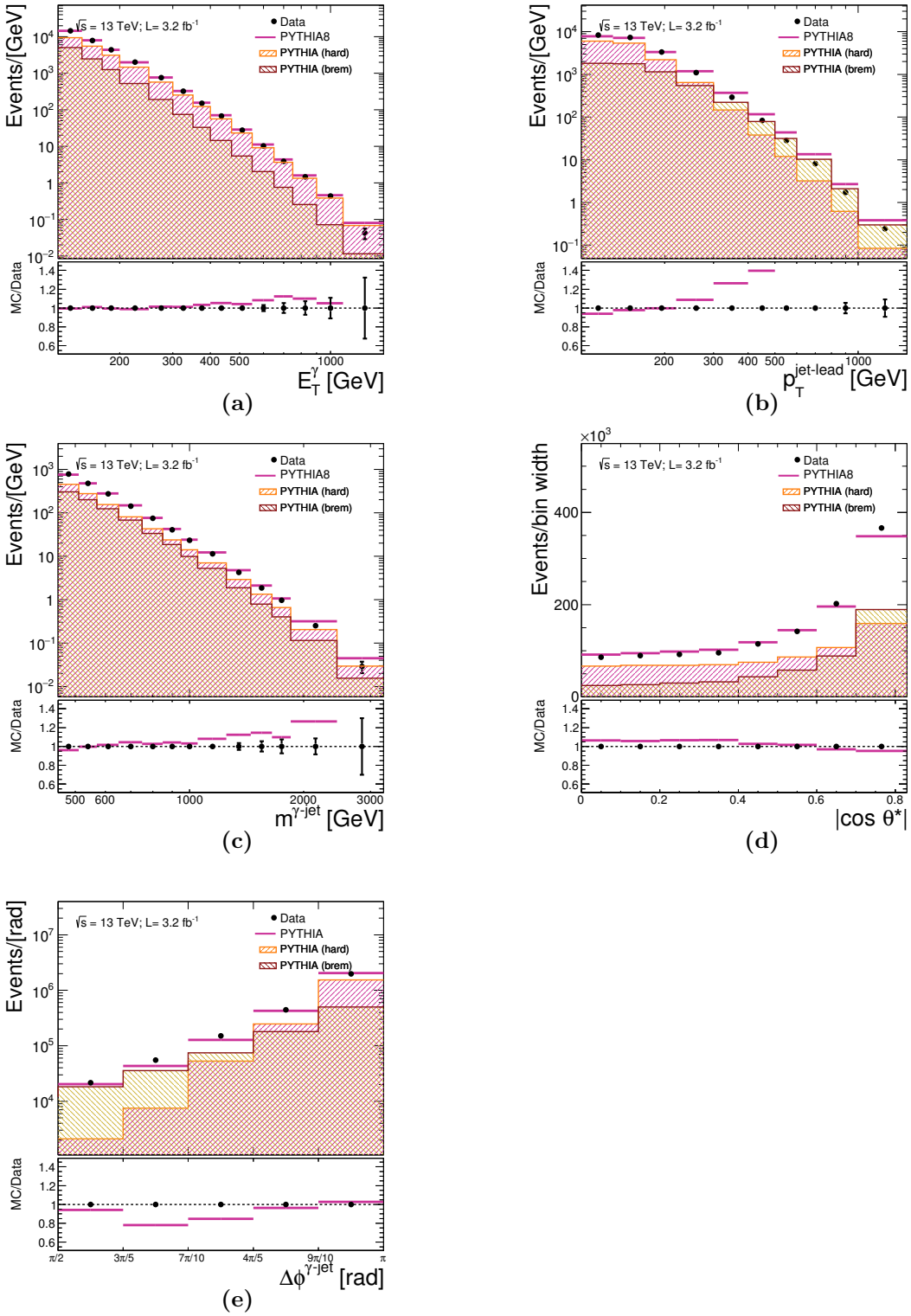


Figure 8.18: The estimated signal yields in data (dots) using signal leakage fractions from PYTHIA default as functions of (a) E_{T}^{γ}, (b) $p_{\mathrm{T}}^{\mathrm{jet-lead}}$, (c) $m^{\gamma-\mathrm{jet}}$, (d) $|\cos\theta^{\star}|$ and (e) $\Delta\phi^{\gamma-\mathrm{jet}}$. For comparison, the MC simulations of the signal from PYTHIA default (solid histograms) are also included. The MC distributions are normalised to the total number of data events. The hard (right-hatched histogram) and bremsstrahlung (left-hatched histogram) components of PYTHIA default are also shown and mixed according to the MC prediction. The ratio of the MC to the data is shown in the lower part of the figures.

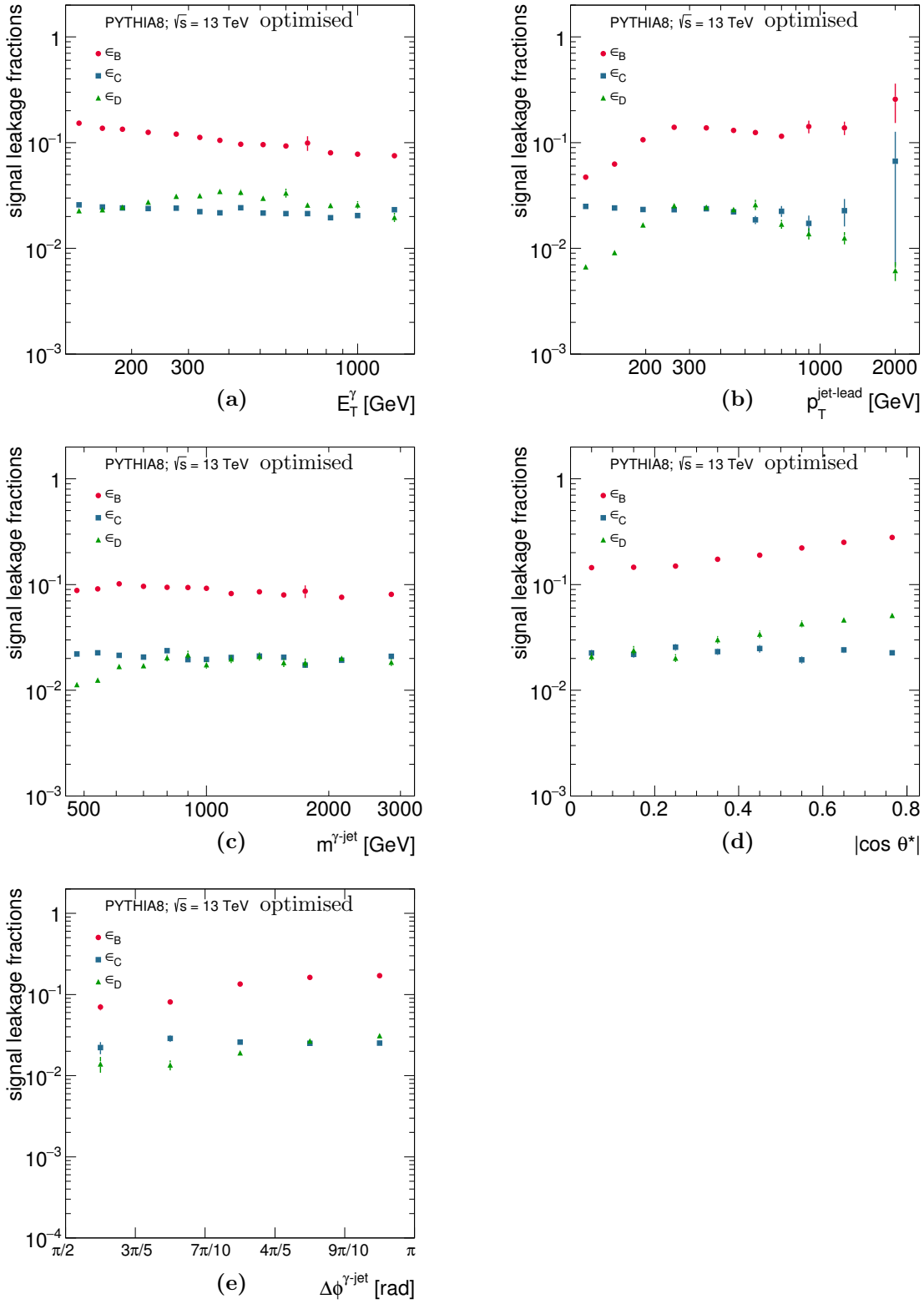


Figure 8.19: Signal leakage fractions from PYTHIA optimised for the B (dots), C (squares) and D (triangles) control regions as functions of the observables studied.

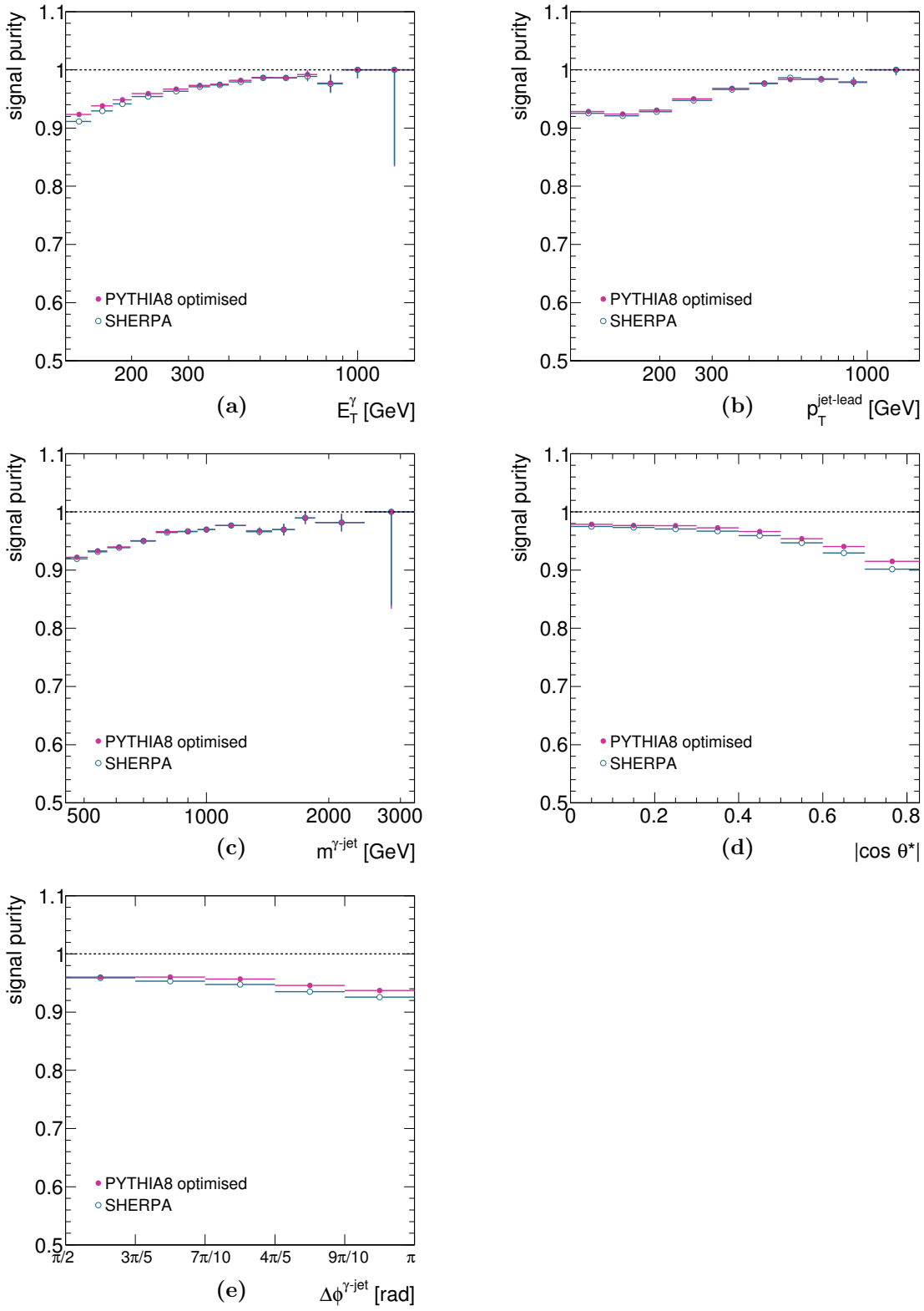


Figure 8.20: Estimated signal purities in data using signal leakage fractions from PYTHIA optimised (dots) and SHERPA (open circles) as functions of (a) E_{T}^{γ}, (b) $p_{\mathrm{T}}^{\mathrm{jet-lead}}$, (c) $m^{\gamma-\mathrm{jet}}$, (d) $|\cos\theta^{\star}|$ and (e) $\Delta\phi^{\gamma-\mathrm{jet}}$.

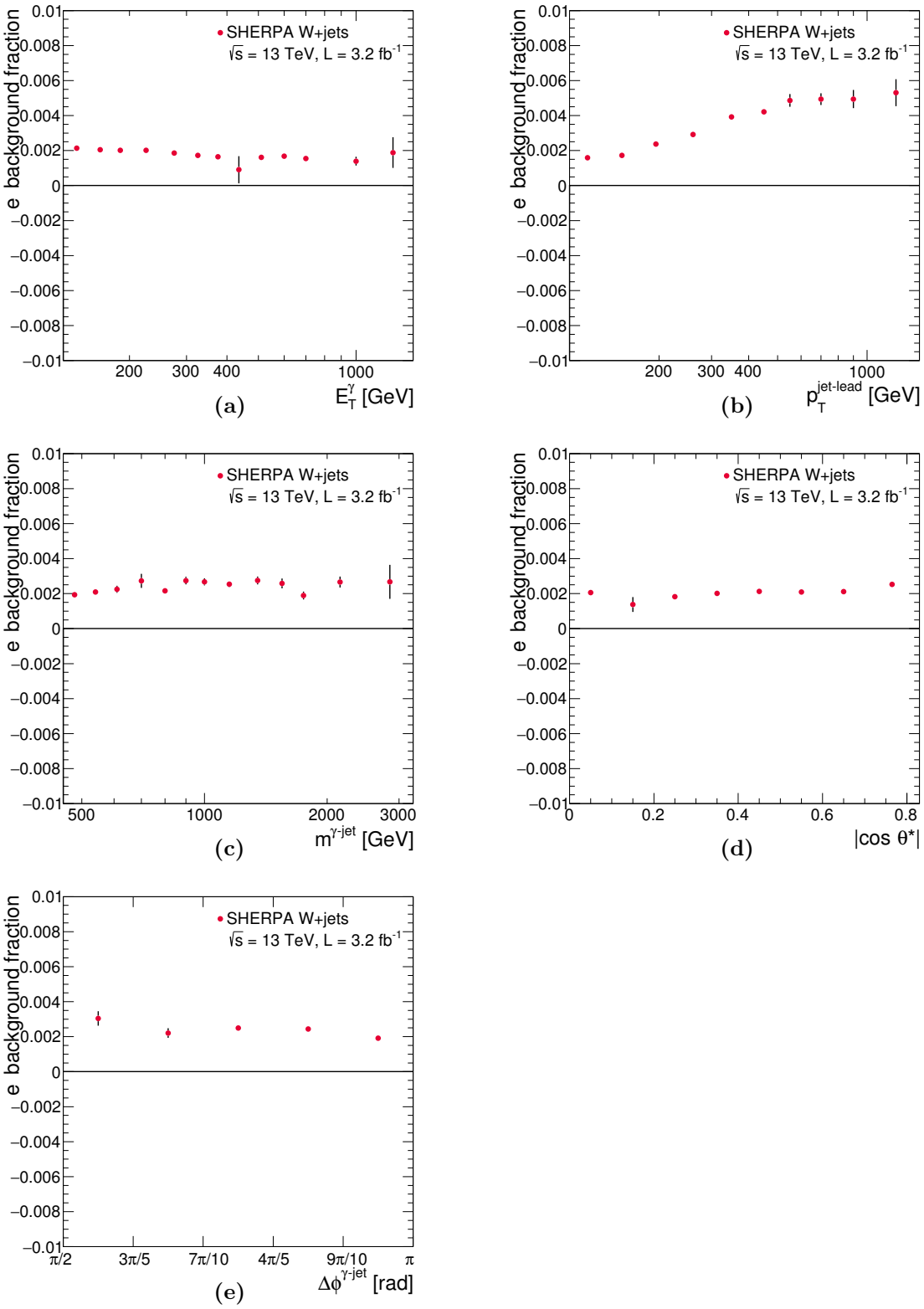


Figure 8.21: Fraction of W + jets background to photon+jet production as a function of (a) E_{T}^{γ}, (b) $p_{\mathrm{T}}^{\mathrm{jet-lead}}$, (c) $m^{\gamma-\mathrm{jet}}$, (d) $|\cos\theta^{\star}|$ and (e) $\Delta\phi^{\gamma-\mathrm{jet}}$ using the MC samples of SHERPA2.2. Truth matching to $e^{\pm}$ is applied with $\Delta R < 0.2$. The error bars represent the statistical uncertainties of the MC samples.

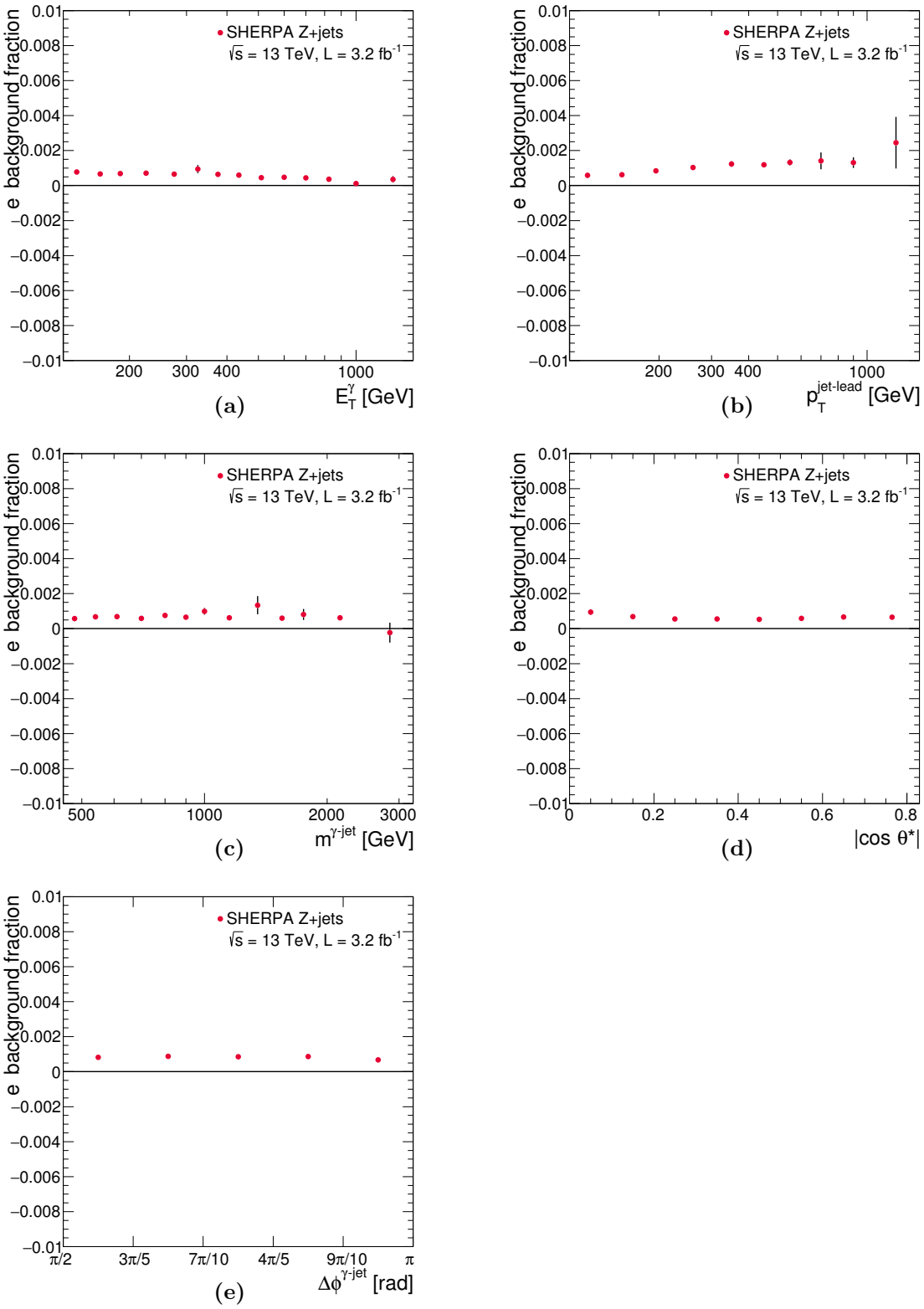


Figure 8.22: Fraction of Z + jets background to photon+jet production as a function of (a) E_{T}^{γ}, (b) $p_{\mathrm{T}}^{\mathrm{jet-lead}}$, (c) $m^{\gamma-\mathrm{jet}}$, (d) $|\cos\theta^{\star}|$ and (e) $\Delta\phi^{\gamma-\mathrm{jet}}$ using the MC samples of SHERPA2.2. Truth matching to $e^{\pm}$ is applied with $\Delta R < 0.2$. The error bars represent the statistical uncertainties of the MC samples.

8.3 Control Plots

Figure 8.23 shows the data distributions after background subtraction using Pythia optimised for the signal leakage fractions compared to the MC simulations of Pythia optimised and Sherpa. An improved description of the data is obtained with Pythia optimised. An adequate description of the shape of the observables is provided by Pythia or Sherpa except in the tail of $m^{\gamma-\text{jet}}$.

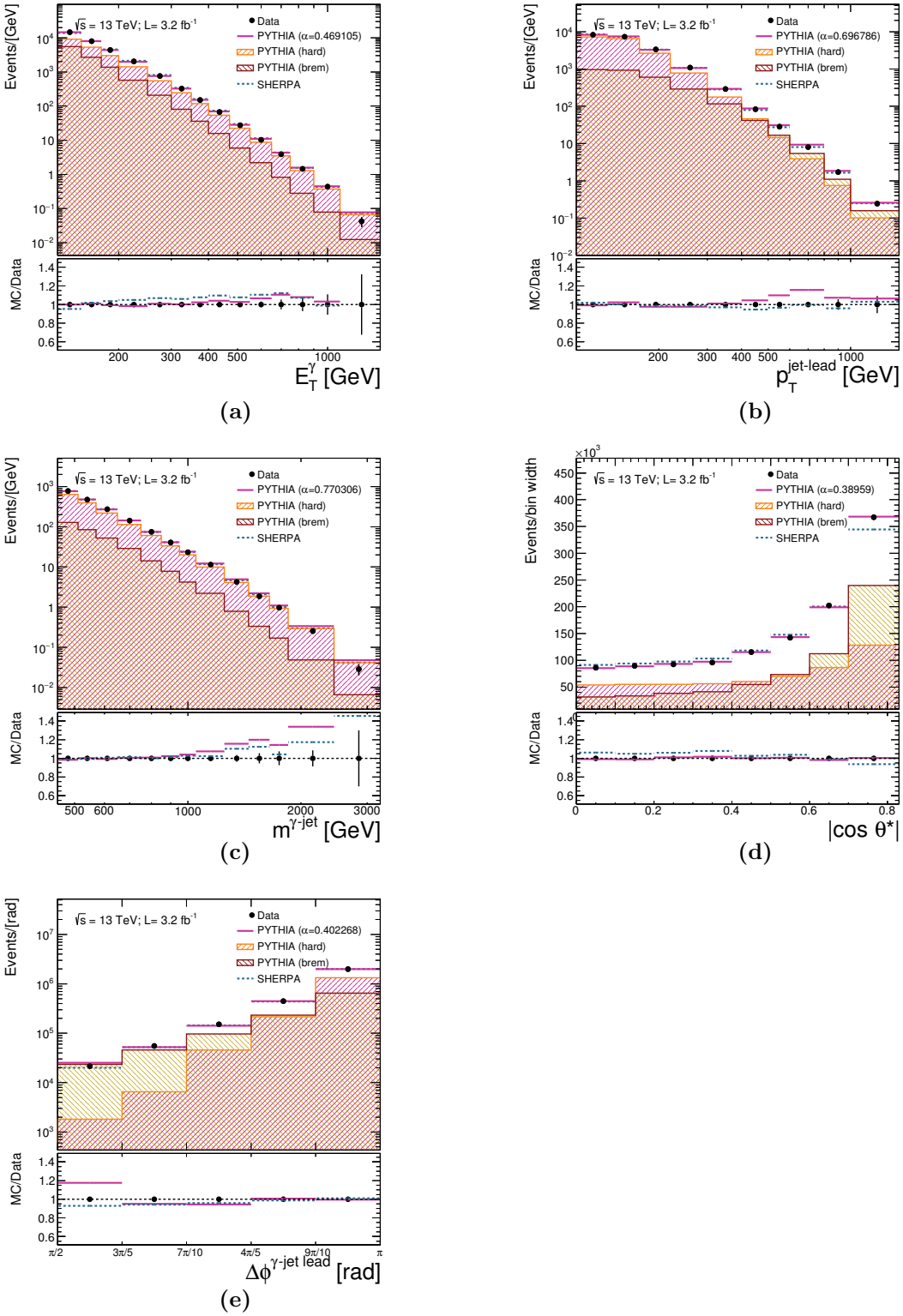


Figure 8.23: The estimated signal yields in data (dots) using signal leakage fractions from PYTHIA optimised as functions of (a) E_{T}^{γ}, (b) $p_{\mathrm{T}}^{\mathrm{jet-lead}}$, (c) $m^{\gamma-\mathrm{jet}}$, (d) $|\cos\theta^{\star}|$ and (e) $\Delta\phi^{\gamma-\mathrm{jet}}$. For comparison, the MC simulations of the signal from PYTHIA optimised and SHERPA are also included. The MC distributions are normalised to the total number of data events. The hard (right-hatched histograms) and bremsstrahlung (left-hatched histograms) components of PYTHIA are also shown and mixed according to the optimised α value shown. The ratio of the MC to the data is shown in the lower part of the figures.

8.4 Unfolding

The measurements were corrected for detector resolution and inefficiencies using a bin-by-bin unfolding method as described in Section 6.5. The adequacy of this method for the present analysis was studied by checking the quality of the reconstruction and the efficiency and purity of the selection using the MC simulations.

8.4.1 Fiducial phase space

The measurements presented in this chapter refer to isolated photons, with $E_{\mathrm{T}}^{\gamma} > 125$ GeV and $|\eta^{\gamma}| < 2.37$ (excluding the region $1.37 < |\eta^{\gamma}| < 1.56$), plus at least one jet with $p_{\mathrm{T}}^{\mathrm{jet-lead}} > 100$ GeV and $|y^{\mathrm{jet}}| < 2.37$. Differential cross sections were measured as functions of E_{T}^{γ}, $p_{\mathrm{T}}^{\mathrm{jet}}$ and $\Delta\phi^{\gamma-\mathrm{jet}}$. A more restricted phase-space region with $|\eta^{\gamma}| + |y^{\mathrm{jet-lead}}| < 2.37$ and $m^{\gamma-\mathrm{jet}} > 450$ GeV was defined for the measurement of the cross sections as functions of $m^{\gamma-\mathrm{jet}}$ and $|\cos\theta^{\star}|$. The fiducial volume to which the measurements are unfolded is also defined by the photon isolation requirement. To define the phase-space region that corresponds to the selection applied at reconstruction level, where an E_{T}^{γ}-dependent isolation was applied, the isolation at particle level was studied. The equivalent requirement at particle level was determined by studying the correlation between the reconstruction and particle levels as a function of $E_{\mathrm{T}}^{\mathrm{iso}}$. The $E_{\mathrm{T}}^{\mathrm{iso}}$ variable at particle level is computed using all the hadrons in the final state (those arising from the hard interaction as well as those arising from the underlying-event simulation) and is also corrected using the jet-area method. Figures 8.24(c) and 8.24(d) show the efficiencies at particle level for Pythia and Sherpa MC samples, respectively. The particle-level efficiency was computed using two different E_{T}^{γ}-dependent requirements and for several fixed-$E_{\mathrm{T}}^{\mathrm{iso}}$ requirements. The efficiency for Sherpa is independent of E_{T}^{γ} and of the isolation requirement and amounts to $\approx 90\%$. For Pythia, the efficiency grows from $\approx 75\%$ at $E_{\mathrm{T}}^{\gamma} = 125$ GeV up to $\approx 85\%$ for $E_{\mathrm{T}}^{\gamma} = 1500$ GeV; this behaviour originates from the different values of the efficiency for the hard (similar to Sherpa) and bremsstrahlung[2] components (see Figure 8.25) convoluted with the E_{T}^{γ}-dependence of the fraction of the bremsstrahlung component (also included in Figure 8.25).

To determine which requirement at particle level would provide the smallest extrapolation in the cross section, studies of the correlation between isolation energy at reconstruction and particle levels were performed and explained below.

Figure 8.26(a,b) shows the profiles for Pythia and Sherpa for $125 < E_{\mathrm{T}}^{\gamma} < 150$ GeV and $750 < E_{\mathrm{T}}^{\gamma} < 900$ GeV. These plots confirm that there is a small dependence of the profile at the reconstruction level with E_{T}^{γ} in the signal region. The same trend is observed in the signal region for both MC samples and for Pythia hard and bremsstrahlung, separately, as can be seen in the comparisons of Figs. 8.26(c,d) and 8.26(e,f). Thus, the same behaviour is seen for Pythia hard, Pythia bremsstrahlung and Sherpa in each E_{T}^{γ} region.

The requirement on $E_{\mathrm{T}}^{\mathrm{iso}}$ at particle level equivalent to the E_{T}^{γ}-dependent one applied at reconstruction level was determined by performing a linear fit to the profiles in the region $5 < E_{\mathrm{T}}^{\mathrm{iso}} < 20$ GeV in each E_{T}^{γ} region. The fits are displayed in Figs. 8.27 to 8.30 for Pythia

[2]The separation of the events due to the hard and bremsstrahlung components in Pythia is achieved by scanning the MC event record and tracing back the origin of the generated photon.

and SHERPA in each E_{T}^{γ} region. The uncertainty in each point takes into account the uncertainty of the fit and the fact that the centre of each E_{T}^{γ} region was used. A summary of the values obtained for the requirement at particle level as a function of E_{T}^{γ} is shown in Figure 8.31. A χ^2 linear fit to the results obtained gives 9.63 ± 0.11 (9.91 ± 0.11) GeV for PYTHIA (SHERPA) for the intercept, p_0, and 0.0039 ± 0.0004 (0.0043 ± 0.0004) for the slope, p_1. Therefore, a requirement on $E_{\mathrm{T}}^{\mathrm{iso}}$ of $4.2 \cdot 10^{-3} \cdot E_{\mathrm{T}}^{\gamma} + 10$ GeV was used at particle level.

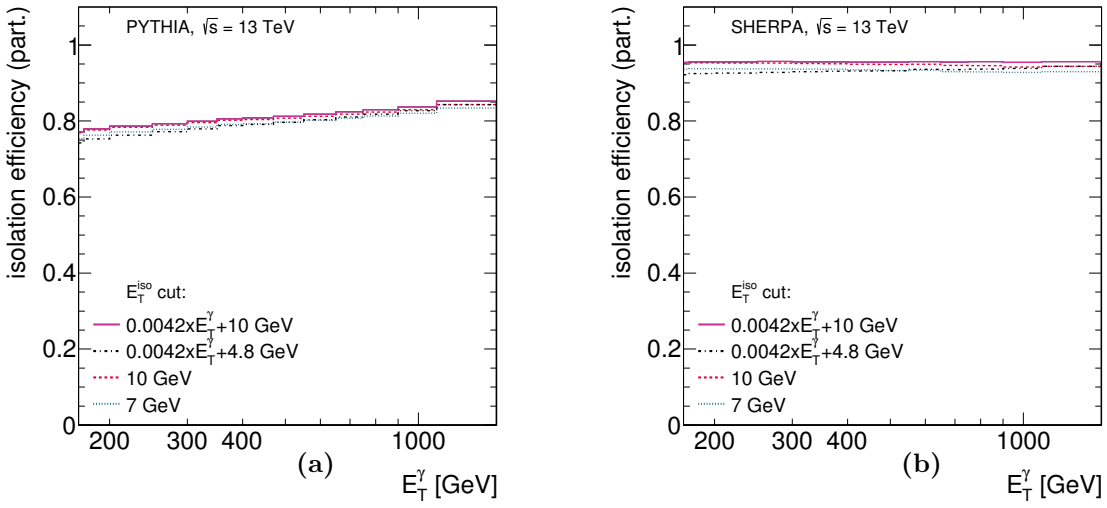


Figure 8.24: Probability for a true photon to pass different isolation requirements with different $E_{\mathrm{T}}^{\mathrm{iso}}$ values for the (a) PYTHIA and (b) SHERPA MC samples at particle level.

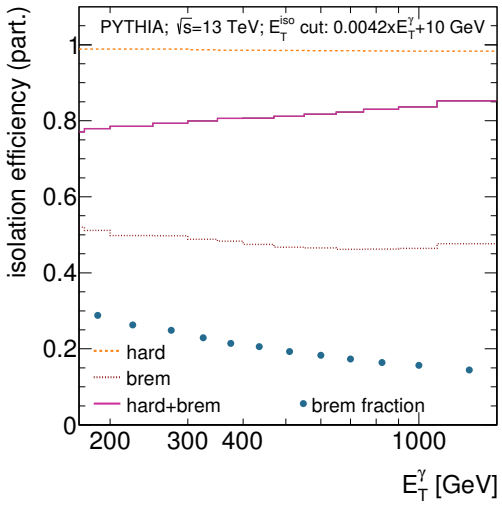


Figure 8.25: Probability for a true photon candidate to pass an isolation requirement, $4.2 \cdot 10^{-3} \cdot E_{\mathrm{T}}^{\gamma} + 10$ GeV, for the hard (dashed line), bremsstrahlung (dotted line) and hard+bremsstrahlung (solid line) components in PYTHIA MC. Also shown is the fraction of bremsstrahlung component as a function of E_{T}^{γ} (dots).

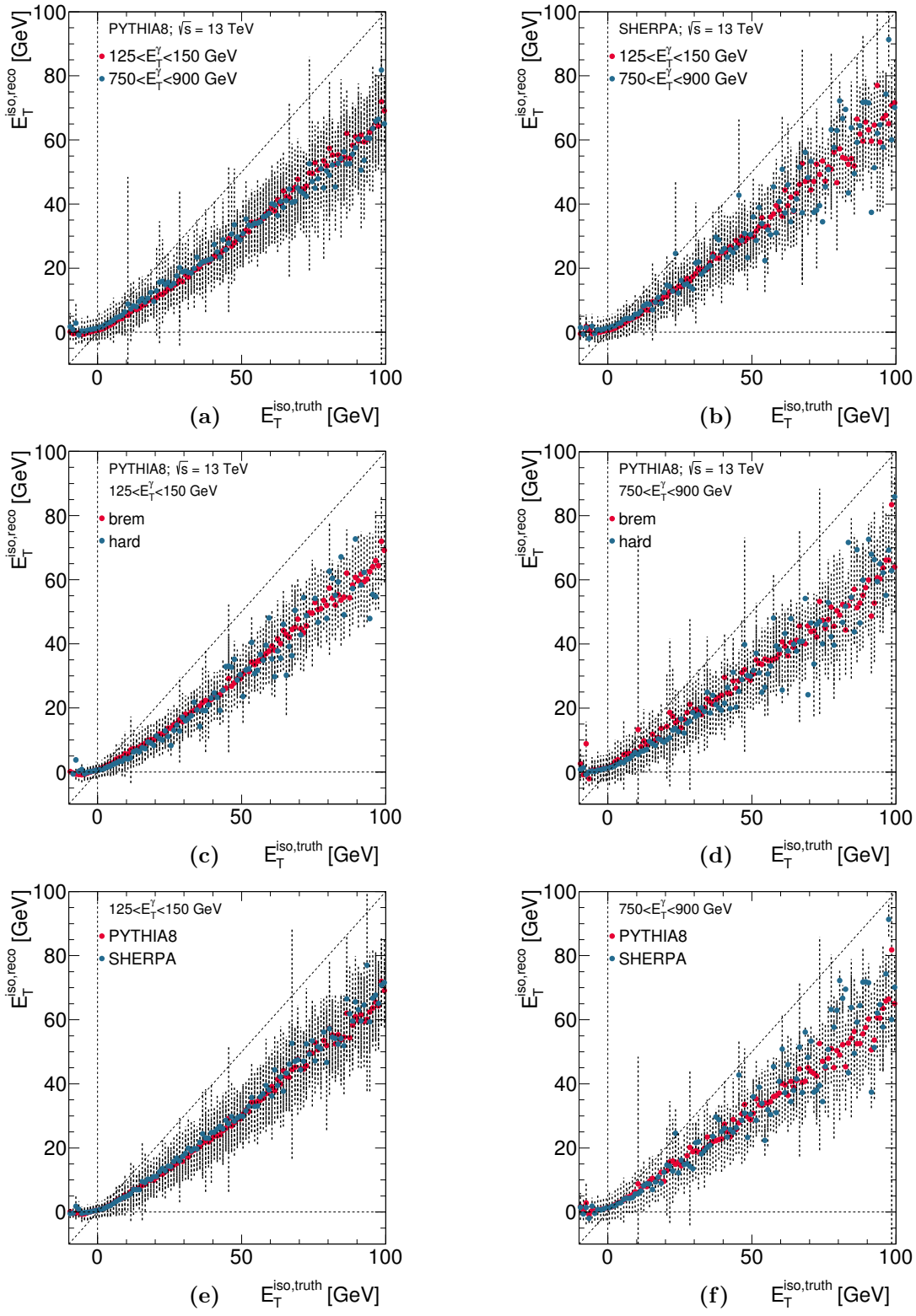


Figure 8.26: Profiles of $E_{\mathrm{T}}^{\mathrm{iso,reco}}$ vs. $E_{\mathrm{T}}^{\mathrm{iso,truth}}$ correlation (dots) for Pythia hard+bremsstrahlung (a) and Sherpa (b) in different E_{T}^{γ} regions, Pythia hard and bremsstrahlung separately for (c) $125 < E_{\mathrm{T}}^{\gamma} < 150$ GeV and (d) $750 < E_{\mathrm{T}}^{\gamma} < 900$ GeV, and Pythia hard+bremsstrahlung and Sherpa for (e) $125 < E_{\mathrm{T}}^{\gamma} < 150$ GeV and (f) $750 < E_{\mathrm{T}}^{\gamma} < 900$ GeV. The error bars represent the width of the distribution in each $E_{\mathrm{T}}^{\mathrm{iso}}$ bin.

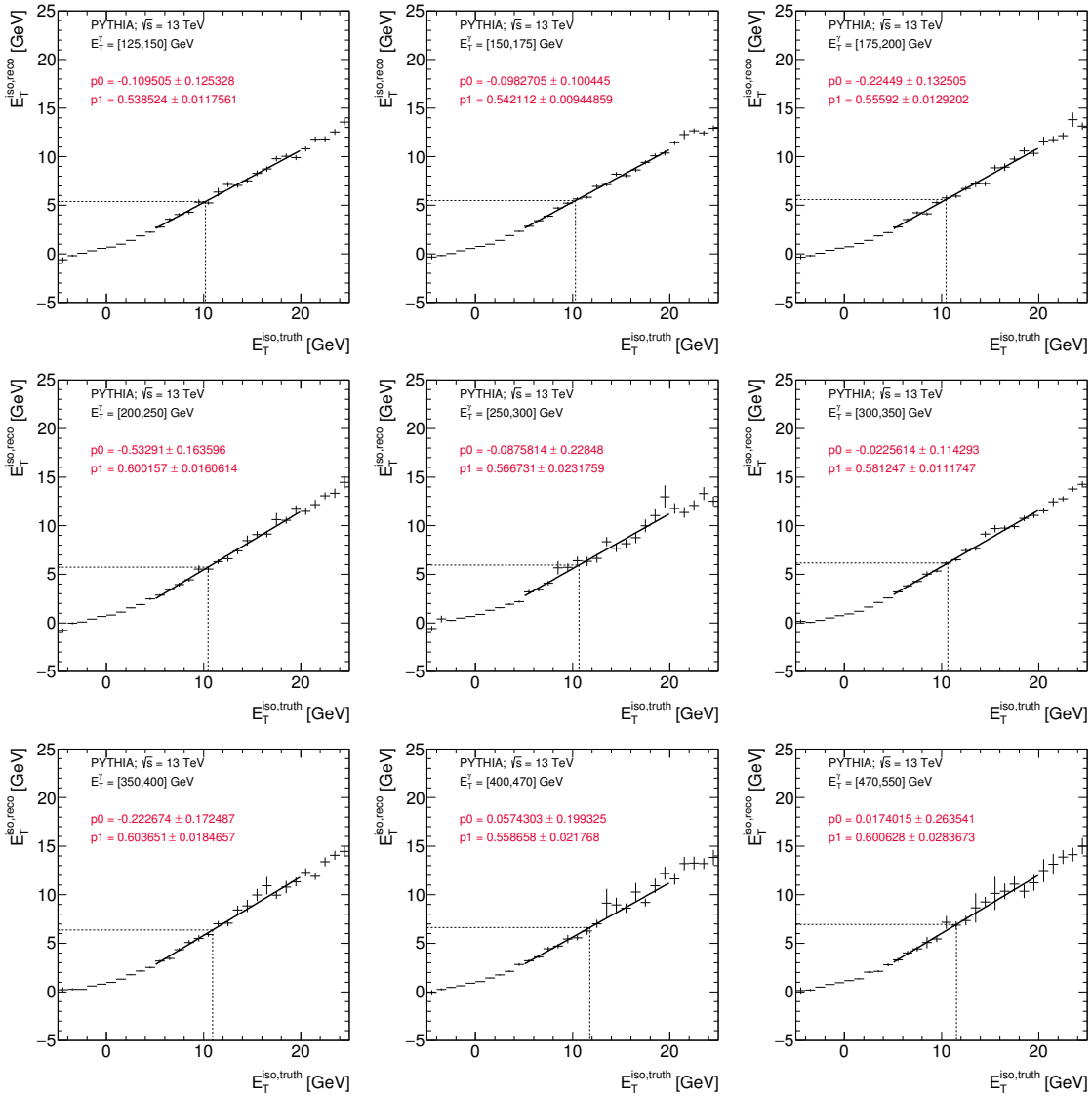


Figure 8.27: $E_{\mathrm{T}}^{\mathrm{iso}}$ reconstruction vs. particle profiles in different E_{T}^{γ} regions (dots) for Pythia hard+bremsstrahlung. The solid line displays the χ^2 linear fit performed to the profile. The horizontal dashed line corresponds to the $E_{\mathrm{T}}^{\mathrm{iso}}$ requirement at reconstruction level, whereas the vertical dashed line is the extrapolated requirement at particle level.

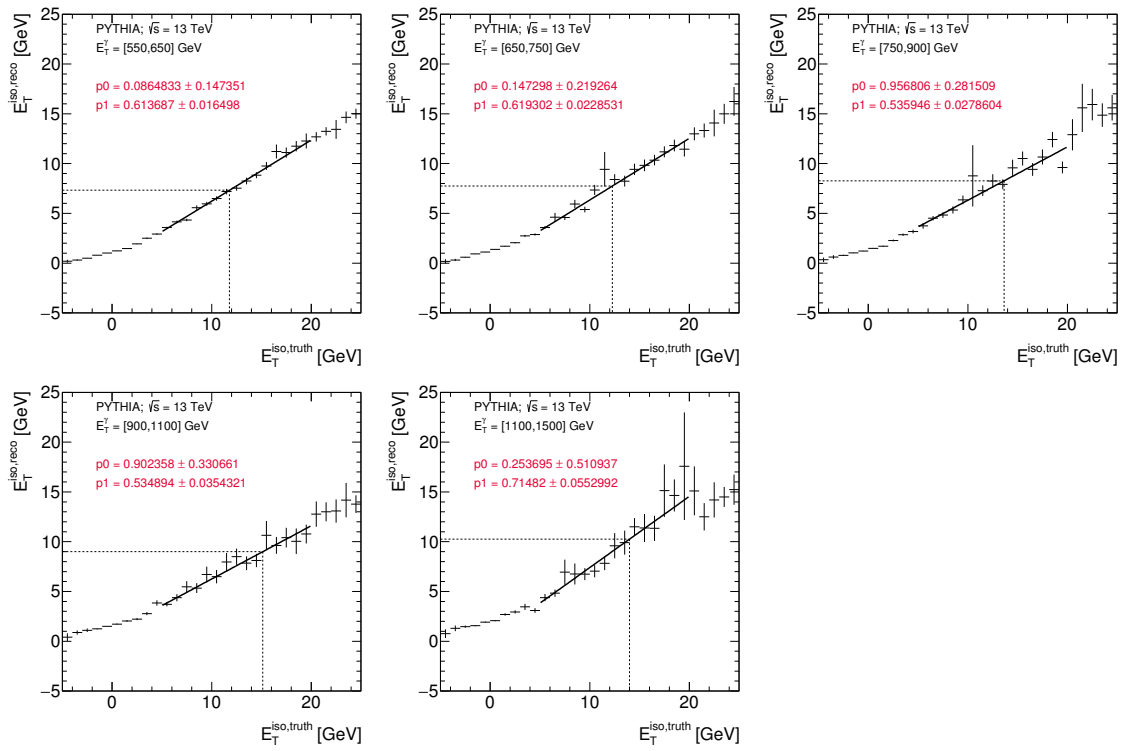


Figure 8.28: $E_{\mathrm{T}}^{\mathrm{iso}}$ reconstruction vs. particle profiles in different E_{T}^{γ} regions (dots) for Pythia hard+bremsstrahlung. The solid line displays the χ^2 linear fit performed to the profile. The horizontal dashed line corresponds to the $E_{\mathrm{T}}^{\mathrm{iso}}$ requirement at reconstruction level, whereas the vertical dashed line is the extrapolated requirement at particle level.

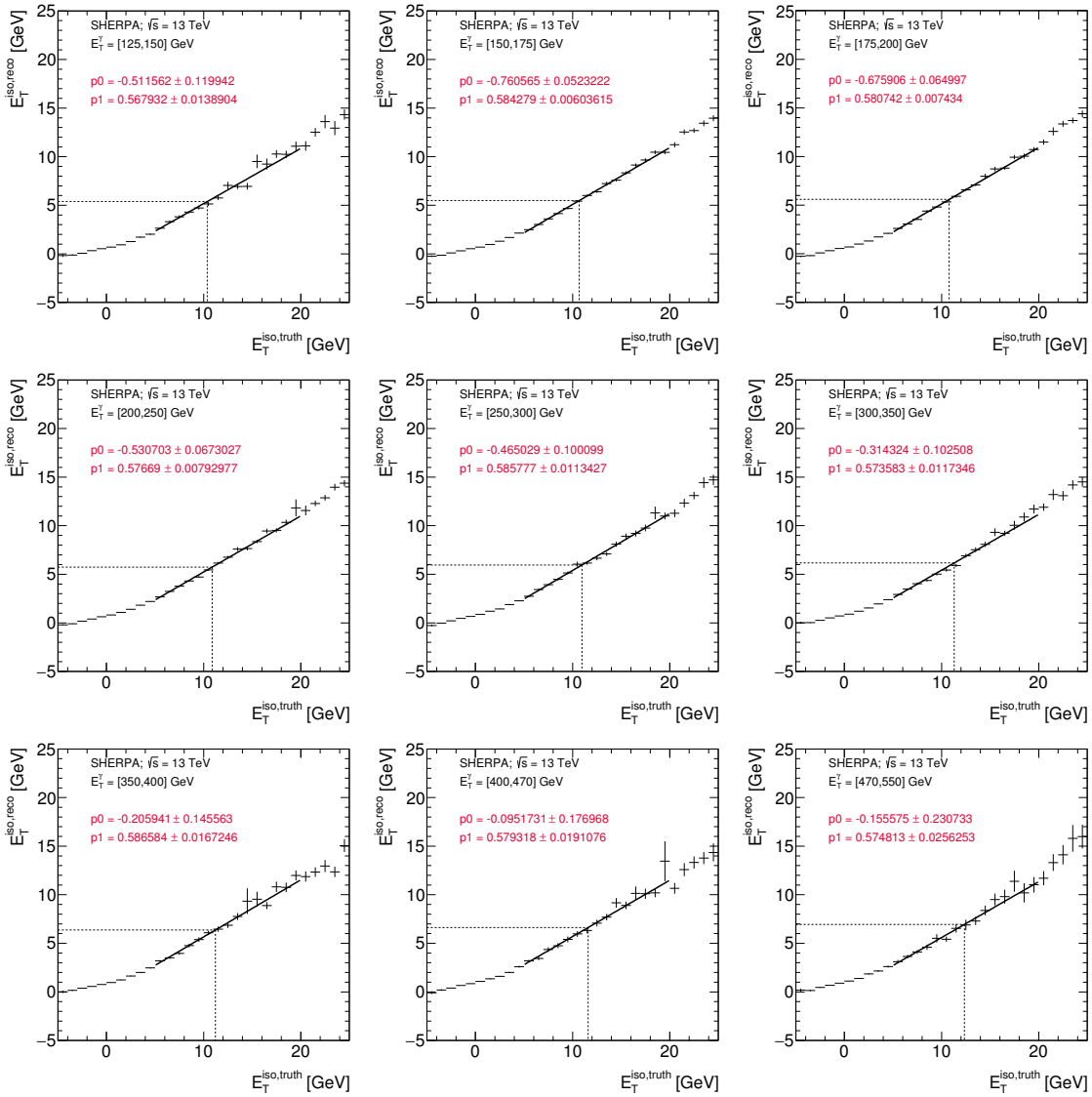


Figure 8.29: $E_{\mathrm{T}}^{\mathrm{iso}}$ reconstruction vs. particle profiles in different E_{T}^{γ} regions (dots) for SHERPA. The solid line displays the χ^2 linear fit performed to the profile. The horizontal dashed line corresponds to the $E_{\mathrm{T}}^{\mathrm{iso}}$ requirement at reconstruction level, whereas the vertical dashed line is the extrapolated requirement at particle level.

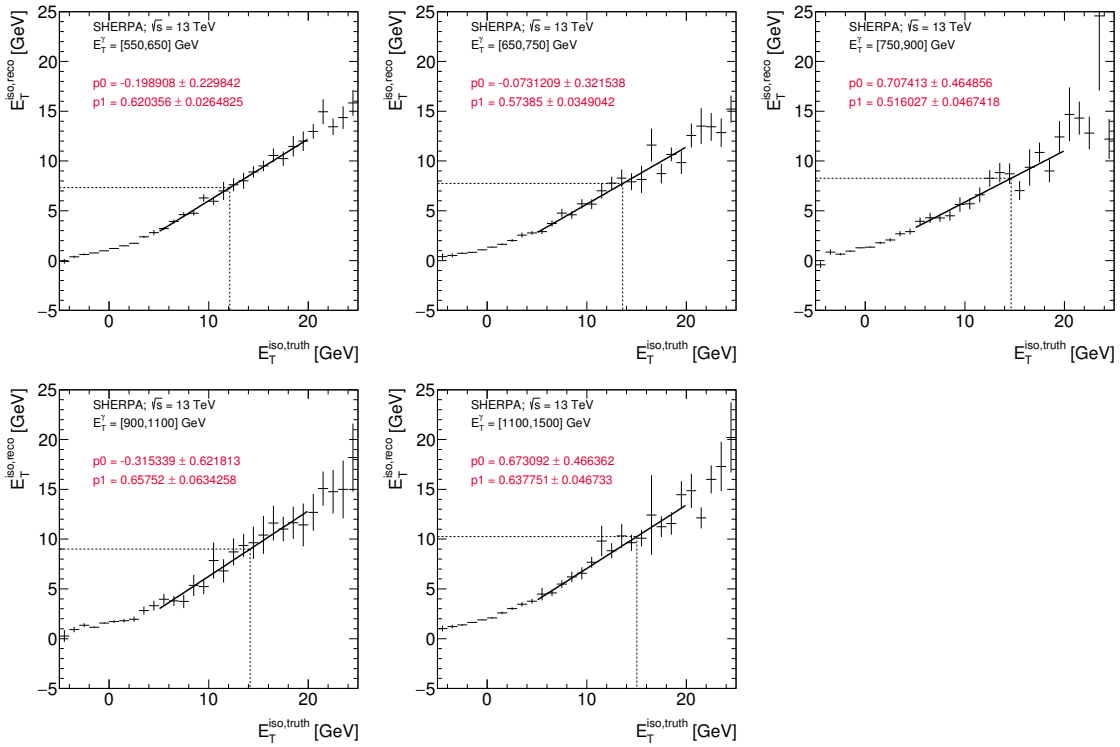


Figure 8.30: $E_{\mathrm{T}}^{\mathrm{iso}}$ reconstruction vs. particle profiles in different E_{T}^{γ} regions (dots) for SHERPA. The solid line displays the χ^2 linear fit performed to the profile. The horizontal dashed line corresponds to the $E_{\mathrm{T}}^{\mathrm{iso}}$ requirement at reconstruction level, whereas the vertical dashed line is the extrapolated requirement at particle level.

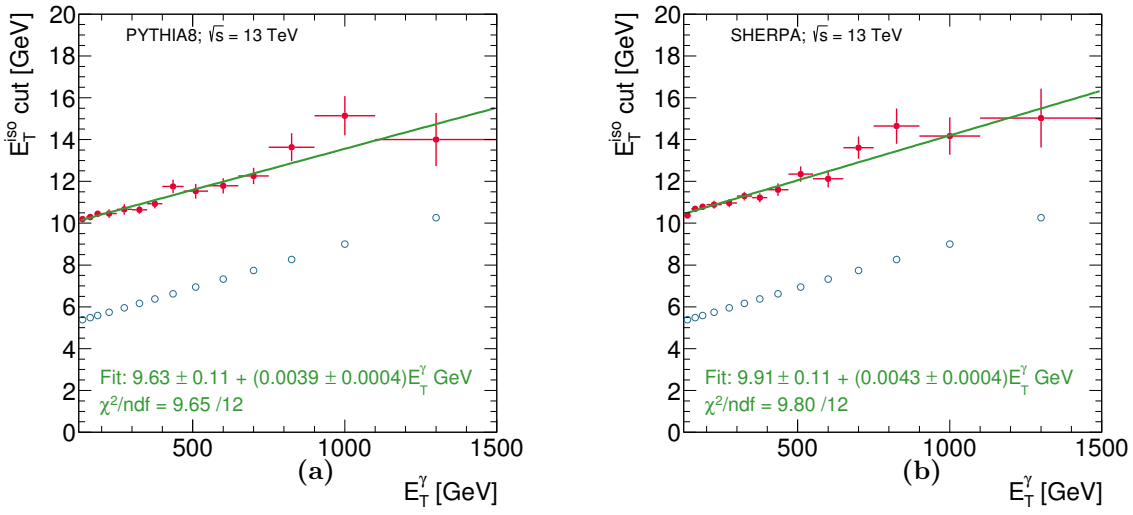


Figure 8.31: Summary of the values obtained for the requirement at particle level as a function of E_{T}^{γ} for (a) PYTHIA and (b) SHERPA (dots). The open circles represent the E_{T}^{γ}-dependent requirement used at reconstruction level evaluated at the centre of each bin. The solid line is the result of a straight-line fit to the values obtained for the requirement at particle level.

8.4.2 Reconstruction quality

To assess the quality of the reconstruction of the variables studied, the observables at reconstructed and particle levels were compared in an event-by-event basis. Each MC event was required to fulfil the requirements at both the reconstruction and particle levels. Additional criteria were imposed at reconstruction level to the jets in this study. They were required to be matched to the particle-level leading jet with $\Delta R = 0.4$. This requirement was only imposed to study the correlation between reconstruction and particle levels and not applied to the nominal simulations at reconstruction level.

Figures 8.32 to 8.37 show the correlation between the reconstruction and particle levels for the observables studied for the samples of Pythia optimised and Sherpa. The spread in $p_{\mathrm{T}}^{\mathrm{jet-lead}}$ and $m^{\gamma-\mathrm{jet}}$ is larger than in E_{T}^{γ}, $\Delta\phi^{\gamma-\mathrm{jet}}$ and $\cos\theta^{\star}$ due to the better resolution in the photon transverse energy and angular variables. A good reconstruction quality is obtained for all observables.

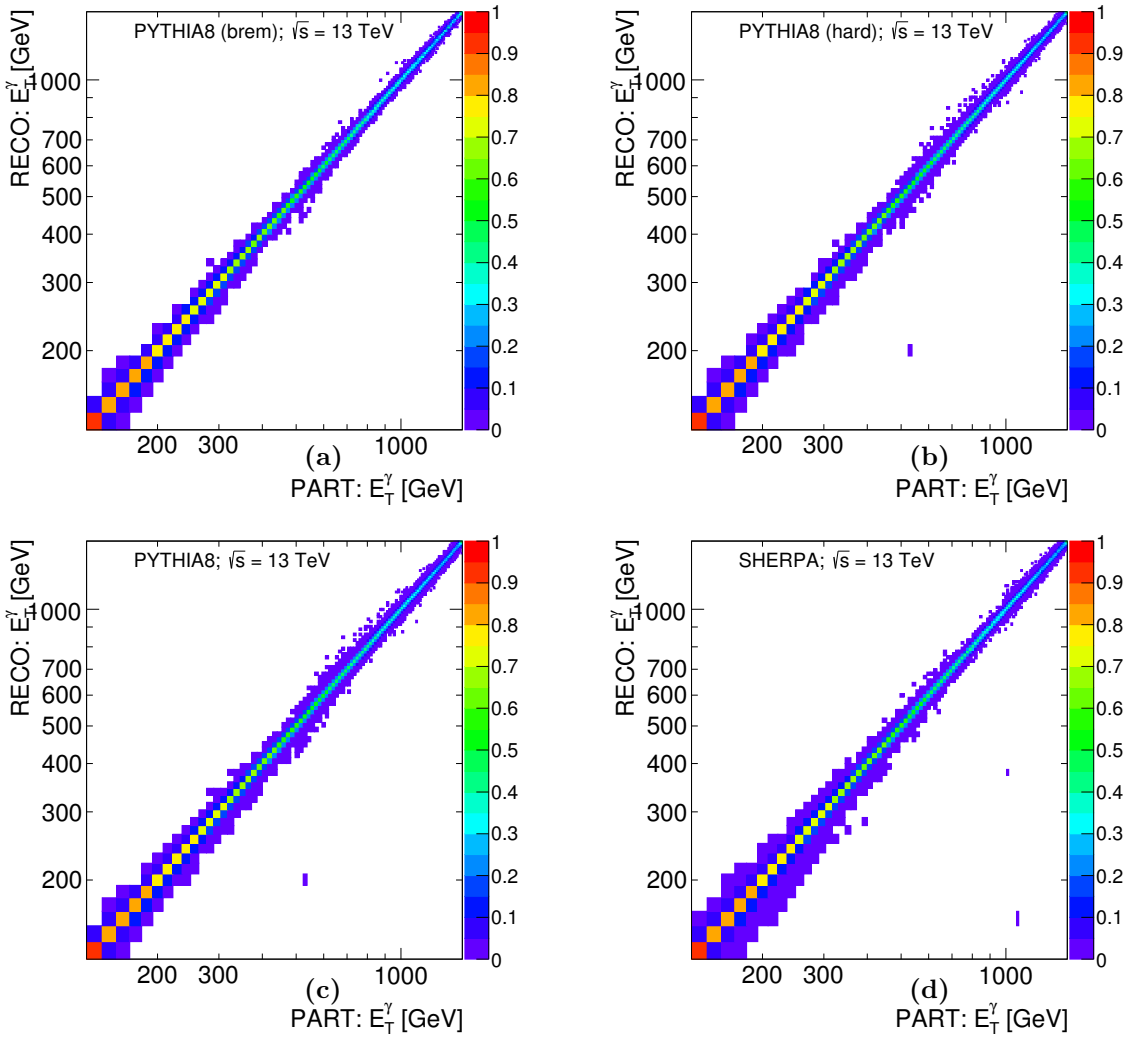


Figure 8.32: The $(E_{\mathrm{T}}^{\gamma})_{\mathrm{reco}}$ vs. $(E_{\mathrm{T}}^{\gamma})_{\mathrm{part}}$ correlation for the photon+one-jet selection for (a) Pythia bremsstrahlung, (b) Pythia hard, (c) Pythia bremsstrahlung plus hard (optimised) and (d) Sherpa.

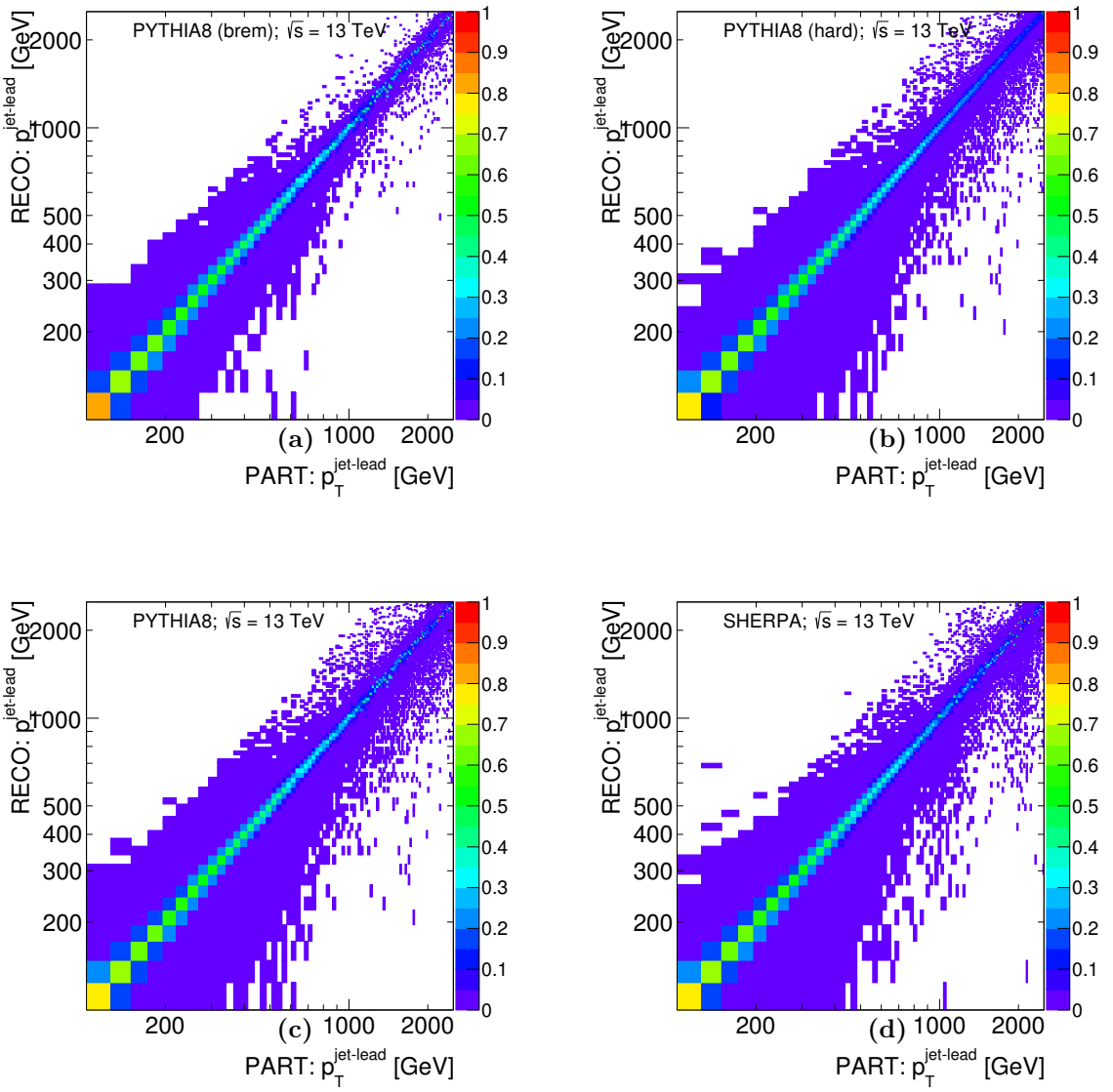


Figure 8.33: The $(p_{\mathrm{T}}^{\mathrm{jet-lead}})_{\mathrm{reco}}$ vs. $(p_{\mathrm{T}}^{\mathrm{jet-lead}})_{\mathrm{part}}$ correlation for the photon+one-jet selection for (a) Pythia bremsstrahlung, (b) Pythia hard, (c) Pythia bremsstrahlung plus hard (optimised) and (d) Sherpa.

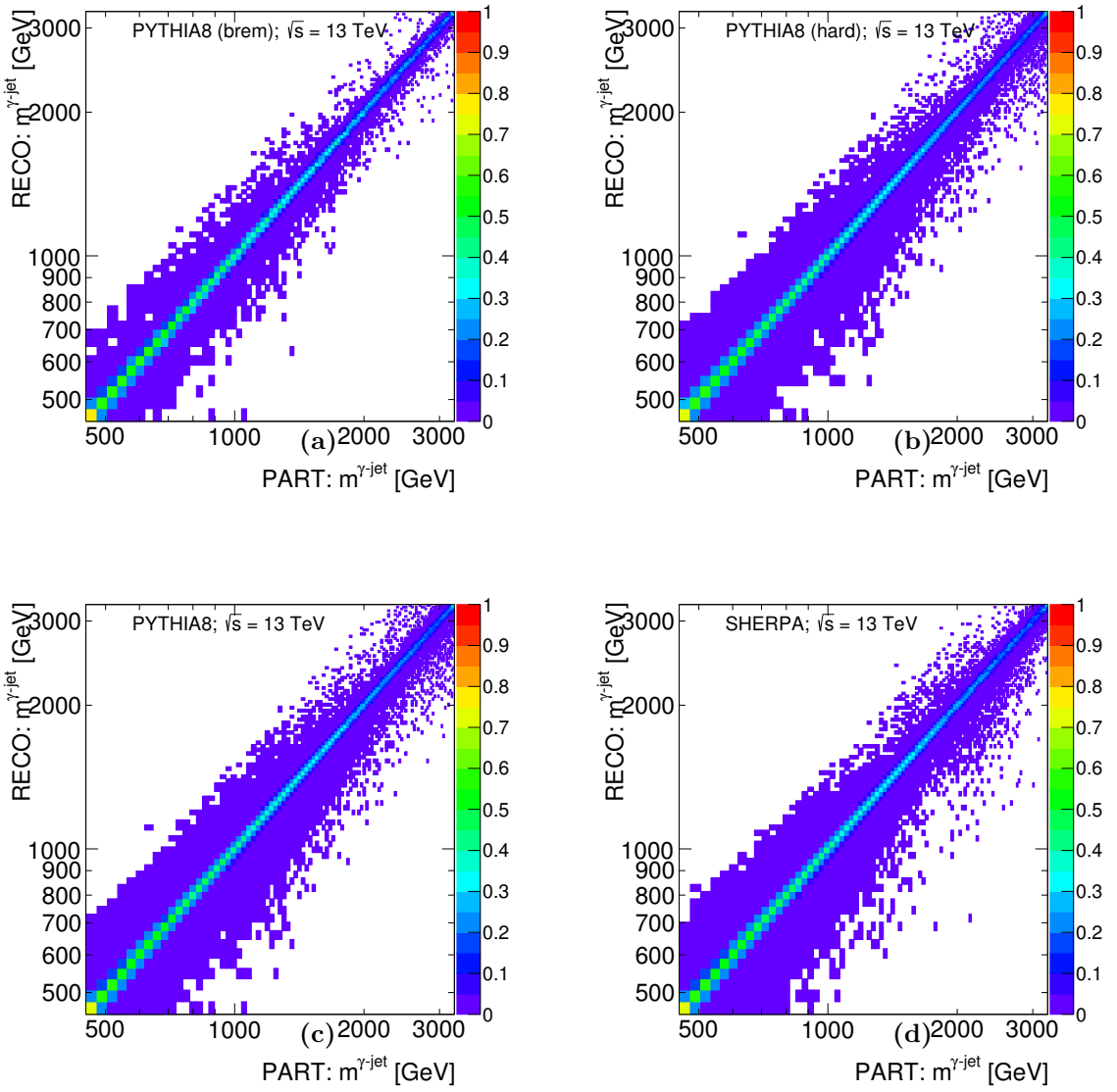


Figure 8.34: The $(m^{\gamma-\text{jet}})_{\text{reco}}$ vs. $(m^{\gamma-\text{jet}})_{\text{part}}$ correlation for the photon+one-jet $m^{\gamma-\text{jet}} - \cos\theta^{\star}$ selection for (a) Pythia bremsstrahlung, (b) Pythia hard, (c) Pythia bremsstrahlung plus hard (optimised) and (d) Sherpa.

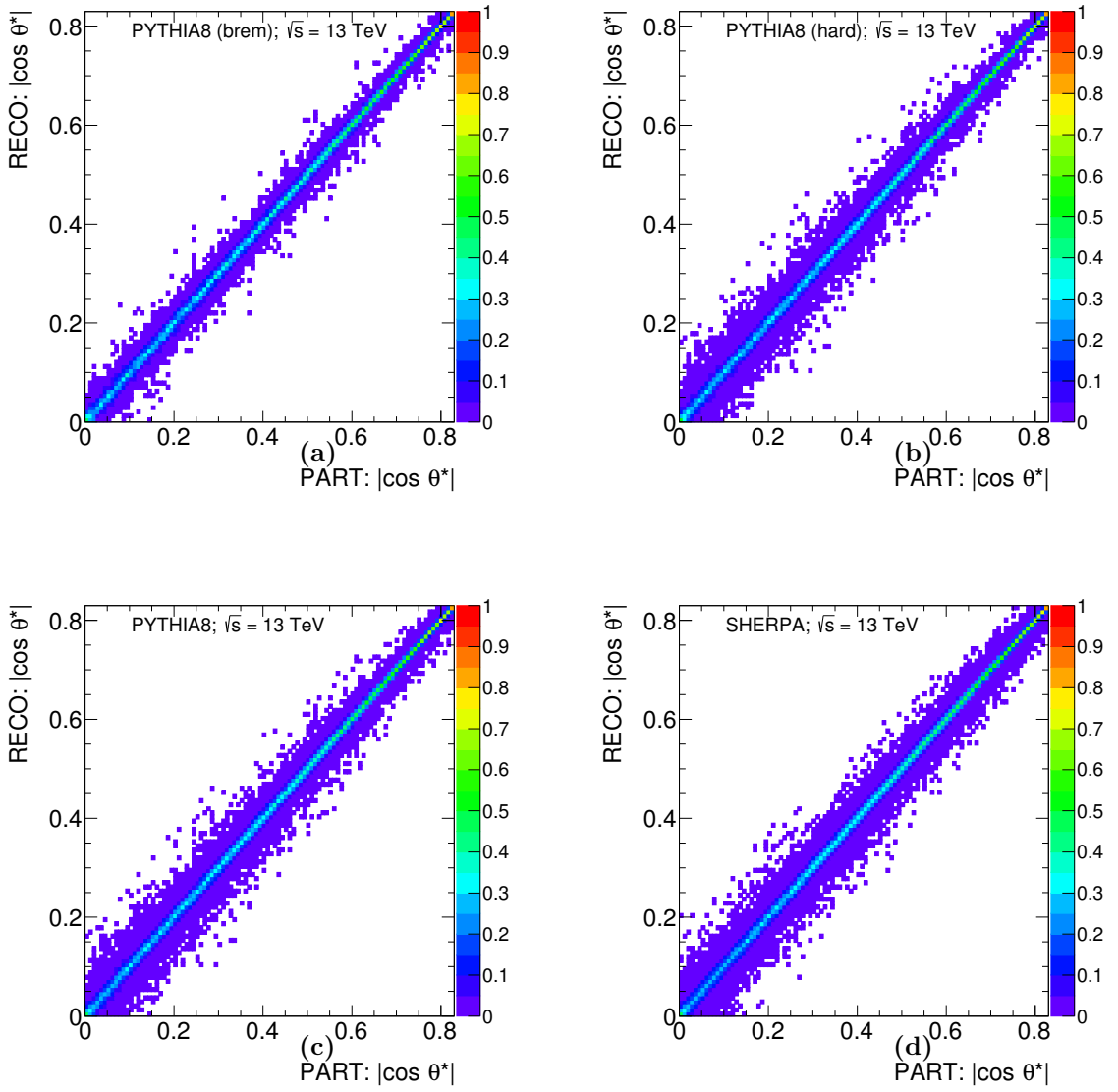


Figure 8.35: The $(|\cos\theta^{\star}|)_{\text{reco}}$ vs. $(|\cos\theta^{\star}|)_{\text{part}}$ correlation for the photon+one-jet $m^{\gamma-\text{jet}} - \cos\theta^{\star}$ selection for (a) Pythia bremsstrahlung, (b) Pythia hard, (c) Pythia bremsstrahlung plus hard (optimised) and (d) Sherpa.

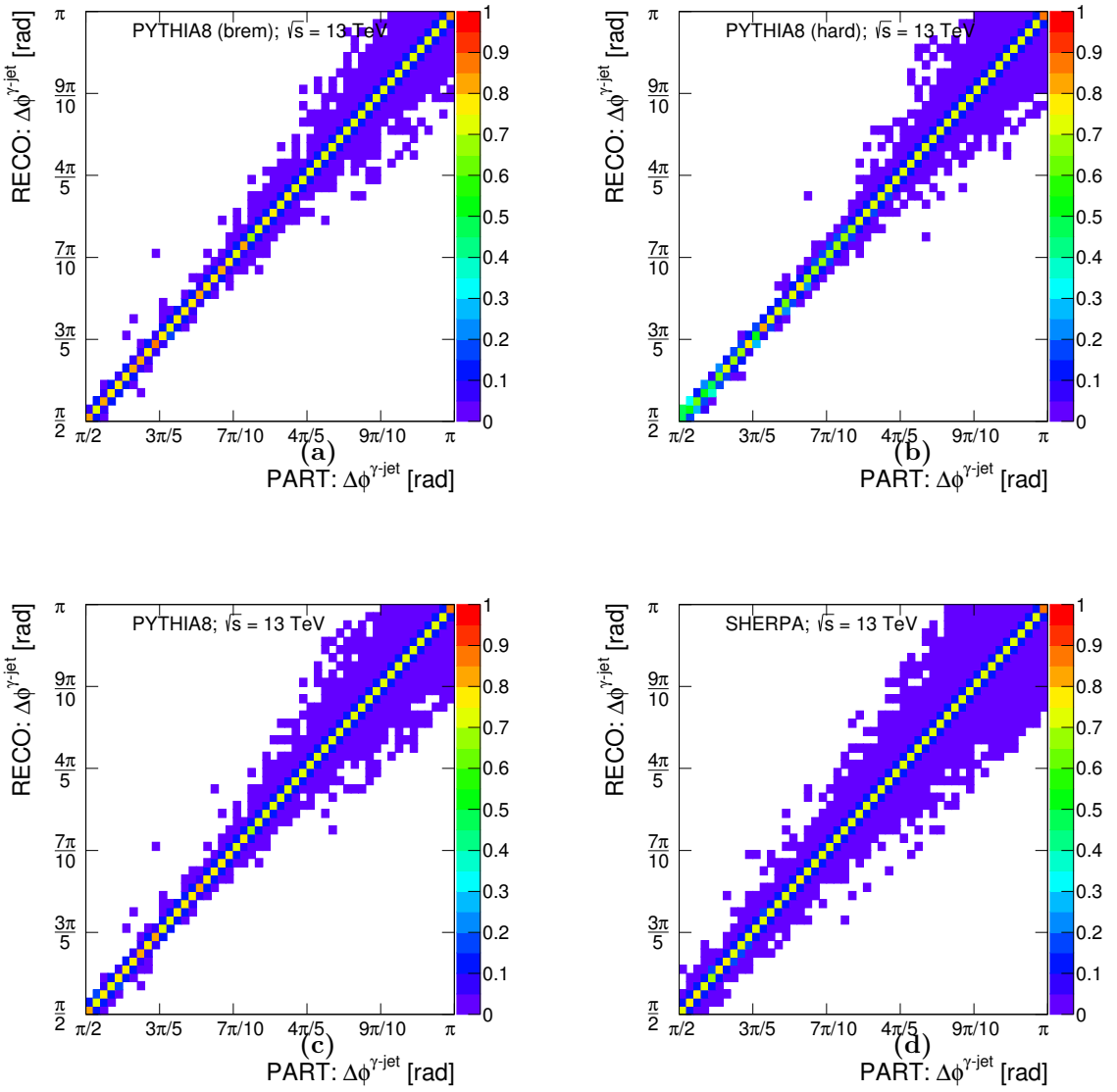


Figure 8.36: The $(\Delta\phi^{\gamma-\mathrm{jet}})_{\mathrm{reco}}$ vs. $(\Delta\phi^{\gamma-\mathrm{jet}})_{\mathrm{part}}$ correlation for the photon+one-jet selection for (a) Pythia bremsstrahlung, (b) Pythia hard, (c) Pythia bremsstrahlung plus hard (optimised) and (d) Sherpa.

8.4.3 Selection efficiency and purity

The selection efficiency and purity, as defined in Section 6.5, were evaluated using the MC samples of Pythia optimised and Sherpa. The integrated selection efficiency was found to be 83% (83%) from the Pythia (Sherpa) samples. The bin-to-bin selection efficiency is above 60% and is very similar for Pythia and Sherpa (see Figure 8.37). The lower values obtained with respect to the inclusive photon analysis are due to the jet requirements. The integrated selection purity was found to be 93% (94%) from the Pythia (Sherpa) samples. The bin-to-bin selection purity is shown in Figure 8.38 and is above 70% and is very similar for Pythia and Sherpa.

8.4.4 Cross-section measurement

The data distributions, after background subtraction, were corrected to particle level using bin-by-bin unfolding correction factors determined using the MC samples. These correction factors take into account the efficiency of the selection criteria and the purity and efficiency of the jet and the photon reconstruction. For this approach to be valid, the uncorrected distributions of the data must be adequately described by the MC simulations at the detector level. This condition was mostly satisfied by both Pythia optimised and Sherpa MC samples. Pythia optimised describes better than Sherpa the measured E_{T}^{γ} distributions, whereas the Sherpa simulation performs better in the description of the $p_{\mathrm{T}}^{\mathrm{jet-lead}}$, $m^{\gamma-\mathrm{jet}}$ and $\Delta\phi^{\gamma-\mathrm{jet}}$. Therefore, samples of Sherpa were chosen to compute the nominal unfolding corrections. For the nominal signal leakage fractions, Pythia optimised was used since, as argued in Section 8.2, it includes the contribution from photons radiated off quarks without any restriction on the opening angle.

The differential cross section in each bin i was computed as in Equation 6.8, where the nominal unfolding corrections (see Equation 6.7) were computed using Sherpa. For the systematic uncertainties on the unfolding performed with the samples of Pythia optimised, the unfolding corrections were computed as

$$C^{\mathrm{MC}}(i) = \frac{\alpha\ N_{\mathrm{part}}^{\mathrm{PYTHIA,H}}(i) + (1-\alpha)\ N_{\mathrm{part}}^{\mathrm{PYTHIA,B}}(i)}{\alpha\ N_{\mathrm{reco}}^{\mathrm{PYTHIA,H}}(i) + (1-\alpha)\ N_{\mathrm{reco}}^{\mathrm{PYTHIA,B}}(i)}, \tag{8.1}$$

where α is the value obtained from the fit to the data distribution of each observable (see Table 8.1). Both unfolding corrections are shown in Figure 8.39 and differ from unity by typically $\lesssim 20\%$. The correction factors are very similar for Pythia and Sherpa.

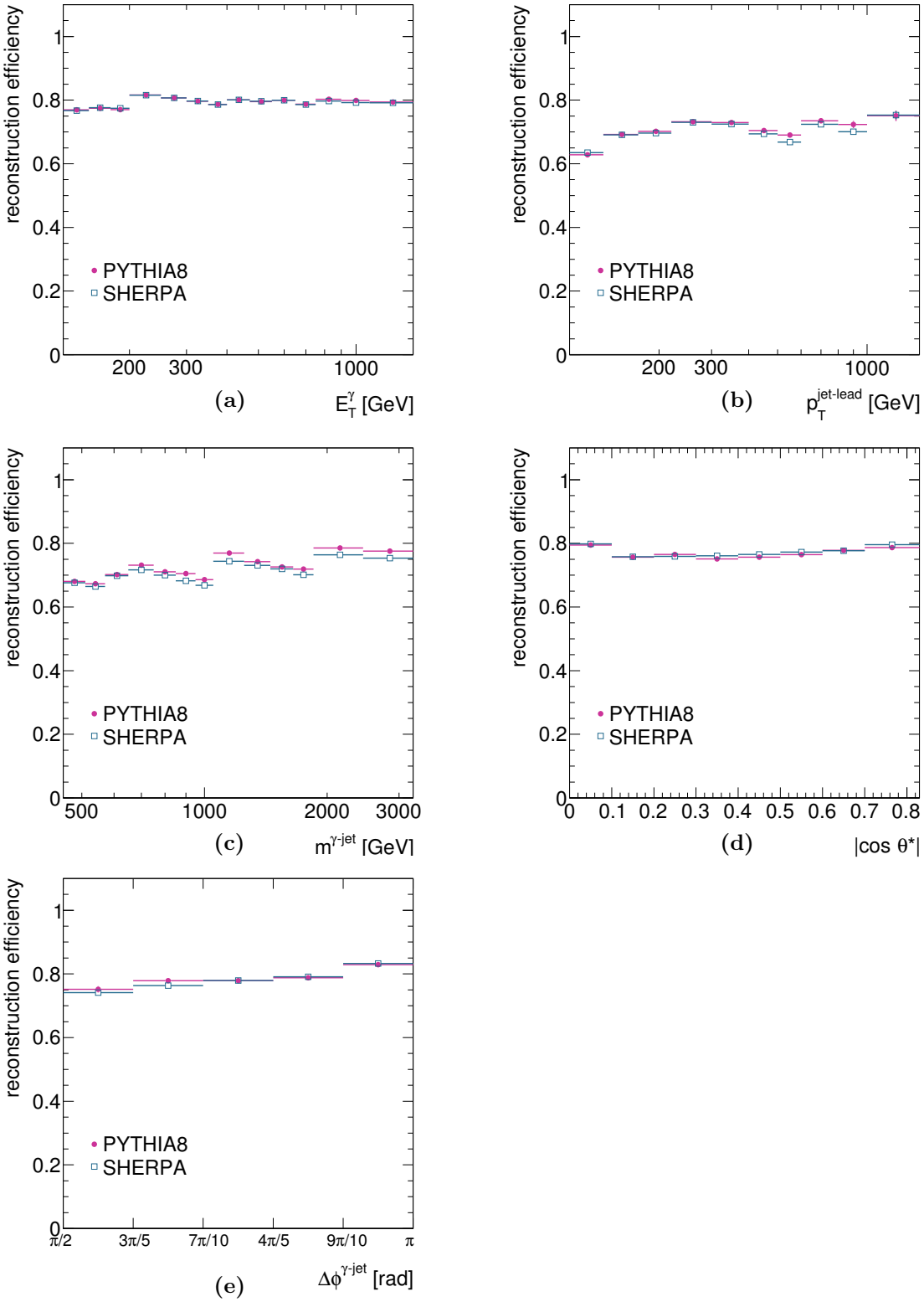


Figure 8.37: Selection efficiency from PYTHIA optimised (dots) and SHERPA (squares) as a function of (a) E_{T}^{γ}, (b) $p_{\mathrm{T}}^{\mathrm{jet-lead}}$, (c) $m^{\gamma-\mathrm{jet}}$, (d) $|\cos\theta^{\star}|$ and (e) $\Delta\phi^{\gamma-\mathrm{jet}}$.

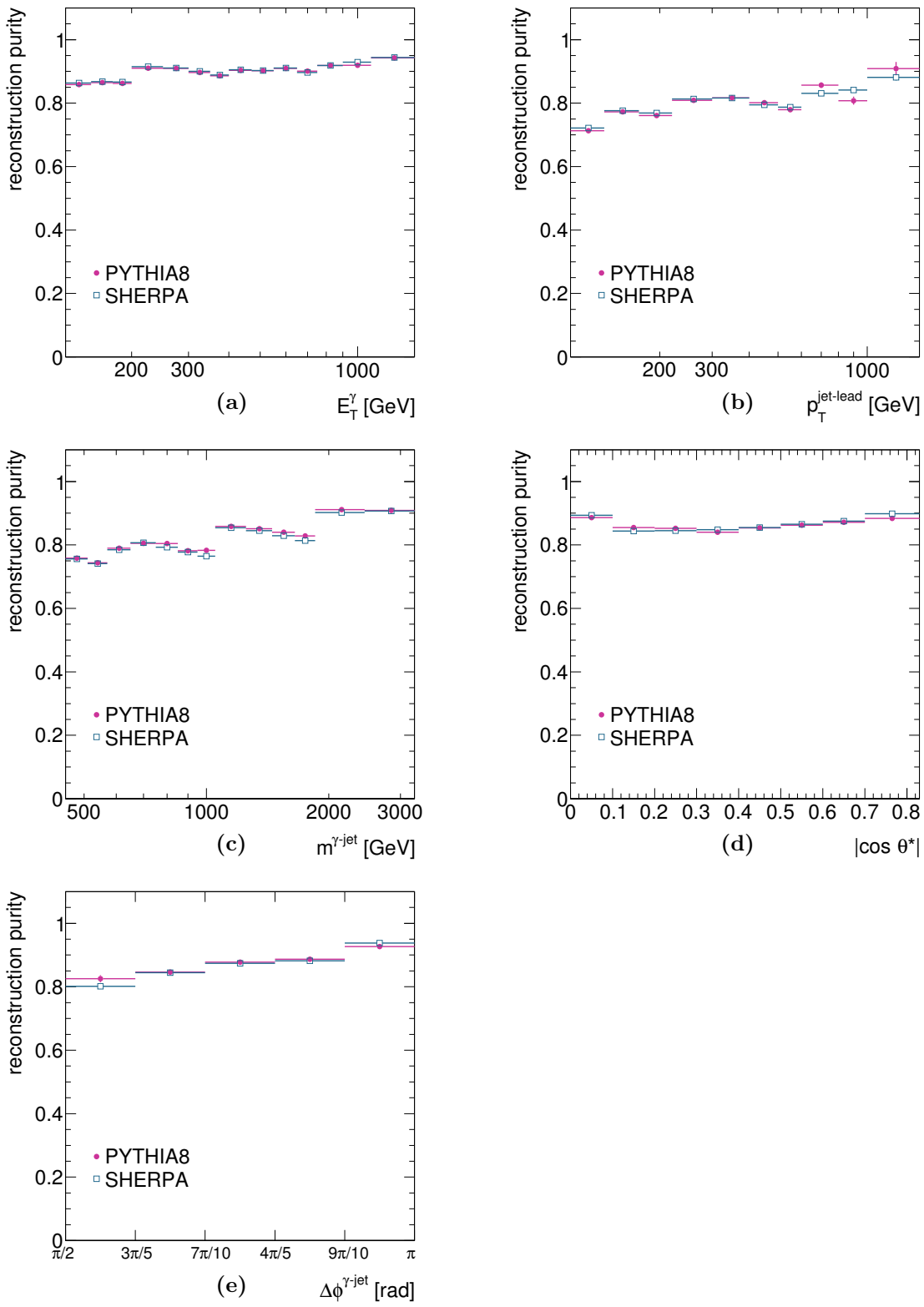


Figure 8.38: Selection purity from PYTHIA optimised (dots) and SHERPA (squares) as a function of (a) E_{T}^{γ}, (b) $p_{\mathrm{T}}^{\mathrm{jet-lead}}$, (c) $m^{\gamma-\mathrm{jet}}$, (d) $|\cos\theta^{\star}|$ and (e) $\Delta\phi^{\gamma-\mathrm{jet}}$.

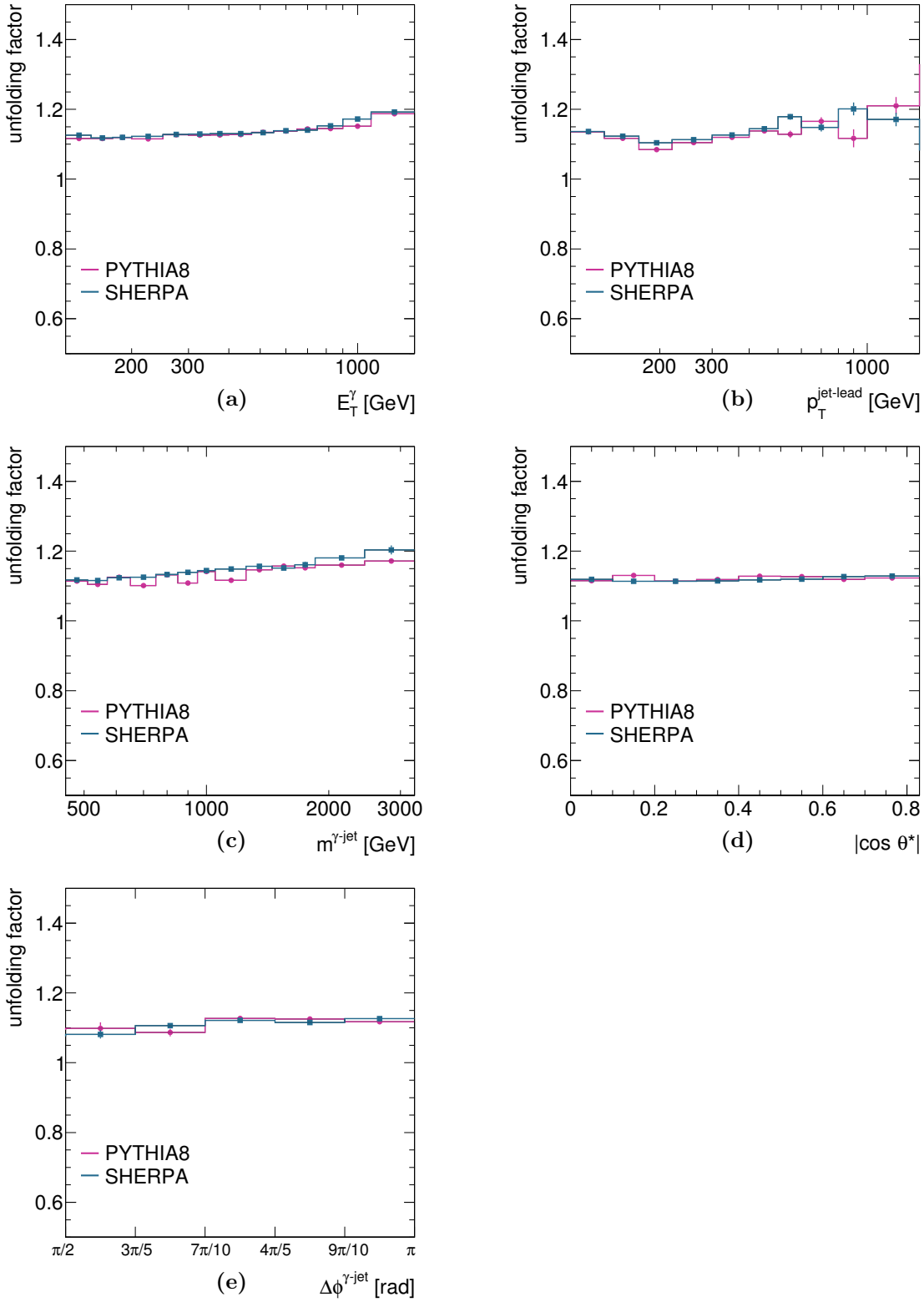


Figure 8.39: Unfolding factors from PYTHIA optimised (dots) and SHERPA (squares) as functions of (a) E_{T}^{γ}, (b) $p_{\mathrm{T}}^{\mathrm{jet-lead}}$, (c) $m^{\gamma-\mathrm{jet}}$, (d) $|\cos\theta^{\star}|$ and (e) $\Delta\phi^{\gamma-\mathrm{jet}}$.

8.4.5 Cross-check using reweighted MC

A cross-check of the bin-by-bin unfolding was performed by reweighting the MC distributions at reconstruction level to the data. The ratio of the data to the MC distributions was fitted according to a χ^2 fit. This is shown in Figure 8.40. Both the particle and reconstruction level distributions were weighted with a factor extracted from the fitting function of each observable evaluated at the particle level for a given observable. After such a reweighting, the ratio between data and the MC predictions at reconstruction level is expected to be close to unity. This ratio is shown in Figure 8.41.

The cross-check was performed by measuring the cross sections with the reweighted version of SHERPA for the estimation of the unfolding correction factors. The relative difference with respect to the measurement obtained using SHERPA default for the unfolding is shown in Figure 8.42 and reflects the dependence of the measured cross section on the predicted shape of the distributions by the simulations. It was observed that the use or not of reweighted SHERPA does not change the measurements, validating the use of a bin-by-bin unfolding: the deviations are smaller than 0.15%, except for the first bin of $\Delta\phi^{\gamma-\text{jet}}$, in which the difference is 0.4% (see Figure 8.42).

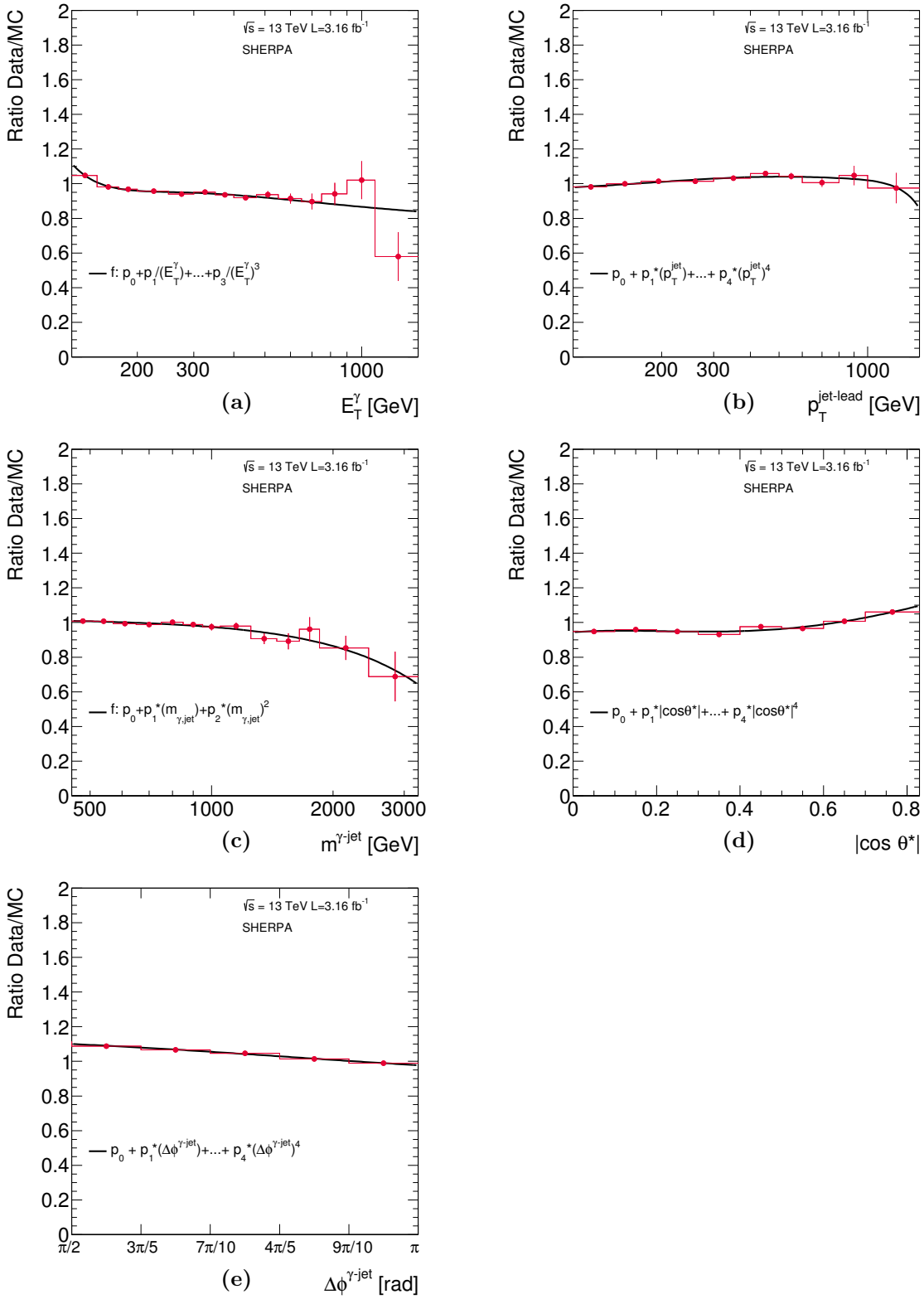


Figure 8.40: Ratio of the data and SHERPA distributions (dots) as a function of (a) E_{T}^{γ}, (b) $p_{\mathrm{T}}^{\mathrm{jet-lead}}$, (c) $m^{\gamma-\mathrm{jet}}$, (d) $|\cos\theta^{\star}|$ and (e) $\Delta\phi^{\gamma-\mathrm{jet}}$. The solid line represents the fit to the ratio. The error bars are statistical only.

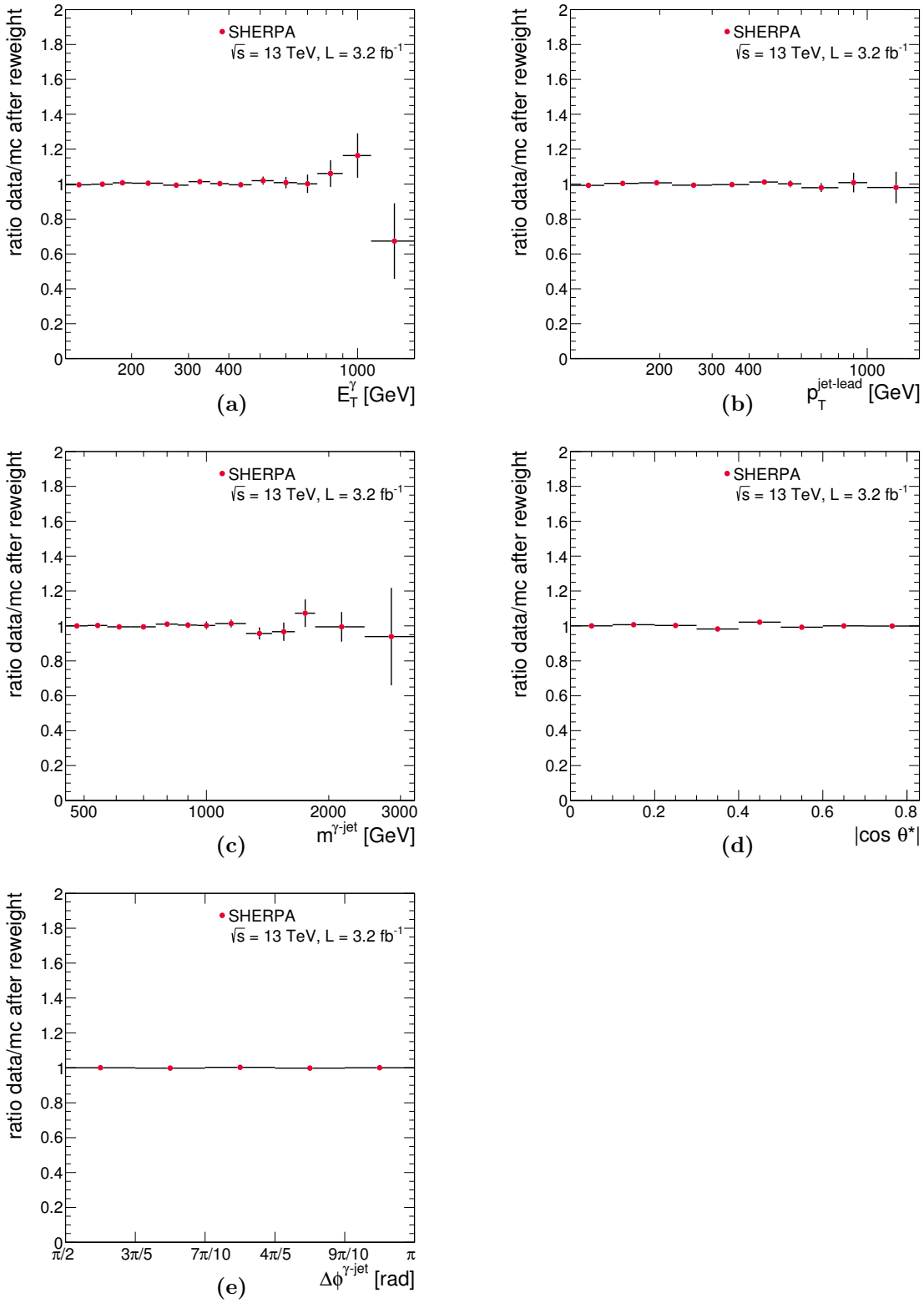


Figure 8.41: Ratio of data and reweighted SHERPA distributions (dots) as a function of (a) E_{T}^{γ}, (b) $p_{\mathrm{T}}^{\mathrm{jet-lead}}$, (c) $m^{\gamma-\mathrm{jet}}$, (d) $|\cos\theta^{\star}|$ and (e) $\Delta\phi^{\gamma-\mathrm{jet}}$. The error bars are statistical only.

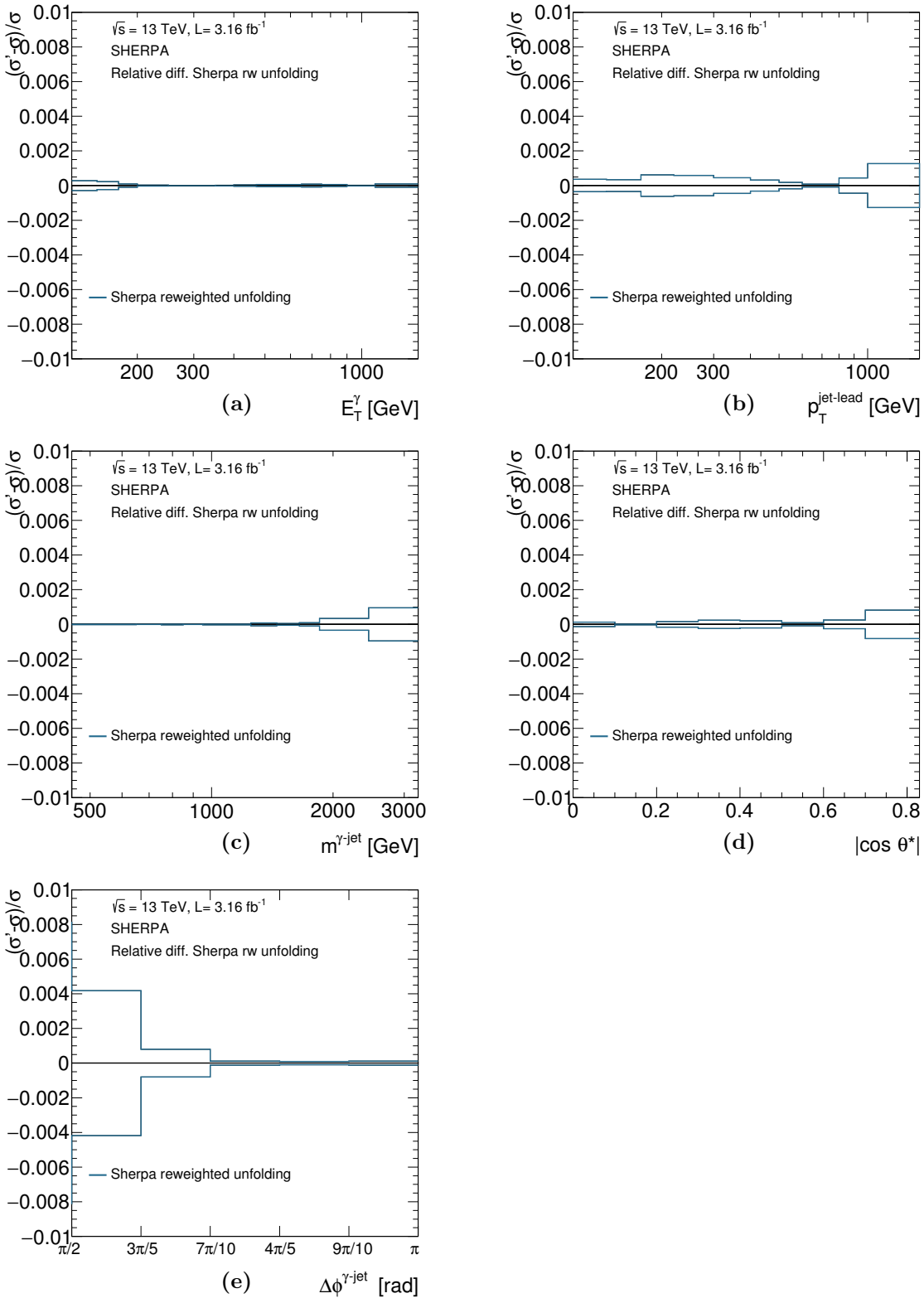
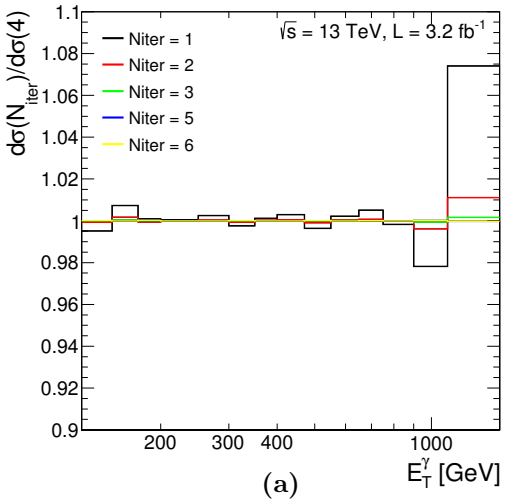


Figure 8.42: Relative difference between the cross section measured using the reweighted SHERPA for the estimation of the bin-by-bin unfolding corrections and those using SHERPA default as a function of (a) E_{T}^{γ}, (b) $p_{\mathrm{T}}^{\mathrm{jet-lead}}$, (c) $m^{\gamma-\mathrm{jet}}$, (d) $|\cos\theta^{\star}|$ and (e) $\Delta\phi^{\gamma-\mathrm{jet}}$.

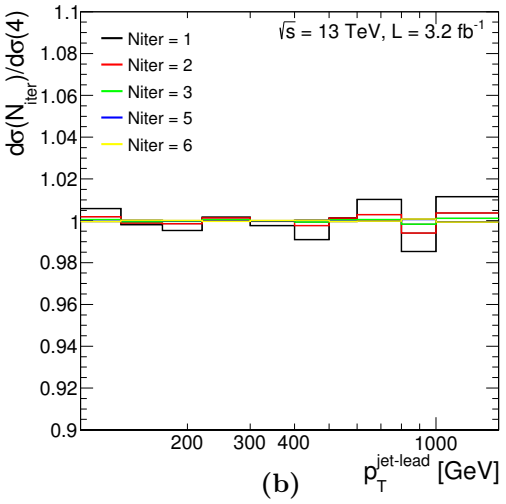
8.4.6 Cross-check using Bayesian unfolding

The measurements obtained with a bin-by-bin unfolding were cross-checked with the Bayesian unfolding explained in Section 6.5.1. Figure 8.43 shows the relative difference between the results obtained using different number of iterations, N, with respect to those obtained using 4 iterations as a function of E_{T}^{γ}, $p_{\mathrm{T}}^{\mathrm{jet-lead}}$, $m^{\gamma-\mathrm{jet}}$, $|\cos\theta^{\star}|$ and $\Delta\phi^{\gamma-\mathrm{jet}}$. The oscillations on the results for $N < 4$ are quite large; these oscillations disappear for $N > 4$. Therefore, the nominal Bayes' unfolding was performed using 4 iterations.

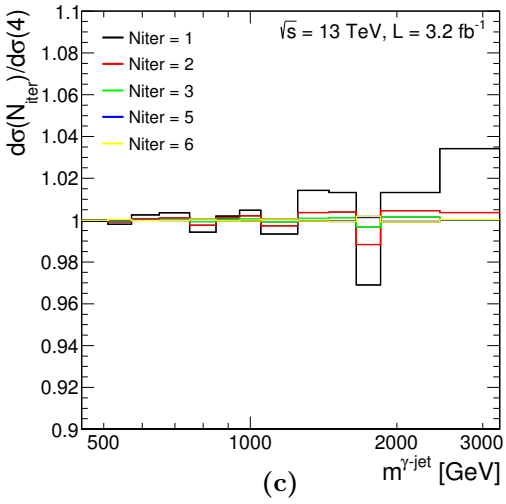
The comparison between the cross sections unfolded via the bin-by-bin and the Bayes (using $N = 4$ iterations) methods is shown in Figure 8.44. The differences between the cross sections obtained via the two methods are generally much smaller than 1%. In the regions of phase space where the MC statistics is poor some larger deviations are observed, but they are smaller than the statistical uncertainty of the data. For comparison, the statistical uncertainty of the cross section is also included in the figures and shows that the size of this uncertainty is much bigger than the difference of the cross sections obtained with the two methods. The correlation matrix used in the Bayes unfolding is shown in Figure 8.45.



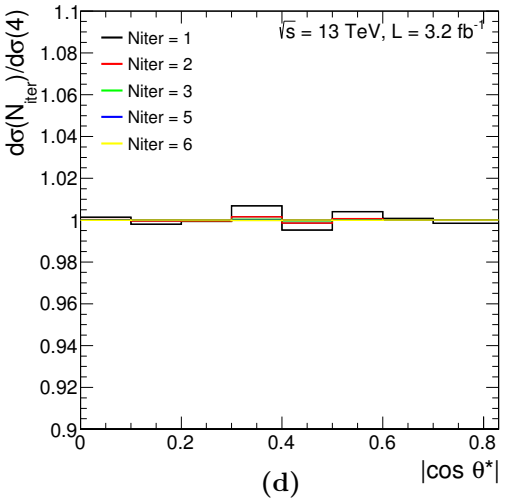
(a)



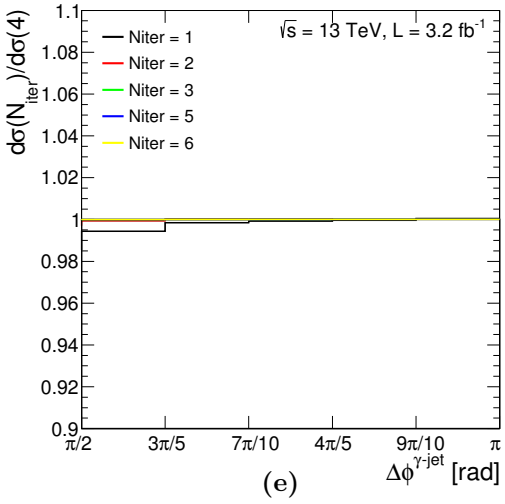
(b)



(c)

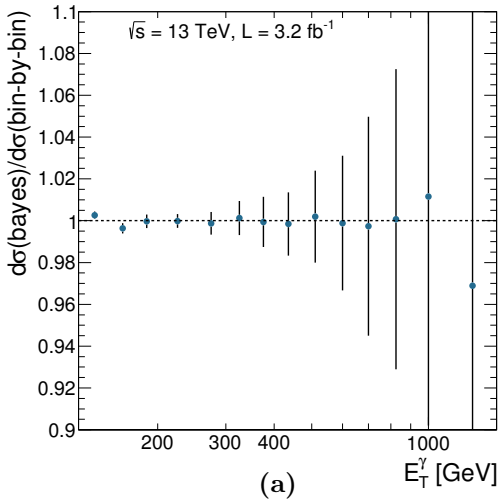


(d)

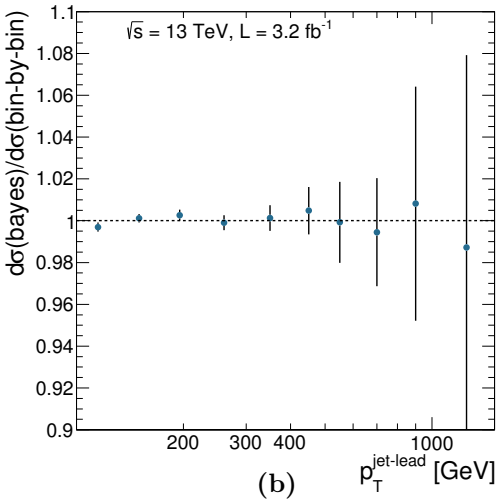


(e)

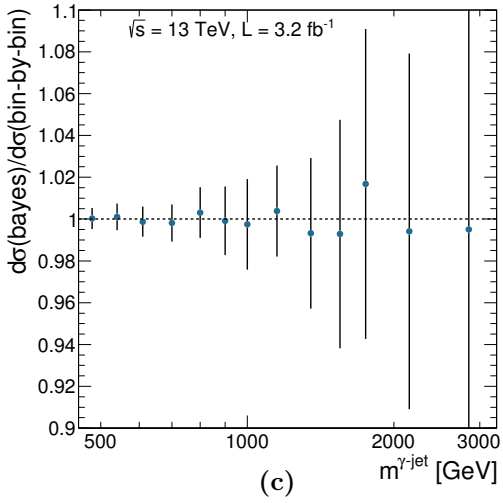
Figure 8.43: Ratios between the cross sections unfolded using the Bayesian method with N iterations and the results unfolded using 4 iterations as functions of (a) E_{T}^{γ}, (b) $p_{\mathrm{T}}^{\mathrm{jet-lead}}$, (c) $m^{\gamma-\mathrm{jet}}$, (d) $|\cos\theta^{\star}|$ and (e) $\Delta\phi^{\gamma-\mathrm{jet}}$.



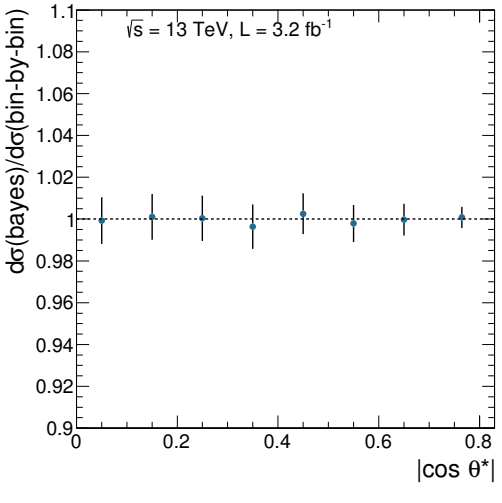
(a)



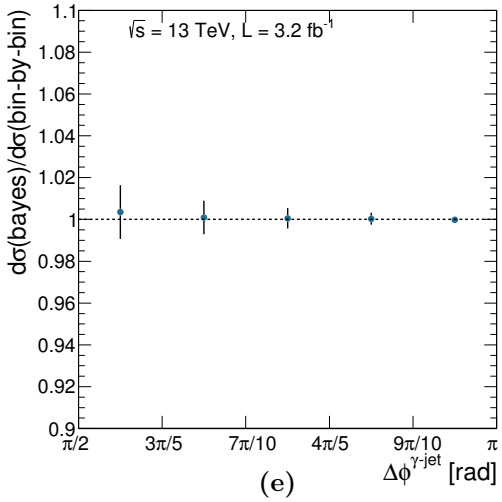
(b)



(c)



(d)



(e)

Figure 8.44: Ratios between the cross sections unfolded using the Bayesian method with four iterations and the nominal cross sections as functions of (a) E_{T}^{γ}, (b) $p_{\mathrm{T}}^{\mathrm{jet-lead}}$, (c) $m^{\gamma-\mathrm{jet}}$, (d) $|\cos\theta^{\star}|$ and (e) $\Delta\phi^{\gamma-\mathrm{jet}}$. For illustration, the relative statistical uncertainties of the nominal cross sections are shown as error bars.

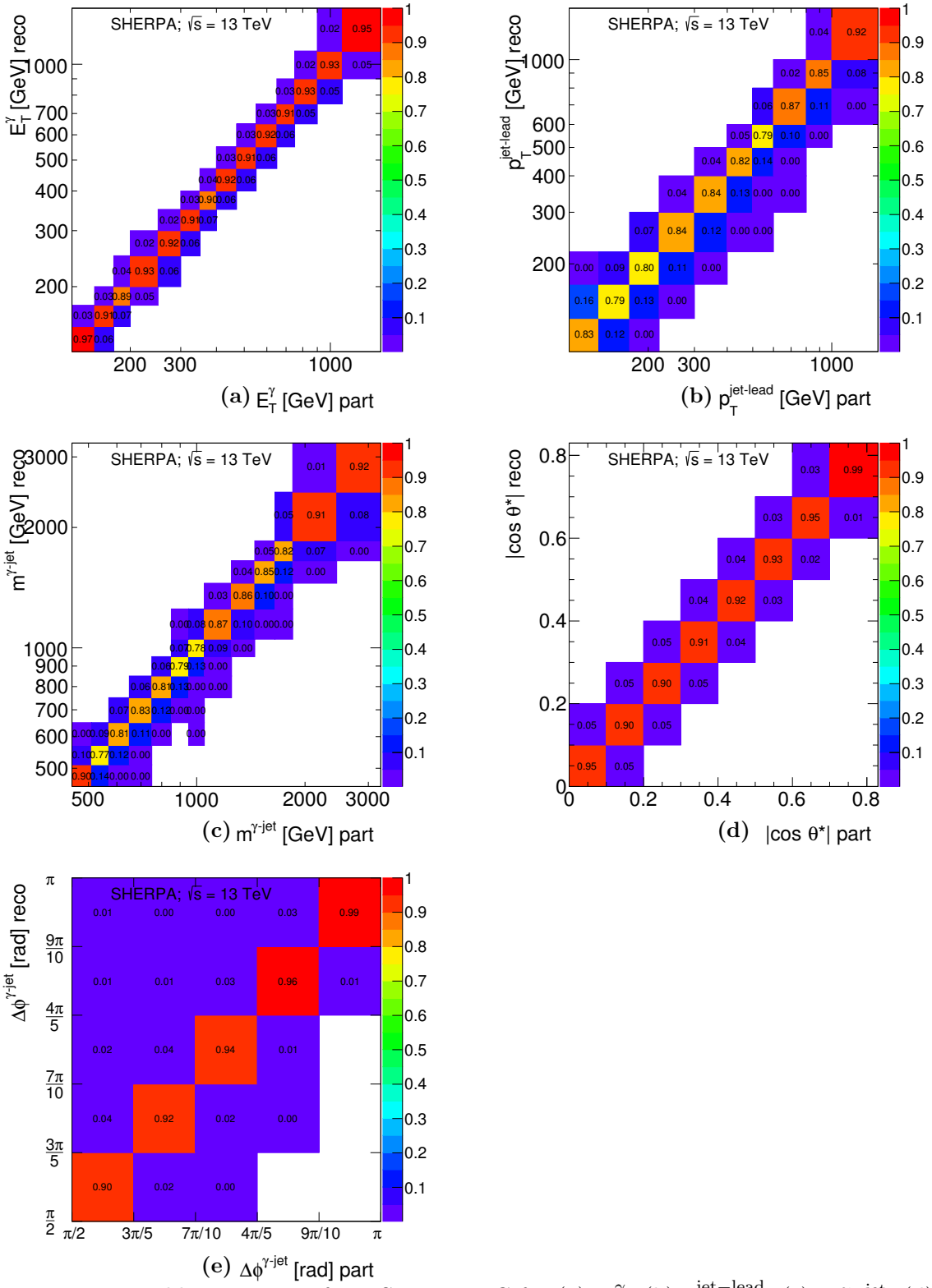


Figure 8.45: Folding matrices from SHERPA MC for (a) E_{T}^{γ}, (b) $p_{\mathrm{T}}^{\mathrm{jet-lead}}$, (c) $m^{\gamma-\mathrm{jet}}$, (d) $|\cos\theta^{\star}|$ and (e) $\Delta\phi^{\gamma-\mathrm{jet}}$.

8.5 Systematic uncertainties

The sources of systematic uncertainty that affect the measurements were investigated. These sources include the photon energy scale and resolution, the jet energy scale and resolution, the QCD-cascade and hadronisation model dependence, the photon identification efficiency, the MC isolation correction, the choice of background control regions, the identification and isolation correlation in the background, the signal modelling, pile-up reweighting, MC sample statistics, the trigger efficiency and the luminosity uncertainties. Each source is discussed below.

8.5.1 Photon energy scale and resolution

The uncertainty on the cross-section measurement due to the uncertainty on the photon energy scale and resolution was investigated following the same scheme as explained in Section 6.6.1. The final value of the uncertainty was estimated using a bootstrap technique to smooth the results obtained, which are shown in Figure 8.46 and compared to the size of the uncertainty before the smoothing. The dominant component of the uncertainty is that due to the relative intercalibration between the medium and high gain used to collect data in the second layer of the EM calorimeter ("L2Gain"). The second and third most important contributions are those due to the LAr calorimeter intercalibration with muons between the first and second layer in the central region of the detector ("LArCalib_etabin0") and the systematic uncertainties for the measurement of data and MC energy scale using electrons coming from Z boson decays ("ZeeSyst"). They are shown in Figure 8.47.

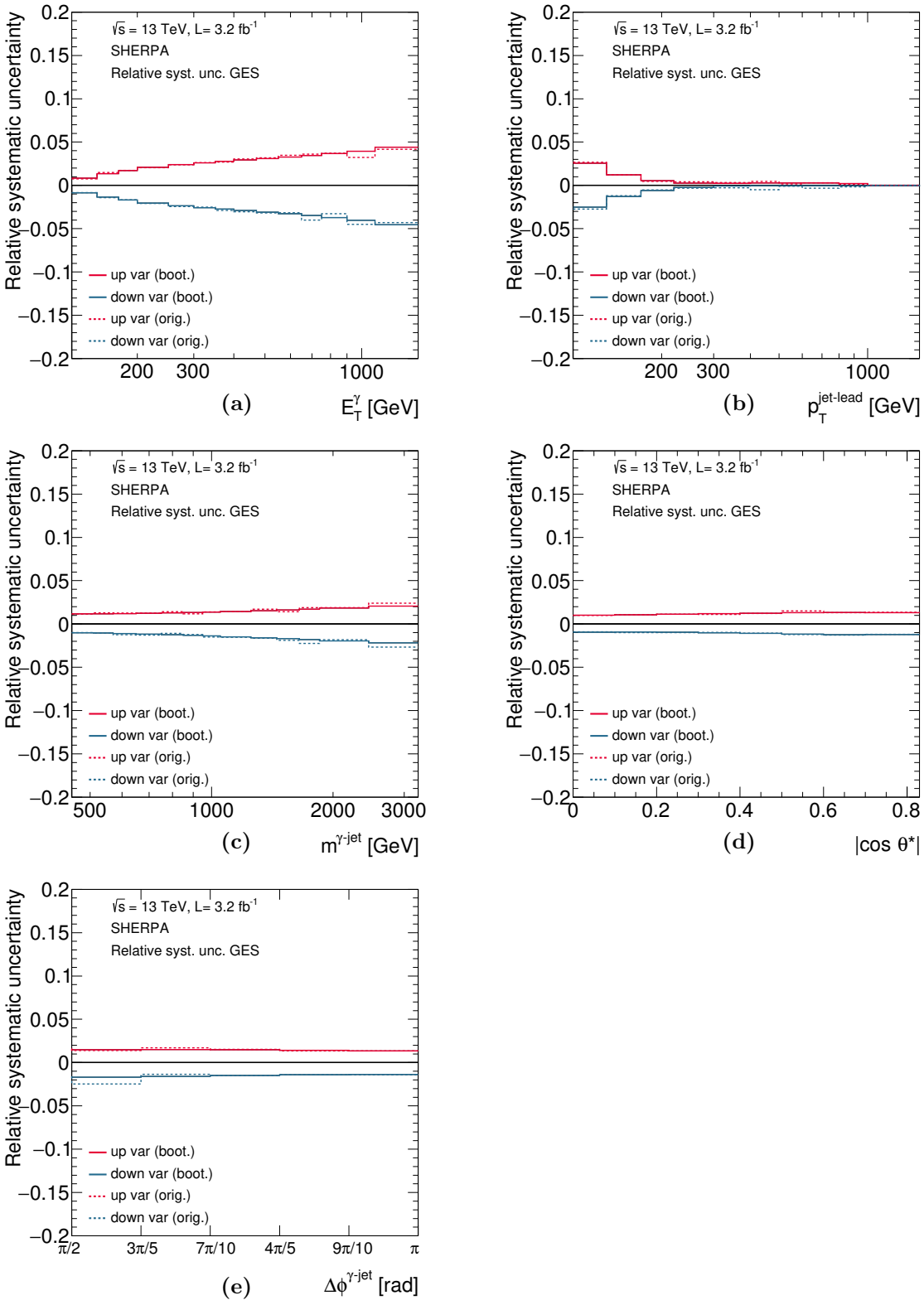


Figure 8.46: Systematic uncertainties on the measured cross section due to the uncertainty in the photon energy scale and resolution as functions of (a) E_{T}^{γ}, (b) $p_{\mathrm{T}}^{\mathrm{jet-lead}}$, (c) $m^{\gamma-\mathrm{jet}}$, (d) $|\cos\theta^{\star}|$ and (e) $\Delta\phi^{\gamma-\mathrm{jet}}$. The solid (dashed) lines display the estimations with (without) bootstrap.

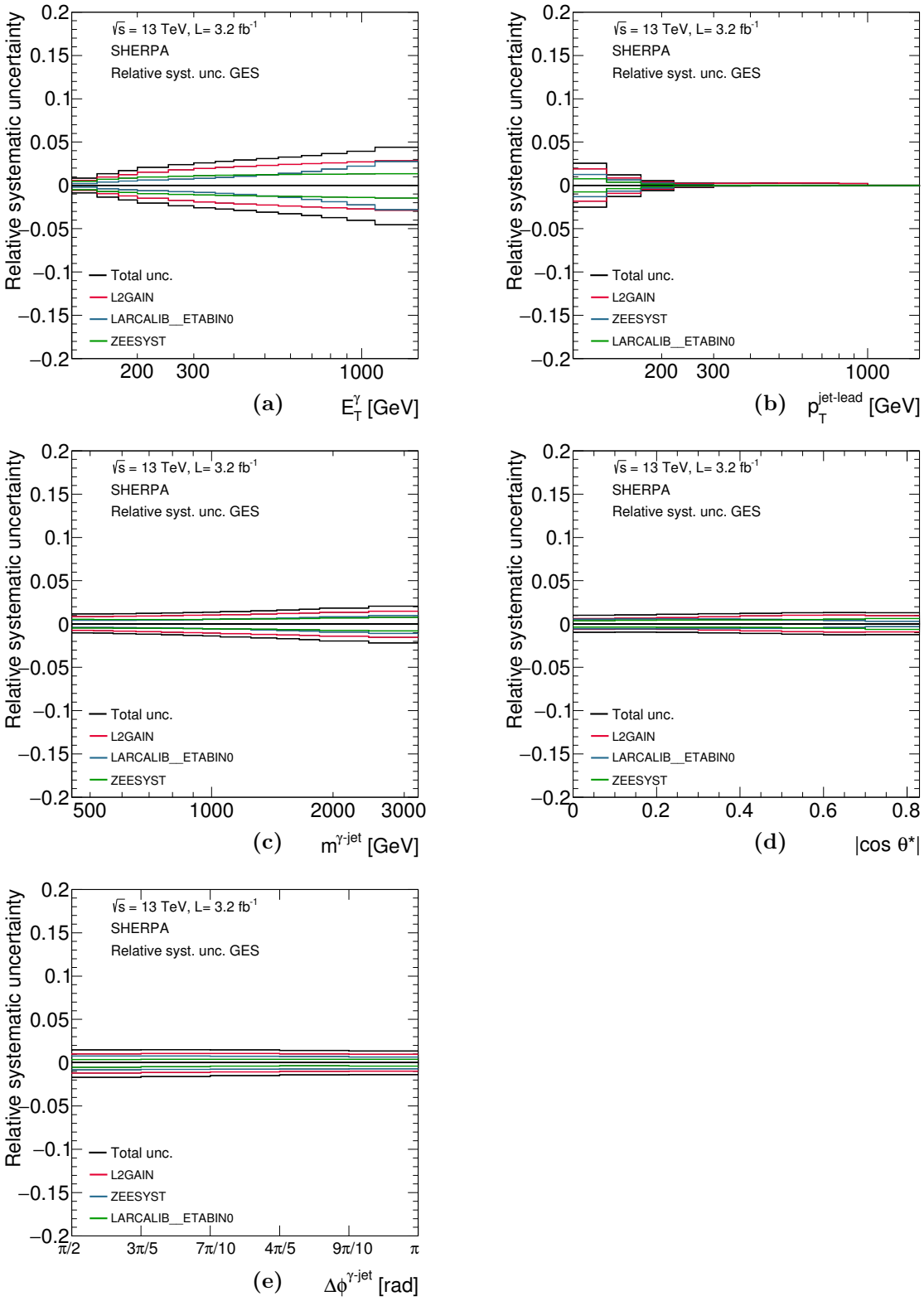


Figure 8.47: Systematic uncertainties on the measured cross section due to the uncertainty in the photon energy scale and resolution as functions of (a) E_{T}^{γ}, (b) $p_{\mathrm{T}}^{\mathrm{jet-lead}}$, (c) $m^{\gamma-\mathrm{jet}}$, (d) $|\cos\theta^{\star}|$ and (d) $\Delta\phi^{\gamma-\mathrm{jet}}$ (black lines). The red, blue and green lines represent the largest, second-largest and third-largest contributions to this uncertainty.

8.5.2 Jet energy scale

The effect on the cross section due to the uncertainty on the jet energy scale was evaluated. For this analysis, the pre-recommendation released for 2015 was used and contains a full treatment of bin-to-bin correlations for the individual sources of uncertainties. This is achieved through the splitting of the nuisance parameters coming from the various in-situ techniques. More details are found in Chapter 5.

Each individual source was varied in the MC simulations and then added in quadrature. The uncertainties were smoothed using the same bootstrap technique as described in Section 6.6.1. They are shown in Figure 8.48 and compared to the total uncertainty before the smoothing. The estimations using bootstrap for the three largest contributions to this uncertainty are shown in Figures 8.49. The four major uncertainties are due to the flavour composition of the sample ("Flavor_Composition"), the response to quark- and gluon-initiated jets ("Flavor_Response"), the electron and photon energy scale in the in situ measurements ("LAr_ESZee") and the generator used in the γ+jet in situ measurement ("Gjet_generator").

8.5.3 Jet energy resolution

The jet energy resolution source of systematic accounts for the fact that the simulated sample has better energy resolution than the data. The impact of this difference was estimated by smearing the MC simulated distributions and comparing the smeared and non-smeared results. The results were smoothed for the $p_{\mathrm{T}}^{\mathrm{jet-lead}}$ distribution.

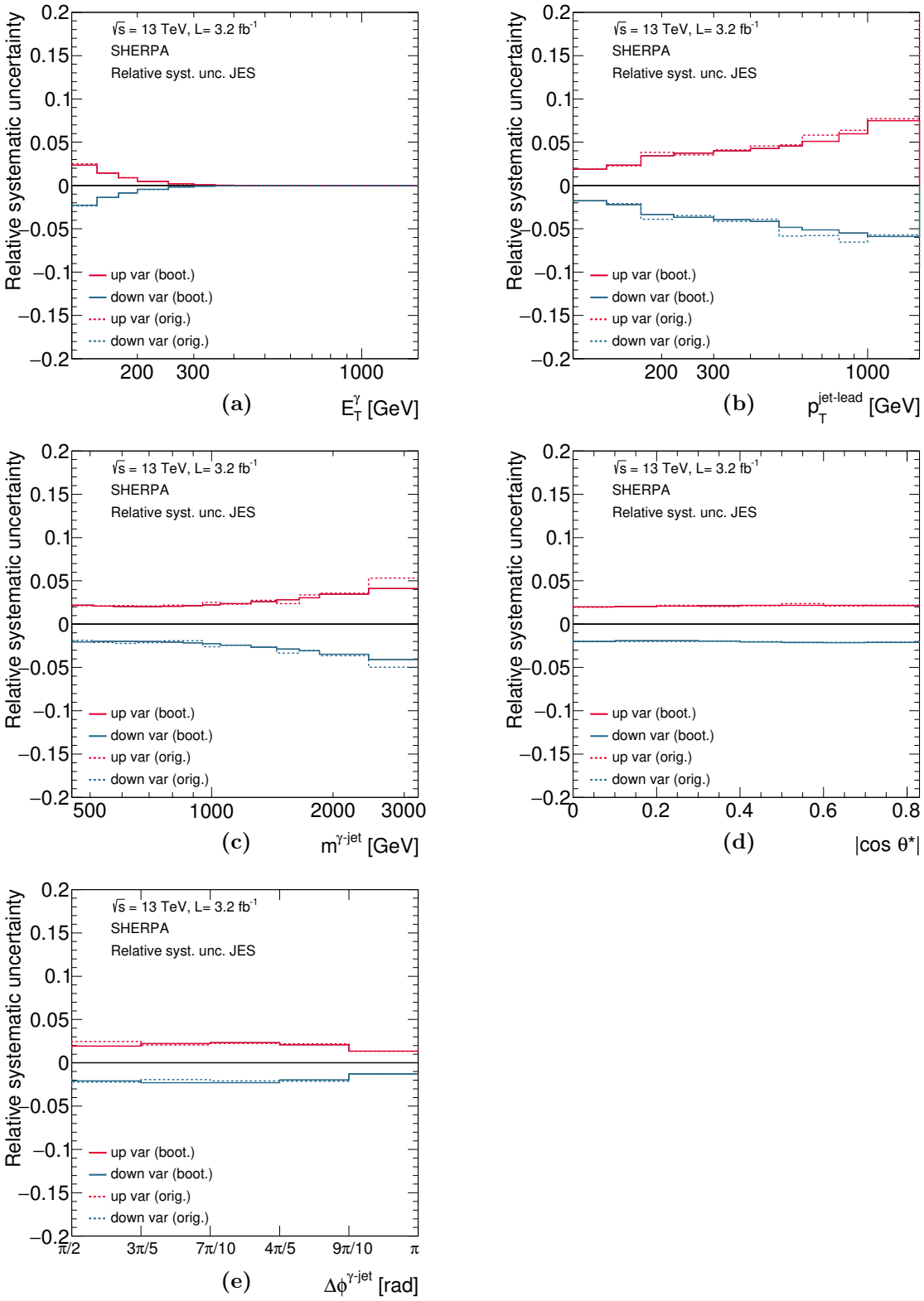


Figure 8.48: Systematic uncertainties on the measured cross section due to the uncertainty in the jet energy scale as functions of (a) E_{T}^{γ}, (b) $p_{\mathrm{T}}^{\mathrm{jet-lead}}$, (c) $m^{\gamma-\mathrm{jet}}$, (d) $|\cos\theta^{\star}|$ and (e) $\Delta\phi^{\gamma-\mathrm{jet}}$. The solid (dashed) lines display the estimations with (without) bootstrap.

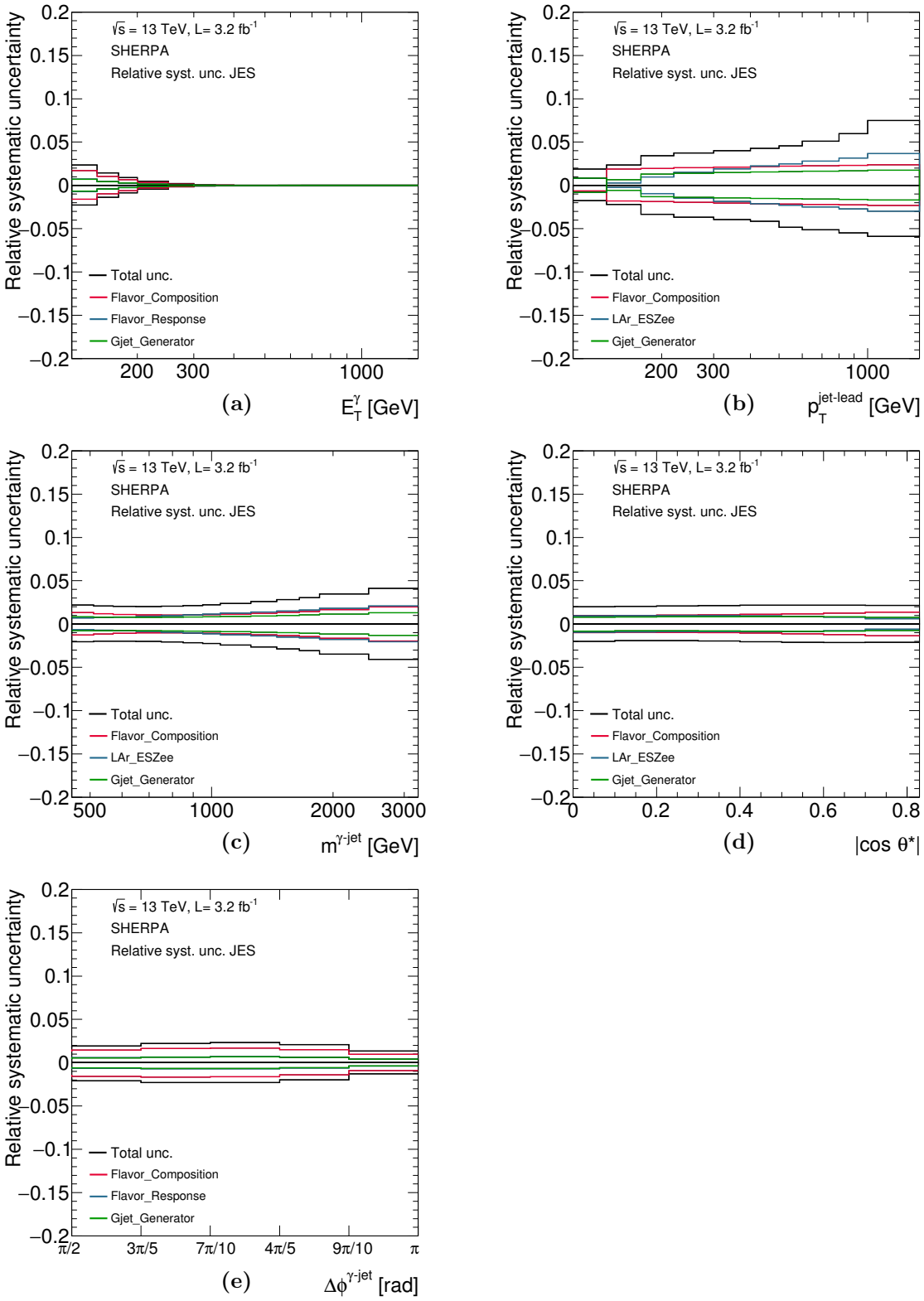


Figure 8.49: Systematic uncertainties on the measured cross section due to the uncertainty in the jet energy scale as functions of (a) E_{T}^{γ}, (b) $p_{\mathrm{T}}^{\mathrm{jet-lead}}$, (c) $m^{\gamma-\mathrm{jet}}$, (d) $|\cos\theta^{\star}|$ and (e) $\Delta\phi^{\gamma-\mathrm{jet}}$ (black lines). The red, blue and green lines represent the largest, second-largest and third-largest contributions to this uncertainty.

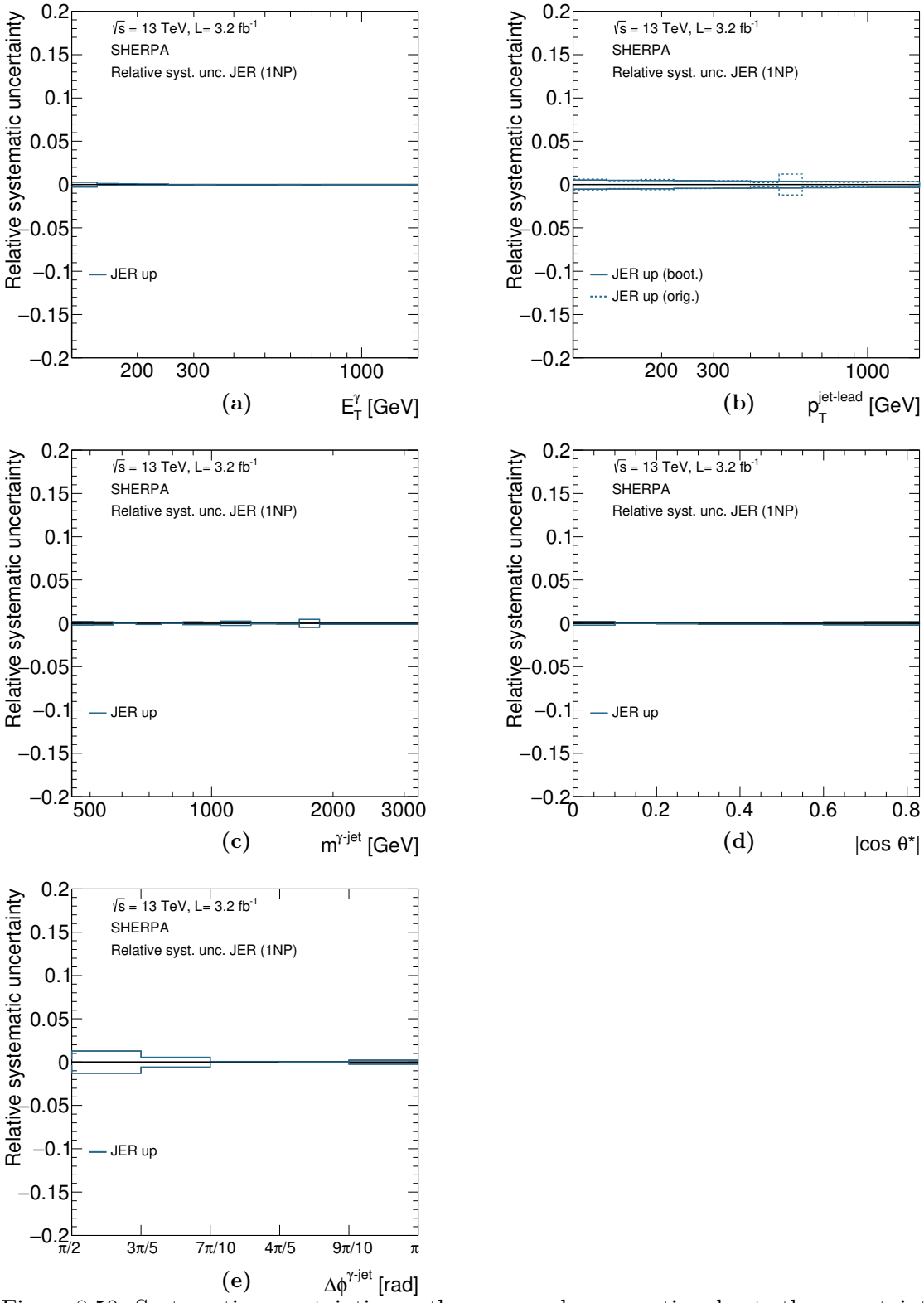


Figure 8.50: Systematic uncertainties on the measured cross section due to the uncertainty in the jet energy resolution as functions of (a) E_{T}^{γ}, (b) $p_{\mathrm{T}}^{\mathrm{jet-lead}}$, (c) $m^{\gamma-\mathrm{jet}}$, (d) $|\cos\theta^{\star}|$ and (e) $\Delta\phi^{\gamma-\mathrm{jet}}$. The estimations for (b) with (without) bootstrap are shown as solid (dashed) lines; for the other variables, the estimations without bootstrap are shown as solid lines.

8.5.4 Parton-shower and hadronisation model dependence

The effects due to the parton-shower and hadronisation models in the signal leakage fractions and unfolding corrections were estimated as the deviations observed from the nominal results by using alternate MC simulations of the signal. Figures 8.51 and 8.52 show the resulting uncertainties:

- signal leakage fractions: the signal leakage fractions of Pythia optimised were used to subtract the background via the 2D-sideband method for the nominal cross sections. The effects on the measured cross sections of using either Pythia default or Sherpa for the signal leakage fractions are shown in Figure 8.51. The envelope of these two variations was used to estimate the final uncertainty. In the cases in which both variations had the same sign, the largest absolute value of the change was taken as the uncertainty and symmetrised. In every case the unfolding is performed with Sherpa;
- unfolding corrections: Sherpa was used for the nominal cross sections. The effects on the measured cross sections of using Pythia optimised for the unfolding are shown in Figure 8.52. In every case the signal leakage fractions of Pythia optimised are used.

Separated in this way, possible partial cancellations of the two effects were avoided. The resulting uncertainties from these two effects were added in quadrature when estimating the total systematic uncertainty following a conservative approach.

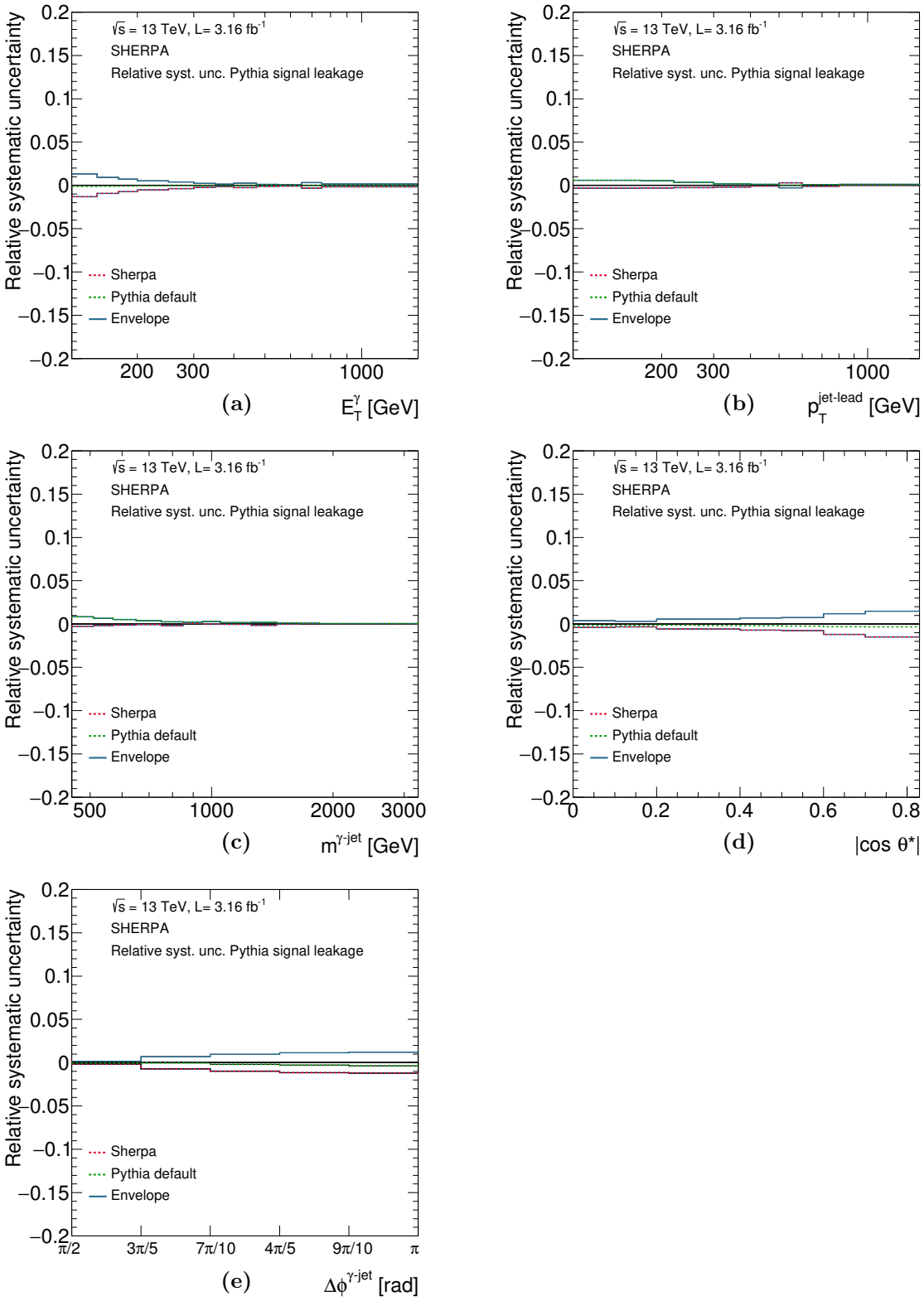


Figure 8.51: Systematic uncertainties on the measured cross section due to the parton shower and hadronisation models as functions of (a) E_{T}^{γ}, (b) $p_{\mathrm{T}}^{\mathrm{jet-lead}}$, (c) $m^{\gamma-\mathrm{jet}}$, (d) $|\cos\theta^{\star}|$ and (e) $\Delta\phi^{\gamma-\mathrm{jet}}$ using either PYTHIA default (green dashed lines) or SHERPA (red dashed lines) to estimate the signal purity. The envelope is shown as the blue solid line.

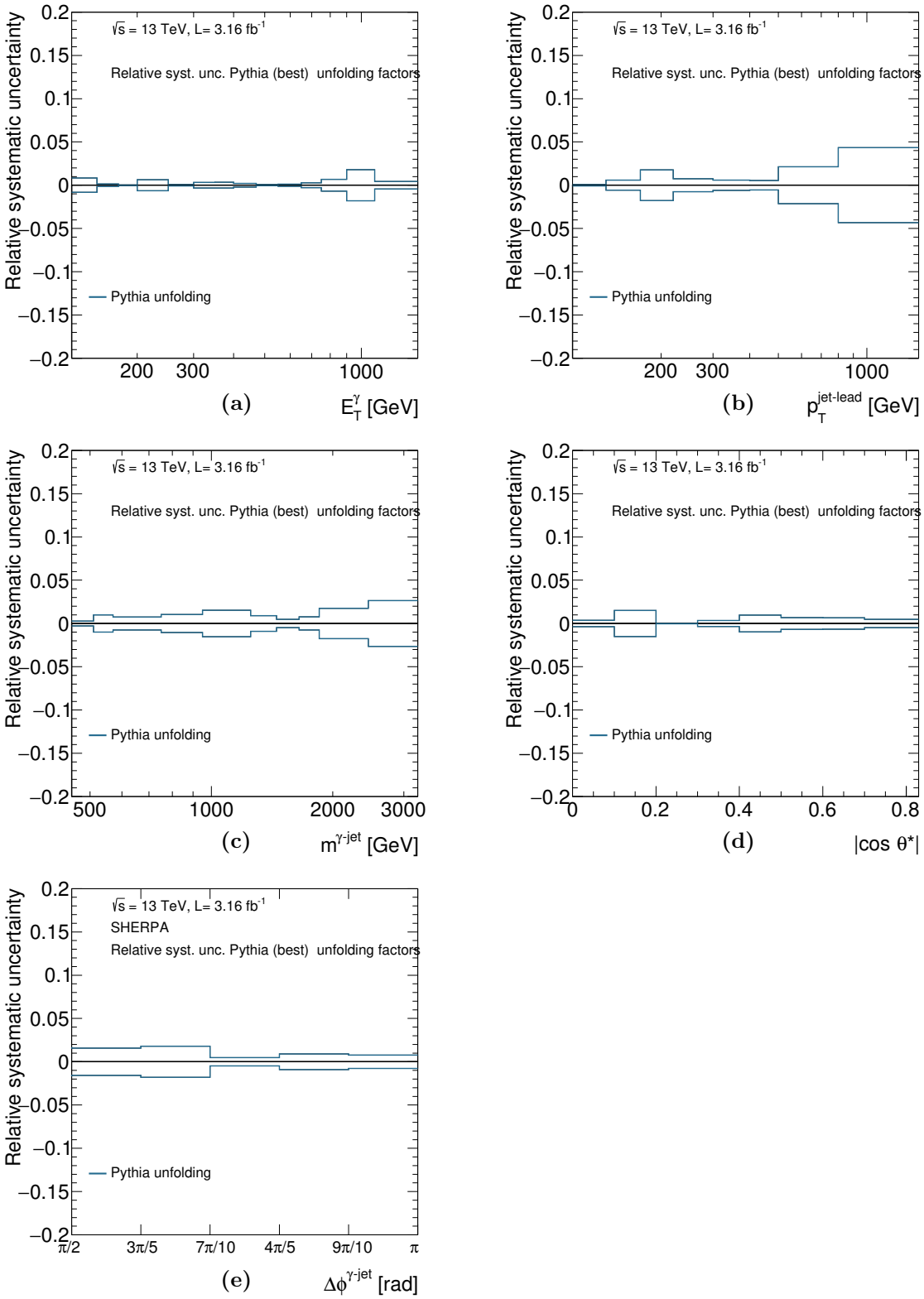


Figure 8.52: Systematic uncertainties on the measured cross section due to the parton-shower and hadronisation models as functions of (a) E_{T}^{γ}, (b) $p_{\mathrm{T}}^{\mathrm{jet-lead}}$, (c) $m^{\gamma-\mathrm{jet}}$, (d) $|\cos\theta^{\star}|$ and (e) $\Delta\phi^{\gamma-\mathrm{jet}}$ using Pythia optimised to estimate the unfolding corrections. This uncertainty has been symmetrised. The unfolding is performed with Pythia using the optimal admixture of the hard and bremsstrahlung components (denoted by "best" in the legends).

8.5.5 Photon identification

The effect in the cross sections due to the photon tight identification efficiency was evaluated by switching on and off the corrections applied to the shower-shape variables. The resulting uncertainties are shown in Figure 8.53.

8.5.6 Isolation correction

The resulting uncertainty due to the isolation correction in the MC are shown in Figure 8.54 (see Section 6.6.4 for details).

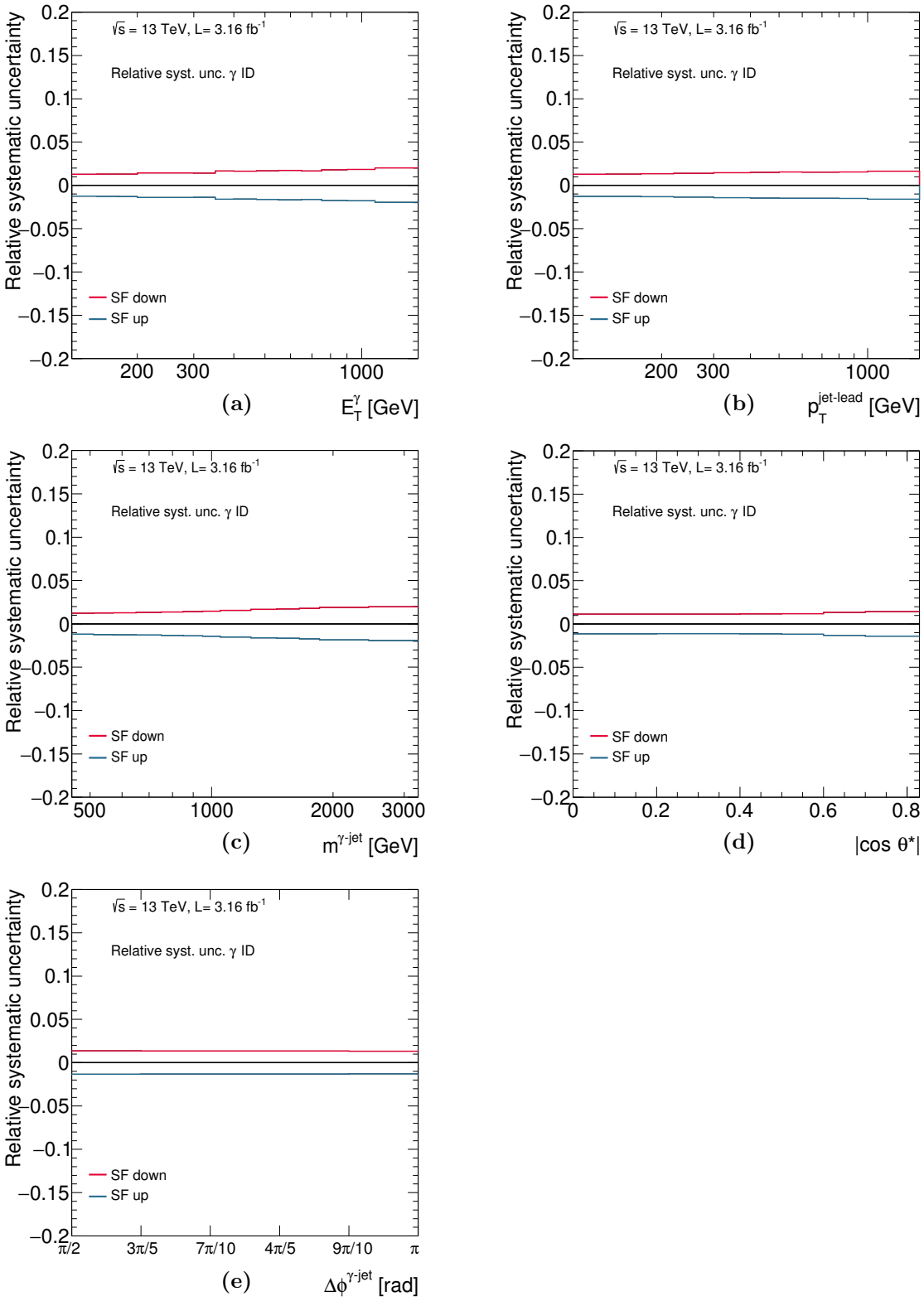


Figure 8.53: Systematic uncertainties on the measured cross sections due to the uncertainty in the photon-ID efficiency as functions of (a) E_{T}^{γ}, (b) $p_{\mathrm{T}}^{\mathrm{jet-lead}}$, (c) $m^{\gamma-\mathrm{jet}}$, (d) $|\cos\theta^{\star}|$ and (e) $\Delta\phi^{\gamma-\mathrm{jet}}$.

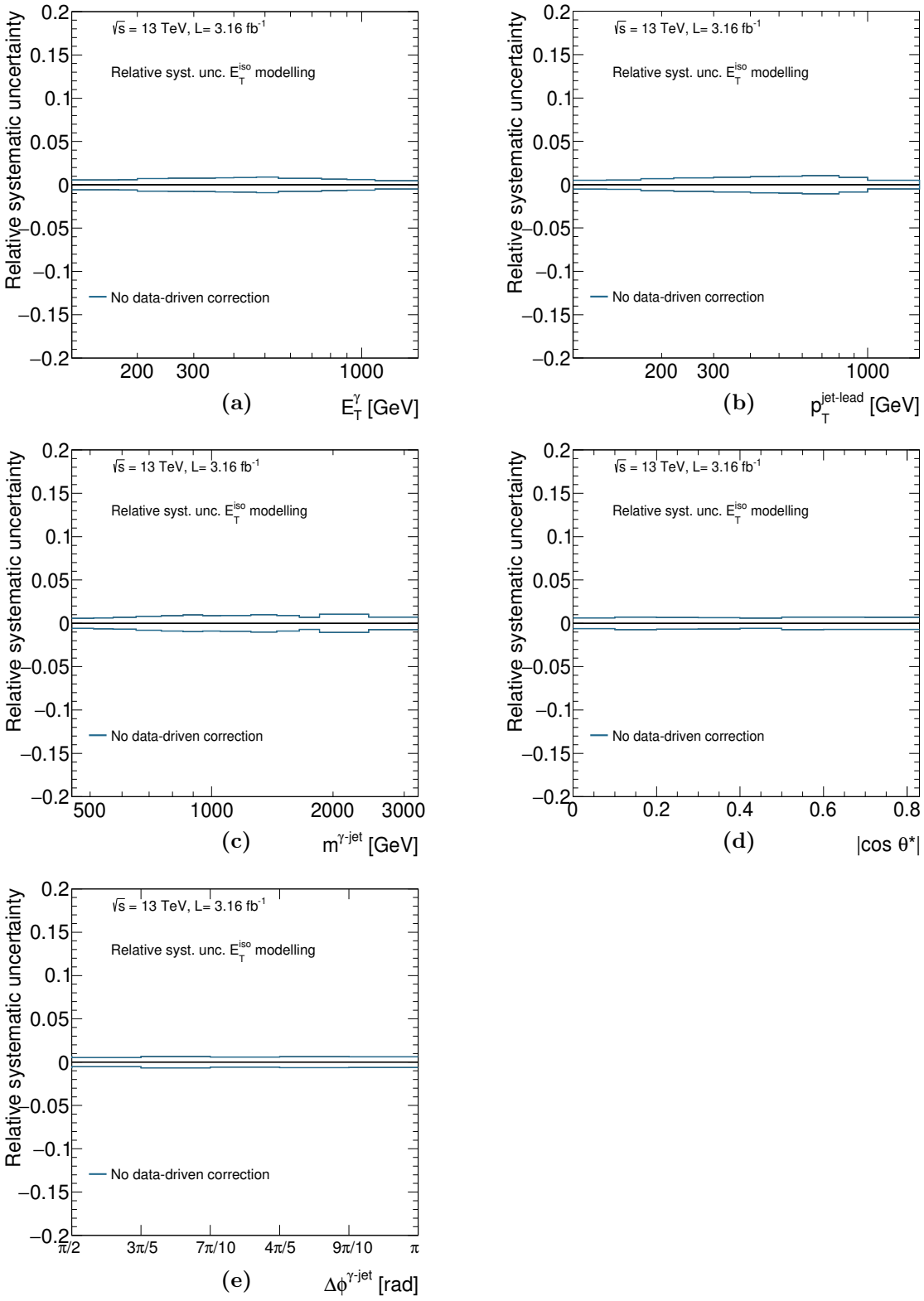


Figure 8.54: Systematic uncertainties on the measured cross sections due to the effect of the isolation corrections as functions of (a) E_{T}^{γ}, (b) $p_{\mathrm{T}}^{\mathrm{jet-lead}}$, (c) $m^{\gamma-\mathrm{jet}}$, (d) $|\cos\theta^{\star}|$ and (e) $\Delta\phi^{\gamma-\mathrm{jet}}$.

8.5.7 Choice of background control regions

The effect of the alternative definitions of the background control regions on the signal yield and, therefore, in the cross sections were evaluated. The variations considered are the same ones as explained in Section 6.6.5. The relative differences in the cross sections due to the variation of the lower limit in isolation of the non-isolated control regions are shown in Figure 8.55. The effect of removing the upper limit of these non-isolated control region is shown in Figure 8.56. The definition of the non-tight control regions was varied with three different loose' definitions: the looser loose' (LoosePrime5) and the two alternatives of tighter loose' (LoosePrime3 and LoosePrime2). The uncertainties were computed separately for each definition and smoothed (if fluctuations were observed) following a bootstrap technique (see Figures 8.57 to 8.59). The envelope of the three variations after smoothing was taken as the final systematic uncertainty, which is shown in Figure 8.60.

8.5.8 Identification and isolation correlation in the background

The same procedure as presented in Section 6.6.6 was followed to check the correlation between the photon identification shower-shape variables used in the loose' and tight definitions and the isolation. The largest deviations from unity in the values of R^{bg} estimated in the high-$E_{\mathrm{T}}^{\mathrm{iso}}$ region are observed with Pythia optimised and shown in Figure 8.61. The values of R^{bg} estimated using the signal leakage fractions extracted from Sherpa are shown in Figure 8.62. The size of the deviations are shown as a dotted black line in the figures and were used to vary R^{bg} from the nominal value, $R^{\mathrm{bg}} = 1$. The final uncertainty in the cross sections is shown in Figure 8.63.

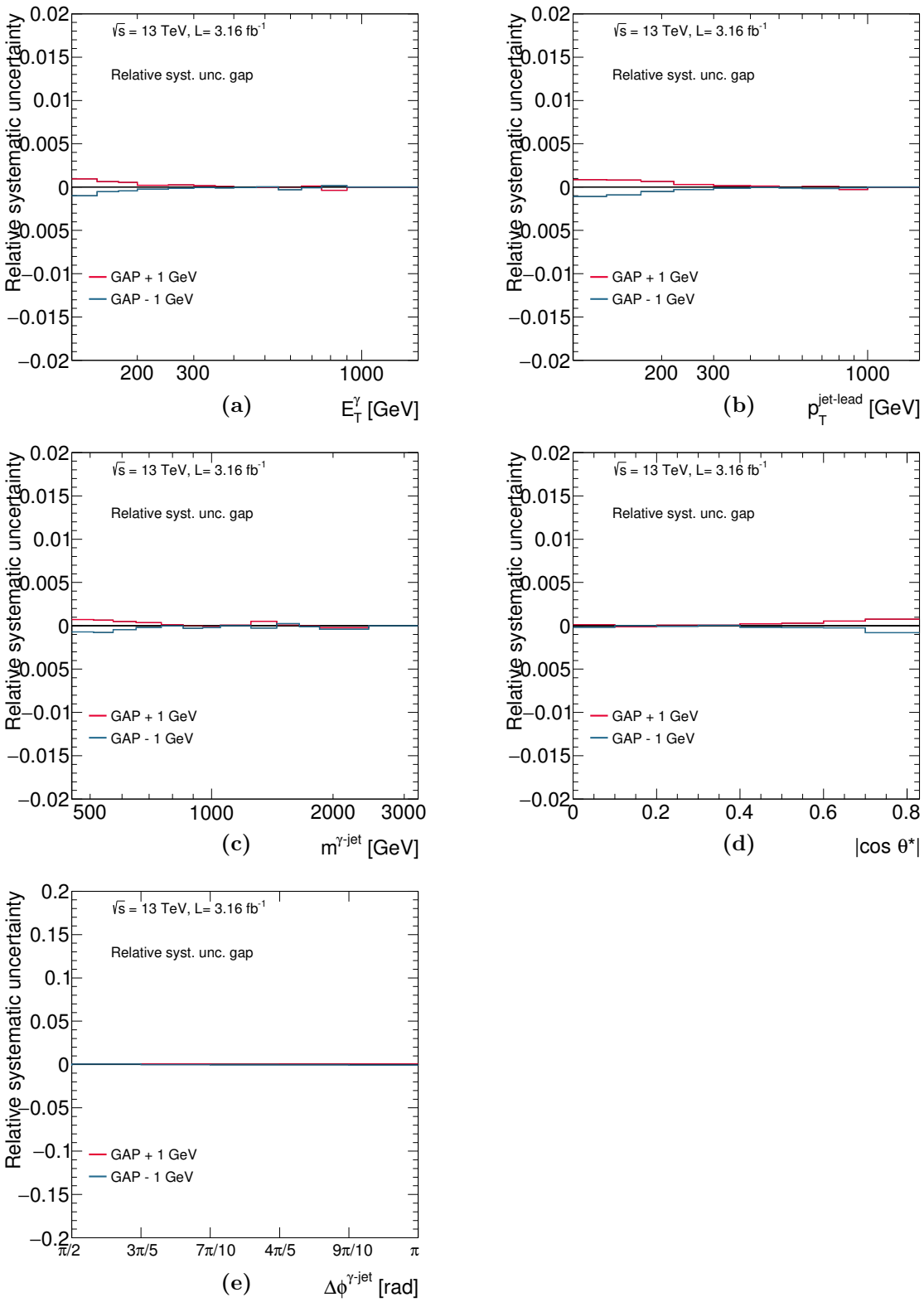


Figure 8.55: Systematic uncertainties on the measured cross sections due to the choice of background control regions (different $E_{\mathrm{T}}^{\mathrm{iso}}$ requirements) as functions of (a) E_{T}^{γ}, (b) $p_{\mathrm{T}}^{\mathrm{jet-lead}}$, (c) $m^{\gamma-\mathrm{jet}}$, (d) $|\cos\theta^{\star}|$ and (e) $\Delta\phi^{\gamma-\mathrm{jet}}$.

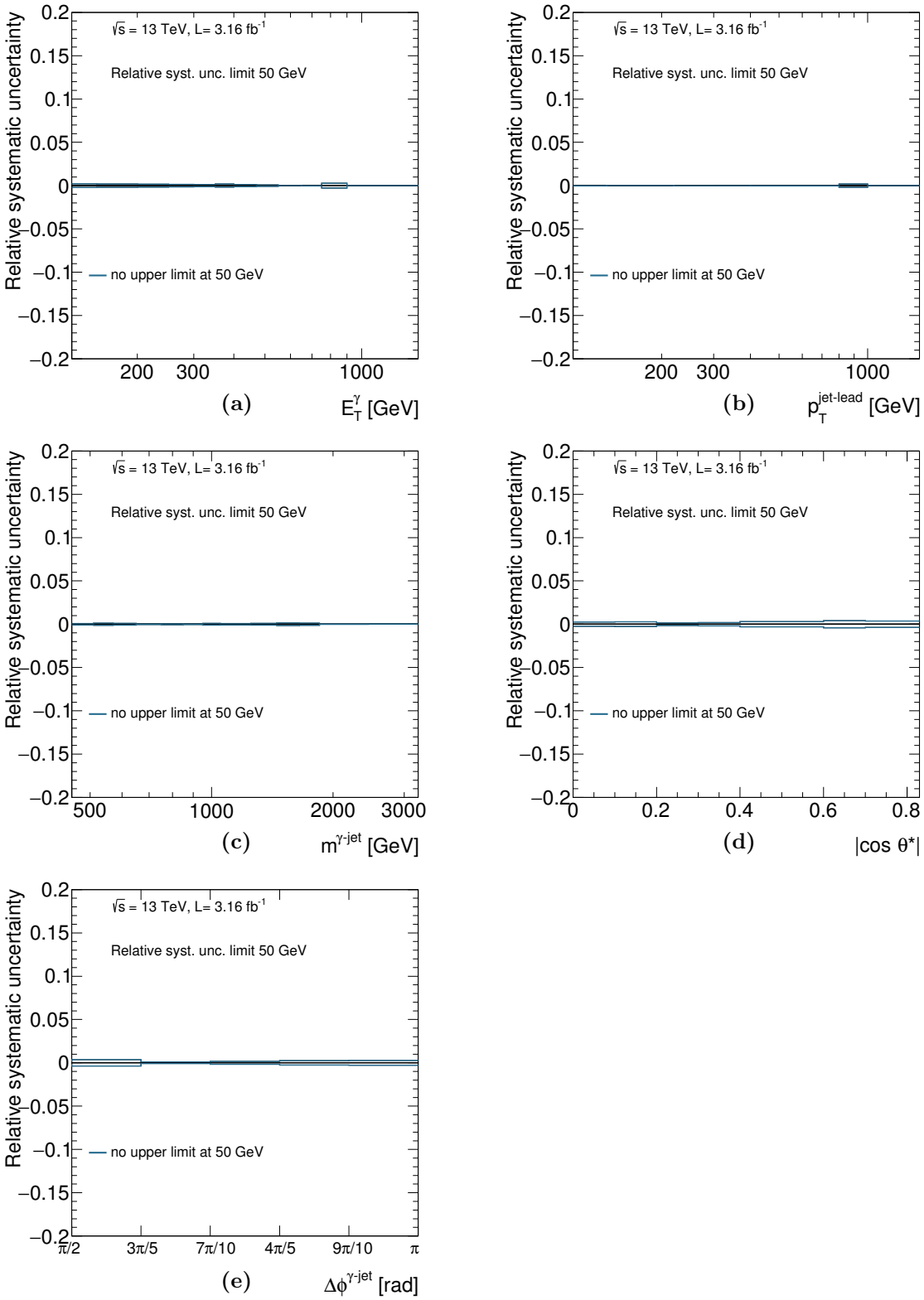


Figure 8.56: Systematic uncertainties on the measured cross sections due to the choice of background control regions (removal of the upper cuts on $E_{\mathrm{T}}^{\mathrm{iso}}$ for regions B and D) as functions of (a) E_{T}^{γ}, (b) $p_{\mathrm{T}}^{\mathrm{jet-lead}}$, (c) $m^{\gamma-\mathrm{jet}}$, (d) $|\cos\theta^{\star}|$ and (e) $\Delta\phi^{\gamma-\mathrm{jet}}$.

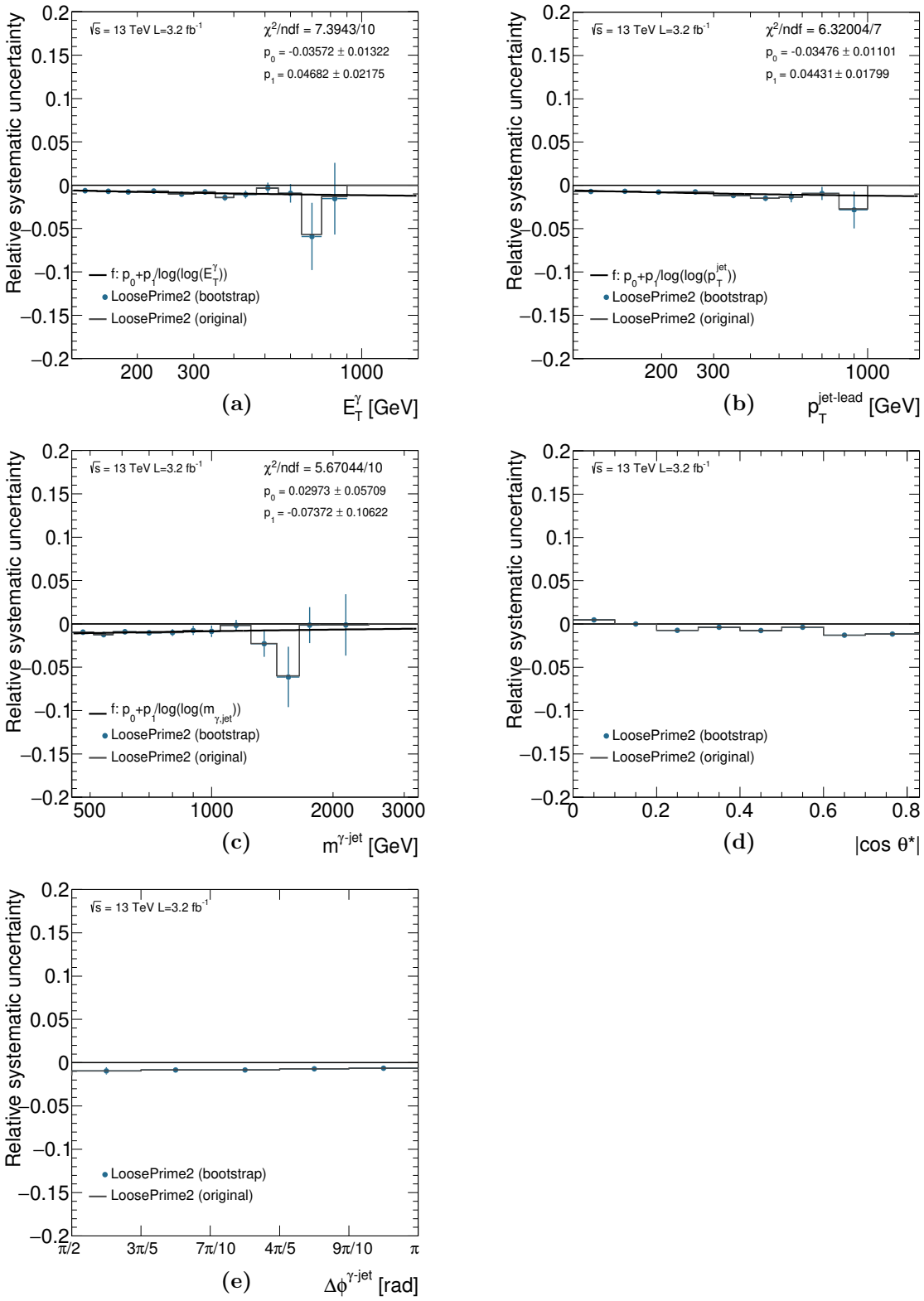


Figure 8.57: Systematic uncertainties on the measured cross sections due to the choice of background control regions (LoosePrime2 definition) as functions of (a) E_{T}^{γ}, (b) $p_{\mathrm{T}}^{\mathrm{jet-lead}}$, (c) $m^{\gamma-\mathrm{jet}}$, (d) $|\cos\theta^{\star}|$ and (e) $\Delta\phi^{\gamma-\mathrm{jet}}$. The results of the bootstrap method, the fits and the lower and upper bounds are also shown.

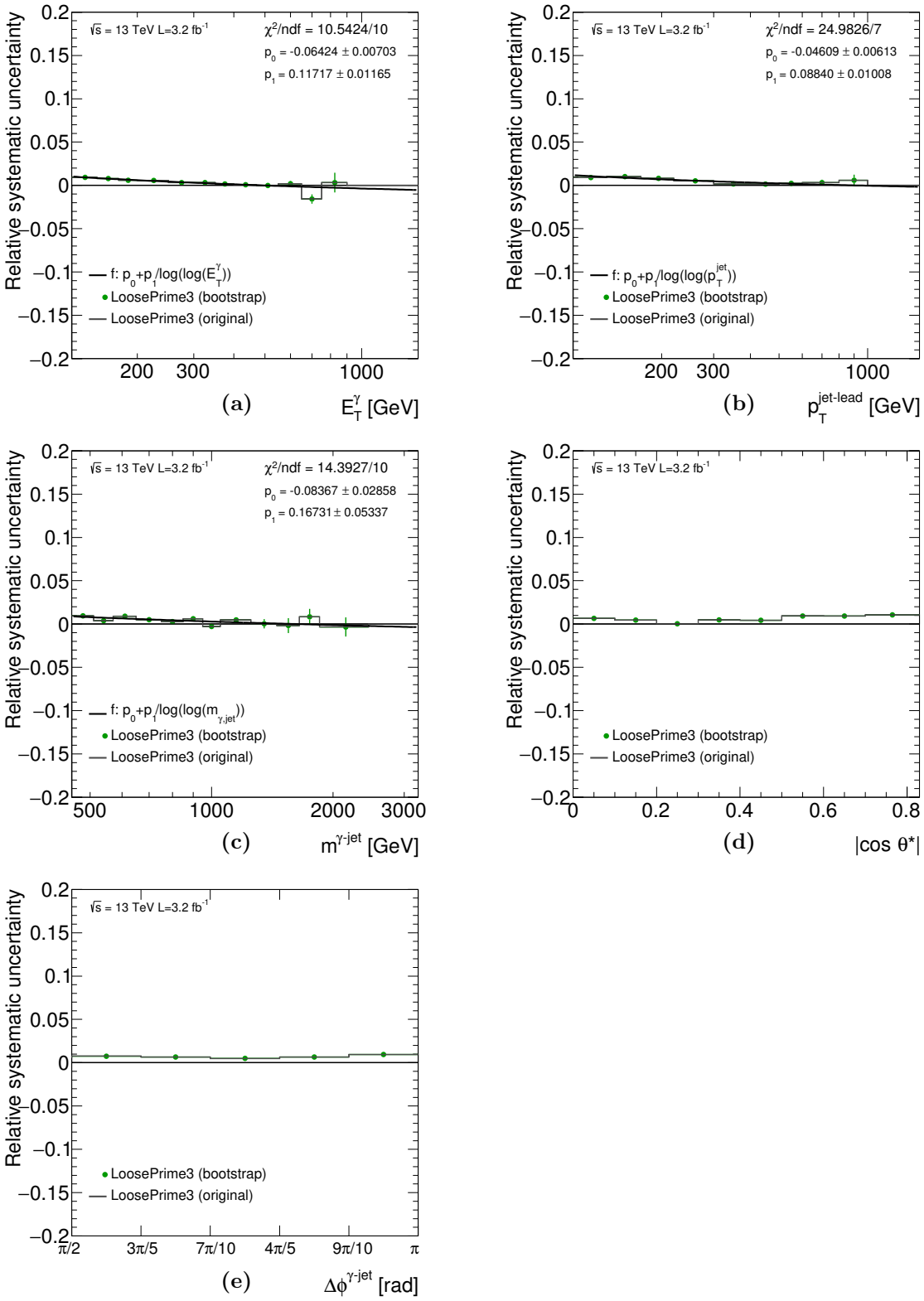


Figure 8.58: Systematic uncertainties on the measured cross sections due to the choice of background control regions (LoosePrime3 definition) as functions of (a) E_{T}^{γ}, (b) $p_{\mathrm{T}}^{\mathrm{jet-lead}}$, (c) $m^{\gamma-\mathrm{jet}}$, (d) $|\cos\theta^{\star}|$ and (e) $\Delta\phi^{\gamma-\mathrm{jet}}$. The results of the bootstrap method, the fits and the lower and upper bounds are also shown.

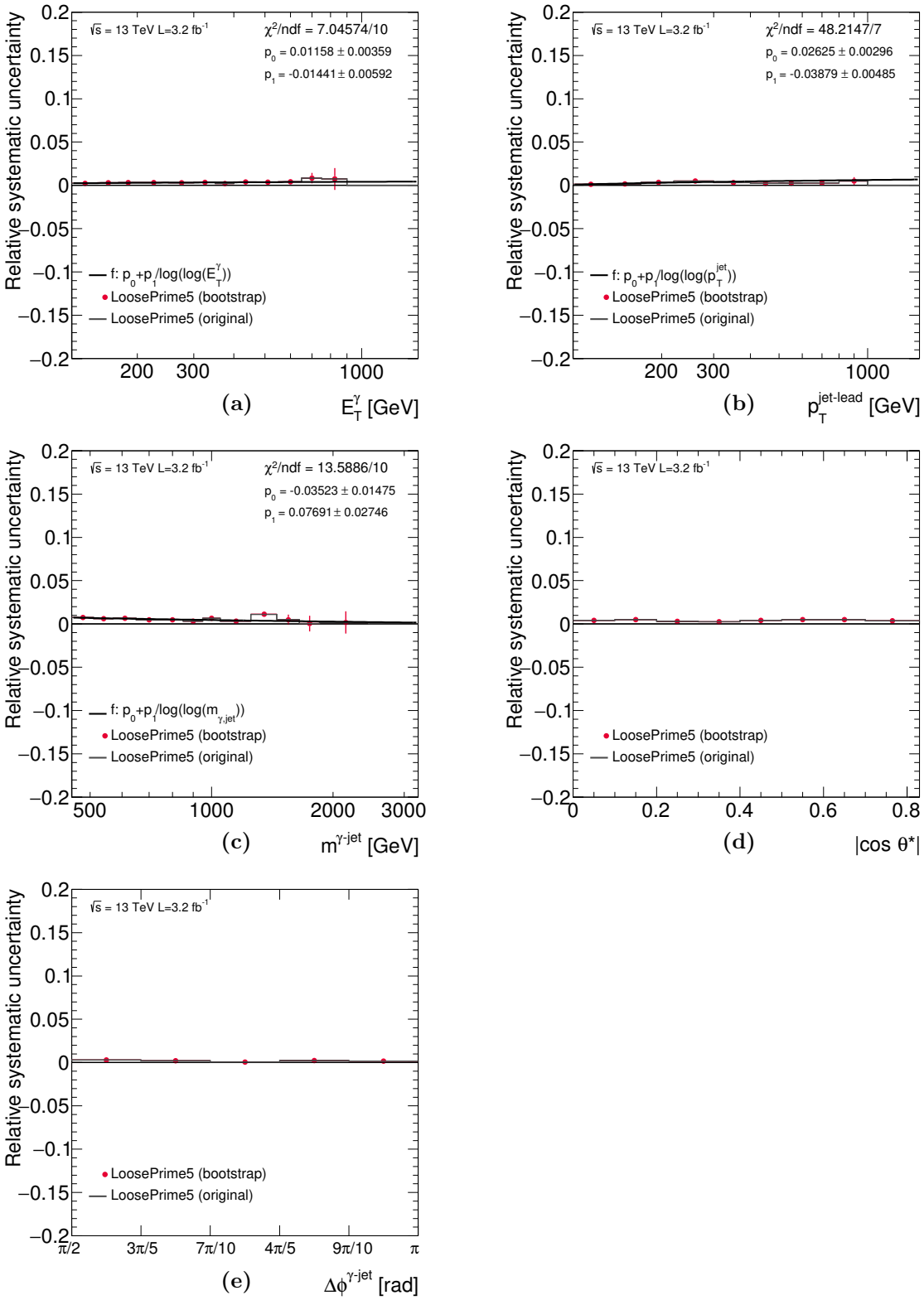


Figure 8.59: Systematic uncertainties on the measured cross sections due to the choice of background control regions (LoosePrime5 definition) as functions of (a) E_{T}^{γ}, (b) $p_{\mathrm{T}}^{\mathrm{jet-lead}}$, (c) $m^{\gamma-\mathrm{jet}}$, (d) $|\cos\theta^{\star}|$ and (e) $\Delta\phi^{\gamma-\mathrm{jet}}$. The results of the bootstrap method, the fits and the lower and upper bounds are also shown.

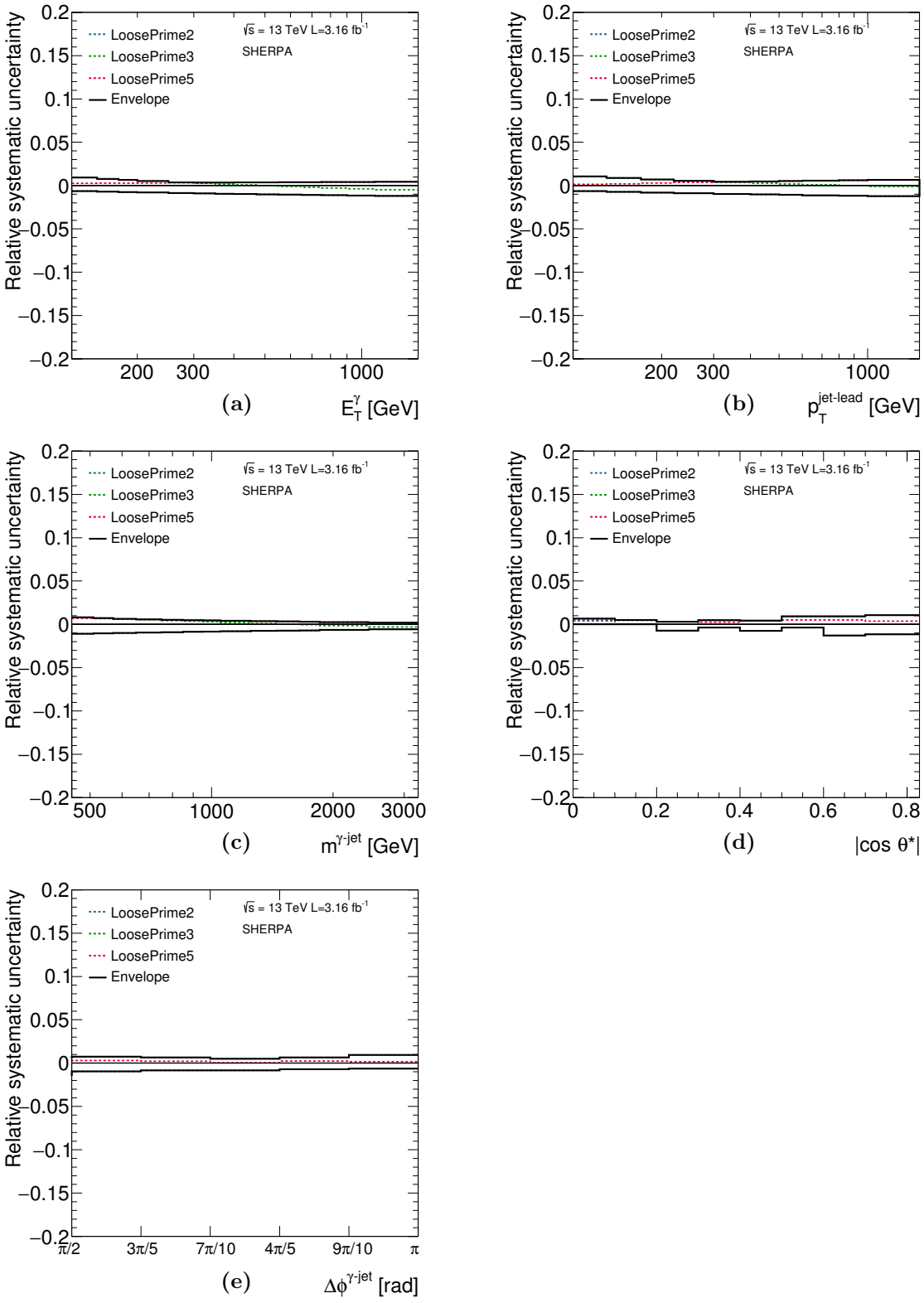


Figure 8.60: Systematic uncertainties on the measured cross sections due to the choice of background control regions (different loose′ definitions) as functions of (a) E_{T}^{γ}, (b) $p_{\mathrm{T}}^{\mathrm{jet-lead}}$, (c) $m^{\gamma-\mathrm{jet}}$, (d) $|\cos\theta^{\star}|$ and (e) $\Delta\phi^{\gamma-\mathrm{jet}}$.

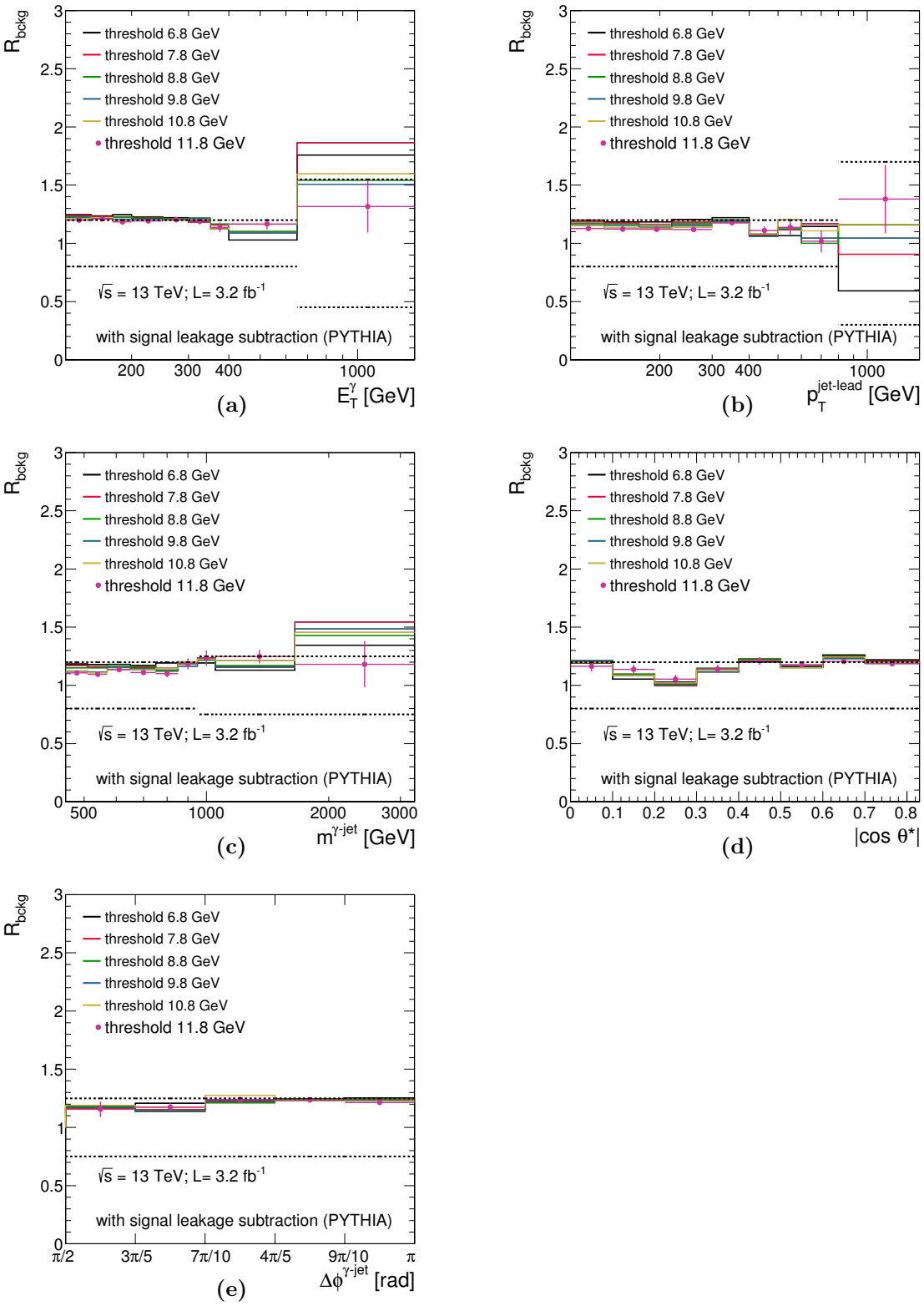


Figure 8.61: R_{bckg} as a function of (a) E_{T}^{γ}, (b) $p_{\mathrm{T}}^{\mathrm{jet-lead}}$, (c) $m^{\gamma-\mathrm{jet}}$, (d) $|\cos\theta^{\star}|$ and (e) $\Delta\phi^{\gamma-\mathrm{jet}}$ and for different definitions of the control regions. The signal leakage contributions in the control regions were removed using PYTHIA optimised. The range in R_{bckg}, which was taken as the uncertainty, is indicated by the dotted lines.

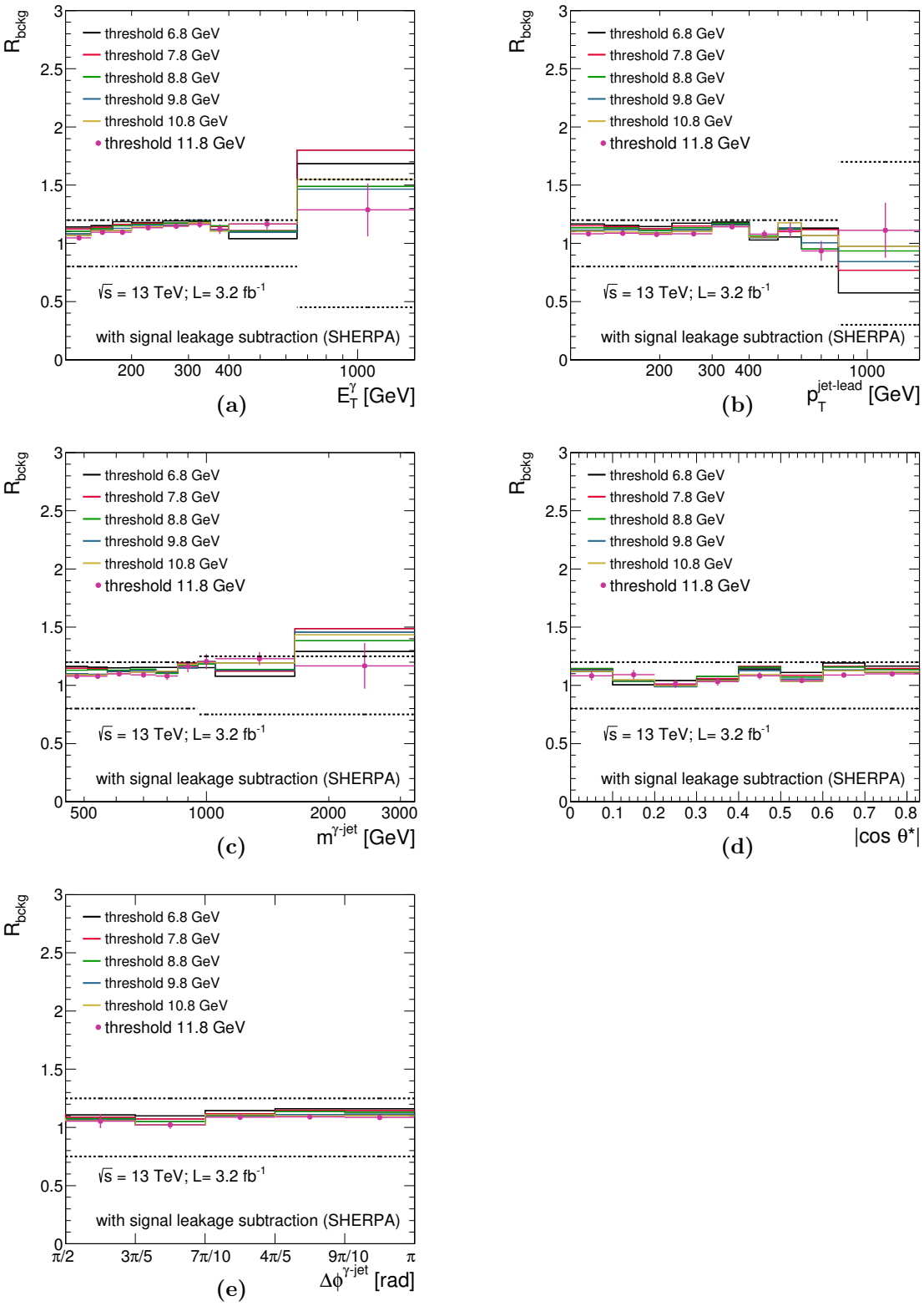


Figure 8.62: R_{bckg} as a function of (a) E_{T}^{γ}, (b) $p_{\mathrm{T}}^{\mathrm{jet-lead}}$, (c) $m^{\gamma-\mathrm{jet}}$, (d) $|\cos\theta^{\star}|$ and (e) $\Delta\phi^{\gamma-\mathrm{jet}}$ and for different definitions of the control regions. The signal leakage contributions in the control regions were removed using SHERPA. The range in R_{bckg}, which was taken as the uncertainty, is indicated by the dotted lines.

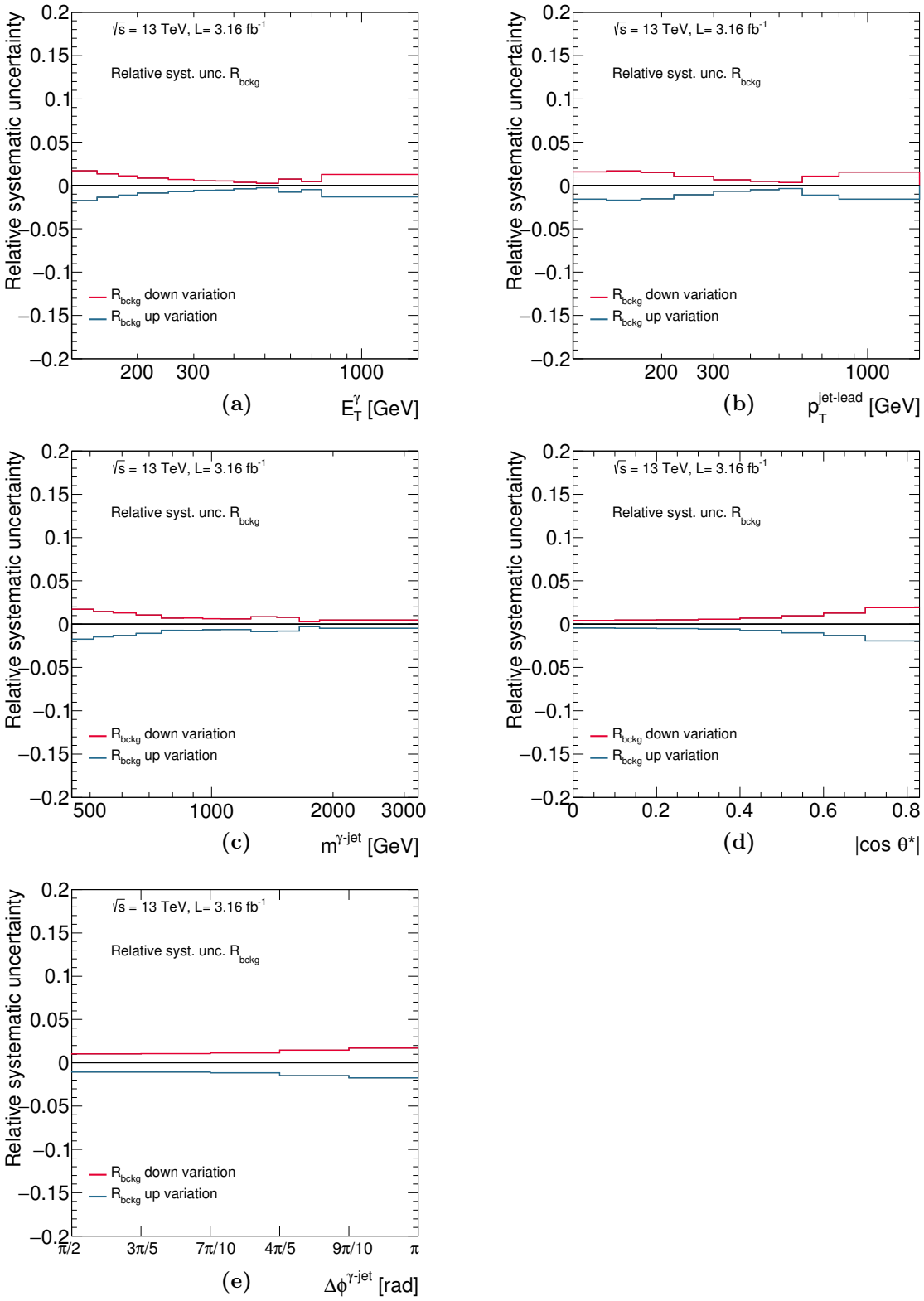


Figure 8.63: Systematic uncertainties on the measured cross sections due to the photon ID and $E_{\mathrm{T}}^{\mathrm{iso}}$ correlation in background events (R_{bckg}) as functions of (a) E_{T}^{γ}, (b) $p_{\mathrm{T}}^{\mathrm{jet-lead}}$, (c) $m^{\gamma-\mathrm{jet}}$, (d) $|\cos\theta^{\star}|$ and (e) $\Delta\phi^{\gamma-\mathrm{jet}}$.

8.5.9 Pile-up reweighting

To match the in-time and out-of-time pile-up conditions in the data, the distribution as a function of $\langle\mu\rangle$ in simulated events was reweighted to that of the data after applying a factor 1/1.16 (see Section 6.1.4). An uncertainty due to this reweighting was estimated by changing this factor applied to the data to 1/1.09 or 1/1.23 and, consequently, the reweighting factors applied to the MC. Figure 8.64 shows the resulting uncertainties on the cross sections.

8.5.10 MC sample statistics

The limited MC statistics affects mainly the bin-by-bin correction factors. Figure 8.65 shows the statistical uncertainty of the MC samples.

8.5.11 Uncertainty on the trigger efficiency

The uncertainty on the trigger efficiency (see Section 8.1.3) was propagated into the measured cross sections.

8.5.12 Uncertainty on the measurement of the integrated luminosity

The uncertainty on the integrated luminosity is ±2.1% [115]. This uncertainty is fully correlated in all bins of all the measured cross sections.

8.5.13 Total systematic uncertainty

The total systematic uncertainty was computed by adding in quadrature the sources of uncertainty listed above, except that on the integrated luminosity. Figure 8.66 shows the resulting total systematic uncertainty, together with the statistical uncertainty, which takes into account the statistical uncertainties in the data for the signal region A as well as for the control regions B, C and D. For $E_{\mathrm{T}}^{\gamma} \lesssim 600$ GeV, the systematic uncertainty dominates while for higher E_{T}^{γ} values, the statistical uncertainty of the data limits the precision of the measurements. The same happens for $m^{\gamma-\mathrm{jet}} \lesssim 1600$ GeV and $p_{\mathrm{T}}^{\mathrm{jet-lead}} \lesssim 1000$ GeV. For $|\cos\theta^{\star}|$, the systematic uncertainties dominate in the whole measured range. Figure 8.67 shows the main contributions to the total systematic uncertainty: photon energy scale (GES), jet energy scale (JES) and photon identification (γID).

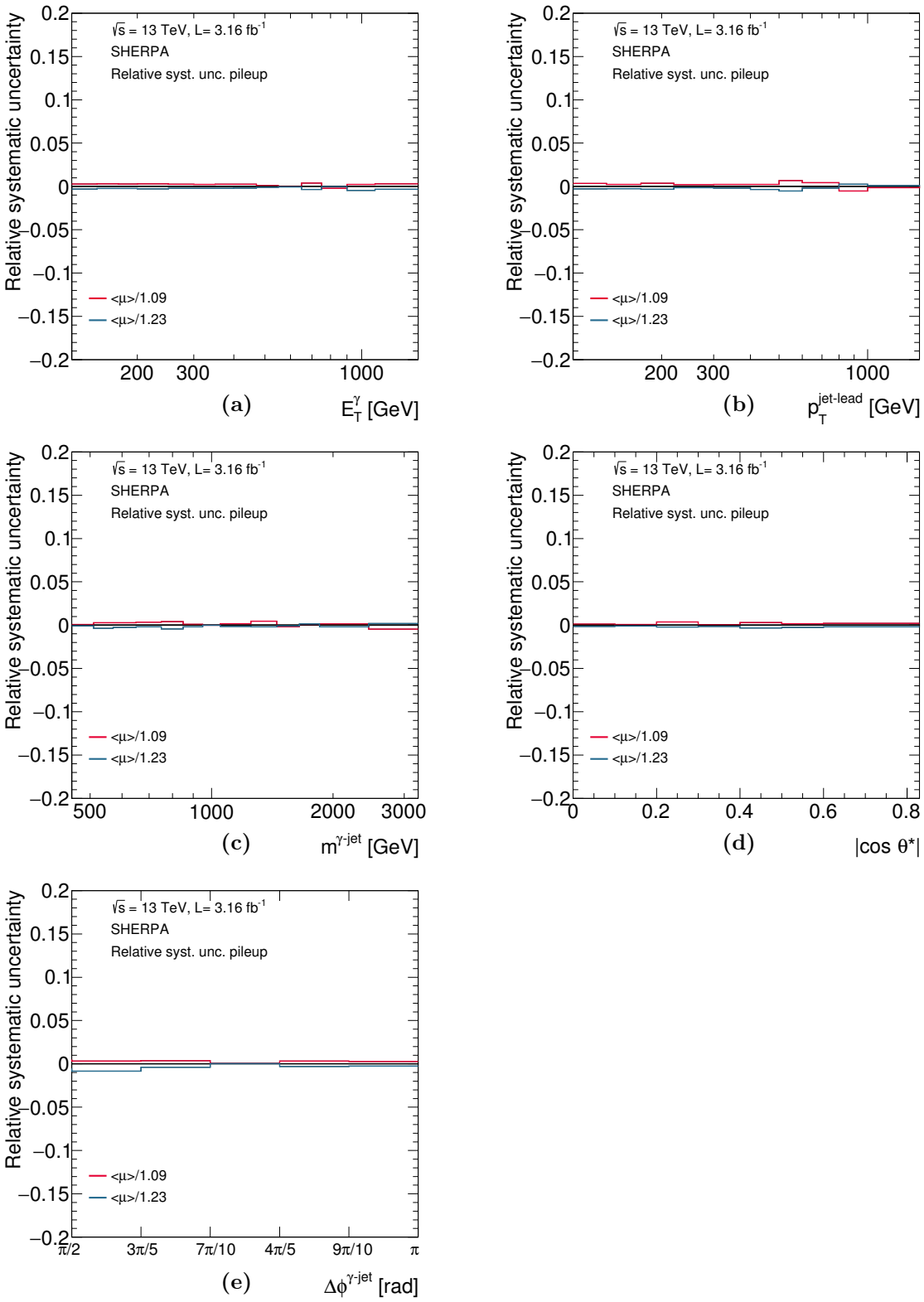


Figure 8.64: Systematic uncertainties on the measured cross sections due to the pile-up reweighting as functions of (a) E_{T}^{γ}, (b) $p_{\mathrm{T}}^{\mathrm{jet-lead}}$, (c) $m^{\gamma-\mathrm{jet}}$, (d) $|\cos\theta^{\star}|$ and (e) $\Delta\phi^{\gamma-\mathrm{jet}}$.

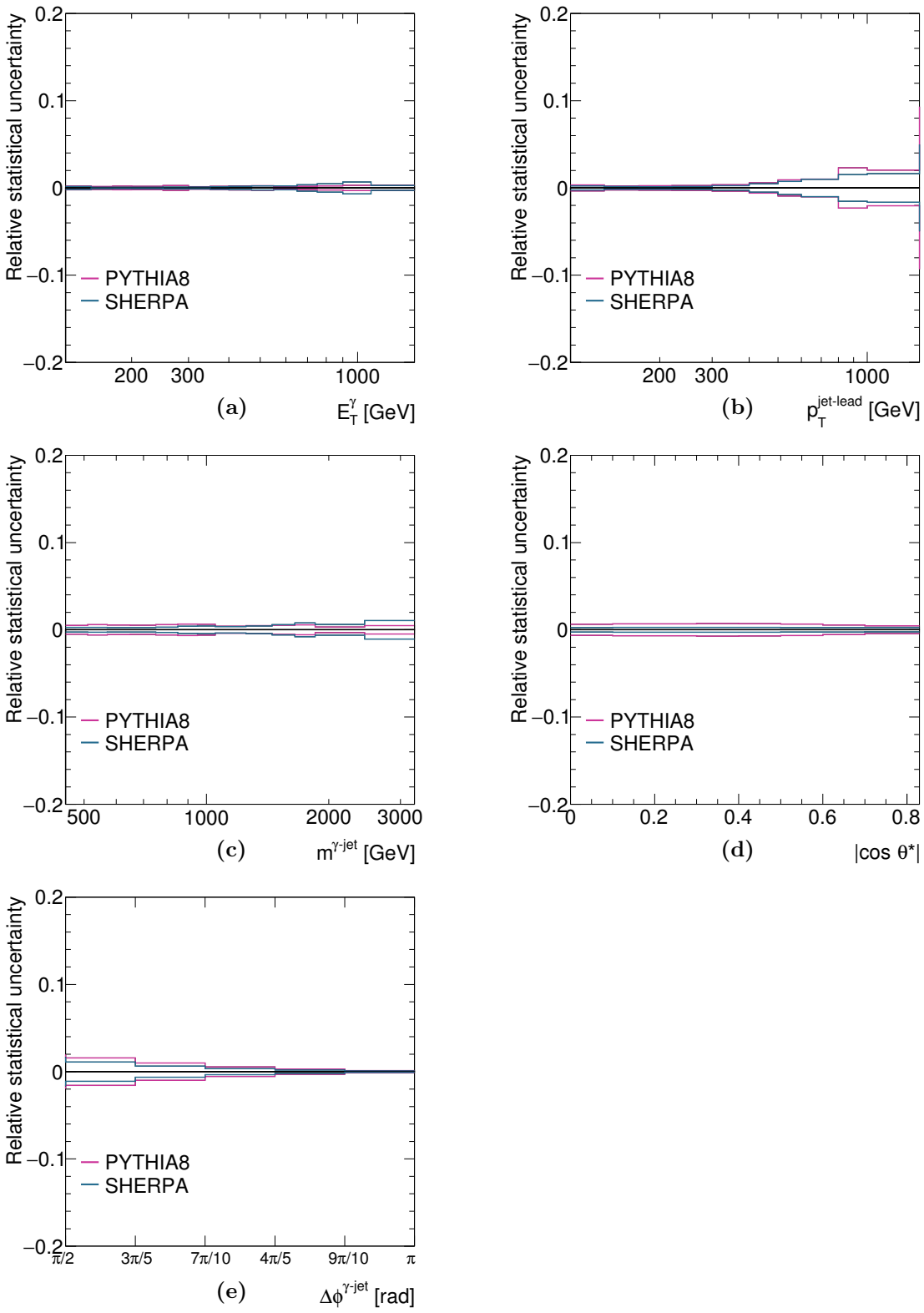


Figure 8.65: Statistical uncertainty of the MC samples as a function of (a) E_{T}^{γ}, (b) $p_{\mathrm{T}}^{\mathrm{jet-lead}}$, (c) $m^{\gamma-\mathrm{jet}}$, (d) $|\cos\theta^{\star}|$ and (e) $\Delta\phi^{\gamma-\mathrm{jet}}$.

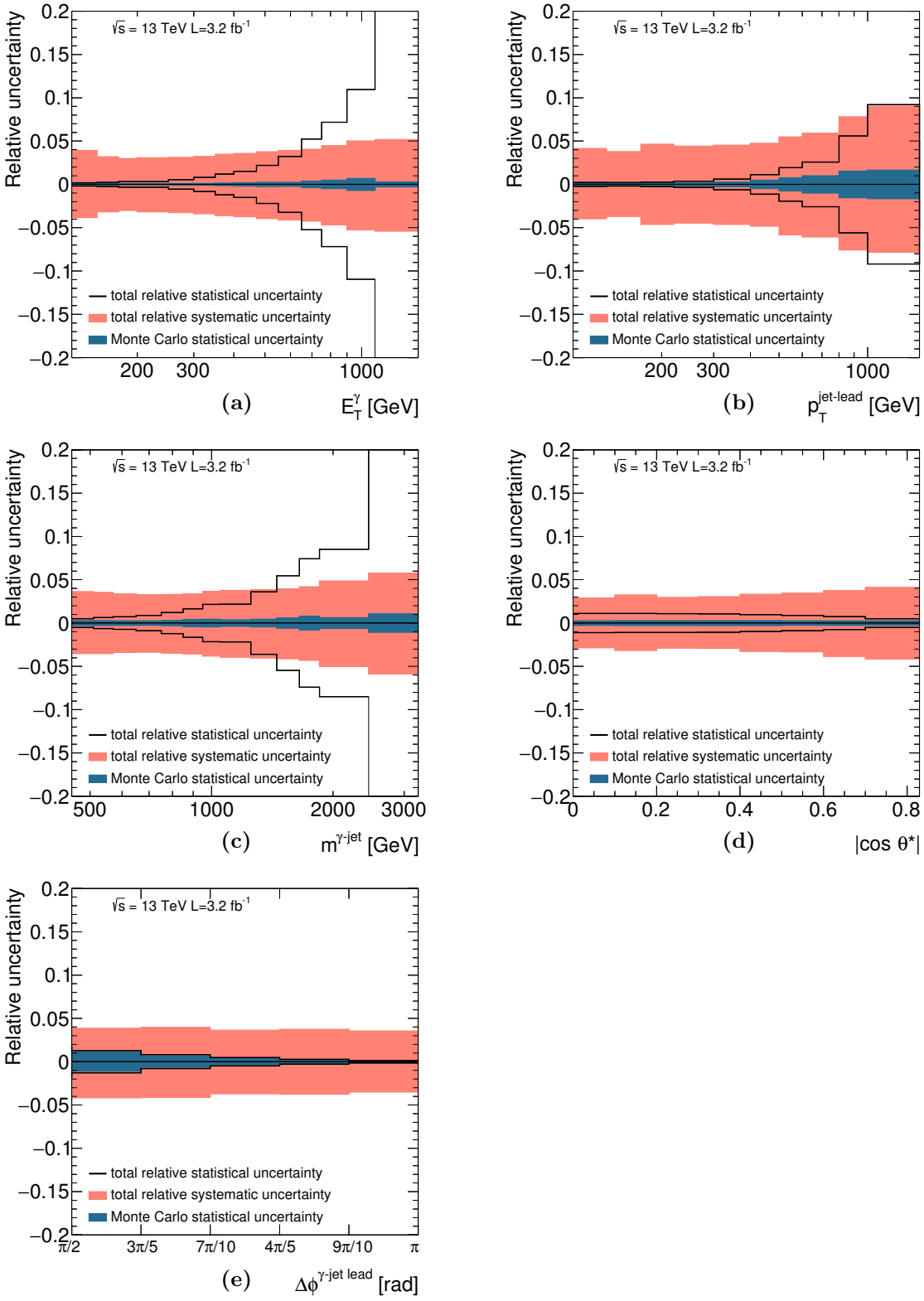


Figure 8.66: Total systematic (pink shaded area) and statistical uncertainties from the data (white histogram) and MC (blue shaded area) as functions of (a) E_{T}^{γ}, (b) $p_{\mathrm{T}}^{\mathrm{jet-lead}}$, (c) $m^{\gamma-\mathrm{jet}}$, (d) $|\cos\theta^{\star}|$ and (e) $\Delta\phi^{\gamma-\mathrm{jet}}$.

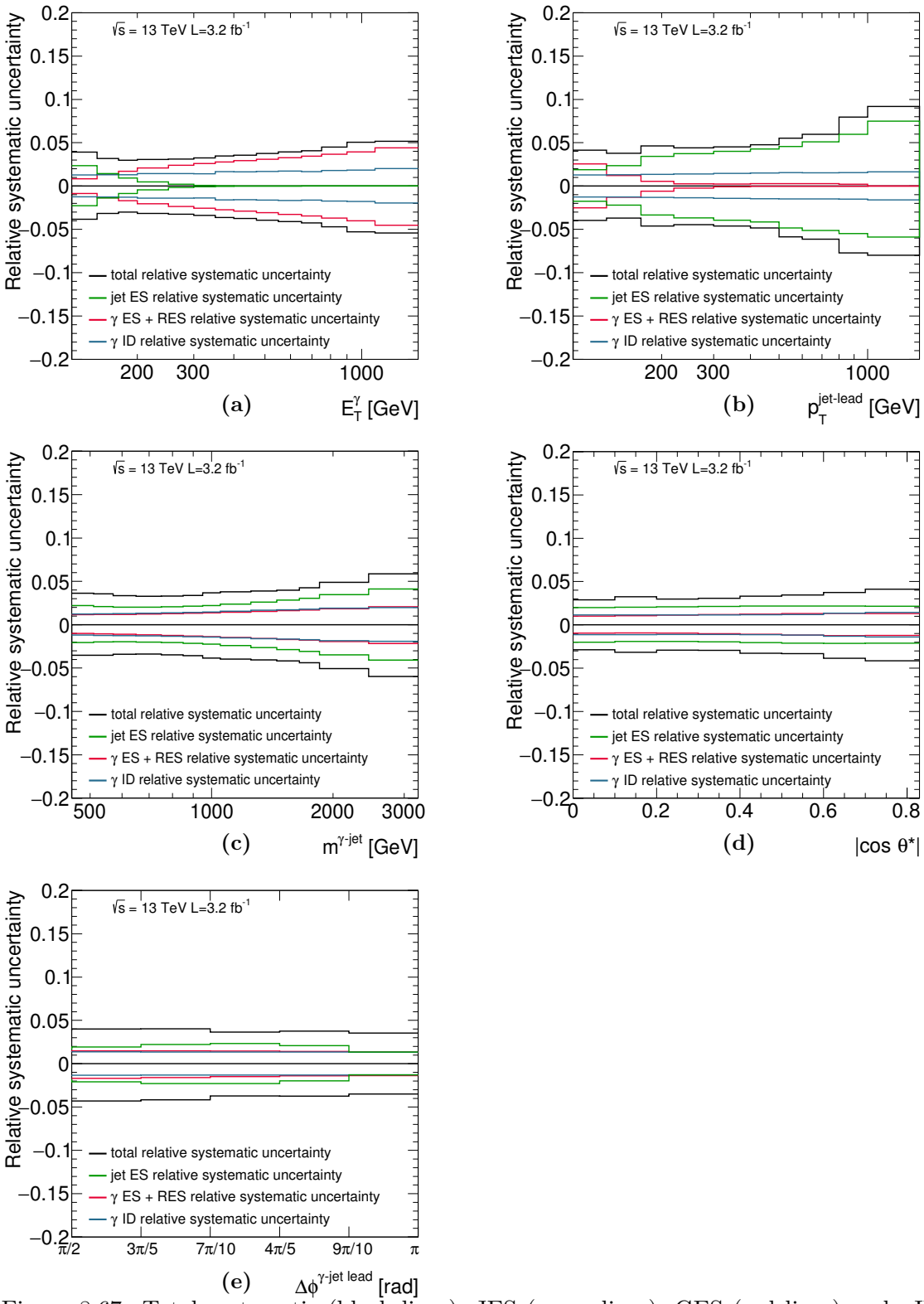


Figure 8.67: Total systematic (black lines), JES (green lines), GES (red lines) and γID (blue lines) uncertainties as functions of (a) E_{T}^{γ}, (b) $p_{\mathrm{T}}^{\mathrm{jet-lead}}$, (c) $m^{\gamma-\mathrm{jet}}$, (d) $|\cos\theta^{\star}|$ and (e) $\Delta\phi^{\gamma-\mathrm{jet}}$.

8.6 Next-to-leading-order QCD calculations

The fixed-order calculations of JetPhox and predictions of Sherpa NLO matched to a parton shower were compared to the cross-section measurements. The predictions of JetPhox were compared to all the observables except for $\Delta\phi^{\gamma-\text{jet}}$ since the NLO QCD calculations are only a lowest-order estimation for $\Delta\phi^{\gamma-\text{jet}}$. More details of the calculations are given in Section 3.5.7.

The calculations were performed using a parton-level isolation cut, which required a total transverse energy below $4.2 \cdot 10^{-3} \cdot E_{\text{T}}^{\gamma} + 10$ GeV (see Section 8.4.1) from the partons inside a cone of radius $R = 0.4$ around the photon direction. The anti-k_t algorithm with radius parameter $R = 0.4$ was applied to the partons in the events generated by this program to compute the cross-section predictions.

Figure 8.68 shows the predicted cross sections for the observables studied. The calculations based on the MMHT2014, CT14 and NNPDF3.0 PDFs are shown.

The parton-level predictions of Pythia nominal and Pythia optimised are compared to the NLO QCD calculations based on MMHT2014 in Figure 8.69. The Pythia optimised predictions at parton-level were obtained using the same method as described in Section 8.2, adjusting in this case the hard and bremsstrahlung Pythia components at parton level. After this optimisation, the parton-level cross sections of Pythia give an adequate description of the NLO QCD predictions, which is required to use these samples for the estimation of the hadronisation corrections.

8.6.1 Non-perturbative corrections to the NLO QCD calculations of JetPhox

The parton-level predictions of JetPhox were corrected for hadronisation and underlying-event effects using samples of Pythia 8.165 generated with the AU2 CTEQ6L1 (AU2) tune, as explained in Section 3.5.7. Figure 8.70 shows the C_{NLO} correction factors for each cross section. The dependence of C_{NLO} with $p_{\text{T}}^{\text{jet}-\text{lead}}$ is due to the photon isolation requirement in the bremsstrahlung component, as can be seen in Figure 8.71. Figure 8.71(a) shows C_{NLO} separately for the bremsstrahlung and hard components in Pythia. Figure 8.71 (b) shows C_{NLO} with and without the application of the photon isolation requirement.

Uncertainties on the non-perturbative corrections

The uncertainties on the non-perturbative corrections were estimated using samples of Pythia 8.186 with the LO NNPDF2.3 A14 (A14) tune and compared to the estimations with the AU2 tune. These two tunes provide different models of the PDFs, multiparton interactions, the parton shower, beam remnants, colour reconnection strength, etc. The most relevant parameters are:

Parameter	AU2 value	A14 value
SigmaProcess:alphaSvalue	0.135	0.140
SpaceShower:rapidityOrder	off	on
SpaceShower:alphaSvalue	0.137	0.127
TimeShower:alphaSvalue	0.1383	0.127
MultipartonInteractions:alphaSvalue	0.135	0.126

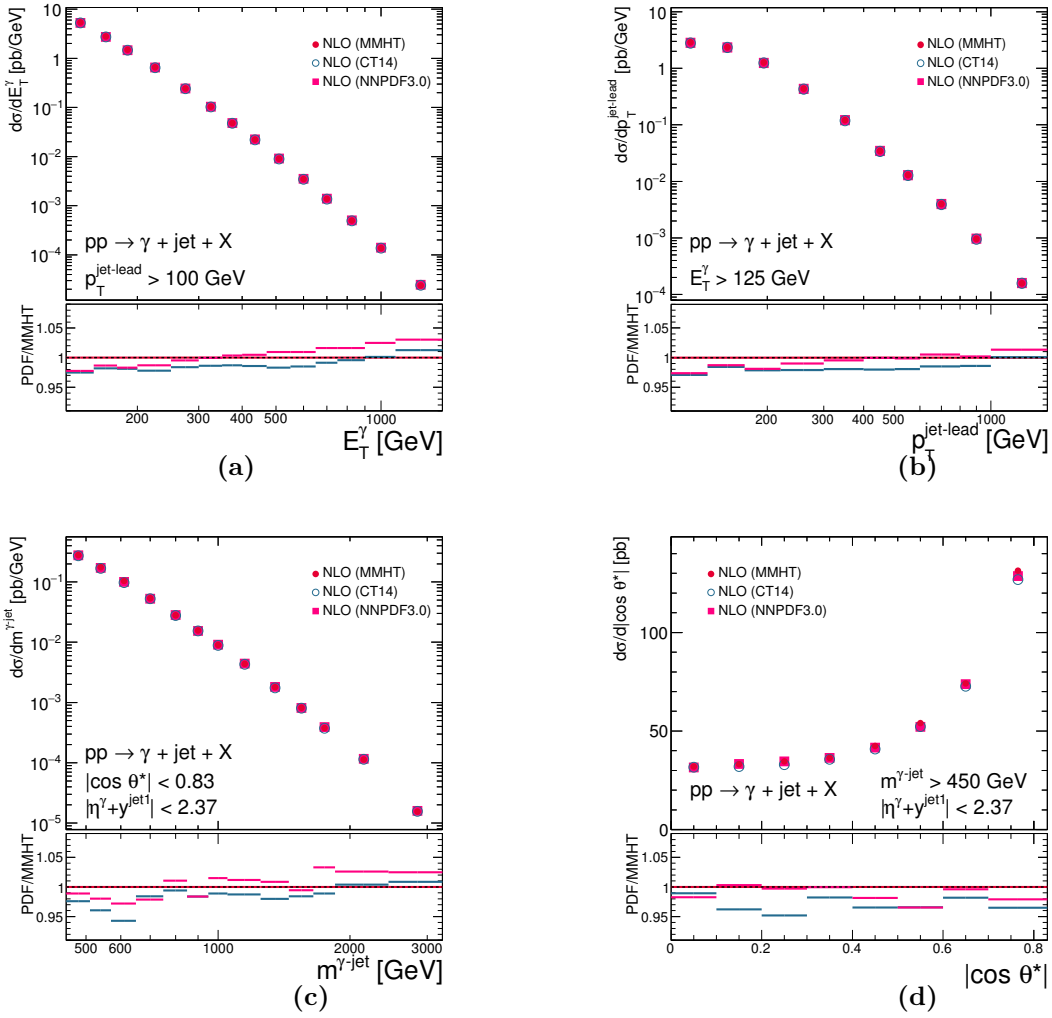


Figure 8.68: Predicted NLO QCD cross sections based on the MMHT2014 (dots), CT14 (open circles) and NNPDF3.0 (squares) proton PDFs as functions of (a) E_{T}^{γ}, (b) $p_{\mathrm{T}}^{\mathrm{jet-lead}}$, (c) $m^{\gamma-\mathrm{jet}}$ and (d) $|\cos\theta^{\star}|$. The lower part of the figures shows the ratio of the NLO calculations to that based on MMHT2014.

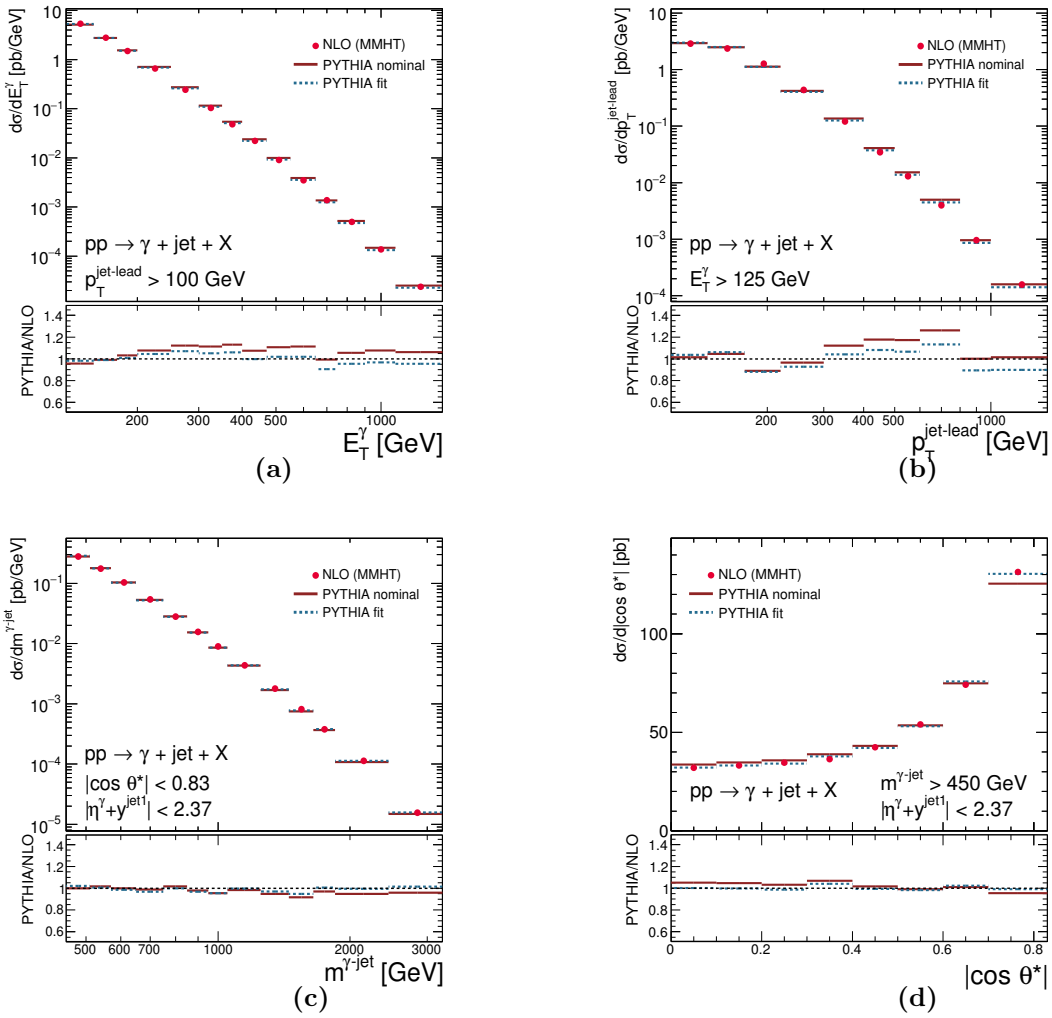


Figure 8.69: Predicted NLO QCD cross sections based on the MMHT2014 calculations (dots) as functions of (a) E_{T}^{γ}, (b) $p_{\mathrm{T}}^{\mathrm{jet-lead}}$, (c) $m^{\gamma-\mathrm{jet}}$ and (d) $|\cos\theta^{\star}|$. The predictions at parton level of Pythia (solid lines) and Pythia optimised (dashed lines) are also shown. The MC predictions are normalised to the integrated NLO QCD calculations. The lower part of the figures shows the ratio of the parton-level MC and NLO QCD calculations.

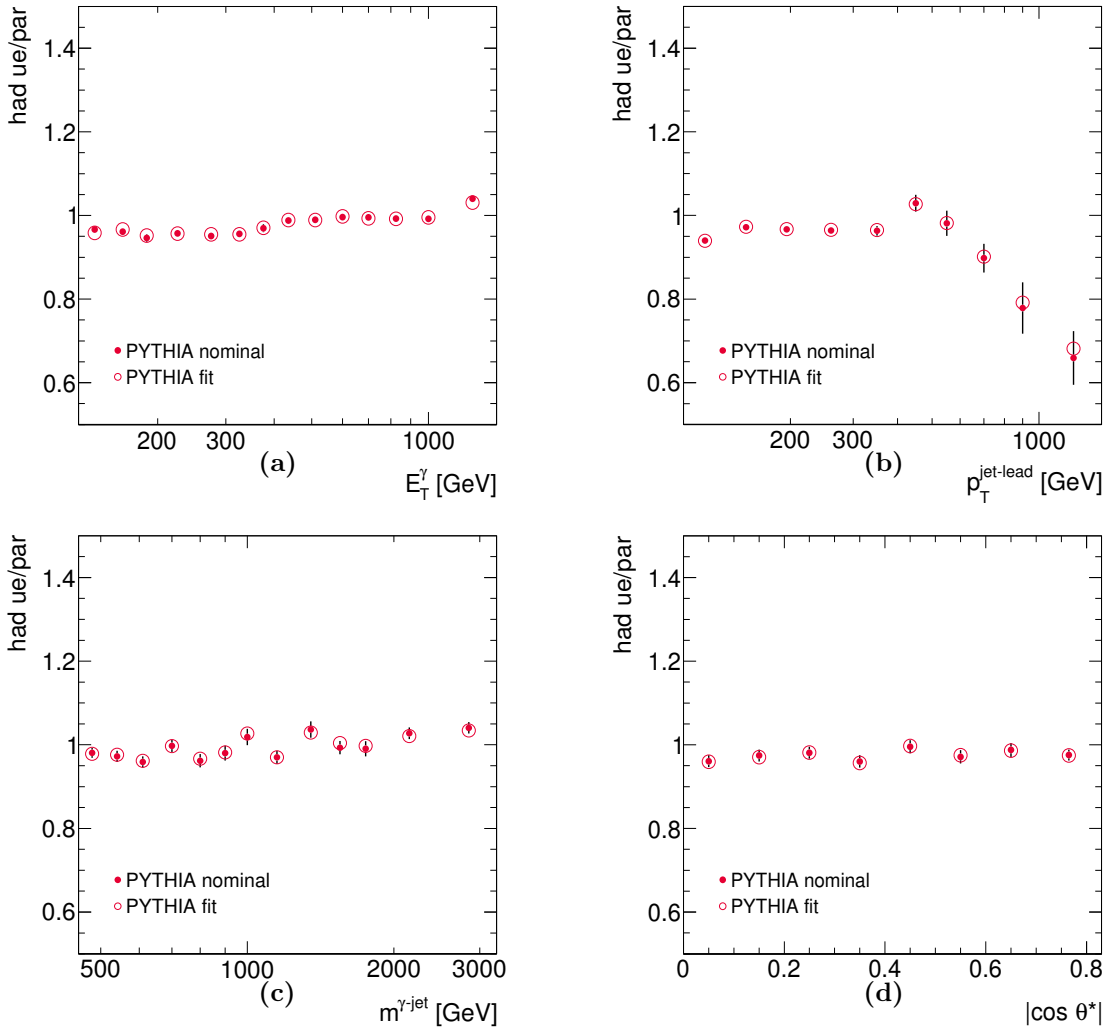


Figure 8.70: C_{NLO} correction factors from PYTHIA nominal (dots) and PYTHIA fitted (open circles) as functions of (a) E_{T}^{γ}, (b) $p_{\mathrm{T}}^{\mathrm{jet-lead}}$, (c) $m^{\gamma-\mathrm{jet}}$ and (d) $|\cos\theta^{\star}|$.

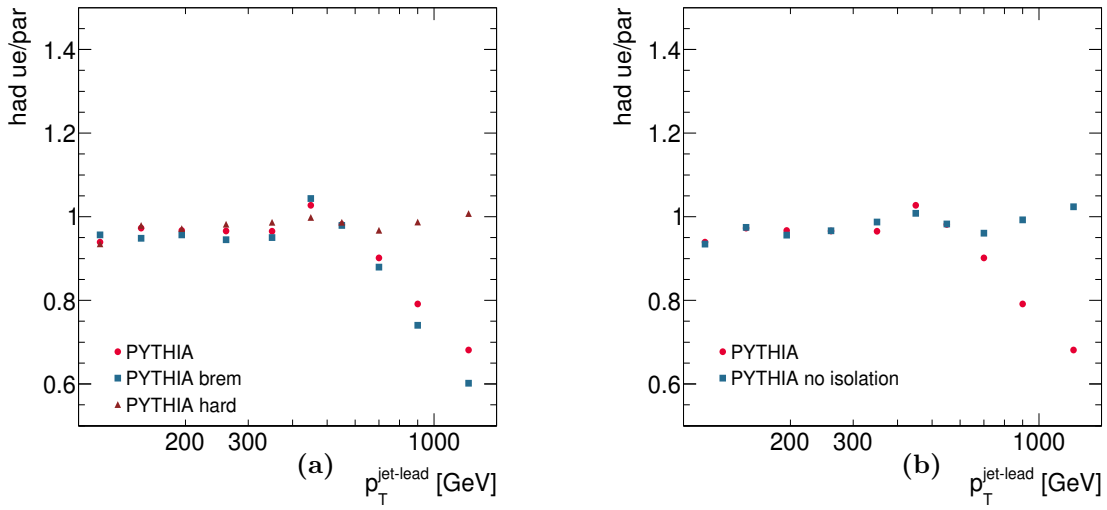


Figure 8.71: (a) C_{NLO} correction factor from PYTHIA fitted (dots), as well as for the hard (triangles) and bremsstrahlung (squares) components, as a function of $p_{\mathrm{T}}^{\mathrm{jet-lead}}$. (b) C_{NLO} correction factor from PYTHIA fitted with (dots) and without (squares) the photon isolation requirement as a function of $p_{\mathrm{T}}^{\mathrm{jet-lead}}$.

A higher value for α_{s} is chosen in the A14 tune for the hard process, whereas a lower value was taken for the parton shower and multiparton interactions. This choice is expected to predict lower activity in the event than in the AU2 tune and affect less the isolation requirement at particle level. The differences between both tunes could also lead to differences in the jet modelling; however, this has been shown to not be the case in the inclusive-jet analysis [129], where the tunes studied yielded similar non-perturbative corrections and close to unity. In addition, two additional variations of the A14 tune were considered, namely Var1Up and Var1Down. For these two variations, all parameter settings were fixed to the value of the A14 tune except for:

- **"MultipartonInteractons:alphaSvalue"** for which the central value of 0.126 was varied to 0.131 for Var1Up and to 0.121 for Var1Down;
- **"BeamRemnants:reconnectRange"** for which the value of 1.71 in the A14 tune was varied to 1.73 for Var1Up and to 1.69 for Var1Down.

The non-perturbative corrections for the nominal corrections with the AU2 tune are shown in Figure 8.72 together with the variations considered. It turned out that the A14 tune and its variations yield corrections closer to unity than those of the AU2 tune; this is explained by the different parameters of the settings. Given the differences in $p_{\mathrm{T}}^{\mathrm{jet-lead}}$, the nominal non-perturbative corrections and its related uncertainties were chosen as follows:

- the average of the corrections obtained using the AU2 CTEQ6L1 and LO NNPDF2.3 A14 tunes was taken as the nominal correction;
- half of the difference between the corrections obtained using the AU2 and A14 tunes was taken as the uncertainty.

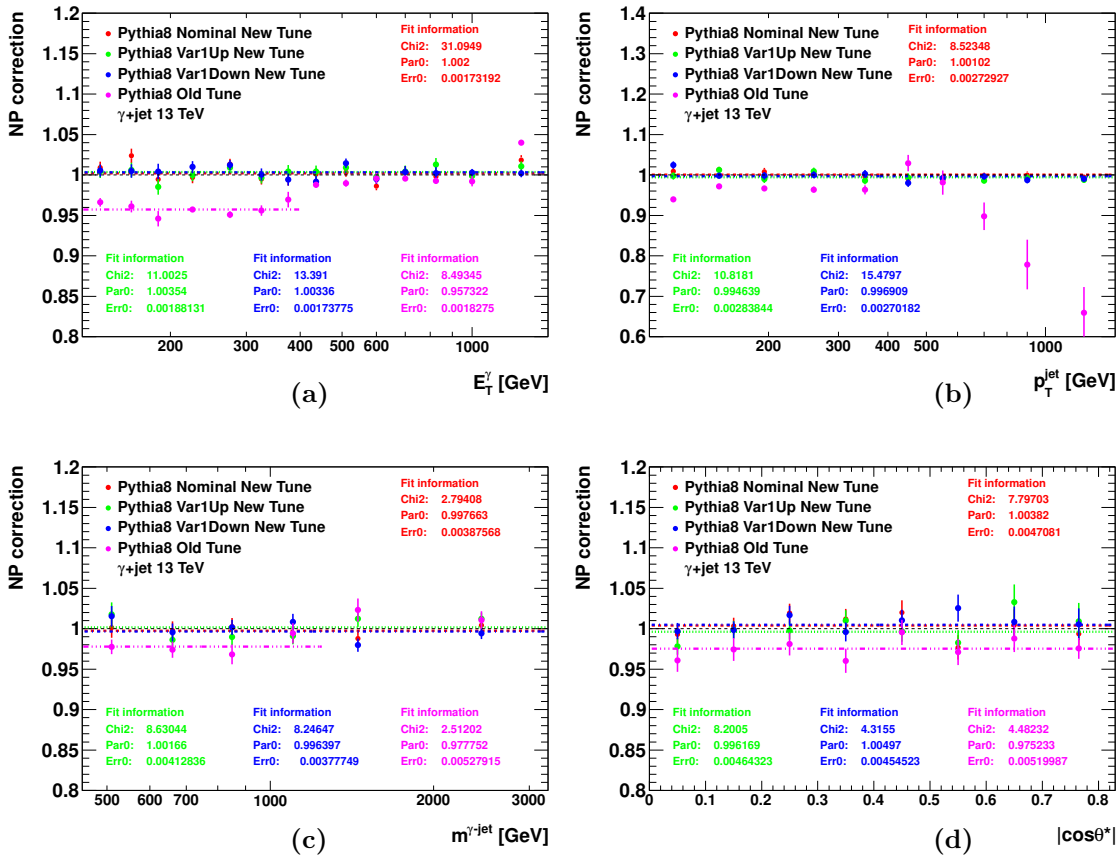


Figure 8.72: Non-perturbative corrections from PYTHIA as functions of (a) E_{T}^{γ}, (b) $p_{\mathrm{T}}^{\mathrm{jet-lead}}$, (c) $m^{\gamma-\mathrm{jet}}$ and (d) $|\cos\theta^{\star}|$ for different tunes: the AU2 ("Old tune", magenta dots), the A14 tune ("Nominal New tune", red dots) and the variations A14 Var1Up ("Var1Up New Tune", green dots) and A14 Var1Up ("Var1Down New Tune", blue dots).

This approach represents the less-biased compromise and the estimated uncertainty envelops the estimations obtained with the AU2 and A14 tunes. To suppress the influence of the statistical fluctuations, in the regions where the corrections are approximately flat, the result of a fit to a constant function was used. The value in each bin was kept otherwise. The results are shown in Figure 8.73. The uncertainties obtained for the non-perturbative corrections are as follows: below 2.2% for the E_{T}^{γ} distribution; approximately 1% for the $m^{\gamma-\mathrm{jet}}$ distribution; approximately 1.5% for the $|\cos\theta^{\star}|$ distribution; and for the $p_{\mathrm{T}}^{\mathrm{jet-lead}}$ distribution the uncertainty is below 3.2% for $p_{\mathrm{T}}^{\mathrm{jet-lead}} < 600$ GeV and increases up to 21% for $p_{\mathrm{T}}^{\mathrm{jet-lead}} \sim 1.5$ TeV.

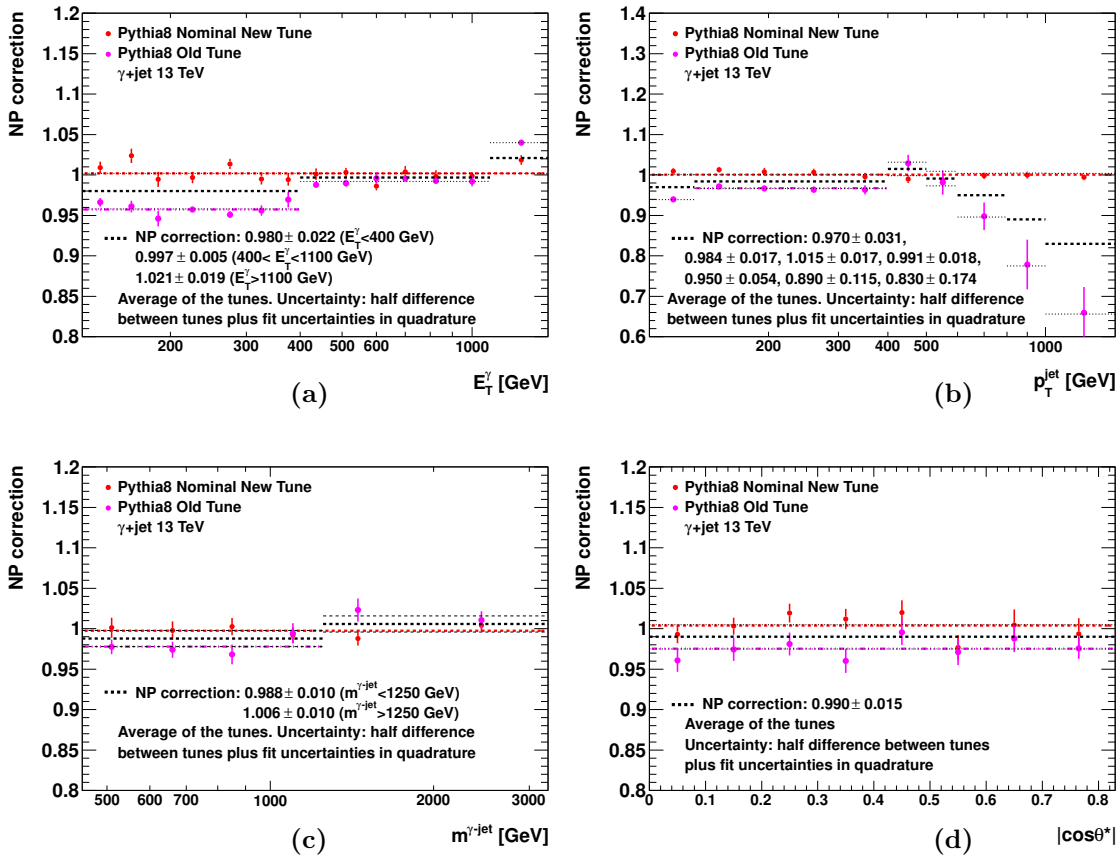


Figure 8.73: Non-perturbative corrections from PYTHIA as functions of (a) E_{T}^{γ}, (b) $p_{\mathrm{T}}^{\mathrm{jet-lead}}$, (c) $m^{\gamma-\mathrm{jet}}$ and (d) $|\cos\theta^{\star}|$ for different tunes: the AU2 tune ("Old tune", magenta dots) and the A14 tune ("Nominal New tune", red dots). The new nominal corrections are shown as the dashed black lines and the uncertainty on the corrections is shown by the dotted black lines (see text).

8.6.2 Theoretical uncertainties for JETPHOX predictions

The baseline settings for the JETPHOX predictions and estimation of the theoretical uncertainties were the same as presented in Section 6.7.2, except for that on the non-perturbative predictions, which has been described in Section 8.6.1.

The dominant theoretical uncertainty is that arising from terms beyond NLO, which is mostly determined by the simultaneous variation of the renormalisation, factorisation and fragmentation scales. The envelope of the 14 possible variations is shown in Figure 8.74. The PDF- and α_s-induced uncertainties are shown in Figures 8.75 and 8.76, respectively. The total theoretical uncertainty for JETPHOX was computed by adding in quadrature the uncertainties mentioned above and is shown in Figure 8.77.

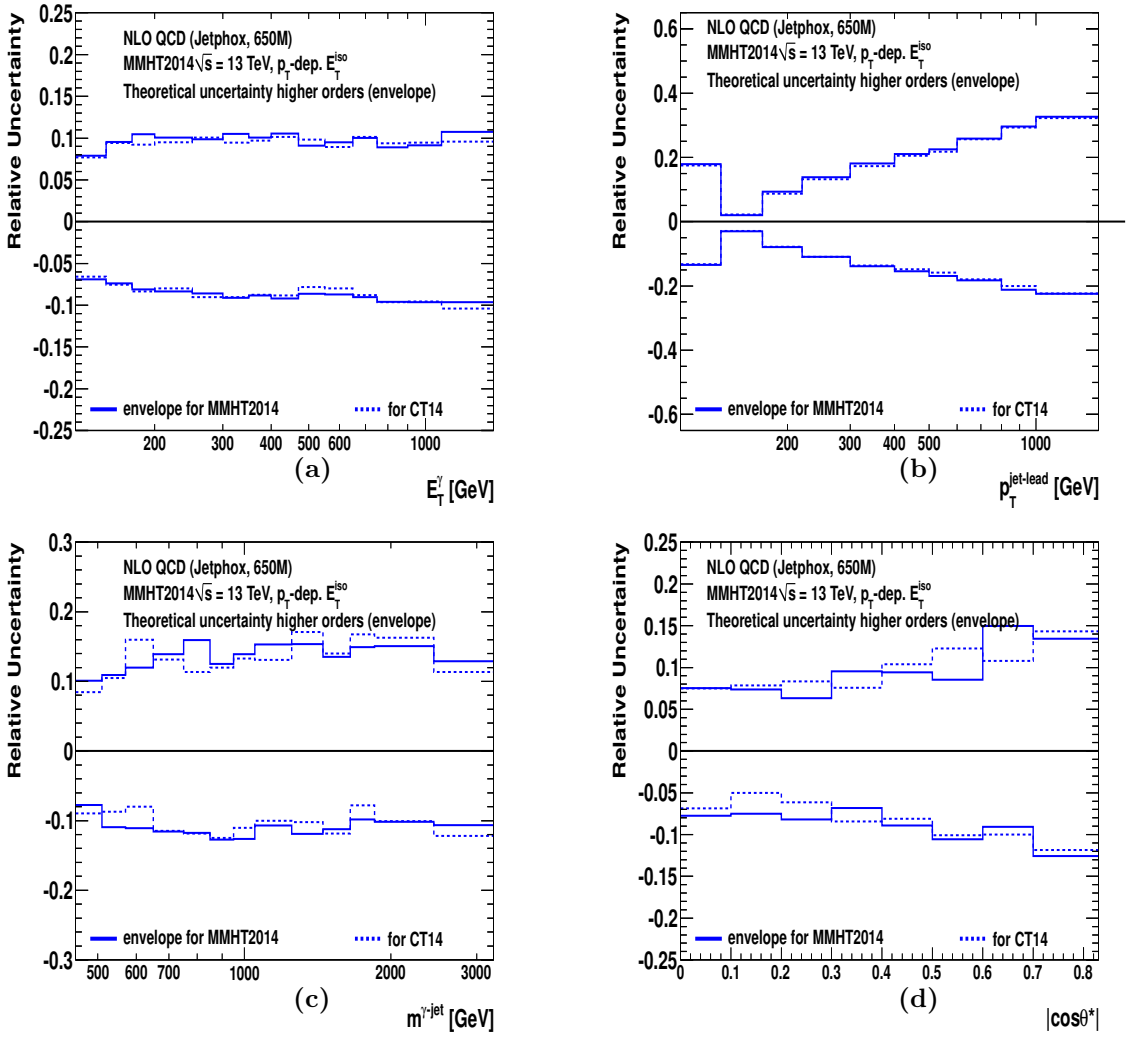


Figure 8.74: Theoretical uncertainty arising from terms beyond NLO (envelope of all 14 variations) using MMHT2014 (solid lines) and CT14 (dotted lines) as a function of (a) E_{T}^{γ}, (b) $p_{\mathrm{T}}^{\mathrm{jet-lead}}$, (c) $m^{\gamma-\mathrm{jet}}$ and (d) $|\cos\theta^{\star}|$.

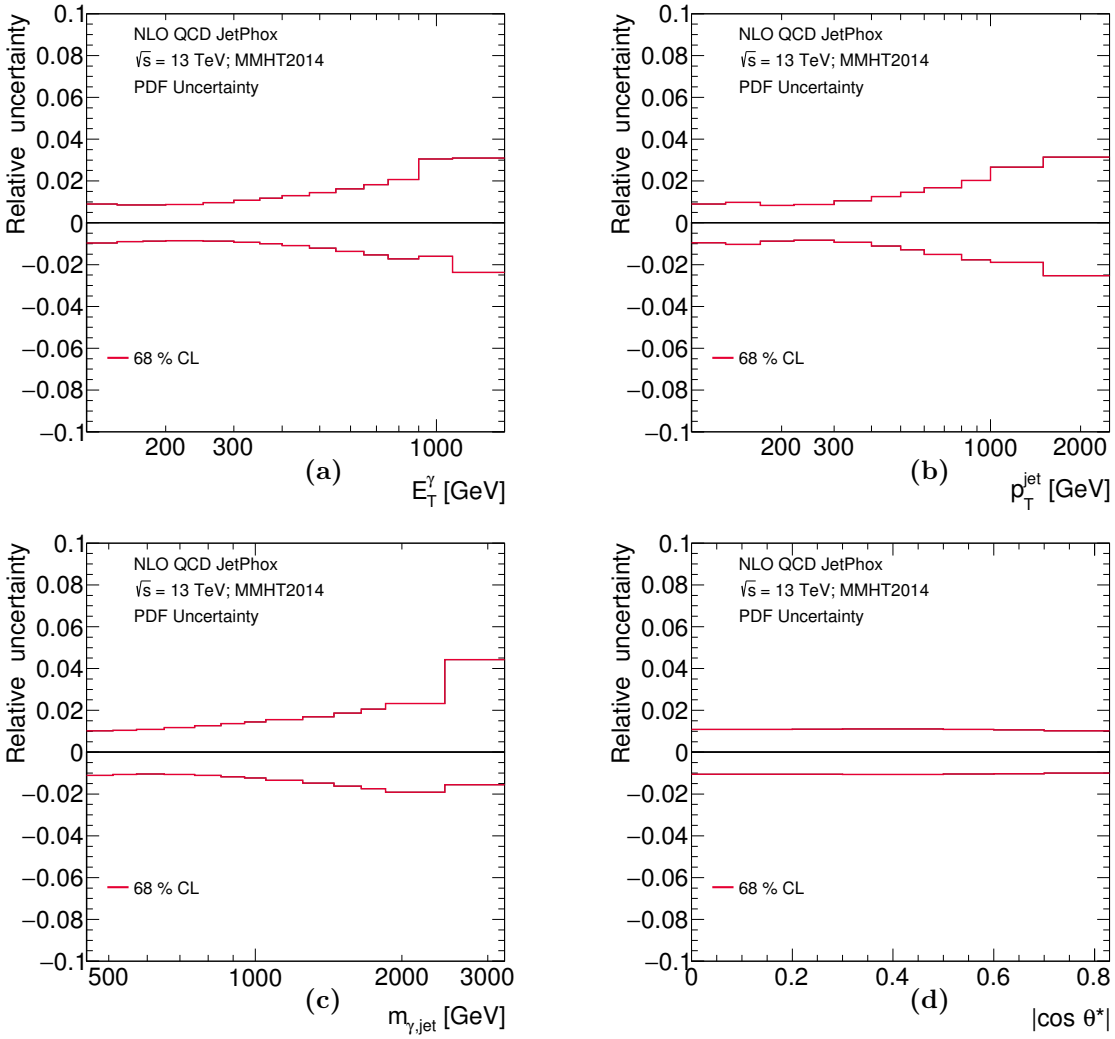


Figure 8.75: Theoretical uncertainty arising from the uncertainty in the PDFs as a function of (a) E_{T}^{γ}, (b) $p_{\mathrm{T}}^{\mathrm{jet-lead}}$, (c) $m^{\gamma-\mathrm{jet}}$ and (d) $|\cos\theta^{\star}|$.

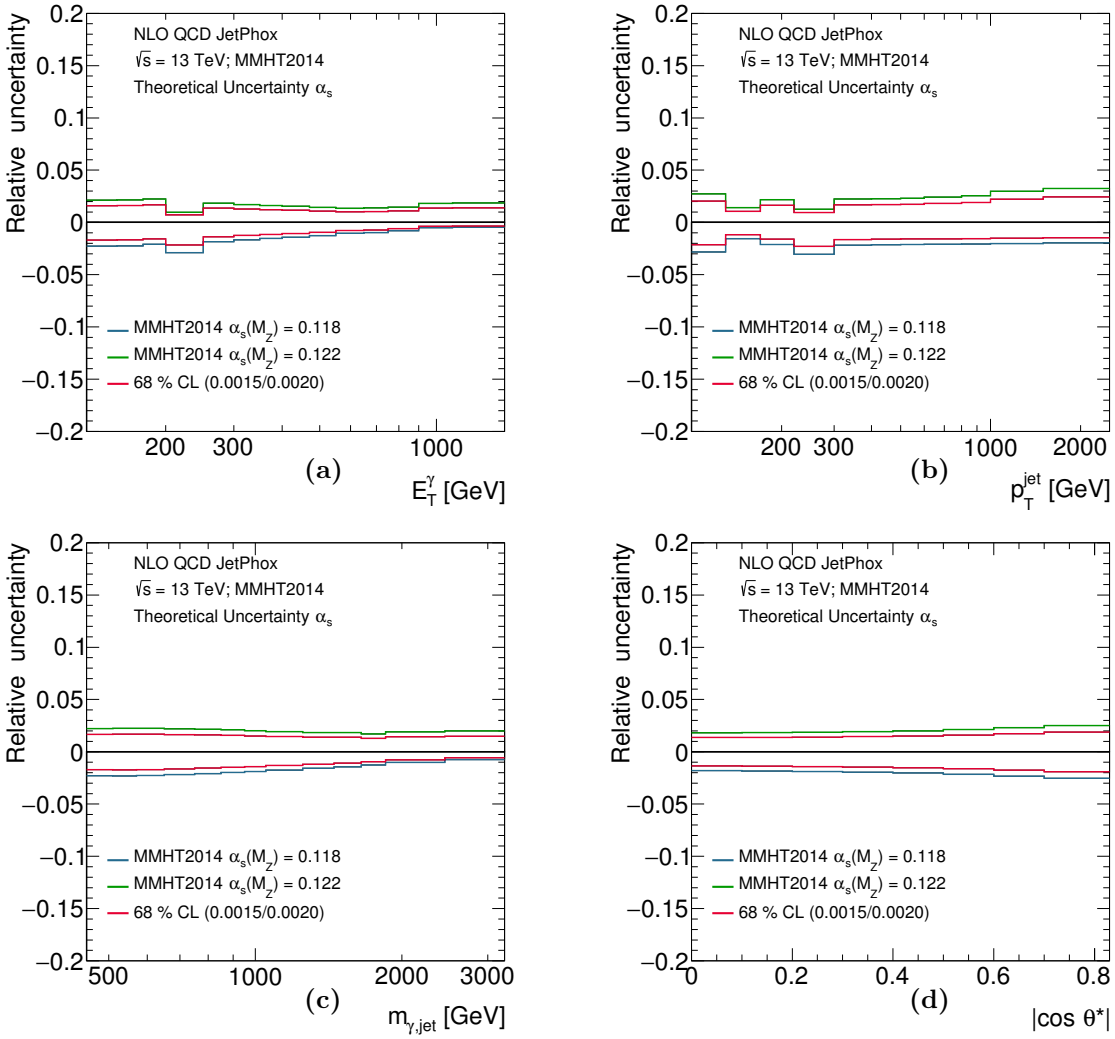


Figure 8.76: Theoretical uncertainty arising from the uncertainty in α_s as a function of (a) E_{T}^{γ}, (b) $p_{\mathrm{T}}^{\mathrm{jet-lead}}$, (c) $m^{\gamma-\mathrm{jet}}$ and (d) $|\cos\theta^{\star}|$.

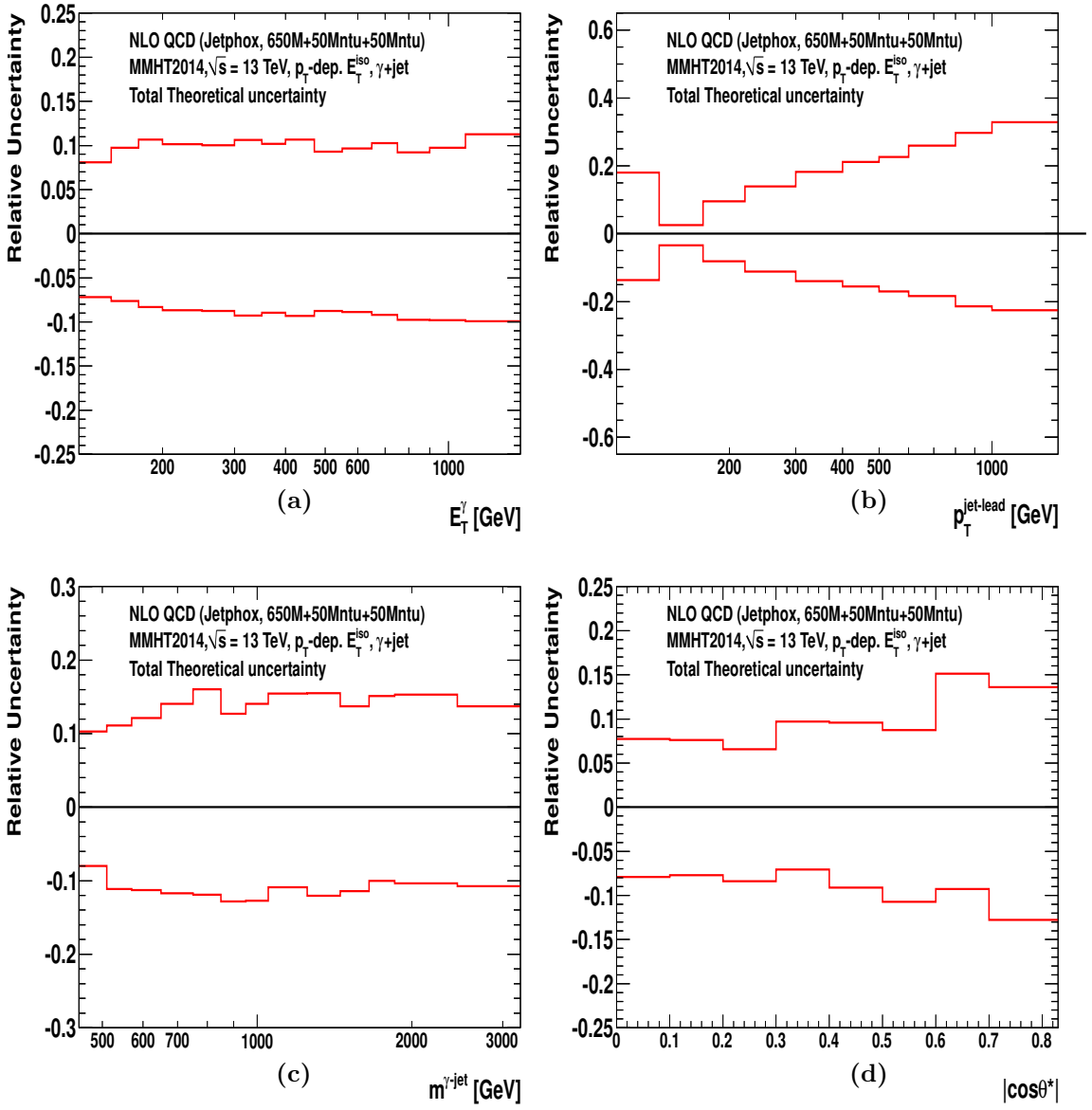


Figure 8.77: Total theoretical uncertainty, excluding that due to the non-perturbative corrections, as a function of (a) E_{T}^{γ}, (b) $p_{\mathrm{T}}^{\mathrm{jet-lead}}$, (c) $m^{\gamma-\mathrm{jet}}$ and (d) $|\cos\theta^{\star}|$.

8.6.3 Predictions using SHERPA 2.2.2

The predictions of SHERPA NLO (see Section 3.5.7) are shown in Figure 8.78. The NNPDF3.0NNLO PDFs [59] are used for the nominal results and compared with the calculations based on MMHT2014 and CT14 PDFs. The differences between the predictions based on different proton PDFs are smaller than 3%.

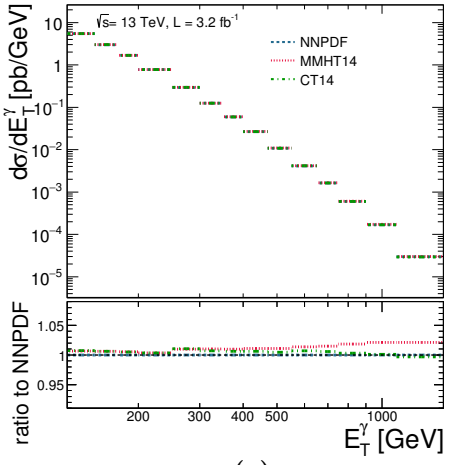
Theoretical uncertainties of the predictions using SHERPA 2.2.2

The following sources of uncertainties in the theoretical predictions were considered:

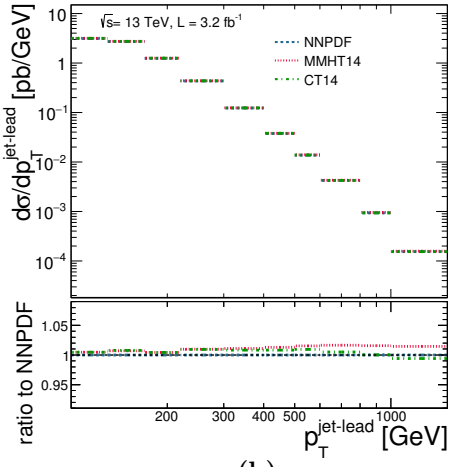
- the uncertainty on the NLO SHERPA calculations due to terms beyond NLO was estimated by comparing the nominal predictions to those obtained using values of μ_R and μ_F scaled by factors of 0.5 and 2. The two scales were either varied simultaneously or individually avoiding variations in which the ratio of scales was larger than or equal to four. The final uncertainty was taken as the largest deviation from the nominal value among the 6 possible variations;
- the uncertainty on the NLO SHERPA due to those on the proton PDFs was estimated by repeating the calculations using 100 replicas from the NNPDF3.0 error analysis;
- the uncertainty induced by the imperfect knowledge of the value of $\alpha_s(m_Z)$ was estimated by repeating the calculations using two additional sets of the proton PDFs from the NNPDF3.0 analysis, for which different values of $\alpha_s(m_Z)$ were assumed in the fits: $\alpha_s(m_Z)$ =0.117 and $\alpha_s(m_Z)$ =0.119. The observed relative differences were scaled by a factor 1.5/1.0 to quote the final uncertainty at a 68% confidence level.

Also here, the dominant theoretical uncertainties come from the uncertainty arising from the terms beyond NLO. Figures 8.79 to 8.81 show an overview of the relative theoretical uncertainties in the kinematic region of the measurements. The total theoretical uncertainty was obtained by adding in quadrature the individual uncertainties listed above.

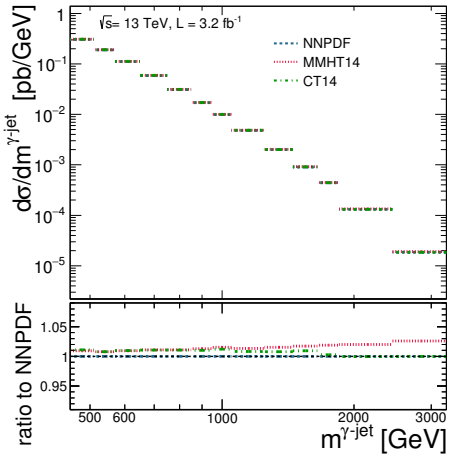
The results of SHERPA 2.2.2 were obtained directly at particle level and contained the effects of hadronisation and UE and there was no need to apply non-perturbative corrections. Nevertheless, an uncertainty should be assigned for this effect. No alternative tune to the nominal one was available making impossible an estimation of such uncertainty. It is expected that the uncertainty should be of similar size as that evaluated using PYTHIA.



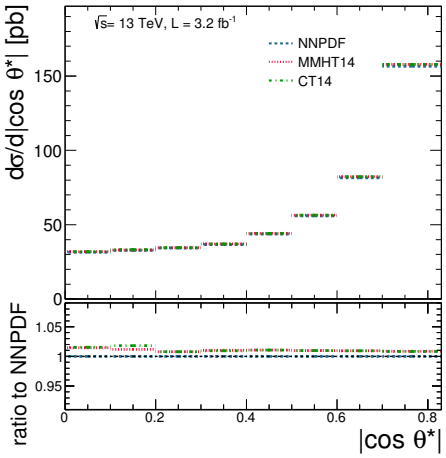
(a)



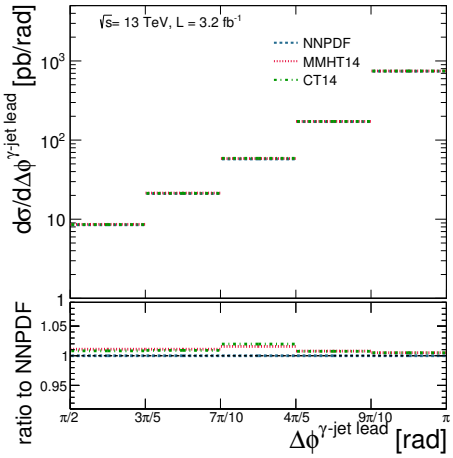
(b)



(c)



(d)



(e)

Figure 8.78: Predictions of NLO Sherpa based on the NNPDF3.0NNLO (blue dashed lines), MMHT2014 (red dotted lines) and CT14 (green dot-dashed lines) proton PDFs for the cross sections for isolated-photon plus one-jet production as functions of the different observables. The lower part of each figure shows the ratio of the predictions to that based on the NNPDF3.0NNLO PDFs.

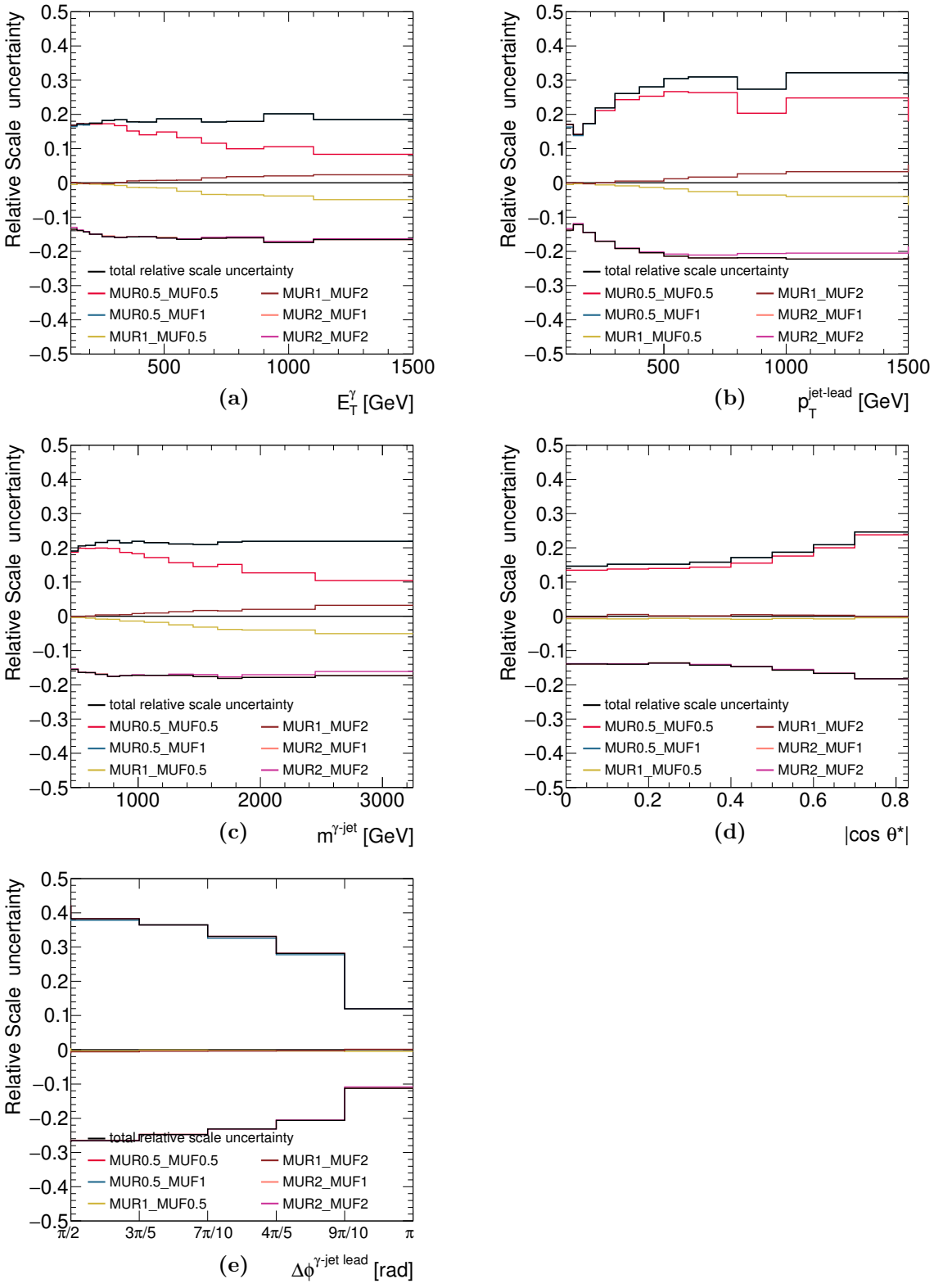


Figure 8.79: Relative uncertainties of the NLO SHERPA predictions based on the NNPDF3.0NNLO PDF set as functions of the different observables arising from the variation of the scales: $\mu_R = \mu_F = 0.5 \cdot E_T^\gamma$ (red histograms); $\mu_R = 0.5 \cdot E_T^\gamma$ and $\mu_F = E_T^\gamma$ (blue histograms); $\mu_R = E_T^\gamma$ and $\mu_F = 0.5 \cdot E_T^\gamma$ (yellow histograms); $\mu_R = E_T^\gamma$ and $\mu_F = 2 \cdot E_T^\gamma$ (brown histograms); $\mu_R = 2 \cdot E_T^\gamma$ and $\mu_F = E_T^\gamma$ (pink histograms); $\mu_R = \mu_F = 2 \cdot E_T^\gamma$ (magenta histograms). The envelope of the six variations is represented by the black histogram.

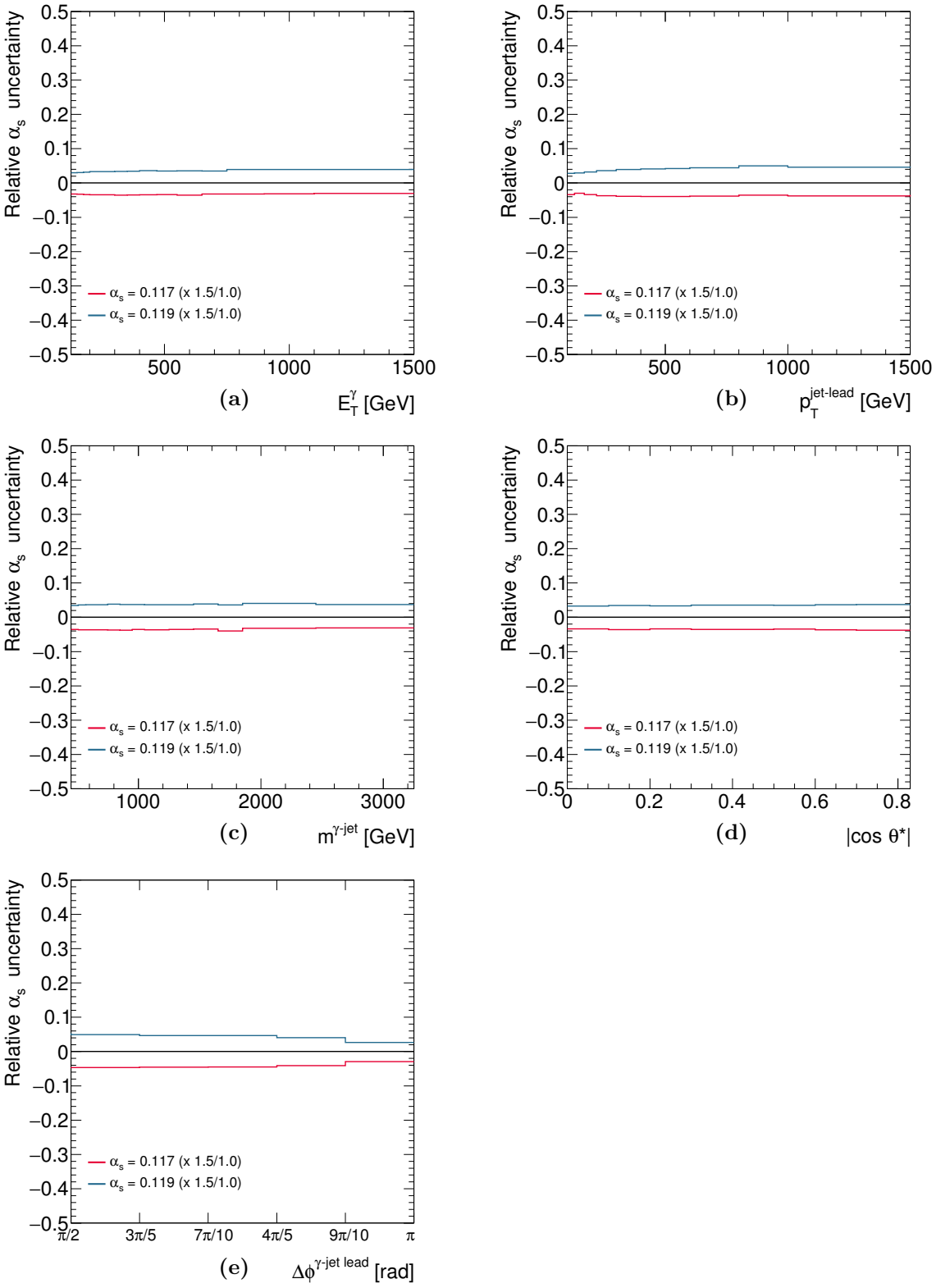


Figure 8.80: Relative uncertainties of the NLO SHERPA predictions based on the NNPDF3.0NNLO PDF set as functions of the different observables arising from the uncertainty in α_s.

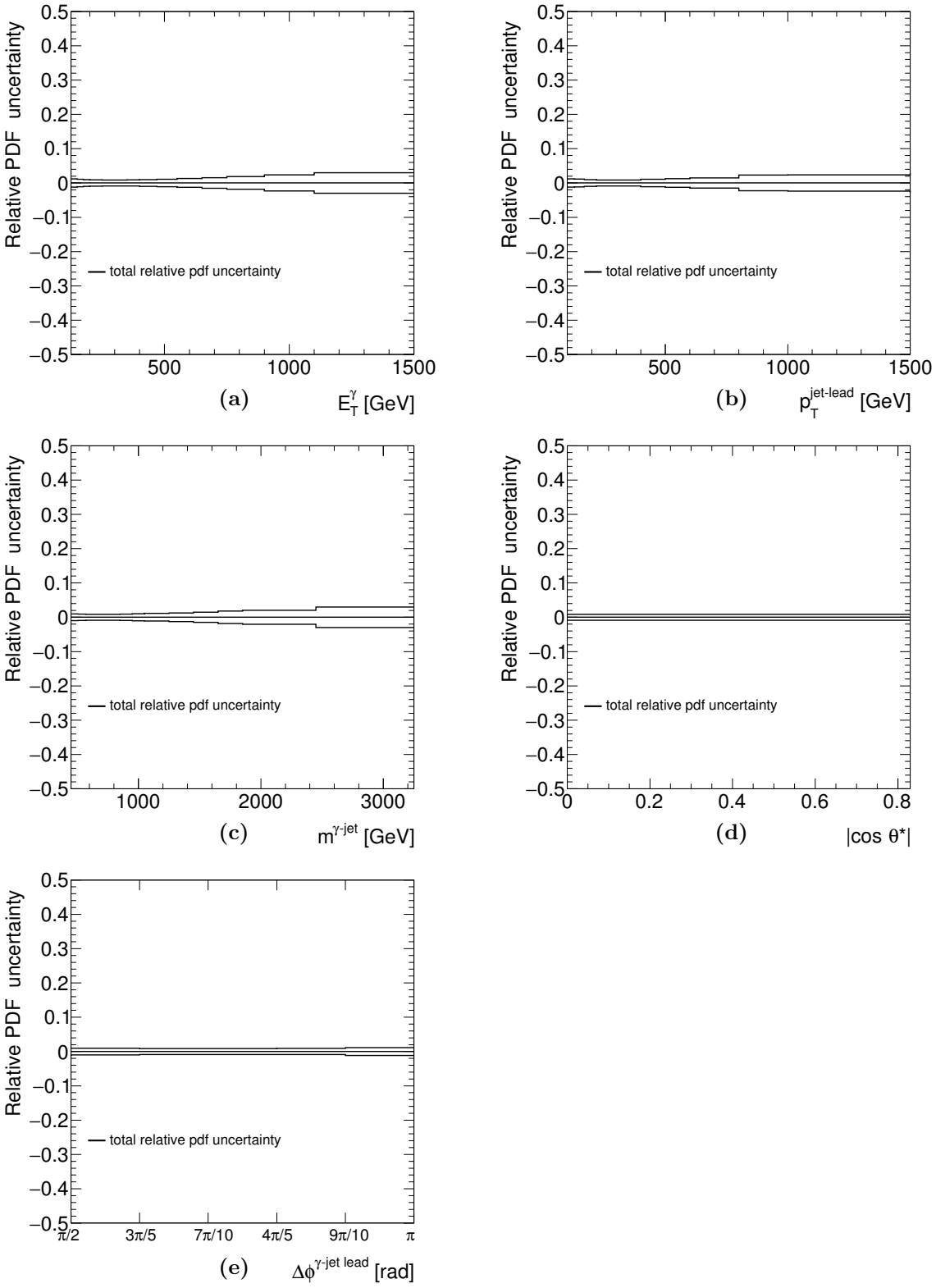


Figure 8.81: Relative uncertainties of the NLO SHERPA predictions based on the NNPDF3.0NNLO PDF set as functions of the different observables arising from the uncertainty in the PDFs.

8.7 Results

The measurements presented here refer to isolated prompt photons with $E_{\mathrm{T}}^{\mathrm{iso}} < 4.2 \cdot 10^{-3} \cdot E_{\mathrm{T}}^{\gamma} + 10$ GeV and jets of hadrons. The measured fiducial cross section for isolated-photon plus one-jet production is

$$\sigma_{\mathrm{meas}} = 300 \pm 10 \text{ (exp.) } \pm 6 \text{ (lumi.) pb},$$

where "exp." denotes the sum in quadrature of the statistical and systematic uncertainties and "lumi." denotes the uncertainty due to that in the integrated luminosity. The fiducial cross sections predicted by NLO QCD JetPhox (multi-leg NLO QCD plus parton-shower Sherpa) using the MMHT2014 (NNPDF3.0NNLO) PDFs are

$$\sigma_{\mathrm{JETPHOX}} = 291^{+25}_{-21} \text{ (scale)}^{+2}_{-3} \text{ (PDF)}^{+4}_{-5} \text{ } (\alpha_{\mathrm{s}}) \pm 6 \text{ (non} - \text{perturb.) pb}$$

and

$$\sigma_{\mathrm{SHERPANLO}} = 319^{+54}_{-45} \text{ (scale) } \pm 3 \text{ (PDF)}^{+10}_{-11} \text{ } (\alpha_{\mathrm{s}}) \text{ pb},$$

which are consistent with the measurement within the theoretical uncertainties.

Figure 8.82 shows the isolated-photon plus jet cross sections as functions of E_{T}^{γ}, $p_{\mathrm{T}}^{\mathrm{jet-lead}}$, $\Delta\phi^{\gamma-\mathrm{jet}}$, $m^{\gamma-\mathrm{jet}}$ and $|\cos\theta^{\star}|$.

The measured $d\sigma/dE_{\mathrm{T}}^{\gamma}$ decreases by almost six orders of magnitude over the complete E_{T}^{γ} range. Values of E_{T}^{γ} up to 1.5 TeV are measured. The experimental uncertainty, excluding that in the luminosity, is below 5% in most of the measured range, dominated by the photon energy scale uncertainty for $E_{\mathrm{T}}^{\gamma} \lesssim 700$ GeV, and it grows up to 33% at $E_{\mathrm{T}}^{\gamma} \sim 1.5$ TeV, dominated by the statistical uncertainty in this region. The measured $d\sigma/p_{\mathrm{T}}^{\mathrm{jet-lead}}$ decreases by more than four orders of magnitude from $p_{\mathrm{T}}^{\mathrm{jet-lead}} \sim 100$ GeV up to the highest measured value, $p_{\mathrm{T}}^{\mathrm{jet-lead}} \approx 1.5$ TeV. The experimental uncertainty, excluding that in the luminosity, is below 5% for $p_{\mathrm{T}}^{\mathrm{jet-lead}} < 500$ GeV. It is dominated by the uncertainty on the jet energy scale.

The measurement of $d\sigma/d\Delta\phi^{\gamma-\mathrm{jet}}$ is restricted to $\Delta\phi^{\gamma-\mathrm{jet}} > \pi/2$ to avoid the phase-space region dominated by photon production in association with a multi-jet system. The measured $d\sigma/d\Delta\phi^{\gamma-\mathrm{jet}}$ increases as $\Delta\phi^{\gamma-\mathrm{jet}}$ increases. The experimental uncertainty, excluding that in the luminosity, is $\approx 4\%$. The measured $d\sigma/dm^{\gamma-\mathrm{jet}}$ decreases by more than four orders of magnitude up to the highest measured value, $m^{\gamma-\mathrm{jet}} = 3.25$ TeV. The experimental uncertainty, excluding that in the luminosity, is $\approx 4\%$ for $m^{\gamma-\mathrm{jet}} \lesssim 1.5$ TeV, dominated by the jet and photon energy scales; for $m^{\gamma-\mathrm{jet}} > 1.5$ TeV, the statistical uncertainty dominates. The measured $d\sigma/d|\cos\theta^{\star}|$ increases as $|\cos\theta^{\star}|$ increases. The experimental uncertainty, excluding that in the luminosity, is $3-4\%$; the only significant contributions arise from the photon and jet energy scale uncertainties and the photon identification efficiency.

The tree-level predictions of the Pythia and LO Sherpa MC models are compared to the measurements in Figure 8.82. These predictions are normalised to the measured integrated fiducial cross section. The difference in normalisation between data and Pythia (LO Sherpa) is $\sim +10\%$ ($+40\%$) and attributed to the fact that these generators are based on tree-level matrix elements, which are affected by a large normalisation uncertainty

due to missing higher-order terms; for this reason, the theoretical uncertainties are not included in Figure 8.82. Both predictions give an adequate description of the shape of the measured $d\sigma/dE_{\mathrm{T}}^{\gamma}$, though Pythia is slightly better than LO Sherpa for $E_{\mathrm{T}}^{\gamma} \lesssim 600$ GeV. For $d\sigma/p_{\mathrm{T}}^{\mathrm{jet-lead}}$, the prediction from LO Sherpa gives an adequate description of the data in the whole measured range, whereas that from Pythia overestimates the data for $p_{\mathrm{T}}^{\mathrm{jet-lead}} \gtrsim 200$ GeV; this overestimation is attributed to a large contribution from photon bremsstrahlung predicted by the tune of Pythia used. The prediction from LO Sherpa gives a good description of the measured $d\sigma/d\Delta\phi^{\gamma-\mathrm{jet}}$, whereas Pythia underestimates the data for $3\pi/5 < \Delta\phi^{\gamma-\mathrm{jet}} < 4\pi/5$ rad. Both predictions give a good description of the data for $m^{\gamma-\mathrm{jet}} < 1.25$ TeV and for all the measured $|\cos\theta^{\star}|$ range.

The predictions of the fixed-order NLO QCD calculations of JetPhox based on the MMHT2014 proton PDF set and corrected for hadronisation and UE effects as explained in Section 8.6.1 are compared to the measurements[3] in Figure 8.83. The predictions of the multi-leg NLO QCD plus parton-shower calculations of Sherpa based on the NNPDF3.0NNLO PDF set are also compared to the measurements in Figure 8.83. Both types of predictions describe the data within the experimental and theoretical uncertainties. For the cross section as a function of $\Delta\phi^{\gamma-\mathrm{jet}}$, the only meaningful prediction is that of NLO Sherpa, which is able to reproduce the data down to $\Delta\phi^{\gamma-\mathrm{jet}} = \pi/2$ due to the inclusion of the matrix elements for $2 \to n$ processes with $n = 4$ and 5. For most of the points, the theoretical uncertainties are larger than those of experimental origin.

Predictions for JetPhox (Sherpa NLO) are also obtained with other parameterisations of the proton PDFs, namely CT14 and NNPDF3.0NLO (CT14 and MMHT2014), and differ by less than 5%. Thus, the description of the data achieved by the predictions does not depend significantly on the specific PDF set used. It is concluded that the NLO pQCD predictions provide an adequate description of the measurements within the uncertainties. Furthermore, the normalisation of the differential cross sections provided by JetPhox as a function of E_{T}^{γ} is closer to the data in the phase space of this measurement than in the inclusive-photon analysis, for which no requirements on jets were imposed. The tendency to provide a different shape of the differential cross section than the one measured for $m^{\gamma-\mathrm{jet}}$ at high $m^{\gamma-\mathrm{jet}}$ by both NLO generators could be due to the missing electroweak corrections.

The measured increase of the $d\sigma/d|\cos\theta^{\star}|$ cross section with $|\cos\theta^{\star}|$ is reproduced by the predictions. To illustrate the sensitivity to the t-channel quark or gluon exchange, the predicted $d\sigma/d|\cos\theta^{\star}|$ cross section for LO direct and fragmentation processes are compared to the measurement in Figure 8.84. Even though the two components are no longer distinguishable at NLO, the LO calculations are useful in illustrating the basic differences in the dynamics of the two processes. The contribution from fragmentation, dominated by gluon exchange, shows a steeper increase as $|\cos\theta^{\star}| \to 1$ than that from direct processes, dominated by quark exchange. The shape of the measured $d\sigma/d|\cos\theta^{\star}|$ cross section is closer to that of the direct processes than that of fragmentation. This is consistent with the dominance of processes in which the exchanged particle is a quark.

[3] As shown in [18], the NLO QCD predictions of JetPhox cannot describe $d\sigma/d\Delta\phi^{\gamma-\mathrm{jet}}$ due to the limited number of final-state partons.

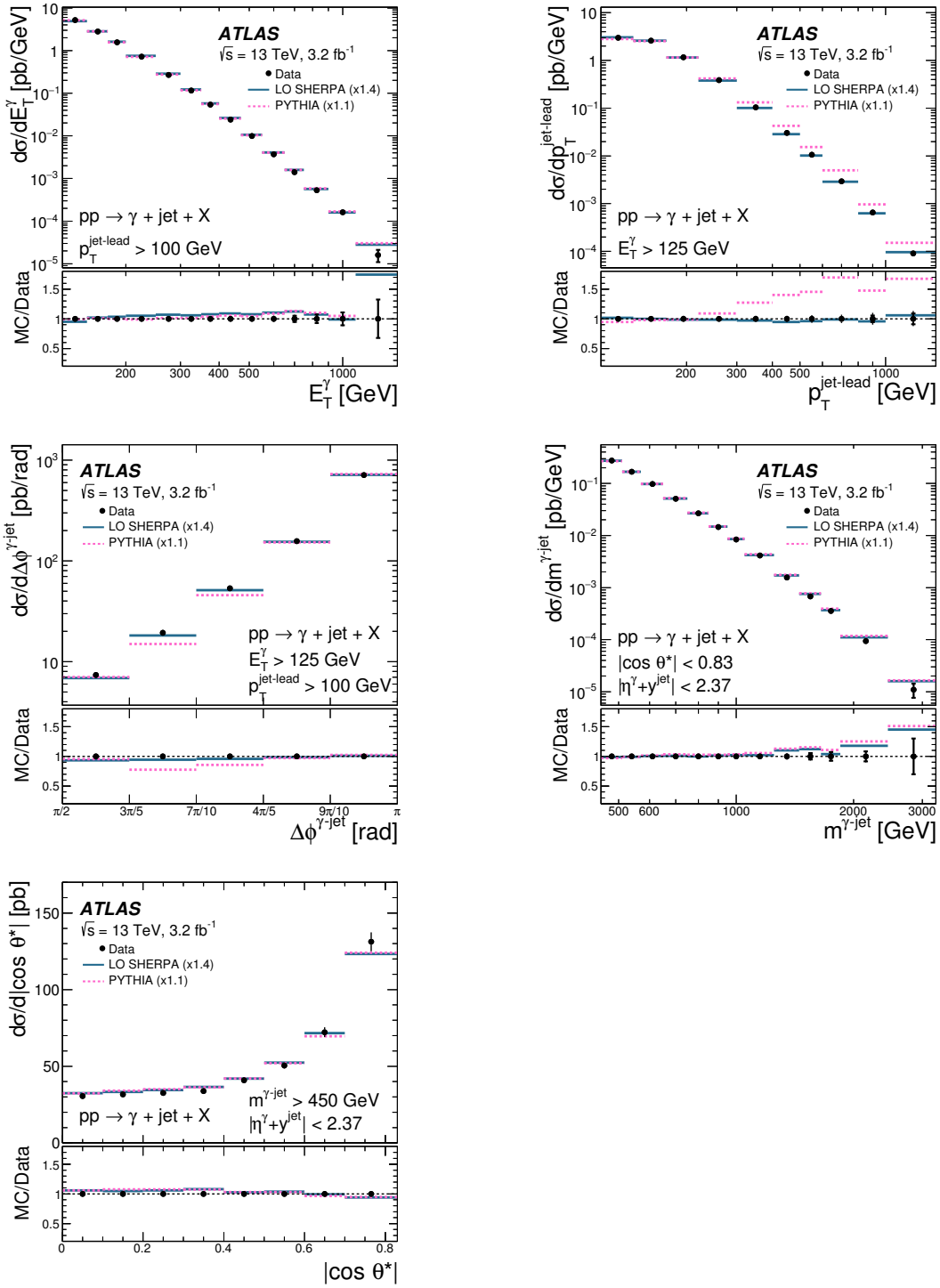


Figure 8.82: Measured cross sections for isolated-photon plus one-jet production (dots) as functions of E_{T}^{γ}, $p_{\mathrm{T}}^{\mathrm{jet-lead}}$, $\Delta\phi^{\gamma-\mathrm{jet}}$, $m^{\gamma-\mathrm{jet}}$ and $|\cos\theta^{\star}|$. For comparison, the tree-level plus parton-shower predictions from LO Sherpa (solid lines) and Pythia (dashed lines) normalised to the integrated measured cross sections (using the factors indicated in parentheses) are also shown. The theoretical uncertainties associated to the tree-level predictions are not included. The bottom part of each figure shows the ratios of the MC predictions to the measured cross section. The inner (outer) error bars represent the statistical uncertainties (the statistical and systematic uncertainties added in quadrature). For most of the points, the inner error bars are smaller than the marker size and, thus, not visible.

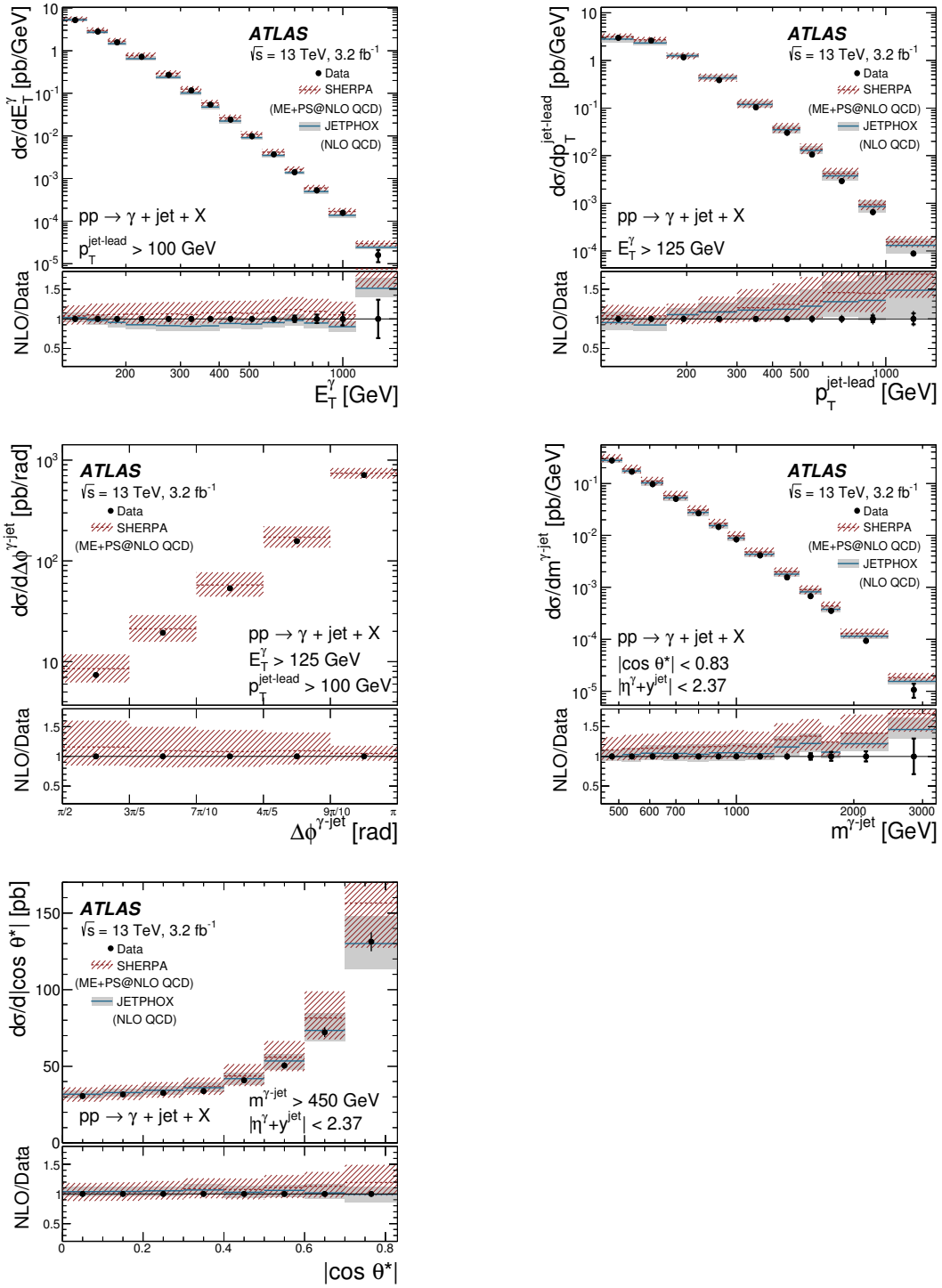


Figure 8.83: Measured cross sections for isolated-photon plus one-jet production (dots) as functions of E_{T}^{γ}, $p_{\mathrm{T}}^{\mathrm{jet-lead}}$, $\Delta\phi^{\gamma-\mathrm{jet}}$, $m^{\gamma-\mathrm{jet}}$ and $|\cos\theta^{\star}|$. For comparison, the multi-leg NLO QCD plus parton shower predictions from SHERPA (dashed lines) and the NLO QCD predictions from JETPHOX corrected for hadronisation and underlying-event effects (solid lines) are also shown. The bottom part of each figure shows the ratios of the predictions to the measured cross section. The inner (outer) error bars represent the statistical uncertainties (the statistical and systematic uncertainties added in quadrature) and the bands display the theoretical uncertainty. For most of the points, the inner error bars are smaller than the marker size and, thus, not visible.

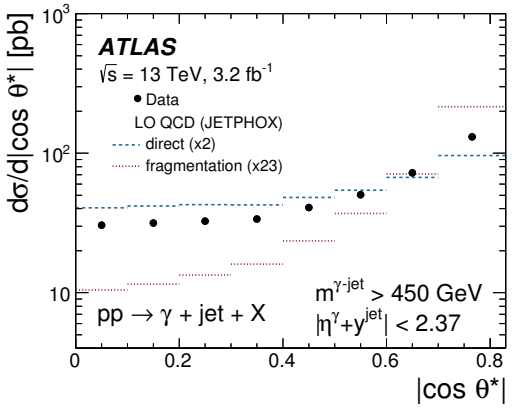


Figure 8.84: Measured cross section for isolated-photon plus one-jet production (dots) as a function of $|\cos\theta^{\star}|$. For comparison, the LO QCD predictions from JetPhox, normalised to the integrated measured cross section by the factors shown in parentheses, of direct (dashed lines) and fragmentation (dotted lines) processes are shown separately. The error bars are smaller than the marker size and, thus, not visible.

9

Cross-section measurements for isolated-photon production plus two jets

In this chapter, the study of the dynamics of isolated-photon plus two-jet events in pp collisions at a centre-of-mass energy of 13 TeV is presented. Three different phase-space regions were investigated to enhance the interplay of the underlying processes. The kinematics of the photon plus two-jet system was studied in this analysis via the measurements of the cross sections as functions of E_{T}^{γ}, $p_{\mathrm{T}}^{\mathrm{jet}}$ and y^{jet}. The dynamics of the photon plus two-jet system was studied by measuring the azimuthal angular separation between the photon and each of the jets ($\Delta\phi^{\gamma-\mathrm{jet}}$), the difference in rapidity between the photon and each of the jets ($|\Delta y^{\gamma-\mathrm{jet}}|$), the invariant mass of the two-jet system ($m^{\mathrm{jet}-\mathrm{jet}}$), the azimuthal angular separation between the jets ($\Delta\phi^{\mathrm{jet}-\mathrm{jet}}$), the difference in rapidity between the two jets ($|\Delta y^{\mathrm{jet}-\mathrm{jet}}|$) and the invariant mass of the photon–jet–jet system ($m^{\gamma-\mathrm{jet}-\mathrm{jet}}$). Next-to-leading-order QCD calculations using Sherpa matrix elements at NLO supplemented with parton showers were compared to the measurements. The predictions of the leading-logarithm parton-shower of Pythia and Sherpa were also compared to the measurements.

9.1 Data selection

The data used in this analysis were collected with the ATLAS detector during the pp collision running periods of 2015 and 2016, when the LHC operated at a centre-of-mass-energy of $\sqrt{s} = 13$ TeV.

The corresponding luminosity of this data set is 36.1 ± 0.8 fb^{-1} [115]. Data passing the on-line requirements of the HLT_g140_loose trigger were used. This is a single-photon high-level trigger with a nominal transverse energy threshold of 140 GeV seeded by a level-1 trigger with a nominal threshold equal to 22 GeV. A brief description of the photon triggers is given in Section 6.1.1. Events were rejected if the inner detector or calorimeters were not fully operational based on the GRL information or showed data-quality problems. The same event requirements as in the inclusive-photon and the photon plus jet analyses were applied (see Section 6.1.2).

9.1.1 Photon and jet selection

The photon and jet selection follows the same criteria as presented in Section 6.1.3 and 8.1.1. The main differences are listed below:

- events with a leading photon with a transverse energy $E_{\mathrm{T}}^{\gamma} > 150$ GeV were selected;
- events with at least two jets at a distance $\Delta R > 0.8$ from the photon with $|y^{\mathrm{jet}}| < 2.5$ were retained;
- the event was discarded if the subleading jet had a transverse energy lower than $p_{\mathrm{T}}^{\mathrm{jet}} < 100$ GeV.

9.1.2 Data samples

Measurements were performed in three different phase-space regions:

1. the sample with $E_{\mathrm{T}}^{\gamma} > 150$ GeV and two jets of $p_{\mathrm{T}}^{\mathrm{jet}} > 100$ GeV (*inclusive* sample);
2. the sample with $E_{\mathrm{T}}^{\gamma} > 150$ GeV, two jets of $p_{\mathrm{T}}^{\mathrm{jet}} > 100$ GeV and $E_{\mathrm{T}}^{\gamma} < p_{\mathrm{T}}^{\mathrm{jet2}}$, where $p_{\mathrm{T}}^{\mathrm{jet2}}$ is the second-highest $p_{\mathrm{T}}^{\mathrm{jet}}$ jet; this sample is enriched in the fragmentation component (*fragmentation-enriched* sample);
3. the sample with $E_{\mathrm{T}}^{\gamma} > 150$ GeV, two jets of $p_{\mathrm{T}}^{\mathrm{jet}} > 100$ GeV and $E_{\mathrm{T}}^{\gamma} > p_{\mathrm{T}}^{\mathrm{jet1}}$, where $p_{\mathrm{T}}^{\mathrm{jet1}}$ is the highest $p_{\mathrm{T}}^{\mathrm{jet}}$ jet; this sample is enriched in the direct component (*direct-enriched* sample).

Figures 9.1 to 9.3 show the distributions as functions of the observables studied in the total sample, fragmentation-enriched and direct-enriched samples. The normalised-to-data predictions of Pythia and Sherpa are included as well as the direct and the fragmentation contributions as simulated by the Pythia MC.

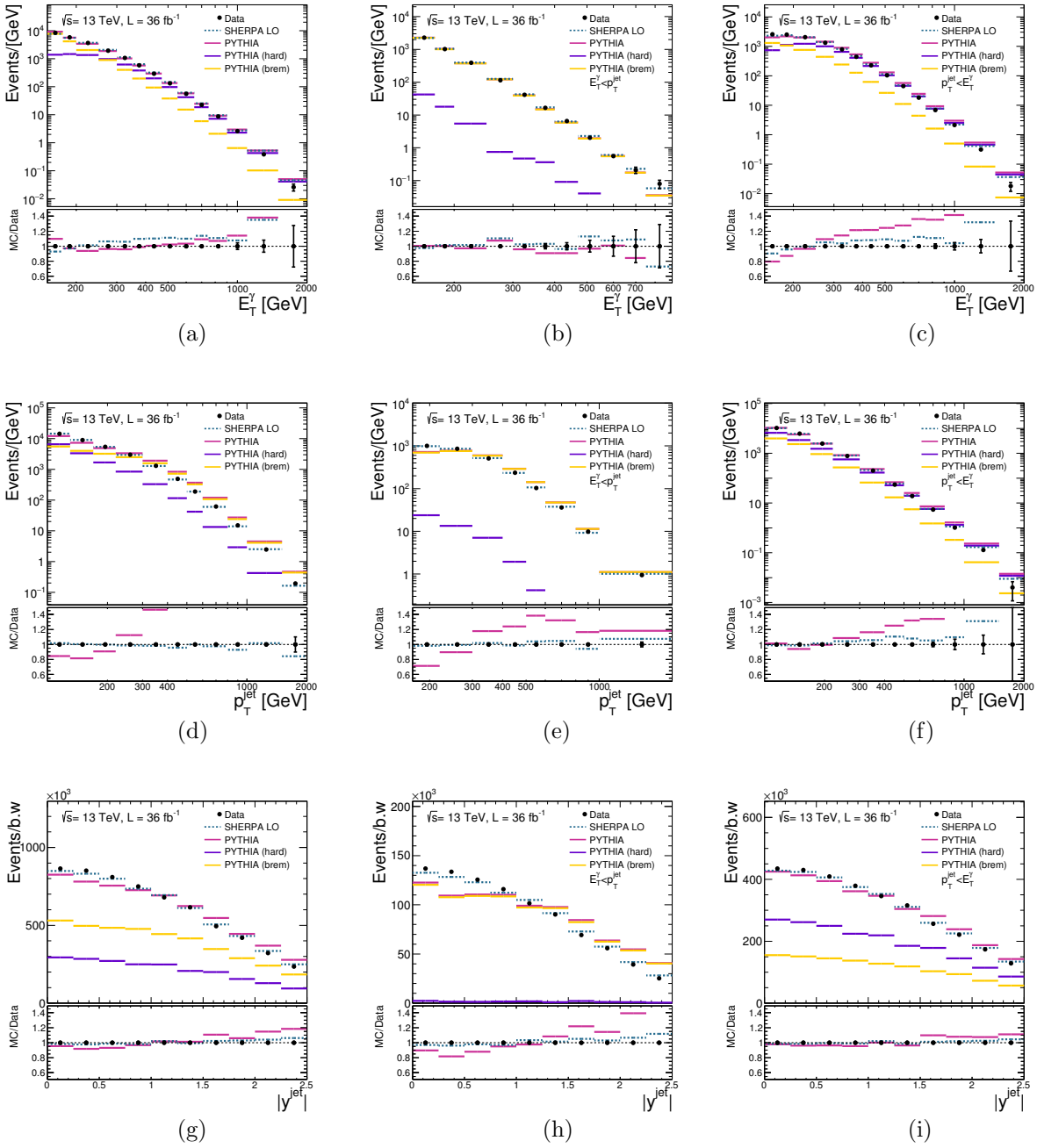


Figure 9.1: The measured E_{T}^{γ} (a,b,c), $p_{\mathrm{T}}^{\mathrm{jet}}$ (d,e,f) and $|y^{\mathrm{jet}}|$ (g,h,i), distributions divided by the bin width (dots) for the total (first column), fragmentation-enriched (second column) and direct-enriched (third column) samples. The measured distributions include background, which has not been subtracted. For comparison, the MC simulations of the signal from PYTHIA (magenta histograms), PYTHIA hard (blue histograms), PYTHIA bremsstrahlung (orange histograms) and SHERPA (dashed histograms) are also included. The MC distributions are normalised to the data. The lower part of the figure shows the ratio of the MC and data distributions.

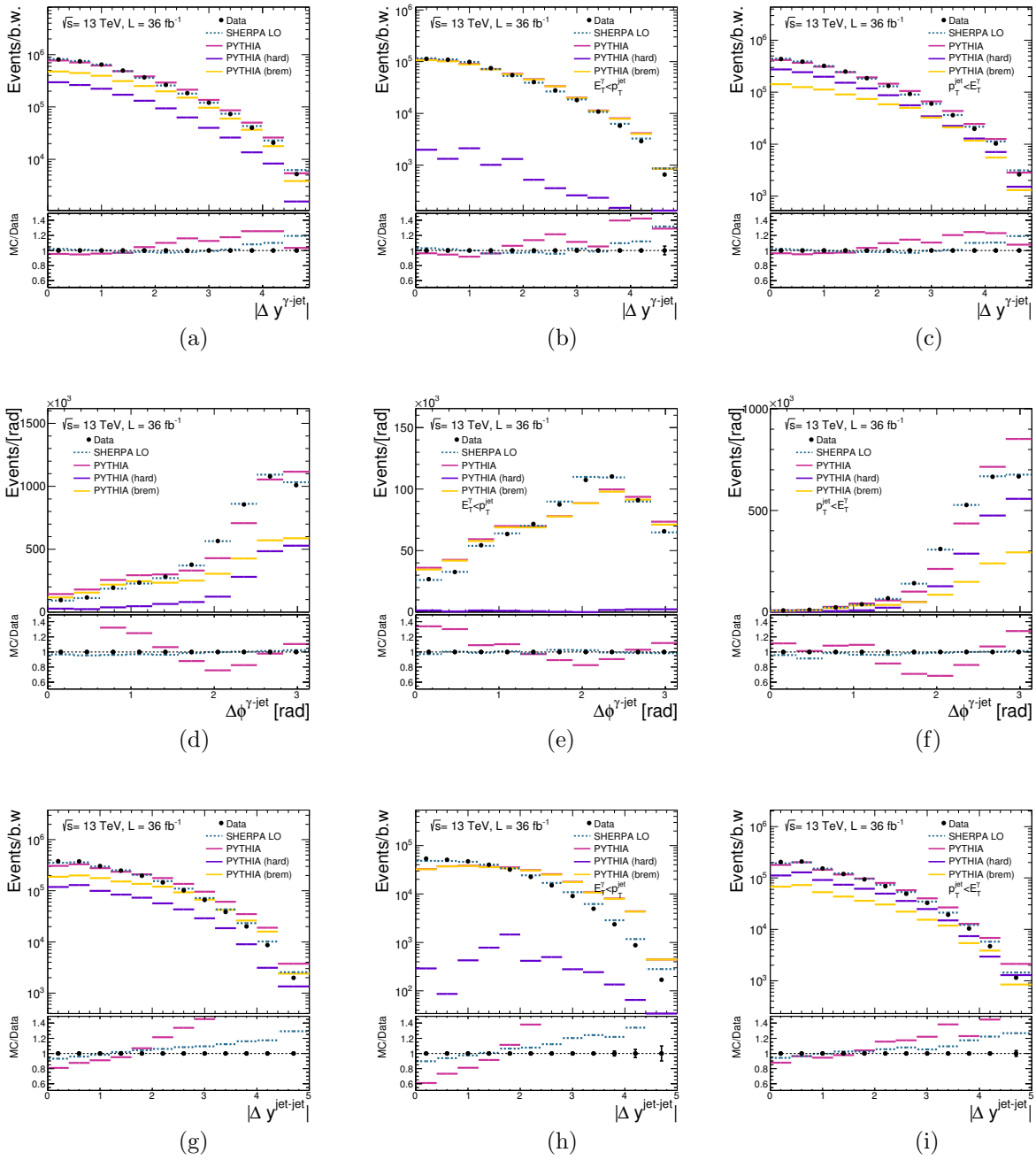


Figure 9.2: The measured $|\Delta y^{\gamma-\text{jet}}|$ (a,b,c), $\Delta\phi^{\gamma-\text{jet}}$ (d,e,f) and $|\Delta y^{\text{jet}-\text{jet}}|$ (g,h,i), distributions divided by the bin width (dots) for the total (first column), fragmentation-enriched (second column) and direct-enriched (third column) samples. The measured distributions include background, which has not been subtracted. For comparison, the MC simulations of the signal from PYTHIA (magenta histograms), PYTHIA hard (blue histograms), PYTHIA bremsstrahlung (orange histograms) and SHERPA (dashed histograms) are also included. The MC distributions are normalised to the data. The lower part of the figure shows the ratio of the MC and data distributions.

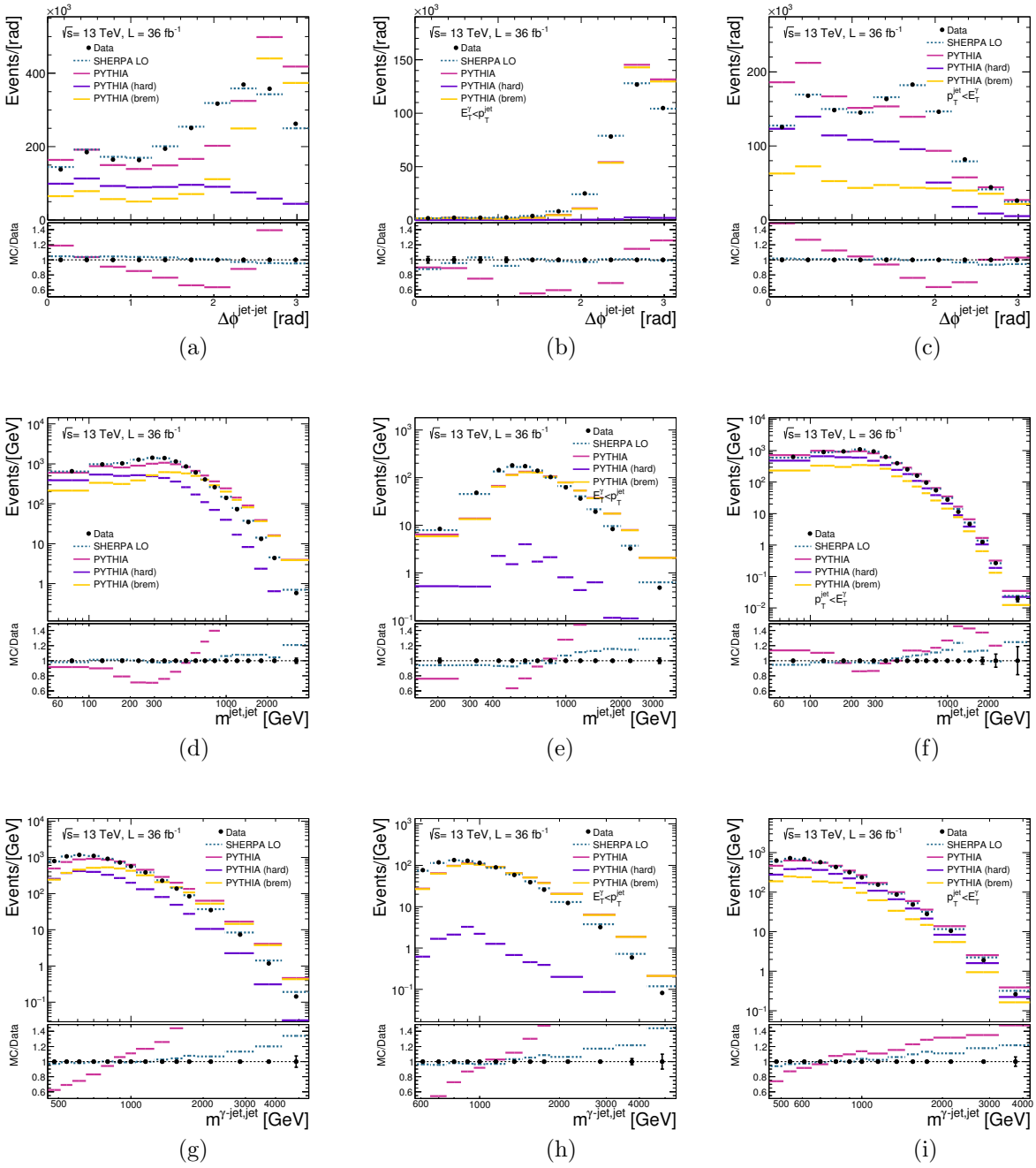


Figure 9.3: The measured $\Delta\phi^{\text{jet}-\text{jet}}$ (a,b,c), $m^{\text{jet}-\text{jet}}$ (d,e,f) and $m^{\gamma-\text{jet}-\text{jet}}$ (g,h,i), distributions divided by the bin width (dots) for the total (first column), fragmentation-enriched (second column) and direct-enriched (third column) samples. The measured distributions include background, which has not been subtracted. For comparison, the MC simulations of the signal from PYTHIA (magenta histograms), PYTHIA hard (blue histograms), PYTHIA bremsstrahlung (orange histograms) and SHERPA (dashed histograms) are also included. The MC distributions are normalised to the data. The lower part of the figure shows the ratio of the MC and data distributions.

9.1.3 Trigger efficiency

The HLT_g140_loose trigger efficiency was measured using a bootstrap method in which the HLT_g120_loose was used as the reference trigger. The efficiency was measured in the four different regions used for background subtraction as described in Section 6.3. It was found that the signal yield obtained after correcting the number of events observed in the signal region and the three background-control regions by the trigger efficiency was essentially the same that applying the estimated correction for the signal region to the signal yield, N_A^{sig}. The measured efficiency shows a dependence with respect to E_{T}^{γ} and $p_{\text{T}}^{\text{jet}}$ in the direct-enriched and fragmentation-enriched samples and no dependence with respect to the other observables studied. The corrections applied to the signal yields $(1/\varepsilon_{\text{trig}})$ were: $\approx 1/0.9988$ for the total sample, $\approx 1/0.9981$ for the fragmentation-enriched sample and $1/0.9992$ for the direct-enriched sample.

The methodology described assumes that the HLT_g120_loose was fully efficient for $E_{\text{T}}^{\gamma} > 150$ GeV. A systematic uncertainty on the trigger efficiency was assigned to cover the inefficiencies of the reference trigger. It was evaluated by measuring the efficiency of the HLT_g120_loose trigger by bootstrapping over a level-1 trigger with a transverse momentum threshold of 15 GeV. A conservative constant uncertainty of 0.22% was considered for all the observables, except for E_{T}^{γ}, in all the phase-space regions. It corresponds to the deviations from unity measured at $E_{\text{T}}^{\gamma} = 150$ GeV, as shown in Figure 9.4. The statistical uncertainties in this figure were computed following the same Bayesian technique described in Section 6.2. For E_{T}^{γ}, the uncertainty considered is collected in Table 9.1 and was computed as the HLT_g120_loose inefficiencies added in quadrature to the statistical uncertainty.

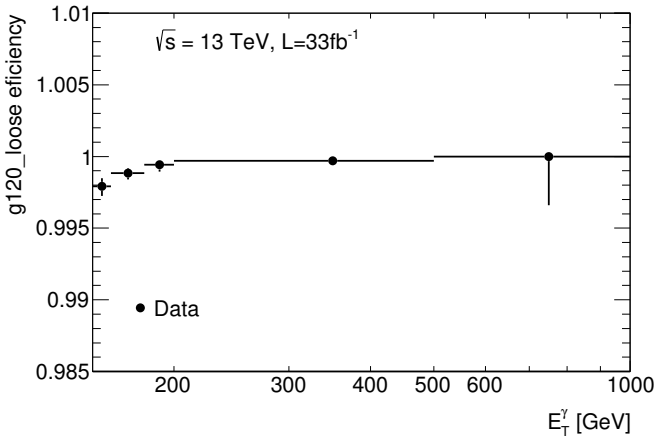


Figure 9.4: HLT_g120_loose trigger efficiency as a function of E_{T}^{γ} for photon candidates reconstructed offline passing the tight identification selection with $|\eta^{\gamma}| < 2.37$, excluding the transition region between the barrel and end-cap calorimeter, at $1.37 < |\eta^{\gamma}| < 1.52$. The error bars represent the Bayesian statistical uncertainty. The data trigger efficiency estimations were provided by the authors of [130].

E_{T}^{γ} range [GeV]	uncertainty
150-175	0.22%
175-200	0.08%
200-470	0.04%
470-2000	0.40%

Table 9.1: Trigger uncertainty in different ranges of E_{T}^{γ}.

9.1.4 Corrections to simulated events

As described in Section 6.1.4, corrections were applied to the MC simulated events to match the overall event conditions of the data sample and to account for known differences between data and simulations. These corrections are:

- the shower-shape discriminant variables used for the photon identification are shifted in the MC to match the shapes observed in data. Additional scales factors were applied to the MC to match the photon-identification efficiency in data. Details on how these were estimated are presented in Section 4.3;
- a correction was applied to the photon isolation (see Section 4.4) to remove the effect of the pile-up and underlying event. The average ambient transverse-energy density is shown in Figure 9.5 and was typically 7 GeV in the central region. Therefore, the average correction in the isolation cone with $R = 0.4$ was 3.5 GeV;
- the isolation value in the MC simulations was further corrected so that the isolation peak observed in data is correctly described. More details are given in Section 6.6.4;
- to match the in-time and out-of-time pile-up conditions in the data, the distribution of $\langle\mu\rangle$ in simulated events was reweighted to that of the data. Figure 9.6 shows the distribution of $\langle\mu\rangle$ for data, after applying a general scale factor of 1/1.09, to achieve a better agreement between data and MC for the distribution on the number of primary vertices, and Sherpa MC before and after this reweighting was applied. The reweighting factors for both Pythia or Sherpa MC simulations are very similar.

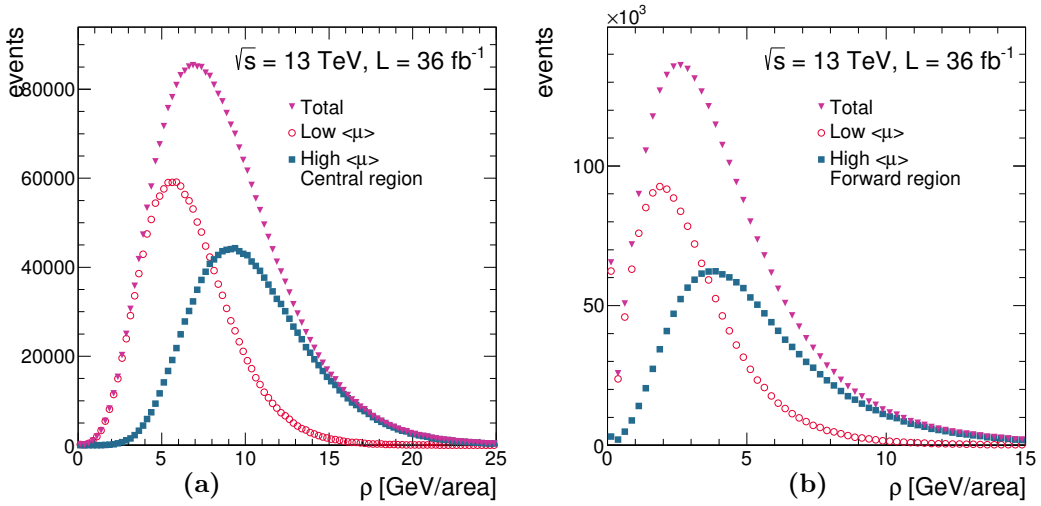


Figure 9.5: Distribution of the ambient transverse-energy density ρ in the (a) central and (b) forward regions for 2015+2016 data.

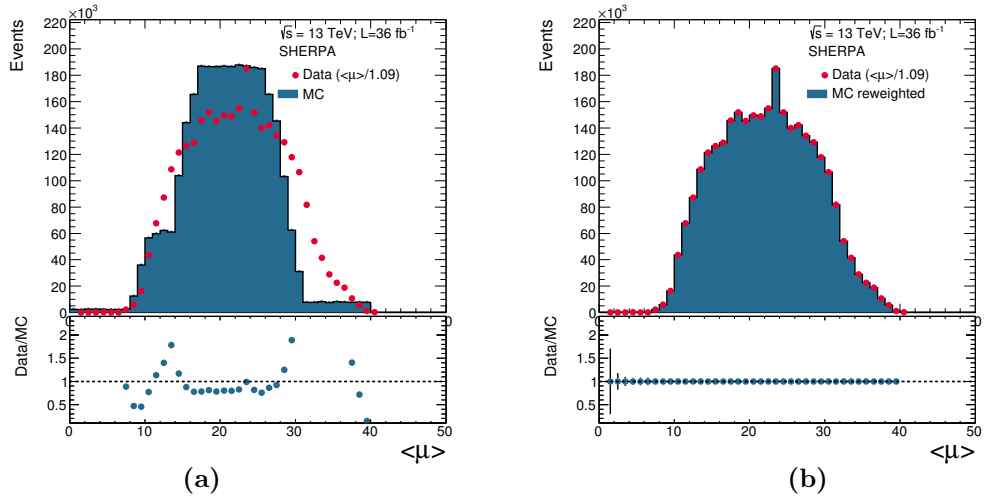


Figure 9.6: Distribution of the average number of interactions per bunch crossing for the sample of tight and isolated photons in data (dots) and SHERPA MC (histograms) (a) before and (b) after reweighting. The lower part of the figures shows the ratio between data and MC.

9.2 Background estimation and subtraction

The background-subtraction technique applied here is the same followed in the inclusive photon analysis (see Section 6.3). A comparison of the distributions in $E_{\mathrm{T}}^{\mathrm{iso}}$ for tight and non-tight photon candidates in data after the leading-photon and jets selection for this analysis was made to support the adequacy of the background control regions in the 2D-sideband method. This is shown in Figure 9.7. It was checked that, as expected, the distribution in $E_{\mathrm{T}}^{\mathrm{iso}}$ from the non-tight photon candidates in data reproduces the tail of the distribution of tight-photon candidates and that the MC simulations of signal photons exhibit a peak around $E_{\mathrm{T}}^{\mathrm{iso}} \approx 0$ GeV that reproduces the one in the data, thanks to the data-driven corrections applied to $E_{\mathrm{T}}^{\mathrm{iso}}$ in the MC. To avoid the effect of fake photons in the simulations, a geometrical matching criteria was imposed between particle and reconstruction level with $\Delta R = 0.2$.

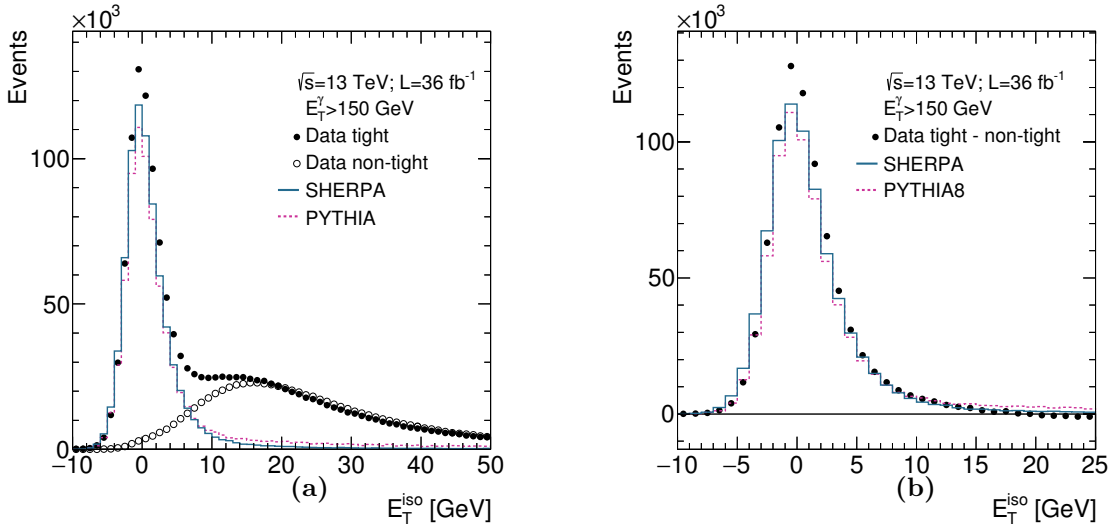


Figure 9.7: (a) The measured $E_{\mathrm{T}}^{\mathrm{iso}}$ distribution before the isolation requirement and after applying the tight identification requirement (black dots) and for those events which fail the tight identification (*non-tight*, open circles). The non-tight distribution was normalised so that the integral of the tight and non-tight distributions for $E_{\mathrm{T}}^{\mathrm{iso}} > 10$ GeV coincides. For comparison, the MC simulations of the signal from Pythia (dashed histogram) and Sherpa (solid histogram) are also included. The MC distributions are normalised to the number of data events in the tight distribution for $E_{\mathrm{T}}^{\mathrm{iso}} < 10$ GeV. (b) The measured $E_{\mathrm{T}}^{\mathrm{iso}}$ distribution before the isolation requirement and after applying the tight identification requirement and after subtracting the non-tight events (dots).

It was also checked that the shape of the isolation tail of tight-photon candidates observed in data was well described by the isolation distribution of non-tight candidates in every region of the phase space. This was studied for each bin of each observable studied and examples for $p_{\mathrm{T}}^{\mathrm{jet}}$ and $\Delta\phi^{\gamma-\mathrm{jet}}$ are shown in Figure 9.8.

The signal leakage fractions extracted from the MC simulations of Pythia and Sherpa are shown in Figures 9.9 to 9.11. The fraction ϵ_C, which represents the signal leaking into the non-tight and isolated control region, is approximately constant for all observables and around $0.02-0.04$ and very similar for Pythia and Sherpa. The fraction

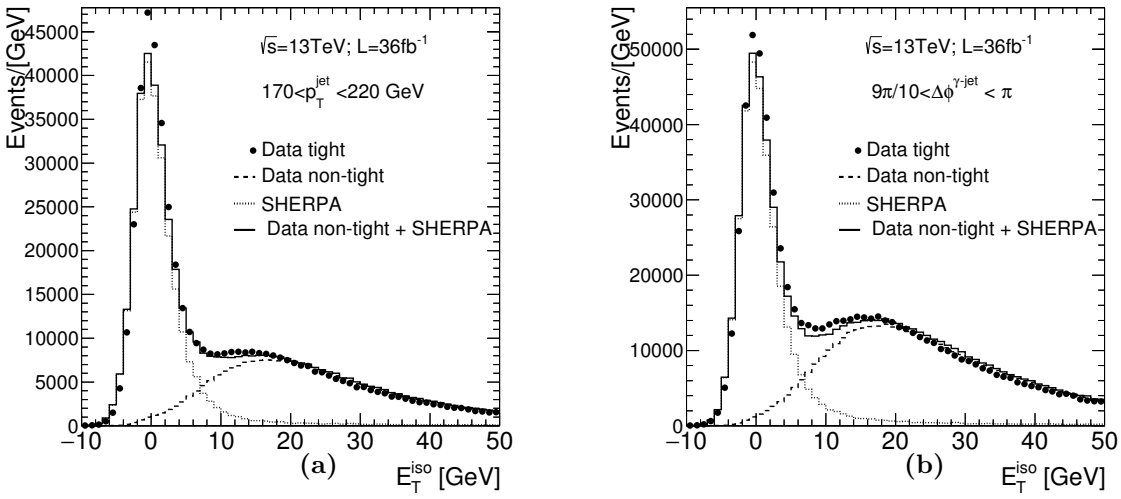


Figure 9.8: Measured $E_{\mathrm{T}}^{\mathrm{iso}}$ distribution before the isolation requirement and after applying the tight identification requirement (black dots) and for those events which fail the tight identification (non-tight, dashed histogram) for (a) $170 < p_{\mathrm{T}}^{\mathrm{jet}} < 220$ GeV and (b) $9\pi/10 < \Delta\phi^{\gamma-\mathrm{jet}} < \pi$. For comparison, the MC simulations of the signal from SHERPA (dotted histogram) are also included. The non-tight photon candidates distribution in data and the simulation were added according to a χ^2 fit (solid histogram).

ϵ_B, signal leakage into the tight and non-isolated control region, is smaller for SHERPA than for PYTHIA; this is due to the different treatment of the bremsstrahlung component in PYTHIA and SHERPA. The background region B is the one with a higher population of signal photons. The fraction ϵ_D, the signal leakage into the non-tight non-isolated control region, is very different for PYTHIA and SHERPA; this is the control region most affected by the different treatment of the bremsstrahlung component in both models.

The purity of the signal region is shown in Figures 9.12 to 9.14. The values of the purity were found to be typically $\gtrsim 95\%$, being somewhat higher in the fragmentation-enriched sample. The jet-faking-photon background was found to be negligible for high values of E_{T}^{γ}, $p_{\mathrm{T}}^{\mathrm{jet}}$, $m^{\mathrm{jet-jet}}$ and $m^{\gamma-\mathrm{jet}-\mathrm{jet}}$. The error bars account for the statistical uncertainties in data for the signal and background control regions. They were computed analytically and truncated to unity.

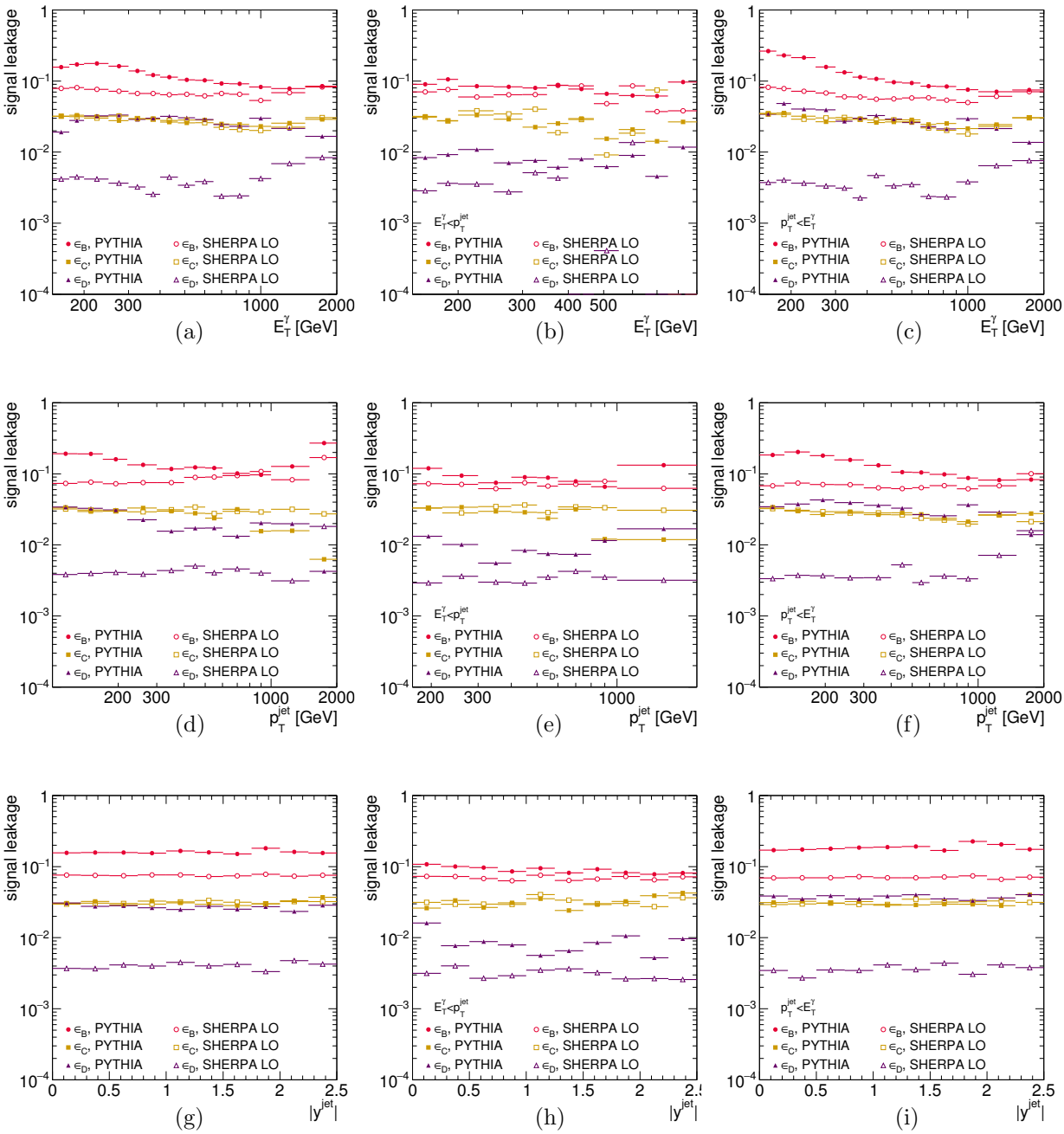


Figure 9.9: Signal leakage fractions from PYTHIA (solid markers) and SHERPA (open markers) for the B (dots), C (squares) and D (triangles) control regions as functions of E_{T}^{γ} (a,b,c), $p_{\mathrm{T}}^{\mathrm{jet}}$ (d,e,f) and $|y^{\mathrm{jet}}|$ (g,h,i) for the total (first column), fragmentation-enriched (second column) and direct-enriched (third column) samples.

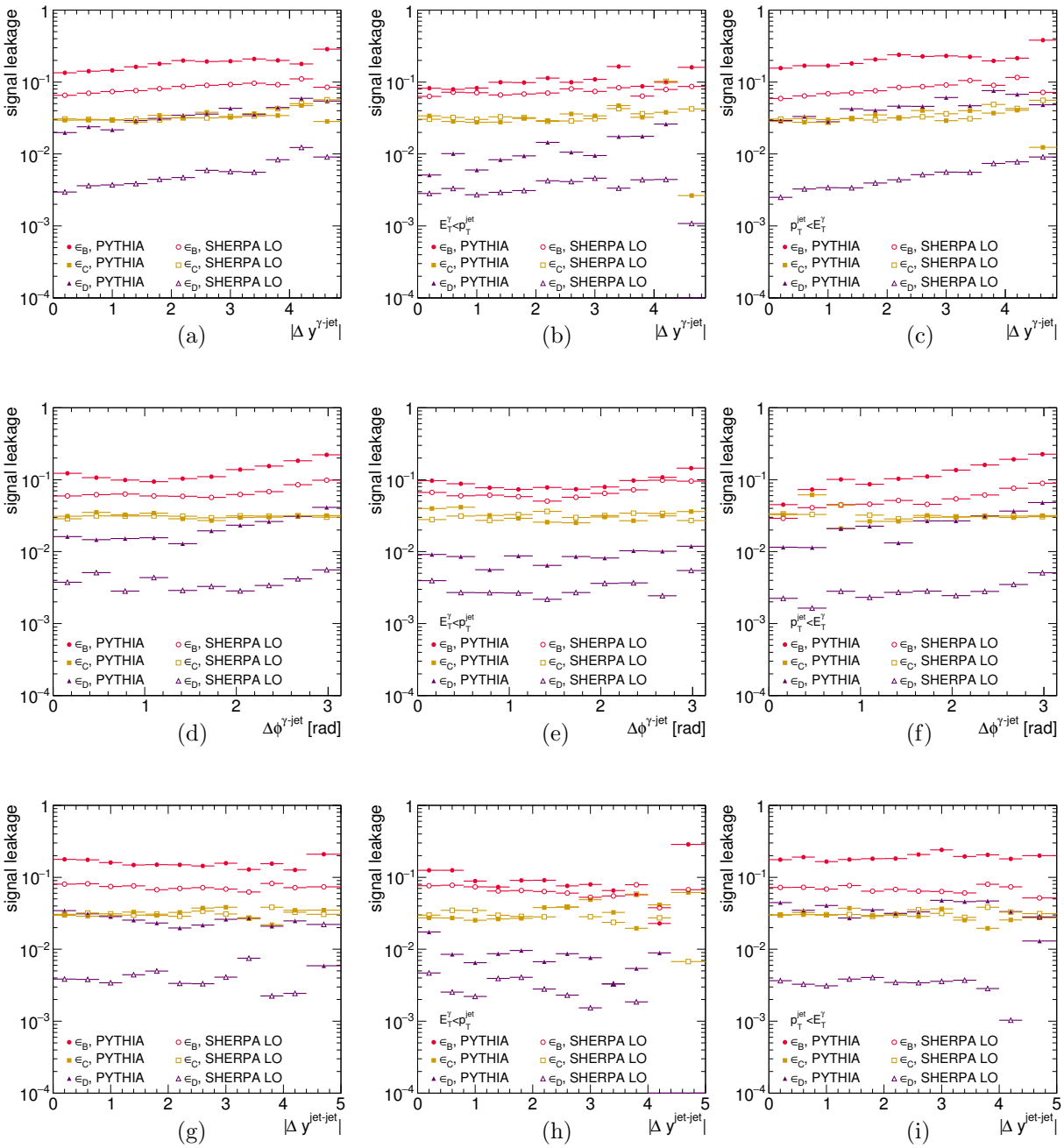


Figure 9.10: Signal leakage fractions from PYTHIA (solid markers) and SHERPA (open markers) for the B (dots), C (squares) and D (triangles) control regions as functions of $|\Delta y^{\gamma-\text{jet}}|$ (a,b,c), $\Delta\phi^{\gamma-\text{jet}}$ (d,e,f) and $|\Delta y^{\text{jet}-\text{jet}}|$ (g,h,i) for the total (first column), fragmentation-enriched (second column) and direct-enriched (third column) samples.

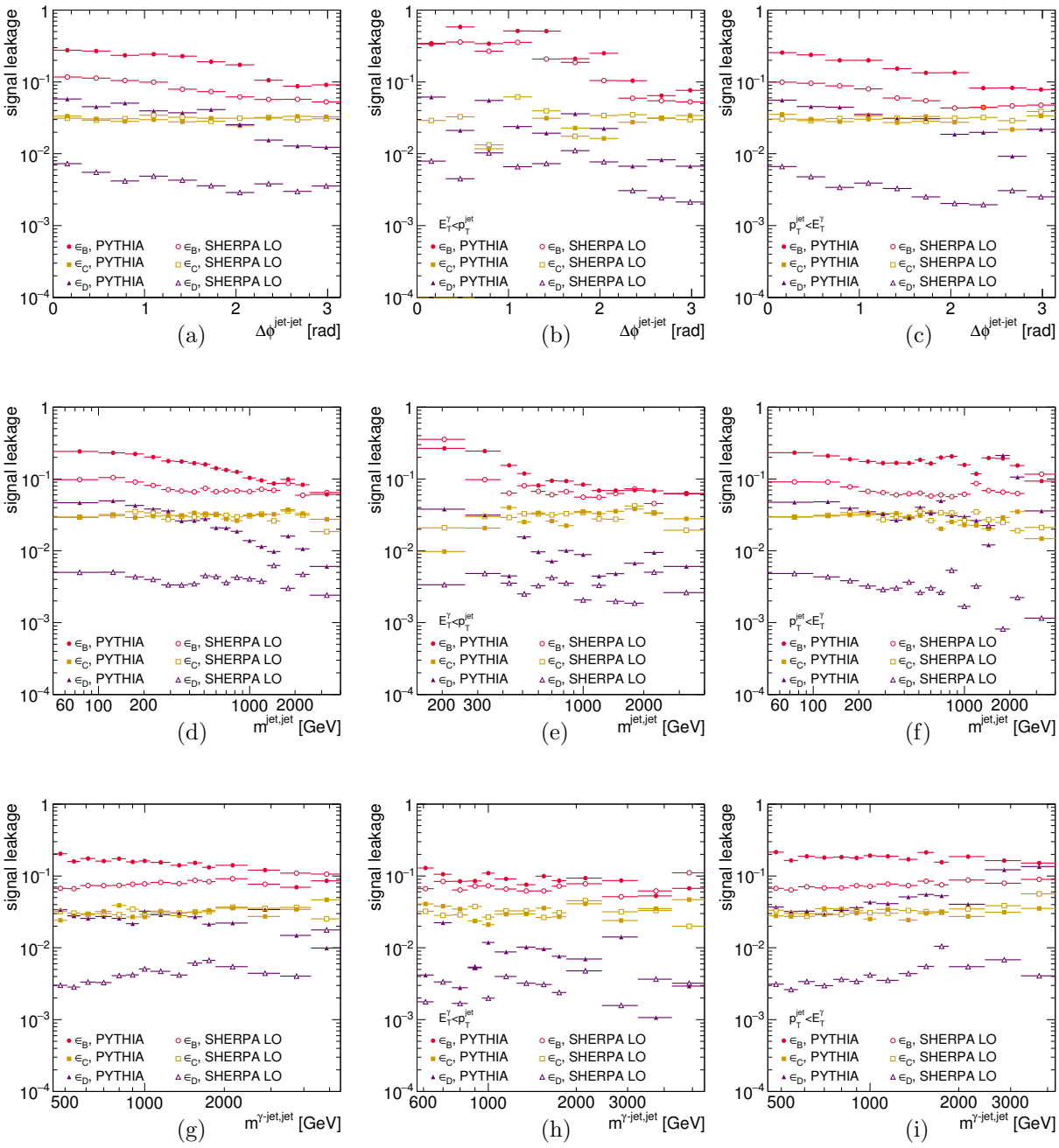


Figure 9.11: Signal leakage fractions from PYTHIA (solid markers) and SHERPA (open markers) for the B (dots), C (squares) and D (triangles) control regions as functions of $\Delta\phi^{\text{jet}-\text{jet}}$ (a,b,c), $m^{\text{jet}-\text{jet}}$ (d,e,f) and $m^{\gamma-\text{jet}-\text{jet}}$ (g,h,i) for the total (first column), fragmentation-enriched (second column) and direct-enriched (third column) samples.

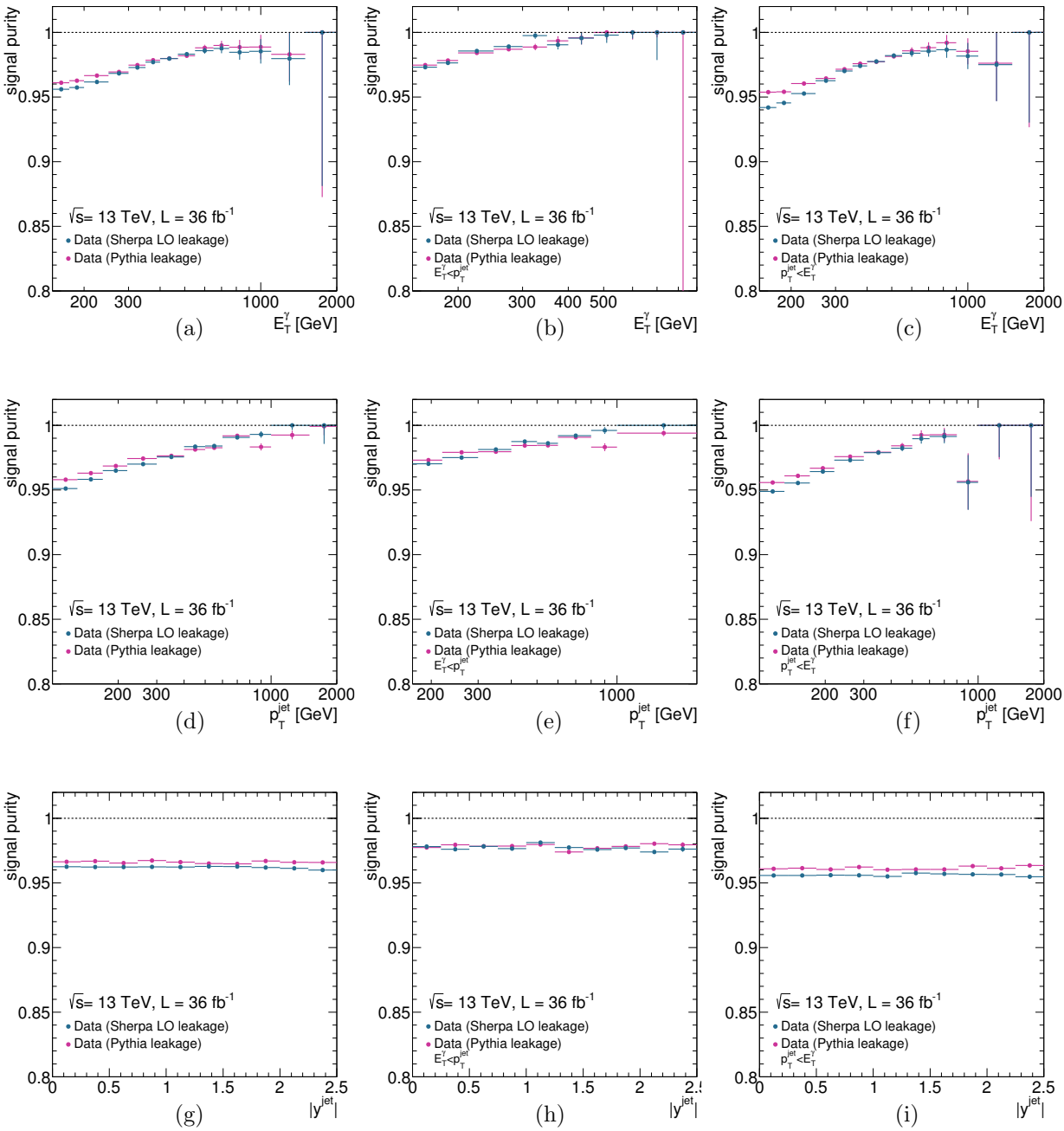


Figure 9.12: Estimated signal purities in data using signal leakage fractions from PYTHIA (pink dots) and SHERPA (blue dots) as functions of E_{T}^{γ} (a,b,c), $p_{\mathrm{T}}^{\mathrm{jet}}$ (d,e,f) and $|y^{\mathrm{jet}}|$ (g,h,i) for the total (first column), fragmentation-enriched (second column) and direct-enriched (third column) samples.

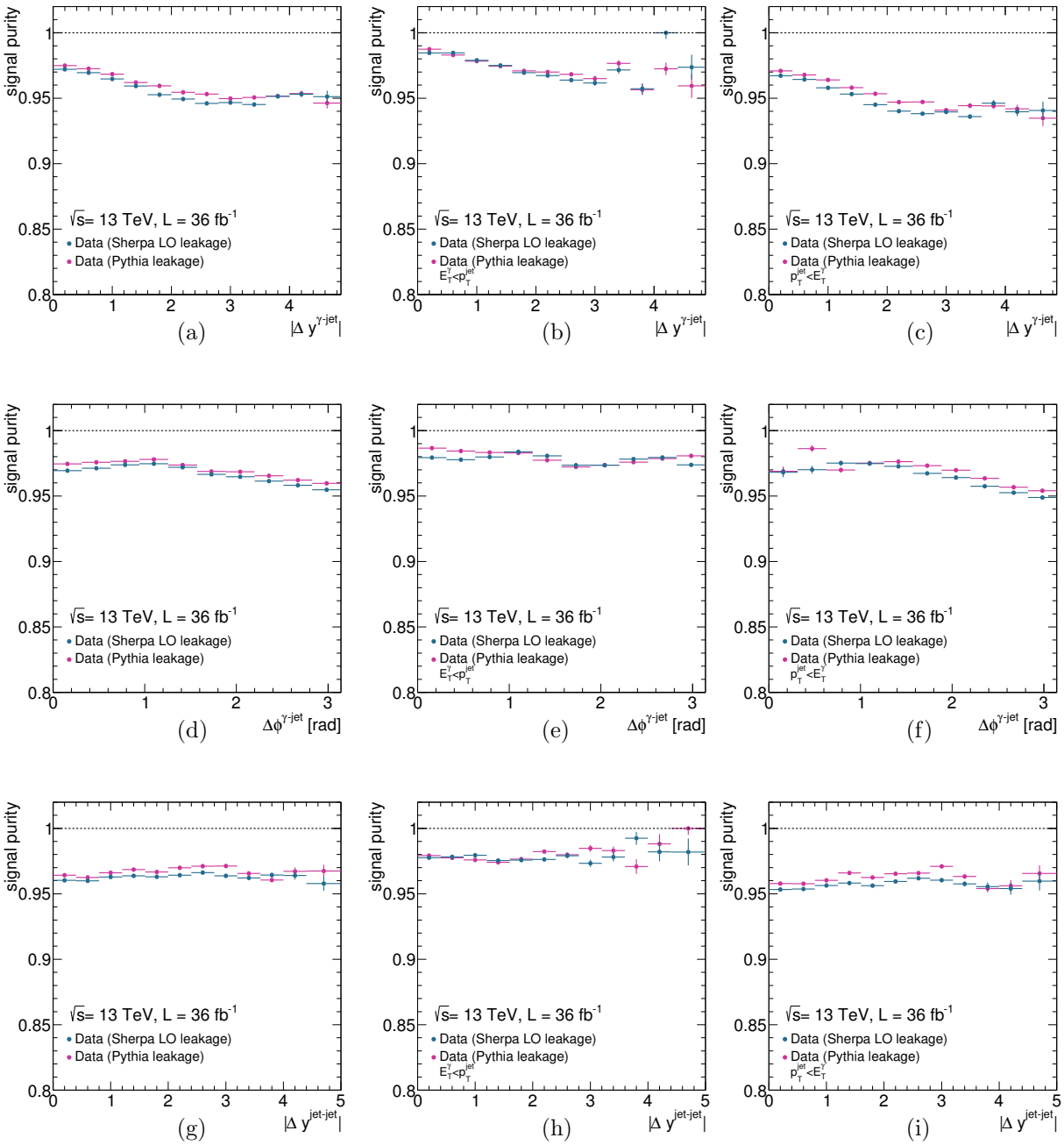


Figure 9.13: Estimated signal purities in data using signal leakage fractions from Pythia (pink dots) and Sherpa (blue dots) as functions of $|\Delta y^{\gamma-\mathrm{jet}}|$ (a,b,c), $\Delta\phi^{\gamma-\mathrm{jet}}$ (d,e,f) and $|\Delta y^{\mathrm{jet}-\mathrm{jet}}|$ (g,h,i) for the total (first column), fragmentation-enriched (second column) and direct-enriched (third column) samples.

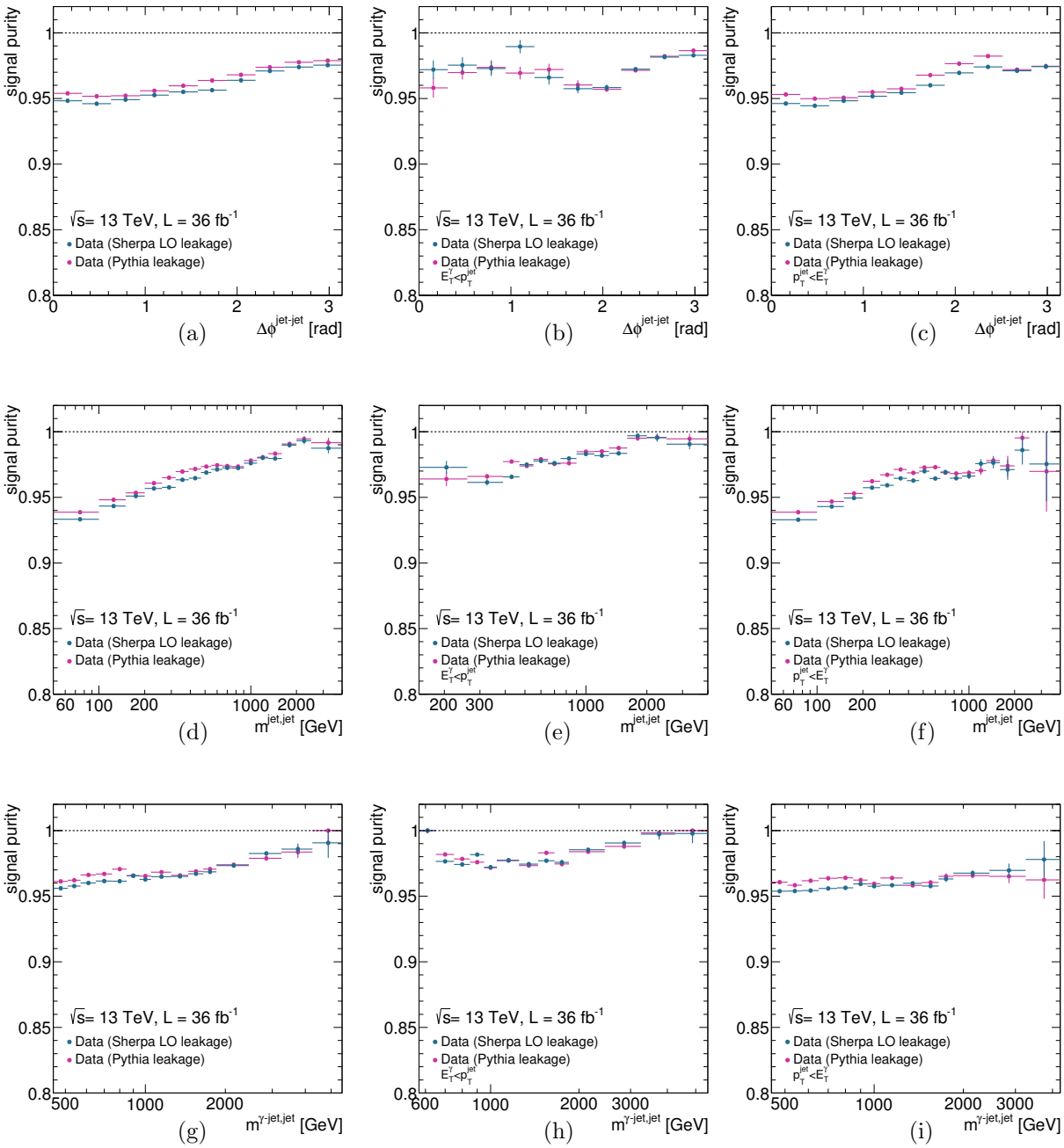


Figure 9.14: Estimated signal purities in data using signal leakage fractions from PYTHIA (pink dots) and SHERPA (blue dots) as functions of $\Delta\phi^{\mathrm{jet-jet}}$ (a,b,c), $m^{\mathrm{jet-jet}}$ (d,e,f) and $m^{\gamma-\mathrm{jet-jet}}$ (g,h,i) for the total (first column), fragmentation-enriched (second column) and direct-enriched (third column) samples.

9.2.1 Background from electrons faking photons

The background from electrons (or positrons) faking photons was estimated using the MC samples of SHERPA 2.2 for W + jets and Z + jets. The fraction of W + jets and Z + jets background as functions of the observables studied in the three samples, with truth matching to $e^{\pm}$ using $\Delta R < 0.2$, is shown in Figs. 9.15 to 9.20. The size of this background was found to be larger than in the analyses presented in Chapter 6 and 8 due to changes in the electron and photon reconstruction. The relative contribution of the electron-faking-photon background from W + jets (Z + jets) was estimated to be 0.48% (0.18%) for the total sample, 0.39% (0.16%) for the direct-enriched sample and 0.61% (0.21%) for the fragmentation-enriched sample [1]. The MC statistics was not sufficient to perform a bin-by-bin subtraction of this background and thus was not taken into account in the nominal results for the signal yield. An uncertainty of the size of the estimated background was included instead.

[1] The numbers were estimated for the $|y^{\text{jet}}|$ distribution for which the electron background is approximately constant.

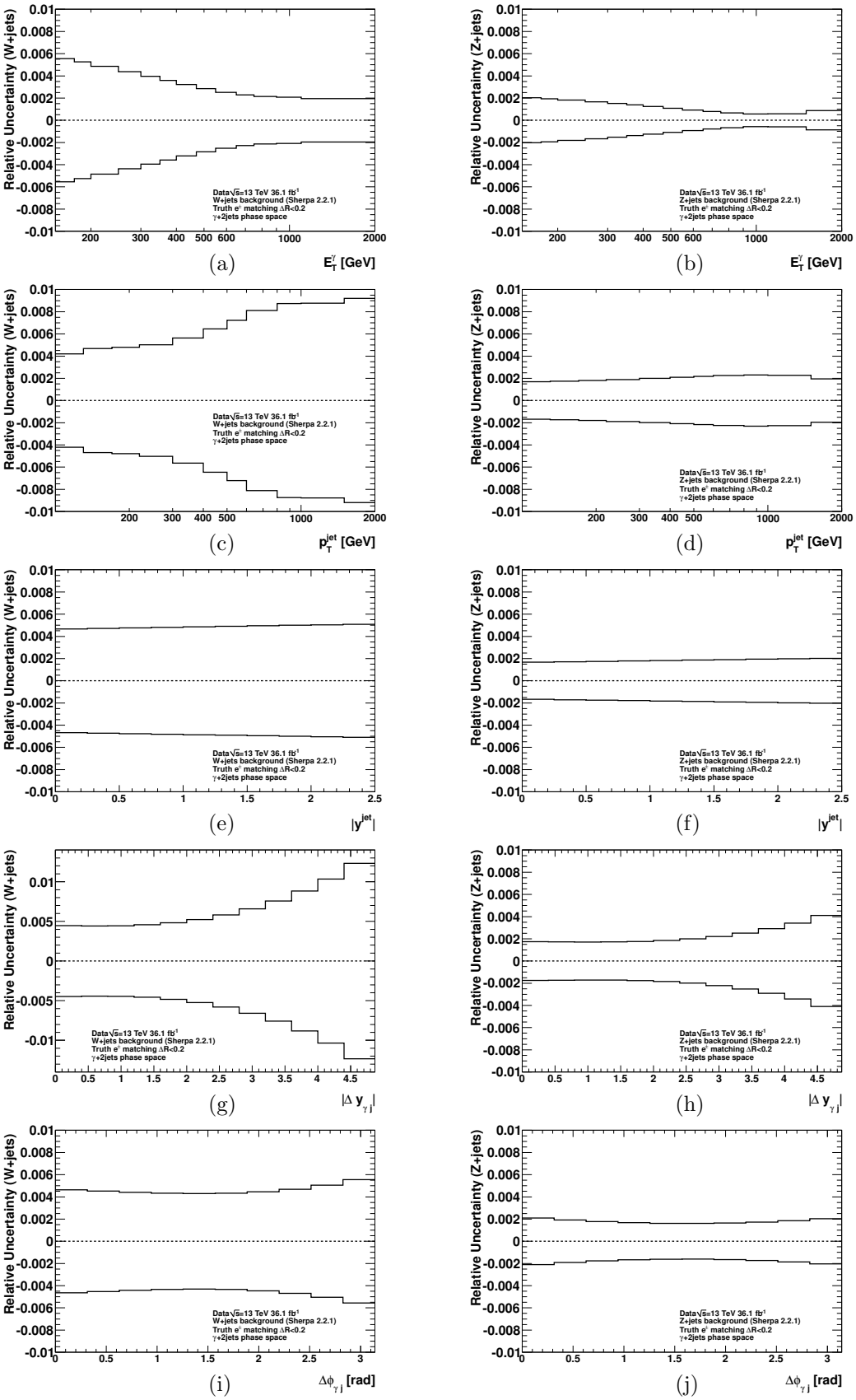


Figure 9.15: Fraction of W+jets (a,c,e,g,i) and Z+jets (b,d,f,h,j) background as a function of different observables for the total sample. See text for details.

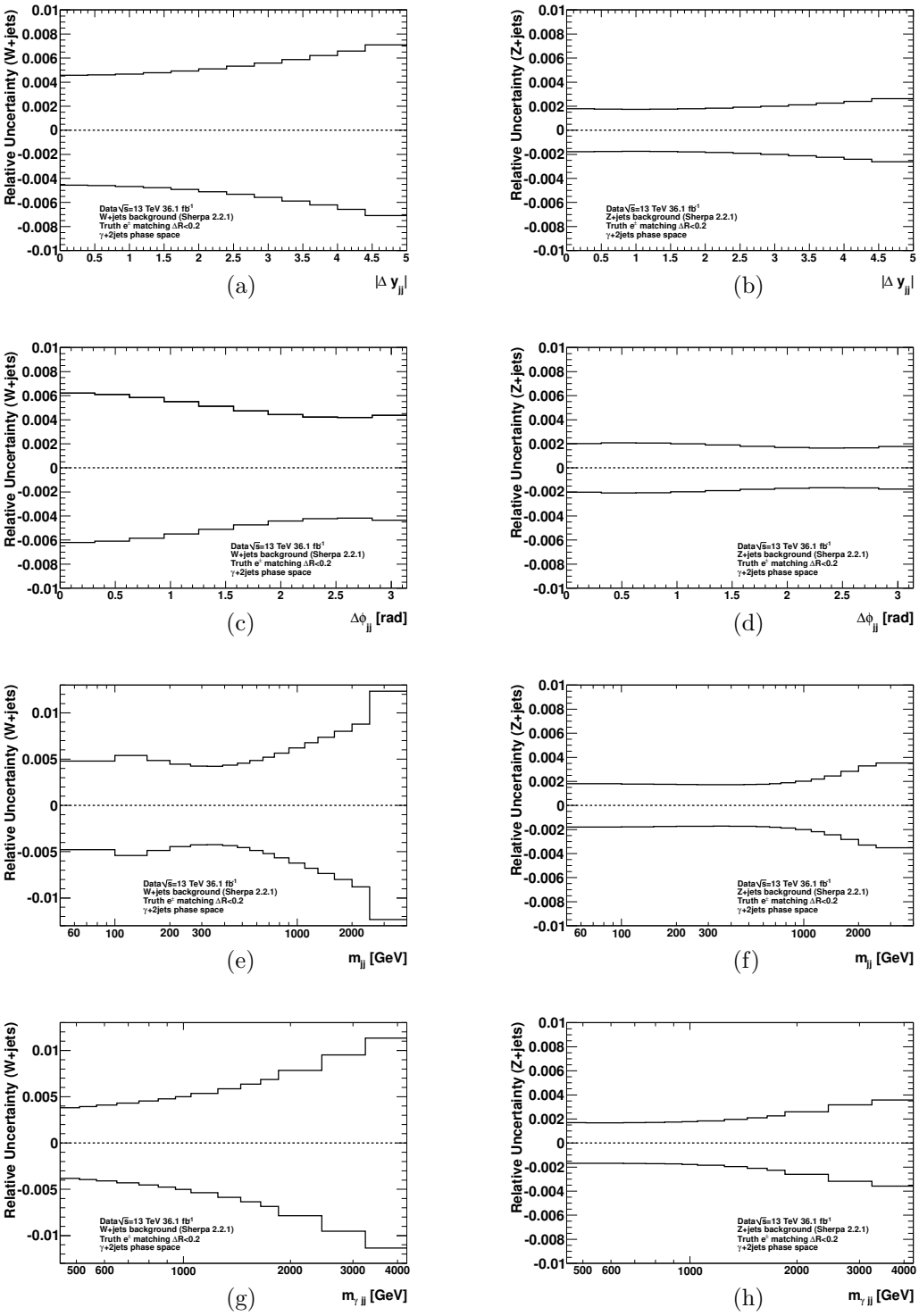


Figure 9.16: Fraction of $W+$jets (a,c,e,g) and $Z+$jets (b,d,f,h) background as a function of different observables for the total sample. See text for details.

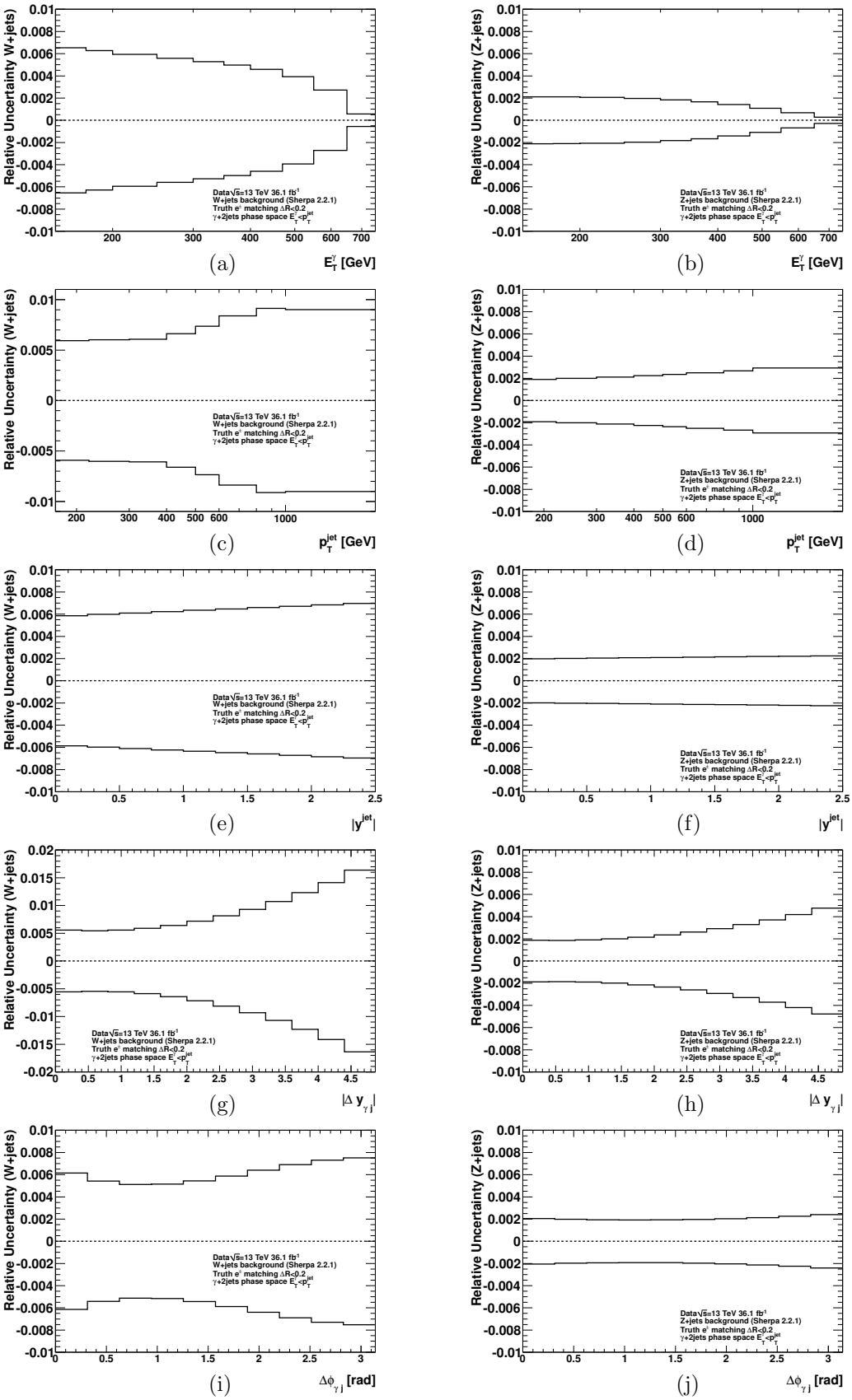


Figure 9.17: Fraction of W+jets (a,c,e,g,i) and Z+jets (b,d,f,h,j) background as a function of different observables for the fragmentation-enriched sample. See text for details.

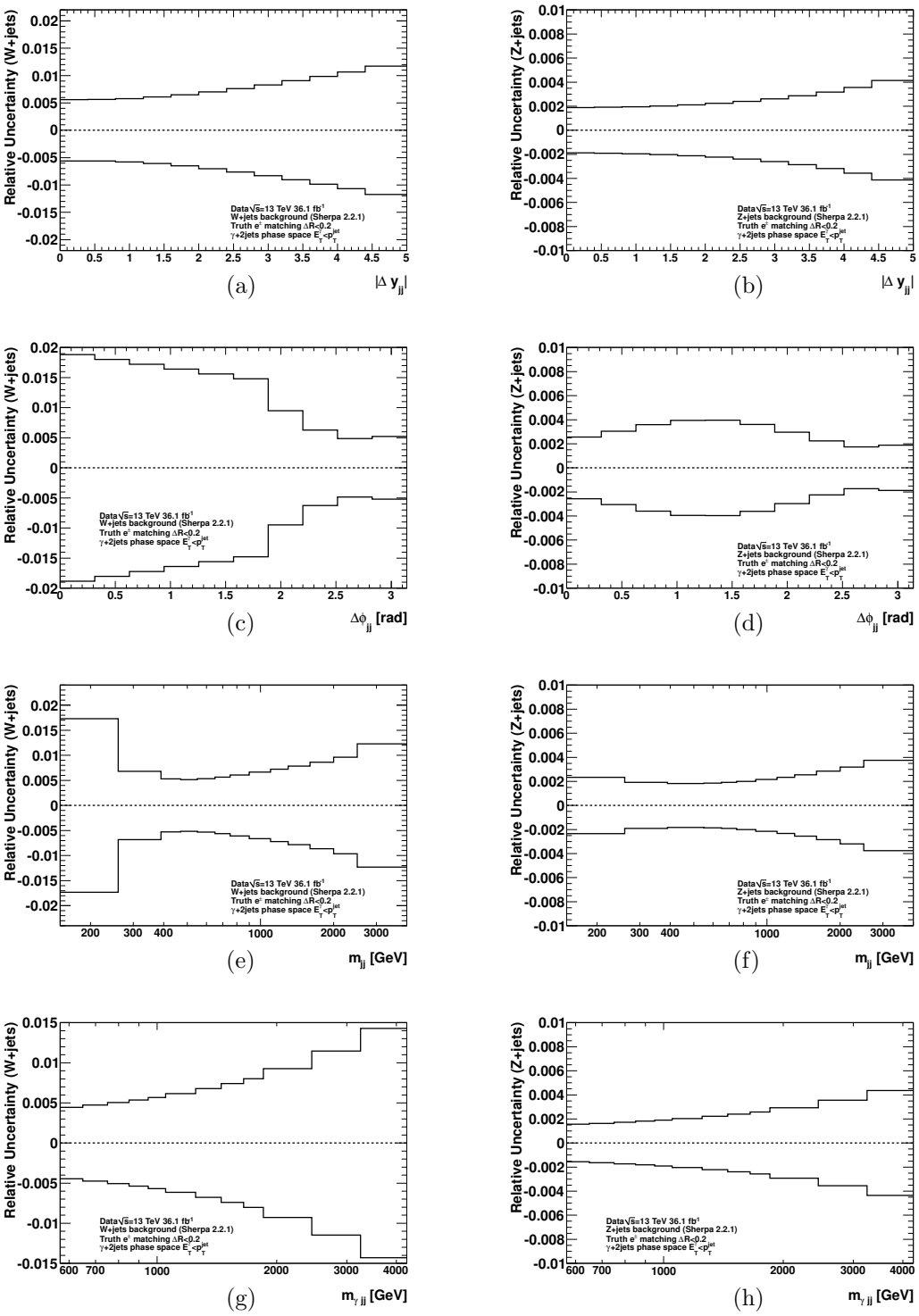


Figure 9.18: Fraction of $W+$jets (a,c,e,g) and $Z+$jets (b,d,f,h) background as a function of different observables for the fragmentation-enriched sample. See text for details.

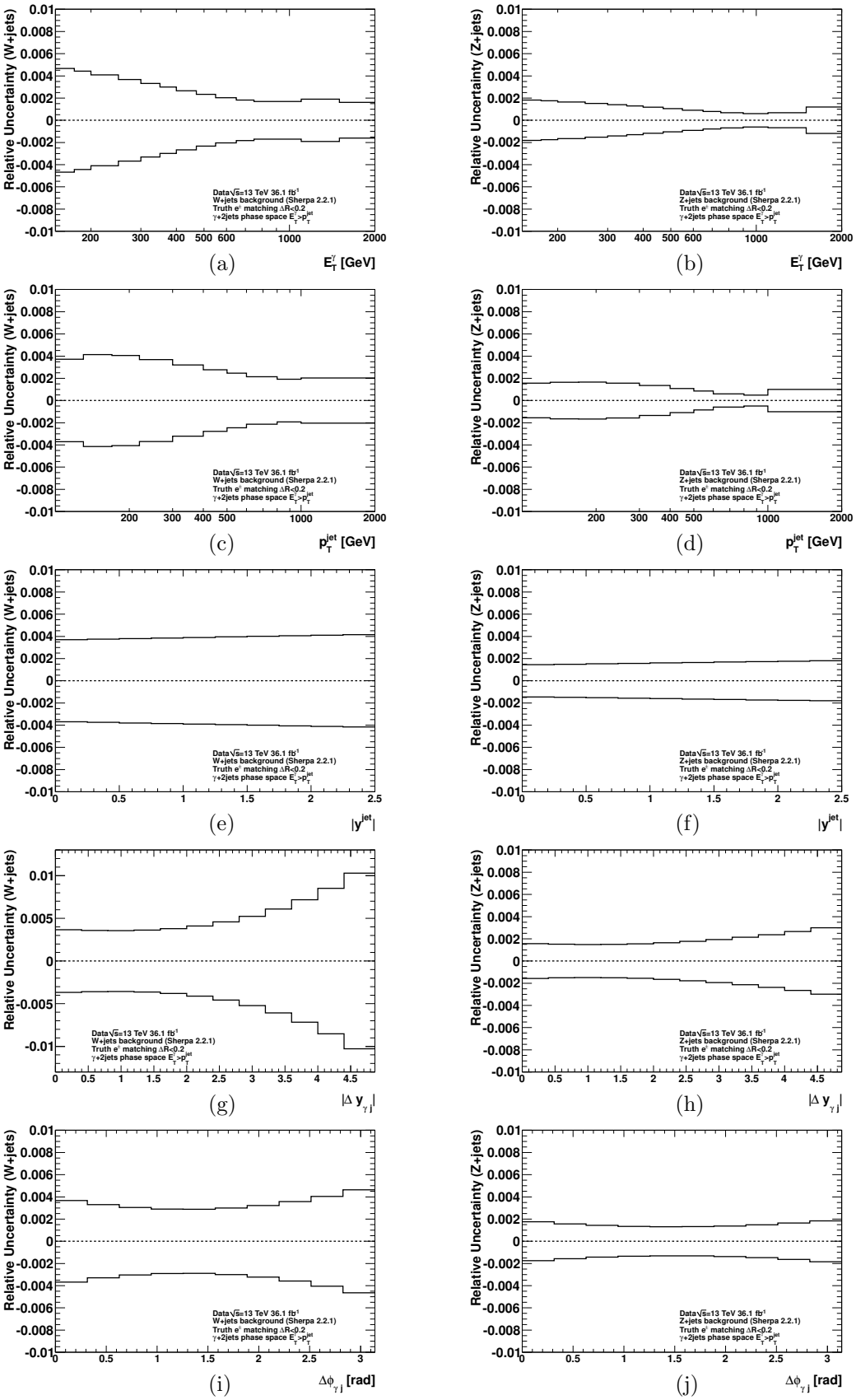


Figure 9.19: Fraction of W+jets (a,c,e,g,i) and Z+jets (b,d,f,h,j) background as a function of different observables for the direct-enriched sample. See text for details.

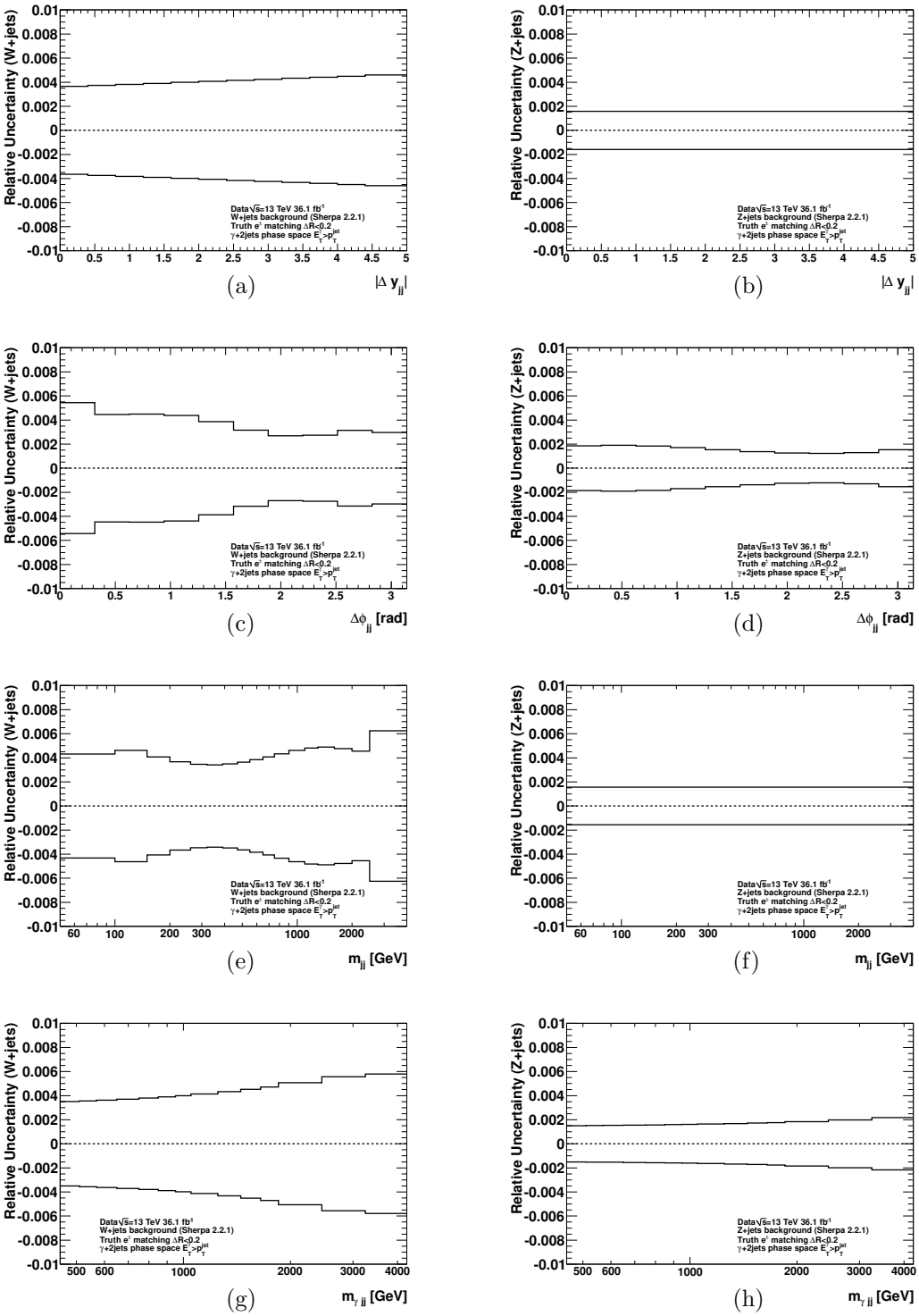


Figure 9.20: Fraction of $W+$jets (a,c,e,g) and $Z+$jets (b,d,f,h) background as a function of different observables for the direct-enriched sample. See text for details.

9.3 Control plots

The estimated signal yields using the signal leakage fractions from SHERPA are shown in Figures 9.21 to 9.23 and compared to the predictions of PYTHIA and SHERPA.

Figure 9.21 (a,b,c) shows the measured E_{T}^{γ} distribution for the three samples. Both PYTHIA and SHERPA provide an adequate description of the data in the total and fragmentation-enriched samples, except in the tail of the distributions. SHERPA also provides a good description of the data in the direct-enriched sample, while PYTHIA fails. The E_{T}^{γ} spectrum for the direct-enriched sample is harder than that in the fragmentation-enriched sample.

Figure 9.21 (d,e,f) shows the measured $p_{\mathrm{T}}^{\mathrm{jet}}$ distribution for the three samples. PYTHIA fails to describe this distribution, whereas SHERPA gives a good description of the data in the full measured range. The $p_{\mathrm{T}}^{\mathrm{jet}}$ distribution in the fragmentation-enriched sample is harder than in the direct-enriched sample.

Figure 9.21 (g,h,i) shows the measured $|y^{\mathrm{jet}}|$ distribution for the three samples. Both PYTHIA and SHERPA provide an adequate description of the data. The shape of these distribution are similar for $|y^{\mathrm{jet}}| < 1$, but for $1 < |y^{\mathrm{jet}}| < 2.5$, the spectrum of the direct-enriched sample is harder.

The $|\Delta y^{\gamma-\mathrm{jet}}|$ and $\Delta\phi^{\gamma-\mathrm{jet}}$ measured distributions are shown in Figures 9.22 (a,b,c) and 9.22 (d,e,f), respectively. SHERPA provides a good description of the data, except at high $|\Delta y^{\gamma-\mathrm{jet}}|$, whereas PYTHIA fails to describe the distributions. The $|\Delta y^{\gamma-\mathrm{jet}}|$ distributions have similar shape in the fragmentation- or direct-enriched samples. The $\Delta\phi^{\gamma-\mathrm{jet}}$ distribution for the direct-enriched sample peaks towards higher $\Delta\phi^{\gamma-\mathrm{jet}}$ values than the distribution for the fragmentation-enriched sample.

The $|\Delta y^{\mathrm{jet}-\mathrm{jet}}|$ and $\Delta\phi^{\mathrm{jet}-\mathrm{jet}}$ measured distributions are shown in Figures 9.22 (g,h,i) and 9.23 (a,b,c), respectively. SHERPA provides a good description of the data, except at high $|\Delta y^{\mathrm{jet}-\mathrm{jet}}|$, whereas PYTHIA fails to describe the distributions. The $|\Delta y^{\mathrm{jet}-\mathrm{jet}}|$ distributions have similar shape in the fragmentation- or direct-enriched samples. The $\Delta\phi^{\mathrm{jet}-\mathrm{jet}}$ distributions are very different for the fragmentation- or the direct-enriched samples.

The $m^{\mathrm{jet}-\mathrm{jet}}$ and $m^{\gamma-\mathrm{jet}-\mathrm{jet}}$ measured distributions are shown in Figures 9.23 (d,e,f) and 9.23 (g,h,i), respectively. SHERPA provides a good description of the data, except in the tail of the distributions, whereas PYTHIA fails. The $m^{\gamma-\mathrm{jet}-\mathrm{jet}}$ distributions have similar shape in the fragmentation- or direct-enriched samples. The $m^{\mathrm{jet}-\mathrm{jet}}$ distributions are very different for the fragmentation- or the direct-enriched samples.

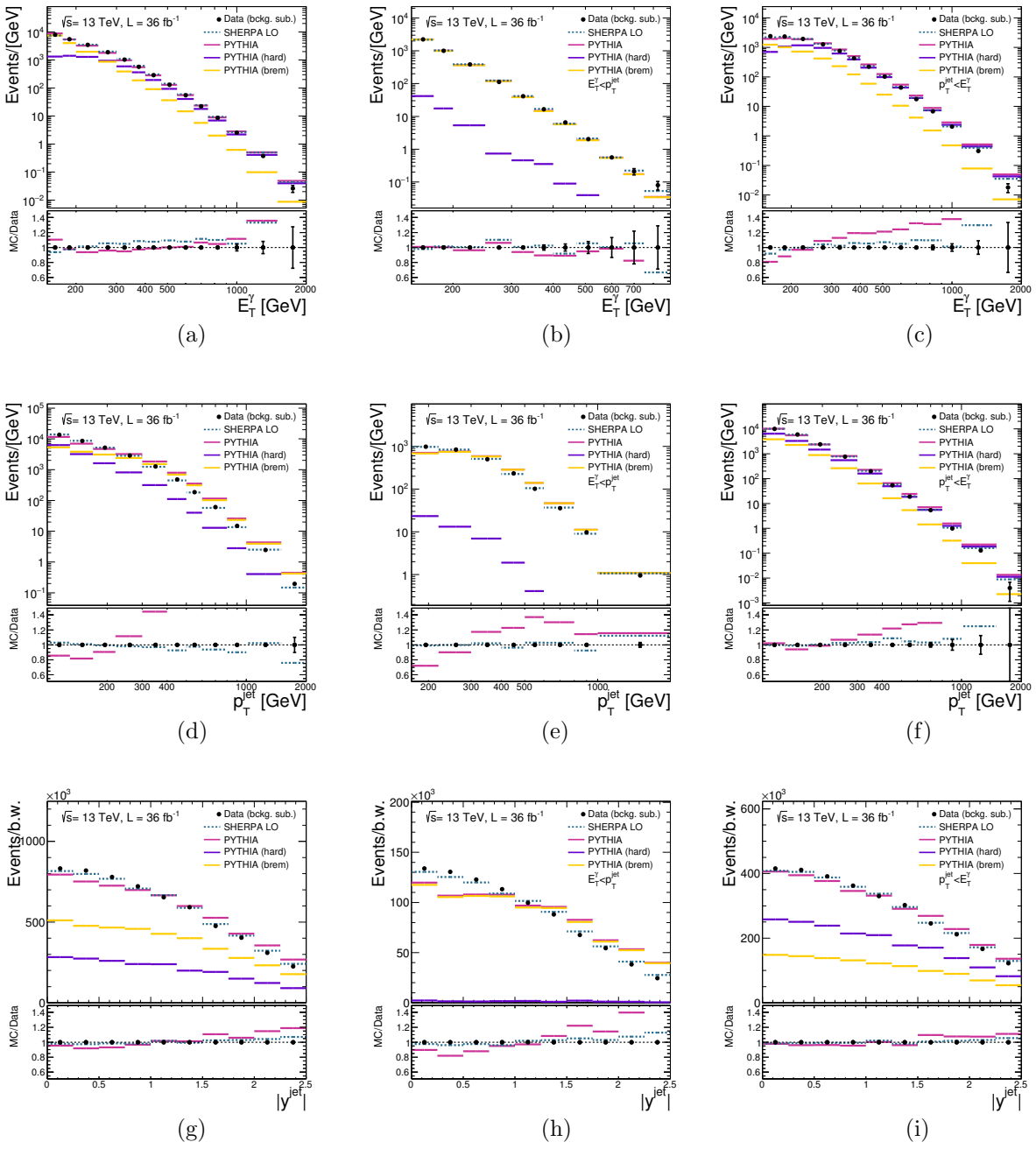


Figure 9.21: The measured E_{T}^{γ} (a,b,c), $p_{\mathrm{T}}^{\mathrm{jet}}$ (d,e,f) and $|y^{\mathrm{jet}}|$ (g,h,i) distributions divided by the bin width (dots) for the total (first column), fragmentation-enriched (second column) and direct-enriched (third column) samples. For comparison, the MC simulations of the signal from Pythia (magenta histograms), Pythia hard (blue histograms), Pythia bremsstrahlung (orange histograms) and Sherpa (dashed histograms) are also included. The MC distributions are normalised to the data. The lower part of the figure shows the ratio of the MC and data distributions.

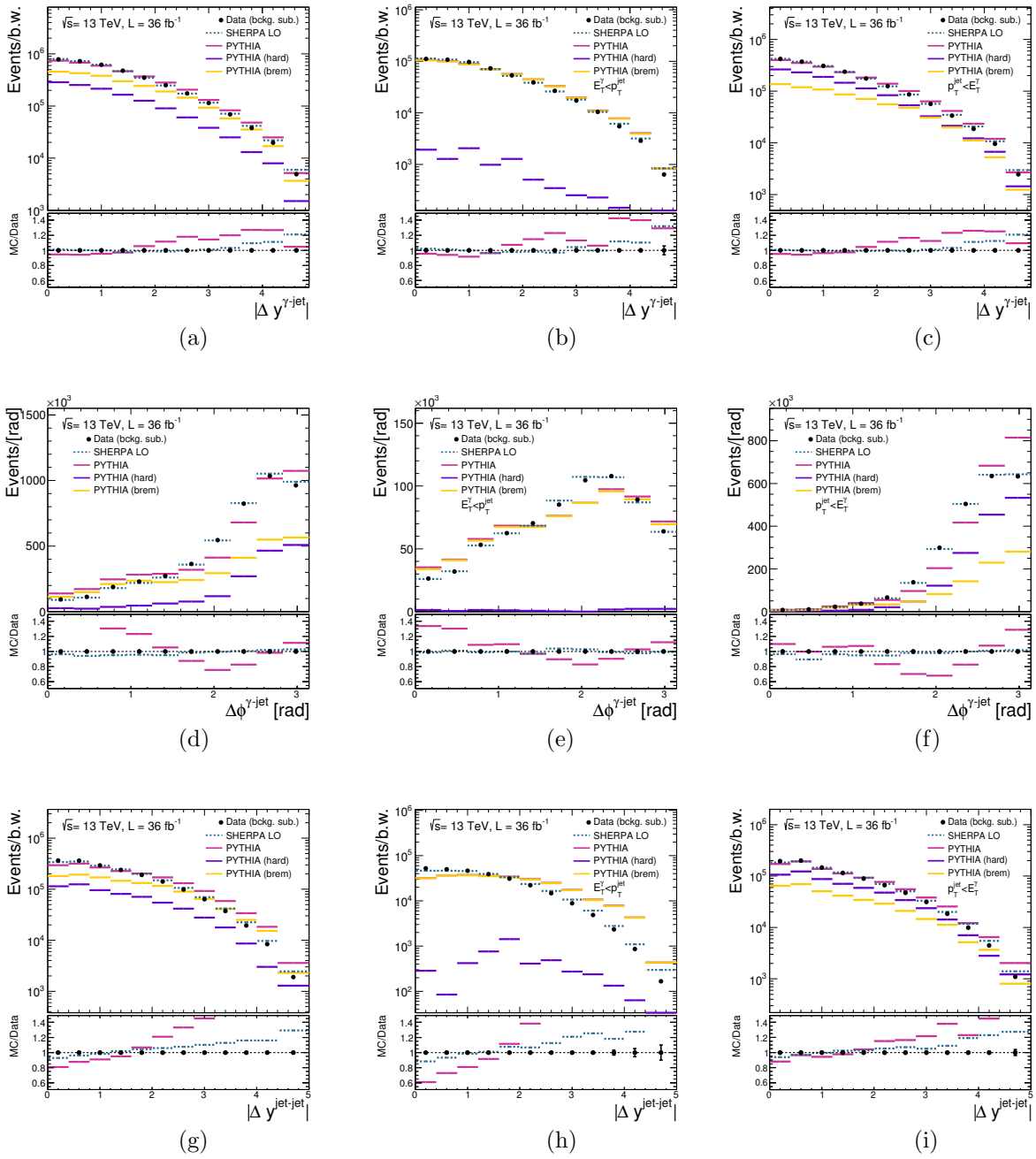


Figure 9.22: The measured $|\Delta y^{\gamma-\text{jet}}|$ (a,b,c), $\Delta\phi^{\gamma-\text{jet}}$ (d,e,f), $|\Delta y^{\text{jet}-\text{jet}}|$ (g,h,i) distributions divided by the bin width (dots) for the total (first column), fragmentation-enriched (second column) and direct-enriched (third column) samples. For comparison, the MC simulations of the signal from PYTHIA (magenta histograms), PYTHIA hard (blue histograms), PYTHIA bremsstrahlung (orange histograms) and SHERPA (dashed histograms) are also included. The MC distributions are normalised to the data. The lower part of the figure shows the ratio of the MC and data distributions.

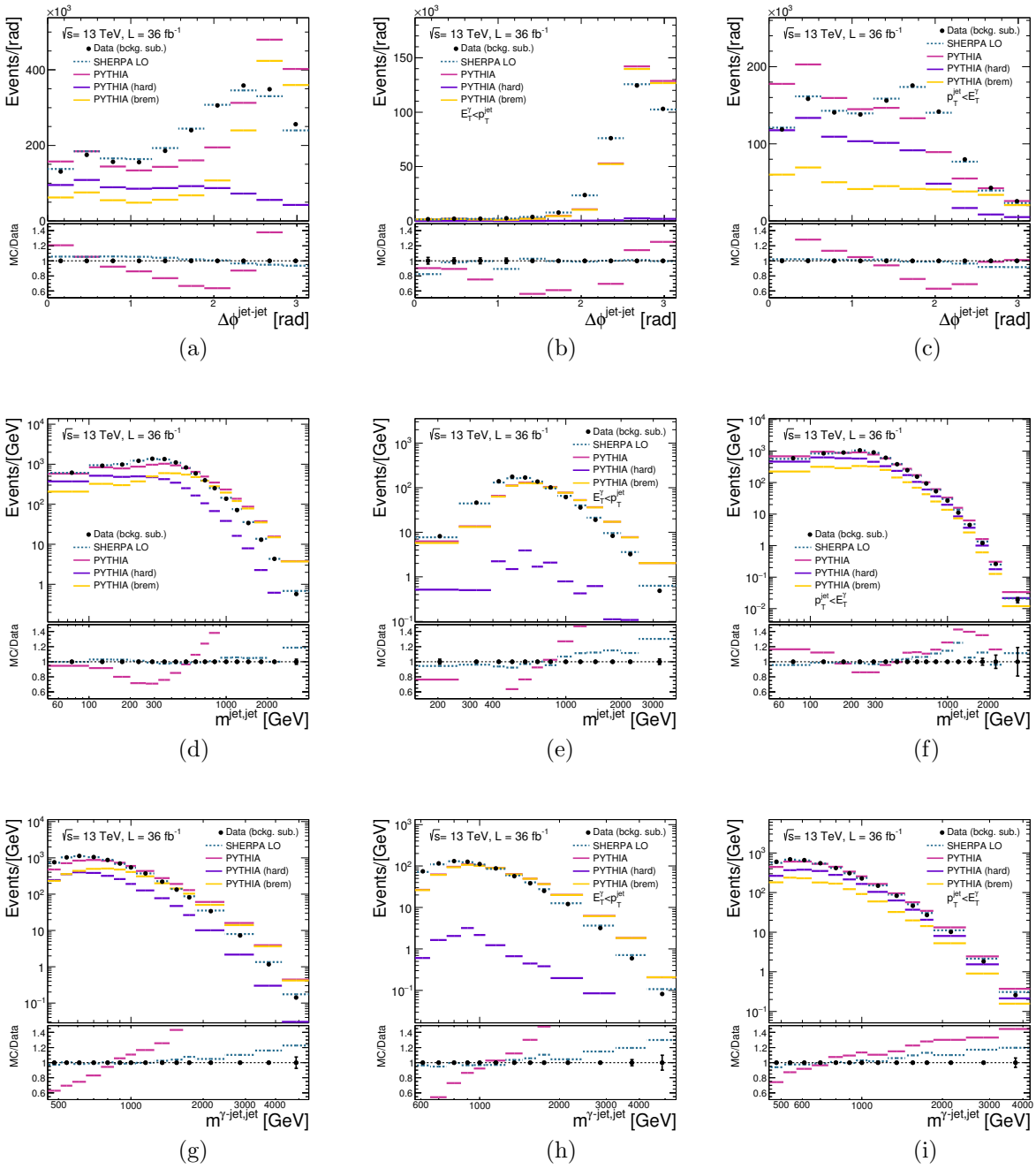


Figure 9.23: The measured $\Delta\phi^{\text{jet}-\text{jet}}$ (a,b,c), $m^{\text{jet}-\text{jet}}$ (d,e,f), $m^{\gamma-\text{jet}-\text{jet}}$ (g,h,i) distributions divided by the bin width (dots) for the total (first column), fragmentation-enriched (second column) and direct-enriched (third column) samples. For comparison, the MC simulations of the signal from PYTHIA (magenta histograms), PYTHIA hard (blue histograms), PYTHIA bremsstrahlung (orange histograms) and SHERPA (dashed histograms) are also included. The MC distributions are normalised to the data. The lower part of the figure shows the ratio of the MC and data distributions.

9.4 Unfolding

The measurements were corrected for detector resolution and inefficiencies through the unfolding. The quality of the reconstruction and the efficiency and purity of the selection using the MC simulations was studied. Since the values of the reconstruction efficiency can be lower than 60% (see Section 9.4.2), a Bayesian unfolding method was used for the nominal results in this analysis, as described in Section 6.5.

9.4.1 Fiducial phase space

The particle-level photon isolation was built summing the transverse energy of all stable particles, except for muons and neutrinos, in a cone of size $\Delta R = 0.4$ around the photon direction after the contribution from the UE is subtracted through the jet-area method. As presented in Section 8.4.1, the isolation requirement at particle level was chosen so that only a small extrapolation from the reconstruction to the particle level was necessary. The same procedure as in Section 8.4.1 was followed. The same requirement on $E_{\mathrm{T}}^{\mathrm{iso}}$ as in the photon plus jet analysis, $4.2 \cdot 10^{-3} \cdot E_{\mathrm{T}}^{\gamma} + 10$ GeV, was imposed at particle level. The differences in phase-space selection between both analyses did not alter the value of the particle-level isolation that corresponds to the one at reconstruction level. Figure 9.24 summarizes the particle-level isolation requirement which corresponds to the reconstruction-level one as a function of E_{T}^{γ}. A χ^2 linear fit to the results shown in Figure 9.24 gives 9.70 ± 0.36 (9.73 ± 0.86) GeV for Pythia (Sherpa) for the intercept and 0.0044 ± 0.0012 (0.0050 ± 0.0012) for the slope.

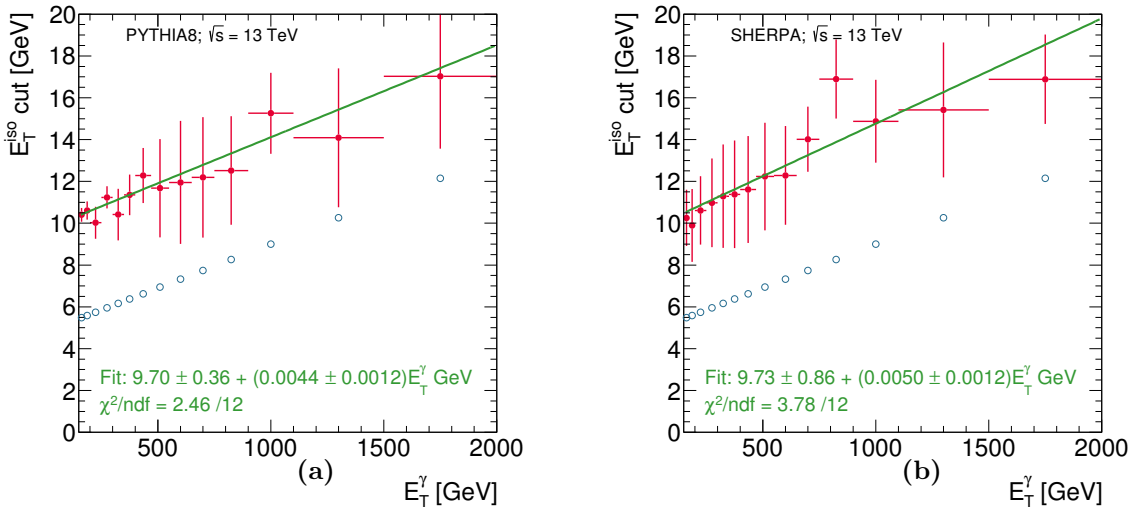


Figure 9.24: Summary of the values obtained for the requirement at particle level as a function of E_{T}^{γ} for (a) Pythia and (b) Sherpa (dots). The open circles represent the E_{T}^{γ}-dependent requirement used at reco level evaluated at the center of each bin. The solid line is the result of a straight-line fit to the values obtained for the requirement at particle level.

9.4.2 Selection purity and efficiency

The selection efficiency and purity, as defined in Section 6.5, were evaluated using the MC samples of PYTHIA and SHERPA. The bin-to-bin selection efficiency is typically $\gtrsim 60\%$ (there are regions where it can be $\approx 40\%$ such as at low values of $m^{\text{jet}-\text{jet}}$ and $m^{\gamma-\text{jet}-\text{jet}}$) and is similar for PYTHIA and SHERPA (see Figures 9.25 to 9.27). The presence of jet requirements lowers the value of the selection efficiency making the use of the bin-by-bin unfolding questionable and thus a Bayesian unfolding was used for the nominal results. The bin-to-bin selection purity is shown in Figures 9.28 to 9.30 and lies typically between 60–80% and is similar for PYTHIA and SHERPA.

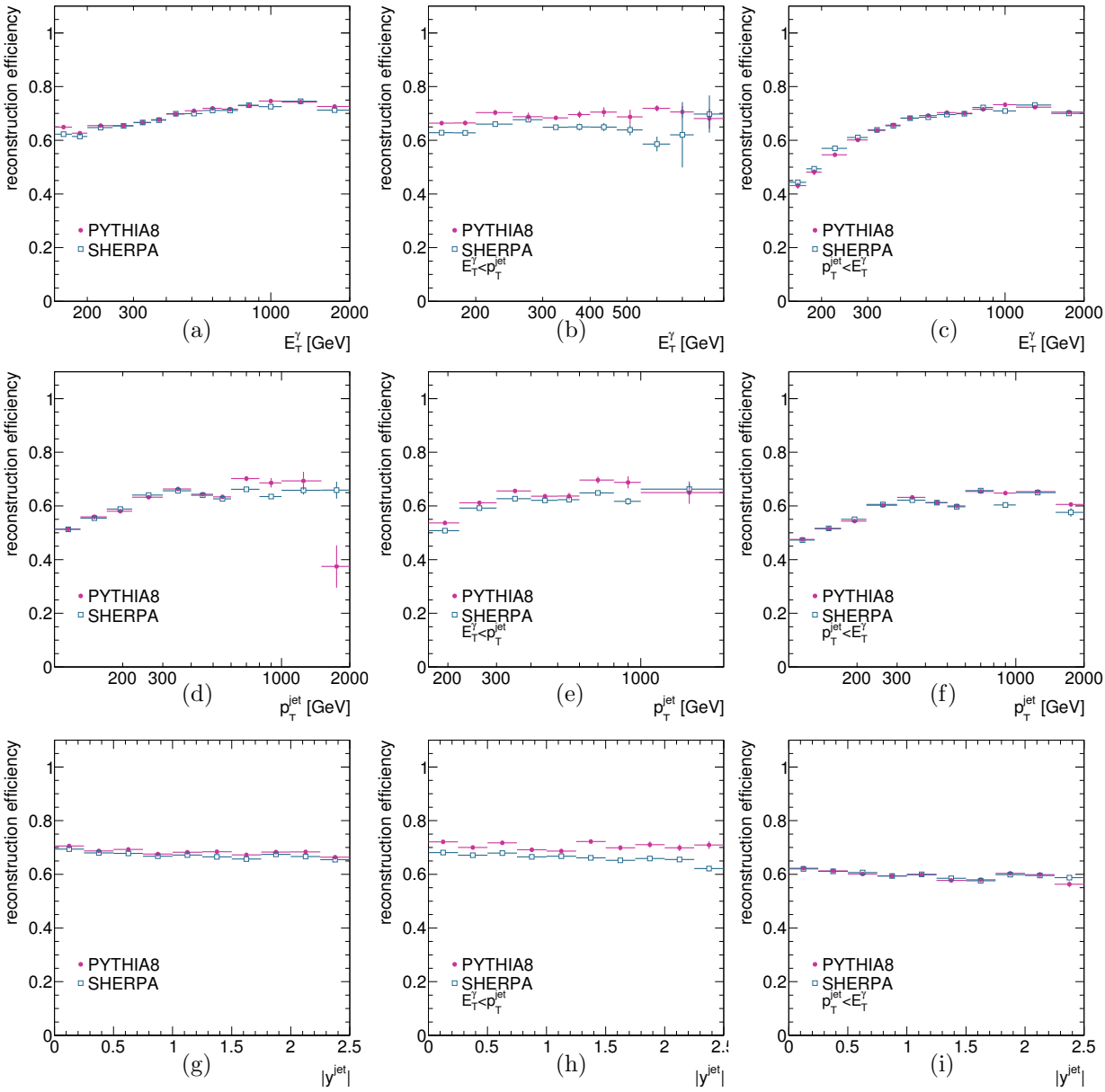


Figure 9.25: Selection efficiencies from PYTHIA (dots) and SHERPA (squares) as functions of E_{T}^{γ} (a,b,c), $p_{\text{T}}^{\text{jet}}$ (d,e,f) and $|y^{\text{jet}}|$ (g,h,i) for the total (first column), fragmentation-enriched (second column) and direct-enriched (third column) samples.

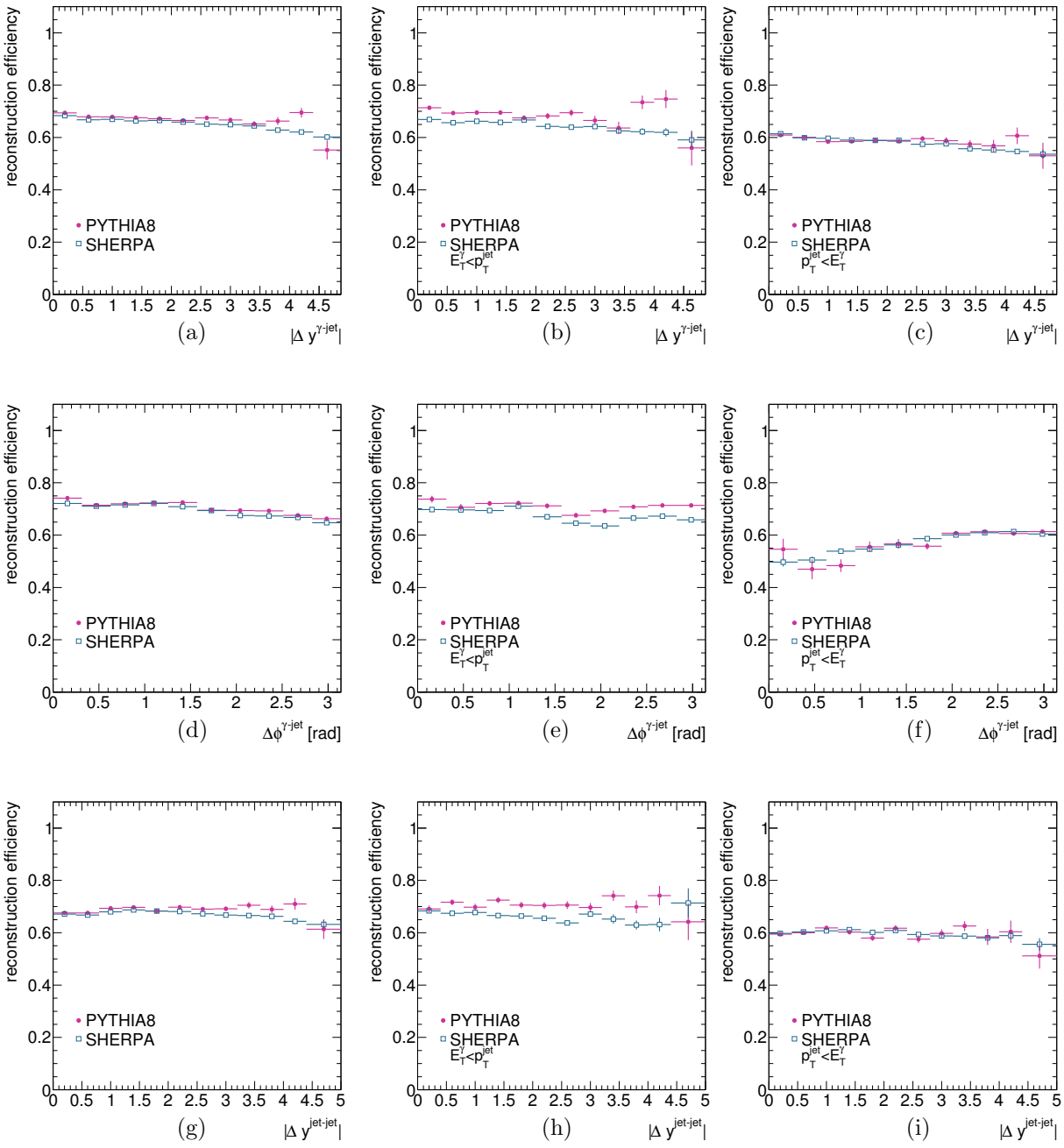


Figure 9.26: Selection efficiencies from PYTHIA (dots) and SHERPA (squares) as functions of $|\Delta y^{\gamma-\text{jet}}|$ (a,b,c), $\Delta\phi^{\gamma-\text{jet}}$ (d,e,f) and $|\Delta y^{\text{jet}-\text{jet}}|$ (g,h,i) for the total (first column), fragmentation-enriched (second column) and direct-enriched (third column) samples.

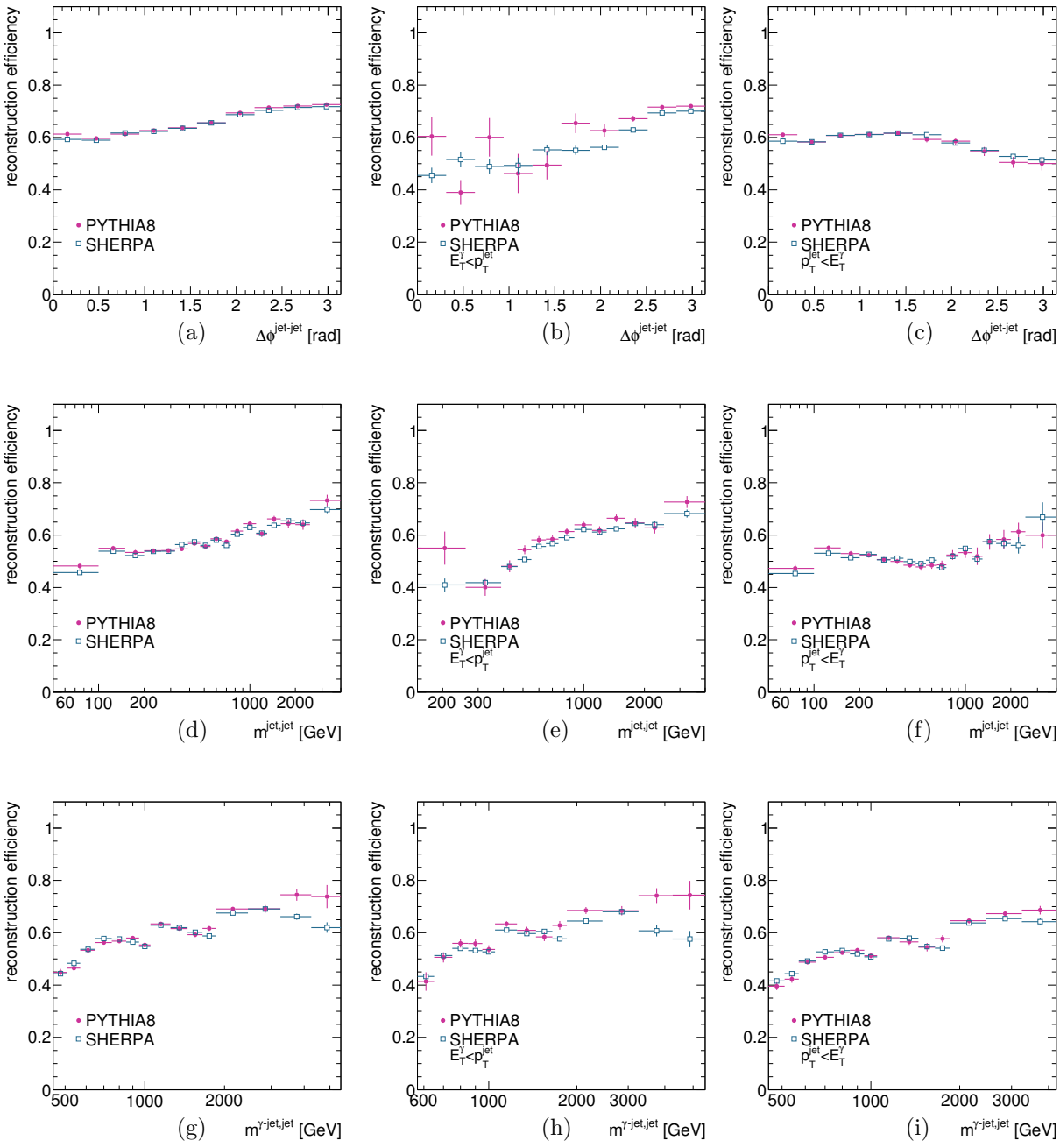


Figure 9.27: Selection efficiencies from PYTHIA (dots) and SHERPA (squares) as functions of $\Delta\phi^{\text{jet}-\text{jet}}$ (a,b,c), $m^{\text{jet}-\text{jet}}$ (d,e,f) and $m^{\gamma-\text{jet}-\text{jet}}$ (g,h,i) for the total (first column), fragmentation-enriched (second column) and direct-enriched (third column) samples.

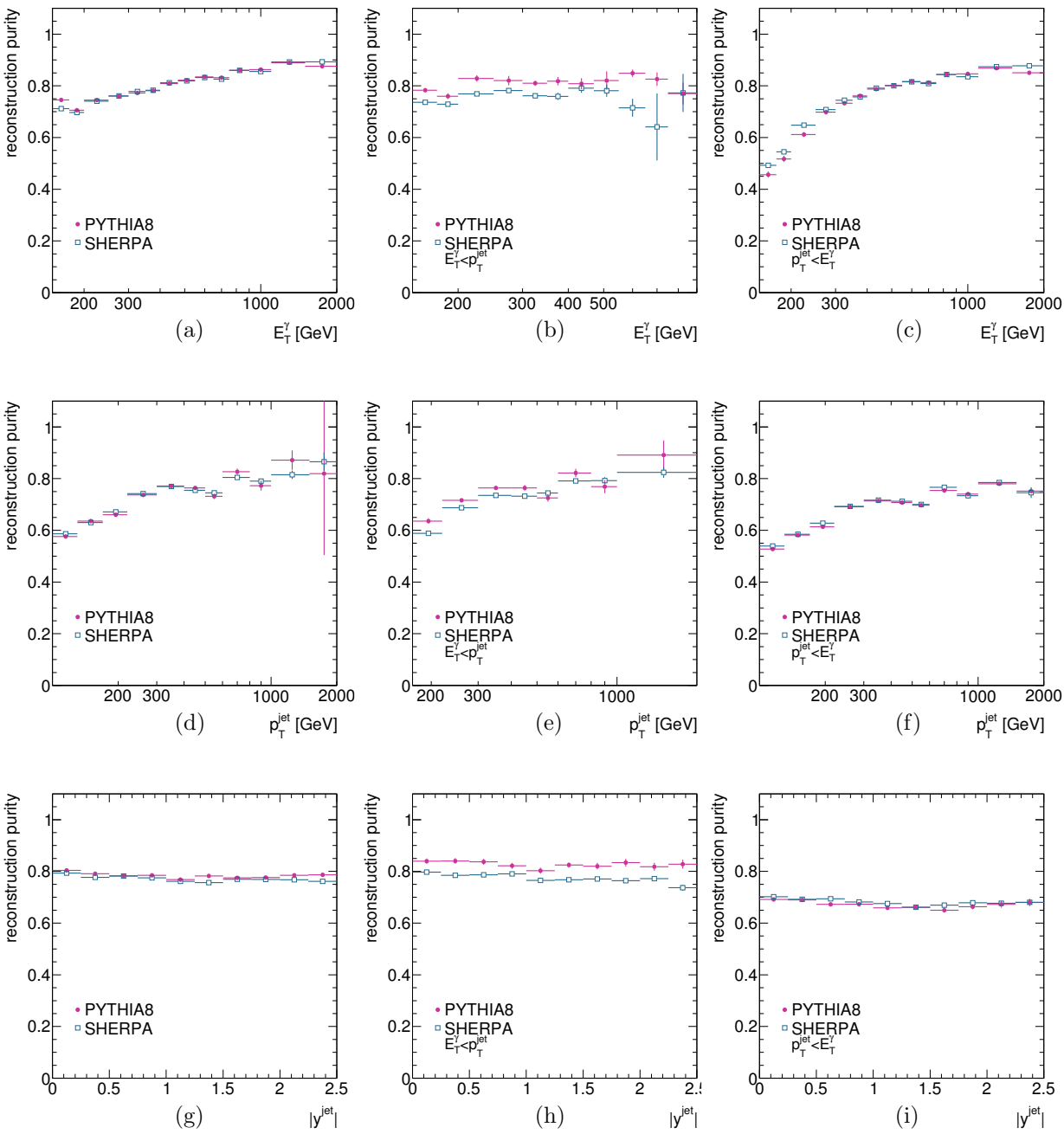


Figure 9.28: Selection purities from PYTHIA (dots) and SHERPA (squares) as functions of E_{T}^{γ} (a,b,c), $p_{\mathrm{T}}^{\mathrm{jet}}$ (d,e,f) and $|y^{\mathrm{jet}}|$ (g,h,i) for the total (first column), fragmentation-enriched (second column) and direct-enriched (third column) samples.

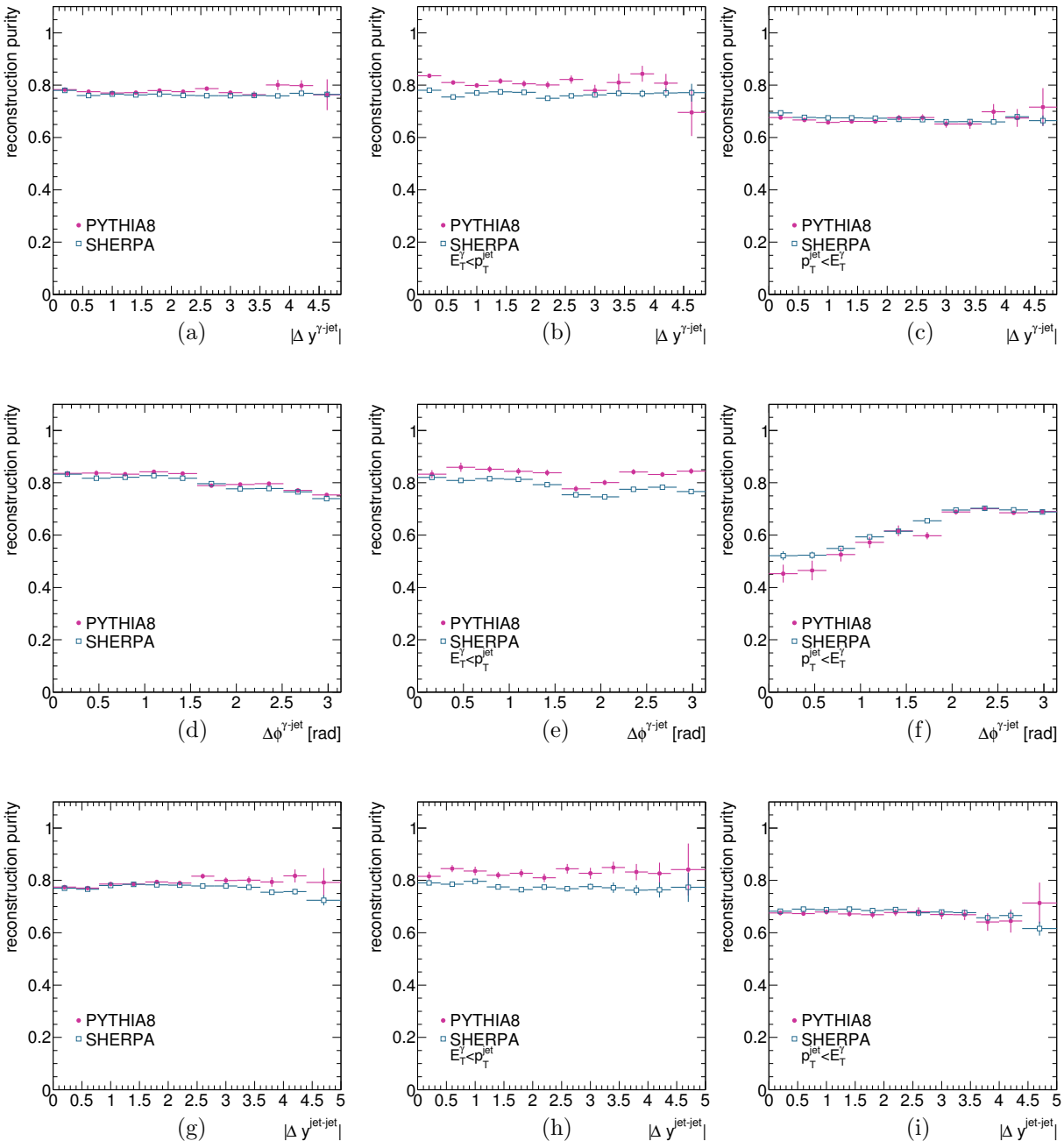


Figure 9.29: Selection purities from PYTHIA (dots) and SHERPA (squares) as functions of $|\Delta y^{\gamma-\text{jet}}|$ (a,b,c), $\Delta\phi^{\gamma-\text{jet}}$ (d,e,f) and $|\Delta y^{\text{jet}-\text{jet}}|$ (g,h,i) for the total (first column), fragmentation-enriched (second column) and direct-enriched (third column) samples.

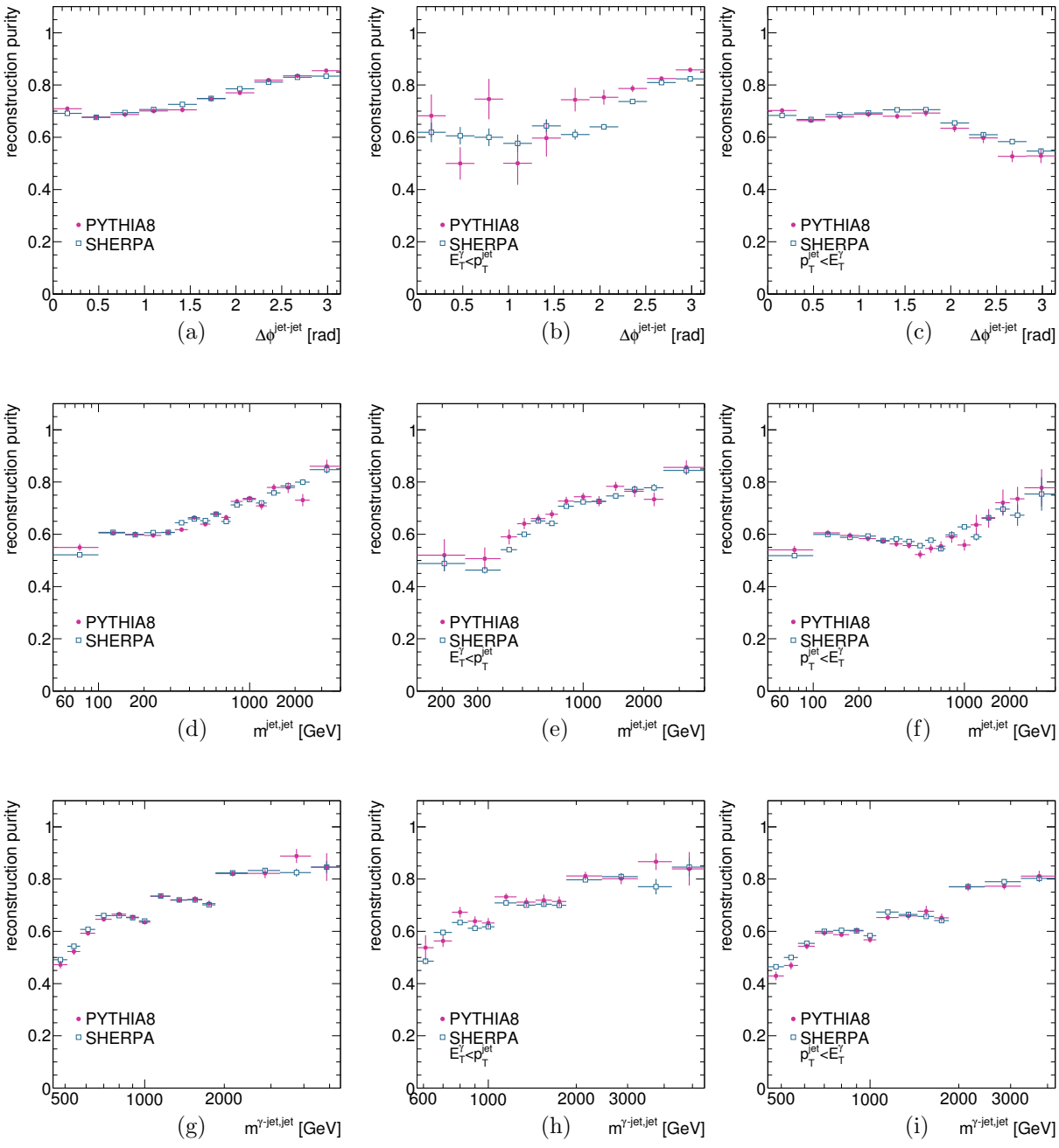


Figure 9.30: Selection purities from Pythia (dots) and Sherpa (squares) as functions of $\Delta\phi^{\text{jet}-\text{jet}}$ (a,b,c), $m^{\text{jet}-\text{jet}}$ (d,e,f) and $m^{\gamma-\text{jet}-\text{jet}}$ (g,h,i) for the total (first column), fragmentation-enriched (second column) and direct-enriched (third column) samples.

9.4.3 Cross-section measurement procedure

The data distributions, after background subtraction, were unfolded to particle level using an iterative Bayesian unfolding, as explained in Section 6.5.1.

The matrices used in the unfolding are shown in Figures 9.31 to 9.33. They were constructed with the events which fulfil the particle- and reconstruction-level requirements. The reconstructed photons or jets which are not matched to a truth photon or jet (*reco unmatched*) as well as reconstruction inefficiencies (*truth unmatched*) were also taken into account in the Bayesian method and the corresponding fractions are shown in Figures 9.34 to 9.36.

The regularisation parameter of the unfolding is the number of iterations. Figures 9.37 to 9.39 show the relative difference between the result obtained using N iterations with respect to those obtained using 4 iterations. The oscillations on the results for $N < 4$ are relatively large and disappear for $N > 4$. Therefore, the nominal Bayes' unfolding was performed using 4 iterations.

The comparison between the cross sections unfolded via the bin-by-bin and the Bayes (using $N = 4$ iterations) methods is shown in Figures 9.40 to 9.42. The differences between the cross sections obtained via the two methods are generally much smaller than 1%. In the regions of phase space where the MC statistics is poor, some deviations are observed, but they are within the statistical uncertainty of the data. The good agreement between both methods was obtained thanks to the good description by Sherpa of the data distributions at reconstruction level. The Pythia simulations fail in general to describe the shape of the data distributions and larger differences are observed between both unfolding methods, especially for $p_{\mathrm{T}}^{\mathrm{jet}}$, $m^{\mathrm{jet-jet}}$ and $m^{\gamma-\mathrm{jet}-\mathrm{jet}}$. For comparison, the relative statistical uncertainty of the cross section is also included in the figures and shows that the size of this uncertainty is typically much bigger than the difference of the cross sections obtained with the two methods.

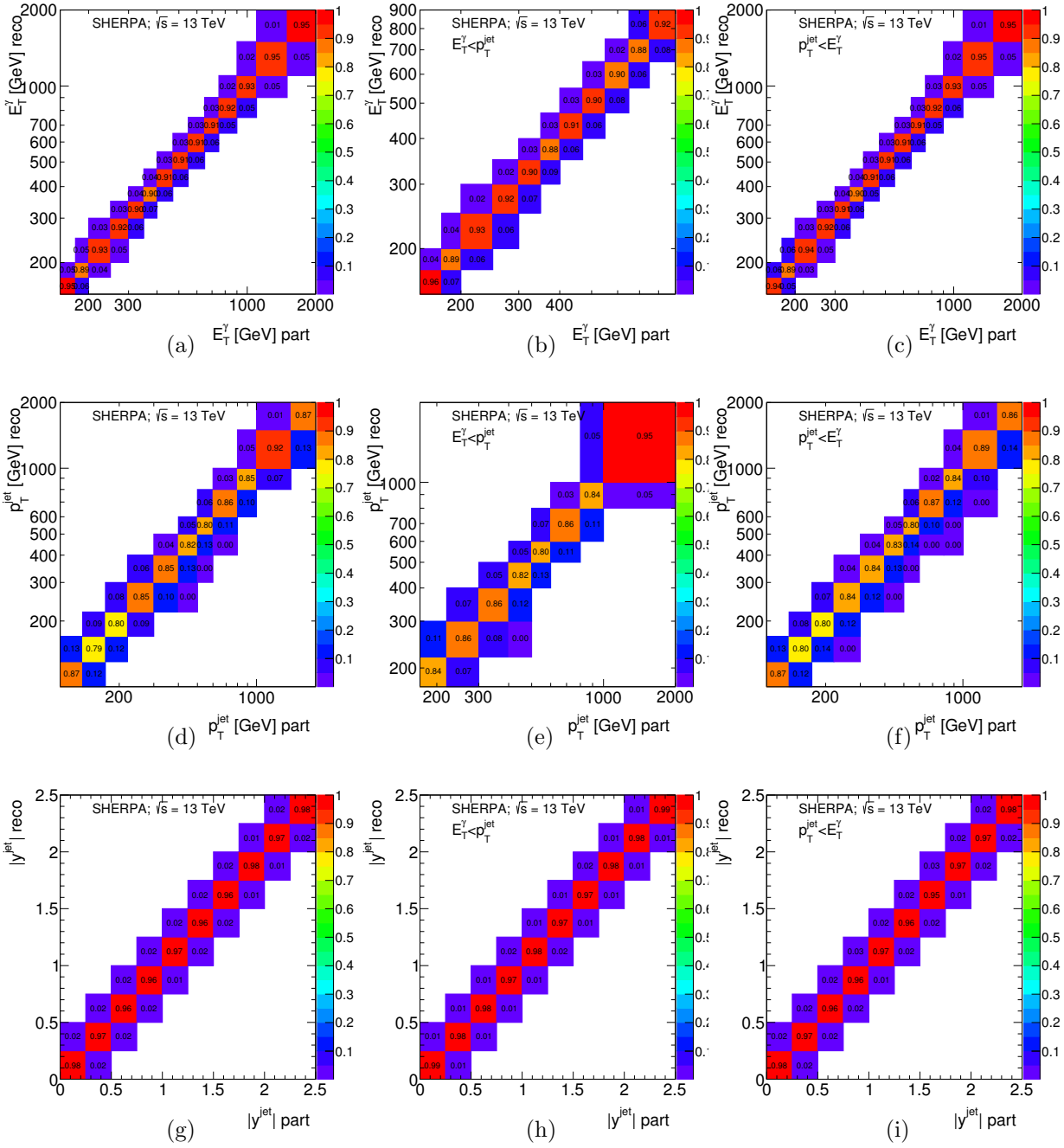


Figure 9.31: Folding matrices used in the iterative Bayesian unfolding for E_{T}^{γ} (a,b,c), $p_{\mathrm{T}}^{\mathrm{jet}}$ (d,e,f) and $|y^{\mathrm{jet}}|$ (g,h,i) for the total (first column), fragmentation-enriched (second column) and direct-enriched (third column) samples.

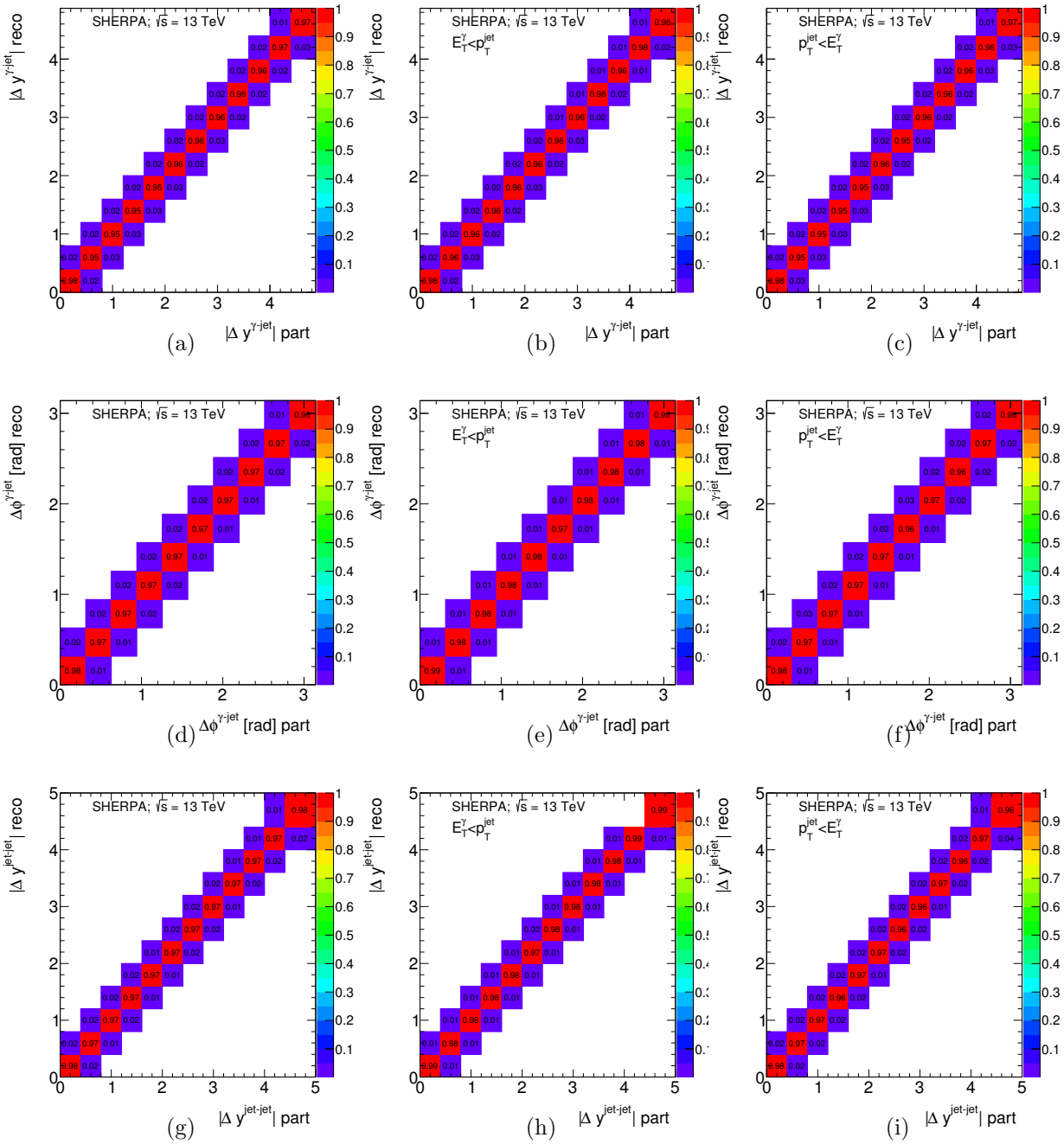


Figure 9.32: Folding matrices used in the iterative Bayesian unfolding for $|\Delta y^{\gamma-\text{jet}}|$ (a,b,c), $\Delta\phi^{\gamma-\text{jet}}$ (d,e,f) and $|\Delta y^{\text{jet}-\text{jet}}|$ (g,h,i) for the total (first column), fragmentation-enriched (second column) and direct-enriched (third column) samples.

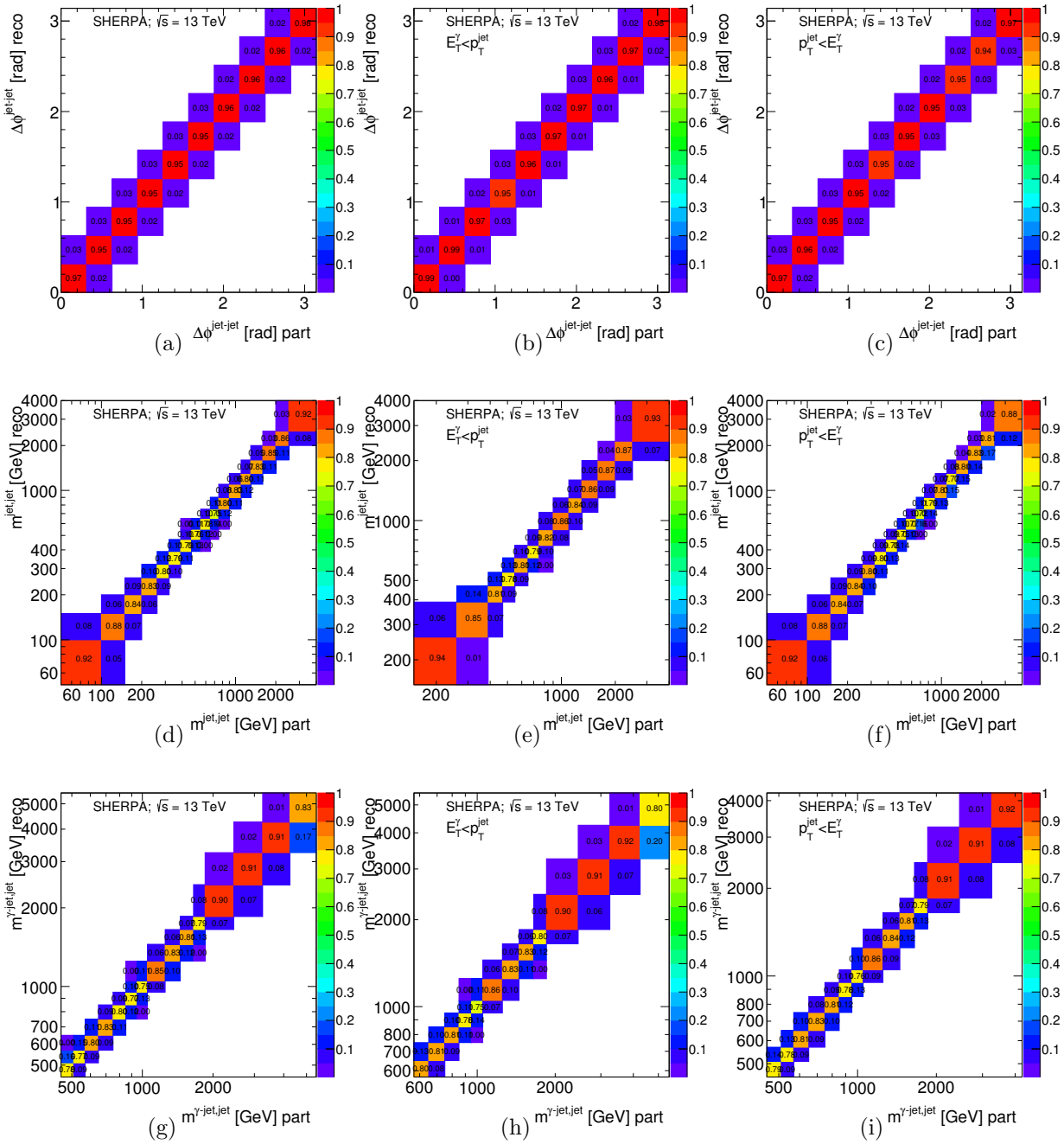


Figure 9.33: Folding matrices used in the iterative Bayesian unfolding for $\Delta\phi^{\text{jet}-\text{jet}}$ (a,b,c), $m^{\text{jet}-\text{jet}}$ (d,e,f) and $m^{\gamma-\text{jet}-\text{jet}}$ (g,h,i) for the total (first column), fragmentation-enriched (second column) and direct-enriched (third column) samples.

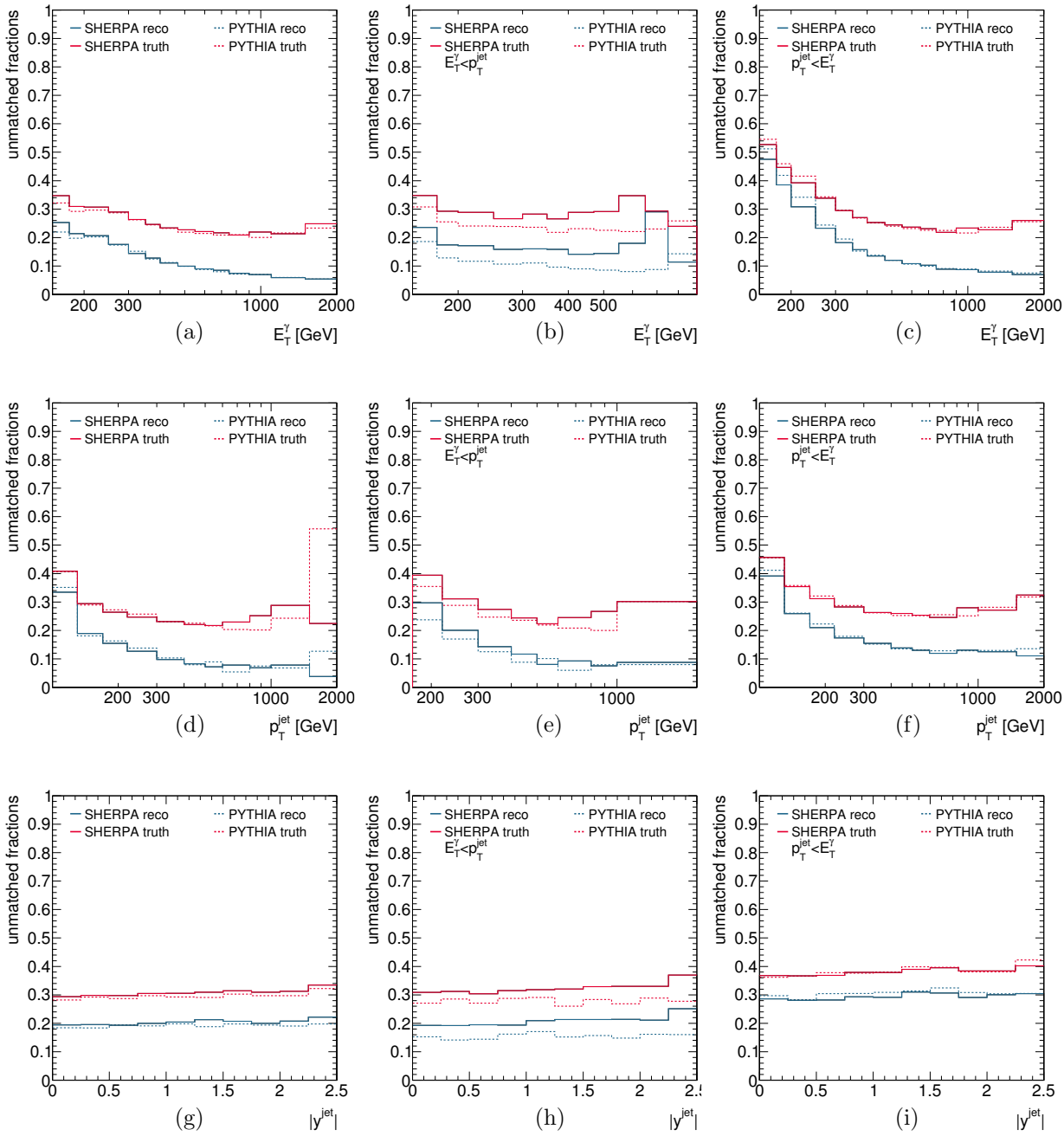


Figure 9.34: Fractions of unmatched truth (red lines) and reco (blue lines) as functions of E_{T}^{γ} (a,b,c), $p_{\mathrm{T}}^{\mathrm{jet}}$ (d,e,f) and $|y^{\mathrm{jet}}|$ (g,h,i) for the total (first column), fragmentation-enriched (second column) and direct-enriched (third column) samples.

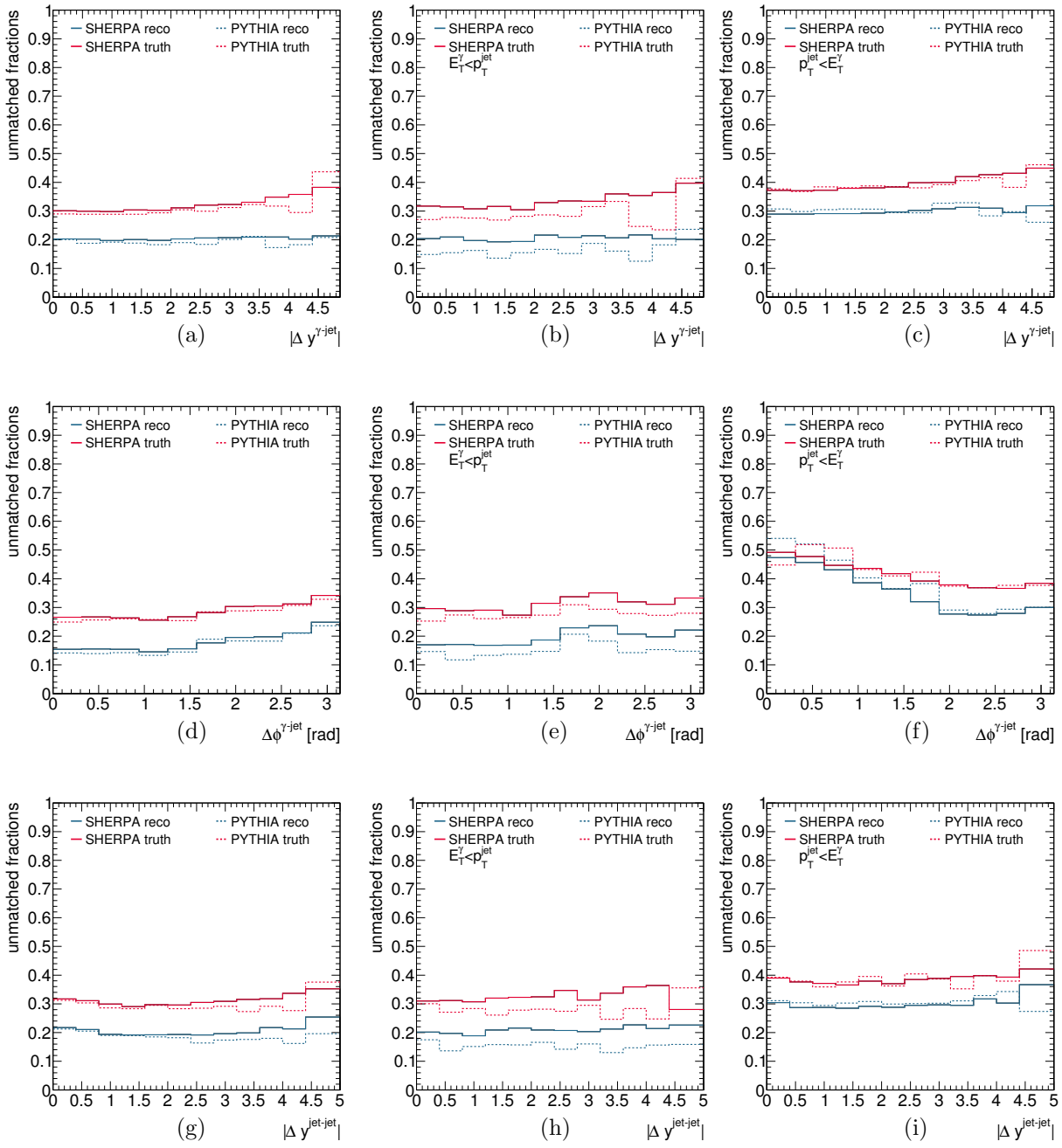


Figure 9.35: Fractions of unmatched truth (red lines) and reco (blue lines) as functions of $|\Delta y^{\gamma-\text{jet}}|$ (a,b,c), $\Delta\phi^{\gamma-\text{jet}}$ (d,e,f) and $|\Delta y^{\text{jet}-\text{jet}}|$ (g,h,i) for the total (first column), fragmentation-enriched (second column) and direct-enriched (third column) samples.

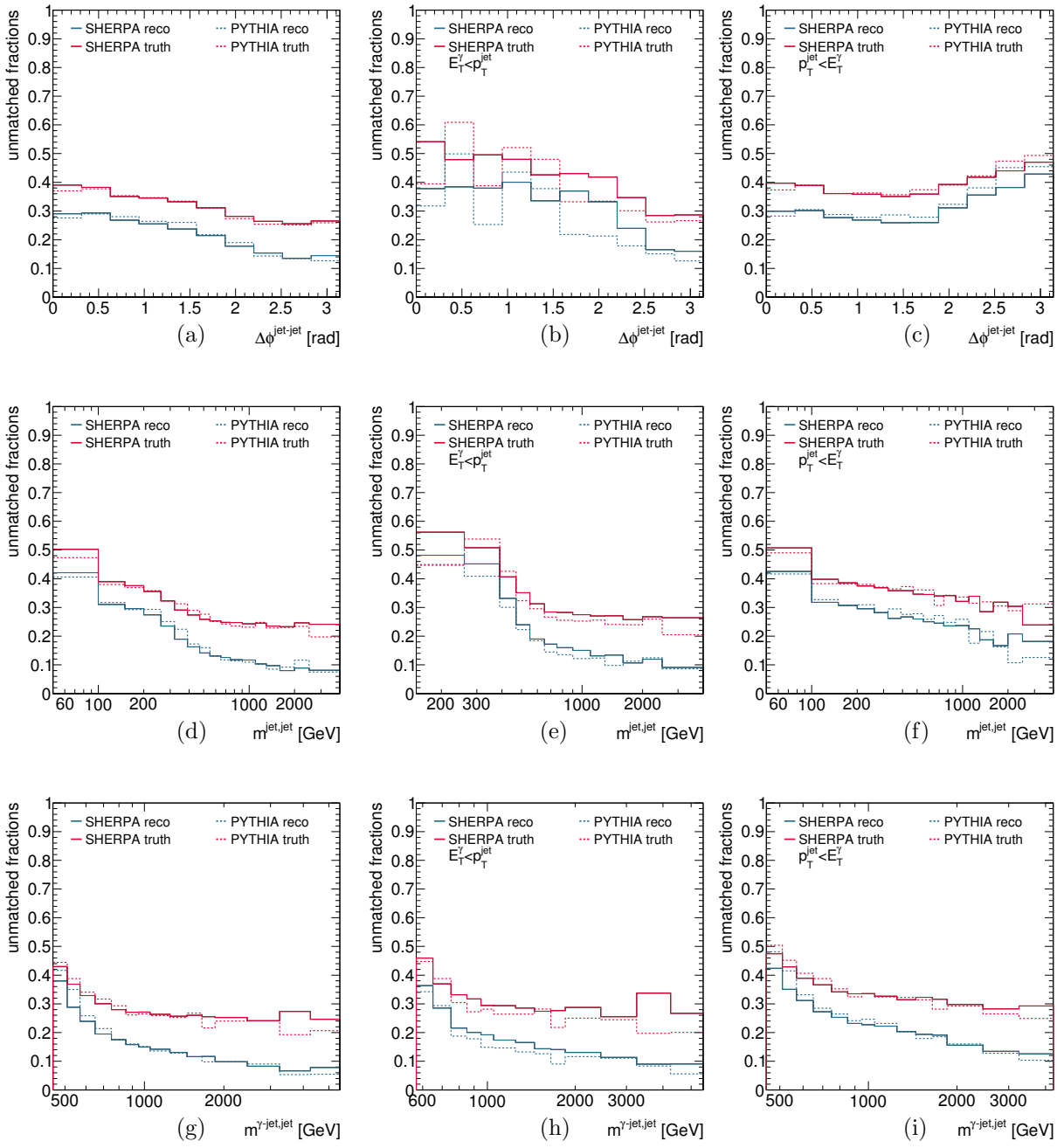


Figure 9.36: Fractions of unmatched truth (red lines) and reco (blue lines) as functions of $\Delta\phi^{\text{jet}-\text{jet}}$ (a,b,c), $m^{\text{jet}-\text{jet}}$ (d,e,f) and $m^{\gamma-\text{jet}-\text{jet}}$ (g,h,i) for the total (first column), fragmentation-enriched (second column) and direct-enriched (third column) samples.

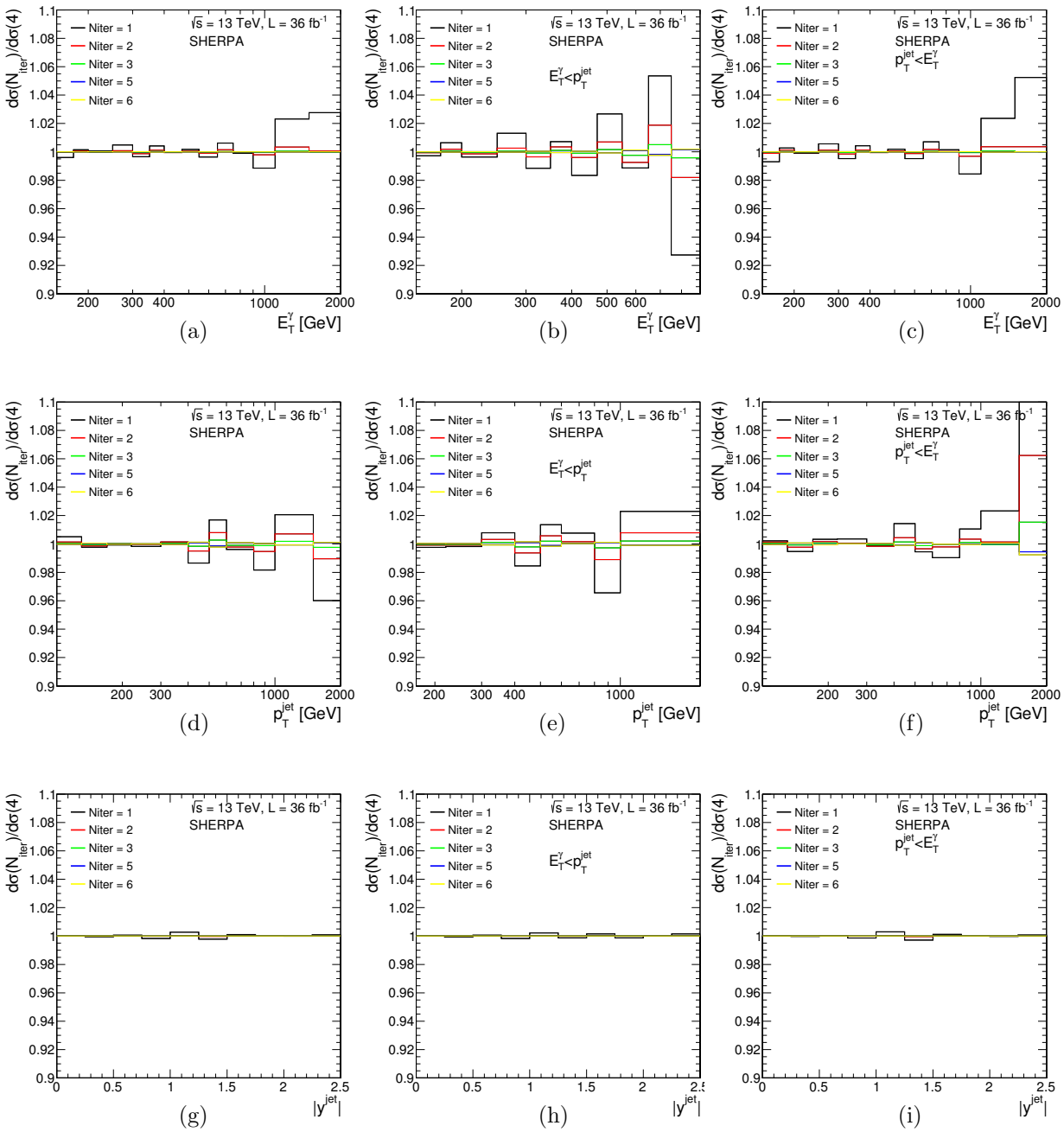


Figure 9.37: Ratios between the cross sections unfolded using the Bayesian method with N iterations and the results unfolded using four iterations and SHERPA MC as functions of E_{T}^{γ} (a,b,c), $p_{\mathrm{T}}^{\mathrm{jet}}$ (d,e,f) and $|y^{\mathrm{jet}}|$ (g,h,i) for the total (first column), fragmentation-enriched (second column) and direct-enriched (third column) samples.

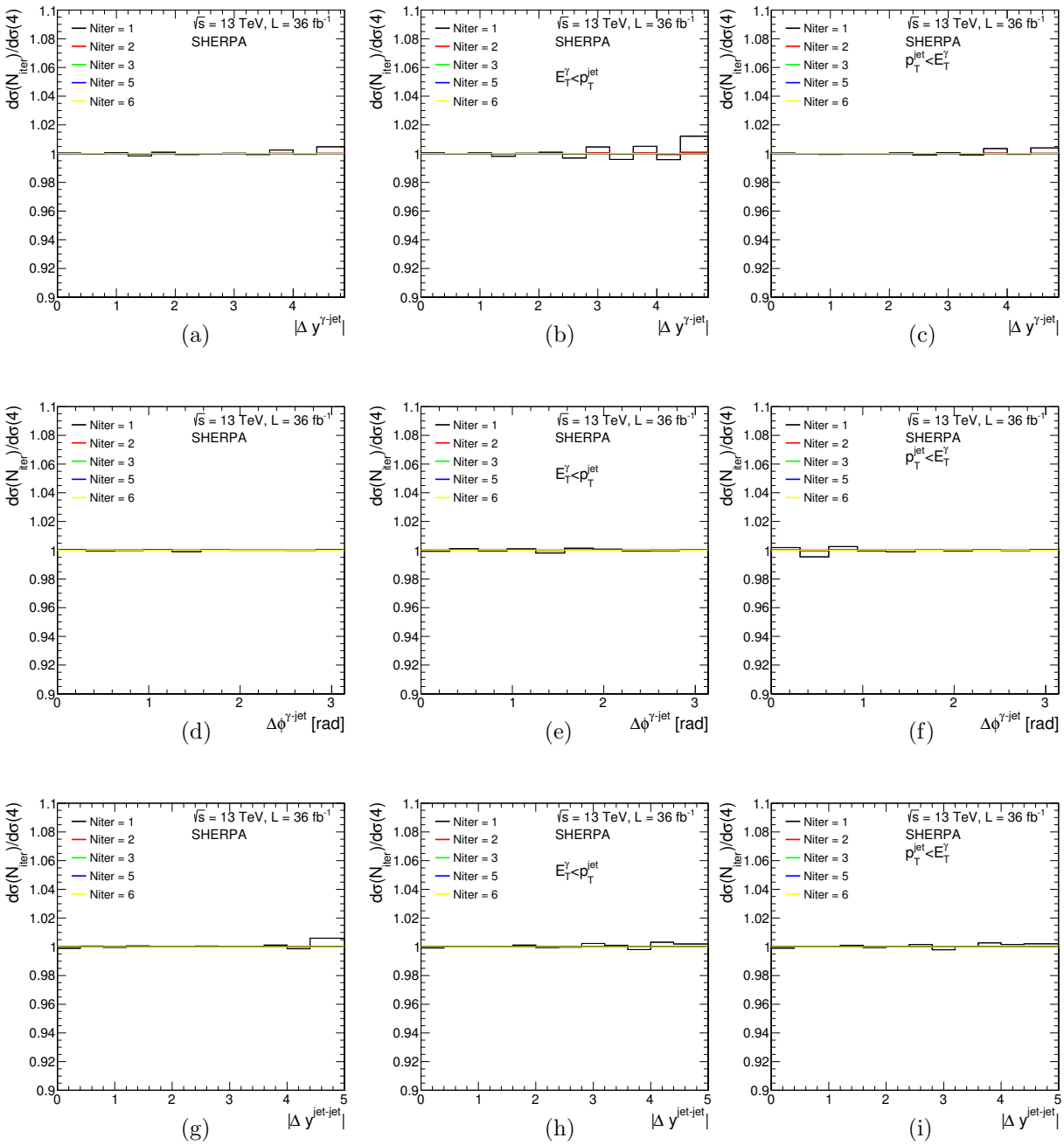


Figure 9.38: Ratios between the cross sections unfolded using the Bayesian method with N iterations and the results unfolded using four iterations and SHERPA MC as functions of $|\Delta y^{\gamma-\text{jet}}|$ (a,b,c), $\Delta\phi^{\gamma-\text{jet}}$ (d,e,f) and $|\Delta y^{\text{jet}-\text{jet}}|$ (g,h,i) for the total (first column), fragmentation-enriched (second column) and direct-enriched (third column) samples.

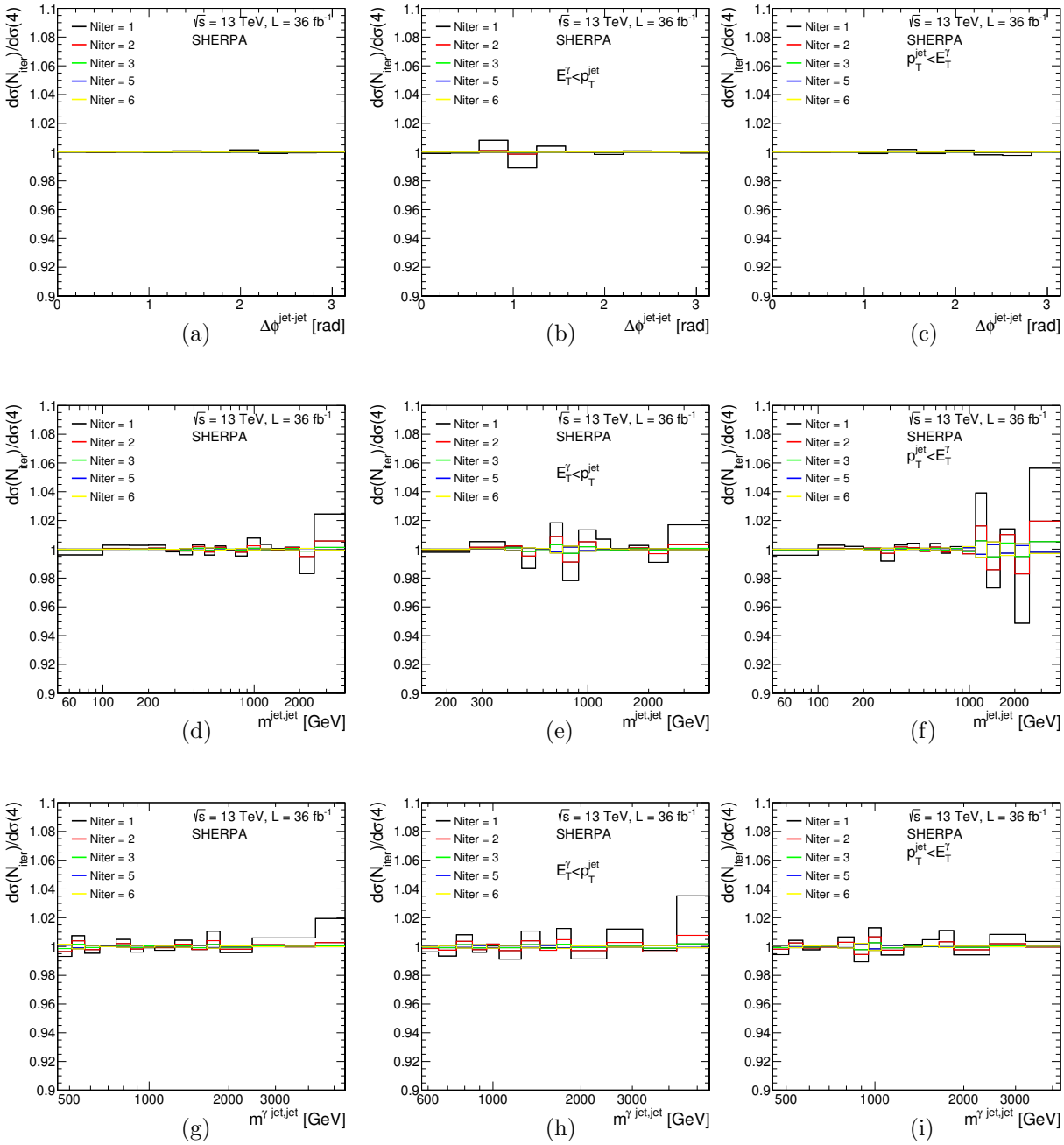


Figure 9.39: Ratios between the cross sections unfolded using the Bayesian method with N iterations and the results unfolded using four iterations and SHERPA MC as functions of $\Delta\phi^{\text{jet}-\text{jet}}$ (a,b,c), $m^{\text{jet}-\text{jet}}$ (d,e,f) and $m^{\gamma-\text{jet}-\text{jet}}$ (g,h,i) for the total (first column), fragmentation-enriched (second column) and direct-enriched (third column) samples.

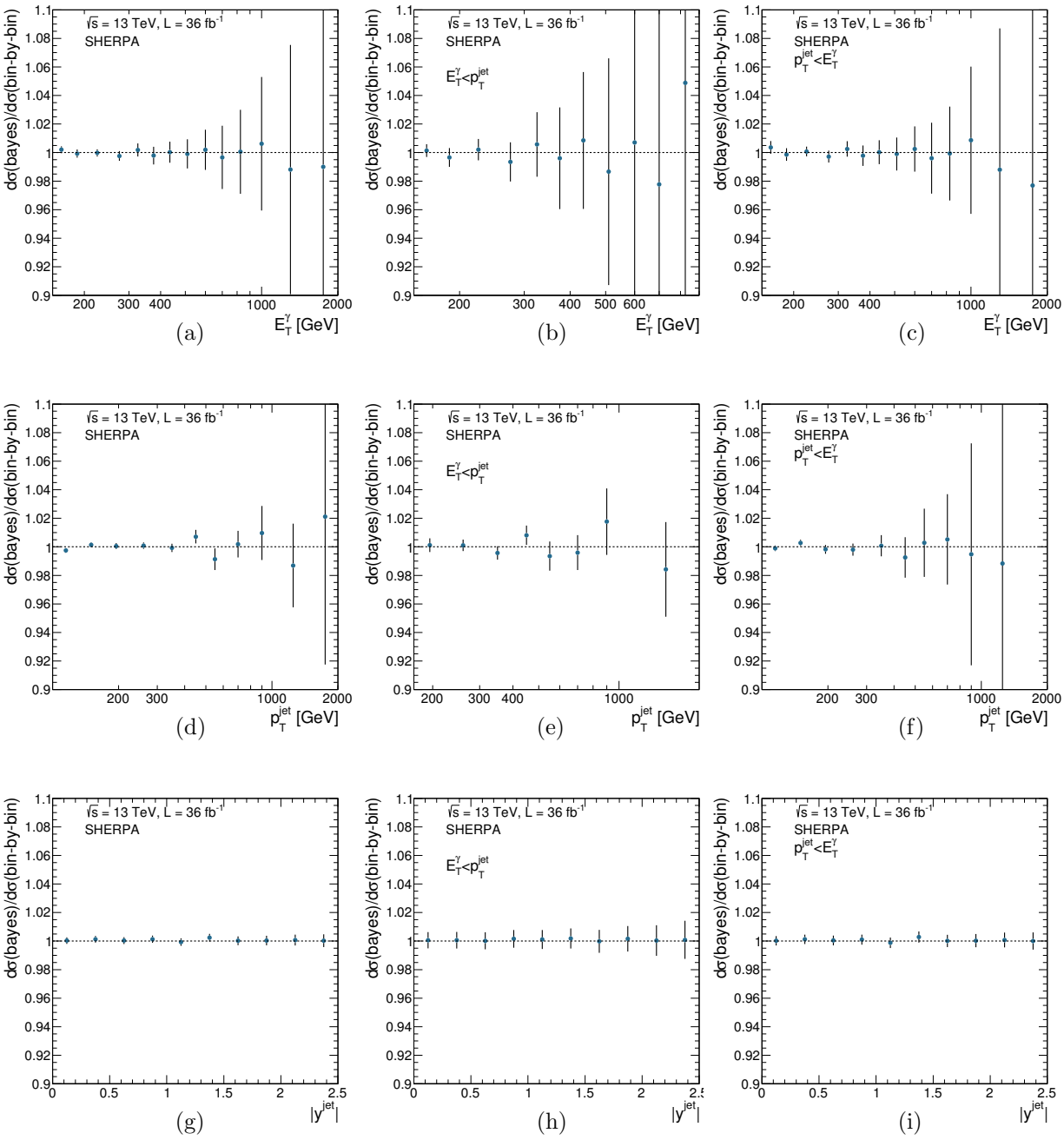


Figure 9.40: Cross-section ratios between results obtained using the iterative Bayesian unfolding with four iterations and those obtained with the bin-by-bin unfolding as functions of E_{T}^{γ} (a,b,c), $p_{\mathrm{T}}^{\mathrm{jet}}$ (d,e,f) and $|y^{\mathrm{jet}}|$ (g,h,i) for the total (first column), fragmentation-enriched (second column) and direct-enriched (third column) samples. For illustration, the relative statistical uncertainties of the cross sections are shown as error bars.

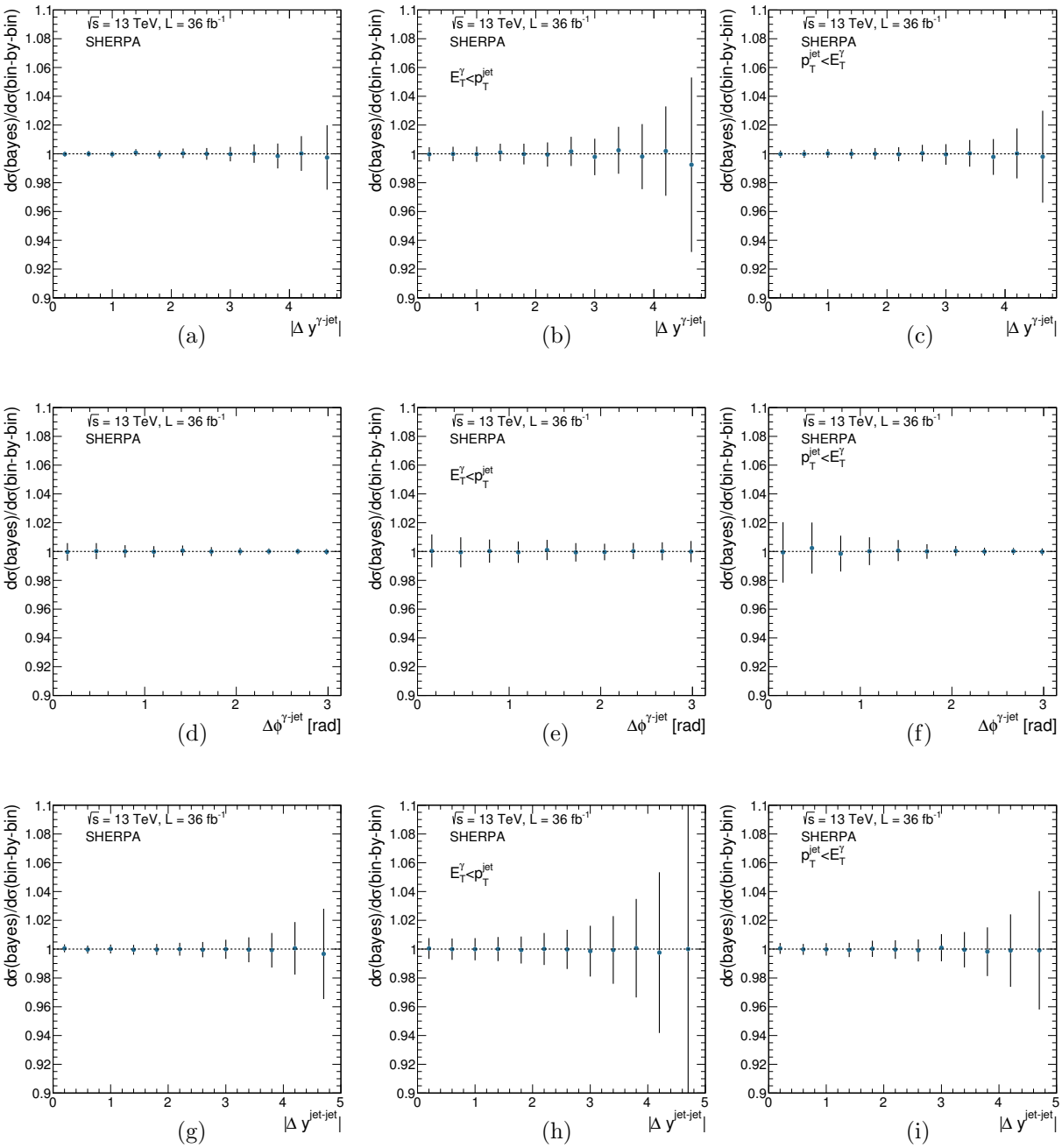


Figure 9.41: Cross-section ratios between results obtained using the iterative Bayesian unfolding with four iterations and those obtained with the bin-by-bin unfolding as functions of $|\Delta y^{\gamma-\mathrm{jet}}|$ (a,b,c), $\Delta\phi^{\gamma-\mathrm{jet}}$ (d,e,f) and $|\Delta y^{\mathrm{jet}-\mathrm{jet}}|$ (g,h,i) for the total (first column), fragmentation-enriched (second column) and direct-enriched (third column) samples. For illustration, the relative statistical uncertainties of the cross sections are shown as error bars.

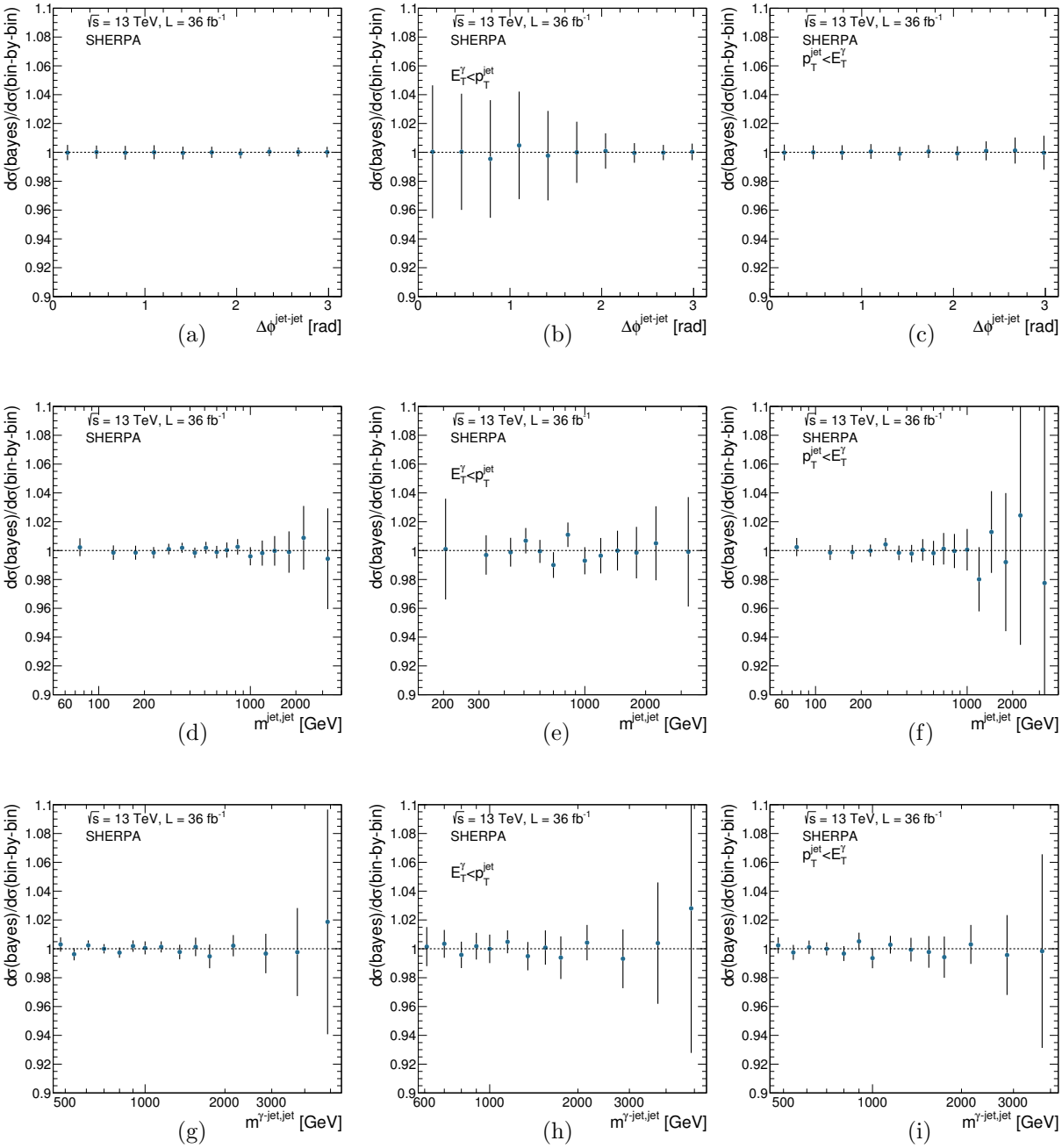


Figure 9.42: Cross-section ratios between results obtained using the iterative Bayesian unfolding with four iterations and those obtained with the bin-by-bin unfolding as functions of $\Delta\phi^{\text{jet}-\text{jet}}$ (a,b,c), $m^{\text{jet}-\text{jet}}$ (d,e,f) and $m^{\gamma-\text{jet}-\text{jet}}$ (g,h,i) for the total (first column), fragmentation-enriched (second column) and direct-enriched (third column) samples. For illustration, the relative statistical uncertainties of the cross sections are shown as error bars.

9.5 Systematic uncertainties

The sources of systematic uncertainties that affect the measurements were investigated. These sources include the photon energy scale and resolution, the jet energy scale and resolution, the QCD-cascade and hadronisation model dependence, the photon identification efficiency, the MC isolation correction, the choice of background control regions, the identification and isolation correlation in the background, the electron-faking-photon background, pile-up reweighting, MC sample statistics, the trigger efficiency and the luminosity uncertainties. Each source of uncertainty was propagated into the cross sections following the same unfolding method as for the nominal results, that is, the iterative Bayesian unfolding with four iterations.

9.5.1 Photon energy scale and resolution

The sources of uncertainty affecting the determination of the photon energy scale and resolution were determined using Run-2 data and parameterised with a total of 67 nuisance parameters for the energy scale and 9 for the energy resolution. The different sources of uncertainty were varied separately in the MC simulations and then added in quadrature. For each nuisance parameter, the impact in the signal yield and the unfolding was taken into account to determine a modified cross section, σ_i', in each bin i which was then compared to the nominal one, σ_i, to assess the contribution of the parameter to the total systematic uncertainty.

The statistical uncertainty of the systematic variations was obtained by a bootstrap technique using 100 MC replicas and used in the smoothing of the uncertainty as described in Section 6.6.1. Figures 9.43 to 9.45 show the resulting total uncertainty after smoothing.

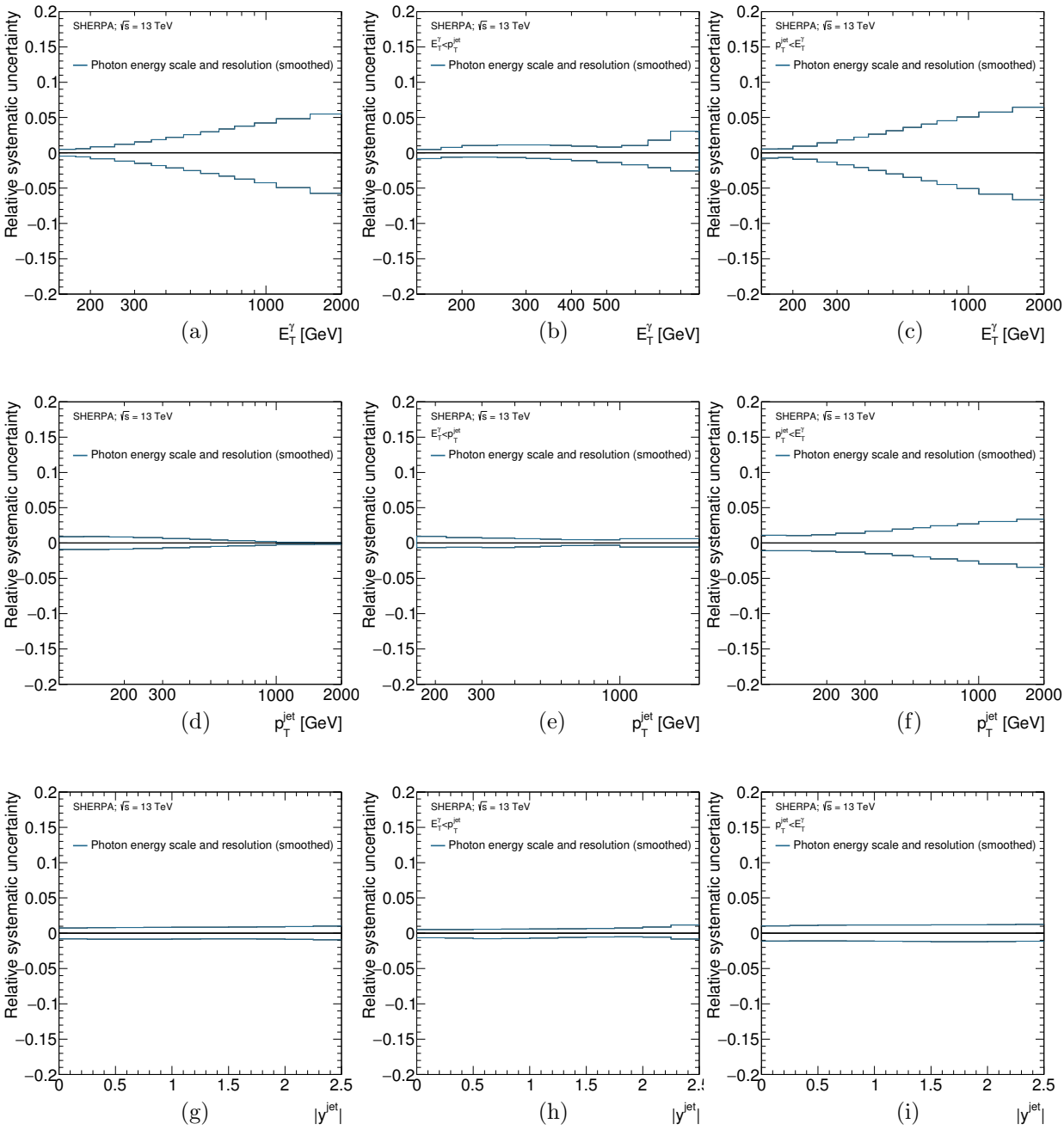


Figure 9.43: Systematic uncertainties on the measured cross section due to the uncertainty in the photon energy scale and resolution as functions of E_{T}^{γ} (a,b,c), $p_{\mathrm{T}}^{\mathrm{jet}}$ (d,e,f) and $|y^{\mathrm{jet}}|$ (g,h,i) for the total (first column), fragmentation-enriched (second column) and direct-enriched (third column) samples.

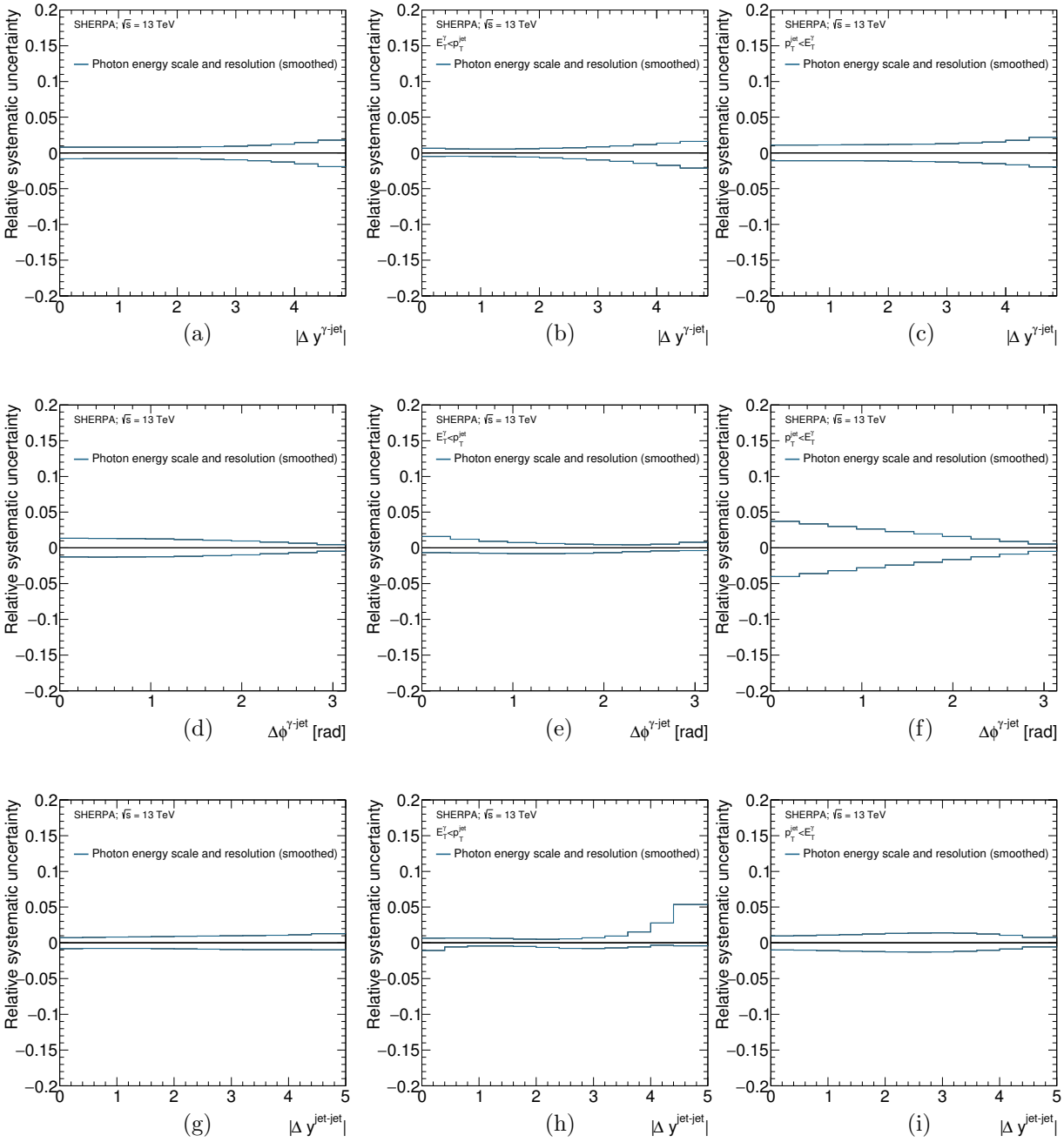


Figure 9.44: Systematic uncertainties on the measured cross section due to the uncertainty in the photon energy scale and resolution as functions of $|\Delta y^{\gamma-\text{jet}}|$ (a,b,c), $\Delta\phi^{\gamma-\text{jet}}$ (d,e,f) and $|\Delta y^{\text{jet}-\text{jet}}|$ (g,h,i) for the total (first column), fragmentation-enriched (second column) and direct-enriched (third column) samples.

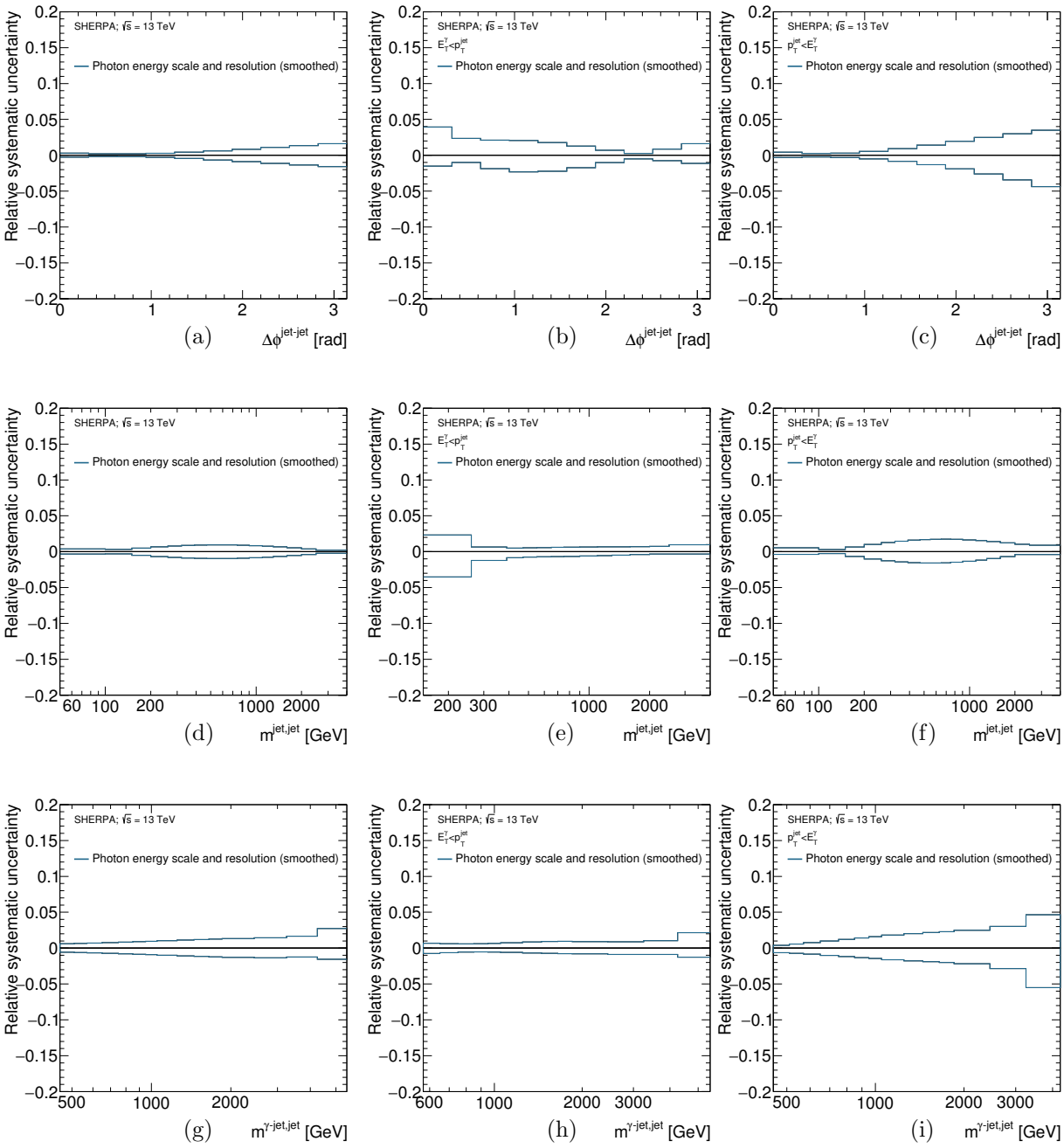


Figure 9.45: Systematic uncertainties on the measured cross section due to the uncertainty in the photon energy scale and resolution as functions of $\Delta\phi^{\text{jet}-\text{jet}}$ (a,b,c), $m^{\text{jet}-\text{jet}}$ (d,e,f) and $m^{\gamma-\text{jet}-\text{jet}}$ (g,h,i) for the total (first column), fragmentation-enriched (second column) and direct-enriched (third column) samples.

9.5.2 Jet energy scale

The 86 individual components influencing the energy scale measurement of the jets were studied and varied within their uncertainties to assess the overall uncertainty on the jet energy measurement. These variations were propagated through the analysis separately to maintain the full information on the correlations. Only the effect on the unfolding was taken into account.

The contribution of each nuisance parameter was smoothed and added in quadrature to obtain the total systematic uncertainty on the jet energy scale which is presented in Figures 9.46 to 9.48

9.5.3 Jet energy resolution

The jet energy resolution uncertainty was estimated by smearing the MC simulated distribution and comparing the cross-section measurements with and without the smearing. Figures 9.49 to 9.51 show the resulting uncertainty.

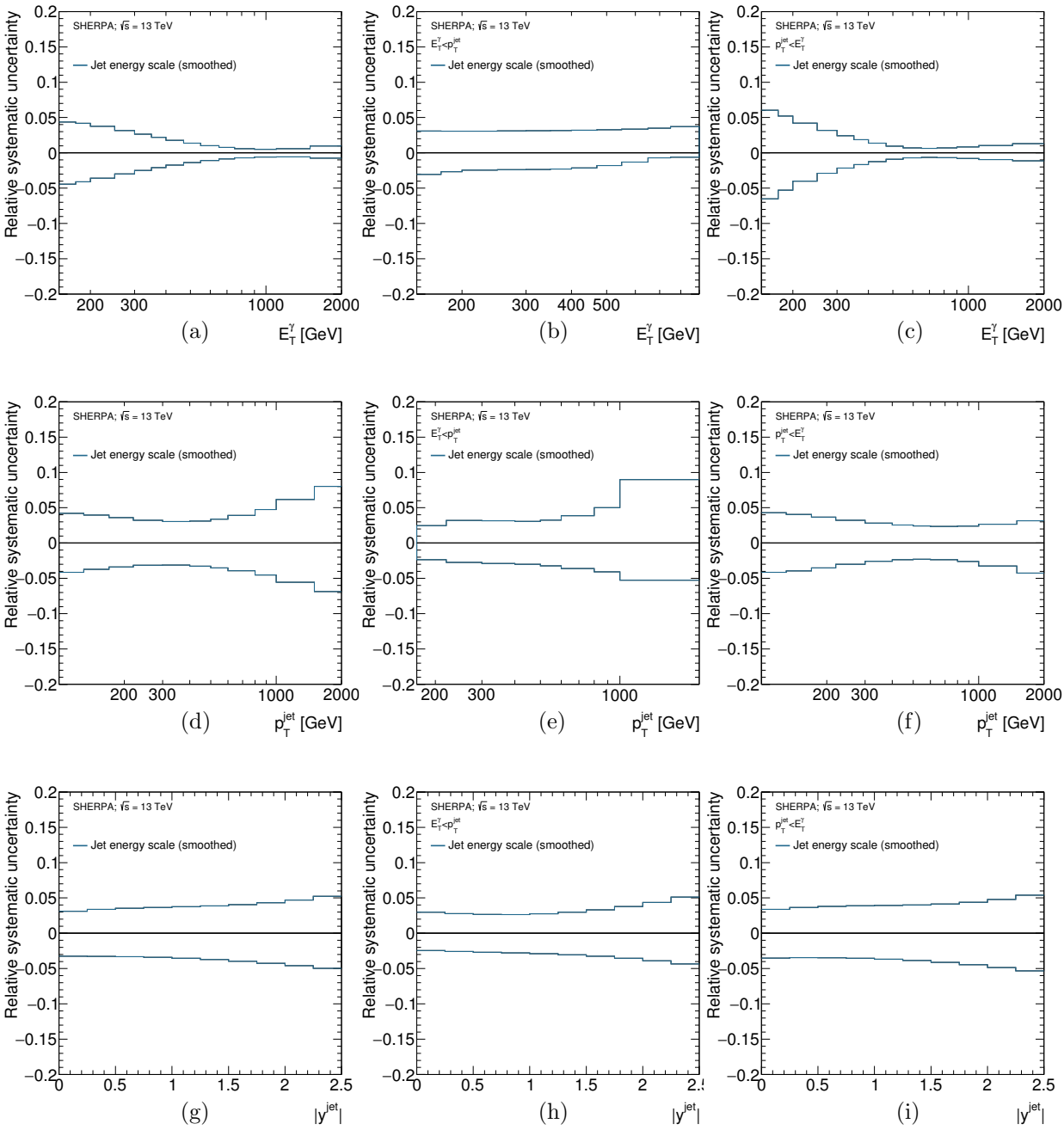


Figure 9.46: Systematic uncertainties on the measured cross section due to the uncertainty in the jet energy scale as functions of E_{T}^{γ} (a,b,c), $p_{\mathrm{T}}^{\mathrm{jet}}$ (d,e,f) and $|y^{\mathrm{jet}}|$ (g,h,i) for the total (first column), fragmentation-enriched (second column) and direct-enriched (third column) samples.

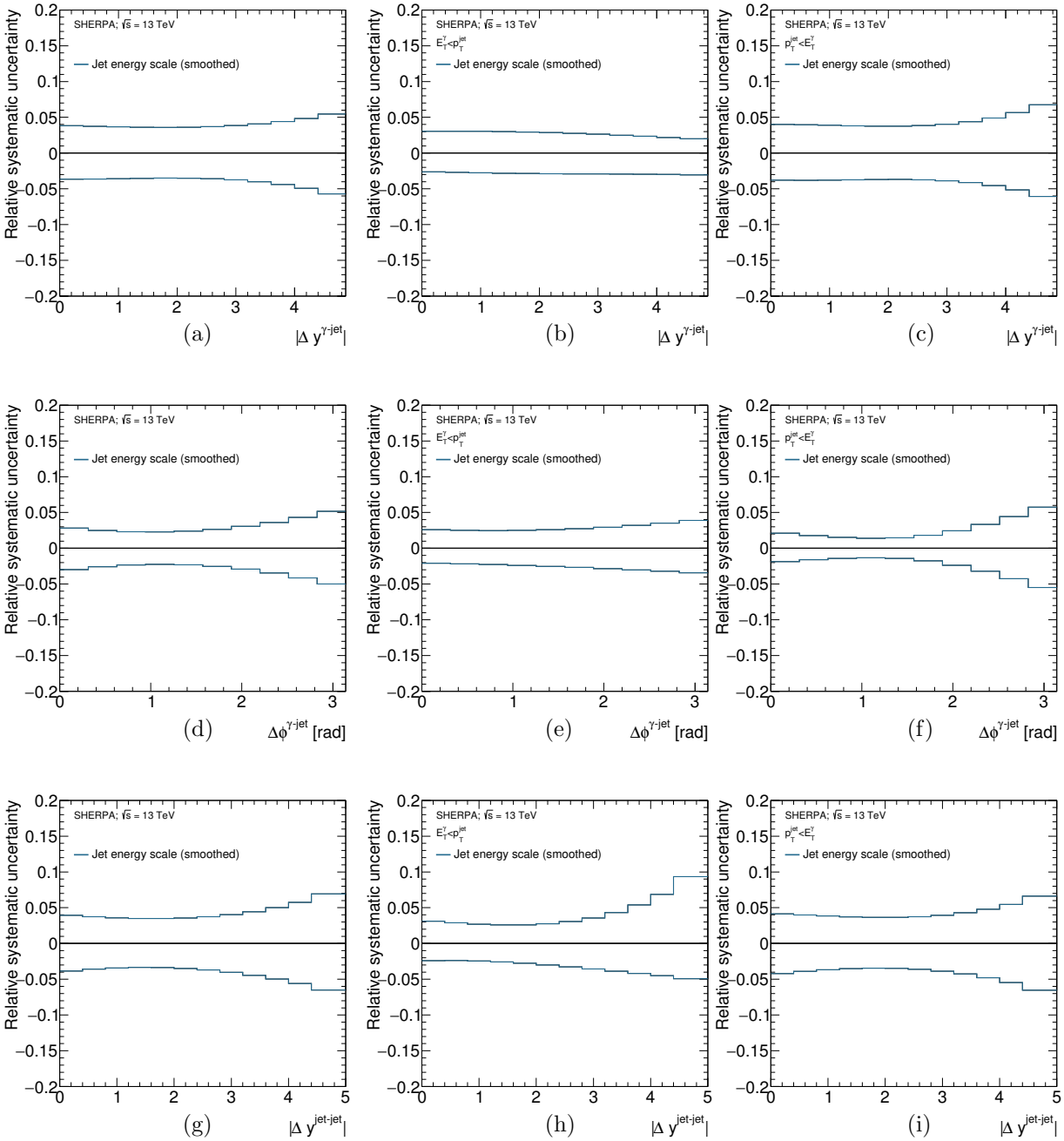


Figure 9.47: Systematic uncertainties on the measured cross section due to the uncertainty in the jet energy scale as functions of $|\Delta y^{\gamma-\text{jet}}|$ (a,b,c), $\Delta\phi^{\gamma-\text{jet}}$ (d,e,f) and $|\Delta y^{\text{jet}-\text{jet}}|$ (g,h,i) for the total (first column), fragmentation-enriched (second column) and direct-enriched (third column) samples.

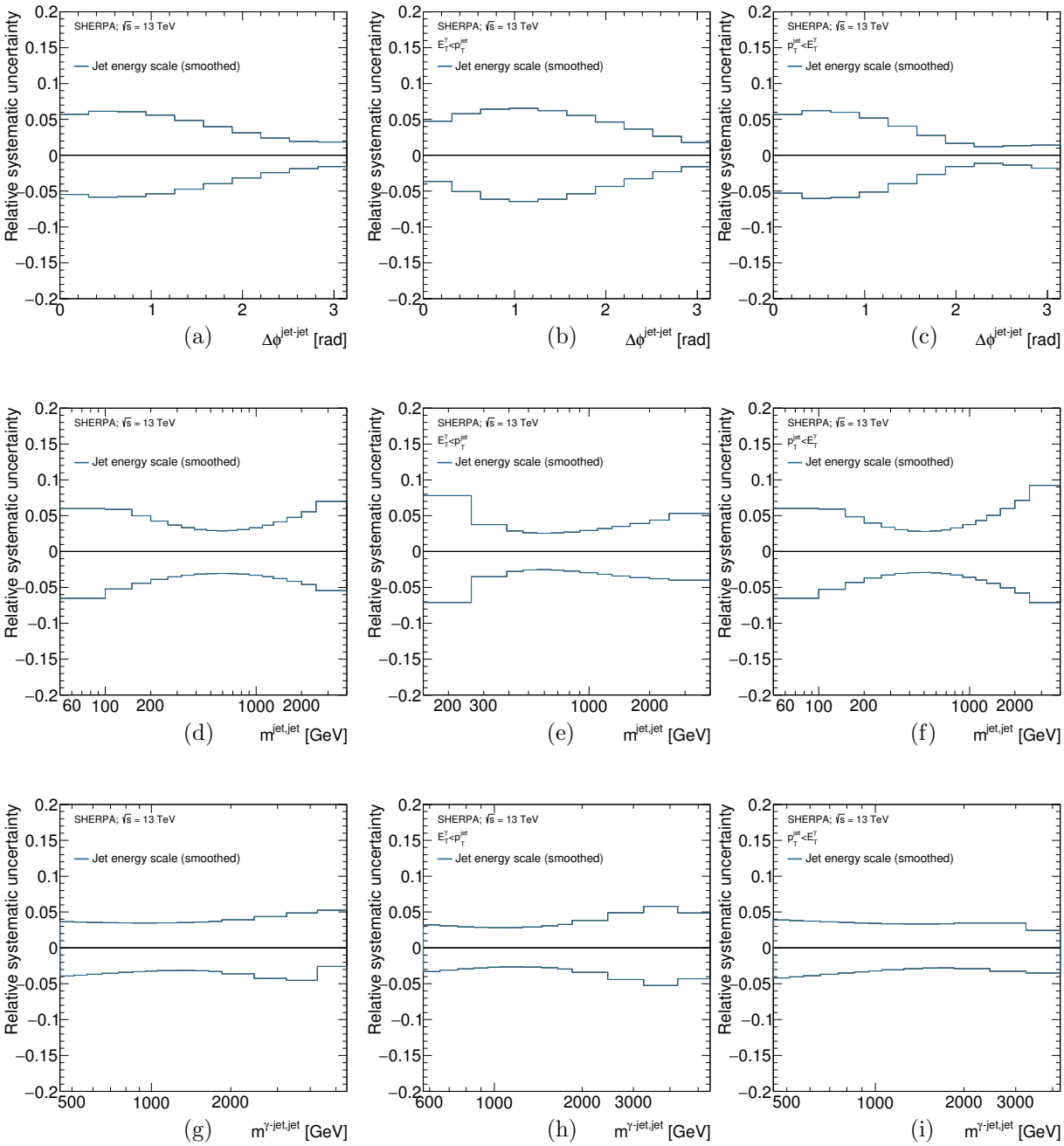


Figure 9.48: Systematic uncertainties on the measured cross section due to the uncertainty in the jet energy scale as functions of $\Delta\phi^{\text{jet}-\text{jet}}$ (a,b,c), $m^{\text{jet}-\text{jet}}$ (d,e,f) and $m^{\gamma-\text{jet}-\text{jet}}$ (g,h,i) for the total (first column), fragmentation-enriched (second column) and direct-enriched (third column) samples.

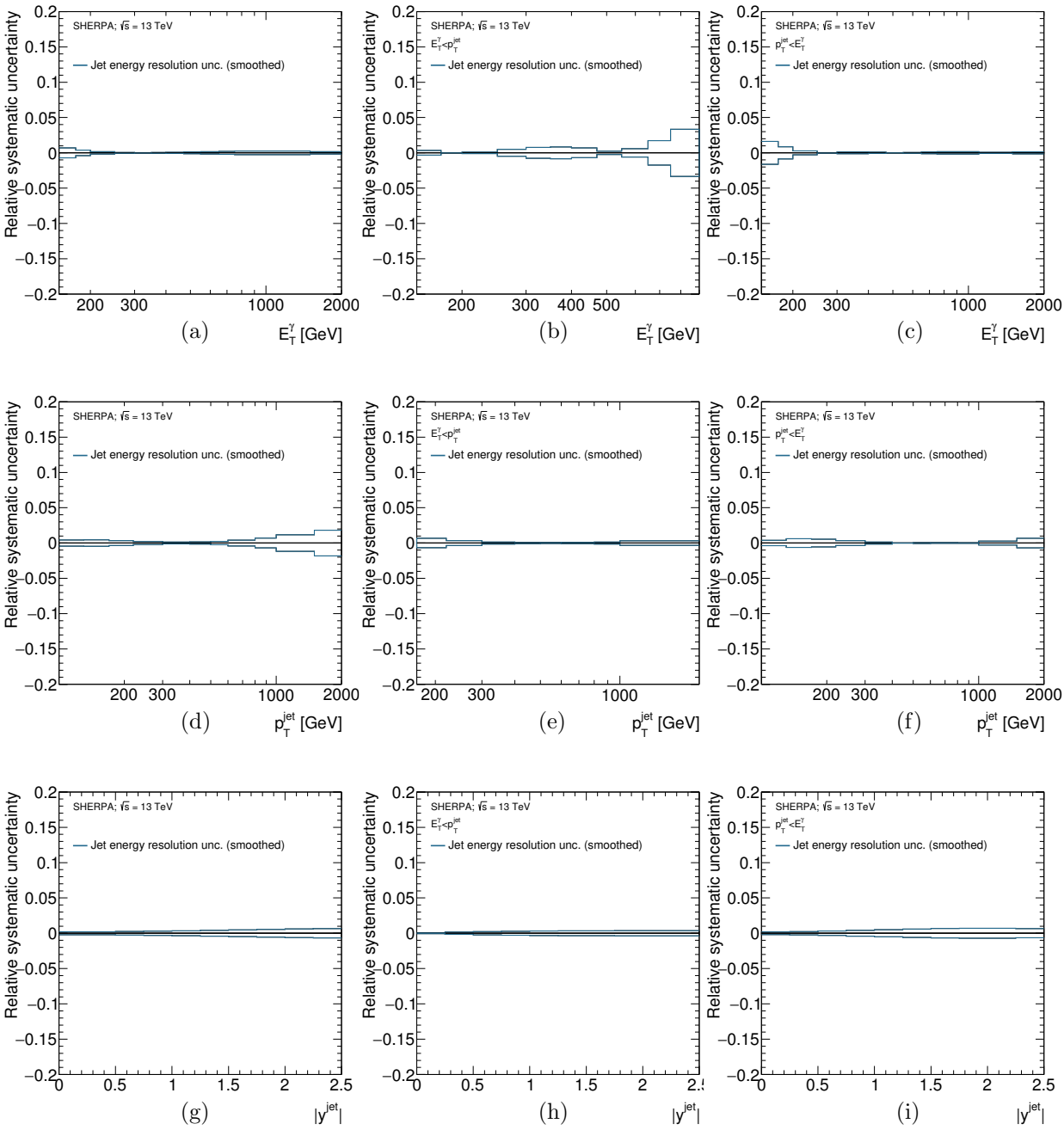


Figure 9.49: Systematic uncertainties on the measured cross section due to the uncertainty in the jet energy resolution as functions of E_{T}^{γ} (a,b,c), $p_{\mathrm{T}}^{\mathrm{jet}}$ (d,e,f) and $|y^{\mathrm{jet}}|$ (g,h,i) for the total (first column), fragmentation-enriched (second column) and direct-enriched (third column) samples.

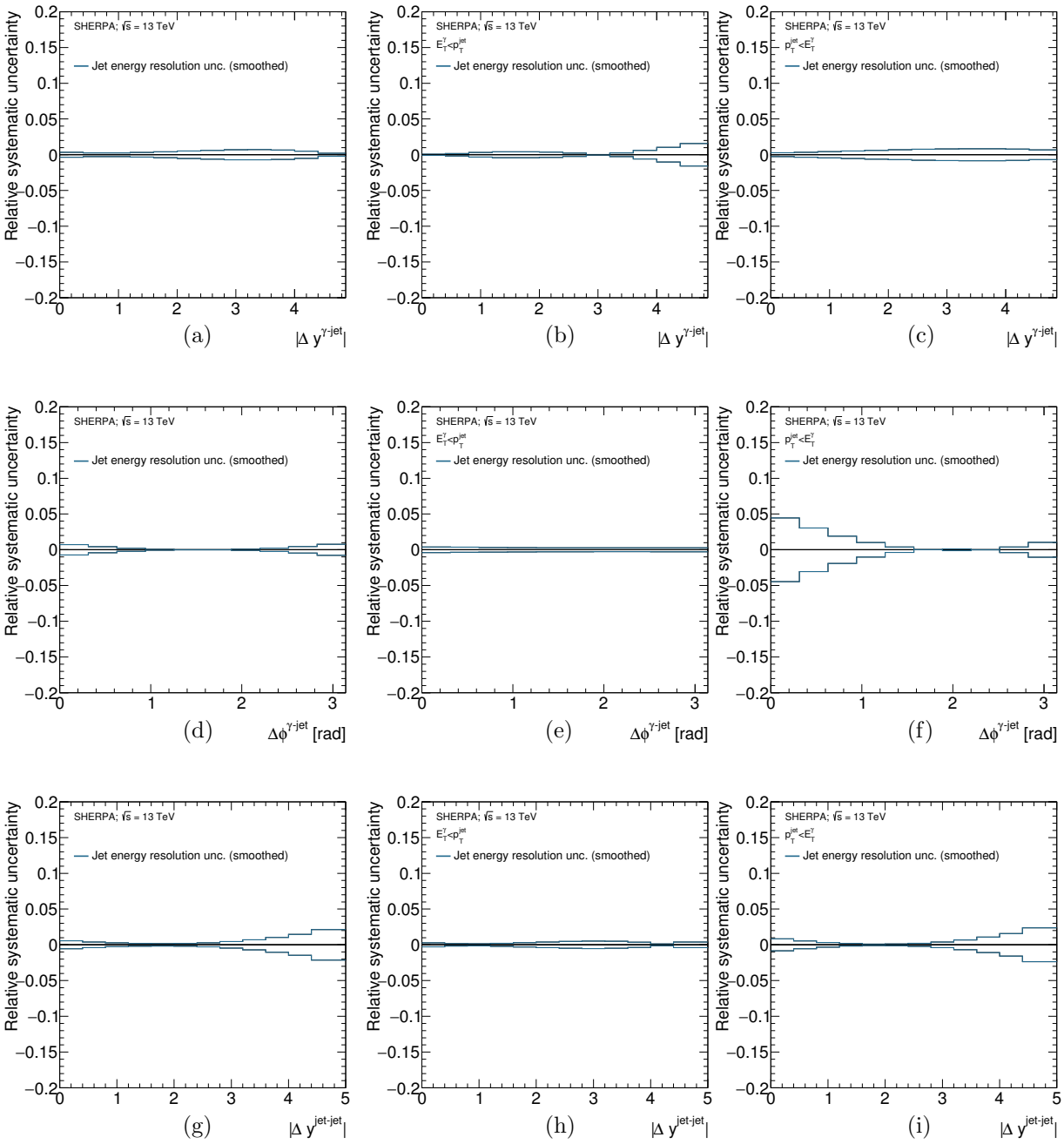


Figure 9.50: Systematic uncertainties on the measured cross section due to the uncertainty in the jet energy resolution as functions of $|\Delta y^{\gamma-\text{jet}}|$ (a,b,c), $\Delta\phi^{\gamma-\text{jet}}$ (d,e,f) and $|\Delta y^{\text{jet}-\text{jet}}|$ (g,h,i) for the total (first column), fragmentation-enriched (second column) and direct-enriched (third column) samples.

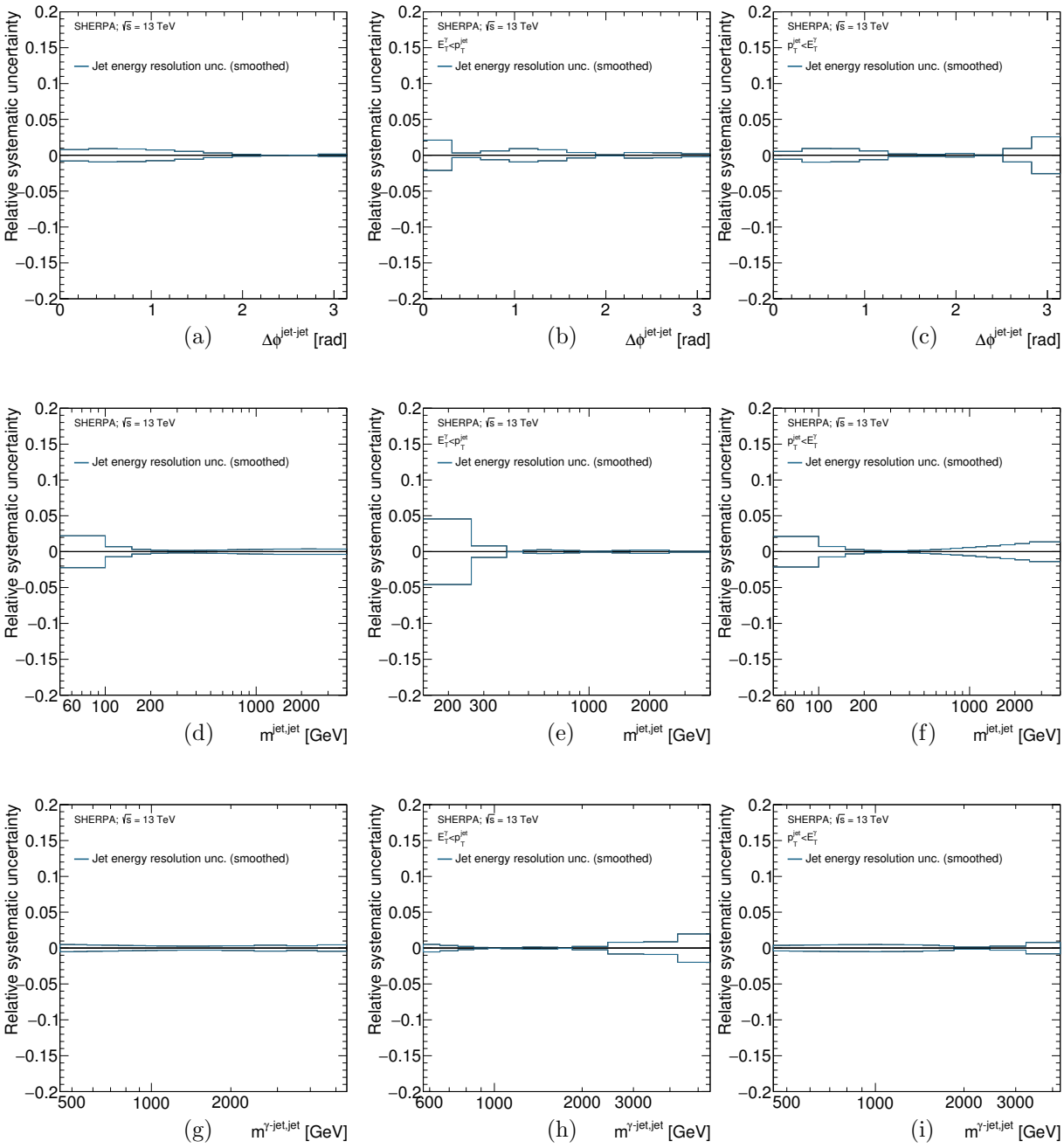


Figure 9.51: Systematic uncertainties on the measured cross section due to the uncertainty in the jet energy resolution as functions of $\Delta\phi^{\mathrm{jet-jet}}$ (a,b,c), $m^{\mathrm{jet-jet}}$ (d,e,f) and $m^{\gamma-\mathrm{jet-jet}}$ (g,h,i) for the total (first column), fragmentation-enriched (second column) and direct-enriched (third column) samples.

9.5.4 Parton shower and hadronisation model dependence

The effect due to the parton shower and hadronisation models of the generators used in the simulations was investigated in two separated ways:

- Signal leakage fractions: the signal leakage fractions of SHERPA were used to subtract the background via the 2D-sideband method for the nominal cross sections. The effects on the measured cross sections of using PYTHIA for the signal leakage fractions are shown in Figures 9.52 to 9.54. In every case the unfolding was performed with SHERPA.
- Unfolding corrections: SHERPA was used for the nominal cross sections. The effects on the measured cross sections of using PYTHIA for the unfolding are shown in Figures 9.55 to 9.57. In every case the signal leakage fractions of SHERPA are used.

Separated in this way, possible partial cancellations of the two effects are avoided. The resulting uncertainties from these two effects are added in quadrature when estimating the total systematic uncertainty.

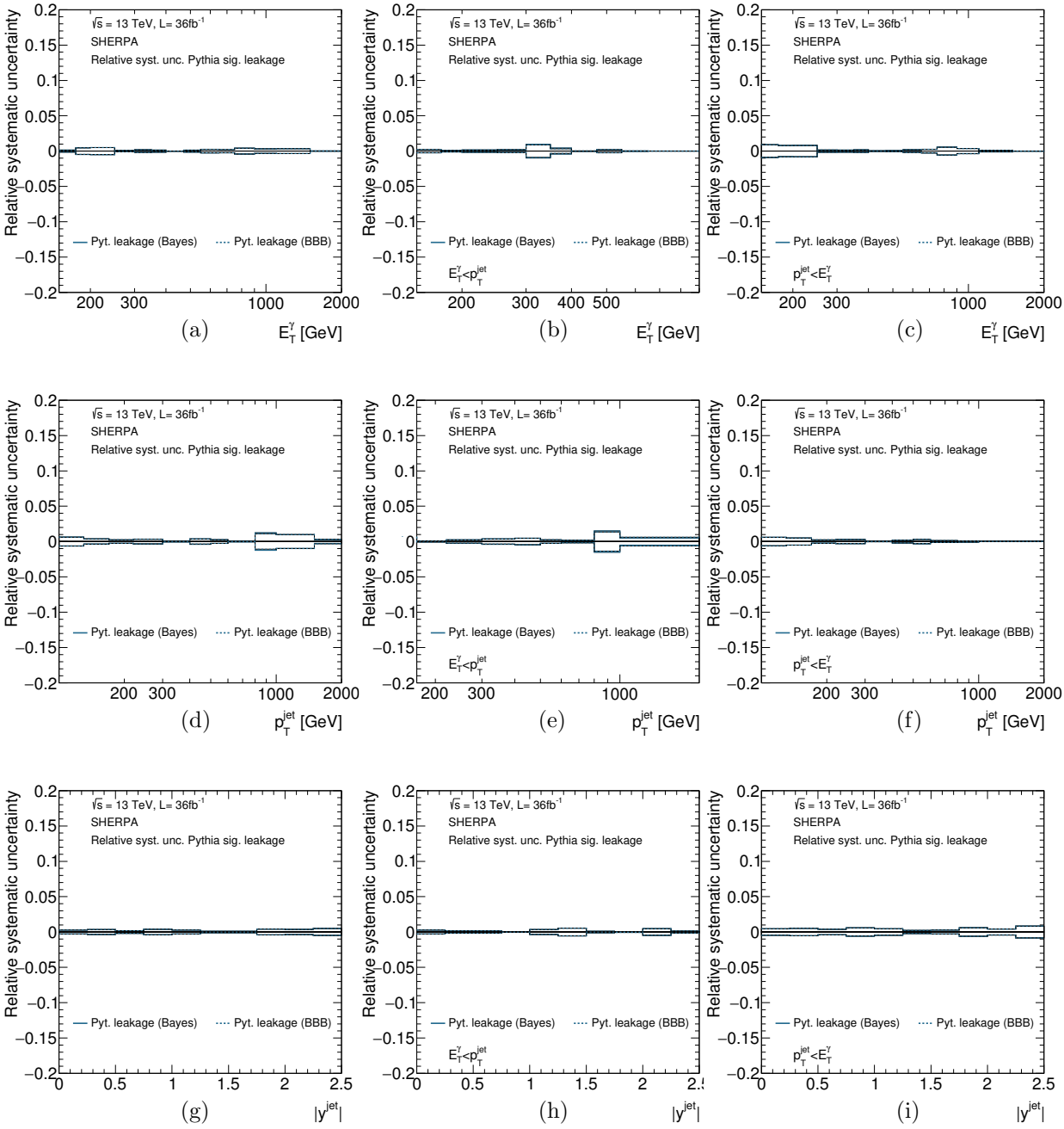


Figure 9.52: Systematic uncertainties on the measured cross sections due to the parton shower and hadronisation models as functions of E_{T}^{γ} (a,b,c), $p_{\mathrm{T}}^{\mathrm{jet}}$ (d,e,f) and $|y^{\mathrm{jet}}|$ (g,h,i) for the total (first column), fragmentation-enriched (second column) and direct-enriched (third column) samples. The signal purity was estimated alternatively using Pythia MC. For comparison, the uncertainty computed using the bin-by-bin unfolding is also shown (dashed lines).

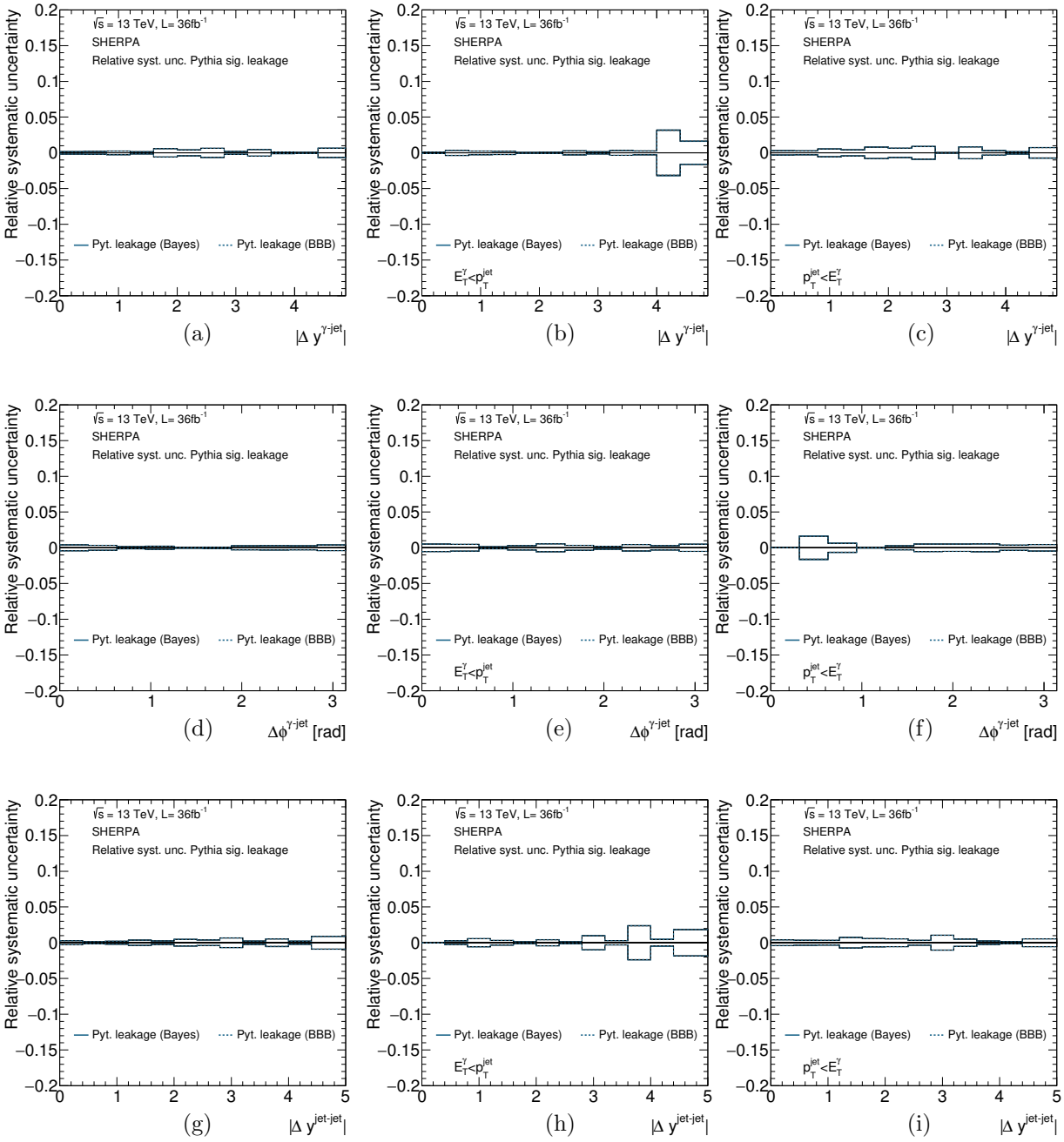


Figure 9.53: Systematic uncertainties on the measured cross sections due to the parton shower and hadronisation models as functions of $|\Delta y^{\gamma-\mathrm{jet}}|$ (a,b,c), $\Delta\phi^{\gamma-\mathrm{jet}}$ (d,e,f) and $|\Delta y^{\mathrm{jet}-\mathrm{jet}}|$ (g,h,i) for the total (first column), fragmentation-enriched (second column) and direct-enriched (third column) samples. The signal purity was estimated alternatively using PYTHIA MC. For comparison, the uncertainty computed using the bin-by-bin unfolding is also shown (dashed lines).

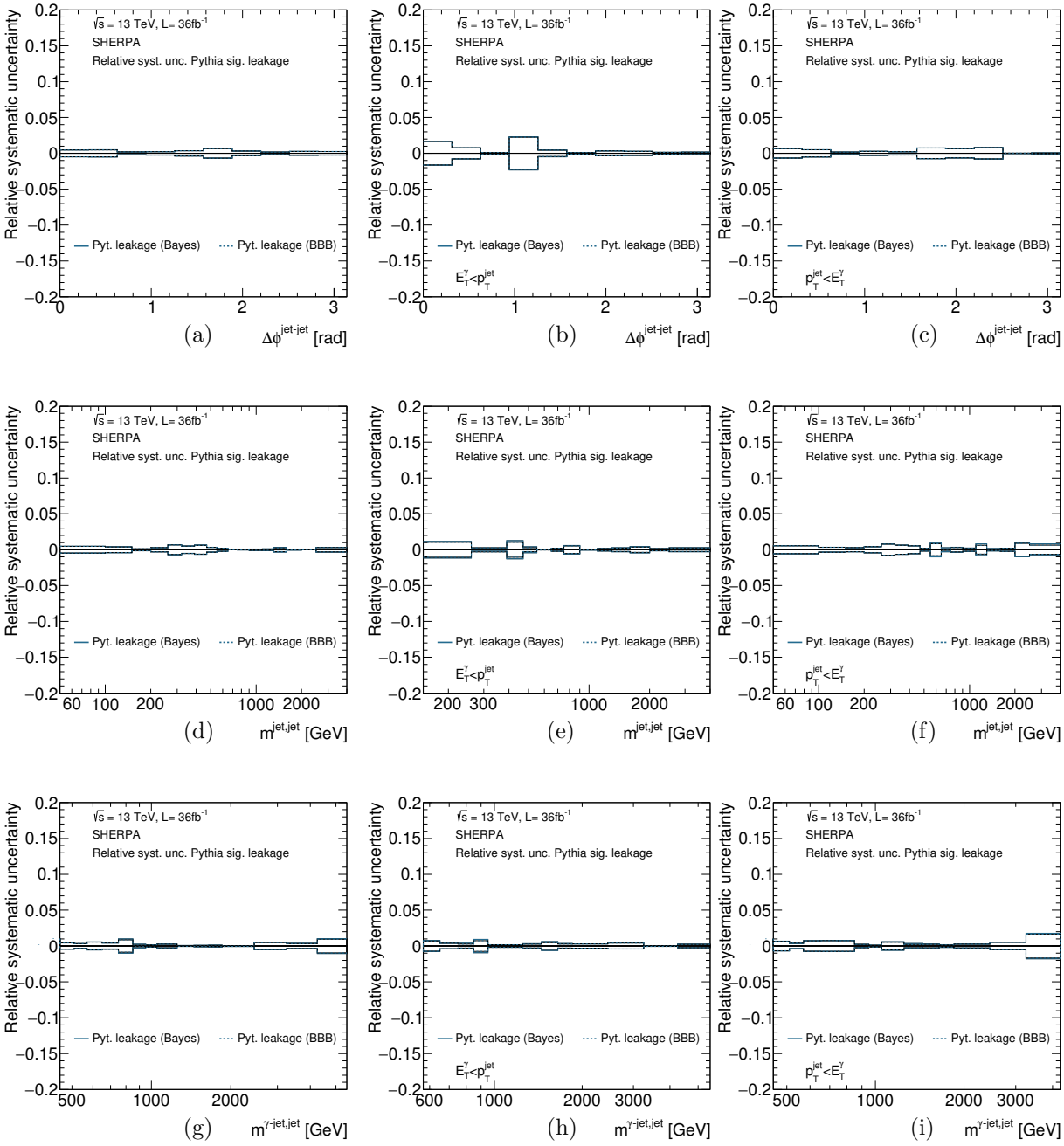


Figure 9.54: Systematic uncertainties on the measured cross sections due to the parton shower and hadronisation models as functions of $\Delta\phi^{\text{jet}-\text{jet}}$ (a,b,c), $m^{\text{jet}-\text{jet}}$ (d,e,f) and $m^{\gamma-\text{jet}-\text{jet}}$ (g,h,i) for the total (first column), fragmentation-enriched (second column) and direct-enriched (third column) samples. The signal purity was estimated alternatively using PYTHIA MC. For comparison, the uncertainty computed using the bin-by-bin unfolding is also shown (dashed lines).

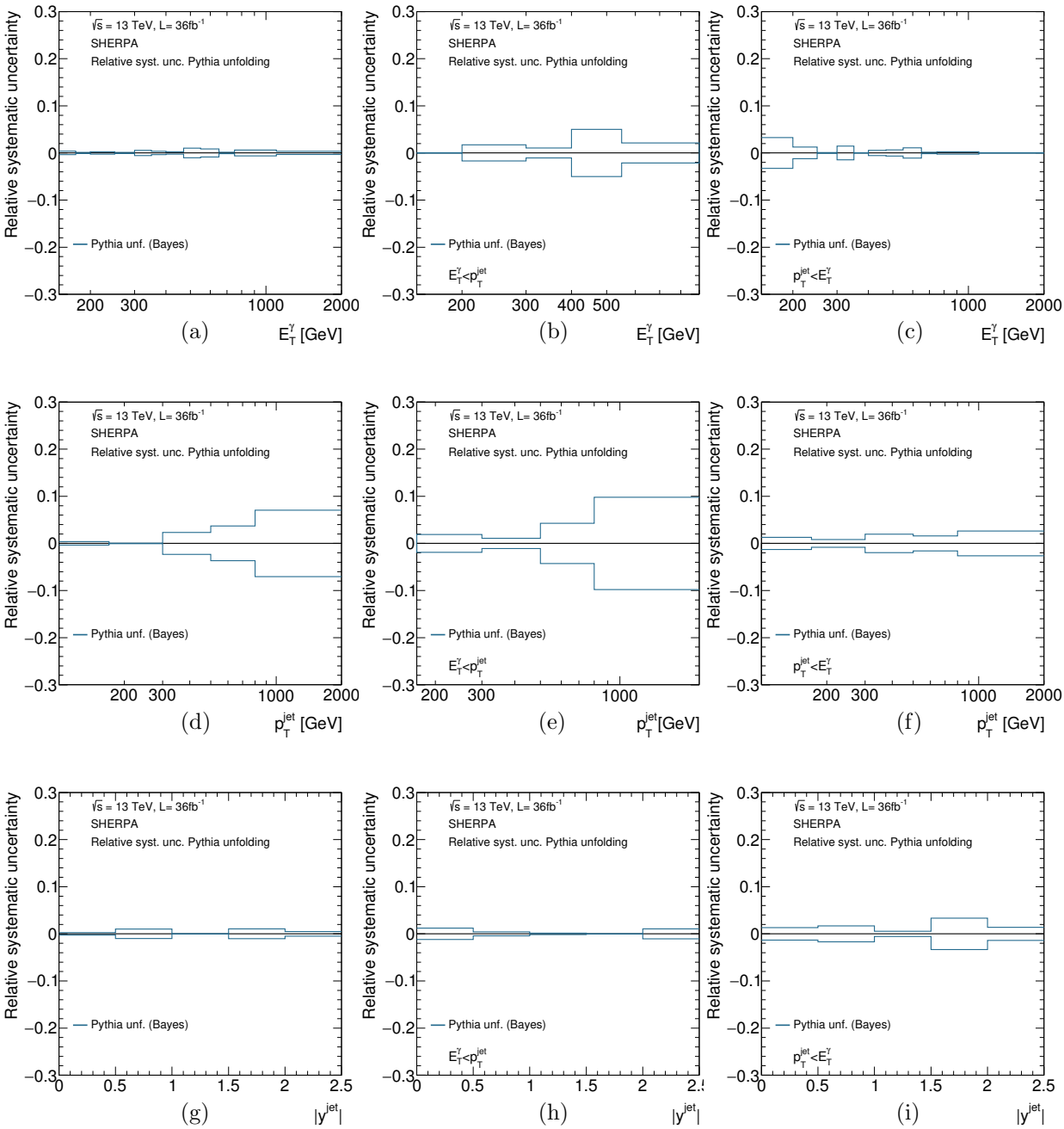


Figure 9.55: Systematic uncertainties on the measured cross section due to the parton shower and hadronisation models as functions of E_{T}^{γ} (a,b,c), $p_{\mathrm{T}}^{\mathrm{jet}}$ (d,e,f) and $|y^{\mathrm{jet}}|$ (g,h,i) for the total (first column), fragmentation-enriched (second column) and direct-enriched (third column) samples. The unfolding was alternatively performed using Pythia MC.

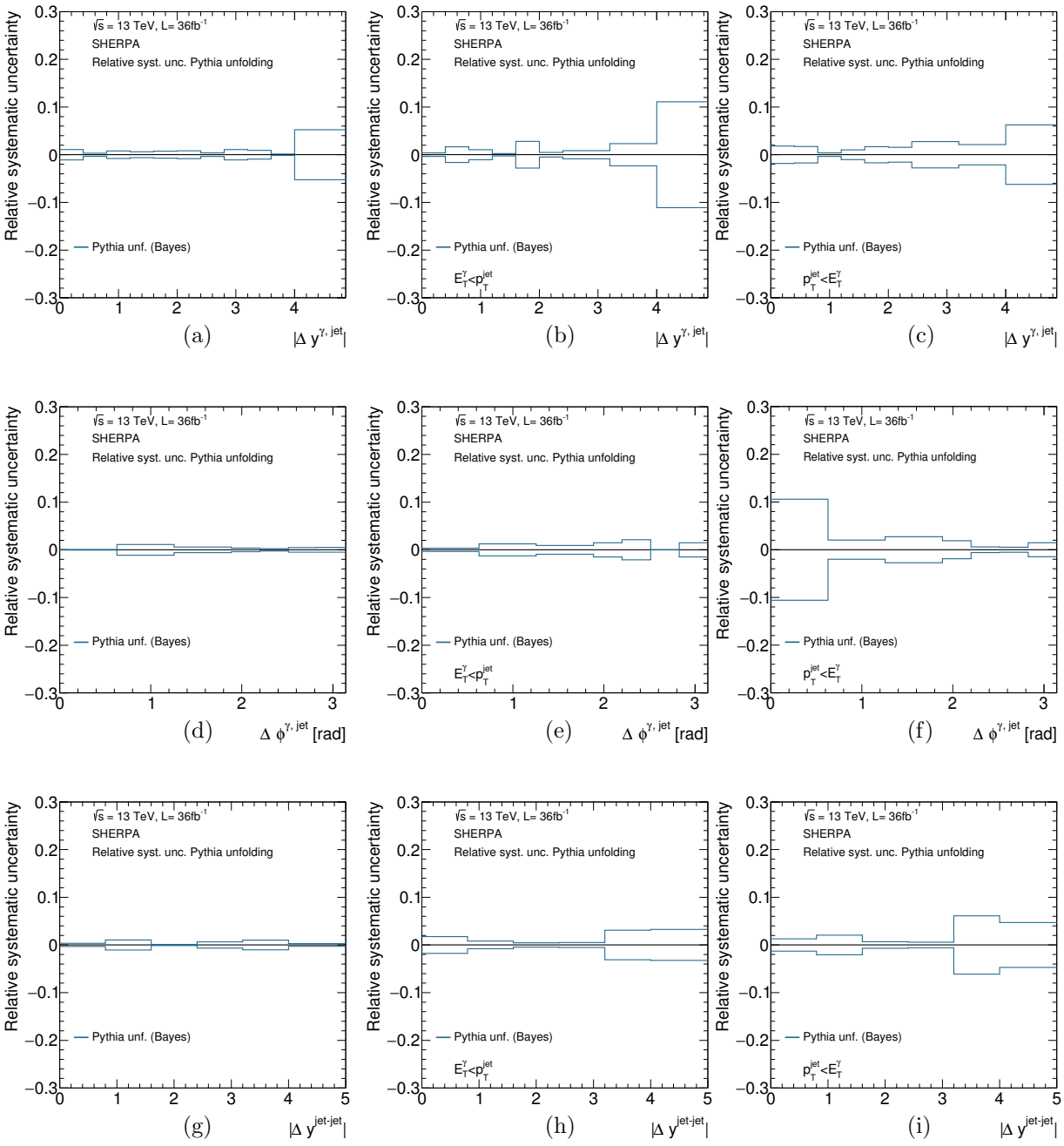


Figure 9.56: Systematic uncertainties on the measured cross section due to the parton shower and hadronisation models as functions of $|\Delta y^{\gamma-\text{jet}}|$ (a,b,c), $\Delta\phi^{\gamma-\text{jet}}$ (d,e,f) and $|\Delta y^{\text{jet}-\text{jet}}|$ (g,h,i) for the total (first column), fragmentation-enriched (second column) and direct-enriched (third column) samples. The unfolding was alternatively performed using Pythia MC.

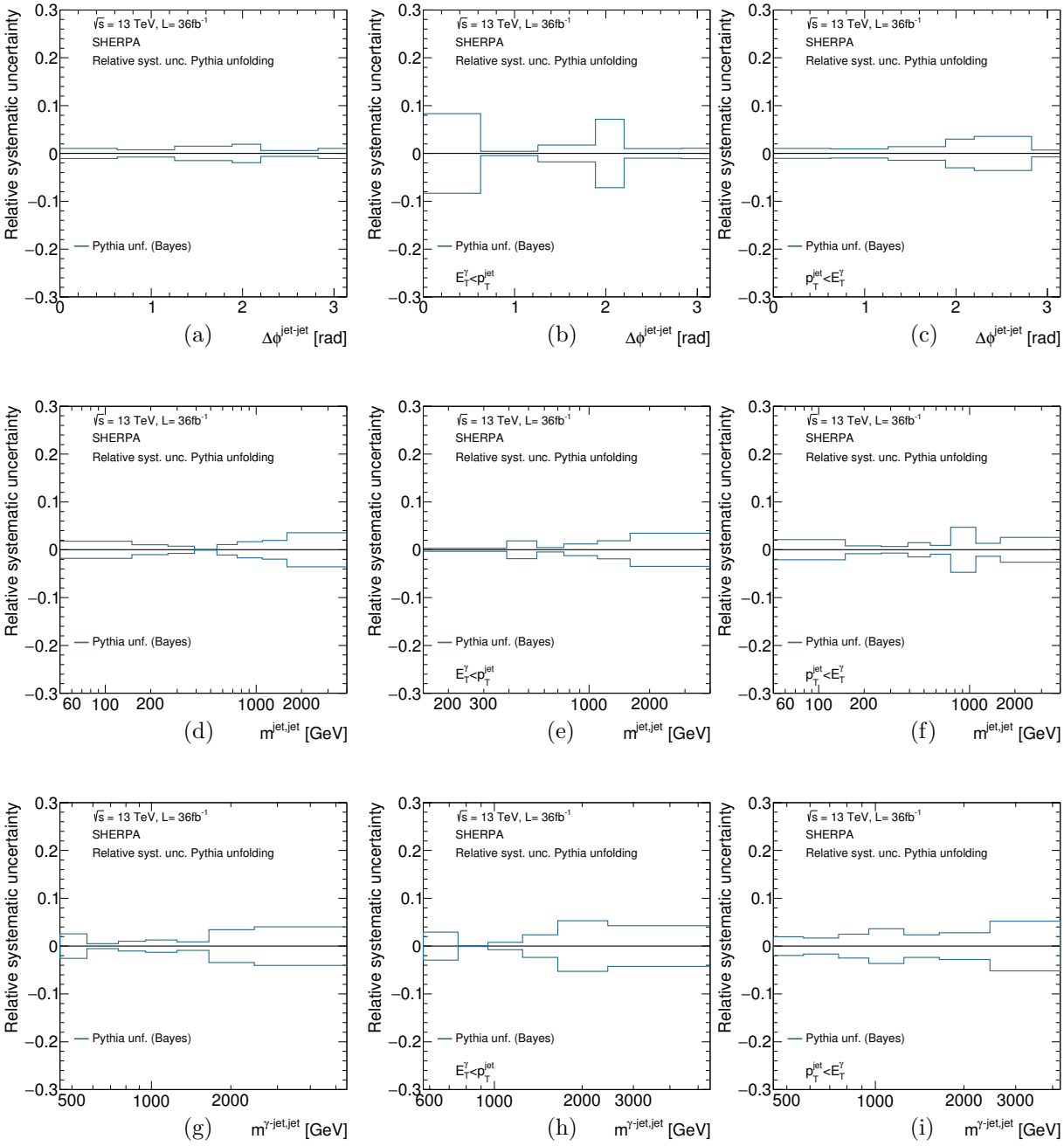


Figure 9.57: Systematic uncertainties on the measured cross section due to the parton shower and hadronisation models as functions of $\Delta\phi^{\text{jet}-\text{jet}}$ (a,b,c), $m^{\text{jet}-\text{jet}}$ (d,e,f) and $m^{\gamma-\text{jet}-\text{jet}}$ (g,h,i) for the total (first column), fragmentation-enriched (second column) and direct-enriched (third column) samples. The unfolding was alternatively performed using Pythia MC.

9.5.5 Photon-identification efficiency

The uncertainty on the photon identification efficiency was estimated by propagating the uncertainties in the scale factors, which were applied to the MC events to match the tight identification efficiency between data and simulation, to the cross section. Figures 9.58 to 9.60 show the resulting uncertainties.

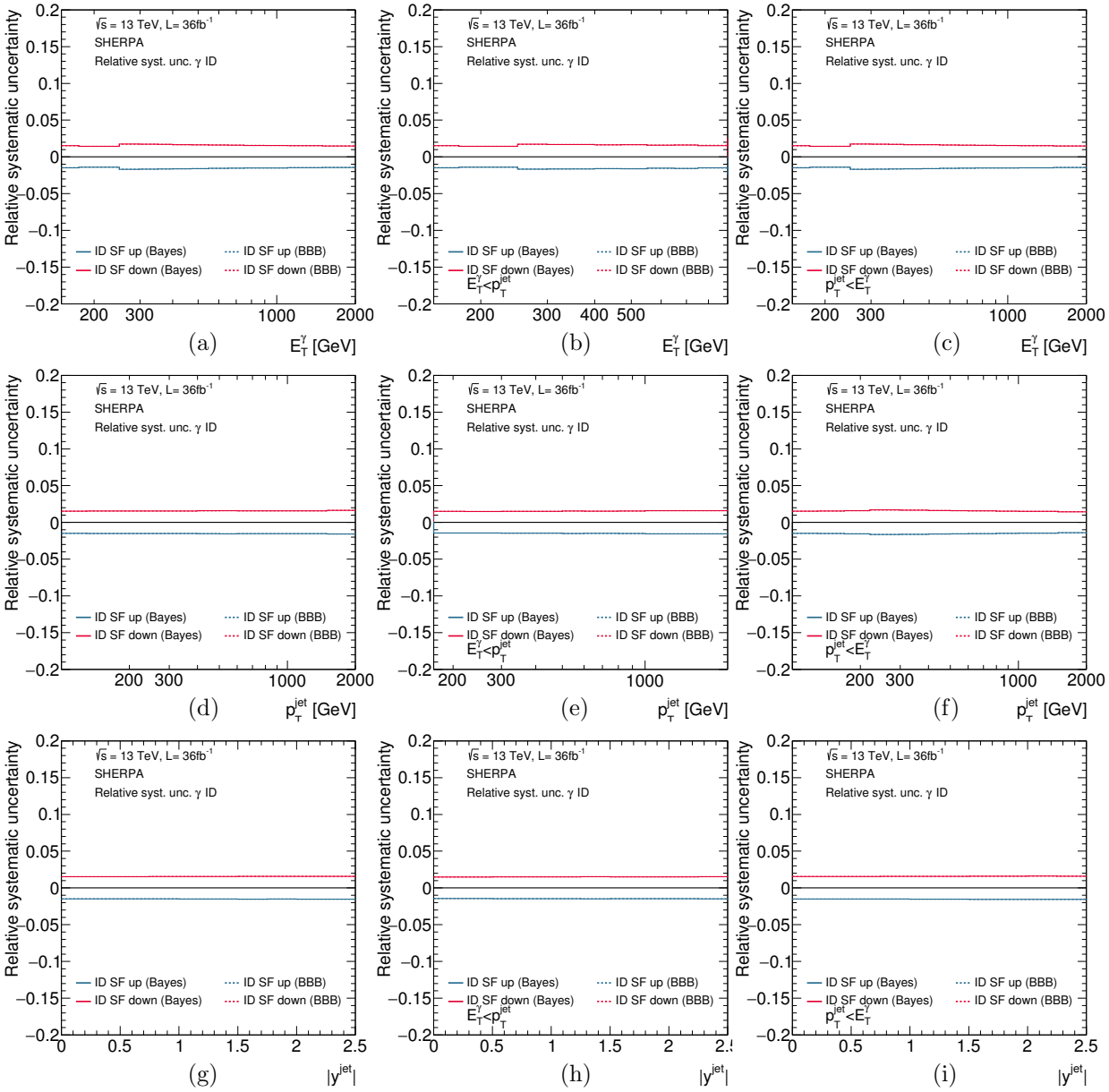


Figure 9.58: Systematic uncertainties on the measured cross sections due to the photon-ID efficiency as functions of E_{T}^{γ} (a,b,c), $p_{\mathrm{T}}^{\mathrm{jet}}$ (d,e,f) and $|y^{\mathrm{jet}}|$ (g,h,i) for the total (first column), fragmentation-enriched (second column) and direct-enriched (third column) samples. For comparison, the uncertainty computed using the bin-by-bin unfolding is also shown (dashed lines).

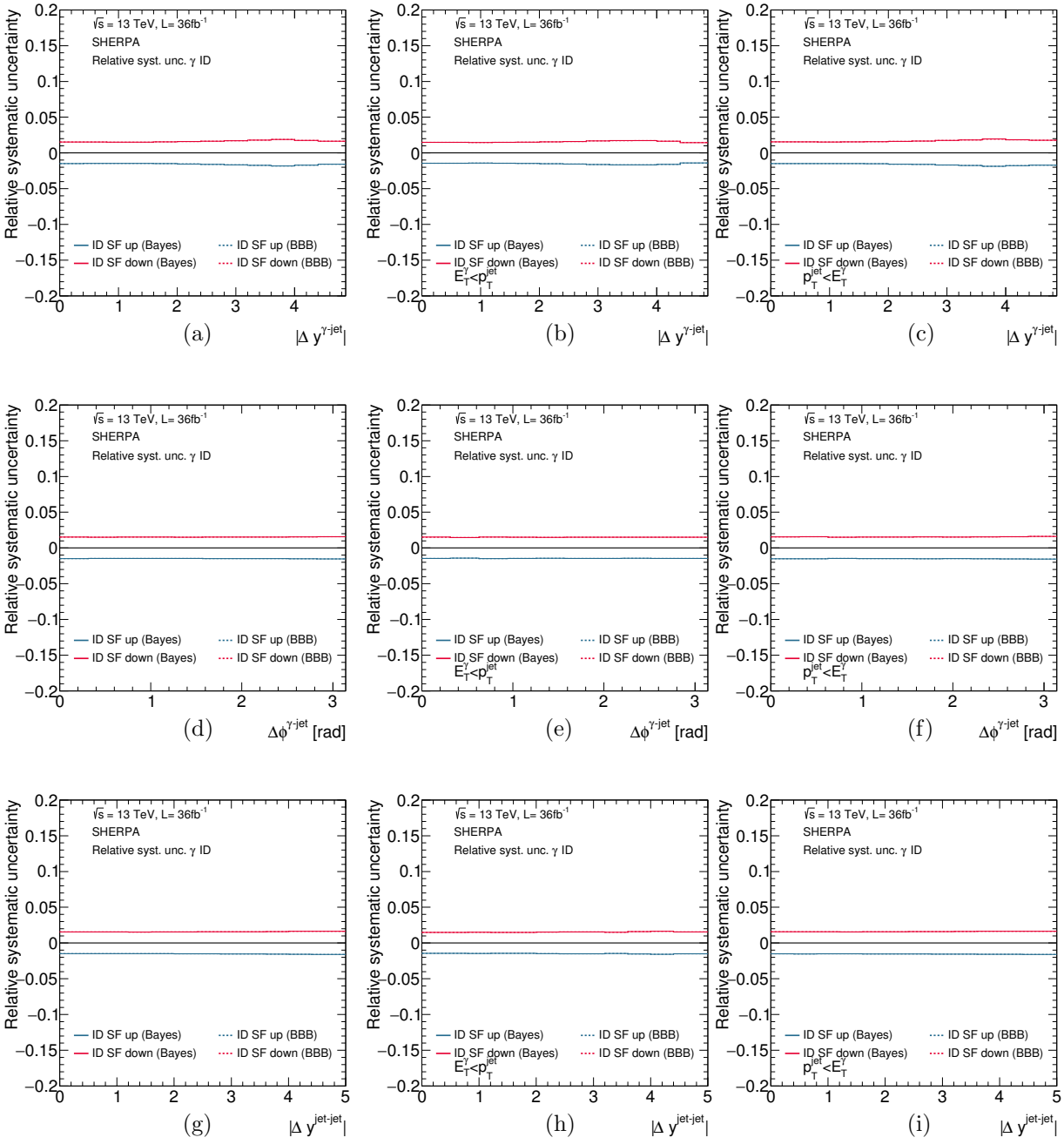


Figure 9.59: Systematic uncertainties on the measured cross sections due to the photon-ID efficiency as functions of $|\Delta y^{\gamma-\text{jet}}|$ (a,b,c), $\Delta\phi^{\gamma-\text{jet}}$ (d,e,f) and $|\Delta y^{\text{jet}-\text{jet}}|$ (g,h,i) for the total (first column), fragmentation-enriched (second column) and direct-enriched (third column) samples. For comparison, the uncertainty computed using the bin-by-bin unfolding is also shown (dashed lines).

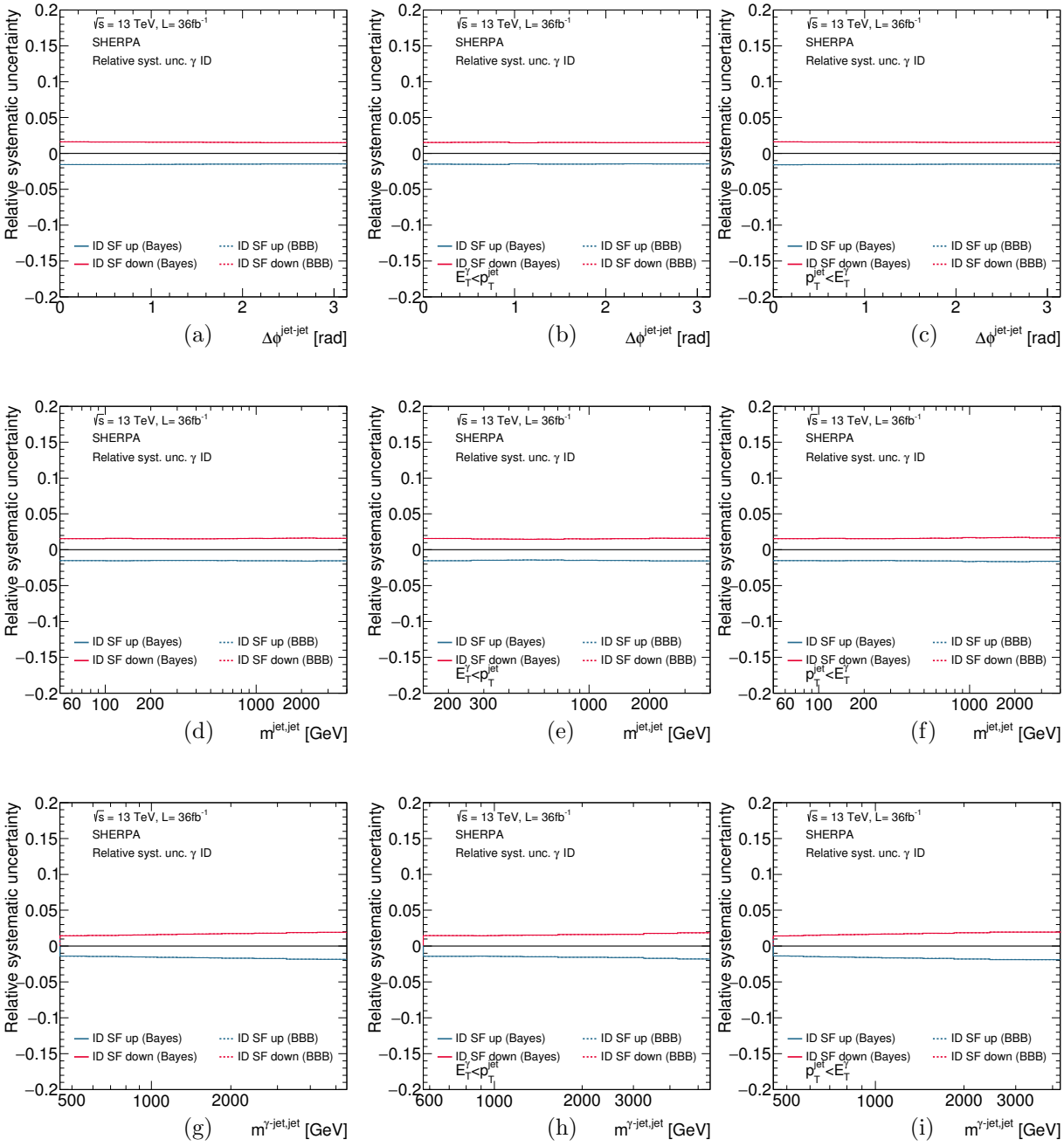


Figure 9.60: Systematic uncertainties on the measured cross sections due to the uncertainty in the photon-ID efficiency as functions of $\Delta\phi^{\text{jet}-\text{jet}}$ (a,b,c), $m^{\text{jet}-\text{jet}}$ (d,e,f) and $m^{\gamma-\text{jet}-\text{jet}}$ (g,h,i) for the total (first column), fragmentation-enriched (second column) and direct-enriched (third column) samples. For comparison, the uncertainty computed using the bin-by-bin unfolding is also shown (dashed lines).

9.5.6 Choice of background control regions

The effect of the alternative definitions of the background control regions on the signal yield and, therefore, in the cross sections were evaluated. The considered variations are the same ones as explained in Section 6.6.5. The relative differences in the cross sections due to the variation of the lower limit in isolation of the non-isolated control regions are shown in Figures 9.61 to 9.63. The effect of removing the upper limit of these non-isolated control region is shown in Figure 9.64 to 9.66. The definition of the non-tight control regions was varied with three different loose' definitions: the looser loose' (LoosePrime5) and the two alternatives of tighter loose' (LoosePrime3 and LoosePrime2). The envelope of the three variations after smoothing was taken as the final systematic uncertainty, which is shown in Figures 9.67 to 9.69.

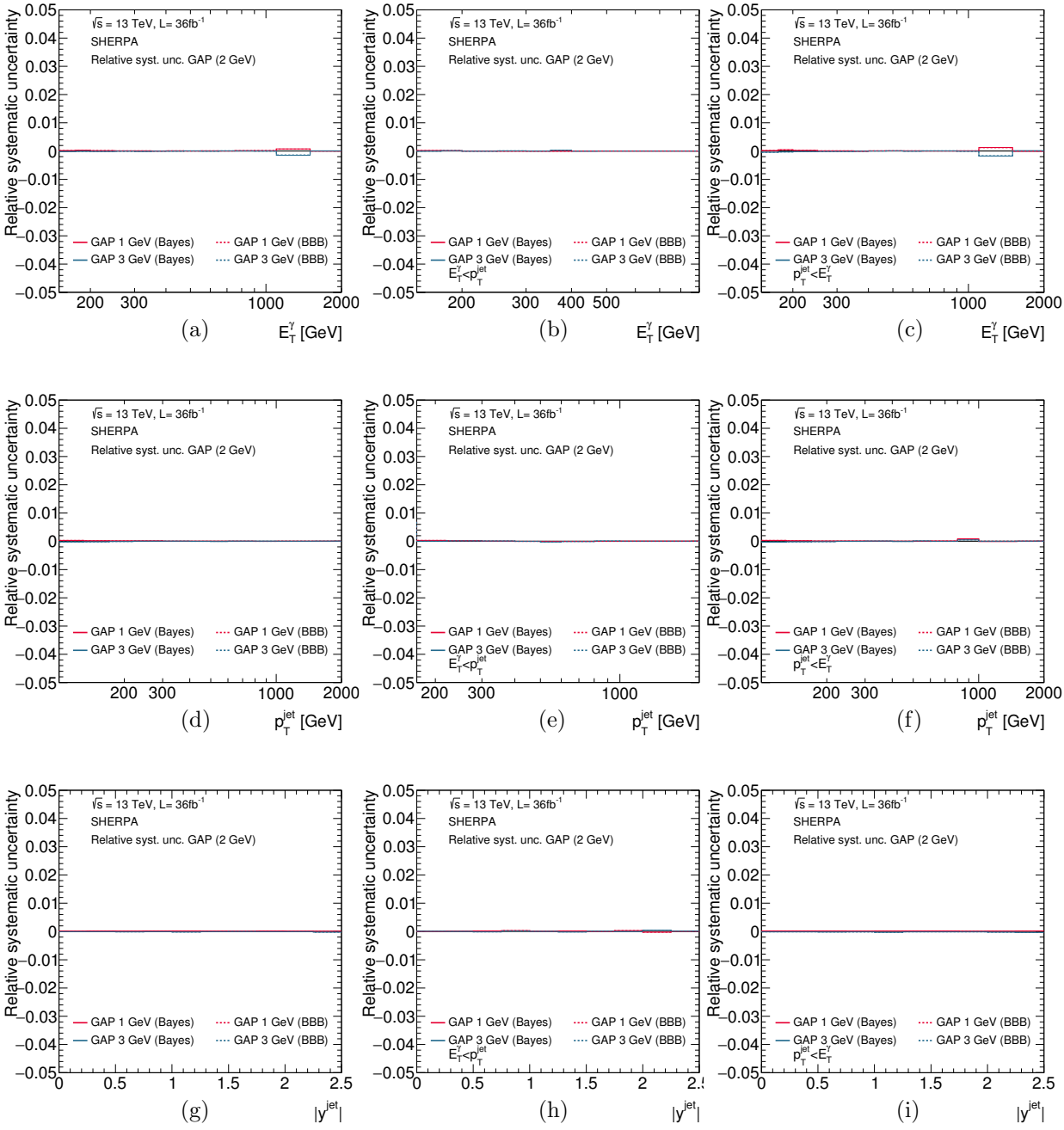


Figure 9.61: Systematic uncertainties on the measured cross sections due to the choice of the $E_{\mathrm{T}}^{\mathrm{iso}}$ lower limit of the non-isolated control regions as functions of E_{T}^{γ} (a,b,c), $p_{\mathrm{T}}^{\mathrm{jet}}$ (d,e,f) and $|y^{\mathrm{jet}}|$ (g,h,i) for the total (first column), fragmentation-enriched (second column) and direct-enriched (third column) samples. For comparison, the uncertainty computed using the bin-by-bin unfolding is also shown (dashed lines).

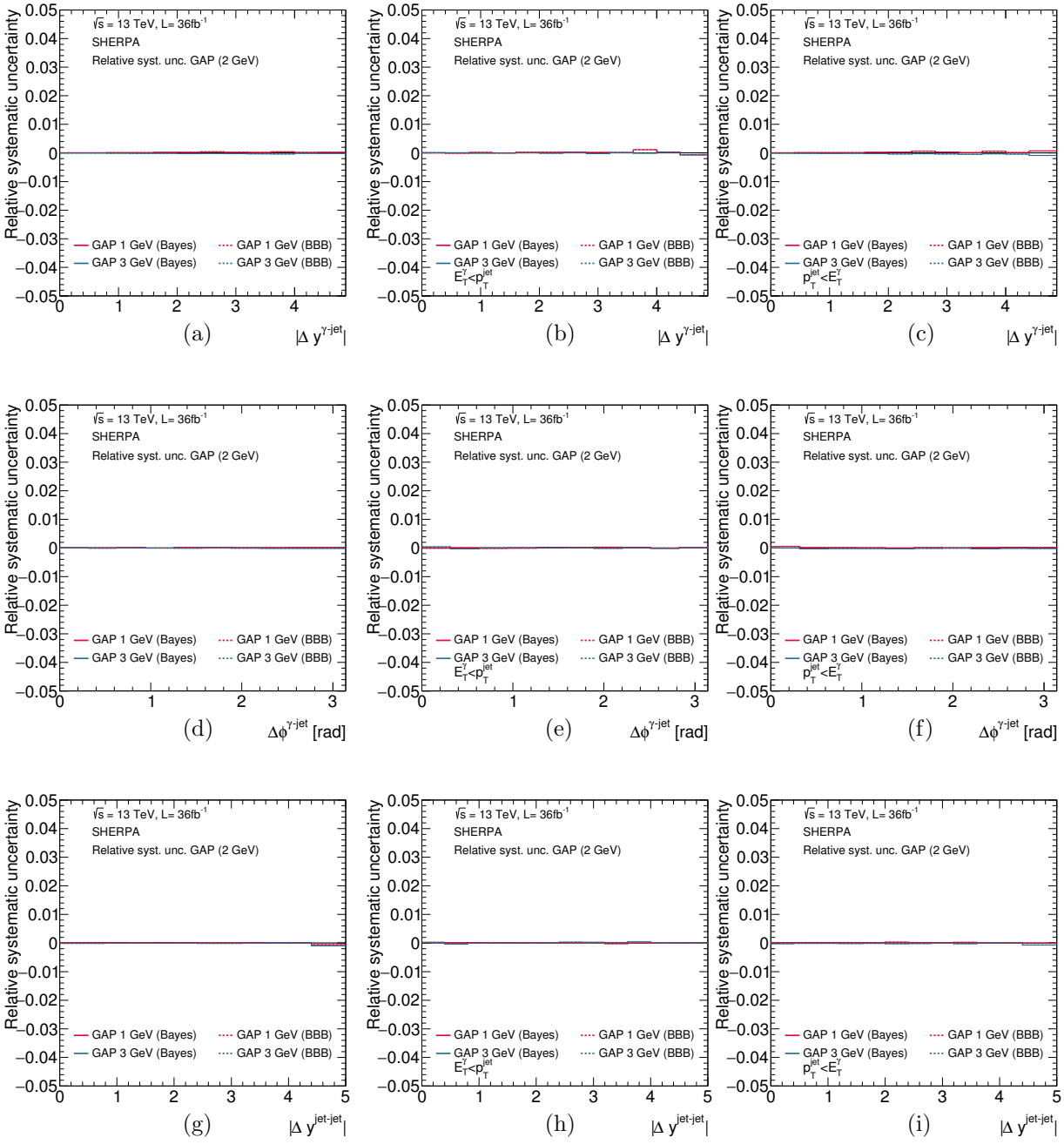


Figure 9.62: Systematic uncertainties on the measured cross sections due to the choice of the $E_{\mathrm{T}}^{\mathrm{iso}}$ lower limit of the non-isolated control regions as functions of $|\Delta y^{\gamma-\mathrm{jet}}|$ (a,b,c), $\Delta\phi^{\gamma-\mathrm{jet}}$ (d,e,f) and $|\Delta y^{\mathrm{jet}-\mathrm{jet}}|$ (g,h,i) for the total (first column), fragmentation-enriched (second column) and direct-enriched (third column) samples. For comparison, the uncertainty computed using the bin-by-bin unfolding is also shown (dashed lines).

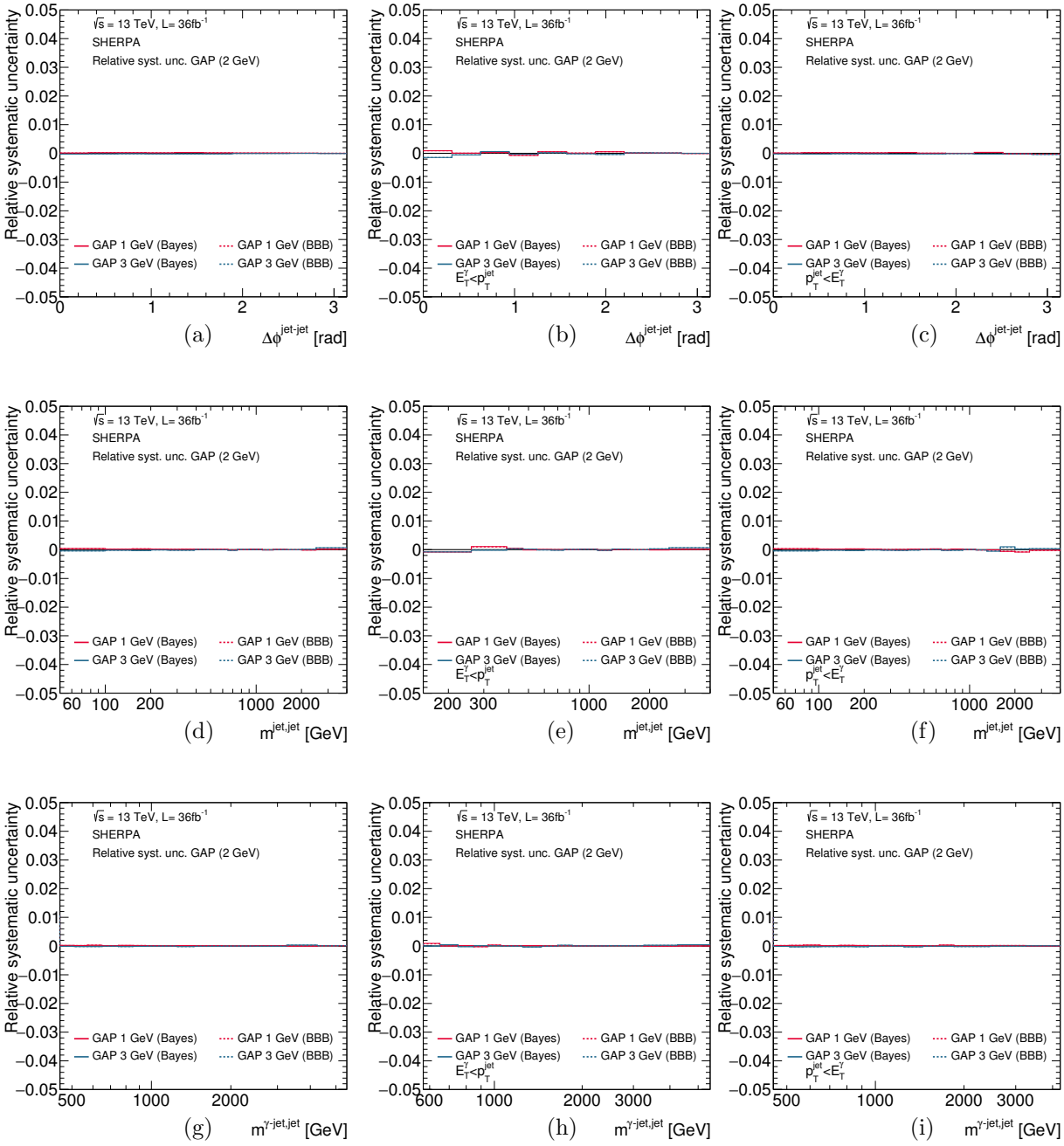


Figure 9.63: Systematic uncertainties on the measured cross sections due to the uncertainty in the choice of the $E_{\mathrm{T}}^{\mathrm{iso}}$ lower limit of the non-isolated control regions as functions of $\Delta\phi^{\mathrm{jet-jet}}$ (a,b,c), $m^{\mathrm{jet-jet}}$ (d,e,f) and $m^{\gamma-\mathrm{jet-jet}}$ (g,h,i) for the total (first column), fragmentation-enriched (second column) and direct-enriched (third column) samples. For comparison, the uncertainty computed using the bin-by-bin unfolding is also shown (dashed lines).

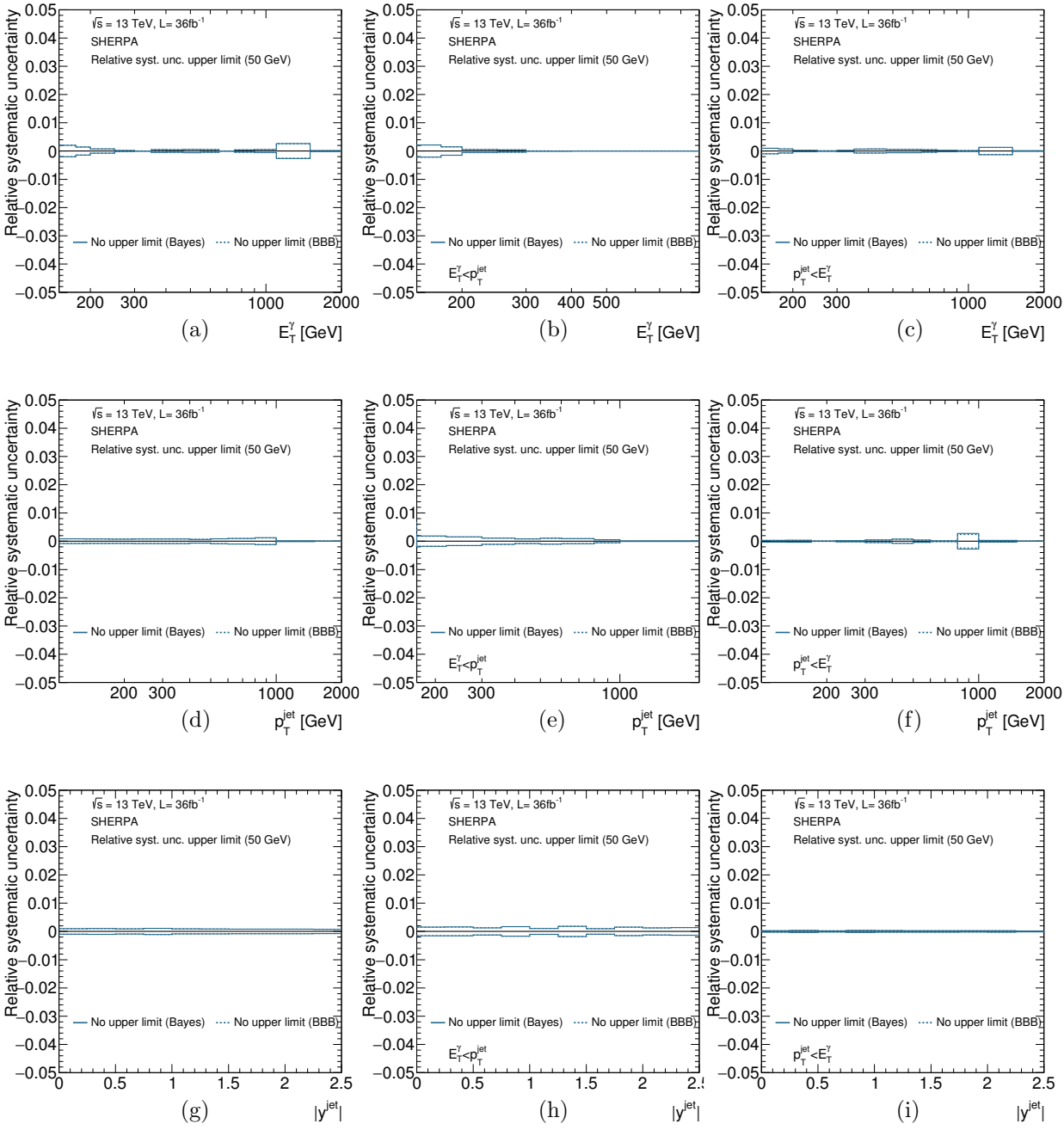


Figure 9.64: Systematic uncertainties on the measured cross sections due to the choice of the $E_{\mathrm{T}}^{\mathrm{iso}}$ upper limit of the non-isolated control regions as functions of E_{T}^{γ} (a,b,c), $p_{\mathrm{T}}^{\mathrm{jet}}$ (d,e,f) and $|y^{\mathrm{jet}}|$ (g,h,i) for the total (first column), fragmentation-enriched (second column) and direct-enriched (third column) samples. For comparison, the uncertainty computed using the bin-by-bin unfolding is also shown (dashed lines).

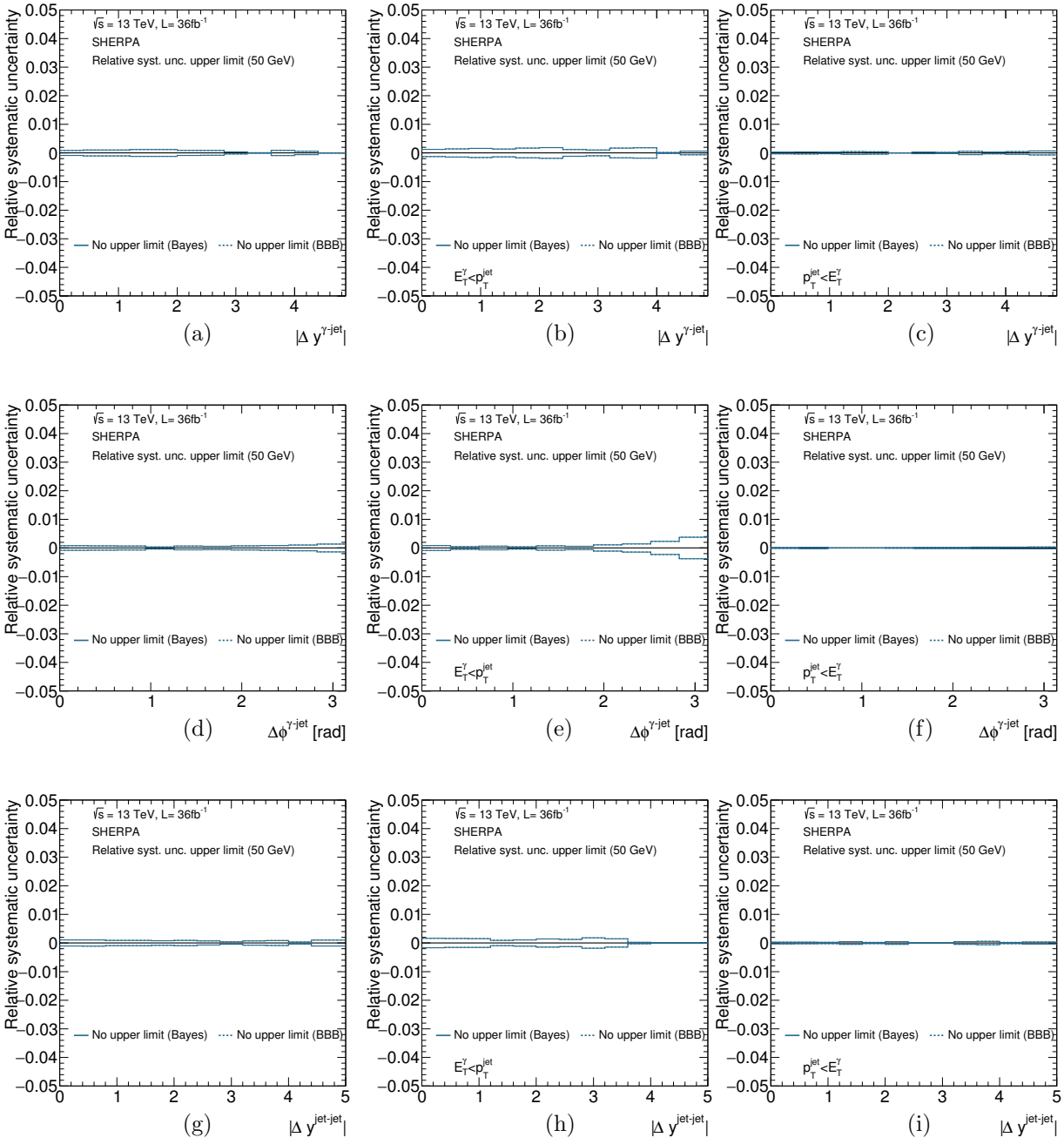


Figure 9.65: Systematic uncertainties on the measured cross sections due to the choice of the $E_{\mathrm{T}}^{\mathrm{iso}}$ upper limit of the non-isolated control regions as functions of $|\Delta y^{\gamma-\mathrm{jet}}|$ (a,b,c), $\Delta\phi^{\gamma-\mathrm{jet}}$ (d,e,f) and $|\Delta y^{\mathrm{jet}-\mathrm{jet}}|$ (g,h,i) for the total (first column), fragmentation-enriched (second column) and direct-enriched (third column) samples. For comparison, the uncertainty computed using the bin-by-bin unfolding is also shown (dashed lines).

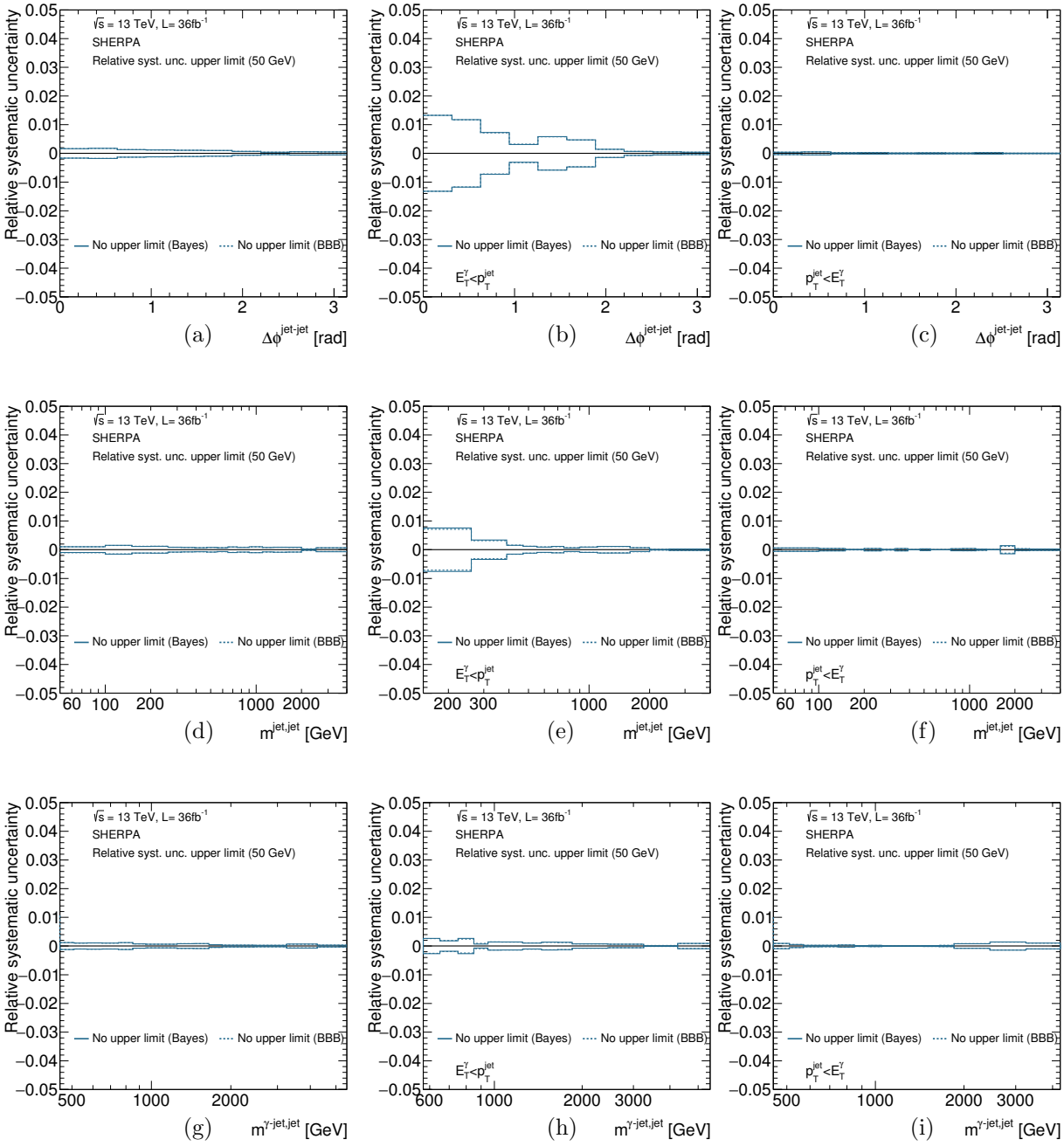


Figure 9.66: Systematic uncertainties on the measured cross sections due to the uncertainty in the choice of the $E_{\mathrm{T}}^{\mathrm{iso}}$ upper limit of the non-isolated control regions as functions of $\Delta\phi^{\mathrm{jet-jet}}$ (a,b,c), $m^{\mathrm{jet-jet}}$ (d,e,f) and $m^{\gamma-\mathrm{jet-jet}}$ (g,h,i) for the total (first column), fragmentation-enriched (second column) and direct-enriched (third column) samples. For comparison, the uncertainty computed using the bin-by-bin unfolding is also shown (dashed lines).

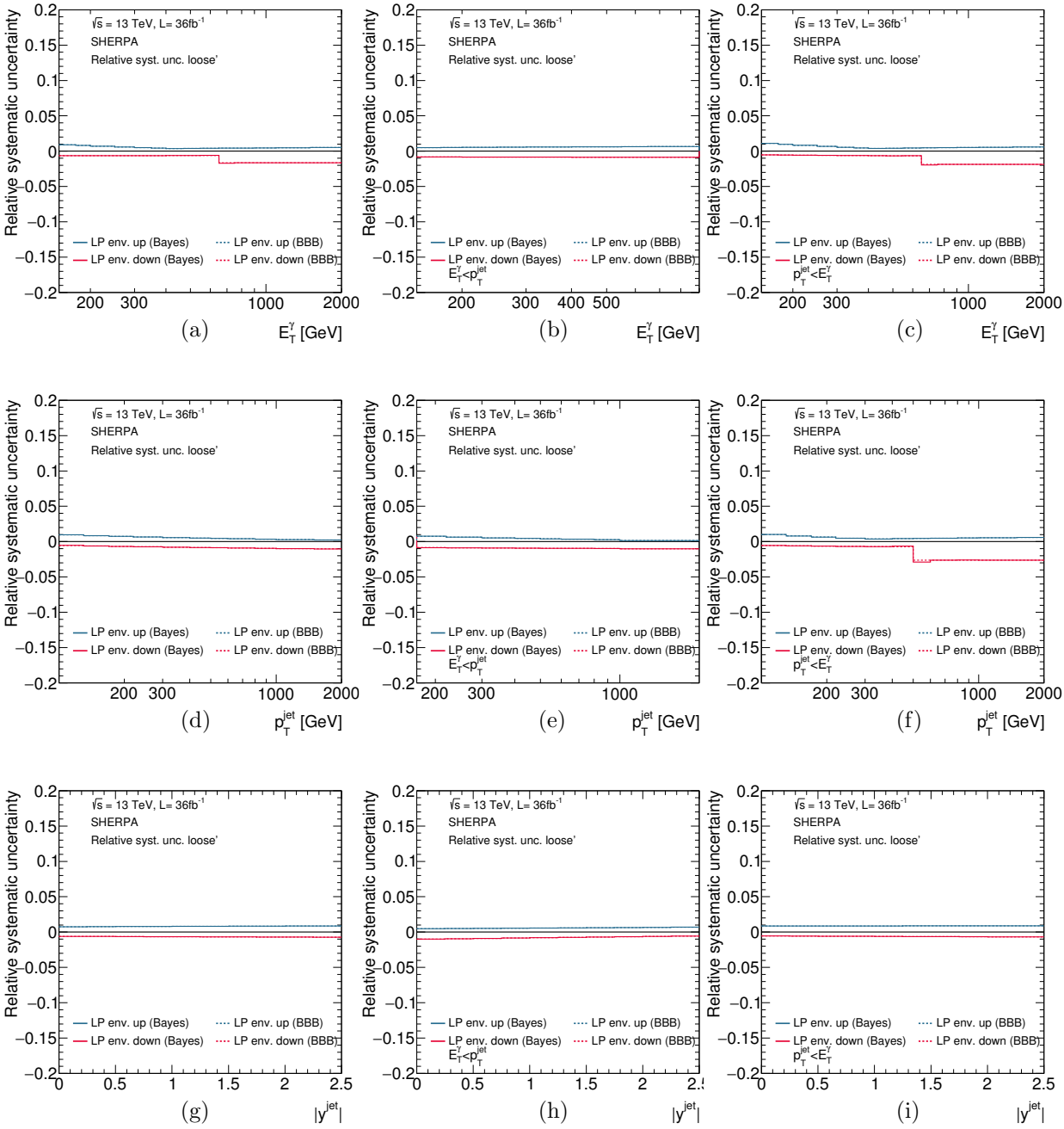


Figure 9.67: Systematic uncertainties on the measured cross sections due to the choice of the non-tight control regions as functions of E_{T}^{γ} (a,b,c), $p_{\mathrm{T}}^{\mathrm{jet}}$ (d,e,f) and $|y^{\mathrm{jet}}|$ (g,h,i) for the total (first column), fragmentation-enriched (second column) and direct-enriched (third column) samples. For comparison, the uncertainty computed using the bin-by-bin unfolding is also shown (dashed lines).

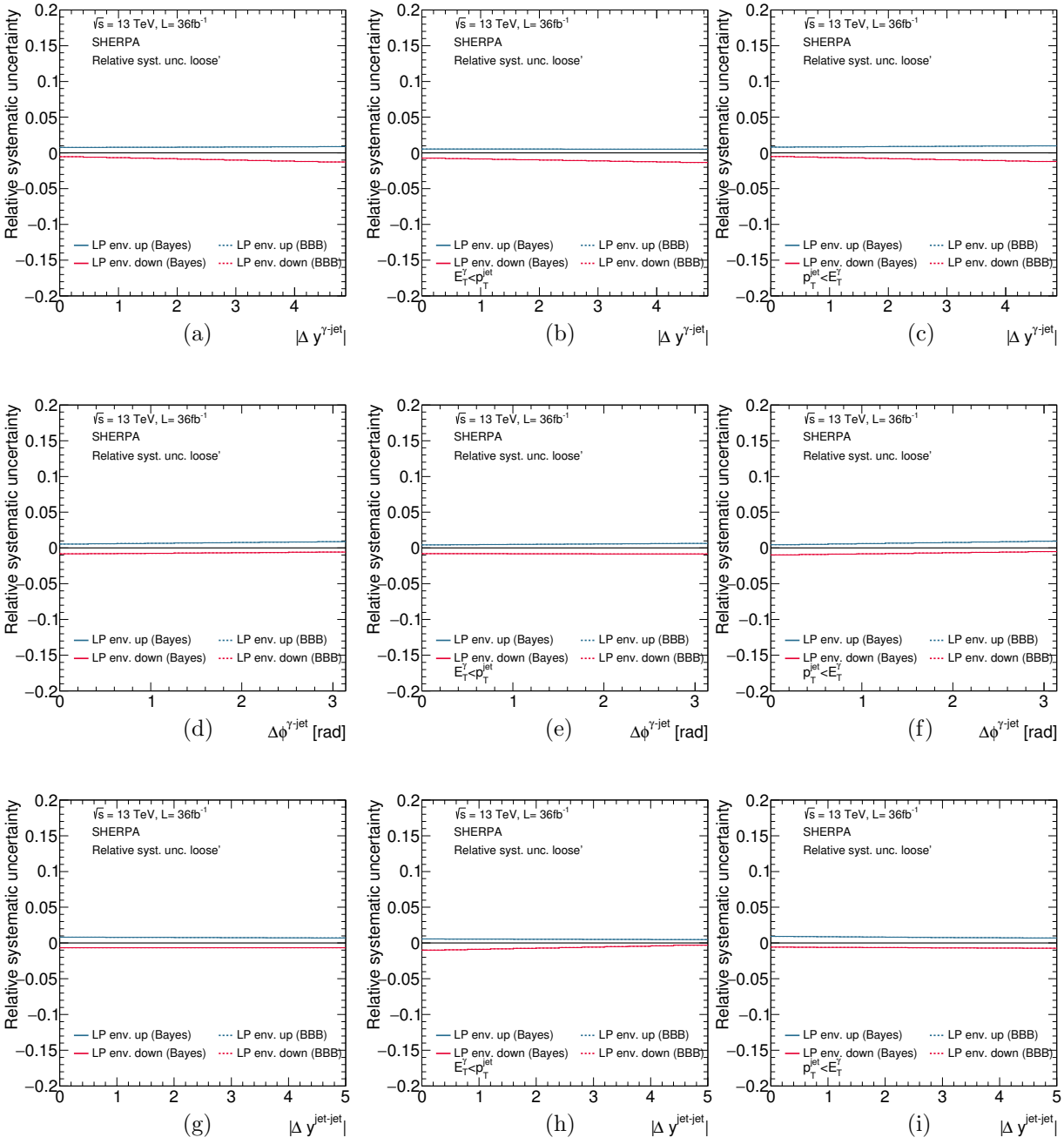


Figure 9.68: Systematic uncertainties on the measured cross sections due to the choice of the non-tight control regions as functions of $|\Delta y^{\gamma-\text{jet}}|$ (a,b,c), $\Delta\phi^{\gamma-\text{jet}}$ (d,e,f) and $|\Delta y^{\text{jet}-\text{jet}}|$ (g,h,i) for the total (first column), fragmentation-enriched (second column) and direct-enriched (third column) samples. For comparison, the uncertainty computed using the bin-by-bin unfolding is also shown (dashed lines).

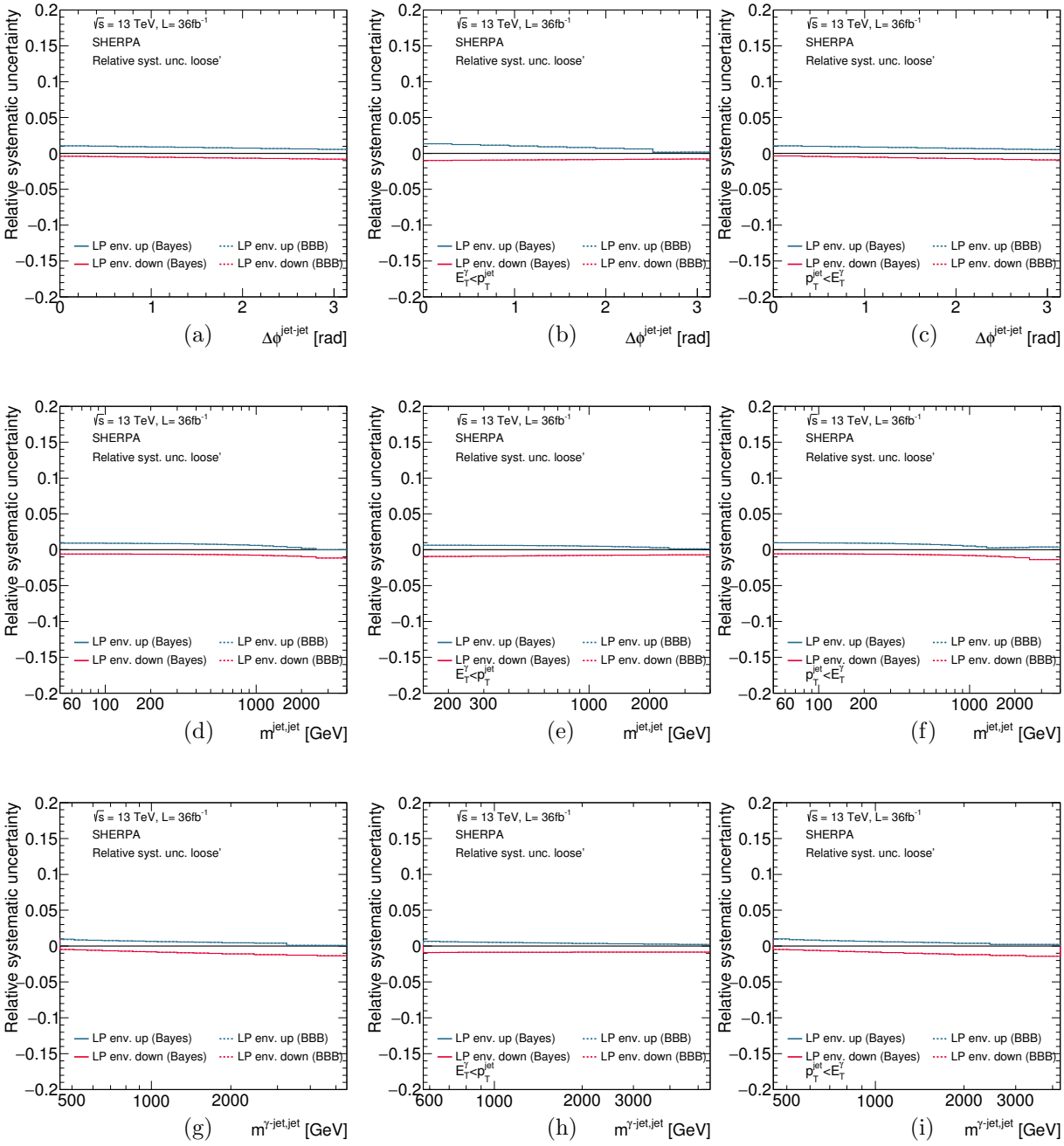


Figure 9.69: Systematic uncertainties on the measured cross sections due to the uncertainty in the choice the non-tight control regions as functions of $\Delta\phi^{\text{jet}-\text{jet}}$ (a,b,c), $m^{\text{jet}-\text{jet}}$ (d,e,f) and $m^{\gamma-\text{jet}-\text{jet}}$ (g,h,i) for the total (first column), fragmentation-enriched (second column) and direct-enriched (third column) samples. For comparison, the uncertainty computed using the bin-by-bin unfolding is also shown (dashed lines).

9.5.7 Isolation correction

Data-driven corrections to $E_{\mathrm{T}}^{\mathrm{iso}}$ were included in the MC samples, which lead to an improved description of the $E_{\mathrm{T}}^{\mathrm{iso}}$ distributions in the data by the MC simulations. A systematic uncertainty was assigned to the modelling of the $E_{\mathrm{T}}^{\mathrm{iso}}$ distribution in MC by comparing the nominal results (with data-driven corrections applied to MC) with those obtained without the application of the data-driven corrections to the simulated events; the resulting uncertainties on the cross sections are shown in Figs. 9.70 to 9.72.

9.5.8 Identification and isolation correlation in the background

The same procedure as presented in Section 6.6.6 was followed to check the correlation between the photon identification shower-shape variables used in the loose' and tight definitions and the isolation. The largest deviations from unity in the values of R^{bg} estimated in the high-$E_{\mathrm{T}}^{\mathrm{iso}}$ region were observed using the signal leakage fractions extracted from Pythia. The size of the deviations were found to be typically 20%, except in a few regions of the phase-space where it increased up to 30% and were used to vary R^{bg} from the nominal value, $R^{\mathrm{bg}} = 1$. The final uncertainty in the cross sections are shown in Figures 9.73 to 9.75.

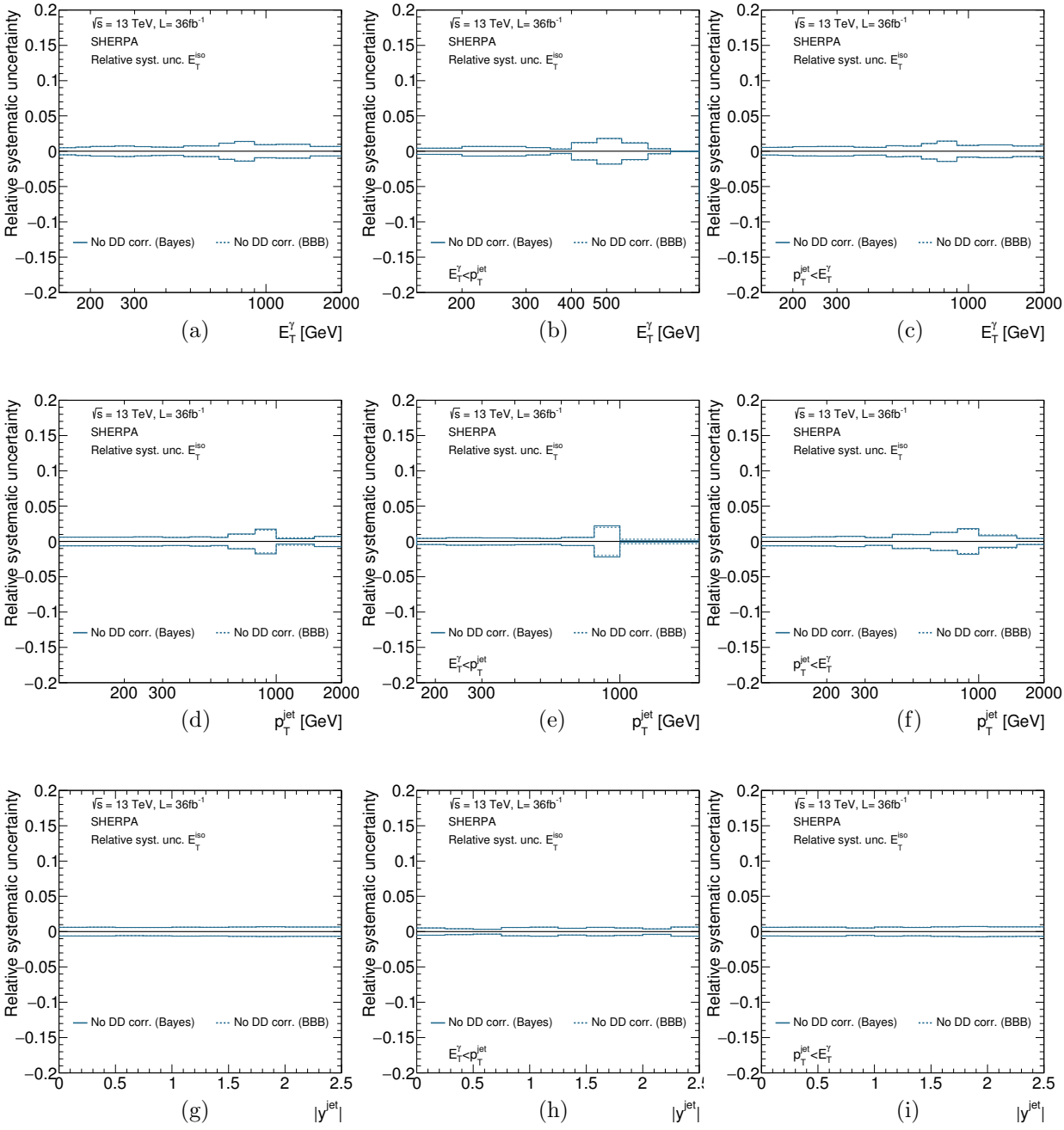


Figure 9.70: Systematic uncertainties on the measured cross sections due to the $E_{\mathrm{T}}^{\mathrm{iso}}$ modelling as functions of E_{T}^{γ} (a,b,c), $p_{\mathrm{T}}^{\mathrm{jet}}$ (d,e,f) and $|y^{\mathrm{jet}}|$ (g,h,i) for the total (first column), fragmentation-enriched (second column) and direct-enriched (third column) samples. For comparison, the uncertainty computed using the bin-by-bin unfolding is also shown (dashed lines).

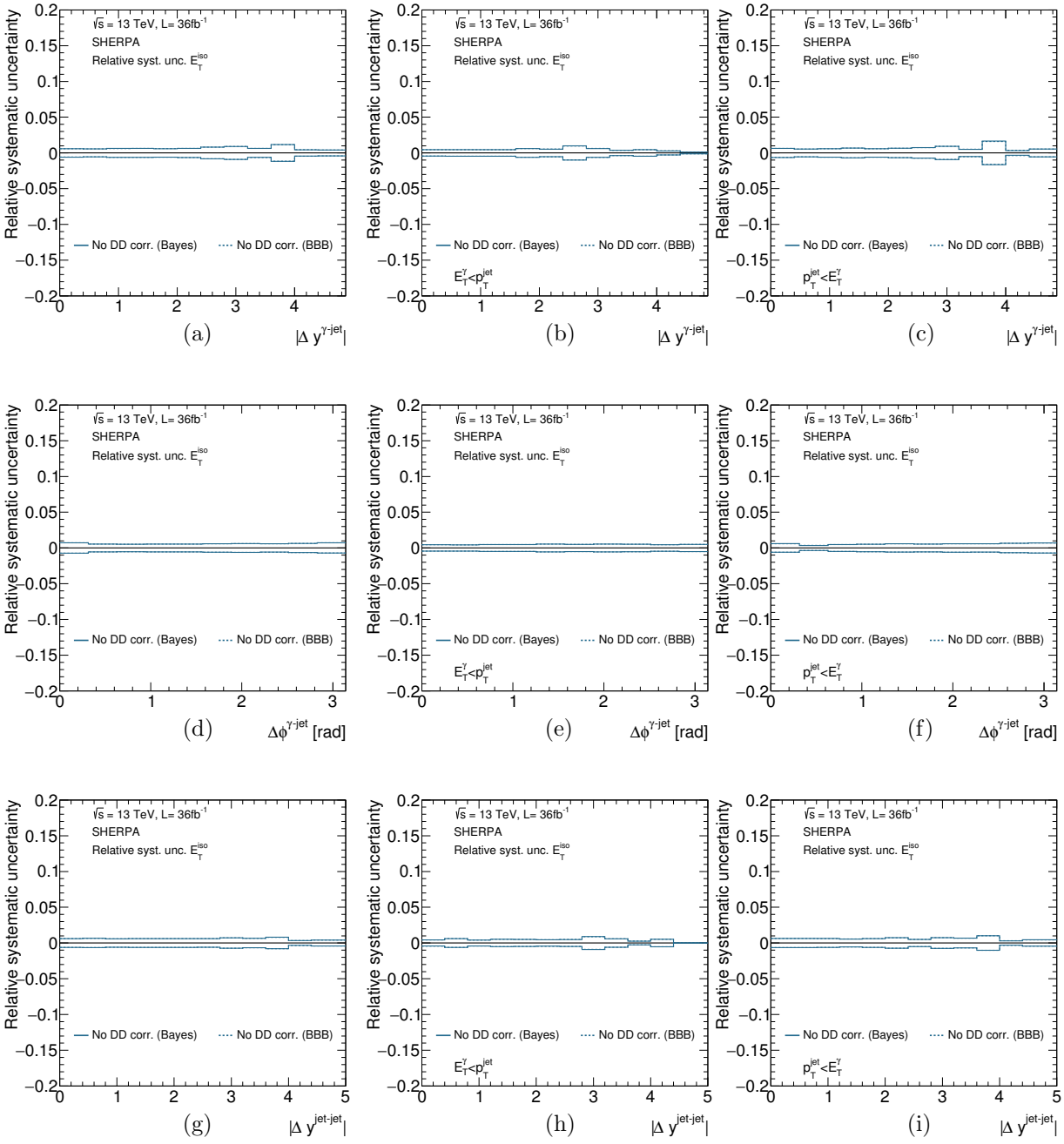


Figure 9.71: Systematic uncertainties on the measured cross sections due to the $E_{\mathrm{T}}^{\mathrm{iso}}$ modelling as functions of $|\Delta y^{\gamma-\mathrm{jet}}|$ (a,b,c), $\Delta\phi^{\gamma-\mathrm{jet}}$ (d,e,f) and $|\Delta y^{\mathrm{jet}-\mathrm{jet}}|$ (g,h,i) for the total (first column), fragmentation-enriched (second column) and direct-enriched (third column) samples. For comparison, the uncertainty computed using the bin-by-bin unfolding is also shown (dashed lines).

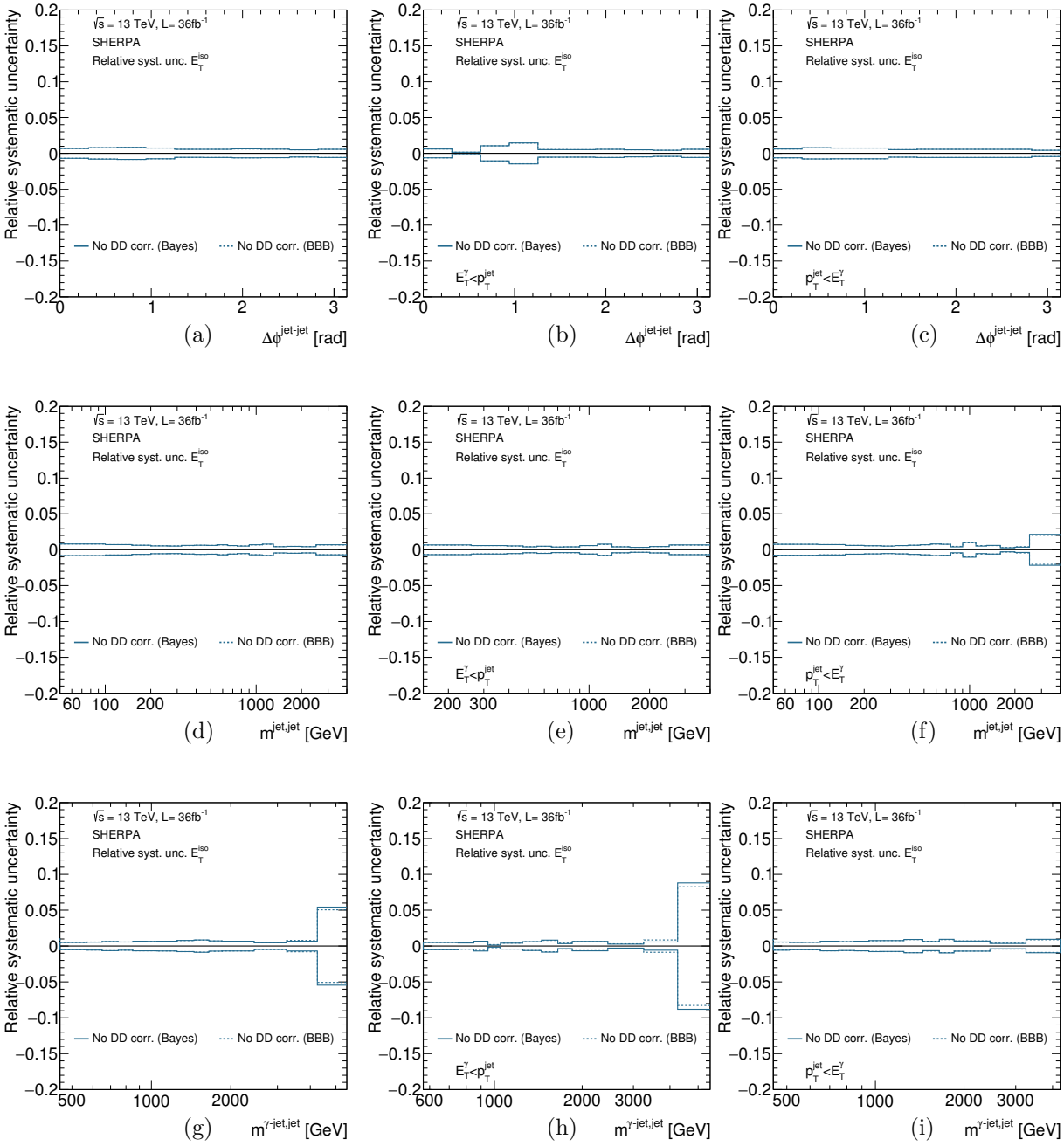


Figure 9.72: Systematic uncertainties on the measured cross sections due to the uncertainty in the $E_{\mathrm{T}}^{\mathrm{iso}}$ modelling as functions of $\Delta\phi^{\mathrm{jet-jet}}$ (a,b,c), $m^{\mathrm{jet-jet}}$ (d,e,f) and $m^{\gamma-\mathrm{jet-jet}}$ (g,h,i) for the total (first column), fragmentation-enriched (second column) and direct-enriched (third column) samples. For comparison, the uncertainty computed using the bin-by-bin unfolding is also shown (dashed lines).

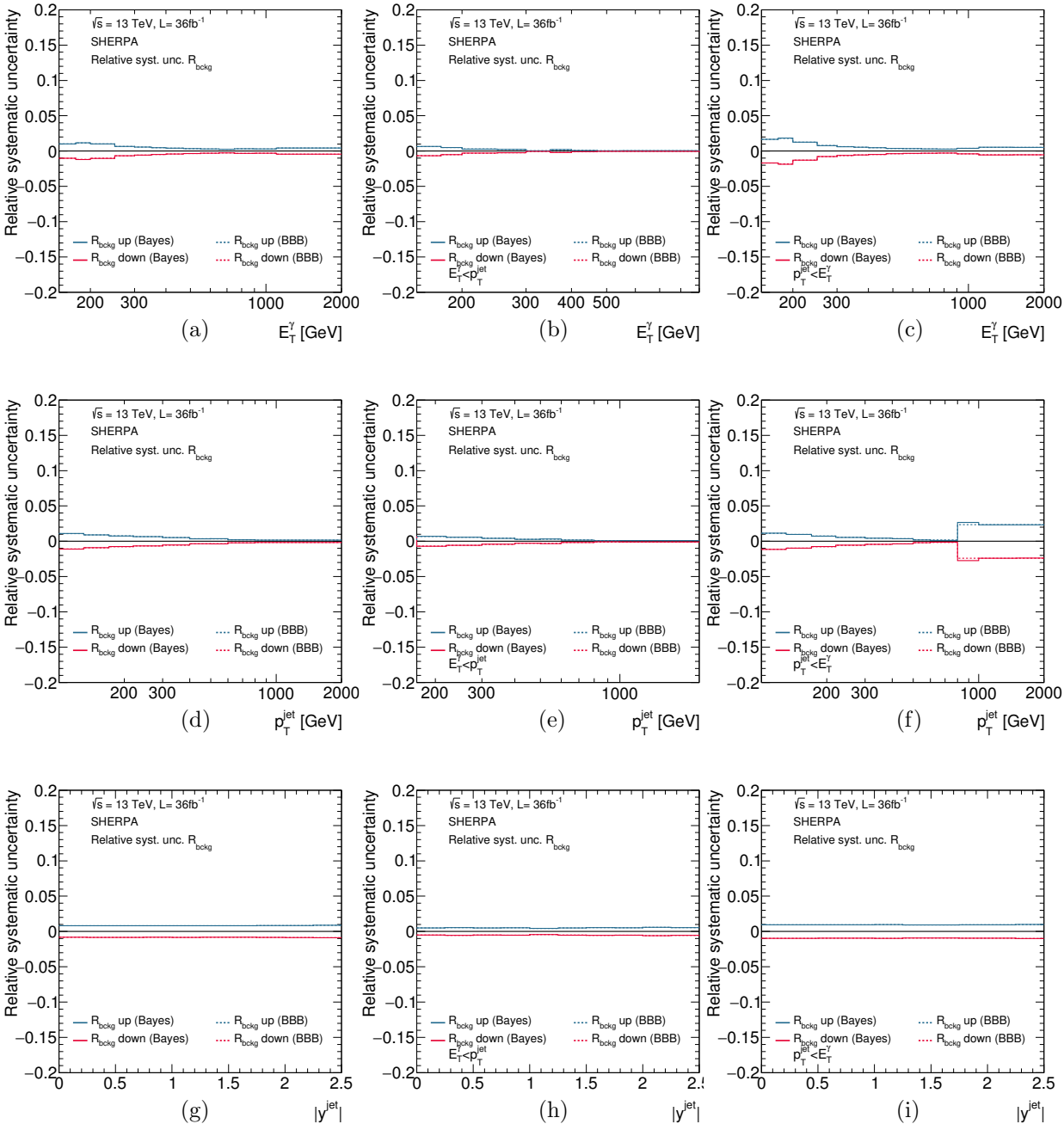


Figure 9.73: Systematic uncertainties on the measured cross sections due to the photon ID and $E_{\mathrm{T}}^{\mathrm{iso}}$ correlation in background events as functions of E_{T}^{γ} (a,b,c), $p_{\mathrm{T}}^{\mathrm{jet}}$ (d,e,f) and $|y^{\mathrm{jet}}|$ (g,h,i) for the total (first column), fragmentation-enriched (second column) and direct-enriched (third column) samples. For comparison, the uncertainty computed using the bin-by-bin unfolding is also shown (dashed lines).

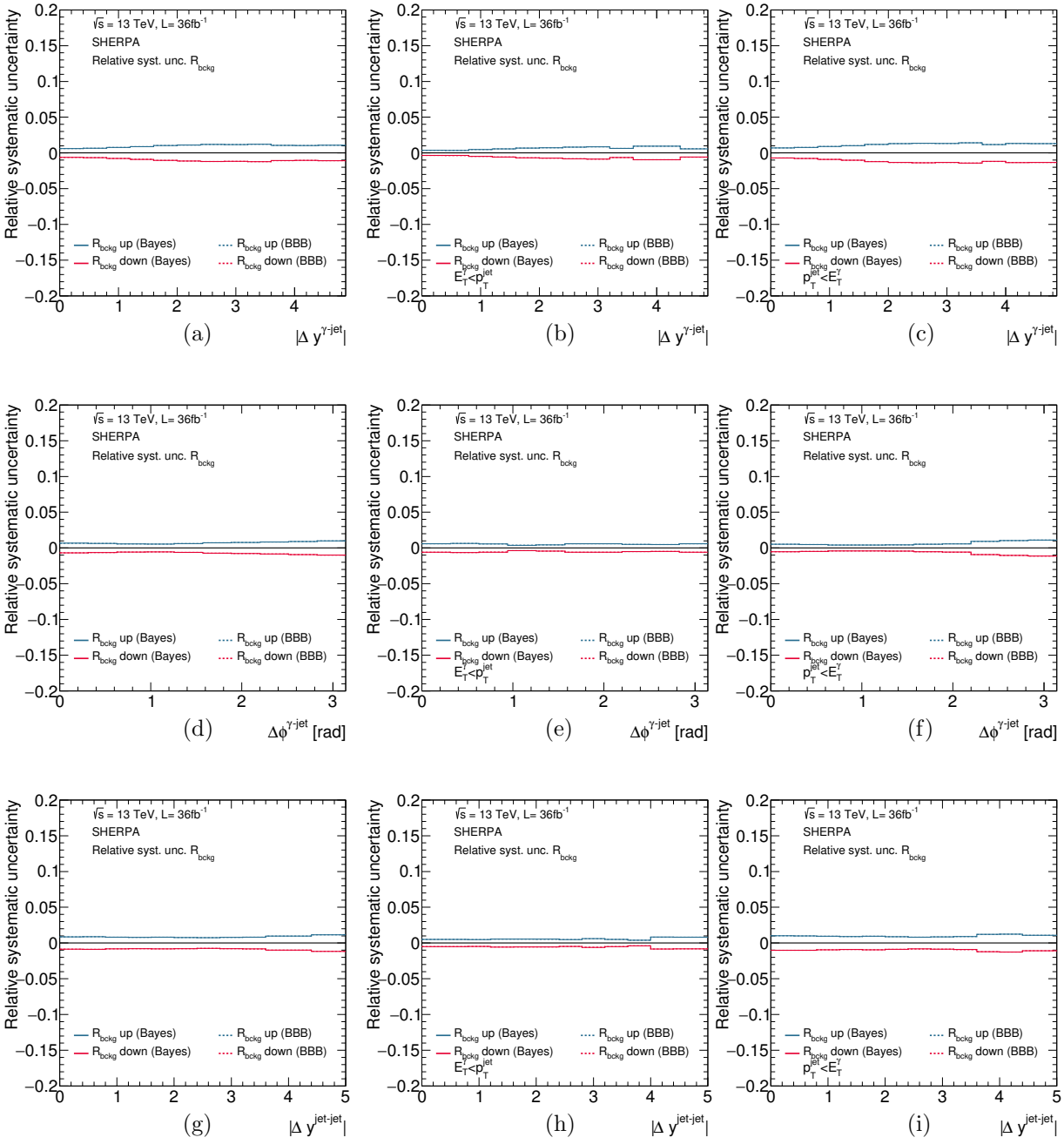


Figure 9.74: Systematic uncertainties on the measured cross sections due to the photon ID and $E_{\mathrm{T}}^{\mathrm{iso}}$ correlation in background events as functions of $|\Delta y^{\gamma-\mathrm{jet}}|$ (a,b,c), $\Delta\phi^{\gamma-\mathrm{jet}}$ (d,e,f) and $|\Delta y^{\mathrm{jet}-\mathrm{jet}}|$ (g,h,i) for the total (first column), fragmentation-enriched (second column) and direct-enriched (third column) samples. For comparison, the uncertainty computed using the bin-by-bin unfolding is also shown (dashed lines).

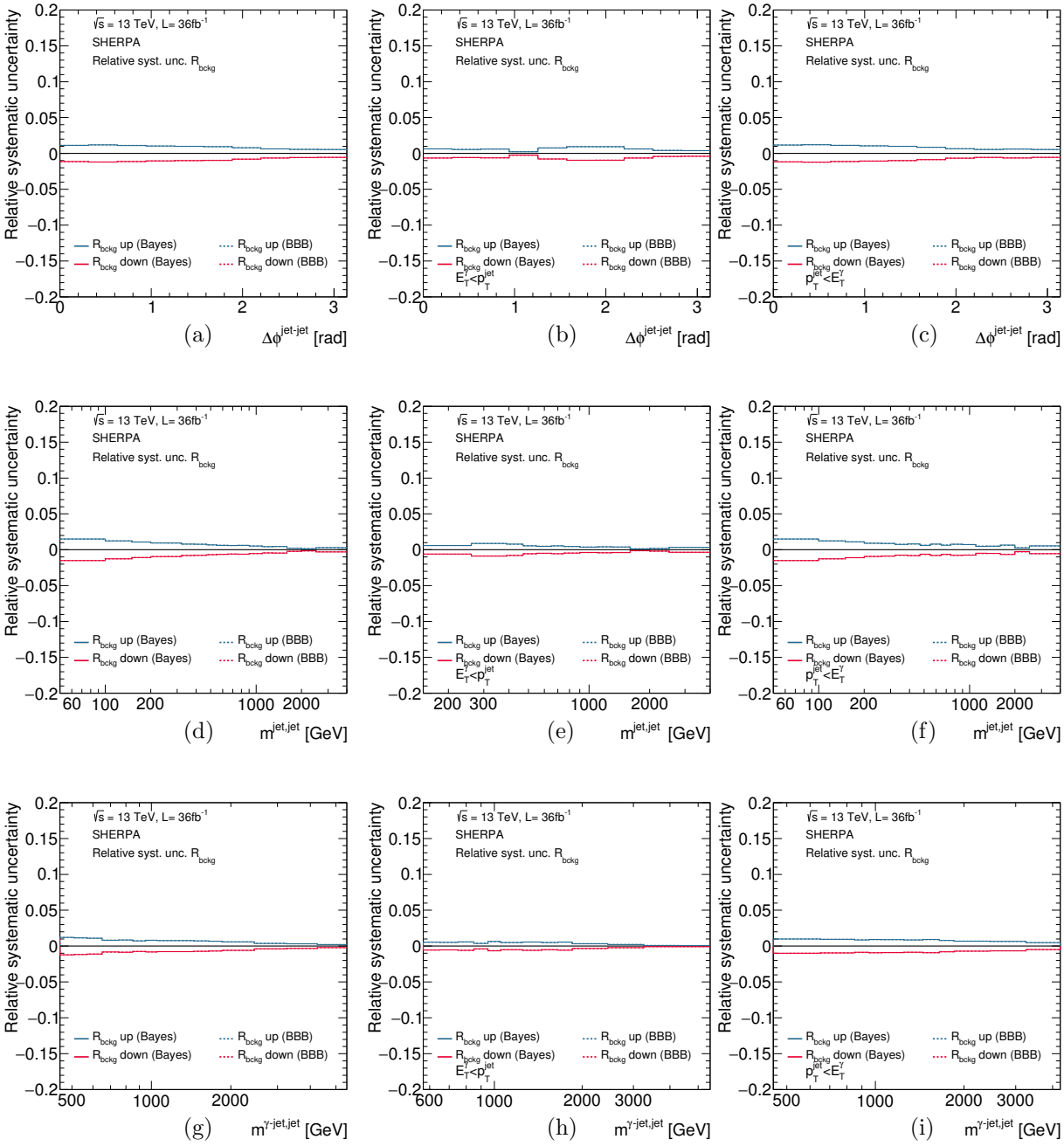


Figure 9.75: Systematic uncertainties on the measured cross sections due to the photon ID and $E_{\mathrm{T}}^{\mathrm{iso}}$ correlation in background events as functions of $\Delta\phi^{\mathrm{jet-jet}}$ (a,b,c), $m^{\mathrm{jet-jet}}$ (d,e,f) and $m^{\gamma-\mathrm{jet}-\mathrm{jet}}$ (g,h,i) for the total (first column), fragmentation-enriched (second column) and direct-enriched (third column) samples. For comparison, the uncertainty computed using the bin-by-bin unfolding is also shown (dashed lines).

9.5.9 Pile-up reweighting

An uncertainty due to the pile-up reweighting (see Section 9.1.4) in the MC simulations was estimated by measuring the cross sections with the MC corrected by $\langle\mu\rangle$-dependent weights. The $\langle\mu\rangle$ distribution in data with a scaling of 1.0 or 1/1.18 matches that of the simulations after applying the corresponding reweighting. The resulting uncertainties are displayed in Figures 9.76 to 9.78.

9.5.10 MC sample statistic

The statistical uncertainty of the MC samples was estimated using 500 MC replicas and following a bootstrap technique. The resulting MC statistical uncertainty is shown in Figures 9.79 to 9.81.

9.5.11 Uncertainty on the trigger efficiency

An uncertainty on the trigger efficiency of 0.22% was considered for all the observables except for E_{T}^{γ} (see Section 9.1.3).

9.5.12 Uncertainty on the electron-faking-photon background

The estimated contribution of the electron-faking-photon background was considered a source of systematic uncertainty. It is presented in Section 9.2.1 and the uncertainties presented in Figures 9.15 to 9.20.

9.5.13 Uncertainty on the measurement of the integrated luminosity

The uncertainty on the integrated luminosity of $\pm 2.1\%$ [115] has been considered.

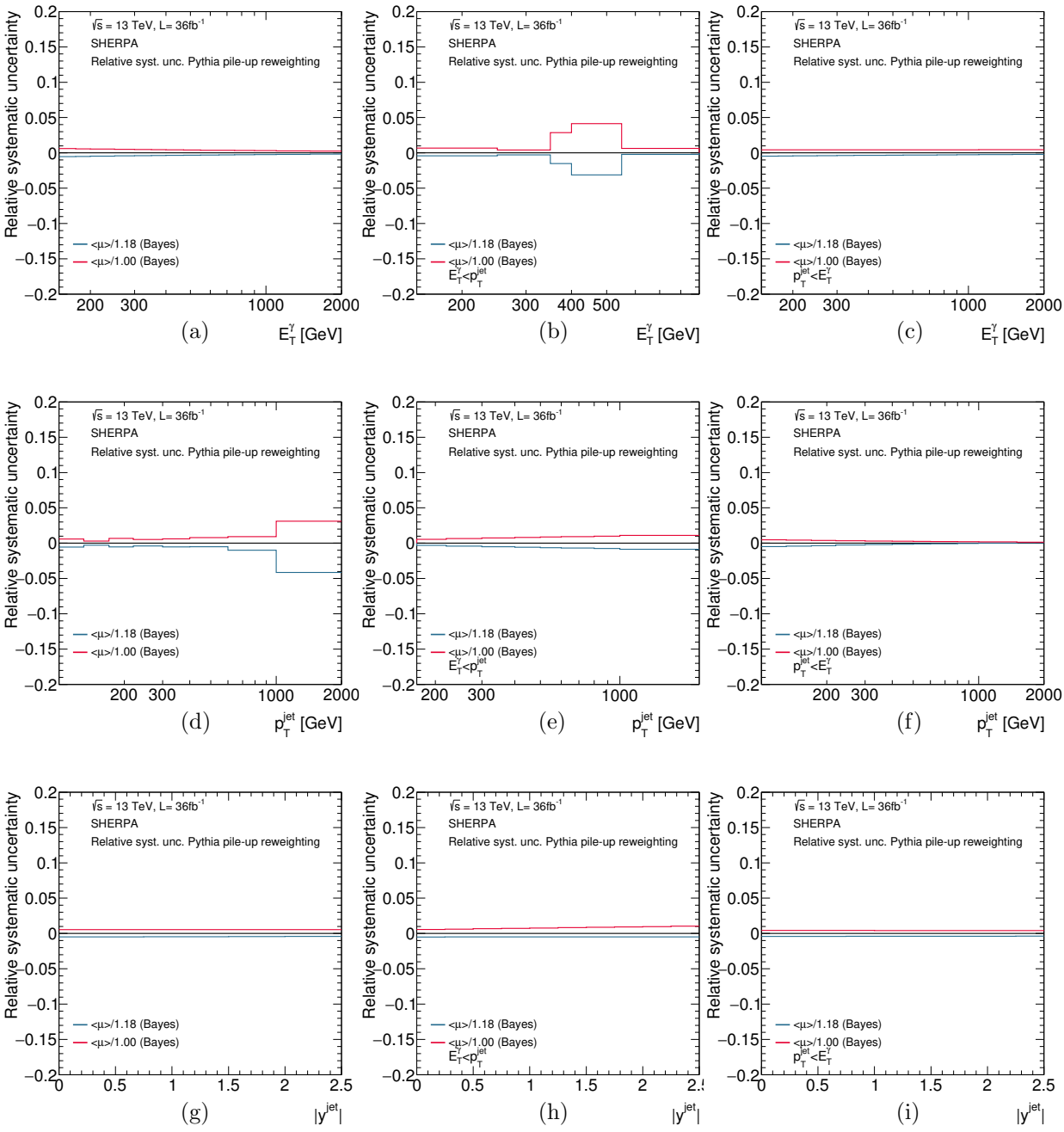


Figure 9.76: Systematic uncertainties on the measured cross section due to the pile-up reweighting as functions of E_{T}^{γ} (a,b,c), $p_{\mathrm{T}}^{\mathrm{jet}}$ (d,e,f) and $|y^{\mathrm{jet}}|$ (g,h,i) for the total (first column), fragmentation-enriched (second column) and direct-enriched (third column) samples.

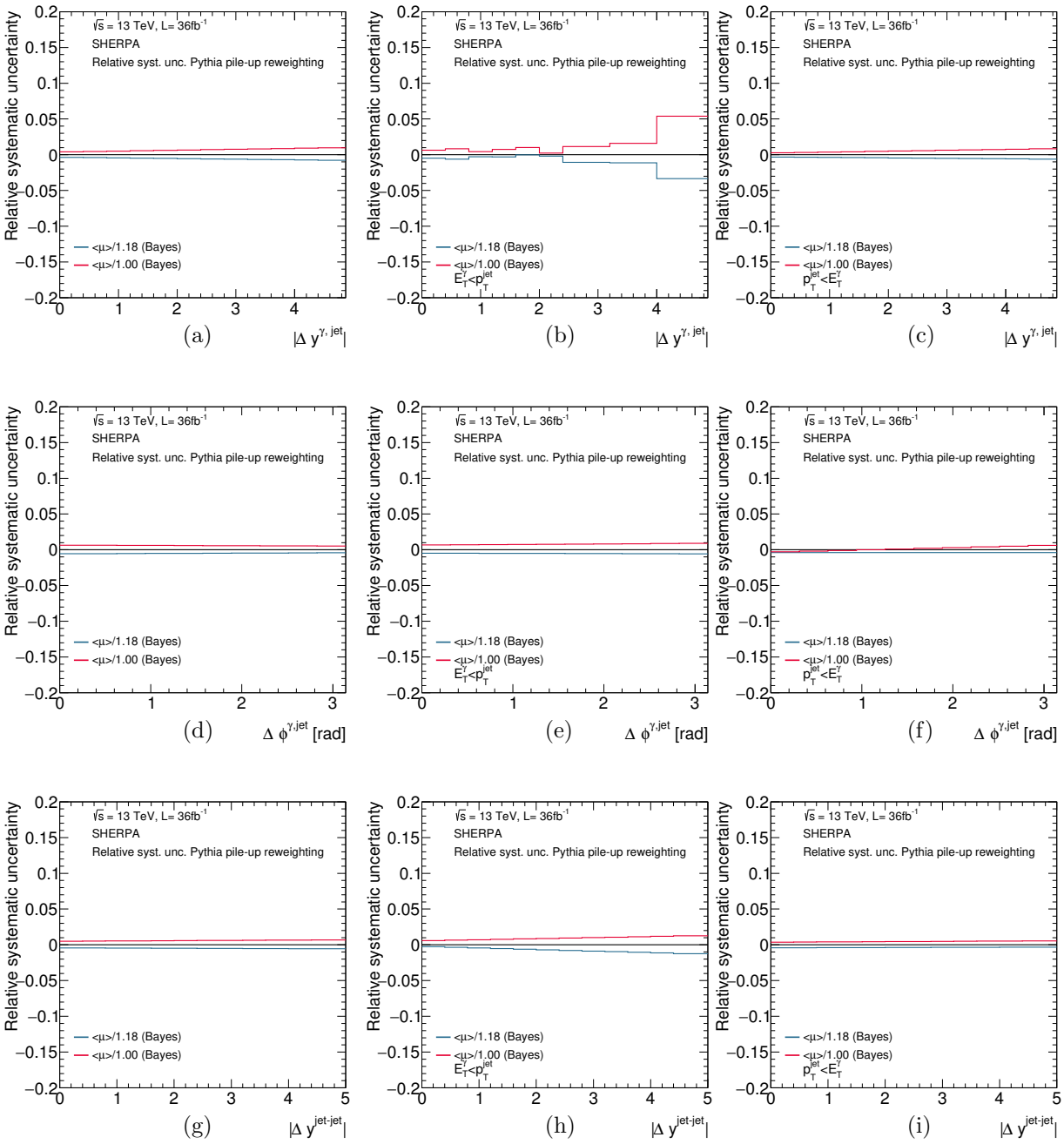


Figure 9.77: Systematic uncertainties on the measured cross section due to the pile-up reweighting as functions of $|\Delta y^{\gamma-\text{jet}}|$ (a,b,c), $\Delta\phi^{\gamma-\text{jet}}$ (d,e,f) and $|\Delta y^{\text{jet}-\text{jet}}|$ (g,h,i) for the total (first column), fragmentation-enriched (second column) and direct-enriched (third column) samples.

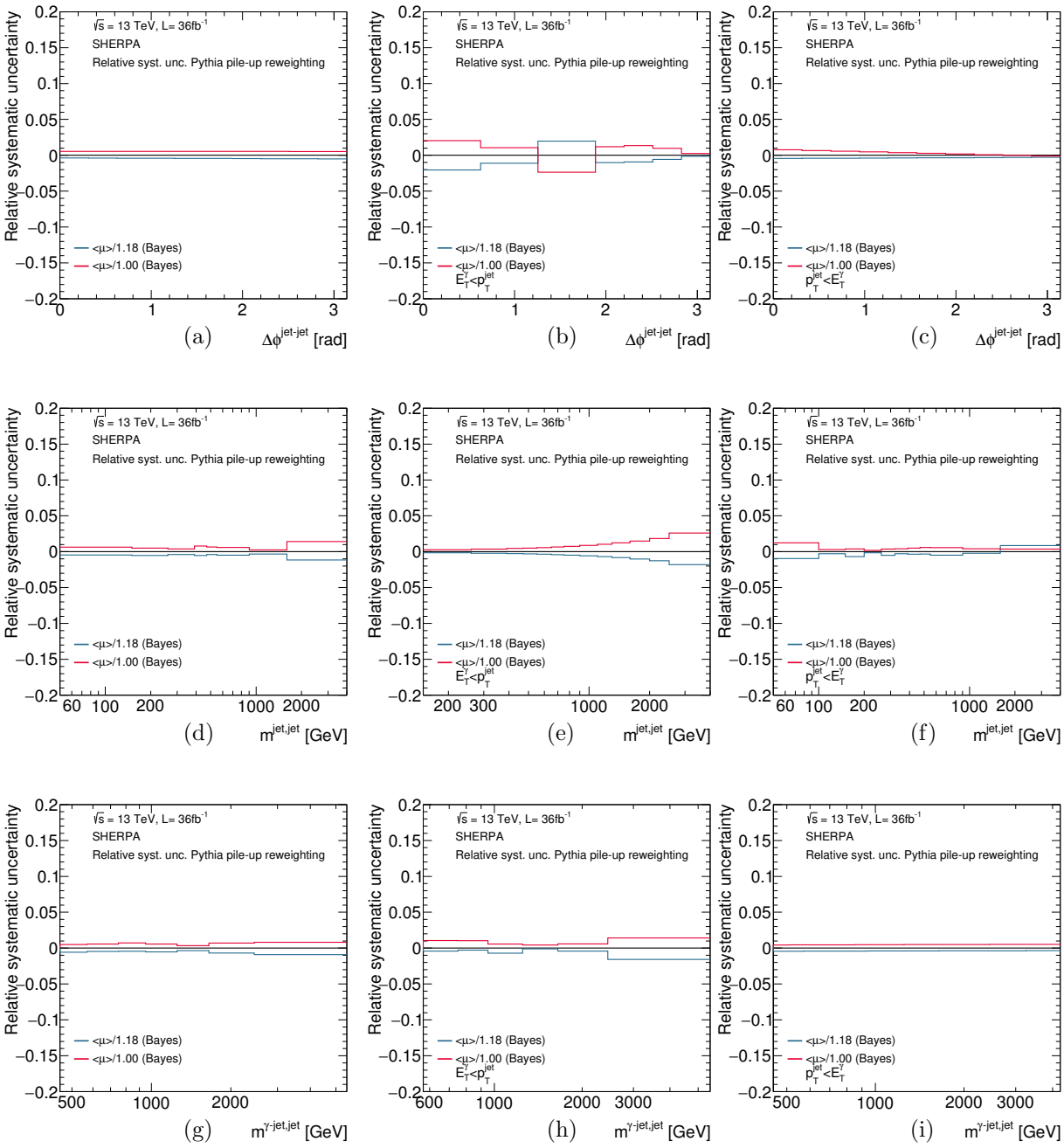


Figure 9.78: Systematic uncertainties on the measured cross section due to the pile-up reweighting as functions of $\Delta\phi^{\text{jet}-\text{jet}}$ (a,b,c), $m^{\text{jet}-\text{jet}}$ (d,e,f) and $m^{\gamma-\text{jet}-\text{jet}}$ (g,h,i) for the total (first column), fragmentation-enriched (second column) and direct-enriched (third column) samples.

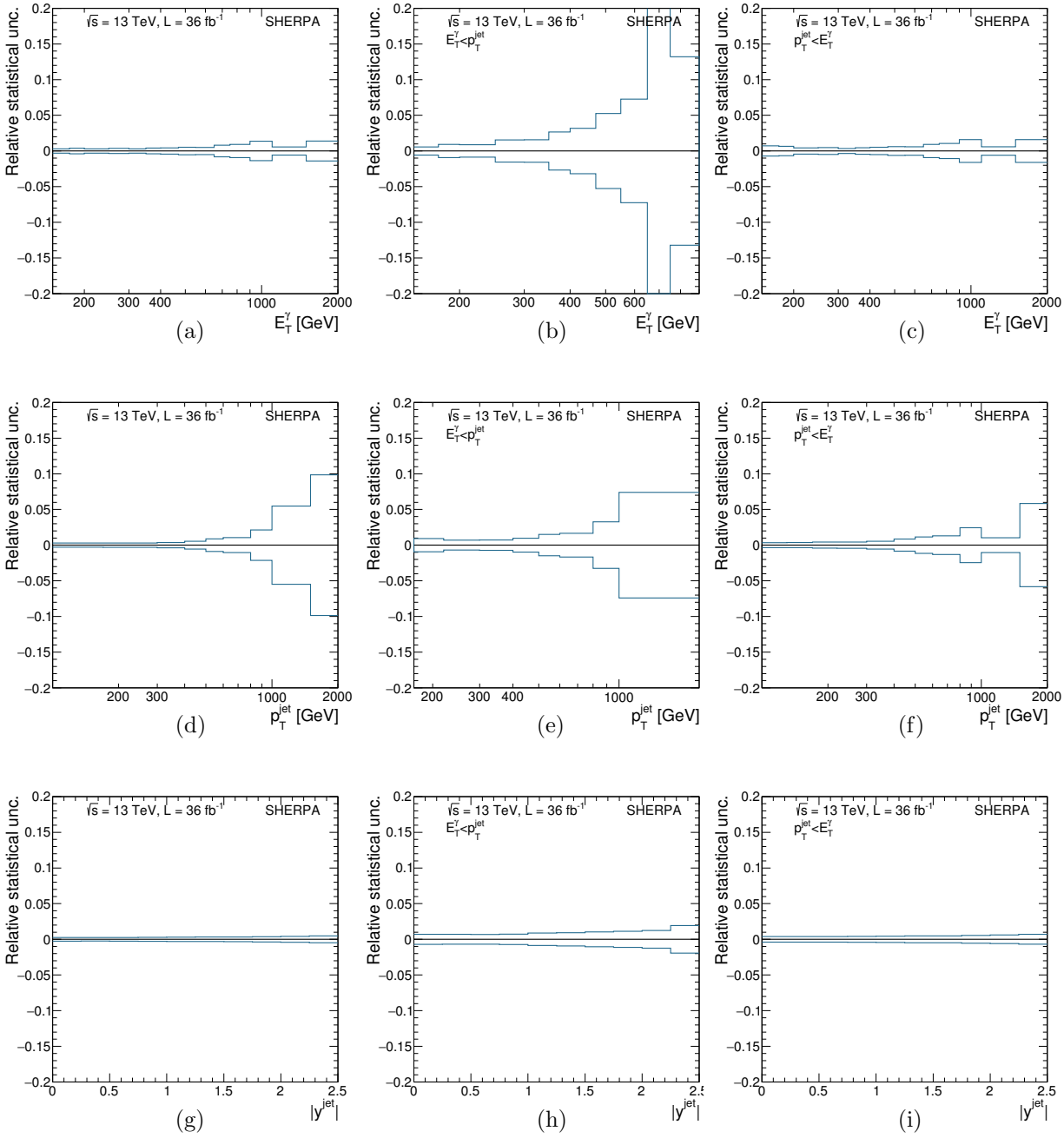


Figure 9.79: Systematic uncertainties on the measured cross section due to the limited MC statistics as functions of E_{T}^{γ} (a,b,c), $p_{\mathrm{T}}^{\mathrm{jet}}$ (d,e,f) and $|y^{\mathrm{jet}}|$ (g,h,i) for the total (first column), fragmentation-enriched (second column) and direct-enriched (third column) samples.

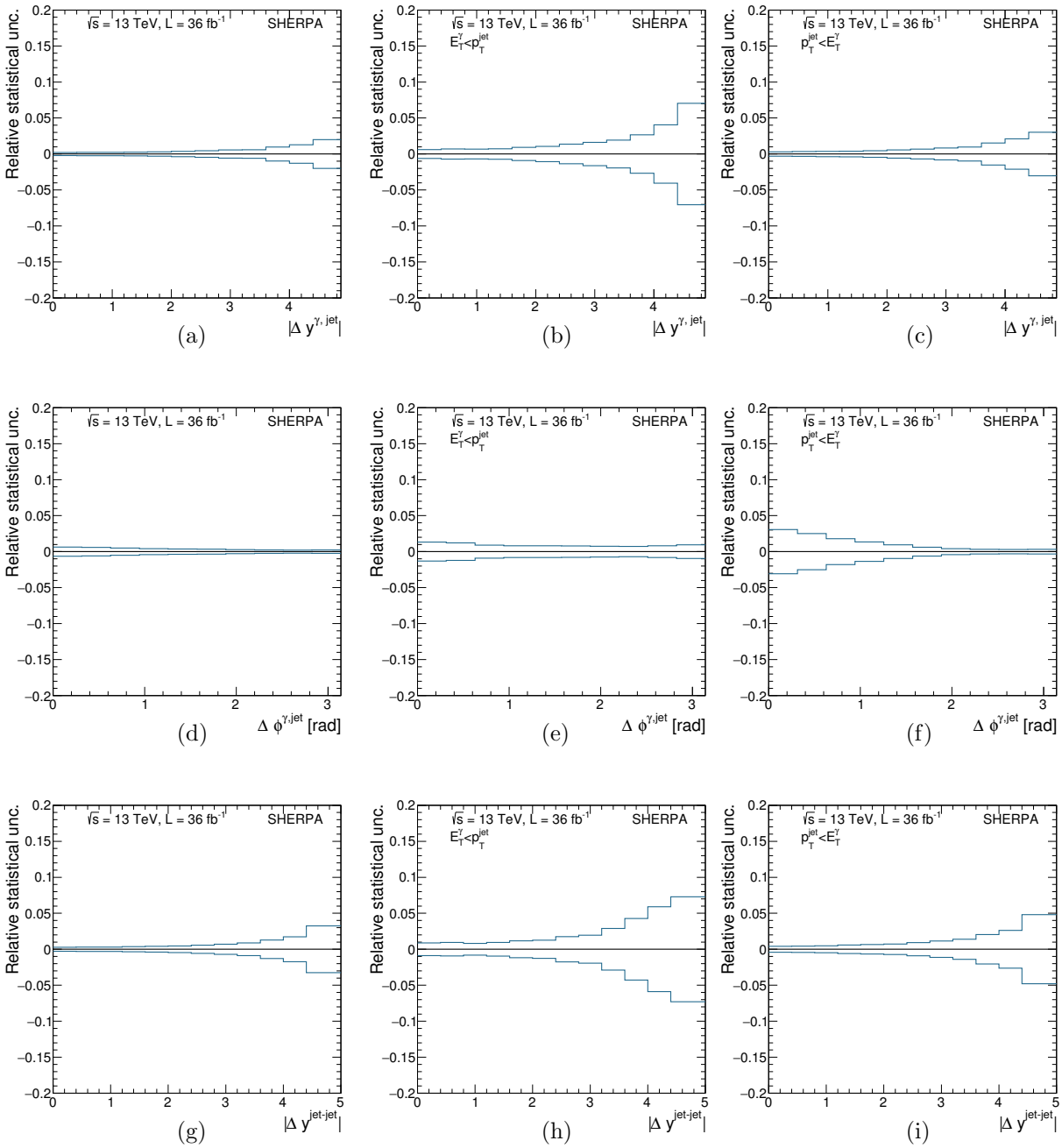


Figure 9.80: Systematic uncertainties on the measured cross section due to the limited MC statistics as functions of $|\Delta y^{\gamma-\text{jet}}|$ (a,b,c), $\Delta\phi^{\gamma-\text{jet}}$ (d,e,f) and $|\Delta y^{\text{jet}-\text{jet}}|$ (g,h,i) for the total (first column), fragmentation-enriched (second column) and direct-enriched (third column) samples.

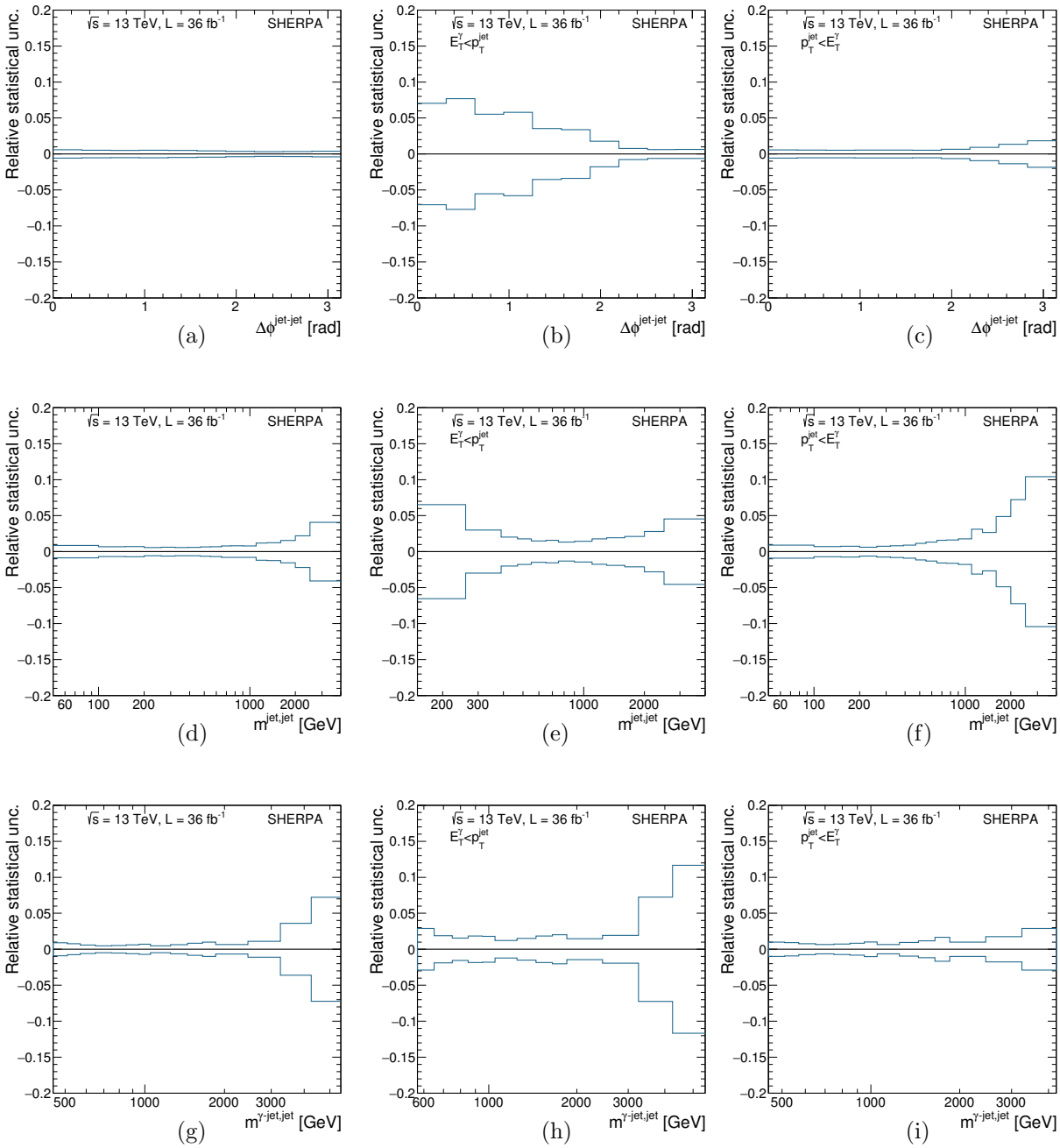


Figure 9.81: Systematic uncertainties on the measured cross section due to the limited MC statistics as functions of $\Delta\phi^{\text{jet}-\text{jet}}$ (a,b,c), $m^{\text{jet}-\text{jet}}$ (d,e,f) and $m^{\gamma-\text{jet}-\text{jet}}$ (g,h,i) for the total (first column), fragmentation-enriched (second column) and direct-enriched (third column) samples.

9.5.14 Total systematic uncertainty

The total systematic uncertainty was computed by adding in quadrature the sources of uncertainty listed above. Figures 9.82 to 9.84 show the resulting total systematic uncertainty (excluding the uncertainty due to the MC statistics and to the integrated luminosity), together with the statistical uncertainty. For most observables, the systematic uncertainty of the measurements dominate, except for cases such as the tail of E_{T}^{γ} and $p_{\mathrm{T}}^{\mathrm{jet}}$, for which the statistical uncertainty of the data is larger. In some regions, also the statistical uncertainty of the MC becomes large.

Figures 9.85 to 9.87 show the first three main contributions to the total systematic uncertainty (excluding the uncertainty on the integrated luminosity): jet energy scale, photon energy scale and photon identification.

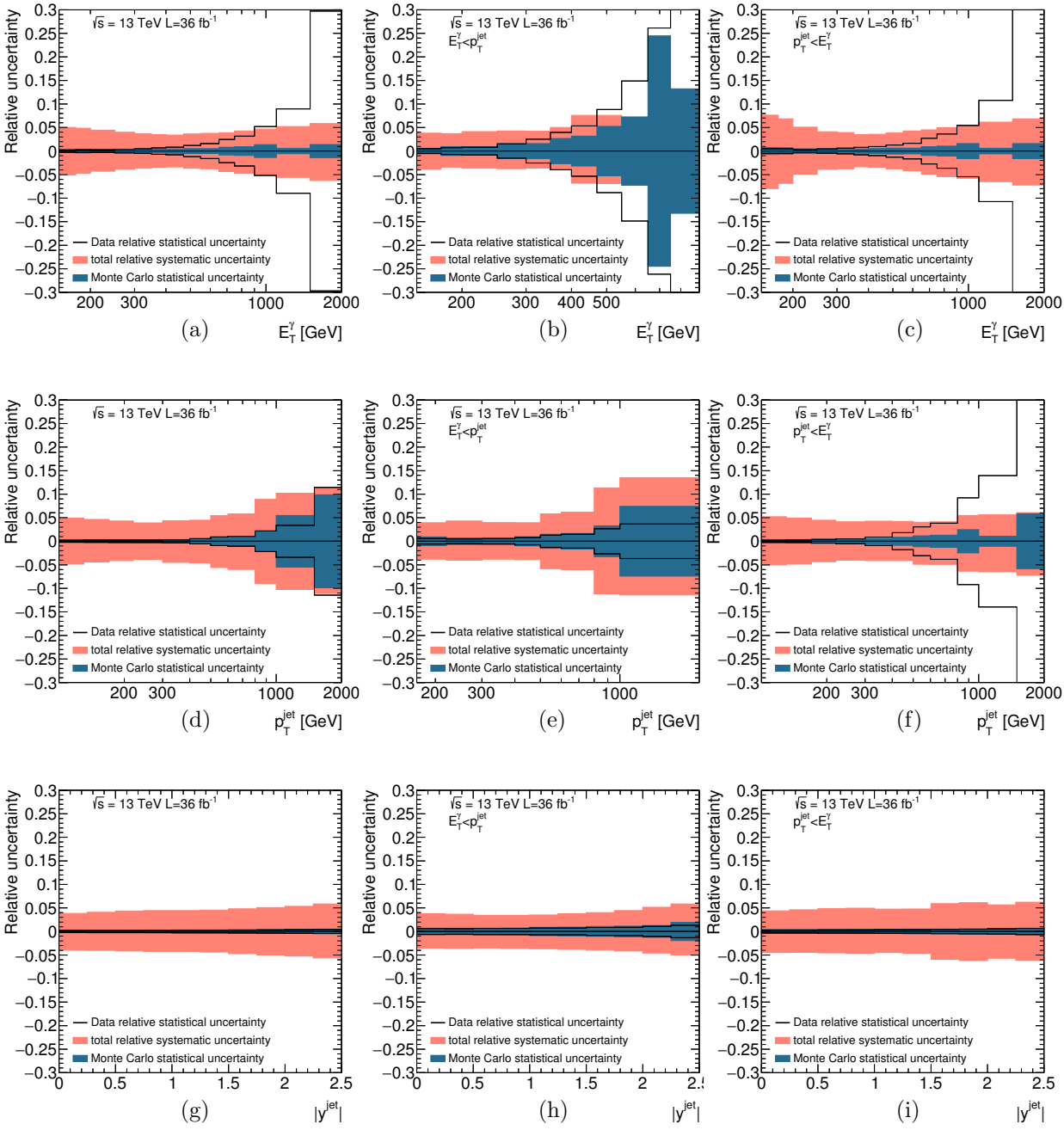


Figure 9.82: Total systematic (pink shaded area), excluding those on the integrated luminosity and MC statistics, and statistical uncertainties from the data (white histogram) and MC (blue shaded area) as functions of E_{T}^{γ} (a,b,c), $p_{\mathrm{T}}^{\mathrm{jet}}$ (d,e,f) and $|y^{\mathrm{jet}}|$ (g,h,i) for the total (first column), fragmentation-enriched (second column) and direct-enriched (third column) samples.

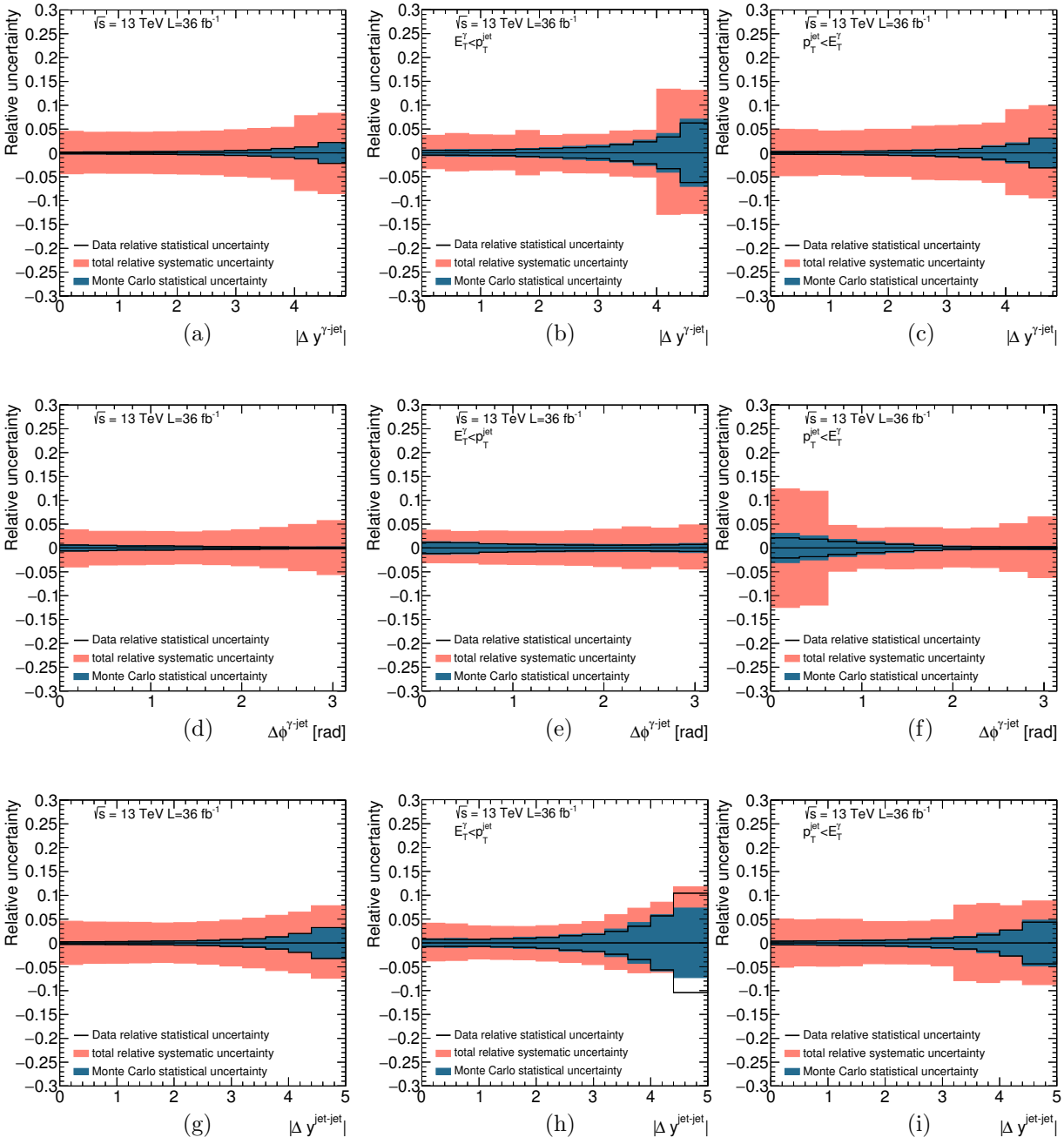


Figure 9.83: Total systematic (pink shaded area), excluding those on the integrated luminosity and MC statistics, and statistical uncertainties from the data (white histogram) and MC (blue shaded area) as functions of $|\Delta y^{\gamma-\text{jet}}|$ (a,b,c), $\Delta\phi^{\gamma-\text{jet}}$ (d,e,f) and $|\Delta y^{\text{jet}-\text{jet}}|$ (g,h,i) for the total (first column), fragmentation-enriched (second column) and direct-enriched (third column) samples.

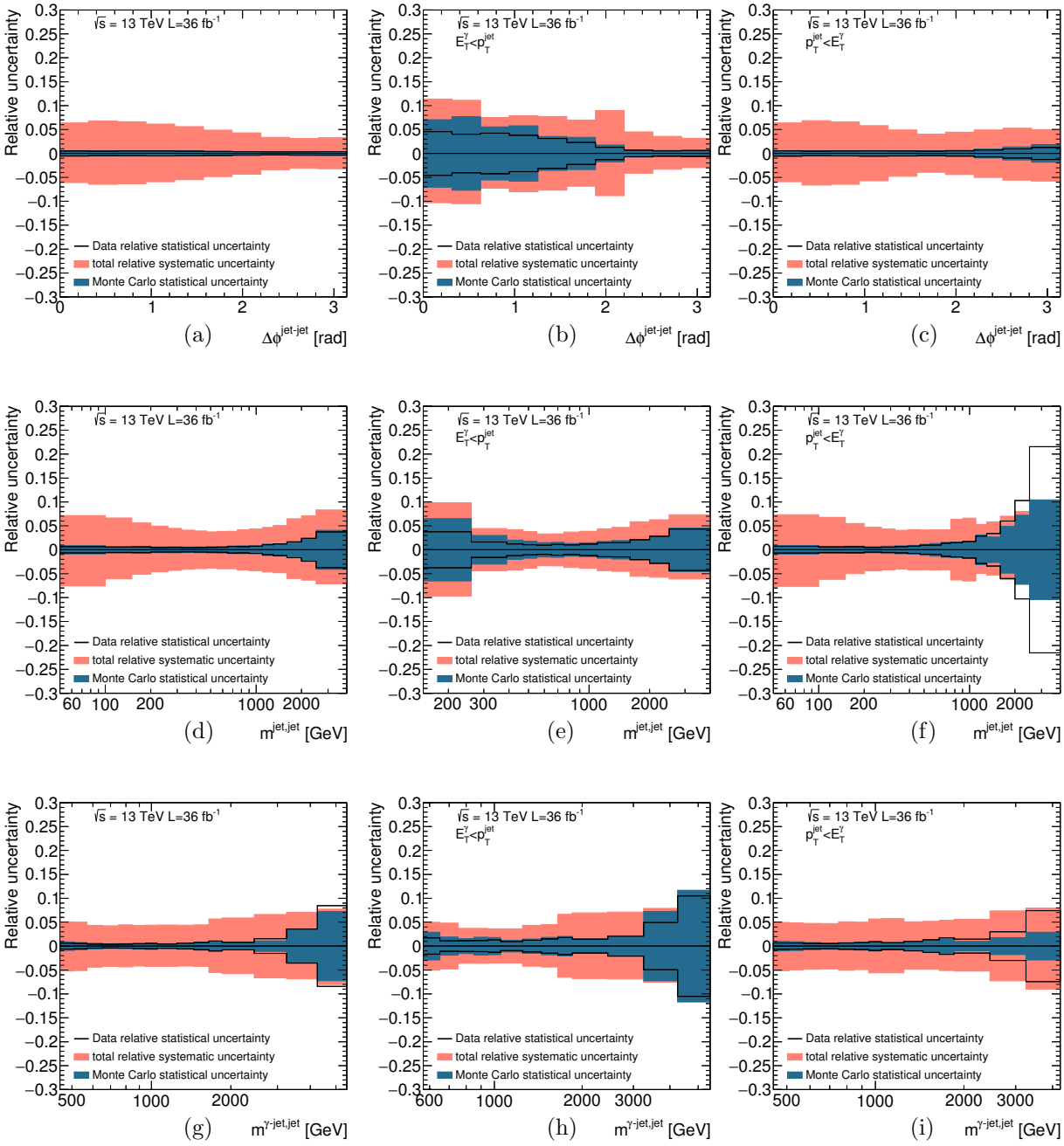


Figure 9.84: Total systematic (pink shaded area), excluding those on the integrated luminosity and MC statistics, and statistical uncertainties from the data (white histogram) and MC (blue shaded area) as functions of $\Delta\phi^{\text{jet}-\text{jet}}$ (a,b,c), $m^{\text{jet}-\text{jet}}$ (d,e,f) and $m^{\gamma-\text{jet}-\text{jet}}$ (g,h,i) for the total (first column), fragmentation-enriched (second column) and direct-enriched (third column) samples.

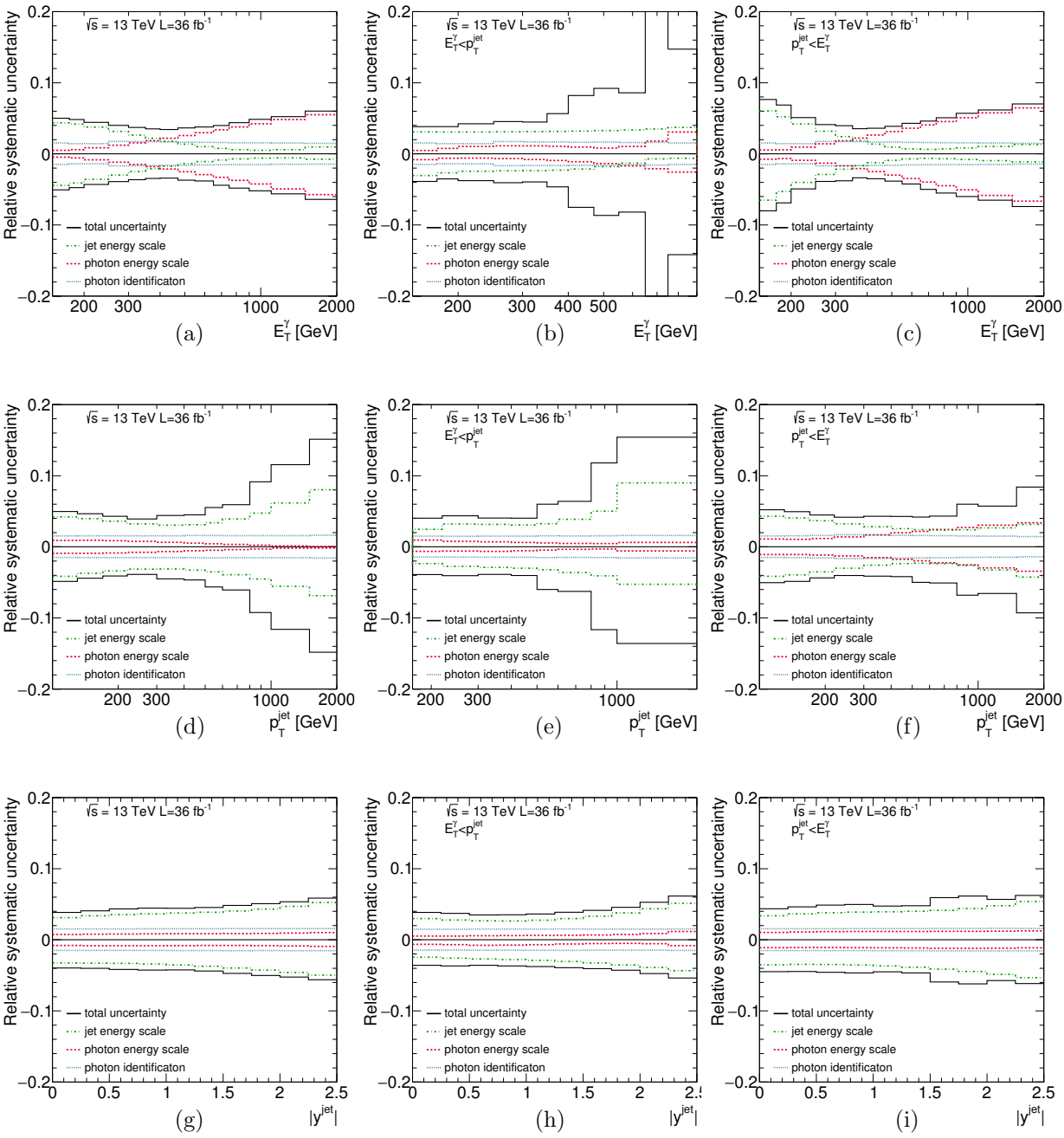


Figure 9.85: Total systematic uncertainty (black lines), excluding that on the integrated luminosity, together with the three main contributions: jet energy scale (dot-dashed lines), photon energy scale (dashed lines) and the photon identification (dotted lines) as functions of E_{T}^{γ} (a,b,c), $p_{\mathrm{T}}^{\mathrm{jet}}$ (d,e,f) and $|y^{\mathrm{jet}}|$ (g,h,i) for the total (first column), fragmentation-enriched (second column) and direct-enriched (third column) samples.

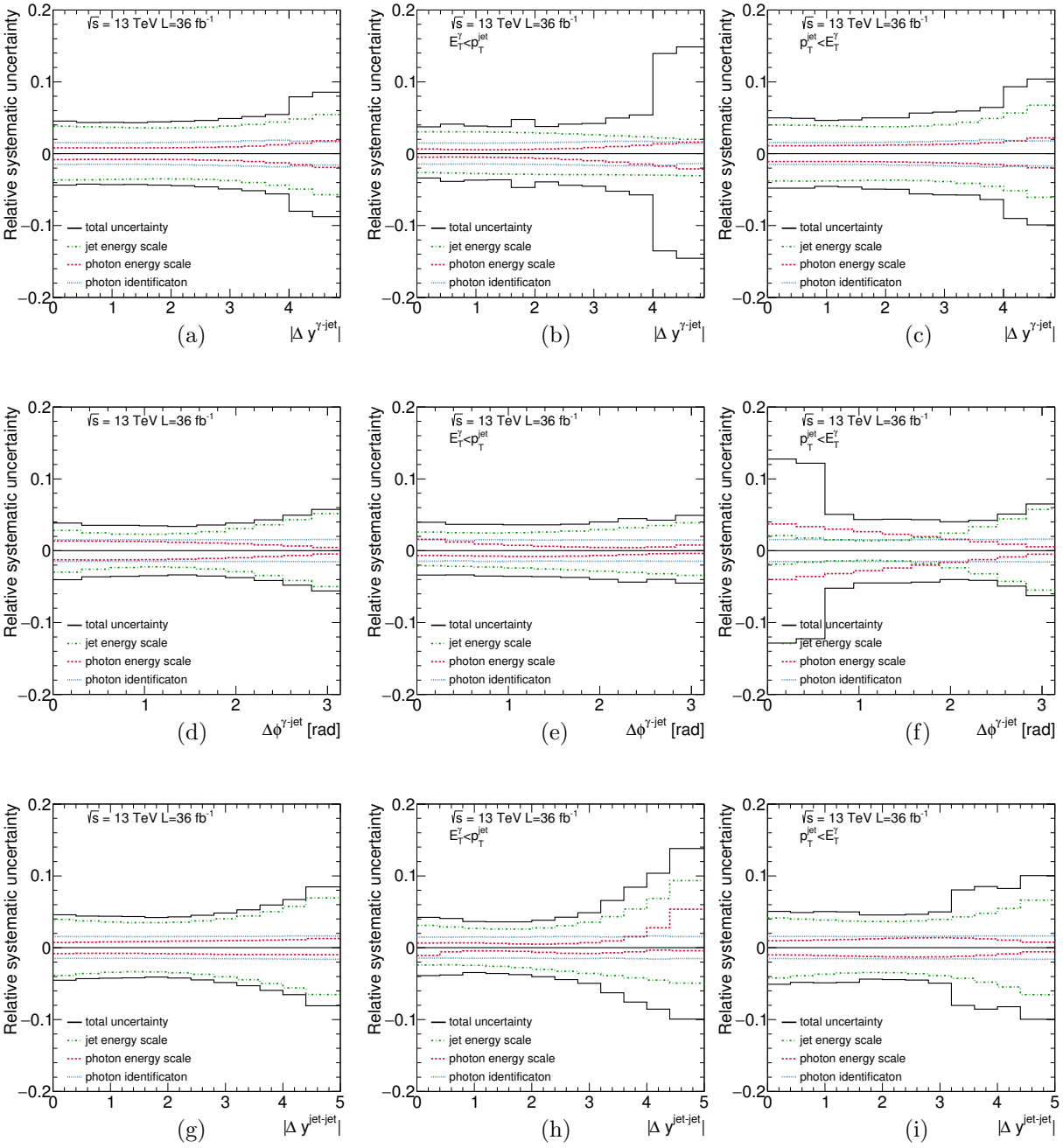


Figure 9.86: Total systematic uncertainty (black lines), excluding that on the integrated luminosity, together with the three main contributions: jet energy scale (dot-dashed lines), photon energy scale (dashed lines) and the photon identification (dotted lines) as functions of $|\Delta y^{\gamma-\mathrm{jet}}|$ (a,b,c), $\Delta\phi^{\gamma-\mathrm{jet}}$ (d,e,f) and $|\Delta y^{\mathrm{jet}-\mathrm{jet}}|$ (g,h,i) for the total (first column), fragmentation-enriched (second column) and direct-enriched (third column) samples.

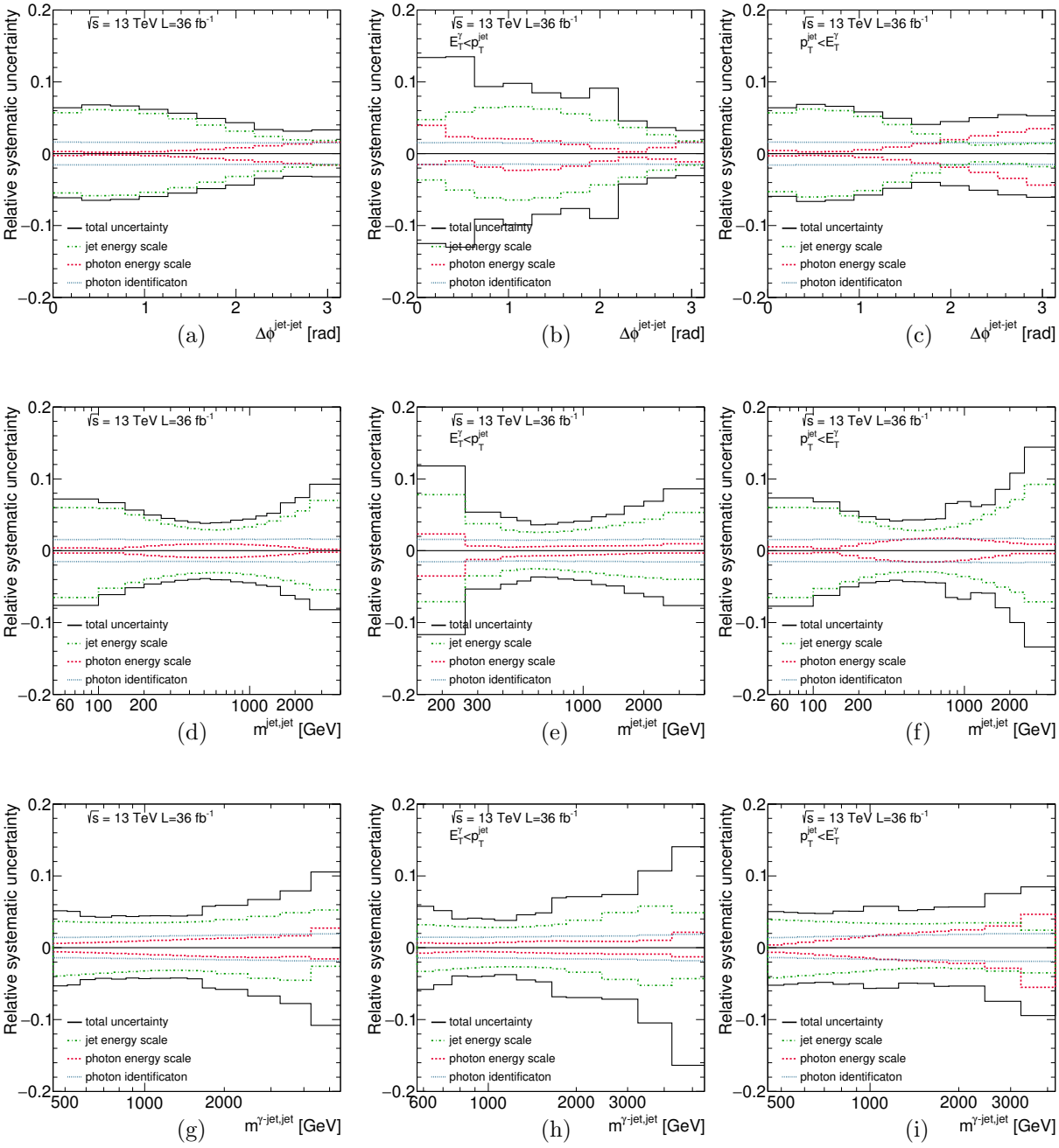


Figure 9.87: Total systematic uncertainty (black lines), excluding that on the integrated luminosity, together with the three main contributions: jet energy scale (dot-dashed lines), photon energy scale (dashed lines) and the photon identification (dotted lines) as functions of $\Delta\phi^{\text{jet}-\text{jet}}$ (a,b,c), $m^{\text{jet}-\text{jet}}$ (d,e,f) and $m^{\gamma-\text{jet}-\text{jet}}$ (g,h,i) for the total (first column), fragmentation-enriched (second column) and direct-enriched (third column) samples.

9.6 Results

Figures 9.88 to 9.93 show the measured isolated-photon plus two jets cross sections in the three phase-space regions.

Figure 9.88(a) shows the measured $\mathrm{d}\sigma/\mathrm{d}E_{\mathrm{T}}^{\gamma}$ for the total sample. The measured cross section decreases by approximately five orders of magnitude in the measured range. Values of E_{T}^{γ} up to 2 TeV are measured with the current integrated luminosity. The measured $\mathrm{d}\sigma/\mathrm{d}E_{\mathrm{T}}^{\gamma}$ for the fragmentation- and direct-enriched samples are shown in Figures 9.90(a) and 9.92(a), respectively; the E_{T}^{γ} spectrum for the direct-enriched sample is harder than that in the fragmentation-enriched sample.

Figure 9.88(b) shows the measured $\mathrm{d}\sigma/\mathrm{d}p_{\mathrm{T}}^{\mathrm{jet}}$ for the total sample. The measured cross section decreases by approximately five orders of magnitude in the measured range. Values of $p_{\mathrm{T}}^{\mathrm{jet}}$ up to 2 TeV are measured with the current integrated luminosity. The measured $\mathrm{d}\sigma/\mathrm{d}p_{\mathrm{T}}^{\mathrm{jet}}$ for the fragmentation- and direct-enriched samples are shown in Figures 9.90(b) and 9.92(b), respectively; the $p_{\mathrm{T}}^{\mathrm{jet}}$ spectrum for the fragmentation-enriched sample is harder than that in the direct-enriched sample.

Figure 9.88(c) shows the measured $\mathrm{d}\sigma/\mathrm{d}|y^{\mathrm{jet}}|$ for the total sample. The measured cross section decreases as $|y^{\mathrm{jet}}|$ increases. The measured $\mathrm{d}\sigma/\mathrm{d}|y^{\mathrm{jet}}|$ for the fragmentation- and direct-enriched samples are shown in Figures 9.90(c) and 9.92(c), respectively, and the shapes are similar for $|y^{\mathrm{jet}}| < 1$, but for $1 < |y^{\mathrm{jet}}| < 2.5$, the spectrum for the direct-enriched sample is harder.

Figure 9.88(d) shows the measured $\mathrm{d}\sigma/\mathrm{d}|\Delta y^{\gamma-\mathrm{jet}}|$ for the total sample. The measured cross section decreases as $|\Delta y^{\gamma-\mathrm{jet}}|$ increases. The measured $\mathrm{d}\sigma/\mathrm{d}|\Delta y^{\gamma-\mathrm{jet}}|$ for the fragmentation- and direct-enriched samples are shown in Figures 9.90(d) and 9.92(d), respectively, and the shapes are similar.

Figure 9.88(e) shows the measured $\mathrm{d}\sigma/\mathrm{d}\Delta\phi^{\gamma-\mathrm{jet}}$ for the total sample. The measured cross sections for the total and direct-enriched (see Figure 9.92(e)) samples have similar shapes, but in the fragmentation-enriched sample (see Figures 9.90(e)), the measured $\mathrm{d}\sigma/\mathrm{d}\Delta\phi^{\gamma-\mathrm{jet}}$ peaks towards lower $\Delta\phi^{\gamma-\mathrm{jet}}$ values.

Figures 9.89(b), 9.91(b) and 9.93(b) show the measured $\mathrm{d}\sigma/\mathrm{d}\Delta\phi^{\mathrm{jet}-\mathrm{jet}}$ for the total, fragmentation- and direct-enriched samples, respectively. The measured cross sections have very different shapes in the three phase-space regions. The same can be observed for the measured $\mathrm{d}\sigma/\mathrm{d}m^{\mathrm{jet}-\mathrm{jet}}$ (see Figures 9.89(c), 9.91(c) and 9.93(c)).

The characteristics observed in the measured cross sections in the fragmentation- and direct-enriched phase-space regions are in agreement with the expectations based on the two underlying mechanisms, which dominate each sample.

The predictions of the LO calculations of Pythia and Sherpa are compared to the data in Figs. 9.88 to 9.93. These predictions are normalised to the measured integrated cross section in each phase-space region. The predictions of Sherpa LO provide a good description of the shape of the data, except at high E_{T}^{γ}, $|\Delta y^{\mathrm{jet}-\mathrm{jet}}|$ and $m^{\gamma-\mathrm{jet}-\mathrm{jet}}$. The predictions of Pythia fail in general to describe the shape of the data.

The predictions of the NLO calculations of Sherpa are compared to the data in Figs. 9.94 to 9.99. The details of these calculations together with its associated uncertainties are described in Appendix G. These predictions describe the data adequately in shape and normalisation within the experimental and theoretical uncertainties; the

latter are much larger than the experimental ones. However, there is a tendency of the predictions to have a different shape than the measurements for some observables, most noticeably for the $|\Delta y^{\gamma-\text{jet}}|$, $\Delta\phi^{\gamma-\text{jet}}$, $m^{\text{jet}-\text{jet}}$ and $m^{\gamma-\text{jet}-\text{jet}}$ cross sections. These differences are more evident in the fragmentation-enriched phase-space region. Similar discrepancies in the shape of the $m^{\text{jet}-\text{jet}}$ and $|\Delta y^{\gamma-\text{jet}}|$ predictions have been found in other boson plus jets SHERPA samples and can be observed in the ATLAS Z+jets analysis at $\sqrt{s} = 13$ TeV [131] or in the vector boson fusion W production analysis at $\sqrt{s} = 7$ and 8 TeV [132]. This is believed to be due to a combination of the shower activity as well as the scale choice for NLO real emissions.

All these studies provide stringent tests of pQCD and validate the description of the dynamics of isolated-photon plus two jets production in pp collisions up to $\mathcal{O}(\alpha_{\text{em}}\alpha_{\text{s}}^3)$.

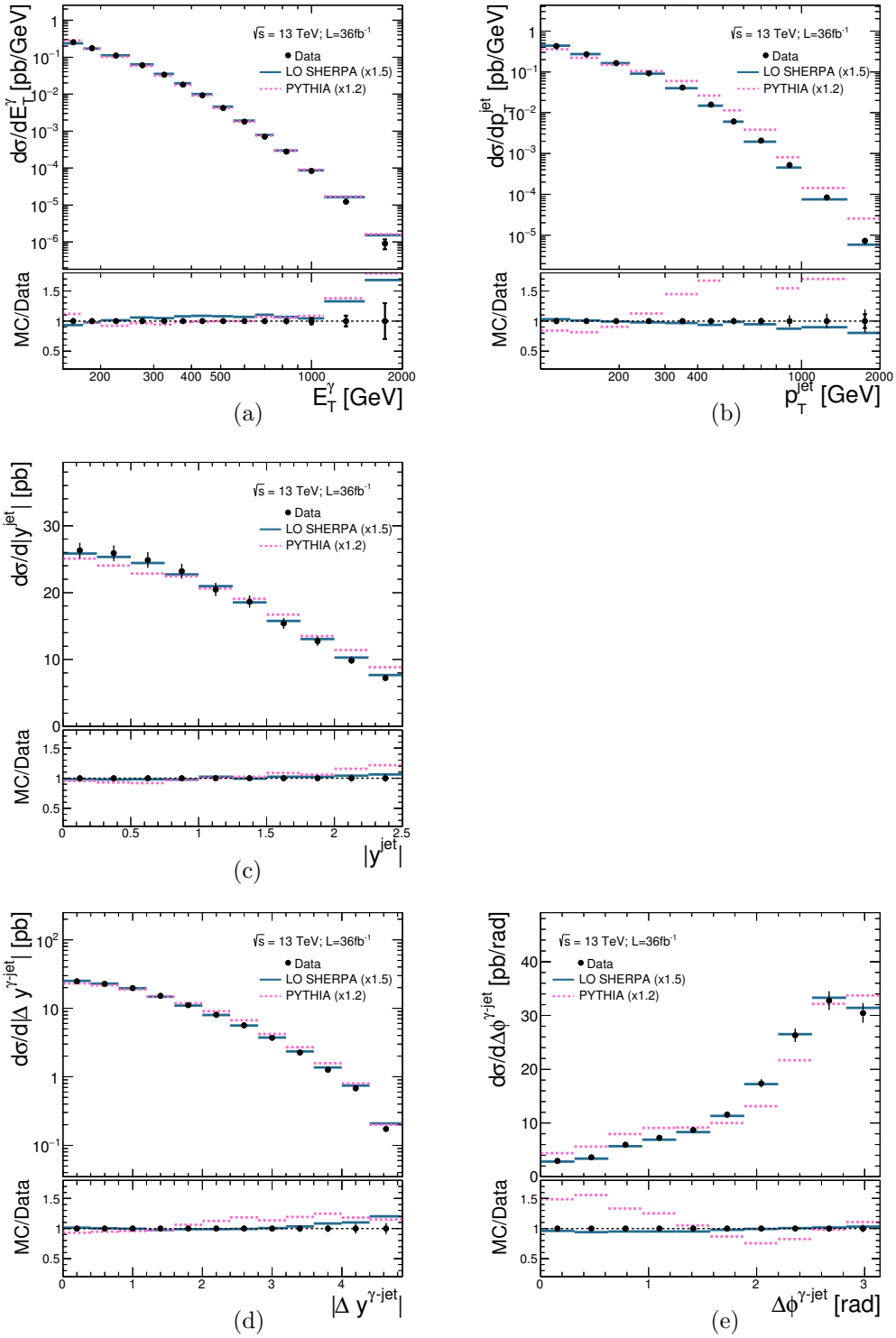


Figure 9.88: Measured cross sections for isolated-photon plus two jets production (dots) as functions of (a) E_{T}^{γ}, (b) $p_{\mathrm{T}}^{\mathrm{jet}}$, (c) $|y^{\mathrm{jet}}|$, (d) $|\Delta y^{\gamma-\mathrm{jet}}|$ and (e) $\Delta\phi^{\gamma-\mathrm{jet}}$ for the total sample. The predictions from PYTHIA (dashed lines) and SHERPA (solid lines) are also shown; these predictions are normalised to the measured integrated cross section using the values indicated in parentheses. The bottom part of each figure shows the ratio of the MC predictions to the measured cross section. The inner (outer) error bars represent the statistical uncertainties (the statistical and systematic uncertainties added in quadrature). For most of the points, the error bars are smaller than the marker size and, thus, not visible.

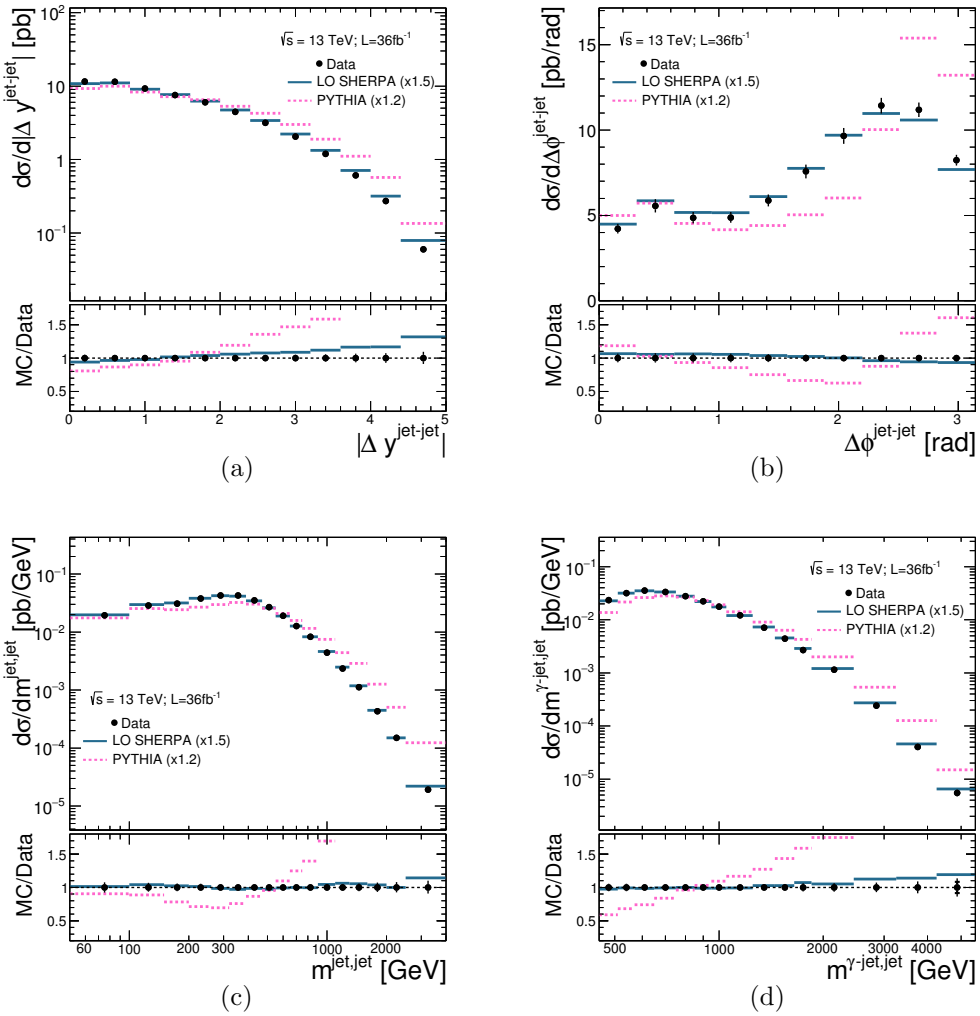


Figure 9.89: Measured cross sections for isolated-photon plus two jets production (dots) as functions of (a) $|\Delta y^{\text{jet}-\text{jet}}|$, (b) $\Delta\phi^{\text{jet}-\text{jet}}$, (c) $m^{\text{jet}-\text{jet}}$ and (d) $m^{\gamma-\text{jet}-\text{jet}}$ for the total sample. The predictions from PYTHIA (dashed lines) and SHERPA (solid lines) are also shown; these predictions are normalised to the measured integrated cross section using the values indicated in parentheses. The bottom part of each figure shows the ratio of the MC predictions to the measured cross section. The inner (outer) error bars represent the statistical uncertainties (the statistical and systematic uncertainties added in quadrature). For most of the points, the error bars are smaller than the marker size and, thus, not visible.

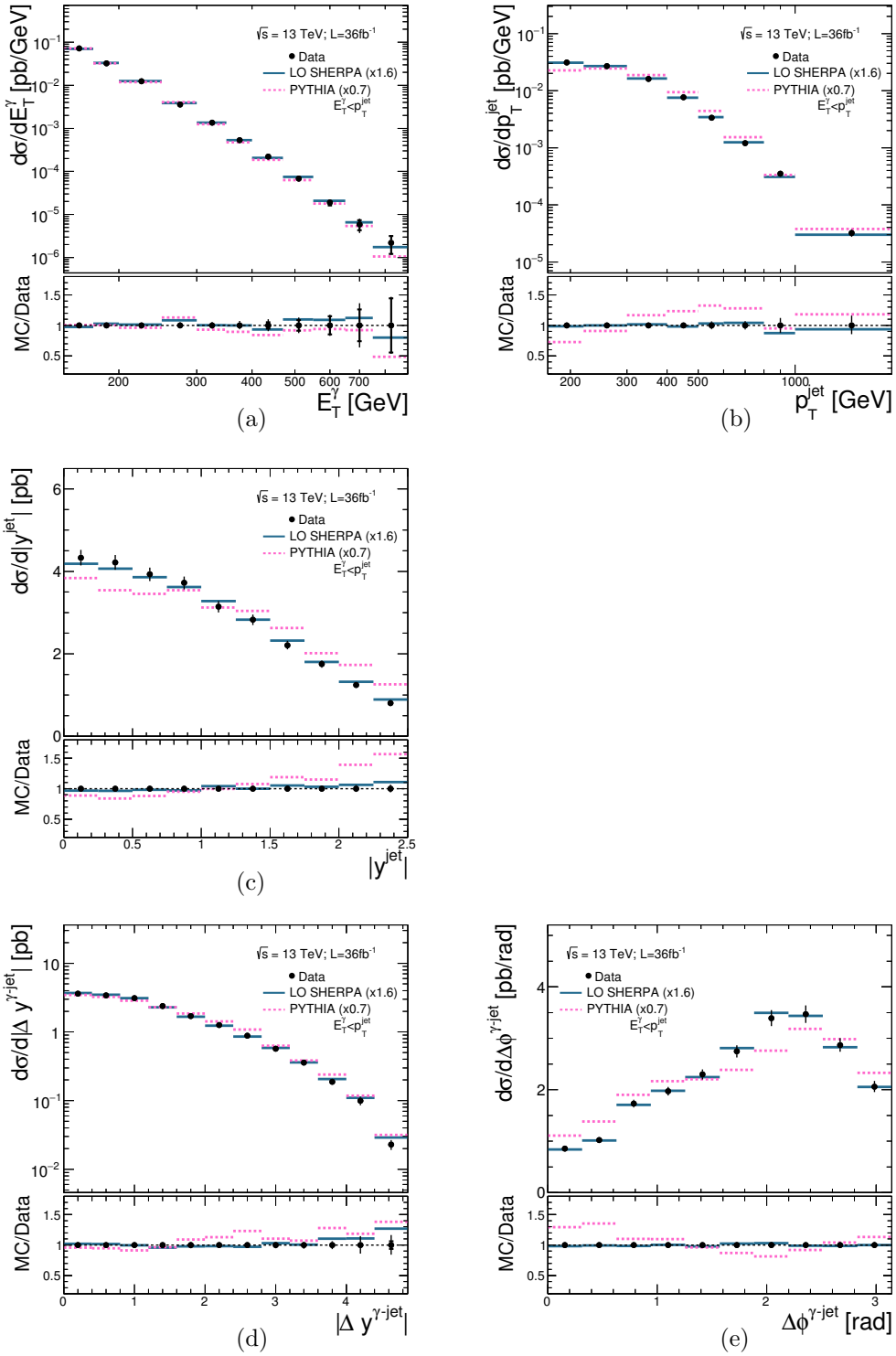


Figure 9.90: Measured cross sections for isolated-photon plus two jets production (dots) as functions of (a) E_{T}^{γ}, (b) $p_{\mathrm{T}}^{\mathrm{jet}}$, (c) $|y^{\mathrm{jet}}|$, (d) $|\Delta y^{\gamma-\mathrm{jet}}|$ and (e) $\Delta\phi^{\gamma-\mathrm{jet}}$ for the fragmentation-enriched sample. The predictions from PYTHIA (dashed lines) and SHERPA (solid lines) are also shown; these predictions are normalised to the measured integrated cross section using the values indicated in parentheses. The bottom part of each figure shows the ratio of the MC predictions to the measured cross section. The inner (outer) error bars represent the statistical uncertainties (the statistical and systematic uncertainties added in quadrature). For most of the points, the error bars are smaller than the marker size and, thus, not visible.

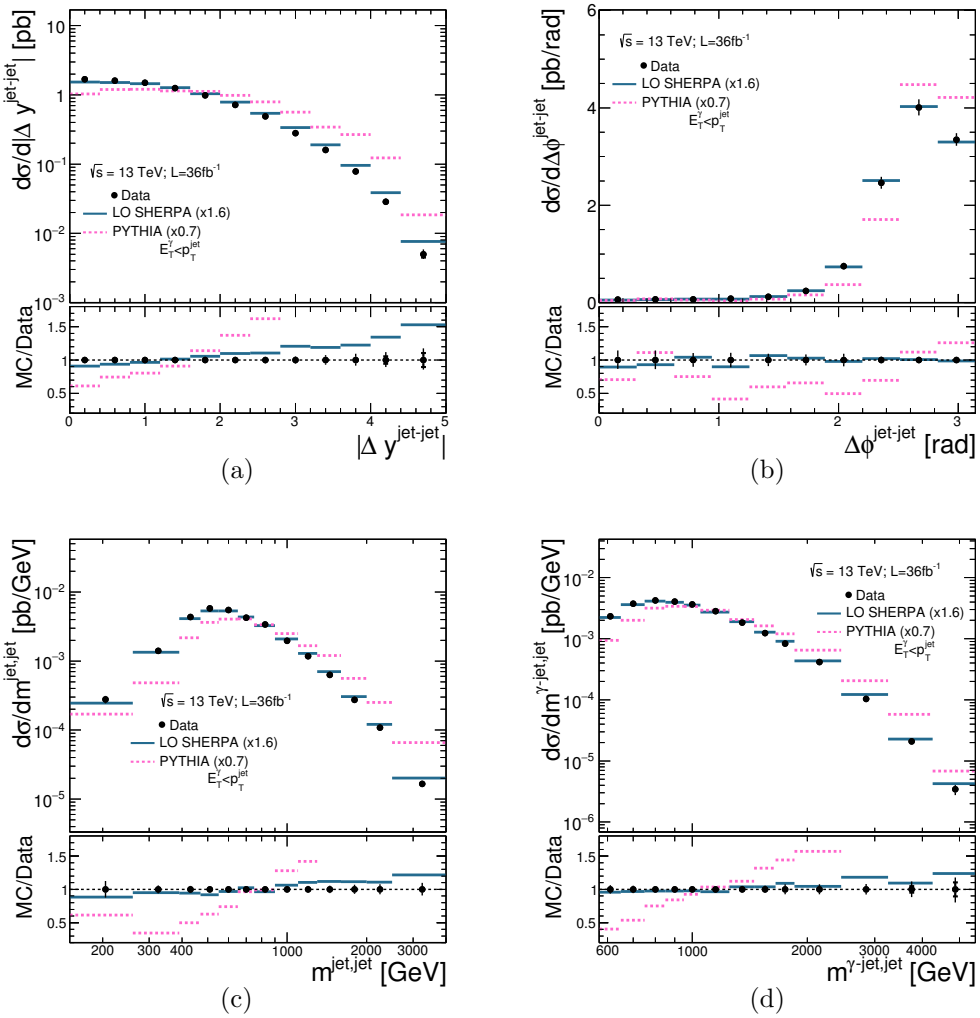


Figure 9.91: Measured cross sections for isolated-photon plus two jets production (dots) as functions of (a) $|\Delta y^{\text{jet}-\text{jet}}|$, (b) $\Delta\phi^{\text{jet}-\text{jet}}$, (c) $m^{\text{jet}-\text{jet}}$ and (d) $m^{\gamma-\text{jet}-\text{jet}}$ for the fragmentation-enriched sample. The predictions from PYTHIA (dashed lines) and SHERPA (solid lines) are also shown; these predictions are normalised to the measured integrated cross section using the values indicated in parentheses. The bottom part of each figure shows the ratio of the MC predictions to the measured cross section. The inner (outer) error bars represent the statistical uncertainties (the statistical and systematic uncertainties added in quadrature). For most of the points, the error bars are smaller than the marker size and, thus, not visible.

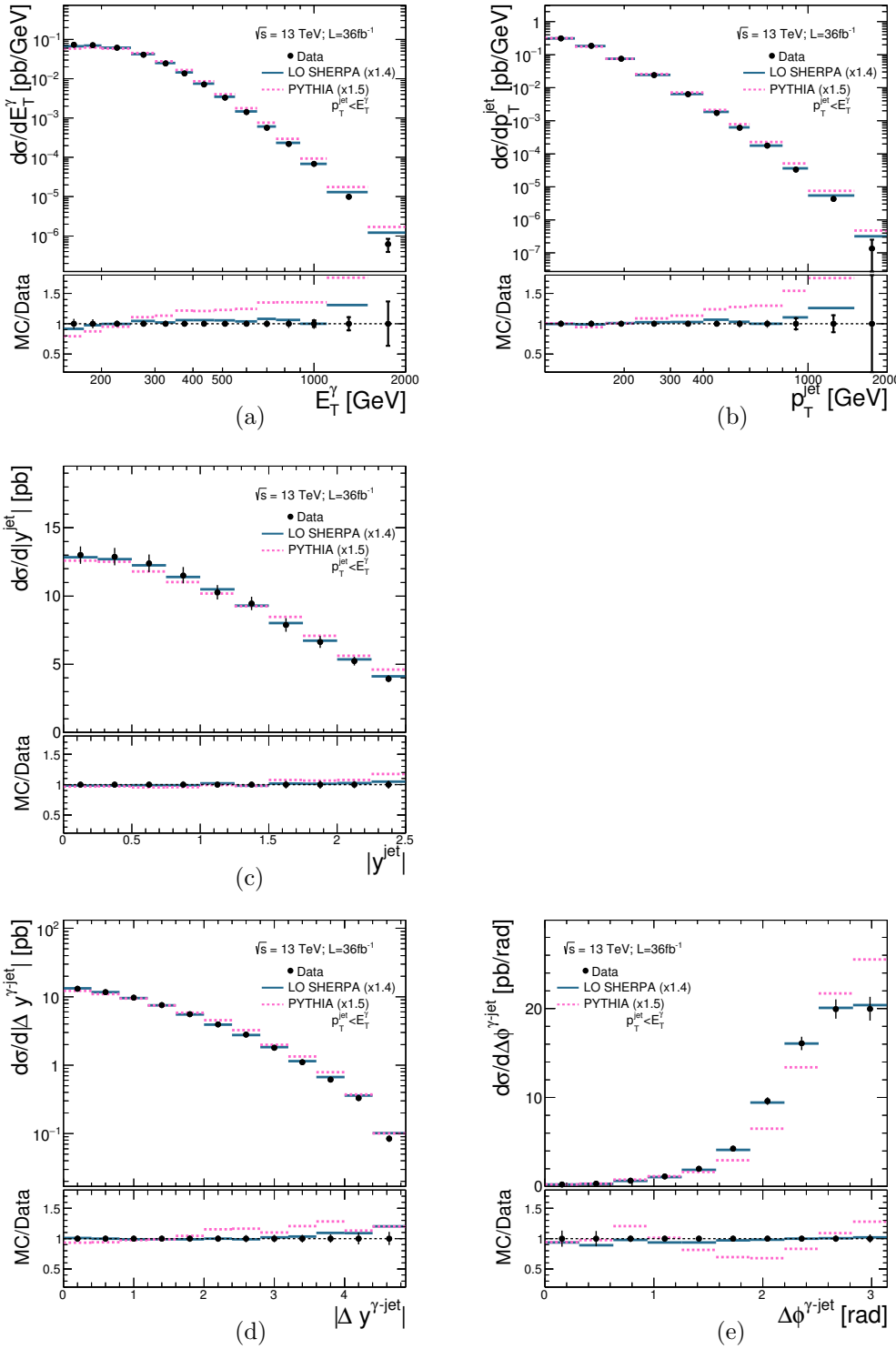


Figure 9.92: Measured cross sections for isolated-photon plus two jets production (dots) as functions of (a) E_{T}^{γ}, (b) $p_{\mathrm{T}}^{\mathrm{jet}}$, (c) $|y^{\mathrm{jet}}|$, (d) $|\Delta y^{\gamma-\mathrm{jet}}|$ and (e) $\Delta\phi^{\gamma-\mathrm{jet}}$ for the direct-enriched sample. The predictions from PYTHIA (dashed lines) and SHERPA (solid lines) are also shown; these predictions are normalised to the measured integrated cross section using the values indicated in parentheses. The bottom part of each figure shows the ratio of the MC predictions to the measured cross section. The inner (outer) error bars represent the statistical uncertainties (the statistical and systematic uncertainties added in quadrature). For most of the points, the error bars are smaller than the marker size and, thus, not visible.

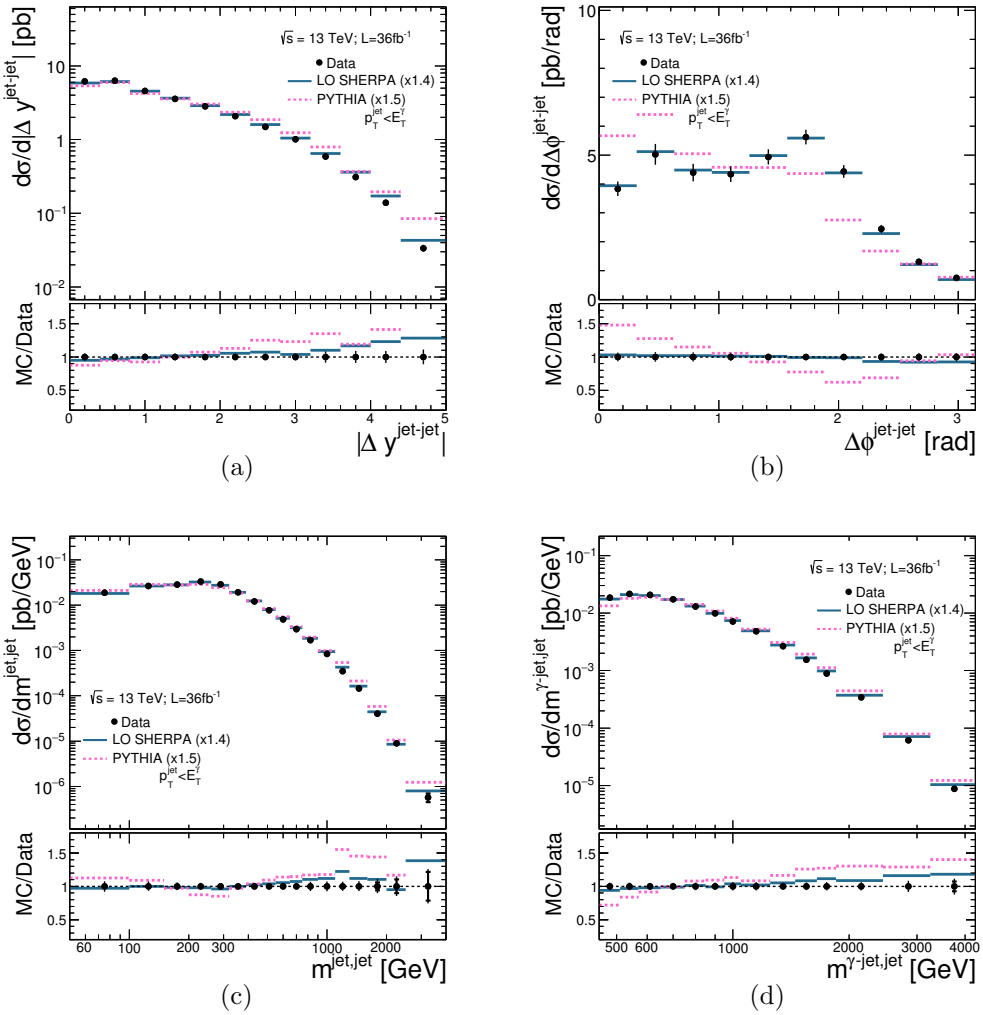


Figure 9.93: Measured cross sections for isolated-photon plus two jets production (dots) as functions of (a) $|\Delta y^{\text{jet}-\text{jet}}|$, (b) $\Delta\phi^{\text{jet}-\text{jet}}$, (c) $m^{\text{jet}-\text{jet}}$ and (d) $m^{\gamma-\text{jet}-\text{jet}}$ for the direct-enriched sample. The predictions from Pythia (dashed lines) and Sherpa (solid lines) are also shown; these predictions are normalised to the measured integrated cross section using the values indicated in parentheses. The bottom part of each figure shows the ratio of the MC predictions to the measured cross section. The inner (outer) error bars represent the statistical uncertainties (the statistical and systematic uncertainties added in quadrature). For most of the points, the error bars are smaller than the marker size and, thus, not visible.

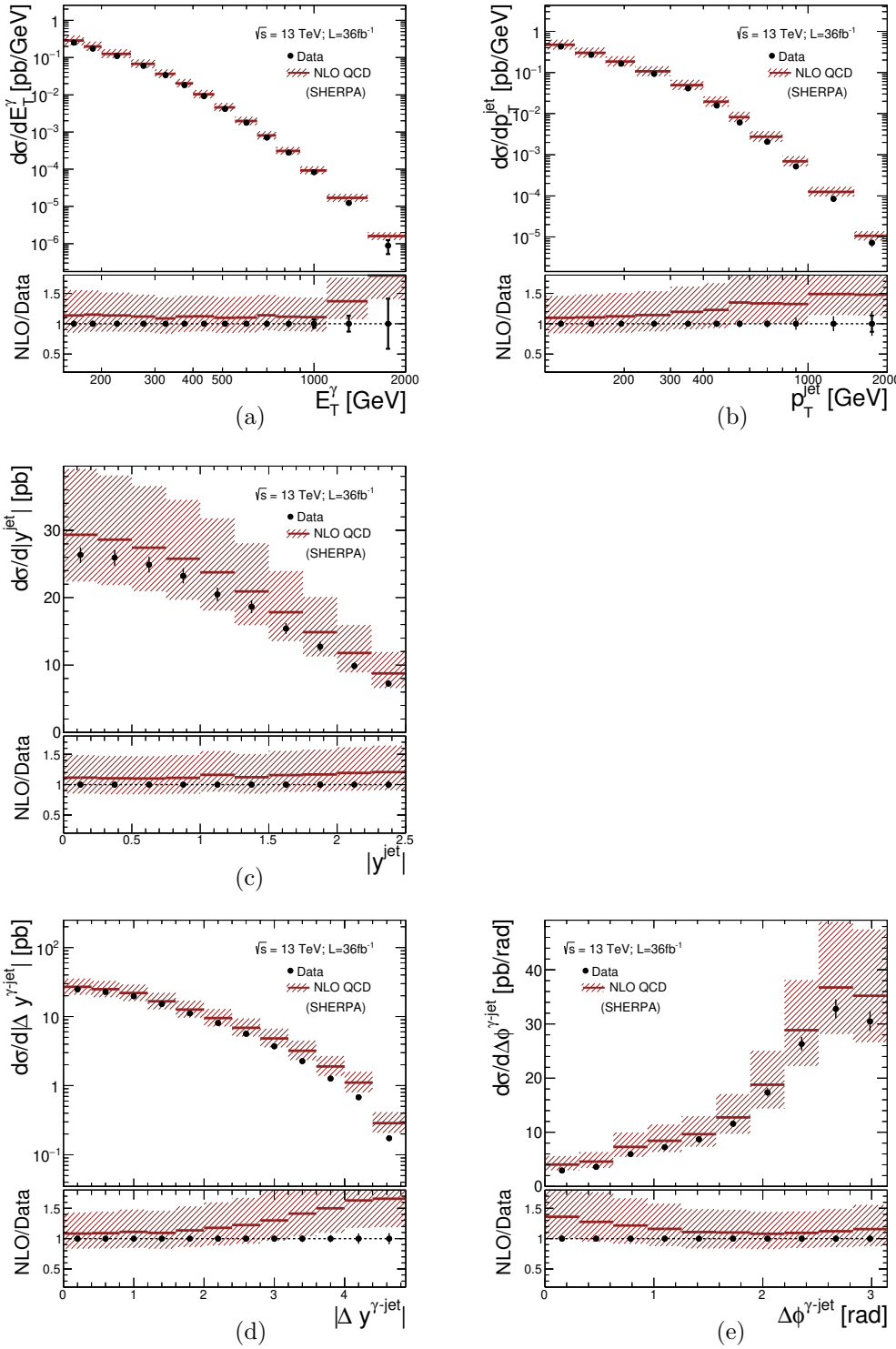


Figure 9.94: Measured cross sections for isolated-photon plus two jets production (dots) as functions of (a) E_{T}^{γ}, (b) $p_{\mathrm{T}}^{\mathrm{jet}}$, (c) $|y^{\mathrm{jet}}|$, (d) $|\Delta y^{\gamma-\mathrm{jet}}|$ and (e) $\Delta\phi^{\gamma-\mathrm{jet}}$ for the total sample. The NLO QCD predictions from SHERPA (solid lines) based on the NNPDF3.0 PDFs are also shown. The bottom part of each figure shows the ratio of the predictions to the measured cross section. The inner (outer) error bars represent the statistical uncertainties (the statistical and systematic uncertainties added in quadrature) and the hatched bands represent the theoretical uncertainty. For most of the points, the error bars are smaller than the marker size and, thus, not visible.

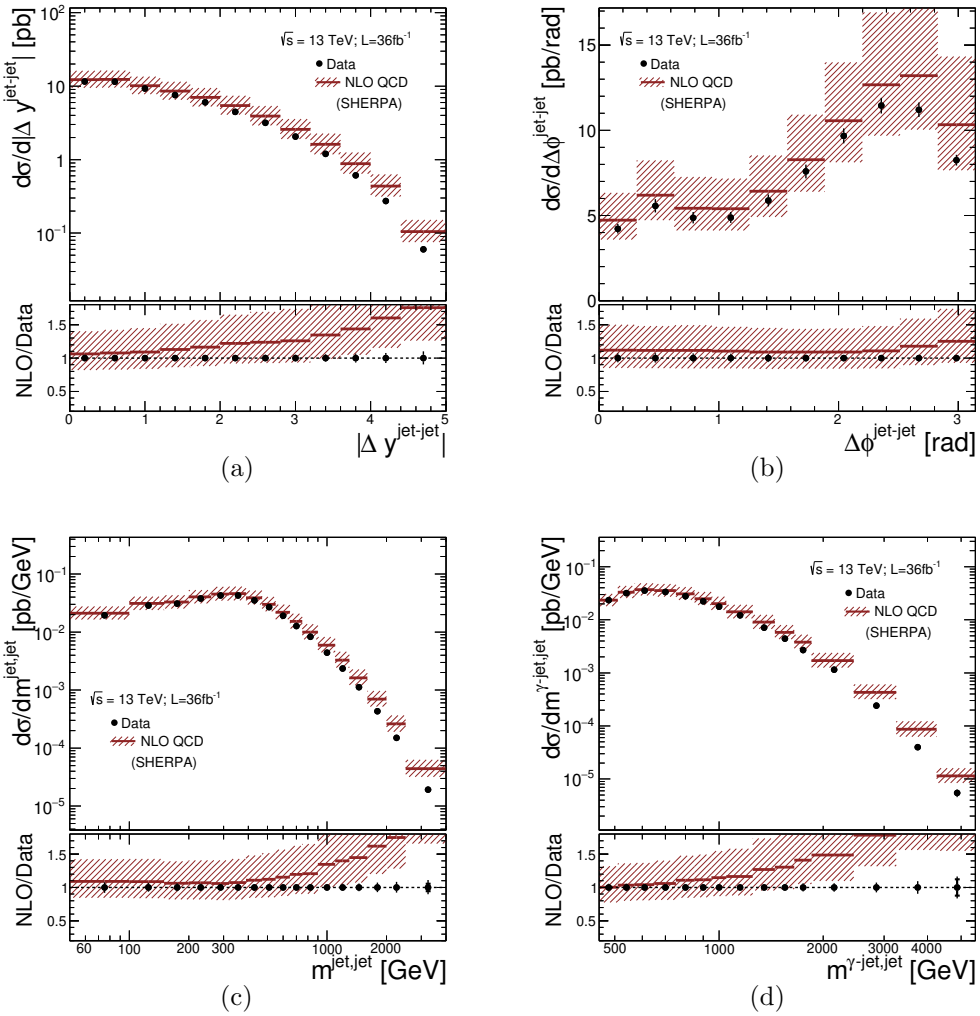


Figure 9.95: Measured cross sections for isolated-photon plus two jets production (dots) as functions of (a) $|\Delta y^{\text{jet}-\text{jet}}|$, (b) $\Delta\phi^{\text{jet}-\text{jet}}$, (c) $m^{\text{jet}-\text{jet}}$ and (d) $m^{\gamma-\text{jet}-\text{jet}}$ for the total sample. The NLO QCD predictions from SHERPA (solid lines) based on the NNPDF3.0 PDFs are also shown. The bottom part of each figure shows the ratio of the predictions to the measured cross section. The inner (outer) error bars represent the statistical uncertainties (the statistical and systematic uncertainties added in quadrature) and the hatched bands represent the theoretical uncertainty. For most of the points, the error bars are smaller than the marker size and, thus, not visible.

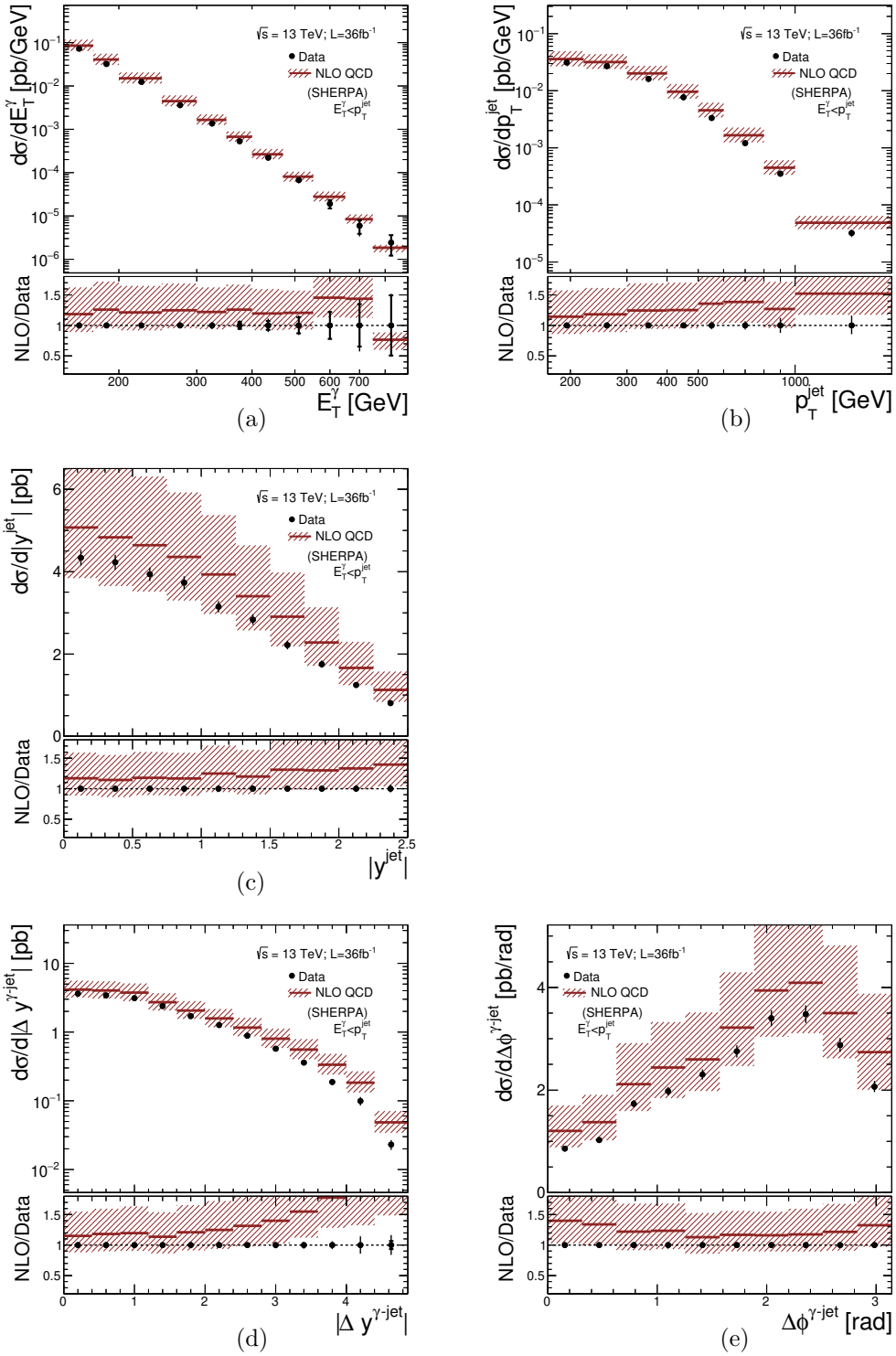


Figure 9.96: Measured cross sections for isolated-photon plus two jets production (dots) as functions of (a) E_{T}^{γ}, (b) $p_{\mathrm{T}}^{\mathrm{jet}}$, (c) $|y^{\mathrm{jet}}|$, (d) $|\Delta y^{\gamma-\mathrm{jet}}|$ and (e) $\Delta\phi^{\gamma-\mathrm{jet}}$ for the fragmentation-enriched sample. The NLO QCD predictions from SHERPA (solid lines) based on the NNPDF3.0 PDFs are also shown. The bottom part of each figure shows the ratio of the predictions to the measured cross section. The inner (outer) error bars represent the statistical uncertainties (the statistical and systematic uncertainties added in quadrature) and the hatched bands represent the theoretical uncertainty. For most of the points, the error bars are smaller than the marker size and, thus, not visible.

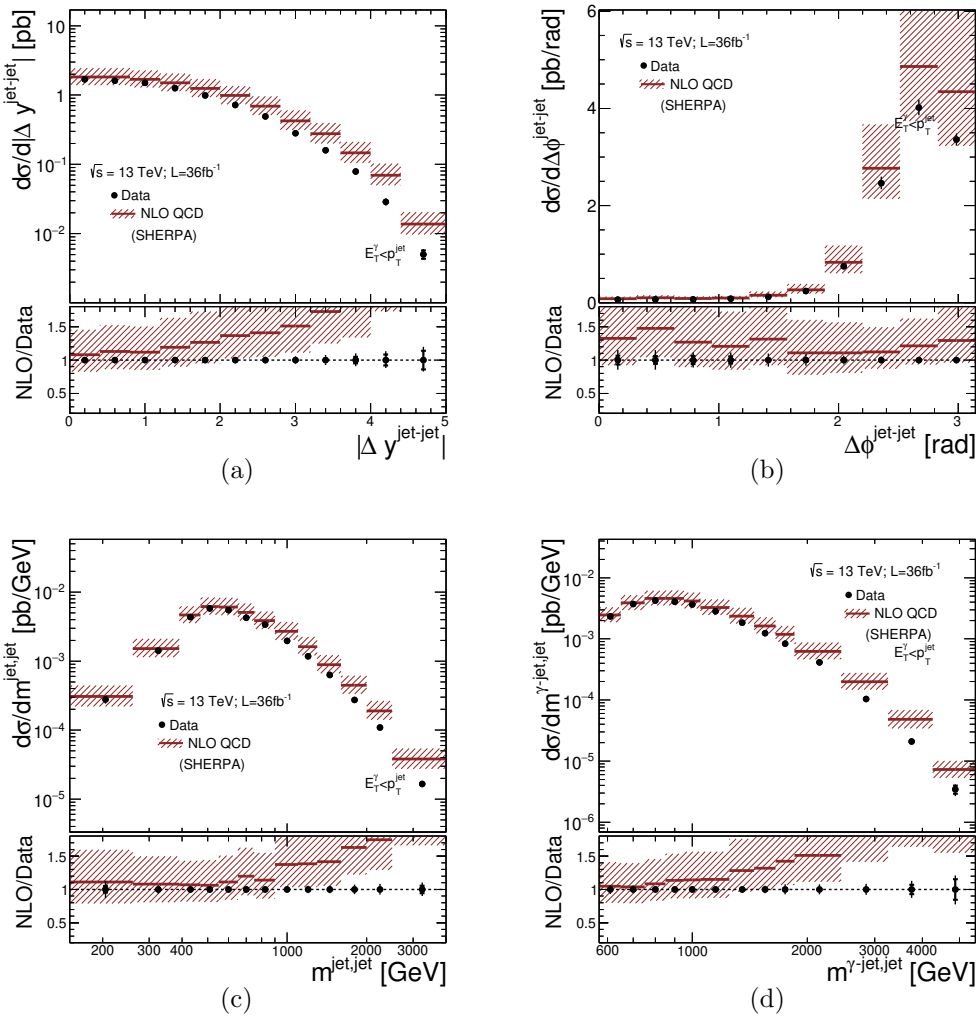


Figure 9.97: Measured cross sections for isolated-photon plus two jets production (dots) as functions of (a) $|\Delta y^{\text{jet}-\text{jet}}|$, (b) $\Delta\phi^{\text{jet}-\text{jet}}$, (c) $m^{\text{jet}-\text{jet}}$ and (d) $m^{\gamma-\text{jet}-\text{jet}}$ for the fragmentation-enriched sample. The NLO QCD predictions from SHERPA (solid lines) based on the NNPDF3.0 PDFs are also shown. The bottom part of each figure shows the ratio of the predictions to the measured cross section. The inner (outer) error bars represent the statistical uncertainties (the statistical and systematic uncertainties added in quadrature) and the hatched bands represent the theoretical uncertainty. For most of the points, the error bars are smaller than the marker size and, thus, not visible.

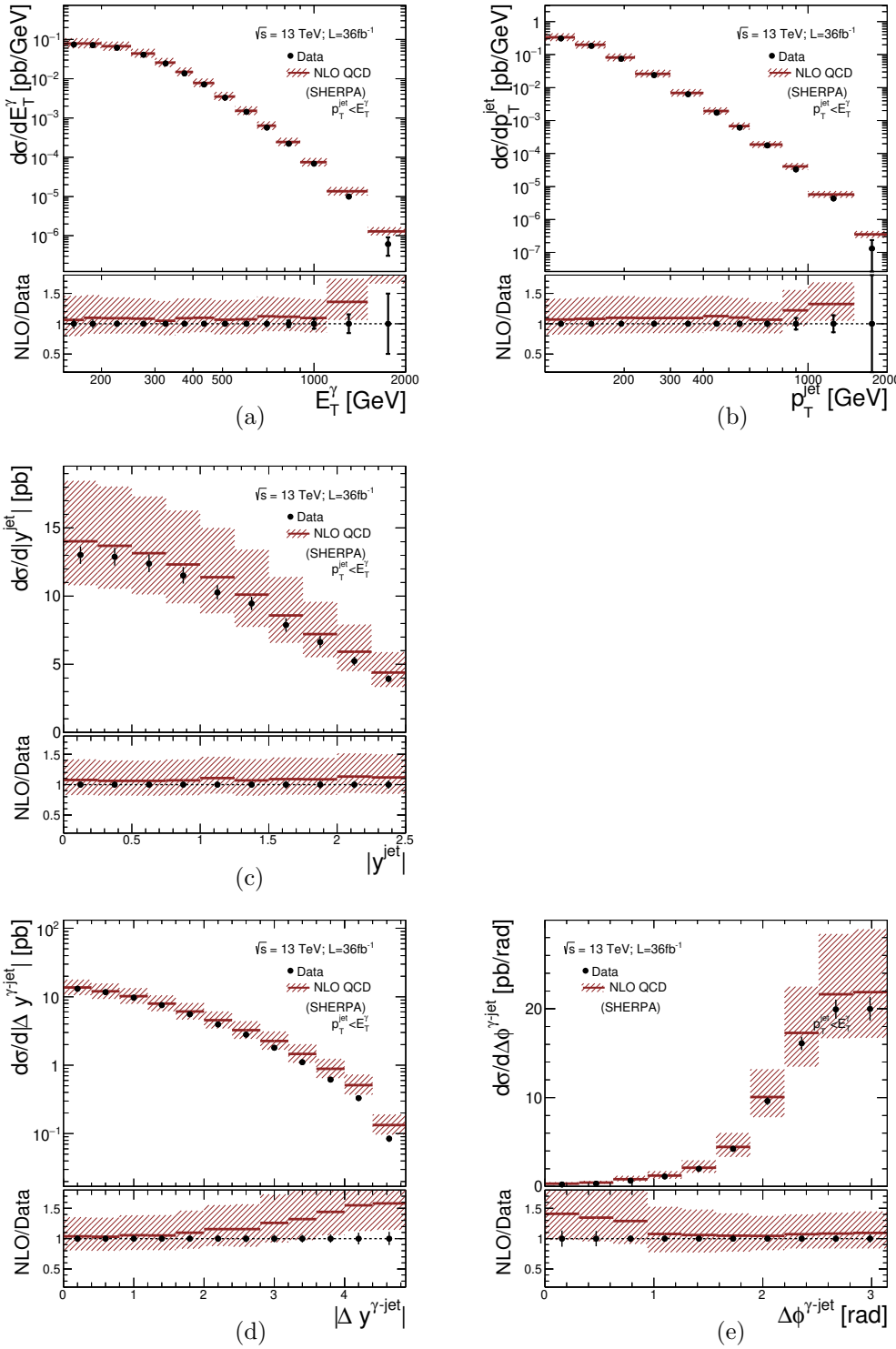


Figure 9.98: Measured cross sections for isolated-photon plus two jets production (dots) as functions of (a) E_{T}^{γ}, (b) $p_{\mathrm{T}}^{\mathrm{jet}}$, (c) $|y^{\mathrm{jet}}|$, (d) $|\Delta y^{\gamma-\mathrm{jet}}|$ and (e) $\Delta\phi^{\gamma-\mathrm{jet}}$ for the direct-enriched sample. The NLO QCD predictions from SHERPA (solid lines) based on the NNPDF3.0 PDFs are also shown. The bottom part of each figure shows the ratio of the predictions to the measured cross section. The inner (outer) error bars represent the statistical uncertainties (the statistical and systematic uncertainties added in quadrature) and the hatched bands represent the theoretical uncertainty. For most of the points, the error bars are smaller than the marker size and, thus, not visible.

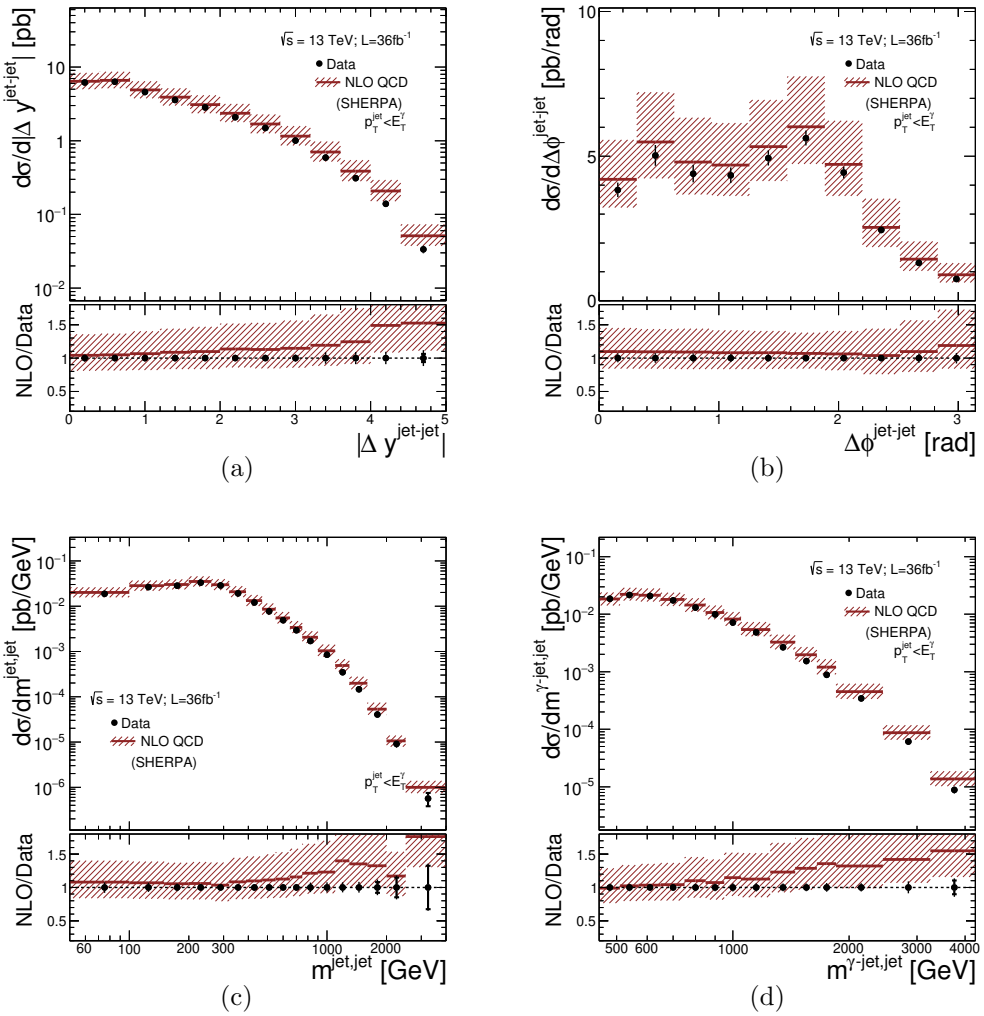


Figure 9.99: Measured cross sections for isolated-photon plus two jets production (dots) as functions of (a) $|\Delta y^{\text{jet}-\text{jet}}|$, (b) $\Delta\phi^{\text{jet}-\text{jet}}$, (c) $m^{\text{jet}-\text{jet}}$ and (d) $m^{\gamma-\text{jet}-\text{jet}}$ for the direct-enriched sample. The NLO QCD predictions from SHERPA (solid lines) based on the NNPDF3.0 PDFs are also shown. The bottom part of each figure shows the ratio of the predictions to the measured cross section. The inner (outer) error bars represent the statistical uncertainties (the statistical and systematic uncertainties added in quadrature) and the hatched bands represent the theoretical uncertainty. For most of the points, the error bars are smaller than the marker size and, thus, not visible.

10
Summary and conclusions

Cross sections for isolated prompt-photon production were measured inclusively or in association with jets in the four analyses presented in this dissertation. The results obtained provide stringent tests of QCD and a wealth of data that can be useful for validating theoretical calculations, tuning MC generators or to constrain the gluon density inside the proton.

The **cross sections for inclusive isolated-photon production in pp collisions at $\sqrt{s} = 13$ TeV** using a data set with an integrated luminosity of 3.2 fb^{-1} were measured. Cross sections were measured as functions of E_{T}^{γ} in four different regions of η^{γ} for photons with $E_{\mathrm{T}}^{\gamma} > 125$ GeV and $|\eta^{\gamma}| < 2.37$, excluding the region $1.37 < |\eta^{\gamma}| < 1.56$. The isolation of photons was ensured by requiring that the transverse energy in a cone of size $\Delta R = 0.4$ around the photon is smaller than $4.8\ \mathrm{GeV} + 4.2 \cdot 10^{-3} \cdot E_{\mathrm{T}}^{\gamma}$ [GeV]. Values of E_{T}^{γ} up to 1.5 TeV were accessed. The fiducial cross section was measured to be $\sigma_{\mathrm{meas}} = 399 \pm 13$ (exp.) ± 8 (lumi.) pb. The experimental systematic uncertainties were evaluated such that the correlations with previous ATLAS measurements of prompt-photon production can be used in the fits of the proton parton distribution functions. A combined fit of the measurements in pp collisions at centre-of-mass energies of 8 and 13 TeV which takes into account the correlated systematic uncertainties has a stronger constraining power in the evolution of the proton PDFs than either set of measurements alone.

The predictions of the Pythia and Sherpa Monte Carlo models give a good description of the shape of the measured cross-section distributions except for $E_{\mathrm{T}}^{\gamma} \gtrsim 500$ GeV in the regions $|\eta^{\gamma}| < 0.6$ and $0.6 < |\eta^{\gamma}| < 1.37$. The NLO QCD predictions, using JetPhox and based on different sets of proton PDFs, provide an adequate description of the data within the experimental and theoretical uncertainties. For most of the phase space, the theoretical uncertainties are larger than those of experimental nature and dominated by the terms beyond NLO. The NNLO pQCD with LL electroweak corrections provide a more stringent test of the theory and describe the data within the reduced theoretical uncertainties.

The **ratio of cross sections for inclusive isolated-photon production in pp collisions at $\sqrt{s} = 13$ and 8 TeV ($R_{13/8}$)** was measured as a function of E_{T}^{γ} in different regions of η^{γ} for photons with $E_{\mathrm{T}}^{\gamma} > 125$ GeV and $|\eta^{\gamma}| < 2.37$, excluding the region $1.37 < |\eta^{\gamma}| < 1.56$. In the estimation of the experimental systematic uncertainties for $R_{13/8}$, the correlations between the measurements at the two centre-of-mass energies were taken into account. The systematic uncertainty arising from the photon energy scale, which is dominant for the individual cross sections, is reduced significantly in $R_{13/8}$ and is no longer the dominant experimental uncertainty. The total systematic uncertainty for $R_{13/8}$ is below 5% in most of the phase space of the measurement.

The predictions from NLO QCD calculations were compared to the measured $R_{13/8}$. The theoretical uncertainties affecting these predictions were also evaluated taking into account the correlations between the two centre-of-mass energies. A significant reduction in the uncertainty of the ratio is achieved when the calculations are considered as fully correlated at both centre-of-mass energies. The theoretical uncertainties in the ratio are below 2% for most of the phase space of the measurement. Within these reduced experimental and theoretical uncertainties, the NLO QCD predictions based on current parameterisations of the proton PDFs agree with the data. The level of agreement achieved validates the description of the evolution of isolated-photon production in pp collisions from $\sqrt{s} = 8$ to 13 TeV.

The comparison of the measured $R_{13/8}$ with the predictions represents a more stringent test of the pQCD calculations than it is possible at NLO with the individual cross sections. The theoretical uncertainties due to the variations of the scales, which are dominant, are approximately 10–15% for the cross-section predictions whereas for $R_{13/8}$, they are below 2% for most of the phase space considered. The use of $R_{13/8}$ as a probe of the evolution, having significantly reduced experimental and theoretical uncertainties, provides a tighter constraint on possible deviations from the Standard Model predictions. Even if some sensitivity to the proton PDF is lost by taking the ratio of cross-section measurements, the reduction achieved in the experimental uncertainties implies that the measured $R_{13/8}$ is still interesting to constrain further the gluon PDF and its uncertainty when this measurement is included in a global QCD fit, especially once the often-ignored theoretical uncertainties are taken into account in such fits.

To reduce further the experimental uncertainty, measurements were also presented of the double ratio of $R_{13/8}$ over the ratio of the fiducial cross sections for Z boson production at 13 and 8 TeV ($D_{13/8}^{\gamma/Z}$). In $D_{13/8}^{\gamma/Z}$, the uncertainty due to the luminosity cancels out at the expense of a small increase in the systematic uncertainty leading to a more precise measurement of the evolution of the inclusive-photon cross section with the centre-of-mass energy. The theoretical prediction, based on NNLO (NLO) QCD calculations for Z boson (inclusive-photon) production, describes well the measurements within the reduced experimental and theoretical uncertainties.

The 2015 data set was also used in the **measurement of the cross sections for the production of one isolated photon in association with one jet in proton–proton collisions at $\sqrt{s} = 13$ TeV**. The photon was required to have $E_{\mathrm{T}}^{\gamma} > 125$ GeV and $|\eta^{\gamma}| < 2.37$, excluding the region $1.37 < |\eta^{\gamma}| < 1.56$. The jets were reconstructed using the anti-k_t algorithm with radius parameter $R = 0.4$.

The cross sections were measured as functions of E_{T}^{γ}, $p_{\mathrm{T}}^{\mathrm{jet-lead}}$ and $\Delta\phi^{\gamma-\mathrm{jet}}$ with $p_{\mathrm{T}}^{\mathrm{jet-lead}} > 100$ GeV and $|y^{\mathrm{jet}}| < 2.37$; the measurements extend up to values of 1.5 TeV in E_{T}^{γ} and $p_{\mathrm{T}}^{\mathrm{jet-lead}}$. The dependence with $m^{\gamma-\mathrm{jet}}$ and $|\cos\theta^{\star}|$ was measured for $m^{\gamma-\mathrm{jet}} > 450$ GeV and $|y^{\mathrm{jet}}| + |\eta^{\gamma}| < 2.37$.

The predictions of the tree-level plus parton-shower Monte Carlo models Pythia and LO Sherpa give a reasonable description of the shape of the data, except for $p_{\mathrm{T}}^{\mathrm{jet-lead}}$ in the case of Pythia. The fixed-order NLO QCD calculations of JetPhox, corrected for hadronisation and underlying-event effects, and the multi-leg NLO QCD plus parton-shower calculations of Sherpa describe the measured cross sections within the experimental and theoretical uncertainties. Interestingly, the normalisation of the measured cross section as a function of E_{T}^{γ} is described better by the NLO calculations in this more

restricted phase space than in the inclusive-photon measurements, in which no jet requirements are imposed. The comparison of predictions based on different parameterisations of the proton PDFs shows that the description of the data does not depend significantly on the specific PDF set used. The only meaningful prediction for $\mathrm{d}\sigma/\mathrm{d}\Delta\phi^{\gamma-\mathrm{jet}}$ is that of NLO Sherpa, which is able to reproduce the data down to $\Delta\phi^{\gamma-\mathrm{jet}} = \pi/2$ due to the inclusion of the matrix elements for $2 \to n$ processes with $n = 4$ and 5. The measured dependence with $|\cos\theta^{\star}|$ is consistent with the dominance of processes in which a quark is being exchanged; the experimental (theoretical) uncertainty on $\mathrm{d}\sigma/\mathrm{d}|\cos\theta^{\star}|$ amounts to $3-4\%$ (10% for JetPhox and $15-25\%$ for Sherpa NLO). All these studies provide stringent tests of pQCD and validate the description of the dynamics of isolated-photon plus jet production in pp collisions at $\sqrt{s} = 13$ TeV.

Measurements of the cross sections for the production of an isolated photon in association with two jets in pp collisions at $\sqrt{s} = 13$ TeV, $pp \to \gamma$ + jet + jet + X, were also presented. These measurements were based on an integrated luminosity of 36.1 fb^{-1} of ATLAS data recorded at the LHC. The photon was required to have $E_{\mathrm{T}}^{\gamma} > 150$ GeV and $|\eta^{\gamma}| < 2.37$, excluding the region $1.37 < |\eta^{\gamma}| < 1.56$. The jets were reconstructed using the anti-k_t algorithm with radius parameter $R = 0.4$. The cross sections were measured as functions of E_{T}^{γ}, $p_{\mathrm{T}}^{\mathrm{jet}}$, $|y^{\mathrm{jet}}|$, $\Delta\phi^{\gamma-\mathrm{jet}}$, $|\Delta y^{\gamma-\mathrm{jet}}|$, $m^{\mathrm{jet}-\mathrm{jet}}$, $\Delta\phi^{\mathrm{jet}-\mathrm{jet}}$, $|\Delta y^{\mathrm{jet}-\mathrm{jet}}|$ and $m^{\gamma-\mathrm{jet}-\mathrm{jet}}$ in three different regions of phase space, namely the total region, the fragmentation-enriched region where $E_{\mathrm{T}}^{\gamma} < p_{\mathrm{T}}^{\mathrm{jet2}}$ and the direct-enriched region where $E_{\mathrm{T}}^{\gamma} > p_{\mathrm{T}}^{\mathrm{jet1}}$. The measurements extend up to values of 2 TeV in E_{T}^{γ} and $p_{\mathrm{T}}^{\mathrm{jet}}$. The dependence of the cross sections on $m^{\mathrm{jet}-\mathrm{jet}}$ and $m^{\gamma-\mathrm{jet}-\mathrm{jet}}$ were measured up to values of 4 TeV and 5.5 TeV, respectively. The characteristics observed in the measured cross sections in the fragmentation- and direct-enriched phase-space regions are in agreement with the expectations based on the two underlying mechanisms, which dominate each sample.

The predictions of the tree-level plus parton-shower MC model of LO Sherpa, with up to four additional partons at the matrix-element level, give a good description of the shape of the data distributions, except at high E_{T}^{γ}, $|\Delta y^{\mathrm{jet}-\mathrm{jet}}|$ and $m^{\gamma-\mathrm{jet}-\mathrm{jet}}$. The predictions of Pythia, in general, fail to describe the shape of the data. In Pythia, one of the three final-state objects comes from the parton shower making difficult a precise description of the kinematic properties and angular correlations between the photon and the jets. Besides, the fragmentation contribution in this sample tends to be overestimated, biasing the shape description of the observables. The predictions of the NLO calculations of Sherpa describe the data adequately in shape and normalisation within the experimental and theoretical uncertainties; the latter are much larger than the experimental ones. However, there is a tendency of the predictions to have a different shape than the measurements for some observables, most noticeably for the $|\Delta y^{\gamma-\mathrm{jet}}|$, $\Delta\phi^{\gamma-\mathrm{jet}}$, $m^{\mathrm{jet}-\mathrm{jet}}$ and $m^{\gamma-\mathrm{jet}-\mathrm{jet}}$ cross sections in the fragmentation-enriched phase-space region. The tendency to overestimate the tail in $m^{\mathrm{jet}-\mathrm{jet}}$ has been observed in other Sherpa NLO boson plus jets processes. This is believed to be due to a combination of the shower activity as well as the scale choice for NLO real emissions. All these studies provide stringent tests of pQCD and scrutinise the description of the dynamics of isolated-photon plus two jets production in pp collisions up to $\mathcal{O}(\alpha_{\mathrm{em}}\alpha_{\mathrm{s}}^{3})$.

Resumen en español

La producción de fotones aislados ha sido medida de manera inclusiva o acompañada de jets en los cuatro análisis presentados en esta tesis. Estos análisis proporcionan test estrictos de cromodinámica cuántica y una riqueza de datos que pueden ser empleados para la validación de cálculos teóricos, ajustes de generadores Monte Carlo o para restringir la densidad de gluones dentro del protón.

Las **sección eficaz inclusiva de la producción de fotones aislados en colisiones** pp **a** $\sqrt{s} = 13$ **TeV** fue medida usando un conjunto de datos con una luminosidad integrada de 3.2 fb^{-1}. Las secciones eficaces fueron medidas en función de E_{T}^{γ} en cuatro regiones diferentes de η^{γ} para fotones con $E_{\mathrm{T}}^{\gamma} > 125$ GeV and $|\eta^{\gamma}| < 2.37$, excluyendo la región $1.37 < |\eta^{\gamma}| < 1.56$. La selección de fotones aislados se asegura requiriendo que la energía transversa en un cono de radio $\Delta R = 0.4$ alrededor del fotón sea menor que $4.8\ \mathrm{GeV} + 4.2 \cdot 10^{-3} \cdot E_{\mathrm{T}}^{\gamma}$ [GeV]. Se alcanzan valores de E_{T}^{γ} de hasta 1.5 TeV. La sección eficaz fiducial medida es $\sigma_{\mathrm{meas}} = 399 \pm 13$ (exp.) ± 8 (lumi.) pb. Las incertidumbres sistemáticas experimentales fueron evaluadas de forma que las correlaciones con medidas previas de la producción de fotones aislados con el detector ATLAS puedan ser usadas en los ajustes de la distribución de partones en el protón. Un ajuste combinado de las medidas en colisiones pp a un centro de masas de 8 y 13 TeV, teniendo en cuenta las correlaciones de las incertidumbres sistemáticas, tienen un poder restrictivo más fuerte en la evolución de las PDFs del protón que cualquier conjunto de medidas por separado.

Las prediciones de los modelos de Monte Carlo de Pythia y Sherpa dan una buena descripción de la forma de las distribuciones de las secciones eficaces medidas excepto para $E_{\mathrm{T}}^{\gamma} \gtrsim 500$ GeV en las regiones $|\eta^{\gamma}| < 0.6$ y $0.6 < |\eta^{\gamma}| < 1.37$. Las predicciones de pQCD al siguiente orden en la serie perturbativa de Jetphox basadas en diferentes conjuntos de PDF del protón, proporcionan una descripción adecuada de los datos dentro de las incertidumbres experimentales y teóricas. Para la mayor parte del espacio de fases, las incertidumbres teóricas son mayores que aquellas de naturaleza experimental y están dominadas por los términos más allá de NLO. Correcciones a NNLO en pQCD incluyendo correcciones electrodébiles a LL representan un test más robusto de la teoría; estas predicciones describen los datos dentro de las incertidumbres teóricas reducidas.

El **cociente entre las secciones eficaces de la producción de fotones aislados en colisiones** pp **a** $\sqrt{s} = 13$ **y** 8 **TeV** ($R_{13/8}$) fue medido en función de E_{T}^{γ} en diferentes regiones de η^{γ} para fotones con $E_{\mathrm{T}}^{\gamma} > 125$ GeV y $|\eta^{\gamma}| < 2.37$, excluyendo la región $1.37 < |\eta^{\gamma}| < 1.56$.

En la estimación de las incertidumbres sistemáticas experimentales de $R_{13/8}$, las correlaciones entre las medidas a ambas energías en el centro de masas se tuvieron en cuenta. Las incertidumbres sistemáticas debidas a la escala de energía del fotón, dominante para las secciones eficaces individuales, se reduce significativamente para $R_{13/8}$ dejando de ser la incertidumbre experimental dominante. La incertidumbre total sistemática sobre $R_{13/8}$ está por debajo del 5% en la mayor parte del espacio de fases de la medida.

Las predicciones de los cálculos a NLO en pQCD fueron comparados con la medida de $R_{13/8}$. Las incertidumbres teóricas que afectan a estas predicciones también han sido evaluadas teniendo en cuenta las correlaciones entre ambas energías en el centro de masas. Se obtiene una reducción significante en la incertidumbre de $R_{13/8}$ cuando los cálculos se consideran totalmente correlacionados. Las incertidumbres teóricas en el cociente de secciones eficaces están por debajo del 2% para la mayor parte del espacio de fases

de la medida. Dentro de estas incertidumbres teóricas y experimentales reducidas, las predicciones de QCD a NLO basadas en parametrizaciones actuales de las PDFs del protón están de acuerdo con los datos. El nivel de acuerdo alcanzado valida la descripción de la evolución de la producción de fotones aislados en colisiones pp desde $\sqrt{s} = 8$ a 13 TeV.

La comparación de la medida de $R_{13/8}$ con las predicciones representa un test más estricto de los cálculos de pQCD que el posible usando las medidas de las secciones eficaces individuales por separado. Las incertidumbres teóricas debidas a la variación de escalas, las cuales son dominantes, son aproximadamente 10–15% para las predicciones de la sección eficaz mientras que para $R_{13/8}$ están por debajo del 2% para la mayor parte del espacio de fases considerado. El uso de $R_{13/8}$ como prueba de la evolución, teniendo incertidumbres teóricas y experimentales significativamente reducidas, refuerza unos límites más rígidos a las posibles desviaciones de las predicciones del Modelo Estándar. Además, la reducción de las incertidumbres experimentales implica que las medidas de $R_{13/8}$ tienen el potencial de poder restringir más las PDFs del protón cuando esta medida se incluya en los ajustes globales de QCD.

Para reducir aún más las incertidumbres experimentales, se presentan las medidas del doble cociente de $R_{13/8}$ sobre la razón de las secciones eficaces fiduciales de la producción de bosones Z a 13 y 8 TeV ($D^{\gamma/Z}_{13/8}$). En $D^{\gamma/Z}_{13/8}$, la incertidumbre debida a la medida de la luminosidad se cancela a costa de un pequeño incremento en la incertidumbre sistemática estableciendo una medida más precisa de la evolución de la sección eficaz inclusiva de la producción de fotones con el incremento en la energía del centro de masas. Las predicciones teóricas, basada en cálculos de QCD a NNLO (NLO) para la producción de bosones Z (fotones aislados), describe bien las medidas dentro de las incertidumbres experimentales y teóricas reducidas.

El mismo conjunto de datos se usó para las **medidas de la sección eficaz de la producción de fotones aislados acompañados de un jet en colisiones protón–protón a $\sqrt{s} = 13$ TeV**. Los requerimientos impuesto sobre el fotón implican que este tenga $E^{\gamma}_{\mathrm{T}} > 125$ GeV y $|\eta^{\gamma}| < 2.37$, excluyendo la región $1.37 < |\eta^{\gamma}| < 1.56$. Los jets fueron reconstruidos usando el algoritmo anti-k_t con un parámetro de radio de $R = 0.4$.

Las secciones eficaces fueron medidas en función de E^{γ}_{T}, $p^{\mathrm{jet-lead}}_{\mathrm{T}}$ y $\Delta\phi^{\gamma-\mathrm{jet}}$ con $p^{\mathrm{jet-lead}}_{\mathrm{T}} > 100$ GeV y $|y^{\mathrm{jet}}| < 2.37$; las medidas se extienden hasta valores de 1.5 TeV en E^{γ}_{T} y $p^{\mathrm{jet-lead}}_{\mathrm{T}}$. La dependencia con $m^{\gamma-\mathrm{jet}}$ y $|\cos\theta^{\star}|$ fue medida para $m^{\gamma-\mathrm{jet}} > 450$ GeV y $|y^{\mathrm{jet}}| + |\eta^{\gamma}| < 2.37$.

Las predicciones a nivel árbol complementadas con cascada de partones en los modelos de Monte Carlo de Pythia y Sherpa a LO dan una descripción razonable de la forma de los datos, excepto para $p^{\mathrm{jet-lead}}_{\mathrm{T}}$ en el caso de Pythia. Los cálculos de QCD a orden fijo NLO de Jetphox, corregidos por efectos de hadronización y evento subyacente, y los cálculos de γ+1,2 jet a NLO y γ+3,4 jet a LO complementados con cascada de partones de Sherpa NLO describen las medidas de las sección eficaz dentro de las incertidumbres experimentales y teóricas. La normalización de la sección eficaz medida como función de E^{γ}_{T} está mejor descrita por los cálculos a NLO en este espacio de fases más restringido que en las medidas inclusivas de fotones en las que no se impuso ningún requerimiento sobre el jet. La comparación de las predicciones basadas en diferentes parametrizaciones de las PDFs del protón muestran que la descripción conseguida de los datos no depende significativamente de un conjunto de PDFs concreto. La única predicción relevante para $\mathrm{d}\sigma/\mathrm{d}\Delta\phi^{\gamma-\mathrm{jet}}$ es la de NLO Sherpa, capaz de reproducir los datos hasta

$\Delta\phi^{\gamma-\text{jet}} = \pi/2$ gracias a la inclusión de elementos de matriz para $2 \to n$ con $n = 4$ y 5. La dependencia medida con respecto a $|\cos\theta^{\star}|$ es consistente con la dominancia del proceso en el que un quark es intercambiado; las incertidumbres experimentales (teóricas) para $\mathrm{d}\sigma/\mathrm{d}|\cos\theta^{\star}|$ son del $3-4\%$ (10% para JetPhox y 15–25% para Sherpa NLO). Todos estos estudios proporcionan un test estricto de QCD perturbativa y validan la descripción de la dinámica de la producción de fotones aislados acompañados de un jet a $\sqrt{s} = 13$ TeV.

Por último, las **medidas de la sección eficaz de producción de un fotón aislado acompañado de dos jets en colisiones** pp **a** $\sqrt{s} = 13$ **TeV**, también han sido presentadas. Estas medidas están basadas en un conjunto de datos recogidos con el detector ATLAS con una luminosidad integrada de 36.1 fb^{-1}. Los requerimientos impuestos sobre el fotón implican que éste tenga $E_{\mathrm{T}}^{\gamma} > 125$ GeV y $|\eta^{\gamma}| < 2.37$, excluyendo la región $1.37 < |\eta^{\gamma}| < 1.56$. Los jets fueron reconstruidos usando el algoritmo anti-k_t con un parámetro de radio de $R = 0.4$. Las secciones eficaces fueron medidas en función de E_{T}^{γ}, $p_{\mathrm{T}}^{\mathrm{jet}}$, y^{jet}, $\Delta\phi^{\gamma-\mathrm{jet}}$, $|\Delta y^{\gamma-\mathrm{jet}}|$, $m^{\mathrm{jet}-\mathrm{jet}}$, $\Delta\phi^{\mathrm{jet}-\mathrm{jet}}$, $|\Delta y^{\mathrm{jet}-\mathrm{jet}}|$ y $m^{\gamma-\mathrm{jet}-\mathrm{jet}}$ en tres regiones diferentes del espacio de fases, en concreto la región total, la región enriquecida en fotones de fragmentación en la que $E_{\mathrm{T}}^{\gamma} < p_{\mathrm{T}}^{\mathrm{jet2}}$ y la región enriquecida en fotones directos en la que $E_{\mathrm{T}}^{\gamma} > p_{\mathrm{T}}^{\mathrm{jet1}}$.

Las medidas se extienden hasta valores de 2 TeV en E_{T}^{γ} y $p_{\mathrm{T}}^{\mathrm{jet}}$. La dependencia de la sección eficaz en $m^{\mathrm{jet}-\mathrm{jet}}$ y $m^{\gamma-\mathrm{jet}-\mathrm{jet}}$ fue medida hasta valores de 4 TeV y 5.5 TeV, respectivamente. Las características observadas en las secciones eficaces medidas en las regiones enriquecidas en fotones directos o de fragmentación están en acuerdo con las expectativas basadas en los dos mecanismos subyacentes que dominan cada muestra.

Las predicciones a nivel árbol complementadas con cascada de partones de acuerdo al modelo del Monte Carlo Sherpa, con hasta cuatro partones adicionales a nivel del elemento de matriz, dan una buena descripción de la forma de la distribución de los datos, excepto a valores altos de E_{T}^{γ}, $|\Delta y^{\mathrm{jet}-\mathrm{jet}}|$ and $m^{\gamma-\mathrm{jet}-\mathrm{jet}}$. Las predicciones de Pythia, en general, fallan en la descripción de la forma de los datos. En Pythia uno de los tres objetos del estado final proviene de la cascada de partones, dificultando una descripción precisa de las propiedades cinemáticas de las partículas y las correlaciones angulares entre el fotón y los jets. Además, la contribución de fragmentación en las muestras de Pythia tiende a estar sobrestimada por lo que ofrece una descripción sesgada de los observables. Las predicciones de los cálculos a NLO de Sherpa describen los datos adecuadamente en forma y normalización dentro de las incertidumbres teóricas y experimentales; siendo las primeras de mayor tamaño que las experimentales. Sin embargo, las predicciones exhiben una tendencia a tener una forma distinta a la medida en los datos para algunos observables. Éstas son especialmente notables para las secciones eficaces en función de $|\Delta y^{\gamma-\mathrm{jet}}|$, $\Delta\phi^{\gamma-\mathrm{jet}}$, $m^{\mathrm{jet}-\mathrm{jet}}$ y $m^{\gamma-\mathrm{jet}-\mathrm{jet}}$ del espacio de fases dominado por fotones de fragmentación. La tendencia a sobrestimar la cola de $m^{\mathrm{jet}-\mathrm{jet}}$ ha sido observada en otros procesos de Sherpa NLO para bosón más jets. Se cree que esto se debe a una combinación de la actividad de la cascada de partones y la elección de escala para las emisiones reales. Todos estos estudios proporcionan tests estrictos de pQCD y examinan a fondo la descripción de la dinámica de la producción de fotones aislados acompañados de dos jets en colisiones pp hasta el orden $\mathcal{O}(\alpha_{\mathrm{em}}\alpha_{\mathrm{s}}^{3})$.

A

Cross check for converted photon fraction

A good description of the converted photon fraction in data must be provided by the MC. The fraction of converted photons for signal photons is shown in Figure A.1.

After background subtraction, the fraction of converted photons in data is constant as a function of E_{T}^{γ} in the different η^{γ} regions and increases with η^{γ} due to the larger presence of material upstream of the calorimeter. The MC simulations of the signal from Pythia and Sherpa are also included in Figure A.1 and describe reasonably well the data in all η^{γ} regions. The small discrepancies observed between data and MC are better seenin the ratios shown in Figure A.2. The number of converted photons was raised (lowered) by 10% at "truth" level[1] and the ratio of the converted-photon fraction between data and MC simulations is also shown in the ratio in Figure A.2. The relative differences in the cross sections due to the changes mentioned are presented in Figure A.3. The effect is negligible for $|\eta^{\gamma}| < 1.81$ and smaller than 0.5% in the most forward η^{γ} region. No systematic uncertainty was thus considered for this effect.

The same cross check was performed for the photon+jet analysis presented in Chapter 8. The relative differences in the cross sections due to this effect are negligible and shown in Figure A.4.

[1]The photon conversion definition at "truth" level is that of photons with a decay vertex within a radius of 800mm, in which a good efficient reconstruction of photon conversions in the inner detector is achieved.

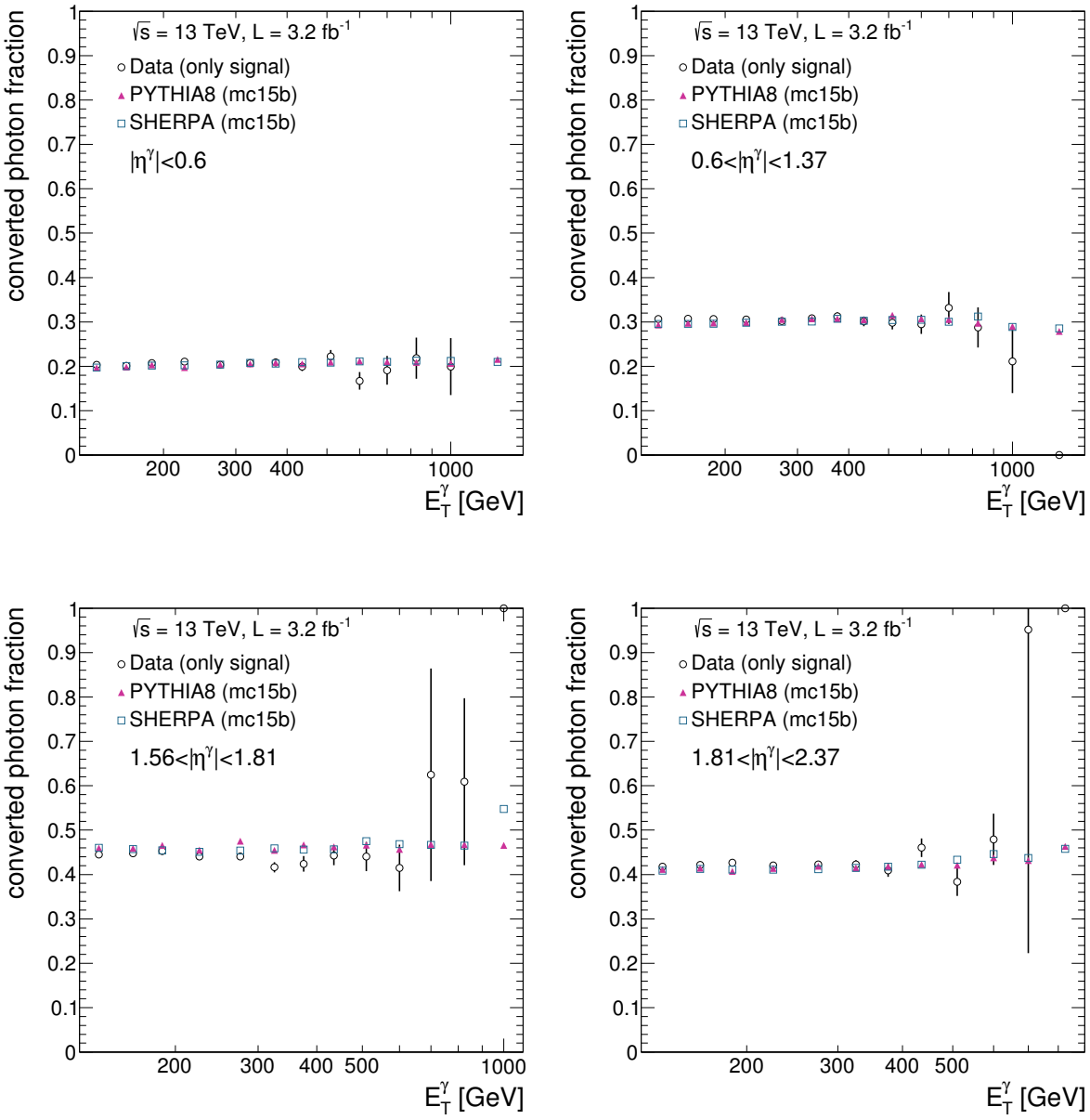


Figure A.1: Measured fractions of converted photons as functions of E_{T}^{γ} in different regions of η^{γ} after background subtraction (open circles). For comparison, the fractions computed with the Pythia (triangles) and Sherpa (open squares) signal MC samples are also included.

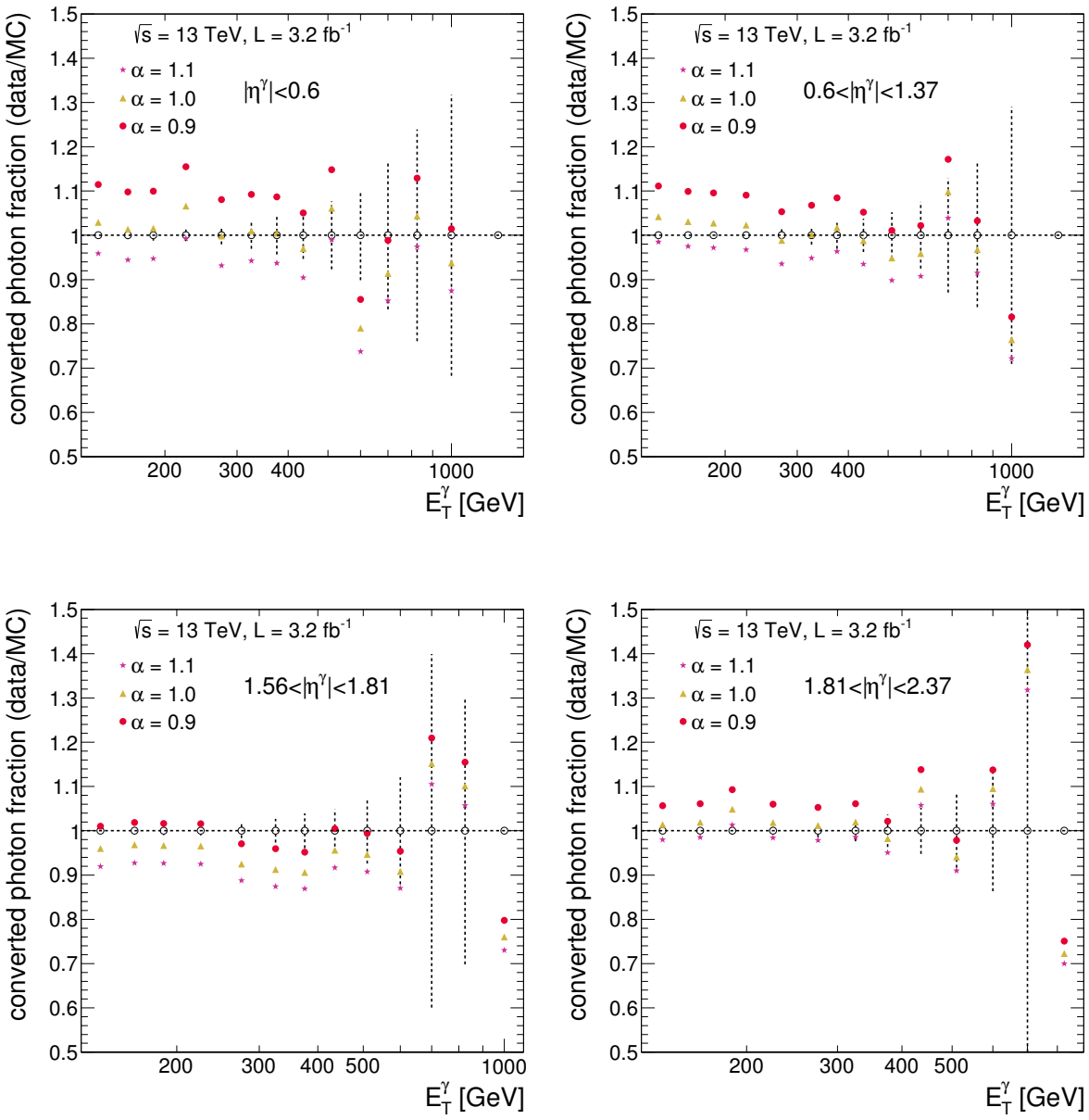


Figure A.2: Ratios of the fraction of converted photons in data and Pythia MC from Fig. A.1 as functions of E_{T}^{γ} in different regions of η^{γ} (upwards triangles). The ratios of the fractions in data and MC when the amount of converted photons in the MC was increased or decreased by the α value are also included. The vertical dashed lines display the relative statistical uncertainty in the data.

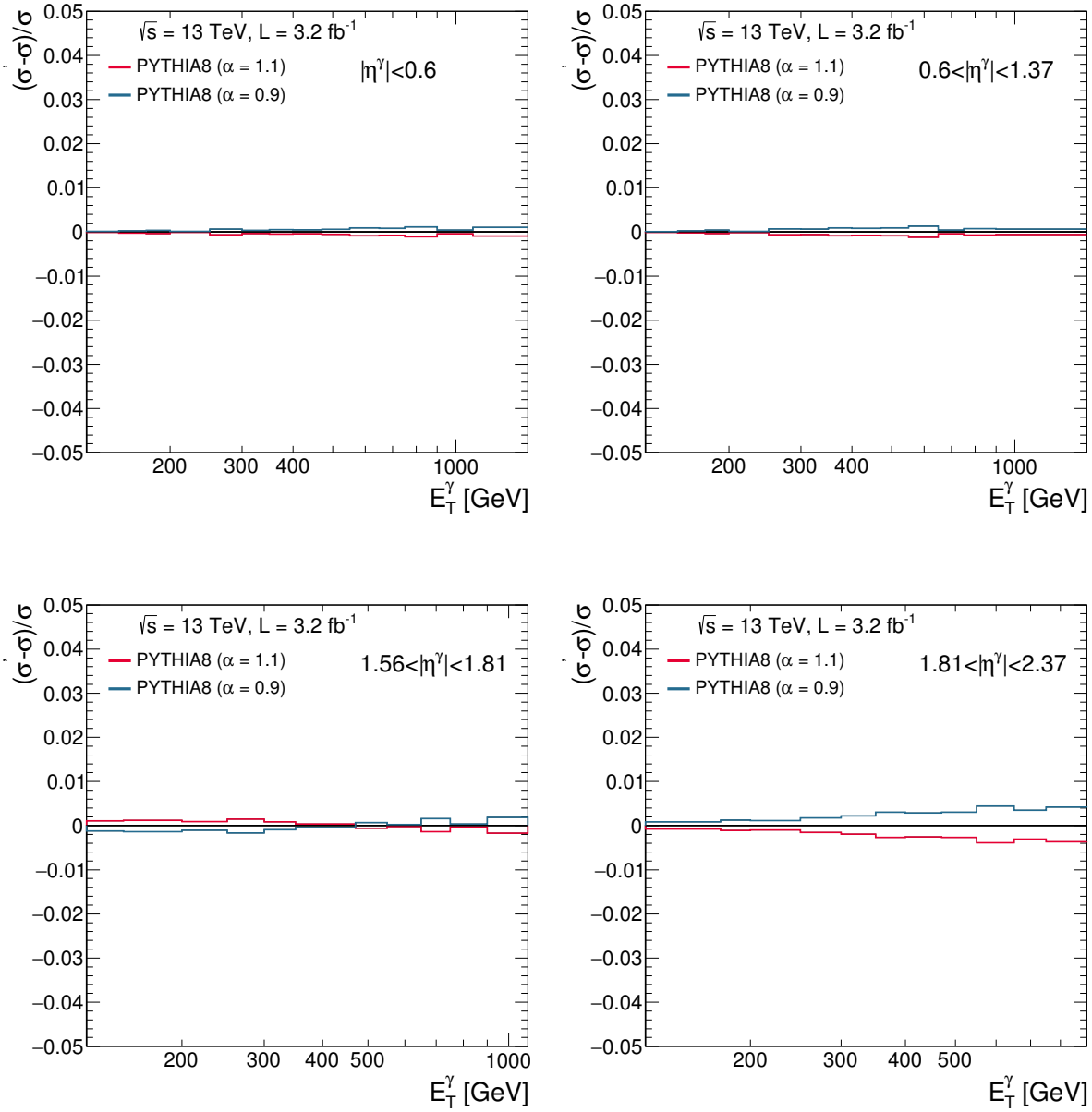


Figure A.3: Relative differences between the cross sections measured using MC samples with a fraction of converted photons increased or decreased by 10% and the nominal cross sections as functions of E_{T}^{γ} in different regions of η^{γ}.

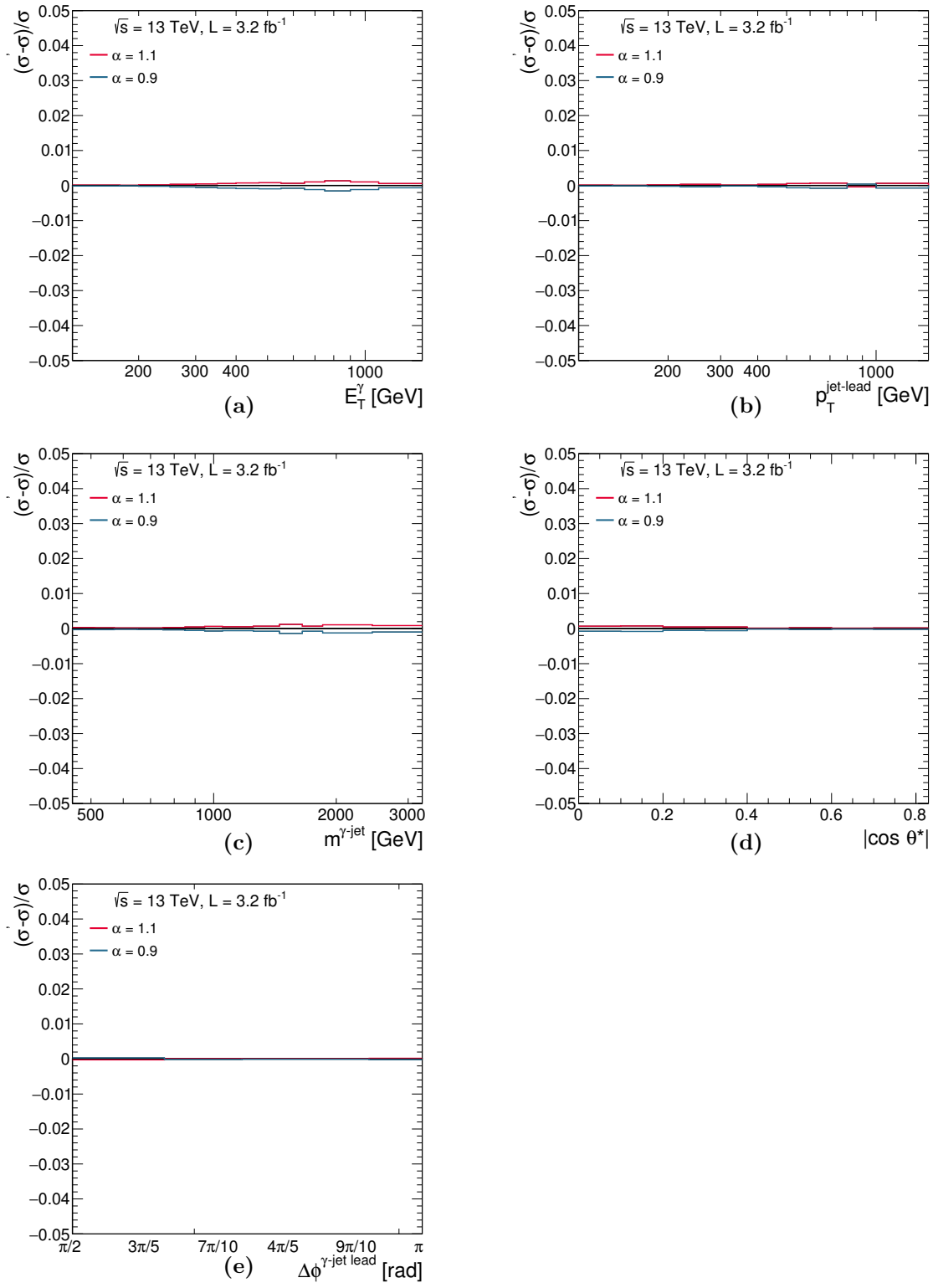


Figure A.4: Relative differences between the cross sections measured using MC samples with the contribution of true converted photons increased or decreased by 10% and the nominal cross sections as functions of (a) E_{T}^{γ}, (b) $p_{\mathrm{T}}^{\mathrm{jet-lead}}$, (c) $m^{\gamma-\mathrm{jet}}$, (d) $|\cos\theta^{\star}|$ and (e) $\Delta\phi^{\gamma-\mathrm{jet}}$.

B
Event displays

Figure B.1 shows the display of two events selected in the inclusive-photon analysis during the 2015 data-taking period. The events show different features regarding the number of jets recoiling against the photon. Figure B.2 shows the display of two events selected in the photon plus two jet analysis during the 2016 data-taking period. The event displays show typical topologies of direct-like (upper figure) and fragmentation-like (bottom figure).

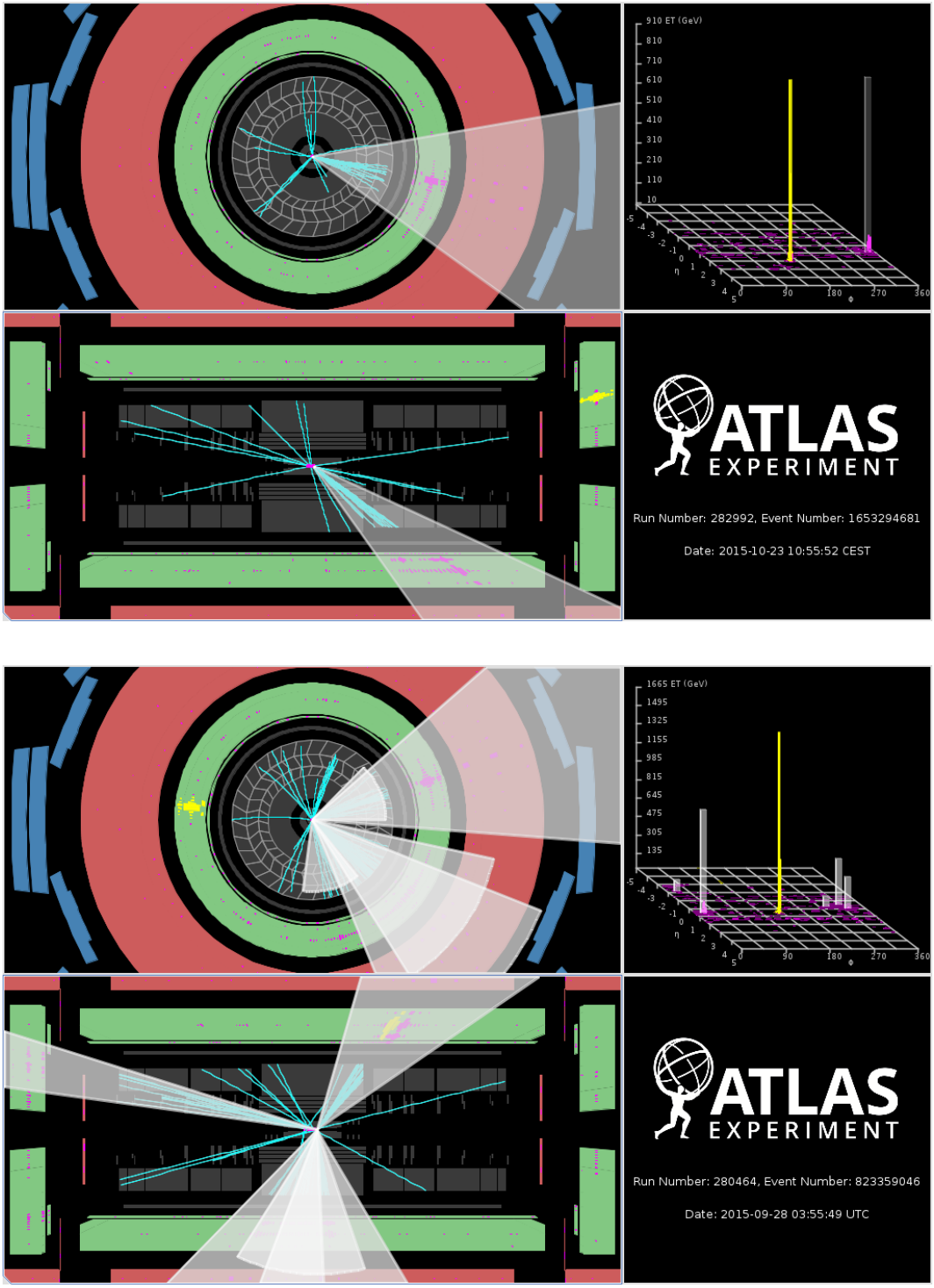


Figure B.1: Display of events 1653294681 in run 282992 (up) and 823359046 in run 280464 (bottom). The events contain a photon candidate with $E_{\mathrm{T}}^{\gamma} = 0.90$ TeV, $\eta^{\gamma} = 2.0$ and $\phi^{\gamma} = 2.9$ rad (up) and $E_{\mathrm{T}}^{\gamma} = 1.6$ TeV, $\eta^{\gamma} = 0.6$ and $\phi^{\gamma} = 3.0$ rad (bottom). The energy deposits associated to the photon candidate in the LAr calorimeter (green shaded areas) are represented by yellow boxes. The jets reconstructed with the anti-k_T algorithm using $R = 0.4$ with $p_{\mathrm{T}} > 50$ GeV are represented by the overlaid white cones. In the lego plot, the photon (jet) candidate is represented by the yellow (grey) coloured tower.

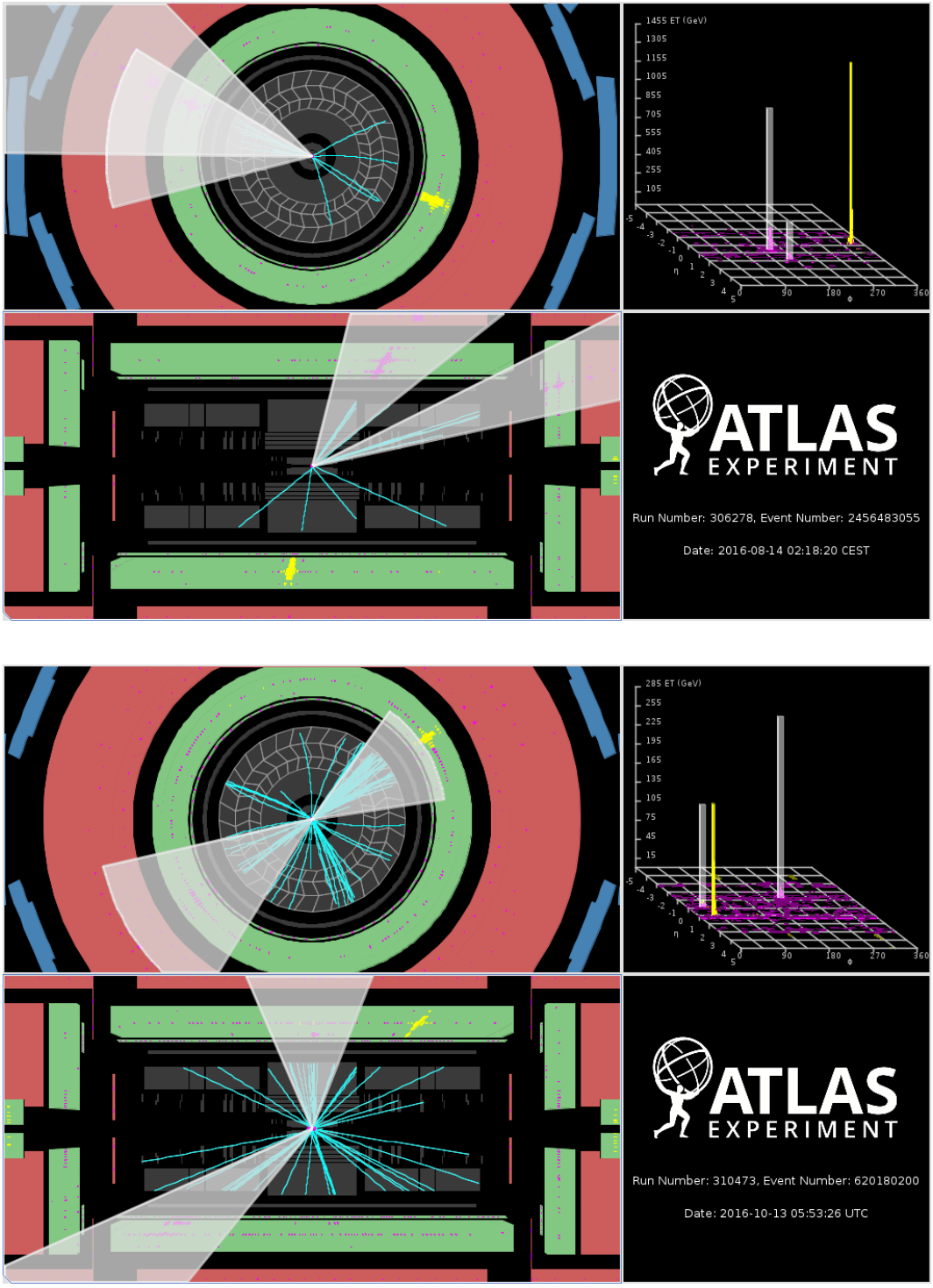


Figure B.2: Display of events 2456483055 in run 306278 (up) and 620180200 in run 310473 (bottom). The events are examples of the direct-like (up) and fragmentation-like (bottom) topologies. The energy deposits associated to the photon candidate in the LAr calorimeter (green shaded areas) are represented by yellow boxes. The jets reconstructed with the anti-k_T algorithm using $R = 0.4$ with $p_{\mathrm{T}} > 50$ GeV are represented by the overlaid white cones. In the lego plot, the photon (jet) candidate is represented by the yellow (grey) coloured tower.

C

Sources of photon energy scale systematic uncertainties

The photon energy scale calibration along with the main sources of associated uncertainties is presented in Section 4.2. The nomenclature of these uncertainties as they are used in Chapter 7 are described below:

- From the $Z \to ee$ in situ measurements two uncertainties were considered:
  - *ZeeStatUncert:* Statistical uncertainty from the data set used to extract the overall energy scale corrections.
  - *ZeeSystUncert:* Systematic uncertainties from the method used to extract the electron energy scale from $Z \to ee$ decays: event and electron selections, trigger, identification and reconstruction efficiencies, bremsstrahlung electrons, pile-up, background processes (electroweak, top and QCD).

  For Run-2 additional uncertainties were considered due to the difference in the number of η_{calo} bins and to cover the difference in the centre-of-mass energy (see Section 4.2).

- The residual mismodelling of the pedestal after pile-up correction is taken into account in *PedestalUncert*.

- Two uncertainties are related to the gain in which the signal is shaped:
  - *L1GainUncert* covers the dependence of the energy response gain (HG or MG) used in the readout chain in the first layer of the EM calorimeter. It is determined from a special run data taken with a lowered HG/MG gain threshold switch.
  - *L2GainUncert* covers the dependence of the energy response gain (HG or MG) used in the readout chain in the second layer of the EM calorimeter. It is determined from a special run data taken with a lowered HG/MG gain threshold switch.

- *PSUncert* is the uncertainty on the determination of the α_{PS} scale factor.

- Several LAr-related uncertainties are considered to take into account the lack of knowledge of the internal calorimeter geometry and the effect of cross-talk between layers:

  - *LArUnconvCalibUncert:* it is the uncertainty on the LAr $E_{1/2}$ modelling for unconverted photons.
  - *LArElecCalibUncert:* it is the uncertainty on the LAr $E_{1/2}$ modelling for electrons.
  - *LArElecUnconvUncert:* it is the uncertainty on the modelling differences between electrons and unconverted photons.
  - *LArCalibUncert:* is the uncertainty arising from the measurement of the layer intercalibration scale factors, $\alpha_{1/2}$, using $Z \to \mu\mu$ events.
  - *LARTEMPERATURE_EXTRA2015PRE*: this uncertainty covers the difference in the LAr temperature between Run-1 and Run-2.

- The uncertainties related to the $E_{1/2}$ scale are:
  - *S12Uncert*: uncertainty from the fit procedure in the measurement of $\alpha_{1/2}$.
  - *LARCALIB_EXTRA2015PRE*: it covers the Run-2 to Run-1 discrepancies in $E_{1/2}$ as Run-1 corrections were used.

- Three uncertainties are considered due to the lack of knowledge of the detector material. They are determined using MC samples with distorted geometry:
  - *MatIDUncert:* uncertainty on the inner detector material estimated using MC samples with distorted geometry in the configuration A, that is, with 5% more material in the whole inner detector.
  - *MatCryoUncert:* uncertainty on the cryostat passive material located between the inner detector and the presampler. It is estimated by scaling the differences between configuration A to the pessimistic configuration L (X), which adds a 10% (30%) of extra material in front of the barrel (end-cap) calorimeter at fixed radius (fixed $|z|$).
  - *MatCaloUncert:* uncertainty on the passive material located between the presampler and the first layer of the EM calorimeter. It is estimated by scaling the difference between configuration A to configuration M (N), which adds 5% of additional material between the barrel (end-cap) and the first layer.

- The GEANT4 modelling uncertainty *G4Uncert* takes into account the difference in the shower shape description in various physics modelling options in GEANT4.

- Several uncertainties are considered from the extrapolation of the energy scale from electrons to photons:
  - *LeakageConvUncert* and *LeakageUnconvUncert* are estimated from the differences in the lateral leakage e/γ between data and MC for converted and unconverted photons, respectively.
  - *ConvEfficiencyUncert* is estimated from the fraction of converted photons reconstructed as unconverted ones.
  - *ConvFakeRateUncert* is estimated from the fraction of unconverted photons reconstructed as converted ones.
  - *ConvRadiusUncert* is estimated from the differences observed between the conversion radius in data and MC.

D

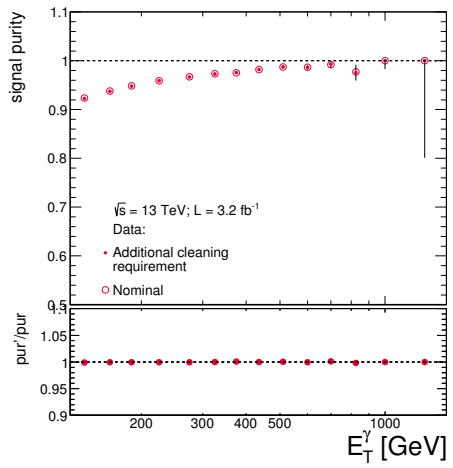
Additional cleaning requirement on jets

The presence of jets near the photon can contaminate the photon isolation cone. The impact of rejecting events in which there is at least one jet with $p_{\mathrm{T}}^{\mathrm{jet}} > 60$ GeV within a distance of $0.4 < \Delta R < 0.8$ was checked and compared to the nominal results which did not include such requirement in the selection.

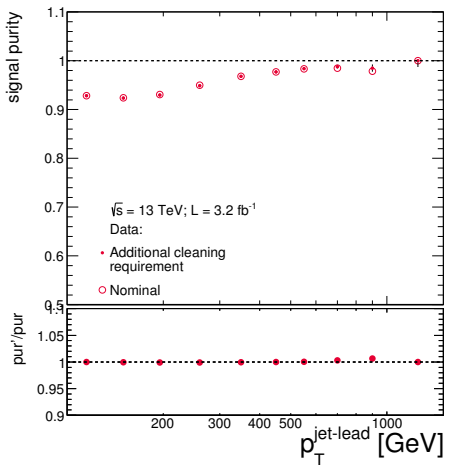
Figure D.1 shows the signal purity for the extraction with this additional requirement and that for the nominal selection as a function of the observables studied. It is observed that the signal purity remains unchanged whether this additional requirement is included in the selection or not. Therefore, the inclusion of this additional requirement does not improve the signal yield.

Figure D.2 shows the comparison of the nominal measured cross sections and the cross sections measured including the additional requirement described above. It is observed that the measured cross sections for both selections are typically consistent to better than 1%. The small differences come from the unfolding factors and, in particular, from the description of the ΔR distribution by the MC. Hence, if such additional criteria were applied, an extra uncertainty would had to be considered. Since Sherpa is a multi-leg generator, an adequate description of this complicated distribution is obtained, as demonstrated by the fact that the cross sections obtained with or without this additional requirement are consistent; however, extra jets in Pythia come only from the parton shower and so it is not guaranteed that it would also be the case. Given the fact that this requirement does not improve the signal yield, i.e. it does not reduce the background contribution, there is no reason to add an additional requirement for which the description by the MC simulation would involve an extra uncertainty.

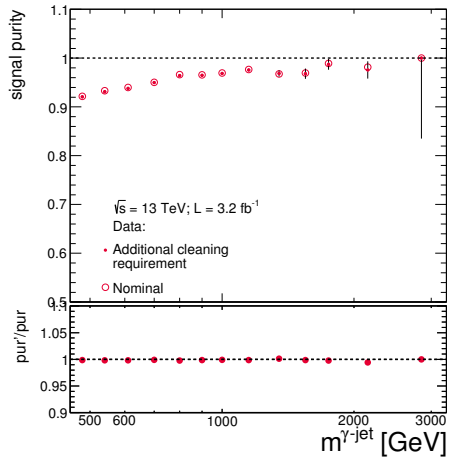
Furthermore, the NLO pQCD calculations cannot account accurately for this effect since there is at most one additional jet. As a result, the accuracy of the pQCD calculation would be degraded. In fact, applying jet vetoes in the region $0.4 < \Delta R < 0.8$ around the photon, breaks the inclusiveness of the final state considered (the rest of the final state "X" in $pp \to \gamma$+jet+X) and is prone to larger theoretical uncertainties; one could think that this requirement might help to suppress the fragmentation contribution, but, at distances of $\Delta R > 0.4$, the veto would be artificially separating contributions (in the pQCD calculation) which truly are not distinguishable. It should be noted that the fragmentation and direct contributions cannot be longer distinguished beyond LO.



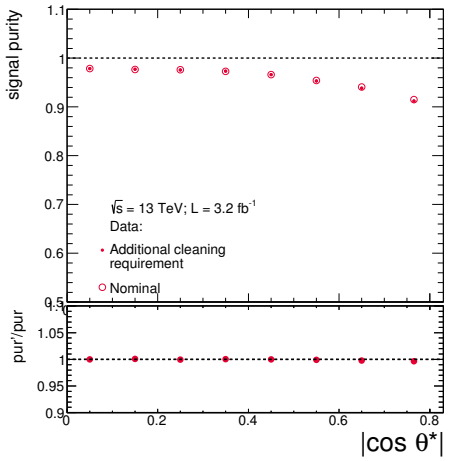
(a)



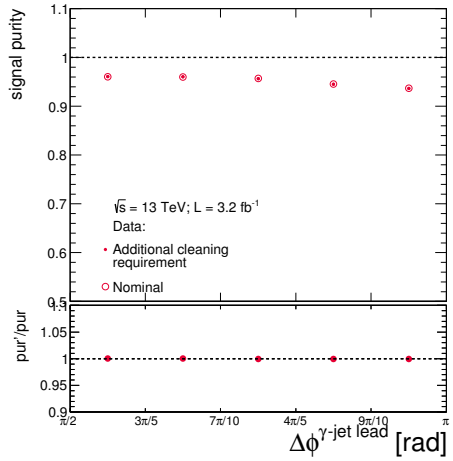
(b)



(c)

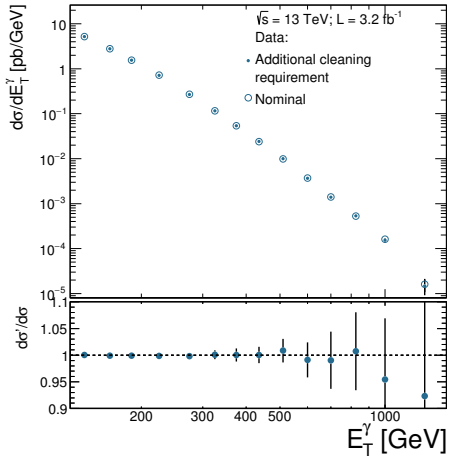


(d)

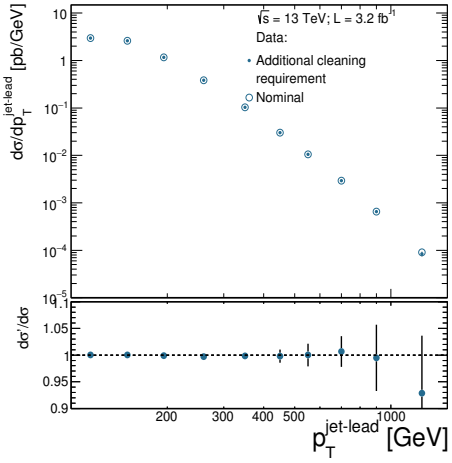


(e)

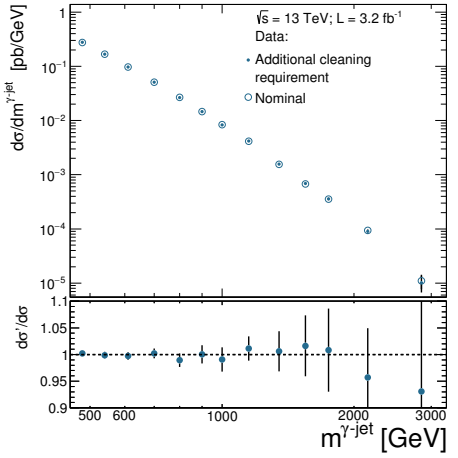
Figure D.1: Signal purity for the nominal selection (open circles) and for the selection with the additional removal of events if there is at least one jet with $p_{\mathrm{T}}^{\mathrm{jet}} > 60$ GeV within a distance $0.4 < \Delta R < 0.8$ from the photon (dots) as a function of (a) E_{T}^{γ}, (b) $p_{\mathrm{T}}^{\mathrm{jet-lead}}$, (c) $m^{\gamma-\mathrm{jet}}$, (d) $|\cos\theta^{\star}|$ and (e) $\Delta\phi^{\gamma-\mathrm{jet}}$. The lower part of the figures shows the ratio of the signal purity for both selections.



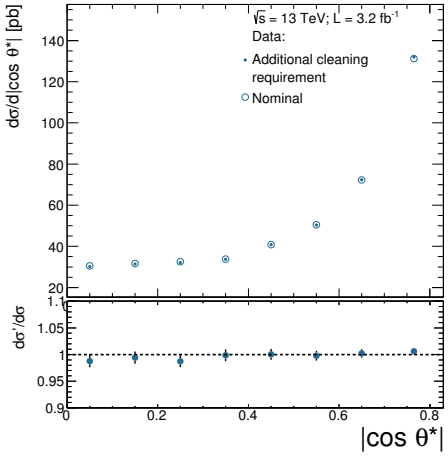
(a)



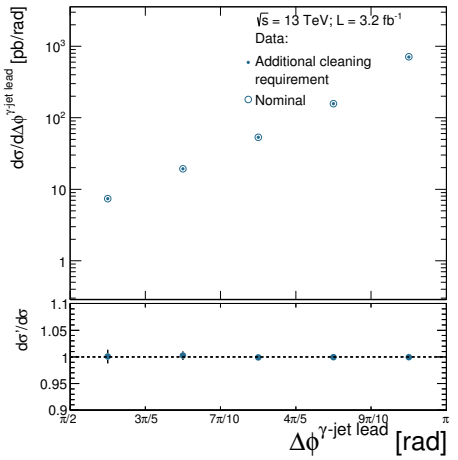
(b)



(c)



(d)



(e)

Figure D.2: Measured cross sections for the nominal selection (open circles) and for the selection with the additional removal of events if there is at least one jet with $p_{\mathrm{T}}^{\mathrm{jet}} > 60$ GeV within a distance $0.4 < \Delta R < 0.8$ from the photon (dots) as functions of (a) E_{T}^{γ}, (b) $p_{\mathrm{T}}^{\mathrm{jet-lead}}$, (c) $m^{\gamma-\mathrm{jet}}$, (d) $|\cos\theta^{\star}|$ and (e) $\Delta\phi^{\gamma-\mathrm{jet}}$. The lower part of the figures shows the ratio of the cross sections for both selections. In both cases, the samples of SHERPA are used to unfold the data.

E

Correlation between the jet and photon energy scale

The jet energy scale (JES) calibration relies on the balance of the photon+jet system to perform one of the in situ corrections (see Section 5). Therefore, there exists in principle a correlation between the uncertainties on both objects. A cross-check of this correlation was performed, taking into account that the photon energy scale (GES) uncertainty used in the JES uncertainties uses a different mode than the one adopted in this analysis to obtain the GES uncertainty, i.e. the full decorrelation model (FULL, 67 individual components, see Section 4.2) was used in this analysis, whereas the uncertainty derived in the jet calibration is based on the simple model of only one nuisance parameter (1NP) for the GES uncertainty in the JES in situ measurements.

First, a comparison of the total GES uncertainty in the FULL and the 1NP was made. The results of both types of variations are presented in Figure E.1. The differences between the two configurations are largest for the E_{T}^{γ} distribution, which is the most sensitive distribution to the GES. It is clear from this comparison that the 1NP configuration overestimates the uncertainty and that the use of the FULL configuration is the most advantageous to obtain a precision measurement. Nevertheless, such a configuration is not available for the JES and so the studies on the correlations presented here are an overestimation of the effects. The study of the correlation was performed in the following way:

1. the JES component related to the photon+jet in situ scale was identified: LAr_ESZee. Unfortunately, this component also contains the effect of the $Z \to e^{+}e^{-}$ in situ calibration (not possible to decouple); thus, this also adds an additional overestimation;

2. the uncertainty due to the photon energy scale was computed in two different ways:

   - uncorrelated mode: the effect of the 1NP uncertainty on the photon was added in quadrature to the effect of the LAr_ESZee JES uncertainty on the jets; i.e. the effects in the cross sections were estimated separately for the photon and the jets, and the results were added in quadrature;
   - correlated mode: the effect of the 1NP uncertainty on the photon and the effect of the LAr_ESZee JES uncertainty on the jets were considered simultaneously on an event-by-event basis; i.e. the effects in the cross sections were estimated in a fully correlated way.

The comparison of these two configurations is shown in Figure E.2. Since the

uncertainty due to GES is largest when the JES uncertainty is smallest and viceversa for E_{T}^{γ} and $p_{\mathrm{T}}^{\mathrm{jet-lead}}$ (see Figures 8.46(a), 8.46(b), 8.48(a) and 8.48(b)), the effect due to the correlation is very small in these distributions. A somewhat larger effect is observed for the $m^{\gamma-\mathrm{jet}}$ and $|\cos\theta^{\star}|$ observables.

The effect of the correlation on the total systematic uncertainty is illustrated in Fig. E.3 by comparing the total systematic uncertainty when using the correlated or uncorrelated mode as described above. For E_{T}^{γ} and $p_{\mathrm{T}}^{\mathrm{jet-lead}}$, the relative difference in the total systematic uncertainty between the two configurations is smaller than 3.5% in average. For $m^{\gamma-\mathrm{jet}}$ and $|\cos\theta^{\star}|$, the relative difference in the two uncertainty modes is smaller than 12% in average.

Therefore, these studies show that the GES uncertainty would change from 5% to 5.6% at most (it is noted, as mentioned above, that this is an overestimation) when taking into account the correlation with the JES.

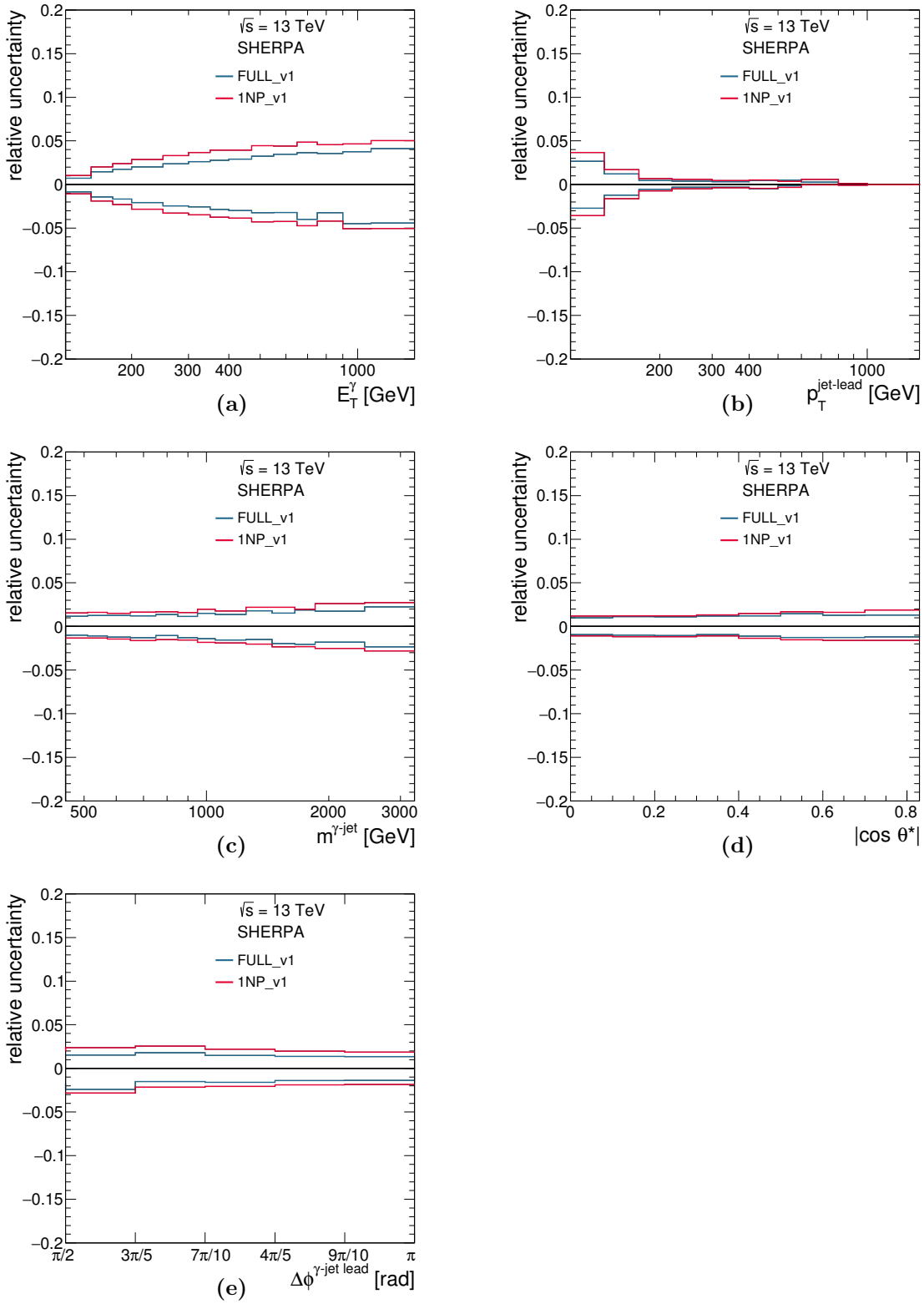


Figure E.1: Comparison between the photon-energy scale uncertainty using the FULL (blue lines) and the 1NP (red lines) configurations as a function of (a) E_{T}^{γ}, (b) $p_{\mathrm{T}}^{\mathrm{jet-lead}}$, (c) $m^{\gamma-\mathrm{jet}}$, (d) $|\cos\theta^{\star}|$ and (e) $\Delta\phi^{\gamma-\mathrm{jet}}$.

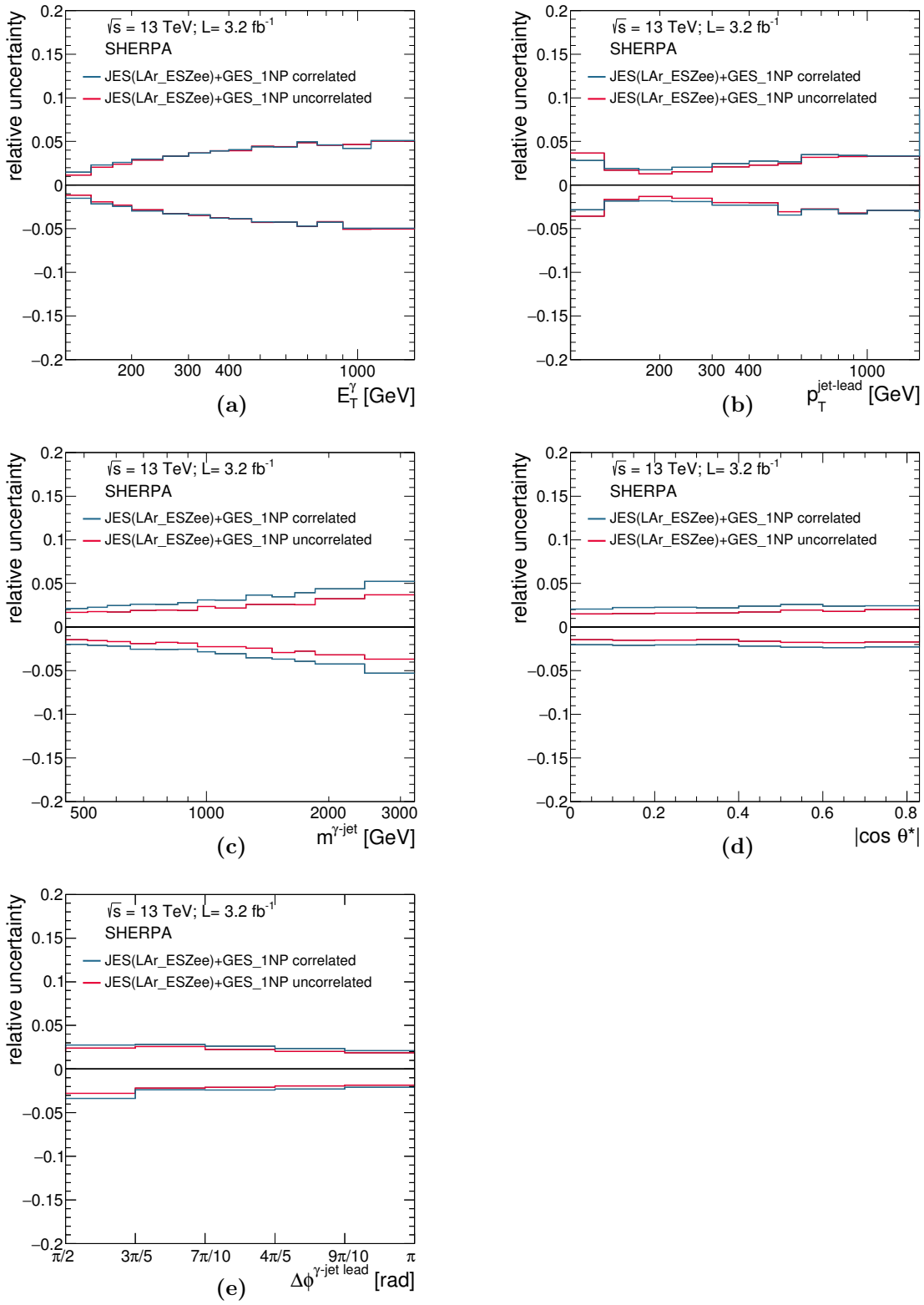


Figure E.2: Comparison of the LAr_ESZee JES and GES_1NP scale uncertainties added in quadrature (red lines) and when the variations were performed in a correlated mode (blue lines) as functions of (a) E_{T}^{γ}, (b) $p_{\mathrm{T}}^{\mathrm{jet-lead}}$, (c) $m^{\gamma-\mathrm{jet}}$, (d) $|\cos\theta^{\star}|$ and (e) $\Delta\phi^{\gamma-\mathrm{jet}}$.

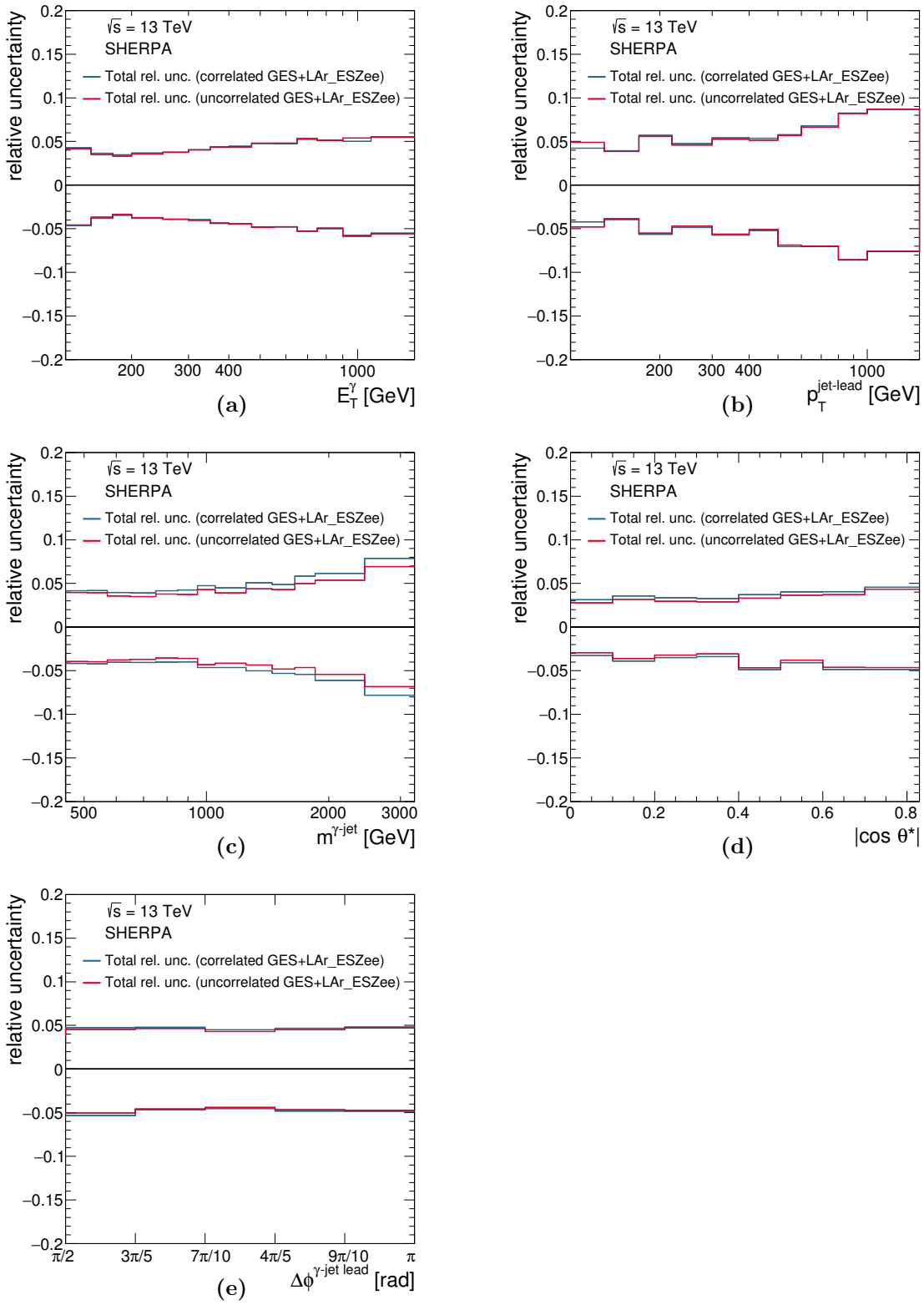


Figure E.3: Comparison of the total systematic uncertainty when varying the JES and GES uncertainties in a correlated (blue lines) or uncorrelated (red lines) mode as a function of (a) E_{T}^{γ}, (b) $p_{\mathrm{T}}^{\mathrm{jet-lead}}$, (c) $m^{\gamma-\mathrm{jet}}$, (d) $|\cos\theta^{\star}|$ and (e) $\Delta\phi^{\gamma-\mathrm{jet}}$.

F

Tables of results

F.1 Tables for the inclusive photon analysis

Tables F.1 to F.4 show the measured cross sections for isolated-photon production as a function of E_{T}^{γ} for each region in $|\eta^{\gamma}|$ (in pb/GeV) together with the statistical uncertainty in the data (in %), the total systematic uncertainty excluding that in the luminosity (in %) and the contributions from the different sources of systematic uncertainty (in %).

Table F.1: The measured cross section for isolated-photon production as a function of E_{T}^{γ} for $|\eta^{\gamma}| < 0.6$ (in pb/GeV) together with the statistical uncertainty in the data (in %), the total systematic uncertainty excluding that in the luminosity (in %) and the contributions from the different sources of systematic uncertainty (in %): photon identification ("γ ID"), photon energy scale and resolution ("γ ES+γ RES"), lower limit in $E_{\mathrm{T}}^{\mathrm{iso}}$ in regions B and D ("$E_{\mathrm{T}}^{\mathrm{iso}}$ gap"), removal of upper limit in $E_{\mathrm{T}}^{\mathrm{iso}}$ in regions B and D ("$E_{\mathrm{T}}^{\mathrm{iso}}$ upp. lim."), variation of the inverted photon identification variables ("γ invert. var."), correlation between γ ID and isolation in background ("R^{bg}"), signal leakage fractions of Sherpa ("Leak."), unfolding with Sherpa ("Unf."), modelling of $E_{\mathrm{T}}^{\mathrm{iso}}$ in MC simulation ("$E_{\mathrm{T}}^{\mathrm{iso}}$ MC"), mixture of hard and bremsstrahlung components in MC samples ("Hard and brem"), pile-up ("Pileup"), statistical uncertainty in MC samples ("MC stat.") and trigger ("Trigger").

E_{T}^{γ} [GeV]	$\mathrm{d}\sigma/\mathrm{d}E_{\mathrm{T}}^{\gamma}$ [pb/GeV]	Stat. (%)	Total syst. (%)		γ ID (%)		γ ES+γ RES (%)		E_{T}^{iso} gap (%)		E_{T}^{iso} upp. lim. (%)	γ invert. var. (%)	
			Up	Down	Up	Down	Up	Down	+1 GeV	−1 GeV		Up	Down
125 - 150	2.27	± 0.3	3.1	-3.0	1.0	-1.0	1.4	-1.3	0.0	-0.1	0.1	0.7	-0.6
150 - 175	1.02	± 0.4	2.7	-2.5	1.0	-1.0	1.6	-1.4	0.1	0.0	0.2	0.7	-0.6
175 - 200	0.521	± 0.5	2.5	-2.4	1.0	-1.0	1.7	-1.5	0.0	0.0	0.2	0.7	-0.6
200 - 250	0.225	± 0.6	2.5	-2.4	1.1	-1.1	1.8	-1.6	0.0	0.0	0.2	0.7	-0.6
250 - 300	0.0827	± 0.9	2.5	-2.4	1.1	-1.1	1.9	-1.8	0.0	0.0	0.1	0.7	-0.6
300 - 350	0.0357	± 1.4	2.8	-2.6	1.1	-1.1	2.0	-1.9	0.0	0.0	0.1	0.7	-0.6
350 - 400	0.0173	± 2.1	2.7	-2.6	1.3	-1.3	2.1	-2.0	0.0	0.0	0.1	0.7	-0.6
400 - 470	0.00804	± 2.5	2.8	-2.7	1.3	-1.3	2.2	-2.2	0.0	0.0	0.1	0.7	-0.6
470 - 550	0.00351	± 3.6	3.0	-2.9	1.4	-1.4	2.3	-2.4	0.0	0.0	0.0	0.7	-0.6
550 - 650	0.00133	± 5.2	3.1	-3.0	1.5	-1.5	2.5	-2.5	0.0	0.0	0.0	0.7	-0.6
650 - 750	0.000557	± 8.2	3.2	-3.2	1.5	-1.5	2.7	-2.7	0.0	0.0	0.0	0.7	-0.6
750 - 900	0.000227	± 10.8	3.7	-3.6	1.8	-1.7	3.0	-2.8	-0.2	0.1	0.6	0.7	-0.6
900 - 1100	0.0000925	± 14.1	4.1	-3.7	1.9	-1.9	3.3	-2.9	0.0	0.0	0.0	0.7	-0.6
1100 - 1500	0.0000085	± 33.2	4.7	-3.8	2.2	-2.1	4.0	-3.1	0.0	0.0	0.0	0.7	-0.6

E_{T}^{γ} [GeV]	R^{bg} (%)		Leak. (%)	Unf. (%)	E_{T}^{iso} MC (%)	Hard and brem (%)		Pileup (%)		MC stat. (%)	Trigger (%)
	Up	Down				Brem×0	Brem×2	Reweight up	Reweight down		
125 - 150	1.4	-1.4	± 1.6	± 0.9	-0.3	0.0	0.0	0.5	-0.5	± 0.3	± 0.1
150 - 175	1.1	-1.1	± 1.2	± 0.4	-0.1	0.4	-0.2	0.4	-0.3	± 0.2	± 0.1
175 - 200	0.9	-0.9	± 1.0	± 0.3	-0.1	0.2	-0.1	0.2	-0.1	± 0.4	± 0.1
200 - 250	0.7	-0.7	± 0.6	± 0.5	-0.3	0.5	-0.3	0.3	-0.2	± 0.3	± 0.1
250 - 300	0.5	-0.5	± 0.6	± 0.4	-0.2	0.3	-0.2	0.2	-0.3	± 0.5	± 0.1
300 - 350	0.5	-0.5	± 0.3	± 0.7	-0.2	0.9	-0.6	0.4	-0.3	± 0.3	± 0.1
350 - 400	0.5	-0.5	± 0.2	± 0.3	-0.1	0.3	-0.2	0.1	-0.1	± 0.3	± 0.1
400 - 470	0.4	-0.4	± 0.2	± 0.5	0.0	0.2	-0.1	0.2	0.0	± 0.4	± 0.1
470 - 550	0.1	-0.1	± 0.1	± 0.6	-0.1	0.5	-0.3	0.4	-0.4	± 0.4	± 0.1
550 - 650	0.3	-0.3	± 0.1	± 0.4	-0.1	0.2	-0.2	0.3	-0.2	± 0.2	± 0.1
650 - 750	0.3	-0.3	± 0.2	± 0.1	0.0	0.4	-0.3	0.2	-0.2	± 0.3	± 0.1
750 - 900	1.1	-1.1	± 0.3	± 0.2	0.0	-0.3	0.2	0.1	0.0	± 0.3	± 0.1
900 - 1100	0.0	0.0	± 0.0	± 0.7	0.0	0.6	-0.4	-0.2	0.2	± 0.4	± 0.1
1100 - 1500	0.0	0.0	± 0.0	± 0.1	0.0	0.2	-0.2	-0.1	0.2	± 0.4	± 0.1

Table F.2: The measured cross section for isolated-photon production as a function of E_{T}^{γ} for $0.6 < |\eta^{\gamma}| < 1.37$ (in pb/GeV) together with the statistical uncertainty in the data (in %), the total systematic uncertainty excluding that in the luminosity (in %) and the contributions from the different sources of systematic uncertainty (in %): photon identification ("γ ID"), photon energy scale and resolution ("γ ES+γ RES"), lower limit in $E_{\mathrm{T}}^{\mathrm{iso}}$ in regions B and D ("$E_{\mathrm{T}}^{\mathrm{iso}}$ gap"), removal of upper limit in $E_{\mathrm{T}}^{\mathrm{iso}}$ in regions B and D ("$E_{\mathrm{T}}^{\mathrm{iso}}$ upp. lim."), variation of the inverted photon identification variables ("γ invert. var."), correlation between γ ID and isolation in background ("R^{bg}"), signal leakage fractions of Sherpa ("Leak."), unfolding with Sherpa ("Unf."), modelling of $E_{\mathrm{T}}^{\mathrm{iso}}$ in MC simulation ("$E_{\mathrm{T}}^{\mathrm{iso}}$ MC"), mixture of hard and bremsstrahlung components in MC samples ("Hard and brem"), pile-up ("Pileup"), statistical uncertainty in MC samples ("MC stat.") and trigger ("Trigger").

E_{T}^{γ} [GeV]	$\mathrm{d}\sigma/\mathrm{d}E_{\mathrm{T}}^{\gamma}$ [pb/GeV]	Stat. (%)	Total syst. (%)		γ ID (%)		γ ES+γ RES (%)		E_{T}^{iso} gap (%)		E_{T}^{iso} upp. lim. (%)	γ invert. var. (%)	
			Up	Down	Up	Down	Up	Down	+1 GeV	−1 GeV		Up	Down
125 - 150	2.93	± 0.2	4.1	-3.9	1.0	-1.0	1.9	-1.9	0.1	-0.1	0.2	1.4	-0.2
150 - 175	1.32	± 0.4	3.5	-3.3	1.0	-1.0	2.0	-2.0	0.1	-0.1	0.2	1.2	-0.2
175 - 200	0.665	± 0.5	3.5	-3.2	1.0	-1.0	2.2	-2.1	0.1	-0.1	0.1	1.0	-0.2
200 - 250	0.285	± 0.5	3.2	-3.1	1.1	-1.1	2.3	-2.3	0.0	0.0	0.1	0.9	-0.2
250 - 300	0.105	± 0.8	3.1	-3.1	1.1	-1.1	2.5	-2.4	0.0	0.0	0.1	0.8	-0.2
300 - 350	0.0452	± 1.3	3.2	-3.3	1.1	-1.1	2.7	-2.6	0.0	0.0	0.1	0.8	-0.2
350 - 400	0.0211	± 1.9	3.3	-3.5	1.2	-1.1	2.8	-2.7	0.0	0.0	0.2	0.8	-0.2
400 - 470	0.00959	± 2.4	3.4	-3.7	1.2	-1.1	3.0	-2.9	0.0	0.0	0.0	0.8	-0.2
470 - 550	0.00401	± 3.4	3.5	-3.8	1.2	-1.2	3.2	-3.1	0.0	0.0	0.0	0.8	-0.2
550 - 650	0.00166	± 4.8	3.8	-3.9	1.3	-1.3	3.4	-3.3	0.0	0.0	0.0	0.8	-0.2
650 - 750	0.000623	± 7.7	4.0	-4.1	1.3	-1.3	3.6	-3.5	0.0	0.0	0.0	0.8	-0.2
750 - 900	0.000248	± 10.2	4.2	-4.3	1.5	-1.4	3.8	-3.8	0.0	0.0	0.0	0.8	-0.2
900 - 1100	0.0000569	± 17.7	4.8	-4.9	1.5	-1.5	4.1	-4.1	0.0	0.0	0.0	0.8	-0.2
1100 - 1500	0.0000072	± 67.6	5.0	-5.1	1.7	-1.7	4.6	-4.6	0.0	0.0	0.0	0.8	-0.2

E_{T}^{γ} [GeV]	R^{bg} (%)		Leak. (%)	Unf. (%)	E_{T}^{iso} MC (%)	Hard and brem (%)		Pileup (%)		MC stat. (%)	Trigger (%)
	Up	Down				Brem×0	Brem×2	Reweight up	Reweight down		
125 - 150	2.3	-2.3	± 1.5	± 1.4	-0.9	0.6	-0.3	0.4	-0.3	± 0.3	± 0.2
150 - 175	1.8	-1.8	± 1.0	± 0.7	-0.9	1.0	-0.6	0.2	-0.2	± 0.2	± 0.2
175 - 200	1.4	-1.4	± 0.8	± 0.9	-0.8	1.4	-0.8	0.0	0.1	± 0.3	± 0.2
200 - 250	1.1	-1.1	± 0.5	± 0.4	-1.1	0.8	-0.5	0.4	-0.3	± 0.3	± 0.2
250 - 300	0.8	-0.8	± 0.3	± 0.3	-1.2	0.7	-0.4	0.2	0.0	± 0.4	± 0.2
300 - 350	0.6	-0.6	± 0.2	± 0.1	-1.5	0.7	-0.4	0.2	-0.2	± 0.2	± 0.2
350 - 400	0.5	-0.5	± 0.1	± 0.2	-1.7	0.7	-0.5	0.1	-0.1	± 0.3	± 0.2
400 - 470	0.3	-0.3	± 0.1	± 0.1	-1.7	0.6	-0.4	-0.2	0.2	± 0.4	± 0.2
470 - 550	0.2	-0.2	± 0.0	± 0.3	-1.6	0.2	-0.2	0.2	-0.5	± 0.4	± 0.2
550 - 650	0.2	-0.3	± 0.1	± 0.5	-1.5	0.6	-0.4	0.1	-0.1	± 0.2	± 0.2
650 - 750	0.0	0.0	± 0.0	± 0.8	-1.5	0.1	-0.1	0.3	-0.3	± 0.3	± 0.2
750 - 900	0.0	0.0	± 0.0	± 0.4	-1.4	0.5	-0.4	0.0	0.2	± 0.4	± 0.2
900 - 1100	0.0	0.0	± 0.0	± 1.7	-1.2	0.7	-0.5	0.2	-0.2	± 0.5	± 0.2
1100 - 1500	0.0	0.0	± 0.0	± 0.2	-1.3	0.1	-0.1	-0.2	0.1	± 0.5	± 0.2

Table F.3: The measured cross section for isolated-photon production as a function of E_{T}^{γ} for $1.56 < |\eta^{\gamma}| < 1.81$ (in pb/GeV) together with the statistical uncertainty in the data (in %), the total systematic uncertainty excluding that in the luminosity (in %) and the contributions from the different sources of systematic uncertainty (in %): photon identification ("γ ID"), photon energy scale and resolution ("γ ES+γ RES"), lower limit in $E_{\mathrm{T}}^{\mathrm{iso}}$ in regions B and D ("$E_{\mathrm{T}}^{\mathrm{iso}}$ gap"), removal of upper limit in $E_{\mathrm{T}}^{\mathrm{iso}}$ in regions B and D ("$E_{\mathrm{T}}^{\mathrm{iso}}$ upp. lim."), variation of the inverted photon identification variables ("γ invert. var."), correlation between γ ID and isolation in background ("R^{bg}"), signal leakage fractions of Sherpa ("Leak."), unfolding with Sherpa ("Unf."), modelling of $E_{\mathrm{T}}^{\mathrm{iso}}$ in MC simulation ("$E_{\mathrm{T}}^{\mathrm{iso}}$ MC"), mixture of hard and bremsstrahlung components in MC samples ("Hard and brem"), pile-up ("Pileup"), statistical uncertainty in MC samples ("MC stat.") and trigger ("Trigger").

E_{T}^{γ} [GeV]	$\mathrm{d}\sigma/\mathrm{d}E_{\mathrm{T}}^{\gamma}$ [pb/GeV]	Stat. (%)	Total syst. (%)		γ ID (%)		γ ES+γ RES (%)		$E_{\mathrm{T}}^{\mathrm{iso}}$ gap (%)		$E_{\mathrm{T}}^{\mathrm{iso}}$ upp. lim. (%)	γ invert. var. (%)	
			Up	Down	Up	Down	Up	Down	+1 GeV	−1 GeV		Up	Down
125 - 150	0.944	± 0.4	8.2	-7.3	1.6	-1.5	7.4	-6.5	0.1	-0.1	0.1	1.6	-1.6
150 - 175	0.419	± 0.6	8.3	-7.8	1.6	-1.5	7.7	-7.1	0.1	-0.1	0.1	1.6	-1.6
175 - 200	0.211	± 0.8	8.6	-8.1	1.6	-1.5	7.9	-7.5	0.1	0.0	0.1	1.6	-1.6
200 - 250	0.0916	± 0.9	8.8	-8.5	1.7	-1.6	8.3	-7.8	0.0	0.0	0.1	1.6	-1.6
250 - 300	0.0334	± 1.5	9.3	-8.7	1.6	-1.6	8.8	-8.1	0.0	0.0	0.1	1.6	-1.6
300 - 350	0.0138	± 2.3	9.7	-8.9	1.7	-1.6	9.3	-8.4	0.0	0.0	0.1	1.6	-1.6
350 - 400	0.00600	± 3.5	10.4	-9.3	2.3	-2.2	9.8	-8.8	0.0	0.0	0.1	1.6	-1.6
400 - 470	0.00293	± 4.3	11.1	-9.9	2.3	-2.2	10.6	-9.3	0.0	0.0	0.1	1.6	-1.6
470 - 550	0.00110	± 6.6	12.1	-10.8	2.4	-2.3	11.5	-10.1	0.0	0.0	0.2	1.6	-1.6
550 - 650	0.000340	± 10.6	13.2	-11.7	2.5	-2.4	12.7	-11.2	0.0	0.0	0.1	1.6	-1.6
650 - 750	0.000109	± 19.4	15.1	-13.7	2.5	-2.4	14.1	-12.6	-0.1	-0.1	-0.2	1.6	-1.6
750 - 900	0.0000297	± 37.6	16.4	-15.1	3.2	-3.0	15.9	-14.6	0.0	0.0	0.0	1.6	-1.6
900 - 1100	0.0000057	± 57.9	19.3	-18.5	3.4	-3.1	18.4	-17.7	0.0	0.0	0.0	1.6	-1.6

E_{T}^{γ} [GeV]	R^{bg} (%)		Leak. (%)	Unf. (%)	$E_{\mathrm{T}}^{\mathrm{iso}}$ MC (%)	Hard and brem (%)		Pileup (%)		MC stat. (%)	Trigger (%)
	Up	Down				Brem×0	Brem×2	Reweight up	Reweight down		
125 - 150	1.6	-1.6	± 0.9	± 1.0	-0.9	0.8	-0.4	0.4	-0.5	± 0.5	± 1.0
150 - 175	1.5	-1.5	± 0.6	± 0.6	-0.9	1.0	-0.5	0.2	-0.2	± 0.4	± 1.0
175 - 200	1.5	-1.5	± 0.4	± 0.1	-1.1	1.4	-0.7	0.1	0.2	± 0.6	± 1.0
200 - 250	1.1	-1.1	± 0.4	± 0.7	-1.1	0.5	-0.3	0.5	-0.8	± 0.6	± 1.0
250 - 300	1.0	-1.0	± 0.2	± 0.9	-1.0	0.5	-0.3	0.1	0.0	± 0.9	± 1.0
300 - 350	1.0	-1.0	± 0.2	± 0.5	-0.8	0.8	-0.5	0.4	-0.1	± 0.4	± 1.0
350 - 400	0.7	-0.7	± 0.0	± 0.2	-0.8	0.7	-0.5	-0.4	0.1	± 0.6	± 1.0
400 - 470	0.6	-0.6	± 0.4	± 1.3	-0.7	0.5	-0.3	-0.1	0.3	± 0.8	± 1.0
470 - 550	0.6	-0.6	± 0.1	± 1.8	-0.7	-0.2	0.2	0.2	-0.6	± 1.0	± 1.0
550 - 650	0.6	-0.6	± 0.1	± 1.2	-0.5	0.3	-0.2	0.4	-0.2	± 0.5	± 1.0
650 - 750	1.1	-1.2	± 1.4	± 3.9	-0.8	-0.6	0.4	0.2	-0.2	± 0.9	± 1.0
750 - 900	0.0	0.0	± 0.0	± 0.1	-0.4	-0.3	0.2	0.6	-0.5	± 1.2	± 1.0
900 - 1100	0.0	0.0	± 0.0	± 3.1	-0.4	0.1	-0.1	1.8	-0.9	± 1.9	± 1.0

Table F.4: The measured cross section for isolated-photon production as a function of E_{T}^{γ} for $1.81 < |\eta^{\gamma}| < 2.37$ (in pb/GeV) together with the statistical uncertainty in the data (in %), the total systematic uncertainty excluding that in the luminosity (in %) and the contributions from the different sources of systematic uncertainty (in %): photon identification ("γ ID"), photon energy scale and resolution ("γ ES+γ RES"), lower limit in $E_{\mathrm{T}}^{\mathrm{iso}}$ in regions B and D ("$E_{\mathrm{T}}^{\mathrm{iso}}$ gap"), removal of upper limit in $E_{\mathrm{T}}^{\mathrm{iso}}$ in regions B and D ("$E_{\mathrm{T}}^{\mathrm{iso}}$ upp. lim."), variation of the inverted photon identification variables ("γ invert. var."), correlation between γ ID and isolation in background ("R^{bg}"), signal leakage fractions of Sherpa ("Leak."), unfolding with Sherpa ("Unf."), modelling of $E_{\mathrm{T}}^{\mathrm{iso}}$ in MC simulation ("$E_{\mathrm{T}}^{\mathrm{iso}}$ MC"), mixture of hard and bremsstrahlung components in MC samples ("Hard and brem"), pile-up ("Pileup"), statistical uncertainty in MC samples ("MC stat.") and trigger ("Trigger").

E_{T}^{γ} [GeV]	$\mathrm{d}\sigma/\mathrm{d}E_{\mathrm{T}}^{\gamma}$ [pb/GeV]	Stat. (%)	Total syst. (%)		γ ID (%)		γ ES+γ RES (%)		E_{T}^{iso} gap (%)		E_{T}^{iso} upp. lim. (%)	γ invert. var. (%)	
			Up	Down	Up	Down	Up	Down	+1 GeV	−1 GeV		Up	Down
125 - 150	1.87	± 0.3	3.5	-4.5	2.0	-1.9	1.9	-2.0	0.1	-0.1	0.1	0.2	-2.7
150 - 175	0.816	± 0.4	3.6	-4.5	2.1	-2.0	2.2	-2.2	0.0	0.0	0.1	0.2	-2.7
175 - 200	0.404	± 0.6	3.6	-4.5	2.1	-2.0	2.4	-2.4	0.0	0.0	0.2	0.2	-2.7
200 - 250	0.168	± 0.7	3.9	-4.7	2.5	-2.3	2.8	-2.8	0.0	0.0	0.1	0.2	-2.6
250 - 300	0.0553	± 1.2	4.3	-5.0	2.5	-2.3	3.3	-3.2	0.0	0.0	0.1	0.2	-2.6
300 - 350	0.0217	± 1.9	4.6	-5.2	2.5	-2.4	3.7	-3.6	0.0	0.0	0.2	0.2	-2.6
350 - 400	0.00899	± 3.0	5.4	-5.8	3.3	-3.1	4.1	-4.0	0.0	0.0	0.3	0.2	-2.6
400 - 470	0.00326	± 4.2	5.8	-6.2	3.4	-3.2	4.5	-4.4	0.0	0.1	0.6	0.2	-2.6
470 - 550	0.00115	± 6.8	6.6	-6.8	4.0	-3.7	5.0	-4.9	0.1	0.0	0.0	0.2	-2.6
550 - 650	0.000317	± 11.5	7.3	-7.3	4.5	-4.2	5.6	-5.4	0.0	-0.1	0.3	0.2	-2.5
650 - 750	0.000117	± 26.5	8.4	-8.4	4.8	-4.4	6.2	-5.9	0.0	0.0	0.0	0.2	-2.5
750 - 900	0.0000219	± 33.3	11.6	-11.3	5.2	-4.7	6.9	-6.5	0.0	0.0	0.0	0.2	-2.5

E_{T}^{γ} [GeV]	R^{bg} (%)		Leak. (%)	Unf. (%)	E_{T}^{iso} MC (%)	Hard and brem (%)		Pileup (%)		MC stat. (%)	Trigger (%)
	Up	Down				Brem×0	Brem×2	Reweight up	Reweight down		
125 - 150	1.8	-1.8	± 0.9	± 0.5	-0.8	-0.2	0.1	0.2	-0.3	± 0.3	± 0.2
150 - 175	1.4	-1.5	± 0.6	± 0.9	-0.7	0.4	-0.2	0.5	-0.4	± 0.3	± 0.2
175 - 200	1.3	-1.3	± 0.5	± 0.1	-0.9	0.7	-0.4	0.5	-0.5	± 0.4	± 0.2
200 - 250	1.0	-1.0	± 0.4	± 0.1	-0.8	0.2	-0.1	0.3	0.0	± 0.4	± 0.2
250 - 300	0.9	-0.9	± 0.2	± 0.2	-0.8	0.8	-0.5	0.3	-0.1	± 0.6	± 0.2
300 - 350	0.7	-0.7	± 0.2	± 0.4	-0.5	0.4	-0.2	0.4	-0.6	± 0.3	± 0.2
350 - 400	0.8	-0.8	± 0.0	± 0.4	-0.5	0.4	-0.3	0.3	-0.1	± 0.5	± 0.2
400 - 470	0.9	-0.9	± 0.4	± 0.2	-0.4	0.6	-0.4	0.5	-0.2	± 0.6	± 0.2
470 - 550	1.1	-1.1	± 0.4	± 0.3	-0.5	-0.4	0.2	-0.1	-0.1	± 0.9	± 0.2
550 - 650	0.7	-0.7	± 0.3	± 0.1	-0.6	0.7	-0.5	0.2	0.0	± 0.5	± 0.2
650 - 750	0.0	0.0	± 0.0	± 3.0	-0.3	-0.4	0.2	0.0	-0.3	± 1.0	± 0.2
750 - 900	0.0	0.0	± 0.0	± 7.4	-0.5	0.8	-0.5	0.9	-0.1	± 1.5	± 0.2

F.2 Tables for the photon plus jet analysis

Tables F.5 to F.9 show the measured cross sections for isolated-photon plus one-jet production as a function of different observables together with the statistical uncertainty in the data (in %), the total systematic uncertainty excluding that in the luminosity (in %) and the contributions from the different sources of systematic uncertainty (in %).

Table F.5: The measured cross section for isolated-photon plus one-jet production as a function of E_{T}^{γ} (in pb/GeV) together with the statistical uncertainty in the data (in %), the total systematic uncertainty excluding that in the luminosity (in %) and the contributions from the different sources of systematic uncertainty (in %): photon energy scale ("γ ES"), photon energy resolution ("γ RES"), jet energy scale ("Jet ES"), jet energy resolution ("Jet RES"), signal leakage fractions ("Leak."), photon identification ("γ ID"), lower limit in $E_{\mathrm{T}}^{\mathrm{iso}}$ in regions B and D ("$E_{\mathrm{T}}^{\mathrm{iso}}$ gap"), variation of the inverted photon identification variables ("γ invert. var."), removal of upper limit in $E_{\mathrm{T}}^{\mathrm{iso}}$ in regions B and D ("$E_{\mathrm{T}}^{\mathrm{iso}}$ upp. lim."), modelling of $E_{\mathrm{T}}^{\mathrm{iso}}$ in MC simulation ("$E_{\mathrm{T}}^{\mathrm{iso}}$ MC"), correlation between γ ID and isolation in background ("R^{bg}"), pile-up ("Pile-up"), unfolding ("Unf."), statistical uncertainty in MC samples ("MC stat."), trigger ("Trigger") and luminosity ("Lumi.").

E_{T}^{γ} [GeV]	$\mathrm{d}\sigma/\mathrm{d}E_{\mathrm{T}}^{\gamma}$ [pb/GeV]	Stat. (%)	Total syst. (%)		γ ES (%)		γ RES (%)		Jet ES (%)		Jet RES (%)		Leak. (%)		γ ID (%)	
			Up	Down	Up	Down	Up	Down	Up	Down	Up	Down	Up	Down	Up	Down
125 - 150	5.191	± 0.2	3.9	-3.8	0.8	-0.9	< 0.1	< 0.1	2.4	-2.3	0.3	-0.3	1.3	-1.3	1.3	-1.2
150 - 175	2.796	± 0.2	3.2	-3.2	1.4	-1.3	< 0.1	< 0.1	1.4	-1.4	0.1	-0.1	0.9	-0.9	1.3	-1.3
175 - 200	1.561	± 0.3	3.0	-3.0	1.7	-1.7	< 0.1	-0.1	0.9	-0.9	0.1	-0.1	0.7	-0.7	1.3	-1.3
200 - 250	0.7184	± 0.3	3.1	-3.2	2.1	-2.0	< 0.1	-0.1	0.5	-0.4	0.1	-0.1	0.5	-0.5	1.4	-1.4
250 - 300	0.2696	± 0.5	3.1	-3.2	2.4	-2.4	< 0.1	-0.1	0.2	-0.2	< 0.1	< 0.1	0.4	-0.4	1.4	-1.4
300 - 350	0.1161	± 0.8	3.2	-3.4	2.6	-2.6	< 0.1	-0.2	0.1	-0.1	< 0.1	< 0.1	0.2	-0.2	1.4	-1.4
350 - 400	0.05370	± 1.2	3.5	-3.6	2.8	-2.7	< 0.1	-0.2	< 0.1	< 0.1	< 0.1	< 0.1	0.1	-0.1	1.7	-1.6
400 - 470	0.02408	± 1.5	3.6	-3.7	2.9	-2.9	< 0.1	-0.2	< 0.1	< 0.1	< 0.1	< 0.1	0.3	-0.3	1.6	-1.6
470 - 550	0.009892	± 2.2	3.7	-3.9	3.1	-3.1	< 0.1	-0.3	< 0.1	< 0.1	< 0.1	< 0.1	0.1	-0.1	1.7	-1.6
550 - 650	0.003711	± 3.2	3.9	-4.0	3.3	-3.3	< 0.1	-0.3	< 0.1	< 0.1	< 0.1	< 0.1	0.1	-0.1	1.7	-1.7
650 - 750	0.001411	± 5.2	4.1	-4.3	3.4	-3.5	< 0.1	-0.4	< 0.1	< 0.1	< 0.1	< 0.1	0.3	-0.3	1.7	-1.6
750 - 900	0.0005304	± 7.2	4.5	-4.7	3.7	-3.7	< 0.1	-0.4	< 0.1	< 0.1	< 0.1	< 0.1	0.2	-0.2	1.8	-1.7
900 - 1100	0.0001615	± 10.9	5.1	-5.3	3.9	-4.0	< 0.1	-0.4	< 0.1	< 0.1	< 0.1	< 0.1	0.2	-0.2	1.8	-1.8
1100 - 1500	0.00001605	± 32.4	5.2	-5.4	4.4	-4.5	< 0.1	-0.5	< 0.1	< 0.1	< 0.1	< 0.1	0.2	-0.2	2.0	-1.9

E_{T}^{γ} [GeV]	$E_{\mathrm{T}}^{\mathrm{iso}}$ gap (%)		γ invert. var. (%)		$E_{\mathrm{T}}^{\mathrm{iso}}$ upp. lim. (%)	$E_{\mathrm{T}}^{\mathrm{iso}}$ MC (%)	R^{bg} (%)		Pile-up (%)		Unf. (%)	MC stat. (%)	Trigger (%)	Lumi. (%)
	Up	Down	Up	Down			Up	Down	Up	Down				
125 - 150	0.1	-0.1	0.9	-0.6	± 0.2	± 0.6	1.7	-1.7	0.3	-0.3	± 0.8	± 0.2	± 1.0	± 2.1
150 - 175	0.1	-0.1	0.8	-0.7	± 0.2	± 0.6	1.3	-1.4	0.3	-0.2	± 0.2	± 0.1	± 1.0	± 2.1
175 - 200	0.1	< 0.1	0.7	-0.7	± 0.2	± 0.6	1.1	-1.1	0.3	-0.2	< 0.1	± 0.1	± 1.0	± 2.1
200 - 250	< 0.1	< 0.1	0.5	-0.8	± 0.2	± 0.7	0.9	-0.9	0.3	-0.3	± 0.6	± 0.1	± 1.0	± 2.1
250 - 300	< 0.1	< 0.1	0.4	-0.9	± 0.1	± 0.8	0.7	-0.7	0.3	-0.2	± 0.1	± 0.1	± 1.0	± 2.1
300 - 350	< 0.1	< 0.1	0.3	-0.9	± 0.1	± 0.8	0.6	-0.6	0.2	-0.2	± 0.3	± 0.1	± 1.0	± 2.1
350 - 400	< 0.1	< 0.1	0.3	-0.9	± 0.2	± 0.8	0.5	-0.5	0.3	-0.2	± 0.3	± 0.2	± 1.0	± 2.1
400 - 470	< 0.1	< 0.1	0.4	-1.0	± 0.1	± 0.8	0.4	-0.4	0.2	-0.2	± 0.2	± 0.2	± 1.0	± 2.1
470 - 550	< 0.1	< 0.1	0.4	-1.0	± 0.1	± 0.9	0.3	-0.3	0.1	-0.1	± 0.1	± 0.2	± 1.0	± 2.1
550 - 650	< 0.1	< 0.1	0.4	-1.0	< 0.1	± 0.8	0.3	-0.3	< 0.1	-0.1	± 0.1	± 0.2	± 1.0	± 2.1
650 - 750	< 0.1	< 0.1	0.4	-1.1	< 0.1	± 0.8	0.5	-0.5	0.4	-0.3	± 0.3	± 0.4	± 1.0	± 2.1
750 - 900	< 0.1	< 0.1	0.4	-1.1	± 0.3	± 0.7	1.3	-1.3	< 0.1	< 0.1	± 0.7	± 0.5	± 1.0	± 2.1
900 - 1100	< 0.1	< 0.1	0.4	-1.1	< 0.1	± 0.6	1.3	-1.3	0.2	-0.5	± 1.8	± 0.7	± 1.0	± 2.1
1100 - 1500	< 0.1	< 0.1	0.4	-1.2	< 0.1	± 0.5	1.3	-1.3	0.3	-0.3	± 0.4	± 0.3	± 1.0	± 2.1

Table F.6: The measured cross section for isolated-photon plus one-jet production as a function of $p_{\mathrm{T}}^{\mathrm{jet-lead}}$ (in pb/GeV) together with the statistical uncertainty in the data (in %), the total systematic uncertainty excluding that in the luminosity (in %) and the contributions from the different sources of systematic uncertainty (in %): photon energy scale ("γ ES"), photon energy resolution ("γ RES"), jet energy scale ("Jet ES"), jet energy resolution ("Jet RES"), signal leakage fractions ("Leak."), photon identification ("γ ID"), lower limit in $E_{\mathrm{T}}^{\mathrm{iso}}$ in regions B and D ("$E_{\mathrm{T}}^{\mathrm{iso}}$ gap"), variation of the inverted photon identification variables ("γ invert. var."), removal of upper limit in $E_{\mathrm{T}}^{\mathrm{iso}}$ in regions B and D ("$E_{\mathrm{T}}^{\mathrm{iso}}$ upp. lim."), modelling of $E_{\mathrm{T}}^{\mathrm{iso}}$ in MC simulation ("$E_{\mathrm{T}}^{\mathrm{iso}}$ MC"), correlation between γ ID and isolation in background ("R^{bg}"), pile-up ("Pile-up"), unfolding ("Unf."), statistical uncertainty in MC samples ("MC stat."), trigger ("Trigger") and luminosity ("Lumi.").

$p_{\mathrm{T}}^{\mathrm{jet-lead}}$ [GeV]	$d\sigma/dp_{\mathrm{T}}^{\mathrm{jet}}$ [pb/GeV]	Stat. (%)	Total syst. (%)		γ ES (%)		γ RES (%)		Jet ES (%)		Jet RES (%)		Leak. (%)		γ ID (%)	
			Up	Down	Up	Down	Up	Down	Up	Down	Up	Down	Up	Down	Up	Down
100 - 130	2.979	± 0.2	4.1	-4.0	2.6	-2.5	< 0.1	-0.1	1.9	-1.8	0.5	-0.5	0.6	-0.3	1.3	-1.3
130 - 170	2.597	± 0.2	3.8	-3.7	1.2	-1.3	< 0.1	< 0.1	2.4	-2.2	0.5	-0.5	0.6	-0.3	1.3	-1.3
170 - 220	1.166	± 0.3	4.6	-4.6	0.5	-0.6	< 0.1	< 0.1	3.4	-3.3	0.5	-0.5	0.5	-0.3	1.3	-1.3
220 - 300	0.3849	± 0.4	4.4	-4.5	0.3	-0.2	< 0.1	< 0.1	3.7	-3.7	0.5	-0.5	0.3	-0.3	1.4	-1.4
300 - 400	0.1037	± 0.6	4.5	-4.6	0.2	-0.1	< 0.1	< 0.1	4.0	-3.9	0.4	-0.4	0.2	-0.2	1.5	-1.4
400 - 500	0.03028	± 1.1	4.8	-4.8	0.3	< 0.1	< 0.1	< 0.1	4.3	-4.1	0.4	-0.4	0.1	-0.1	1.5	-1.5
500 - 600	0.01057	± 1.9	5.5	-5.9	0.3	< 0.1	< 0.1	< 0.1	4.6	-4.8	0.4	-0.4	0.3	-0.3	1.5	-1.5
600 - 800	0.002926	± 2.6	6.0	-6.1	0.3	< 0.1	< 0.1	< 0.1	5.1	-5.1	0.4	-0.4	0.1	-0.1	1.5	-1.5
800 - 1000	0.0006549	± 5.6	8.0	-7.7	0.2	< 0.1	< 0.1	< 0.1	6.0	-5.5	0.3	-0.3	0.1	-0.1	1.5	-1.5
1000 - 1500	0.00009047	± 9.2	9.2	-8.0	< 0.1	< 0.1	< 0.1	< 0.1	7.5	-5.9	0.3	-0.3	0.1	-0.1	1.6	-1.6

$p_{\mathrm{T}}^{\mathrm{jet-lead}}$ [GeV]	$E_{\mathrm{T}}^{\mathrm{iso}}$ gap (%)		γ invert. var. (%)	$E_{\mathrm{T}}^{\mathrm{iso}}$ upp. lim. (%)	$E_{\mathrm{T}}^{\mathrm{iso}}$ MC (%)	R^{bg} (%)		Pile-up (%)		Unf. (%)	MC stat. (%)	Trigger (%)	Lumi. (%)
	Up	Down	Up	Down		Up	Down	Up	Down				
100 - 130	0.1	-0.1	1.1	-0.6	< 0.1	± 0.5	1.6	-1.6	0.3	-0.3	± 0.1	± 0.2	± 1.0	± 2.1
130 - 170	0.1	-0.1	0.9	-0.7	< 0.1	± 0.5	1.7	-1.7	0.2	-0.3	± 0.6	± 0.2	± 1.0	± 2.1
170 - 220	0.1	-0.1	0.7	-0.8	< 0.1	± 0.7	1.5	-1.5	0.4	-0.3	± 1.8	± 0.1	± 1.0	± 2.1
220 - 300	< 0.1	< 0.1	0.5	-0.9	< 0.1	± 0.8	1.1	-1.1	0.2	-0.1	± 0.8	± 0.2	± 1.0	± 2.1
300 - 400	< 0.1	< 0.1	0.4	-1.0	< 0.1	± 0.9	0.7	-0.7	0.2	-0.2	± 0.6	± 0.3	± 1.0	± 2.1
400 - 500	< 0.1	< 0.1	0.5	-1.0	< 0.1	± 0.9	0.5	-0.5	0.2	-0.3	± 0.6	± 0.5	± 1.0	± 2.1
500 - 600	< 0.1	< 0.1	0.5	-1.1	< 0.1	± 1.0	0.3	-0.3	0.7	-0.5	± 2.1	± 0.7	± 1.0	± 2.1
600 - 800	< 0.1	< 0.1	0.6	-1.1	< 0.1	± 1.0	0.3	-0.3	0.4	-0.2	± 2.1	± 1.0	± 1.0	± 2.1
800 - 1000	< 0.1	< 0.1	0.6	-1.2	± 0.2	± 0.8	1.5	-1.6	0.2	-0.5	± 4.3	± 1.5	± 1.0	± 2.1
1000 - 1500	< 0.1	< 0.1	0.7	-1.2	< 0.1	± 0.5	1.5	-1.6	0.1	-0.2	± 4.3	± 1.6	± 1.0	± 2.1

Table F.7: The measured cross section for isolated-photon plus one-jet production as a function of $\Delta\phi^{\gamma-\text{jet}}$ (in pb/rad) together with the statistical uncertainty in the data (in %), the total systematic uncertainty excluding that in the luminosity (in %) and the contributions from the different sources of systematic uncertainty (in %): photon energy scale ("γ ES"), photon energy resolution ("γ RES"), jet energy scale ("Jet ES"), jet energy resolution ("Jet RES"), signal leakage fractions ("Leak."), photon identification ("γ ID"), lower limit in $E_{\text{T}}^{\text{iso}}$ in regions B and D ("$E_{\text{T}}^{\text{iso}}$ gap"), variation of the inverted photon identification variables ("γ invert. var."), removal of upper limit in $E_{\text{T}}^{\text{iso}}$ in regions B and D ("$E_{\text{T}}^{\text{iso}}$ upp. lim."), modelling of $E_{\text{T}}^{\text{iso}}$ in MC simulation ("$E_{\text{T}}^{\text{iso}}$ MC"), correlation between γ ID and isolation in background ("R^{bg}"), pile-up ("Pile-up"), unfolding ("Unf."), statistical uncertainty in MC samples ("MC stat."), trigger ("Trigger") and luminosity ("Lumi.").

$\Delta\phi^{\gamma-\text{jet}}$ [rad]	$\text{d}\sigma/\text{d}\Delta\phi^{\gamma-\text{jet}}$ [pb/rad]	Stat. (%)	Total syst. (%)		γ ES (%)		γ RES (%)		Jet ES (%)		Jet RES (%)		Leak. (%)		γ ID (%)	
			Up	Down	Up	Down	Up	Down	Up	Down	Up	Down	Up	Down	Up	Down
$\pi/2-3\pi/5$	7.377	$\pm$ 1.3	4.0	-4.3	1.5	-1.7	0.1	-0.2	1.9	-2.1	1.3	-1.3	0.2	-0.2	1.4	-1.3
$3\pi/5-7\pi/10$	19.34	$\pm$ 0.8	4.0	-4.2	1.5	-1.6	0.1	<0.1	2.2	-2.3	0.6	-0.6	0.7	-0.7	1.4	-1.3
$7\pi/10-4\pi/5$	53.49	$\pm$ 0.5	3.6	-3.7	1.5	-1.5	0.1	<0.1	2.3	-2.3	0.1	-0.1	1.0	-1.0	1.3	-1.3
$4\pi/5-9\pi/10$	157.2	$\pm$ 0.3	3.8	-3.7	1.4	-1.4	<0.1	<0.1	2.1	-2.0	<0.1	<0.1	1.1	-1.1	1.3	-1.3
$9\pi/10-\pi$	710.3	$\pm$ 0.1	3.5	-3.5	1.3	-1.4	<0.1	-0.1	1.4	-1.3	0.2	-0.2	1.2	-1.2	1.3	-1.3

$\Delta\phi^{\gamma-\text{jet}}$ [rad]	$E_{\text{T}}^{\text{iso}}$ gap (%)		γ invert. var. (%)		$E_{\text{T}}^{\text{iso}}$ upp. lim. (%)	$E_{\text{T}}^{\text{iso}}$ MC (%)	R^{bg} (%)		Pile-up (%)		Unf. (%)	MC stat. (%)	Trigger (%)	Lumi. (%)
	Up	Down	Up	Down			Up	Down	Up	Down				
$\pi/2-3\pi/5$	0.1	<0.1	0.8	-0.9	$\pm$ 0.4	$\pm$ 0.5	1.0	-1.1	0.3	-0.8	$\pm$ 1.6	$\pm$ 1.1	$\pm$ 1.0	$\pm$ 2.1
$3\pi/5-7\pi/10$	0.1	<0.1	0.7	-0.8	$\pm$ 0.1	$\pm$ 0.7	1.1	-1.1	0.4	-0.4	$\pm$ 1.8	$\pm$ 0.6	$\pm$ 1.0	$\pm$ 2.1
$7\pi/10-4\pi/5$	<0.1	<0.1	0.5	-0.8	$\pm$ 0.2	$\pm$ 0.6	1.1	-1.2	0.1	<0.1	$\pm$ 0.5	$\pm$ 0.3	$\pm$ 1.0	$\pm$ 2.1
$4\pi/5-9\pi/10$	0.1	<0.1	0.7	-0.7	$\pm$ 0.3	$\pm$ 0.6	1.5	-1.5	0.3	-0.3	$\pm$ 0.9	$\pm$ 0.2	$\pm$ 1.0	$\pm$ 2.1
$9\pi/10-\pi$	0.1	-0.1	0.9	-0.6	$\pm$ 0.3	$\pm$ 0.6	1.7	-1.7	0.3	-0.3	$\pm$ 0.8	$\pm$ 0.1	$\pm$ 1.0	$\pm$ 2.1

Table F.8: The measured cross section for isolated-photon plus one-jet production as a function of $m^{\gamma-\text{jet}}$ (in pb/GeV) together with the statistical uncertainty in the data (in %), the total systematic uncertainty excluding that in the luminosity (in %) and the contributions from the different sources of systematic uncertainty (in %): photon energy scale ("γ ES"), photon energy resolution ("γ RES"), jet energy scale ("Jet ES"), jet energy resolution ("Jet RES"), signal leakage fractions ("Leak."), photon identification ("γ ID"), lower limit in $E_{\text{T}}^{\text{iso}}$ in regions B and D ("$E_{\text{T}}^{\text{iso}}$ gap"), variation of the inverted photon identification variables ("γ invert. var."), removal of upper limit in $E_{\text{T}}^{\text{iso}}$ in regions B and D ("$E_{\text{T}}^{\text{iso}}$ upp. lim."), modelling of $E_{\text{T}}^{\text{iso}}$ in MC simulation ("$E_{\text{T}}^{\text{iso}}$ MC"), correlation between γ ID and isolation in background ("R^{bg}"), pile-up ("Pile-up"), unfolding ("Unf."), statistical uncertainty in MC samples ("MC stat."), trigger ("Trigger") and luminosity ("Lumi.").

$m^{\gamma-\text{jet}}$ [GeV]	$\text{d}\sigma/\text{d}m^{\gamma-\text{jet}}$ [pb/GeV]	Stat. (%)	Total syst. (%)		γ ES (%)		γ RES (%)		Jet ES (%)		Jet RES (%)		Leak. (%)		γ ID (%)	
			Up	Down	Up	Down	Up	Down	Up	Down	Up	Down	Up	Down	Up	Down
450 - 510	0.2760	± 0.5	3.6	-3.5	1.2	-1.0	0.1	< 0.1	2.2	-2.0	0.2	-0.2	0.8	-0.3	1.2	-1.2
510 - 570	0.1682	± 0.6	3.6	-3.5	1.2	-1.0	0.1	< 0.1	2.1	-2.0	0.2	-0.2	0.7	-0.2	1.3	-1.2
570 - 650	0.09722	± 0.7	3.4	-3.4	1.2	-1.1	0.1	< 0.1	2.0	-2.0	< 0.1	< 0.1	0.5	-0.1	1.3	-1.3
650 - 750	0.05070	± 0.9	3.3	-3.4	1.2	-1.2	< 0.1	< 0.1	2.0	-2.0	0.1	-0.1	0.4	-0.1	1.3	-1.3
750 - 850	0.02667	± 1.2	3.3	-3.5	1.3	-1.2	< 0.1	< 0.1	2.1	-2.1	< 0.1	< 0.1	0.3	-0.2	1.4	-1.3
850 - 950	0.01461	± 1.6	3.4	-3.6	1.3	-1.3	< 0.1	< 0.1	2.1	-2.2	0.2	-0.2	0.2	-0.2	1.4	-1.4
950 - 1050	0.008384	± 2.2	3.6	-3.8	1.4	-1.4	< 0.1	-0.1	2.2	-2.3	0.2	-0.2	0.3	-0.3	1.5	-1.4
1050 - 1250	0.004129	± 2.2	3.8	-4.0	1.4	-1.5	< 0.1	-0.1	2.4	-2.4	0.3	-0.2	0.2	< 0.1	1.6	-1.5
1250 - 1450	0.001555	± 3.6	3.9	-4.1	1.5	-1.6	< 0.1	-0.1	2.6	-2.6	0.1	-0.1	0.2	-0.2	1.7	-1.6
1450 - 1650	0.0006754	± 5.5	4.0	-4.2	1.6	-1.7	< 0.1	-0.1	2.8	-2.9	0.1	-0.1	0.1	< 0.1	1.7	-1.7
1650 - 1850	0.0003545	± 7.4	4.3	-4.4	1.7	-1.8	< 0.1	-0.1	3.1	-3.1	0.4	-0.4	0.1	-0.1	1.8	-1.7
1850 - 2450	0.00009419	± 8.5	4.9	-5.1	1.8	-1.9	< 0.1	-0.2	3.5	-3.5	0.1	-0.1	0.1	-0.1	1.9	-1.8
2450 - 3250	0.00001096	± 30.0	5.9	-6.0	2.1	-2.2	0.1	-0.2	4.1	-4.1	0.1	-0.1	0.1	-0.1	2.0	-1.9

$m^{\gamma-\text{jet}}$ [GeV]	$E_{\text{T}}^{\text{iso}}$ gap (%)		γ invert. var. (%)		$E_{\text{T}}^{\text{iso}}$upp. lim. (%)	$E_{\text{T}}^{\text{iso}}$ MC (%)	R^{bg} (%)		Pile-up (%)		Unf. (%)	MC stat. (%)	Trigger (%)	Lumi. (%)
	Up	Down	Up	Down			Up	Down	Up	Down				
450 - 510	0.1	-0.1	0.8	-1.1	± 0.1	± 0.6	1.7	-1.7	0.1	-0.1	± 0.3	± 0.3	± 1.0	± 2.1
510 - 570	0.1	-0.1	0.7	-1.0	± 0.1	± 0.6	1.5	-1.5	0.3	-0.4	± 1.0	± 0.3	± 1.0	± 2.1
570 - 650	0.1	< 0.1	0.6	-1.0	± 0.1	± 0.7	1.3	-1.3	0.3	-0.2	± 0.8	± 0.3	± 1.0	± 2.1
650 - 750	< 0.1	< 0.1	0.6	-1.0	< 0.1	± 0.8	1.1	-1.1	0.3	-0.2	± 0.8	± 0.3	± 1.0	± 2.1
750 - 850	< 0.1	< 0.1	0.5	-0.9	± 0.1	± 0.9	0.7	-0.7	0.4	-0.4	± 1.0	± 0.3	± 1.0	± 2.1
850 - 950	< 0.1	< 0.1	0.5	-0.9	< 0.1	± 1.0	0.7	-0.7	0.1	-0.2	± 1.0	± 0.4	± 1.0	± 2.1
950 - 1050	< 0.1	< 0.1	0.5	-0.8	± 0.1	± 0.9	0.6	-0.6	< 0.1	< 0.1	± 1.5	± 0.4	± 1.0	± 2.1
1050 - 1250	< 0.1	< 0.1	0.4	-0.8	± 0.1	± 0.9	0.6	-0.6	0.2	-0.1	± 1.5	± 0.4	± 1.0	± 2.1
1250 - 1450	0.1	< 0.1	0.4	-0.8	± 0.1	± 1.0	0.9	-0.9	0.5	-0.2	± 0.9	± 0.4	± 1.0	± 2.1
1450 - 1650	< 0.1	< 0.1	0.3	-0.7	± 0.1	± 0.9	0.8	-0.8	< 0.1	-0.1	± 0.5	± 0.6	± 1.0	± 2.1
1650 - 1850	< 0.1	< 0.1	0.3	-0.7	± 0.1	± 0.7	0.3	-0.3	< 0.1	< 0.1	± 0.8	± 0.8	± 1.0	± 2.1
1850 - 2450	< 0.1	< 0.1	0.3	-0.6	< 0.1	± 1.1	0.5	-0.5	0.2	-0.2	± 1.8	± 0.6	± 1.0	± 2.1
2450 - 3250	< 0.1	< 0.1	0.2	-0.6	< 0.1	± 0.7	0.5	-0.5	0.2	-0.5	± 2.6	± 1.1	± 1.0	± 2.1

Table F.9: The measured cross section for isolated-photon plus one-jet production as a function of $|\cos\theta^{\star}|$ (in pb) together with the statistical uncertainty in the data (in %), the total systematic uncertainty excluding that in the luminosity (in %) and the contributions from the different sources of systematic uncertainty (in %): photon energy scale ("γ ES"), photon energy resolution ("γ RES"), jet energy scale ("Jet ES"), jet energy resolution ("Jet RES"), signal leakage fractions ("Leak."), photon identification ("γ ID"), lower limit in $E_{\mathrm{T}}^{\mathrm{iso}}$ in regions B and D ("$E_{\mathrm{T}}^{\mathrm{iso}}$ gap"), variation of the inverted photon identification variables ("γ invert. var."), removal of upper limit in $E_{\mathrm{T}}^{\mathrm{iso}}$ in regions B and D ("$E_{\mathrm{T}}^{\mathrm{iso}}$ upp. lim."), modelling of $E_{\mathrm{T}}^{\mathrm{iso}}$ in MC simulation ("$E_{\mathrm{T}}^{\mathrm{iso}}$ MC"), correlation between γ ID and isolation in background ("R^{bg}"), pile-up ("Pile-up"), unfolding ("Unf."), statistical uncertainty in MC samples ("MC stat."), trigger ("Trigger") and luminosity ("Lumi.").

$\lvert\cos\theta^{\star}\rvert$	$\mathrm{d}\sigma/\mathrm{d}\lvert\cos\theta^{\star}\rvert$ [pb]	Stat. (%)	Total syst. (%)		γ ES (%)		γ RES (%)		Jet ES (%)		Jet RES (%)		Leak. (%)		γ ID (%)	
			Up	Down	Up	Down	Up	Down	Up	Down	Up	Down	Up	Down	Up	Down
0.0 - 0.10	30.56	± 1.1	2.9	-2.9	1.0	-1.0	< 0.1	< 0.1	2.0	-2.0	0.2	-0.2	0.4	-0.4	1.1	-1.1
0.10 - 0.20	31.61	± 1.1	3.3	-3.2	1.1	-0.9	< 0.1	< 0.1	2.0	-1.9	< 0.1	< 0.1	0.3	-0.3	1.1	-1.1
0.20 - 0.30	32.57	± 1.1	3.0	-2.9	1.1	-1.0	< 0.1	< 0.1	2.1	-1.9	0.1	-0.1	0.6	-0.6	1.1	-1.1
0.30 - 0.40	33.79	± 1.1	3.1	-2.9	1.2	-1.0	0.1	< 0.1	2.1	-2.0	0.1	-0.1	0.6	-0.6	1.1	-1.1
0.40 - 0.50	40.79	± 1.0	3.3	-3.3	1.2	-1.1	0.1	< 0.1	2.2	-2.0	0.1	-0.1	0.7	-0.7	1.2	-1.1
0.50 - 0.60	50.47	± 0.9	3.5	-3.3	1.3	-1.2	0.1	< 0.1	2.2	-2.1	0.1	-0.1	0.7	-0.7	1.2	-1.2
0.60 - 0.70	72.22	± 0.8	3.7	-3.9	1.3	-1.2	0.1	< 0.1	2.2	-2.1	0.2	-0.2	1.2	-1.2	1.3	-1.3
0.70 - 0.83	131.2	± 0.5	4.1	-4.1	1.3	-1.2	0.1	-0.1	2.2	-2.1	0.2	-0.2	1.5	-1.5	1.4	-1.4

$\lvert\cos\theta^{\star}\rvert$	$E_{\mathrm{T}}^{\mathrm{iso}}$ gap (%)		γ invert. var. (%)		$E_{\mathrm{T}}^{\mathrm{iso}}$ upp. lim. (%)	$E_{\mathrm{T}}^{\mathrm{iso}}$ MC (%)	R^{bg} (%)		Pile-up (%)		Unf. (%)	MC stat. (%)	Trigger (%)	Lumi. (%)
	Up	Down	Up	Down			Up	Down	Up	Down				
0.0 - 0.10	< 0.1	< 0.1	0.7	< 0.1	± 0.2	± 0.6	0.4	-0.4	0.1	-0.1	± 0.4	± 0.2	± 1.0	± 2.1
0.10 - 0.20	< 0.1	< 0.1	0.5	< 0.1	± 0.3	± 0.7	0.5	-0.5	0.1	-0.1	± 1.5	± 0.3	± 1.0	± 2.1
0.20 - 0.30	< 0.1	< 0.1	0.3	-0.7	± 0.2	± 0.7	0.5	-0.5	0.4	-0.2	< 0.1	± 0.3	± 1.0	± 2.1
0.30 - 0.40	< 0.1	< 0.1	0.5	-0.4	± 0.2	± 0.6	0.6	-0.6	< 0.1	-0.2	± 0.4	± 0.3	± 1.0	± 2.1
0.40 - 0.50	< 0.1	< 0.1	0.4	-0.8	± 0.3	± 0.6	0.7	-0.7	0.3	-0.3	± 1.0	± 0.3	± 1.0	± 2.1
0.50 - 0.60	< 0.1	< 0.1	0.9	-0.4	± 0.3	± 0.7	1.0	-1.0	0.2	-0.3	± 0.7	± 0.3	± 1.0	± 2.1
0.60 - 0.70	0.1	< 0.1	0.9	-1.3	± 0.4	± 0.7	1.3	-1.3	0.2	-0.2	± 0.7	± 0.3	± 1.0	± 2.1
0.70 - 0.83	0.1	-0.1	1.1	-1.1	± 0.4	± 0.7	1.9	-1.9	0.2	-0.2	± 0.5	± 0.2	± 1.0	± 2.1

F.3 Tables for the ratio of cross sections for inclusive-photon production

The results for the measured $R_{13/8}$ ($D_{13/8}^{\gamma/Z}$) as a function of E_{T}^{γ} together with the statistical uncertainty and the total systematic uncertainty for different regions in $|\eta^{\gamma}|$ are listed in Table F.10 (F.11).

Table F.10: The measured $R_{13/8}$ as a function of E_{T}^{γ} together with the statistical uncertainty and the total systematic uncertainty for different regions in $|\eta^{\gamma}|$.

E_{T}^{γ} [GeV]	$R_{13/8} \pm$ statistical uncertainty $\pm$ systematic uncertainty			
	$\lvert\eta^{\gamma}\rvert < 0.6$	$0.6 < \lvert\eta^{\gamma}\rvert < 1.37$	$1.56 < \lvert\eta^{\gamma}\rvert < 1.81$	$1.81 < \lvert\eta^{\gamma}\rvert < 2.37$
125–150	$2.08 \pm 0.01 \pm 0.09$	$2.11 \pm 0.01 \pm 0.11$	$2.16 \pm 0.01 \pm 0.12$	$2.25 \pm 0.01 \pm 0.12$
150–175	$2.12 \pm 0.01 \pm 0.08$	$2.15 \pm 0.01 \pm 0.10$	$2.22 \pm 0.02 \pm 0.12$	$2.46 \pm 0.05 \pm 0.13$
175–200	$2.23 \pm 0.02 \pm 0.09$	$2.21 \pm 0.02 \pm 0.10$	$2.35 \pm 0.03 \pm 0.12$	$2.66 \pm 0.03 \pm 0.14$
200–250	$2.28 \pm 0.02 \pm 0.09$	$2.28 \pm 0.02 \pm 0.10$	$2.63 \pm 0.03 \pm 0.14$	$3.10 \pm 0.03 \pm 0.16$
250–300	$2.42 \pm 0.03 \pm 0.09$	$2.43 \pm 0.03 \pm 0.10$	$3.06 \pm 0.06 \pm 0.16$	$3.89 \pm 0.06 \pm 0.21$
300–350	$2.53 \pm 0.04 \pm 0.10$	$2.72 \pm 0.04 \pm 0.12$	$3.67 \pm 0.12 \pm 0.22$	$5.2 \pm 0.1 \pm 0.3$
350–400	$2.64 \pm 0.07 \pm 0.11$	$2.78 \pm 0.07 \pm 0.13$	$3.95 \pm 0.20 \pm 0.27$	$6.7 \pm 0.3 \pm 0.4$
400–470	$2.83 \pm 0.09 \pm 0.11$	$3.11 \pm 0.09 \pm 0.15$	$5.7 \pm 0.3 \pm 0.5$	$8.4 \pm 0.6 \pm 0.6$
470–550	$3.11 \pm 0.14 \pm 0.13$	$3.46 \pm 0.15 \pm 0.18$	$8.7 \pm 0.9 \pm 0.8$	$16.1 \pm 2.0 \pm 1.2$
550–650	$3.28 \pm 0.21 \pm 0.14$	$4.35 \pm 0.27 \pm 0.24$	$12.5 \pm 2.3 \pm 1.4$	$29 \pm 8 \pm 3$
650–750	$4.0 \pm 0.4 \pm 0.2$	$5.0 \pm 0.5 \pm 0.3$		
750–900	$5.2 \pm 0.8 \pm 0.3$	$8.4 \pm 1.3 \pm 0.5$		
900–1100	$9.9 \pm 2.3 \pm 0.5$	$7.9 \pm 2.4 \pm 0.5$		
1100–1500	$13.9 \pm 9.8 \pm 0.8$			

Table F.11: The measured $D_{13/8}^{\gamma/Z}$ as a function of E_{T}^{γ} together with the statistical uncertainty and the total systematic uncertainty for different regions in $|\eta^{\gamma}|$.

E_{T}^{γ} [GeV]	$D_{13/8}^{\gamma/Z} \pm$ statistical uncertainty $\pm$ systematic uncertainty			
	$\lvert\eta^{\gamma}\rvert < 0.6$	$0.6 < \lvert\eta^{\gamma}\rvert < 1.37$	$1.56 < \lvert\eta^{\gamma}\rvert < 1.81$	$1.81 < \lvert\eta^{\gamma}\rvert < 2.37$
125–150	$1.35 \pm 0.01 \pm 0.04$	$1.37 \pm 0.00 \pm 0.06$	$1.40 \pm 0.01 \pm 0.07$	$1.46 \pm 0.01 \pm 0.07$
150–175	$1.38 \pm 0.01 \pm 0.04$	$1.40 \pm 0.01 \pm 0.05$	$1.44 \pm 0.01 \pm 0.06$	$1.60 \pm 0.03 \pm 0.07$
175–200	$1.45 \pm 0.01 \pm 0.04$	$1.44 \pm 0.01 \pm 0.05$	$1.53 \pm 0.02 \pm 0.07$	$1.73 \pm 0.02 \pm 0.08$
200–250	$1.49 \pm 0.01 \pm 0.04$	$1.49 \pm 0.01 \pm 0.05$	$1.71 \pm 0.02 \pm 0.08$	$2.02 \pm 0.02 \pm 0.09$
250–300	$1.57 \pm 0.02 \pm 0.04$	$1.58 \pm 0.02 \pm 0.05$	$1.99 \pm 0.04 \pm 0.09$	$2.53 \pm 0.04 \pm 0.12$
300–350	$1.65 \pm 0.03 \pm 0.05$	$1.77 \pm 0.03 \pm 0.06$	$2.39 \pm 0.08 \pm 0.13$	$3.37 \pm 0.10 \pm 0.17$
350–400	$1.72 \pm 0.04 \pm 0.05$	$1.81 \pm 0.04 \pm 0.07$	$2.57 \pm 0.13 \pm 0.16$	$4.3 \pm 0.2 \pm 0.3$
400–470	$1.84 \pm 0.06 \pm 0.05$	$2.02 \pm 0.06 \pm 0.08$	$3.7 \pm 0.2 \pm 0.3$	$5.5 \pm 0.4 \pm 0.3$
470–550	$2.02 \pm 0.09 \pm 0.06$	$2.25 \pm 0.10 \pm 0.10$	$5.6 \pm 0.6 \pm 0.5$	$10.5 \pm 1.3 \pm 0.7$
550–650	$2.13 \pm 0.14 \pm 0.07$	$2.83 \pm 0.18 \pm 0.14$	$8.2 \pm 1.5 \pm 0.9$	$19 \pm 5 \pm 2$
650–750	$2.6 \pm 0.3 \pm 0.1$	$3.3 \pm 0.3 \pm 0.2$		
750–900	$3.4 \pm 0.5 \pm 0.1$	$5.5 \pm 0.9 \pm 0.3$		
900–1100	$6.4 \pm 1.5 \pm 0.3$	$5.1 \pm 1.6 \pm 0.3$		
1100–1500	$9.1 \pm 6.4 \pm 0.5$			

G

NLO calculations for $pp \to \gamma + \text{jet} + \text{jet} + \text{X}$

The cross-section measurements were compared to the predictions of Sherpa NLO matched to a parton shower as detailed in Section 3.5.7 in the same fiducial phase-space volume as the measurements (see Section 9.4.1).

The predictions of Sherpa NLO are shown in Figures G.1 to G.3. The NNPDF3.0-NNLO PDFs used for the nominal results are compared to the calculations based on MMHT2014 and CT14 PDFs. The differences between the predictions based on different proton PDFs are typically smaller than 3%.

The theoretical uncertainties were estimated as described in Section 8.6.3. An overview of the relative theoretical uncertainties in the kinematic region of the measurements is shown in Figures G.4 to G.12. The dominant sources of theoretical uncertainty were found to be the ones related to the renormalisation scale variations.

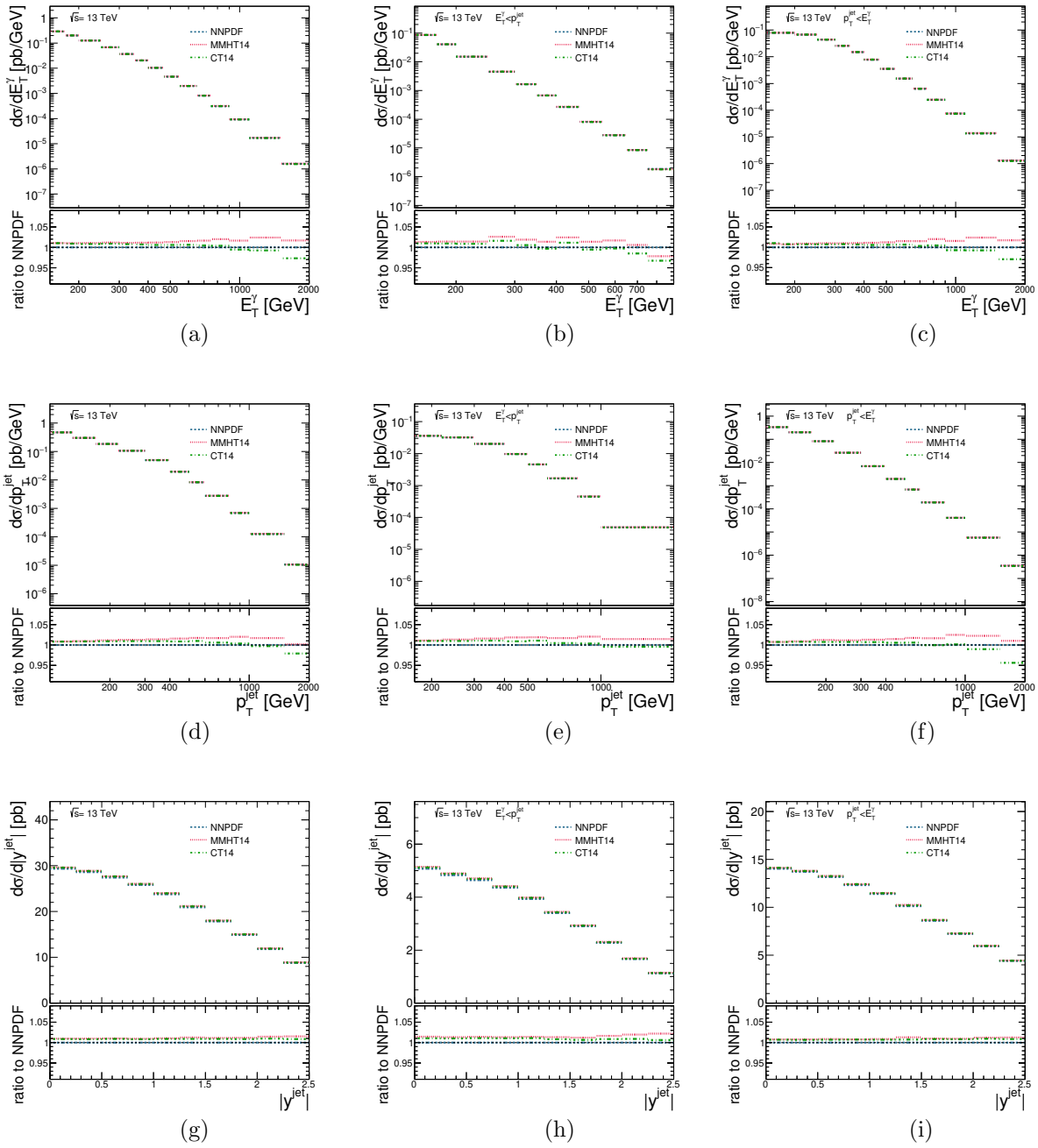


Figure G.1: Predictions of SHERPA NLO based on the NNPDF3.0NNLO (dashed lines), MMHT2014 (dotted lines) and CT14 (dot-dashed lines) proton PDFs for the cross sections for isolated-photon plus two-jet production as functions of E_{T}^{γ} (a,b,c), $p_{\mathrm{T}}^{\mathrm{jet}}$ (d,e,f) and $|y^{\mathrm{jet}}|$ (g,h,i) for the total (first column), fragmentation-enriched (second column) and direct-enriched (third column) samples. The lower part of each figure shows the ratio of the predictions to that based on the NNPDF3.0NNLO PDFs.

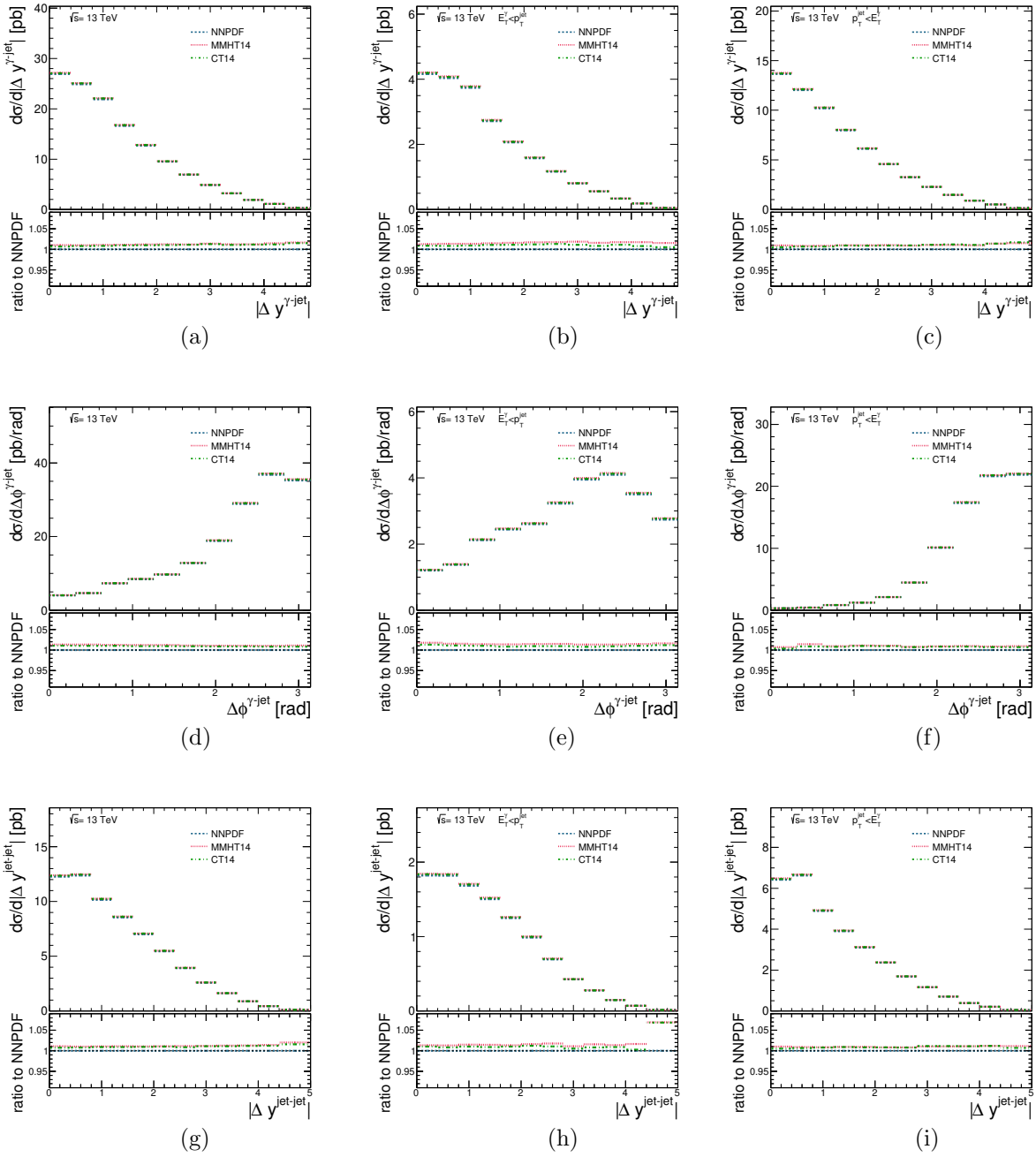


Figure G.2: Predictions of Sherpa NLO based on the NNPDF3.0NNLO (dashed lines), MMHT2014 (dotted lines) and CT14 (dot-dashed lines) proton PDFs for the cross sections for isolated-photon plus two-jet production as functions of $|\Delta y^{\gamma-\mathrm{jet}}|$ (a,b,c), $\Delta\phi^{\gamma-\mathrm{jet}}$ (d,e,f) and $|\Delta y^{\mathrm{jet}-\mathrm{jet}}|$ (g,h,i) for the total (first column), fragmentation-enriched (second column) and direct-enriched (third column) samples. The lower part of each figure shows the ratio of the predictions to that based on the NNPDF3.0NNLO PDFs.

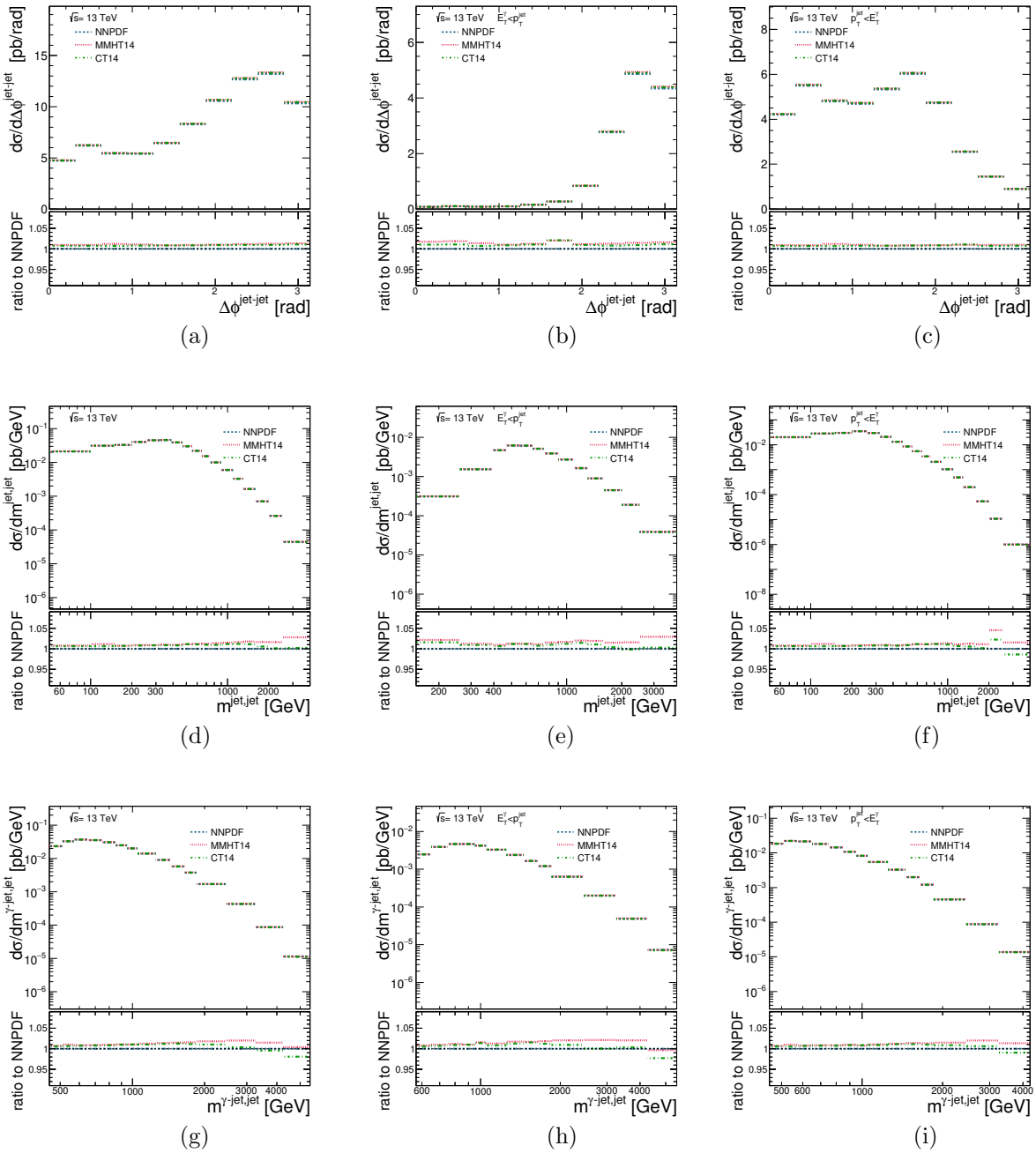


Figure G.3: Predictions of SHERPA NLO based on the NNPDF3.0NNLO (dashed lines), MMHT2014 (dotted lines) and CT14 (dot-dashed lines) proton PDFs for the cross sections for isolated-photon plus two-jet production as functions of $\Delta\phi^{\text{jet}-\text{jet}}$ (a,b,c), $m^{\text{jet}-\text{jet}}$ (d,e,f) and $m^{\gamma-\text{jet}-\text{jet}}$ (g,h,i) for the total (first column), fragmentation-enriched (second column) and direct-enriched (third column) samples. The lower part of each figure shows the ratio of the predictions to that based on the NNPDF3.0NNLO PDFs.

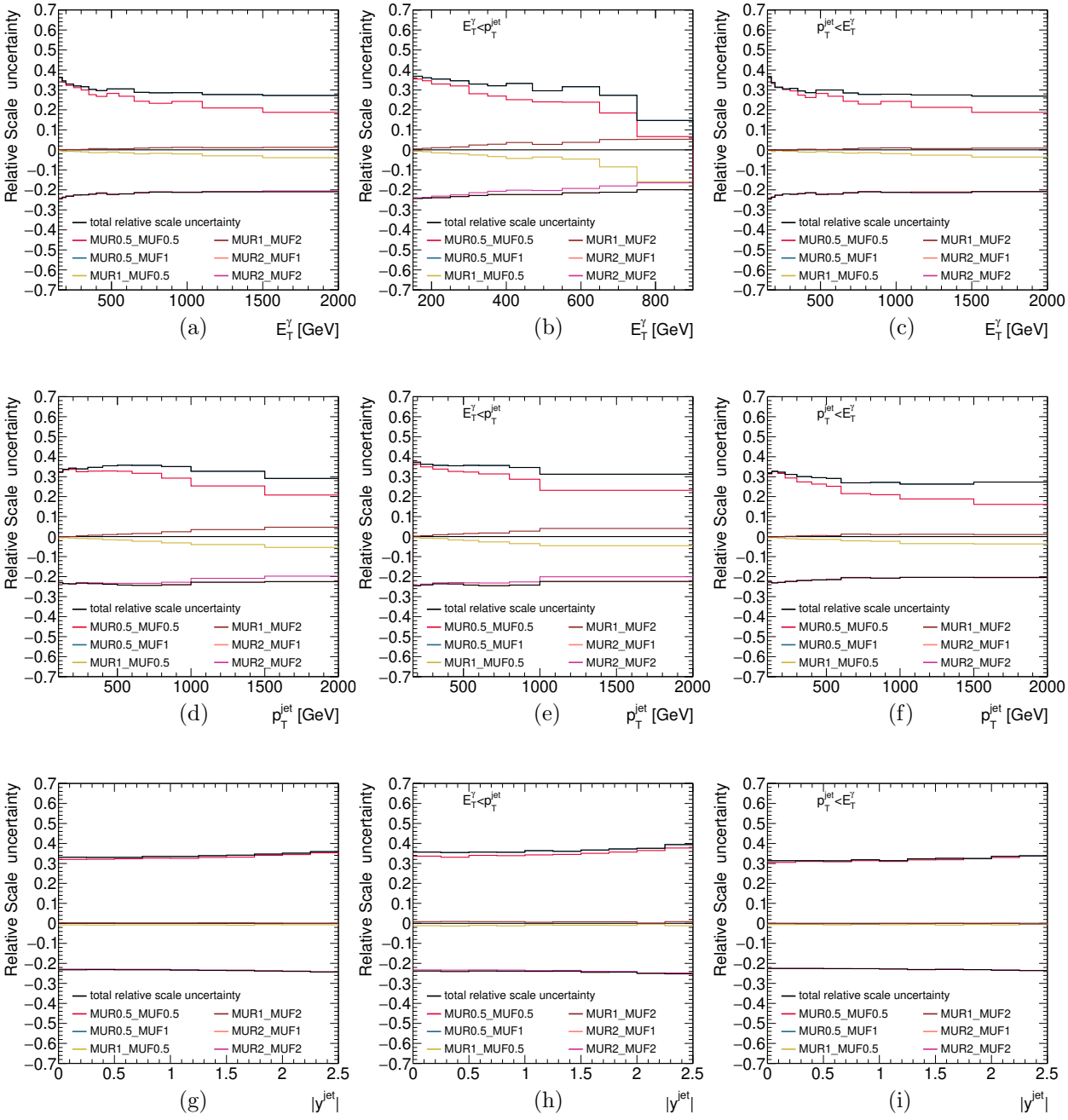


Figure G.4: Relative scale uncertainty as a function of E_{T}^{γ} (a,b,c), $p_{\mathrm{T}}^{\mathrm{jet}}$ (d,e,f) and $|y^{\mathrm{jet}}|$ (g,h,i) for the total (first column), fragmentation-enriched (second column) and direct-enriched (third column) samples. Uncertainties arising from the variations of the μ_R and μ_F scales: $\mu_{\mathrm{R}} = \mu_{\mathrm{F}} = 0.5 \cdot E_{\mathrm{T}}^{\gamma}$ (red histograms); $\mu_{\mathrm{R}} = 0.5 \cdot E_{\mathrm{T}}^{\gamma}$ and $\mu_{\mathrm{F}} = E_{\mathrm{T}}^{\gamma}$ (blue histograms); $\mu_{\mathrm{R}} = E_{\mathrm{T}}^{\gamma}$ and $\mu_{\mathrm{F}} = 0.5 \cdot E_{\mathrm{T}}^{\gamma}$ (yellow histograms); $\mu_{\mathrm{R}} = E_{\mathrm{T}}^{\gamma}$ and $\mu_{\mathrm{F}} = 2 \cdot E_{\mathrm{T}}^{\gamma}$ (brown histograms); $\mu_{\mathrm{R}} = 2 \cdot E_{\mathrm{T}}^{\gamma}$ and $\mu_{\mathrm{F}} = E_{\mathrm{T}}^{\gamma}$ (orange histograms); $\mu_{\mathrm{R}} = \mu_{\mathrm{F}} = 2 \cdot E_{\mathrm{T}}^{\gamma}$ (magenta histograms). The envelope of the six variations is represented by the black histograms.

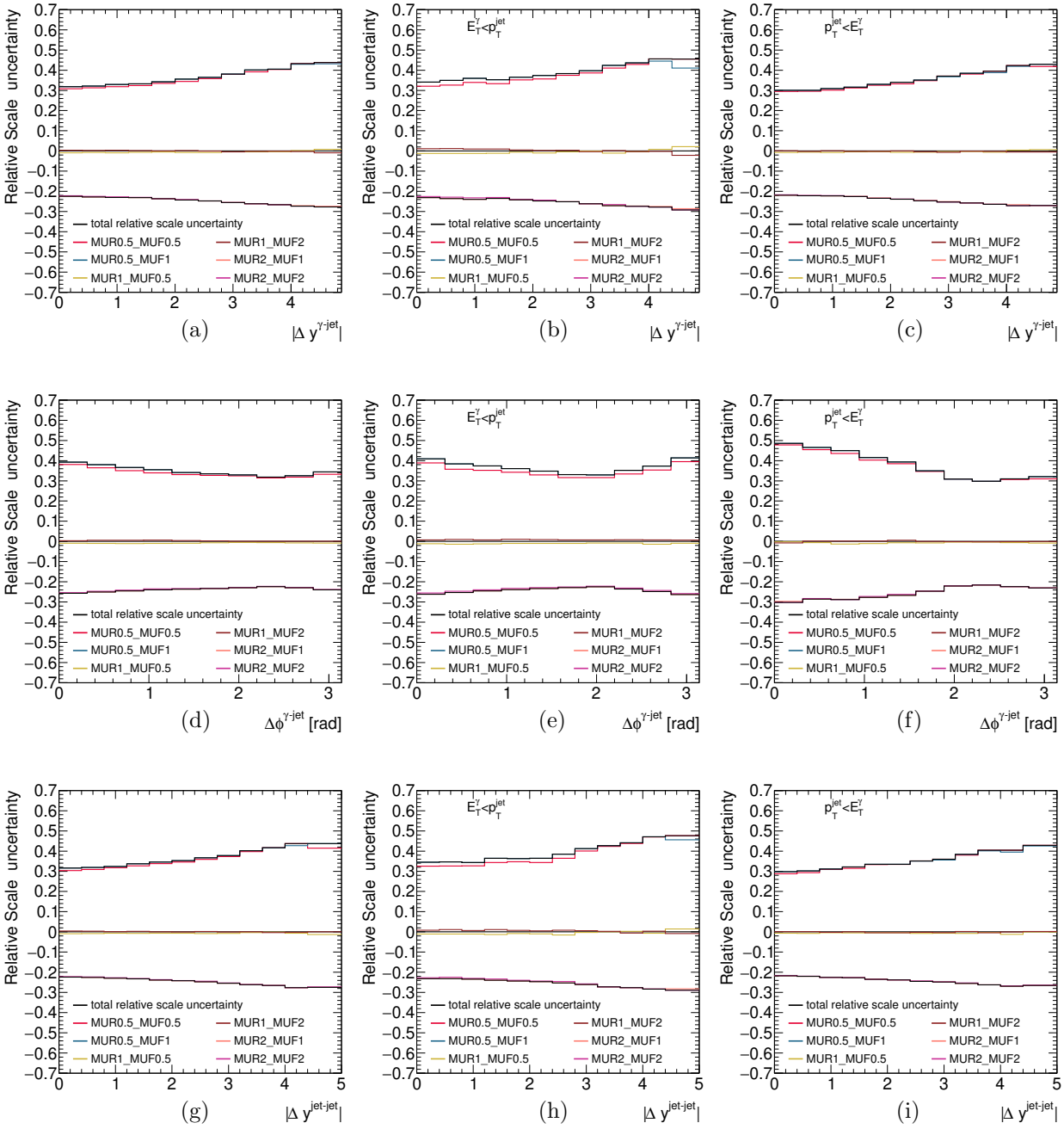


Figure G.5: Relative scale uncertainty as a function of $|\Delta y^{\gamma-\text{jet}}|$ (a,b,c), $\Delta\phi^{\gamma-\text{jet}}$ (d,e,f) and $|\Delta y^{\text{jet}-\text{jet}}|$ (g,h,i) for the total (first column), fragmentation-enriched (second column) and direct-enriched (third column) samples. Uncertainties arising from the variations of the μ_R and μ_F scales: $\mu_\text{R} = \mu_\text{F} = 0.5 \cdot E_\text{T}^\gamma$ (red histograms); $\mu_\text{R} = 0.5 \cdot E_\text{T}^\gamma$ and $\mu_\text{F} = E_\text{T}^\gamma$ (blue histograms); $\mu_\text{R} = E_\text{T}^\gamma$ and $\mu_\text{F} = 0.5 \cdot E_\text{T}^\gamma$ (yellow histograms); $\mu_\text{R} = E_\text{T}^\gamma$ and $\mu_\text{F} = 2 \cdot E_\text{T}^\gamma$ (brown histograms); $\mu_\text{R} = 2 \cdot E_\text{T}^\gamma$ and $\mu_\text{F} = E_\text{T}^\gamma$ (orange histograms); $\mu_\text{R} = \mu_\text{F} = 2 \cdot E_\text{T}^\gamma$ (magenta histograms). The envelope of the six variations is represented by the black histograms.

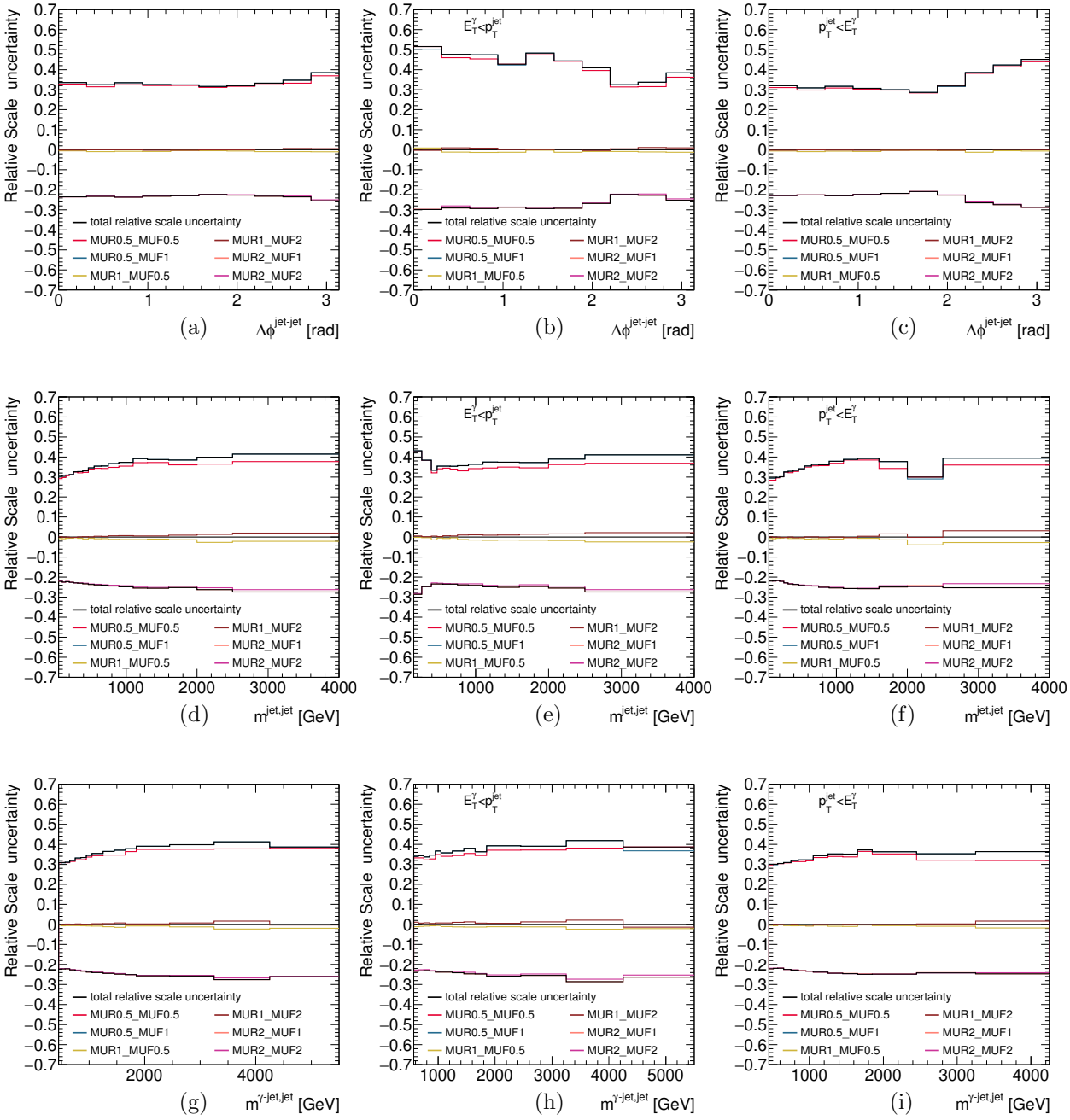


Figure G.6: Relative scale uncertainty as a function of $\Delta\phi^{\text{jet}-\text{jet}}$ (a,b,c), $m^{\text{jet}-\text{jet}}$ (d,e,f) and $m^{\gamma-\text{jet}-\text{jet}}$ (g,h,i) for the total (first column), fragmentation-enriched (second column) and direct-enriched (third column) samples. Uncertainties arising from the variations of the μ_R and μ_F scales: $\mu_\text{R} = \mu_\text{F} = 0.5 \cdot E_\text{T}^\gamma$ (red histograms); $\mu_\text{R} = 0.5 \cdot E_\text{T}^\gamma$ and $\mu_\text{F} = E_\text{T}^\gamma$ (blue histograms); $\mu_\text{R} = E_\text{T}^\gamma$ and $\mu_\text{F} = 0.5 \cdot E_\text{T}^\gamma$ (yellow histograms); $\mu_\text{R} = E_\text{T}^\gamma$ and $\mu_\text{F} = 2 \cdot E_\text{T}^\gamma$ (brown histograms); $\mu_\text{R} = 2 \cdot E_\text{T}^\gamma$ and $\mu_\text{F} = E_\text{T}^\gamma$ (orange histograms); $\mu_\text{R} = \mu_\text{F} = 2 \cdot E_\text{T}^\gamma$ (magenta histograms). The envelope of the six variations is represented by the black histograms.

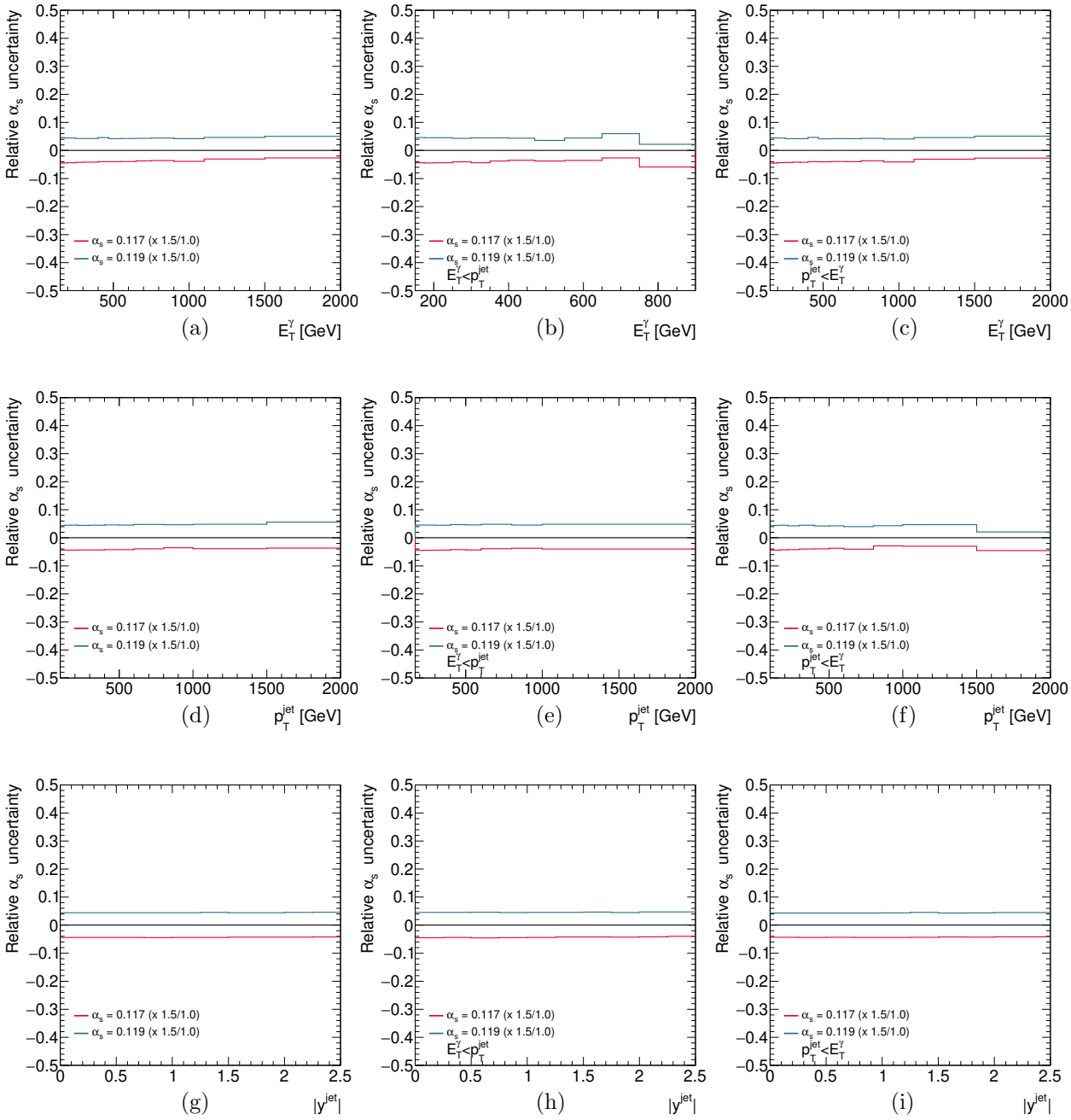


Figure G.7: Relative $\alpha_s(m_Z)$-induced uncertainty as a function of E_{T}^{γ} (a,b,c), $p_{\mathrm{T}}^{\mathrm{jet}}$ (d,e,f) and $|y^{\mathrm{jet}}|$ (g,h,i) for the total (first column), fragmentation-enriched (second column) and direct-enriched (third column) samples.

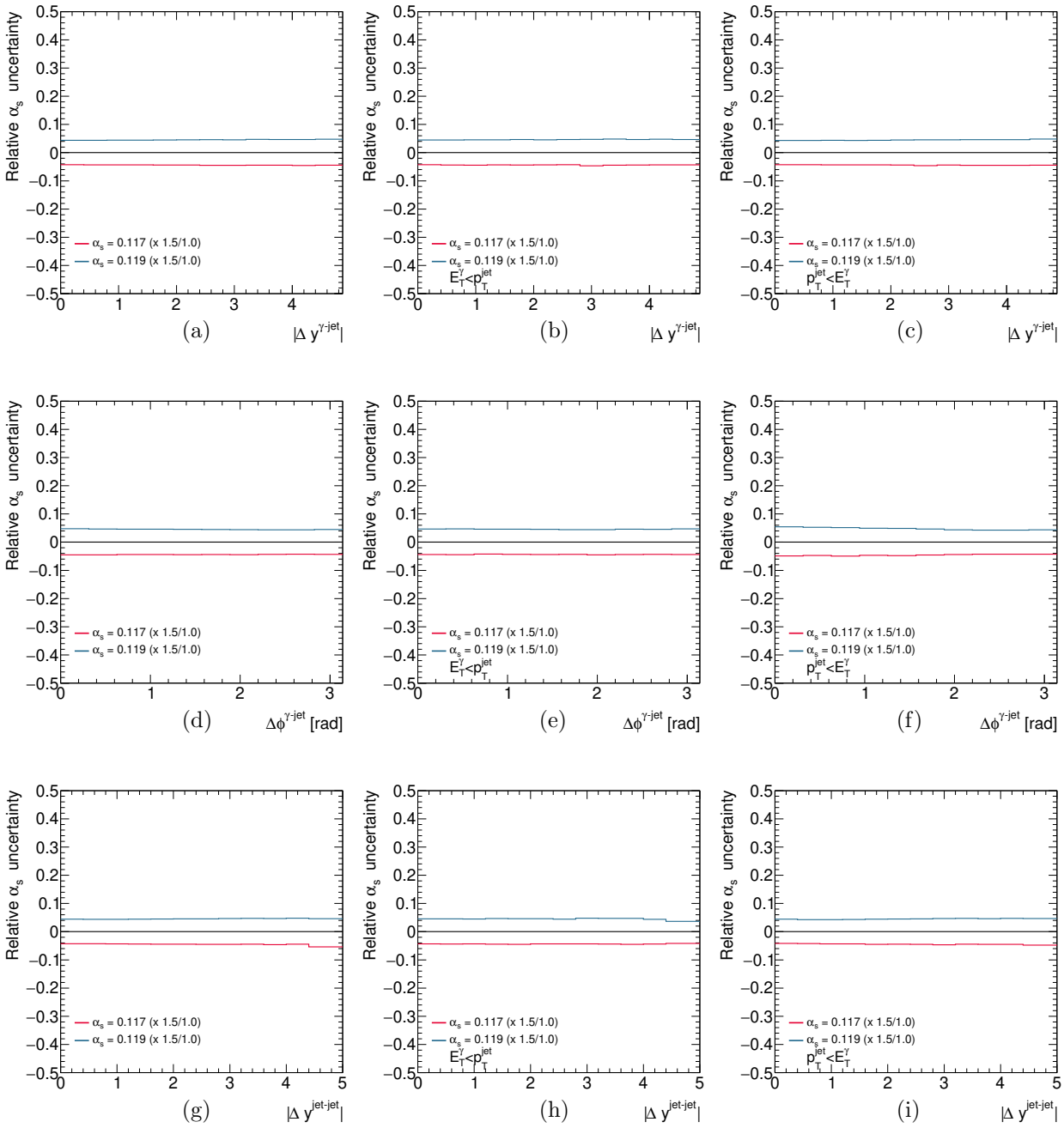


Figure G.8: Relative $\alpha_s(m_Z)$-induced uncertainty as a function of $|\Delta y^{\gamma-\text{jet}}|$ (a,b,c), $\Delta\phi^{\gamma-\text{jet}}$ (d,e,f) and $|\Delta y^{\text{jet}-\text{jet}}|$ (g,h,i) for the total (first column), fragmentation-enriched (second column) and direct-enriched (third column) samples.

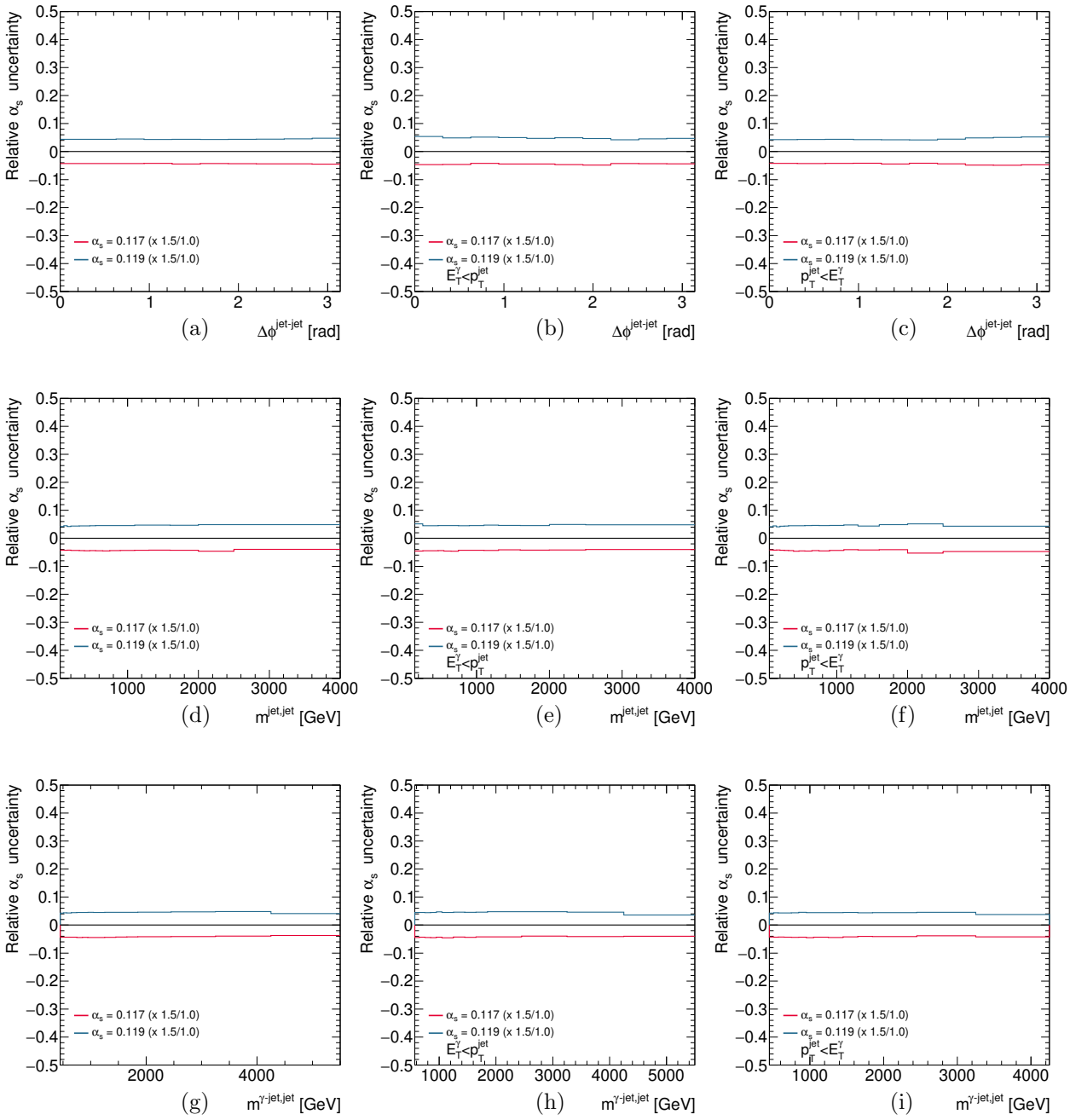


Figure G.9: Relative $\alpha_s(m_Z)$-induced uncertainty as a function of $\Delta\phi^{\text{jet}-\text{jet}}$ (a,b,c), $m^{\text{jet}-\text{jet}}$ (d,e,f) and $m^{\gamma-\text{jet}-\text{jet}}$ (g,h,i) for the total (first column), fragmentation-enriched (second column) and direct-enriched (third column) samples.

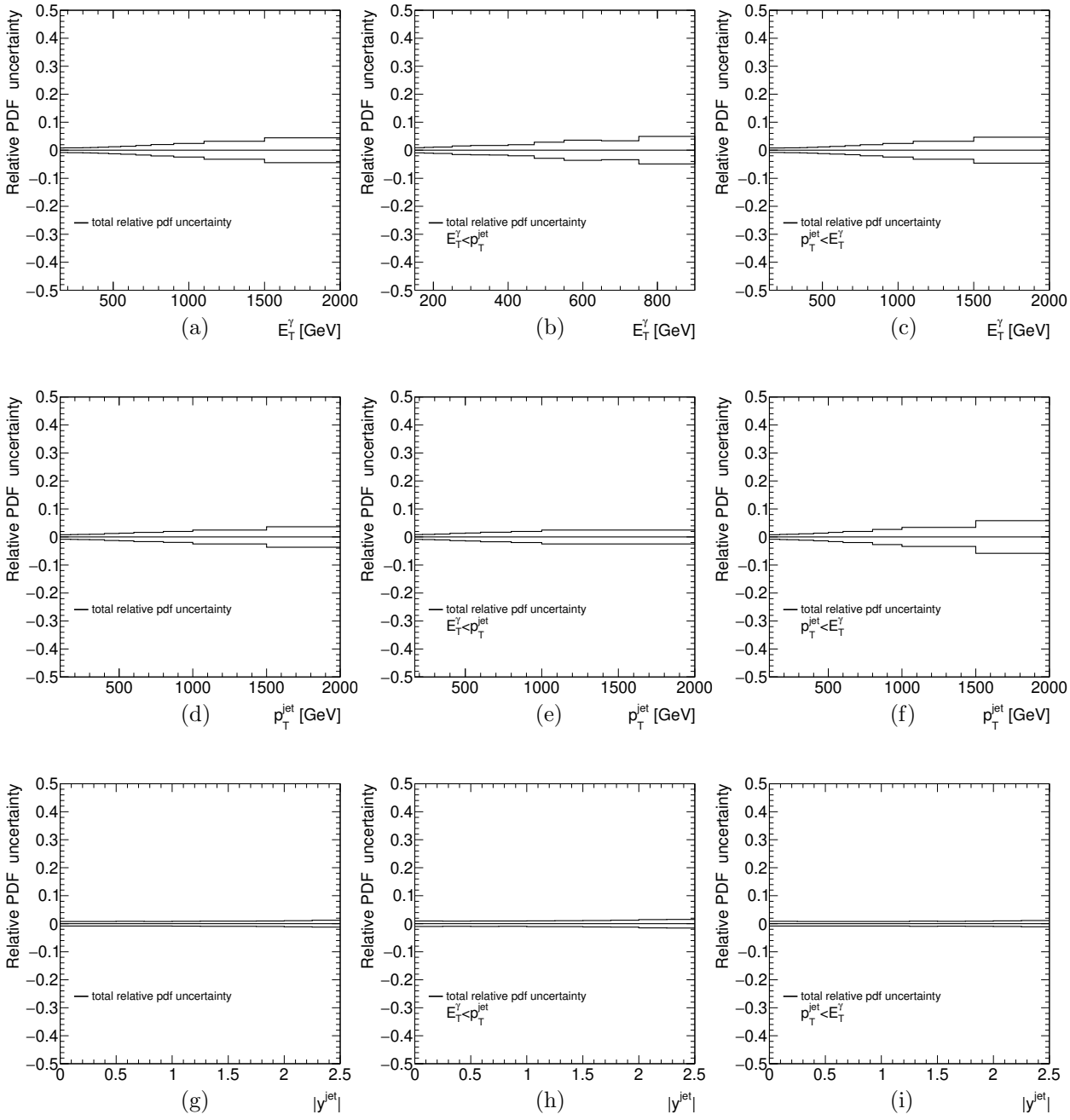


Figure G.10: Relative PDF-induced uncertainty as a function of E_{T}^{γ} (a,b,c), $p_{\mathrm{T}}^{\mathrm{jet}}$ (d,e,f) and $|y^{\mathrm{jet}}|$ (g,h,i) for the total (first column), fragmentation-enriched (second column) and direct-enriched (third column) samples.

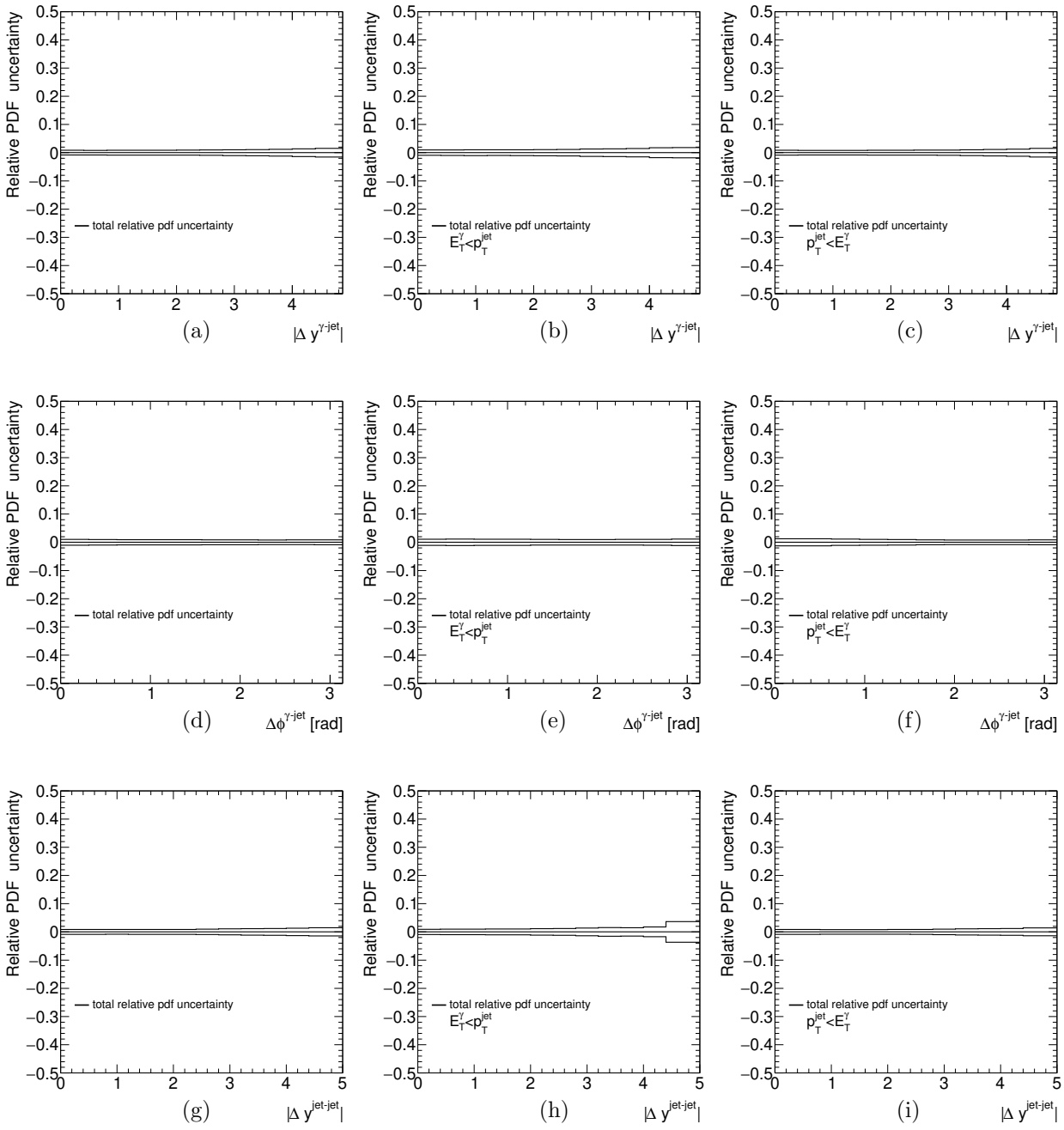


Figure G.11: Relative PDF-induced uncertainty as a function of $|\Delta y^{\gamma-\text{jet}}|$ (a,b,c), $\Delta\phi^{\gamma-\text{jet}}$ (d,e,f) and $|\Delta y^{\text{jet}-\text{jet}}|$ (g,h,i) for the total (first column), fragmentation-enriched (second column) and direct-enriched (third column) samples.

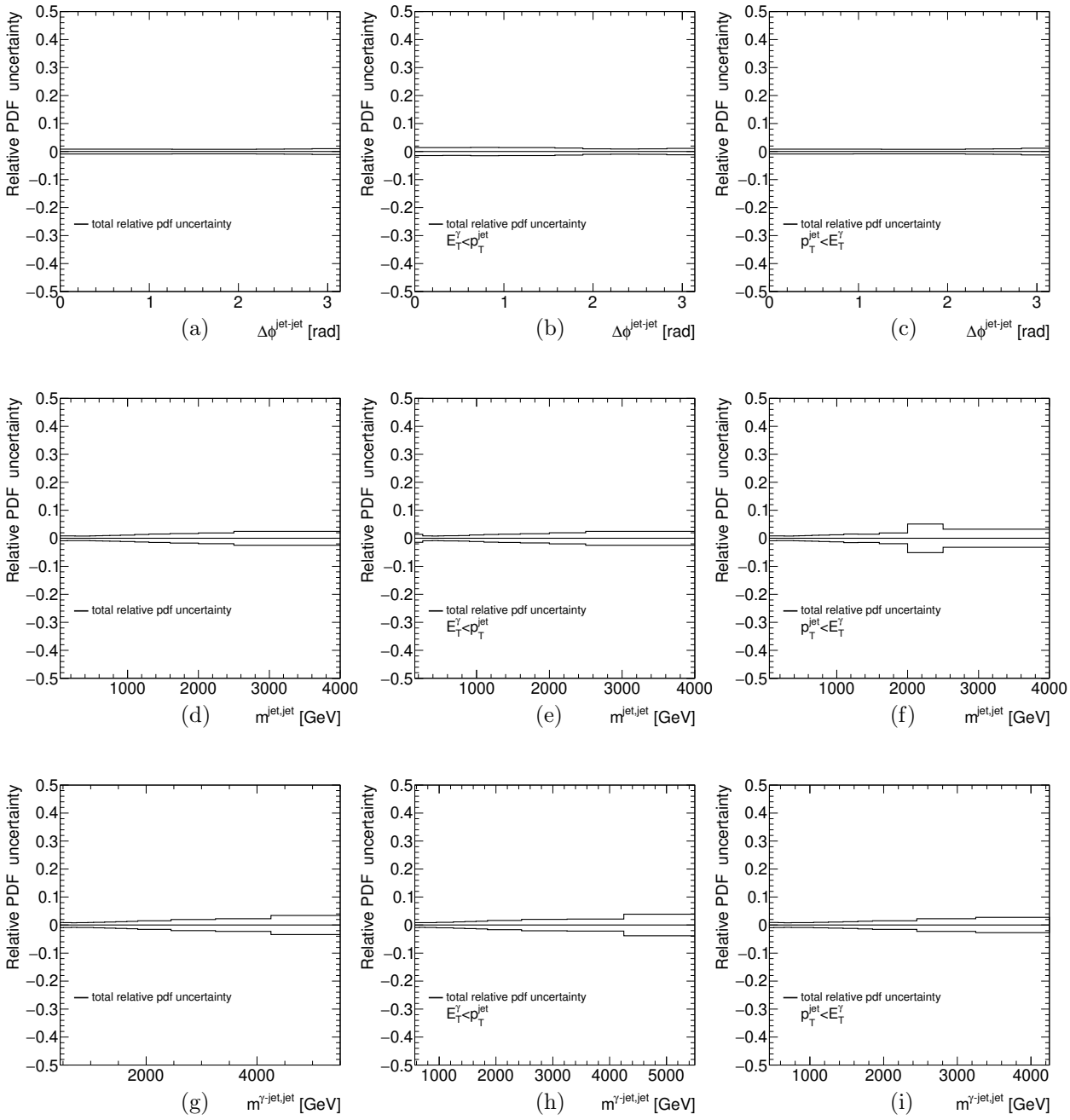


Figure G.12: Relative PDF-induced uncertainty as a function of $\Delta\phi^{\mathrm{jet-jet}}$ (a,b,c), $m^{\mathrm{jet-jet}}$ (d,e,f) and $m^{\gamma-\mathrm{jet-jet}}$ (g,h,i) for the total (first column), fragmentation-enriched (second column) and direct-enriched (third column) samples.

Agradecimientos

Comenzar un doctorado quizá fuese la opción más cómoda para mi hace cuatro años. Me permitía seguir en el mundo académico que bien conocía y que me apasionaba sin tener que enfrentarme a explorar el competitivo mundo laboral. A pesar de los altibajos típicos de estos años, me puedo sentir afortunada de que el camino desde el principio hasta el final del doctorado haya sido agradable, de que me ha dado más momentos de satisfacción que de frustración y de que me ha ayudado a evolucionar como científica y persona. Sin duda, esta etapa habría sido mucho más complicada sin las personas que de una forma u otra han estado conmigo.

El mérito de esta tesis lo comparto con mis supervisores, Claudia y Juan. Tenerlos como referencia me ha servido para aprender de muchos de mis errores, tener un pensamiento más crítico, diferenciar los aspectos realmente importantes a los que dedicar mi tiempo y valorar el trabajo bien hecho. Gracias por vuestras continuas enseñanzas, por darme voz en las decisiones del grupo y por vuestra disposición a ayudarme con cualquier tipo de problema que haya surgido durante estos años.

Durante el primer año de doctorado en Madrid pude compartir quejas, entusiasmo y preocupaciones con aquellos que también empezaban este camino como Isabel, Ana Isabel o Sergio. Recuerdo con especial cariño las cenas, conversaciones y paseos con Pedro y Nieves. En las reuniones con Marina, Blanca, Gloria, Maribel, Nuria o Mónica podía disfrutar hablando de todo como si el tiempo no hubiese pasado desde que nos conocimos en Heidelberg, aunque han sido menos frecuentes de lo que me hubiese gustado. Las visitas a Fuengirola no hubiesen sido tan entretenidas sin los reencuentros con Sarah, Marina, Elena y Claudia.

En los últimos años en el CERN, han sido muchas las personas que he tenido la oportunidad de conocer y con las que he podido compartir experiencias. A los que formaron parte de la UAM: Josu, Javier y Héctor, me gustaría agradecerles su disponibilidad cuando he necesitado que me resolvieran alguna duda o perdirles algún favor. Gracias a Pili, Carlos, Mercedes, Emma, María, Daniel, Manuel, Andrea R., Andrea S., Roger, todos los Javis, Jose, Nacho y Cecilia por amenizar muchas de las comidas, tardes de viernes en el R1 y fines de semana en Ginebra o en el emocionante Saint Genis.

Mi familia ha sido un pilar esencial en esta y todas las etapas de mi vida. A mis padres les tengo que agradecer su incondicional apoyo. Gracias por darme la libertad y responsabilidad de tomar mis propias decisiones sin oponeros, por escuchar mis logros y momentos de desesperación aunque os costara entenderme, por tratar de darme los mejores consejos y por inculcarme los valores que me han hecho ser quien soy. A mi imparable abuela por todo su cariño. A mi hermano Fran y a Sara por preocuparse por mi y acogerme cada vez que lo he necesitado. A mis sobrinos, María y Fran, porque sin saberlo son una fuente inigualable de felicidad. A mis tíos y primos que siempre han estado dispuestos a ofrecerme su ayuda.

El último párrafo se lo dedico a Pablo. Gracias por ser mi confidente y soporte fundamental, por traerme la paz y la alegría cada vez que nos encontramos y por tu amor. Yo también espero que nuestra vida juntos sea larga, buena y feliz.

Madrid, Junio de 2018

Bibliography

[1] ATLAS Collaboration, "Observation of a new particle in the search for the Standard Model Higgs boson with the ATLAS detector at the LHC", Phys. Lett. B **716**, 1 (2012), doi:10.1016/j.physletb.2012.08.020, arXiv:1207.7214 [hep-ph].

[2] CMS Collaboration, "Observation of a new boson at a mass of 125 GeV with the CMS experiment at the LHC", Phys. Lett. B **716**, 30 (2012), doi:10.1016/j.physletb.2012.08.021, arXiv:1207.7235 [hep-ex].

[3] S. Catani, M. Fontannaz and E. Pilon, "Factorization and soft gluon divergences in isolated photon cross-sections", Phys. Rev. D **58** (1998) 094025, doi:10.1103/PhysRevD.58.094025, arXiv:hep-ph/9803475.

[4] L. Bourhis, M. Fontannaz and J. P. Guillet, "Quarks and gluon fragmentation functions into photons", Eur. Phys. J. C **2**, 529 (1998), doi:10.1007/s100520050158, arXiv:hep-ph/9704447.

[5] T. Pietrycki and A. Szczurek, "Photon-jet correlations in pp and p anti-p collisions", Phys. Rev. D **76**, 034003 (2007), doi:10.1103/PhysRevD.76.034003, arXiv:0704.2158 [hep-ph].

[6] Z. Belghobsi, M. Fontannaz, J.-P. Guillet, G. Heinrich, E. Pilon and M. Werlen, "Photon - Jet Correlations and Constraints on Fragmentation Functions", Phys. Rev. D **79**, 114024 (2009), doi:10.1103/PhysRevD.79.114024, arXiv:0903.4834 [hep-ph].

[7] L. Carminati, G. Costa, D. D'Enterria, I. Koletsou, G. Marchiori, J. Rojo, M. Stockton and F. Tartarelli, "Sensitivity of the LHC isolated-gamma+jet data to the parton distribution functions of the proton", EPL **101**, no. 6, 61002 (2013), doi:10.1209/0295-5075/101/61002, arXiv:1212.5511 [hep-ph].

[8] D. d'Enterria and J. Rojo, "Quantitative constraints on the gluon distribution function in the proton from collider isolated-photon data", Nucl. Phys. B **860**, 311 (2012), doi:10.1016/j.nuclphysb.2012.03.003, arXiv:1202.1762 [hep-ph].

[9] P. Aurenche, M. Fontannaz, J. P. Guillet, E. Pilon and M. Werlen, "A New critical study of photon production in hadronic collisions", Phys. Rev. D **73** (2006) 094007, doi:10.1103/PhysRevD.73.094007, arXiv:hep-ph/0602133.

[10] R. Ichou and D. d'Enterria, "Sensitivity of isolated photon production at TeV hadron colliders to the gluon distribution in the proton", Phys. Rev. D **82**, 014015 (2010), doi:10.1103/PhysRevD.82.014015, arXiv:1005.4529 [hep-ph].

[11] J. M. Campbell, J. Rojo, E. Slade and C. Williams, "Direct photon production and PDF fits reloaded", arXiv:1802.03021 [hep-ph].

[12] A. V. Lipatov and M. A. Malyshev, "Reconsideration of the inclusive prompt photon production at the LHC with k_T-factorization", Phys. Rev. D **94**, no. 3, 034020 (2016), doi:10.1103/PhysRevD.94.034020, arXiv:1606.02696 [hep-ph].

[13] M. D. Schwartz, "Precision direct photon spectra at high energy and comparison to the 8 TeV ATLAS data", JHEP **1609**, 005 (2016), doi:10.1007/JHEP09(2016)005, arXiv:1606.02313 [hep-ph].

[14] J. M. Campbell, R. K. Ellis and C. Williams, "Direct Photon Production at Next-to–Next-to-Leading Order", Phys. Rev. Lett. **118** (2017) no.22, 222001, doi:10.1103/PhysRevLett.118.222001 arXiv:1612.04333 [hep-ph].

[15] ATLAS Collaboration, "Measurement of the inclusive isolated prompt photon cross section in pp collisions at $\sqrt{s}$ = 8 TeV with the ATLAS detector", JHEP **1608** (2016) 005, doi:10.1007/JHEP08(2016)005, arXiv:1605.03495 [hep-ex].

[16] M. L. Mangano and J. Rojo, "Cross Section Ratios between different CM energies at the LHC: opportunities for precision measurements and BSM sensitivity", JHEP **1208**, 010 (2012), doi:10.1007/JHEP08(2012)010, arXiv:1206.3557 [hep-ph].

[17] ATLAS Collaboration, "Measurement of the production cross section of an isolated photon associated with jets in proton-proton collisions at $\sqrt{s}$ = 7 TeV with the ATLAS detector", Phys. Rev. D **85**, 092014 (2012), doi:10.1103/PhysRevD.85.092014, arXiv:1203.3161 [hep-ex].

[18] ATLAS Collaboration, "Dynamics of isolated-photon plus jet production in pp collisions at $\sqrt{(s)}$ = 7 TeV with the ATLAS detector", Nucl. Phys. B **875**, 483 (2013), doi:10.1016/j.nuclphysb.2013.07.025 arXiv:1307.6795 [hep-ex].

[19] ATLAS Collaboration, "High-E_{T} isolated-photon plus jets production in pp collisions at $\sqrt{s}$ = 8 TeV with the ATLAS detector", Nucl. Phys. B **918**, 257 (2017), doi:10.1016/j.nuclphysb.2017.03.006, arXiv:1611.06586 [hep-ex].

[20] CMS Collaboration, "Rapidity distributions in exclusive Z + jet and γ + jet events in pp collisions at $\sqrt{s}$ = 7 TeV", Phys. Rev. D **88**, no. 11, 112009 (2013), doi:10.1103/PhysRevD.88.112009, arXiv:1310.3082 [hep-ex].

[21] CMS Collaboration, "Measurement of the triple-differential cross section for photon+jets production in proton-proton collisions at $\sqrt{s}$=7 TeV", JHEP **1406**, 009 (2014), doi:10.1007/JHEP06(2014)009, arXiv:1311.6141 [hep-ex].

[22] CMS Collaboration, "Comparison of the Z/γ^* + jets to γ + jets cross sections in pp collisions at $\sqrt{s}$ = 8 TeV", JHEP **1510** (2015) 128, Erratum: [JHEP **1604** (2016) 010], doi:10.1007/JHEP04(2016)010, doi:10.1007/JHEP10(2015)128, arXiv:1505.06520 [hep-ex].

[23] ATLAS Collaboration, "Search for new phenomena with photon+jet events in proton-proton collisions at $\sqrt{s}$ = 13 TeV with the ATLAS detector", JHEP **1603**, 041 (2016), doi:10.1007/JHEP03(2016)041, arXiv:1512.05910 [hep-ex].

[24] ATLAS Collaboration, "Search for new phenomena in high-mass final states with a photon and a jet from pp collisions at $\sqrt{s}$ = 13 TeV with the ATLAS detector", Eur. Phys. J. C **78**, no. 2, 102 (2018), doi:10.1140/epjc/s10052-018-5553-2, arXiv:1709.10440 [hep-ex].

[25] S. Keller and J.F. Owens, "Event structure in photon plus two-jet final states", Phys. Lett. B **269**, (1991) 445, doi:10.1016/0370-2693(91)90198-Y.

[26] M. Aleksa *et al.*, "ATLAS Liquid Argon Calorimeter Phase-I Upgrade Technical Design Report", CERN-LHCC-2013-017, ATLAS-TDR-022, cds.cern.ch/record/1602230.

[27] ATLAS Collaboration, "Measurement of the cross section for inclusive isolated-photon production in pp collisions at $\sqrt{s} = 13$ TeV using the ATLAS detector", Phys. Lett. B **770**, 473 (2017), doi:10.1016/j.physletb.2017.04.072, arXiv:1701.06882 [hep-ex].

[28] A. Cueto (ATLAS Collaboration), "Inclusive isolated-photon production in pp collisions at $\sqrt{s} = 13$ TeV", Nuovo Cim. C **40**, no. 5, 185 (2018), doi:10.1393/ncc/i2017-17185-3.

[29] A. Cueto, C. Glasman, J. Terrón, "Measurement of the ratio of cross sections for inclusive isolated-photon production in pp collisions at $\sqrt{s} = 13$ and 8 TeV with the ATLAS detector", cds.cern.ch/record/2274526.

[30] ATLAS Collaboration, "Measurement of the cross section for isolated-photon plus jet production in pp collisions at $\sqrt{s} = 13$ TeV using the ATLAS detector", Phys. Lett. B **780**, 578 (2018), doi:10.1016/j.physletb.2018.03.035, arXiv:1801.00112 [hep-ex].

[31] A. Cueto, C. Glasman, J. Terrón, "Measurement of isolated-photon plus two-jet production in pp collisons at $\sqrt{s} = 13$ TeV with the ATLAS detector", cds.cern.ch/record/2308741.

[32] O. S. Bruning, P. Collier, P. Lebrun, S. Myers, R. Ostojic, J. Poole and P. Proudlock, "LHC Design Report Vol.1: The LHC Main Ring", CERN-2004-003-V1, CERN-2004-003, CERN-2004-003-V-1.

[33] ATLAS Collaboration, "The ATLAS Experiment at the CERN Large Hadron Collider", JINST **3**, S08003 (2008), doi:10.1088/1748-0221/3/08/S08003.

[34] "LEP Design Report: Vol.2. The LEP Main Ring", CERN-LEP-84-01.

[35] ALICE Collaboration, "The ALICE experiment at the CERN LHC", JINST **3**, S08002 (2008), doi:10.1088/1748-0221/3/08/S08002.

[36] CMS Collaboration, "The CMS Experiment at the CERN LHC", JINST **3**, S08004 (2008), doi:10.1088/1748-0221/3/08/S08004.

[37] LHCb Collaboration, "The LHCb Detector at the LHC", JINST **3**, S08005 (2008), doi:10.1088/1748-0221/3/08/S08005.

[38] TOTEM Collaboration, "The TOTEM Experiment at the LHC", arXiv:0905.2936 [hep-ex].

[39] LHCf Collaboration, "The LHCf detector at the CERN Large Hadron Collider", JINST **3**, S08006 (2008), doi:10.1088/1748-0221/3/08/S08006.

[40] MoEDAL Collaboration, "Technical Design Report of the MoEDAL Experiment", CERN-LHCC-2009-006, MoEDAL-TDR-001, cds.cern.ch/record/1181486.

[41] C. de Melis, "The CERN accelerator complex", OPEN-PHO-ACCEL-2016-001, cds.cern.ch/record/2119882.

[42] ATLAS Collaboration, "Measurement of the Inelastic Proton-Proton Cross Section at $\sqrt{s} = 13$ TeV with the ATLAS Detector at the LHC", Phys. Rev. Lett. **117**, no. 18, 182002 (2016), doi:10.1103/PhysRevLett.117.182002, arXiv:1606.02625 [hep-ex].

[43] ATLAS Collaboration, "ATLAS Insertable B-Layer Technical Design Report", CERN-LHCC-2010-013, ATLAS-TDR-19, cds.cern.ch/record/1291633.

[44] L. Adamczyk *et al.*, "Technical Design Report for the ATLAS Forward Proton Detector", CERN-LHCC-2015-009, ATLAS-TDR-024, cds.cern.ch/record/2017378.

[45] ATLAS/LUCID Collaboration, "The new ATLAS/LUCID detector", doi:10.1109/ANIMMA.2015.7465502.

[46] ATLAS Collaboration, "Zero degree calorimeters for ATLAS", CERN-LHCC-2007-01, cds.cern.ch/record/1009649.

[47] S. Abdel Khalek *et al.*, "The ALFA Roman Pot Detectors of ATLAS", JINST **11**, no. 11, P11013 (2016), doi:10.1088/1748-0221/11/11/P11013, arXiv:1609.00249.

[48] ATLAS Collaboration, "Technical Design Report for the Phase-I Upgrade of the ATLAS TDAQ System", CERN-LHCC-2013-018, ATLAS-TDR-023, cds.cern.ch/record/1602235.

[49] ATLAS Collaboration, "Monitoring and data quality assessment of the ATLAS liquid argon calorimeter", JINST **9**, P07024 (2014), doi:10.1088/1748-0221/9/07/P07024, arXiv:1405.3768 [hep-ex].

[50] T. Golling, H. S. Hayward, P. U. E. Onyisi, H. J. Stelzer and P. Waller, "The ATLAS Data Quality Defect Database System", Eur. Phys. J. C **72**, 1960 (2012), doi:10.1140/epjc/s10052-012-1960-y, arXiv:1110.6119.

[51] H. Abreu *et al.*, "Performance of the electronic readout of the ATLAS liquid argon calorimeters", JINST **5**, P09003 (2010), doi:10.1088/1748-0221/5/09/P09003.

[52] S. L. Glashow, "Partial Symmetries of Weak Interactions", Nucl. Phys. **22**, 579 (1961), doi:10.1016/0029-5582(61)90469-2.

[53] S. Weinberg, "A Model of Leptons", Phys. Rev. Lett. **19**, 1264 (1967), doi:10.1103/PhysRevLett.19.1264.

[54] A. Salam, "Gauge Unification of Fundamental Forces", Rev. Mod. Phys. **52**, 525 (1980), [Science **210**, 723 (1980)], doi:10.1103/RevModPhys.52.525.

[55] A. Pich, "Quantum chromodynamics", In *Sorrento 1994, High energy physics* 157-207, arXiv:hep-ph/9505231.

[56] R. K. Ellis, W. J. Stirling and B. R. Webber, "QCD and collider physics", Camb. Monogr. Part. Phys. Nucl. Phys. Cosmol. **8**, 1 (1996).

[57] E. C. G. Stueckelberg and A. Petermann, "The normalPization group in quantum theory", Helv. Phys. Acta **24**, 317 (1951).

[58] R. P. Feynman, "Photon-hadron interactions," Reading 1972, 282p.

[59] R. D. Ball *et al.* [NNPDF Collaboration], "Parton distributions for the LHC Run II", JHEP **1504**, 040 (2015), doi:10.1007/JHEP04(2015)040, arXiv:1410.8849 [hep-ph].

[60] C. Patrignani *et al.* [Particle Data Group], "Review of Particle Physics", Chin. Phys. C **40**, no. 10, 100001 (2016), doi:10.1088/1674-1137/40/10/100001.

[61] H1 and ZEUS Collaborations, "Combination of measurements of inclusive deep inelastic $e^{\pm}p$ scattering cross sections and QCD analysis of HERA data", Eur. Phys. J. C **75**, no. 12, 580 (2015), doi:10.1140/epjc/s10052-015-3710-4, arXiv:1506.06042 [hep-ex].

[62] ATLAS Collaboration, atlas.web.cern.ch/Atlas/GROUPS/PHYSICS/CombinedSummaryPlots/SM.

[63] CMS Collaboration, twiki.cern.ch/twiki/bin/view/CMSPublic/PhysicsResultsCombined.

[64] S. Catani, M. Fontannaz, J. P. Guillet and E. Pilon, "Cross-section of isolated prompt photons in hadron hadron collisions", JHEP **0205**, 028 (2002), doi:10.1088/1126-6708/2002/05/028, arXiv:hep-ph/0204023.

[65] E. W. N. Glover and A. G. Morgan, "Measuring the photon fragmentation function at LEP", Z. Phys. C **62**, 311 (1994), doi:10.1007/BF01560245.

[66] S. Frixione, "Isolated photons in perturbative QCD", Phys. Lett. B **429**, 369 (1998), doi:10.1016/S0370-2693(98)00454-7, arXiv:hep-ph/9801442.

[67] J. M. Campbell and R. K. Ellis, "An Update on vector boson pair production at hadron colliders", Phys. Rev. D **60**, 113006 (1999), doi:10.1103/PhysRevD.60.113006, arXiv:hep-ph/9905386.

[68] L. Cieri, "Diphoton isolation studies", Nucl. Part. Phys. Proc. **273-275**, 2033 (2016); doi:10.1016/j.nuclphysbps.2015.09.329; arXiv:1510.06873 [hep-ph].

[69] T. Gehrmann, N. Greiner and G. Heinrich, "Photon isolation effects at NLO in $\gamma\gamma$ + jet final states in hadronic collisions", JHEP **1306**, 058 (2013), Erratum: [JHEP **1406**, 076 (2014)], doi:10.1007/JHEP06(2014)076,doi:10.1007/JHEP06(2013)058, arXiv:1303.0824 [hep-ph].

[70] S. Catani, L. Cieri, D. de Florian, G. Ferrera and M. Grazzini, "Diphoton production at the LHC: a QCD study up to NNLO", arXiv:1802.02095 [hep-ph].

[71] J. M. Lindert *et al.*, "Precise predictions for $V+$ jets dark matter backgrounds", Eur. Phys. J. C **77**, no. 12, 829 (2017), doi:10.1140/epjc/s10052-017-5389-1, arXiv:1705.04664 [hep-ph].

[72] J. M. Campbell, R. K. Ellis and C. Williams, "Driving missing data at the LHC: NNLO predictions for the ratio of $\gamma + j$ and $Z + j$", Phys. Rev. D **96**, no. 1, 014037 (2017), doi:10.1103/PhysRevD.96.014037, arXiv:1703.10109 [hep-ph].

[73] M. Diemoz, F. Ferroni, E. Longo and G. Martinelli, "Parton Densities from Deep Inelastic Scattering to Hadronic Processes at Super Collider Energies", Z. Phys. C **39** (1988) 21, doi:10.1007/BF01560387.

[74] P. N. Harriman, A. D. Martin, W. J. Stirling and R. G. Roberts, "Parton Distributions Extracted From Data on Deep Inelastic Lepton Scattering, Prompt Photon Production and the Drell-Yan Process", Phys. Rev. D **42** (1990) 798, doi:10.1103/PhysRevD.42.798.

[75] J. G. Morfin, W. K. Tung, "Parton distributions from a global QCD analysis of deep inelastic scattering and lepton pair production", Z. Phys. **C52** (1991) 13-30, doi:10.1007/BF01412323.

[76] T. Sjostrand, S. Mrenna and P. Z. Skands, "A Brief Introduction to PYTHIA 8.1", Comput. Phys. Commun. **178** (2008) 852, doi:10.1016/j.cpc.2008.01.036, arXiv:0710.3820 [hep-ph].

[77] T. Gleisberg, S. Hoeche, F. Krauss, M. Schonherr, S. Schumann, F. Siegert and J. Winter, "Event generation with SHERPA 1.1", JHEP **0902** (2009) 007, doi:10.1088/1126-6708/2009/02/007, arXiv:0811.4622 [hep-ph].

[78] S. Agostinelli *et al.* [GEANT4 Collaboration], "GEANT4: A Simulation toolkit", Nucl. Instrum. Meth. A **506**, 250 (2003), doi:10.1016/S0168-9002(03)01368-8.

[79] D. J. Lange, "The EvtGen particle decay simulation package", Nucl. Instrum. Meth. A **462**, 152 (2001), doi:10.1016/S0168-9002(01)00089-4.

[80] R. D. Ball *et al.*, "Parton distributions with LHC data", Nucl. Phys. B **867**, 244 (2013), doi:10.1016/j.nuclphysb.2012.10.003, arXiv:1207.1303 [hep-ph].

[81] H. L. Lai, M. Guzzi, J. Huston, Z. Li, P. M. Nadolsky, J. Pumplin and C.-P. Yuan, "New parton distributions for collider physics", Phys. Rev. D **82**, 074024 (2010), doi:10.1103/PhysRevD.82.074024, arXiv:1007.2241 [hep-ph].

[82] ATLAS Collaboration, "ATLAS Run 1 Pythia8 tunes", ATL-PHYS-PUB-2014-021, cds.cern.ch/record/1966419.

[83] F. Krauss, R. Kuhn and G. Soff, "AMEGIC++ 1.0: A Matrix element generator in C++", JHEP **0202**, 044 (2002), doi:10.1088/1126-6708/2002/02/044, arXiv:hep-ph/0109036.

[84] S. Schumann and F. Krauss, "A Parton shower algorithm based on Catani-Seymour dipole factorisation", JHEP **0803**, 038 (2008), doi:10.1088/1126-6708/2008/03/038, arXiv:0709.1027 [hep-ph].

[85] S. Hoeche, F. Krauss, M. Schonherr and F. Siegert, "QCD matrix elements + parton showers: The NLO case", JHEP **1304**, 027 (2013), doi:10.1007/JHEP04(2013)027, arXiv:1207.5030 [hep-ph].

[86] F. Siegert, "A practical guide to event generation for prompt photon production with Sherpa", J. Phys. G **44**, no. 4, 044007 (2017), doi:10.1088/1361-6471/aa5f29, arXiv:1611.07226 [hep-ph].

[87] L. A. Harland-Lang, A. D. Martin, P. Motylinski and R. S. Thorne, "Parton distributions in the LHC era: MMHT 2014 PDFs", Eur. Phys. J. C **75**, no. 5, 204 (2015), doi:10.1140/epjc/s10052-015-3397-6, arXiv:1412.3989 [hep-ph].

[88] M. Cacciari and G. P. Salam, "Pileup subtraction using jet areas", Phys. Lett. B **659**, 119 (2008), doi:10.1016/j.physletb.2007.09.077, arXiv:0707.1378 [hep-ph].

[89] W. Lample *et al.*, "Calorimeter Clustering Algorithms: Description and Performance", ATL-LARG-PUB-2008-002, cds.cern.ch/record/1099735.

[90] ATLAS Collaboration, "Measurement of the photon identification efficiencies with the ATLAS detector using LHC Run-1 data", Eur. Phys. J. C **76** (2016) no.12, 666, doi:10.1140/epjc/s10052-016-4507-9, arXiv:1606.01813 [hep-ex].

[91] ATLAS Collaboration, "Electron and photon energy calibration with the ATLAS detector using data collected in 2015 at $\sqrt{s} = 13$ TeV", ATL-PHYS-PUB-2016-015, cds.cern.ch/record/2203514.

[92] ATLAS Collaboration, "Energy calibration prerecommendation for Run 2" ATL-COM-PHYS-2015-1300, cds.cern.ch/record/2196992.

[93] ATLAS Collaboration, "Electron and photon energy calibration with the ATLAS detector using LHC Run 1 data", Eur. Phys. J. C **74**, no. 10, 3071 (2014), doi:10.1140/epjc/s10052-014-3071-4, arXiv:1407.5063 [hep-ex].

[94] ATLAS Collaboration, "Photon identification in 2015 ATLAS data", ATL-COM-PHYS-2016-855, cds.cern.ch/record/2195848.

[95] W. Lample, S. Laplace, D. Lelas, P. Loch, H. Ma, S. Menke, S. Rajagopalan, D. Snyder, G. Unal "Calorimeter Clustering Algorithms: Description and Performance", ATL-LARG-PUB-2008-002, cds.cern.ch/record/1099735.

[96] J. E. Gaiser, "Charmonium Spectroscopy From Radiative Decays of the J/ψ and ψ'", SLAC Stanford - SLAC-255 (82,REC.JUN.83) 194p.

[97] M. Cacciari, G. P. Salam and G. Soyez, "FastJet User Manual", Eur. Phys. J. C **72**, 1896 (2012), doi:10.1140/epjc/s10052-012-1896-2, arXiv:1111.6097 [hep-ph].

[98] ATLAS Collaboration, "Jet energy scale measurements and their systematic uncertainties in proton-proton collisions at $\sqrt{s} = 13$ TeV with the ATLAS detector", Phys. Rev. D **96**, no. 7, 072002 (2017), doi:10.1103/PhysRevD.96.072002, arXiv:1703.09665 [hep-ex].

[99] ATLAS collaboration, "Determination of the jet energy scale and resolution at ATLAS using Z/γ–jet events in data at $\sqrt{s} = 8$ TeV", ATLAS-CONF-2015-057.

[100] V. Lendermann, J. Haller, M. Herbst, K. Kruger, H. C. Schultz-Coulon and R. Stamen, "Combining Triggers in HEP Data Analysis", Nucl. Instrum. Meth. A **604**, 707 (2009), doi:10.1016/j.nima.2009.03.173, arXiv:0901.4118 [hep-ex].

[101] ATLAS Collaboration, "Jet energy measurement with the ATLAS detector in proton-proton collisions at $\sqrt{s} = 7$ TeV", Eur. Phys. J. C **73**, no. 3, 2304 (2013), doi:10.1140/epjc/s10052-013-2304-2, arXiv:1112.6426 [hep-ex].

[102] ATLAS Collaboration, "Measurement of the inclusive isolated prompt photon cross section in pp collisions at $\sqrt{s} = 7$ TeV with the ATLAS detector", Phys. Rev. D **83**, 052005 (2011), doi:10.1103/PhysRevD.83.052005, arXiv:1012.4389 [hep-ex].

[103] ATLAS Collaboration, "Measurement of the inclusive isolated prompt photon cross-section in pp collisions at $\sqrt{s} = 7$ TeV using 35 pb^{-1} of ATLAS data", Phys. Lett. B **706**, 150 (2011), doi:10.1016/j.physletb.2011.11.010, arXiv:1108.0253 [hep-ex].

[104] ATLAS Collaboration, "Measurement of the inclusive isolated prompt photons cross section in pp collisions at $\sqrt{s} = 7$ TeV with the ATLAS detector using 4.6 fb^{-1}",Phys. Rev. D **89** (2014) no.5, 052004, doi:10.1103/PhysRevD.89.052004, arXiv:1311.1440 [hep-ex].

[105] CMS Collaboration, "Measurement of the Isolated Prompt Photon Production Cross Section in pp Collisions at $\sqrt{s} = 7$ TeV", Phys. Rev. Lett. **106**, 082001 (2011), doi:10.1103/PhysRevLett.106.082001, arXiv:1012.0799 [hep-ex].

[106] CMS Collaboration, "Measurement of the Differential Cross Section for Isolated Prompt Photon Production in pp Collisions at 7 TeV", Phys. Rev. D **84** (2011) 052011, doi:10.1103/PhysRevD.84.052011, arXiv:1108.2044 [hep-ex].

[107] ATLAS Collaboration, "Performance of the ATLAS Trigger System in 2015", Eur. Phys. J. C **77**, no. 5, 317 (2017), doi::10.1140/epjc/s10052-017-4852-3, arXiv:1611.09661 [hep-ex].

[108] ATLAS Collaboration, "Photon trigger performance in 2015 ATLAS data", twiki.cern.ch/twiki/bin/view/AtlasPublic/EgammaTriggerPublicResults.

[109] ATLAS Collaboration, "Search for new phenomena with the ATLAS detector in monophoton events from proton-proton collisions at $\sqrt{s}$ =13 TeV", ATL-COM-PHYS-2015-291, cds.cern.ch/record/2010478.

[110] ATLAS Collaboration, "Measurement of the production cross section of a Z boson in association with jets at $\sqrt{s} = 13$ TeV with the ATLAS detector", ATL-COM-PHYS-2016-017, cds.cern.ch/record/2119923.

[111] ATLAS Collaboration, "Measurement of $W^{\pm}$ and Z-boson production cross sections in pp collisions at $\sqrt{s} = 13$ TeV with the ATLAS detector", Phys. Lett. B **759** (2016) 601, doi:10.1016/j.physletb.2016.06.023, arXiv:1603.09222 [hep-ex].

[112] D. Casadei, "Estimating the selection efficiency", JINST **7**, P08021 (2012), doi:10.1088/1748-0221/7/08/P08021, arXiv:0908.0130.

[113] G. D'Agostini, "A Multidimensional unfolding method based on Bayes' theorem", Nucl. Instrum. Meth. A **362**, 487 (1995), doi:10.1016/0168-9002(95)00274-X.

[114] T. Adye, "Unfolding algorithms and tests using RooUnfold", doi:10.5170/CERN-2011-006.313, arXiv:1105.1160.

[115] ATLAS Collaboration, "Improved luminosity determination in pp collisions at sqrt(s) = 7 TeV using the ATLAS detector at the LHC", Eur. Phys. J. C **73** (2013) no.8, 2518, doi:10.1140/epjc/s10052-013-2518-3, arXiv:1302.4393 [hep-ex].

[116] S. Dulat *et al.*, "New parton distribution functions from a global analysis of quantum chromodynamics", Phys. Rev. D **93**, no. 3, 033006 (2016), doi:10.1103/PhysRevD.93.033006 arXiv:1506.07443 [hep-ph].

[117] S. Alekhin, J. Blümlein and S. O. Moch, 'ABM11 parton distributions and benchmarks", doi:10.3204/DESY-PROC-2012-02/302 arXiv:1[hep-ph]208.1444.

[118] J. Pumplin, D. Stump, R. Brock, D. Casey, J. Huston, J. Kalk, H. L. Lai and W. K. Tung, "Uncertainties of predictions from parton distribution functions. 2. The Hessian method", Phys. Rev. D **65**, 014013 (2001), doi:10.1103/PhysRevD.65.014013, arXiv:hep-ph/0101032.

[119] D. Bourilkov, R. C. Group and M. R. Whalley, "LHAPDF: PDF use from the Tevatron to the LHC", arXiv:hep-ph/0605240.

[120] L. A. Harland-Lang, A. D. Martin, P. Motylinski and R. S. Thorne, "Uncertainties on α_S in the MMHT2014 global PDF analysis and implications for SM predictions", Eur. Phys. J. C **75**, no. 9, 435 (2015), doi:10.1140/epjc/s10052-015-3630-3, arXiv:1506.05682 [hep-ph].

[121] M. Klasen, C. Klein-Bösing and H. Poppenborg, "Prompt photon production and photon-jet correlations at the LHC", arXiv:1709.04154 [hep-ph].

[122] ATLAS Collaboration, "Measurements of top-quark pair to Z-boson cross-section ratios at $\sqrt{s} = 13, 8, 7$ TeV with the ATLAS detector", JHEP **1702**, 117 (2017), doi:10.1007/JHEP02(2017)117, arXiv:1612.03636 [hep-ex].

[123] ATLAS Collaboration, "Measurement of $t\bar{t}$ to Z boson production cross-section ratio and double ratio using pp collisions at $\sqrt{s}$ = 7,8, and 13 TeV", ATL-COM-PHYS-2015-1573, cds.cern.ch/record/2117165.

[124] S. Alekhin, J. Blümlein, S. Moch and R. Placakyte, "Parton distribution functions, α_s, and heavy-quark masses for LHC Run II", Phys. Rev. D **96**, no. 1, 014011 (2017), doi:10.1103/PhysRevD.96.014011, arXiv:1701.05838 [hep-ph].

[125] S. Catani and M. Grazzini, "An NNLO subtraction formalism in hadron collisions and its application to Higgs boson production at the LHC", Phys. Rev. Lett. **98**, 222002 (2007), doi:10.1103/PhysRevLett.98.222002, arXiv:hep-ph/0703012.

[126] S. Catani, L. Cieri, G. Ferrera, D. de Florian and M. Grazzini, "Vector boson production at hadron colliders: a fully exclusive QCD calculation at NNLO", Phys. Rev. Lett. **103** (2009) 082001, doi:10.1103/PhysRevLett.103.082001, arXiv:0903.2120 [hep-ph].

[127] A. Gehrmann-De Ridder, G. Kramer and H. Spiesberger, "Photon plus jet production in large Q**2 e p collisions at next-to-leading order QCD", Phys. Lett. B **459**, 271 (1999), doi:10.1016/S0370-2693(99)00646-2, arXiv:hep-ph/9903377.

[128] M. Cacciari, G. P. Salam and G. Soyez, "The Anti-k(t) jet clustering algorithm", JHEP **0804**, 063 (2008), doi:10.1088/1126-6708/2008/04/063, arXiv:0802.1189 [hep-ph].

[129] ATLAS Collaboration, "Measurement of inclusive jet and dijet cross-sections in proton-proton collisions at $\sqrt{s} = 13$ TeV with the ATLAS detector", ATLAS-CONF-2017-048, cdsweb.cern.ch/record/2273864.

[130] ATLAS Collaboration, "Electron/photon trigger efficiency plots for ICHEP2016", ATL-COM-DAQ-2016-086, cds.cern.ch/record/2200359.

[131] ATLAS Collaboration, "Measurements of the production cross section of a Z boson in association with jets in pp collisions at $\sqrt{s} = 13$ TeV with the ATLAS detector", Eur. Phys. J. C **77** (2017) no.6, 361, doi:10.1140/epjc/s10052-017-4900-z, arXiv:1702.05725 [hep-ex].

[132] ATLAS Collaboration, "Measurements of electroweak Wjj production and constraints on anomalous gauge couplings with the ATLAS detector", Eur. Phys. J. C **77** (2017) no.7, 474, doi:10.1140/epjc/s10052-017-5007-2, arXiv:1703.04362 [hep-ex].

[133] S. Frixione, "Colourful FKS subtraction", JHEP **1109** (2011) 091, doi:10.1007/JHEP09(2011)091, arXiv:1106.0155 [hep-ph].